

RAPID SOLIDIFICATION PROCESSING PRINCIPLES AND TECHNOLOGIES, III



*Third Conference on
**Rapid Solidification
Processing***

held at the

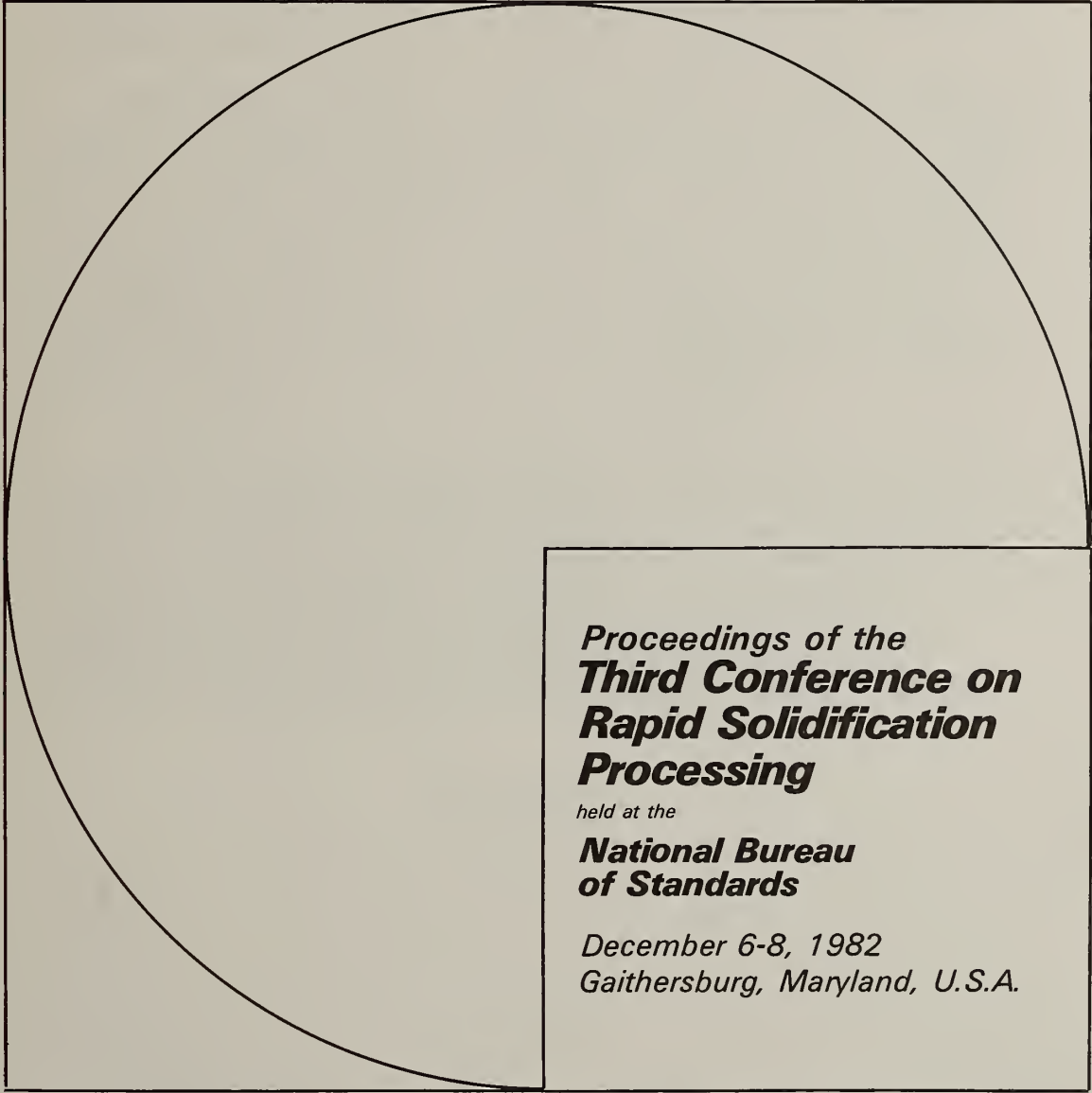
***National Bureau
of Standards***

*Gaithersburg, Maryland
December, 1982*

Editor—Robert Mehrabian

This document contains information which is subject to special export controls. It should not be transferred to foreign nationals in the U.S. or abroad without a validated export license. (Reference Export Administration Regulations, Section 387.1, 1 October 1980 and Federal Register, 1 October 1980. Volume 45, No. 192, Page 65014.)

RAPID SOLIDIFICATION PROCESSING PRINCIPLES AND TECHNOLOGIES, III



*Proceedings of the
**Third Conference on
Rapid Solidification
Processing***

held at the

***National Bureau
of Standards***

*December 6-8, 1982
Gaithersburg, Maryland, U.S.A.*

Edited by: Robert Mehrabian

PREFACE

The general aim of this Third Conference on Rapid Solidification Processing was to review the advances in our understanding of principles as well as technological progress achieved during the past two and one-half years. As in the previous two Conferences, emphasis was placed on rapidly solidified crystalline materials, rather than on amorphous solids which have been adequately treated at other meetings. However, attention was given to the amorphous state and its controlled thermal decomposition as a possible "pathway" toward attaining unique crystalline structures.

The Conference comprised five plenary sessions, five poster sessions of relevance to the plenary sessions, and a panel/workshop session. The topics covered in the plenary and the corresponding poster sessions were: fundamentals of rapid solidification, microstructures and properties, surface layers and thin filaments, consolidation and forming, and applications. A panel/workshop session was also convened to address critical questions in rapid solidification processing (RSP) such as: roadblock to RSP, alternatives to RSP, and new horizons for RSP. In these proceedings no distinction has been made between the invited lectures given at the plenary sessions and the shorter poster presentations. Instead, the eighty-three papers have been arranged sequentially, according to the subject areas covered. A summary of the presentations and discussions from the panel/workshop is given at the end of this volume.

The members of the Steering Committee are listed in front of this book. The Committee wishes to thank Ms. Joyce Harris and Mrs. Kathy C. Stang for organization, arrangements, and operations of the Conference, and for efficient handling of the finances involved, Ms. CaRole Lamb for her invaluable help in the final typing of some of the manuscripts and the overall supervision over reproduction of this book. The Committee also acknowledges the financial assistance provided by the following sponsors: the Air Force Wright Aeronautics Laboratory, the Army Research Office, the Defense Advanced Research Projects Agency, the Office of Naval Research, the National Aeronautics and Space Administration, and the National Bureau of Standards.

Robert Mehrabian
Washington, DC

CHAIRMEN AND COMMITTEE MEMBERS

STEERING COMMITTEE

A. M. Adair
M. Cohen
L. A. Davis
M. A. Greenfield
Lt. Col. L. A. Jacobson
B. H. Kear
J. R. Manning
R. Mehrabian--Chairman
J. B. Moore
P. Parrish
D. E. Polk
B. B. Rath
R. A. Sprague
E. C. van Reuth
J. C. Williams

SESSION CHAIRMAN AND MODERATORS

I : M. Cohen and J. R. Manning
II : B. B. Rath and J. C. Williams
III: B. H. Kear and D. E. Polk
IV : A. M. Adair and R. A. Sprague
V : L. A. Jacobson and J. E. Moore
VI : Panel/Workshop (organizers and reporters)
Roadblocks to RSP: M. Cohen and J. B. Moore
M. A. Greenfield and J. R. Manning
Alternatives to RSP: J. C. Williams and R. A. Sprague
A. M. Adair and L. A. Jacobson
New Horizons for RSP: B. H. Kear and L. A. Davis
D. E. Polk and B. B. Rath

AFFILIATIONS OF CHAIRMEN AND COMMITTEE MEMBERS

- A. M. Adair, Air Force Aeronautical Laboratory, Wright-Patterson Air Force Base, OH 45333
- M. Cohen, Massachusetts Institute of Technology, Cambridge, MA 02139
- L. A. Davis, Allied Corporation, Morristown, NJ 07960
- M. A. Greenfield, National Aeronautics and Space Administration, Washington, DC 20546
- Lt. Col. L. A. Jacobson, Lawrence Livermore National Laboratory, Livermore, CA 94550
- B. H. Kear, Exxon Research and Engineering Company, Linden, NJ 07036
- J. R. Manning, National Bureau of Standards, Washington, DC 20234
- R. Mehrabian, National Bureau of Standards, Washington, DC 20234
- J. B. Moore, Pratt and Whitney Aircraft, West Palm Beach, FL 33402
- P. Parrish, U.S. Army Research Office, Research Triangle Park, NC 27709
- D. E. Polk, Office of Naval Research, Arlington, VA 22217
- B. B. Rath, U.S. Naval Research Laboratory, Washington, DC 20375
- R. A. Sprague, General Electric Company, Cincinnati, OH 45215
- E. C. van Reuth, Defense Advanced Research Projects Agency, Arlington, VA 22209
- J. C. Williams, Carnegie-Mellon University, Pittsburgh, PA 15213

ACKNOWLEDGMENT

This Conference was supported by grants from the following U.S. Government agencies:

Defense Advanced Research Projects Agency
Office of Naval Research
Army Research Office
Air Force Wright Aeronautical Laboratory
National Aeronautics and Space Administration
National Bureau of Standards

TABLE OF CONTENTS

	<u>Page</u>
I. <u>FUNDAMENTALS</u>	
SOME FUNDAMENTAL ASPECTS OF RAPID SOLIDIFICATION--M. Cohen and R. Mehrabian	1
SOLIDIFICATION OF UNDERCOOLED LIQUIDS--J. H. Perepezko, Y. Shiohara, J. S. Paik, and M. C. Flemings	28
MECHANISMS OF SEGREGATION-FREE SOLIDIFICATION--W. J. Boettinger, S. R. Coriell, and R. F. Sekerka	45
MICROSTRUCTURAL CHARACTERIZATION OF RAPIDLY SOLIDIFIED MATERIALS--H. L. Fraser and J. B. Vander Sande	56
ASPECTS OF SOLIDIFICATION IN THE RSR POWDER PROCESS--R. J. Patterson, II and C. M. Adam	70
OSTWALD RIPENING OF RAPIDLY SOLIDIFIED SOLID-LIQUID MIXTURES--P. W. Voorhees and M. E. Glicksman	83
SOLIDIFICATION MICROSTRUCTURES OF UNDERCOOLED DROPLETS--J. J. Richmond, J. H. Perepezko, S. E. LeBeau, and K. P. Cooper	90
MICROSTRUCTURAL STUDIES ON SUPERCOOLED SUB-MICROMETER POWDER PARTICLES--D. Schechtman, S. D. Ridder, and R. Mehrabian	96
AN EXPERIMENTAL TECHNIQUE FOR DETERMINING THE DEGREE OF PARTICLE MELTING IN A PLASMA JET OPERATING AT LOW PRESSURE--R. W. Smith, M. Paliwal, and D. Apelian	105
AN ATOMISTIC MODEL OF SOLUTE TRAPPING--M. J. Aziz	113
TEMPERATURE EFFECTS ON PLASMA DEPOSITION OF Ni-BASE MATERIALS--T. L. Cheeks, M. E. Glicksman, M. R. Jackson, and E. L. Hall	118
SUPERSATURATED SOLID SOLUTIONS BY MASSIVE SOLIDIFICATION: OBSERVATIONS AND IMPLICATIONS--T. F. Kelly, M. Cohen, and J. B. Vander Sande	124
SOLUTE REDISTRIBUTION DURING SOLIDIFICATION OF SUPERCOOLED ALLOYS--S. D. Peteves, D. D. McDevitt, and G. J. Abbaschian	129
II. <u>MICROSTRUCTURES AND PROPERTIES</u>	
MICROSTRUCTURE-PROPERTY RELATIONS AND THEIR ROLE IN RSP MATERIALS--J. C. Williams and J. P. Hirth	135
THE EFFECT OF RAPID SOLIDIFICATION ON THE MICROSTRUCTURES AND PROPERTIES OF ALUMINUM POWDER METALLURGY ALLOYS--J. R. Pickens and E. A. Starke, Jr.	150
STRUCTURE-PROPERTY RELATIONSHIPS IN RSP STEELS--G. B. Olson, M. Cohen, and G. J. Yurek	171
STRUCTURE AND PROPERTIES OF RSP COPPER-BASED ALLOYS--I. E. Anderson, R. A. Masumura, B. B. Rath, and C. L. Vold	178
FUNDAMENTALS OF RAPID SOLIDIFICATION PROCESSING IN NICKEL-BASE SUPERALLOYS--E. H. Aigeltinger, A. F. Giamei, and D. M. Dimiduk	186
THE MECHANICAL BEHAVIOR OF RSPD MATERIALS--M. R. Jackson, R. W. Smashey, and L. G. Peterson	198
NOTCHED TENSILE PROPERTIES OF RAPIDLY SOLIDIFIED AND INGOT-BASED ALUMINUM ALLOYS--S. Kang and N. J. Grant	209
RAPIDLY SOLIDIFIED O.D. IN-100: STRUCTURE AND PROPERTIES--C. H. Smith and N. J. Grant	215

THE MICROSTRUCTURE OF TOOL STEELS PROCESSED FROM RAPIDLY SOLIDIFIED POWDERS--S. Kumar, A. Lawley, and M. J. Koczak	223
STRUCTURE AND PROPERTIES OF A POWDER-PROCESSED HIGH-CHROMIUM ION--S. Mohan, A. Lawley, L. R. Woodyatt, and K. S. Brosius	229
THE EFFECT OF POWDER COOLING RATE AND THERMAL EXPOSURE ON THE TENSILE PROPERTIES OF A RAPIDLY SOLIDIFIED NICKEL BASE SUPERALLOY--D. B. Miracle, K. A. Williams, and H. A. Lipsitt	234
TENSILE BEHAVIOR OF RSR IRON-ALUMINIDES--M. G. Mendiratta, S. K. Ehlers, D. K. Chatterjee, and H. A. Lipsitt	240
MICROSTRUCTURE AND MECHANICAL PROPERTIES OF RAPIDLY-SOLIDIFIED WHITE-CAST IRON POWDERS--L. E. Eiselstein, O. A. Ruano, O. D. Sherby, and J. Wadsworth	246
MICROSTRUCTURE EVOLUTION IN RAPIDLY SOLIDIFIED $Ni_3(Mo,X)$ ALLOYS--P. L. Martin and J. C. Williams	252
COMPARATIVE FINE STRUCTURE, MICROCHEMISTRY AND MORPHOLOGY OF RENE' 95 SUPERALLOY POWDERS PRODUCED BY ARGON ATOMIZATION AND CENTRIFUGAL ATOMIZATION--J. A. Domingue, R. D. Kissinger, W. J. Boesch, and J. K. Tien	259
RAPID SOLIDIFICATION STUDIES OF Ni_3Al ALLOYS--C. C. Koch, J. A. Horton, C. T. Liu, O. B. Cavin, and J. O. Scarbrough	264
MICROSTRUCTURAL CHARACTERIZATION OF RSPD STRUCTURES--A. M. Ritter and M. R. Jackson	270
PRECIPITATION SEQUENCES IN A RAPIDLY SOLIDIFIED Ni-Al-Mo-W ALLOY--D. M. Dimiduk	276
EFFECT OF THE RAPID-SOLIDIFICATION METHOD ON MICROSTRUCTURES AND PROPERTIES OF Al-Li ALLOYS--P. J. Meschter, J. E. O'Neal, and R. J. Lederich	281
AGING BEHAVIOR OF DEVITRIFIED Ti RICH ALLOYS CONTAINING METALLOIDS--S. H. Whang and Y. Z. Lu	286
 III. SURFACE LAYERS AND THIN FILAMENTS	
DIRECTED ENERGY SURFACE PROCESSING OF METALS--T. R. Tucker and A. H. Clauer	291
INTERFACE RESPONSE IN LASER-MELTED ALLOYS--S. M. Copley, D. Beck, and M. Bass	303
INFLUENCE OF ELECTRON BEAM SCANNING PARAMETERS ON SURFACE MELTING AND HEAT TREATMENT CHARACTERISTICS--P. R. Strutt, M. Kurup, and A. Taquir	312
IMPROVED IRON BASE ALLOYS MADE USING A RAPID SOLIDIFICATION PROCESS--R. Ray, V. Panchanathan, and S. Isserow	323
BORIDE AND CARBIDE DISPERSION IN MELT SPUN SUPERALLOYS--S. C. Huang, K. M. Chang, and E. L. Hall	337
HIGH TEMPERATURE OXIDATION OF RAPIDLY SOLIDIFIED Ni-Al-Mo-W ALLOYS--G. H. Meier, F. S. Pettit, and A. S. Khan	348
RAPIDLY SOLIDIFIED CARBIDE POWDERS PRODUCED BY SPARK MACHINING OF Ti AND Zr--C. S. Pande and J. D. Ayers	360
PROCESSING, MICROSTRUCTURE, AND PROPERTIES OF MELT SPUN AND CONSOLIDATED SUPERALLOYS--R. H. VanStone, J. R. Hughes, R. E. Maxwell, H. H. Liebermann, and R. G. Rowe	365
M_3B_2 BORIDE IN MELT-SPUN SUPERALLOYS--S. C. Huang, E. L. Hall, and T. K. Glasgow	377
PREPARATION OF METALLIC GLASSES WITH SECOND PHASE PARTICLES--D. G. Ast and P. G. Zielinski	384
THE EFFECT OF SOLIDIFICATION VELOCITY ON THE MICROSTRUCTURE OF Ag-Cu ALLOYS--W. J. Boettinger, R. J. Schaefer, F. Biancaniello, and D. Shechtman	390

NONDESTRUCTIVE CHARACTERIZATION OF RAPIDLY SOLIDIFIED Al-Mn ALLOYS--R. J. Schaefer, M. Rosen, J. J. Smith, D. Shechtman, and R. Mehrabian	397
EXPERIMENTAL STUDIES OF THE DYNAMICS OF RAPID SOLIDIFICATION USING ACOUSTIC EMISSION--R. B. Clough, H. Wadley, and R. Mehrabian	403
CRYSTALLIZATION KINETICS OF AMORPHOUS ALLOYS BY ULTRASONIC MEASUREMENTS--M. Rosen, E. Horowitz, H. N. G. Wadley, and R. Mehrabian	416
OXIDATION RESISTANCE OF A FINE-GRAINED RAPIDLY SOLIDIFIED 18-8 STAINLESS STEEL--G. J. Yurek	424
CHARACTERIZATION OF METASTABLE PHASE POWDERS PREPARED BY ELECTROLESS DEPOSITION--L. V. Meisel, P. J. Cote, and D. M. Quinn	429
PREPARATION OF GLASSY METALS AS POWDERS VIA HYDROGEN EMBRITTLEMENT--B. C. Giessen, S. H. Whang, and F. Dabkowski	435
AN ARC FURNACE MELT SPINNER FOR THE RSR PROCESSING OF REFRACTORY AND REACTIVE ALLOYS--S. H. Whang and B. C. Giessen	439
A NEW HIGH STRENGTH NICKEL-BASE MICROCRYSTALLINE ALLOY VIA RAPID SOLIDIFICATION TECHNOLOGY--V. Panchanathan, S. Sastri, and S. Hahn	443
DYNAMIC WETTING/SOLIDIFICATION PHENOMENA--R. P. I. Adler and S. C. Hsu	448
RAPID-SOLIDIFICATION PROCESSING OF TITANIUM ALLOYS--T. C. Peng, S. M. L. Sastry, and J. E. O'Neal	452
THE MICRO-PARTICLE PROCESSOR TO PRODUCE FINE POWDERS AND COATINGS--J. Perel, J. F. Mahoney, S. Taylor, Z. Shanfield, and C. Levi	458
RAPID SOLIDIFICATION SURFACE TREATMENT OF DISCS AND RINGS BY ELECTRON BEAM PROCESSING--M. Tuli and P. R. Strutt	464
PLASMA DEPOSITION EFFECTS ON STRUCTURES AND PROPERTIES OF RSPD SUPERALLOYS--R. W. Smith, D. V. Rigney, J. S. Smith, and J. R. Rairden	468
THE MICROSTRUCTURE OF RAPIDLY SOLIDIFIED NiAl-Cr QUASIBINARY EUTECTIC--D. Shechtman, T. Z. Kattamis, F. S. Biancaniello, and W. J. Boettinger	476
WEAR PROPERTIES OF RAPIDLY SOLIDIFIED SURFACES OF A PSEUDO-BINARY Fe-TiC ALLOY--P. R. Strutt, B. G. Lewis, S. F. Wayne, S. L. Rice, and B. H. Kear	483
IV. <u>CONSOLIDATION AND FORMING</u>	
FABRICATION OF ORIENTED SINGLE CRYSTAL WAFER STOCK FROM Ni-Al-Mo-X ALLOY POWDERS--R. E. Anderson, H. A. Chin, S. E. Hughes, and B. B. Rath	488
DEFECT ANALYSES OF P/M SUPERALLOYS--W. H. Chang, H. M. Green, and R. A. Sprague	500
INTERPRETIVE REVIEW OF COMPARATIVE MICROSTRUCTURES OF POWDERS AND CONSOLIDATES OF P/M SUPERALLOYS PRODUCED BY MODERN ATOMIZATION PROCESSES--R. D. Kissinger and J. K. Tien	510
CONSOLIDATION AND FORMING OF P/M POROUS BILLETS--H. L. Gegel, J. S. Gunasekera, S. M. Doraivelu, J. C. Malas, J. T. Morgan, and L. E. Matson	519
PROCESSING OF P/M ALUMINUM ALLOYS X7090 AND X7091--F. R. Billman, J. C. Kuli, Jr., G. J. Hildeman, J. I. Petit, and J. A. Walker	532
POST RSPD PROCESSING EFFECTS ON GRAIN GROWTH--R. A. Amato, M. R. Jackson, and P. A. Siemers	547
Ni-Mo-B ALLOYS: METALLIC GLASS TO DUCTILE CRYSTALLINE SOLID--S. K. Das, L. A. Davis, J. R. Y. Wang, and D. Kapoor	559

MICROSTRUCTURAL MODIFICATION OF ALUMINUM-SILICON ALLOY POWDERS DURING DYNAMIC CONSOLIDATION--W. H. Gourdin and J. E. Smugeresky	565
MICROSTRUCTURE OF RAPIDLY SOLIDIFIED STAINLESS STEEL AND SUPERALLOY POWDERS: A COMPARISON OF POWDER-MAKING TECHNIQUES--J. E. Smugeresky	572
CONSOLIDATION, THERMOMECHANICAL PROCESSING, AND MECHANICAL PROPERTIES OF RAPIDLY SOLIDIFIED, DISPERSION-STRENGTHENED TITANIUM ALLOYS--S. M. L. Sastry, T. C. Peng, J. E. O'Neal, and L. P. Beckerman	579
EFFECT OF AGING ON THE MICROSTRUCTURE OF RAPIDLY COOLED Ti-5Al-2.5Sn WITH Si ADDITIONS--A. G. Jackson, T. F. Broderick, F. H. Froes, and J. Moteff	585
ON THE TEXTURE DEVELOPMENT--DIRECTIONAL RECRYSTALLIZATION INTERACTION OF RAPIDLY SOLIDIFIED Ni-Mo-Al-W AND Ni-Cr-Al-W ALLOYS--H. A. Chin, S. E. Hughes, J. S. Andrus, and J. L. Larson	590
THERMAL STABILITY OF HIGH TEMPERATURE P/M ALUMINUM ALLOYS--Y.-W. Kim, M. M. Cook, and W. M. Griffith	597
EVALUATION OF VOIDS IN POWDER CONSOLIDATES USING LONG WAVELENGTH NEUTRONS--M. Fatemi and B. B. Rath	603

V. APPLICATIONS

RAPID SOLIDIFICATION--PAST PROMISES AND CURRENT REALITY--A. M. Adair, L. A. Jacobson, E. C. van Reuth, and J. Dickson	609
AEROSPACE STRUCTURAL APPLICATIONS OF RAPIDLY SOLIDIFIED ALUMINUM-LITHIUM ALLOYS--R. E. Lewis, I. G. Palmer, J. C. Ekvall, I. F. Sakata, and W. E. Quist	615
APPLICATIONS OF RAPIDLY SOLIDIFIED ALUMINUM ALLOYS AT ELEVATED TEMPERATURES--C. M. Adam, J. W. Simon, and S. Langenbeck	629
GAS TURBINE APPLICATIONS OF RST ALLOYS--D. B. George, R. G. Bourdeau, and J. A. Miller	640
AIRCRAFT ENGINE GAS TURBINE COMPONENT FABRICATION CONCEPTS USING RSPD--A. M. Johnson, J. S. Keim, R. W. Smashey, D. V. Rigney, and T. G. Wakeman	650
RECENT APPLICATIONS OF ULTRA RAPID SOLIDIFICATION TECHNOLOGY (URST) MICROCRYSTALLINE AND AMORPHOUS POWDER MATERIALS--J. H. Kushnick and D. L. Sawhney	662
SHOCK COMPACTION OF FERROUS ALLOY POWDERS--T. J. Ahrens, D. Koska, P. Kasiraj, T. Vreeland, Jr., A. W. Hare, F. D. Lemkey, and E. R. Thompson	672
ULTRASONIC GAS ATOMIZED POWDERS OF MAGNETIC ALLOYS--R. C. O'Handley, P. Domalavage, B. W. Corb, Y. Hara, and N. J. Grant	678
PRODUCTION APPLICATIONS OF RAPIDLY SOLIDIFIED TOOL STEELS, SUPERALLOYS, TITANIUM ALLOYS, AND CORROSION-RESISTANT ALLOYS--J. H. Moll and F. J. Rizzo	686
COMMERCIAL RAPID SOLIDIFICATION (CRS) PROCESSING FOR ADVANCED TURBINE DISK APPLICATIONS--R. Beck, W. Kent, and C. S. Kortovich	692

VI. PANEL/WORKSHOP ON CRITICAL QUESTIONS IN RAPID SOLIDIFICATION PROCESSING

ROADBLOCKS TO RAPID SOLIDIFICATION PROCESSING--T. Tietz, M. DeCrescente, S. Copley, and T. Kearns	697
ALTERNATIVES TO RAPID SOLIDIFICATION PROCESSING--C. Kortovich, C. Blankenship, L. Johnson, and W. Boesch	699
NEW HORIZONS FOR RAPID SOLIDIFICATION PROCESSING--R. Schaefer, P. Strutt, R. Maringer, B. Giessen, H. Fraser, and M. Flemings	701

M. Cohen
Massachusetts Institute of Technology
Cambridge, MA 02139

and

R. Mehrabian
National Bureau of Standards
Washington, DC 20234

ABSTRACT

Detailed consideration is given to the interplay of supercooling and rapid heat-extraction rate in controlling the mode and kinetics of solidification processes. Achievable external heat extraction rates impose strict limitations on solid/liquid interfacial velocities in the absence of bulk supercooling. On the other hand, for the case of supercooling, the recalescence rate at the interface almost always predominates the external heat-extraction rate. Particular attention is directed to the resulting degrees of solute partitioning at the moving solid/liquid interface, and also to the special conditions which achieve partitionless (or massive) solidification. The required conditions for the latter are an interfacial temperature below the $T_0^{L/\alpha}$ line, and an interfacial velocity which exceeds the diffusive velocity of solute in the liquid. The complete trapping of solute elements in the solidifying phase is potentially of major significance from the standpoint of microstructural control and alloy design because extremely high supersaturations of very stable (low solid solubility) phases can thereby be obtained. Subsequent precipitation leads to ultrafine (~ 100 Å) dispersions of second-phase particles which resist coalescence and re-resolution in the solid matrix at elevated temperatures. Such dispersions are unusually effective in pinning grain boundaries and inhibiting grain growth.

A further question now arises concerning an appropriate definition of rapid solidification, in view of the fact that the conventionally specified "cooling rate" does not always properly express a "solidification rate." Accordingly, an attempt will be made to describe various modes of solidification in terms of interfacial velocities.

Introduction

At the Second International Conference on Rapid Solidification Processing: Principles and Technologies [1] about three years ago, considerable emphasis was directed to the microstructural refinement achieved in cellular and dendritic morphologies by rapid cooling from the liquid state. Even though almost equilibrium partitioning of solute and impurity atoms may still occur at the advancing solid/liquid interfaces, there is substantial refinement in the scale of the resulting microsegregations and second-phase dispersions due to the fact that rapid cooling allows less time for the coarsening of morphological features during the solidification growth process. The conditions for such rapid cooling are typically attained by setting up positive temperature gradients in the melt ahead of the moving interfaces, and efficiently extracting heat through the solid phase to the external surroundings as the solidification proceeds.

In the present paper, more attention is given to solidification under conditions of bulk melt supercooling such that the temperature gradients ahead of the solidifying front become negative, and then the heat of solidification can flow into the remaining supercooled liquid even more rapidly than to the surroundings. This mode of solidification leads to high interfacial velocities and, in turn, to solute trapping in the advancing solid, i.e., nonequilibrium partitioning at the interfaces. We shall be especially interested in the limiting case in which the partition ratio reaches unity, thus attaining partitionless (or massive) solidification. Under these circumstances, the solid phase not only inherits the same compositional uniformity as prevails in the melt, but it may also be highly supersaturated with respect to very stable second phases which have been previously dissolved in the liquid state. This supersaturation in the solid state then permits the precipitation of extremely fine dispersions which are otherwise impossible to dissolve in the solidified alloy.

Some microstructural consequences of massive solidification will then be discussed, particularly from the standpoint of high-temperature grain-growth resistance arising from the grain-boundary pinning effect of stable second-phase dispersions. These characteristics have important implications in structure/property relationships.

In dealing with rapid solidification phenomena, it is well to recognize two conditions of extreme heat flow. In the first, the solid/liquid interface moves into a superheated melt, and the latent heat of fusion is withdrawn through the solid. Typical cases are atomization, melt spinning, and surface melting when there is no bulk supercooling. The resulting achievable interfacial velocities are then limited by the rate of external heat extraction and the thickness of the material being processed, assuming that no restraints are imposed on the interfacial motion by local atomic rearrangements [2]. The second situation involves solid growth into a supercooled melt, where most of the latent heat of fusion can be absorbed by the liquid itself and so the external rate of heat extraction is less important. In such instances, the temperature of the liquid rises (recalescence) and must be taken into account in the accompanying heat-flow kinetics. Nevertheless, sufficiently high interfacial velocities can be attained in this type of solidification to reach complete solute trapping.

In this paper, we shall describe modes of solidification in two ways: (1) according to the morphology of growth (i.e., plane-front, cellular, or dendritic), and (2) according to compositional changes at the solid/liquid interface (i.e., with equilibrium, partial, or no partitioning of solute atoms between the liquid and solid phases). Clearly, these are related but different kinds of classification. The variations in solidification behavior will depend on the transport of heat and solute from the interface, and in some cases on atomic rearrangement processes at the interface. It is necessary to take these interdependent factors into account in order to deal with the microstructural consequences of rapid solidification and, hence, with processing/structure/property relationships. Special emphasis will be placed on the solid/liquid interfacial velocity which is generated under the operative conditions of nucleation (usually heterogeneous) and heat flow.

We shall first review some fundamentals of solidification when compositional equilibrium is maintained locally at the moving growth front (no supercooling). Figure 1 shows that the interfacial morphology is a function of the thermal gradient (G_L) in the melt at the interface and the interfacial velocity or growth rate (R). The slope of the line AB is given by [3]:

$$\text{AVERAGE COOLING RATE } \dot{T} = G_L R$$

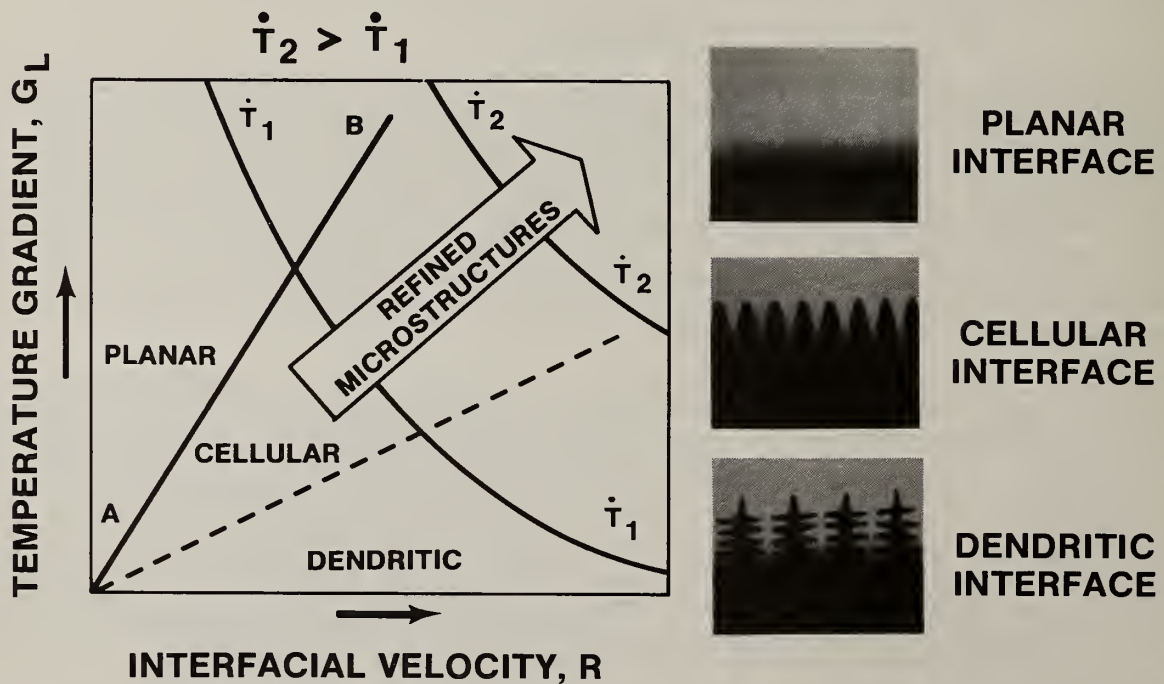


Figure 1. Mode of solidification as a function of temperature gradient in the liquid (G_L) and interfacial velocity or growth rate (R). Microstructural refinement due to increasing the cooling rate ($\dot{T}=G_L R$) is indicated by the arrow [1]. Line AB is given by eq. (1).

$$\frac{G_L}{R} = \frac{m_L C_0 (k_E - 1)}{D_L k_E} \quad (1)$$

where C_0 = solute concentration in the bulk liquid,
 D_L = diffusivity of solute in liquid,
 k_E = equilibrium partition ratio (< 1 as in figure 12), and
 m_L = slope of liquidus line (negative as in figure 12).

When G_L/R is greater than the right-hand side of eq. (1), the interface advances on a planar (or smooth) front as heat is withdrawn through the solid phase. Under these conditions, the interface tends to be stabilized in that chance protuberances on the solid front are "melted back" by the steep temperature gradient in the liquid relative to the interfacial velocity. Moreover, at steady state, there will be no microsegregation of solute atoms behind the advancing front, except possibly at the very end of solidification.

In contrast, when G_L/R is less than the right-hand side of eq. (1), the interface becomes morphologically unstable in as much as protuberances tend to grow ahead preferentially into combinations of liquid temperature and composition where the melt would otherwise be supercooled (or supersaturated) with respect to the solid phase. Another way of putting it is that, when R is increased relative to G_L , the solute concentration gradient ahead of the interface can become steep enough to induce morphological instability. This situation leads to cellular or dendritic growth morphologies, with solute-enriched microsegregations building up in the remaining liquid between the cells or dendritic arms*. These microstructural regions are also locations where other solid phases usually precipitate near the end of the solidification process.

For the case of cellular or dendritic solidification, the temperature gradient and interfacial velocity in figure 1 could represent averages for the liquid-plus-solid "mushy" region. The product $G_L R$ then expresses the average cooling rate (\dot{T}) and, as the sloping arrow indicates, the cellular or dendritic arm spacings decrease in scale with increasing \dot{T} . This trend comes about because interfacial energy associated with these morphological features causes them to coarsen as a function of the available time for solidification. Accordingly, such coarsening can be reduced by increasing the average cooling rate during cellular or dendritic solidification. Thus, even with equilibrium partitioning being substantially maintained at the moving interfaces, accelerated cooling can provide significantly smaller distances between microsegregated regions and precipitated second phases in the final microstructure.

Figure 1 must be modified in important ways at very high interfacial velocities (very rapid solidification rates), and then the regime of morphological instability is capped off, as illustrated in figure 2. When R is sufficiently large, beyond line EF, morphological stability is reestablished and plane-front growth ensues, still under the assumption of equilibrium partitioning or no supercooling. The reason for this interesting behavior is that, when the limiting interfacial velocity at EF is approached, potential perturbations in the growth front become so fine in scale that surface tension imposes a dominant stabilizing influence toward establishing a smooth interface. Coriell and Sekerka [5] have solved this complex solidification problem, taking into account these capillary forces as well as the solute and thermal diffusion fields in front of the interface (including the effect of latent heat evolution). The solute field is always destabilizing, while the capillary forces always oppose the growth of perturbations. The thermal field will be stabilizing if the net flow of heat flow is toward the solid. Calculated results for an aluminum-silicon alloy are represented in figure 2 [6].

The line AB in figure 2 has the same significance as in figure 1, but the regime of cellular and dendritic solidification is now confined to the dome-shaped region in figure 2. Therefore, plane-front growth is obtained not only to the left of line AB, as discussed in connection with eq. (1), but also above and to the right of line BFE. The condition represented by line EF is often referred to as absolute morphological stability. The corresponding velocity is given by [5,7]:

*The morphological instability attending cellular or dendritic solidification is often termed constitutional supercooling [4]. However, local compositional equilibrium at the advancing growth front is still assumed, and so this is not supercooling in the usual sense.

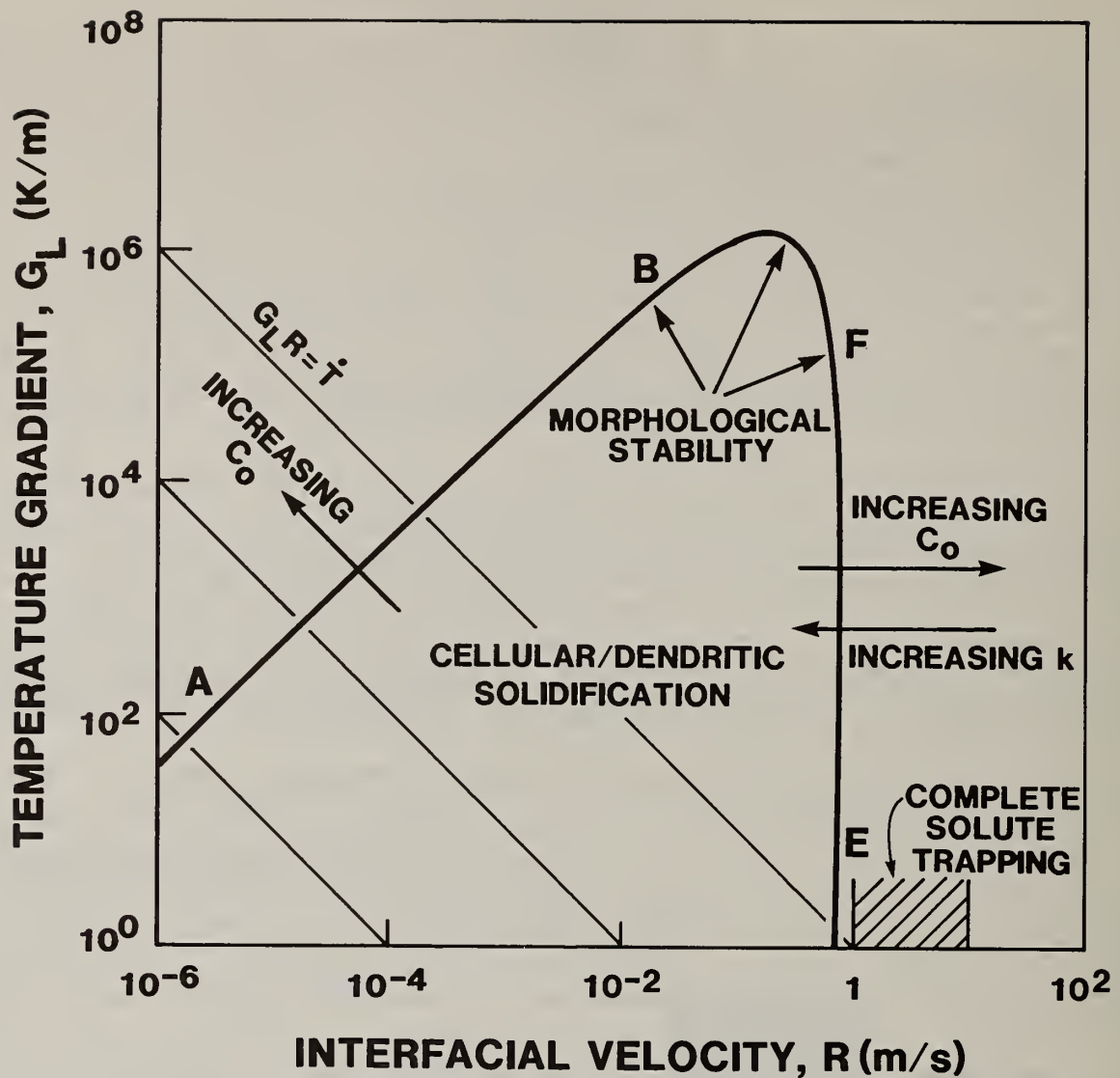


Figure 2 Regimes of liquid temperature gradient (G_L) and interfacial velocity (R) for plane-front growth (morphologically stable interface) and for cellular/dendritic growth. The boundary ABFE between these two regimes is calculated for an Al-0.1 wt.% Si alloy, assuming equilibrium partitioning of Si at the moving interface [6]. Cross-hatched band indicates estimated interfacial velocity which is fast enough to achieve partitionless solidification.

$$R(\text{at EF}) = \frac{m_L D_L (k_E - 1) C_0}{k_E^2 T_M \Gamma}, \quad (2)$$

where T_M = melting temperature of the interface without solute, and

Γ = is the ratio of solid/liquid surface energy to the latent heat of fusion per unit volume.

According to eq. (2), the boundary EF is shifted to higher velocities with increase C_0 and with decreasing k_E . Some typical calculations in table I for aluminum alloys, with solute contents in the range of their solid solubility limits, indicate that interfacial velocities of the order of 3 to 13 m s^{-1} are required to achieve absolute morphological stability, under the assumption of equilibrium partitioning. However, such velocities lie beyond the range that can be attained by maximum external heat-extraction rates or feasible cooling rates, as shown by the heat-flow calculations in table II for 10 μm melts of Al, Fe, and Ni when cooled by processes of atomization, melt spinning, and substrate self-quenching.

Table I. Interfacial Velocity for Absolute Morphological Stability in Binary Aluminum Alloys; Equilibrium at Interface

	Al-Cu	Al-Fe	Al-Si
Maximum Solid Solubility (at.%)	2.5	0.025	1.6
$\frac{(k_E - 1)}{k_E^2} m_L$	~ 265	~ 7000	~ 388
$R \text{ (m s}^{-1}\text{)} \geq$	~ 13.2	3.5	~ 12.4

k_E Equilibrium Partition Coefficient

m_L Slope of Liquidus Line

Table II. Cooling-Rate and Interfacial-Velocity Limitations in RSP of 10 μm Size Al, Fe, Ni Specimens; No Supercooling

	Heat Transfer Coefficient	Avg. Max. Cooling Rate in Liquid	Max. Interfacial Velocity	Fraction Solid
Atomization	$\sim 5 \times 10^4 \text{ W m}^{-2} \text{ K}^{-1}$	$\sim 7 \times 10^6 \text{ K s}^{-1}$	$0.1 - 0.27 \text{ m s}^{-1*}$	0.1 to 0.95
Melt Spinning	$\sim 10^6$	$\sim 2.5 \times 10^7$	$0.6 - 0.75^*$	0 to 1.0
Self Quenching	Tends to infinity	$\sim 10^8$	$1.5 - 2.3 \text{ Al}^{**}$ $0.35 - 0.65 \text{ Fe, Ni}$	0.1 to 1.0

* Independent of Size for Newtonian Cooling

** Inversely Proportional to Melt Thickness

The equilibrium-partitioning assumption is not realistic at the high growth rates in question. Various relationships have been proposed for the dependence of nonequilibrium partitioning on interfacial velocity [8]. For present purposes, a convenient form is:

$$k(R) = \frac{R\lambda/D_L + k_E}{R\lambda/D_L + 1}, \quad (3)$$

where λ = effective diffusion distance in the liquid concentration gradient at the interface, $\sim 10 \times$ interatomic distance (ξ).

$k(R)$ is plotted as a function of R in figure 3 for Al-Si alloys, taking $D_L = 2.3 \times 10^{-9} \text{ m}^2 \text{ s}^{-1}$, and $\xi \sim 2.3 \times 10^{-10} \text{ m}$. It will be seen that $k(R)$ increases progressively (signifying more solute trapping) with increasing interfacial velocity. If the form of eq. (2) is now adopted for general values of k (instead of only for k_E), the resulting connection between alloy composition and the velocity for absolute morphological stability can also be plotted in figure 3. Because of the enhanced values of k , absolute stability may be attained at growth rates of less than 1 m s^{-1} even with concentrated alloys (up to 5 wt.% Si), but the solidification is then far ($k \approx 0.5$) from being partitionless.

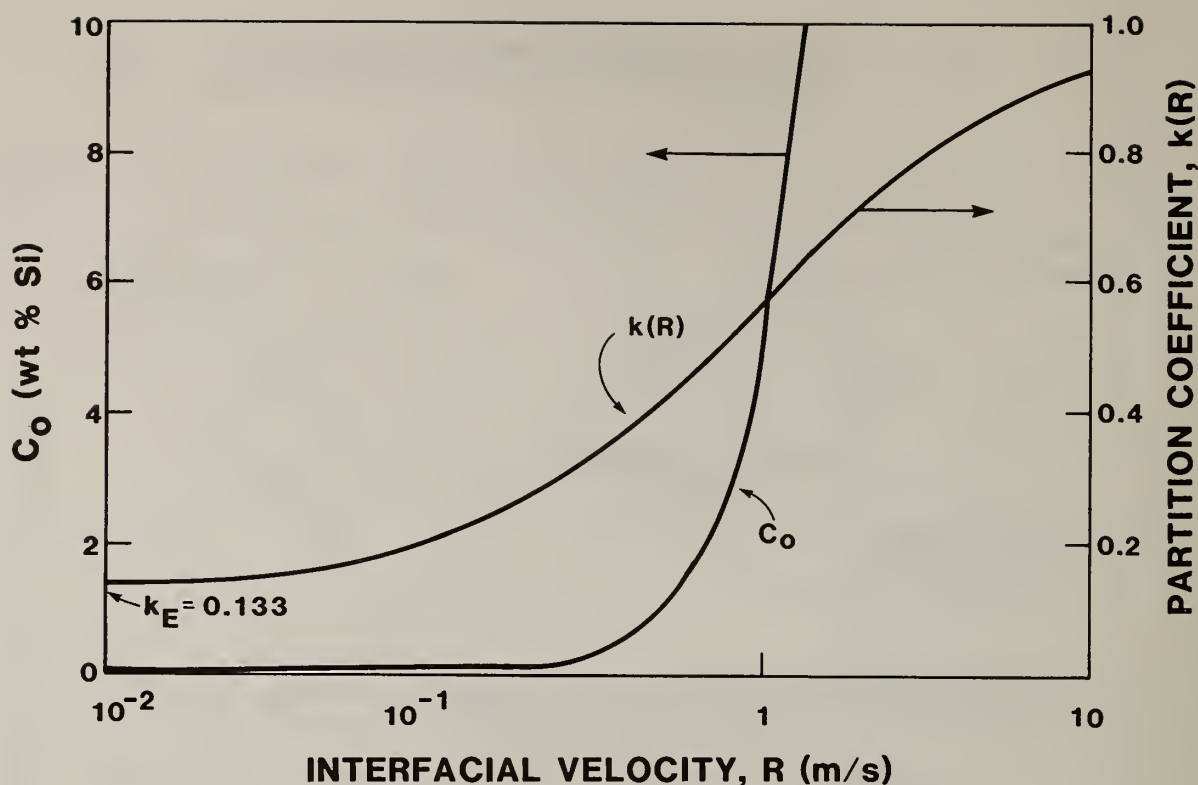


Figure 3 Calculated changes in partition coefficient ($k(R)$) and composition (C_0) for partitionless solidification as a function of interfacial velocity (R) in Al-Si alloys. $k(R)$ vs R is given by eq. (3) and C_0 vs R is given by eq. (2) with $k(R)$ substituted for k_E .

Shortcomings of the above approach include the fact that eq. (3) has been derived for dilute alloys. Furthermore, substitution of $k(R)$ for k_E in the absolute morphological stability eq. (2) should only be made when the change of partition coefficient with velocity ($\partial k(R)/\partial R$) is small and/or the interfacial kinetics are sluggish [9]. The latter condition implies a small interfacial kinetic coefficient $K_M = \partial R/\partial T_i \leq 1.0 \text{ cm s}^{-1}\text{K}^{-1}$, where T_i is the interfacial temperature.

In general, solidification under conditions of absolute morphological stability is not necessarily partitionless. From its very nature, the plane-front growth characteristic of absolute stability means that there will then be no lateral partitioning, but partitioning may still take place between the solid and the liquid in the direction of growth. In fact, in order to avoid the latter type of partitioning, the interface will have to move at a rate in excess of the diffusive velocity (D_L/ξ), or at least with an effective diffusive velocity such as $D_L/\lambda \sim D_L/10 \xi$. This range of velocities is shown as a cross-hatched bar in figure 2 and, for the case at hand, happens to lie beyond the velocity where absolute stability should set in. Experimental evidence of such a situation has been observed [10] and will be discussed later.

It is worth noting that in the modes of solidification which have been analyzed in this section, the net heat flux is always from the liquid to the solid. In contrast, when bulk melt supercooling is involved, as will be covered in the following section, the heat flow may be reversed, and then the latent heat of fusion can be discharged into the supercooled liquid. This circumstance contributes substantially to the interfacial velocities that can be attained during the solidification process.

Solidification of Supercooled Droplets

In this section, the thermal history during solidification of supercooled droplets is described using enthalpy/temperature diagrams. Newtonian heat-flow conditions, i.e., negligible temperature gradients inside the droplets, are first assumed in order to portray the thermal history of pure aluminum droplets during solidification. Conditions for hypercooling are described and related to

the overall recalescence of the droplet. It is shown that the Newtonian model is reasonable under either of two conditions: first, when the atomic rearrangement process at the interface is slow compared to thermal diffusion (motion is then "interface limited"), and second, when the number of nucleation events is large. Next, the general case of solidification of a supercooled droplet is described when the temperature gradients are not negligible. Sample calculations are presented from reference [11] to describe temperature profiles and interfacial velocities as a function of initial supercooling, droplet size, and interfacial kinetics. The necessary conditions for partitionless solidification of an alloy are given in terms of $T_0^{L\alpha}$ curves and interfacial velocities. Finally, microstructural observations on submicron and commercial-sized powders are correlated with the predictions of the heat-flow solidification model.

Three general "paths" portraying the thermal history for Newtonian solidification of pure aluminum droplets are designated in the enthalpy/temperature diagram of figure 4 [10]. These "paths" express the relative enthalpy per mole of the system ($H - H_{SM}$) as a function of temperature and weight fraction solid (g) based on the following equation:

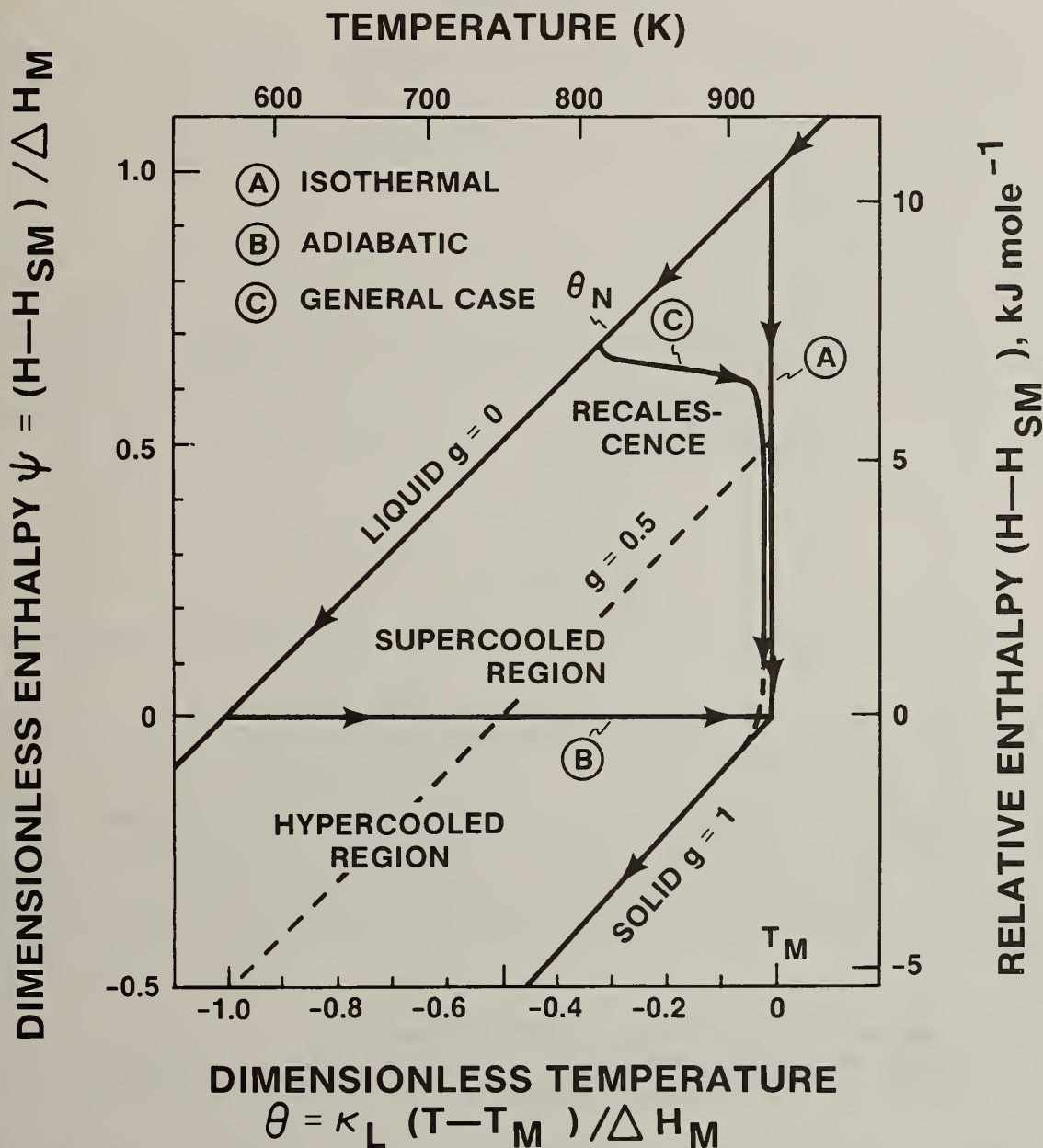


Figure 4 Enthalpy-temperature diagram for aluminum, showing three solidification "paths." In "path" C, θ_N is the dimensionless nucleation temperature on supercooling. Other symbols are defined in text [10].

$$H - H_{SM} = [\Delta H_M + \kappa_L(T - T_M)][1 - g] + \kappa_S(T - T_M)g \quad (4)$$

where: H = enthalpy per mole of the system
 H_{SM} = enthalpy per mole of the solid phase at the melting temperature, T_M ,
 ΔH_M = latent heat of fusion,
 κ_S, κ_L = specific heats of solid and liquid (assumed constant unless otherwise indicated).

The two terms on the right-hand side of eq. (4) represent the enthalpies of the liquid and solid fractions in the droplet. The relationship in eq. (4) can also be written in terms of dimensionless enthalpy ψ and temperature θ , where:

$$\psi = (H - H_{SM})/\Delta H_M, \text{ and} \quad (5)$$

$$\theta = \kappa_L(T - T_M)/\Delta H_M. \quad (6)$$

These parameters are also shown in figure 4. For a volume of liquid at or above its melting point ($T \geq T_M$, $g = 0$), $\theta \geq 0$ and $\psi \geq 1.0$. On the other hand, for a volume of solid at or below its melting point ($T \leq T_M$, $g = 1.0$), $\theta \leq 0$ and $\psi \leq 0$. A volume of partially solid material at T_M ($\theta = 0$) will have a dimensionless enthalpy equal to the fraction of liquid ($1 - g$). This is because lines of constant fraction solid intersect the melting temperature axis at $\psi = 1 - g$; the lines for $g = 0$, $g = 0.5$, and $g = 1.0$ are drawn in figure 4.

Isothermal solidification in the diagram of figure 4 follows a vertical "path". For example, in the simple case of a liquid droplet solidifying without supercooling ($T = T_M$, $\theta = 0$), "path" A is followed from $\psi = 1.0$, $g = 0$ to $\psi = 0$, $g = 1.0$ where the droplet is completely solid. A horizontal "path" represents adiabatic solidification without any external heat extraction. If a liquid droplet is supercooled to the temperature T_H ($\theta = -1.0$), an amount of enthalpy equivalent to the heat of fusion is withdrawn prior to nucleation, and the droplet can then solidify adiabatically along "path" B. In general, the critical hypercooling temperature, T_H , of a pure metal is defined by:

$$\int_{T_H}^{T_M} \kappa_L dT = \Delta H_M \quad (7)$$

A pure metal droplet is then said to be hypercooled when its temperature at nucleation, T_N , is equal to or less than T_H ($\theta_N \leq -1.0$).

When nucleation is suppressed below the melting temperature T_M , but not into the hypercooled region, the system can follow an intermediate "path" such as C in figure 4, starting at the nucleation temperature $-1 < \theta_N < 0$ on the liquid ($g = 0$) line and ending at some point on the solid ($g = 1$) line. Two heat-flow regimes are identified when the thermal history follows "path" C. The first is a "rapid solidification" stage accompanied by recalescence, where the supercooled droplet absorbs most of the liberated heat of fusion, and external heat extraction from the droplet surface plays a relatively minor role. For the case at hand (Newtonian model), no distinction is made between the interfacial temperature and the remainder of the solidifying droplet. Near-adiabatic solidification exhausts the available supercooling and the partially solid droplet continues to solidify at a much reduced rate dg/dt on a near isothermal (vertical $\psi - \theta$) "path." This slower solidification stage is predominantly controlled by the rate of heat extraction through the droplet surface.

For the Newtonian model, the thermal history and the smooth-front interfacial velocity of a single nucleus formed at the droplet surface are only functions of the nucleation temperature θ_N and the dimensional ratio K/Bi [11]. K is a dimensionless interfacial kinetic coefficient defined as:

$$K = (r_o \alpha_L)(\Delta H_M/\kappa_L) K_M \quad (8)$$

where r_o = droplet radius,
 α_L = thermal diffusivity of liquid;

$$Bi = (r_o/k_L)/(1/h),$$

(9)

where k_L = thermal conductivity of liquid, and

h = heat transfer coefficient at droplet/environment interface.

Bi , the Biot number, is the ratio of resistance to heat flow inside the droplet to that at the droplet/environment interface. Thus, the K/Bi parameter is a measure of the degree of predominance of the recalescence rate over the rate of heat loss to the environment.

Figure 5 shows the effect of initial supercooling, θ_N , on the $\psi - \theta$ "path" for $K/Bi = 100$ [11]. This value corresponds to a relatively low interfacial kinetic coefficient ($K_M = 2 \text{ cm s}^{-1}\text{K}^{-1}$) and a very high rate of external heat extraction ($h = 2 \times 10^5 \text{ W m}^{-1}\text{K}^{-1}$) from aluminum droplets [11]. The

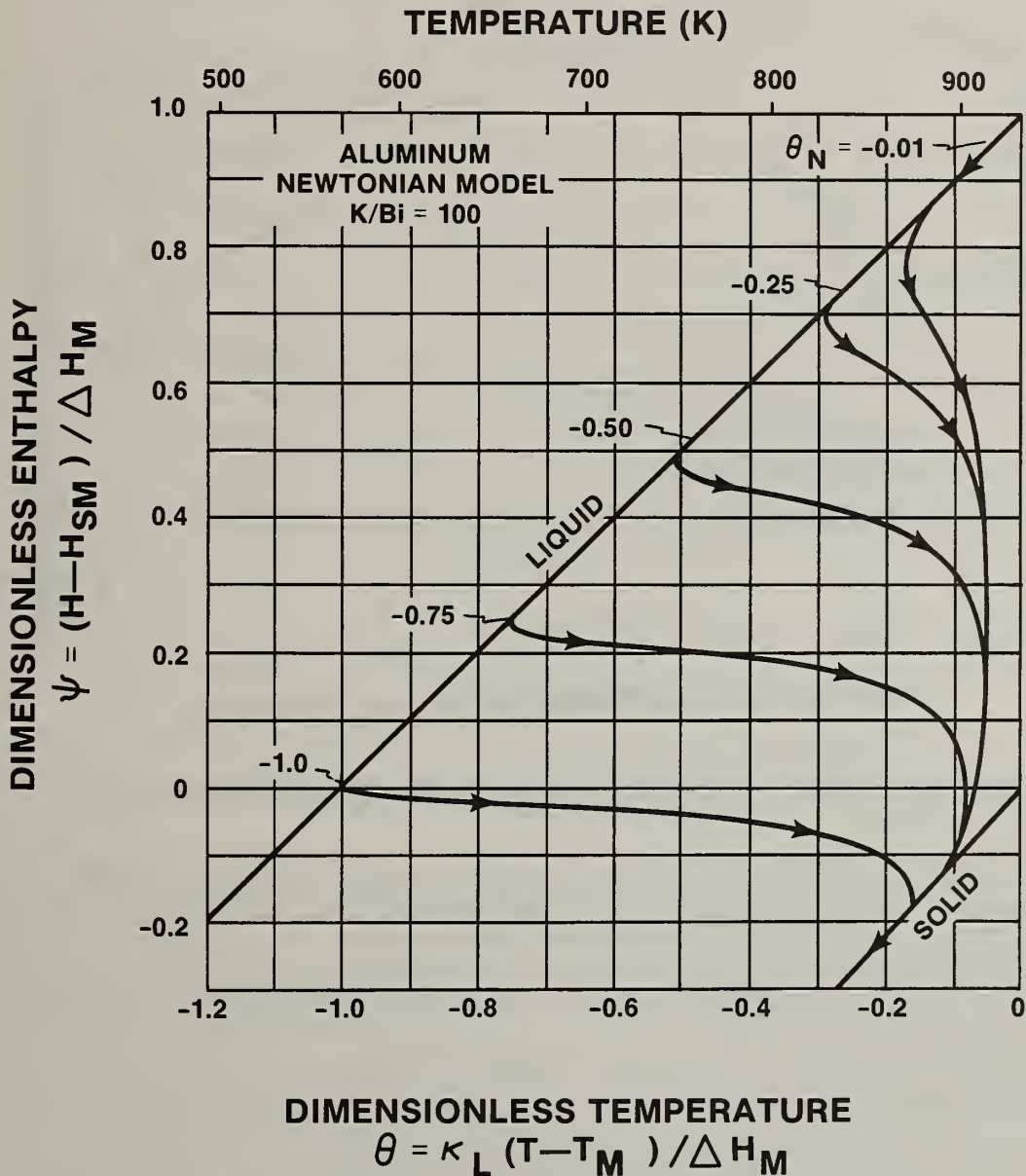


Figure 5 Calculated enthalpy-temperature curves for the solidification of aluminum droplets after different degrees of supercooling over the range of $\theta_N = -0.01$ to -1.0 . Newtonian heat flow is assumed; the ratio $K/Bi = 100$ corresponds to extremely rapid cooling conditions for atomized aluminum droplets [11].

curves demonstrate that as the supercooling prior to nucleation increases, so does the extent of adiabatic solidification; this manifests itself in flatter $\psi - \theta$ curves and larger fractions of solid at the end of recalescence. The same trend is observed when the K/Bi ratio is raised for a given initial supercooling θ_N . An increase in K/Bi signifies faster interfacial kinetics or increased solid/liquid interfacial area (i.e., increased number of nucleation events or dendritic vs smooth-front solidification), and a corresponding decrease in the contribution made by the external heat extraction (i.e., more adiabatic solidification during recalescence). Figure 6 illustrates this trend; here a factor $2r_0/d_{MX}$ is introduced to represent multiple nucleation events (d_{MX} is the mean distance between adjacent nuclei). Starting with a K/Bi ratio of 50 and a single nucleus, the successive curves indicate the thermal histories of droplets with 1, 8, 64, and 1000 nucleation events, respectively [11]. It is important to note that with increasing number of nuclei, the distances over which temperature gradients occur decrease from r_0 to $d_{MX}/2$, thus improving the validity of the Newtonian approximation.

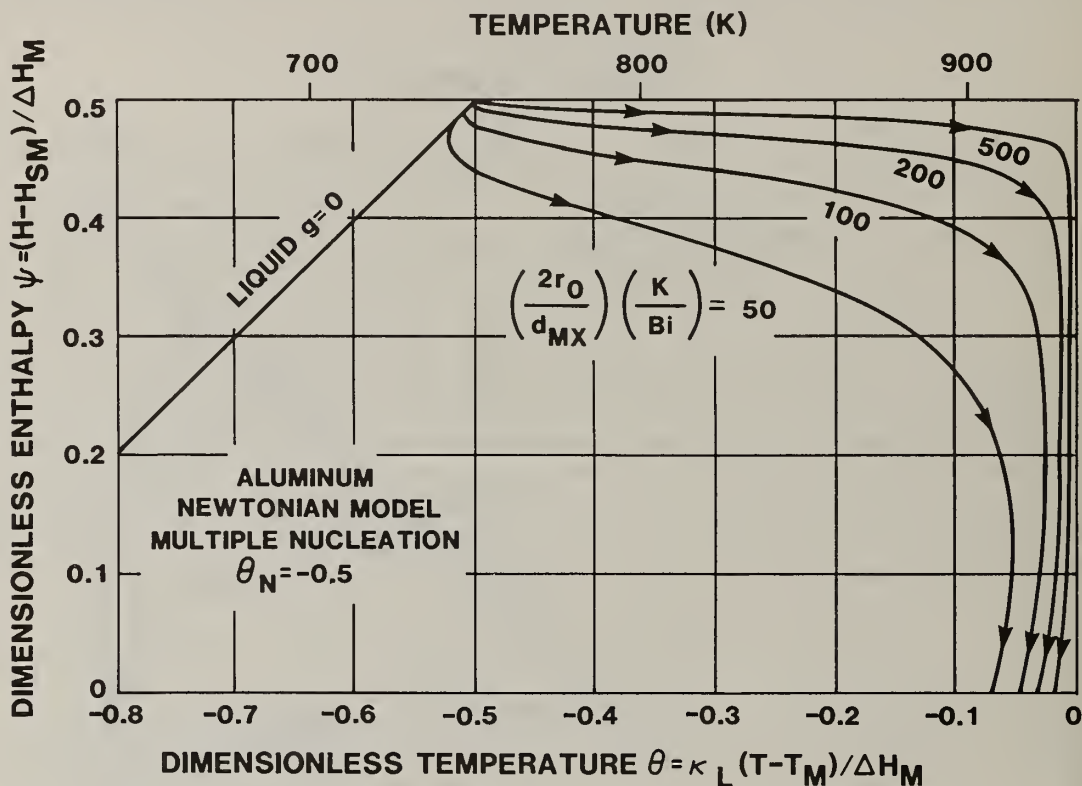


Figure 6 Effect of the number of nucleation events on the thermal history of supercooled droplets solidifying under Newtonian conditions [11].

For the case of one or a few nucleation events, the Newtonian assumption becomes invalid when substantial supercooling prior to nucleation is achieved--the local recalescence of the interface is likely to be faster than the overall recalescence of the droplet. In the extreme, when the rates of interfacial rearrangement processes are high, the crystal growth into the bulk supercooled liquid approaches the "heat transport limited" regime. In a recent paper, Coriell and Turnbull [2] estimated interfacial kinetic coefficients as high as $K_M = 200 \text{ cm s}^{-1}\text{K}^{-1}$ for growth of pure nickel dendrites into bulk supercooled melts. This kinetic coefficient was based on the speed of sound in liquid nickel which establishes an upper bound for the collision frequency of atoms from the liquid to the interface.

Figure 7 shows calculated [11] temperature profiles, at discrete fractions of solid, along the growth axis of a $10 \mu\text{m}$ droplet supercooled to $\theta_N = -0.5$. Substantial temperature gradients in the liquid, in front of the interface, are evidenced even for as low an interfacial kinetic coefficient as $K_M = 2 \text{ cm s}^{-1}\text{K}^{-1}$. The corresponding calculated interfacial profiles and velocities are illustrated in figure 8 along with two other droplet sizes of $1 \mu\text{m}$ and $100 \mu\text{m}$ in diameter [11]. In all

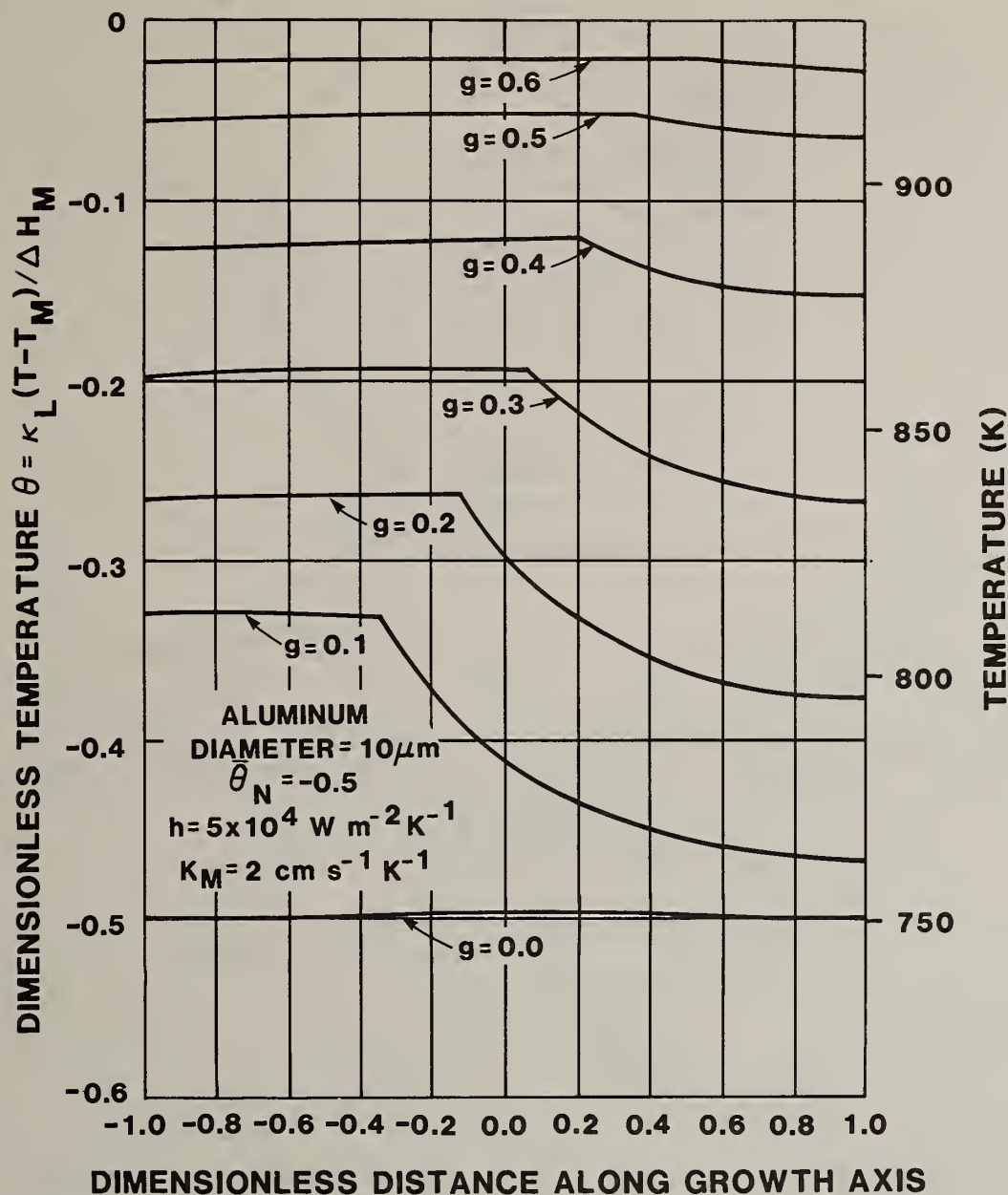
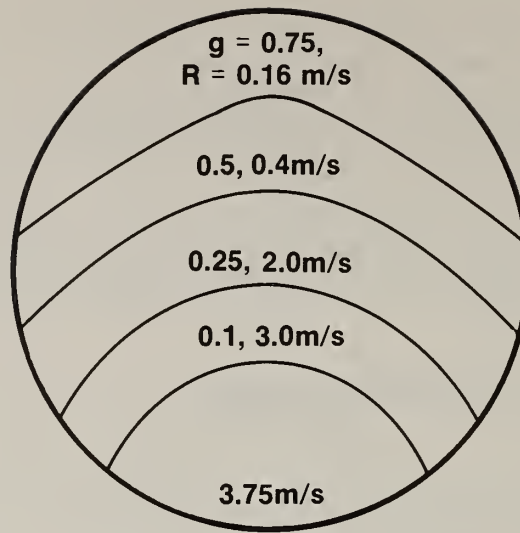


Figure 7 Thermal profiles developed in a supercooled aluminum droplet during solidification from a single nucleation event at the droplet surface [11].

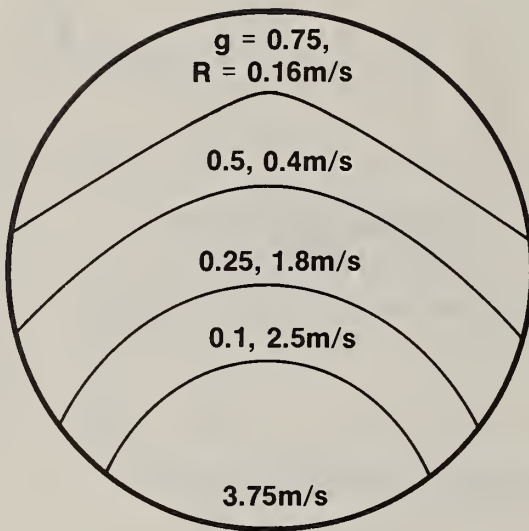
three sizes, the interfacial velocity (R) decreases with increasing fraction solid (g) due to recalescence as expected, but remains substantially faster than the highest values of ~ 0.1 to 0.27 m s^{-1} reported for the case of no supercooling in table II.

Figure 9 presents calculated [11] interfacial velocities as a function of fraction solid for different initial supercoolings. R is larger than 1.5 m s^{-1} throughout the solidification (recalcescence) process when the droplet is hypercooled ($\theta_N \leq -1.0$) prior to nucleation.

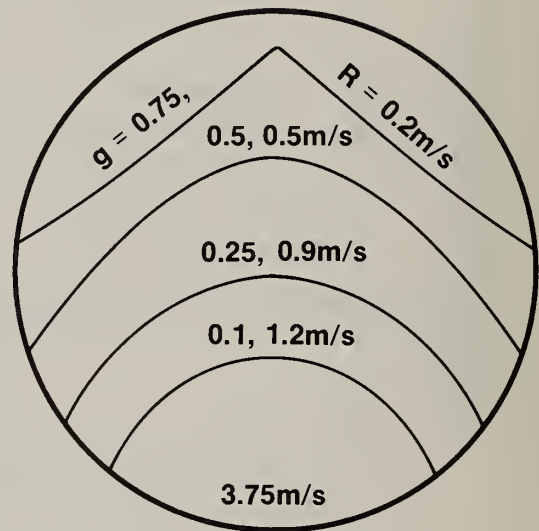
For the non-Newtonian cases noted above, the enthalpy/temperature curves are evaluated in terms of the weighed averages of ψ and θ over the entire droplet. The thermal history can no longer be expressed just in terms of θ_N and K/Bi , but depends on the particular values of droplet diameter, interfacial kinetic coefficient, and heat-transfer coefficient at the droplet surface. Figure 10 indicates how increasing the droplet size shifts the $\psi - \theta$ curve away from the Newtonian case [11]. Interfacial recalescence introduces large temperature gradients, especially in the coarser particles.



a. DIAMETER = 1 μm



b. DIAMETER = 10 μm



c. DIAMETER = 100 μm

$\bar{\theta}_N = -0.5$	$K_M = 2 \text{ cm s}^{-1} \text{ K}^{-1}$
$K/Bi = 400$	$h = 5 \times 10^4 \text{ Wm}^{-2} \text{ K}^{-1}$

Figure 8 Interfacial positions and velocities as a function of fraction solidified (g) for three sizes of atomized aluminum droplets, supercooled to $\bar{\theta}_N = -0.5$. Calculations based on non-Newtonian heat-flow model [11].

Locations far removed from the interface are not influenced by the heat released at the interface, and may even cool slightly below their original supercooling temperature due to heat extraction by the surroundings. It can be postulated that the larger particles maintain these supercooled regions for longer times, and are therefore better candidates for multiple nucleation events.

Increasing the interfacial kinetic coefficient (K_M) increases the growth velocity, interfacial recalescence rate, and temperature gradients. Figure 11 shows calculated [11] temperature profiles

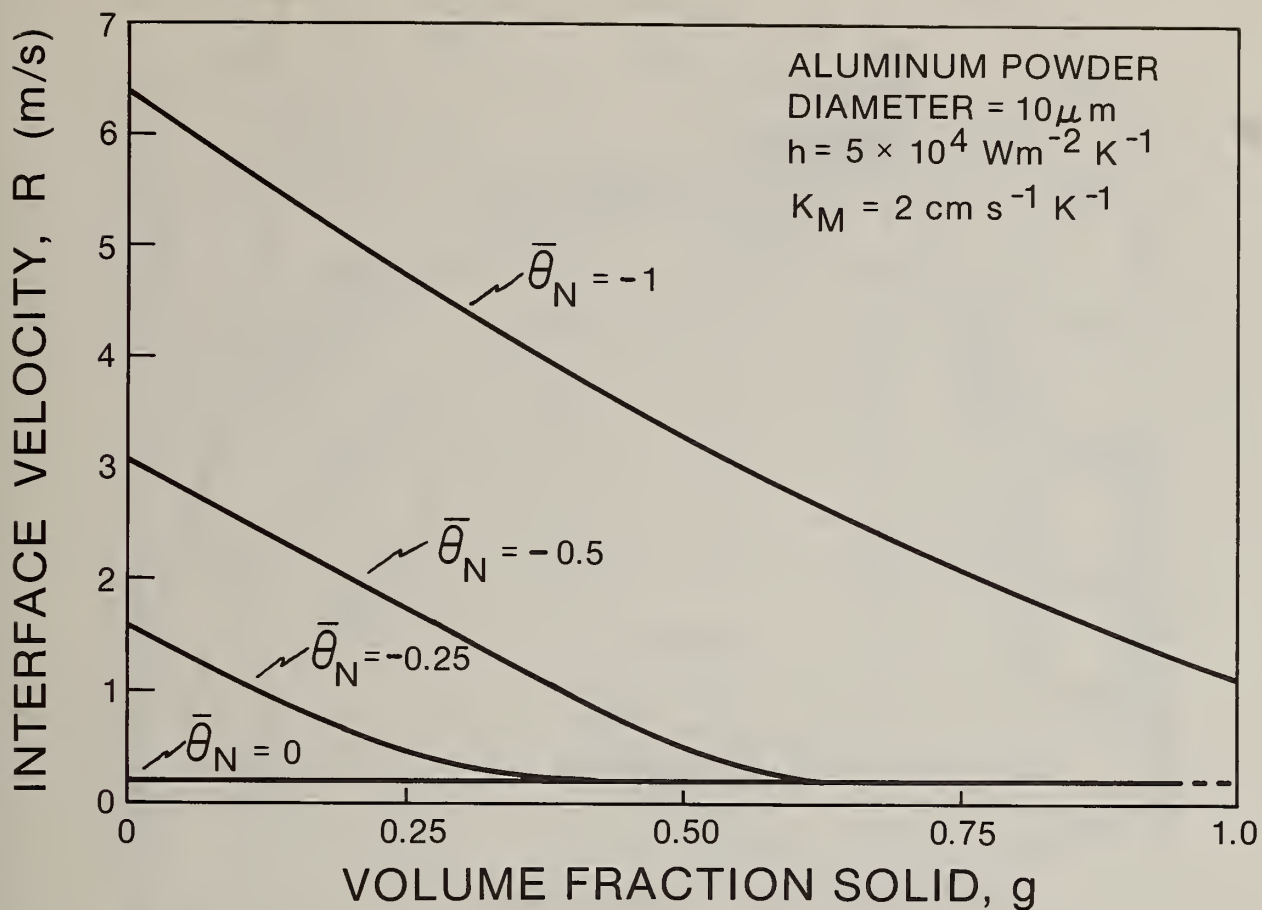


Figure 9 Calculated interfacial velocities (R) as a function of volume fraction solidified (g) for different initial average supercoolings ($\bar{\theta}_N$).

in 1 and $10 \mu\text{m}$ diameter droplets at $g = 0.1$. Increasing the kinetic coefficient from 2 to $50 \text{ cm s}^{-1} \text{ K}^{-1}$ increases the maximum temperature difference inside a $1 \mu\text{m}$ droplet from 7 to 82 K, and in a $10 \mu\text{m}$ droplet from 52 to 154 K, both for an initial average supercooling of 182 K ($\bar{\theta}_N = -0.5$) [11]. The larger interfacial kinetic coefficient is in line with current estimates for "heat transport limited" growth into bulk supercooled melts [2]. Again, note the near-absence of temperature gradients in the solid compared to the large negative gradients in the liquid. The influence of K_M on interfacial velocities is given in table III. For high interfacial rearrangement processes ($K_M = 50 \text{ cm s}^{-1} \text{ K}^{-1}$), the interfacial velocity (R) remains above 1 m s^{-1} for over half of the solidification process. Minimum R values of $\sim 0.14 \text{ m s}^{-1}$ are calculated after the loss of bulk supercooling at which time interfacial velocities are controlled by the rate of heat extraction from the droplet surface. The data in figure 9 and table III illustrate that in atomized droplets the supercooling prior to nucleation is perhaps the only realistic way of achieving interfacial velocities necessary for partitionless solidification.

Extension of the above kinetic considerations to the solidification of alloy (in contrast to pure metal) droplets requires a brief description of thermodynamic restrictions on partitionless solidification. Consider the binary phase diagram in figure 12. The diagram includes metastable extensions of the solidus α/L and liquidus L/α curves (dashed lines), and the $T_0^{L/\alpha}$ curve for partitionless solidification. The $T_0^{L/\alpha}$ curve is the locus of temperatures and compositions where the α -solid and liquid have the same free energy. Partitionless solidification to a crystalline solid can only occur at temperatures below this curve. A liquid solution, such as C_0' , C_0'' , and C_0''' , can solidify to the α -phase of the same composition if the interfacial temperature lies below the $T_0^{L/\alpha}$ curve. Kinetic considerations also require interfacial velocities in excess of the diffusive velocity of the solute in front of the interface; otherwise partitioning will occur in the

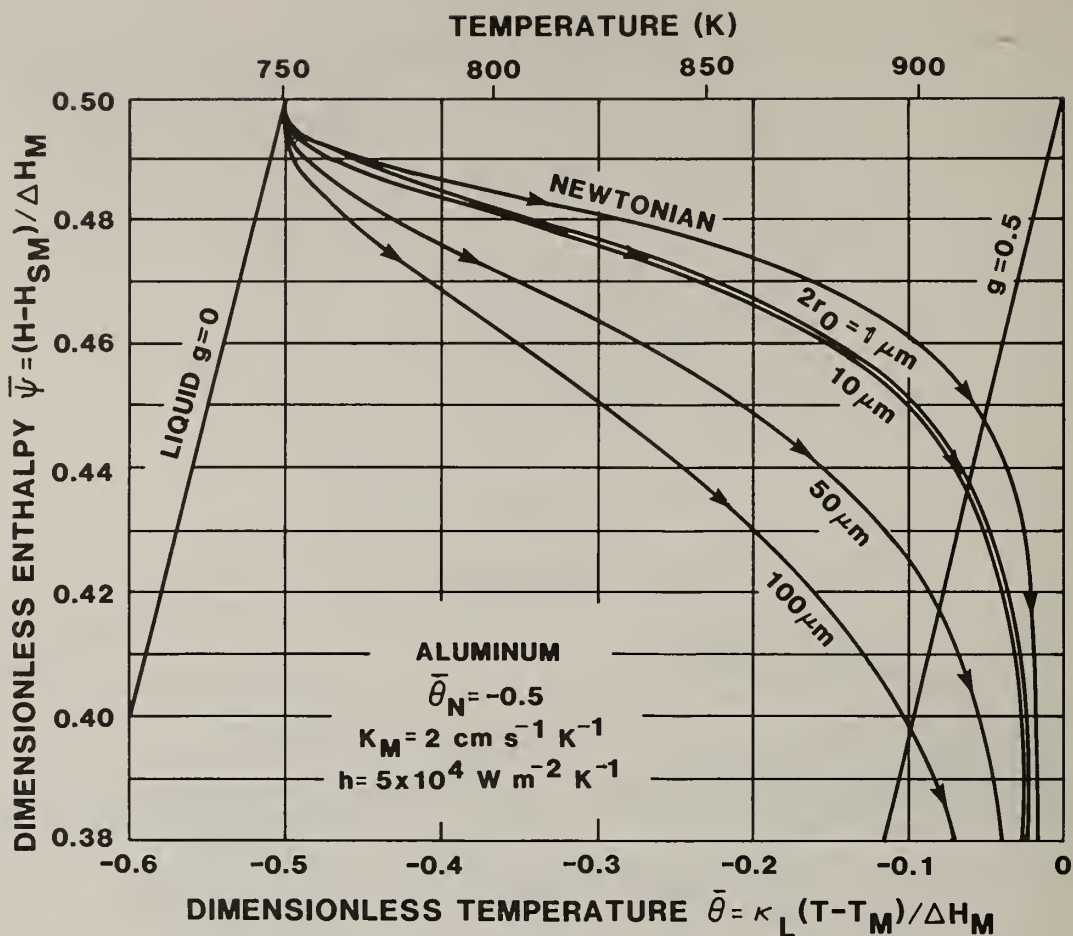


Figure 10 Departure from Newtonian thermal history as droplet size increases. Note that dimensionless enthalpy and temperature are now averaged over the entire droplet [11].

Table III. Effect of Kinetic Coefficient on Interfacial Velocity, $R(\text{m s}^{-1})$; from Reference (11).

Fraction Solid, g	$K_M (\text{cm s}^{-1} \text{K}^{-1})$		
	2	8	50
0.1	2.4	6.4	14.6
0.3	1.5	4.0	10.1
0.5	0.41	0.64	1.3
Minimum Velocity	0.14	0.14	0.12

Particle Diameter $10 \mu\text{m}$, $\bar{\theta}_N = -0.5$, $h = 5 \times 10^4 \text{ W m}^{-2} \text{K}^{-1}$

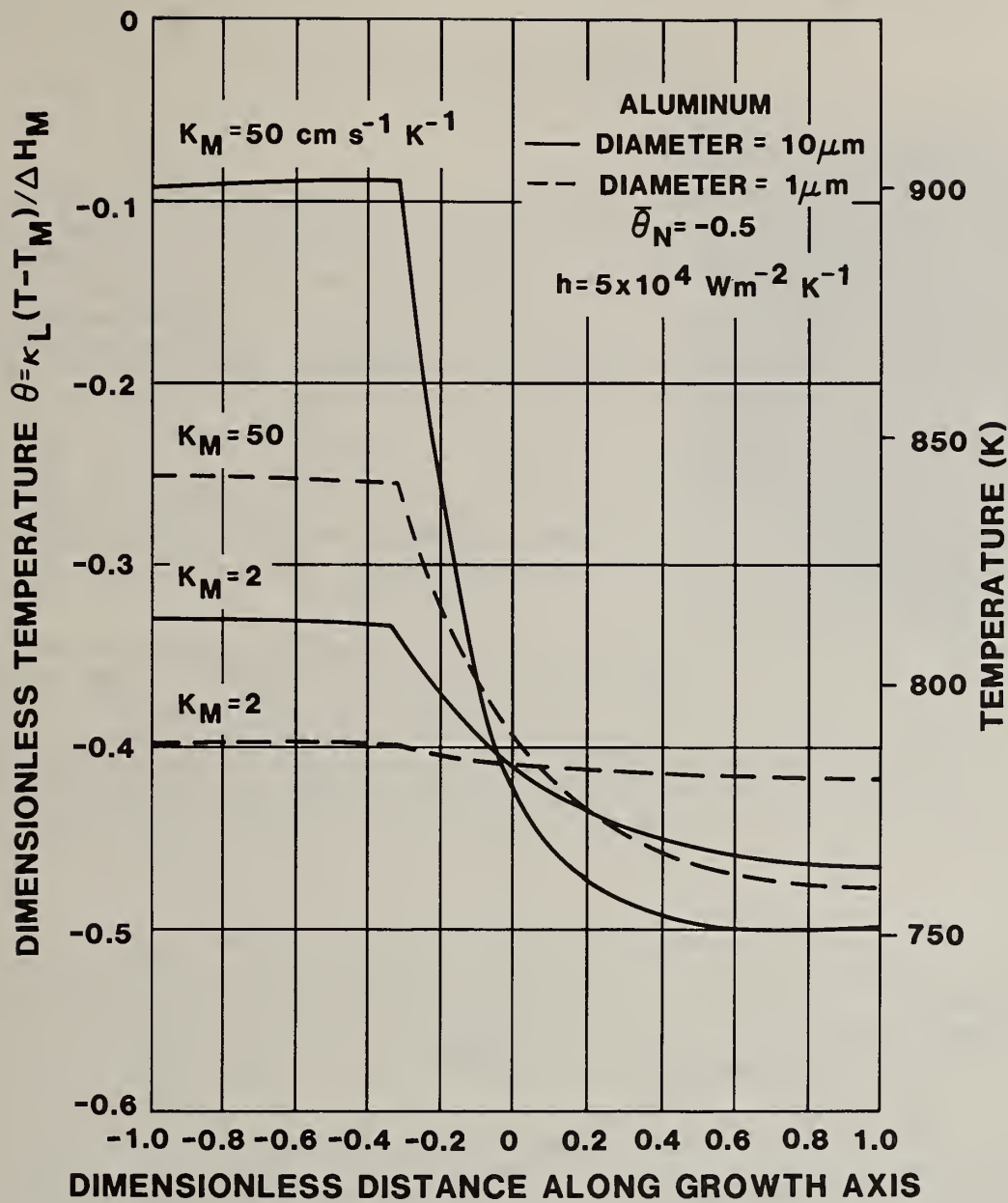


Figure 11 Temperature profiles during solidification of supercooled droplets, at a constant fraction solid $g = 0.1$, for two droplet sizes and two values of the interfacial kinetic coefficient K_M [11].

stable or metastable two-phase ($\alpha + \text{liquid}$) region. Calculations presented earlier show that these two conditions can be met in significantly supercooled droplets. The alloy C_0'''' cannot be supercooled below the $T_0^{L/\alpha}$ curve and so partitionless solidification to the α -phase is thermodynamically forbidden in this instance.

The degree of supercooling required to achieve complete partitionless solidification of an alloy system must be such that the growth velocity will remain sufficiently fast to avoid solute partitioning despite the rising interfacial temperature due to the evolving heat of fusion. Once solidification sets in after supercooling, both the degree of supercooling and resulting interfacial velocity will decrease progressively because of the attendant recalescence. Accordingly, during this process, the growth rate may fall below that needed for complete solute trapping at some temperature, T_C , where $T_C < T_0^{L/\alpha}$. In other words, the entire solidification will be partitionless if the interfacial temperature remains below T_C . Hence, complete solute trapping (massive solidification) requires an initial supercooling temperature, T_N :

$$\int_{T_N}^{T_C} \kappa_L dT \geq \Delta H_M \quad (10)$$

Experimental observations on fine (less than $1 \mu\text{m}$ diameter) electron-transparent powders of Al-4.5 wt.% Cu and Al-6 wt.% Si alloys confirm the above concepts [10]. The segregated cellular structures in figure 13 are evidence that this Al-4.5 wt.% Cu alloy particle solidified in a more-or-less conventional manner. Solidification was probably initiated at $T_N = T_L$ ($\theta_N \sim 0$), with interfacial breakdown soon thereafter due to constitutional supercooling. The thermodynamic conditions at the solid/liquid interface, i.e., temperature and composition, would seem to have corresponded fairly closely to those dictated by the equilibrium phase diagram. It appears that solidification occurred over the temperature range $T_L \leq T \leq T_E$ with the solid and liquid compositions and temperatures at the interface following the liquidus and solidus lines, respectively.

Figure 14 shows the Al-rich corner of the Al-Si binary phase diagram. The diagram includes metastable extensions of the solidus and liquidus lines as well as the $T_0^{L/\alpha}$ curve. Figures 15 and 16 show two particles of Al-6 wt.% Si alloy that solidified with different degrees of initial bulk supercooling: $T_N \sim 664 \text{ K}$ ($\theta_N \sim -0.5$), and $T_N < 482 \text{ K}$ ($\theta_N < -1.0$).

The micrograph of figure 15 suggests that region A underwent partitionless solidification while both the interface and the average droplet temperature θ recalesced up to T_C along the vertical line shown in this figure. During this stage, the solidification evidently proceeded with a smooth-front morphology, and the entrapped solute precipitated out subsequent to solidification on cooling to room temperature. The reported [10] crystallographic relationship between the precipitates and the matrix supports this observation. Region B corresponds to a solute-poor precipitation-free zone, which delineates the smooth interface at a stage when the interfacial velocity had slowed down to the point

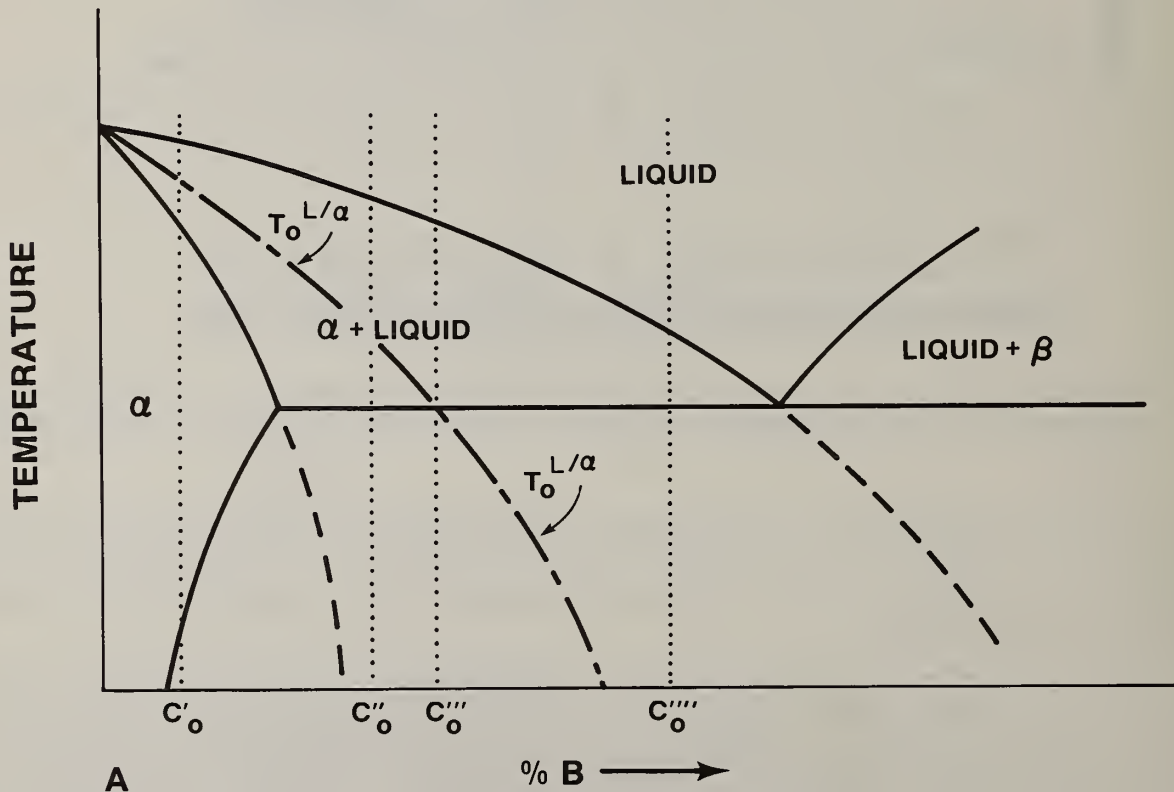


Figure 12 A schematic binary phase diagram, showing the $T_0^{L/\alpha}$ curve where liquid and α -solid solutions of the same composition have the same free energy. The metastable extensions of the solidus and liquidus lines are also shown. Alloy C''''_0 does not have a $T_0^{\alpha/L}$ temperature.

NO SUPERCOOLING

TEMPERATURE

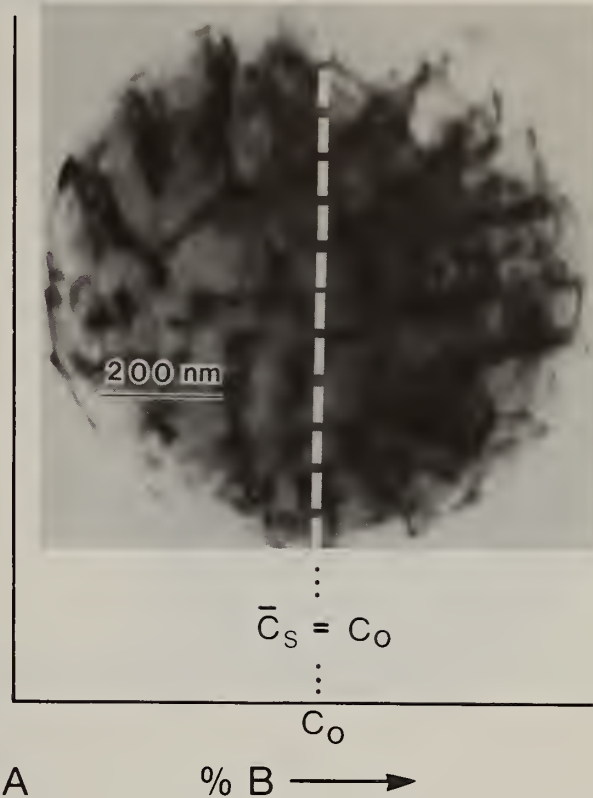
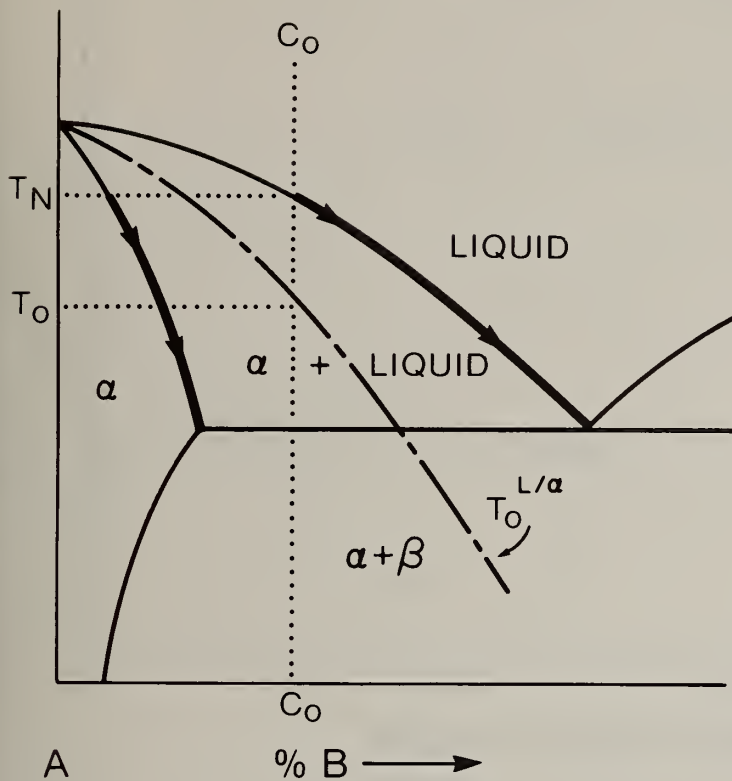


Figure 13 Schematic phase diagram of Al-Cu system and electron-transparent micrograph of a rapidly solidified Al-4.5 wt.% Cu submicron droplet. The cellular (segregated) structure in the particle resulted from nucleation at $T = T_L$ (no supercooling) with interfacial breakdown due to constitutional supercooling. Liquid and solid compositions at the interface followed the "paths" shown on the phase diagram. The micrograph is from reference [10].

that solute partitioning set in, although the velocity was high enough to maintain morphological stability. Solute was rejected ahead of the solidification front as the solid and liquid composition at the interface moved up along the dashed "path" in the phase diagram to a maximum recalescence temperature T_R . In region C the further reduction in growth rate rendered the interface unstable, and cellular solidification then took place with segregation of silicon to the cell walls. The postulated solidification "path" at the interface(s) is noted by arrows in figure 15. The calculated thermal profiles in figures 7 and 11 show little or no thermal gradients in the solid during recalescence. It is conceivable that some of the supersaturated solid behind the interface could have been heated above its $T_0^{L/\alpha}$ temperature. However, even if this were the case, no remelting seems to have occurred due to the short times available. Remelting after recalescence has been observed in larger dendritically solidified particles where heat-flow conditions were more sluggish [12]. Finally, the smaller droplet in figure 16 was probably supercooled sufficiently so that complete partitionless solidification prevailed during the recalescence.

Figure 17 presents an SEM view of a large ($\sim 500 \mu\text{m}$ in size) powder particle of a maraging 300 steel alloy. The corn-on-the-cob dendritic structure emanating from a nucleation point on the top surface at the top right-hand corner is fairly characteristic of structures observed in large complex alloy powders [13]. There is also evidence that a substantial number of droplets like the one in figure 17 were supercooled prior to solidification. The light etching in the center of the dendritic arms (figure 18) is evidence of high solute cores, which were verified by microprobe analysis [14]. This indicates some solute trapping early in the solidification process when the dendrites were growing into a bulk supercooled melt.

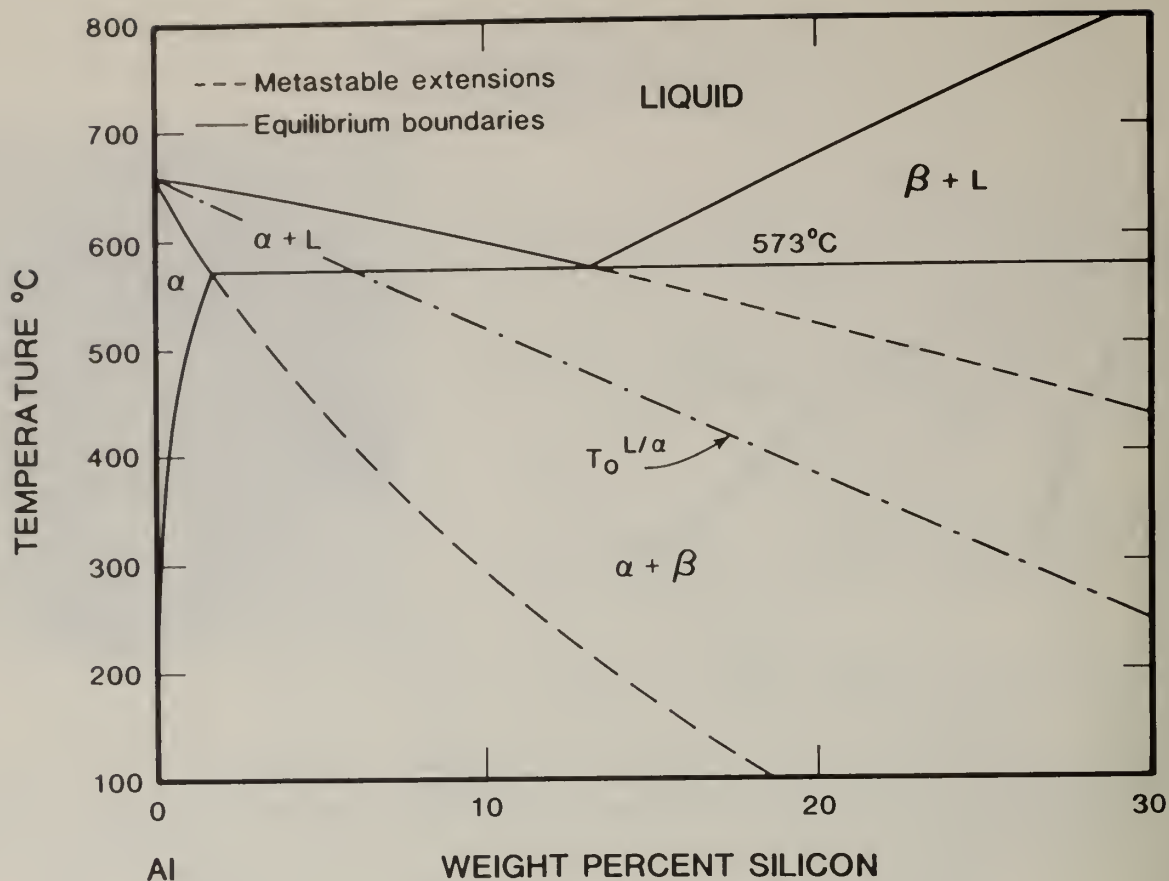


Figure 14 Al-rich corner of the Al-Si phase diagram, indicating the $T_0^{L/\alpha}$ curve and metastable extensions of the solidus and liquidus lines.

Figure 19 illustrates some calculated [11] growth fronts in large (1000 μm) diameter droplets of pure aluminum with and without initial supercooling. The overall interfacial shapes are concave toward the liquid in contrast to the case of the smaller particles shown in figures 8 and 19a where the interfaces are convex. In large-sized droplets, positive temperature gradients exist in the melt prior to nucleation, ~ 90 K in the 1000 μm particles of figure 19 [11]. Therefore, the solid growing along the symmetry axis faces a superheated liquid, whereas dendrites initially growing along the surface encounter a supercooled liquid as well as some external heat extraction. In the limit, the droplet can become rapidly covered with a solid "shell" after several nucleation events along its surface, and further solidification then proceeds in a fairly concentric pattern. Increasing K_M from 2 to 50 $\text{cm s}^{-1}\text{K}^{-1}$ magnifies the concavity of the interface, as in figure 19c.

Importance of Second-Phase Dispersions

The mode of solidification which we have referred to as partitionless (or massive) provides a pathway for obtaining especially fine dispersions of very stable second-phase precipitates. Such solidification, from its very nature, is synonymous with complete solute trapping of all the atomic species previously dissolved in the liquid state. In this manner, second phases which are highly insoluble in the solid matrix of the alloy system can be retained in solid solution, thus attaining exceptional degrees of supersaturation as a stepping-stone to subsequent precipitation in the solid state. These circumstances result in finer and more uniformly distributed dispersions than can be achieved when the second-phase precipitation occurs directly from the melt, i.e., as a part of the solute-partitioning type of solidification.

An interesting example of these phenomena is illustrated in figure 20, based on MnS dispersions in 303 (high-sulfur) stainless steel [15]. After conventional metallurgical practice, the MnS inclusions are on the order of 10 μm in size; however, after rapid solidification even with compositional partitioning, the size is reduced to about 0.1 μm (figure 20a), and after massive solidification,

$$\int_{T_N}^{T_C} \kappa_L dT < \Delta H_M$$

TEMPERATURE

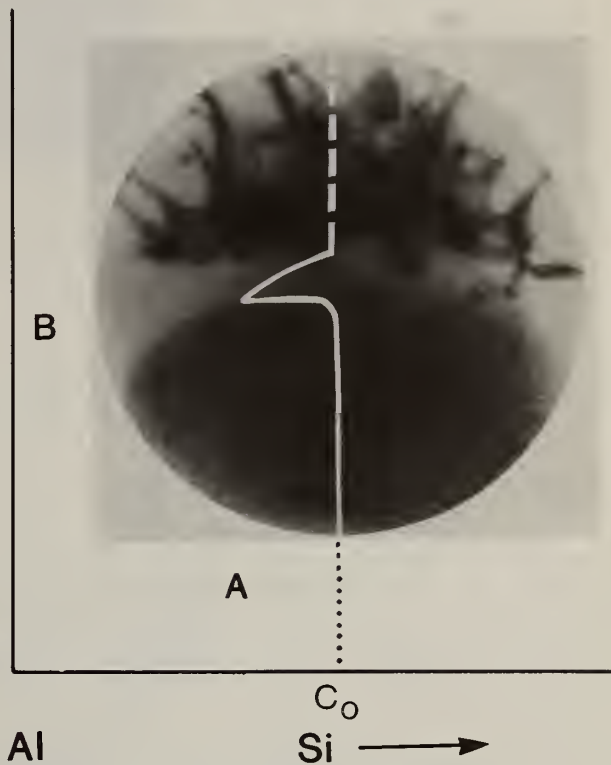
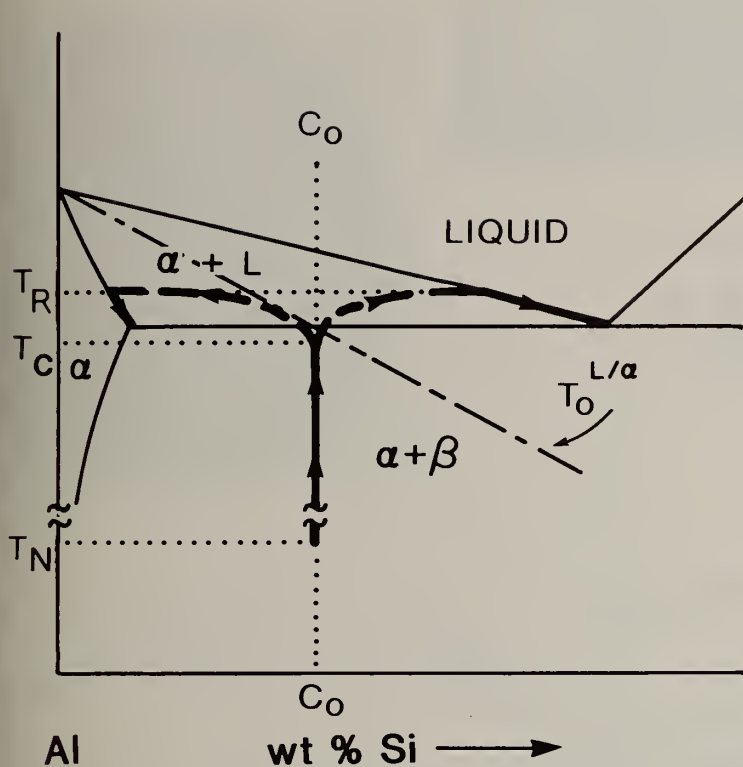


Figure 15 Schematic phase diagram of the Al-Si system showing the solidification "path" of the rapidly solidified Al-6 wt.% Si droplet illustrated on the right. The electron-transparent micrograph indicates three sequential modes of solidification. Region A is due to partitionless solidification during interfacial recalescence from T_N to T_C ; region B continued to solidify in a smooth-front mode with partitioning at the interface as suggested by solid and liquid compositions moving along the dashed lines to the liquidus and solidus phase boundaries; region C has solidified in the cellular mode due to onset of morphological instability with silicon precipitation at the cell walls. The micrograph is from reference [10].

there is a further refinement to about $0.01 \mu\text{m}$ (figure 20b). In the latter case, the MnS precipitation has taken place after the completion of solidification during the subsequent cooling to room temperature. Under more extreme conditions, as shown in figure 20c, the MnS precipitation can be suppressed entirely.

Such dispersions of relatively stable second-phase precipitates are very effective in pinning grain boundaries at elevated temperatures, and so they play a significant role in retarding grain growth during the hot consolidation of atomized powders as well as during later heat treatment. A relationship between the limiting grain diameter D which comes into interfacial-tension balance with the dispersed precipitates is given by [16]:

$$D = \frac{\pi}{6} \frac{\bar{d}}{f_v} \left(\frac{3}{2} - \frac{2}{Z} \right) \quad (11)$$

$$\int_{T_N}^{T_C} \kappa_L dT \geq \Delta H_M$$

**PARTITIONLESS
SOLIDIFICATION**

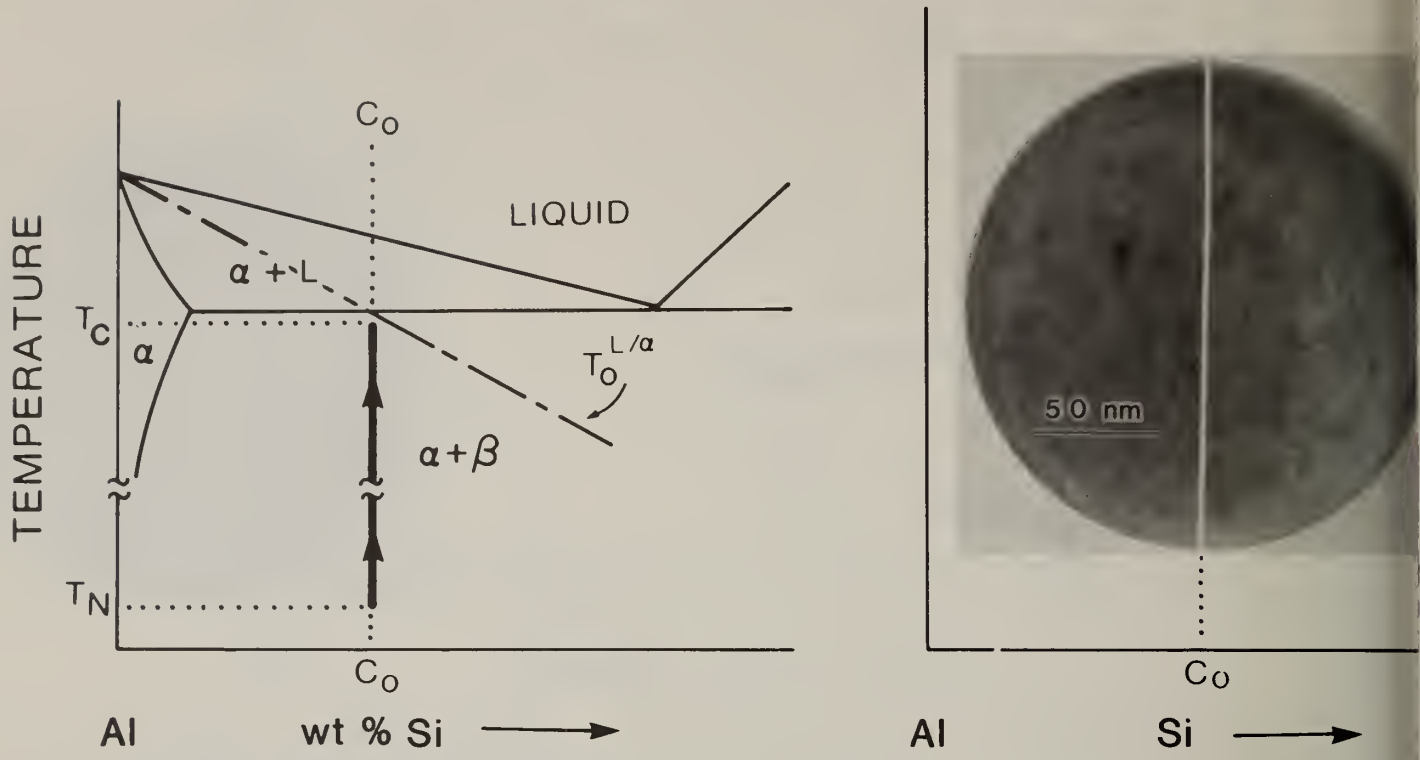


Figure 16 Schematic phase diagram of the Al-Si system showing the solidification "path" of a massively solidified Al-6 wt.% Si droplet illustrated on the right. Partitionless solidification occurred during recalescence from T_N to T_C . The micrograph is from reference [10].

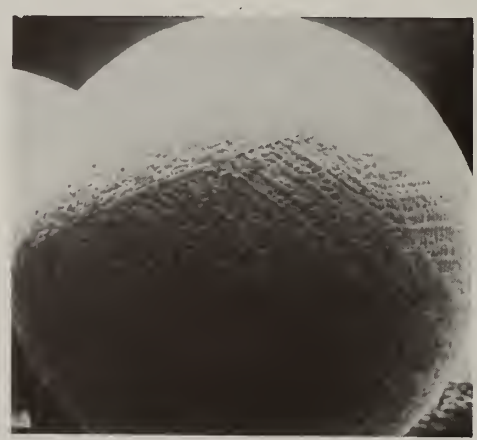


Figure 17 SEM view of a rapidly solidified maraging 300 steel alloy powder. Magnification 240 x. See text for details.

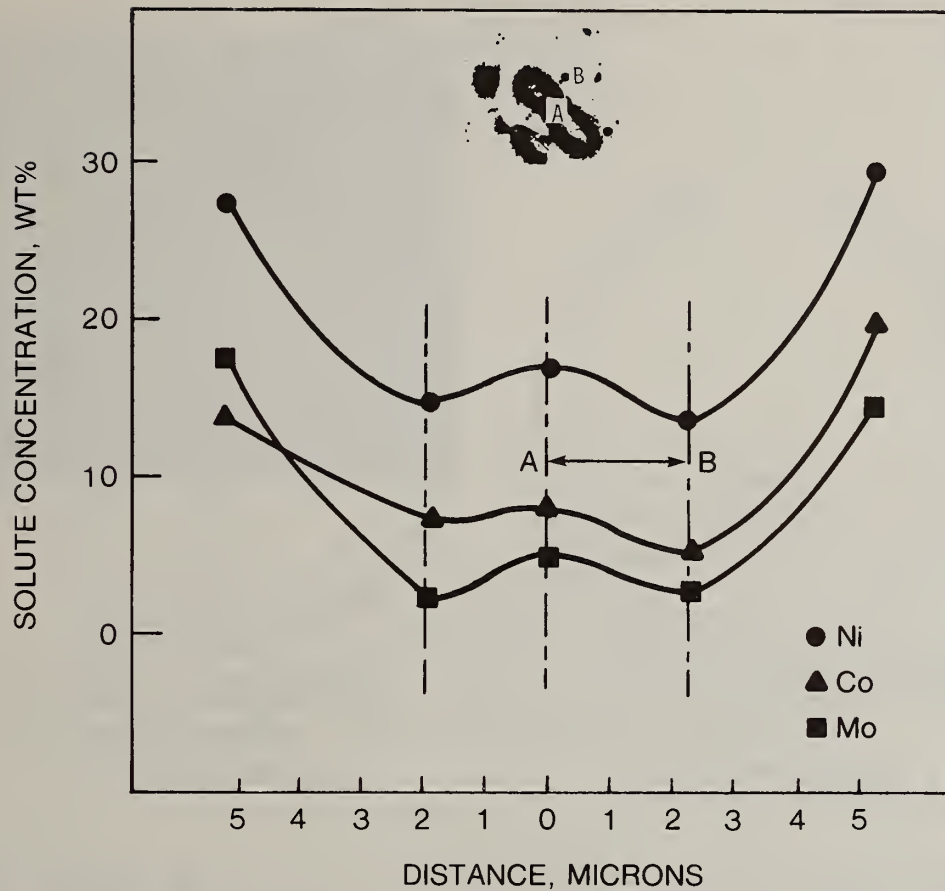
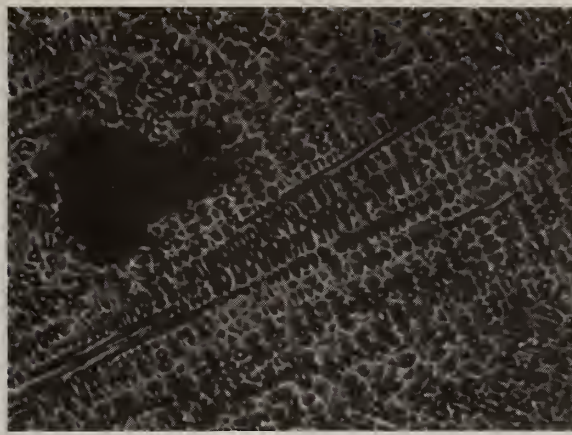
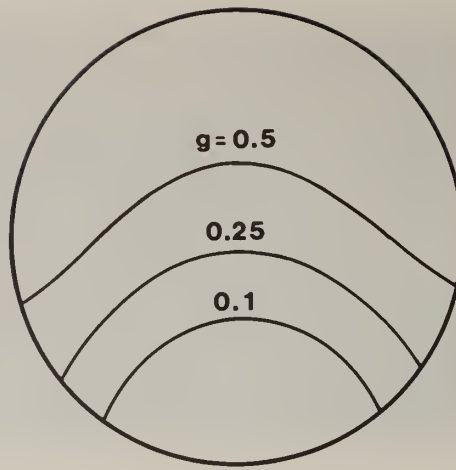


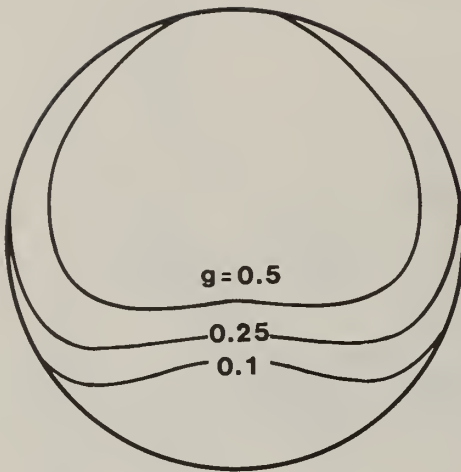
Figure 18 Photomicrograph and microsegregation in a supercooled powder particle of maraging 300 steel alloy. (a) Photomicrograph at 250X, (b) distribution of Ni, Co, and Mo concentrations measured at various points along the chosen microprobe path across a dendritic arm [14].

where \bar{d} = mean diameter of the precipitates,
 f_v = volume fraction of the precipitates, and
 Z^V = ratio of the largest to the mean grain diameter.

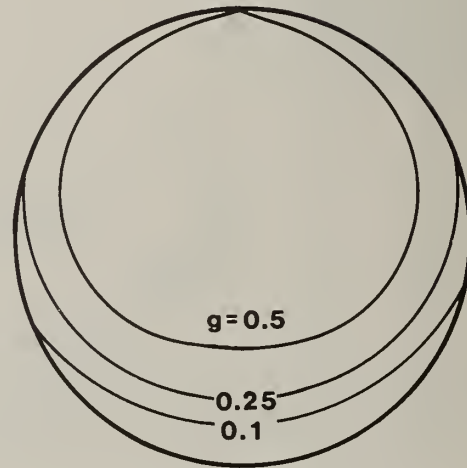
It is evident, then, that the pinned grain size is smaller, the smaller the precipitate size and the larger its volume fraction, both of which are favored by rapid solidification, and especially by partitionless solidification.



a) DIAMETER = $100\mu\text{m}$
 $\bar{\theta}_N = -0.25$
 $K_M = 2\text{ cm s}^{-1}\text{ K}^{-1}$



b) DIAMETER = $1000\mu\text{m}$
 $\bar{\theta}_N = -0.25$
 $K_M = 2\text{ cm s}^{-1}\text{ K}^{-1}$



c) DIAMETER = $1000\mu\text{m}$
 $\bar{\theta}_N = -0.01$
 $K_M = 50\text{ cm s}^{-1}\text{ K}^{-1}$

Figure 19 Interfacial positions as a function of fraction solidified (g) for two sizes of atomized aluminum droplets. Transition from concave to convex interfacial profiles is produced by increasing droplet size at a given initial supercooling and also by increasing the interfacial kinetic coefficient [11].

However, the \bar{d}/f_v ratio in eq. (11) tends to increase with increasing temperature because of precipitate coalescence (Ostwald ripening) and resolution in the solid matrix. The kinetics of coalescence can be expressed by [17]:

$$\bar{d}^3 - \bar{d}_0^3 = \frac{64 D_s C_s}{9 R T} \sigma V_p^2 t \quad (12)$$

where \bar{d}_0 = mean precipitate diameter at zero time,

D_s = diffusivity (in the solid-solution matrix) of the rate-controlling species,

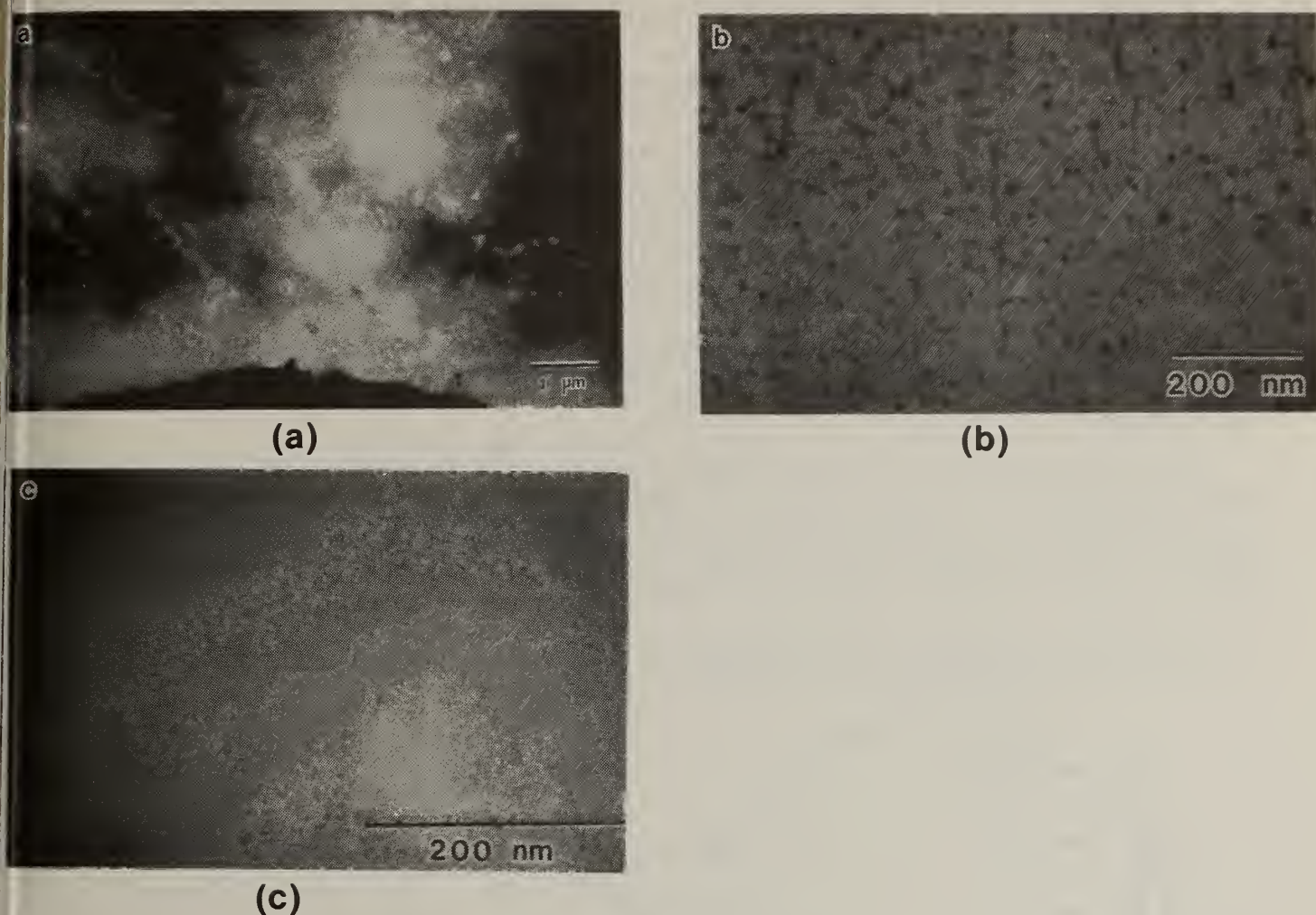


Figure 20 Electron transmission micrographs of centrifugally atomized high-sulfur 303 stainless steel, illustrating (a) cellular, and (b and c) massive solidification. (a) MnS dispersion in fcc matrix; precipitate formed as part of solidification process. Dark-field image. (b) MnS dispersion in bcc matrix; precipitate formed from solid solution after massive solidification. Bright-field image. (c) Bcc matrix after massive solidification, but with MnS precipitation suppressed. Bright-field image [15].

C_s = concentration (in the solid-solution matrix) of the rate-controlling species,

R_g = gas constant,

T = absolute temperature,

σ = specific interfacial energy,

V_p = molar volume of the precipitate phase, and

t = time at temperature T .

The rate-controlling species, e.g., M or X if the dispersed phase is taken as MX , is that for which the product DC is the smallest. Combining eqs. (11) and (12) yields a $t^{1/3}$ time dependence for grain coarsening when controlled by particle pinning of the grain boundaries. It turns out [18] that d is dominated by the initial precipitate size d_0 when $d_0 > 2(d^3 - d_0^3)^{1/3}$, and is dominated by precipitate coalescence when $d_0 < 2(d^3 - d_0^3)^{1/3}$.

Concomitantly, f_v of the dispersed phase MX is maximized if the alloy composition in M and X corresponds to the stoichiometric ratio of MX [18]. This condition guarantees that the kinetics of Ostwald ripening will be controlled by the slower diffusing species. The coarsening rate can be further diminished by using second phases of higher stability, i.e., having still lower solubility products relative to the solid-solution matrix; this serves to decrease the concentration C in eq. (12).

An example of the resistance to austenitic grain growth after rapid solidification is given in figure 21 for a 9Ni-4Co-0.2C steel [19]. Very little grain growth takes place in the rapidly solidified material up to 16 hours at 1100 °C, and even after coarsening sets in, the grain size remains very much smaller than in the conventionally processed steel. Such unusual grain-growth characteristics have been observed in a number of steels [20].

The fracture toughness of some ultrahigh-strength steels can be significantly improved by austenizing at relatively high temperatures, but other adverse effects may result from the attendant grain coarsening. On the other hand, with steels that are processed by rapid solidification, the resistance to grain growth should favor more attractive combinations of properties. An illustrative trend is shown in figure 22 for an 0.25C-4Mo martensitic steel after tempering at 150 °C [21]. In this instance, whether the steel is processed conventionally or by rapid solidification, both the sharp-crack and blunt-notch fracture toughness are enhanced by raising the austenitizing temperature. However, the influence of the difference in grain size is clearly manifested when the toughness testing is carried out at subzero temperatures, as plotted in figure 22c. The shelf energy and the ductile condition are maintained to much lower temperatures, comparing the rapidly solidified to the conventional materials, because of the small grain size retained in the former after high austenitizing treatments.

The fine dispersions of very stable phases, made possible by rapid solidification, also play a beneficial role in oxidation resistance. For those alloys which tend to form protective oxide films at high temperatures, the stable second-phase precipitates seem to improve the adherence of surface films via a keying action due to fine-scale interfacial penetration around the uniformly distributed particles [22]. An example of this favorable effect is shown in figure 23 for rapidly solidified Fe₃Al containing TiB₂ as the dispersed second phase [23].

Of course, all of these second-phase considerations, when applied to larger volume fractions, can lead to interesting possibilities with regard to dispersion strengthening.

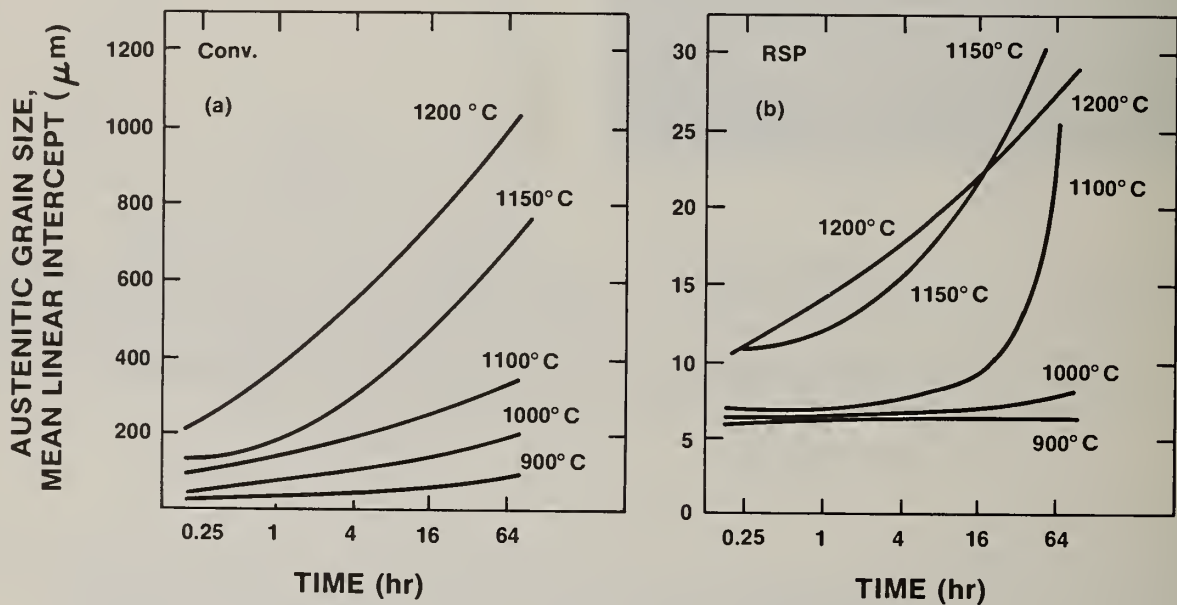


Figure 21 Grain-growth characteristics of 9Ni-4Co-0.2C steel (a) after conventional processing (normal ingot and hot-rolling practice) and (b) after rapid solidification processing. The latter involved centrifugal atomizing and consolidation by hot extrusion [19].

Closure

The fundamental modes of solidification have been described according to the morphological stability of the advancing growth front and the extent of solute partitioning at the interface. In the regime of cellular and dendritic morphologies, even with no appreciable supercooling, rapid cooling through the solidification range modifies the microstructure by refining the scale of the

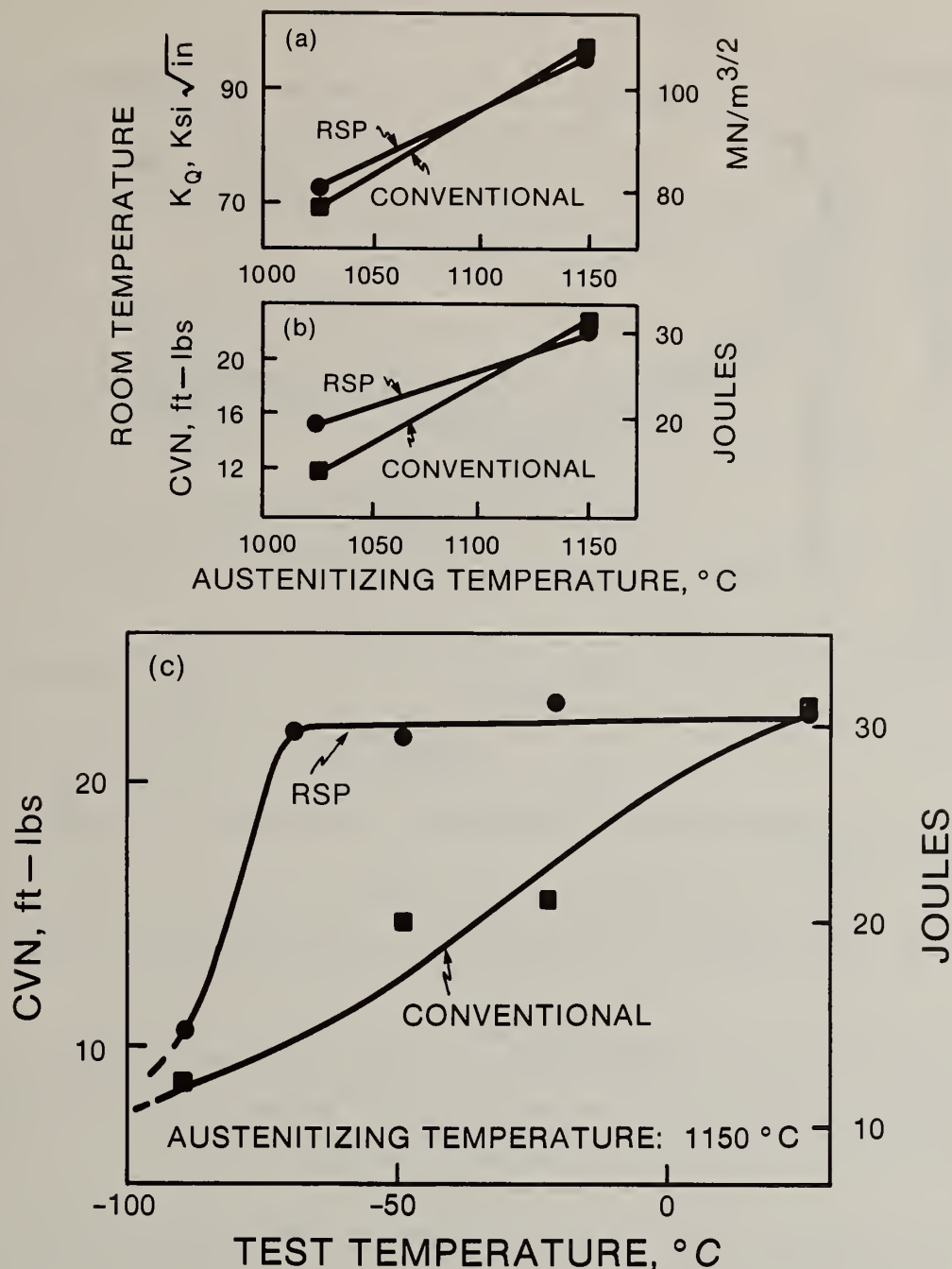


Figure 22 Fracture-toughness characteristics of conventionally processed and RSP 0.25C-4Mo steel; water quenched from austenitizing temperatures shown and tempered at 150 $^{\circ}\text{C}$ for 1 hr. (a) and (b) Effect of austenitizing temperature on room-temperature properties, and (c) effect of test temperature on fracture toughness after austenitizing at 1150 $^{\circ}\text{C}$. K_Q is the plane-strain fracture toughness based on the maximum load vs crack-opening displacement for a fatigue-precracked specimen in a slow-bend test [21].

microsegregated regions which result from solute partitioning; the accompanying dispersions of second-phase precipitates are also refined. Of further interest is the attainment of massive (partitionless) solidification via supercooling in which solute trapping is substantially complete. By this means, extremely high supersaturations relative to very stable phases are obtained which, in turn, can be precipitated subsequently from the solid matrix. The required conditions for massive solidification are both thermodynamic and kinetic; the interfacial temperature must be below $T_0^{L/\alpha}$, and the interfacial velocity must exceed the diffusive velocity to avoid solute partitioning.

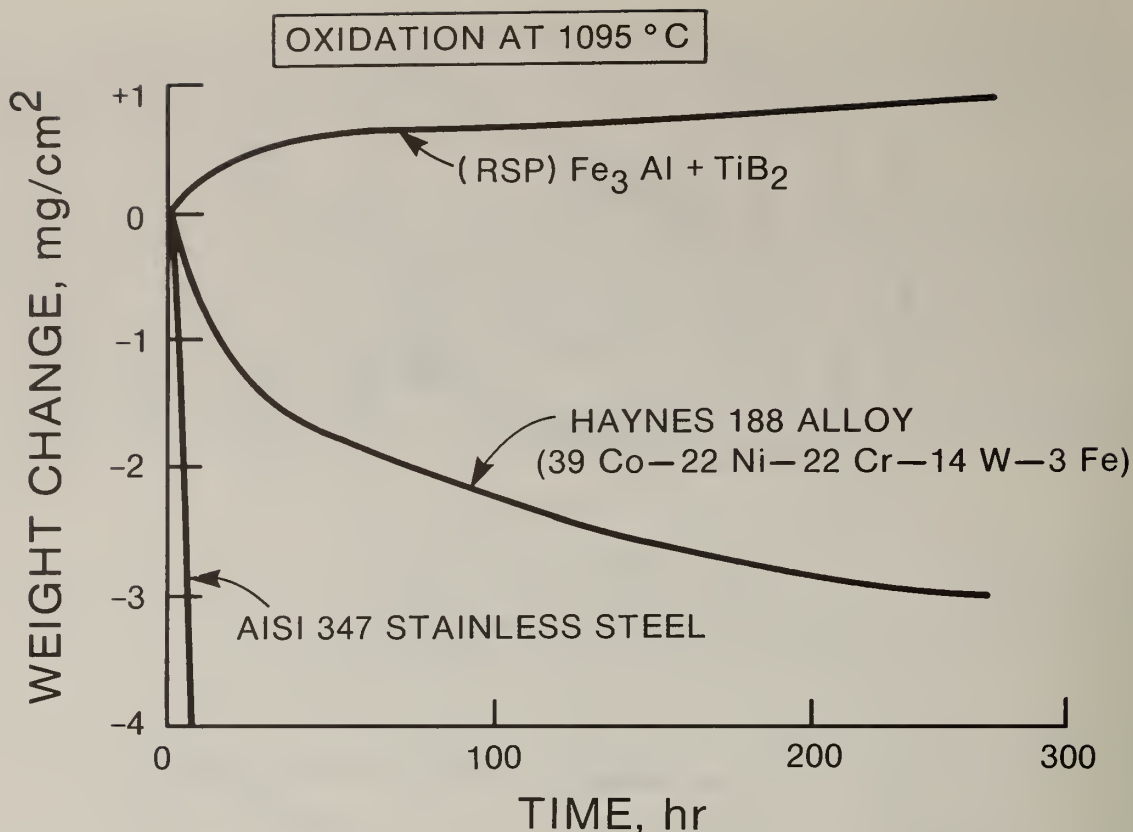


Figure 23 Effect of RSP and a dispersed second phase (TiB_2) on cyclic oxidation resistance of Fe_3Al at 1095 °C [23].

Stable second-phase dispersions resist coalescence on heating and so remain effective in pinning grain boundaries even at unusually high temperatures. Some consequences of these microstructural features have been discussed with respect to mechanical and oxidation behavior.

A proper definition of rapid solidification has still not been established. When dealing with cellular or dendritic modes of solidification, it is found that increased rates of cooling from the melt are beneficial because they lead to enhanced compositional uniformity and second-phase refinement. In this sense, cooling faster than about 200 K s^{-1} has been regarded as a rapid cooling rate inasmuch as significant changes in microstructure can thereby be obtained [1]. Nevertheless, cooling rates of 10^4 to 10^6 K s^{-1} are often sought for further benefits.

However, it is obvious that a cooling rate cannot be synonymous with a solidification rate. In connection with smooth-front solidification, as achieved by appropriate supercooling, the solidification rate can be identified with an interfacial velocity, at least for a given nucleation event. Under such circumstances, the interfacial velocity has further significance from the standpoint of affecting the degree of solute trapping. In the limiting case, to reach the highest levels of compositional uniformity and of stable second-phase refinement, a solidification growth rate commensurate with the diffusive velocity might be considered as rapid solidification, since this condition reflects substantial amount of solute trapping. In the present work which focuses on the solidification of atomized droplets, it appears that interfacial velocities greater than about 1 m s^{-1} might be regarded as "rapid solidification." Solidification rates of this magnitude are obtained more readily by supercooling than by rapid cooling per se without supercooling.

Acknowledgments

We wish to express our appreciation to several agencies who have sponsored various aspects of our respective research programs on rapid solidification: the Office of Naval Research under Contract No. N00014-81-K-0013 at the Massachusetts Institute of Technology; the National Bureau of Standards under Contract No. NB83NAHA4004 at the Massachusetts Institute of Technology; the Defense Advanced Research Projects Agency under DARPA Order Number 3751 at the National Bureau of Standards. Enlightening discussions with Drs. J. W. Cahn, W. J. Boettinger, and S. R. Coriell of the National Bureau of Standards are gratefully acknowledged.

References

- [1] M. Cohen, B. H. Kear, and R. Mehrabian, Proc. 2nd Intl. Conf. Rapid Solidification Processing: Principles and Technologies II, R. Mehrabian, B. H. Kear, and M. Cohen, eds., Claitor's Publishing Division, Baton Rouge, p. 1 (1980).
- [2] S. R. Coriell and D. Turnbull, Acta Metall. 30, 2135 (1982).
- [3] M. C. Flemings, Solidification Processing, McGraw-Hill Book Co., p. 60 (1974).
- [4] B. Chalmers, Physical Metallurgy, John Wiley, New York, p. 258 (1959).
- [5] S. R. Coriell and R. F. Sekerka, Rapid Solidification Processing: Principles and Technologies II, R. Mehrabian, B. H. Kear, and M. Cohen, eds., Claitor's Publishing Division, Baton Rouge, p. 35 (1980).
- [6] S. R. Coriell, private communication.
- [7] R. F. Sekerka, Crystal Growth: An Introduction, North-Holland Amsterdam, p. 403 (1973).
- [8] M. J. Aziz, J. Appl. Phys. 53, 1158 (1982).
- [9] W. J. Boettinger, S. R. Coriell, and R. F. Sekerka, these proceedings.
- [10] C. G. Levi and R. Mehrabian, Metall. Trans. A 13A, 13 (1982).
- [11] C. G. Levi and R. Mehrabian, Metall. Trans. A 13A, 221 (1982).
- [12] J. H. Perepezko, Y. Shiohara, J. S. Paik, and M. C. Flemings, these proceedings.
- [13] P. A. Joly and R. Mehrabian, J. of Mat. Sci. 9, 1446 (1974).
- [14] T. Z. Kattamis and R. Mehrabian, J. of Mat. Sci. 9, 1040 (1974).
- [15] T. F. Kelly, M. Cohen, and J. B. VanderSande, submitted to Metall. Trans. for publication.
- [16] T. Gladman, Proc. Roy. Soc. A 294, 298 (1966).
- [17] I. M. Lifshitz and V. V. Slyozov, J. Phys. Chem. Solids 19, 35 (1961); C. Wagner, Z. Electrochem. 65, 581 (1961).
- [18] G. B. Olson, H. C. Ling, J. S. Montgomery, and J. B. VanderSande, Rapidly Solidified Amorphous and Crystalline Alloys, B. H. Kear, B. C. Giessen, and M. Cohen, eds., North-Holland Publishing, NY, p. 355 (1982).
- [19] M. Suga, J. L. Gross, G. B. Olson, and J. B. VanderSande, Rapid Solidification Processing: Principles and Technologies II, R. Mehrabian, B. H. Kear, and M. Cohen, eds., Claitor's Publishing Division, Baton Rouge, p. 364 (1980).
- [20] G. B. Olson, M. Cohen, and G. J. Yurek, these proceedings.
- [21] P. M. Fleyshman, Fracture Toughness of Rapidly Solidified Martensitic Steels, S. M. Thesis, MIT, Cambridge (1982).
- [22] G. J. Yurek, D. Eisen, and A. Garratt-Reed, Metall. Trans. A 13A, 473 (1982).
- [23] E. R. Slaughter, C. Adam, M. J. Blackburn, R. G. Bourdeau, and C. V. Law, unpublished research (1982).

SOLIDIFICATION OF UNDERCOOLED LIQUIDS

J.H. Perepezko^{*}, Y. Shiohara⁺, J.S. Paik^{*} and M.C. Flemings⁺

^{*}Department of Metallurgical and Mineral Engineering
University of Wisconsin-Madison
Madison, Wisconsin 53706

⁺Department of Materials Science and Engineering
Massachusetts Institute of Technology
Cambridge, Massachusetts 02139

ABSTRACT

During rapid solidification processing (RSP) the amount of liquid undercooling is an important factor in determining microstructural development by controlling phase selection during nucleation and morphological evolution during crystal growth. While undercooling is an inherent feature of many techniques of RSP, the deepest undercoolings and most controlled studies have been possible in carefully prepared fine droplet samples. From past work and recent advances in studies of nucleation kinetics it has become clear that the initiation of crystallization during RSP is governed usually by heterogeneous sites located at surfaces. With known nucleant sites, it has been possible to identify specific pathways of metastable phase formation and microstructural development in alloys. These advances have allowed for a clearer assessment of the interplay between undercooling, cooling rate and particle size statistics in structure formation. New approaches to the examination of growth processes have been developed to follow the thermal behavior and morphology in small samples in the period of rapid crystallization and recalescence. Based upon the new experimental information from these studies, useful models can be developed for the overall solidification process to include nucleation behavior, thermodynamic constraints, thermal history, growth kinetics, solute redistribution and resulting structures. From the refinement of knowledge concerning the underlying factors that govern RSP a basis is emerging for an effective alloy design and processing strategy.

Introduction

The main attention in rapid solidification (RSP) methods has been focused upon the attainment of high cooling rates in the range of 10^4 to 10^8 °C/sec. With these methods small liquid volumes are quenched either in contact with a substrate as in melt spinning and directed energy beam processing or in an inert gas as in atomization. However, the most important impact of RSP can be related directly to the solidification structures and the new opportunities for structure control by innovative alloy design and processing strategies. The wide range of reported microstructural variations encompass not only equilibrium phase mixtures with refined microstructural scale, but also novel microstructures such as supersaturated solid solutions, metastable intermediate phases and amorphous solids.

The existence and understanding of novel microstructures representing non-equilibrium phases requires a consideration of the level of undercooling at the onset of nucleation in addition to rapid growth kinetics. In fact, the available free energy for non-equilibrium phase formation is directly related to the amount of undercooling. With increasing levels of undercooling the product phase selection involved in nucleation can be expanded to involve an increased variety and to allow competitive growth kinetics to play an important role in the evolution of different microstructural morphologies. Accordingly, the examination of solidification in undercooled liquids can contribute to the basic understanding necessary for an effective microstructure control and alloy design in the optimization of RSP.

Experimental Techniques for High Undercooling

Even with liquid metals of high purity the attainment of a high level of undercooling is precluded usually by the catalytic action of residual impurities or container walls. In order to observe extensive undercooling it is necessary to circumvent the catalytic effects of the active nucleants. An effective experimental approach that may be applied to yield large undercooling prior to solidification involves the slow cooling (10-30°C/min) from the melt of a dispersion of stabilized fine metal

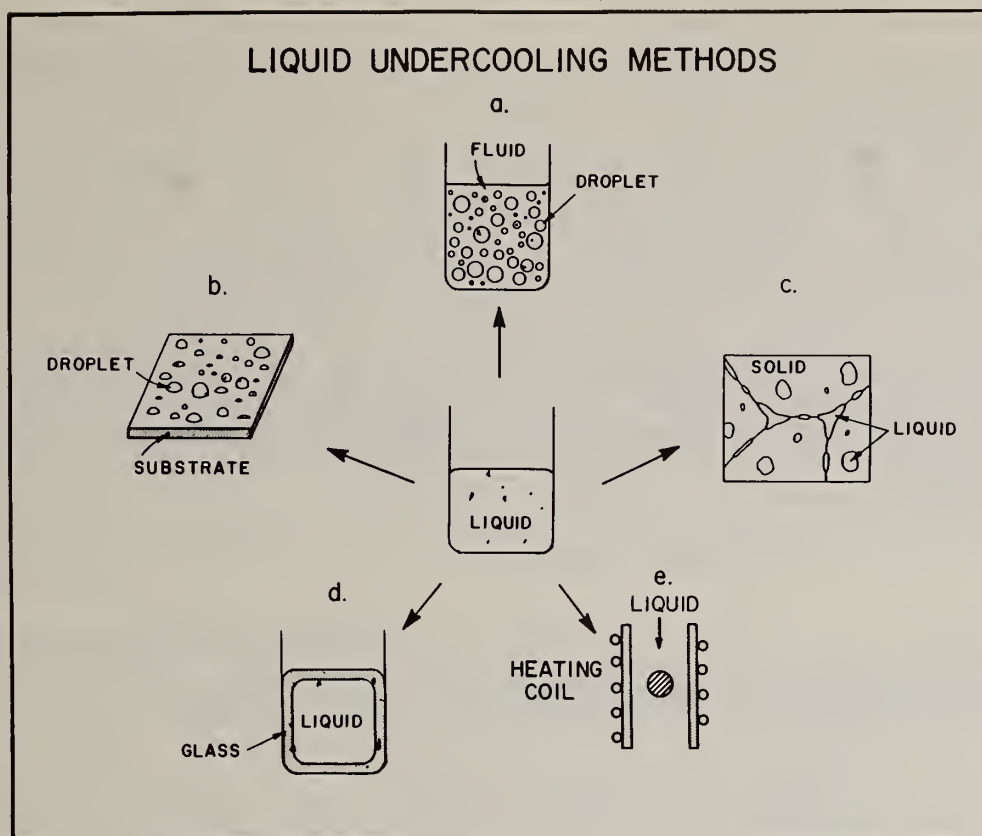


Fig. 1 Liquid undercooling methods

droplets [1]. By starting with high purity metal and dispersing the liquid into a large number of small droplets ($<20\mu$) within a suitable medium, the catalytic effects of active nucleants may be restricted to a small fraction of the total droplet population. A suitable means of carrying out the nucleant isolation operation is illustrated schematically in fig. 1.

In considering the droplet approach to undercooling, a distinction should be made between the several modifications of this technique which have been employed by a number of investigators in the past. For example in the droplet substrate method [2], a small sample of liquid metal is placed on an inert glass substrate in a chamber with an inert or reducing atmosphere. With this approach the onset of solidification is determined by visual observation of the change in surface reflectivity of a metal droplet which is about $50\text{--}100\mu$ in diameter. In the entrained droplet technique [3] a bulk alloy sample is equilibrated in a liquid-solid two phase field with the temperature and alloy composition selected so that only a small fraction of the volume will be liquid in contact with a primary solid solution phase, as a potential heterogeneous nucleant. In addition, several other procedures have been developed for generating liquid metal droplet dispersions which exhibit a propensity for substantial undercooling. These droplet forming techniques involve exploding wires [4], shotting [5] and the containerless solidification in drop tubes [6]. While the majority of droplet undercooling schemes have a provision for some method of temperature measurement, the undercooling tendency of liquid droplets in several cases including all atomization methods is judged usually from microstructural observations.

With bulk samples, the removal of active nucleation sites usually involves a physical separation of the sites from the melt or a chemical treatment either to incorporate or to deactivate possible catalytic sites in the presence of an inorganic containment layer. These approaches which include a bulk sample encased in organic glasses [7] as well as a bulk melt levitated by induction [8] indicate that some remarkably large levels of undercooling (i.e. $0.2 T_m$) may be achieved. The inorganic glass encasing is believed to promote undercooling not only by isolating the liquid from possible catalytic sites on container walls, but also by a possible scavenging action on nucleating centers that may be distributed within the volume of the melt. It is worthwhile to note that in principle the undercooling attained in properly conditioned bulk samples should approach the levels in droplet samples. Besides these specific undercooling techniques, it is clear that atomization of liquids is a commercial RSP method which incorporates an effective nucleant isolation operation as well as rapid quenching.

Nucleation Kinetics in Undercooled Liquids

In the present discussion the main interest in nucleation kinetics will be focused on the possible relationships between undercooling and cooling rate during the solidification of a distribution of liquid droplets. These relationships may be examined by nucleation rate calculations, but the computed results are highly dependent on the specific values assigned to the kinetic rate parameters. Reliable information is available for some parameters, however, in most cases the kinetic parameters are assigned values based upon theoretical models which require experimental verification. To minimize the uncertainty associated with calculations based model dependent parameter values, it is of interest to examine the range of droplet nucleation kinetics in a general manner. With this approach it is possible to deduce several useful guiding relationships for rapid solidification behavior.

Nucleation of a crystalline phase in an undercooled liquid phase may be classified into two mechanistic types. When nucleation occurs without an association with any catalytic nucleation sites, it can be classified as homogeneous nucleation. In the vast majority of experimental conditions nucleation is initiated at some catalytic nucleation site as heterogeneous nucleation. For a heterogeneous nucleation, an expression for the nucleation rate, J , has been developed on the basis of homogeneous nucleation theory [9] as:

$$J = \Omega_a \exp [-\Delta G(n^*)/kT] \quad (1)$$

where Ω_a is proportional to the number of liquid atoms in contact with unit area of the catalytic surface as well as the jumping frequency of atoms, $\Delta G(n^*)$ is the activation barrier for nucleation and kT has the usual meaning. For nuclei having the form of a spherical sector,

$$\Delta G(n^*) = (16/3) \pi \sigma^3 f(\theta) / (\Delta G_V)^2 \quad (2)$$

where σ is the interfacial energy between the nucleus and the liquid, ΔG_V is the driving free energy for nucleation of unit volume of the product phase and $f(\theta) = (2 - 3 \cos \theta + \cos^3 \theta)/4$ is a contact angle factor. In the description of nucleation kinetics during rapid liquid quenching, steady state nucleation conditions may be considered in general, except for glass forming alloys [9].

Nucleation Rate Parameters

The nucleation rate is a relatively steep function of temperature with a steady state magnitude determined principally by the value of the exponential terms in $\Delta G(n^*)$ at the nucleation temperature T_n and to a lesser amount by the prefactor. In evaluating the temperature dependence of J usually a constant value based on theory is taken for Ω_a even though the catalytic site may vary. Similarly, little information is available to judge the catalytic potency, $f(\theta)$ so that a range of values is used in calculations. However, the most important parameters in determining J and hence the undercooling level are ΔG_V and σ which have received continued experimental and theoretical study.

In pure metals, the recent measurements of the heat capacity for undercooled liquids [10] have allowed for a direct evaluation of ΔG_V . In general, the experimental values are represented to within a few percent by the relation proposed by Turnbull [11,12].

$$\Delta G_V = -\Delta H_V (\Delta T/T_m) = -\Delta H_V (1 - T_r) \quad (3)$$

where ΔH_V is the heat of fusion per unit volume of product phase, ΔT is the undercooling and T_m is the melting point of the product phase. For alloys the value of ΔG_V is determined from the composition of the nucleating phase at T_n . The composition dependence of ΔG_V can be expressed as

$$\Delta G_V = [X_A \Delta \mu^A + (1 - X_A) \Delta \mu^B] / \bar{v} \quad (4)$$

where $\Delta \mu^A$ and $\Delta \mu^B$ are the chemical potential differences between the undercooled liquid and crystal and \bar{v} is the molar volume for the crystalline phase at composition X_A . It is apparent from eq. 4 that ΔG_V is maximized when $\Delta \mu^A = \Delta \mu^B$ so that $\Delta G_V = \Delta \mu^A / \bar{v}$. This condition has been proposed by Hillert [13] to assess the nucleus composition. However, the favored nucleus composition should yield a minimum value of $\Delta G(n^*)$. Only if \bar{v} and σ are not composition dependent can the maximum ΔG_V value occur at the same

composition as that for a minimum in $\Delta G(n^*)$. Apparently this behavior may be approached in some alloys. For example, recent calculations [14] of the composition dependence of the nucleation temperature, $T_n(x)$ have reproduced the observed experimental trends [1] which reflect the composition dependence of the liquidus, but the generality of the calculated behavior requires further examination.

In the study of nucleation one of the most important parameters is the solid-liquid interfacial energy. Since the nucleation rate is proportional to $\exp -(\sigma)^3$ as shown in eqs. 1 and 2, it is very sensitive to even slight errors in the σ value [15]. A direct measurement of σ is very difficult even with a large uncertainties because of sensitivity to impurity effects. Usually values of σ are calculated from classical nucleation theory by assuming that experimentally obtained maximum undercooling values are associated with homogeneous nucleation. Unless the maximum undercooling value is proven to refer to homogeneous nucleation, the estimated σ value is expected to underestimate the true value. There have been a number of theoretical approaches to study the structure and properties of the solid-liquid interface on the basis of various model constructions. The models range from the limiting cases in which σ values are calculated from enthalpic bond breaking arguments [16] or derived solely from a basis of entropic considerations [17] to intermediate approaches where a weighted contribution of enthalpic and entropic terms [18-20] is incorporated into the evaluation. At the present time, the theoretical values appear to underestimate σ compared to values calculated from nucleation undercooling results [15]. Certainly, an improvement in the independent experimental determination of σ would be invaluable in allowing for a clear evaluation of theoretical models and more reliable nucleation calculations.

Effect of Cooling Rate on Nucleation Kinetics

Since the onset of nucleation in a highly undercooled liquid is expected to be a sharp function of temperature it is useful to consider a limiting case for the effect of cooling rate on nucleation temperature. In general, for a given nucleation kinetics the critical condition to observe nucleation experimentally in a time, t , in a droplet of volume, v , and catalytic surface area, a , is given by $Jvt \approx 1$ for homogeneous nucleation and by $Jat \approx 1$ for heterogeneous nucleation. From eq. 1, the heterogeneous nucleation time can be represented as a function of temperature as:

$$\ln t = -\ln[a (\Omega_a)] + 16 \pi \sigma^3 f(\theta) / [3 k (\Delta H_v)^2 T_m (1-T_r)^2 T_r] \quad (4)$$

where a Ω_a represents the heterogeneous nucleation site population associated with a droplet of volume v .

Furthermore, the rate dependence of the nucleation temperature which represents the shape of the T-T-T diagram associated with a specific nucleation kinetics is represented in general as

$$\frac{dT_r}{d(\ln t)} = \frac{3k (\Delta H_v)^2 T_m}{16 \pi \sigma^3 f(\theta)} \left[\frac{(1-T_r)^3 T_r^2}{(3 T_r - 1)} \right] \quad (5)$$

where the possible temperature dependence of Ω_a , ΔH_v , σ and $f(\theta)$ has been neglected in order to examine a limiting value and minimize the uncertainty of model dependent values. For homogeneous nucleation $f(\theta) = 1$, but for a heterogeneous nucleation $0 < f(\theta) < 1$. Therefore, T-T-T diagrams for heterogeneous nucleation can have different breadths representing a different temperature dependence of the nucleation rate for different heterogeneous sites. In eq. 5, $dT_r/d(\ln t)$ becomes infinite at $T_r = 1/3$ as the nucleation time is minimized. Therefore, $T_r = 1/3$ is believed to estimate a lower bound to the onset of sensible nucleation of a crystalline phase during slow cooling [21]. If the undercooling limit of the droplet sample represents the solidification of the nucleant-free droplet population, the crystallization temperature is determined either by the catalytic nature of the droplet surface coating or by the intervention of homogeneous nucleation kinetics. Also, during cooling the operation of a given catalyst kinetics and the kinetic competition between different catalysts and different product phase structures will be influenced strongly by the active catalyst distribution at the undercooling limit. In order to reach this limiting undercooling the size refinement of droplets becomes one of the most important factors. Further analysis on the distribution of active nucleants among droplets then becomes necessary to understand the undercooling behavior of droplet samples.

Nucleation Kinetics and Size Distribution Statistics

As long as a single nucleation kinetics with a steep temperature dependence is operating the effect of droplet size on the nucleation temperature is relatively small. In fact, if the size distribution is the only factor associated with the nucleation temperature range during cooling, a

sharp nucleation peak over a narrow temperature range ($<10^{\circ}\text{C}$) is expected even with a sample of a rather broad droplet size distribution. However, droplet emulsion samples of pure metals and alloys often show a broad crystallization peak over a wide temperature range ($>20^{\circ}\text{C}$). In this case the operation of a single nucleation kinetics is unlikely but the broad crystallization peak can be associated with multiple nucleation events continuously activated during the cooling process [21]. Moreover, at a given cooling rate, nucleation of the crystalline phase in each droplet is associated with the catalytic potency of the most active nucleant. As a result, nucleation at different levels of undercooling due to crystallization over a wide temperature range can result in the formation of different structures in different droplets. Even if the same structure is nucleated at different levels of undercooling, this structure will not necessarily be retained completely in the final solidification pattern. For example, the final product structure can develop variations due to a different thermal history associated with the recalescence period following nucleation at different undercooling levels in separate droplets.

An example of the nucleation of different phases due to crystallization behavior over a broad undercooling range may be illustrated by considering the careful studies on Fe-Ni alloys reported by Cech [22]. In fine droplet samples, ($<40\mu$), Cech demonstrated the presence of droplets of a metastable bcc structure in addition to droplets of the equilibrium fcc structure. Size distribution analysis results showed that small droplets less than 13μ are more likely nucleated at high undercooling since the major fraction had a metastable bcc structure. Since there were also droplets of the metastable structure within the large size grouping ($d > 20\mu$), it is necessary to consider the mode of nucleant distribution among droplets. When all possible nucleation sites which can be activated at lower levels of undercooling than that necessary to retain the metastable phase are considered to be nucleants, a Poisson distribution function may be introduced to describe the random distribution of these nucleants among droplets [21,23]. In this case the fraction of droplets free from active nucleants is represented by

$$X = \exp [-m(v)] \quad (6)$$

where $m(v)$ is the average number of active nucleants in each droplet of volume V . Depending on the distribution mechanism of nucleants during the atomization process $m(v)$ is proportional either to the volume or to the corresponding surface area of the droplet. Since a nucleant distribution proportional to the droplet volume would result in a rapid decrease in the yield of metastable product with increasing droplet size, it appears that for the Fe-Ni case, a surface area dependent nucleant distribution is most probable. A further application of the Poisson distribution has been reported for the solidification of Pd-Si droplet samples [24]. In this case the droplet fraction which solidified continuously as glass represents X in eq. 6 which can also be written in terms of droplet diameter, d , as $X = \exp [-(d/d_0)^n]$. When $m(v)$ is proportional to the droplet surface area, $n=2$ for a heterogeneous surface nucleation. For heterogeneous volume nucleation $n=3$ and for homogeneous nucleation $n=4.6$. As in other droplet studies the solidification behavior of Pd-Si droplets was described most closely by a heterogeneous surface nucleation kinetics.

Metastable Phase Formation

Thermodynamic Features

A large number of examples of metastable phase formation have been demonstrated during rapid quenching experiments [25]. While the possible reaction paths leading to metastable phase formation in alloy systems are numerous a consideration of thermodynamic constraints can be useful in providing guidelines and limiting bounds on the reaction sequences in undercooled liquids. For example the free energy relationships that are relevant to the generation of solid solutions are illustrated in fig. 2. Two features are of interest in this case. For the formation of an equilibrium solid solution of composition C_0 at temperature T_N an overall free energy change of ΔG_1 is involved in reaction. However, in the early nucleation stage of reaction when a small amount of α forms from the liquid the driving free energy is maximized for α with a composition C_1 rather than C_0 . When the molar volume of solution does not change appreciably with composition, the C_1 composition may be determined by constructing a tangent to the α free energy curve which is parallel to a tangent to the liquid free energy. As noted previously, this consideration indicates that α with solute content different from C_0 can develop initially during nucleation [13]. Another feature of interest in fig. 2 concerns the bound set by the T_0 dashed curve between the liquidus and solidus [26], which represents the locus of equal free energy between liquid and solid. Formation of α product with the same composition as the liquid is excluded at compositions beyond the T_0 limit.

A thermodynamic consideration is of most value when the analysis also can provide an estimate of potential metastable intermediate phases that can enter in the kinetic competition. For example, in alloys the requirement that the free energy, ΔG , exhibit an overall decrease with reaction can lead to several interesting possibilities for phase reaction sequences [26] as illustrated by one example in

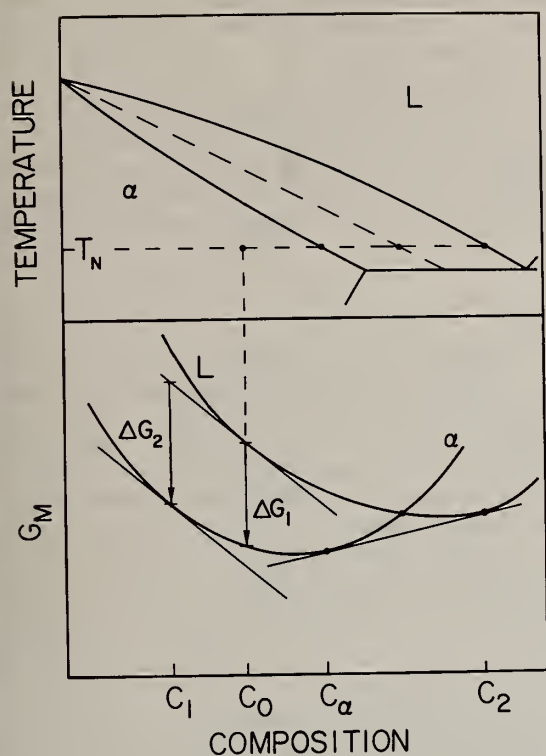


Fig. 2 Free energy relationship between under-cooled liquid and α phase.

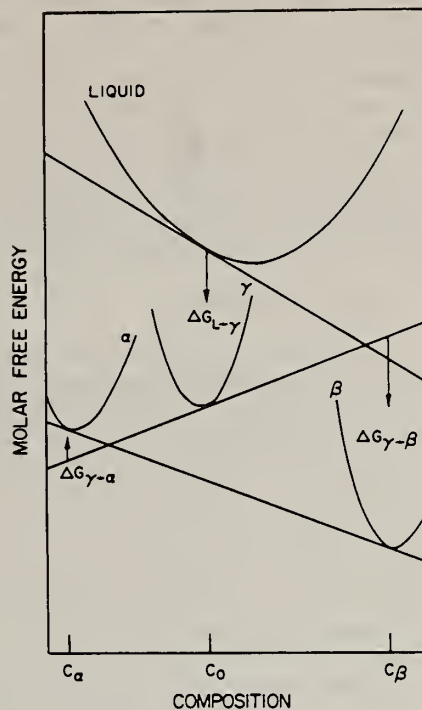
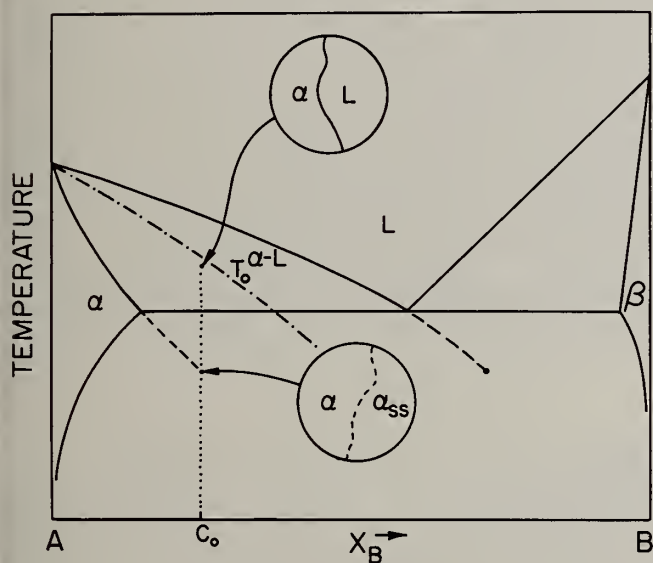
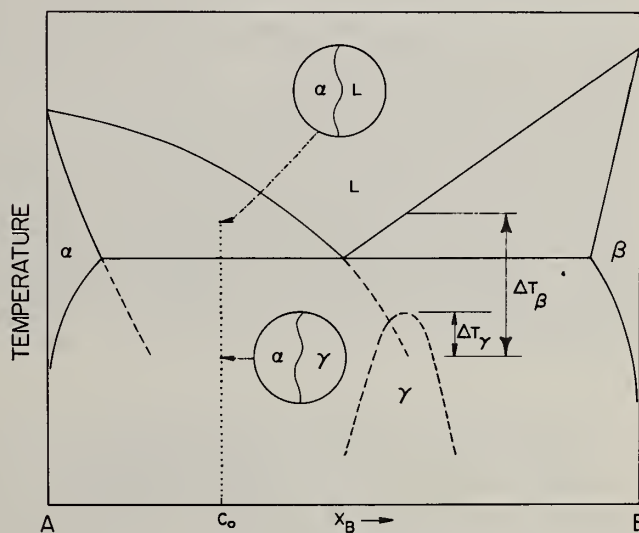


Fig. 3 Free energy relationship between under-cooled liquid and several crystalline phases [26].



(a)



(b)

Fig. 4 Schematic illustration of a possible reaction path for primary phase catalysis of a metastable solid solution (a) and a metastable γ intermediate phase (b).

fig. 3. In this case the equilibrium solidification of liquid of composition C_0 would yield a two-phase mixture of α with composition C_α and β with composition C_β . However, if the nucleation kinetics are favorable, an intermediate reaction step can occur involving the formation of the metastable γ phase with composition C_0 and free energy reduction $\Delta G(L \rightarrow \gamma)$. The presence of γ phase affects the reaction sequence in that α phase cannot form since the free energy change $\Delta G(\gamma \rightarrow \alpha)$ is positive. Only after the γ phase transforms into β phase can the α phase form with a free energy reduction. When there are several metastable phases possible, the number of intermediate reaction steps can increase and present interesting opportunities for structure control during both solidification and subsequent solid state processing. One way of summarizing the potential for structure modification in alloys is to construct a metastable phase diagram [25,27].

Competitive Kinetics Analysis

Since the driving force for the formation of a metastable phase is related directly to the amount of undercooling below the melting temperature of the phase, a high level of undercooling can expand the product selection involved in nucleation to an increased variety of types of structures. This is illustrated by the nucleation transition from fcc to bcc in Fe-Ni alloys [22], stainless steels [28] and tool steels [29]. Other examples have been reported in Pb-Bi, Bi-Cd and Pb-Sn alloys as well as Ga and Bi [1,10,21]. For Pb-Bi alloys a multiple phase selection transition has been observed in droplets [1]. As the level of undercooling increases an equilibrium eutectic mixture is replaced by a supersaturated (hcp) phase which in turn is superceded by a metastable intermediate phase at the highest undercooling. In addition for Pb-Sn, Sn-Ge and Cd-Sb alloys the operation of the nucleation product transition has been related to the catalytic effect of specific heterogeneous sites [21,30]. One type of effective nucleation site is a primary solid solution which can participate in catalysis reactions such as those illustrated in fig. 4 [21]. When the α phase is a potent catalyst, a continued growth of α is possible during cooling to form a supersaturated α product as in fig. 4a. When α is strongly catalytic in promoting the nucleation of a metastable intermediate γ phase as indicated in fig. 4b, the formation of an equilibrium β phase may be bypassed as the liquid is undercooled below the metastable γ phase melting point. Thus, for an alloy that may exhibit metastable products, it is possible to select a particular phase by controlling the degree of undercooling prior to solidification and by providing a high density of favorable catalytic sites.

In order to understand the kinetic competition between different phases during nucleation in an undercooled liquid, the comparison of thermodynamic stability may not be sufficient. In terms of overall nucleation kinetics, the driving free energy is not the only parameter of importance, but also nucleation site density and the magnitude of $\Delta G(n^*)$ associated with a given phase are critical. As an illustration of the application of nucleation kinetics to reveal the relationships between cooling rate, undercooling and phase selection, it is useful to consider the competition between two nucleation kinetics during continuous cooling of a droplet in several different situations that are illustrated in fig. 5. As an initial example, when two catalysts of different nucleation site density and potency are in the same droplet (B and C), the undercooling limit of the droplet at T_{r1} is determined by catalyst C at cooling rate \dot{T}_1 . At cooling rate \dot{T}_2 , however, the undercooling of the droplet increases to T_{r2} by circumventing the catalytic effect of C. Thus at a continually increasing level of cooling rate, there can be a significant improvement of undercooling as the catalytic effects of highly potent nucleants are circumvented. During this process the controlling nucleation kinetics involves catalysts of decreasing potency. When two different phases are competing with each other on the same catalytic surface present in a highly undercooled liquid, according to nucleation theory, the magnitude of the activation free energy barrier becomes the most dominant factor. Therefore, in order to favor nucleation of a metastable phase at a given cooling rate the activation energy barrier for the metastable phase should be lower than that for the equilibrium phase. In terms of eq. 1 this condition may be expressed as

$$\frac{\sigma_{LM}^3 f(\theta')}{(\Delta H_V^m)^2 (1-T_r')^2} < \frac{\sigma^3 f(\theta)}{(\Delta H_V)^2 (1-T_r)^2} \quad (7)$$

where σ_{LM} and θ' are the interfacial energy and the contact angle between the metastable phase and the catalytic surface, ΔH_V^m is the heat of fusion per unit volume of the metastable phase and T_r' is the relative nucleation temperature of the metastable phase. It has been shown in eq. 5 that the breadth of the T-T-T diagram associated with different nucleation kinetics is proportional to $(\Delta H_V)^2 T_m / \sigma^3 f(\theta)$. When the melting temperatures of two different phases nucleated by the same catalysts are very close and the metastable phase is dominant, the condition given by eq. 7 may be approximated by

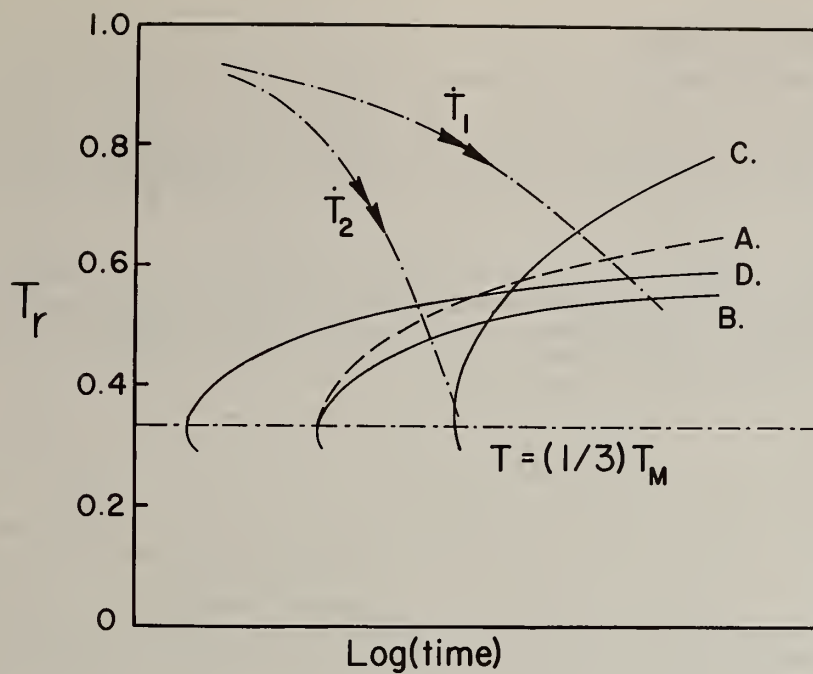


Fig. 5 T-T-T diagram representing different nucleation kinetics that may occur during a continuous cooling in undercooled droplets.

$$\frac{(\Delta H_V^m)^2}{\sigma_{LM}^3 f(\theta')^2} > \frac{(\Delta H_V)^2}{\sigma^3 f(\theta)^2} \quad (8)$$

In this case, the breadth of the T-T-T diagram for the nucleation of the metastable phase (A) is larger than that for the equilibrium phase (B), but the noses of these two diagrams are placed at the same position as illustrated in fig. 5 schematically (A and B). Unless there are nucleants of higher catalytic potency for nucleation of the equilibrium phase (for example C in fig. 5), the equilibrium phase is always masked by nucleation of the metastable phase regardless of the cooling rate. In fact, the droplet emulsion technique which disperses potent nucleants of small population into a minor fraction of the droplet sample can be viewed as eliminating the possible activation of nucleation kinetics C in the major fraction of the sample. Alternatively, if the activation barrier for A is higher than that for B, the equilibrium phase will nucleate at all cooling rates. In addition, it is also possible for the nucleation of the equilibrium phase to be favored by an increase of the cooling rate if the nucleation site density for the equilibrium phase (curve D) is greater than that for the metastable phase. For these conditions an increase in cooling rate can result in a decreasing yield of a metastable product. In fact, a transition in nucleation from surface dependent to volume dependent kinetics with increasing cooling rate such as C to D in fig. 5 can yield a large increase in rate and may contribute to a propensity for multiple nucleation as reported in quenched Al-Si alloy droplets [31]. However, other factors involving the specific thermal history of droplets are also likely to contribute to the development of multiple nucleation.

In summary, the examination of the simple competitive kinetics examples reveals several types of general behavior. First, for a single operating kinetics an increase in cooling rate translates usually into some increase in undercooling. With several competing kinetics the increase in undercooling with cooling rate may not be uniform. For several competing kinetics and possible product structures, an increase in cooling rate can allow for nucleation of a metastable phase to be favored or for an increase in the yield of a metastable phase product, but this is not a general rule. Depending on the density of catalytic sites, it is possible for an increase in cooling rate to result in no change in phase selection or to result in a decreasing yield of a given metastable phase in favor of another metastable product or even an equilibrium phase product. From these examples illustrating the possible synergistic effects between high undercooling and rapid quenching to yield unique product structures, it is clear that attention to catalyst potency and site distribution as affected by surface conditions during atomization can be as important as cooling rate in optimizing RSP treatments.

Heat Flow and Pure Metal Solidification

In solidification of small droplets, two extreme heat flow situations may arise. In the first one, the solidification front moves into a liquid at its melting point or above, and the latent heat of fusion must be withdrawn through the solid. The second situation involves solidification into a supercooled melt. Nucleation occurs only after substantial supercooling, and initial solidification then occurs primarily by flow of heat into the liquid itself, thereby resulting in droplet recalescence.

For solidification without undercooling, the Newtonian approximation is applicable when the dimensionless Biot number, Bi , is lower than 0.1, where $Bi = h r_0/k_m$. The Biot number is the ratio of the surface conductance or heat transfer coefficient, h to the metal conductance (k_m/r_0): k_m is the thermal conductivity of the metal and r_0 is the droplet radius. The heat transfer coefficient is determined from the Nusselt number [32]:

$$Nu = 2 h r_0/k_f = 2 + 0.6 Re^{1/2} Pr^{1/3} \quad (9)$$

where Re and Pr are Reynolds and Prandtl numbers respectively and k_f is the thermal conductivity of the fluid. In the case of solidification of metal droplets in a quiescent liquid or gas, the Nusselt number reduces to 2, and the Biot number is simplified to k_f/k_m . In the case of pure tin droplets emulsified in oil (polyphenylether), the Biot number is about 4.4×10^{-3} , since k_f is 0.112 kcal/m hr °C and k_m is 25.3 kcal/m hr °C. Thus, the dominant resistance to heat flow in this example occurs at the surface and no significant temperature gradients can develop inside the droplet in absence of undercooling. Similarly in most if not all gas atomization processes, heat transfer is limited by the solid-gas heat transfer resistance.

Thus, the simple Newtonian model is widely and correctly used for single phase cooling and solidification without undercooling [33]. Table 1 shows cooling rates for aluminum gas atomized droplets calculated in this way. Table 2 shows comparable cooling rates for atomized or emulsified metals in several liquid media.

When supercooling occurs in atomized or emulsified droplets, it is not obvious that the droplet will have a uniform temperature distribution during the recalescing period of solidification;

Table 1. Calculated Cooling Rates of Pure Aluminum at 660°C During Gas Atomization (in Helium at 300°K): (°K/sec)

Relative Gas Velocity		Particle Diameter (μm)	
mach	V_∞ (m s ⁻¹)	10	100
0	0	7.21×10^6	7.21×10^5
0.1	97	1.00×10^7	1.56×10^6
0.3	290	1.22×10^7	2.26×10^6
0.5	483	1.36×10^7	2.69×10^6
1.0	965	1.56×10^7	3.53×10^6

Table 2. Calculated Cooling Rates of Pure Metal Droplets (10μm dia.) Cooled in Different Media at Low Reynolds Numbers

Metal and Quench Medium	Cooling Rate at Equilibrium Melting Point (°K/sec)
Aluminum in Helium gas at 27°C	7.21×10^6
Aluminum in Argon gas at 27°C	9.68×10^5
Aluminum in Liquid Gallium at 30°C	2.12×10^9
Tin in Argon at 27°C	4.57×10^5
Tin in Oil at 100°C	2.28×10^6
Tin in Oil/CCl ₄ (1/2) at -25°C	3.77×10^6
Iron in Argon at 27°C	1.15×10^6
Iron in Glass at 1000°C	3.99×10^7
Iron in Molten Salt at 482°C	3.11×10^8

i.e., the temperature of the growing interface may rise faster than the average temperature of the droplet. In this case, the validity of the Newtonian approximation during recalescence will depend not only on the Biot number, but also on interface velocity and interface morphology.

Levi and Mehrabian [34] have considered in some detail the solidification of undercooled droplets of pure metals, assuming a planar (non-dendritic) interface and the interface kinetic relationship suggested by Turnbull [35] and modified by Cahn [36] for the steady state continuous growth of a planar front. Figure 6 is an example of results of their computer calculations for an aluminum droplet with a single nucleation event. For the conditions chosen, significant temperature differences develop within the liquid during recalescence. Of course, as pointed out by Levi and Mehrabian, the magnitude and longevity of internal temperature differences depend sensitively on the number of nuclei growing, and on whether or not the interface is dendritic. In the case of multiple nucleation, the scale of the heat transfer problem is reduced from that of the droplet radius, r_0 , to that of half of the interparticle spacing $d_{mx}/2$. In the limit of lacy dendrites (or, dendrites that become unstable and break into individual particles), the heat transfer scale is similarly reduced. Figure 7, also from Levi and Mehrabian, shows schematically how decreasing d_{mx} alters the "enthalpy path" during solidification. Decreasing d_{mx} moves paths more toward the top and right of the diagram and here recalescence becomes more rapid, more adiabatic, and more Newtonian.

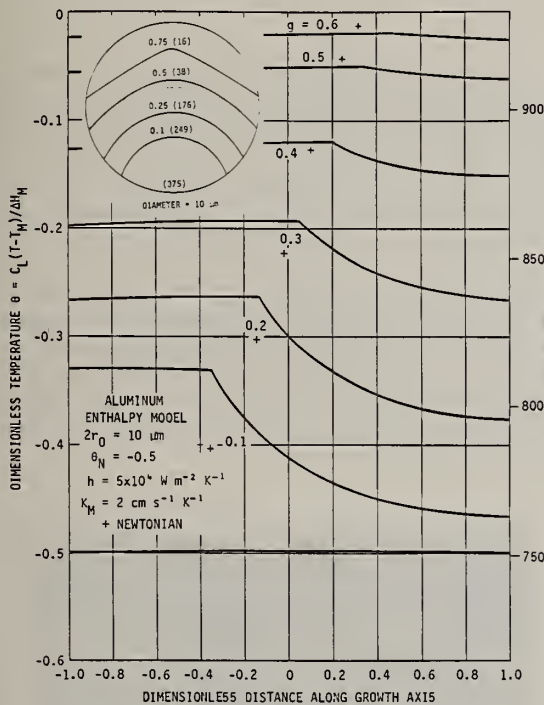


Figure 6. Thermal profiles for a recalescing pure aluminum droplet, 10 μ m dia. Advancing liquid solid front shown in insert which denotes fraction solid and interface velocity (cm s⁻¹), from Levi and Mehrabian [34].

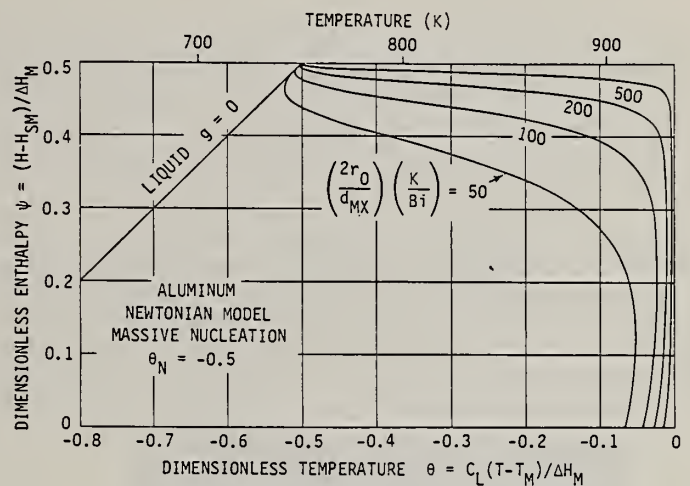


Figure 7. Effect of the ratio K/Bi on the thermal history of undercooled droplets for a fixed nucleation temperature. Note that for typical atomization conditions ($k/Bi > 100$) the external cooling is not able to slow down recalescence to a significant extent, from Levi and Mehrabian [34].

We do not yet have experimental measurements of growth velocities or interface morphology in undercooled pure metal droplets. We can, however, turn to other studies where growth of crystals into pure undercooled liquids has been measured, and where this growth is apparently dendritic. Perhaps the highest measured crystal growth velocities are those of nickel and cobalt into their pure undercooled melts, reported by Walker [37], Colligan and Bayles [38]. In their experiments, columns of the bulk melt were undercooled by varying amounts up to 250-300°C and then seeded at one end. The velocity was determined from the times at which the freely moving dendrite tip passed thermal sensors sited along the column. Similar experiments have been performed by Glicksman et al [39] on succinonitrile, and successfully analyzed by combining heat flow and interface stability theory. By addition of interface kinetics to this analysis, Coriell and Turnbull [40] showed excellent agreement of theory with experiment, for the undercooled nickel experiments described above. These experimental studies, as well as interface stability theory suggest solidification of undercooled pure metals (and alloys) should be dendritic. Nonetheless, there are indications that undercooled alloy droplets at high undercooling solidify in a non-dendritic fashion. Perhaps this is because of transient effects, or perhaps because the wavelength of the stability is long compared

with the droplet size [41].

Alloy Solidification

In an earlier section, the possibility has been described of achieving non-equilibrium phases through undercooling (e.g. obtaining a BCC phase in a normally austenitic steel). And of course, glassy structures can also be obtained. In this section, we focus on structure and segregation in alloys where the expected phases are formed (i.e. those obtained in usual solidification process).

A number of investigators have shown that solidification in bulk iron, nickel, and copper alloys is dendritic at moderate undercoolings, with the dendrite structure becoming gradually a simple rod-like structure with increasing undercooling. Then, at a critical undercooling which often seems to be about 100-200°C grain size drops abruptly; an example is shown in Figure 8 [42]. For undercoolings greater than the critical, the dendrite structure is completely absent, replaced by more-or-less spherical "elements" which are the separate grains [7,42]. Both the dendrite arm spacing in moderately undercooled specimens, and the size of the spherical elements are strongly dependent on cooling rate after recalescence. Hence, it is clear that the structures we see are strongly affected by ripening and are not therefore the actual structures that grew during recalescence. The abrupt grain size reduction has been alternately explained by an acoustic nucleation mechanism, and by a ripening or dendrite remelting mechanism.

Especially at intermediate to rapid rates of heat extraction during and/or immediately after recalescence, a number of investigators have observed solute rich cores within the dendrites or "elements" in undercooled alloys. Figure 9 is an example from work of Wu [43] showing high solute cores in 5mm dia. Fe-25%Ni alloy that was undercooled 90°C. The solute rich cores certainly formed during recalescence. Perhaps they grew in diffusionless fashion below the T_0 , but the probable remelting, coarsening, and solid state diffusion occurring during and after recalescence did not completely eliminate these traces of the original structure.

Related structures have been obtained by Levi and Mehrabian in aluminum rapidly solidified droplets. Homogeneous solute rich material is found in a portion (or all) of the droplets when a given droplet is not completely homogeneous it contains also a solute depleted zone and dendritic or cellular region as well. The homogeneous solute rich region must have formed at some temperature below the thermodynamic T_0 temperature, and grew in an apparently non-dendritic manner, at some critical temperature during recalescence, solute began to be rejected, eventually rendering it unstable and resulting in the cellular structure at the upper right.

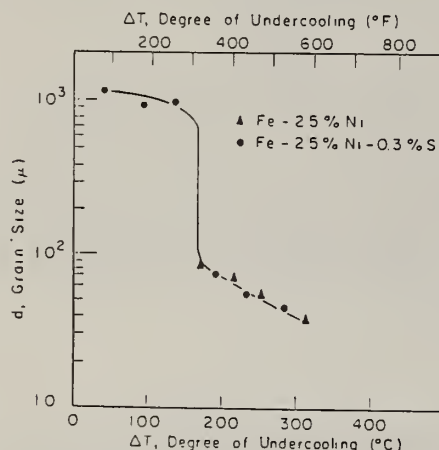


Figure 8. Grain size versus undercooling in a bulk undercooled melt, from Kattamis and Flemings [42].

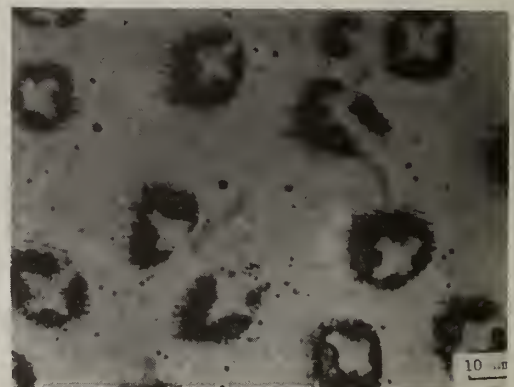


Figure 9. Solute rich cores in undercooled Fe-25%Ni alloy, $\Delta T = 90^\circ\text{C}$, 700X, from Wu [43].

With sufficient undercooling and sufficiently rapid heat extraction, supersaturated structures and non-equilibrium phases can be retained to room temperature. Kelly, Vander Sande and Cohen [28] have obtained a homogeneous (non-cellular), non equilibrium BCC structure in atomized 303 stainless steel powder in diameter up to about 70 microns. Figure 10 shows similar homogeneous structures in 316 stainless steel obtained by MacIsaac [44] in thesis work at MIT. These latter structures are of both the equilibrium FCC phase and the non-equilibrium BCC phase; they were obtained in an emulsification of steel in glass. These structures also appear to have grown in non-dendritic manner.

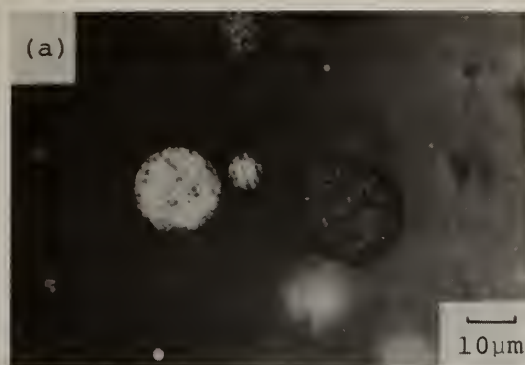


Figure 10. (a) Optical micrograph of cross-sectioned and etched 316 BCC and FCC particles after undercooling. Fcc particles are light in color. (b) Backscattered electron micrograph of the same particles, from MacIsaac [44].

The attributes of high undercooling and rapid heat extraction are optimized in emulsions when the emulsion itself is rapidly cooled by external means. One way to do this is shown in Figure 11 [45], where an emulsion of a metal in a carrier fluid is injected into a cooler miscible fluid that is being vigorously agitated. This is a technique developed by M.G. Chu in his doctoral thesis work at MIT. Figure 12 shows two structures of Sn-5%Pb alloy illustrating the importance of this external cooling. When the alloy is emulsified in such a way that it can achieve an undercooling of 100°C or more at slow cooling rates, and then is rapidly cooled using the apparatus of Figure 11, a fully homogeneous, non-dendritic structure is obtained, at least at 1000X, Figure 12a. This is in spite of the fact that the maximum equilibrium solid solubility of lead in tin is 2.5%. When, however, these samples are more slowly cooled, or reheated, or held for an extended period of time at room temperature, substantial precipitation of lead rich phase occurs, Figure 12b. In the case of Chu's work, the effect of the quench was probably primarily in preventing solid state decomposition. In other cases (e.g.) quenching liquid iron in molten salt. Table 2, heat extraction rates might conceivably be increased enough by the cold salt to influence solidification kinetics.

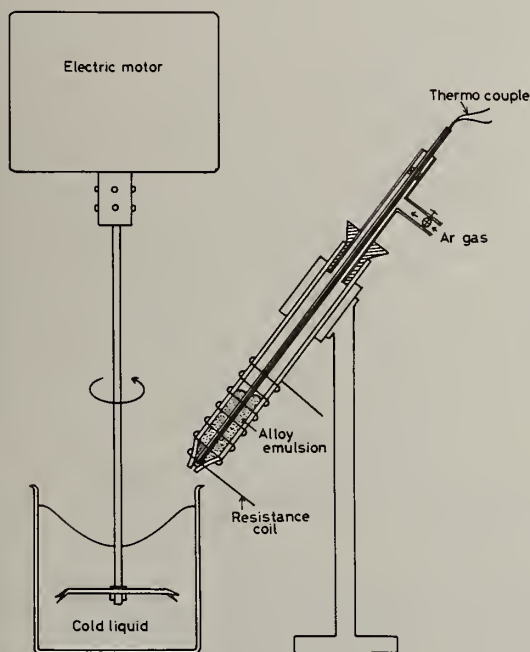


Figure 11. Diagram of apparatus for rapid quenching of molten emulsified droplets, from Chu et al [45].



Figure 12. Microstructures of emulsified droplets of Sn-5%Pb: (a) Rapidly cooled to -25°C, (b) Rapidly cooled and then held one month at room temperature 1000X.

Quite complex solidification structures can be obtained in undercooled alloys when more than one phase forms during recalescence. Chu has studied a wide variety of such structures in tin-lead alloys; the structures obtained depend on alloy, undercooling and rate of heat extraction during and after recalescence. with the particular emulsification technique he used, and a moderate cooling rate (10°C/min), he found the nucleation temperatures plotted in the phase diagram in Figure 13a. A tin rich phase forms at T_n and a lead rich phase at T'_n . Perepezko [21] previously had found similar nucleation temperatures, Figure 13b, and by using a different emulsification medium, he was able to get the lower nucleation temperatures also shown in Figure 13b.

Solidification of hyper-eutectic tin-lead alloys was found to occur in the following sequence: (a) nucleation at T'_n of a lead rich phase, (b) dendritic growth of this phase, first during recalescence and then during subsequent cooling T_n , where a tin rich phase nucleates, (c) growth of the tin rich phase during recalescence and during subsequent cooling. Note that the recalescence and solute distribution during growth of the second phase can be expected to influence the first phase to form. In addition the intervention of the formation of a metastable phase prior to the tin rich phase due to catalysis by the lead rich phase [16] can also influence the overall solidification sequence and microstructure. Figure 14 shows examples of solidification structures of such an alloy. Figure 14a is a structure that was undercooled and rapidly quenched. Lead rich dendrites (white) first formed and tin rich phase (dark) later filled in within the interstices. Both the tin rich and lead rich phases shown substantial second phase with themselves, presumably from solid state precipitation. Figure 14b is a sample that was allowed to nucleate on slow cooling and then rapidly solidified. The dendritic structure formed as before, and the final structure is very little different. The sample allowed to cool slowly (10°C/min) however, shows massive ripening of the original lead rich phase, Figure 14c.

Three different tin-lead structures of eutectic composition are shown in Figure 15. The first is comparable to the slowly cooled Sn-45%Pb alloy discussed above, in that it shows primary, ripened lead rich phase (with entrapped and precipitated tin rich phase), Figure 15a. The second shows the same alloy rapidly cooled, Figure 15b. Apparently the rapid cooling suppressed the nucleation temperature of the lead rich phase, T'_n below that of the tin rich phase, T_n . The third structure, Figure 15c, from work of Cooper, Anderson and Perepezko [46] is similar to 15b, but somewhat coarser. In this case the nucleation temperature T'_n was depressed below T_n by a modified emulsion; this depression is shown in figure 13. The second two eutectic structures are similar to those obtained in conventional rapid solidification processes, e.g. wheel casting [47].

Recalescence Measurements in Droplet Solidification

Ewasko [48] and Wu [43] in separate theses at MIT are attempting to gain some experimental understanding of the "solidification paths" of undercooled alloys by looking at thermal behavior and structure of 5mm dia. metal droplets undercooled in molten glass. Their results to date illustrate well how much we do not understand yet about this process.

As one example, the rate of recalescence of the droplet surface increases dramatically with increasing undercooling, Figure 16. We believe that this cannot be a heat flow caused phenomenon since experiments on pure nickel show orders of magnitude faster recalescence. Thus, a preliminary conclusion is that these rates of recalescence (at least at temperatures approaching and above the calculated T_0) are limited by solute transport. The T_0 temperature in Figure 16, incidentally, was calculated from a regular solution model.

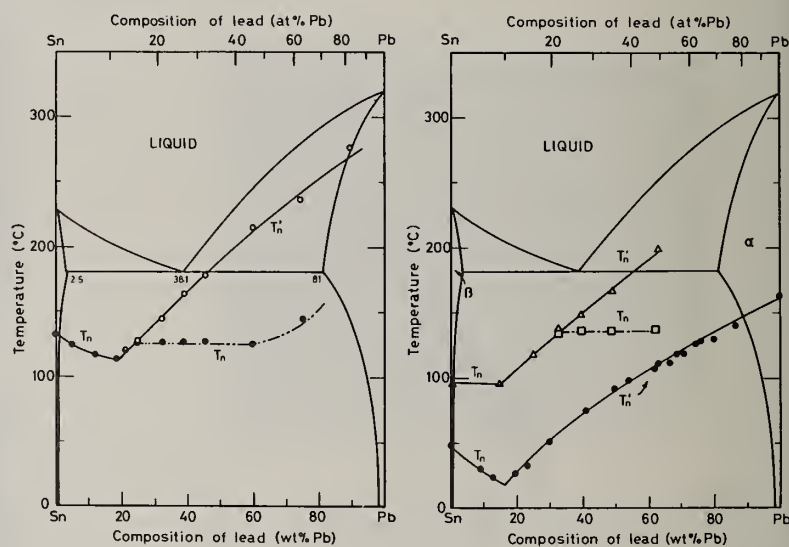


Figure 13. Nucleation temperature in supercooled Sn-Pb alloys. T_n is nucleation temperature of tin rich phase and T'_n of lead rich phase. Diagram on left is from Chu et al [45] and on the right is from Cooper et al [46]. Exact amounts of undercooling depend on emulsification procedure. The two different sets of curves in diagram on the right result from the different emulsification procedures.

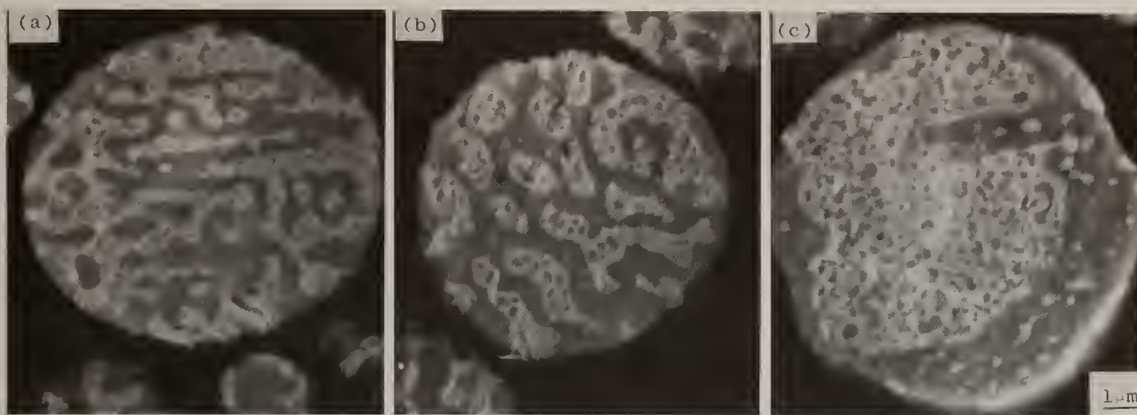


Figure 14. Microstructures of Sn-45%Pb alloy droplets, 7000X. (a) Rapidly quenched (b) Slowly cooled to just below T_n and quenched (c) Slowly cooled to room temperature.

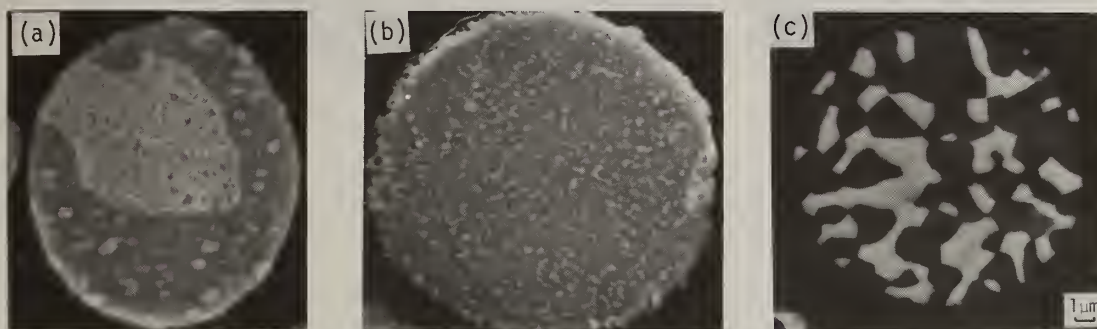


Figure 15. Microstructures of emulsified droplets of eutectic Sn-Pb alloy. (a) Slowly cooled, moderate undercooling, (b) Undercooled and rapidly solidified, (c) Slowly cooled, high undercooling.

The photomicrographs in Figure 17 provide some insight into factors influencing this recalescence, by showing the very different structures at different undercoolings. At moderate undercooling where temperature is estimated to be above the thermodynamic T_0 temperature, recalescence is very slow, and a two phase structure results that has a coarse dendritic appearance, Figure 17a. Initial results show the core of this "dendrite" is of approximately C_0 composition, the periphery is depleted, and the interdendritic regions appear to be somewhat above C_0 , possibly it grew as a single phase initially into solute redistribution at least during later stages of growth. If so, we would expect re-melting on a fine scale within the dendrites as it recalesces above some temperature approaching T_0 ; the liquid pools remelting could lead to the finely distributed second phase within the "dendrite".

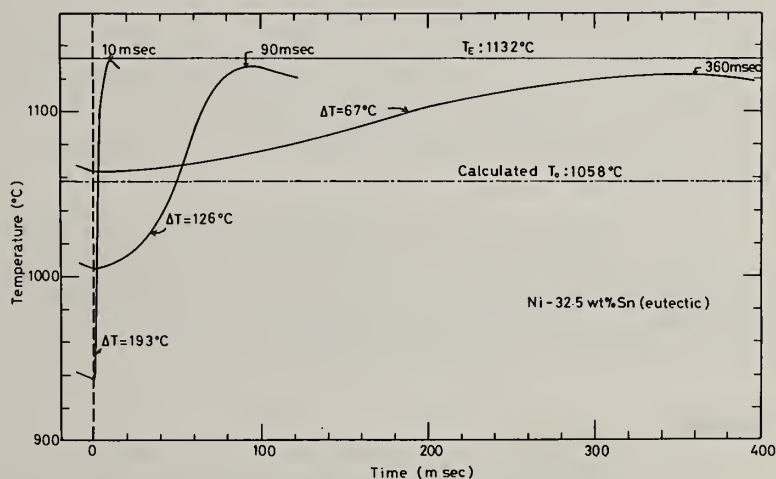


Figure 16. Recalescence curves from 5mm droplets of Ni-Sn eutectic alloy at several undercoolings, from Ewasko [48].

The sample at the intermediate undercooling in Figure 17 show a fine grain structure with a multiplicity of growth sites, each of which has a central region (two phase) that may well have

initially grown in a diffusionless manner below T_0 and later partially remelted during recalescence. The fine scale of this structure due to the multiplicity of growth sites would explain the more rapid recalescence, even above T_0 . This qualitative description of solidification behavior for such an alloy is largely conjecture, but the approach suggests an experimental direction toward an eventual fuller thermal and solidification description of undercooled alloys.

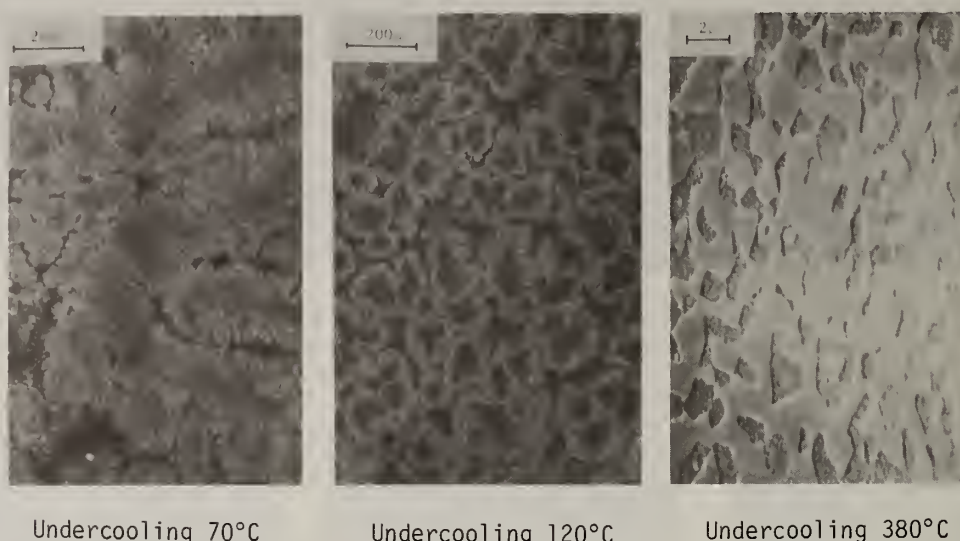


Figure 17. Structure of 5mm droplets of Ni-Sn eutectic alloy solidified at 3 different undercoolings, from Wu [43].

Conclusions

In examining the nucleation and solidification of undercooled liquid metals it is apparent that the experimental and theoretical understanding has made good progress since the initial pioneering work of Turnbull. From the present experience with droplets studies it has been possible to identify some general guidelines for the interplay between process variables such as cooling rate, undercooling, alloy composition and particle size and the nucleation phase selection involved in RSP. With droplet samples and controlled undercooling conditions new understanding has been gained into the development of solidification microstructure and the influence of thermal history on the final microstructural morphology. This area of research in the study of RSP, we believe, has a great potential for the further development of nucleation and solidification theory. It also has the potential for the development of new processes of engineering importance. In this regard it seems possible that we can someday learn to enhance undercooling with controlled surface treatments in existing RSP methods, and perhaps, as well, find ways to bring other processes such as emulsification to the point of engineering usefulness.

Acknowledgement

The support and the ARO (DAAG29-80-K-0068) for studies on solidification structures and the NSF (DMR-79-15802) for work on nucleation catalysis kinetics at the University of Wisconsin-Madison is gratefully acknowledged. Portions of this work (those at MIT) were sponsored by NASA Grant No. NSG 7645, from Materials Processing & Space Division, NASA office, with Dr. Louis Testardi, project monitor.

References

- [1]. J. H. Perepezko, in Proceedings of Rapid Solidification Processing: Principles and Technologies II, R. Mehrabian, B. H. Kear and M. Cohen eds., Claitor's Pub., Baton Rouge, La. 56 (1980).
- [2]. D. Turnbull and R. E. Cech, J. Appl. Phys. 21, 804 (1950).
- [3]. C. C. Wang and C. S. Smith, Trans. AIME 188, 136 (1950).
- [4]. E. Meyer and L. Rinderer, J. Crystal Growth, 28, 199 (1975).
- [5]. R. E. Cech and D. Turnbull, Trans, AIME, 206, 124 (1956).

- [6]. L. L. Lacy, M. B. Robinson and T. J. Rathz, J. Crystal Growth 51, 47 (1980).
- [7]. T. Z. Kattamis and M. C. Flemings, Trans. AIME 236, 1523 (1966).
- [8]. S. Y. Shirashi and R. G. Ward, Canadian Met. Quaterly, 3, 117 (1964).
- [9]. D. Turnbull, J. Chem. Phys., 20, 411 (1952).
- [10]. J. H. Perepezko and J. S. Paik, in Proceedings of the 29th Midwest Solid State Conference: Novel Materials and Techniques in Condensed Matter, G. Crabtree and P. Vashishta eds., North Holland, N.Y., 57 (1982).
- [11]. D. Turnbull, J. Chem. Phys., 18, 198 (1951).
- [12]. C. V. Thompson and F. Spaepen, Acta. Met., 27, 1855 (1979).
- [13]. M. Hillert, Acta Met., 1, 763 (1953).
- [14]. C. V. Thomson and F. Spaepen, in Proceedings of the Materials Research Society Symposium: Materials Processing in the Reduced Gravity Environment of Space, G. E. Rindone eds., North Holland, N.Y., 603 (1982).
- [15]. J. S. Paik and J. H. Perepezko, to be published.
- [16]. A. S. Skapski, Acta Met., 4, 576 (1956).
- [17]. F. Spaepen and R. B. Meyer, Scripta Met., 10, 257 (1976).
- [18]. R. H. Ewing, Phil. Mag., 25, 778, 1972.
- [19]. A. Bonnissent, J. L. Finney and B. Mutaftschiev, Phil. Mag. B, 42, 2, 233 (1980).
- [20]. Y. Waseda and W. A. Miller, Trans. JIM, 19, 547 (1978).
- [21]. J. H. Perepezko and J. S. Paik, in Proceedings of the Material Research Society Symposium: Rapidly Solidified Amorphous and Crystalline Alloys, B. H. Kear, B. C. Giessen and M. Cohen eds., North Holland, N.Y., 49 (1982).
- [22]. R. E. Cech, J. Metals, 8, 565 (1956).
- [23]. D. Turnbull, Acta Met., 1, 8 (1953).
- [24]. A. J. Drehman and D. Turnbull, Scripta Met., 15, 543 (1981).
- [25]. B. C. Giessen and R. H. Willens in Phase Diagrams: Materials Science and Technology Vol. III, A. M. Alper ed., Academic Press, N.Y., 104 (1970).
- [26]. J. C. Baker and J. W. Cahn, in Solidification, ASM, Metals Park, Ohio, 23 (1971).
- [27]. J. L. Murray, to be published
- [28]. T. F. Kelly, M. Cohen and J. B. Vander Sande, submitted to Metal Trans. A, (1982).
- [29]. C. M. Adam, Private Communication.
- [30]. I. E. Anderson, J. H. Perepezko and B. C. Giessen, to be published.
- [31]. C. G. Levi and R. Mehrabian, Met. Trans. 13A 13, 221 (1982).
- [32]. G.H. Geiger and D.R. Poirier: "TRANSPORT PHENOMENA IN METALLURGY", Addison-Wesley Publishing Company, Reading, MA(1973).
- [33]. N.J. Grant, in "RAPID SOLIDIFICATION PROCESSING-PRINCIPLES AND TECHNOLOGIES I", Baton Rouge, Claitor Publishing Division, 230(1978).
- [34]. C.G. Levi and R. Mehrabian, "HEAT FLOW DURING SOLIDIFICATION OF UNDERCOOLED METAL DROPLETS", to be published.

- [35] D. Turnbull, "THERMODYNAMICS IN PHYSICAL METALLURGY", American Society for Metals, Metals Park, OH(1949).
- [36] J.W. Cahn, W.B. Hilling and G.W. Sears, Acta. Met., 12, 1421(1964).
- [37] J.L. Walker, unpublished work presented in "PRINCIPLES OF SOLIDIFICATION", B. Chalmers, Chapter 4, John Wiley(1964).
- [38] G.A. Colligan and B.J. Bayles, Acta. Met., 10, 895(1962).
- [39] M.E. Glicksman, R.J. Schaefer, and J.D. Hyers, Metall. Trans. 74, 1947(1976).
- [40] S.R. Coriell and D. Turnbull, submitted Acta. Met.(1981).
- [41] W.J. Boettenger, S.C. Coriell, R.E. Sekerka, RAPID SOLIDIFICATION PROCESSING PRINCIPLES AND TECHNOLOGIES III., to be published.
- [42] T.Z. Kattamis and M.C. Flemings, Trans. A.F.S., 75, 191(1967).
- [43] Yan-Zhong Wu, unpublished work, Massachusetts Institute of Technology.
- [44] D.G. MacIsaac, Y. Shiohara, M.G. Chu and M.C. Flemings submitted Proc. AIME Fall Meeting (St. Louis 1982).
- [45] M.G. Chu, Y. Shiohara, M.C. Flemings, submitted Proc. AIME Fall Meeting (St. Louis 1982).
- [46] K.P. Cooper, I.E. Anderson and J.H. Perepezko, Proc. 4th Int. Conf. on "RAPIDLY QUENCHED METALS VOL. 1" 107, Sendai, Japan(1981).
- [47] R. Cheese and B. Cantor, Materials Science and Engineering, 45, 83(1980).
- [48] Ricky Ewasko, S.M. Thesis, Department of Materials Science and Engineering, Massachusetts Institute of Technology(1982).

MECHANISMS OF SEGREGATION-FREE SOLIDIFICATION

W. J. Boettinger, S. R. Coriell

Metallurgy Division
National Bureau of Standards
Washington, DC 20234

and

R. F. Sekerka*

Carnegie-Mellon University
Pittsburgh, PA 15213

ABSTRACT

A frequent microstructural feature of rapidly solidified alloys is the absence of cellular or dendritic microsegregation, often accompanied by incorporation of solute in excess of the equilibrium solid solubility. Two solidification mechanisms can produce microsegregation-free crystalline solids: planar growth and partitionless solidification. The solidification conditions required for planar growth with equilibrium partitioning at the interface are well known. For growth at high velocities, capillarity provides a stabilization of the planar interface. This regime is referred to as absolute stability and applies only when the net heat flow is toward the solid. Partitionless solidification arises from the kinetics of interface motion. These kinetics can involve the trapping of solute by the moving interface, causing the partition coefficient to deviate from the equilibrium value. Solute trapping generally occurs at high interface velocities and may be pronounced when the interface temperature is far below the liquidus. In the limit of partitionless solidification, when the partition coefficient is unity, the interface temperature is below the T_0 temperature for the composition at the interface. Partitionless solidification provides a mechanism for the formation of segregation-free crystalline alloys when the net heat flow is toward the liquid or when the interface is not planar. Recent work has combined a velocity dependent partition coefficient with interface stability theory to predict the solidification conditions required for microsegregation-free solidification. Under some conditions, oscillatory instabilities are predicted. The relation of the interface temperature to the liquidus, solidus and T_0 temperatures as a function of growth rate and considerations necessary to predict the conditions of microsegregation-free solidification in concentrated alloys are discussed.

Introduction

Microsegregation-free crystalline alloys including those with solute in excess of equilibrium solubility provide an ideal starting microstructure for the development of interesting mechanical properties during subsequent thermomechanical processing [1]. In this paper, the following three topics related to the solidification conditions required to produce such microstructures will be described: the interface temperature during solute trapping; the interface stability theory; and the conditions for microsegregation-free solidification of concentrated alloys. It will be assumed that the phase which is forming from the melt has been selected previously by nucleation kinetics or by competition among growing crystalline phases. Under this assumption, the primary role of nucleation is to allow the development of a large bulk undercooling of the liquid into which growth can occur quite rapidly. This paper focuses on the conditions at the solid-liquid interface, with the realization that a full analysis of heat and solute transport must be conducted to form the basis for a final choice of processing conditions.

*Consultant, National Bureau of Standards

In 1971, Baker and Cahn [2] posed the solidification problem of a binary alloy using two response functions. One choice for the response functions describes the interface temperature, T_I , and the composition of the solid at the interface, C_S^* . These response functions can be written as follows:

$$T_I = f(V, C_L^*) - T_M \Gamma K \quad (1)$$

$$C_S^* = C_L^* k(V, C_L^*) \quad (2)$$

where V is the local interface velocity, C_L^* is the composition of the liquid at the interface, $T_M \Gamma$ is a capillarity constant, and K is the mean curvature of the solid-liquid interface. At zero velocity, the functions f and k are very simply related to the phase diagram: $f(0, C_L^*)$ is the equation for the phase diagram liquidus and $k(0, C_L^*)$ is the equation for the equilibrium partition coefficient, k_E , which can depend on composition.

These response functions are constrained by thermodynamics. Fig. 1 shows the molar free energy versus composition for a liquid and a solid phase at a fixed temperature. During solidification, the temperature and the compositions at the interface are constrained by the fact that there must be a net decrease in the free energy per mole, ΔG , needed to form an infinitesimal amount of solid of composition C_S^* from liquid of composition C_L^* [2]. The free energy change is shown in Fig. 1, and is given by

$$\Delta G = (\mu_S^A - \mu_L^A)(1 - C_S^*) + (\mu_S^B - \mu_L^B)C_S^*. \quad (3)$$

Under the usual assumption of local equilibrium at the solid-liquid interface, believed to be valid at slow rates of solidification, the chemical potentials of the liquid, μ_L^i , and solid, μ_S^i , for each species, i , must be equal. During rapid rates of solidification, this is not necessarily the case and nonequilibrium conditions at the interface can exist. The term solute trapping is loosely applied to conditions when the partition coefficient deviates from the equilibrium value, but as originally defined, is restricted to the case when the chemical potential of the solute increases during solidification. Baker and Cahn showed that the restriction that ΔG be negative could be represented on a figure where, for constant temperature, the range of possible solid and liquid

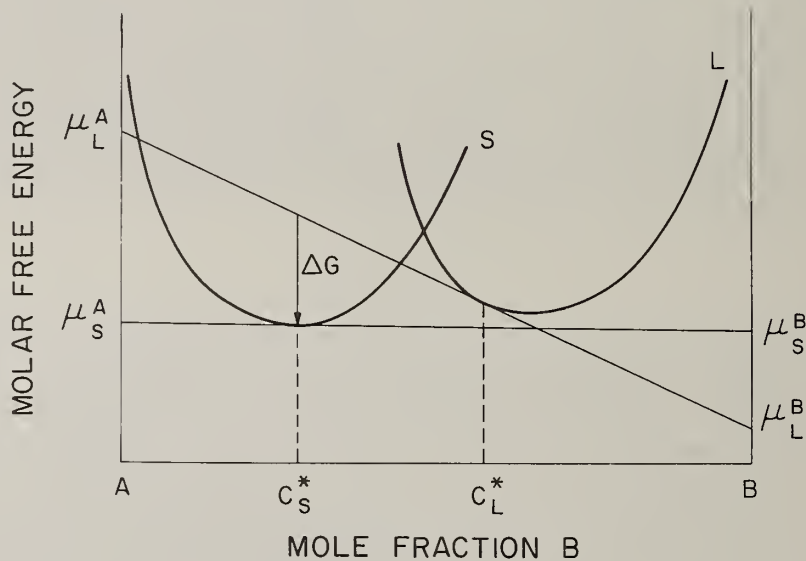


Fig. 1. Construction to show the Gibbs free energy per mole, ΔG , for solidification of an infinitesimal amount of solid of composition C_S^* from a liquid of composition C_L^* under non-equilibrium conditions for which the chemical potentials $\mu_L^A \neq \mu_S^A$ and $\mu_L^B \neq \mu_S^B$.

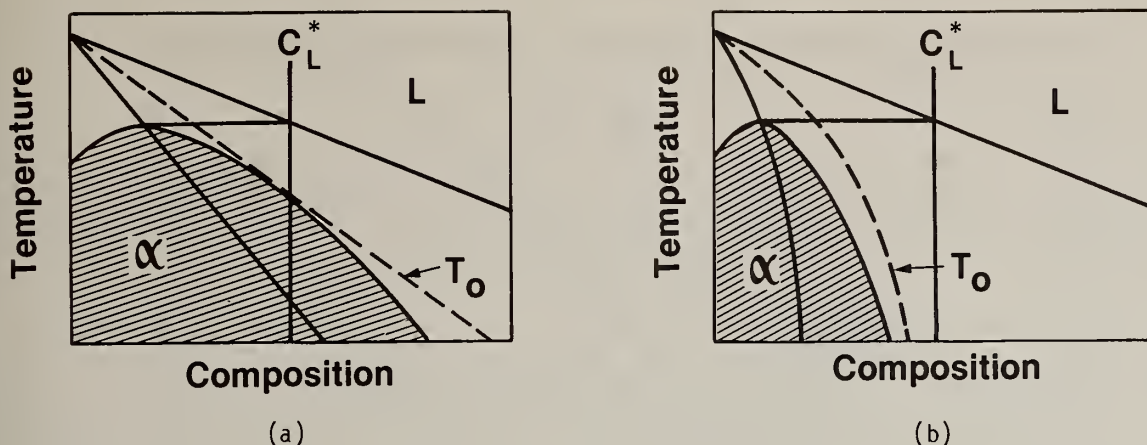


Fig. 2. Regions (cross-hatched) of thermodynamically allowed solid compositions that may be formed when solid solidifies from liquid of composition C_L^* at various temperatures. The value of T_0 is the highest temperature at which partitionless solidification of a liquid of given composition can occur. In (b), the T_0 curve plunges and partitionless solidification is impossible for liquid of composition C_L^* . (From reference [3]).

concentrations are shown. Fig. 2 shows an alternate representation of this restriction [3]. The cross-hatched region shows the range of possible solid compositions that can form from a liquid of composition C_L^* at various temperatures. When the temperature is equal to the liquidus temperature for the composition C_L^* , the only possible solid composition is the equilibrium solid composition. For interface temperatures below the liquidus, the range of allowable solid composition expands. Of particular interest is the T_0 curve which lies between the liquidus and solidus. The T_0 curve is the locus of compositions and temperatures for which the molar free energy of the liquid and solid phases are equal. When the temperature of the liquid at the interface reaches the T_0 curve, the solid can have the same composition as the liquid, i.e., partitionless solidification. Fig. 2b shows a case where the T_0 curve plunges quite steeply. In this case, for the composition C_L^* , partitionless solidification is not possible, i.e., the partition coefficient, k , cannot approach unity at high velocity.

Many models for the dependence of the partition coefficient on velocity have been formulated [4-7]. This dependence on velocity constitutes one of the two response functions required to analyze rapid solidification problems. The model formulated by Baker [4] is quite general and includes a wide variety of possibilities. Fig. 3 shows the results of more recent theories which predict that the partition coefficient changes monotonically from its equilibrium value to unity as the growth velocity increases. In these models the interface partition coefficient is a function of a dimensionless velocity, $\beta_0 V$, where β_0 is the ratio of a length scale, a_0 , normally related to the interatomic distance and a diffusion coefficient, D . The diffusion coefficient in the various models ranges between a liquid diffusion coefficient and a diffusion coefficient characteristic of the interface itself. The functional form of the model proposed by Aziz [5] and Jackson, Gilmer and Leamy [6] for continuous growth is given as

$$k(V) = \frac{k_E + \beta_0 V}{1 + \beta_0 V} \quad (4)$$

where $\beta_0 = a_0/D$. At a velocity of $1/\beta_0$, the partition coefficient is the average of the equilibrium partition coefficient and unity. If we choose a liquid diffusion coefficient typical of metals (10^{-5} cm²/s) and the length scale to be 5 \AA , $1/\beta_0$ is 200 cm/s. However, the value of $1/\beta_0$ which best fits [5] recent experimental data for doped Si is 10 m/s; for Si, $D = 5 \times 10^{-4}$ cm²/s [8], and hence $a_0 = 50\text{ \AA}$. It remains a challenge to design good experiments to determine the velocity required for solute trapping in metallic alloys.

There are significant shortcomings in the present models of the dependence of the partition coefficient on velocity. The models primarily treat dilute alloys so there is no explicit dependence on composition. For the case of Fig. 2b, where the T_0 curve plunges, the partition coefficient cannot approach unity at high velocity. A second shortcoming of the present trapping models is that the response function for the interface temperature is not treated.

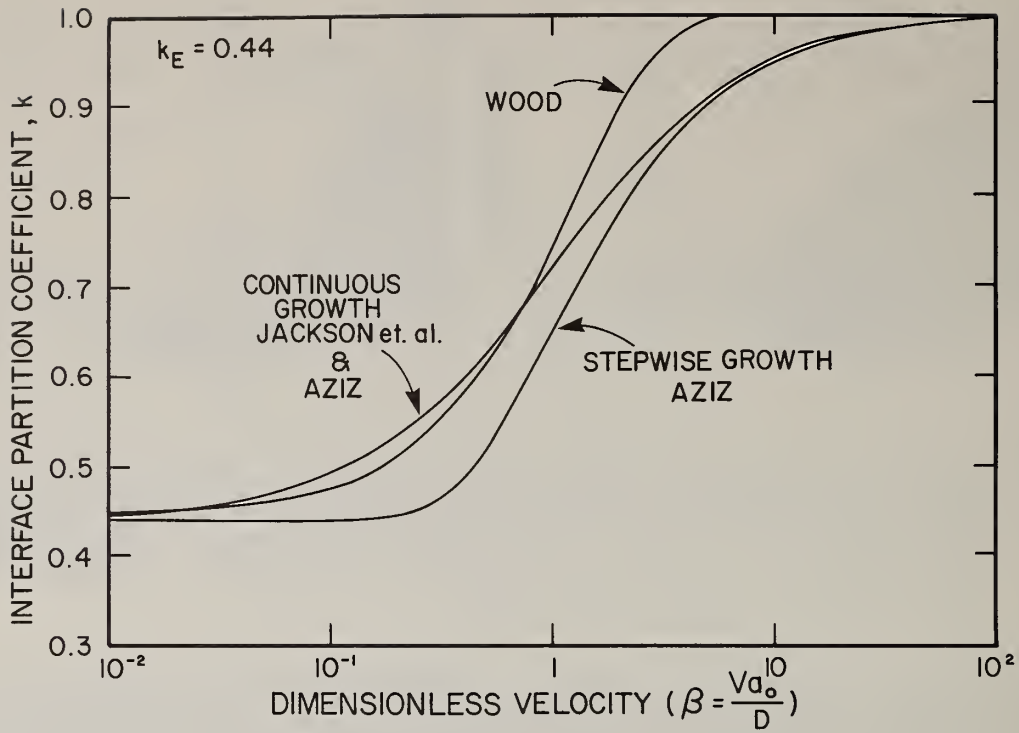


Fig. 3. Curves showing the dependence of the interface partition coefficient, k , on velocity according to the models of various investigators.

Following the suggestion of Aziz [5] a model for the response function for the interface temperature can be formulated. For pure materials Turnbull et al. [9,10] have suggested that the rate at which atoms attach to the growing crystalline solid may only be limited by their rate of collision with the solid. In such a case, the interface velocity is related to the interface temperature, T_I , by an expression

$$V = fV_0\{1 - \exp(\Delta G/RT_I)\} \quad (5)$$

where f is the fraction of sites on the solid-liquid interface available for attachment, V_0 is the speed of sound in the liquid metal, ΔG is the molar free energy for solidification and R is the gas constant. For most metals, f is thought to be close to unity and for velocities much less than the speed of sound, this expression can be written as

$$V = -V_0 \left(\frac{\Delta G}{RT_I} \right). \quad (6)$$

For the solidification of disordered crystals, this collision limited model of solidification may apply as well. This model will be employed to formulate a response function for the interface temperature for a binary alloy. The molar free energy for solidification is evaluated from Eq. (3) and, in special cases, can be described simply in terms of undercooling. When solute trapping occurs a simple expression in terms of undercooling is not possible. For pure metals ΔG reduces to

$$\Delta G \approx \frac{-L(T_M - T_I)}{T_M} \quad (7)$$

where L is a latent heat and T_M is the melting point of the pure metal. For dilute alloys, when the partition coefficient equals the equilibrium partition coefficient, k_E , the thermodynamic driving force for solidification is given by

$$\Delta G \approx \frac{-L(T_L - T_I)}{T_L} \quad (8)$$

where T_L is the liquidus temperature for the concentration of the liquid at the interface C_L^* . When the partition coefficient is identically equal to one, ΔG has a similar form,

$$\Delta G \approx \frac{-L(T_0 - T_I)}{T_0} \quad (9)$$

where the undercooling ($T_0 - T_I$) is referred to the T_0 temperature for the interface composition. The similarity of the expressions for the case where k equals one, i.e., partitionless solidification, and the expression for pure metals, is the origin of the often stated idea that the kinetics of partitionless solidification are quite rapid and similar to that for the solidification of a pure metal. In the general case when the partition coefficient is not the equilibrium value, the thermodynamic driving force for solidification must be evaluated from the full expression given by Eq. (3). In this expression the chemical potentials are functions of concentration and temperature that may be determined by modelling the phase diagram. This demonstrates the importance of modelling phase diagrams, even for applications to rapid solidification. If Eqs. (3 & 5) are combined with, for example, the trapping model of Aziz, Eq. (4), the interface temperature can be determined as a function of the interface velocity and the concentration of the liquid at the interface. A similar calculation for other models of solute trapping or interface temperature can be performed. Alternatively, part of the free energy for solidification can be dissipated by solute drag, as reported by Aziz in the current proceedings [11].

Fig. 4 shows a composite plot of the two response functions obtained by using Eqs. (3-5) superimposed on the phase diagram including the liquidus, solidus and T_0 curve. The composition of the solid at the interface and the interface temperature are plotted along a curve parameterized by interface velocity for a given fixed liquid concentration at the interface. The figure is based on thermodynamic data for Ag-Cu [12], a liquid composition of 8.2 at% Cu, a value of β_0 of 10^{-2} s/cm and for two values of V_0 (infinity and 2×10^5 cm/s). At zero velocity, the composition of the solid lies on the solidus curve. At intermediate velocities (~ 10 cm/s), the concentration of the solid moves towards the concentration of the liquid with a small increase in the undercooling. At high velocities the solid composition at the interface approaches the liquid concentration at the interface near the T_0 curve. The dashed curve shows the case where V_0 is infinite. This corresponds to the thermodynamic bound on the solid concentration at the interface given in the Fig. 2. The dashed curve can also be obtained by letting $\Delta G = 0$ in Eq. (3). The solid curve, for a finite value of V_0 , shows the interface temperature plunging quite rapidly. This analysis provides, for the first time, a pair of response functions for the conditions at the liquid-solid interface, thus permitting the analysis of rapid solidification problems when combined with solute redistribution and heat flow analysis. Such curves are of interest during recalescence when the velocity of the interface starts out at a high value and decreases due to the evolution of latent heat. They are also required for a detailed analysis of the stability of the solid-liquid interface during solute trapping.

Interface Stability

Interface stability theory is of interest because, during planar growth, solidification occurs with no lateral microsegregation. The theory was first developed by Mullins and Sekerka [13] and has been extended and discussed in more detail for rapid solidification by Coriell and Sekerka [14-15]. The present paper is restricted to a discussion of the simple asymptotic form of the stability theory relevant at high velocity. This asymptotic form is known as absolute stability and is given by the expression

$$V = \frac{mD(1-k_E)C}{k_E^2 T_M \Gamma} \quad (10)$$

where m is the liquidus slope, D is the liquid diffusion coefficient and C is the alloy composition. Whenever V exceeds the value given in Eq. (10), a planar liquid-solid interface is stable. Absolute stability of a planar interface occurs because of the influence of capillarity. At high growth velocities, there is only limited time available so lateral solute segregation in the liquid can

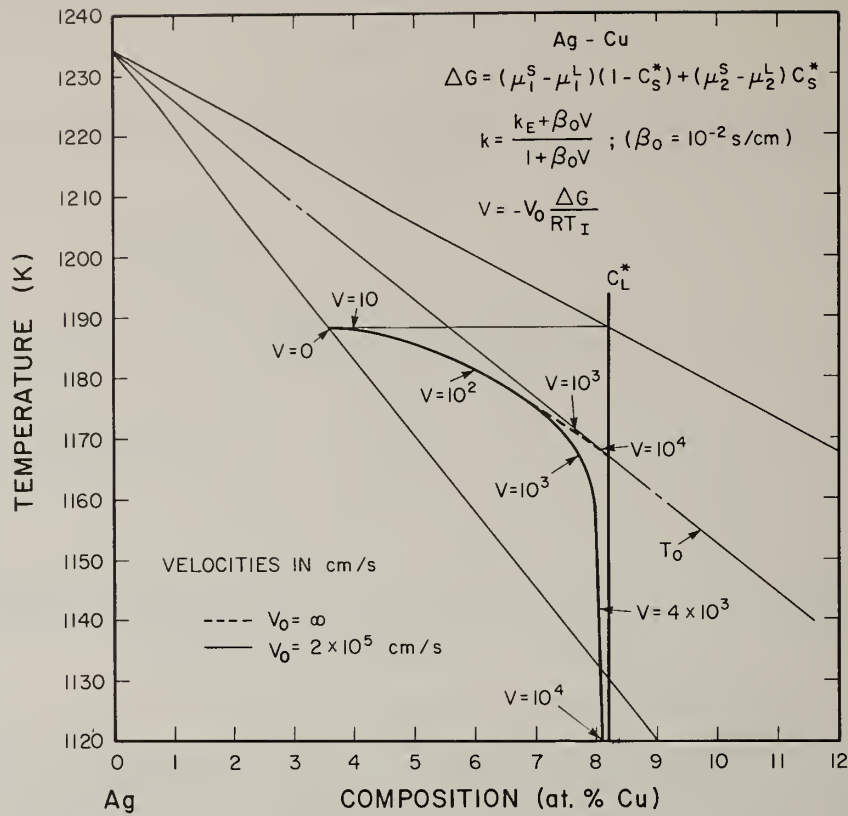


Fig. 4. Interface temperature and solid compositions for solid that forms at the indicated velocities from a liquid of fixed composition C_L^* at the interface. Thermodynamic parameters are for Cu in Ag for a specific kinetic law with $V_0 = 2 \times 10^5$ cm/s (full curve) and $V_0 \rightarrow \infty$ (dashed curve).

only occur for perturbations of the solid-liquid interface with very short wavelengths. These short wavelengths require such a large increase in the area of the interface that the perturbations are retarded by capillary forces and the interface is stable.

There are several restrictions on the use of the simple asymptotic form given by Eq. (10). First, rather trivially, this form is only valid if the partition coefficient is the equilibrium partition coefficient. Modifications required when the partition coefficient depends on the velocity will be discussed in a later section. A second restriction is that the net heat flow must be into the solid, i.e.,

$$G^* = \frac{k_L G_L + k_S G_S}{k_L + k_S} > 0. \quad (11)$$

Here k_L and k_S are the thermal conductivities of the liquid and solid respectively. G_L and G_S are the temperature gradients in the liquid and solid respectively. In the case of solidification following surface melting, the conduction of heat is almost completely into the solid and G^* is always positive. For quenching against a substrate or for atomization, the sign of G^* is less clear. What is important is the relative amount of heat flowing into the solid and flowing into the liquid. For quenching against a substrate, bulk undercooling of the liquid can occur if nucleation is difficult. In this case, during solidification heat can flow both into the solid and into the liquid to remove the latent heat evolved at the liquid-solid interface. An experimental observation in which planar growth is stable, and G^* is negative, would require a reexamination of the assumptions

in the present stability theory. In this event two possible modifications [14] would be an allowance for a velocity of solidification that depends on time or an analysis of solidification in samples in which the wavelength of the fastest growing instability is of the same order as the sample itself. A third restriction on the use of the absolute stability equation is that one must be far from the modified constitutional supercooling regime of the full stability theory. This condition will be satisfied whenever the velocity

$$V \gg \frac{LD^2}{(k_s + k_L)T_M \Gamma k_E}, \quad (12)$$

provided also that the temperature gradient in the liquid is not too large [$G_L \ll VL/(2k_L)$] as is usually the case for rapid solidification. Here, L is the latent heat per unit volume. This restriction is more important for doped Si [15] than for metallic alloys due to the relatively high latent heat and diffusion coefficient for Si.

In a recent set of experiments employing electron beam surface melting [16-17] the applicability of the morphological stability theory to rapid solidification has been demonstrated. Fig. (5) shows the transition from cellular to cell-free structure which occurs in Ag-1 wt% Cu and Ag-5 wt% Cu alloys. For the former, the transition occurs between 10 and 20 cm/s, and for the latter, the transition occurs between 50 and 60 cm/s. Fig. 6 shows a summary of the experimental results for the two alloys. The transition from cellular to cell-free material is seen to occur at velocities roughly a factor of 2 less than the theoretical predictions. Such agreement is considered reasonable in view of the imprecise knowledge of the materials parameters required for the theory. A more complete discussion of these results occurs elsewhere [16].

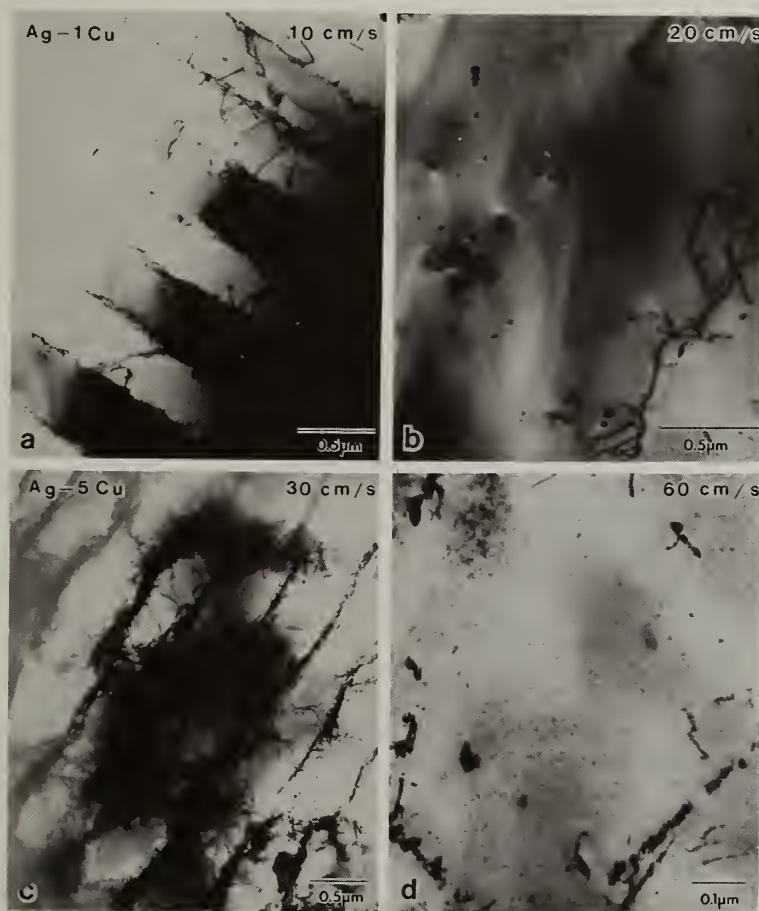


Fig. 5. a) Cellular and b) cell-free structures obtained in Ag-1 wt% Cu alloys rapidly solidified at 10 and 20 cm/s respectively. c) Cellular and d) cell-free structures obtained in Ag-5 wt% Cu alloys rapidly solidified at 30 and 60 cm/s respectively [16], TEM.

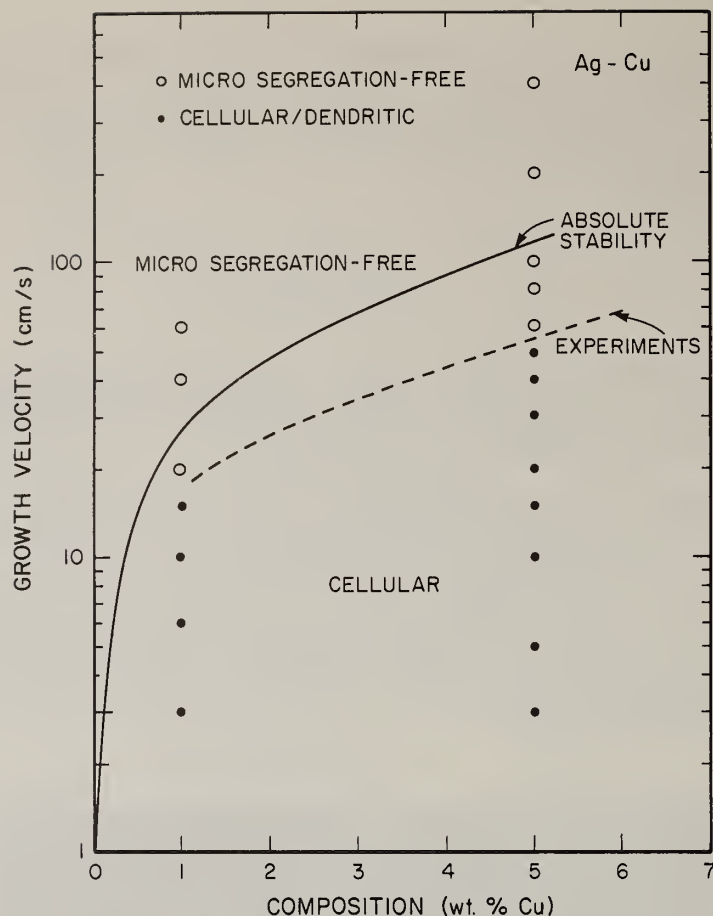


Fig. 6. Summary of structures obtained [16] by electron beam surface melting and resolidification of Ag-1 and 5 wt% Cu alloys at various growth rates. The comparison of the absolute stability theory with experiments is shown.

When the partition coefficient depends on the interface velocity, the stability theory must be modified [18]. This modified analysis of stability suggests the possibility of increased instability of a planar liquid-solid interface, attributed to a feature called the "solute pump mechanism". Physically, the partition coefficient will vary across a perturbed solid-liquid interface because of local differences in velocity. This leads to a variation of the solute rejection rate along the interface and produces lateral solute segregation without the necessity of lateral diffusion. Hence perturbations with wavelengths much longer than those normally encountered at high growth velocity can occur and capillarity is less effective in stabilizing such perturbations. The results of the theory are complex and will only be described qualitatively here. It is found that the actual value of the partition coefficient can be substituted into the absolute stability equation only under certain conditions. If the rate of change of the partition coefficient with velocity is relatively small, and/or the absolute value of the rate of change of the interface temperature with respect to velocity is relatively large, this simple substitution method is valid. On the other hand, if the rate of change of the partition coefficient with velocity is large and/or the absolute value of the rate of change of the interface temperature with velocity is small, the simple substitution is not valid. Clearly the details of the size of these derivatives depends critically on the parameters β_0 and V_0 described in the previous section. Fig. 7 shows a plot of the demarcation between stability and instability for Ag-Cu alloys for a choice of β_0 of 10^{-2} s/cm and for various values of μ_T where $\mu_T = -\partial V/\partial T_I$. On the right side of the figure is shown the variation of the partition coefficient with velocity. On the left side is shown the demarcation between stability and instability. Depending upon the value of μ_T , the stability criterion can change dramatically.

It should be pointed out that the instability in the case of the "solute pump mechanism" is oscillatory in nature. This arises because of the temporal phase difference between the local velocity of the interface and the interface shape. Such oscillatory instabilities lead to microsegregation patterns that are three dimensional, whereas an ordinary microsegregation pattern is two dimensional (in directions transverse to the growth direction). Such oscillatory instabilities have not been observed, and only future experiments will determine their importance.

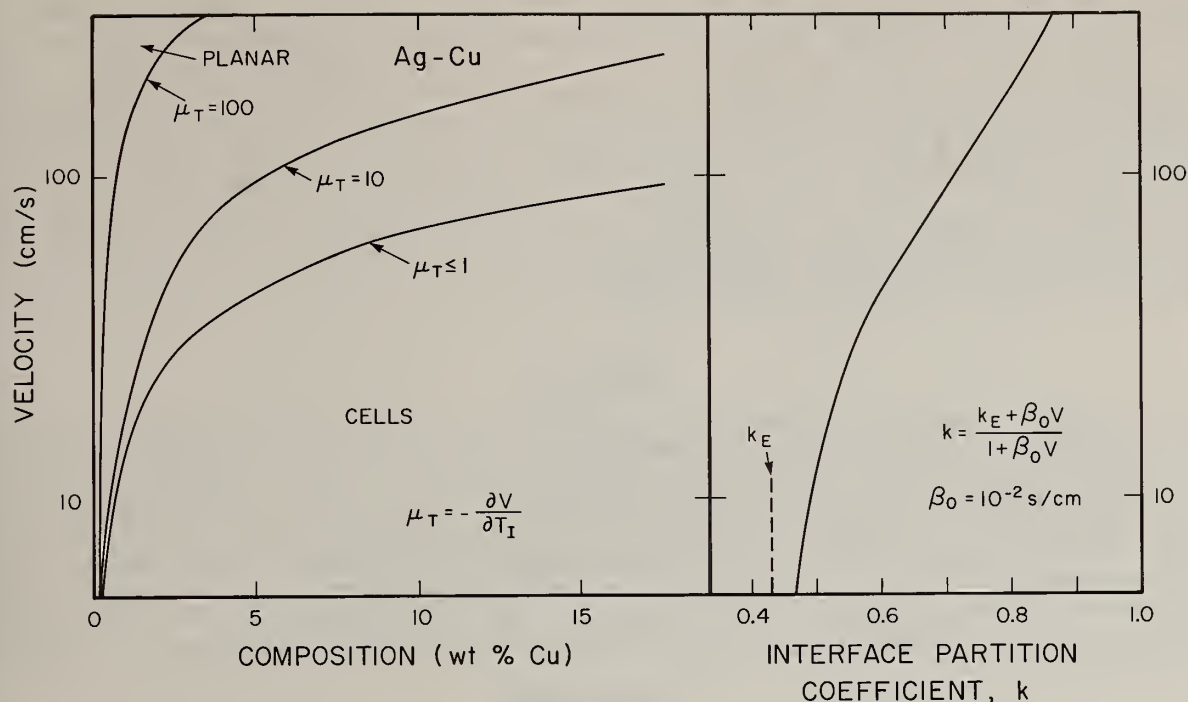


Fig. 7. Curves showing the onset of morphological instability for nonequilibrium conditions for which the partition coefficient, k , varies with V as shown on the right. Velocity for instability is shown as a function of the composition of bulk liquid for various values of the kinetic coefficient μ_T . For $\mu_T \leq 1$, the transition to instability is non-oscillatory in time and corresponds to a simple substitution of $k(V)$ into the standard criterion for instability. The units of μ_T are cm/(Ks).

Concentrated Alloys

The solidification conditions required to produce microsegregation-free crystalline structures for concentrated alloys are generally associated with the temperature difference between the liquidus curve and the T_0 curve. For most terminal solid solutions, this difference increases with increasing concentration. The usual idea is that, compared to dilute alloys, such alloys require more rapid solidification or higher undercooling to produce microsegregation-free crystalline alloys. The simple trapping models presented earlier in this paper involve no explicit concentration dependence. Furthermore, a recent set of experiments conducted on Ag-rich Ag-Cu alloys [16-17], suggest that as the composition approaches the eutectic composition, the growth velocity required to form microsegregation-free structures decreases. At 15 wt% Cu, an interface velocity of approximately 2 m/s is required. At the eutectic composition (28 wt% Cu), a velocity of only 70 cm/s is required. Therefore, in this alloy, it is actually easier to form the microsegregation-free structure for the very concentrated alloys. Such results have several possible origins and one possibility is related to the dependence of the liquid diffusion coefficient on temperature, as discussed below.

The dependence of the liquid diffusion coefficient on temperature is generally neglected in ordinary solidification theory. Such is the case because of the fact that solidification almost always takes place very close to the liquidus temperature. Diffusion data is often described by an Arrhenius equation. For a melting point of 1000K and an activation energy of 10 kcal/mol, an undercooling of 300K will reduce the diffusion coefficient by an order of magnitude.

The dependence of the diffusion coefficient on temperature can affect substantially various ideas in solidification. In the following, it is assumed that the diffusion coefficient is only a function of temperature. The first example involves solute redistribution in the growth of concentrated alloys. In particular it has been noted previously [3] that the dependence of the diffusion coefficient on temperature can lead to a maximum in eutectic growth rate of approximately 10 cm/s. This maximum velocity has origins that are identical with the nose of the C curve for eutectoid growth observed in solid state transformations. Such a maximum eutectic growth rate is consistent with the fact that eutectic spacings are rarely observed to be finer than 200 Å. A second example may occur in the stability theory. For planar growth with equilibrium at the solid-liquid interface, the interface temperature is at the solidus for the average alloy concentration. In many concentrated

alloys, the solidus may easily lie 300 K below the liquidus. An order of magnitude change in the diffusion coefficient can affect the prediction of the stability theory significantly. A third example involves a very simple modification of the trapping model presented previously. The parameter β_0 involves a diffusion coefficient. A simple approach to include composition dependence in a trapping theory would be to calculate the diffusion coefficient at the T_0 curve for various compositions. For pure silver, the diffusion coefficient is $2 \times 10^{-5} \text{ cm}^2/\text{s}$ at its melting point. For the eutectic composition the T_0 temperature is approximately 670 °C and the diffusion coefficient, based on an activation energy of 10 kcal/mole, is $6 \times 10^{-6} \text{ cm}^2/\text{s}$. This simple idea leads to the conclusion that the growth velocity required for significant levels of solute trapping would be reduced by a factor of 3.5 as the composition changes from pure Ag to the eutectic composition. Such a trend is consistent with the observed data.

Conclusion

In this paper, a response function for the temperature of the interface during solute trapping has been discussed. This model for the temperature is consistent with thermodynamics and with models of solute trapping and collision limited growth. Such interface response functions should permit a rational approach to the solidification problem in a wide variety of conditions of heat flow and solute redistribution. Secondly, circumstances where the absolute stability equation can be used in lieu of the full stability theory have been addressed. Experimental results obtained by using electron beam surface melting of Ag-Cu alloys are consistent with the stability theory. Thirdly, a few comments have been presented on the conditions for microsegregation-free solidification of concentrated alloys. This area obviously remains ripe for experimental and theoretical investigation.

Acknowledgment

This work was partially sponsored by the Defense Advanced Research Projects Agency. One of us (RFS) received partial support from the National Science Foundation.

We would like to thank M. J. Aziz, J. W. Cahn, and D. Turnbull for helpful discussions.

References

- [1] M. Cohen and R. Mehrabian, these proceedings.
- [2] J. C. Baker and J. W. Cahn, in Solidification (ASM, Metals Park, 1971) p. 23.
- [3] W. J. Boettinger, in Rapidly Solidified Amorphous and Crystalline Alloys, ed by B. H. Kear, B. C. Giessen and M. Cohen (Elsevier, 1982) p. 15.
- [4] J. C. Baker, Interfacial Partitioning During Solidification, Ph.D. Thesis, MIT (1970) Chapter V. Also reported by J. W. Cahn, S. R. Coriell and W. J. Boettinger, in Laser and Electron Beam Processing of Materials, ed. by C. W. White and P. S. Peercy (Academic Press, NY, 1980) p. 89-103.
- [5] M. J. Aziz, J. Appl. Phys. 53, 1158 (1982).
- [6] K. A. Jackson, G. H. Gilmer, and H. J. Leamy, in: Laser and Electron Beam Processing of Materials, ed. by C. W. White and P. S. Peercy (Academic, NY, 1980) p. 104.
- [7] R. F. Wood, Phys. Rev. B25, 2786 (1982).
- [8] See, e.g., J. Narayan, J. Crystal Growth 59, 583 (1982).
- [9] F. Spaepen and D. Turnbull, in Rapidly Quenched Metals, ed by N. J. Grant and B. C. Giessen (MIT Press, Cambridge, MA, 1976) p. 205.
- [10] D. Turnbull and B. G. Bagley, in Treatise on Solid State Chemistry, ed. by N. B. Hannay (Plenum, New York, 1975) Vol. 5, p. 513.
- [11] M. J. Aziz, these proceedings.
- [12] J. L. Murray, Met. Trans. A, to be published.
- [13] W. W. Mullins and R. F. Sekerka, J. Appl. Phys. 35, 444 (1964).

- [14] S. R. Coriell and R. F. Sekerka, in Rapid Solidification Processing Principles and Technologies II, ed. by R. Mehrabian, B. H. Kear, and M. Cohen (Claitor, Baton Rouge, LA, 1980) p. 35.
- [15] J. W. Cahn, S. R. Coriell, and W. J. Boettinger, in Laser and Electron Beam Processing of Materials, ed. by C. W. White and P. S. Peercy (Academic Press, New York, 1980) p. 89.
- [16] W. J. Boettinger, R. J. Schaefer, F. S. Biancaniello, and D. Shechtman, Met. Trans. A, to be published.
- [17] W. J. Boettinger, R. J. Schaefer, F. S. Biancaniello, and D. Shechtman, these proceedings.
- [18] S. R. Coriell and R. F. Sekerka, J. Crystal Growth, to be published.

*Department of Metallurgy and the Materials Research Laboratory
University of Illinois, Urbana, IL 61801

**Department of Materials Science and Engineering
Massachusetts Institute of Technology, Cambridge, MA 02139

Introduction

It is now well established that rapid solidification of alloys holds considerable advantage over conventional processing because of the fuller potential for microstructural control realizable through rapid solidification. With this new emphasis on microstructural control via rapid solidification processing has come the need for detailed microstructural analysis. Also, with the reduction in size of characteristic microstructural entities that occurs on rapid solidification, there developed a need for new experimental techniques that could probe both structure and composition with much higher resolution than was previously available. Fortunately, the advent of scanning transmission electron microscopy (STEM) occurred virtually simultaneously with the developments of rapid solidification technologies. With STEM, the capability for compositional analysis by x-ray fluorescence spectroscopy with a spatial resolution on the order of 5 nm in electron transparent sections has been realized.

Instrumentation

The commercial instrument used in the part of this work conducted at MIT was a Vacuum Generator HB5 field emission STEM [1]. Using a cold tungsten field emitter as an electron source and a two lens probe forming system, 2 nA of 100 kV electrons can be formed into a probe of approximately 1.5 nm diameter on the specimen. The vacuum in the specimen chamber is $\sim 2 \times 10^{-9}$ torr, which minimizes the problem of specimen contamination. The instrument used in the part of this work conducted at the University of Illinois was a Philips EM400T. The EM400T can operate as a conventional transmission electron microscope or as a STEM instrument, and has excellent selected area and convergent beam diffraction capabilities. An energy dispersive x-ray (EDX) analysis system as well as an electron energy loss spectrometer (EELS) are available on both the HB5 and the 400T. In each instrument, the Si(Li) EDX detector and EELS system are coupled to a multi-channel analyzer and minicomputer system for spectral manipulation.

Interpretation of energy-dispersive x-ray data requires a great deal of care. The usual way to consider the effects of x-ray production is to employ the sensitivity factor method due to Cliff and Lorimer [2], embodied in the equation:

$$\frac{C_A}{C_B} = \frac{I_A K_A}{I_B K_B} \quad (1)$$

where C_A/C_B is the ratio of the concentrations of the elements A and B in a specimen; I_A and I_B are the integrated x-ray counts in chosen lines due to each element; and K_A and K_B are sensitivity factors. Often the ratio K_A/K_B is used as a relative sensitivity factor denoted by K_{AB} , relating the sensitivities of the two elements.

If the x-rays were generated in an infinitely thin specimen in free space, the measured x-ray signals would correspond exactly to the generated x-ray intensities. Such, however, is not the case, and it is necessary to consider (a) the modification to the x-ray intensities as they travel through adjacent material and selective absorption occurs, and (b) generation of spurious x-rays from remote parts of the specimen and the microscope as a result of spurious radiation (electrons and x-rays) generated in the microscope column or as a result of interaction of the main electron beam with the specimen itself.

It has been shown that in the HB5 fitted with the so-called "virtual objective aperture," the contribution of spurious radiation generated by the microscope is negligible compared with that generated by the interaction of the beam with the specimen. Further, if the microscope is not so equipped, this "hole count" can simply be recorded by passing the beam through a hole in the specimen, and subtracting the resulting x-ray spectrum from that recorded while the beam is incident on a

fracture in the specimen. The main disadvantage of this latter procedure is the large increase in the background noise level.

For uniform thin foils, correction equations have been developed to allow for the effects of selective absorption [3]. In such cases fluorescence is usually of less importance. However, in multiphase materials the situation is not so simple. In general the x-ray path through each phase is not known, and the distance from the x-ray source to different fluorescing phases is not well characterized. Thus accurate correction of the x-ray intensities is not usually possible in such cases. To some extent the problems may be overcome by the use of extraction replica techniques, but these cannot be employed in cases where it is required to measure the compositions of, say, precipitates and matrix in immediately adjoining regions. In such instances it is of some assistance to use specimen geometries in which the extent of interaction between the various phases is minimized.

Applications to Rapidly Solidified Fe-Based Alloys

Research at MIT has centered on microstructures and properties produced in rapidly solidified steels. Of particular importance in this research has been the construction of composition profiles across solidification-related microstructural features. Where grain boundaries or cell walls have been analyzed, the analysis was performed by orienting the grain boundaries parallel to the electron beam and then manually stepping the electron probe along a line perpendicular to the boundary. After each point has been analyzed, the boundary was examined to ensure that no specimen drift had occurred before repositioning the probe at the next data point. Whenever possible, boundaries were selected that were perpendicular to the edge of the foil so that the step scan occurred in a region of uniform thickness. Additionally, the line of the step scan was oriented perpendicular to the line between the specimen and the x-ray detector.

303 Stainless Steel

A notable finding in the course of investigation into the microstructures of a rapidly solidified austenitic 303 stainless steel is the presence of a distinct ferromagnetic component in the centrifugally atomized powders. It became evident that the ferromagnetic particles are the smallest of the powder particle population. X-ray-diffraction analysis of the magnetically separated particles shows that the nonferromagnetic powder is 100 percent fcc. The ferromagnetic powder is predominately bcc but has as much as 30 volume percent fcc. Light microscopy of metallographic sections of the ferromagnetic powder using a "dark etch" on the bcc phase indicates that the smallest ferromagnetic particles are 100 percent bcc. Some of the larger ferromagnetic particles have both fcc and bcc grains present.

The microstructure of the fcc particles if found, in all cases, to be that of a cellular or dendritic solidification. The microstructures of the bcc particles, however, are found to be of two types; cellular and noncellular. As described below, important differences exist between the fcc and bcc structures in regard to solute segregation patterns and resultant precipitate morphologies.

Rapidly Solidified Cellular FCC

The microstructure of a cellular fcc powder particle is shown in figure 1 with a corresponding composition profile. Precipitate particles 100 to 200 nm diameter reside at the cell walls of this structure and delineate the cellular geometry. These cell-wall precipitates are observed to be about the same size in both cellular fcc and cellular bcc rapidly solidified structures. This cell-wall type of precipitate will be referred to as the 100 nm precipitate. X-ray fluorescence spectra indicate that these precipitate particles are nominally manganese sulfide.

With reference to figure 1, note that there is an increase in nickel content and corresponding decrease in iron content associated with the cell walls in the microstructure. The chromium content of these cells appears to be uniform though there is indication of a relatively slight increase at the cell wall. Other profiles in these fcc cellular structures have shown slight chromium enrichment, coincident with more pronounced nickel enrichment at cell walls.

A notable aspect of the manganese variation along the profile is a decrease in concentration in the vicinity of the cell wall. Since manganese must be segregating to the cell walls to form the precipitates, this observed decrease in manganese must be due to manganese redistribution along the cell wall during formation of the precipitates in the late stages of solidification.

Changes in silicon concentration within the structure appear counter-variant with those of manganese. This may be evidence of a coupling of the partitioning behavior of manganese and silicon during solidification. Similarly, changes in sulfur concentration in the structure appear covariant with manganese.

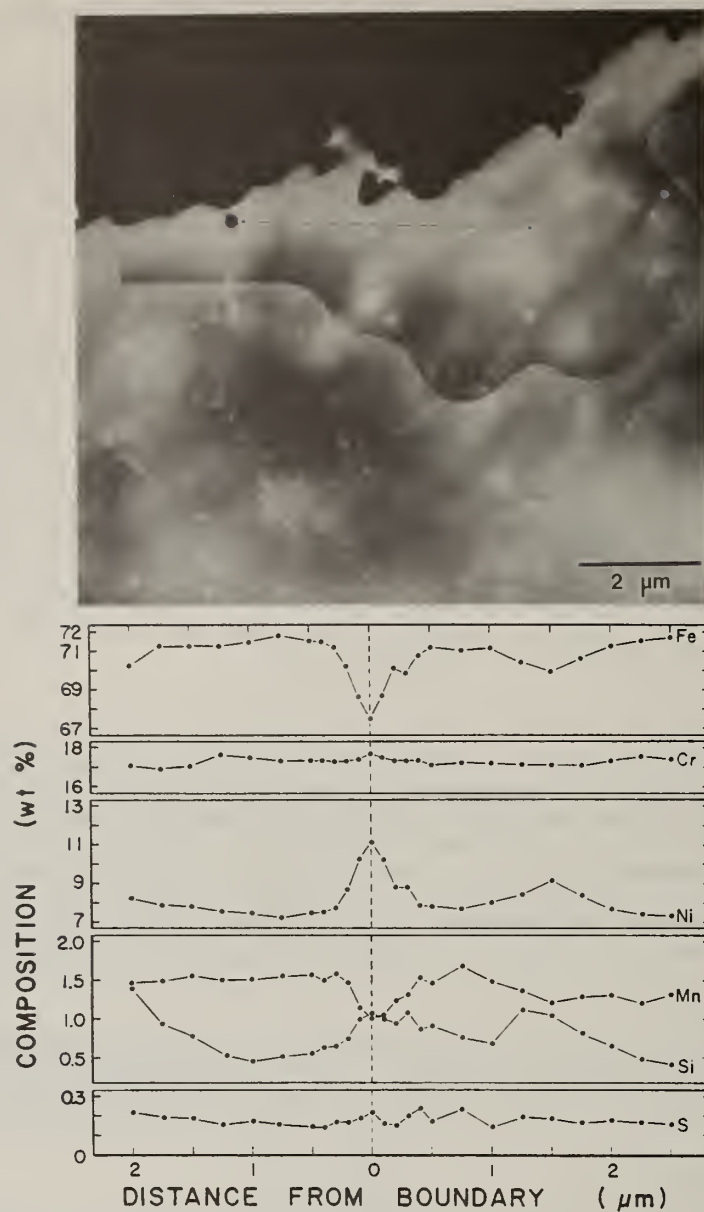


Figure 1. Rapidly solidified cellular fcc structure of 303 stainless steel. Montage of two scanning transmission electron microscopy annular dark-field images and composition profile.

Note that compositional redistribution in the solid in this rapidly solidified structure is calculated to be on the scale of 8 nm or less, for example, for chromium and nickel using recently measured diffusion data for stainless steels [4,5]. It appears that compositional redistribution in the solid does not significantly alter the observed composition profiles in these rapidly solidified powders. Though these variations are not extreme, this cellular fcc structure of the rapidly solidified powder does exhibit some partitioning of both the metal and metalloid solute species.

Rapidly Solidified Cellular BCC

A view of the cellular bcc structure is shown in figure 2. Cells appear delineated by sulfide precipitates of 100 to 200 nm diameter, similar to the rapidly solidified cellular fcc structure with the 100 nm precipitates at the cell walls. The elongated cells in figure 2 are apparently longitudinal sections of cells. A notable feature of this structure is the presence of the small precipitates, 10 to 20 nm diameter, within the cell. These 10 nm precipitates are observed in the bcc

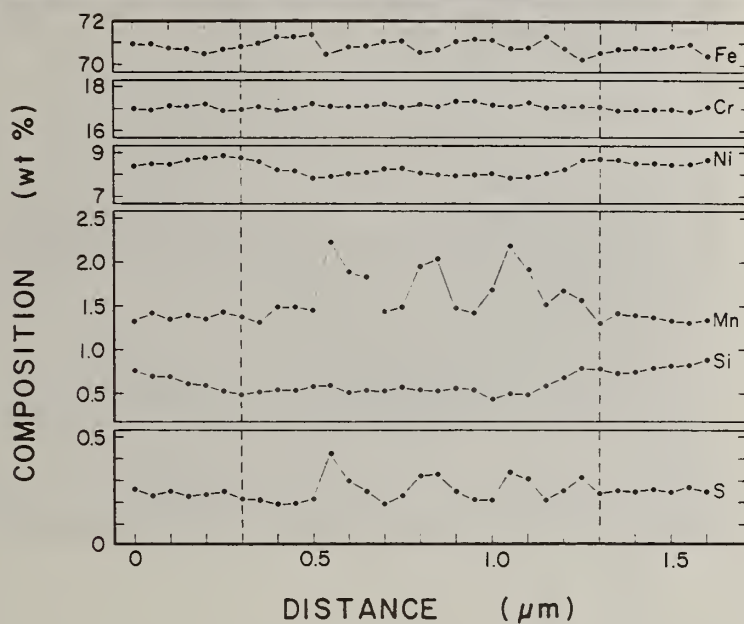
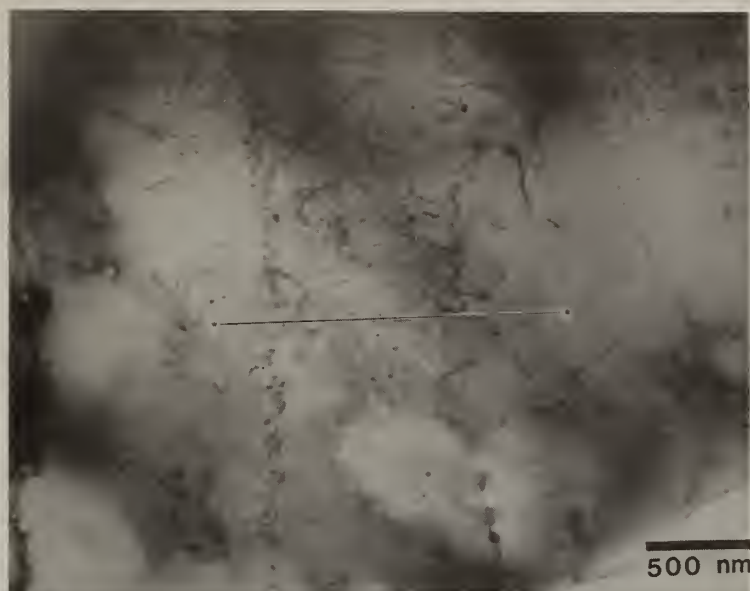


Figure 2. Rapidly solidified cellular bcc structure of 303 stainless steel. Scanning transmission electron microscopy bright-field image and composition profile.

structures only. There appears to be a decrease in the volume fraction of 10 nm precipitates at the cell walls commensurate with the appearance of the 10 nm precipitates in the cell interiors. In situ x-ray fluorescence analysis of the 10 nm precipitates indicates that they are nominally manganese sulfide.

The location of these 10 nm precipitates within the cells corresponds with the position in the composition profile at which the concentrations of manganese and sulfur go through large variations. These peaks in concentration are about 0.2 micron in spatial extent and correlate with localized maxima in the number density of the 10 nm precipitates in the central region of the cell. It should be noted here that care has been taken to distinguish the observed increases in manganese and sulfur concentrations as due to local increases in the matrix concentration and not simply due to the presence of a precipitate in the volume of material analyzed at a given point. The composition profile of this rapidly solidified cellular bcc indicates that the structure is homogeneous with respect to iron, chromium, nickel, and silicon.

The term "noncellular" is used here to mean that solidification occurred without the formation of a cellular liquid/solid interface morphology. Indications are that a smooth-front growth of the solid took place without development of solute partitioning; hence, this solidification mode is termed massive solidification.

The microstructure of a noncellular bcc particle is shown in figure 3. There is no suggestion of a cellular solidification structure, especially as would be delineated by precipitates. The matrix composition of this noncellular bcc structure is characterized by a lack of microsegregation. The composition profiles of figure 3 indicates virtually complete homogeneity over a distance of nearly 5 microns. The most significant variation in composition observed here is that associated with manganese. As pointed out earlier in connection with the cellular bcc structure, there appears a periodic variation in manganese concentration along the profile. In the noncellular bcc structure, however, the period of the variation is about 2 microns as compared with about 0.2 micron in the case of the cellular bcc.

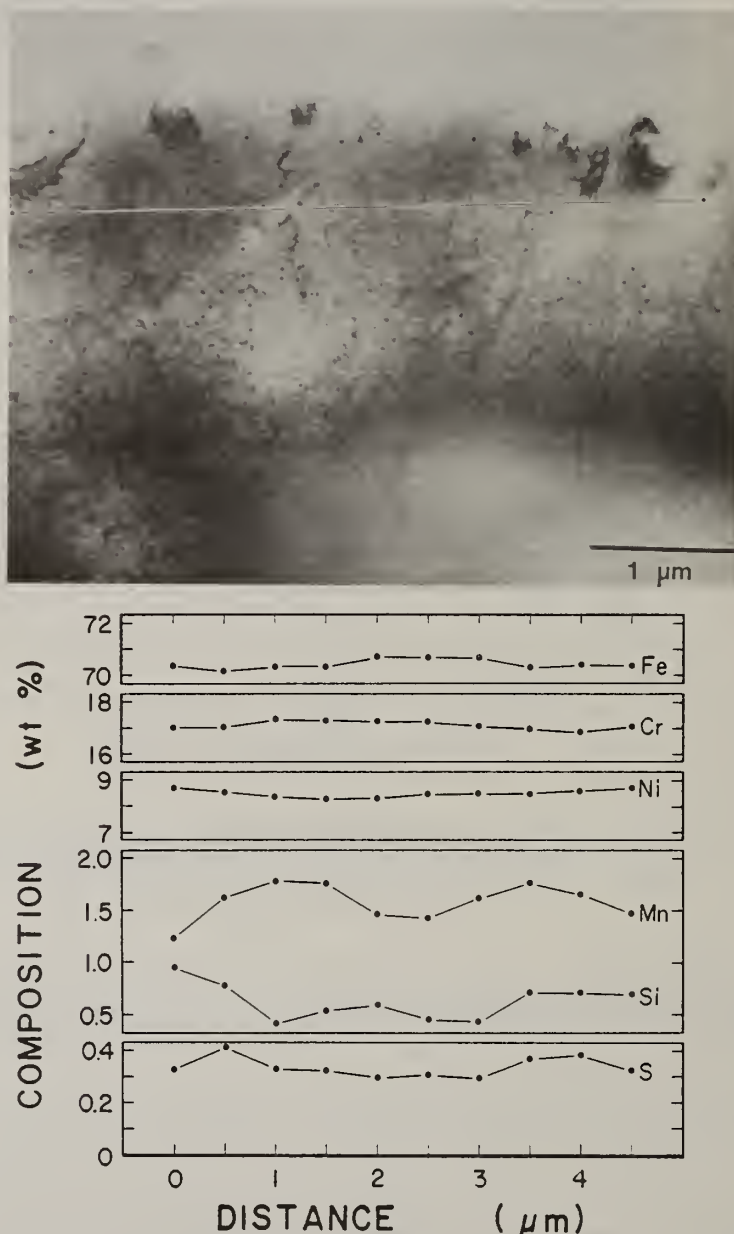


Figure 3. Rapidly solidified noncellular bcc structure of 303 stainless steel. Scanning transmission electron microscopy bright-field image and compositional profile.

A predominant feature of some bcc noncellular particles is a large number density of small precipitates (10 to 20 nm diameter) throughout the entire microstructure. This feature is readily seen in the image of figure 3. The morphology of these 10 nm precipitates is similar to that noted in the intracellular region of the cellular bcc structure (fig. 2). Not all noncellular bcc particles are found to have the 10 nm precipitates. This latter microstructure is the result of retention of the solid solution that was produced during massive solidification. This precipitate-free noncellular bcc microstructure was only observed in a sample of very small (20 ± 3 micron diameter) powder particles. Since the cooling rate in the processing of these powders increases with decreasing particle size, it appears that the supersaturated solid can be retained to room temperature as a result of greater cooling rates from solidification temperatures.

High Phosphorus Steel

A Fe-16Cr-10Ni-0.4P steel also produced by centrifugal atomization has been under investigation. As in the 303 stainless steel, there exists in these powders a fcc and a bcc fraction with the smaller powder particles being bcc. The range of solidification microstructures encountered can be seen in figure 4. The intercellular phase observed in figure 4 is glassy [6]. Of particular interest are the two powder particles which do not exhibit a dendritic structure. These observations exhibit the same trends as seen in 303 stainless steel suggesting that, at the smallest ($< 20 \mu\text{m}$) powder particle sizes massive solidification may be at play.

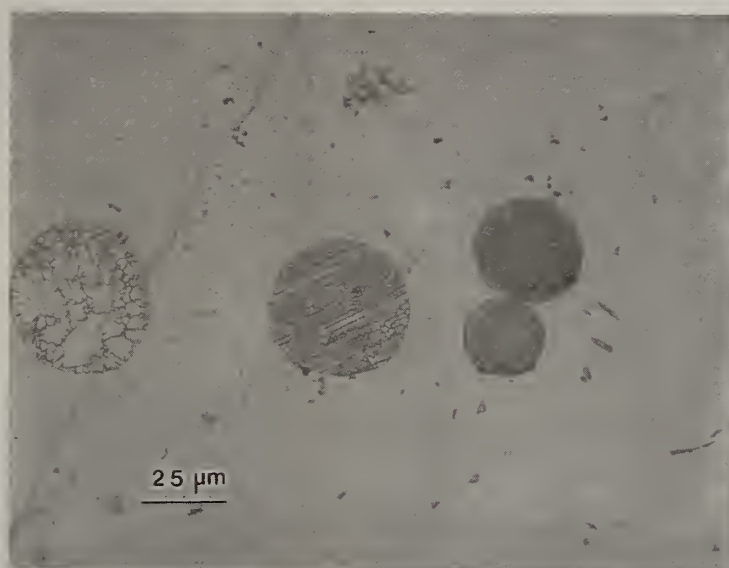


Figure 4. Rapidly solidified high phosphorus austenitic steel powders exhibiting three different solidification microstructures. All of the powders are $\sim 45 \mu\text{m}$ in diameter.

Al Alloys

There are several potentially beneficial modifications to microstructure which may be effected by rapid solidification processing (RSP). One of these is the possibility of metastable phase formation. Two studies are currently underway at Illinois involving metastability in Al alloys, the first of which is directly aimed at developing an understanding of metastable phase formation in Al-Ge alloys during rapid solidification. The second is part of a program attempting to improve the elevated temperature properties of Al alloys by developing a very fine scale dispersion of intermetallic compounds using RSP. In this study, metastable phases form as a result of rapid solidification, and an example of this will be given.

In the first set of experiments, alloys from the Al-Ge system are used, because there is in the literature a number of reports of metastable phase formation resulting from the application of various means of rapid solidification [7-11]. In the present study, a new technique for the direct in situ observations of rapid solidification using transmission electron microscopy (TEM) has been

developed, where the incident electron beam is used as a local heat source to cause melting of individual alloy powders [12]. The powders are produced by electrohydrodynamic atomization (the EHD process), and were kindly supplied by Phrasor Scientific Inc. and the National Bureau of Standards. As has been reported previously, such powders when supported on a thin carbon film may be introduced readily into a TEM, and are often sufficiently thin for microstructural analysis [13]. When using the *in situ* method for melting of powders, a range of cooling rates may be achieved; the slowest is produced by slowly defocusing the condenser lens. Intermediate rates of cooling may be effected by deflecting the electron beam using electromagnetic coils, and the fastest rate of cooling is produced by inserting an opaque stop between the electron gun and sample.

For the case of Al-Ge powders of eutectic composition, the microstructure following *in situ* rapid solidification has been shown to vary widely depending on cooling rate [14]. For the slowest rate, a metastable phase forms, the structure of which has been determined as hexagonal (space group $P6_3/mmm$) with $a = 1.42$ nm and $c = 0.74$ nm [15]. At intermediate cooling rates, a refined distribution of randomly oriented crystals of α -Al and β -Ge (solid solutions) was observed. These phases are those which are predicted by the equilibrium phase diagram. At the most rapid rate of cooling, a microstructure is produced which consists of single crystal α -Al, in either cellular or dendritic form, surrounded by a Ge-rich amorphous phase. This microstructure is shown in figure 5, for the case of the cellular Al, and figure 6 for the dendritic morphology. Included in both figures are selected area diffraction patterns recorded, in each case, with the whole powder being irradiated; the single crystal nature of the crystalline phase is evident. Microdiffraction patterns of the interdendritic phase and carbon film are shown in figure 6, and the former pattern is consistent with the amorphous nature of the Ge-rich phase. Energy dispersive x-ray spectra show that this amorphous phase is considerably enriched in Ge (~ 50 at.%).

The mechanism of formation of the mixed crystalline/amorphous structure has not been established. However, it is possible to hypothesize that when the beam is occluded from the specimen, undercooling of the molten droplet occurs to a temperature where α -Al nucleates. The α -Al phase will grow in size, rejecting Ge-rich solute ahead of the advancing interface, until the liquid composition and temperature are such that a glassy metal forms. The glass transition temperature for hypereutectic compositions in this alloy system is, over a certain range, expected to increase with increasing Ge concentration because of the difficulty in nucleating β -Ge.

An interesting aspect of the present observations is that the metastable hexagonal structure forms at a lower level of undercooling than that required to produce a mixture of α -Al and β -Ge phases as predicted by the equilibrium phase diagram. This is the subject of further study.

In the second set of experiments, metastable phases have been observed in Al-Fe alloys following laser surface melting, and Al-Mo alloys which has been processed into ribbon using melt spinning. In this latter case, an example will be given for melt spinning of Al-1.75 wt.% Mo. The microstructure of this material is shown in figure 7. A number of precipitates may be seen, the size of which is typically ~ 0.1 μ m. One of these precipitates is shown at a higher magnification in figure 8, and it can be seen that the phase is somewhat faulted. Selected area diffraction patterns were recorded with the incident electron beam parallel to a number of low index zone axes, but it was not possible to interpret these data on the basis of any of the reported phases in the Al-Mo system [16].

In an attempt to identify the second phase shown in figures 7 and 8, the techniques of energy dispersive x-ray analysis and convergent beam electron diffraction were used. The chemical composition of the phase was determined in this way and corresponds to Al_5Mo ; for this stoichiometry, the previously reported crystal structure is hexagonal (space group $P6_3$), and $a = 4.89$ Å and $c = 8.80$ Å. Convergent beam electron diffraction patterns with the electron beam parallel to the $\langle 100 \rangle$ and $\langle 111 \rangle$ zone axes are given in figure 9. These various patterns may be interpreted using the tables in reference [17]. Thus the projection diffraction and whole pattern symmetries for the $\langle 100 \rangle$ zone axis patterns are both 4 mm, so that this diffraction group may be deduced as being either 4 mm or 4 mm_R. In the case of patterns produced with the beam parallel to the $\langle 111 \rangle$ zone axis, the projection diffraction symmetry is 6 mm, and the bright field and whole pattern symmetries are both 3 m; the deduced diffraction group is 6 mm_R. Consideration of these possible diffraction groups leads to the conclusion that the point group of the precipitated phase is $m3m$. The space group may be determined by projecting the reflections contained in the first and second order Laue zones onto the zero order zone of the $\langle 100 \rangle$ pattern. When this is done, a face centered reciprocal lattice results, which corresponds to a body centered real lattice cell. There are two space groups that possess the $m3m$ point group and exhibit a body centered cell, namely $Im3m$ and $Ia3d$. The intensities recorded in the convergent beam patterns is only consistent with the $Im3m$ space group. The lattice parameter has been determined from the diffraction patterns, and is given by $a = 5.39 \pm 0.01$ Å. The occurrence of this phase, Al_5Mo , possessing the space group $Im3m$, has not been reported previously in the literature and is presumably a metastable phase formed on rapid quenching of the alloy.

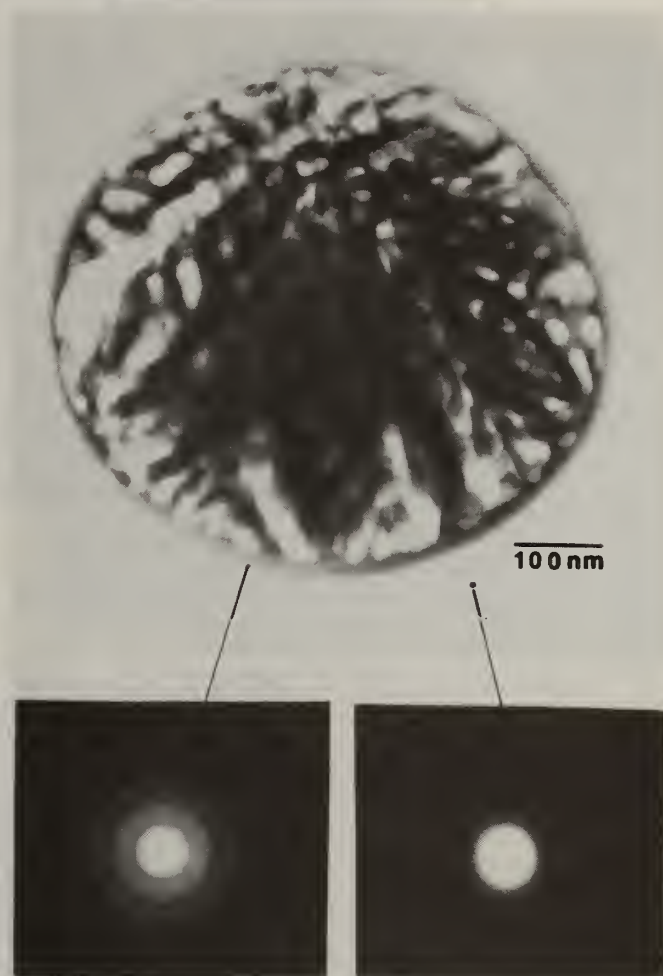
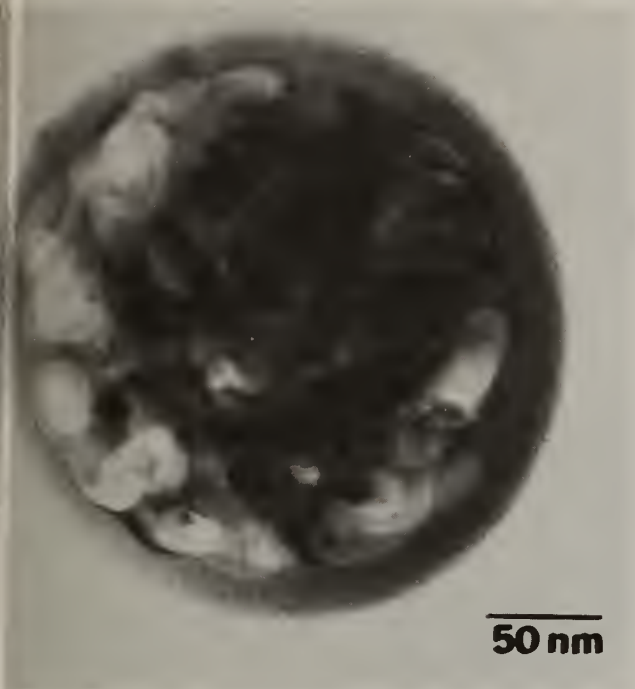


Figure 5. Two phase (cellular, single crystal interior plus amorphous shell) structure with corresponding SAD pattern produced by interrupting the beam from a molten droplet with the condenser aperture mechanism.

Figure 6. Larger two phase (dendritic, single crystal interior plus amorphous shell) with corresponding SAD pattern and micro-diffraction patterns from the shell and the carbon film. Structure was produced by interrupting the beam from a molten droplet with the condenser aperture mechanism.

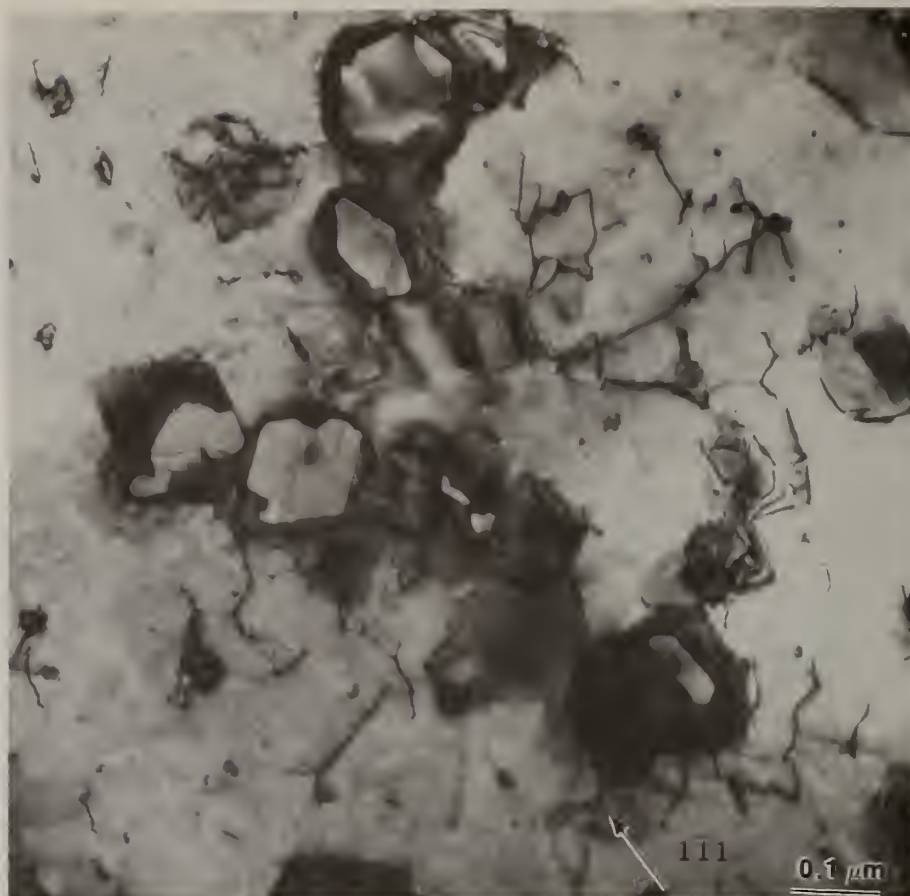


Figure 7. TEM micrograph showing the precipitates and associated dislocation structure in Al-1.75 wt.% Mo ribbon. Beam direction close to $\langle 101 \rangle$.

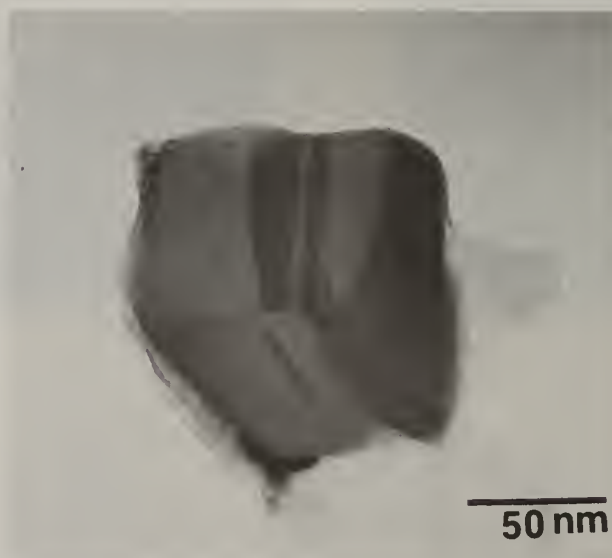


Figure 8. TEM micrograph of precipitate in Al-1.75 wt.% Mo ribbon. This precipitate was used in the convergent beam diffraction studies. The electron probe was focused in the unfaulted region in the upper left corner.

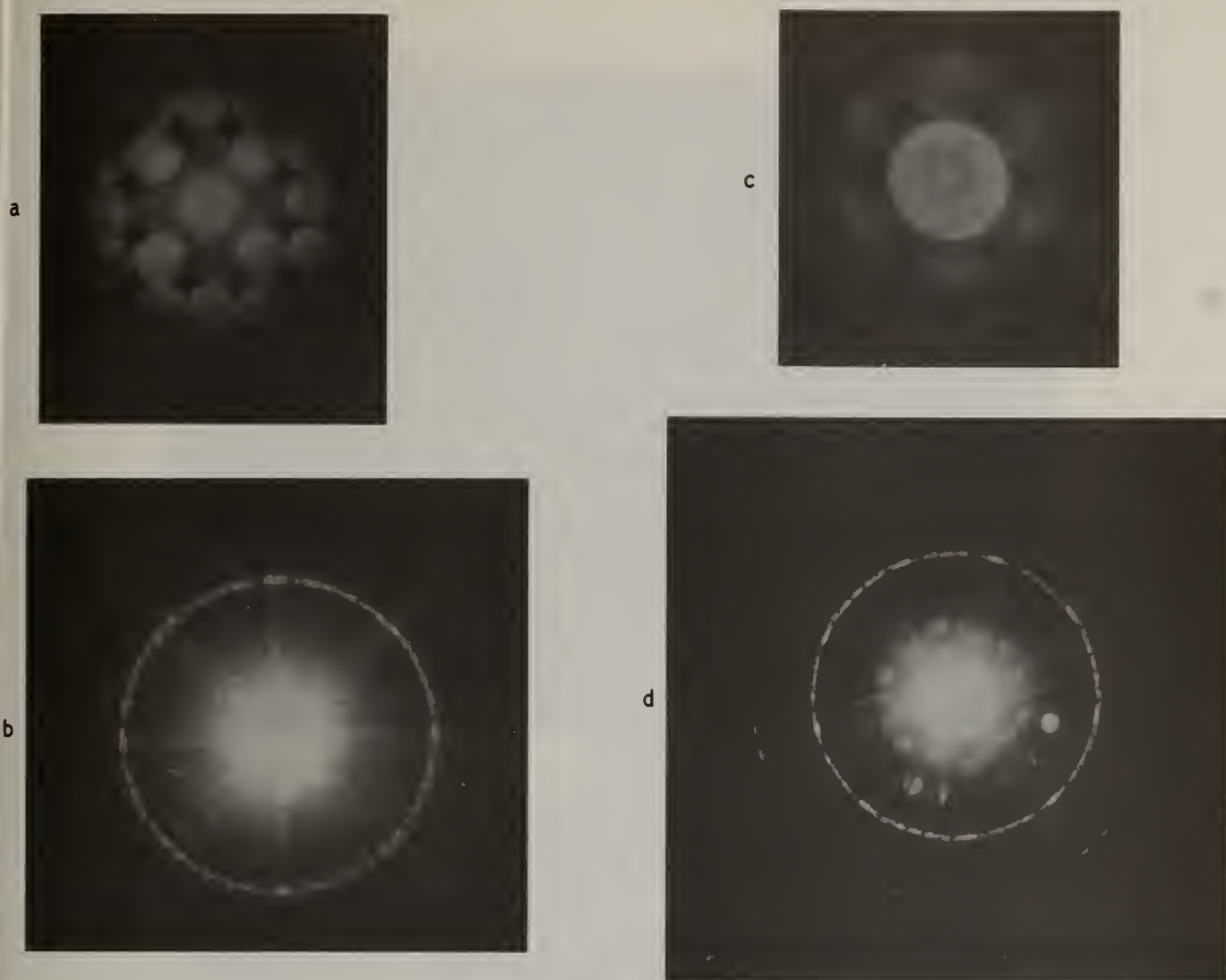


Figure 9. Convergent beam electron diffraction patterns from the precipitate shown in figure 5. (a) $\langle 100 \rangle$ zone axis, zero order Laue zone projection. (b) $\langle 100 \rangle$ zone axis, whole pattern. (c) $\langle 111 \rangle$ zone axis, bright field and zero order Laue zone projection. (d) $\langle 111 \rangle$ whole pattern. Patterns recorded on a Philips EM400T operating at 120 kV.

Ti Alloys

Research in the area of RSP of Ti alloys has generally concentrated on the possibility of producing ultrafine dispersions of rare-earth oxides in an α -Ti matrix (e.g. [18]). Such a study is currently underway at Illinois where it is intended to produce rapidly solidified powders of Ti and Ti-8Al (at.%) containing refined dispersions of Y_2O_3 , Nd_2O_3 , and Er_2O_3 . Initially, the response of the alloys Ti and Ti-8Al with additions of elemental Y, Nd, and Er to rapid solidification is being established. In this case, laser surface melting is being used as a convenient and efficient method of obtaining small volumes of rapidly solidified material. An example of this study is given for the case of Y containing alloys.

Figure 10 shows a backscattered electron image obtained in the scanning electron microscope of the interface between as-arc melted and laser surface melted Ti-8Al-4Y (at.%). The as-arc melted alloy consists of a relatively coarse dendritic microstructure, whereas a substantial refinement in this microstructure has been effected in the laser affected region. A comparison between the microstructures of as-arc melted and laser surface melted materials is given in figure 11. The as-arc melted alloy is seen to consist of a dispersion of second phase within an α -Ti matrix, where the average size of the dispersoids is 0.1 μm . Following rapid solidification, the matrix consists of laths of α' martensite, and there is a refined dispersion of second phase present, the average size



Figure 10. The microstructure of an arc-melted Ti-8Al-4Y specimen which has been subjected to laser surface melting. Backscattered electron image recorded in scanning electron microscope.

of these precipitates being $\sim 120 \text{ \AA}$ in diameter. It is necessary to determine the nature of these particles, since in preparing the alloy, elemental additions of Y (nominal metallic purity of 99.95%) have been made. Such characterization has been performed, and the identity of these second phase dispersoids has been established [17].

The identity of all particles with diameters $> 400 \text{ \AA}$ in both the as-arc melted and laser surface melted samples has been determined. All these particles were found to have identical crystal structures; the nature of the smaller precipitates in the rapidly solidified samples has not been uniquely determined. For the precipitates with sizes $> 400 \text{ \AA}$, selected area diffraction patterns corresponding to a number of low index zone axes were recorded. It was not possible to interpret these patterns in terms of one crystal structure, and so convergent beam patterns were recorded with the electron beam parallel to the $\langle 100 \rangle$ and $\langle 111 \rangle$ zone axes. These are shown in figure 12. The projection diffraction, bright field and whole pattern symmetries for the $\langle 100 \rangle$ patterns are all 2mm. In this case, the deduced diffraction group is either $2mm$ or $2mm1_P$. For the $\langle 111 \rangle$ patterns, the projection diffraction symmetry is 6, and the bright field and whole pattern symmetries are both 3; the deduced diffraction group in this case is 6_P . The only point group containing these deduced diffraction groups is $m3$. By projecting the reflections contained in the higher order Laue zones onto the zero order zone, it is possible to deduce that the reciprocal lattice cell is face-centered so that the unit cell of the real lattice is body-centered cubic. The space group can be determined by combining the determinations of point group and cell type with information concerning kinematically forbidden reflections. In this case, 011 reflections are absent from $\langle 001 \rangle$ patterns, and so it is possible to assign the space group $Ia3$. The lattice parameter may also be determined from the diffraction patterns and is given by $a = 10.6 \pm 0.05 \text{ \AA}$. Since previous work [20] has determined that Y_2O_3 has the same space group and lattice parameter as that given above, it is reasonable to assume that the second phases observed in the present study are, in fact, Y_2O_3 .



a



b

Figure 11. Transmission electron micrographs of Ti-8Al-4Y alloy. (a) as-arc melted. (b) laser surface melted.

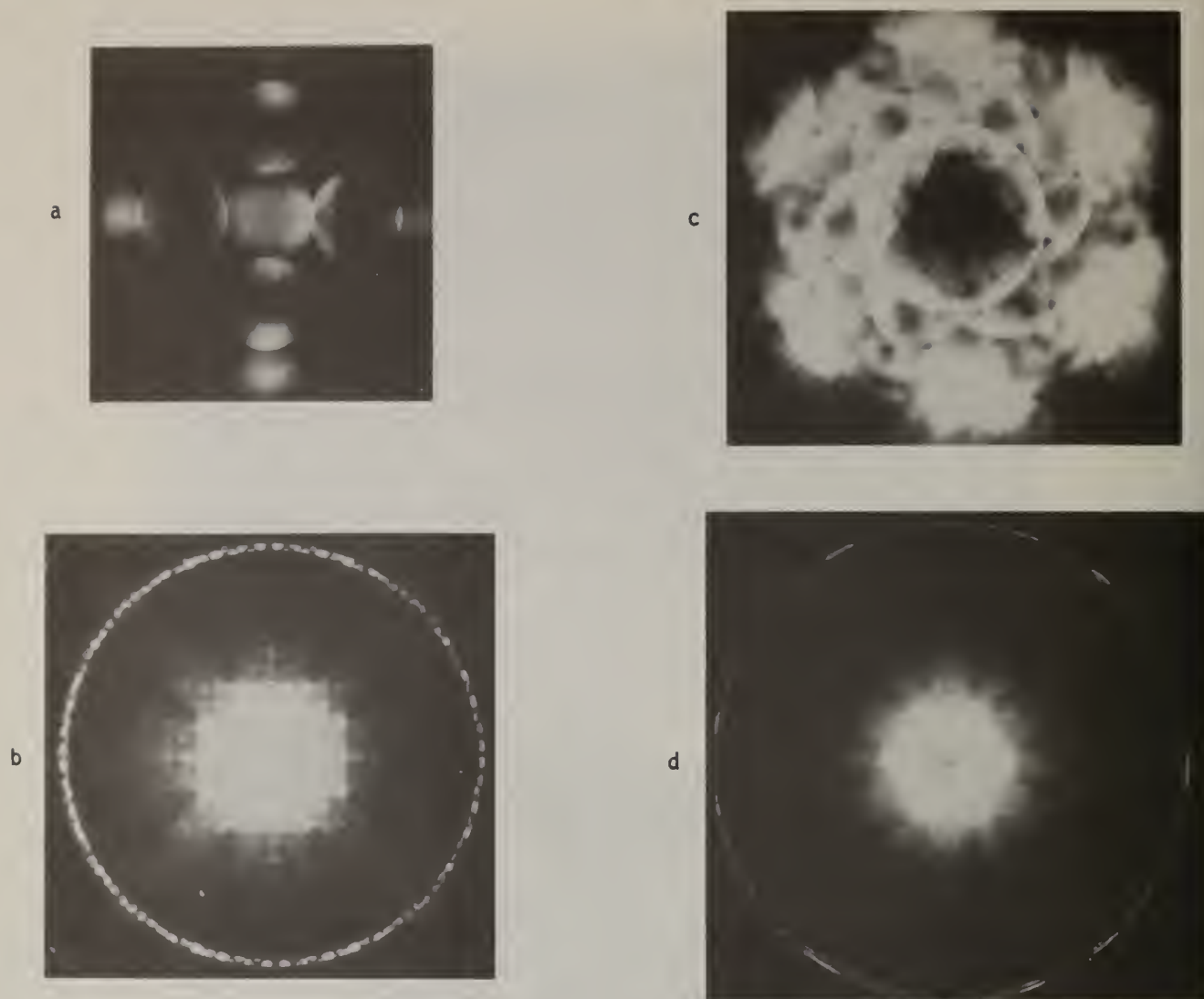


Figure 12. Convergent beam electron diffraction patterns from the second phase precipitates found in Ti-8Al-4Y alloy. (a) $\langle 100 \rangle$ zone axis, bright field and zero order Laue zone projection. (b) $\langle 100 \rangle$ zone axis, whole pattern. (c) $\langle 111 \rangle$ zone axis, bright field and zero order Laue zone projection. (d) $\langle 111 \rangle$ zone axis, whole pattern. Patterns recorded on a Philips EM400T operating at 120 kV.

Summary

Examples of microstructural characterization of Fe-, Al-, and Ti-based alloys following rapid solidification processing have been presented. Since the products of such processing are often extremely fine, it is necessary to make use of the recently developed techniques of analytical transmission electron microscopy. This is absolutely necessary, not only to aid in the understanding of the mechanism of microstructural formation, but also in developing microstructure/property relationships.

Acknowledgments

The MIT research was conducted by Dr. Thomas F. Kelly and Mr. Matthew Libera under ONR sponsorship (N00014-81-K-0013). Extensive use was made of central facilities provided through the Center for Materials Science and Engineering (NSF-MRL).

The Illinois research was conducted by Michael J. Kaufman, Fritz C. Grensing, and Douglas G. Konitzer. The work on Al-Ge and the Ti alloys was sponsored by the U.S. Department of Energy, Division of Materials Sciences, under Contract # DE AC02 76ER01198. The studies involving Al-Mo were sponsored by the U.S. AFOSR, under Contract # AFOSR 82-0186, with Dr. Alan H. Rosenstein as Technical Monitor. The electron microscopy studies were performed using the facilities of the Center for the Microanalysis of Materials in the Materials Research Laboratory of the University of Illinois.

References

1. I. R. M. Wardell, J. Morphew, and P. E. Bovey, in "Scanning Electron Microscopy Systems and Applications," Inst. Phys. Conf. Series No. 18 (1973) p. 182.
2. G. Cliff and G. W. Lorimer, J. Microsc. 103 (1975) p. 203.
3. J. I. Goldstein, "Introduction to Analytical Electron Microscopy," (eds. J. J. Hren, J. I. Goldstein, and D. C. Joy) Plenum Press, (1979).
4. R. A. Perkins, Metall. Trans. 4 (1973) p. 1665.
5. R. A. Perkin, R. A. Podgett, and N. K. Tunala, Metall. Trans. 4 (1973) p. 2535.
6. T. F. Kelly, G. B. Olson, and J. B. Vander Sande, "Rapidly Solidified Amorphous and Crystalline Alloys," (eds. B. M. Kear, B. C. Giessen, M. Cohen), Elsevier Science Publ. Co. (1982).
7. M. Laridjani, K. D. Krishnanand and R. W. Cahn, J. Mater. Sci. 11 (1976) p. 1643.
8. M. Laridjani and R. W. Cahn, Mat. Sci. Eng. 23 (1976) p. 125.
9. V. Köster, Z. Metallk. 63 (1972) p. 472.
10. P. Ramachandrarao, M. G. Scott, and G. A. Chadwick, Phil. Mag. 5 (1972) p. 961.
11. C. Suryanarayana and T. R. Anantharaman, J. Mater. Sci. 5 (1970) p. 992.
12. M. J. Kaufman and H. L. Fraser, Scripta Met. 17 (1983) p. 141.
13. C. G. Levi and R. Mehrabian, Metall. Trans. 13A (1982) p. 13.
14. M. J. Kaufman and H. L. Fraser, Metall. Trans. (1983) in press.
15. M. J. Kaufman and H. L. Fraser, Mats. Sci. and Eng. 57 (1983) p. 117.
16. Bulletin of Alloy Phase Diagrams, 1 (1980) p. 71.
17. B. F. Buxton, J. A. Eades, J. W. Steeds, and G. M. Rackham, Phil. Trans. Roy. Soc. A281 (1976) p. 171.
18. K. K. Sankaran, S. M. L. Sastry, and P. S. Pao, Metall. Trans. 11A (1980) p. 196.
19. D. G. Konitzer, B. C. Muddle, and H. L. Fraser, Metall. Trans. (1983) in press.
20. M. G. Paton and E. N. Maslen, Acta Cryst. 19 (1965) p. 307.

ASPECTS OF SOLIDIFICATION IN THE RSR POWDER PROCESS

R. J. Patterson, II and C. M. Adam*

Pratt & Whitney Aircraft
P. O. Box 2691
West Palm Beach, Fl. 33402

ABSTRACT

Early work in rapid solidification suggested that the production of new structures, metastable phases, and in particular the amorphous state, is a strong function of quench rate. More recent work suggests that in addition to quench rate, nucleation plays a substantial role. We report here work related to nucleation in the glassy alloy $\text{Ni}_{75}\text{B}_{17}\text{Si}_8$ and also a study of undercooling in rapidly solidified alloy steel powders.

The characterization of the glassy powders consisted of differential scanning calorimetry (DSC) on precisely sized fractions from a number of powder runs where both quench gas and other process parameters were varied. The results suggest that any of a number of nucleation modes may occur, including heterogeneous volume nucleation and homogeneous volume nucleation. The possibility of other modes is also raised.

The results on the alloy steel powders were obtained by x-ray diffraction (XRD) and transmission electron microscopy (TEM). Both the body centered cubic phase ferrite and the face centered cubic phase austenite were observed. Preliminary evidence indicates that the ferrite phase results from solidification of liquid droplets supercooled by a few hundred degrees, producing carbon supersaturation approaching 0.5 wt%, while the austenitic powder results from the solidification of droplets which have experienced lower levels of supercooling.

INTRODUCTION

The possibility of producing new alloys with novel properties by rapidly solidifying multi-component liquid metals was recognized some three decades ago by Duwez [1]. Several conferences have since provided increasing metallurgical data about the solidification behavior, phase stability, and phase transformations of alloys solidified at cooling rates above 10^5K/sec [2,3]. There exist several laboratory scale devices which produce liquid cooling rates greater than 10^5K/sec in bulk quantities. One such device, developed by the Government Products Division of Pratt & Whitney Aircraft, has been used for the past six years to produce quantities of powder quenched from the liquid at cooling rates from about 10^5 to 10^6K/sec [4]. This device consists of a rapidly rotating disk onto which is directed a liquid metal stream, producing a normal distribution of liquid metal droplets ranging in size up to about $200\text{ }\mu\text{m}$ in diameter with a mean particle size of up to about $90\text{ }\mu\text{m}$. Inert gas is used to provide forced convective cooling at rates between 10^5 and 10^6K/sec , with the quench rate depending on the type of gas used and the particle size produced.

The bulk of work published during the first decade or so of rapid solidification implied that the controlling factor in the production of new phases, structures, and the amorphous state was the rate of quenching of the melt. Early work at Pratt & Whitney on rapidly solidified powders suggested that the situation must be more complex: Holiday et al. [4] reported on two structures found in nickel-base superalloy powders, a conventional dendritic structure and a previously unreported "microcrystalline" structure. STEM analysis by Field and Fraser [5] suggested that the latter structure consisted of discrete crystallites exhibiting lower levels of segregation than found in the former structure. The former authors observed that both structures were found in different particles of any given particle size fraction, though the occurrence of the microcrystalline form was found to depend on both alloy chemistry and particle size, increasing rapidly as particle size decreased.

*Now with Allied Corporation, Corporate Technology, Morristown, N.J. 07960.

This work plus unpublished data on powders produced from 99.97+ wt% nickel led us [6] to conclude that in addition to quench rate, the effects of nucleation must be considered. In any given size fraction of the nickel powder, structures ranging from a very fine microcrystalline to a very coarse dendritic structure were observed, as shown in Figure 1. This structural difference seemed difficult to explain on the basis of quench rate alone since the quench rate of this powder process should be quite uniform for any given particle size. The heat transfer work of Glickstein *et al.* [7] also suggested that recalescence should occur during nucleation and growth due to the release and conduction of the latent heat of fusion; their model indicated that internal conduction should dominate over the rate of heat removal from the droplet surface during solidification. These factors suggested that the occurrence of nucleation at varying levels of supercooling might give rise to the variety of microstructures which had been observed.

Figure 1. Scanning electron micrograph of the -230+270 mesh size fraction of RSR processed 99.97+ weight percent nickel powder.



It thus seemed desirable to investigate the effect of process parameters on supercooling and nucleation. Unfortunately, for many alloys this would imply the metallographic examination of large numbers of particles from each of many size fractions, in order to insure that conclusions drawn would be statistically valid. Systems were sought for which other criteria might be used in order to avoid this laborious effort: Two, studied here, seemed reasonable. First, in the case of metallic glasses, the amorphous state would only be reached if nucleation and growth of the crystalline phases did not occur, and one could then evaluate large numbers of particles simultaneously by DSC to determine the variation of the heat released during crystallization of the glassy particles as a function of powder particle size and of process parameters; earlier results have been presented elsewhere [8]. Another system which might be useful would be one in which a series of crystalline phases could form on solidification at various levels of supercooling, some of which might be magnetic. For such a system, magnetic separation of each particle size fraction, coupled with x-ray diffraction, could then shed light on the significance of alloy chemistry and operational parameters in achieving the various levels of supercooling and resultant microstructures.

The work reported here is thus separated into two sections: One on the glass forming alloy $\text{Ni}_{75}\text{B}_{17}\text{Si}_8$ (atom percent) and the other on a series of alloy steels containing C, Cr, Mo, and V. In the former case, the powders were precision sieved into 5 μm or 10 μm size fractions, which were then subjected to DSC. The results suggest that a number of nucleation modes can occur, sometimes in different size ranges of the same powder lot, and that run to run results can vary widely. For the steels, the structures described resulted from a wider systematic study of the solidification behavior of a wide compositional range of alloy steels [9]. Normal metallographic techniques suggested that in all cases the crystalline solidification structure observed was cellular-dendritic, as shown in Figure 2, with dendrite arm spacings less than one micrometer indicating liquid quench rates on the order of 10^5K/sec or slightly higher. Subsequent XRD studies on these steels showed that in many cases the powders had solidified as the body centered cubic phase ferrite (Figure 3a), or alternatively as the face centered cubic phase austenite (Figure 3b), without any evidence of the metastable martensite phase, and that the alloy preference for ferritic or austenitic solidification did not appear to be easily related to chemistry. Also, some alloy compositions (e.g. Fe-1.2C-19Cr-2Mo-1V and Fe-1.15C-

14.7Cr-4Mo-1V, wt%) showed almost equal quantities of austenitic and ferritic phase powder (Figure 3c).

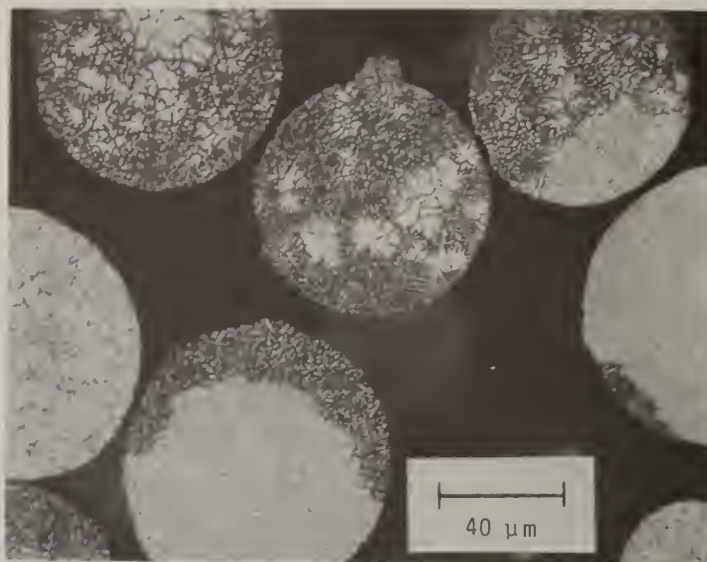


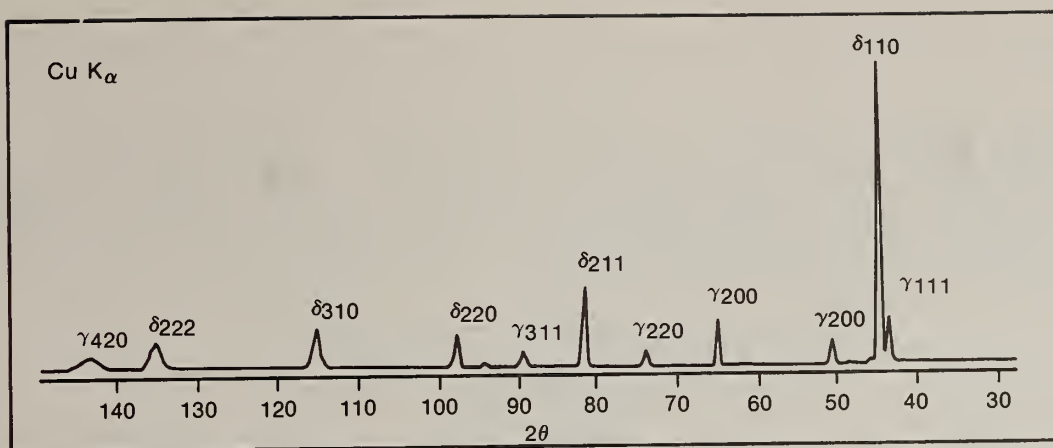
Figure 2. Cellular-dendritic solidification structure of 14-19 wt% Cr alloy steels. Light etching powder particles are austenitic; the darker areas are ferritic.

Since the austenitic powder is non-magnetic it was possible to separate the ferrite phase powder particles magnetically and examine the distributions of the two phases independently. The non-magnetic austenite phase was found to be confined to the coarser size fractions, above about 80 μm diameter, while the magnetic ferrite phase was confined to particle diameters finer than 50 μm . A further test of correlation between particle size and austenite/ferrite phase separation was obtained by selectively removing the -25 μm fraction by sieving. This powder was found to be entirely ferritic, indicating that a strong correlation existed between particle size and phase distribution. This was later confirmed independently for a commercial 303 stainless steel (Fe-17Cr-8Ni-1.6Mn, wt%) converted to powder by the P&WA process [10]. The structures found in both phases, shown in Figure 2 above, indicate direct solidification from the liquid rather than solid state transformation.

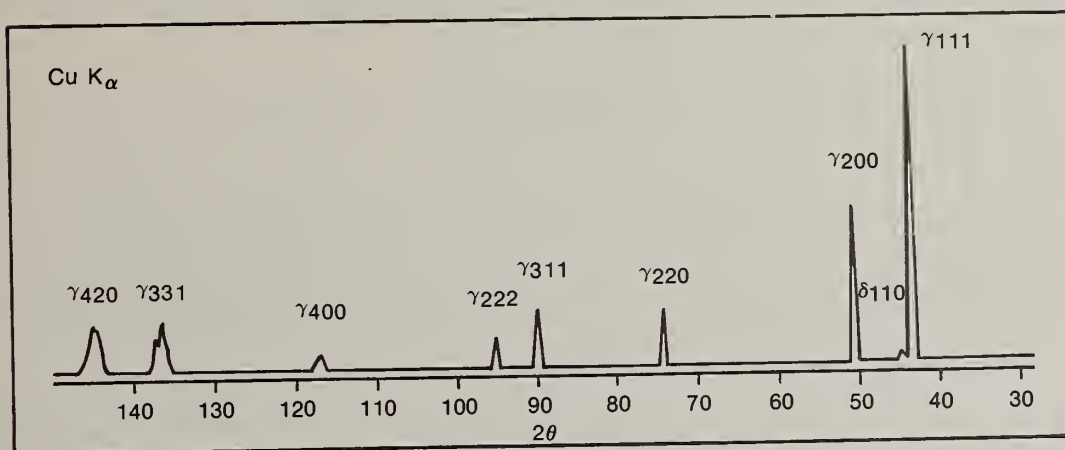
AMORPHOUS POWDERS

In previous work on amorphous powders [8,11] preliminary evidence has suggested that individual particles are either glassy or crystalline. In our work, limited microscopy on particle diameters to about 100 μm has shown no particles exhibiting both crystalline and glassy regions. For processes and alloys for which this occurs, the size distribution of the amorphous particles can be determined by measuring the heat released upon crystallization (by DSC) as a function of powder particle size. Since we have yet to produce a fraction which has been determined to be totally amorphous by x-ray diffraction, the results we have obtained are relative to the most energetic fraction observed to date.

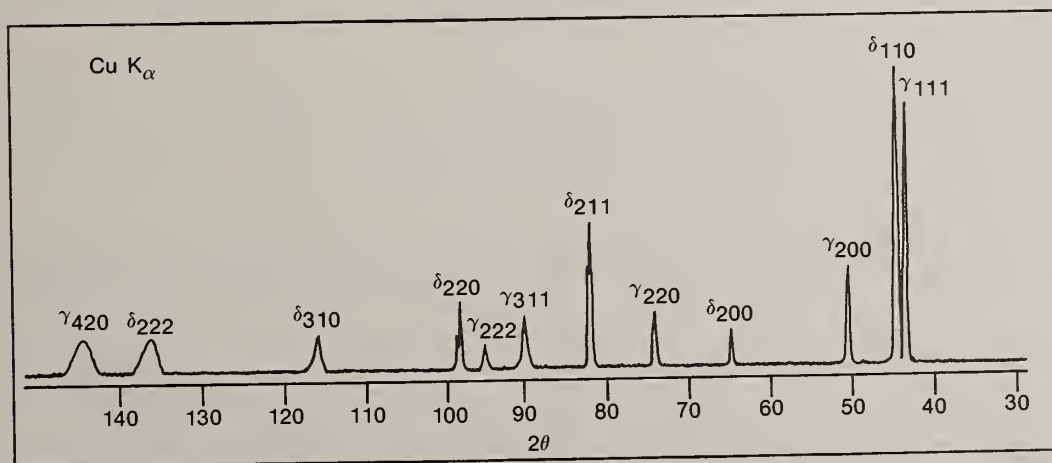
Arguments have been raised that the presence of crystalline particles implies that the quench rate necessary for glass formation does not exist. However, since glassy particles can be found in the same size fractions, the quench rate would seem to be satisfactory and the more pertinent question is: What events transpired which prevented the crystalline particles from reaching the glassy state. Nucleation and subsequent growth due to the presence of moles or nucleation sites would seem to be a more plausible explanation than the presumption that the quench rate varies in some complex fashion, allowing most (but not all) of the smaller particles and some (but not most) of the coarser particles to be glassy. Perepezko and Anderson [12] suggest that if heterogeneous volume nucleation is the dominant nucleation mode, then the probability x that a droplet of volume v will NOT contain a nucleation site when it is produced from a melt containing M sites per unit volume is given by a Poisson distribution of the form:



(a)



(b)



(c)

Figure 3. X-ray diffraction patterns of ferritic and austenitic alloy steel powders. (a) Fe-1.15C-14.7Cr-6Mo-1V; (b) Fe-1.15C-14.7Cr-2Mo-1V; (c) Fe-1.15C-14.7Cr-4Mo-1V.

$$X = \exp(-Mv) \quad (1)$$

This form is not explicit, since M is seldom known and must be back-calculated to fit the expression to the experimental data. A more useful form is obtained, following Drehman and Turnbull [11], by converting the volume to a particle diameter and by realizing that at some point the product Mv must be unity, at which point the expression (1) takes on the value $X \approx 0.3679$. We may thus normalize the equation through the use of a particle diameter d_0 , which will be that diameter at which $X \approx 0.3679$:

$$X = \exp\left\{-\left(\frac{d}{d_0}\right)^3\right\} \quad (2)$$

Unfortunately, the use of graphical analysis in Cartesian coordinates is also cumbersome. First, Drehman and Turnbull point out that there may be other nucleation modes; they suggest that for heterogeneous surface nucleation the exponent on d should be 2.0, while for homogeneous volume nucleation they expect the exponent to be on the order of 4.6. The latter exponent results from considering that the time available for nucleation is inversely proportional to quench rate, which in turn depends roughly on particle diameter to the -1.6 power.

Further difficulties may also confound the analysis. First, one must expect a degree of uncertainty in the experimental data so that exact agreement between such data and expressions such as (2) with exponents as suggested by Drehman and Turnbull is unlikely. Second, only three nucleation modes have been mentioned but others are not outside the realm of possibility. For example, the heat transfer work of Glickstein *et al.* [7] implies that thermal gradients should exist within rapidly quenched droplets, resulting in a droplet surface which is colder than the interior, and which will thus also begin to supercool sooner than the interior. This suggests that homogeneous surface nucleation may also be possible. Third, beyond the normal uncertainties encountered with experimental data, "outliers" may be encountered which would be difficult to detect when fitting an exponential function in Cartesian coordinates. Fourth, if a variety of modes having different catalytic activity exist in the melt, then the mode of nucleation encountered in the data might vary with particle size fraction.

To circumvent these difficulties, it is preferable to use a general expression in which the exponent is to be determined from the data:

$$X = \exp\left\{-\left(\frac{d}{d_0}\right)^y\right\} \quad (3)$$

If we then take successive logarithms we arrive at:

$$\ln(-\ln X) = y \ln(d) - y \ln(d_0) \quad (4)$$

Since this expression is linear in $\ln X$ and d , linear regression analysis may be performed to determine not only the best exponent, y , for the data, but also the correlation coefficient, R , of the data to the line of best fit. This still does not solve the problem of faulty data points or the presence of different nucleation modes in different size fractions, but these may be readily determined by graphical analysis: Data fitting the expression (4) will be linear when $-\ln X$ is plotted against d on log-log paper. Unfortunately, the price for this convenience is that this form puts heavy emphasis on the data when x is large. Thus, a small (1% or so) change in a large value of x (which we recall is the relative energy of crystallization determined by DSC) can cause a substantial shift in the location of the point. If other nearby points also shift (perhaps data are being remeasured), the slope (exponent) y will also change.

Experimental Results

Data were obtained using a DuPont 1090 thermal analysis system on small samples (3 to 15 mg, depending on absolute energy release) of powder which had been precisely sized into 5 or 10 μm fractions using an ATM Model L3P sonic sifter equipped with precision electroformed sieves. A few of the sieves were found to deviate from the stated size by a few microns, so a few fractions were as small as 3 μm or as large as 10 μm in range. Powder was obtained from remelting one of three masterheats which had

been produced by vacuum induction melting lots of from 35 to 40 Kg. Each lot was then poured to form ingots weighing about 12Kg. The remelting of each ingot was done under vacuum in the RSR device; upon melting, the chamber was backfilled with the gas to be used for quenching and the melt temperature was then increased to provide the necessary superheat. Argon was used as the quench gas for two of the runs, while helium was used for the other three. The data obtained from DSC are presented graphically in Figures 4 (argon quench) and 5. Values of the slopes of the various segments, determined by linear regression, are presented in Table I along with the correlation coefficient determined for the data of each segment:

TABLE I

Figure Number	Slope y	Correlation Coefficient, R
4A	1.01	0.9987
	2.45	0.9990
4B	1.50	0.9973
	2.75	0.9994
	4.31	0.9999
5A	2.36	0.9995
5B	0.617	0.9972
	0.992	0.9967
5C	2.94	0.9956

Two of the exponents can be correlated with the work of Drehman and Turnbull. The exponent for Figure 5C is sufficiently close to 3.0 to suggest that in this instance, heterogeneous volume nucleation has occurred. The exponent for the third segment of Figure 4B, at 4.31, is reasonably close to the analytically determined 4.6 and sufficiently far above the 3.0 expected for heterogeneous volume nucleation that homogeneous volume nucleation is likely the origin of the crystalline particles. At 2.75 the exponent of the second segment of Figure 4B may be sufficiently close to 3.0 to again indicate that volumetric heterogeneous nucleation has occurred. However, exponent values between 2.0 and 3.0 may imply an interchange of heterogeneous surface nucleation ($y=2.0$) and heterogeneous volume nucleation ($y = 3.0$); that is, a form of heterogeneous nucleation which is not site specific. This may be the case for the values of 2.75 of Figure 4B and 2.36 of Figure 5A; although the latter value may, with the uncertainties present in the data, be sufficiently close to 2.0 to indicate the heterogeneous surface nucleation observed by Drehman and Turnbull [11]. The latter situation may also apply to the slope of 2.45 of Figure 4A.

Then we have the seemingly low values of 1.01, 1.50, 0.617 and 0.992 tabulated above for various segments of Figures 4A, 4B and 5B. Whether these represent new modes of nucleation or are the result of a superposition of several modes remains to be determined, but some speculation may be warranted. For example, the dependence of the film coefficient, which relates the rate of heat removal from the surface of a droplet, on diameter is of the order of $d^{-0.6}$ while the bulk quench rate dependence is of the order of $d^{-1.6}$. Along the lines of a surface to volume ratio, the ratio of film coefficient to quench rate is on the order of $d^{1.0}$. The value of 0.617 for a segment of Figure 5B thus suggests a dependence on film coefficient, while the value of 1.50 of a segment of Figure 4B is close to the 1.6 expected for quench rate dependence.

It would thus appear that there are some operational regimes of the P&WA process where nucleation may be controlled by macroscopic quench rate, however little correlation to run conditions has yet been found. This is due in part to the number of operational parameters in the process, and also to the fact that for us, this is a relatively new alloy; our past experience has indicated that as many as twenty runs may be needed to determine the conditions necessary for proper atomization. Presently, operating variables have been selected not so much to study their effect on nucleation as to learn of their effect on atomization. In most of these runs we have obtained a log normal particle size distribution which is not characteristic of proper atomization by this process, and the general appearance, as observed via closed circuit TV and high speed film, suggests that a multiplicity of atomization modes are occurring. It may be that this factor is confounding the data presented; surely, more work is needed to distinguish between competitive nucleation modes.

ALLOY STEEL POWDERS

There has been continuing controversy in metallurgical literature over the respective roles of

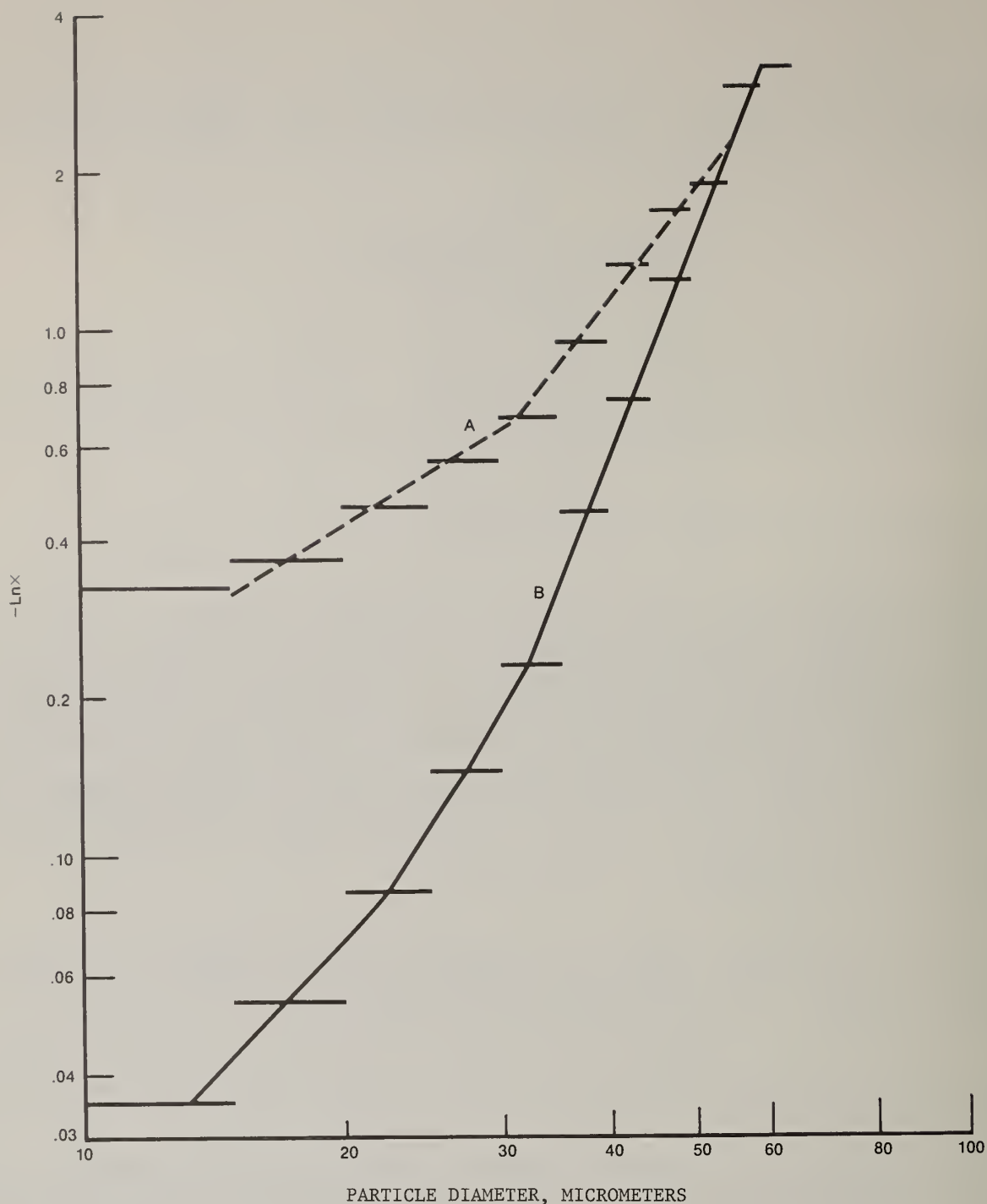


Figure 4. Variation in the relative volume fraction of amorphous powder, X , with particle size for two argon quenched runs of $\text{Ni}_{75}\text{B}_{17}\text{Si}_8$ (atom%), plotted according to Equation 4. Data were obtained by differential scanning calorimetry at a scan rate of 50K/min. The width of the data bars represents the nominal range between the precision sieves used for each size fraction. The slopes of the various segments of the curves are presented in Table I and discussed in the text.

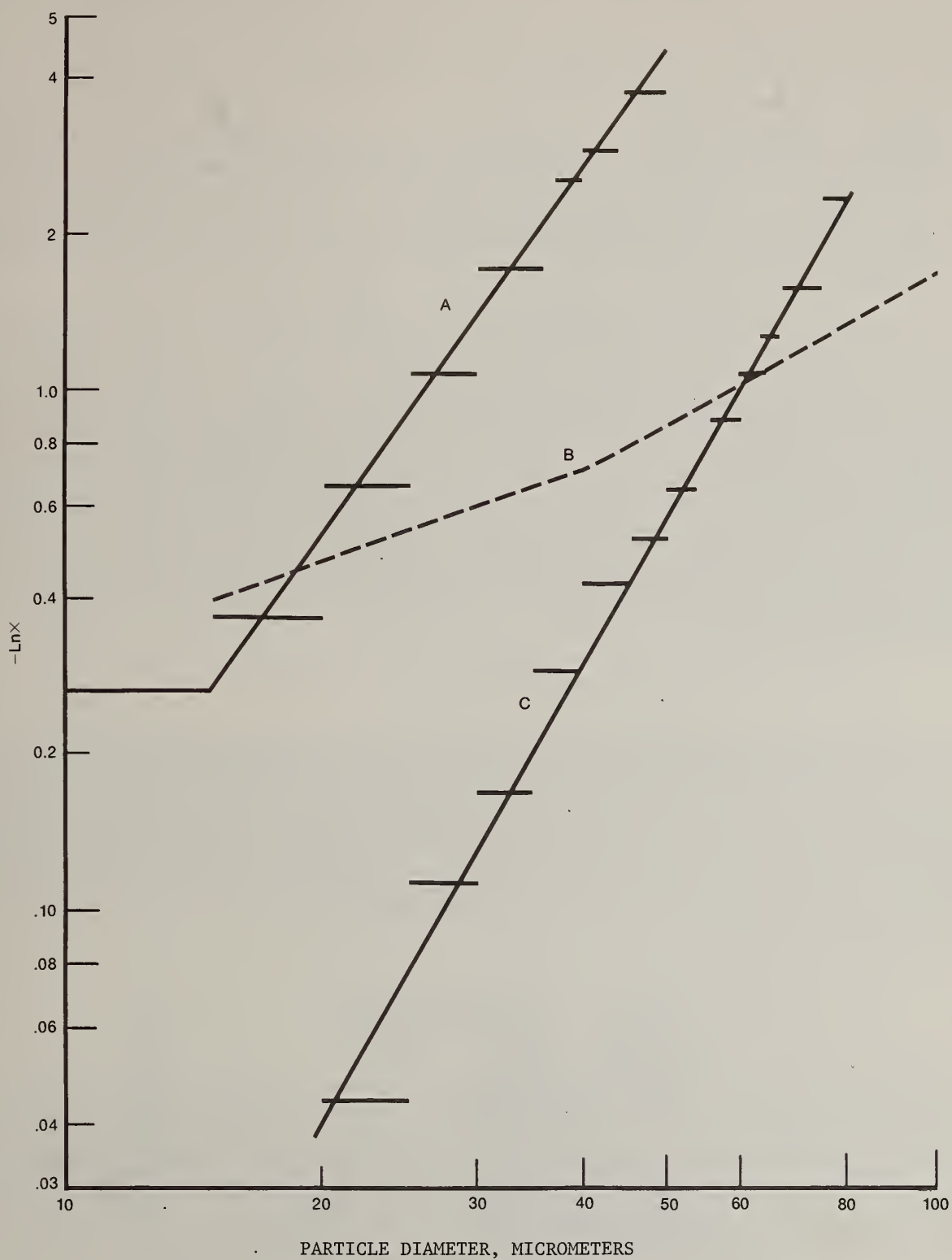


Figure 5. Data for three helium quenched RSR powder runs of $\text{Ni}_{75}\text{B}_{17}\text{Si}_8$, obtained and plotted as in the previous figure.

nucleation kinetics and subsequent growth kinetics during the solidification of metals. It has been generally considered that bulk liquid metals are incapable of massive supercooling because of the large number of heterogeneous catalytic nucleants normally present in commercial liquid metals, and that continuous dendritic growth at low supercooling levels is kinetically easier than repeated renucleation. However, the undercooling experiments of Cech [13] on Fe-Ni droplets, of Powell and Hogan on copper alloys [14], and more recently of Perepezko and Paik [15] on low melting point alloys has shown that in the absence of suitable heterogeneous nucleants, bulk (1g or more) quantities of liquid metal can be supercooled to $0.4 T_m$, where T_m is the normal pure metal thermodynamic freezing point. This work suggests that in general the degree of supercooling achieved before nucleation occurs increases as particle size decreases. Thus in our work it is reasonable to assume that supercooling levels in the finer ferritic powders are greater than those achieved in the coarser austenitic powders, using the same arguments as advanced by Perepezko and his co-workers. It is thus instructive to calculate the undercoolings for ferrite and austenite nucleation and to speculate why higher supercooling might lead to ferritic rather than austenitic solidification in the finer powder size fractions.

The iron-carbon equilibrium diagram can be viewed as a stable-metastable system in which either δ ferrite or γ austenite is stable, depending on the variables of composition and temperature. Cech [13] showed this situation qualitatively; based on such phase diagrams, one expects solidification of high-chromium (14-19 wt%) steels containing 1% carbon to be austenitic. The work of Kaufman and Bernstein on phase diagram calculation allowed Kelly [10] to calculate the relative free energies of the reactions $\text{Liq} \rightarrow \delta$ and $\text{Liq} \rightarrow \gamma$ for a commercial grade 303 stainless steel which is typical of many of the highly alloyed steels used in our investigation. This work indicated that the relative free energy changes are very similar and that there is no overwhelming free energy growth advantage for the subsequent solidification of either ferrite or austenite. This observation then leads to the conclusion that the presence of ferrite or austenite in rapidly solidified alloy steel powders is controlled by a critical nucleation energy, ΔG^* , with some energetic advantage being enjoyed by ferrite at high supercooling levels and by austenite at lower levels, for high-chromium steels containing 1 wt% C. The homogeneous nucleation rate, J_v , in an undercooled liquid may be expressed in simple form by the Turnbull equation:

$$J_v = \Omega_v \exp\left\{-\frac{16 \pi \sigma^3}{3(\Delta G_v)^2 kT}\right\} = \Omega_v \exp\left(-\frac{\Delta G^*}{kT}\right) \quad (5)$$

where Ω_v is a pre-factor of the order of $10^{35} \text{ cm}^{-3} \text{ sec}^{-1}$, σ is the interfacial energy between the nucleus and the undercooled liquid, ΔG_v is the driving force for nucleation of the product phase, k is the Boltzmann constant, and T is the absolute temperature. It is therefore useful to determine the relative values of σ and ΔG_v for austenite and ferrite and to speculate on how undercooling to different supercooling temperatures must affect the ferrite and austenite nucleation rates. Growth of ferrite or austenite can then proceed according to the free energy driving forces calculated from Kaufman-Bernstein data. Since $\Delta G_v = \Delta H \Delta T / T_m$, we can substitute in Equation (5) for ΔG_v in terms for which data are available, yielding:

$$J_v = \Omega_v \exp\left\{-\frac{16 \pi \sigma^3 T_m^2}{3 \Delta H_v^2 \Delta T^2 kT}\right\} \quad (6)$$

The nucleation event in a droplet can be observed [16] when the product $J_v \tau \approx 1$, where τ is the droplet volume and τ is time of flight in the temperature range over which freezing occurs. The nucleation rates in droplets 30 μm and 100 μm in diameter differ by roughly one order of magnitude based on their relative volumes, while the difference is roughly two orders of magnitude between 20 and 100 micrometer droplets. If we calculate the nucleation rate for a 20 μm ferrite droplet arbitrarily based on the time spent in a 500K temperature range below the equilibrium liquidus temperature, using a nominal liquid cooling rate of 10^6 K/sec [17], then the nucleation rate for such ferrite droplets is:

$$J_v \approx \frac{1}{\tau t} = \frac{3}{(5 \times 10^{-4}) 4\pi (10)^3 \times 10^{-12}} = 4.775 \times 10^{11}$$

$$\text{and} \quad \frac{16 \pi \sigma^3 T_m^2}{3 \Delta H_v^2 \Delta T^2 kT} = \ln\left\{\frac{10^{35}}{4.8 \times 10^{11}}\right\} = 53.70 \quad (7)$$

Using the latent heat of fusion, ΔH_v , of iron as $2.1 \times 10^9 \text{ J/m}^3$, the surface energy, σ , as 0.2 J/m^2 , and

$T_m = 1812\text{K}$ and $T = 1500\text{K}$, the undercooling for ferrite nucleation becomes:

$$\Delta T_\alpha = \left\{ \frac{16 \pi (0.2)^3 (1812)^2}{3(2.1 \times 10^9)^2 (1.38 \times 10^{-23}) \times 1500 \times 53.7} \right\}^{1/2} \approx 300\text{K} \quad (8)$$

Coarser droplets cool at somewhat slower rates, e.g. $5 \times 10^4 \text{K/sec}$ for a $100 \mu\text{m}$ diameter particle. Over the same temperature range (500K), $t \approx 10^{-2} \text{sec}$, and the nucleation rate for austenitic droplets becomes:

$$J_v = 1.6 \times 10^8 \text{ cm}^{-3} \text{ s}^{-1}$$

$$\text{and} \quad \frac{16 \pi \sigma^3 T_m^2}{3 \Delta H_v^2 \Delta T^2 k T} = \ln \left\{ \frac{10^{35}}{1.6 \times 10^8} \right\} = 61.7 \quad (9)$$

Solving for ΔT_γ yields a value of 260K . These calculations indicate that ferrite enjoys a nucleation advantage at undercoolings of about 300K , but the available free energy data for subsequent growth indicates that this advantage becomes suppressed by the faster growth of austenite at these undercooling levels. There is not sufficient precision in either the calculated undercoolings or in the Kaufman-Bernstein free energy data to be completely accurate in a predictive sense, in determining where austenite or ferrite nucleate in strongly undercooled liquid steel droplets, however the available data does indicate that a nucleation advantage enjoyed by ferrite overcomes a free energy disadvantage for subsequent growth. At droplet undercoolings of about $260\text{--}300\text{K}$ one would expect to find evidence of both ferrite and austenite nucleation and subsequent growth, and indeed that is the case for powder particles of intermediate size, i.e. between 50 and $100 \mu\text{m}$ diameter. In these powder particles both ferrite and austenite nucleate, but it is apparent that austenite has a substantial growth advantage.

Carbon Supersaturation

The x-ray diffraction data shown in Figure 3 have been used to calculate accurate lattice parameters for rapidly solidified austenite and ferrite present in high chromium content alloy steels containing up to 1.2 wt\% carbon. By using a standard Nelson-Riley extrapolation technique precise lattice parameters have been determined for a number of steels. The distribution of austenite and ferrite as a function of the particle size distribution obtained for one such alloy, Fe-1.15C-14.7Cr-4Mo-1V, is shown in Figure 6.

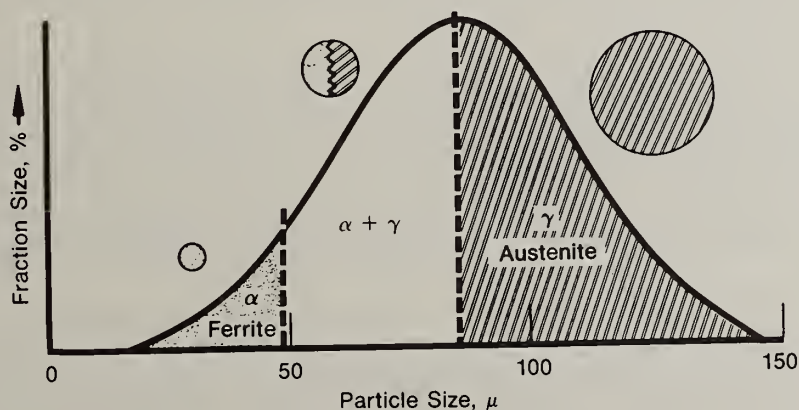


Figure 6. Austenite-ferrite distribution in Fe-1.15C-14.7Cr-4Mo-1V as a function of particle size.

Table II presents x-ray data obtained for two alloys: One (Fe-1.15C-14.7Cr-4Mo-1V) with fine ferritic and coarse austenitic powder and the other (Fe-1.2C-19Cr-2Mo-1V) with a range of austenitic and ferritic powders for which lattice parameters varied systematically with powder size. For both ferritic and austenitic powder the lattice parameters increased systematically with decreasing powder particle size. We expect that this data reflects both increased undercooling and subsequently a faster solidification rate for finer powder particles, with a consequent increase in solute supersaturation.

TABLE II

Lattice parameter data for austenite and ferrite phases in 14-19wt% Cr steels

Alloy Chemistry	Particle Diameter, μm	Lattice Parameter, nm	
		Austenite	Ferrite
Fe-1.15C-14.7Cr-4Mo-1V	<45	-----	0.2880
	80 to 105	0.3623	-----
Fe-1.2C-19Cr-2Mo-1V	>180	0.2867	0.3617
	150 to 180	0.2868	0.3617
	105 to 150	0.2869	0.3616
	75 to 105	0.2870	0.3617
	45 to 75	0.2873	0.3617
	38 to 45	0.2873	0.3619
	<38	0.2872	0.3620

Lattice parameters determined for the alloys of Table II are understandably greater than the usual lattice parameters for ferrite and austenite [18] indicating that the alloy solutes have expanded the basic crystal lattices. The lattice parameter of austenite is related to alloy chemistry by the following relationship:

$$a_0(\gamma) = 3.578 + 0.033\%C + 0.0031\%Mo + 0.0018\%V + 0.0006\%Cr \quad (10)$$

in weight percent, from which it is clear that interstitial carbon exercises the greatest effect on lattice parameter expansion. Lattice parameter determinations of the ferritic phase (Table II) yielded $a_0(\alpha)$ values between 0.2867 and 0.2872 nm (Fe-1.25C-19Cr-2Mo-1V) and 0.2880 nm (Fe-1.15C-14.7Cr-4Mo-1V). Using relationships determined for the lattice parameter of ferrite [19], $a_0(\alpha) = 2.8664 + 0.0084\%C$ (atom percent), solidification of the ferrite droplets thus resulted in substantial carbon supersaturation, varying from 0.4 to 0.6 wt% for the alloys shown in Table II. This calculated carbon supersaturation is imprecise due to lack of data about the magnitude of the ferrite lattice dilation by the substitutional elements vanadium and molybdenum. Chromium produces an almost negligible change in lattice parameter of ferrite [20] (0.005 nm/atom %) and molybdenum and vanadium appear to have an effect similar in magnitude to chromium in ferrite [21].

The measured ferrite lattice parameters are due to supersaturated solid solutions of carbon in the δ ferrite phase field, for which maximum solid solubility is 0.09 wt% at 1811K. There is no readily available data relating δ ferrite lattice parameters to alloy composition, however it is conceivable that the measured values represent an extension of the stable solid solubility limit of carbon in δ ferrite into the metastable region. Extrapolation of the δ ferrite solidus line to a temperature some 300K below the ferrite melting point produces a carbon solubility of about 0.6 wt% in δ ferrite. This value is close to the carbon supersaturation calculated from the x-ray measurements reported in Table II.

Equilibrium solid solubility data for the Fe-Cr-C alloys [21] indicated that the maximum carbon solid solubility in austenite in Fe-12Cr alloys is 0.92 wt% at 1500K, and for Fe-17Cr alloys, 0.65 wt% at 1533K. Using the experimental lattice parameters determined for the high-chromium alloys, the concentration of carbon in austenite was calculated at about 0.8%. Knowledge of the partition of carbon between complex $M_{23}C_6$ carbides and austenite is unavailable, however TEM showed that the volume fraction of $M_{23}C_6$ present in Fe-1.15C-14.7Cr-4Mo-1V austenitic powder was that expected from the balance of the alloy carbon content, e.g. 0.35 wt% C, producing about six volume percent $M_{23}C_6$ in the as-solidified austenitic powder. The carbon content of the austenite is roughly that predicted by the equilibrium diagram with no extreme supersaturation, but there is a general trend apparent in Table II for the finer size fractions of austenitic powder to contain more solute carbon than the coarser powder.

SUMMARY

The results of preliminary studies of undercooling and nucleation in rapidly solidified powders have been presented. Calorimetry on a glass-forming alloy has been used to evaluate nucleation. Suggested improvements to the analysis of data coupled with the data obtained suggest that a number of nucleation modes may occur, including heterogeneous and homogeneous volume nucleation. The work presented on alloy steel powders implies that supercoolings of a few degrees in the coarser particles, and a few hundred degrees in the finer particles, may be anticipated. In addition, extension of the solid solubility limit of carbon in ferrite into the metastable region is suggested by the work on the lattice parameters in the finer ferritic powder, while the work on the coarser austenitic powder suggests that the carbon content is roughly that predicted by the equilibrium diagram.

ACKNOWLEDGMENTS

We are indebted to Pratt & Whitney Aircraft for the support of the work on the metallic glass powders, and to the Defense Advanced Research Projects Agency, the Materials Laboratory of the Air Force Wright Aeronautical Laboratories, and to the Office of Naval Research for their support of various aspects of the work on alloy steel powders. In particular, we thank A.R. Cox, R.L. Athey and J. B. Moore of P&WA, Drs. E.C. vanReuth and L.A. Jacobson of DARPA, A.M. Adair of AFWAL/ML, and Dr. Bruce MacDonald of ONR for their interest and support.

The views and conclusions herein are those of the authors and should not be interpreted as necessarily representing the official policies, either expressed or implied, of the Defense Advanced Research Projects Agency, the U.S. Air Force, the U.S. Navy, or the U.S. Government.

REFERENCES

- [1]. P. Duwez, R.H. Willens and W. Klement, J.App. Phys. 31 (1960) 1136, and Trans. Met. Soc. A.I.M.E. 227(1963) 362.
- [2]. N.J. Grant and B.C. Giessen, eds., Proc. Second International Conf. on Rapidly Quenched Metals, Materials Sci. and Eng. V23 (1976); Proc. Third International Conf. on Rapidly Quenched Metals, B. Cantor, ed., The Metals Society, VI and II(1978); Proc. Fourth International Conf. on Rapidly Quenched Metals, H. Jones, ed., Japanese Inst. Metals (1981).
- [3]. Proc. First and Second Int. Conf. on Rapid Solidification Processing: Principles and Technologies, R. Mehrabian, B.H. Kear and M. Cohen, eds., Claitor's Publishing Division, Baton Rouge LA, 1978, 1980.
- [4]. P.R. Holiday, A.R. Cox and R.J. Patterson II, in Ref. [3] (1978) pp.246.
- [5]. R.D. Field and H.L. Fraser, *ibid.*, 270.
- [6]. R.J. Patterson, II, unpublished, West Palm Beach FL June 1977 and La Jolla CA July 1977.
- [7]. M.R. Glickstein, R.J. Patterson, II and N.E. Shockey in Rapid Solidification Processing: Principles and Technologies, R. Mehrabian, B.H. Kear and M. Cohen, eds., Claitor's Publishing Division, Baton Rouge, LA (1978) 46.
- [8]. R.J. Patterson, II, D.L. Ledwith and J.C. Dwyer, in Proc. ACS-AIME Powder Processing Symposium, K.W. Lay and R.M. German, eds., TMS-AIME, Warrendale, PA (1982).
- [9]. C.M. Adam *et al.*, AFWAL Final Report, Contract F33615-76-C-5136, P&WA/GPD Report FR15325, September 1981.
- [10]. T. Kelly, Ph.D. Thesis, M.I.T., Cambridge, Massachusetts, 1981.
- [11]. A.J. Drehman and D. Turnbull, Scripta Met. 15 (1981) 543.
- [12]. J.H. Perepezko and I.E. Anderson in Synthesis and Properties of Metastable Phases, E.S. Machlin and T.J. Rowland, eds., TMS-AIME, Warrendale, PA (1980) 31.
- [13]. R.E. Cech, Trans. A.I.M.E. 206 (1956) 585.

- [14]. G.L.F. Powell and L.M. Hogan, Trans. Met. Soc. A.I.M.E. 242 (1968) 2133.
- [15]. J.H. Perepezko and J.S. Paik in Rapidly Solidified Amorphous and Crystalline Alloys, B.H. Kear, B.C. Giessen and M. Cohen, eds., North-Holland, N.Y., NY (1982) 49.
- [16]. J.P. Hirth, Met. Trans. 9A (1978) 401.
- [17]. C.G. Levi and R. Mehrabian, Met. Trans. 11B (1980) 21.
- [18]. D.J. Dyson and B. Holmes, J. Iron and Steel Inst. 208 (1970) 469.
- [19]. F.J. Fasiska and H. Wagenblast, Trans. Met. Soc. A.I.M.E. 239 (1967) 1818.
- [20]. W.C. Leslie, Met. Trans. 3 (1972) 5.
- [21]. F.B. Pickering, Physical Metallurgy and the Design of Steels, Applied Science, London, 1978.

OSTWALD RIPENING OF RAPIDLY SOLIDIFIED SOLID-LIQUID MIXTURES

P. W. Voorhees* and M. E. Glicksman

Materials Engineering Department
Rensselaer Polytechnic Institute
Troy, NY 12181

ABSTRACT

A new theory of Ostwald ripening in two-phase mixtures has been developed which explicitly accounts for the diffusional interaction between the dispersed coarsening second phase. This theory predicts the morphology of coarsening solid/liquid mixtures in terms of time invariant distributions of interfacial curvature. The theory also predicts a dependence of the curvature distributions and ripening kinetics on the volume fraction solidified. Experiments were performed to measure the response of an ultra-precise thermal probe immersed in a coarsening rapidly solidified solid/liquid mixture of high purity white phosphorous over a wide range of fraction solids. Through this theory it is now possible to interpret the experimental results to gain a deeper insight into the nature of Ostwald ripening following rapid solidification.

Introduction

Ostwald ripening has long been viewed as a slow morphological relaxation process which follows the initial phase transformation. The concept of ripening or coarsening as a kinetically slow process no doubt stems from the extensive investigation of the effects of coarsening on the microstructure of slowly solidified castings. The work of Kattamis, et al., has established that in large castings, where the local solidification times are on the order of many minutes or hours, ripening plays a major role in determining the size scale of the as-solidified microstructure [1].

By contrast, most rapid solidification processes are associated with far higher interfacial velocities and generally shorter local solidification times. The influence of coarsening of the microstructure of rapidly solidified materials is commonly thought to be negligible because of a pre-conception of coarsening as a kinetically slow relaxation process.

A major impediment in the assessment of coarsening processes in rapidly solidified materials is the extremely short local solidification times which are commonly encountered. These brief local solidification times--often as short as 10^{-4} s--preclude the use of standard experimental techniques, such as quenches at different aging times for determining the role of coarsening in the morphological progression of solid-liquid mixtures. As a result, there is little direct experimental evidence to indicate that coarsening plays any role in the microstructural development of rapidly solidified materials. A second impediment in the study of dendritic ripening in solid-liquid mixtures is the lack of cogent theoretical guidance. This is due primarily to the difficulty in constructing a theory of coarsening in solid-liquid mixtures which realistically accounts for the diffusional interactions among regions of the system with differing interfacial curvature and, consequently, differing chemical potential.

To address these current deficiencies in our understanding of coarsening following rapid solidification, experimental measurements were made of the kinetics of coarsening in rapidly solidified solid-liquid mixtures and a realistic theory of microstructural relaxation in solid-liquid mixtures was developed which is capable of providing new insights into the dendrite ripening problem.

*Presently at the National Bureau of Standards, Washington, DC 20234

Experimental

A novel experimental procedure was employed to produce rapidly solidified mixtures with local solidification times on the order of many hours. These long local solidification times were essential in permitting the coarsening kinetics of a rapidly solidified solid-liquid mixture to be measured experimentally. The following is a brief description of the apparatus and procedure used to measure the kinetics of dendritic coarsening in rapidly solidified solid-liquid mixtures. A more detailed description of the procedure and apparatus can be found elsewhere [2].

Measurements of the coarsening kinetics were made using rapidly solidified, high purity, white phosphorus (αP_4). αP_4 was chosen as the model material because of the relative ease in achieving large supercooling. The supercooling tendency of αP_4 enabled precise control of both the interfacial velocity and the volume fraction of solid transformed during solidification. The volume fraction of solid, rapidly solidified under adiabatic conditions, is numerically equal to the normalized supercooling, $\Delta\phi = C\Delta T/L$ where L is the latent heat of fusion, ΔT is the supercooling, and C is the specific heat of the liquid [2]. The interfacial velocities achieved in αP_4 were usually on the order of 200 cm/sec, and thus were of the same magnitude as interfacial velocities commonly reported for other rapid solidification processes. To preserve the adiabaticity of the two-phase mixture immediately following nucleation of the supercooled melt, the 30 ml bulb containing the solid-liquid mixture was transferred immediately to a stirred bath carefully thermostatted approximately 4mK below the bulk melting temperature (44.1°C). Placing the bulb in the thermostat greatly reduced the heat loss from the bulb, thus preserving the solid-to-liquid ratio in the two-phase mixture for periods of many hours.

The equilibrium temperature of an interface is directly related to its curvature, κ , via the Gibbs-Thomson equation, viz.,

$$T(\kappa^*) = T_m - \frac{\gamma}{\Delta S_f} \kappa^*, \quad (1)$$

where κ^* is the total dimensional curvature at a point on the interface, γ is the solid-liquid interfacial energy, T_m is the bulk melting point, and ΔS_f is the entropy of fusion. The progress of dendritic coarsening can, in principle, be measured in situ via a precision thermometer capable of resolving temperature changes of 10^{-4} K within the two-phase mixture.

Results

A typical log-temperature vs. log-time output from the thermistor is shown in Fig. 1. The slow rise in thermistor temperature with time is consistent with increasing interfacial radii of curvature linked to the ripening of the solid-liquid mixture. To determine the rate of Ostwald ripening at times too short to be directly measurable with the instrumentation used in this experiment, it is necessary to assume that the power-law kinetics shown at long times in Fig. 1 can be extrapolated

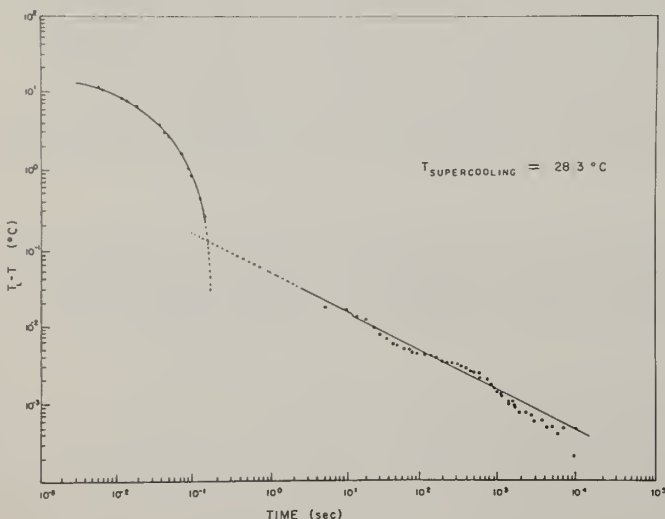


Fig. 1. Liquidus temperature, T_l , minus the thermistor temperature versus time (log-log scale) showing short-time response of the thermistor (due to thermal inertia) and long-time response due to Ostwald ripening. The two kinetic processes are easily distinguished here, as is the power-law character of the dendritic coarsening.

back toward shorter times. Theoretical justification for this back extrapolation is found in ripening theory which asserts that power law coarsening kinetics exist as long as the system is at steady-state. Theory also indicates that steady-state ripening should occur under most circumstances in a very short time compared to the duration of the steady-state coarsening process. Further discussion of this point can be found elsewhere [2]. The equation of the line shown in Fig. 1 is

$$T = T_L - Bt^{-n}. \quad (2)$$

It has been shown theoretically that the temperature of a thermistor immersed in a coarsening solid-liquid mixture is related to the average radius of curvature by [2],

$$T = T_L - \frac{A\gamma}{\Delta S_f \langle R \rangle}, \quad (3)$$

where A is a constant of order unity and $\langle R \rangle$ is the average total radius of curvature of the solid-liquid interface.

Substituting eq. 3 into eq. 2 yields

$$\langle R \rangle = \frac{A\gamma}{B \Delta S_f} t^n. \quad (4)$$

It is possible to compute the coarsening rate from eq. 4 as,

$$\frac{d\langle R \rangle}{dt} = \dot{\langle R \rangle} = \frac{A\gamma n}{B \Delta S_f} t^{n-1}. \quad (5)$$

The data in Fig. 1 yield values of B and n of 0.0486 and 0.476, respectively. The coarsening rates and average radii of curvature of the solid-liquid mixture at shorter times can now be found by extrapolating the data of Fig. 1 backwards in time. Clearly, extrapolation to $t = 0$ is precluded because eq. 5 diverges as $t \rightarrow 0$. A reasonable estimate for the time corresponding to the beginning of steady-state coarsening in these experiments is 10^{-3} seconds. Inserting the materials constants of αP_4 into eqs. 4 and 5 and taking $A = 1$ yields the average interfacial radius of curvature and coarsening rates as functions of time, respectively, as shown in Fig. 2. A number of interesting observations can be made on the basis of Fig. 2: 1) the average radius of curvature soon after solidification, $\sim 10^{-3}$ s, is indeed small, but well above the atomic scale; 2) this small radius of curvature gives rise to an extraordinarily rapid coarsening rate. Our experimental measurements and subsequent order-of-magnitude estimates of coarsening rates in rapidly solidified solid-liquid mixtures have shown that significant coarsening of the structure can occur with local solidification times on the order of 10^{-3} s. Further insights into the morphology and kinetics of dendritic coarsening in solid-liquid mixtures can be obtained by considering the theory of Ostwald ripening.

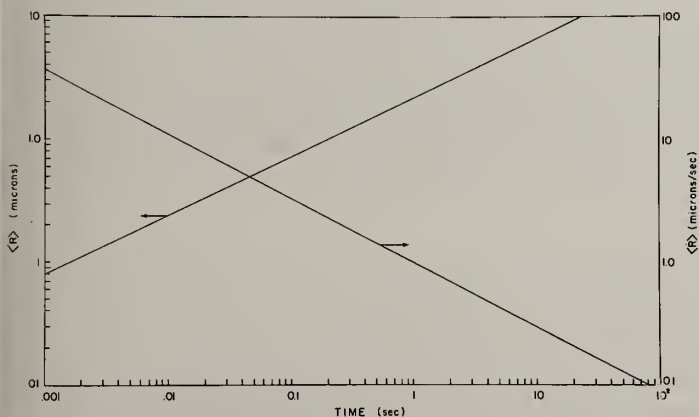


Fig. 2. Average interfacial radius of curvature $\langle R \rangle$ and $\dot{\langle R \rangle}$ versus time. These plots correspond to the thermal response data shown in Fig. 1, as interpreted through Equations 4 and 5 in the text.

Theory

Developing a predictive theory of dendritic coarsening in solid-liquid mixtures which is based upon detailed interfacial morphology is virtually impossible. We shall therefore consider the solid-liquid mixture present following rapid solidification in a topological sense whereby only the statistical distribution of interfacial curvature associated with the mixture will be considered, and not its detailed morphology. A distribution of interfacial curvature at some instant of time following rapid solidification will be modeled in a statistical sense with a distribution of spherical solid particles having the same distribution of local equilibrium temperatures. Using this approach it is possible to gain considerable insight into the coarsening behavior of solid-liquid mixtures.

Recently, the authors have developed a fast algorithm for accurate numerical solution to the multi-particle diffusion problem (MDP) [3]. The MDP has been employed to determine the temperature field within a coarsening solid-liquid mixture, and as a result interparticle thermal interactions are realistically included in the theory. Interparticle interactions allow the volume fraction of coarsening phase to play a role in determining the ripening kinetics and morphology. A detailed description of the theory of the MDP can be found elsewhere [3]. The theory indicates that coarsening solid-liquid mixtures quickly reach a steady-state, wherein the inverse of the cube of the average curvature grows linearly with time, i.e.,

$$\langle \kappa(t) \rangle^{-3} - \langle \kappa(0) \rangle^{-3} = Kt. \quad (6)$$

Here $\langle \kappa(0) \rangle$ is the dimensionless average curvature at time $t = 0$, $\langle \kappa(t) \rangle$ is the dimensionless average curvature at time t , and K is the rate constant. The theory also shows that the distribution of interfacial curvature, when normalized by the average curvature, is time invariant. The specific predictions on the morphology and coarsening kinetics are discussed below.

Morphology

As was mentioned earlier, under steady-state conditions the distribution of interfacial curvature scaled to the average becomes time invariant. However, theory also indicates that the distribution of interfacial curvature should depend on the volume fraction of solid in the two-phase mixture. The volume fraction dependence of the distribution of curvature results from the diffusional interaction between regions of differing curvature. As the volume fraction of solid is increased, the regions of differing interfacial curvature become closer, on average, which causes the thermal interactions among these regions to increase. The increasing interactions in turn produce a change in the interfacial morphology of the solid-liquid mixture. Since the volume fraction of solid is equal to the normalized supercooling, the morphology of coarsening solid-liquid mixtures should depend on the degree of supercooling prior to nucleation. The changes in interfacial morphology with volume fraction can be seen in the steady-state distribution of curvatures shown in Fig. 3. As is evident, the increased diffusional interaction with increasing volume fraction manifests itself as a broader and more symmetric distribution of interfacial curvature.

Kinetics of Morphological Relaxation

As expected intuitively, the increasing thermal interactions among regions of differing curvature as the volume fraction of solid increases cause an increase in the growth rate of the average interfacial radius of curvature. Such an increase in microstructural coarsening rates is expressed by a change in the rate constant, K , appearing in Eq. 6. The functional dependence of K on volume fraction is shown in Fig. 4. This figure illustrates that partially solidified mixtures with a volume fraction of solid, (or normalized undercooling) approaching 0.5 should coarsen at about four times the rate as that of a mixture with a solid volume fraction near zero. The results shown in Fig. 4, in conjunction with the rate equation, Eq. 6, can be combined to yield specific predictions on the interfacial coarsening rates of solid-liquid mixtures. The coarsening rate for a given average curvature can be found from Eq. 6, viz.

$$\dot{\langle R \rangle} = \frac{dR}{dt} = \frac{K}{3} \langle R \rangle^{-2}, \quad (7)$$

where $\langle R \rangle$ is the dimensionless average radius of curvature of the solid-liquid mixture. The inverse squared dependence of the coarsening rate on the average radius of curvature indicates that mixtures with a small average radius of curvature will coarsen at high rates. If the volume fraction dependence of K is included, then the coarsening rate behaves as is shown in Fig. 5. As was observed

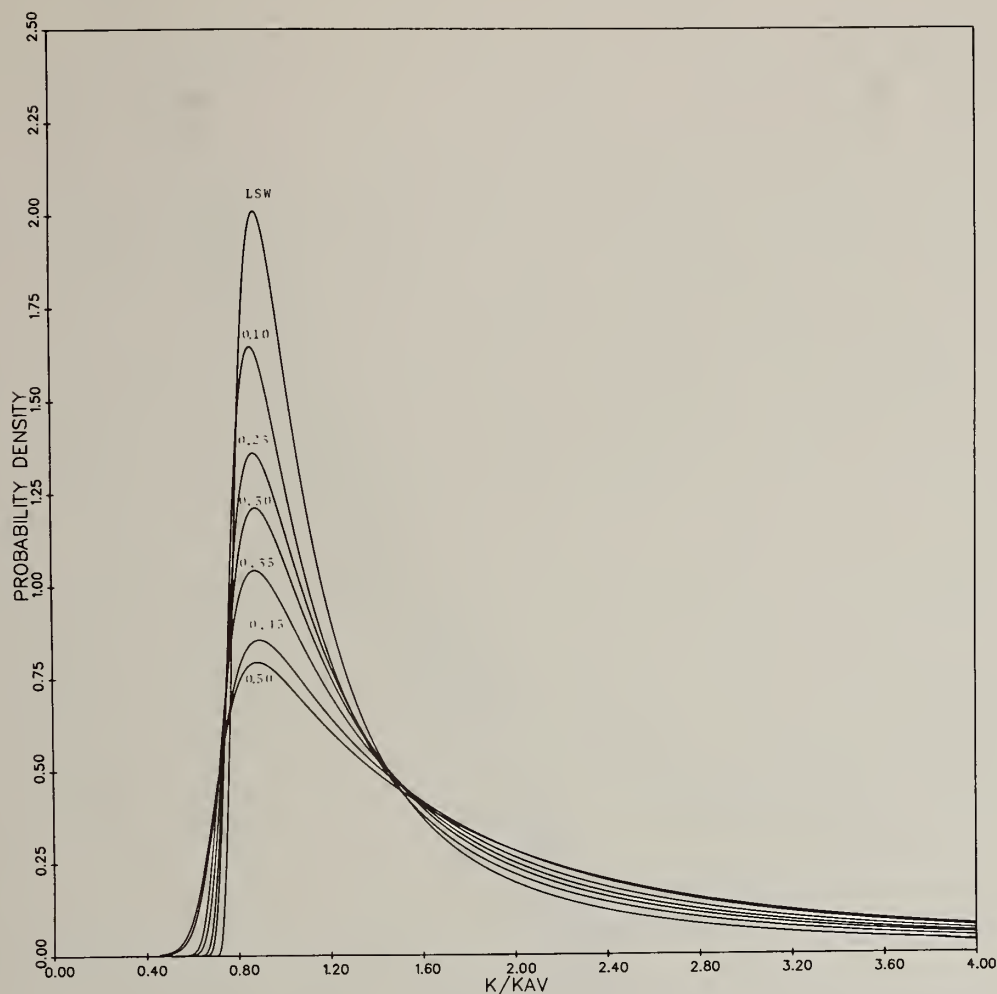


Fig. 3. Theoretical distributions of interfacial curvature. Distribution functions are shown for the various volume fractions of solid studied by computer simulation of the steady-state MDP.

experimentally, the theory predicts that a dendritic solid-liquid system with small radii of curvature will coarsen at high rates relative to the size scale of the microstructure. This can be seen more clearly by denormalizing the variables shown in Fig. 5. For example, choosing a normalized undercooling of 0.35 and $\langle R \rangle = 10^4$ yields a dimensionless coarsening rate of 4.2×10^{-9} . Using the materials constants of α -P4, $\langle R \rangle$ and $\langle R \rangle$ can be dimensionalized to give $\langle R \rangle = 6.51 \mu$ and $\langle R \rangle = 10.4 \mu/s$. These theoretical predictions further reinforce the idea that Ostwald ripening plays an important role in the development of the morphology of rapidly solidified solid-liquid mixtures.

Conclusions

The following can be concluded on the basis of this paper:

1. An experimental procedure has been developed which permits investigation of the coarsening behavior of rapidly solidified solid-liquid mixtures via direct thermometry.
2. The average interfacial radius at the beginning of steady-state dendritic coarsening following rapid solidification is estimated to be a moderately small multiple of the capillary length.

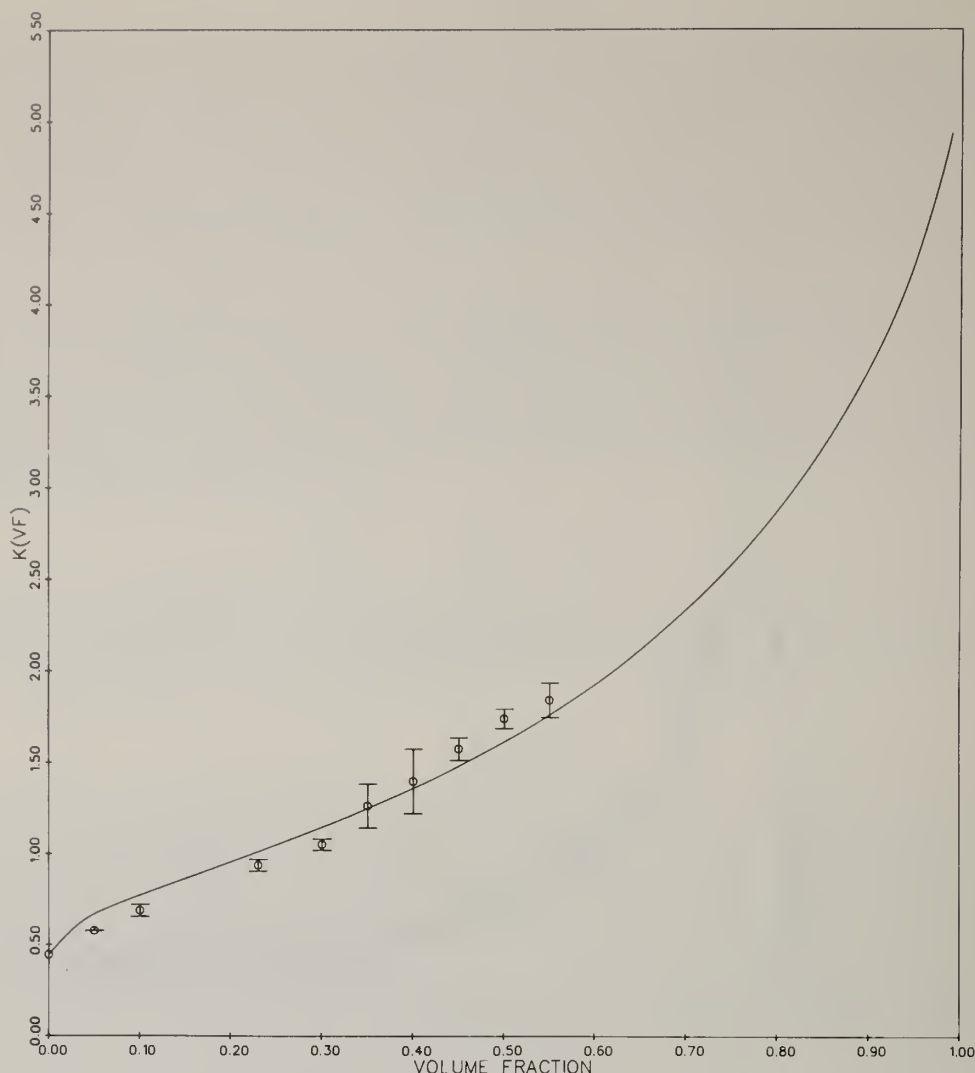


Fig. 4. Dependence of the cubical rate constant K on volume fraction.

3. The large interfacial curvatures following rapid solidification give rise to rapid coarsening rates relative to the size scale of the microstructure. Calculations indicate that α -P₄ in a solid-liquid mixture with an average radius of curvature of 0.1μ will double its radius in approximately 3×10^{-4} s.
4. Steady-state distributions of interfacial curvature can be calculated on the basis of Ostwald ripening theory, and are dependent on the degree of normalized liquid supercooling.
5. At steady-state, the cube of the average radius of curvature grows linearly with time, with the rate of growth being dependent on the normalized liquid supercooling.
6. Theoretical predictions of the coarsening rates of solid-liquid mixtures are in qualitative agreement with experiment.

Acknowledgment

The authors acknowledge the support provided by the National Science Foundation (NSF) through the Division of Materials Research, under contract DMR-7721638. We are especially grateful for the special provision of a Research Creativity Award provided to one of us (MEG) by NSF.

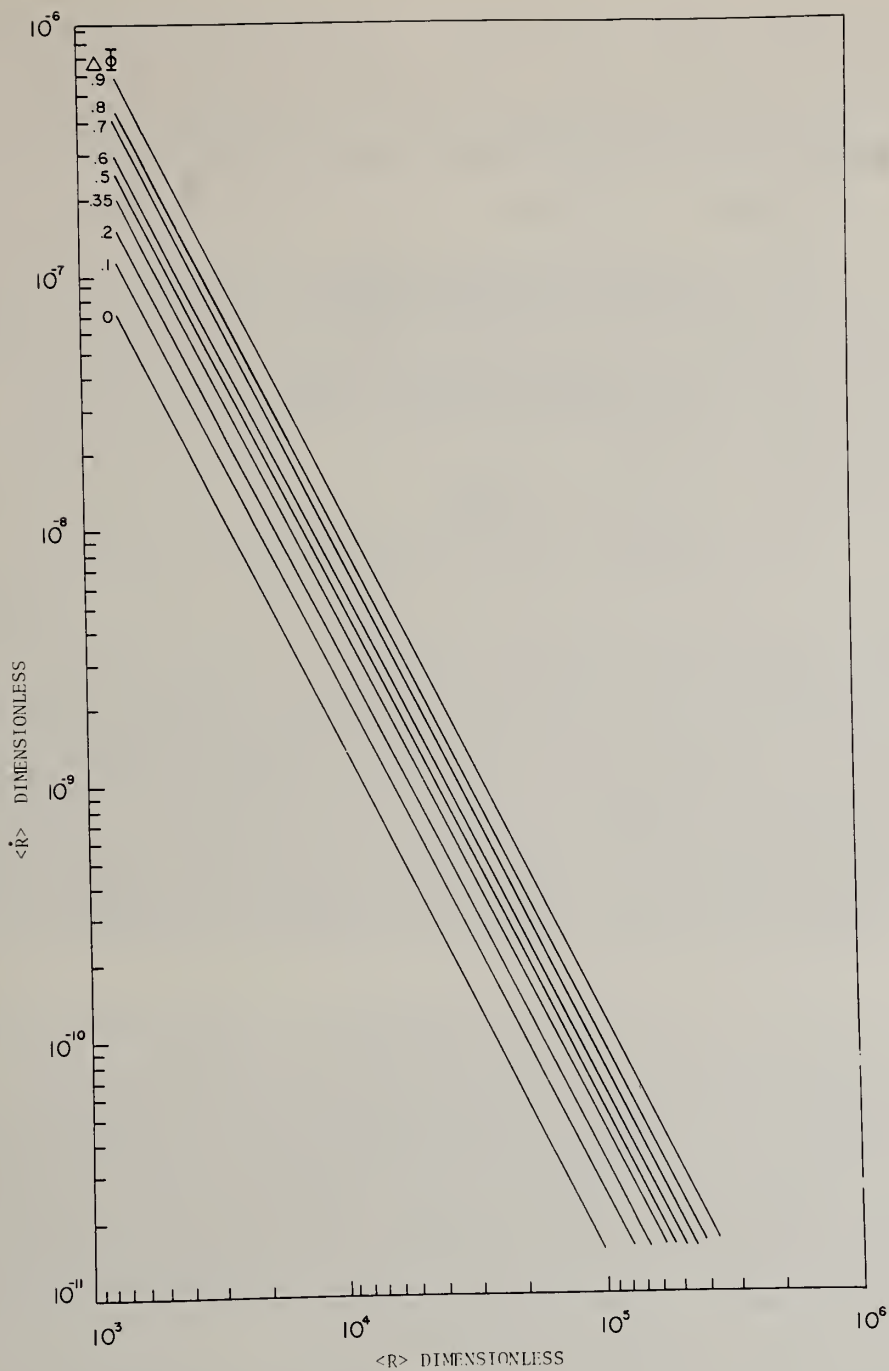


Fig. 5. Coarsening rate \dot{R} versus average interfacial radius of curvature $\langle R \rangle$ for dendritic mixtures supercooled initially an amount $\Delta\phi$.

References

1. T. Z. Katamis, J. C. Coughlin, and M. C. Flemings, Trans. Met. Soc. AIME, 239 (1967) pp. 1504.
2. P. W. Voorhees and M. E. Glicksman, J. Crystal Growth, to be submitted.
3. P. W. Voorhees and M. E. Glicksman, Acta Met., to be submitted.

SOLIDIFICATION MICROSTRUCTURES OF UNDERCOOLED DROPLETS

J. J. Richmond, J. H. Perepezko, S. E. LeBeau and K. P. Cooper⁺

Department of Metallurgical and Mineral Engineering
University of Wisconsin-Madison
Madison, Wisconsin 53706

⁺Olin Metals Research Labs
New Haven, Connecticut 06511

ABSTRACT

Following nucleation in an undercooled liquid the subsequent crystal growth will yield rapid solidification conditions. Fine liquid droplets exhibit large undercoolings which can be measured accurately at a slow cooling rate and can be varied experimentally in a controlled manner. With this approach the development of solidification microstructures as a function of melt undercooling and composition has been examined in several eutectic alloy systems. In Pb-rich Pb-Sb alloys with compositions extending to the eutectic a transition from a segregated, two-phase microstructure to a supersaturated solid solution has been identified with increasing undercooling level. These observations have been related to the onset of hypercooling conditions during isenthalpic solidification. In hypereutectic Al-Fe alloys a transition from growth controlled features to nucleation controlled structures has been observed where formation of the metastable Al_6Fe occurs in undercooled droplets even in the presence of primary Al_3Fe particles. For Pd-Cd alloys the usual eutectic pattern developed at modest undercooling is circumvented by a phase separation reaction as the initially homogeneous alloy liquid enters a miscibility gap region before crystallization at high undercooling. These observations highlight several solidification paths for microstructure development.

Introduction

The emergence of Rapid Solidification Processing (RSP) as an innovative approach to materials processing has been based to a large extent on favorable microstructural features [1-3]. As a broad generalization of the microstructures associated with RSP there appear to be two categories of characteristics. In one case the influence of RSP treatment can be viewed in terms of the decrease in local solidification time and the growth features of the principal microstructural elements. Another category of microstructural development is the evolution of novel structures comprised of phase mixtures that are not associated with the equilibrium features of phase diagrams. The examination of microstructure control in the case of novel structures requires a consideration of nucleation kinetics and significant melt undercooling. In addition, for both general categories the influence of thermal history should be incorporated in the analysis of microstructure.

One approach to the examination of structure development during RSP involves the study of droplet samples. The dispersal of a liquid into fine droplets has been demonstrated to yield very high undercooling levels which can be measured accurately [4]. This feature is a prerequisite for a detailed examination and understanding of the phase selection kinetics involved in nucleation controlled product structures. In addition, with droplet samples and thermal cycling treatments it is possible to examine growth controlled microstructures and thermal history effects associated with RSP. In the present work, the development of solidification microstructures has been examined in highly undercooled droplet samples of Pb-Sb, Al-Fe and Pb-Cd alloys.

Experimental

Droplet samples were prepared by an emulsification process in which a high speed motor (30,000 rpm) attached with a shearing blade assembly disrupts a mixture of carrier fluid and liquid metal under an inert atmosphere into a droplet dispersion. With a large number of droplets only a small fraction of the drops may contain the most potent nucleant sites. The fine droplets ($d < 20\mu$) are maintained independent by the use of thin surface coatings produced by chemical reaction. For metals which melt below $500^\circ C$, a mixture of organic carrier fluid dissolved with organic or inorganic acid surfactants and a liquid metal alloy, which is prepared with metals of 99.999% purity, is sheared at

50 to 100°C above the liquidus temperature. Recently the droplet method has been extended to allow the study of high melting temperature alloys such as Al-Fe with the use of molten salt carrier fluid mixtures. The crystallization temperature and kinetics can be measured accurately by either a differential thermal analysis (DTA) or a differential scanning calorimetry (DSC) technique. Following thermal analysis, the phase selection and solidification microstructure were examined by applying an x-ray diffraction (XRD) technique and by metallographic study of exterior surface and interior droplet sections.

Results and Discussion

A large volume of bulk liquid can be considered to have a distribution of nucleating centers with different catalytic potencies. The amount of undercooling at a given cooling rate is determined by the effect of the most active sites. By progressively removing or isolating nucleation sites from a sample, an undercooling level will be observed which is characteristic of the most active nucleant still remaining [5]. The importance of the degree of the droplet size refinement in promoting a high level of liquid undercooling has been demonstrated clearly [4]. Based upon the current experience, a uniform undercooling characteristic of a single crystallization exotherm far below the melting point is represented usually by droplets in the 5-20 μm size range. In addition it has been demonstrated that in fine droplet dispersions with a narrow size distribution, the extent of liquid undercooling is sensitive also to the surface coating used to maintain droplet independence [4].

Pb-Sb Alloy droplets

An example of uniform undercooling to a single crystallization exotherm is represented in fig. 1 for a Pb-11.4 a/o Sb alloy. The maximum undercooling nucleation temperature, T_N , occurs at 113°C which is equivalent to an undercooling, ΔT , of 162°C below the alloy liquidus, T_L . The sensitivity of the undercooling behavior to alternate nucleation sites is also illustrated in fig. 1 where the cooling trace yielding final crystallization at T_{HET} (185°C) represents the catalysis of an α -Pb primary phase in promoting solidification. In examining the influence of melt undercooling on microstructure development, alternate nucleation sites, that are generated by the application of different surfactant treatments, were used as an effective approach to produce controlled undercooling levels. A summary of the undercooling behavior for Pb-Sb alloys for compositions spanning the eutectic is superimposed on the portion of the phase diagram plotted in fig. 2. As observed in other alloys [5] the trend of undercooling with alloy composition exhibits a pattern which tends to follow roughly the alloy liquidus.

The apparently simple behavior of the undercooling trends reported in fig. 2 however, does not reflect the variety of microstructural patterns developed in droplets following rapid solidification. This variety is illustrated for a Pb 14.4 a/o Sb alloy by the microstructures given in fig. 3. At a low ΔT of 14°C the microstructure in fig. 3a reveals coarse α dendrites with a complex regular eutectic within interdendritic regions [6] and would be representative of a conventional processing treatment. In droplet samples at an undercooling level of 111°C a strongly modified microstructure is evident in fig. 3b. In this case the light, clear regions represent an α primary solid solution which was supersaturated up to the alloy solute content while the remaining region represents a fine scale two-phase mixture. The initial supersaturation of the α phase has been established by separate XRD measurements on droplet samples immediately following thermal analysis. During sample preparation to reveal interior droplet sections, the supersaturated α phase undergoes a precipitation reaction which produces a pattern of fine, dark Sb precipitates. Another stage of microstructure modification is apparent in the micrograph of fig. 3c corresponding to droplet solidification at a ΔT of 162°C. In this case, XRD measurements have been used to establish that the initial solidification structure was essentially entirely a supersaturated α phase. Again, during sample preparation a fine scale precipitation of the Sb phase developed in the single crystal droplets.

Based upon the measured undercooling values and the initial droplet structures, it is possible to develop an understanding of the observed microstructural modifications in terms of an adiabatic solidification model [1,3]. When the nucleation temperature, T_N , is close to T_L , a segregated structure can develop as in fig. 3a. It is possible for crystallization to yield a solid of the alloy composition C_0 as T_N is reduced below T_0 which represents the onset of partitionless solidification [7] and is also drawn schematically in fig. 2. Since the rate of crystal growth following nucleation in a highly undercooled liquid is rapid, the latent heat will evolve at a rapid rate during recalescence. The temperature rise during recalescence reduces the amount of interfacial undercooling and the growth rate which for a solid of composition C_0 can reduce to zero upon reaching T_0 which appears to set a bound on partitionless solidification. Toward the end of recalescence and during final droplet solidification the solid composition can change leading to a segregated structure and a mixed morphology (fig. 3b). With the adiabatic model, when the undercooling is sufficient so that the recalescence temperature rise does not lead to the development of solute partitioning, solidification can occur entirely to a single phase solid as shown in fig. 3c. The limiting undercooling for this process defines the onset of

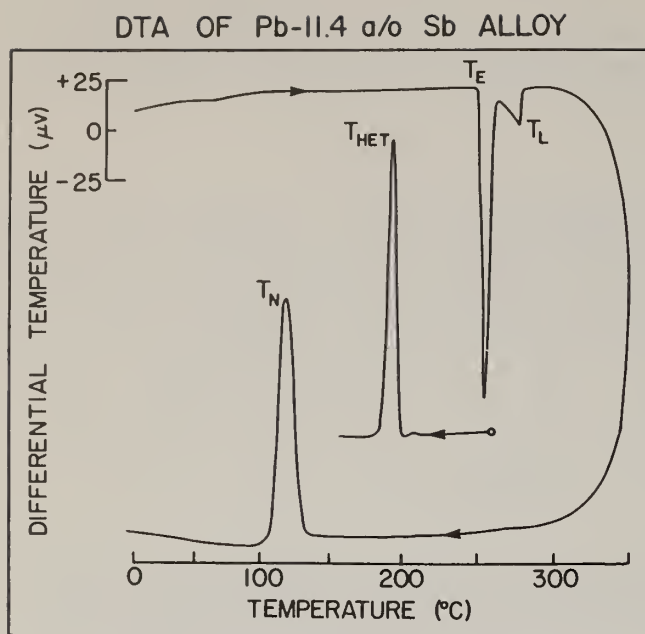


Fig. 1 DTA Thermogram for Pb-11.4 a/o Sb alloy droplets.

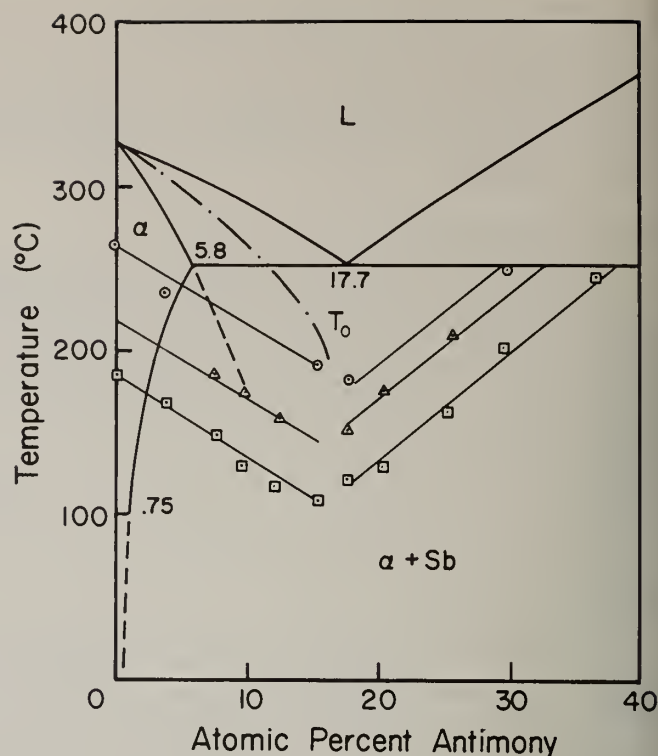
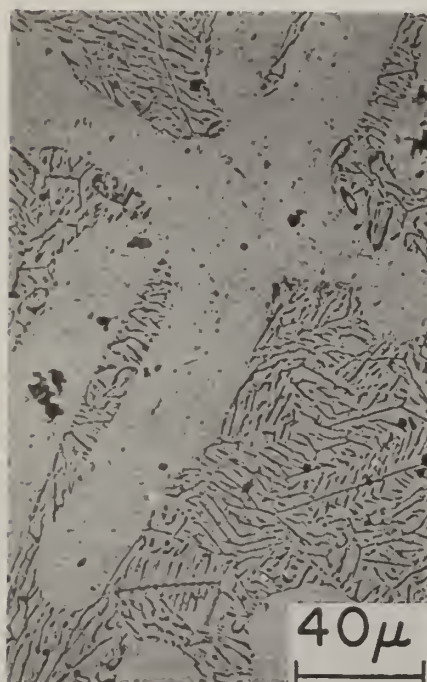
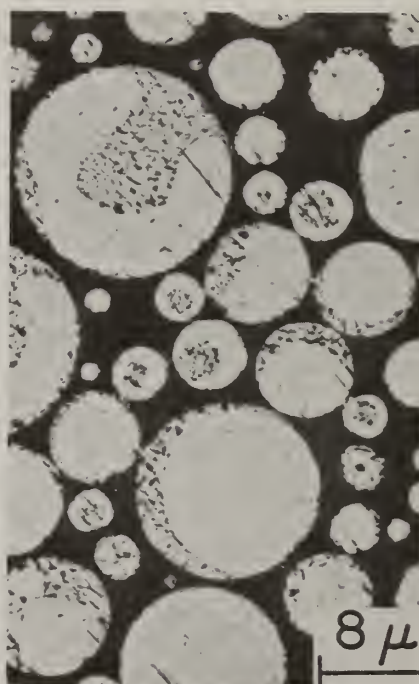


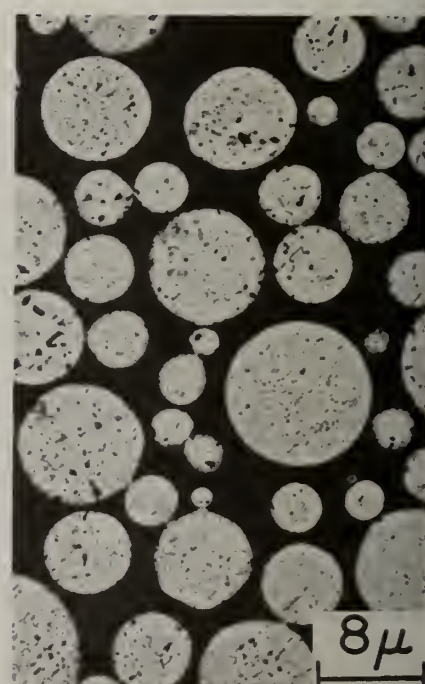
Fig. 2 Summary of undercooling behavior in Pb-Sb alloys. Different symbols refer to undercooling trends produced by different droplet surface coating treatments.



a



b



c

Fig. 3 Solidification microstructures developed in Pb-14.4 a/o Sb alloys at different undercooling levels (a) $\Delta T = 14^\circ\text{C}$; (b) $\Delta T = 111^\circ\text{C}$; (c) $\Delta T = 162^\circ\text{C}$.

hypercooling, ΔT_H which is given to first order by $\Delta T_H = \Delta H_m / C_p$ where ΔH_m is the latent heat and C_p is the liquid heat capacity [3,4]. In Pb-Sb alloys ΔT_H appears to be reduced with solute content from about 157°C for pure Pb [4] to about 130°C for a Pb-14.4 a/o Sb alloy [6]. This is in agreement with the solidification to a supersaturated solid solution in droplets at $\Delta T = 162^\circ\text{C}$ and the formation of partially segregated droplet structures at $\Delta T = 111^\circ\text{C}$.

In a number of hypoeutectic alloy compositions microstructural patterns similar to those reported for the Pb-14.4 a/o Sb alloy have been observed. For alloy compositions near the eutectic however, a different pattern of microstructure was observed as illustrated in fig. 4 for a Pb-17.7 a/o Sb eutectic alloy. At a ΔT of 19°C a complex regular eutectic pattern develops. Also, at undercoolings from 70°C to 130°C the eutectic pattern is replaced by a dendritic microstructure instead of single phase α . This agrees with other rapid melt quenching work [8] where the limit for solubility extension was approximately the eutectic. The transition from a eutectic to a dendritic morphology with increasing undercooling has been observed to occur also in hypereutectic alloys and appears to be related to the location of the coupled zone for eutectic growth [9]. The coupled zone region usually tends to be skewed towards compositions high in the faceting component such as Sb. As a result, with increasing undercooling, a transition can occur from a eutectic to a dendritic structure. In addition, measurements of the secondary dendrite arm spacing (DAS) reveal only a small decrease from 0.37μ at $\Delta T = 70^\circ\text{C}$ to 0.23μ at $\Delta T = 130^\circ\text{C}$ in the eutectic alloy which suggests that a significant structural coarsening may control DAS at high undercooling [10]. In this case the application of DAS measurements to characterize parameters such as solidification rate may not be reliable.

Undercooled Al-Fe Alloys

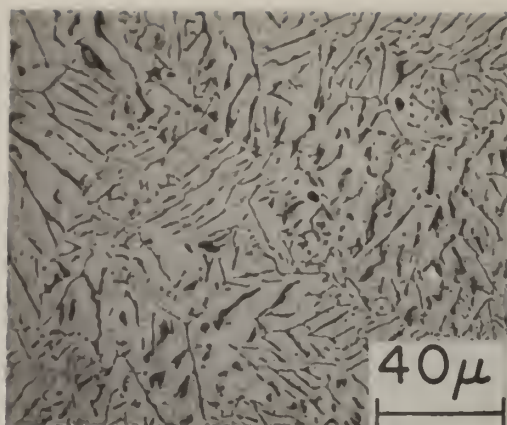
The Al-Fe alloy system exhibits a eutectic reaction at 1/8 w/o Fe and 655°C between Al containing 0.052 w/o Fe and a binary Al-Fe intermetallic compound, Al_3Fe . The Al- Al_3Fe eutectic microstructure at moderate freezing rates is an example of a faceted-nonfaceted irregular eutectic structure consisting of plates of the faceted Al_3Fe phase in an aluminum matrix. A transition from the irregular Al- Al_3Fe structure to a fine fibrous metastable eutectic of Al- Al_6Fe has been observed in chill casting [11] controlled direction solidification studies [12] and in rapid quenching experiments [13]. The potential for Al-Fe based high-strength PM alloys for use at elevated temperatures is receiving continued interest [14].

The eutectic systems of the Al-rich end of the Al-Fe phase diagram have been examined using the droplet-emulsion technique. Fig. 5 is a typical DTA thermogram for a hypereutectic droplet emulsion sample of Al-9 w/o Fe. Upon heating the droplet sample ($\dot{T} = 30\text{ K/min}$) an endothermic peak associated with the melting of the metastable Al- Al_6Fe eutectic, $m-T_E$, occurs at 649°C corresponding to a eutectic composition of the Al- Al_6Fe at 3.8 w/o Fe by a simple linear extrapolation of the solidus and liquidus of the equilibrium phase diagram. Upon further heating the thermal signal returns to the baseline value at a T_L of 875°C. During the subsequent cooling of the sample ($\dot{T} = 30\text{ K/min}$) a small exothermic peak which indicates the crystallization of primary Al_3Fe is observed at 850°C. Any further crystallization and/or growth of the primary phase is not easily distinguished from the normal baseline behavior. Upon cooling below the eutectic temperature a pair of broad crystallization exotherms occurs with peak temperatures of 640°C and 565°C respectively. The DTA thermogram suggests that even in the presence of Al_3Fe primary particles substantial undercoolings of at least 85°C below the eutectic isotherm can be achieved. The relatively low catalytic activity of the Al_3Fe primary phase can be substantiated by reheating the sample above the eutectic temperature to equilibrate a liquid- Al_3Fe primary solid two-phase mixture within each droplet. Subsequently, upon cooling the samples, the crystallization behavior observed was identical to that obtained in the previous cycle during cooling from above T_L . The droplet microstructure obtained after the thermal cycling in fig. 5 is shown in the SEM micrograph in fig. 6. The microstructure consists of a primary Al_3Fe plate which is surrounded by a metastable Al- Al_6Fe eutectic mixture. The undercooling and microstructure characteristics that are presented in figs. 5 and 6 reveal that a distribution of nucleants can be active in a droplet sample. These observations suggest that the range of microstructural variations that have been reported in aluminum base systems in rapid quenching studies may be the result of variations in initial liquid undercooling in addition to variations of cooling rate.

Pb-Cd Alloys

Often it is implicitly assumed in solidification that an initial alloy liquid is compositionally homogeneous. During conventional processing this characteristic may be assessed by examining the equilibrium phase diagram. However, during RSP which can involve liquid undercoolings up to about $0.3 T_m$, it may be necessary to reconsider the assumption of initial melt homogeneity. For example, at high undercooling the alloy liquid may enter into the domain of a metastable miscibility gap. The role of initial melt constitution on microstructural development in rapid solidification has been examined in the Pb-Cd system which exhibits an equilibrium eutectic reaction. However, for hypereutectic alloys, DTA studies on undercooled droplets reveal that prior to crystallization a phase separation can occur in the liquid. The consequences of phase separation on the solidification

(a)



(b)



Fig. 4 Solidification microstructures developed in Pb-17.7 a/o Sb alloys at different undercooling levels. A transition from eutectic (a) [$\Delta T=19^\circ\text{C}$] to a dendritic surface morphology (b) [$\Delta T=130^\circ\text{C}$] is illustrated.



Fig. 6 Solidification microstructure developed in Al-9 w/o Fe droplets.

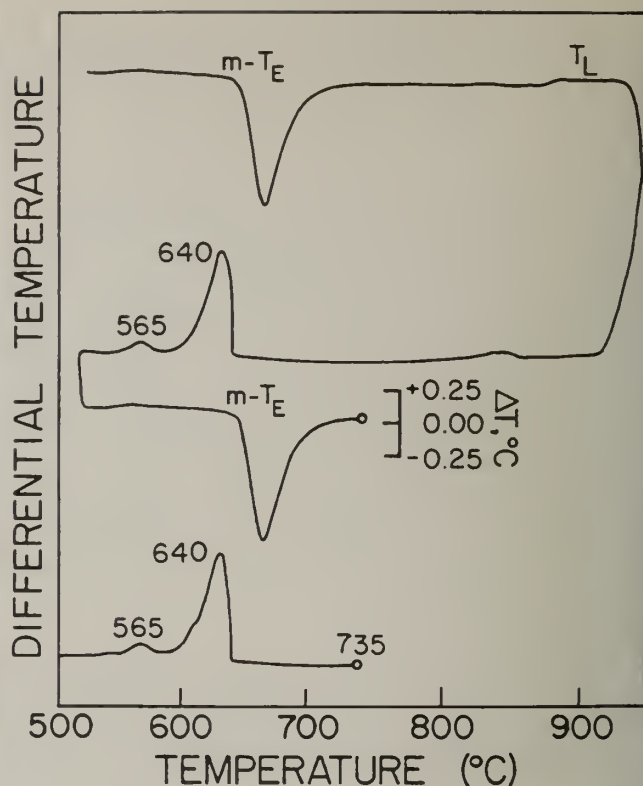


Fig. 5 Undercooling behavior of Al-9 w/o Fe droplets.

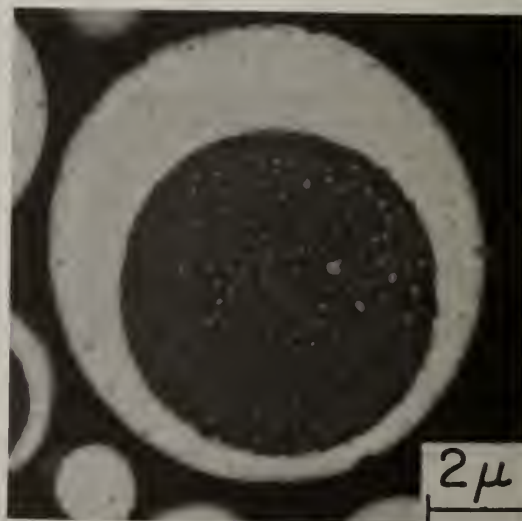


Fig. 7 Microstructure developed in Pb-40 w/o Cd droplets in which phase separation preceded solidification.

microstructure are illustrated strikingly in fig. 7. The interior droplet section reveals a Pb-rich region (light) surrounding a Cd-rich core (dark) which is a substantially different morphology than that developed during usual eutectic solidification. For Pb-Cd alloys the tendency for liquid phase separation may be judged by the shallow Cd liquidus so that the undercooling required to achieve liquid demixing is not large [15]. In general the likelihood of a metastable miscibility gap may not be readily apparent from an equilibrium liquidus without a thermodynamic analysis, but this feature can be encountered more often at large undercooling and for conditions involved in glass formation.

Summary

The controlled undercooling in fine droplet samples provides an effective experimental approach to the study of RSP. In Pb-Sb alloys the capability to vary melt undercooling has allowed for the study of a transition from a segregated two-phase morphology to a single phase solidification microstructure. This microstructural transition has been related to the onset of hypercooling in terms of rapid solidification under adiabatic conditions. Similar studies on eutectic Pb-Sb alloys have revealed only a weak dependence of DAS on undercooling which may be the result of structural coarsening effects. In droplets of Al-Fe alloys a large undercooling and solidification of a metastable Al_6Fe phase has been established even in the presence of primary Al_3Fe nucleants. The microstructural effects of melt inhomogeneity due to a metastable phase separation have been demonstrated in undercooled Pb-Cd alloys. These observations highlight the use of undercooled droplet samples to examine paths for microstructure development during RSP.

Acknowledgement

The authors are grateful for the support of the U.S. Army Research Office (DAAG29-80-K-0068). We are indebted to W. J. Boettinger, G. J. Hildeman and C. M. Adam for discussions and assistance.

References

- [1]. R. Mehrabian, "Rapid Solidification Processing-Principles and Technologies", R. Mehrabian, B. H. Kear and M. Cohen (eds.), p. 9, Claitor Pub. Div., Baton Rouge, LA, (1978).
- [2]. M. Cohen, B. H. Kear and R. Mehrabian, "Rapid Solidification Processing - Principles and Technologies II", R. Mehrabian, B. H. Kear and M. Cohen (eds.), p. 1, Claitor Pub. Div., Baton Rouge, LA, (1980).
- [3]. C. G. Levi and R. Mehrabian, Met. Trans. 13A 13, 221 (1982).
- [4]. J. H. Perepezko, ref. 2 p. 56.
- [5]. J. H. Perepezko and J. S. Paik, "Rapidly Solidified Amorphous and Crystalline Alloys", B. H. Kear, B. C. Giessen, and M. Cohen (eds.) p. 49, Elsevier Pub. Co. N.Y. (1982).
- [6]. J. J. Richmond and J. H. Perepezko (to be published).
- [7]. J. C. Baker and J. W. Cahn, "Solidification" p. 23, ASM, Metals Park, OH (1971).
- [8]. C. Barromée-Gautier, B. C. Giessen and N. J. Grant, J. Chem. Phys. 48, 1905 (1968).
- [9]. W. Kurz and D. J. Fisher, Int. Met. Rev. 5-6 177 (1979).
- [10]. P. W. Voorhees and M. E. Glicksman, ref. 5 p. 33.
- [11]. L. Backerud, Jernkont. Ann. 152 109 (1968).
- [12]. R. Hughes and H. Jones, Jnl. of Mat. Sci. 11 1781 (1976).
- [13]. H. Jones, Mater. Sci. Eng. 5 1 (1969).
- [14]. C. M. Adam and R. G. Bordeau, ref. 2 p. 246.
- [15]. J. H. Perepezko and W. J. Boettinger (to be published).

^{*}Center for Materials Research, The Johns Hopkins University, Baltimore, MD 21218[†]Center for Materials Science, National Bureau of Standards, Washington, DC 20234

ABSTRACT

Various Al-Cu alloy powders were made by the Microparticle Processor and their microstructure studied by transmission electron microscopy. The powder particles which sizes range from 3 nm to a few microns demonstrate different structural characteristics ranging from amorphous to ordered crystalline intermetallic depending upon composition and particle size. Extended solid solubility was observed in all the alloys examined. Some of the results obtained from Al-Cu alloy powders will be shown and discussed. The cooling rates needed to suppress crystallization in some alloys will be calculated.

Introduction

The use of electrohydrodynamics (EHD) in the atomization of metal alloys, in an apparatus hereafter referred to as the micro-particle processor (MPP)¹ has provided a means of producing small quantities of submicrometer size metal particles. These small powders are, in general, transparent to 100 Kev electrons, used in conventional TEM analysis allowing a three-dimensional view of the entire solidification structure. This paper will discuss some aspects of the microstructures observed in aluminum-copper alloy powders produced by this process. Of particular interest here is the formation of metastable solid solutions in many of these powders and powders showing a transition from partitionless (massive) solidification to a segregated solidification mode as described in an earlier paper by Levi and Mehrabian [1] and in this volume by Cohen and Mehrabian [2]. The influence of particle size and composition on microstructure is discussed, especially as it relates to the apparent bulk supercooling achieved prior to nucleation and the solid/liquid interfacial velocity during growth and recalescence.

Experimental Procedure

Al-Cu binary alloy powders were produced using the microparticle processor (MPP) at NBS. A detailed description of this apparatus is given in these proceedings [3]. Droplet generation in the processor essentially involves the application of a very intense electric field on a conductive liquid at the tip of a capillary nozzle (emitter). The alloys contained 0.5, 1, 2, 3, 4.5 and 6 wt.% Cu. The production parameters were 14 kV extraction voltage with an argon feed pressure of 50 mm Hg x cm² against a vacuum of 10⁻⁵ mm Hg cm². The flight distance to the cellulose acetate tape collector (target) was 150 mm. Specimens for transmission electron microscopy were prepared by depositing a thin carbon layer on the monolayer of particles captured on the target tape. The tape was subsequently dissolved in acetone. Specimens thus made were mounted on 400 mesh grids and studied in a scanning transmission electron microscope (STEM) equipped with a nondispersive x-ray fluorescence analysis system. The study of composition variation across a powder particle involves several experimental difficulties, including the proper geometrical positioning of the particle relative to the grid base, the electron beam and the detector. Appropriate adjustments were made to compensate for these so as to produce minimum experimental error. Other difficulties are inherent to the spherical shape and size of the individual particles. These require a correction procedure that will take into account the specific electron beam location on the particle, i.e., the cross-section of the particle at that point and its location relative to the x-ray detector. Such correction procedure was not done, but an attempt was made to measure x-ray intensities generated from points of equal thickness. This may account for some inaccuracies in the composition analysis.

Finally, *in situ* heat treatment of individual powder particles was performed under controlled electron beam in the STEM and the sequence of second phase precipitation from the supersaturated solid solutions was recorded.

¹Disclaimer: Certain trade name and company products are mentioned in the text in order to adequately specify the experimental procedure and equipment used. In no case does identification imply a recommendation or endorsement by the National Bureau of Standards, nor does it imply that products are necessarily the best available for the purpose. This processor uses electrohydrodynamic atomization technique to break a molten metallic droplet situated at the tip of an extractor tube into smaller droplets, which then cool by radiation and solidify.

Results and Discussion

Most of the Al-Cu particles studied were in the size range of 3 nm to 2 μm . In general, larger particles did not solidify in flight. Furthermore, particles larger than $\sim 2 \mu\text{m}$ are not transparent to 100 Kev electrons. Representative microstructures of individual powder particles are shown in Figure 1. Three kinds of microstructures were observed. The first is a segregation-free particle which solidified with no partitioning at the solid/liquid interface, Figure 1a. The second particle solidified in a more-or-less conventional cellular solidification mode, Figure 1c. The powder particle in Figure 1b exhibits a mixed solidification mode with both a segregation-free and cellularly segregated regions. These types of microstructures have previously been reported in fine powders of Al-Si and Al-Cu alloys [1,2].

While the structures in Figure 1 are not restricted to any particular size range or copper content, some general trends were established. At the lower end of the size range (below $\sim 0.5 \mu\text{m}$) and compositions below $\sim 2 \text{ wt.}\% \text{ Cu}$ most of the particles solidified without apparent lateral segregation. With increasing particle size and/or copper content the microstructures in Figure 1b and 1c become predominant. No attempt was made to deduce a statistical correlation between size, composition and mode of solidification.

These observations can be interpreted in terms of bulk supercooling prior to nucleation and interfacial temperatures and velocities during solidification. Partitionless solidification requires an interfacial temperature below the T_0 temperature of the alloy and an interfacial velocity in excess of the diffusive velocity of solute in the liquid in front of the interface. The latter conditions can only be achieved through substantial bulk supercoolings prior to solidification. In the absence of such supercoolings, the rate of external heat extraction limits achievable solid/liquid interfacial velocities to below that required for partitionless solidification [2,4].

Figure 2 shows the proposed solidification "path" of a droplet with no discernible segregation. First, the thermodynamic restriction on partitionless solidification is denoted by the $T_0^{L/\alpha}$ curve on the binary phase diagram. Partitionless solidification of a crystalline solid can only occur while interfacial temperatures are below this curve. On the other hand, kinetic considerations require interfacial velocities in excess of the diffusive velocity of the solute in the liquid. It has been shown that velocities in excess of several meters per second are achievable if the droplet supercools to a temperature T_N prior to nucleation. The supercooling required for the complete partitionless solidification of the powder particle in Figure 2 has previously been defined by the following equation (1):

$$\int_{T_N}^{T_C} C_p dT \geq \Delta H_M \quad (1)$$

where T_C is some temperature below $T_0^{L/\alpha}$ (2).

The solidification "path" is then that depicted by the arrows in Figure 2. After nucleation the evolving heat of fusion increases the interfacial temperature. The growth velocity, while decreasing with rising interfacial temperature, remains fast enough to avoid solute partitioning even at the end of solidification at T_C .

The mixed mode of solidification observed in Figure 1b was studied by establishing the composition profile across an Al-4.5% Cu powder particle. The results are shown in Figure 3. The points on the electron micrograph indicate locations where the microanalysis was performed. The data are plotted on the right-hand side of the figure as a function of distance from the interface delineating the plain-front solidified region from the cellular. The most important finding was the depletion of copper at this interface. This observation verifies earlier hypothesis of solute depletion between partitionless and cellularly solidified structures [1,2,4].

Figure 4 shows the phase diagram and the postulated solidification path of the powder particle with a mixed mode of solidification. The lower region of the powder underwent partitionless solidification while both interface temperature and average droplet temperature recalesced to T_C along the vertical "path" shown. The solute poor region of the particle shown on the right-side of this figure, which is documented in Figure 3, was due to solute partitioning as the interfacial velocity slowed down. The solid and liquid interfacial compositions are indicated by the dashed lines. Solute

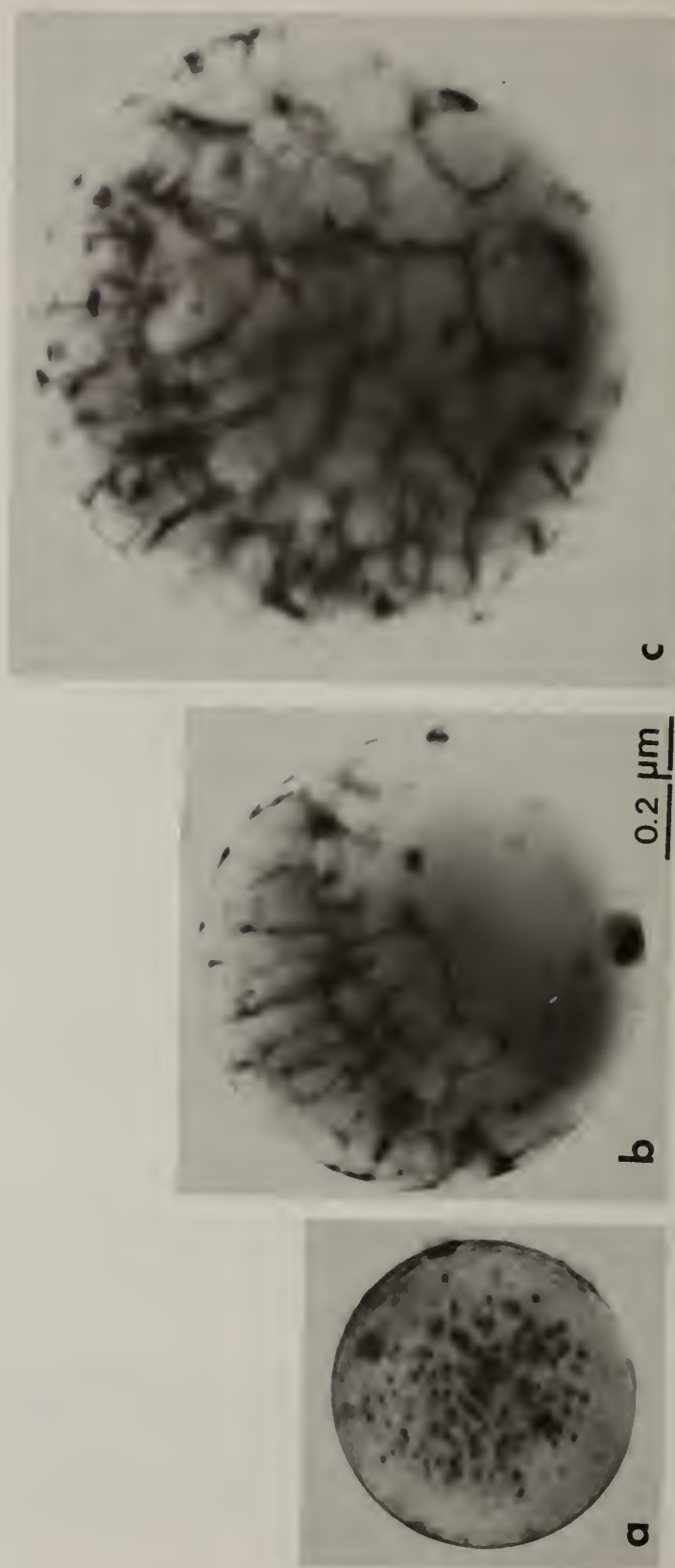


Figure 1 Typical microstructures observed in fine powder particles of Al-Cu alloys produced by EHD; (a) free structure, (b) mixed modes of solidification, and (c) cellular structure with lateral segregation.

$$\int_{T_N}^{T_C} C_p dT \geq \Delta H_M, \text{ HYPERCOOLED}$$

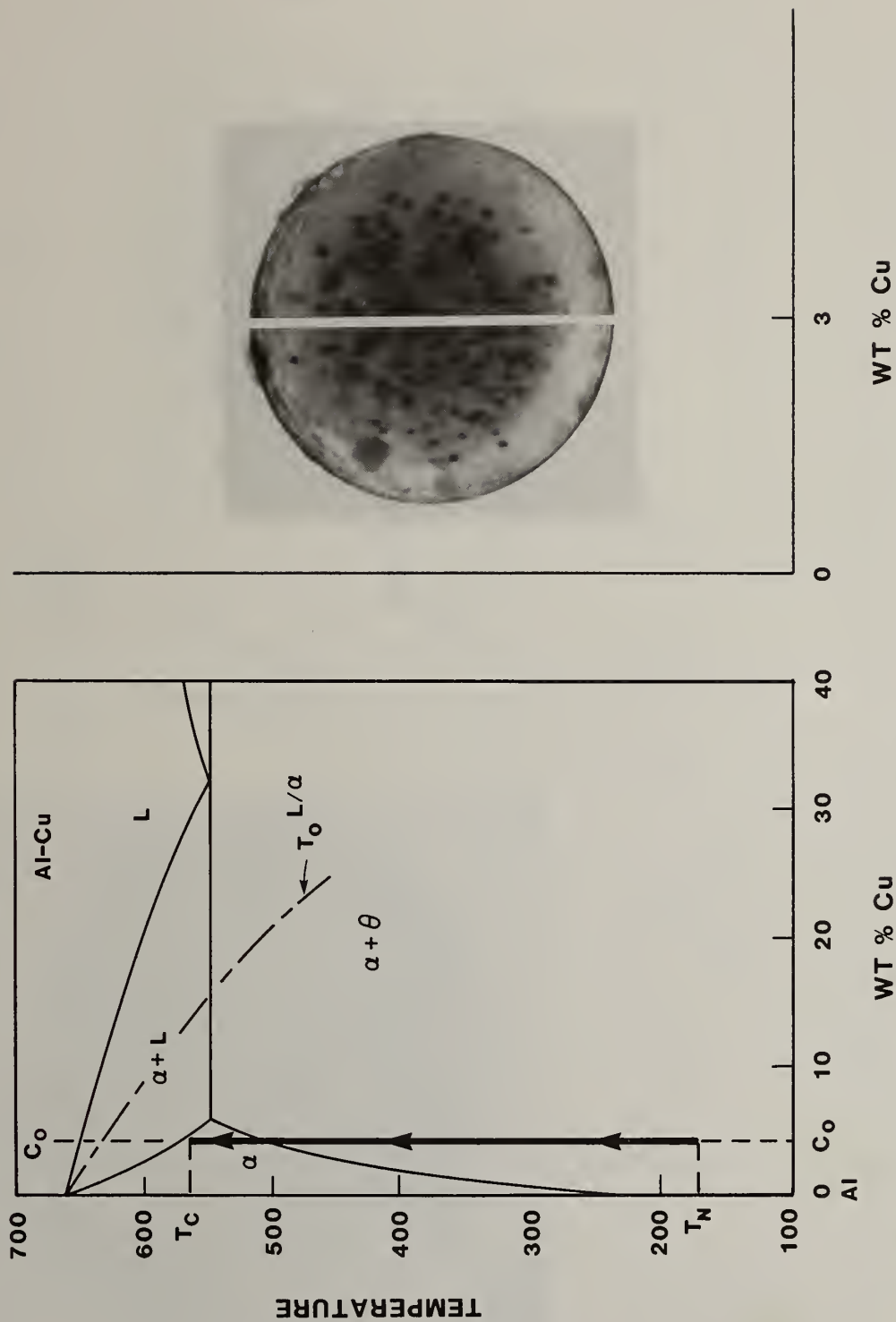


Figure 2. Schematic phase diagram of the Al-Cu system showing the solidification "path" of the rapidly solidified Al-3 wt.% Cu droplet illustrated on the right. Partitionless solidification occurred during recalescence from T_N to T_C .

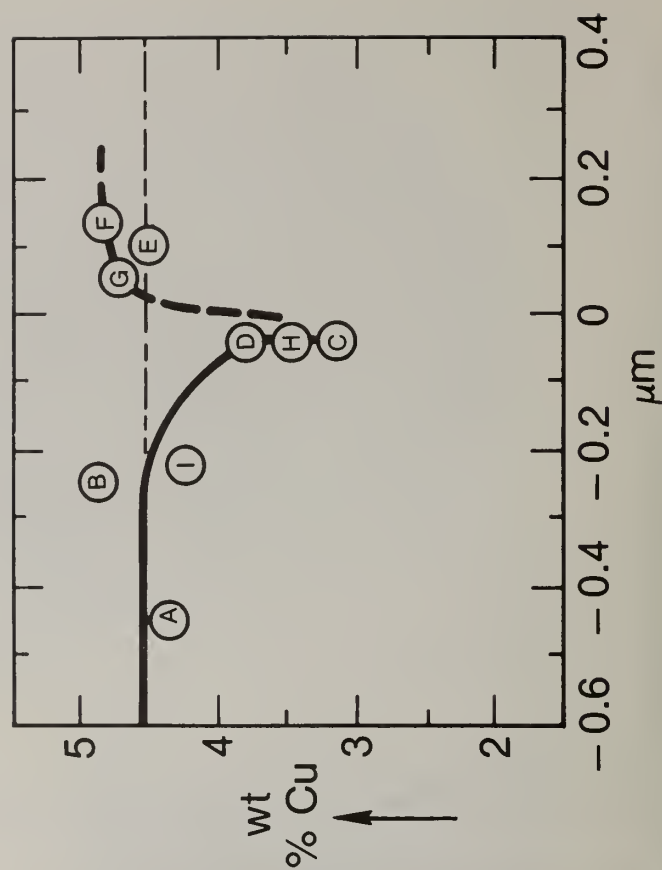
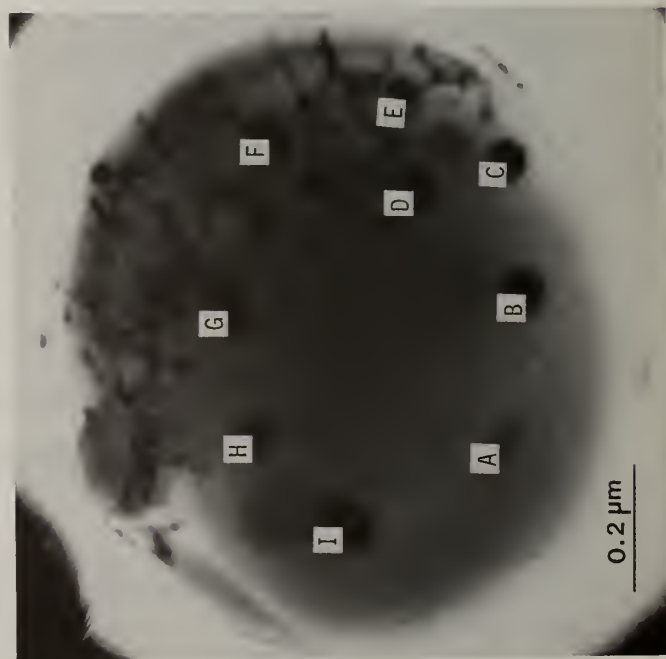


Figure 3 Copper concentration as a function of distance from the interface between the planar (partitionless) and cellular (segregated) regions in a particle containing an average of 4.5 wt.% Cu.

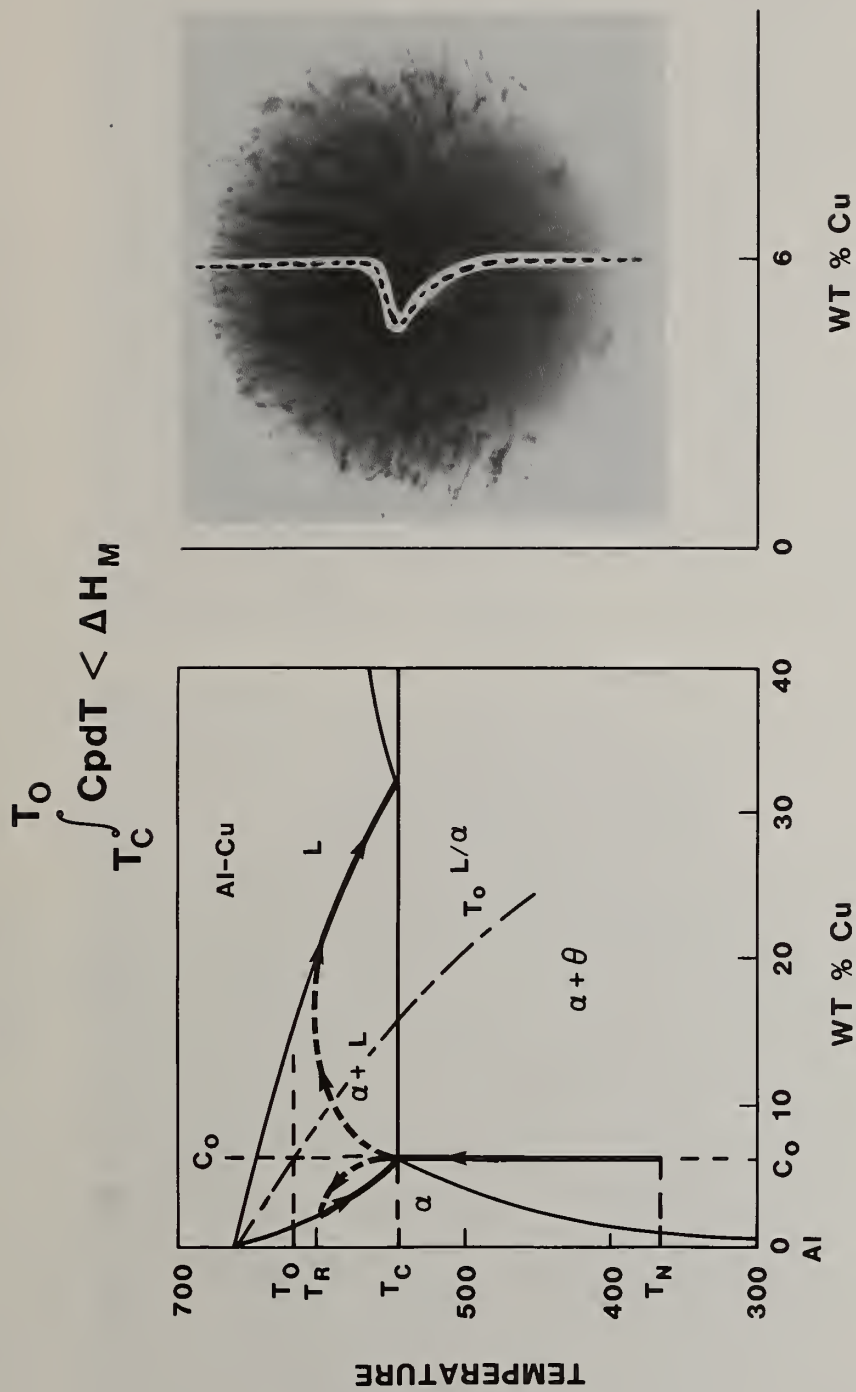


Figure 4 Schematic phase diagram of the Al-Cu system showing the solidification "path" of the Al-4.5 wt.% Cu alloy droplet illustrated on the right. Three sequential solidification modes are depicted in the electron-micrograph. The lower extremity is due to partitionless solidification with high interfacial velocities during recalcence from T_N to T_C ; this region was followed by partitioning at the interface while plane-front mode of solidification continued with solid and liquid composition moving along the dashed lines; the last region solidified in a cellular mode with lateral segregation due to onset of morphological instability.

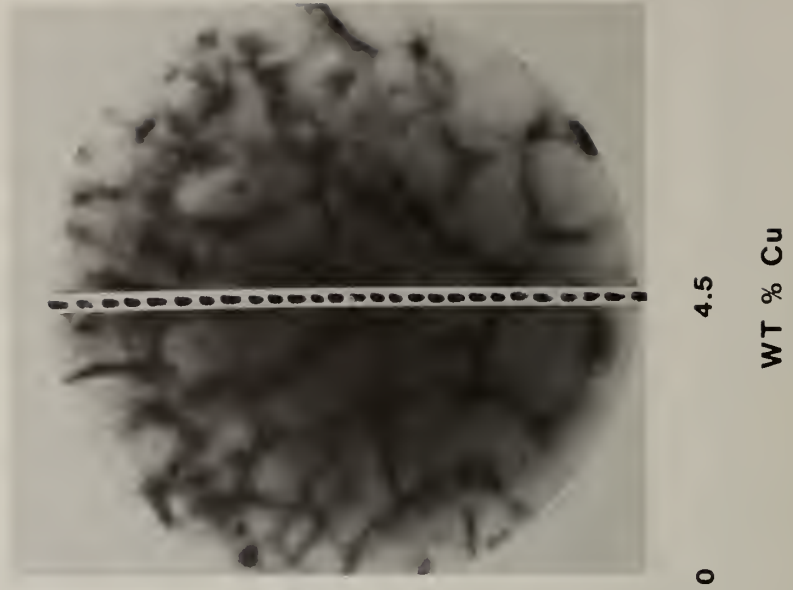
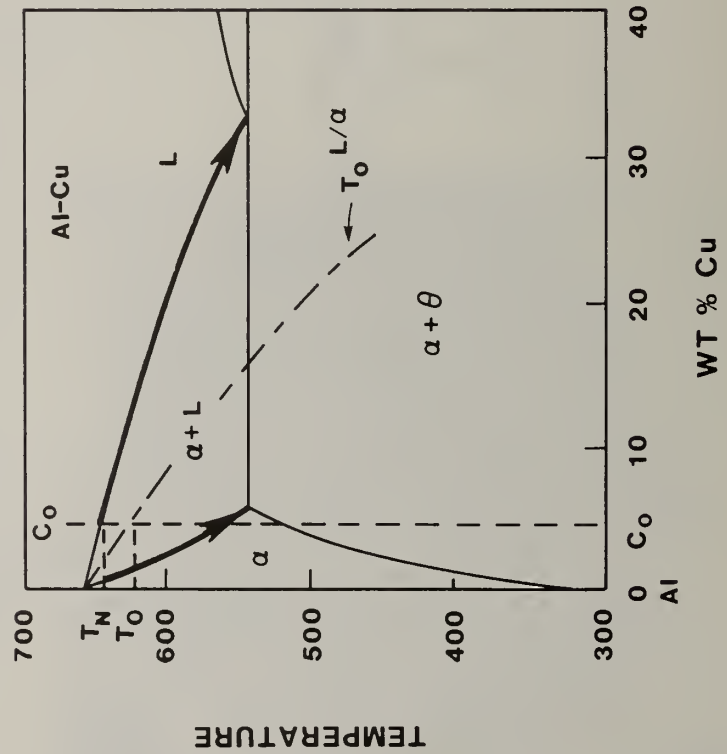


Figure 5 Schematic phase diagram of Al-Cu system and electron-transparent micrograph of a rapidly solidified Al-4.5 wt.% Cu submicron droplet. The particle solidified with no initial bulk supercooling.

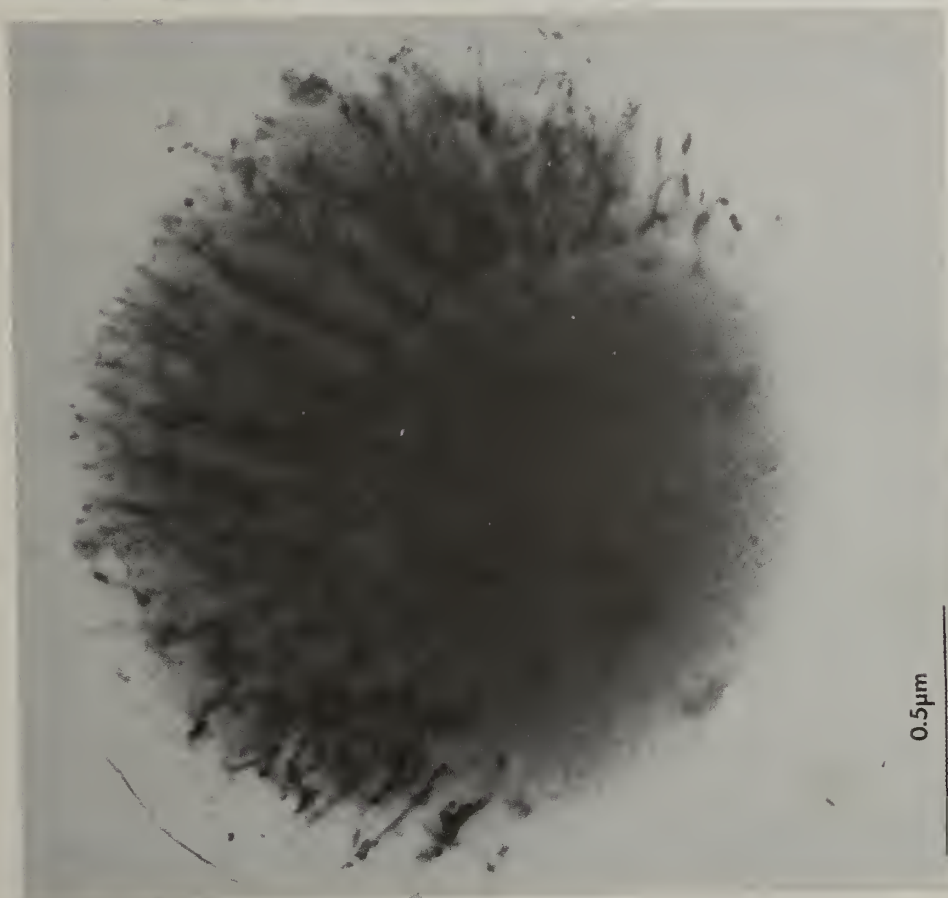
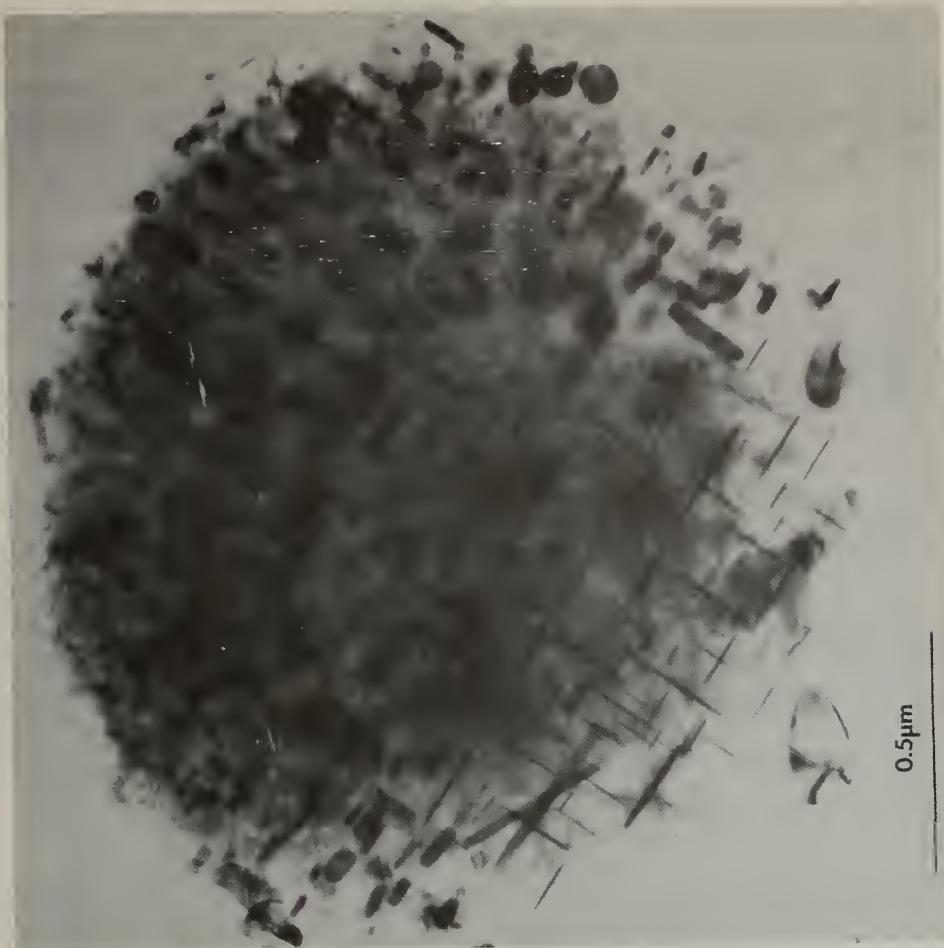


Figure 6 Electron micrographs of as-solidified and heat treated particles of Al-6 wt.% Cu.

rejected ahead of the interface resulted in morphological instability and in the cellular solidification noted in the upper portion of the powder particle.

Figure 5 shows a powder particle that solidified in a more-or-less conventional manner without any bulk supercooling. In this case solidification was initiated at or close to the liquidus temperature. Interfacial breakdown early in the growth process lead to cellular solidification with lateral segregation. The solidification "path" in this figure is that usually expected in slower conventional solidification processes with equilibrium at the solid/liquid interface.

Some of the powder particles were heat treated by the electron beam in the electron microscope, to study precipitation from the supersaturated solid solution. Results obtained are shown in Figure 6. The particle has 6 wt.% Cu and its microstructure contains cells in about 50 percent of its volume. When heat treated, two kinds of precipitates appear. The θ' precipitates which appear in the partitionlessly solidified volume are thin platelets which form on the $\{100\}$ planes. Their diameters vary between 50 nm and 400 nm. The other kind, probably θ precipitates, forms from the cell boundaries which are richer in Cu. These precipitates too, form on the $\{100\}$ planes. They are round, 25 nm thick, and about 75 nm in diameter.

Acknowledgment

This work was sponsored by the Defense Advanced Research Projects Agency.

References

1. C. G. Levi and R. Mehrabian, Met. Trans. 13A, 13 (1982).
2. M. Cohen and R. Mehrabian, in these proceedings.
3. J. Perel, J. F. Mahoney, S. Tayler, L. Shanfield, and G. Levi, in these proceedings.
4. R. Mehrabian, International Metals Reviews 27(4), 185 (1982).

AN EXPERIMENTAL TECHNIQUE FOR DETERMINING THE DEGREE OF
PARTICLE MELTING IN A PLASMA JET OPERATING AT LOW PRESSURE

R. W. Smith

General Electric Gas Turbine Division
Schenectady, NY 12345

M. Paliwal and D. Apelian

Drexel University
Philadelphia, PA 19104

ABSTRACT

Low pressure plasma deposition, a recent advance in plasma spray metallizing, is now being developed for high performance materials applications. A study of particle melting and solidification in the plasma jet, operating at low pressure, will allow one to identify the effect of the process variables and material properties on the resultant structures. In order to study and model the particle melting and solidification phenomena, experimental techniques must be developed to measure the progression of the particle melting that is occurring. In tandem, the experimental results are being utilized in the development of a model describing particle melting in Rapid Solidification by Plasma Deposition (RSPD).

Two methods of determining the degree of powder melting in a plasma jet have been evaluated. The first method intercepts the particle path in the jet with a glass slide and the other method samples the jet with a nozzle, quenching the powder before it impacts the walls of the collector. The splats on the glass slide are studied metallographically using optical and scanning electron microscopes. Changes in splat appearances are documented for the alloys Fe-20 wt% Mn, and Hastelloy Alloy X. The plasma sprayed powders trapped by the collector are evaluated for surface changes via SEM and depth of melting via TEM.

1. Introduction

The plasma spray process has been used as a method of producing rapidly solidified materials since 1963; reported structures are typical of RSR processing (i.e. amorphous phases, metastable phases, extended solid solubility...) [1-3]. However, due to the entrainment of oxygen and nitrogen in the deposits and the high process heat flux causing deposit recrystallization, the plasma process has not previously been used extensively to produce RSR structures for high performance applications. The recent development of low pressure plasma spraying [4] and its subsequent use in the deposition of superalloys [5] has brought the plasma spray process into the forefront in RSR processing and has been named Rapid Solidification by Plasma Deposition (RSPD).

The addition of a low pressure environment to the plasma spray process has introduced several advantages, making possible deposits of highly alloyed materials which can be used for high performance applications. Some of these advantages are: i) inert environment; ii) pre-heat/cleaning ability of plasma transferred arc; iii) process flexibility for spraying alloy particles having different melting ranges, and iv) deposition size/uniformity. Work is now underway to evaluate and optimize this plasma deposition process for producing high quality superalloy deposits which can be used as preformed RSR materials or near net shape structures. This is particularly beneficial in alloy systems which are difficult to cast and forge.

In order to successfully and repetitively produce deposits of good quality, the basic controlling mechanisms of the RSPD process must be understood. Variables which affect the deposit structure (presented by others in this conference [6-8]) include: i) plasma jet enthalpy and velocity (determined by gun design, power level, and arc gas); ii) powder characteristics; iii) powder injection and iv) substrate variables (distance, temperature, thermal properties and geometry). The objective of our study has been to isolate the processes of melting and solidification through experimental techniques and to study each process separately. The experimental results are used to identify the mechanisms of

melting and solidification during RSPD processing. These results are utilized in the development of models describing particle melting and solidification during RSPD.

The predominant requirement for the production of dense high-strength deposits via RSPD is that a large fraction of the particles be in a molten state when they impinge on and impact the substrate (or the previously deposited particles...). Isolating the melting and solidification phenomena in the plasma spray process has been and still is a difficult task. The degree of particle melting, the mode of powder particle melting, the final splat thickness, the particle cooling rate, and the quenched microstructures can be masked by the recrystallization caused by the extensive heat flux from the plasma jet. Recrystallization of the deposits, especially in simple alloys, can be quite extensive due to the low contamination in the low pressure plasma deposits. In addition to deposit recrystallization, the other confounding variables in the process are the non-uniform powder sizes, non-uniform heat flux to the particles, and non-uniform powder trajectories. Experimental techniques used to isolate the melting and solidification phenomena in the RSPD process are subsequently discussed.

2. Experimental Procedure

Two different plasma jets were utilized in this study: i) the Ma 3 plasma jet was an EPI Ar/He jet at 80 kw, Argon 140 liters/min, Helium 40 liters/min, and an EPI03CA-80 anode; ii) the Ma 2.4 plasma jet was an EPI Ar/He (125/30 liters/min) at 72 kw and an EPI03CA-109 anode. Both jets operated in a low pressure, 40 torr, argon atmosphere and incorporated internal anode powder injection.

Glass microscope slides were positioned at various distances from the plasma gun exit, low powder feed rates (<50 gram/min) were set, and the plasma gun was rapidly (>30 cm/sec) traversed over the slides. The slides intercepted varying numbers of powder particles, but all the deposits were less than a single particle thick without major overlaying of particles. The glass slides were then viewed via both optical and scanning electron microscopy (SEM). The powders studied were argon atomized Fe-20 wt% Mn (averages of 16 and 29 μ m; classified), Hastelloy Alloy X (-400, -325+400, -270+325 and -100+270 mesh), and René 80 (-400 mesh). Sampling distances ranged from 20-40 cm downstream from the nozzle exit.

Another technique to sample the powders from the plasma jets was a powder collector whose aperture could be positioned in the plasma jet. The collector was a 45 mm ID by 95 cm long stainless steel tube topped with a 90° stainless steel cone with a 3 mm aperture port drilled in the center, and a stainless steel collector cup at the bottom. This collector was inserted into the jet at 40 cm axial distance to collect powders over a 5 min deposition time. During this time powders deposited onto the cone surface and a small fraction entered the collector aperture and cooled during flight before impacting the collector bottom 95 cm downstream. Hastelloy X, René 80, Fe-20 wt% Mn and Fe-20 wt% Cu powders were sprayed and collected by the collector at 300 and 400 mm, using the two plasma jets.

Evaluation of these small samples required a modified Field and Fraser technique [9]. The powders were spread thinly onto a replica tape and vapor deposited with a thin silver layer. These collected powder samples as well as the "virgin" atomized powder were then evaluated for surface morphology via SEM. The tape was then sandwiched between two washers, plated with 0.1 mm of nickel, the replica tape dissolved off, mounted in a metallographic mount, and finally diamond polished and etched. This technique provides good edge retention and allows a good view of the cross sections. The metallographic evaluation was accomplished using both the SEM and transmission electron microscopy on carbon replicas. The carbon replica technique has some shortcomings caused by the etch "grooves" around the edge of the powder particles, but good resolution of powder particle interiors were obtained.

"Sweet-spot" (where the plasma gun is not traversed) deposits onto substrates were also made to study the microstructural features (unmelted particles, splat thickness, porosity, etc.) of actual built-up deposit. These deposits were made onto 15 cm x 15 cm plates positioned under the two different plasma jets, 30-40 cm downstream. Using spraying times of 1-2 minutes, 2-4 mm thick deposits were made on preheated substrates (800-900°C).

3. Results and Discussion

Glass Slide Experiments

The results of the glass slide experiments are used to study the morphological changes of individual particles which have interacted with the plasma jet and subsequently impacted the glass substrate. Particle morphologies for Hastelloy X powder plasma sprayed using the Ma 2.4 gun are shown in Figure 1. Figure 1a shows the splatting of a partially melted particle which was in a "slushy" state when it impacted. Examples of particle fracturing along the melted interdendritic region in a

partially melted particle, and the splatting of well melted particles can be seen in Figure 1b. A large number of spherical particles much smaller than the starting original powder can be seen in the micrographs. These smaller spherical particles result both from the spheroidization of the edges of the splats as well as in-situ atomization of the particles and their subsequent resolidification within the plasma jet. The in-situ atomization of the particles is more conclusively determined from the results of the powder collector which are discussed below. In addition, Figure 1b shows solidified streaks caused by the branching of molten splats on impact.

The glass slide experiments can also be used to qualitatively assess the degree of particle melting achieved using different gun to substrate distances, plasma gun conditions or the starting particle size. Optical micrographs comparing melting of two different powder sizes for Fe-20 wt% Mn plasma sprayed using the Ma 3 condition are shown in Figure 2a (average particle size 29 μm) and 2b (average particle size 16 μm). More uniform melting achieved using a finer size powder is evident when comparing the two micrographs. The white circular areas seen in the micrographs are the well splatted particles whereas the dark black areas represent the unmelted and partially melted particles.

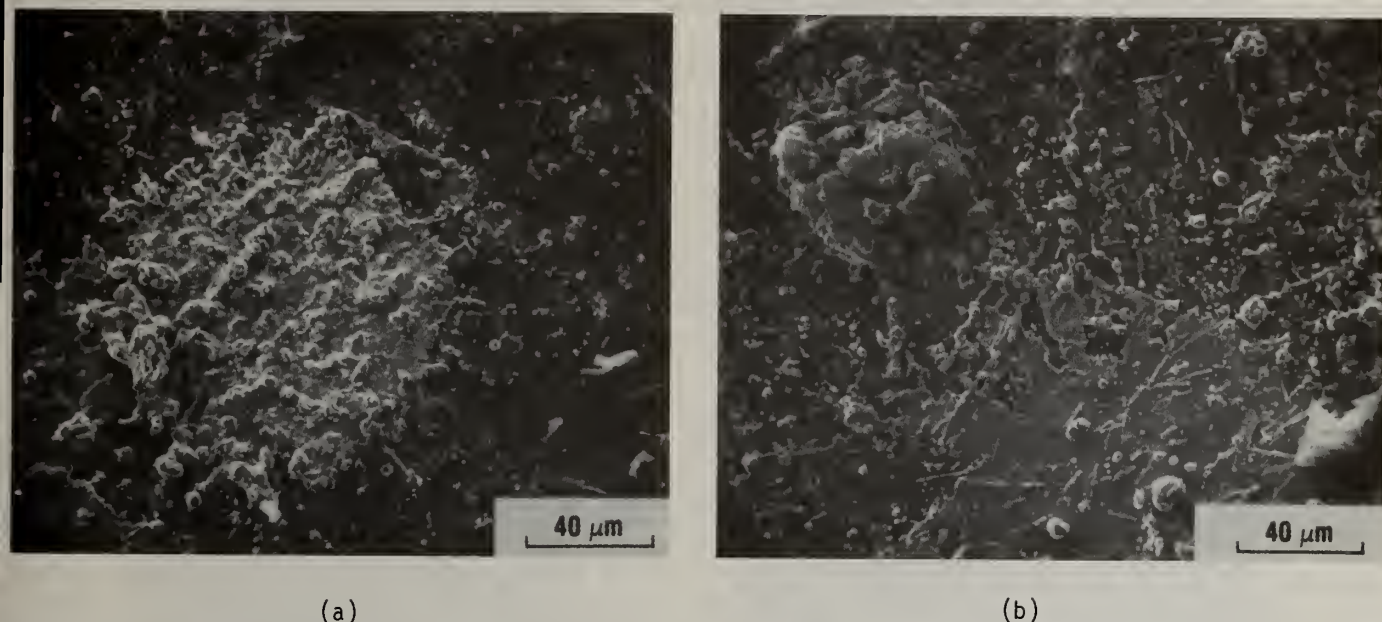


Figure 1: SEM photographs of Hastelloy X powders showing varying amount of melting and splatting upon impact on a glass slide substrate.

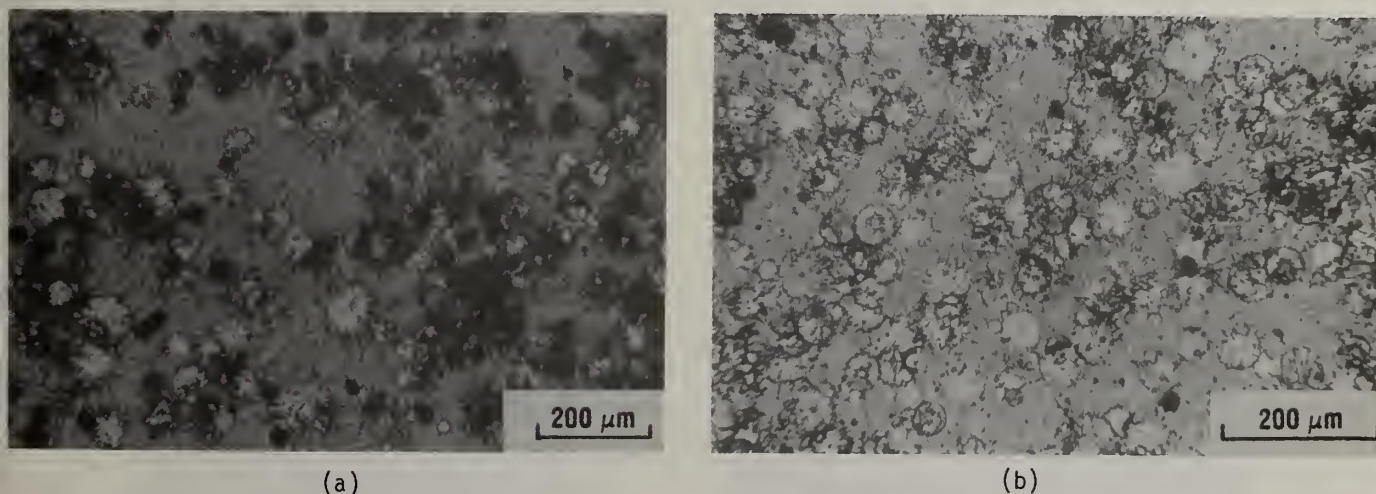


Figure 2: Optical photographs of Fe-20 wt% Mn powders plasma sprayed onto glass slides using the EPI Ma 3 gun. a) Average particle size 29 μm , b) Average particle size, 16 μm .

Figures 3a to 3f are SEM micrographs of "virgin" and plasma sprayed powders of Fe-20 wt% Cu, Fe-20 wt% Mn, Hastelloy X and René 80. Figure 3a is a SEM photomicrograph of the surface morphology of the virgin René 80 powders. It can be seen that the argon gas atomized powders are mostly spherical and quite regular in shape. A few particles which have been impacted or are splatted with another particle, during atomization, can be seen. Figures 3b and 3c show the general distribution of morphologies of the plasma sprayed René 80 and Hastelloy X powders, respectively. When compared to the virgin powders, Figure 3a, the plasma sprayed powders of both alloys show extensive amounts of fine powders, agglomerated fine particles, fractured powder particles, and various other shapes which have been formed in the plasma jet or during collection. Figure 3c shows an example of how a coarser screen fraction of powders has been "atomized" into a distribution of powder that has a large volume fraction of particles below 10 μ m. The probable origin of these fine particles could be i) interdendritic fracturing of powders and their subsequent spheroidization into smaller particles, ii) detachment of the liquid layer from surface melted particles, and iii) secondary atomization of molten droplets into smaller particles. Figures 3d through 3f are examples of the fracturing and spheroidization that has occurred in Hastelloy X, Fe-20 wt% Mn and Fe-20 wt% Cu powders sprayed with the higher enthalpy Ma 2.4 plasma jet. Figure 3e shows that the Fe-20 wt% Mn powder, having the narrowest melting range, was more irregular and less spheroidized than the wider melting range powder, Fe-20 wt% Cu, shown in Figure 3f. Comparison of surface morphologies of plasma sprayed and collected particles using this evaluation technique has also shown that the Ma 2.4, higher enthalpy plasma jet, results in better and more uniform melting of the injected powder particles than the Ma 3 jet.

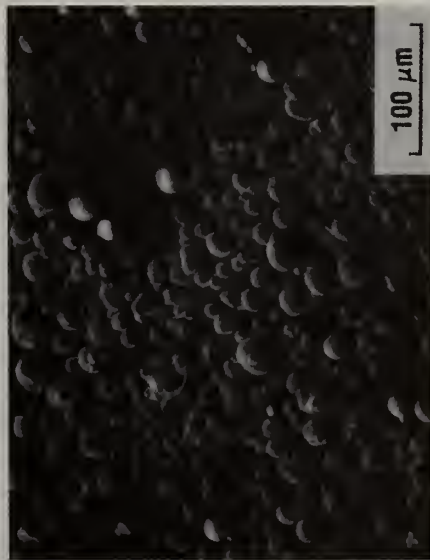
Figures 4a, 4b, and 4c show polished cross-sections of the virgin Fe-20 wt% Mn, René 80 and Hastelloy X, respectively. The SEM photomicrographs of the virgin powders show that Fe-20 wt% Mn and René 80 have solidified dendritically and the Hastelloy X powders solidified cellularly. Figures 5a and 5b are cross-sectioned microstructures of collected plasma sprayed René 80 and Figure 5c is a cross section of a Hastelloy X powder. Microstructural features of the collected powders further augment and confirm previously discussed observations such as the fracture of particles along melted interdendritic regions.

Figures 6a and 6b illustrate that the collector technique may be trapping a large fraction of completely melted particles; therefore not measuring the progress of the melting process. These figures are carbon replica TEM photomicrographs of an as atomized and a plasma sprayed powder particle, respectively. The details of the carbon replica evaluation technique show these particles to differ in dendrite arm spacing and interdendritic MC carbide size. The finer structure of the plasma sprayed powder particle indicates that it has cooled faster than the atomized powder. Moreover, the smaller dendrite arm spacing suggests that this irregularly shaped particle was at one time completely melted. Because the particle was completely melted, all information regarding the progression of melting has been lost. This shortcoming for studying melting of powders can be resolved by using shorter collection distances to catch the particles earlier in flight. Modifications are being made to the collector to include a high temperature ceramic nose cone.

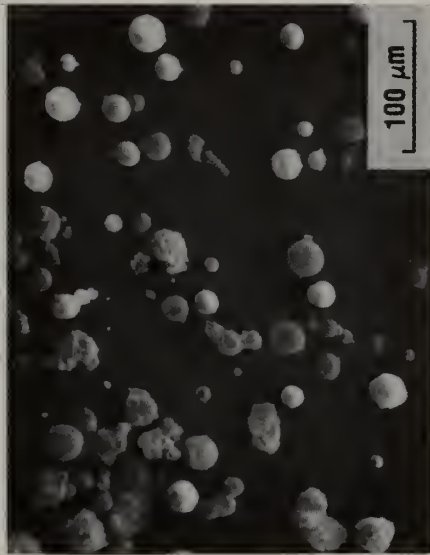
The Fe-20 wt% Cu and Fe-20 wt% Mn powder cross sections have not been shown here because their atomized and subsequent plasma sprayed dendritic structures showed no significant differences, suppressing any conclusions about the progress of melting. Because of this observation, it is believed these powders melted before collection and then cool at a rate similar to the rates of cooling in the atomization process. To be able to distinguish the microstructures of the plasma sprayed and collected powders from the microstructure of the as atomized powders, the starting powder will be pre-annealed to eliminate the initial segregation structure.

Deposits

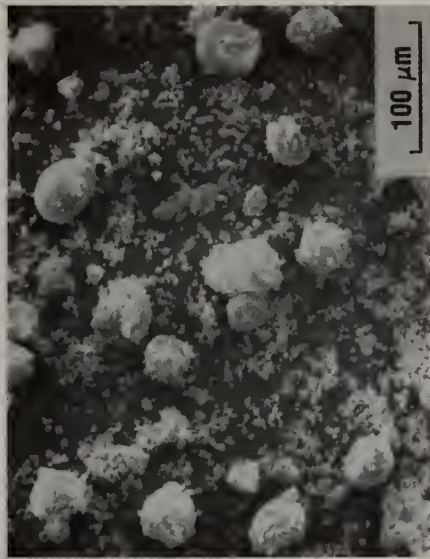
Microstructures of "sweet spot" deposits made using Fe-20 wt% Mn and René 80 powders are shown in Figure 7. The Fe-20 wt% Mn powder (average size 29 μ m) deposited using the Ma 3 gun are essentially unmelted but heated to a temperature sufficient to cause deformation of the particles upon impact (Figure 7a). In contrast, the same powder plasma sprayed using the higher enthalpy Ma 2.4 gun exhibits a structure where the particles are well melted and splat upon impact (Figure 7b). René 80 powder deposits, Figure 7c, consist of splats of melted particles, partially melted particles, and fragments of larger powder particles. In these deposits, particles impact on top of one another, bonding, inter-diffusing, and recrystallizing. These deposits supplement the structural knowledge obtained from the glass slide studies, particularly in terms of observing the individual particle morphologies and their interaction (overlayering) as the deposit builds up. The deposits can thus be used to measure the degree of particle melting and splatting as a function of radial position in the plasma jet.



(a)



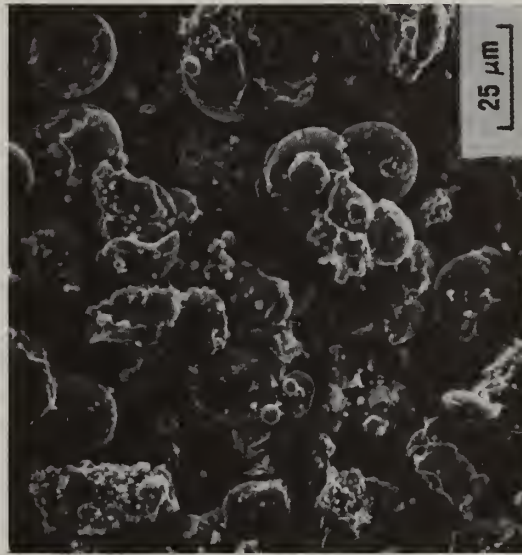
(b)



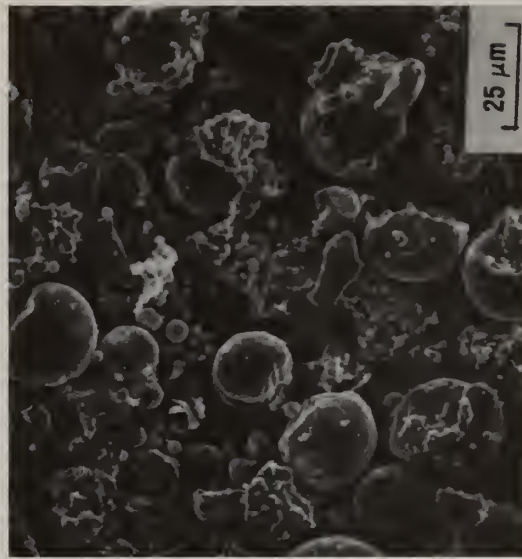
(c)



(d)



(e)



(f)

Figure 3: SEM micrographs of "virgin" and plasma sprayed powders. a) "Virgin" René 80 powder. Plasma sprayed powders; b) René 80, c) and d) Hastelloy X, e) Fe-20 wt% Mn and f) Fe-20 wt% Cu.



(a)



(b)



(c)

Figure 4: Microstructure of as received "Virgin" powders. a) Fe-20 wt% Mn, b) René 80 and c) Hastelloy X.



(a)

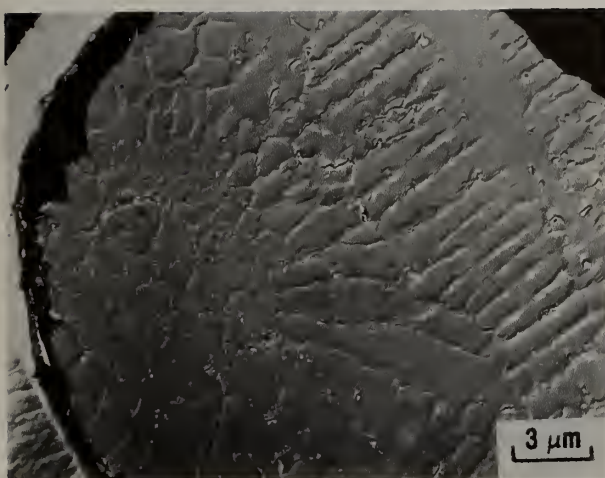


(b)

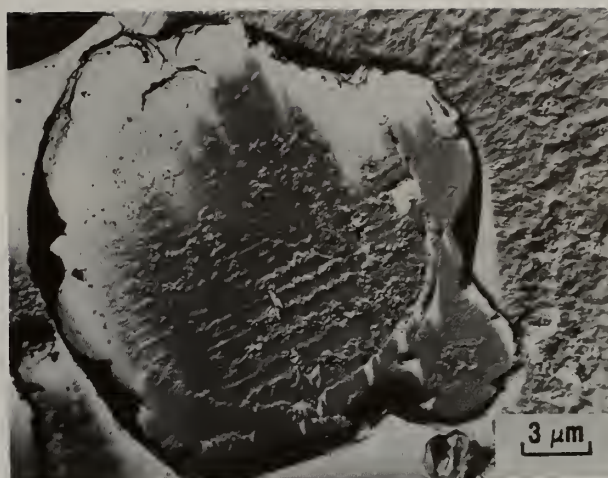


(c)

Figure 5: Microstructure of plasma sprayed powders. a) and b) René 80 powder, c) Hastelloy X powder.



(a)



(b)

Figure 6: Replica TEM photomicrographs of René 80 powder. a) As received and b) plasma sprayed.

Summary

It has been shown that both the glass slide and the powder collector experiments can successfully be used to study the effects of the plasma jet processing variables and those of material parameters (particle size and physical characteristics) on the extent of particle melting.

The results also indicate that the melting of powder particles in the plasma jet is not a classical homogeneous sphere melting problem. A large number of spherical particles smaller than the starting original virgin powder have been observed on the inserted glass slide substrates as well as from the particle collector. These smaller particles are generated from particles fracturing along melted interdendritic regions; melting and spheroidization of the fractured particles; and/or secondary atomization of the melted droplets within the plasma jet.

The powder collector experimental technique is a very useful tool for trapping droplets in flight and for examining the morphological changes experienced by the particles such as fracturing and spheroidization. However, monitoring the progress of powder melting (via the study of the microstructural features of the collected powders) is limited by the capability of differentiating between the resolidified features of the collected particles and the solidification structures of the original powder. In these cases, the injected particles should be treated to erase the features of the initial atomization process - i.e., inject pre-annealed or amorphous particles.

Acknowledgements

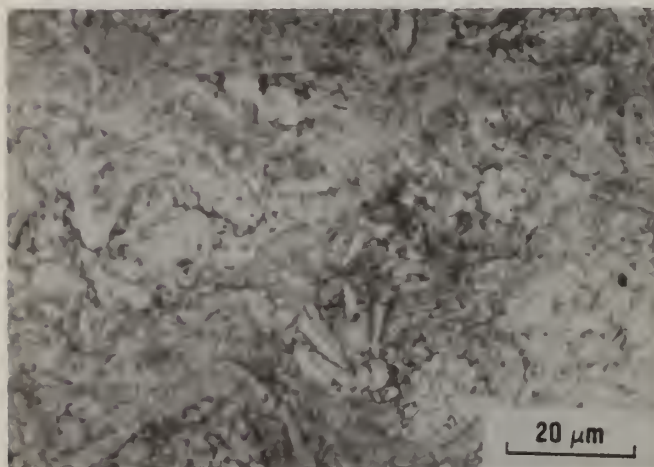
The research reported herein was sponsored by DARPA Contract F33615-81-C-5156 and the authors would like to thank Col. L. Jacobsen and Air Force Project Monitor Dr. H.C. Gegel for their support.



(a)



(b)



(c)

Figure 7: Microstructure of "sweet" deposits. a) Fe-20 wt% Mn plasma sprayed using EPI Ma 3 gun, b) Fe-20 wt% Mn plasma sprayed using EPI Ma 2.4 gun; c) René 80 powder plasma sprayed using EPI Ma 2.4 gun.

References

- [1] M. Moss: Acta. Met., 1968, Vol. 16, No. 3, pp. 321-326.
- [2] K.D. Krishnanand and R.W. Cahn: "Properties of Plasma Sprayed Aluminum-Copper Alloys" in Rapidly Quenched Metals, Eds. N.J. Grant and B.C. Giessen, pp. 67-75, MIT Press, MA, 1976.
- [3] R.W. Cahn: "Rapid Solidification by Plasma Spraying" in Rapid Solidification Processing: Principles and Technologies I, Eds. R. Mehrabian, B.H. Kear and M. Cohen, pp 129-139, Claitor's Publishing Division, Baton Rouge, LA, 1978.
- [4] E. Muehlberger: "A High Energy Plasma Coating Process" in Proceedings of the 7th International Thermal Spray Conference, pp. 245-256, Welding Institute, Abington, Cambridge, U.K., 1974.
- [5] M.R. Jackson et al.: J. of Metals, 1981, Vol. 33, No. 11, pp. 23-27.
- [6] R.W. Smith, D.V. Rigney and J.R. Rairden: "Plasma Deposition Effects on Structure and Properties of RSPD Superalloys", Third Conference on Rapid Solidification Processing, Gaithersburg, MD, Dec. 1982.
- [7] M.R. Jackson, R.W. Smashey and L.G. Peterson: "Structure and Properties of RSPD Materials", Third Conference on Rapid Solidification Processing, Gaithersburg, MD, Dec. 1982.
- [8] T.L. Cheeks et al.: "Temperature Effects on Plasma Deposition of Ni-Base Materials", Third Conference on Rapid Solidification Processing, Gaithersburg, MD, Dec. 1982.
- [9] R.D. Field and H.L. Fraser: Met. Trans., 1978, Vol. 9A, No. 1, pp. 131-134.

AN ATOMISTIC MODEL OF SOLUTE TRAPPING

Michael J. Aziz

Division of Applied Sciences
9 Oxford Street
Harvard University
Cambridge, MA 02138

ABSTRACT

An atomistic model for nonequilibrium solute segregation during rapid solidification is presented in terms of a single unknown parameter, the interfacial diffusivity D_i . The results for stepwise growth and for continuous growth at the same interface velocity differ quantitatively but exhibit the same qualitative features. A transition from equilibrium segregation to complete solute trapping occurs over approximately an order of magnitude in growth velocity, as the interface speed surpasses the maximum speed with which solute atoms can diffuse across the interface to remain ahead of the growing crystal. This diffusive speed is given by D_i/λ , where λ is the interatomic spacing, and is typically of the order 10 meters per second. A solute drag term and an intrinsic interfacial mobility term are included in an equation which predicts the growth velocity of a planar interface. Steady-state solutions are presented for the Ag-Cu system.

INTRODUCTION

Experiments have shown [1,2] that the chemical potential of the minor component of a binary alloy often increases during rapid solidification. This result rules out concepts of local equilibrium and independence of atomic species. In this paper, a simple model is described which predicts suppressed segregation as the solidification velocity becomes faster than the diffusive speed of solute across the interface.

Conventional modelling of interface kinetics uses the same atomic motions to describe crystallization as those to describe interdiffusion. In such a case, the growth speed u can never exceed the maximum diffusive speed D_i/λ , where D_i is the diffusion coefficient at the interface and λ is the interatomic distance. However, the collision-limited growth model developed by Turnbull and coworkers [3-10], which has recently been confirmed by Broughton et. al. [11] indicates that for metallic systems such a scaling is invalid and that u_s , the speed of sound, should be the only limit to the crystal growth rate. Consequently the growth speed can easily exceed the diffusive speed by a large factor, and when it does so in alloys we expect suppressed solute segregation and a diffusionless transformation.

The reason that crystal growth in metals should not scale with diffusion is illustrated in Fig. 1. A crystallization event consists of an atom shifting its position a small distance to move from a potential well in the liquid structure to a well on the crystal lattice. Since no bonds must be broken, the activation barrier for this reaction ought to be quite small; in the Turnbull collision-limited growth model this barrier is zero. A diffusive jump, on the other hand, is a different atomic process in this system. Position shifts of a fraction of an interatomic distance do not accomplish the solute-solvent redistribution which is necessary to avoid solute incorporation into the crystal. A solute atom must accomplish three things to avoid crystallization: It must escape from its potential well, as shown by the dashed arrow in Fig. 1, as the energy of the well increases and the well moves to the lattice site. It must push solvent atoms out of the way. And it must be replaced by a solvent atom on the lattice site, or else it will be pushed right back to where it came from.

Atoms in the interface region tend to interdiffuse in order to establish equilibrium compositions on either side of the interface. As the interface passes, solute-solvent redistribution only occurs during a limited time. Before the interface arrives, the driving force for redistribution is zero; afterwards, atomic mobilities are too low to permit significant interdiffusion. When $u \ll D_i/\lambda$, there is plenty of time for the atoms at the

interface to equilibrate. As the growth velocity becomes greater, solute and solvent atoms have less time while they are in the interface region to interdiffuse and maintain local equilibrium. When $u \gg D_i/\lambda$, the atoms have no time to interdiffuse; the interface passes and locks the liquid composition into the bulk of the solid before the atoms have a chance to react.

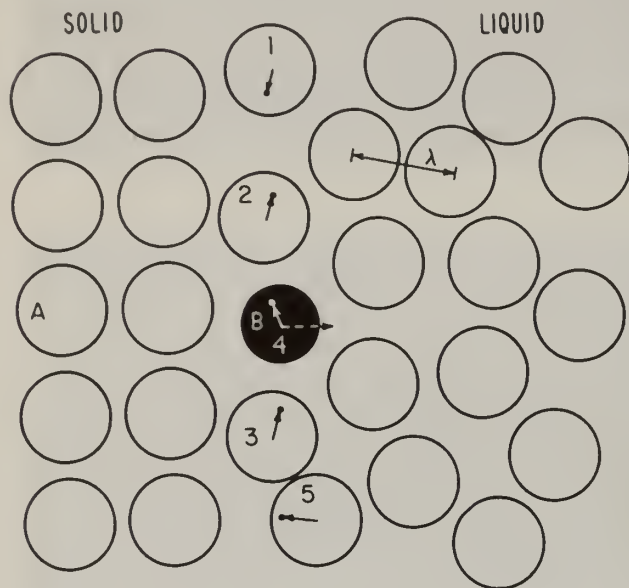


Fig. 1 Choreography of Solute Trapping. In order to avoid incorporation into the crystal (solid arrow), the "B" atom must:
1) ESCAPE from its potential well (dashed arrow) as the well gains energy and moves to the lattice site (solid arrow),
2) PUSH "A" atoms out of the way,
3) BE REPLACED with an "A" atom on the lattice site.

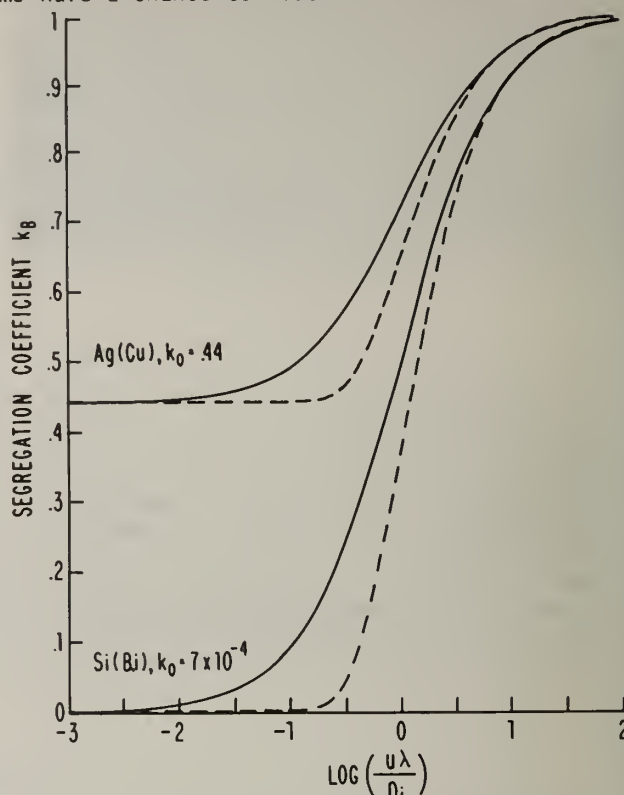


Fig. 2 Variation of segregation coefficient with dimensionless velocity, dilute solution limit. Dashed lines: stepwise growth model (equation 1). Solid lines: continuous growth model (equation 2). k_0 is k_e for a dilute solution; i.e. k_e at the melting point of pure solvent.

SOLUTE TRAPPING MODEL

The mathematical derivation and extensive discussion of the solute trapping model are published elsewhere [12]. A summary is given here of the assumptions that go into the modelling.

Stepwise Growth Model. If growth occurs by the rapid lateral passage of steps of height λ , then the average time between the passage of steps is $\tau = \lambda/u$, where u is the growth velocity. The time it takes solvent atoms to shift to their lattice positions is negligible when compared to τ , and the shifts can be treated as virtually instantaneous. The interface is thus assumed to be planar and executing instantaneous jumps of length λ separated by a time interval $\tau = \lambda/u$. The jump of the interface is assumed to incorporate one liquid monolayer, including all solute atoms, into the crystal lattice. Solute diffuses back into the liquid during the interval τ ; diffusive-style rate equations give the composition in the solid monolayer at the interface as a function of time. (The composition of the liquid at the interface is assumed to be constant and given by the solution to the diffusion equation in the bulk of the liquid.) Solute remaining in the solid monolayer at $t = \tau$ is permanently buried into the bulk of the solid, where diffusion is negligible, by the advance of the interface across the next monolayer. The result for a dilute solution of B in A is

$$k_B(u, T) = k_e(T) + [1 - k_e(T)] \exp(-D_i/u\lambda), \quad (1)$$

where T is the interface temperature, the equilibrium segregation coefficient $k_e(T)$ is the ratio of the solidus composition to the liquidus composition at the undercooled temperature T , and the interface diffusivity D_i is the only fitting parameter in the model. The result for the stepwise-growth model is plotted in Fig. 2, note that $k_B \rightarrow k_e$ when $u \ll D_i/\lambda$ and $k_B \rightarrow 1$ when $u \gg D_i/\lambda$.

Continuous Growth Model. If continuous solidification occurs, the impurity atom is being dragged toward its lattice site during a time period of order τ . The details are complex and unknown, but in the limit of strict steady-state fluxes on a microscopic scale, the problem simplifies. The fluxes and concentrations become time-independent and the same diffusive-style rate equations as before yield, for a dilute solution of B in A,

$$k_B(u, T) = [(u\lambda/D_i) + k_e(T)] / [(u\lambda/D_i) + 1] \quad (2)$$

This function is also plotted in Fig. 2.

GROWTH VELOCITY

Equations (1) and (2) for solute trapping require information, either theoretical or experimental, for the velocity-undercooling function. In many cases the assumption of no interfacial undercooling is a useful one, but the assumption becomes unrealistic at high velocities and solute concentrations. A dissipation-theory treatment of the interfacial undercooling problem for alloys is used below.

For pure systems, the process is easily understood. In equilibrium, the crystallization reaction and the backward (melting) reaction are equal in magnitude. When there is a finite driving force for crystallization, the former exceeds the latter by a Boltzmann factor $\exp(\Delta\mu/RT)$; the growth velocity is given by their difference. The kinetics are lumped into an intrinsic growth-velocity-limit, $u_o(T)$, which is the speed with which the interface would propagate at infinite driving force (i.e. when the back reaction disappears). The growth velocity is then written: $u = u_o(T)[1 - \exp(\Delta\mu/RT)]$. This becomes the familiar $u = M \Delta G$ at small driving forces. Inverting the above expression, we have $\Delta\mu = RT \ln(1 - u/u_o)$. The left-hand side is the driving free energy; the right-hand side can be thought of as the free energy dissipated by the irreversible crystallization reaction at the interface. Thus the velocity-driving force relation can be written $\Delta G_{DF} = \Delta G_F$, where ΔG_{DF} is the driving energy, expressed as free energy per mole, and ΔG_F , the "interface friction energy" due to a finite interfacial mobility, is the free energy dissipated per mole of material solidified. We say that the available driving force is dissipated by the irreversible processes at the interface.

For alloys, we can write
$$\Delta G_{DF} = \Sigma \Delta G_{DISS}, \quad (3)$$

where the ΔG_{DISS} are the losses due to all of the dissipative processes going on simultaneously. In the steady state, this must hold: the driving free energy does no work on the surroundings and so it must be entirely dissipated by irreversible processes during the transformation. If we can calculate the dissipation and the driving force as functions of velocity, we have an equation which predicts the growth velocity. Ignoring heat conduction, the two dissipative processes at the interface are the aforementioned crystallization and redistribution reactions. The dissipative terms associated with them are, respectively, the "interface friction energy" ΔG_F and the "solute drag" ΔG_D [13,14]. By assuming interface friction to be the same for alloys as for pure systems, we can calculate these terms [15]. The results are $\Delta G_F = RT \ln(1 - u/u_o)$ and, for the dilute solution continuous growth model (eq'n 2), $\Delta G_D = X_S RT [(1 - k_B)/k_B] \ln[k_B/k_e(T)]$. The driving force is given by [14] $\Delta G_{DF} = X_S \Delta\mu_B + (1 - X_S) \Delta\mu_A$; the growth velocity equation becomes

$$\Delta G_{DF}(u) = \Delta G_F(u) + \Delta G_D(u) \quad (4)$$

It turns out that one of the dissipative terms is usually negligible compared to the other; the transition occurs over a very small velocity range. Consequently the equation can be simplified away from the transition. For e-beam melting experiments on Ag(Cu), with interface velocities in the centimeter-per-second to meter-per-second range, ΔG_D dominates most of the time; for laser annealing of doped Si with meter-per-second velocities, ΔG_F almost always dominates. During a diffusionless transformation in any system, ΔG_D vanishes.

The dilute solution approximation is invalid when the mole fraction of solute is no longer negligible or when activity coefficients are no longer constants. When the appropriate corrections to the fluxes and driving forces in the continuous growth model are made [15], the results are

$$k_B = [(u\lambda/D_i) + X_o] / [(u\lambda/D_i) + 1 - (1 - X_o)X_{li}], \quad (5)$$

$$\Delta G_D = X_S [(1 - k_B)/k_B] RT \ln[k_B/k_A X_o], \quad (6)$$

where $X_o(X_S, X_{li}, T) = \exp[-\Delta(\mu_B' - \mu_A')/RT]$, $\mu'(X, T) = \mu(X, T) - RT \ln X = \mu^o(T) + RT \ln \gamma(X, T)$, X_{li} is the mole fraction in the liquid at the interface, $k_A = X_S^A/X_{li}^A$, A = solute, B = solvent, and $\Delta =$ "solid minus liquid". The implicit assumption has been made that at the interface the transition state behaves in an ideal manner. In practice, temperature and composition dependence may show up in D_i .

RESULTS

Equations 4, 5, and 6 were solved numerically; some of the results follow. For the Ag-Cu system, the thermodynamic model of J. Murray [16] was used to obtain the chemical potential of Ag and of Cu across the phase diagram. The following parameters were used: $\lambda = 2\text{\AA}$, $u_0 = 340000\text{ cm/s}$, $D_i = .00122 \exp[-(10\text{ kcal/mole})/RT]\text{ cm}^2/\text{s}$. The results are plotted as interface temperature and compositions on the phase diagram in Fig. 3; we see that for a given composition X_{li} in the liquid at the interface, the solid composition increases and the interface temperature drops as the velocity is increased. In a steady-state e-beam melting experiment [17], the solid composition is constrained to be equal to the bulk liquid composition. The velocity is independently controlled; the dependent variables are X_{li} and T . The way they behave is shown in Fig. 4. As the velocity is increased, the liquid composition at the interface decreases due to solute trapping, and the interface temperature actually rises, trying to follow the liquidus. When the T_0 line is reached, a diffusionless transformation becomes thermodynamically possible. However, diffusionless solidification does not commence until some distance beyond the T_0 line, when the velocity is great enough to suppress the redistribution reaction. Fig. 5 illustrates that in the model for the Ag(Cu) system, two effects facilitate trapping at high concentrations. The interface diffusivity drops by a factor of two as we go from the melting point of silver to the eutectic temperature, thus making the redistributive reaction more difficult while not sensibly affecting the growth mobility. In addition, the driving force for redistribution is smaller at high concentrations.

Acknowledgements. The author is indebted to E. Nygren and K.F. Kelton for assistance with the computer calculations; to J.A. Murray for the thermodynamic modelling of the Ag-Cu and Si-Bi systems; to J.W. Cahn, S.R. Coriell, W.J. Boettinger, and F. Spaepen for much helpful discussion; and to D. Turnbull for guidance. This work was supported in part by an Allied Corp. Fellowship Grant and by National Science Foundation Grant DMR-79-23597.

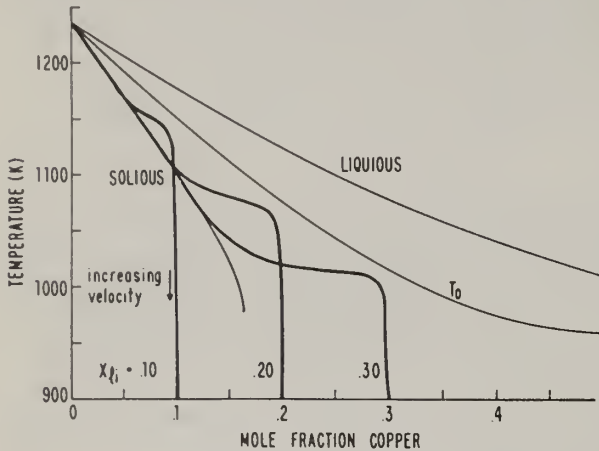


Fig. 3 Interface temperature and solid composition for fixed X_{li} in Ag(Cu). For a given liquid composition X_{li} at the interface, the solid composition increases and the interface temperature drops as the velocity is increased.

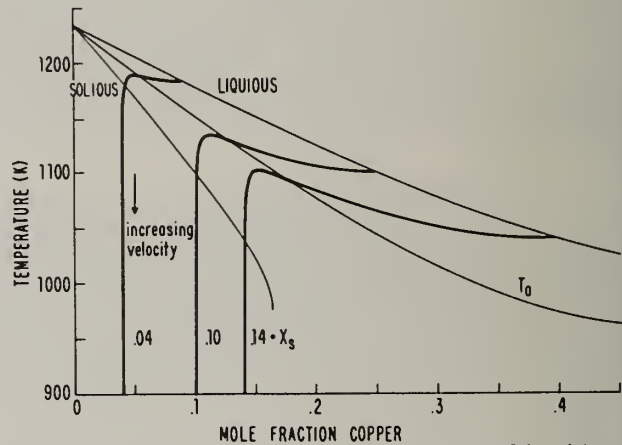
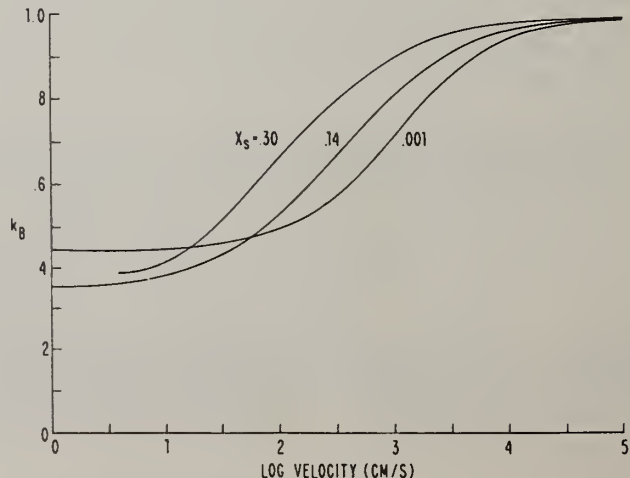


Fig. 4 Interface temperature and liquid composition at interface for fixed X_s . When the T_0 line is crossed the diffusionless transformation becomes thermodynamically possible, but it does not occur until some distance beyond.

Fig. 5 Segregation Coefficient vs. Velocity for Dilute and Concentrated Alloys of Cu in Ag. In this system, two effects facilitate trapping at higher concentrations. The interface diffusivity drops and the driving force for redistribution drops.



REFERENCES

- [1] J.C. Baker and J.W. Cahn, in Solidification (ASM, Metals Park, Ohio, 1970).
- [2] C.W. White, S.R. Wilson, B.R. Appleton, and F.W. Young Jr., J. Appl. Phys. 51, 738 (1980).
- [3] D. Turnbull, Contemp. Phys. 10, 473 (1969).
- [4] D. Turnbull, in Solidification (ASM, Metals Park, Ohio, 1970).
- [5] D. Turnbull, J. de Physique-Colloque C-4, p. 1 (1974).
- [6] D. Turnbull and B. G. Bagley, in Treatise on Solid State Chemistry, ed. N. B. Hannay (Plenum, New York, 1975), vol. 5.
- [7] F. Spaepen and D. Turnbull, in Rapidly Quenched Metals, 2nd International Conf., ed. N.J. Grant and B.C. Giessen (MIT Press, Cambridge, Mass. 1976).
- [8] P. Chaudhari and D. Turnbull, Science 199, 11 (1978).
- [9] F. Spaepen and D. Turnbull, in Laser and Electron Beam Processing of Semiconductor Structures, ed. J. M. Poate and J. W. Mayer (Academic, New York 1981).
- [10] D. Turnbull Met. Trans. 12A, 693 (1981).
- [11] J.Q. Broughton, G.H. Gilmer, and K.A. Jackson, Phys. Rev. Lett. 49, 1496 (1982).
- [12] M.J. Aziz, J. Appl. Phys. 53, 1158 (1982).
- [13] J.W. Cahn, Acta Metall. 10, 789 (1962).
- [14] M. Hillert and B. Sundman, Acta Metall. 25, 11 (1977).
- [15] M.J. Aziz, to be published.
- [16] J.A. Murray, to be published.
- [17] W.J. Boettinger, these proceedings.

TEMPERATURE EFFECTS ON PLASMA DEPOSITION OF Ni-BASE MATERIALS

T.L. Cheeks
Cornell University
Ithaca, New York 14853

M.E. Glicksman
Rensselaer Polytechnic Institute
Troy, New York 12180

M.R. Jackson and E.L. Hall
General Electric Corporate Research and Development
Schenectady, New York 12301

ABSTRACT

Temperature of deposition has been varied from ~500C to the melting range for Ni, NiAl, NiCr and a superalloy, IN-100, in structures produced by rapid solidification plasma deposition. This was accomplished by controlling the spacing between the plasma gun and the substrate on which deposition occurred. Considerable difference in microstructural response was noted for the different alloys. Much of this difference is attributable to grain growth occurring in situ, due to continued heating by the plasma beam for the less heavily alloyed compositions. During deposition at a given distance, a continuous change in temperature measured in the substrate was observed, due to the evolution of the latent heat of solidification of particles impacting the substrate. The rate of change in temperature is a function of the arrival rate of molten particles and the distance the substrate is from the plasma gun.

Introduction

Plasma spraying has been used to produce coatings on substrates to improve resistance to wear or aggressive environments (1,2). The process involves melting individual powder particles, propelling the molten droplets toward the substrate, and solidifying the droplets at the surface. Because of spreading of the droplet at the surface, very great heat extraction rates are attained, and rapid solidification occurs (3,4). When deposition is performed in a low-pressure environment, coating microstructure is significantly improved in density and cleanliness compared to deposition performed in air or under a protective gas shroud (5-7). Low-pressure deposition of structural alloys, rather than coating compositions, to produce free-standing bodies has been termed rapid solidification plasma deposition (RSPD) (8,9). The microstructure of such deposits are typically fine-grained as-sprayed, chemically homogeneous, and consolidated to nearly full density. One of the major features of this rapid solidification technique is the ability to produce structurally sound components without the need of a separate consolidation step (10).

Although the RSPD process is a single step operation, conceptually it can be considered as a series of unit operations. These operations include injection of powder into the plasma arc or jet, transfer of heat and momentum from the gases to melt and transport the particles, and impact and solidification of the droplet against the substrates (11).

The present study treats the last of these unit operations, addressing the interrelationship of substrate surface temperature and RSPD microstructure in Ni-based alloy deposits. Since structures and properties of heat treated deposits may depend on the as-deposited microstructure, it is important to determine if the initial structure can be controlled, and if it can, by what procedure. Substrate temperature might be expected to affect microstructure by influencing the rate of heat extraction and the degree of droplet spreading before solidification begins. The fine scale at which these microstructural changes may occur requires observation by transmission electron microscopy.

Experimental Procedure

Temperature measurements on substrate surfaces during exposure to the plasma were obtained using .050 cm diameter Pt-Rh thermocouple wires that were threaded through previously drilled holes to the front and back surfaces of either Cu substrates of varying thickness or 10 x 10 x 1.25 cm stainless steel substrates.

The thermocouples were spot welded to the front surface and insulated with a both-ends-open ceramic sleeve which was locked into the hole by upsetting the steel surface by hammer peening. The substrates and thermocouples were attached to a fixture which provided stability for the substrate in the plasma stream and also served as a means of connecting substrate thermocouples to other connections leading to the outside of the 150 cm diameter low-pressure chamber. Measurements were recorded using computer-aided devices.

Atomized powders of Ni-7.5 wt% Al, Ni-13.5 wt% Cr and a Ni-based superalloy (Ni-15 wt% Co, 10 wt% Cr, 3 wt% Mo, 5.5 wt% Al, 4.5 wt% Ti, .04 wt% Zr, .015 wt% B, .05 wt% C), as well as pure Cu, were prescreened to -400 mesh (37 μ m or smaller) before spraying. Powder was weighed before filling the powder feeder and unsprayed powder remaining was weighed after spraying in order to determine feed rates and powder usage. A measure of the substrate weight before and after spraying then allowed a determination of deposition yield.

Data from the temperature measurements were taken for gun-to-substrate distances (g-t-s-d) of 20, 25, 30, 37.5 and 45 cm. The measurements began after the process parameters such as voltage, amperage, pressure and gas flow rate were stabilized with the plasma plume off the substrate. Deposition conditions used in all experiments were 52V, 1300A, Ar-He plasma in an EPI, Inc. plasma gun, using a 20° powder-injection angle. Initially the chamber was pumped to 0.5 torr, the arc was ignited, and the vacuum pump was throttled to maintain a pressure of 60 torr due to the plasma gases. With the plasma plume centered on the substrate, temperature measurements were recorded once a second and continued until the surface temperature rise decreased to 1 K/sec. This temperature was denoted "temperature before deposition of powder." Once this increase was achieved, powder injection into the plasma gases began and continued for 55 seconds for most experiments. This corresponded to a powder mass flow of approximately 12 kg/h. The temperature achieved the instant deposition ceased was denoted "temperature after deposition of powder." A temperature vs. time plot was generated using computer-aided graphics to compare the different results.

After deposition the substrates were sliced into sections which encompassed the "sweet-spot," an area of the substrate upon which the deposits were the most homogeneous and uniform, and which varied in diameter from 2 to 5 cm, as g-t-s-d was varied. The sections were subjected to both optical and transmission electron microscopy (TEM), as well as density measurements.

Optical samples were cut, polished and etched using Marble's Reagent. TEM samples were cut and ground to .0075-.0125 cm thickness and mechanically punched into 3 cm diameter disks. The disks were electrochemically polished using a solution of perchloric acid and methanol.

Results and Discussion

Temperature

Typical time-temperature curves are shown in Figure 1 for deposition of Cu on Cu substrates. The curves show a form characteristic of all depositions made, whether Cu or Ni alloys deposited on Cu or stainless steel substrates. As the plasma initially heated the substrate, a rate of temperature rise at the exposed surface of ~ 10 K/sec was observed. Eventually the substrate was hot enough that radiative losses to the nearly-black body chamber walls became significant. The rate of temperature rise then fell rapidly. For the purposes of this experiment, an effective steady state, heating from the plasma nearly equal to radiative loss, was defined when the rate of temperature rise fell to 1 K/sec. At that point, powder was injected into the plasma gases for melting and transport to the substrate. Again, a rapid rise at the substrate surface was

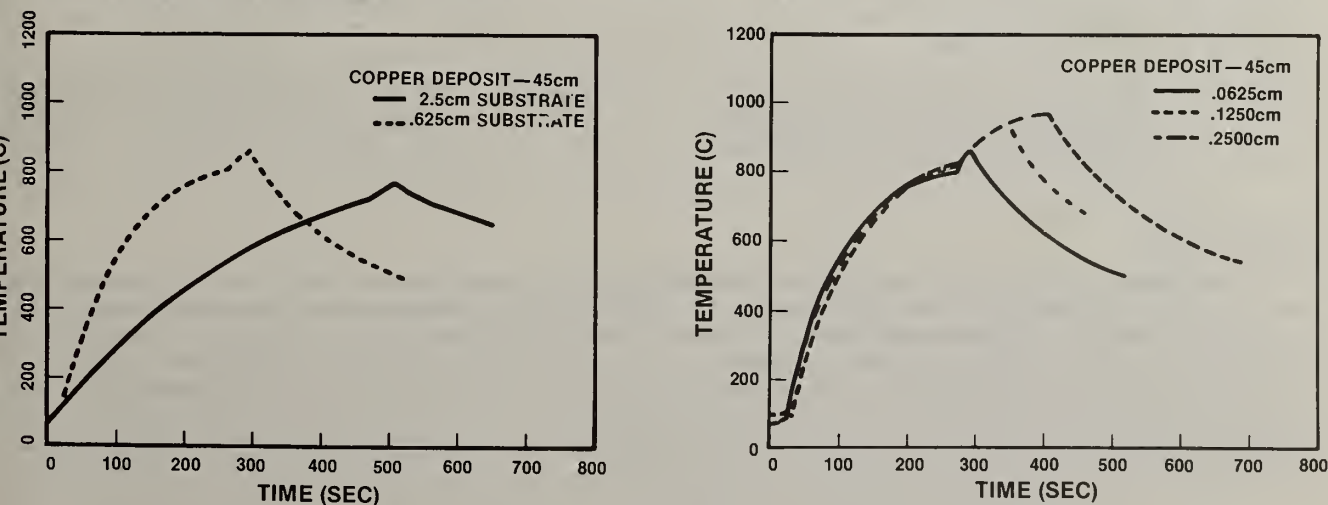


Figure 1. Temperature change with time for Cu deposited on Cu for variation in a) substrate thickness or b) deposit thickness.

observed. Heat transfer now included not only the plasma gas contribution, but also contributions from heated solid (unmelted) particles and from the latent heat evolved by solidification of melted particles. The rate of temperature rise measured at the substrate surface again fell as the exposed (deposit) surface grew away from the substrate surface and the total mass being heated increased. At the termination of deposition, the plasma was extinguished and the substrate-deposit composite cooled due to continued radiative loss.

As seen in Figure 1a, substrate steady-state temperature varies with substrate thickness, although the larger effect is on time to reach steady state. Substrate temperature is also dependent on the total amount of deposition. For very thick deposits, thicker than shown in Figure 1b, the substrate may show a decrease in temperature during deposition, as the system reaches a new equilibrium between heat input and output and the exposed surface moves away from the substrate surface.

The effect of gun-to-substrate distance (g-t-s-d) is shown in Figure 2. Steady-state temperature is a stronger function of g-t-s-d than is the temperature achieved during deposition. It can be assumed that the heat input from latent heat is essentially constant over the range of g-t-s-d. The fraction of that heat lost by radiation will decrease with increasing g-t-s-d because of the lower T^4 losses from less plasma gas heating. As g-t-s-d is increased, not only steady-state temperature decreased, but the time to reach steady state is increased significantly (Figure 3).

The steady state temperatures are actual surface measurements, while the substrate temperatures during deposition are being measured further and further from the deposit surface, as noted earlier. For Cu substrates, front-to-back substrate surface gradients are ~ 10 C/cm, while for Ni and stainless steel substrates, gradients of as much as 75 C/cm were observed. At any g-t-s-d, Cu substrates were hotter, but the differences were < 50 C. Heat capacities are nearly equivalent for these substrate materials, but Cu has about five times the thermal conductivity of stainless steel and Ni. Even for the largest gradient observed in the substrates, the difference between substrate surface temperature and deposit surface temperature is likely to be small. The deposits of this study were typically ~ 0.5 cm thick, so that the deposit surface is expected to be within 40 C of the measured substrate temperature.

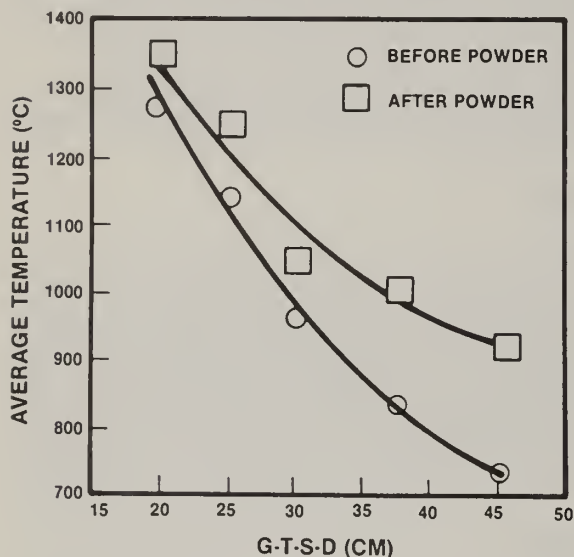


Figure 2. The effect of gun-to-substrate distance on maximum temperature achieved before and after deposition.

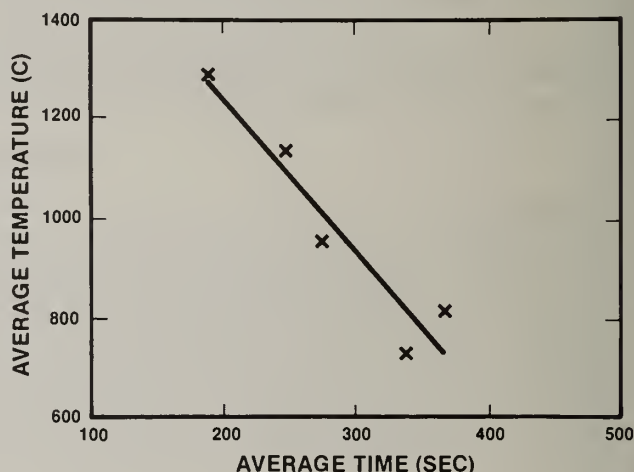


Figure 3. Time to reach maximum temperature before deposition for various g-t-s-d.

Microstructure

The deposits consist of a composite containing small fractions of unmelted particles interspersed in a melted and rapidly solidified matrix. Microstructure of the rapidly solidified regions is shown in Figure 4 for both longitudinal and transverse sections. The thin foil in the longitudinal section is parallel to the plane of the substrate surface, while the transverse section is perpendicular. Thus, the spherical liquid droplets spread on impact (12) and solidify rapidly. Grains are equiaxed columnar in nature. For the powders used, the largest liquid droplets should be $37 \mu\text{m}$ in diameter. The maximum measured splat thicknesses of $1-3 \mu\text{m}$ indicate a spreading to the order of $100 \mu\text{m}$ prior to solidification, assuming no mass loss due to splashing of the droplet.

Temperature gradients can be approximated from the temperature measured and the splat thicknesses. For the heavily alloyed Ni-base material, with a liquidus temperature of 1355 C, a maximum temperature

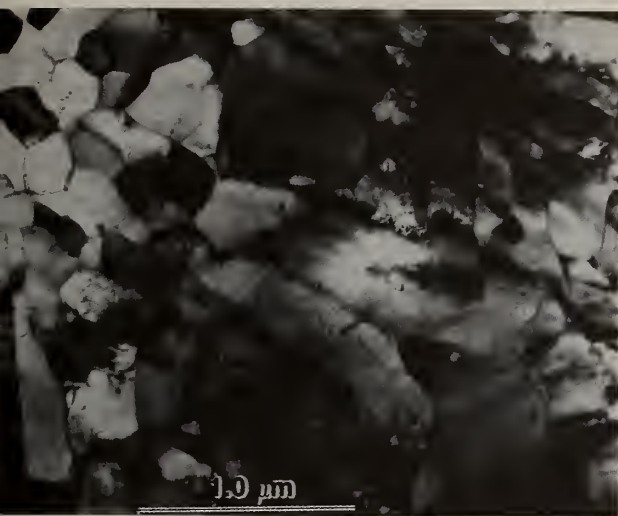


Figure 4. Longitudinal and transverse TEM views in RSPD Ni superalloy.

during deposition of 1164C and splat thickness of $3\text{ }\mu\text{m}$ leads to a temperature gradient of $(1355\text{C}-1164\text{C})/0.0003\text{ cm}$, or $6.4 \times 10^6\text{ K/cm}$, while for a maximum temperature of 731C, the gradient is $2.1 \times 10^6\text{ K/cm}$. A lower limit of growth rates can also be estimated from the measured splat thicknesses. For a powder-feed rate of $\sim 20\text{ kg/h}$, assuming all particles are $37\text{ }\mu\text{m}$ in diameter, approximately a million particles per second enter the plasma. For the degree of spreading noted above, any point on the substrate is covered about 350 times/sec. For $3\text{ }\mu\text{m}$ splat thicknesses, this corresponds to a solidification rate of at least 0.1 cm/sec , if each splat solidifies just as the next one spreads. Assuming solidification occurs well before spreading of the next droplet, the solidification rate is greater than 0.1 cm/sec .

From this upper estimate of particle solidification times and measured substrate temperatures, cooling rates can be estimated. For 350 particles/sec, a solidification time of $\sim 0.0029\text{ sec}$ is obtained. Again, for a liquidus of 1355C and a maximum substrate temperature of 1164C, a cooling rate of $>6.6 \times 10^6\text{ K/sec}$ results, while for a maximum temperature of 731C, a cooling rate of $>2.2 \times 10^6\text{ K/sec}$ results. The degree to which these cooling rates underestimate the actual rates is related to the overestimate of solidification time.

For the temperature gradients, G , and solidification rates, R , a G/R ratio of 0.7 to $2.2 \times 10^7\text{ K/sec/cm}^2$ results. Since a ratio of $\sim 5 \times 10^6\text{ K/sec/cm}^2$ is sufficient to achieve planar growth (13,14), the columnar, equiaxed grains in Figure 4 are, as expected, free of any dendritic or cellular solidification features.

Although the substrate temperature range is quite broad, it results in small ranges in G and therefore in G/R . As would be expected, the variation in splat thickness is also quite small, less than a factor of 2, between the lowest and highest substrate temperatures. The variation in deposit temperature from beginning to end of deposition is smaller than the variations due to $g\text{-t-s-d}$, so similarly the variation in splat thickness from first deposition to last is insignificant.

Other features of the microstructure were alloy dependent, such as fraction of particles unmelted and degree of microstructure modification after solidification. The simple alloys, Ni, Ni-13.5 Cr and Ni-7.2 Al have liquidus temperatures in excess of 1400C while the heavily alloyed composition has a liquidus of 1355C. There were considerably more unmelted particles in the materials with the higher liquidus temperatures, in spite of a plasma gas nearly 10 times hotter than the metal liquidus. This was manifested in deposit density as well. When compared to cast standards, the materials with large fractions of unmelted particles were $\sim 93\%$ as dense as their cast counterparts, while the heavily alloyed material was fully dense (Figure 5).

Comparing the temperatures measured with the optical micrographs of Ni-7.5 wt% Al and Ni-13.5 wt% Cr revealed structures that had experienced an *in situ* anneal. This was evident from the enlarged grains ($\sim 6\text{ }\mu\text{m}$) that are normally not apparent in plasma sprayed materials ($\sim 0.5\text{ }\mu\text{m}$) (Figure 6). The annealing was attributed to the heat of the plasma which in the 20 cm g-t-s-d case caused melting of the deposit during deposition, resulting in a cratered contour. The contours in general, became broader and more uniform as the $g\text{-t-s-d}$ increased. The grain growth due to the anneal was attributed to the low-alloy content and lack of grain boundary inhibitors such as carbides, as compared to a chemistry more typical of a superalloy. The true microstructure of these alloys could not be correlated to the temperatures measured. However, for the case of the melted sample there was evidence that a temperature gradient existed between the substrate surface ($T = 1325\text{C}$) and the liquid deposit surface ($1400\text{-}1450\text{C}$) through a deposit thickness of $\sim 1\text{ cm}$.

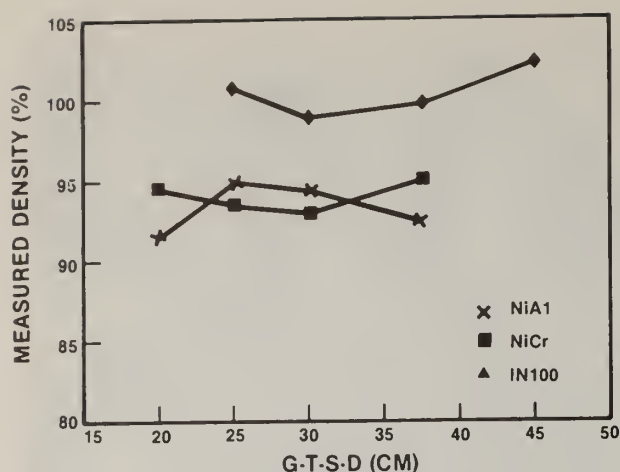


Figure 5. Deposit density for various g-t-s-d for Ni-Al, Ni-Cr and Ni superalloy.

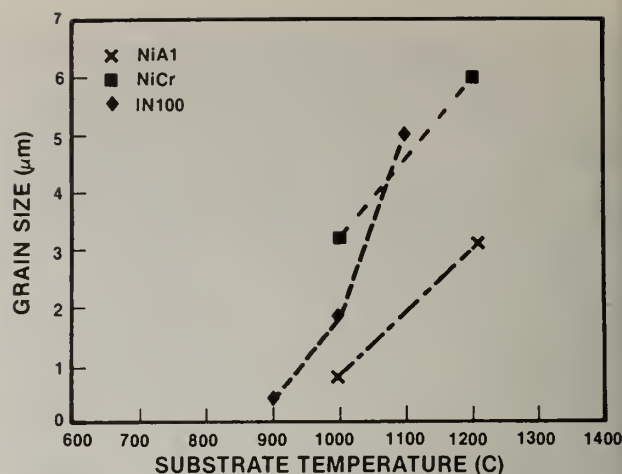


Figure 6. Grain size in as-deposited material as a function of substrate temperature.

Summary

Deposition temperature, as estimated from the substrate temperature, is dependent on distance from the plasma source, substrate thickness (mass), and powder-deposition rate. Heating is due in part to the plasma gases and in part to the heat involved during re-solidification.

Spreading of liquid droplets varies less than a factor of 2 (in thickness of the spread disc) from about 2.5 μm to 4 μm , for the range of cooling rates achievable in RSPD. Cooling rates are $\sim 10^5$ K/sec, and temperature gradient, solidification rate ratios (G/R) are such that planar solidification occurs.

Degree of particle melting is strongly dependent on liquidus temperature. For simpler alloy chemistries, *in situ* annealing can occur for the higher deposition temperatures. This is noted by a loss in remnant splat structure and a growth in grain size.

Acknowledgement

The helpful technical discussions with J.R. Rairden, M.F.X. Gigliotti, D. Lee, F. Zaverl and A.M. Ritter (all of General Electric Company) are gratefully acknowledged. Considerable experimental skills were provided by W.A. Seaman, S.F. Rutkowski and J.A. Resue. R.W. Kopp was responsible for designing temperature measurement equipment.

References

- (1) T.A. Roseberry and F.W. Boulger, "A Plasma Flame Spray Handbook," Rpt. No. MT-043, Naval Sea Systems Command, Dept. of the Navy, March 1977.
- (2) J.R. Rairden, "A Study of the Properties of High-Velocity Arc Plasma Sprayed NiCrAlY Coatings" Proc. 9th Int. Thermal Spray Conf., The Hague, p. 329, 1980.
- (3) R.W. Cahn, "Rapid Solidification by Plasma Spraying," Proc. Int. Conf. on Rapid Solidification Processing, Reston, Va., p. 129, 1977.
- (4) H. Herman, "Metastable Phase Produced by Plasma Spraying," Fall Meeting Program, TMS-AIME, Pittsburgh, p. 22, Oct. 1980.
- (5) R.W. Smith, "Mechanical Properties of a Low-Pressure Plasma Applied CoCrAlY Coating," Proc. Int. Conf. on Metallurgical Coatings, San Francisco, 1981.
- (6) J.R. Rairden, M.R. Jackson, M.F.X. Gigliotti, M.F. Henry, J.R. Ross, W.A. Seaman, D.A. Woodford and S.W. Yang, "Coatings for Balanced Environmental/Mechanical Behavior," Proc. Int. Conf. on High-Temperature Corrosion, NACE, San Diego, p. 72, 1981.
- (7) E. Muehlberger, Proc. 7th Int. Thermal Spray Conf., London, p. 245, 1973.

- (8) M.R. Jackson, J.R. Rairden, J.S. Smith and R.W. Smith, "Production of Metallurgical Structures by Rapid Solidification Plasma Deposition," J. of Metals, p. 23, Nov. 1981.
- (9) M.R. Jackson, R.W. Smashey and L.G. Peterson, "The Mechanical Behavior of RSPD Material," this conference proceedings.
- (10) J.R. Rairden, M.R. Jackson, J.R. Ross and W.A. Seaman, "Plasma Sprayed Alloys Considered for Advanced Concept for a Gas Turbine Bucket," Thin Solid Films, 73, p. 37, 1980.
- (11) M.G. Benz, General Electric Co., Schenectady, NY, private communication, 1981.
- (12) J. Madejski, "Solidification of Droplet on Cold Surface," Int. J. of Heat and Mass Transfer, 19, p. 1009.
- (13) R. Mehrabian, "Relationship of Heat Flow to Structure in Rapid Solidification Processing," Proc. Int. Conf. on Rapid Solidification Processing, Reston, Va., p. 9, 1977.
- (14) H. Matyja, B.C. Giessen and N.J. Grant, "The Effect of Cooling Rate on the Dendrite Spacing in Splat Cooled Aluminum Alloys, J. of the Institute of Metals, p. 30, 1968.

SUPERSATURATED SOLID SOLUTIONS BY MASSIVE SOLIDIFICATION: OBSERVATIONS AND IMPLICATIONS*

Thomas F. Kelly, Morris Cohen, and John B. Vander Sande

Department of Materials Science and Engineering
Massachusetts Institute of Technology
Cambridge, Massachusetts 02139

Abstract

Massive solidification structures have been observed in centrifugally atomized and rapidly solidified bcc powder particles of a 303 stainless steel. These structures are solid solutions of uniform composition throughout. A most important characteristic here is that the as-grown solid solution is highly supersaturated. Normally, large manganese sulfide precipitates form during cellular or dendritic solidification of this steel.

Since the solubility of the liquid state is generally much greater than that of the solid state, massive solidification to supersaturated solid solutions offers great potential for development of new alloy compositions and alloy design concepts. These possibilities and some processing conditions that favor massive solidification are discussed.

* Sponsored by the Office of Naval Research, Contract Number N00014-81-K-0013, NR653-032.

Introduction

303 stainless steel** is an austenitic steel with approximately one volume percent sulfide precipitate due to an intentionally high sulfur content, Table 1. Owing to the low solubility of the solid iron-base matrix for sulfur, partitioning of sulfur during solidification is severe. As a consequence, in conventional ingot processing sulfides, principally of manganese, precipitate from the enriched liquid at dendrite cell walls during the latter stages of solidification.

As the solidification rate increases, it is found that the size of these intercellular precipitates decreases as the size of the cells decreases. At the most extreme solidification rates, solute partitioning is kinetically suppressed and homogeneous solid solutions are produced in a massive solidification. These solid solutions are highly supersaturated with precipitate forming elements even at the moment of solidification which suggests novel processing paths to precipitate-strengthened alloys.

Table 1 - Composition of 303 Stainless Steel in weight percent.

Fe	Cr	Ni	Mn	Cu	Si	Mo	S	Co	C	N	P
bal.	17.3	8.68	1.60	0.78	0.66	0.37	0.34	0.71	0.034	0.032	0.022

**The 303 stainless steel was kindly supplied by Carpenter Technologies Corporation, Reading, Pennsylvania, which had originally requested the rapid solidification processing run.

Microstructural Observations

Light metallographic examination of ingot-processed (cooling rate $< 10^{-1}$ K/s) 303 stainless steel reveals large, 10 to 50 micron diameter manganese sulfide precipitates strung out in the rolling direction, Figure 1a. These are the remnants, after hot rolling, of the more nearly spherical precipitates formed by liquid-phase precipitation at dendrite cell walls in the ingot. Chill casting of this steel (cooling rate $\sim 10^2$ K/s) reduces the precipitate size to 1 micron diameter.

Centrifugal atomization with forced convective cooling* (cooling rate 10^5 to 10^6 K/s) has been used to produce rapidly solidified powder of 303 stainless steel with powder particle sizes in the range 5 to 200 micron diameter. Interestingly, a body-centered cubic (bcc) crystallization phase of the 303 stainless steel nucleates and grows in the smaller powder particles as a result of changing relative nucleation rates of fcc and bcc with increasing liquid supercooling [1]. Face-centered cubic (fcc) is the usual crystallization phase of this steel at small liquid supercoolings and is found in the larger powder particles.

The structure of the fcc powder particles is invariably found to be cellular with sulfide precipitates at the cell walls. These precipitates are about 100 nanometer diameter as a result of rapid solidification but are still formed by a liquid-phase precipitation process as occurs in ingot processing.

It is in the microstructures of the bcc powders that deviations from this solidification scenario are observed. The extreme example of this is a homogeneous [2] solid solution produced by massive (partitionless) solidification with a planar liquid/solid interface, Figure 1c. In this process, the solid grows with the same composition as the liquid. The solid solution of Figure 1c apparently decomposes in some cases, during continuous cooling to ambient, to the structure of Figure 1d. Here, 10nm diameter manganese sulfides have precipitated throughout the structure from the supersaturated solid solution produced during massive solidification.

An intermediate microstructure between the cellular fcc and the noncellular bcc structures is a cellular bcc structure, Figure 1e. Larger, 100 nanometer diameter sulfides that precipitate from the liquid are located at the cell walls of the structure. There is, as well, a massive solidification zone in the central region of each of the cells. Smaller 10 nanometer diameter sulfides have precipitated from the supersaturated solid solution that results from this localized massive solidification.

Preliminary studies indicate that the supersaturated solid solutions of Figure 1c may decompose to ultra-fine, 1 to 2 nanometer sulfide precipitates under controlled precipitation heat treatments at 400°C.

Discussion

Supersaturation

It is important to know whether the solid solution that forms during solidification is supersaturated with respect to manganese and sulfur at solidification temperatures. If the solid solution is not supersaturated, then this is simply the case of a high temperature single phase of high solubility that has been accessed by massive solidification. An important distinction must be made between massive solidification processes that produce homogeneous undersaturated solid solutions and those that produce homogeneous supersaturated solid solutions. Though there might still be some advantages to massive solidification in the former case, the real importance of massive solidification as a processing route lies in the ability to produce supersaturated solid solutions that cannot be produced otherwise.

Turkdogan et. al [3] have determined the solubility product of manganese and sulfur in fcc iron. By their results, the equilibrium solubility product of manganese and sulfur at the melting point of iron, 1800K, is $[Mn(wt\%)][S(wt\%)]_{Fe} = 0.0076$. The composition product of manganese and sulfur in 303 stainless steel is 0.544 which is 72 times this fcc-iron equilibrium solubility product at 1800K.

* The rapidly solidified powder was kindly processed by Pratt and Whitney Aircraft Group, Government Products Division, United Technologies Corporation, West Palm Beach, Florida 33402.

F C C



B C C

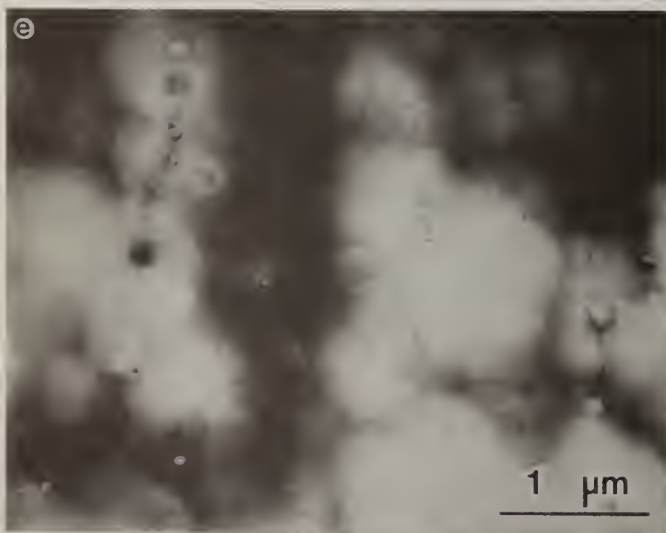


Figure 1 - Process states of 303 Stainless Steel:

- (a) light micrograph of longitudinal section of hot-rolled ingot;
- (b) annular dark-field STEM image of rapidly solidified fcc;
- (c) and (d) bright-field STEM image of rapidly solidified noncellular bcc;
- (e) bright-field STEM image of rapidly solidified cellular bcc.

Complete solid solutions are observed only in the bcc structures. Although the solubility of sulfur may be greater in bcc than in fcc, this is a small effect compared with the large amount of manganese and sulfur in 303 stainless steel. Furthermore, a one hour heat treatment of some rapidly solidified 303 stainless steel at 1600K produced only a small amount of precipitate coarsening: the average precipitate size increased from 10 to 200 nanometer diameter to 0.5 to 1.0 micron diameter. This indicates a low solubility product of the precipitate-forming elements, manganese and sulfur, in this steel. Accordingly, it does appear that a bcc solid solution that is highly supersaturated with respect to manganese and sulfur forms during massive solidification of 303 stainless steel as a bcc structure.

Hypercooling: Fcc vs. Bcc

It is not coincidence that massive solidification is observed only in the bcc structure. There are some compelling reasons why bcc solidification in this steel would be massive more readily than fcc solidification. This difference in solidification behavior between the two structures is associated with the degree of supercooling of the liquid prior to nucleation of the solid.

The onset of massive solidification can be associated with the approach to hypercooling, which is where the specific supercooling goes to unity:

$$\frac{C_p^L \Delta T}{\Delta H^{L \rightarrow S}} \rightarrow 1.$$

For 303 stainless steel, the enthalpy of fusion of fcc, $\Delta H^{L \rightarrow \text{bcc}}$, is calculated to be 19% less than the enthalpy of fusion of fcc, $\Delta H^{L \rightarrow \text{fcc}}$ [1]. This means that, for equivalent supercoolings, ΔT , the specific supercooling of the liquid with respect to bcc,

$$\frac{C_p^L \Delta T}{\Delta H^{L \rightarrow \text{bcc}}}$$

is greater than the specific supercooling of the liquid with respect to fcc,

$$\frac{C_p^L \Delta T}{\Delta H^{L \rightarrow \text{fcc}}}.$$

C_p^L is the heat capacity of the liquid at constant pressure. For an alloy where the equilibrium melting temperature of bcc is not too much lower than the equilibrium melting temperature of fcc, as for 303 stainless steel, the liquid will be hypercooled with respect to bcc at a higher temperature than fcc. Bcc should then be more prone to solidify massively.

Implications and Applications of Massive Solidification

Massive solidification, if it is achieved, offers a means of producing solid solutions in alloy systems in which it may not otherwise be possible to obtain such solid solutions. This could have far-reaching implications for alloy design.

Consider an alloy consisting of a base metal plus elemental additions that will form a precipitate in the base metal. Solidification of this alloy in a cellular or dendritic mode might produce a relatively coarse second-phase morphology. If a phase regime of high solubility for the precipitate were to exist at high temperature for this hypothetical alloy, then solutionizing of the alloy could be carried out. The penalty for this might be excessive grain growth during the solutionizing treatment. If, however, there is no high-temperature regime of high solubility for the precipitate, then there is no possibility of solutionizing the alloy via this type of heat treatment.

On the other hand, processing of such an alloy to obtain massive solidification would offer some advantages. Having achieved the solid solution during solidification, a precipitation heat treatment could be carried out at a low enough temperature that grain growth is negligible. Since the solubility of the precipitate phase is very low, the precipitate dispersion will be very resistant to coarsening even at high temperatures. This fine precipitate dispersion will, in turn, prevent grain coarsening at the high temperatures. Thus, an unusual precipitation-strengthened fine-grain material would result.

An alloy-design approach that utilizes massive solidification may be especially desirable for the design of materials with a large volume fraction of the second phase. With rapid solidification processing, alloy designs would not be limited to those that can be successfully processed by conventional means. New precipitate/metal matrix combinations should be tried on the basis of their potential effectiveness if the solid solution can be achieved by massive solidification. Ideally, the supersaturated solution would be retained to room temperature to allow control of subsequent precipitation processes. Optimal precipitate volume fractions, sizes, and dispersions could then be achieved with this type of processing.

Conclusions

Massive solidification of bcc structures, which occurs in the smaller ($\lesssim 70$ micron diameter) droplets of 303 atomized stainless steel, results in a supersaturated solid solution with respect to the precipitate forming elements, manganese and sulfur. This supersaturated solid solution cannot be produced by conventional solid-state processing of this alloy.

As materials-processing route, the use of massive solidification to produce supersaturated solid solutions appears promising as a means of structural control in a wide range of material systems.

Acknowledgements

Sponsored by the Office of Naval Research, Contract Number N00014-81-K-0013, NR 653-032.

References

1. Thomas F. Kelly, Morris Cohen, and John B. Vander Sande, "Rapid Solidification of Atomized Stainless Steel: Part 2 - Origins of FCC and BCC Solidification Phases," submitted to Metall. Trans. A, 1982.
2. Thomas F. Kelly, Morris Cohen and John B. Vander Sande, "Rapid Solidification of Atomized Stainless Steel: Part 1 - Depressed Partitioning and Supersaturated Solid Solutions in FCC and BCC Solidification Phases," submitted to Metall. Trans. A, 1982.
3. E. T. Turkdogan, S. Ignatowicz and J. Pearson, J. Iron and Steel Inst., 1955, vol. 180, pp. 349-354.

SOLUTE REDISTRIBUTION DURING SOLIDIFICATION OF SUPERCOOLED ALLOYS

S. D. Peteves, D. D. McDevitt and G. J. Abbaschian

Department of Materials Science and Engineering
University of Florida
Gainesville, FL 32611

ABSTRACT

During some rapid solidification processes considerable supercooling is achieved such that nucleation takes place below the solidus temperature. The solidification in such cases is initially partitionless, resulting in the formation of a solid with the composition of the liquid. A simple model based on the heat of fusion, heat capacity, and the supercooling has been proposed to calculate the fraction that solidifies without segregation. Calculations based on this model are compared with STEM measurements of the composition profile in supercooled Fe-25%Ni structures. The results indicate qualitative, but not quantitative, agreement between the two. The discrepancy is explained based on the non-uniformity of temperature, and interfacial curvature and kinetic effects. A model for the associated heat transfer equations is given, which indicates that solidification is kinetically controlled at the beginning of recalescence, but becomes thermally controlled as recalescence progresses.

Introduction

The conventional techniques of obtaining rapidly solidified structures are generally based upon increasing the cooling rate during solidification by improving the heat extraction efficiency between the casting and the heat sink, and/or by reducing the volume of material being solidified. However, rapid solidification can also result from supercooling prior to nucleation, followed by rapid heat removal. With substantial supercooling, the initial solidification rate is large as the heat of fusion is absorbed by the supercooled liquid. In fact, a supercooling exists beyond which the liquid can solidify completely without the need for transfer of heat to the surroundings. Substantial supercoolings before nucleation have been obtained by melting high purity metals within molten glass [1,2], within emulsions [3,4], or by using a levitation technique [5,6]. The latter technique has been recently used [5] to study the effects of supercooling and cooling rate on the solidification structure of Fe-25%Ni samples. The samples, approximately 0.5 cm in diameter, were supercooled as much as 270 K and were solidified in water, molten lead, or a ceramic mold. The sub-grain microstructure was found to fall into three categories: dendritic, spherical, or a mixture of the two. All three morphologies were observed when the samples had solidified with a supercooling less than 175 K. At larger supercoolings, however, the spherical morphology predominated. In addition to the spherical morphology, other segregation patterns were noted at large supercoolings [6].

Numerous studies have been done to relate solute distribution and microstructure to the amount of supercooling prior to nucleation [7-10]. The most widely used model, proposed by Kattamis [7], is based on the relationship between the heat of fusion, heat capacities, and the supercooling. The model indicates that when a liquid is supercooled below the solidus temperature prior to nucleation, the fraction that solidifies segregationless is approximately:

$$f_s^0 = \frac{C_p}{H_f} (T_s - T_n)$$

where C_p is the average heat capacity of the solid and liquid, H_f is the heat of fusion, T_s is the solidus temperature, and T_n is the nucleation temperature. As the temperature recalesces above the solidus, partitioning begins at the interface and solidification continues with the solid decreasing in solute until the maximum recalescence temperature is reached. Beyond this point the solidification continues similar to conventional solidification processes with no supercooling. The equations relating the composition profile to the fraction solid during and after recalescence are given by:

$$C_s = C_0 + \frac{(f_s - f_s^0)H_f}{C_p m_s} \quad \text{for } f_s^0 < f_s < f_{sR} \quad \text{and}$$

$$C_s = C_{sR} \left[1 - \frac{(f_s - f_{sR})}{(1 - f_{sR})} \right]^{k-1} \quad \text{for } f_{sR} < f_s < 1$$

where C_{sR} is the solid composition at the maximum recalescence temperature and where f_{sR} is the fraction solid at maximum recalescence, m_s is the solidus slope, and C_{sR} is the solid composition at the maximum recalescence.

The present paper investigates the applicability of the above mentioned models to the solidification of supercooled Fe-25%Ni alloys.

Experimental Procedure

The experimental procedure consisted of utilizing electromagnetic levitation to levitate and melt one gram samples of Fe-25%Ni [5]. The samples were melted while levitated and supercooled to a desired temperature where they were dropped in a molten lead bath held at 650 K. The quenched samples were then analysed metallographically and by a JOEL 200 scanning transmission electron microscope. For the latter study, the samples were sliced by a diamond saw followed by electrochemical thinning in a solution of 90% acetic - 10% perchloric acid at 280 K. The composition profile in the thinned samples were obtained by using the electron microscope.

Results

Similar to previous studies [5,6], the microstructure was found to fall into three major categories: dendritic, spherical, or a combination of the two. At supercoolings less than 175 K, all three morphologies were frequently observed while at supercoolings exceeding this value, the spherical morphology tended to predominate. The metallographic examination further revealed the presence of a fine dendritic segregation pattern within the larger dendrites, as shown in Figure 1. Surrounding the solute-rich "primary" dendrites is a lightly colored region which gradually darkens toward the edge of the larger dendrite arms. In general, there is a single primary dendrite arm within each larger arm. However, several primary arms were observed within a larger arm in some areas.



Figure 1. The dendritic morphology etched to reveal fine "primary" dendrites within the dendritic arms. The sample was supercooled 175 K before quenching in molten lead.

Samples having the spherical segregation pattern exhibited similar features, containing solute-rich cores, as shown in Figure 2. However, the solute-rich primary cores are not fully developed dendrites but have a simple cross shape. The crosses are surrounded by a lightly colored, solute-poor region, darkening toward the edge of the spherical elements.

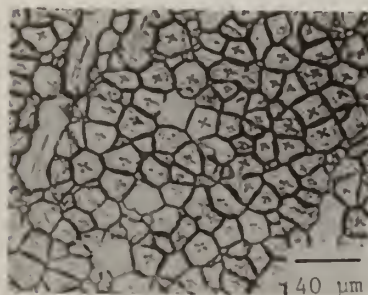
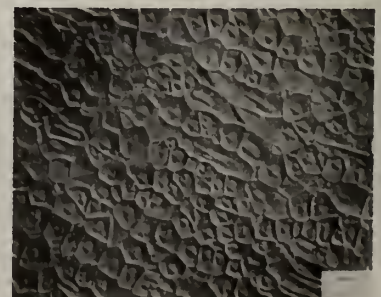


Figure 2. a) Brightfield microscopy of the spherical morphology showing dark colored solute-rich crosses in the center of each element surrounded by a solute-poor region which gradually darkens toward the edge. b) crosses revealed using Nomarski interference contrast.



A scanning transmission micrograph of a spherical element, similar to the ones shown in Figure 2, is shown in Figure 3. The compositional profile along a horizontal line passing through the center

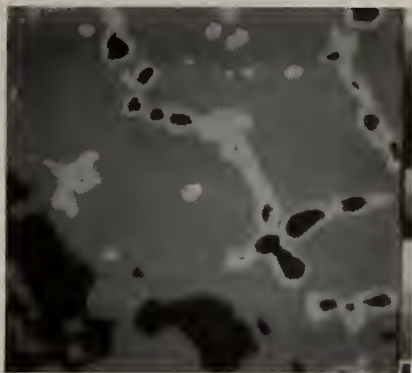


Figure 3. STEM micrograph of spherical element similar to those in Figure 2b.

of the cell was obtained using an energy dispersive spectrometer. The ratio of the intensities of the iron and nickel K_{α} x-ray peaks was used for compositional measurements. The line scan data of a sample supercooled 80 K below the solidus line, is plotted as a function of distance from the center of the cell in Figure 4. The compositional profile based on the model discussed earlier is also shown in the figure.

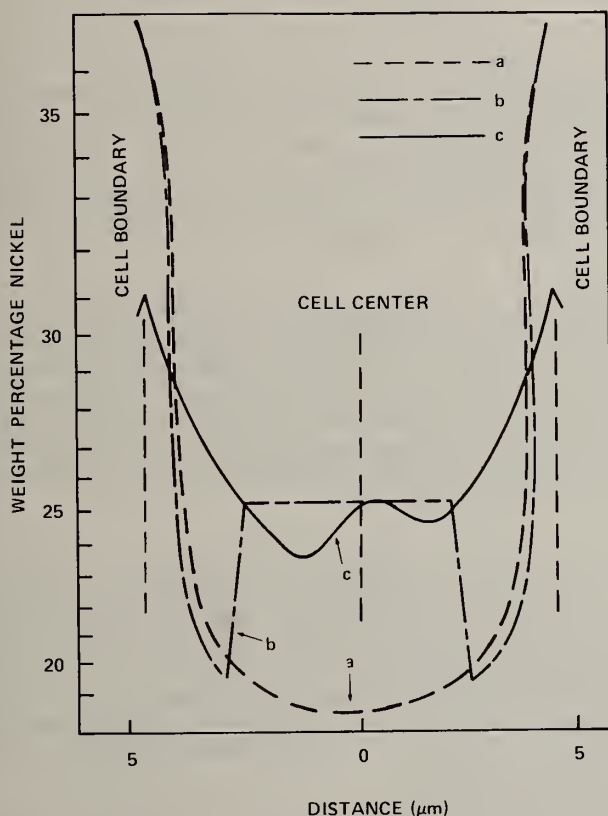


Figure 4. Model and measured compositional profiles: a) and b) Scheil equation and Kattamis' model, respectively, converted to spherical geometry. c) Line scan of measured x-ray intensity ratios converted into concentration.

Discussion

The measured compositional profiles and the results of metallographic examination clearly indicate the existence of a solute rich core within the cast elements. This region is surrounded by a region of lower concentration beyond which the concentration increases to a maximum at the periphery of the cell. The measured compositional profile qualitatively agrees with that of the model but not quantitatively. The experimental results show the region of the partitionless solidification to be much smaller than that of the model, and the measured minimum concentration to be higher than the theoretical one. These discrepancies are believed to be due to the assumptions or simplification which were used in the model. These include: i) adiabatic solidification during recalescence; ii) negligible solid state diffusion; iii) no remelting during recalescence; iv) partitioning at T_S ; v) no curvature effects; and vi) uniform temperature throughout the sample during recalescence.

The assumptions of adiabatic solidification seems to be justified considering the short recalescence time and relatively large volume of the samples about 0.5 cm in diameter. Furthermore, the effect of non-adiabatic conditions will be to increase the extent of partitionless solidification, rather than to reduce it. The solid state diffusion can also be assumed to be negligible because of the relatively short solidification time. The local solidification is approximately 0.007 sec for a sample supercooled 80 K below solidus and quenched in lead [5]. The smaller size of the central core, as compared with the model, may be due to remelting of compositionally unstable solid above the solidus temperature. However, for remelting to take place at the surface of a growing solid, the interfacial movement must cease completely before retreating. The continuous cooling of the sample during this period can lower the temperature enough to eliminate remelting.

Thermodynamic considerations based upon the T_0 concept, detailed by Baker and Cahn [11] indicate that partitionless solidification may continue above the solidus until the temperature reaches T_0 . The T_0 curve is where the free energies of the liquid and solid phases are equal. Above T_0 , solidification must occur by partitioning if the free energy is to be decreased. If partitionless solidification continues past the solidus to the T_0 curve, the volume fraction of the solute-rich core would be larger than the presented model. However, the actual temperature of the partitionless-partitioning demarcation is debatable.

The assumption of the planar interface is not justified when the interface breaks down and forms a dendritic morphology. The dendrites during partitionless solidification are caused by the thermal field, since the solid is growing into a supercooled liquid. According to Gibbs-Tompson effect, the interfacial curvature then shifts the phase diagram downward, leading to an earlier transition into partitioning.

For the sample shown in Figure 1, the size of the primary dendrites is less than 10^{-4} cm. Although, it is rather difficult to determine the tip radius during recalescence, a rough estimate of the radius can be made from the dendritic growth models relating the tip radius to the bath supercooling and growth rate [12]. For 80 K supercooling, the tip radius is estimated to be 10^{-5} - 10^{-4} cm. The corresponding depression of the solidus and liquidus temperatures, as well as T_0 , is in the range of 3-30 K. As a result, the extent of the partitionless solidification will become considerably less than that predicted from the model. It should be noted that a 30 K temperature depression will reduce f_S^0 to a value close to the observed results.

Non-uniformity of the temperature within the sample during recalescence is another major factor that could drastically alter the value f_S^0 . If the solidification process is controlled by the interfacial kinetics, the interface temperature will remain close to that of the bulk sample. However, when the process is heat transfer controlled (i.e., the interfacial kinetics are faster than the rate of the thermal diffusion), the interface temperature will be appreciably higher than the bulk. In this case the interface temperature will eventually rise to the melting point, even though the bulk liquid still remains supercooled. Partitioning in the latter case takes place much sooner than the former case. The former case is used in the derivation discussed earlier.

Numerical techniques have been recently used to calculate temperature profiles during solidification of atomized aluminum powders [13]. The results indicate that substantial temperature differences are developed inside the droplets during recalescence. Obtaining an analytical solution for the associated heat transfer equations during recalescence is rather difficult. Heat transfer solutions of supercooled melts to date have been usually concerned with isothermal solidification of a solid at its melting point into the supercooled liquid. The interfacial temperature is also assumed to be fixed at the melting point and without any kinetic effect. A solution based on these conditions was given by Frank [14] for radially symmetric phase growth controlled by diffusion. The solution, however, is not applicable for transitional heat transfer problem during recalescence.

For a simplified case of a spherical solid growing into a relatively large supercooled bath, a quasi-stationary solution for the heat transfer equations can be given by modifying the analysis given by Frank [13]. Assuming the heat transfer to be by conduction only, the heat capacity of solid to be negligible compared with the heat of fusion, and the solid to have a uniform temperature equal to the interface temperature, the temperature profile in the liquid ahead of the interface is:

$$T(r,t) = T_N + \frac{S(T_i - T_N)}{e^{-\frac{S^2}{4}} - \frac{S}{2} \pi^{1/2} \operatorname{erfc}(\frac{S}{2})} \left\{ \frac{(\alpha t)^{1/2}}{r} e^{-\frac{r^2}{4\alpha t}} - \frac{\pi^{1/2}}{2} \operatorname{erfc}\left(\frac{r}{2(\alpha t)^{1/2}}\right) \right\}$$

where $S = r a^{1/2} t^{-1/2}$, dimensionless "reduced radius," is a root of

$$S^2 \exp\left(\frac{1}{4}S^2\right) \left[\exp\left(-\frac{1}{4}S^2\right) - \frac{1}{2} \pi^{1/2} S \{1 - \operatorname{erf}\left(\frac{1}{2}S\right)\} \right] = 2 \left(\frac{T_i - T_N}{H_f} \right) C_p$$

in which r is the radial distance in the liquid, t is the time, T_i is the interface temperature, T_N is the nucleation temperature, α is thermal diffusivity, C_p is specific heat, and H_f is heat of fusion. The interface temperature can have any value between the nucleation temperature and the melting point.

The above equations were used to calculate the heat transfer controlled interfacial velocity as a function of radius at various interfacial supercoolings. The results are plotted in Figure 5, where the y-axis gives the interfacial velocity while the x-axis gives the radius of the growing solid.

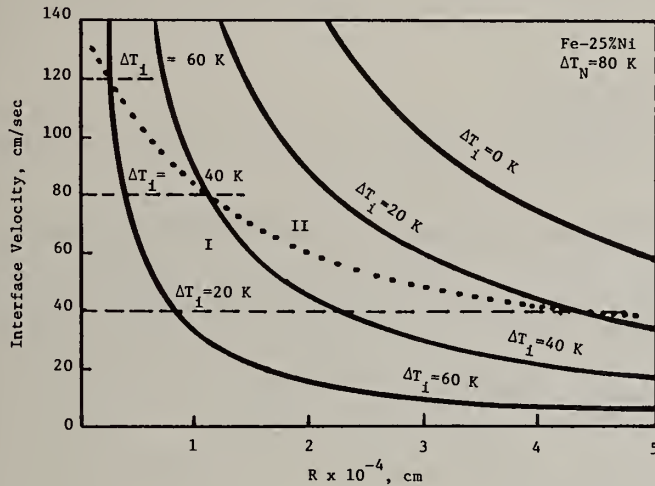


Figure 5. Interface velocity as a function of the radius of solid, growing at various constant interfacial supercoolings: Solid and dashed curves show heat flow and kinetically controlled growth respectively. The dotted curve is the demarcation line between the two growth modes.

The above mentioned calculations are based on the assumption that the interfacial kinetics is infinite. In reality, however, the interface kinetics is limited and it is a function of the material parameters, the supercooling, the orientation and the nature of the interface. Therefore, the heat transfer equations must be coupled with the kinetic equations. There are only limited number of accurate measurements on the solidification kinetics of metals, and these are mostly at low supercoolings [15]. However, at high enough supercoolings, the rate equations are expected [16] to be a linear function of the interfacial supercooling given by

$$V = \frac{\beta D H_f \Delta T_i}{h R T^2}$$

where β is a correction factor for the structure and orientation, D is the liquid diffusivity, R is the gas constant, and h is the distance by which a position on the interface advances when an atom is added or removed. The coefficient β is expected to be of the order of ten for symmetrical molecules and atoms. Using the available data for iron and nickel and $\beta=10$, the coefficient of the linearity is about 2 cm per second per degree of the interfacial supercooling for Fe-25%Ni alloys. The corresponding kinetically controlled solidification rates at various supercoolings are shown by the horizontal dashed lines in Figure 5.

The preceding heat flow and kinetics calculations indicate the limiting cases for the solidification processes. For a given interfacial supercooling, when the radius of the solid is small, the kinetically controlled rate is slower than the heat transfer controlled one. Thus the solidification will be kinetically controlled. The situation is reversed however, as the radius of the sphere becomes large and the process becomes thermally controlled. However, it should be noted that as solidification continues, the interface temperature also rises. This in turn reduces the kinetically controlled rates while it increases the heat transfer rate. Therefore, the various regions shown in Figure 5, can be divided to two zones separated by the dotted curve and marked by I and II. In zone I, where the radius of the solid is small and/or the interfacial supercooling is high, the solidification is kinetically controlled. In zone II, where the fraction solid is larger and/or most of the interfacial supercooling is lost, the solidification process is heat transfer controlled. It is in zone II, that the interface temperature rises rapidly to the melting point and partitioning begins even though the bulk liquid is still supercooled. It should be noted that the time necessary for the solidification to change from kinetically controlled mode to the heat transfer controlled mode is rather short. For example at a 40 K interface supercooling, the time for the transition is estimated at 2×10^{-4} sec.

Summary

The solute distribution profile in highly supercooled Fe-25%Ni was measured by using STEM. The results quantitatively agreed with the model proposed by Kattamis [7], but not quantitatively. The disagreement is believed to be due to certain assumptions made in the theoretical calculations; namely uniformity of temperature during recalescence, no curvature effects, and no interface kinetics. An approximate analytical solution has been given for the associated heat transfer equations. The results are discussed in conjunction with kinetically controlled solidification, which qualitatively indicate the solidification is kinetically controlled at the beginning of recalescence, but becomes thermally controlled as recalescence progresses.

Acknowledgements

The project was sponsored by the National Science Foundation, under grant no. DMR-8202724 to the University of Florida.

References

1. T. Z. Kattamis, and M. C. Flemings, "Solidification of Highly Undercooled Castings," Modern Casting, pp. 97-104, July, (1976).
2. J. L. Walker, "Physical Chemistry of Process Metallurgy, Part I," pp. 845, Interscience, NY, (1961).
3. D. Turnbull, "Kinetics of Solidification of Supercooled Liquid Mercury Droplets," J. Chem. Phys., vol. 20, No. 3, pp. 411-24, (1952).
4. J. H. Perepezko, "Crystallization of Undercooled Liquid Droplets," Conf. Proc. 2nd International Conf. on Rapid Solidification Processing, Reston, VA, March 23-6, (1980).
5. G. J. Abbaschian, and M.C. Flemings, "Supercooling and Structure of Levitated Fe-Ni Alloys," to be published in Met. Trans.
6. D. D. McDevitt, and G. J. Abbaschian, "Microstructure and Solute Distribution in Highly Supercooled Fe-Ni Alloys," to be published in Microstructural Science, vol. 11, 1983.
7. T. Z. Kattamis, "Redistribution of Solute in Highly Undercooled Iron-Nickel Alloy," Z. Metallkunde, pp. 856-60, (1970).
8. T. Z. Kattamis, "Solute Redistribution in Undercooled Alloys," Ph.D. Thesis, MIT, (1965).
9. H. Biloni and B. Chalmers, "Predendritic Solidification," Trans. Met. Soc. AIME, vol. 236, pp. 615-34, (1966).
10. S. P. Iyer and W. V. Youdelis, "Distribution of Bismuth in Primary Sn Crystals of Supercooled Sn-Bi Alloy Ingot," J. of Inst. of Metals, vol. 101, pp. 218-20, (1973).
11. J. C. Baker and J. W. Cahn, "Thermodynamics of Solidification," in Solidification, an ASM publication, (1971).
12. R. Trivedi, "Growth of Dendritic Needles from a Supercooled Melt," Acta. Met., vol. 18, March, pp. 287-96, (1970).
13. C. G. Levi and R. Mehrabian, "Heat Flow During Rapid Solidification of Undercooled Metal Droplets," Met. Trans. A, vol. 13A, pp. 221-34, (1982).
14. F. C. Frank, "Rapidly Symmetric Phase Growth Controlled by Diffusion," Proc. Roy. Soc. A, 201, pp. 586-99, (1950).
15. G. J. Abbaschian, S. F. Ravitz, "Rate Equations for Dislocation-Free and Dislocation-Assisted Growth of Gallium," J. Crystal Growth, 44, pp. 453-66, (1975).
16. J. W. Cahn, W. B. Hillig and G. W. Sears, "The Molecular Mechanism of Solidification," Acta. Met., vol. 12, pp. 1421-39, (1964).

MICROSTRUCTURE-PROPERTY RELATIONS AND THEIR ROLE IN RSP MATERIALS

J. C. Williams^{*} and J. P. Hirth^{**}

^{*}Carnegie-Mellon University
Pittsburgh, PA 15213

^{**}Ohio State University
Columbus, OH 43210

ABSTRACT

The prospect of creating microstructures which are truly optimum for a given application has moved a step closer to reality with the development of Rapid Solidification Processing (RSP) techniques. This paper discusses in general some of the possibilities for creating optimum microstructures using RSP and considers in greater detail the selection of microstructures for combined strength and toughness. Finally, a series of unresolved issues regarding microstructure-property relations are identified and the role that these issues play in restraining the selection of optimum microstructures is discussed.

Introduction

It has become accepted in recent years that optimum performance of a material in a given application can be paced by any of a variety of properties, depending on the details of the loading and service requirements placed on it. In simple cases, where weight is critical, the component may be sized using strength as a primary criterion whereas in many other cases, where fracture resistance is critical, toughness or fatigue-related properties may fix the section size long before strength becomes an issue. Many other comparable situations exist but these are too numerous to describe here. It is clear, however, that the first step in optimizing the performance of a structural component is identification of the pacing property which dominates the design process. As already mentioned, this property may be structure-sensitive such as strength, toughness or fatigue resistance, or it may be one of the so-called structure-insensitive properties such as modulus or density. Irregardless of which of these properties pace the performance of a component, metallurgists have made considerable progress in learning how to enhance the values of each of these properties. Unfortunately, a material cannot be altered so as to maximize a given property without due consideration of the concurrent effect that such alterations may have on other properties.

Among the better known examples of the trade-offs which result from improving one property at the expense of another is the inverse relationship between strength and toughness. Many other comparable trade-offs exist in practice and it is these which often limit the extent to which a particular property can be maximized. Frequently these trade-offs and limitations are the result of the metallurgist's inability to simultaneously control the different microstructural features which affect the various individual properties. If it were possible to synthesize optimum microstructures using a metallurgical equivalent of the molecular engineering methods used so successfully by developers of polymeric materials, then some of these trade-offs might be lessened or eliminated.

One possibility for expanding the range of microstructures and alloy compositions which can be obtained in metallic materials is the use of rapid solidification processing (RSP) techniques. In particular, RSP permits fabrication of alloys which contain either greater concentrations of solute or solutes which are difficult to deal with using ingot metallurgy. Thus, RSP opens new horizons in terms of alloy composition. In addition, RSP offers the potential for creating finer and even novel microstructures which cannot be achieved in alloys fabricated from ingots. These opportunities thus raise an important question: "If we could create any microstructure, what would we specify for a particular application?" It turns out that the answers to this question are more complicated than might be anticipated, especially when fracture-related properties are considered.

The purpose of this paper is to discuss the question of specifying optimum microstructures. To do this, we will address only two properties in any detail; strength and toughness. The discussion of these two properties will be followed by a short summary of key issues which face the metallurgist before true microstructure synthesis can be attempted with confidence. These key issues could also be identified as pacing issues or barriers to success in the implementation of RSP in a broader applications arena. At any rate, we hope that the remainder of this paper will illustrate an approach to considering microstructure-property relationships in a more fundamental way than has been traditionally done in alloy development programs. We also hope that some food for thought can be found herein, even for those who do not share our enthusiasm regarding the opportunities which RSP brings to metallurgical practice.

Strength

If one considers the possibilities for improving the strength of metals and alloys, there are basically three general types of strengthening mechanisms which can be employed. These are: solid solution, particle and boundary hardening. Most articles on strengthening mechanisms list more hardening mechanisms but, after some scrutiny, all of the mechanisms can be grouped in the above three types. From the standpoint of microstructural design or selection, this is a convenient way to consider the possible strengthening contributions since each is readily identifiable and distinct from a microstructural viewpoint. The ensuing discussion will thus examine these three types of hardening, particularly in light of some of the effects that each has on other characteristics or properties. It is not the intent of the discussion to present a rigorous analysis or review of strengthening mechanisms but, rather, to examine the role of microstructure on strength with an eye toward providing some insight into optimizing microstructures of RSP materials with respect to strength. Readers interested in a more rigorous review of strengthening, per se are referred to any of a number of books and reviews on this subject[1-6].

Boundary Hardening

Boundary hardening refers to the strengthening contribution due to the presence of boundaries which act as obstacles to dislocation motion; these may be grain boundaries, interphase boundaries in duplex or microduplex alloys, or sub-boundaries such as cell walls in a polygonized structure. In general, reducing the grain size or slip length of a material leads to increased strength, with these strength increases being proportional to $d^{-1/2}$ where d is the grain diameter. Smaller grains also usually lead to simultaneous improvements in ductility and toughness. However, very fine grains ($\sim 1\text{-}5\mu\text{m}$) may also reduce the resistance to shear localization, thus an optimum grain size no doubt exists for each material. The exact value for optimum grain size depends in a complex way on a variety of factors, including intrinsic work hardening, preferred orientation, slip character and others. Nevertheless, it seems certain that refining the grain size of most structural materials to values in the $1\text{-}10\mu\text{m}$ range can lead to simultaneous increases in strength, toughness and other properties such as fatigue strength, although fatigue crack propagation rates may increase and environmentally-induced cracking may become more severe.

RSP has been used to introduce a uniform distribution of small second phase particles which act as intrinsic grain refining agents[7]. The advantage of RSP in this case is that the particles can be kept small enough that they do not appear to participate in the initiation of microvoids during ductile fracture, yet still stabilize the grain size by preventing growth. As a result, the grain size refinement can be achieved without the deleterious effects associated with large inclusions or second phase particles.

When the grain size is refined to diameters less than $\sim 1\mu\text{m}$, then the strengthening from substructure becomes more important[8]. As a result, this seems to set the low end size limit for grain size strengthening. However, the stabilization of substructure by fine particles is also a useful concept and the use of RSP in producing a uniform distribution of fine particles which aid in stabilizing a substructure with a small cell size seems attractive. This approach has not been extensively studied in RSP materials, but similar structures have been produced in mechanically alloyed materials such as ODS Ni-Cr alloys[9]. In these materials the thoria particles are very effective in stabilizing the substructure.

Thus, while it is still difficult to use first principles to quantitatively specify an optimum grain size, it is clear that grain diameters in the $1\text{-}10\mu\text{m}$ range are attractive and potentially beneficial. Such grain sizes are indeed rare in conventional ingot metallurgy products. As a result, the use of RSP to develop very fine grained materials appears very attractive. The use of very small, stable cells ($< 1\mu\text{m}$) for strengthening also appears attractive, especially if RSP can be used to produce a uniform dispersion of particles which will pin and stabilize these cell walls. In the final analysis, boundary hardening is an attractive means of improving the strength because it typically im-

proves ductility and toughness also. When employing boundary strengthening, however, the earlier comment on fatigue crack growth rates must be borne in mind. Other property compromises may also exist, for example, intragranular environmental cracking is usually more pronounced in fine grained materials.

Particle Hardening

Particle hardening refers to increases in strength due either to dispersoids or to precipitates. The distinction between these is that the former are typically by-passed by mobile dislocations whereas the latter are sheared. This difference has a profound effect on the work hardening characteristics of the material which, in turn, affect the ability of a material to resist localized deformation and plastic instability which leads to premature fracture. Alloys which are hardened by shearable precipitates generally exhibit decreasing strain hardening with increasing strength. As will be discussed below in the section on Toughness, this reduction in strain hardening tends to lead to earlier onset of plastic instability and thus to reduced toughness. The precipitates which form in many of these alloys during aging have a very uniform size and a small spacing as shown in the examples in Figure 1. Since these particles are usually aligned with the matrix via an orientation relation they tend to be readily sheared by matrix dislocations. Extreme examples of this are found in Al-Li alloys where the coherent δ' phase is sheared, leading to intense bands of shear localization and to the premature initiation of cracks along these bands[10]. Essentially all alloys which contain shearable precipitates exhibit this tendency and the differences between alloy systems tends to be one of degree rather than of kind.

Alloys which contain non-shearable particles (dispersoids) tend to exhibit increased strain hardening compared to the equivalent solid solution matrix. The reasons for this are the rapid accumulation of dislocation debris around the particles during the initial stages of straining. The dispersoids also are effective in producing particle strengthening via the Orowan process. In such cases the initial strength varies as the inverse particle spacing. Thus, a fine, uniform distribution of dispersoids is a highly desirable means of producing increased strength without accelerating the onset of strain localization. RSP has been used successfully to produce this type of microstructure in Al alloys[11] and in other alloy systems[7,12]. An example of these dispersoids in Al-Mn alloys is shown in Figure 2. These dispersoids are Al_6Mn [13] but a variety of other particles have been shown to exist in Al-Fe-Ce and in other alloys[11].

The size of the dispersoid is critical to the performance of these materials for several reasons. First, if the volume fraction is fixed by solubility limits or other considerations, then a uniformly small dispersoid size is necessary in order to achieve small spacings and high strengths. Second, the size of the dispersoid is related to the ease with which it can act as a site for void formation as discussed in greater detail below. Third, there is a size below which particles do not appear to act as void initiation sites. This size has been calculated to be $\sim 14\text{nm}$ [14] for the case of uniform strain distribution in the matrix. If the strain is concentrated locally due to inhomogeneous slip or because cross-slip is difficult, then this becomes an underestimate. Also, elongated particles appear to be more prone to decohesion and thus act as more frequent void nuclei. Despite the details of the calculation, it is helpful to recognize that a particle size limit exists below which the particles contribute to strength but do not act as void nuclei for ductile fracture. RSP has the potential to produce a uniform distribution of small particles and thus may be very beneficial as a means of producing dispersion hardened materials which are both strong and tough. There is another consideration regarding dispersoid size and strength. That is the existence of a minimum size below which the dispersoid is readily by-passed by local climb or cross-slip. This size is estimated to be in the range of a few nm. Particles which are smaller than this do not contribute to the flow stress. Thus, the optimum particle size range for dispersion strengthening appears to be bounded on both sides; the upper size bound is fixed by the onset of void nucleation at particles while the lower size bound is fixed by the ease of cross-slip or climb around the particles. These sizes have been subjected to calculation and within the uncertainties of these calculations because of necessary simplifying assumptions the optimum dispersoid size range lies between a few nm and tens of nm. This is indeed a fairly tightly defined range. As a result, RSP may be very useful in providing the processing control necessary to produce this.

Solid Solution Hardening

Solid solution hardening is a well-known and useful means of raising the flow stress. However, solid solution additions can also alter the deformation characteristics of the matrix. For example, in face-centered cubic materials the slip character can change from wavy to planar if solutes which reduce the stacking fault energy are added. Such solute additions not only raise the friction stress but also increase the strain hardening rate. Other solute additions can create short range order which increases the initial flow stress but tend to also cause strain localization and reduced work

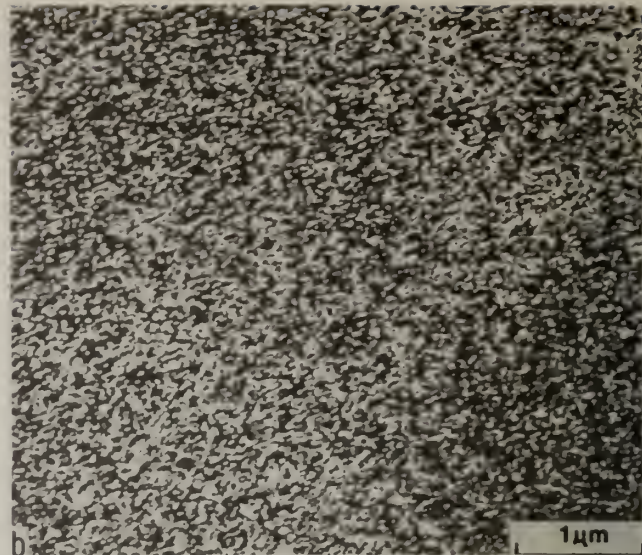


Figure 1. TEM micrographs showing fine, uniformly distributed precipitates typical of most age hardening alloys.

a) Θ'' in Al-4%Cu, bright field micrograph (photo courtesy of S. Dumolt).

b) ω -phase in Ti-12%Mo, dark field micrograph using ω -phase reflection.

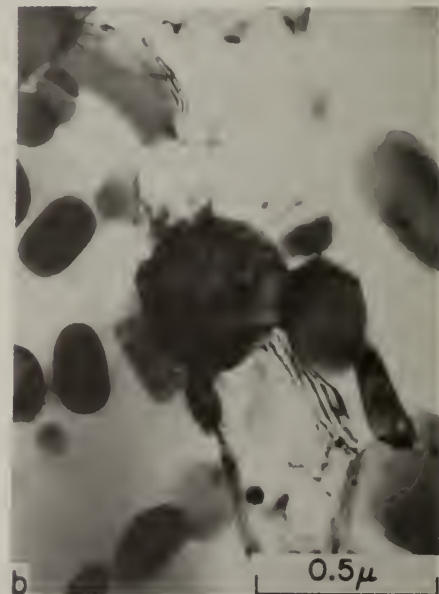


Figure 2. TEM micrographs showing Al_6Mn dispersoids which have formed in a Al-10%Mn powder metallurgy alloy (Ref. 58).

a) hot pressed at 400°C

b) hot pressed at 500°C.

hardening[6]. Thus the choice of solutes to strengthen alloys must be carefully selected if the increases in strength are to be achieved without sacrificing the ductility and toughness of the alloy. There are a number of rules regarding the strengthening contribution of solutes based on size difference, modulus difference, valence, chemical nature, etc., [cf 3,4,14] but these rules only provide insight regarding the expected change in stress. They do not consider, in any direct way, the effect of these solutes on slip character and work hardening rate. It is this latter factor which becomes important when striving for simultaneous improvements in strength and toughness.

Additivity of Strengthening Contributions

The use of two or more types of strengthening contributions is commonplace in commercial alloys. However, the methods for summing the contributions from various hardening mechanisms are not well-developed, as is mentioned later in the key issues section. On the one hand, work on dilute solid solutions containing SiO₂ particles showed that the increased friction stress due to the solid solution additions added linearly to the strengthening due to the SiO₂ particles[15]. However, as the solute concentration is increased or as solutes which affect slip character are added, the attendant creation of stronger or more intense dislocation pileups tends to alter the effectiveness of particle or boundary hardening contributions. In such cases the linear superpositioning of individual hardening contributions can lead to either an underestimate or an overestimate of the true combined strengthening.

One last example of the complexity of strengthening which cannot be dealt with analytically may be useful. Figure 3 shows the microstructure of a Ni-Al-Mo-W alloy which contains at least three distinct hardening precipitates in addition to the solid solution strengthened matrix. Figure 3(a) is a bright field electron micrograph which shows a high volume fraction of cuboidal γ' precipitates separated by a continuous matrix which shows mottled contrast. Selected area diffraction patterns, such as the one shown in Figure 3(b), show that two more ordered phases exist in addition to γ' . These have D0₂₂ and Pt₂Mo prototype structures. Dark field images of the appropriate diffraction spots (Figs. 3(c) and (d)) show that these additional phases lie in the matrix regions between the γ' particles. The point of showing this example is to illustrate the complexity which can arise in concentrated alloys. The current situation with regard to combining strengthening contributions from three coexisting types of particles is such that analysis is not currently possible. Many other examples such as this exist in practice.

In view of the foregoing brief discussion, it is clear that improved insight into the effects of multiple hardening contributions on strength must await development of improved analytically methods for combining the individual contributions. Computer simulation studies coupled with detailed calculations and carefully planned experiments are needed here. The use of RSP to produce more uniform microstructures may be helpful in this regard.

Toughness

The discussion of toughness which follows considers three central elements which affect the performance of a material with regard to toughness. These are plastic instability, ductile fracture and brittle fracture. The factors which affect each of these elements will be discussed below.

Plastic Instability

It has long been known that the condition for macroscopic necking in a tensile test is that

$$\frac{d\sigma}{d\epsilon} \geq \sigma \quad \text{Equation 1}$$

For larger strain rates both rate effects and adiabatic heating can be important and the condition for stable flow becomes[17].

$$\frac{\partial \sigma}{\partial \epsilon} \frac{d\epsilon}{\dot{\epsilon}, T} + \frac{\partial \sigma}{\partial \ln \dot{\epsilon}} \frac{d \ln \dot{\epsilon}}{T, \dot{\epsilon}} + \frac{\partial \sigma}{\partial T} \frac{dT}{\dot{\epsilon}, \epsilon} \geq \sigma d\epsilon \quad \text{Equation 2}$$

In either case, an increase in work hardening rate ($\partial \sigma / \partial \epsilon$) clearly enhances the resistance to plastic instability.

More recently, it has become known that ductile failures often occur as a consequence of plastic instability in the form of localized shear bands initiating either at the surface or in the bulk[18]. Continuum mechanics theories have been developed for the particular case of a yield surface with a

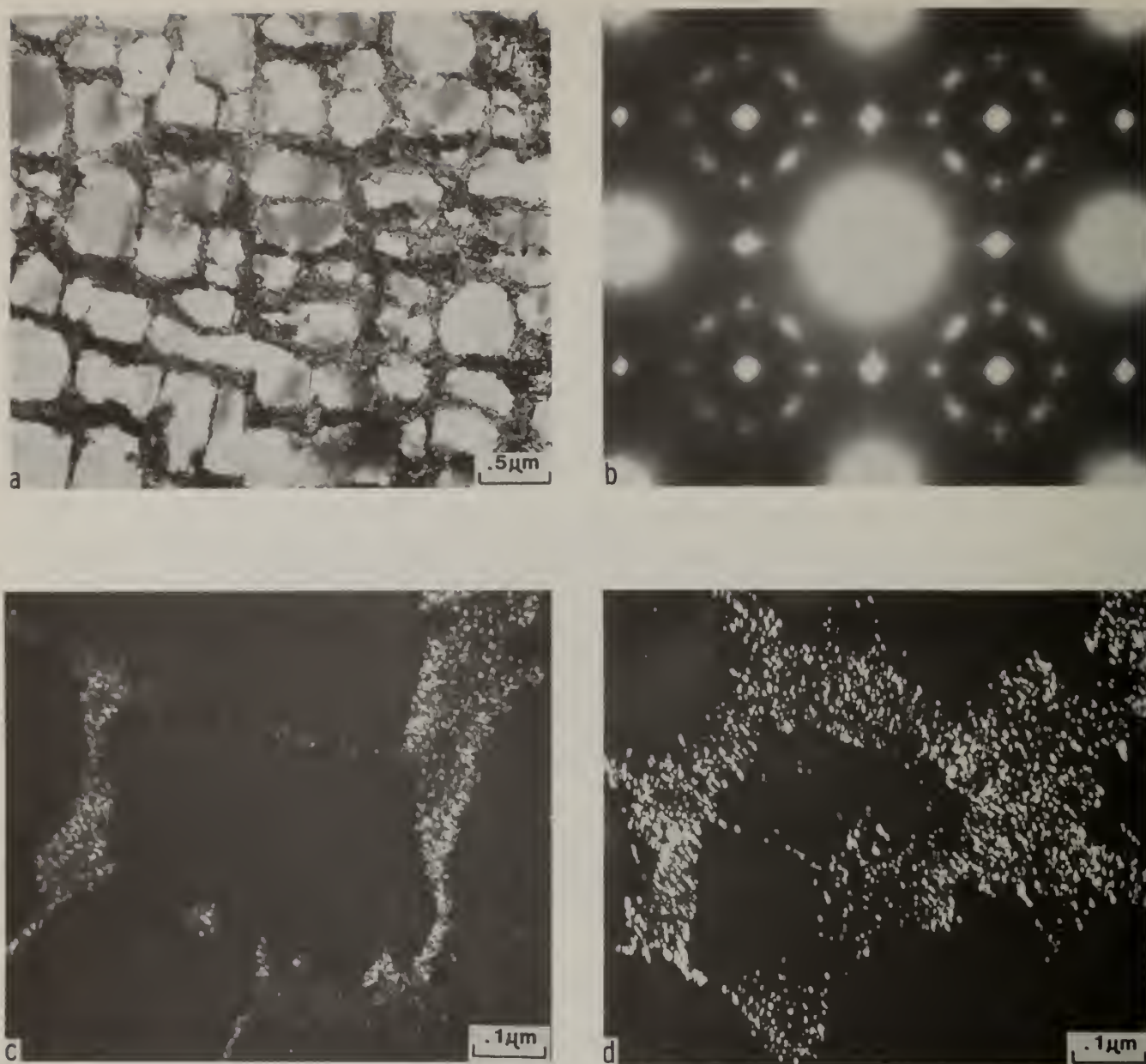


Figure 3. TEM micrographs showing the complex microstructure which exists in a Ni-Al-Mo-W alloy made from RSR powder (Ref. 59).

- a) Bright field micrograph showing large cuboidal γ' and mottled contrast in matrix regions.
- b) Selected area electron diffraction pattern showing γ , γ' , $D0_{22}$, Ni_2Mo reflections.
- c) Dark field micrograph showing Ni_3Mo ($D0_{22}$) precipitates.
- d) Dark field micrograph showing Ni_2Mo (Pt_2Mo type) precipitates.

corner[20], and these give good to fair agreement, respectively, with experiments revealing surface [19,20] or bulk[21,22] initiated instabilities. To illustrate these newer ideas, we present the critical condition for the onset of surface instability in the form of surface roughness which subsequently initiates shear bands propagating into the interior. The condition is expressed in terms of the critical strain in plane strain tension as

$$\frac{E_T}{E_S} = \epsilon^* [1 - \exp(-2\epsilon^*)] \quad \text{Equation 3}$$

where ϵ^* is the critical maximum principal strain and E_T and E_S are the tangent and secant moduli defined in Figure 4. Through the dependence on $E_T = (d\sigma/d\epsilon)$ for slow strain rate tests, again the material is stabilized against local instability by an increased work hardening rate.

Thus, so-called diffuse hardening mechanisms which tend to increase the yield or flow stress but not the work hardening rate are detrimental to ductile fracture in that they increase E_S while leaving E_T constant, thus enhancing the tendency for plastic instability. Diffuse mechanisms include solid solution hardening, precipitation hardening, and grain size hardening. Contrariwise, dispersion hardening promotes multiple slip and large work hardening[2], provided the dispersoid is impenetrable by dislocations. Hence, if impenetrable and if resistant to cracking or decohesion, dispersion hardening should increase the resistance to plastic instability. Therefore, as also mentioned in other sections of this paper, an ideal microstructure for strength and toughness should involve dispersion hardening as the primary hardening mechanism with the diffuse mechanisms as secondary ones.

Once localized shear instability ensues, the detailed mechanism of failure is not clearly understood, but failure is rapid once instability begins. Thus, avoidance of the critical condition for onset of plastic instability is the critical factor for design purposes. Failure can occur by shearing to a chisel-point fracture[23], by void formation and link-up under the influence of incompatibility stresses induced by the instability[24], or by transition from a mixed-mode I-II shear crack to an unstable Mode I brittle crack which propagates by hole growth, by cleavage, or by a mixed mechanism. Conditions which favor the onset of localized shear instability, and hence ones that should be avoided, include plane-strain plastic constraint and low work-hardening rate/yield stress ratio.

Ductile Fracture

Beginning with the early work of McClintock[25], it has become clear that the resistance to ductile fracture is improved by increasing the resistance to particle decohesion or cracking. Since either of these events leads to void growth, whether for smooth or notched specimens, ductile fracture resistance is improved when the cohesion of the particle is above a minimum value. Theories relating to particle decohesion in simple[26,27] or more complex[28,29] ways are available and have been quite successful in explaining some[30] but not all[28], experimental results. If the cohesive strength of a particle is below a certain size-dependent critical value, most of the plastic strain to failure is involved with void growth and there is not much gain in fracture toughness with an increase in cohesive strength. Above this critical value, failure is rapid once void nucleation occurs because the voids enhance shear localization and essentially limit plastic strain prior to failure. Thus, above the critical value, fracture toughness is enhanced directly by an increase in cohesive strength[31].

Once hole nucleation occurs, failure can occur by necking of the ligaments, Figure 5(a) or by shear localization between the ligaments, Figure 5(b)[16,21]. In either case, the amount of plastic work required for crack propagation is limited to a volume of the order of the void spacing, Figure 6. Hence, a decrease in void spacing should enhance toughness as is observed in fractographic correlations of dimple size and toughness. Enhanced resistance of the matrix to plastic instability should enhance toughness in the case where ligaments fail by shear localization, so the matrix properties should follow the design precepts of the previous section.

Decoherence or cracking of a particle becomes more likely for large particles[14,18,32], particle with large aspect ratios[14,18,33], and particles with low intrinsic cohesive strengths[14,31,33]. The cohesive strength for the reversible formation of a decohesive nucleus is

$$\gamma_{coh} = \gamma_{part} + \gamma_{mat} - \gamma_{int} \quad \text{Equation 4}$$

where the surface energies are expressed per unit area and γ_{part} , γ_{mat} and γ_{int} are, respectively, the particle-void, matrix-void and particle-matrix interfacial energies. Values for γ_{part} and γ_{mat} are available at high but not low temperature for some cases but values of γ_{int} are sparse. Hence, data or theory is needed before γ_{coh} can be used as a design parameter. One can crudely say that semi-

conducting particles such as carbides should have lower values of γ_{int} than insulators such as oxides, a factor which would tend to increase γ_{coh} and help resist decohesion.

There is some theoretical indication that the critical stress for decohesion should vary inversely with the square root of particle diameter[14,34]. These models are upper bounds for the stress and a more detailed theory is needed which includes the influence of slip inhomogeneity or dislocation pileups in nucleating decohesion. Nevertheless, they provide a guideline in agreement with experiment that decreasing the size of a dispersoid decreases its decohesion tendency. There is a limit roughly of the order of 10nm diameter below which the particles become effectively penetrable because dislocations can cross-slip or climb around the particles[2]. Again, a more detailed theory is needed to better define this limit.

The particle asymmetry effect is associated with increased stresses favoring decohesion arising from slip inhomogeneity and dislocation pileups. An array of edge dislocation pileups produces larger stress concentrations than a single pileup, and a large aspect ratio particle would be more likely to sustain more than one pileup along its larger dimensions.

Brittle Fracture

Some progress in understanding brittle fracture and relating it to microstructure has been achieved, beginning with the work of Ritchie, Knott and Rice[35]. These authors considered that the critical event was the spreading of a crack from a carbide at a grain boundary one or two grain diameters ahead of a crack tip to link with the main crack. A critical combination of intensified stress and carbide size (crack size) is needed, as illustrated in Figure 7, to initiate matrix cracking. The calculation has been modified recently Evans and Hutchinson[36] who consider a statistical distribution of carbide sizes (crack lengths). In both calculations, the carbides are considered to be at grain boundaries and to be precracked. Since incompatibility and pileup effects are large at boundaries, and since carbides are often larger there because of preferential grain boundary nucleation, the assumption seems plausible. The resulting prediction for the critical stress intensity for cleavage crack initiation is[36].

$$K_{IC} \propto \frac{\gamma_0^{(N+1)/4}}{Y^{(N-1)/2} r^{(N-2)/4} (fd)^{1/4}} \quad \text{Equation 5}$$

where γ_0 is the effective surface energy for crack propagation, Y is the yield stress, r is the average carbide radius, f is the volume fraction of carbides on grain boundaries, and d is the grain diameter. The factor N is the reciprocal of the work hardening coefficient n in a power law description $\sigma \propto \epsilon^n$. Typically $N > 3$ so all exponents are positive in Eq. 5.

The factors in Eq. 5 can be understood qualitatively as follows. An increase in Y shifts the stress to a larger value at a given position, Figure 7, and favors fracture. An increase in α_0 obviously represents increased resistance to cracking. An increase in r means an increase in local stress intensity at the edge of the carbide crack which favors its propagation into the matrix. An increase in f increases the probability of a large carbide at a given position and hence favors fracture. The weak dependence on d arises from the need for a number of cracks spaced at about the grain diameter along the crack tip to propagate locally to lead to overall crack advance. The model agrees well with data of Curry and Knott[37].

The above models are lower bound models in the sense that they underestimate K_{IC} if the carbide particles are not precracked as assumed. The likelihood of carbide cracking or decohesion is related to the magnitude of internal stress concentrations produced by localized slip or dislocation pileups. These factors have been considered quantitatively[38] but they can be understood in qualitative terms. Pileups should be decreased, and fracture resistance promoted, by: a decrease in grain size provided that it and not dispersions controls the wear slip path; increased stacking fault energy which promotes pileup blunting by cross-slip; a large number of available slip systems; also promoting blunting; decreased hardening by solutes or precipitates which would tend to prevent operation of secondary dislocation sources to relieve pileup stresses; decreased dispersoid spacing, which bounds pileup lengths in the dispersion hardening limit; and decreased particle size, which decreases the likelihood of decohesion or cracking in the limit for reasons already discussed. Particle shape anisotropy or greatly asymmetric grains promote pileup stress concentrations and fracture: edge dislocations formed against such asymmetric barriers interact in such a way that the pileup stress concentration is increased by a factor of d/λ , where d is the pileup length (short grain dimension) and λ is the pileup (slip band) spacing.

Another ameliorating factor for the models mentioned above is the possibility that a crack in a carbide may not propagate in a brittle manner into the matrix. At the grain size level, added energy

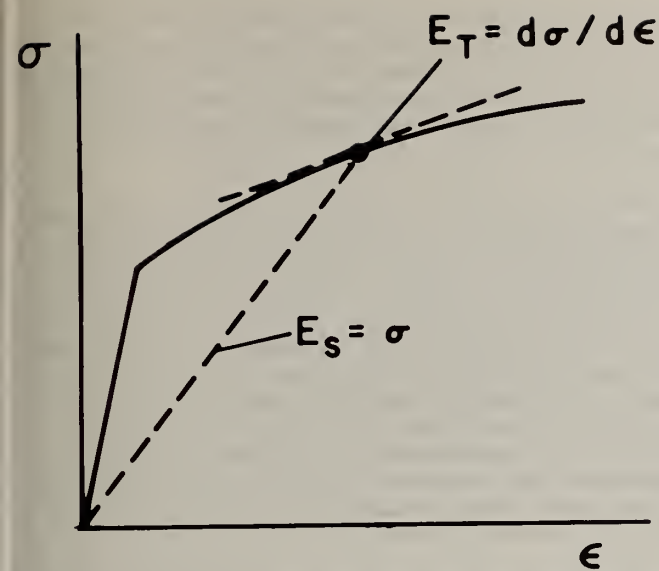


Figure 4. Schematic stress-strain curve showing tangent and secant moduli, E_T and E_s , respectively.

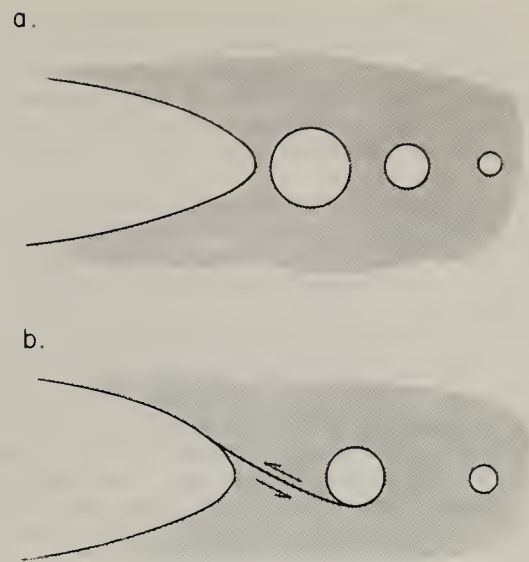


Figure 5. Schematic showing ductile fracture processes which occur in crack tip region.
a) hole formation ahead of crack tip
b) shear localization connecting holes and crack tip.

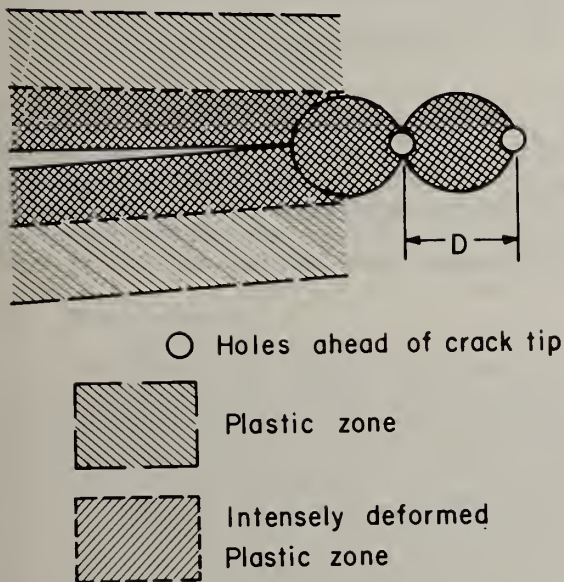


Figure 6. Schematic showing relationship between plastic zone volume and inclusion spacing, D , ahead of crack tip.

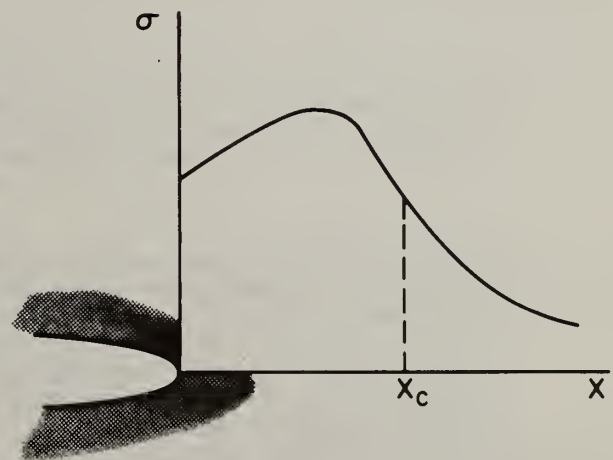


Figure 7. Schematic showing the stress distribution as a function of distance ahead of a crack tip.

must be supplied to create cleavage steps or tear ridges as the cleavage plane changes orientation upon crossing a grain boundary. At a finer scale, a microcrack in, say, a particle must propagate into the matrix locally rather than blunting. The statistics of the probability of this occurrence as a function of particle size distribution were considered by Evans and Hutchinson[36], as discussed previously. There are some other factors at the microstructural level that we now consider briefly for the case of quenched and tempered steel as an example.

The orientation relationship between austenite and ferrite is $(211)_\alpha || (001)_{cm}$; $[001]_\alpha || [100]_{cm}$, $[111]_\alpha || [010]_{cm}$ [37]. Thus, the primary cleavage plane of $(001)_{cm}$ is inclined at 35° or 66° to the 54° to the $\{100\}_\alpha$ planes. Thus, a carbide particle within a grain is not favorably oriented for propagation of a crack into ferrite. Neither are such particles favorably oriented for propagation from ferrite into carbide, a factor that could be important in crack growth. At a grain boundary, the carbides are oriented with respect to one grain to reduce surface energy. However, they are randomly oriented with respect to the second grain. Thus, some fraction of grain boundary carbides are likely to be oriented for cleavage crack propagation and grain boundary carbides can be more detrimental, but on a statistical distribution basis. If recrystallization or grain growth is imposed subsequent to carbide precipitation as in "process-annealing", the orientation relation would be lost for many of the carbides, and bulk carbides could become favorably oriented for cleavage propagation. Thus, in the brittle fracture regime one might be cautious about attributing changes in behavior to grain size changes alone if the changes were accomplished in the above manner.

Carbides have larger volumes per iron atom than the matrix and smaller thermal expansion coefficients. Thus, residual stresses in the particles from precipitation and cooling should be compressive in nature and would tend to reduce the brittle fracture tendency for radial cracks. Circumferential tensile stresses would exist though, and could promote fracture for precipitates with salient corners.

If a crack nucleus starts to grow in a particle or grain boundary, it will gain inertia. This dynamic effect would tend to promote crack propagation into the matrix, but calculations are needed to determine the magnitude of this effect. If a particle decoheres, this effect should be diminished because of the non-planar trajectory of the growing crack nucleus.

Key Issues

As mentioned previously, detailed consideration of the notion of microstructural synthesis brings into focus a number of inadequacies in our current understanding of strengthening and fracture at the fundamental level. We have elected to present these as "Key Issues" since we feel progress toward elucidating these will substantially enable true microstructural synthesis.

1. Effect of dispersion size on properties.

- a. Yield strength: Orowan theory and experiment verify that yield strength should increase as particle spacing decreases (hence as particle size decreases for a fixed volume fraction) provided the particles are impenetrable by dislocations[2]. The trend is reversed only below a particle size where dislocations can readily cross-slip or climb around particles. Rough estimates indicate that this critical size is $\sim 10\text{nm}$, but experiment and theory are needed to verify this.
- b. Ductile fracture: Since ductile fracture (initiation or stable crack growth) occurs by particle decohesion (or, less-often, particle cracking) and finer void spacings enhance Mode I (normal) or mixed Mode I-II (shear) failure[40], it has been suggested that increased interface cohesion of particles would help and that a critical size existed, below which decohesion would not occur[41]. Recent work[36] suggests that increased cohesion helps provided that the cohesion exceeds a critical value which depends on volume fraction, but otherwise that changes in cohesion have little effect in the sense that void growth tends to control fracture.

Also, the estimate of the critical size for decohesion of $\sim 14\text{nm}$ [14] is a lower bound if the local plastic strain is uniform but is an overestimate if plastic strain can be concentrated in dislocation pileups. Experiments to follow up on these ideas, some new, are called for.

- c. Brittle fracture: For years, the ductile-brittle transition has been little understood in terms of mechanism. Ritchie, Knott and Rice[35] focused attention on the possibility of a critical stress being achieved for steel at a grain diameter or so ahead of a crack where a cracked carbide particle could act as a nucleus for cleavage. Yet, many K_{IC} -T plots show an abrupt change at the

DBTT[42] and not a smooth one as predicted by the model, and estimates of the critical distance vary from 1 or 2 to 10 grain diameters[43]. Possibilities include, R-curve type crack resistance with microcracks extending over grains but not propagating further[44], the critical event then being linking of a set of these and dynamic pop-in of a crack from a particle to the matrix; or extension of pre-existing cracks at particles into single grains, with the cracks eventually linking up to form an unstable cleavage crack. Unresolved issues are the requirements to propagate a cleavage crack across a boundary where the crack orientation changes (requiring added crack surface area or linking shear zones); the local events needed for particle cracking and whether these, at the dislocation level, determine the ductile brittle transition temperature; whether microcracks exist in a zone near the crack initiation point as suggested by an R-curve-type model; and whether crack initiation indeed occurs ahead of the precracked region[45]. Also, a statistical distribution of particle sizes and strengths could mean that the critical event occurs from one to ten grain diameters ahead of a crack[36], tying the mechanics of the Ritchie et al model to a perhaps more realistic microstructural mechanism. Some of these new ideas are evidently amenable to experimental test.

2. Effects of grain size.

A decrease in grain size always increases yield strength or flow stress, an effect which is large provided that the size exceeds a critical value of $\sim 1\mu\text{m}$ where substructure becomes a more important strengthening mechanism[46]. Empirical correlations for steels also indicate that decreasing grain size is the only strengthening mechanism that also increases toughness[39]. However, this trend is also limited by the decreased work hardening rate and increased tendency for strain localization associated with it. Thus, an optimum grain size exists for a given material.

3. Dispersion hardening.

Dispersion hardening is attractive compared to other hardening mechanisms because: dispersoids pin grain boundaries and aid in achieving fine grain or substructure sizes (item 2); they provide large increases in yield or flow stress (proportional to the inverse particle spacing) while they are impenetrable and non-by-passable; and they give large values of work-hardening rate which provides resistance to plastic instability. The problems with dispersions are those mentioned in item 1, concerning their role as crack or void sources.

4. Diffuse hardening mechanisms.

Argon[47] classified as "diffuse" hardening mechanisms those which increase yield stress; do not affect slip character or $d\sigma/dT$; have little or no positive effect or a negative effect on work hardening; and as a consequence decrease the resistance to plastic instability. These include grain size hardening (item 2), solid solution hardening, and the various forms of precipitation hardening. Because of the decreased resistance to plastic instability, these mechanisms are not as attractive as primary strengthening mechanisms as they are as secondary mechanisms in conjunction with dispersion hardening. This holds true in particular for RSP materials.

5. Work hardening.

Despite the theoretical and experimental activity since the 1950's, which provide guidelines on work hardening in terms of rough average dislocation properties[48,49], we still have little knowledge of the detailed mechanism of work hardening, particularly in polycrystals or multiphase systems and at high strains.

6. J and tearing modulus as a function of yield stress.

Continuum mechanics models predict that if the critical crack opening displacement for crack nucleation and propagation is constant, that the value of J_{IC} should increase with yield strength while the value of the tearing modulus dJ/da should decrease with increasing yield strength[27,48]. There are data to support the latter effect, but some measurements indicate an inverse relation of J_{IC} and yield strength[49]. Evidently, the experiments also conflict with the mechanics prediction (which has some support in a compilation by Paris[52], although the data is so scattered that the opposite trend would be possible) that materials with large J have small dJ/da and vice-versa. This suggests a possible role of microstructure leading to a dependence of the critical crack opening displacement δ_{IC} on yield strength.

7. Additivity of strengthening mechanisms.

In the absence of detailed studies or predictions, most treatments consider that multiple mechanisms contribute linearly to strength. For the special case of point obstacles and simple dislocation line tension, the rule instead should be the square root of the sum of the squares of the individual contributions[53]. Work is clearly needed to provide better guidelines in this important subject area.

8. Dislocation mechanisms.

A major problem in complex structures in relating microstructural mechanism to macroscopic properties such as flow stress is the statistical averaging problem. To first order, single dislocation models for Orowan hardening, precipitation hardening, etc., are known. However, averaging must be done over $\sim 10^{14}$ segments, each experiencing differing resolved internal stresses arising from interactions with other segments[54]. In the absence of guidelines, simple averaging is assumed, for example in the relation of strain rate to dislocation density and dislocation velocity. Some work on a limited number of segments, but nevertheless distributed realistically in three dimensions, is needed to indicate the accuracy of the simple averaging process. To second order, more refined single dislocation calculations, using anisotropic elasticity, nonlinear inhomogeneity effects for second-phase particles, and dropping the simple line tension model, are needed to better define the force-distance curves necessary in the dislocation rate theories.

9. Limiting volume fraction of dispersoid.

Of importance in RSP alloy design is the issue of the limiting volume fraction of dispersion. Where strength alone is the dominant design criterion or where interface cohesion prevents void formation, properties improve with decreased spacing (or increased volume fraction at constant size). For particles poorly wet by the matrix in the capillarity sense, a limit should be the percolation limit of 18-25 percent, and some work on steels tends to confirm this limit[55]. On the other hand, when the particles are wet by the matrix, as for tungsten carbide in cobalt, the material has useful properties. Wettability increases with decreased surface energy of the particle-matrix interface, or, equivalently with increased interface cohesion. Work is needed to establish alloy design guidelines.

10. Plastic instability.

Some work on the initiation of plastic instability, particularly at surfaces[21] is in quite good agreement with continuum mechanics predictions of critical strains[20]. Yet hydrogen charging has been shown to drastically lower these strains (by about a factor of two)[21]. Work is needed to determine whether strong local defects such as sharp micro-notches could produce such changes in the continuum predictions, and to determine whether the role of hydrogen is to produce such defects.

11. Cyclic crack growth.

In cyclic loading, wavy slip alloys appear superior in low cycle fatigue, where crack initiation is important, but poorer in $da/dN - \Delta K$ crack growth compared to planar slip alloys. This is clearly a microstructural effect and deserves further study.

12. Transformation induced plasticity.

In a number of alloys, resistance to plastic instability is provided by martensite transformation as a function of strain. The J resistance curve does not appear to be optimized at the same conditions of strain rate, temperature and composition as the necking resistance in tension[56]. An important issue is whether martensite forms continuously during the deformation process and influences necking resistance throughout the uniform strain increment or whether it preferentially forms locally at incipient necks. In other words, is the TRIP effect a local or global one. If local, the models for transformation toughening of ceramics by Evans and Hutchinson[36] could apply as well for TRIP materials in the plastic zone at crack tips.

13. Multiaxial stress and strain effects.

Work on multiaxial stress effects is only beginning. Certainly from both a continuum and microstructural viewpoint[23], void formation and the propensity for plastic instability are influenced by hydrostatic tension. Also, the strength-differential effect reflects multiaxial stress influences. Similarly, strain path has been shown to be an important factor influencing strain to failure in sheet steel and aluminum. There is little guideline on how microstructural variables relate to these effects.

14. Design needs.

Alloy design should not be focused on a single property. The potential spectrum of property needs for given designs should be considered. In many cases secondary properties such as buckling resistance or density may be limiting. A systems approach to materials and design seems to be the optimum method for improving overall structural efficiency.

15. Other effects.

Other properties are quite important and could receive equal attention with the yield-toughness properties emphasized in the above enumeration. Environmental interactions can lead to severe degradation and could be limiting in RSP structures. Fatigue properties, particularly initiation, relate perhaps more closely to events at the crystal plasticity-microstructure level than the yield-toughness properties. Optimization of yield-toughness behavior almost certainly would not give optimum corrosion or fatigue resistance.

16. Production of precipitation hardening materials by RSP.

It is fairly clear that materials which are precipitation hardened in the absence of dispersoids or very small grains have a tendency for strain localization. They thus do not typically have particularly attractive ductility. Accordingly, if RSP is used to make materials which are precipitation hardening then it appears to be advantageous to take advantage of this technology to introduce either grain refinement or dispersoids in addition to the intrinsic precipitates which form during aging.

Conclusions

In view of the foregoing discussion we draw the following conclusions.

1. RSP has the potential to fill an important need in the area of microstructural synthesis.
2. Our ability to specify optimum microstructures is not yet fully developed but with respect to improving strength and toughness several trends can be identified as follows:
 - a. grain size and dispersion hardening are the most attractive strengthening mechanisms because they tend to increase strength and work hardening simultaneously
 - b. factors which promote strain localization and/or plastic instability must be avoided
 - c. a relatively narrow size range exists over which dispersoids can provide increased strength without impairing toughness
 - d. other strengthening mechanisms can be used as secondary means for improving strength provided their effect does not override the dispersoids with regard to plastic instability.
3. A number of areas of microstructure-property relations are presently not well-enough understood to permit microstructure design from first principles.
4. RSP can make a significant short term contribution to improving materials by providing a method for preparing more uniform, finer microstructures in conventional alloys.
5. RSP can make an even bigger long term impact on improving materials when and if we can specify optimum microstructures with more precision.

Acknowledgments

The authors gratefully acknowledge useful discussions with other members of the DARPA Materials Research Council. In particular, those with Professors Hutchinson, Evans and Budiansky, and with Dr. Jacobson, formerly of DARPA. The authors, also, acknowledge with gratitude the permission of several collaborators to cite the results of their work prior to publication. Included in the group of collaborators would be Professors Hutchinson and Evans as well as Drs. Terlinde, Martin and Paris.

References

- [1] A. Kelly and R. B. Nicholson, Progress in Matls. Science, Vol. 10, No. 3, Pergamon Press, New York, NY, 1963.
- [2] A. Kelly and R. B. Nicholson, eds., Strengthening Methods in Crystals, John Wiley, New York, NY, 1971.
- [3] Strengthening Mechanisms in Solids, ASM, Metals Park, OH, 1962.
- [4] D. Peckner, ed., The Strengthening of Metals, Reinhold, New York, NY, 1964.
- [5] S. M. Copley and J. C. Williams, in "Alloy and Microstructural Design," Tien and Ansell, eds., Academic Press, New York, NY, 1976, pp 3-63.
- [6] J. C. Williams and A. W. Thompson, "Strengthening of Metals and Alloys," in Metallurgical Treatises, Tien and Elliot, eds., TMS-AIME, Warrendale, PA, 1981, p 487. — Metallurgical
- [7] J. B. Vandersande and M. Cohen, Rapid Solidification Processing, Principles and Technologies, II, Mehrabian, Kear and Cohen, eds., Claitors Press, 1980.
- [8] C. M. Young and O. D. Sherby, Jl. Iron and Steel Inst., 211, 640 (1973).
- [9] c.f. J. C. Williams and N. E. Paton, "Transmission Electron Microscopy," in Systematic Materials Analysis, Richardson and Peterson, eds., Academic Press, New York, NY, 1978, p 408.
- [10] T. H. Sanders, Jr., Mat'ls Sci. and Engr., 43 , 247 (1980).
- [11] E. A. Starke and J. R. Pickens, This conference proceedings, 1982.
- [12] C. H. Smith and N. J. Grant, op cit.
- [13] G. T. Terlinde and J. C. Williams, to be published.
- [14] A. S. Argon and J. Im, Met. Trans., 6A, 815 (1975).
- [15] P. Haasen, Trans. Japan Inst. Met., 9 (supplement), XL(1968).
- [16] R. Ebeling and M. F. Ashby, Phil. Mag., 13, 805 (1966).
- [17] E. W. Hart, Acta Met., 15, 351 (1967).
- [18] T. B. Cox and J. R. Low, Jr., Met. Trans., 5, 1457 (1974).
- [19] J. R. Rice, Proc. 14th Int. Cong. Theor. Appl. Mech., North Holland, Delft, 1976, p 207.
- [20] J. W. Hutchinson and V. Tvergaard, Int. Jl. Mech. Sci., 22, 339 (1980).
- [21] O. A. Onyewuenyi and J. P. Hirth, Met. Trans., 14A (in press).
- [22] L. Anand and W. A. Spitzig, J. Mech. Phys. Solids, 25, 309 (1977).
- [23] J. D. Embury, Proceedings of the 1982 DARPA Materials Research Council Conference, University of Michigan, Ann Arbor, MI, 1983 (to be published).
- [24] T. Goldenberg, T. D. Lee and J. P. Hirth, Met. Trans., 9A, 1663 (1978).
- [25] F. A. McClintock, in Ductility, ASM, Metals Park, OH, 1968, p 255.
- [26] A. A. Wells, Brit. Weld. J., 10, 563 (1963).
- [27] G. T. Hahn and A. R. Rosenfield, ASTM-STP 432, A.S.T.M., Philadelphia, PA 1968, p 5.
- [28] J. P. Hirth and F. H. Froes, Met. Trans., 8A, 1165 (1977).
- [29] B. Budiansky, A. G. Evans and J. W. Hutchinson, Proceedings of the 1982 DARPA Materials Research Council Conference, University of Michigan, Ann Arbor, MI, 1983 (to be published).

- [30] C. Q. Chen and J. F. Knott, *Metal Sci.*, 15, 357 (1981).
- [31] G. T. Hahn, M. F. Kanninen and A. R. Rosenfield, *Ann. Rev. Mater. Sci.*, 2, 381 (1972); G. T. Hahn, R. G. Hoagland and A. R. Rosenfield, *Met. Trans.*, 7, 49 (1976).
- [32] A. Gangulee and J. Gurland, *Trans. TMS-AIME*, 239, 269 (1967).
- [33] A. S. Argon, J. Im and R. Safoglu, *Met. Trans.*, 6A, 825 (1975).
- [34] M. Toya, *Int. J. Fracture*, 9, 463 (1973).
- [35] R. O. Ritchie, J. F. Knott and J. R. Rice, *Jl. Mech. Phys. Solids*, 21, 395 (1973).
- [36] A. G. Evans and J. W. Hutchinson, Proceedings of the 1982 DARPA Materials Research Council Conference, University of Michigan, Ann Arbor, MI, 1983 (to be published).
- [37] D. A. Curry and J. F. Knott, *Met. Sci.*, 10, 1 (1978).
- [38] J. P. Hirth, Proceedings of the 1982 DARPA Materials Research Council Conference, University of Michigan, Ann Arbor, MI, 1983 (to be published).
- [39] W. C. Leslie, The Physical Metallurgy of Steels, McGraw-Hill, New York, NY, 1968, p 100.
- [40] V. Tvergaard, *Int. J. Fracture*, 17, 389 (1981).
- [41] G. T. Hahn, M. F. Kanninen and A. R. Rosenfield, *Ann. Rev. Mater. Sci.*, 2, 381 (1972).
- [42] R. O. Ritchie, W. L. Server and R. A. Wullaert, *Met. Trans.*, 10A, 1557 (1979).
- [43] D. A. Curry and J. F. Knott, *Metal Sci.*, 12, 511 (1978).
- [44] S. P. Rawal and J. Gurland, *Met. Trans.*, 8A, 691 (1977).
- [45] Articles by B. Budiansky, A. G. Evans, J. P. Hirth and J. W. Hutchinson, Proceedings of the 1982 DARPA Materials Research Council Conference, University of Michigan, Ann Arbor, MI, 1983 (to be published).
- [46] A. W. Thompson, Work Hardening in Tension and Fatigue, TMS-AIME, Warrendale, PA, 1977.
- [47] A. S. Argon, Proceedings of the 1982 DARPA Materials Research Council Conference, University of Michigan, Ann Arbor, MI, 1983 (to be published).
- [48] J. P. Hirth and J. Weertman, eds., Work Hardening, Gordon and Breach, New York, NY, 1968.
- [49] J. D. Embury, Strengthening Methods in Crystals, A. Kelly and R. B. Nicholson, eds., John Wiley, New York, NY, 1971, p 331.
- [50] J. R. Rice, in Mechanics of Solids, H. G. Hopkins and M. J. Sewall, eds., Pergamon Press, Oxford, England, 1982.
- [51] M. T. Miglin, I. H. Lin, J. P. Hirth and A. R. Rosenfield, *Proc. 14th National Symposium on Fracture Mech.*, A.S.T.M., Philadelphia, PA, 1983.
- [52] P. Paris, *Elastic-Plastic Fracture*, ASTM-STP 668, A.S.T.M., Philadelphia, PA, 1979, p 5.
- [53] U. F. Kocks, A. S. Argon and M. F. Ashby, *Prog. Mater. Sci.*, 19, 1 (1975).
- [54] J. P. Hirth and J. Lothe, Theory of Dislocations, John Wiley, New York, NY, 1982, p 791.
- [55] J. Gurland, in Quantitative Microscopy, R. T. DeHoff and F. N. Rhines, eds., McGraw-Hill, New York, NY, 1968, p 279.
- [56] M. Cohen, Proceedings of the 1982 DARPA Materials Research Council Conference, University of Michigan, Ann Arbor, MI, 1983 (to be published).
- [57] R. M. McMeeking and A. G. Evans, *J. Am. Ceram. Soc.*, 65, 242 (1982); B. Budiansky, J. W. Hutchinson and J. C. Lambropoulos, *Int. J. Sol. Struct.*, in press (1983).
- [58] G. T. Terlinde, H. G. Paris and J. C. Williams, submitted to *Met. Trans.*
- [59] P. L. Martin, Ph.D. Thesis, Carnegie-Mellon University, 1982.

THE EFFECT OF RAPID SOLIDIFICATION ON THE MICROSTRUCTURES AND PROPERTIES OF ALUMINUM POWDER METALLURGY ALLOYS

J.R. Pickens

Martin Marietta Laboratories
1450 South Rolling Road
Baltimore, MD 21227

and

E.A. Starke, Jr.

Department of Materials Science
University of Virginia
Charlottesville, VA

ABSTRACT

Rapid solidification (RS) applied in conjunction with powder metallurgy (P/M) can be used to improve the microstructures of alloys by refining grain and constituent particle size, increasing solubility limits, and enabling the use of alloying elements not practical by ingot metallurgy (I/M).

RS has been particularly successful in producing improved aluminum P/M alloys, resulting in materials having high room-temperature strength, high specific modulus, and improved elevated temperature properties. This paper reviews the role of the RS microstructure in determining properties such as room and elevated temperature strength, fatigue resistance, toughness, creep resistance, stiffness, and resistance to environmental attack.

I. INTRODUCTION

Rapid solidification (RS) and powder metallurgy (P/M) consolidation are presently being used in aluminum alloy development programs directed towards developing new alloys that combine high strength, fracture toughness, and corrosion resistance with improved thermal stability, reduced density, and greater stiffness. Much of this work has been reviewed recently [1,2] and subsequent research in the RS aluminum P/M field has been so extensive, that a complete state-of-the-art review is an impractical task. Consequently, these authors will not review the work of many ongoing investigations, but will describe in detail the relationships between the microstructure and properties of RS aluminum alloys based on current investigations to which they have access. Since the P/M alloys of interest for structural applications fall into three classes, i.e., high strength, low density/high modulus, and high temperature alloys, we will discuss them in these groupings.

II. HIGH-STRENGTH P/M ALUMINUM ALLOYS

The strengthening mechanisms most often employed for aluminum alloys include those associated with solid solutions, precipitates and dispersions, and grain and subgrain boundary effects [3,4]. Rapid solidification may be used to decrease the grain size, extend solid solubility, refine the intermetallic particle size, and increase chemical homogeneity. Most of the commercial high-strength P/M aluminum alloys are based on the composition of I/M 7XXX series alloys (Al-Zn-Mg-Cu) with relatively small additions of low-solubility transition elements such as Co, Fe, or Ni [2].

A representative alloy of this group that has received much attention is X7091 (nominal composition in weight percent, 6.5 Zn, 2.5 Mg, 1.5 Cu, 0.4 Co, 0.05 Fe, and 0.06 Si). Typical production procedures are as follows: A melt of the desired chemical composition is air atomized with solidification rates in the 10^5 - 10^6 °C/s range to produce irregularly shaped powder particles, sieved to obtain a desired particle-size distribution, isostatically pressed at room temperature to ~ 75% theoretical density, encapsulated in an aluminum can, evacuated at high temperature, hot pressed to 100% theoretical density, and extruded. Subsequent processing is typical of that used for I/M products.

A. Microstructure

The non-axisymmetric geometry of the extrusion die coupled with the cylindrical nature of the hot compacted P/M billet creates non-uniform metal flow during extrusion. The changing nature of flow between the edge and the center of an extruded X7091 plate is shown in Fig. 1 [5]. Metal flow at the center is similar to that which occurs during hot rolling; it gradually deviates to a pseudo-radial nature at the edge similar to that which occurs during axisymmetric extrusion. The closer spacing of the flow contours revealed by etching the short transverse section of the plate corresponds to greater strains [6]. Consequently, variations in the texture, degree of recrystallization, and grain shape are expected within the plate; Walker and Starke [5] have characterized these parameters for extruded X7091 plate.

The texture measured from the interior of the plate is represented by the pole figures in Fig. 2. The texture near the edge of the plate, Fig. 2(a) and (b), contains strong deformation (110) [111] and recrystallization (100)[001] components often observed in axisymmetric extrusions of aluminum alloys. The partial radial metal flow creates a pseudo-fiber texture indicated by a strong [111] peak in the extrusion direction and spreading of the (100) along the fiber orientation. The radial nature of the recrystallization and deformation components of texture are represented by the broken and solid lines in Fig. 2(c). Figure 2(d) contains strong deformation (100)[112] and recrystallization (100)[001] components characteristic of duplex sheet textures. The surface texture is quite different from the interior texture and this is especially true near the center of the plate. The (100) pole figure from the center surface, Fig. 3(a), has a strong deformation component spread over a wide range in the transverse direction and no recrystallization component. However, a recrystallization component is present in the (100) pole figure from the center interior, Fig. 3(b).

The absence of a strong (100)[001] recrystallization component in the surface texture, Fig. 3(a), suggests an unrecrystallized structure, and the presence of a strong (100)[001] component in the interior texture, Fig. 3(b), suggests a partially recrystallized structure. Optical metallography, Fig. 4, appears to support the x-ray results, although it is difficult to distinguish recrystallization from unrecrystallized regions in fine-grained P/M products. Apparently the higher surface temperature, resulting from die friction and large deformation strains, allows extensive dynamic recovery and the formation of a substructure that is stable during subsequent annealing operations. Conversely, the lower temperature experienced in the interior does not allow extensive dynamic recovery, and partial recrystallization occurs during solutionizing treatments. Although an inhomogeneity in grain structure does exist in the P/M product, the degree of inhomogeneity appears to be much smaller than normally found in recrystallized or partially recrystallized I/M products. A fine distribution of oxides, originating from the atomized particulate, work in conjunction with small ($< 0.4 \mu\text{m}$) dispersoids, Fig. 5, to inhibit subgrain and grain boundary migration and prevent the large grains commonly found in I/M products from developing.

The small intermetallic particles that form during solidification and fabrication of the P/M billet do not fracture or coarsen during primary processing as do the large constituent phases present in I/M products. SEM observation of bromine-etched specimens revealed a uniform distribution of dispersoids from the edge to the center of the plate, Fig. 6. Mean particle spacing measurements give no significant statistical variation in interparticle spacing. The dispersoids were identified by x-ray diffraction energy dispersive analysis as $[\text{Co,Fe}]_2\text{Al}_9$. Most dispersoids were less than $0.4 \mu\text{m}$ in diameter although some primary intermetallics, $\sim 2 \mu\text{m}$ in diameter, were uniformly distributed throughout the extruded plate. No large $\text{Al}_7\text{Cu}_2\text{Fe}$ constituents, normally found in I/M 7XXX alloys, were detected. The precipitates that form during aging are the same as those in I/M 7XXX alloys. For the T7E69 aging condition of this study (an overaged temper) the matrix precipitates are metastable η' . Equilibrium η (AlCuMgZn) precipitates are associated with subgrain and grain boundaries, Fig. 7.

Alloy X7090 is similar in composition to X7091, but is more highly alloyed with Zn, contains less Cu, and has four times the Co content (nominal composition in weight percent: 8.0 Zn, 2.5 Mg, 1.0 Cu, 1.6 Co, 0.05 Fe, 0.06 Si). The microstructures of X7090 and X7091 are compared in Fig. 8 and are basically similar, with the exception of the larger size and the larger volume fraction of cobalt-containing particles in the X7090.

B. Mechanical Properties

Tensile tests were conducted at six locations across an X7091 extrusion to evaluate the effect of the microstructural variations on tensile properties. No significant variation was detected, and the fine grain size, particle size, and lack of coarse constituents result in better combinations of tensile properties than observed for I/M 7XXX alloys in similar tempers, Table 1.

TABLE I
Average Tensile Properties of P/M X7091 and Selected I/M Alloys

Alloy	X7091- T7E69	7175- T73511	7178- T76511	7050- T76511
YS (MPa)	571	462	484	514
UTS (MPa)	658	534	554	576
RA (%)	28.6	---	---	31
Elongation	13	14	10	13

The strain-life behavior of P/M X7091 is compared to that of a conventionally processed I/M of similar composition in Fig. 9. Although cyclic deformation was very homogeneous for the P/M product, Fig. 10, no improvement in low cycle fatigue (LCF) life, normally obtained when reducing grain size [7], was observed. Careful examination of the surface of the P/M LCF specimens revealed that cracks initiated at grain boundaries, whereas they initiated at slip bands in I/M samples. The unexpectedly poor LCF behavior of the fine-grained P/M X7091 is most likely due to the presence of oxides at the grain boundaries. This has been confirmed by recent studies of Hirose and Fine [8] and Kuo and Starke [9], which will be described in more detail in the next section.

C. Microstructure and Mechanical Property Modification by ITMT

Kuo and Starke [9] and Chang and Starke [10] have recently studied the effect of microstructure and texture on the monotonic and cyclic properties of X7091-T651 rolled plate. Various structures were developed using conventional I/M, P/M, and intermediate thermal mechanical treatments (ITMT). As mentioned previously, P/M produces a finer grain structure and particle size distribution than I/M. Intermediate thermal mechanical treatments produce a recrystallized grain structure with a weak texture, compared to the unrecrystallized grain structure and sharp texture normally obtained with conventional processing. For the sake of discussion, the following designations will be used: Conventionally processed I/M (IMCP); I/M ITMT to produce a large grain size (IMIP)-L and small grain size (IMIP)-S; conventionally processed P/M (PMCP); and P/M ITMT to produce a fine, recrystallized grain structure (PMIP).

Representative microstructures are shown in Fig. 11 and the basic microstructural data obtained from the optical micrographs are summarized in Table II. Particles larger than 0.1 μm were observed on bromine-etched surfaces by SEM and were coarser in the I/M products; higher volume fractions were observed for the I/M materials, Table III. Intermediate thermal mechanical treatments generally produced a more uniform distribution of particles than their conventionally processed counterparts. The monotonic properties, which were comparable for the different products, are listed in Table IV; they generally have higher yield strengths than those observed for conventional I/M 7XXX alloys.

TABLE II

Basic Microstructural Data of the X7091 Materials

Material	$\bar{L}_L \times \bar{L}_{LT} \times \bar{L}_{ST}$ (μm)	D_{eq} (μm)	Ω_{pl-lin}	DR (%)
IMCP	170 x 61 x 20	81	0.76	20-40
IMIP-L	139 x 109 x 76	130	0.33	100
IMIP-S	11.5 x 10.7 x 9.2	13.0	0.13	100
PMCP	3.2 x 3.4 x 2.0	3.5	0.22	7
PMIP	31.2 x 30.4 x 9.6	25.9	0.53	100

 \bar{L} = mean grain intercept length

L = longitudinal direction

LT = long-transverse direction

 Ω_{pl-lin} = orientation factor of grain shape
(e.g., 0 for a sphere, 1 for a sheet)

ST = short-transverse direction

 D_{eq} = diameter of a sphere of equivalent
volume

DR = degree of recrystallization

TABLE III

Total Volume Fraction of the $(\text{Co,Fe})_2\text{Al}_9$ and Cu-rich Particles
with Sizes Larger than $0.1 \mu\text{m}$ in the X7091 Materials

	Volume Fraction (%)				
	IMCP	IMIP-L	IMIP-S	PMCP	PMIP
Transverse Plane	2.17	2.23	2.69	1.55	1.52
Longitudinal Plane	2.56	1.98	2.77	1.74	1.71
Rolling Plane	2.36	2.12	2.20	1.52	1.42
Average	2.36	2.11	2.55	1.60	1.55

TABLE IV

Mechanical Properties of the X7091 Materials

	Elastic Modulus (GPa)	Yield Strength 0.2% offset (MPa)	ELONG (%)	A_0 $\ln \frac{A_0}{A}$ (%)	Strain Hardening Exp., n	Ductility Coeff. ϵ_f' (%)	Fatigue Ductility Exp., c	Strain Hardening Exp., n'
IMCP	71	549	15.9	40	0.053	92	-0.89	0.071
IMIP-L		543	15.2	37	0.063	16	-0.62	0.075
IMIP-S		545	12.0	42	0.069	51	-0.74	0.076
PMCP		558	14.8	27	0.055	25	-0.74	0.090
PMIP		497	17.7	40	0.065	122	-0.84	0.106

The IMCP failed by transgranular shear, Fig. 12(a), and both the IMIP-L and IMIP-S failed by a mixture of transgranular and intergranular modes, Fig. 12(b) and (c). The lower ductility, highly textured PMCP material failed intergranularly, Fig. 12(d). The fracture features appeared as pulled-out flat grains, corresponding to the shape of the flattened powder particles and indicating fracture along particulate boundaries that had high oxide concentrations. The ITMT of the P/M material changed the fracture mode from intergranular to a mixed mode for the PMIP, Fig. 12(e). The recrystallization process associated with the ITMT moved the grain boundaries away from the oxides and reduced the occurrence of intergranular fracture.

As mentioned previously, reduction in grain size generally decreases strain localization and increases resistance to fatigue crack initiation (FCI) [7]. This was observed for all materials except PMCP, Fig. 13. The PMCP showed the poorest LCF life, even though it had a microstructure conducive for homogeneous deformation. The modified P/M microstructure obtained by ITMT had the best FCI resistance of the materials investigated in this study. The slip in the IMCP was retarded by coarse particle stringers, and fatigue cracks were initiated at slip band particle intersections or at particles lying along slip bands, Fig. 14(a). Fatigue cracks nucleated at slip bands and grain boundaries in the IMIP-L, Fig. 14(b), most likely due to the material's long slip distance and slip compatibility across grain boundaries. Since P/M refined grain structure and homogenized slip, FCI in PMCP was associated with other detrimental features, such as oxide clusters along particulate interfaces, Fig. 14(c). However, the ITMT moved the grain boundaries away from the oxides, and fatigue cracks were nucleated at the slip bands on free surfaces, Fig. 14(d), thus accounting for the improvement in FCI resistance.

The FCGR's of these experimental materials are shown in Fig. 15, by plots of a da/dN versus ΔK . A plateau connects the threshold and Paris regions on the FCGR curves from 10^{-9} to 10^{-8} m/cycle. The FCP resistance was found to be best for the IMCP and IMIP-L ($\Delta K_{th} \sim 3.0 \text{ MPa m}^{1/2}$), intermediate for the PMIP alloy ($\Delta K_{th} \sim 2.5 \text{ MPa m}^{1/2}$), and worst for the PMCP and IMIP-S alloys ($\Delta K_{th} \sim 2.3 \text{ MPa m}^{1/2}$). Hirose and Fine [8] reported similar results for extruded X7091 P/M. Several studies [11,12,13] have suggested that the FCGR's of aluminum alloys decrease with an increase in grain size. This is attributed to the dislocation slip being more reversible [12], to less plastic strain being accumulated [14], or to a greater degree of fatigue crack closure [15].

The ITMT of P/M X7091 produced the optimum microstructure, i.e., that which gives the best combination of mechanical properties. The important features include a small recrystallized grain structure, a fine particle distribution, a weak texture, and a low concentration of oxides at grain boundaries.

D. Properties Relating to Environmental Interactions

The RS microstructure has a beneficial effect on resistance to various types of environmental attack. Much of the improved resistance is caused by the microstructural refinement provided by RS -- finer grain size and reduced segregation. In addition, the fine dispersion of intermetallics that is made possible by RS P/M, and the dispersion of oxides accompanying P/M consolidation, can alter the morphology and the electrochemical nature of the grain boundaries, the regions at which environmental attack is likely to occur.

Little work has been performed concerning the susceptibility of RS aluminum alloys to hydrogen embrittlement (HE). Crack propagation of I/M Al-Zn-Mg alloys during SCC has been shown to heavily involve HE [16,17,18] and the HE studies performed on RS Al P/M alloys to date have been undertaken to elucidate the SCC mechanism.

Green et al. [18] were among the numerous investigators to provide evidence that SCC in Al-Zn-Mg I/M alloys involves HE. They demonstrated greater susceptibility of I/M 7075 to SCC in Mode I (tension) than in Mode III (antiplane shear, i.e., torsion) and demonstrated changes in the susceptibility when the hydrogen recombination inhibitor, As, was added to the environment. In Mode I, a triaxial stress component serves as a driving force for hydrogen to concentrate sufficiently for HE, whereas in Mode III, there is no such triaxiality and SCC is believed to proceed solely by dissolution. Consequently, they [18] interpreted these findings as evidence that HE is operating during SCC. Furthermore, they proposed that HE was more dominant than dissolution in the SCC mechanism.

Pickens et al. [19] recently used the loading mode technique for P/M X7091 in the following test solution developed by Sprowls et al. [20], referred to as chromate-inhibited brine:

0.6M NaCl + 0.02M Na₂Cr₂O₇ + 0.07M Na₂C₂H₅O₂ + HC₂H₅O₂, pH = 4.

They found results similar to those Green et al. [18] found for 7075. Figure 16 shows that time-to-failure (ttf) at a given normalized stress intensity (K_I/K_{IC} or K_{III}/K_{IIIC}) is significantly less in Mode I than in Mode III. This shows that RS Al alloy X7091 is susceptible to HE as are its conventional counterparts and furthermore, that the SCC mechanism is similar in the two-alloy types in that crack advance occurs both by dissolution and HE.

To assess the relative contributions to crack advance during SCC, Pickens et al. [19] measured the plateau crack velocity (v_p) in Mode I using double cantilever-beam specimens and a compliance calibration. They also measured crack velocity in Mode III [21] but, because the Mode III apparatus did not include a torque-angular displacement measurement system, crack velocity could not be precisely measured. However, the total crack advance measured from the Mode III SCC fracture surface (after fracture) was divided by the ttf to give the average crack velocity (v) in Mode III. Because ttf includes both initiation and propagation times, strict comparison of this velocity with v_p in Mode I cannot be done. However, v computed for a specimen loaded to 95% of K_{IIIC} , where initiation time is expected to be short, was 0.28×10^{-6} m/hr, in comparison to a v_p in Mode I of 3.3×10^{-6} m/hr. Thus, the crack advance solely attributed to dissolution (i.e., in Mode III) is an order of magnitude less than that attributed to dissolution and HE (i.e., in Mode I), which suggests that the mechanism of SCC in X7091 is heavily dependent upon crack advance by HE. Thus, microstructural features that trap hydrogen, or serve as recombination sites for H₂, should improve SCC resistance.

Pickens et al. [19] showed that resistance to SCC is enhanced by RS P/M processing and there is a lower v_p for X7091 than I/M alloy 7075 in chromate-inhibited brine, Fig. 17.

Pickens et al. [21] have also examined susceptibility to SCC of X7091 and X7090 in several tempers using double cantilever-beam (DCB) specimens in chromate-inhibited brine. The DCB specimen geometry enables measurement of the SCC threshold stress intensity (K_{ISCC}) as well as v_p . They found that susceptibility in each alloy decreases in the order: underaged temper (UT) > peak aged temper (PA) > overaged temper (OA). Figure 18 shows the v - K curves for each alloy in the UT and PA tempers. For X7090, K_{ISCC} is lower and v_p is higher in the underaged temper than in the peak aged temper, demonstrating greater susceptibility in the UT. Several specimens showed double plateaus which may be caused by corrosion product wedging or may reflect a change in fracture mechanism in different stress intensity regimes. No cracking was observed in the OA tempers for X7090 (T7E71) or X7091 (T7E69). This is significant because each alloy affords a major strength advantage (~100 MPa for X7091, greater for X7090) over comparable 7XXX I/M alloys in the SCC resistant temper (e.g., 7075T73). The stress-corrosion fracture path in both X7090 and X7091 was found to be largely intergranular (Fig. 19) in this work [21] although Swanson et al. [22] have observed transgranular SCC in X7090.

Free Mg has been shown to segregate on the GBs of Al-Zn-Mg I/M alloys [24,25] during solution heat treatment. Viswanadham et al. [26] proposed that this free Mg serves as a means of concentrating hydrogen by forming a Mg-H complex and thereby playing an important role in the SCC mechanism. Pickens et al. [27] found that on high-purity Al-Zn-Mg I/M alloys, this Mg segregation generally decreases with aging time, which is consistent with the decrease in SCC susceptibility found by Speidel [23] on Al-Zn-Mg-Cu alloys. Furthermore, Pickens et al. [27] proposed that the decrease in SCC susceptibility with aging time may in part be caused by the decreasing trend in Mg segregation.

Figure 20 is an Auger depth profile of an X7090 specimen fractured under ultra-high vacuum at 35°C after pre-exposure to liquid gallium (Ga_l) to induce intergranular failure [28]. The Auger beam spreads over many GBs and collects information from GB precipitates and elemental segregants on the GB. Extreme Mg segregation is observed that is much greater than the Zn segregation, and no Cu segregation was found, which indicates that much of the Mg is not bound in precipitates but exists freely. This is also similar to the relative concentrations of Mg and Zn segregation found on I/M grain boundaries [24].

Other studies [28-29], which used the aforementioned Auger technique, measured GB segregation of Mg for I/M 7175 and RS P/M X7091 extruded bar. The magnesium-to-aluminum peak-to-peak height ratio from the Auger spectra (Mg/Al) was used as a measure of GB segregation. Mg/Al was significantly lower for the RS P/M alloys as shown in Table V. Thus, RS P/M processing decreases GB segregation of Mg, which probably is largely caused by the finer grain size in the RS P/M alloy. The X7091 has a nearly equiaxed grain size of $2.0 \times 1.6 \times 1.6 \mu\text{m}$ in the L, LT, and ST

directions, respectively, compared with $\sim 170 \times 17 \times 16 \mu\text{m}$ grain size in the I/M 7175. Therefore, the RS P/M alloy has much greater GB area competing for segregants.

TABLE V

Grain Boundary Composition Measured By Auger Electron Spectroscopy of LT Specimens Fractured Intergranularly at 35°C, Under Ultra-High Vacuum after Pre-Exposure to Liquid Gallium

<u>Alloy</u>	<u>Temper</u>	<u>Mg/Al</u>
7175	T6	1.9 1.5
X7091	T6E192 + 1hr at 157°C	0.24 0.33
X7090	T6511	0.33

A study of SCC initiation in X7091 and I/M 7075 revealed that the surface oxide films -- an alloy's first defense against environmental attack -- are similar in composition and thickness for each alloy [19]. The "thermal" films that form during solution heat treatment of each alloy are magnesia and are 600Å thick, whereas the "natural" films that form after polishing are alumina and are 50Å thick [29]. Therefore, RS does not alter the composition and thickness of the protective surface oxide film. However, RS does eliminate the coarse iron-containing constituent particles that are present in I/M 7XXX alloys; much of the iron goes into the $[\text{Co,Fe}]_2\text{Al}_9$ particles. Figure 21 shows a polished, unstressed I/M 7075 specimen that was exposed to distilled water, a mild SCC environment. Attack is apparent at the constituent/matrix boundary, indicating that these particles serve as SCC initiation sites.

Lyle et al. [30] speculated that the presence of oxides in the RS P/M microstructure decreases SCC susceptibility by changing the electrochemical nature of the GBs. Figure 22 shows a specimen of X7091 that was solutionized and water quenched to reveal the oxides. They clearly serve to pin GBs, thereby refining grain size, and also make the GB surface more irregular, causing an intergranular SCC path to be more circuitous.

A major benefit of RS is that fine dispersions of low-solubility alloying elements can be achieved that are not practical by I/M because these additions segregate coarsely using conventional solidification rates. Cobalt, one such addition, has been particularly successful and was suspected early in RS P/M aluminum alloy development of enhancing SCC resistance [31]. Otto [32] subsequently provided strong evidence of its beneficial effect. Christodoulou et al. [33] studied the mechanism of SCC in X7091-type alloys containing 0, 0.4, and 0.8 wt% Co and having similar compositions and grain sizes. When bolt-loaded and precracked DCB specimens were alternately immersed in chromate-inhibited brine, SCC susceptibility clearly decreased with Co content (see Fig. 23). Both K_{ISCC} and v_p reflect this trend. To understand the mechanism by which Co decreases SCC susceptibility, a specimen of X7091 (0.4 wt% Co) was pre-exposed to salt water at room temperature for 30 min. Attack occurred in the region adjacent to the Co_2Al_9 particles (see Fig. 24), suggesting that the Co_2Al_9 is cathodic with respect to the grain boundary region. This could have a beneficial effect on SCC resistance because this galvanic action could serve to blunt a propagation SCC crack. Furthermore, these cathodic particles may serve as sites for hydrogen recombination, thereby catalyzing hydrogen egress from the alloy during stress-corrosion. This possibility is currently being explored.

Liquid metal embrittlement (LME) is a type of environmental attack studied as much for its insights into mechanisms of bonding and fracture, as for its prevention. The susceptibilities to LME of RS P/M alloys X7091 and I/M 7175, aged to similar strengths, were compared in liquid mercury (Hg_L) and in a liquid mercury - 1.5 at% gallium solution ($\text{Hg} + 1.5 \text{ Ga}_L$) [29]. Specimens were wetted by placing a 2-ml drop of liquid metal on top of a HF layer used to remove the surface oxide films. It was quite apparent that the RS alloy was more difficult to wet. The specimens were fractured in tension at 25°C, 5 or 60 minutes after wetting, at a constant cross-head speed of 0.084 cm/min. All specimens fractured with no measureable ductility, so the decrease in fracture stress is the sole means of assessing susceptibility to LME.

The X7091 was less susceptible to LME in each environment (see Table VI). In addition, susceptibility was generally greater with ($\text{Hg} + 1.5 \text{ Ga}_L$) because of gallium's well-known ability

to penetrate and weaken aluminum grain boundaries [34,35,36]. With Hg_L , susceptibility did not vary significantly with pretest exposure time (t_p) for X7091, but it did increase greatly for 7175. Fracture under the influence of Hg_L , $(Hg + 1.5Ga)_L$, or Ga_L (Fig. 25) was invariably intergranular. Fractographic studies revealed that Hg_L dissolves the grain boundary region, particularly the precipitates on the boundaries, so a GB corrosion reaction occurs simultaneously with adsorption-LME*. Furthermore, the greater GB segregation (Table V) in I/M 7175 than in RS P/M X7091 leads to greater corrosion by the Hg_L . Nevertheless, the susceptibility to adsorption-LME is also greater in the I/M 7175, which is consistent with the observations of Ichinose and Oouchi [37] who found that susceptibility to adsorption-LME generally decreases with decreasing grain size.

TABLE VI

Effect of Pretest Exposure Time (t_p) and Liquid Metal Environment on Fracture Stress, σ_F , at 25°C (LT Orientation) for an RS and a Conventional Aluminum Alloy [29]

Alloy	Heat Treatment	t_p (min)	Liquid Metal	Fracture stress, σ_F (MPa + standard deviation)
X7091	Peak hardness [29]	--	None	586
X7091	Peak hardness	5	Hg	135 \pm 13
X7091	Peak hardness	60	Hg	131 \pm 20
X7091	Peak hardness	5	Hg + 1.5 Ga	119 \pm 12
X7091	Peak hardness	60	Hg + 1.5 Ga	94 \pm 25
7175	T6	--	None	545
7175	T6	5	Hg	80 \pm 15
7175	T6	60	Hg	15 \pm 9
7175	T6	5	Hg + 1.5 Ga	68 \pm 17
7175	T6	60	Hg + 1.5 Ga	22 \pm 6

Thus, RS for aluminum alloys generally decreases susceptibility to a variety of environmental effects ranging from SCC-hydrogen embrittlement to liquid metal embrittlement. The improvement offered by RS often is caused by the refinement of grain size, but also is affected by the reduced segregation and unique dispersions made possible by RS and P/M consolidation.

III. LOW DENSITY, HIGH MODULUS P/M ALUMINUM ALLOYS

Lithium is the lightest metallic element and, with the exception of beryllium, which has manufacturing and health-related problems, is the only metal that improves both the modulus and density when alloyed with aluminum, Fig. 26. Each wt% lithium added to an aluminum alloy reduces the density approximately 3% and increases the elastic modulus approximately 6%, for lithium additions up to 4% [38]. Moreover, Al-Li alloys containing more than about 2 wt% Li can be age-hardened due to the precipitation of the metastable, coherent, and ordered δ' (Al_3Li) phase [39]. However, upon plastic deformation these Al_3Li precipitates are sheared by glide dislocations resulting in strain localization and concomitant fracture at low macroscopic strains [40]. Consequently, research on Al-Li alloys has focused on improving tensile ductility and fracture toughness [41].

* Adsorption-LME is the decrease in fracture stress or strain of a solid metal that occurs during its fracture in a liquid metal environment, without the requirement of diffusion or strong chemical interaction between the two metals.

Previous studies have shown that strain localization due to shearing of coherent precipitates can be reduced by decreasing the grain size and by adding small incoherent dispersoids [42]. The development of Al-Li alloys using rapid solidification and powder metallurgy processing is considered a promising approach for achieving a smaller grain size and high-volume fraction of small dispersoids when compared with conventional ingot metallurgy [43]. Many compositions have been examined [44]; however, those containing large amounts of dispersoid-forming elements have not produced the desired ductility.

The most promising alloys are based on the Al-Li-Cu system. Copper has been shown to be very effective in increasing the strength of Al-Li alloys. The main strengthening precipitates that form during aging of Al-Li-Cu alloys containing 2-3% Li and 2-3% Cu are δ' (Al_3Li), T_1 (Al_2CuLi), and θ' (Al_2Cu) [45]. The T_1 and θ' precipitates have interfacial strains that may aid in homogenizing deformation. The equilibrium precipitates T_2 (Al_6CuLi_3) and δ (AlLi) may also form during aging [46,47]. A composition of Al-3Li-2Cu-0.2Zr was selected in a recent alloy development program [44,48]. Three percent lithium was chosen to maximize the modulus and density effects and eliminate the fabrication problems associated with higher lithium-content alloys. Two percent copper prior to aging, which approaches the solubility that can be obtained in an Al-3Li alloy, was selected for strength considerations. Zirconium was added to inhibit recrystallization. A comparison of the tensile properties of this alloy produced by three methods--I/M, P/M-splat, and P/M-atomized--is given in Table VII. Although the strength-ductility relationship is considerably better than observed for Al-Li binary alloys [49], it is still somewhat below that desired for commercial utilization.

TABLE VII

Comparison of Tensile Properties of I/M, P/M-Splat, and P/M-Atomized Al-3Li-2Cu-0.2Zr Alloy Artificially Aged to Peak Strength

Alloy	Yield Strength, 0.2% offset	Tensile Strength, σ_{uts} (MPa)	Strain to Fracture, ϵ_f (%)
I/M	503	561	4.0
P/M-splat	490	546	4.2
P/M-atomized	443	562	7.3

The low ductility of this alloy was due to strain localization in the precipitate-free zones (PFZ's) along the subgrain boundaries. The unrecrystallized structure has equiaxed subgrains that develop during hot deformation. Preferential precipitation occurs along the subgrain boundaries resulting in the PFZ's, Fig. 27(a). The PFZ's are much weaker than the matrix and many are favorably oriented for slip. Deformation concentrates in these regions and low ductility ensues, Fig. 27(b).

Attempts were made to harden the PFZ by solid solution strengthening and additional precipitation, and to minimize subgrain boundary precipitation by alloy modification and TMT's [44]. Because magnesium is a potent solid solution strengthener in aluminum, it was selected as an additive and one of the alloys had the nominal composition Al-3Cu-2Li-1Mg-0.2Zr. The age-hardened microstructure of this alloy is very complex and contains T_1 (Al_2CuLi)-, δ' (Al_2CuMg)-, and Al_2MgLi -strengthening precipitates [50]. Some δ' (Al_3Li) may also form; however, due to the presence of Al_3Zr , it is difficult to detect [48].

Although the equilibrium T_2 and S phases were detected on the boundaries of the elongated unrecrystallized grains, no preferential precipitation and associated PFZ's were observed at subgrain boundaries in TMT-processed material, Fig. 28. The strength/ductility relationship of this alloy, Fig. 29, exceeds that of I/M 7075-T76. The high ductility is associated with homogeneous deformation and a transgranular fracture mode as shown in the TEM's (Fig. 30) from recent high-voltage electron microscope (HVEM) in situ deformation studies [51].

IV. HIGH-TEMPERATURE P/M ALUMINUM ALLOYS

In the 1950's, attempts were made to produce an aluminum alloy that would be stable at high temperatures by utilizing sintered alloy powder, SAP, containing a high concentration of fine oxide particles [52,53]. Although this product was stable to $\sim 800^\circ \text{K}$, it had limited room-temperature strength, poor reproducibility of mechanical properties, and a tendency toward embrittlement during sustained loading at elevated temperatures [54]. The common aluminum alloys currently being used by the aircraft industry for high-temperature applications are based on the Al-Cu system and include 2219 (Al-Cu-Mn) and 2618 (Al-Cu-Mg-Fe-Ni). The transition elements form intermetallic phases that are stable at elevated temperatures and hinder grain-boundary sliding. However, both alloys derive their strength from coherent and partially coherent intermediate precipitates that coarsen rapidly and transform to equilibrium precipitates at temperatures above 450°K . The rate of coarsening is controlled either by atom transfer across the precipitate/matrix interface, or by volume or bulk diffusion. Low values of interfacial energy, solid solubility, and solute diffusivity are desirable for low coarsening rates [55,56].

The solid solubility and diffusion parameters for a selected number of binary additions to aluminum are given in Table VIII. The alloying elements normally used for precipitation hardening, i.e., Cu, Mg, and Zn, have high solubilities and diffusion rates. However, the dispersoid-forming transition elements and the rare earth Ce have low solubilities and low diffusion rates. A high-volume fraction of small dispersoids formed by these additions can give adequate high-temperature strength. The dispersoids can also slow down all three contributors to steady-state creep; grain boundary sliding, diffusional or "Nabarro-Herring" creep, and dislocation creep [57]. Large additions of the transition elements can significantly increase the elastic modulus of aluminum, Fig. 26(a), making the dispersion-hardened alloys especially attractive for stiffness-critical high-temperature applications. Unfortunately, the limited solid solubility makes it impossible to obtain a fine dispersion of closely spaced incoherent particles using normal ingot-casting procedures. The inherently slow ingot solidification rates enhance the precipitation of coarse particles that lower ductility and fracture toughness values.

TABLE VIII.

Diffusion Parameters and Solid Solubilities of Binary Additions to Aluminum*

Solute	Maximum Solid Solubility (wt%)	Diffusion Coefficient, D_0 (cm^2/s)	Activation Energy (k cal/g atom)
Ce	<0.05	1.9×10^{-6}	26.6
Co	<0.02	1.1×10^{-6}	19.9
Cr	0.72	3.01×10^{-7}	15.4
Cu	5.70	0.15	30.2
Fe	0.05	4.1×10^{-9}	13.9
Mg	17.4	0.12	28.6
Mn	1.4	0.22	28.8
Ni	0.05	2.9×10^{-8}	15.7
Ti	0.24	5×10^{-7}	25.8
V	0.37	6.05×10^{-7}	19.6
Zn	82.2	11.6	27.8

* Data from Hansen, 1958 and Bishop and Fletcher, 1972.

Rapid solidification and P/M consolidation are currently being used in aluminum-alloy development programs aimed at producing elevated temperature properties competitive with those of titanium [58,59,60]. Solute element additions having high liquid solubility, low solid solubility, and low diffusion rates are being used either individually or in combination. These include Co, Fe, Ni, Ce, and Cr. Although strengthening theory predicts an increase in strength with decreasing interparticle spacing, and therefore with volume fraction (V_f) for a constant

particle size, ductility also decreases with V_f thereby placing restrictions on solute concentrations. Argon and Im [61] have shown that when the volume fraction of particles approaches some critical value, interaction effects come into play and interfacial stresses are enhanced due to overlap of the plastic zones around the particles. This results in interface separation at very low strains [62].

The principal characteristics that dominate the microstructure and properties of dispersion-hardened aluminum alloys fabricated from rapidly solidified particulate arise from the size distribution of the particulate and the quality of the interparticulate bonding. A typical microstructure of an Al-Fe-Ni-Co splat-quenched flake is shown in Fig. 31 [63], and contains both coarse and fine precipitates analogous to the microstructure of RS Al-Fe alloys studied by Jones [64]. Jones suggested that the amount of coarse precipitates could be reduced by increasing the solidification rates and/or reducing the solute concentration. Although the bimodal structure normally exists within one splat particle, the relative amounts of coarse and fine structure depend on the splat particulate size. A larger amount of the coarse dispersoids appear in the large particulates because they have a lower degree of undercooling during solidification. Since a range of particulate sizes are used for consolidation, the finished product contains a bimodal particle-size distribution similar to those shown in Fig. 32 for Al-Fe-Ni-Co extruded plate.

The fine structure occupied approximately 95% of the volume of the alloys studied by Mullins [63] and appeared to control the flow stress. Although the yield strength could be correlated with the interparticle spacing of the small particle regions, Fig. 33, no one-to-one relationship existed with calculated values using the Orowan equation. This is probably due to the additional strength contribution associated with the high dislocation densities introduced during compaction and primary processing of the wrought product. Nondeformable dispersoids generate a large number of geometrically necessary dislocations [57], which contribute to the strength when the final product is unrecrystallized, as for the case described here. The coarse structure occupied less than 5% of the extruded plate but most likely controlled the ductility. Cracks were first formed at the large particles, Fig. 34, and final fracture occurred by the coalescence of microvoids associated with the dispersoids. Other research has also shown that even when small particles far outnumber large ones, the larger particles crack first and at lower strains than the smaller particles [65,66]. The difference in strength-ductility relationship of the two alloys of Fig. 34 may be related to more large particles in the higher solute alloy.

As mentioned earlier, Jones suggested that the formation of coarse particles may be suppressed by increasing the degree of undercooling. Because this often is impractical, other approaches must be taken. It is well known that multiple alloy additions can affect precipitation in many aluminum systems [67]. In certain cases, compositional modification can increase the nucleation rate and decrease both the size and coarsening rates of the precipitates, probably by altering interfacial energies and diffusion processes. This has been accomplished for the Al-Fe alloys by additions of Ce. Rapidly solidified Al-Fe binary alloys have microstructures containing both coarse and fine dispersoids [64] similar to those shown in Fig. 31. The coarse precipitates are absent in Al-Fe-Ce alloys, Fig. 35 [68].

Al-8Fe-3.4Ce is a new aluminum alloy that shows promise for high-temperature applications [68]. Figure 36 compares its yield strength at various temperatures with the program goal and the currently used high-temperature alloy 2219-T851. The decrease in strength with temperature is related to both recovery and coarsening processes and occurs at a lower rate than that for 2219-T851 at temperatures up to 505°K. The real advantage of the dispersoid-strengthened material, however, is in its creep resistance, Fig. 37. Note that the creep rate of age-hardened 2219 and 2124 increases rapidly with time, whereas that of the Al-8Fe-3.4Ce alloy seems to level off. The accelerated creep of 2219 and 2124 is associated with extensive overaging that occurs at 505°K. However, coarsening of the dispersoid-strengthened Al-8Fe-3.4Ce alloy is unlikely at 505°K and the initial creep strain is probably associated with recovery processes. Once these are complete, additional creep strain is minimal.

This study clearly demonstrates the feasibility of producing aluminum alloys with usable mechanical properties and creep resistance in the 505-615°K range. However, more work needs to be directed toward improving ductility. The elongation to failure at room temperature is 5% for the Al-Fe-Ce alloy. Argon and Im [61] suggest that some improvement may be obtained by controlled deformation processing, i.e., keeping the increments of strain between annealing operations below the critical strain for dispersoid fracture and interface separation.

V. SUMMARY AND CONCLUSIONS

Rapid solidification combined with powder metallurgy consolidation enables the production of aluminum alloys which often have superior mechanical and corrosion properties with respect to conventional ingot metallurgy alloys. The alloys developed for elevated temperature service have perhaps the greatest advantages over conventional alloys. The superior properties result from increased alloying limits, microstructural refinement of grain and constituent particle sizes, reduced harmful segregation effects, and the ability to finely disperse intermetallic phases and oxides in RS P/M alloys. These unique abilities of RS P/M allow the alloy designer to combine various microstructural improvements to tailor an alloy to specific requirements. As a result, alloy development efforts have been successfully producing promising alloys for applications requiring high room-temperature strength, high modulus and low density, and improved elevated temperature properties.

ACKNOWLEDGEMENTS

Much of the data discussed was generated in projects supported by the following government agencies: AFOSR, ARO, DARPA, and NSF. The authors are grateful to G. Hildeman, R.E. Sanders, M.J. Koczak, R.E. Crooks, V.W.C. Kuo, J.A. Walker, J.W. Mullins, J.A.S. Green and especially L. Christodoulou for providing information described in this paper.

- [1] Pickens, J.R. (1981) *J. Mater. Sci.* 16, 1437-1457.
- [2] Tietz, T.E. and Palmer, I.G. (1981) "Advanced P/M Aluminum Alloys" to be published in *Proc. 1981 ASM Mater. Sci. Sem., Advances in Powder Metallurgy*, Oct 1981, Louisville, KY.
- [3] Starke, E.A., Jr. (1977) *Mater. Sci. Eng.* 29, p. 99.
- [4] Starke, E.A., Jr. (1982) "The Application of the Fundamentals of Strengthening to the Design of New Aluminum Alloys," in *Proc. 6th Int. Conf. on the Strength of Metals and Alloys*, Melbourne, Australia, Aug. 1982.
- [5] Walker, J.A. and Starke, E.A., Jr. (1982) "The Microstructure and Properties of an Extruded P/M X7091 Plate," (submitted to *Powder Metallurgy*).
- [6] Pearson, C. and Parkins, R. (1960) in *The Extrusion of Metals*, New York: John Wiley and Sons, Inc.
- [7] Starke, E.A., Jr. and Lutjering, G. (1979) in *Fatigue and Microstructure*, M. Meshue, ed., Metals Park, OH: ASM, p. 205.
- [8] Hirose, S. and Fine, M. (1982) "Fatigue Crack Initiation and Propagation in High Strength Aluminum P/M Alloys," *Metall. Trans.*, A (in press).
- [9] Kuo, Victor W.C. and Starke, E.A., Jr. (1982) "The Effect of ITMT's and P/M Processing on the Microstructure and Mechanical Properties of X7091 Alloy", *Metall. Trans.*, A (in press).
- [10] Chang, H. and Starke, E.A., Jr., "Effect of an Intermediate Thermal Mechanical Treatment on Fatigue Properties of I/M X7091 Aluminum Alloy," paper presented at the Fall Meeting of The Metallurgical Society of AIME, St. Louis, MO, 25 Oct. 1982 (to be published).
- [11] Sanders, R.E., Jr. and Starke, E.A., Jr. (1978) *Metall. Trans.*, A, 9A, p. 1087.
- [12] Lindigkeit, J., Terlinde, G., Gysler, A., and Lutjering, G. (1979) *Acta Metall.* 27, p.1717.
- [13] Fine, M.E. (1980) *Metall. Trans.*, A, 11A, p. 365.
- [14] Chakraborty, S. (1979) in *Fatigue of Engineering Materials and Structures*, Vol. 2, p. 331.
- [15] Beevers, C.J. (1981) in *Proc. Int. Symp. on Fatigue Thresholds*, Vol. 1, no. 17, arranged by the Aeronautical Res. Inst. of Sweden and the Swedish Plastics and Rubber Inst., Stockholm, Sweden.
- [16] Gruhl, W. (1963) *Z. Metallkd.* 54, p. 86.
- [17] Scamans, G.M., Alani, R., and Swann, P.R. (1976) "Pre-exposure Embrittlement and Stress Corrosion Failure in Al-Zn-Mg Alloys," *Corros. Sci.* 16 (7), p.443.
- [18] Green, J.A.S., Hayden, H.W., and Montague, W.G. (1976) "The Influence of Loading Mode on the Stress Corrosion Susceptibility of Various Alloy/Environment Systems," in *Effect of Hydrogen on Behavior of Materials*, A.W. Thompson and I.M. Bernstein, eds., p.200, Philadelphia, PA: AIME
- [19] Pickens, J.R., Gordon, J.R., and Christodoulou, L. (1982) "Stress-Corrosion Cracking and Hydrogen Embrittlement in P/M X7091 and I/M 7075" in *High Performance Aluminum Powder Metallurgy*, M.J. Koczak and G.J. Hildeman, eds., Warrendale, PA: TMS AIME.
- [20] Sprowls, D.O., Shumaker, M.B., Coursen, J.W., and Walsh, J.D. (1973) Evaluations of Stress Corrosion Cracking Susceptibility Using Fracture Mechanics Techniques," Alcoa Technical Center, Pittsburgh, PA, Final Report, Part I, Contract No. NAS 8-21487, for George C. Marshall Space Flight Center.
- [21] Pickens, J.R., Christodoulou, L., and Gordon, J.R. (1983) Martin Marietta Labs., Baltimore, MD, to be published.
- [22] Swanson, R.E., Bernstein, I.M., and Thompson, A.W. (1982) "Environmental Embrittlement of a High Strength P/M Al Alloy" in *High Performance Aluminum Powder Metallurgy*, M.J. Koczak and G.J. Hildeman, eds., Warrendale, PA: TMS-AIME.
- [23] Speidel, M.O. (1971) in *The Theory of Stress Corrosion Cracking in Alloys*, J.C. Scully, ed., Brussels: NATO, p. 289.
- [24] Green, J.A.S., Viswanadham, R.K., Sun, T.S., and Montague, W.G. (1977) in *Corros./77, Int. Corros. Forum*, Paper 17, p. 71/1, San Francisco, CA: Natl. Assoc. Corros. Eng.
- [25] Sun, T.S., Chen, J.M., Viswanadham, R.K., and Green, J.A.S. (1977) *Appl. Phys. Lett.*, 31 (9), p. 580.
- [26] Viswanadham, R.K., Sun T.S., and Green, J.A.S. (1980) "Grain Boundary Segregation in Al-Zn-Mg Alloys -- Implications to Stress Corrosion Cracking," *Metall. Trans.*, A, 11A, p.85.
- [27] Pickens, J.R., Davis, G.D., Christodoulou, L., Green, J.A.S. (1983) Martin Marietta Labs, Baltimore, MD, to be published.
- [28] Pickens, J.R., Davis, G.D., Christodoulou, L. (1983) Martin Marietta Labs, Baltimore, MD, unpublished research.
- [29] Pickens, J.R., Precht, W., and Westwood, A.R.C. (1982) "Embrittlement of P/M X7091 and I/M 7175 Aluminum Alloys by Mercury Solutions" accepted for publication in *J. Mater. Sci.*
- [30] Lyle, J.P. and Cebulak, W.S. (1975) *Metall. Trans.*, A, 6A, 685-699.
- [31] Haar, A.P. (1965) Final Report on Contract DA-36-034-ORD-3559 RD, 20 Dec. 1965.
- [32] Otto, W.L., Jr. (1976) report #AFML-TR-76-60, May 1976.
- [33] Christodoulou, L., Pickens, J.R., and Gordon, J.R. (1983) Martin Marietta Labs, Baltimore, MD, to be published.

- [34] Roques-Carmes, C., Aucouturier, M., Lacombe, P. (1973) *Met. Sci. J.*, 7, 128-132.
- [35] Goggin, W.R. and Moberly, J.W. (1966) *ASM Trans. Q.* 59, p. 315.
- [36] Preece, C.M., and Westwood, A.R.C. (1969) *Trans. ASM* 62, 418-424.
- [37] Ichinose, H. and Oouchi, C. (1968) *Trans. Jpn. Inst. Met.* 9 (1), 41-47.
- [38] Sankaran, K.K. and Grant, N.J. (1981) in Aluminum Lithium Alloys, T.H. Sanders, Jr. and E.A. Starke, Jr., eds., Warrendale, PA: AIME, p. 205.
- [39] Gysler, A., Crooks A.R., and Starke, E.A., Jr. (1982) "Correlation Between Microstructure and Mechanical Properties of Al-Li-Z Alloys" in Proc. of 7th Int. Light Metals Congress, Leoben, Vienna, p. 50.
- [40] Starke, E.A., Jr., Sanders, T.H., Jr., and Palmer, I.G. (1981) *J. Met.* 33 (8), p. 24.
- [41] Sanders, T.H., Jr. (1979) NADC Contract No. N62269-76-C-0271, Final Report, June, 1979.
- [42] Lutjering, G. and Gysler, A. (1978) in Aluminum Transformation Technology and Application, Metals Park, OH: ASM.
- [43] Lewis, R.E., Webster, D., and Palmer, I.G. (1978) Final Report, contract F33615-77C-5186, Technical Report #AFML-TR-78-102, July 1978.
- [44] Palmer, I.G., Lewis, R.E., and Crooks, D.D. (1981) in Aluminum Lithium Alloys, T.H. Sanders, Jr. and E.A. Starke, Jr., eds., Warrendale, PA: TMS-AIME, p. 241.
- [45] Silcock, J.M. (1959/60) *J. Inst. Met.* 88, p. 357.
- [46] Nobel, B. and Thompson, G.E. (1971) *Met. Sci. J.* 5, p. 114.
- [47] Nobel, B. and Thompson, G.E. (1972) *Met. Sci. J.*, 8, p. 167.
- [48] Lin, F.S., Chakraborty, S.B., and Starke, E.A., Jr. (1982) *Metall. Trans.* 13A, p. 401.
- [49] Sanders, T.H., Jr. and Starke, E.A., Jr. (1982) *Acta Metall.* 30, p. 927.
- [50] Crooks, R.E. (1982) The Influence of Microstructure on the Ductility of an Al-Cu-Li-Mg-Zr Alloy, Ph.D. Thesis, Georgia Institute of Technology, Atlanta, GA.
- [51] Crooks, R.E., Kenik E., and Starke, E.A., Jr. (1982) University of Virginia, Charlottesville, VA, unpublished research.
- [52] Irmann, R. (1952) *Metallurgia* 46, p. 125.
- [53] Bloch, E.A. (1961) *Met. Rev.* 6 (22), p. 193
- [54] Langenbeck, S.L., Wald, G.G., Himmel, E.J., Simenz, R.F., Hildeman, G., Adam, C.M., Hilliard, D., and Bjeletich, J. (1981) "Elevated Temperature Aluminum Alloy Development," Interim Technical Report for Period April-September, 1981, Lockheed-California Company.
- [55] Lifshitz, I.M and Slyosov, V.V. (1961) *J. Phys. Chem. Solids.* 19, p. 35.
- [56] Wagner, C., *Z. Elektrochem*, Vol 65, 1961, p. 581.
- [57] Ashby, M.F. (1968) in Oxide Dispersion Strengthening, G.S. Ansell, T.D. Cooper, and F.V. Linell, eds., NY: Gordon & Breach, p. 143.
- [58] Wald, G.G. (1981) NASA Contractor Report 165676, May 1981.
- [59] Griffith, W., IBID [19].
- [60] Chellman, D.J., Wald, G.G., Paris, H.G., Walker, J.A., IBID [19].
- [61] Argon, A.S. and Im, J. (1975) *Metall. Trans.* 6A, p. 839.
- [62] Tien, J.K. (1975) in Fundamental Aspects of Structural Alloy Design, R.I. Jafee and B.A. Wilcox, eds., NY: Plenum Press, p. 363
- [63] Mullins, J.W. (1982) The Microstructure and Tensile Properties of RSP Al-Fe-Ni-Co Alloys, M.S. Thesis, Georgia Institute of Technology, Atlanta, GA.
- [64] Jones, H. (1969-70) *Mater. Sci. Eng.* 5, p. 1.
- [65] Palmer, I.G. and Smith, G.C. (1968) in Oxide Dispersion Strengthening, G.S. Ansell, T.D. Cooper, and F.V. Linell, eds., NY: Gordon & Breach, p. 253.
- [66] Gangulee, A. and Gurland, J. (1967) *Trans. TMS-AIME*, 239, 269.
- [67] Polmear, I.J. (1966) *J. Aust. Inst. Met.*, 11, p. 246.
- [68] Sanders, R.E., Jr. and Hildeman, G.J. (1981) "Elevated Temperature Aluminum Alloy Development," Final Report AFWAL-TR-81-4076.

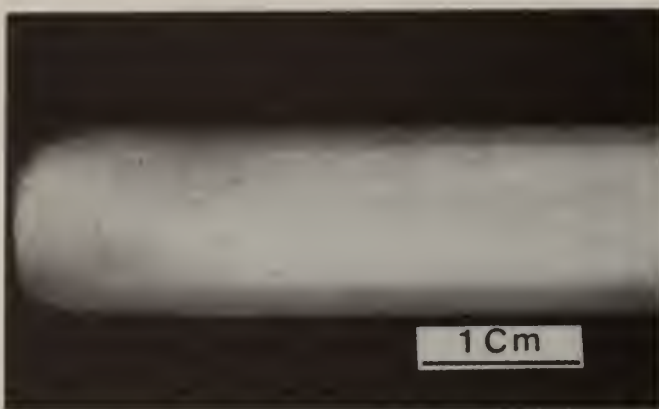


Figure 1. Optical macrograph of the cross section of the extruded P/M plate showing flow lines.

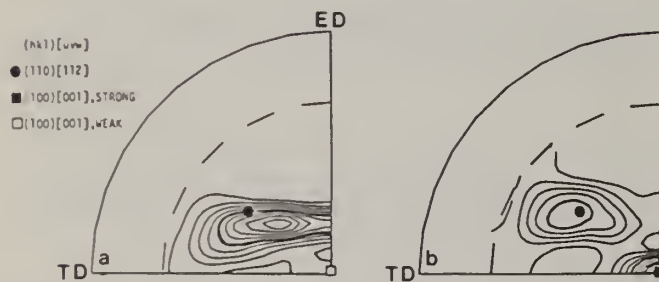


Figure 3. The (100) pole figures from the center of the P/M extrusion showing (a) the absence of the recrystallization component as well as broadening of the deformation component near the surface, and (b) the typical duplex sheet texture at the interior indicating partial recrystallization.

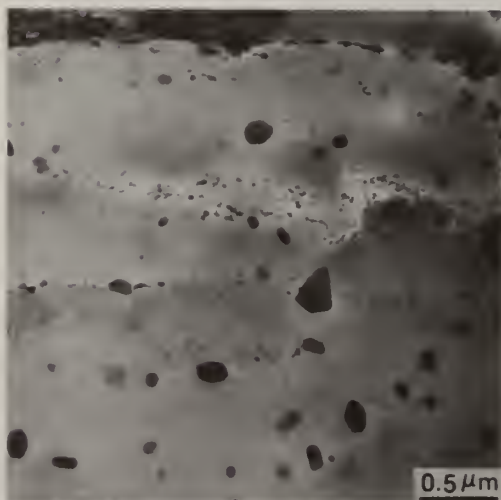


Figure 5. TEM showing oxides along grain and subgrain boundaries and $(\text{Co,Fe})_2\text{Al}_9$ dispersoids.

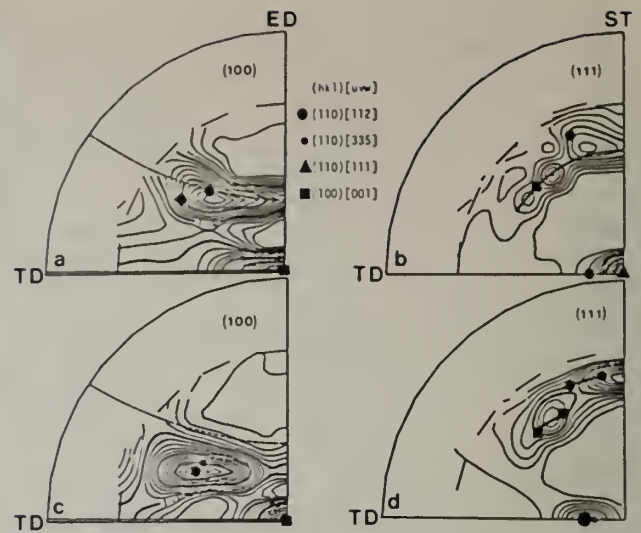


Figure 2. The duplex pseudo-axisymmetric texture from the interior of the edge (a), (b); and the duplex sheet texture from the interior of the center (c), (d), of the P/M extruded plate. ED represents the extrusion direction, T the traverse, and S the short traverse directions.

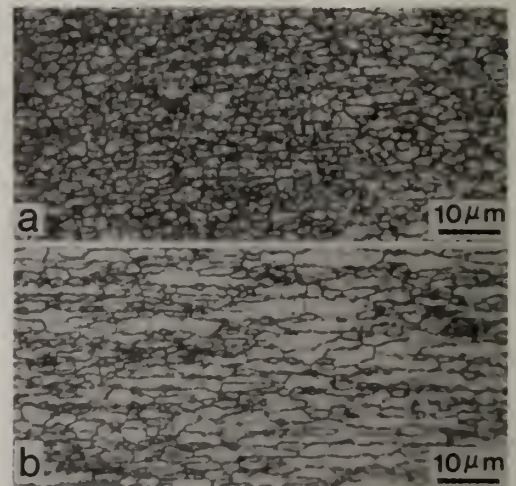


Figure 4. Optical micrographs from center of extrusion showing (a) unrecrystallized sub-structure near the surface; and (b) larger, more inhomogeneous, partially recrystallized grain structure at the interior.



Figure 6. SEM of bromine-etched surface of ST section of the extrusion showing the uniform distribution of $(\text{Co,Fe})_2\text{Al}_9$ dispersoids.

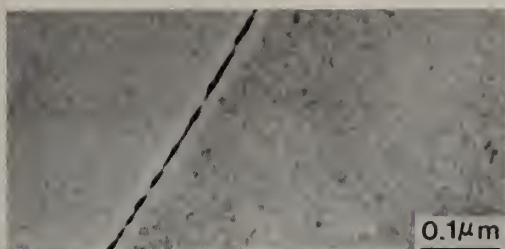


Figure 7. TEM showing uniform distribution of metastable η' precipitates in the matrix and equilibrium η along a grain boundary.

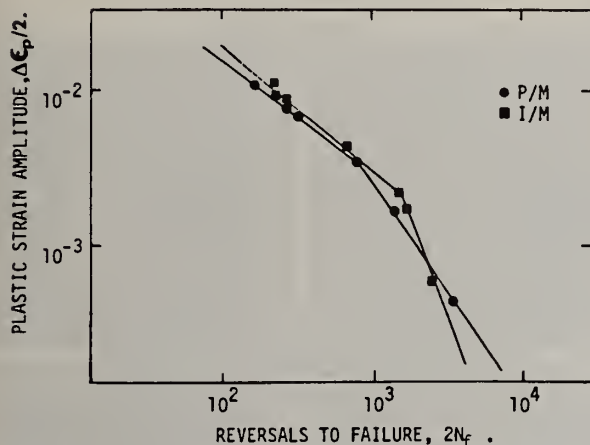


Figure 9. Comparison of strain-life behavior for X7091 and I/M alloy of similar composition.



Figure 8. Microstructure of (a) X7091 (slightly overaged); and (b) X7090 T6511 showing greater number of, and somewhat larger, Co_2Al_9 particles in the X7090.



Figure 10. TEM showing homogeneous deformation in P/M extrusion cycled to failure at $\Delta\epsilon_p/2 = 0.0007$.

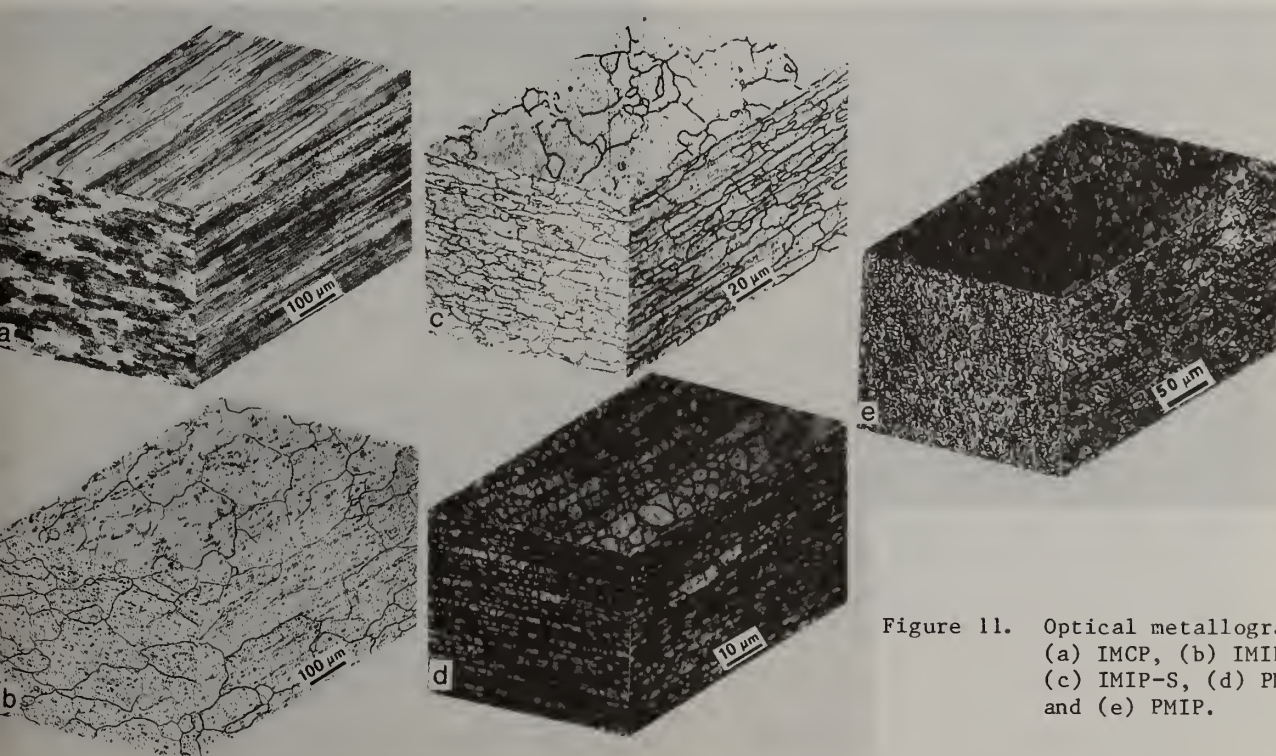


Figure 11. Optical metallographs: (a) IMCP, (b) IMIP-L, (c) IMIP-S, (d) PMCP, and (e) PMIP.

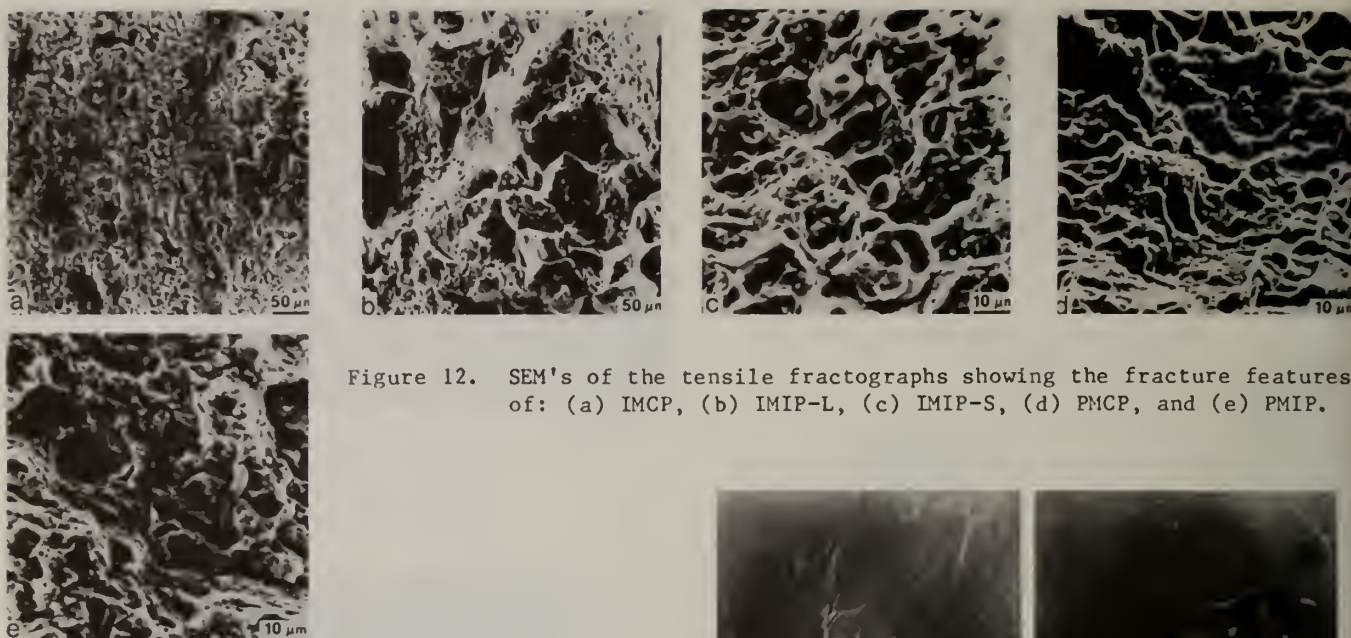


Figure 12. SEM's of the tensile fractographs showing the fracture features of: (a) IMCP, (b) IMIP-L, (c) IMIP-S, (d) PMCP, and (e) PMIP.

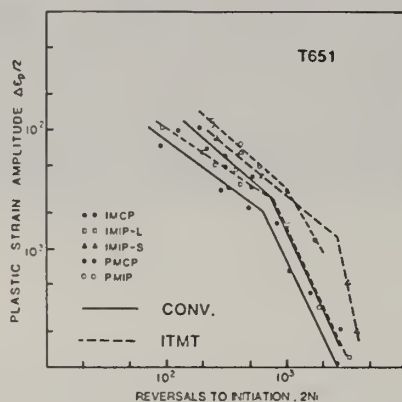


Figure 13. LCF Coffin-Manson plots for crack initiation in dry air, showing variations in FCI resistance.

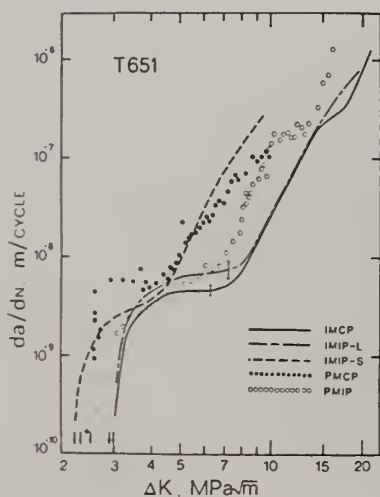


Figure 15. FCGR's of the experimental alloys in dry air with $R = 0.1$, 10 Hz.

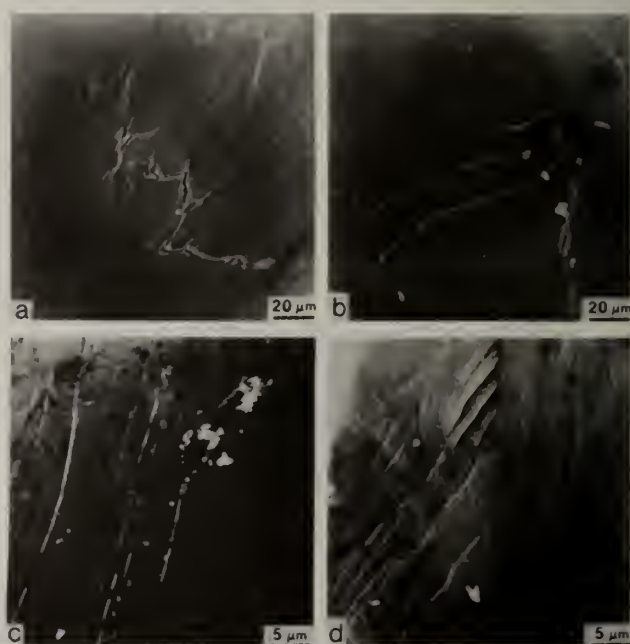


Figure 14. SEM's showing the surface markings and FCI sites of the LCF specimens, $\Delta\epsilon_T/2$ 1/3%: A) IMCP, $N_i = 250$ cycles; (b) IMIP, $N_i = 180$ cycles; (c) PMCP, $N_i = 150$ cycles; and (d) PMIP, $N_i = 290$ cycles.

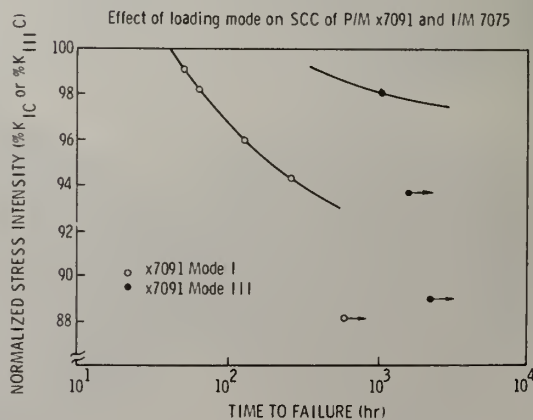


Figure 16. Effect of loading on SCC of P/M X7091.

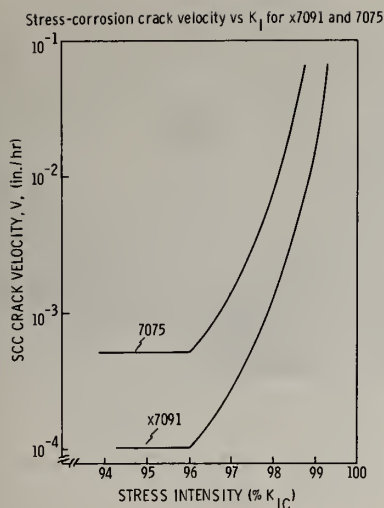


Figure 17. Stress corrosion crack velocity vs K_I for X7091 and 7075.

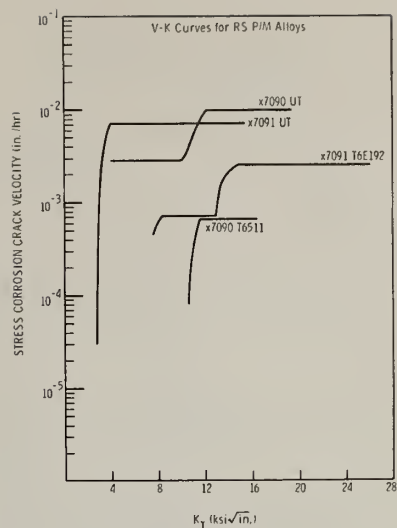


Figure 18. Stress corrosion crack velocity vs K_I for X7091 and X7090.

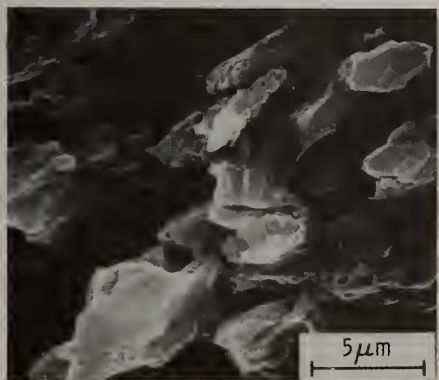


Figure 19. SCC path in X7091 showing largely intergranular fracture.

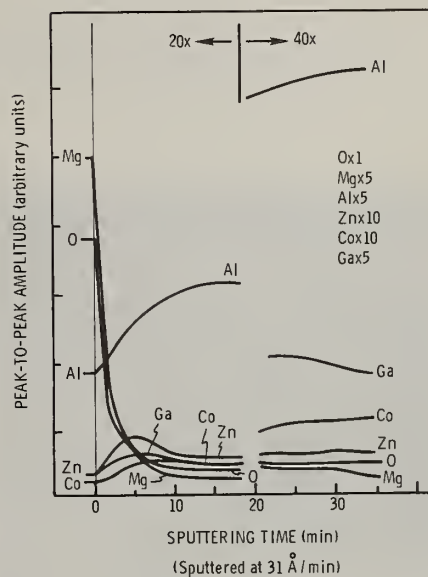


Figure 20. Auger depth profile of intergranular fracture surface of X7090.



Figure 21. SCC initiation at constituent particle in 7075.

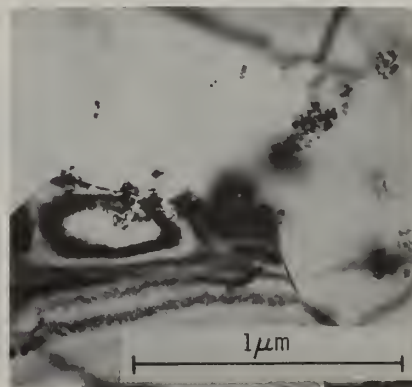


Figure 22. Oxide particles in RS P/M alloy X7091 pin grain boundaries and make an intergranular path more circuitous (from Ref. 31).

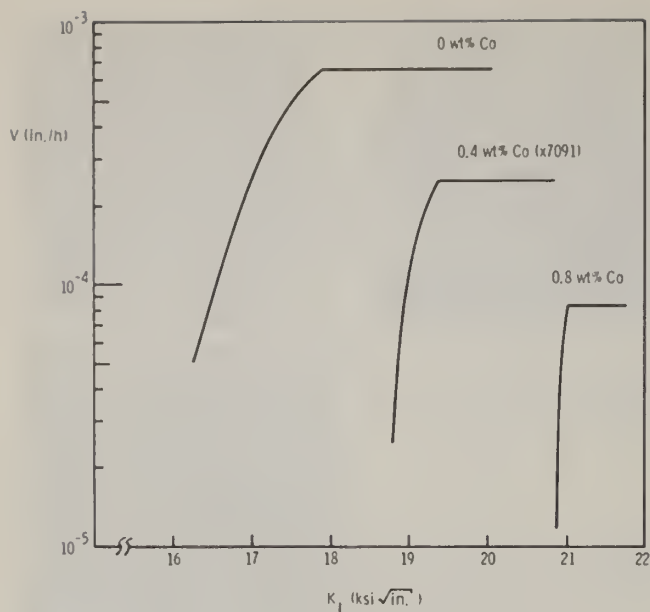


Figure 23. Stress corrosion crack velocity (v) vs K_I for different cobalt contents in X7091-type alloys.



Figure 25. Fracture of X7091 under liquid gallium is intergranular.

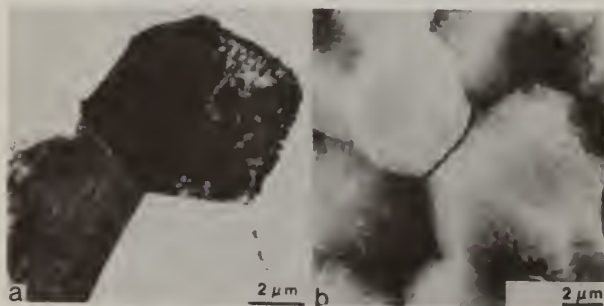


Figure 27. TEM showing (a) PFZ's along subgrains, and (b) intersubgranular fracture of an age-hardened Al-3Li-2Cu-0.2Zr alloy (from Ref. 48).

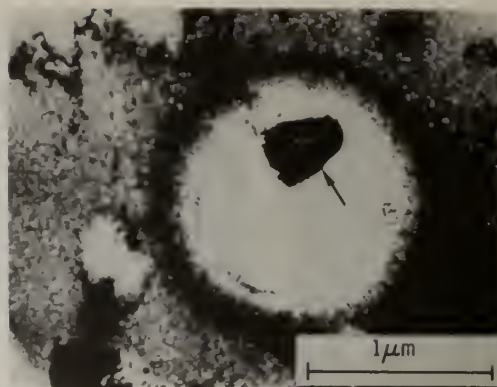


Figure 24. Localized attack around a coarse Co_2Al_9 particle (indicated by arrow) in X7091 after 30-min exposure to 3.5% NaCl solution.

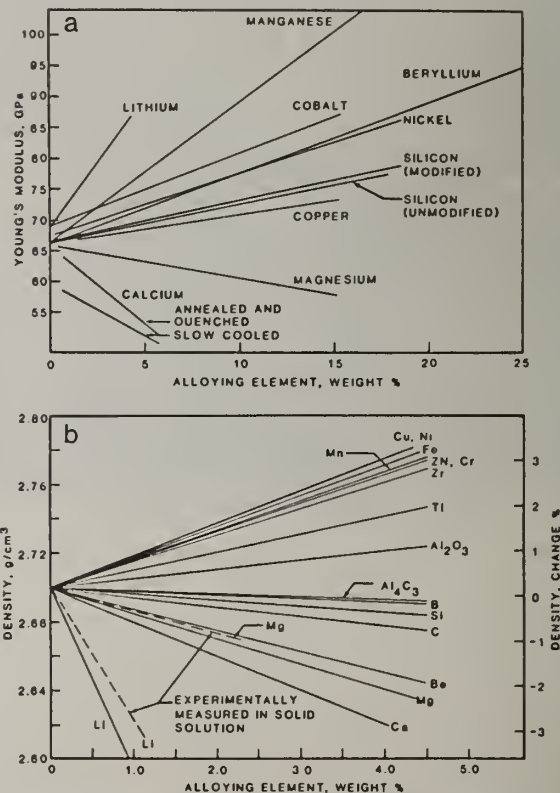


Figure 26. (a) The effect of solute additions on the modulus of aluminum alloys, and (b) the effect of solute additions on the density of aluminum alloys (from Ref. 58).

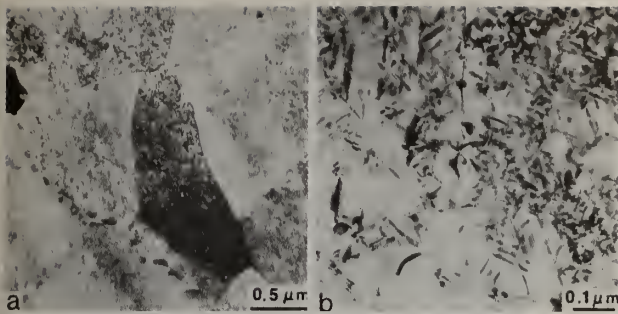


Figure 28. TEM's of Al-3Cu-2Li-1Mg-0.2Zr showing uniformly distributed precipitates and a lack of PFZ's (from Ref. 50).

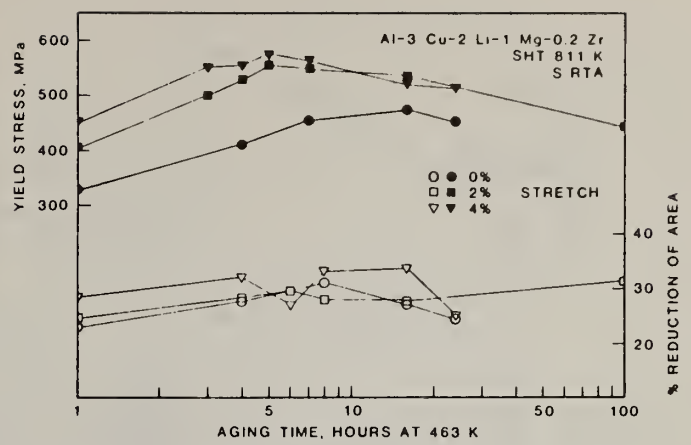


Figure 29. Yield stress and reduction of area versus aging time after various TMT (stretch) (from Ref. 50).

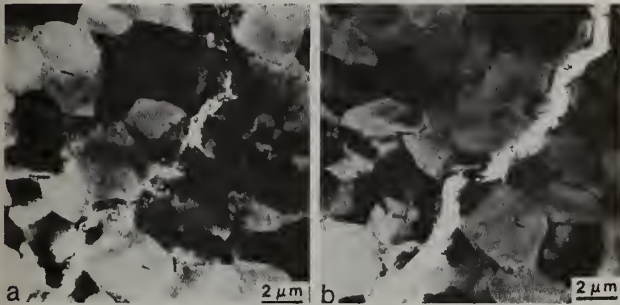


Figure 30. TEM's taken during in situ deformation studies in HVEM, showing homogeneous deformation and transgranular fracture of aged Al-3Cu-2Li-1Mg-0.2Zr alloy (from Ref. 51).

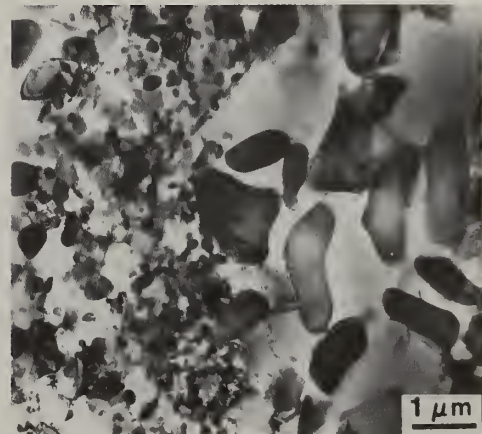


Figure 31. TEM of rapidly solidified Al-3.3Fe-2.3Ni-4.6Co splat-quenched flake showing regions of coarse and fine dispersoids (from Ref. 63).

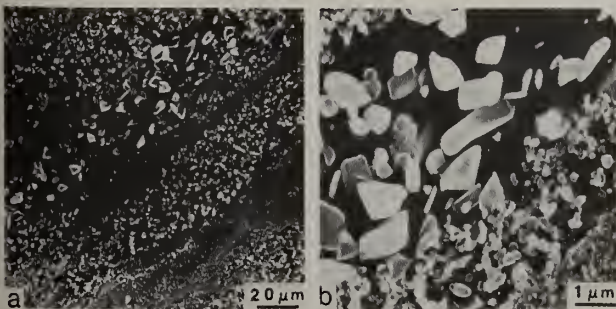


Figure 32. SEM's of bromine-etched surfaces of extruded Al-3.3Fe-2.3Ni-4.6Co plate made from rapidly solidified flake showing coarse and fine dispersoids associated with large and small flake particulate (from Ref. 63).

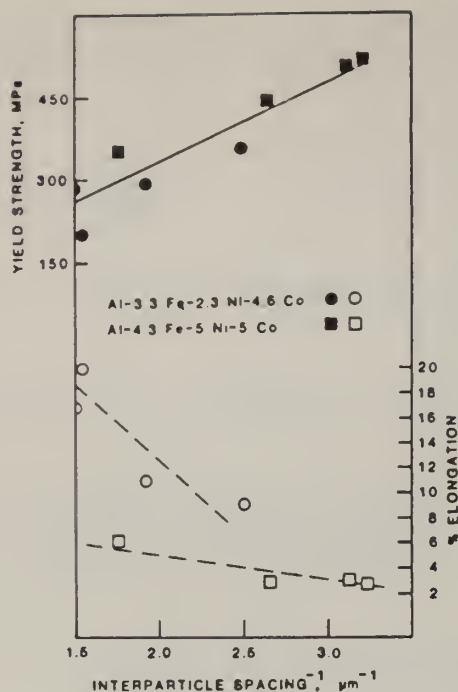


Figure 33. The effect of interparticle spacing on the yield strength of Al-Fe-Ni-Co plate made from P/M consolidation of rapidly solidified particulate (from Ref. 63).

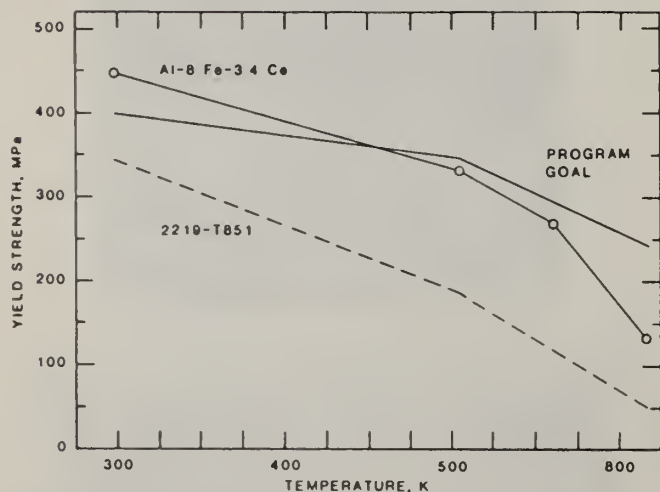


Figure 36. Comparison of yield strength temperature behavior of Al-8Fe-3.4Ce forging made from rapidly solidified particulate with two I/M 2XXX alloys. Tests conducted after 1000-hr exposure at temperature (from Ref. 68).



Figure 34. SEM showing crack nucleation associated with large dispersoids in an Al-3.3Fe-2.3Ni-4.6Co tensile specimens (from Ref. 63).

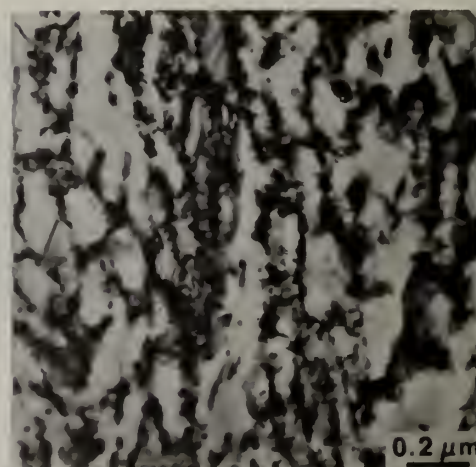


Figure 35. TEM of a rapidly solidified Al-8Fe-3.4Ce alloy (from Ref. 68).

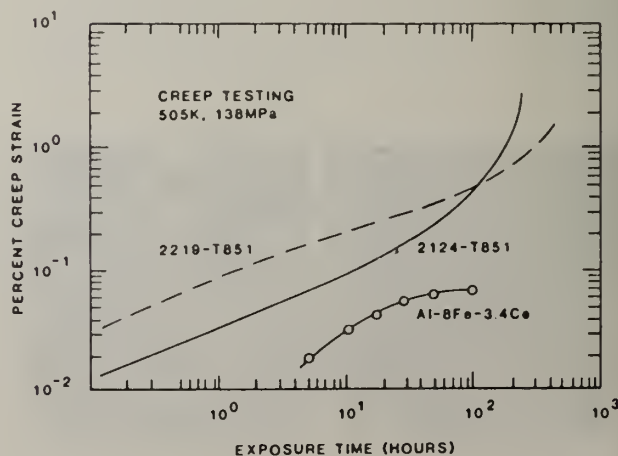


Figure 37. Comparison of creep strain versus exposure time of Al-8Fe-3.4Ce forging made from rapidly solidified particulate with two I/M 2XXX alloys (from Ref. 68).

STRUCTURE-PROPERTY RELATIONSHIPS IN RSP STEELS

G.B. Olson, M. Cohen, and G.J. Yurek
MIT, Cambridge, MA 02139

ABSTRACT

Rapid solidification of austenitic and martensitic steels via centrifugal atomization is found to produce significant refinement of inclusion phases. The thermal stability of the fine inclusions makes them effective grain-boundary pinning particles in hot-consolidated materials, accounting for unusual resistance to grain coarsening at high austenitizing temperatures. This allows the improvement of sharp-crack fracture toughness by high austenitizing treatments without the reduction in blunt-notch toughness and tensile ductility which may otherwise accompany excessive grain coarsening. Experiments on a 4Mo-0.25C martensitic steel demonstrate that high austenitizing significantly improves the K_{IC} toughness of both RSP and conventionally-processed materials, but the finer-grained RSP material has a 60°C lower Charpy ductile-brittle transition temperature. The fine-inclusion dispersion and grain-coarsening resistance also enhances the oxidation resistance of an RSP 303 austenitic stainless steel; this effect is attributed to promotion of oxide scale formation and mechanical keying of the scale by the fine grain size and dispersed inclusions.

Introduction

Rapid solidification processing (RSP) allows the achievement of a wide variety of novel metastable structures, but the range of structures which can be practically exploited is greatly narrowed by the available consolidation techniques through which rapidly solidified powders, flakes, and ribbons are converted into bulk materials. While the development of lower-temperature consolidation methods will expand this range, certain special aspects of structural metastability which survive the high temperatures of currently reliable consolidation processes form the basis of an approach to microstructural control which is ready for practical exploitation today. Investigations of structure/property relationships in rapidly solidified steels produced by centrifugal atomization and consolidated by hot extrusion indicate that the most practical benefit of rapid solidification is the fine dispersion of stable compounds normally regarded as "inclusion" phases. After discussing the role of inclusion refinement in the microstructural development of these steels we propose to illustrate its potential for the improvement of material properties, using examples of fracture toughness in high-strength martensitic steels and oxidation resistance in an austenitic stainless steel.

Inclusion Refinement and Grain-Coarsening Resistance

The refinement of inclusion phases via rapid solidification has been demonstrated in a study by scanning transmission electron microscopy (STEM) of a centrifugally-atomized high-sulfur 303 stainless steel (Table 1) [1]. While coarse powder particles which solidified in a

TABLE 1
Steel Compositions (w/o)

	<u>C</u>	<u>Mn</u>	<u>P</u>	<u>S</u>	<u>Si</u>	<u>Ni</u>	<u>Cr</u>	<u>Mo</u>	<u>V</u>	<u>W</u>	<u>Co</u>	<u>Cu</u>	<u>N</u>
303 Stainless	0.06	1.60	0.028	0.34	0.62	8.68	17.31	0.37	-	-	0.15	0.78	0.032
4Mo-0.25C	0.26	0.51	0.005	0.007	0.05	-	-	4.10	-	-	-	-	0.001
M2 Matrix	0.51	0.22	0.015	0.006	0.19	-	4.68	2.72	1.07	2.02	-	-	0.011

cellular/dendritic mode produced 0.1 μm intercellular manganese sulfides as a part of the solidification process, smaller powder particles which solidified in a massive (segregationless) mode produced 100 Å sulfides, the latter being precipitated from the solid state. After hot consolidation of -140 mesh ($<105 \mu\text{m}$) powder by 10:1 extrusion at 900°C, an average sulfide size of $\sim 0.1 \mu\text{m}$ was maintained. This is in contrast to the 10-100 μm sulfide stringers normally obtained by conventional ingot processing.

As was reviewed recently in the context of alloy design guidelines for rapid solidification [2], the low solubility of inclusion phases, which causes them to precipitate early (and in coarse form) during conventional solidification, provides the basis for unusual coarsening resistance once they are finely dispersed (metastably) via rapid solidification. The rate of inclusion-particle coarsening is proportional to the matrix concentration of the rate-controlling species (the species with the smallest product of diffusivity and matrix concentration), and this matrix concentration is controlled by the inclusion-phase solubility product. For example in the rapidly solidified 303 stainless steel, the ability of the manganese sulfides to maintain during hot consolidation a particle size two to three orders of magnitude smaller than in conventionally processed material arises from the low matrix sulfur concentration associated with the low sulfide solubility in austenite.

The refinement of inclusion phases down to sizes of 0.1 μm and below renders the particles less harmful as initiating defects in fracture and fatigue processes, and also allows them to play a new and beneficial role in the control of microstructure. At inclusion volume fractions of the order of 0.1%, refinement to this size level provides a strong grain-boundary pinning force which results in unusual resistance to grain coarsening at high austenitizing temperatures [3]. Figure 1 summarizes the high-temperature austenitic grain-coarsening behavior (1 hour treatments) of a 4Mo-0.25C martensitic steel (Table 1), comparing the grain size of conventionally processed material with that of hot extruded (9:1 reduction at 900°C) centrifugally-atomized RSP material of two powder sizes, -200 mesh ($<75 \mu\text{m}$) and -140+200 mesh (75-105 μm) [4]. Dissolution of carbides above 1025°C leads to rapid grain coarsening of the conventional steel, whereas the additional pinning effect of the dispersed inclusions causes greatly retarded grain coarsening, and this is slower in the material produced from the finer powder. While there is evidence of enhanced pinning in the region of the prior powder-particle boundaries [3], which may contribute to the powder size dependence of the grain-coarsening behavior, a comparison of hot-extruded and hot-pressed RSP powders of a 9Ni-4Co steel [5] revealed substantial grain-boundary pinning within the powder-particle domains as well. Hence, finer dispersions of inclusions formed by solidification at higher supercoolings may also contribute to enhanced grain-boundary pinning in material formed from finer powders.

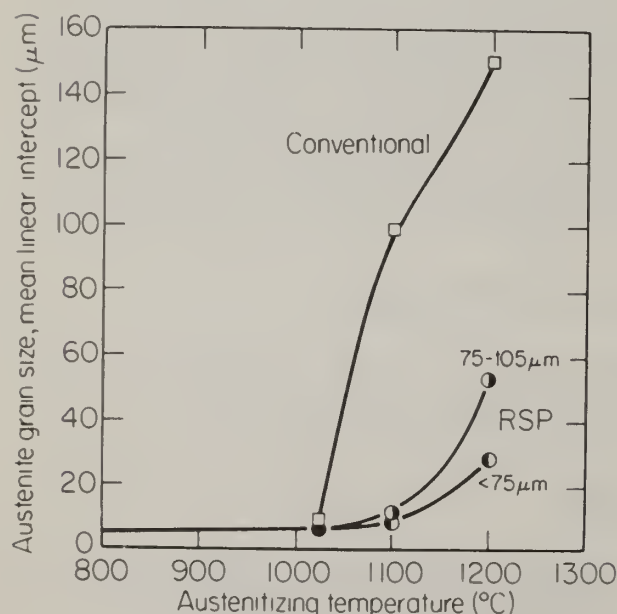


Fig. 1 Comparison of austenitic grain size of conventional and RSP 4Mo-0.25C steel after 1-hour austenitizing treatments [4].

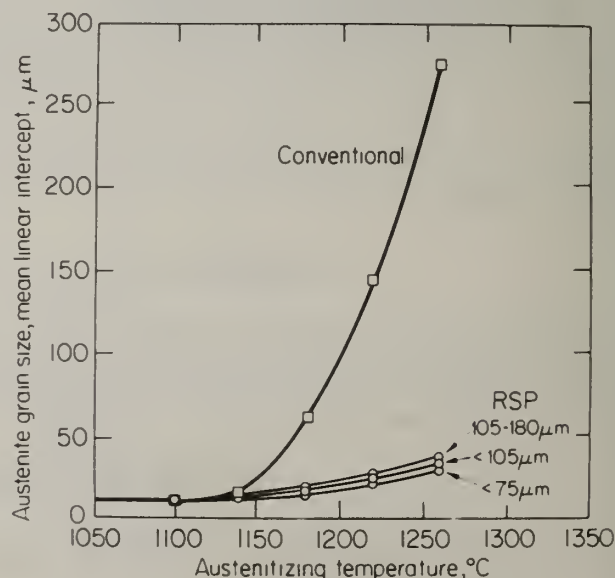


Fig. 2 Comparison of austenitic grain size of conventional and RSP M2 matrix steel after 1-hour austenitizing treatments [6].

Figure 2 shows a similar comparison of the grain-coarsening behavior of a matrix tool steel (VASCO-MA) derived from the matrix composition of M2 (Table 1) [6]. Again the rapid coarsening of the conventional material marks the dissolution of alloy carbides, while the RSP material (consolidated by blank die compaction and 4:1 extrusion at 900°C) exhibits greatly retarded coarsening; in this case the coarsening is less sensitive to powder size. Results of a STEM analysis of the dispersed phases remaining after austenitizing at temperatures above the carbide-dissolution temperature are summarized in Table 2 [6]. Light-element analysis was permitted by the use of an ultrathin-window X-ray detector. Though sulfides make a significant contribution to the boundary-pinning particles at 1180°C, at still higher temperatures the predominant particles are silicates which occasionally possess substantial sulfur contents. Table 2 lists the observed size range of each inclusion phase as well as the total average particle diameter \bar{d} and estimated total volume fraction f at each temperature.

Under conditions of particle-pinning-controlled grain coarsening, the limiting grain diameter at which the total pinning force balances the driving force for grain growth is expressed by [7]:

$$D = \frac{\pi}{6} \frac{\bar{d}}{f} \left(\frac{3}{2} - \frac{2}{Z} \right) \quad (1)$$

where Z is a grain-size distribution factor defined as the ratio of the largest to the average grain diameter. The high-temperature grain-coarsening behavior of the RSP material illustrated by Fig. 2 is in qualitative agreement with eqn. 1 in that the observed D is proportional to the \bar{d}/f determined from the data of Table 2. Adopting an empirical Z parameter of $1.5 < Z < 2.0$ based on previous studies of austenite grain coarsening [8] predicts a grain size smaller than that observed by a factor of 2 to 5. Thus, the observed particles are more than sufficient to account for the observed coarsening resistance. The discrepancy may lie within the accuracy of the particle volume-fraction estimates in as much as these are subject to the uncertainty of foil thickness and degree of both particle-image overlap and truncation in the thin-foil STEM observations.

TABLE 2
Dispersed Phases in RSP M2-Matrix Steel [6]

Austenitizing Temperature (1 hr.)	Stable Particles	$d, \mu\text{m}$	
1180°C	MnS	0.1-0.5	$\bar{d} = 0.18\mu\text{m}$ $f \approx 3.7 \times 10^{-3}$
	VS	0.1-0.5	
	(Mn,V)S	0.15-0.5	
	SiO ₂	0.1-0.5	
	MgO·SiO ₂	0.2-0.6	
	MnS·MgO·SiO ₂	0.2-0.6	
	VS·SiO ₂	0.15-0.6	
1220°C	SiO ₂	0.1-0.5	$\bar{d} = 0.19\mu\text{m}$ $f \approx 2.5 \times 10^{-3}$
	MgO·SiO ₂	0.2-0.6	
	VS·SiO ₂	0.2-0.6	
	MnS·SiO ₂	0.2-0.6	
1260°C	SiO ₂	0.1-0.5	$\bar{d} = 0.23\mu\text{m}$ $f \approx 2.2 \times 10^{-3}$
	MgO·SiO ₂	0.2-0.65	
	VS·SiO ₂	0.2-0.7	

While further refinement of inclusion size would be desirable, the observed dispersion of inclusion particles and associated high-temperature grain coarsening demonstrate that phases which normally play a deleterious role can be made to perform a beneficial function in microstructural control through rapid solidification.

Mechanical Properties

Provided stable boundary-pinning dispersions can be kept sufficiently fine so that they themselves do not limit fracture toughness, significant toughness improvements should be expected from the proper exploitation of the grain-coarsening resistance of RSP steels. It is well established that the sharp-crack fracture toughness (K_{IC}) of medium-carbon ultrahigh-strength steels, such as 4340 and 300M, can be substantially enhanced by the use of high austenitizing temperatures up to 1200°C [9-11]. This toughening effect can be attributed primarily to the dissolution of soluble void-initiating particles [11,12]. However, even though K_{IC} is increased, the blunt-notch toughness (e.g. Charpy energy) and tensile ductility (reduction in area) may decrease due to the excessive grain coarsening which normally accompanies such high austenitizing treatments [12,13]. A recent investigation of the toughening effect in conventional 4340 [5] reveals that the improvement of K_{IC} with high austenitizing treatment persists through the first stage of tempering (ϵ -carbide precipitation) but is lost in the second stage (retained austenite decomposition) due to increased intergranular fracture in the coarse-grained material. On the other hand, the grain-coarsening resistance of RSP steels offers the prospect of using the beneficial solutionizing effect of high austenitizing treatments without the deleterious effects of excessive grain coarsening.

The influence of high austenitizing treatments on the fracture toughness of the 4Mo-0.25C steel of Fig. 1 was examined using the 75-105 μm powder size RSP material [5]. Room-temperature mechanical properties of the conventional and RSP steels tempered 2 hour at 150°C after austenitizing at 1025°C and 1150°C are summarized in Table 3. Due to some decarburization during rapid solidification processing, the RSP material was found to contain 0.03C less than the conventional steel of Table 1. This accounts for the slightly lower hardness and strength level indicated in Table 3. The influence of austenitizing temperature on the room-temperature fracture properties of both materials is depicted in Fig. 3. Sharp-crack fracture toughness, given as K_Q in Table 3 and Fig. 3, was measured on standard pre-cracked single-edge-notched specimens of 0.41 in. thickness. The higher K_Q values in Table 3 fall just outside the range for valid plane-strain K_{IC} values for this size specimen. In both the conventional and RSP materials, this steel exhibits a significant increase in both sharp-crack K_Q toughness and blunt-notch C_v energy with high austenitizing treatment. While the conventional material shows a substantial drop in tensile ductility (%RA) attending the high-temperature grain coarsening, the coarsening-resistant RSP material is not appreciably affected. Although the room-temperature Charpy energies of the two materials are equivalent after 1150°C austenitizing, the advantage of the finer-grain RSP steel shows up clearly in its superior ductile-brittle transition behavior illustrated in Fig. 4. While shelf energies are similar, the onset of the transition is lowered by $\sim 100^\circ\text{C}$ in the RSP material, and the midpoint transition temperature is decreased by 60°C. This dramatic difference is too large to be accounted for by the small carbon and strength differences between the two materials. Hence, the grain-coarsening resistance of the RSP steel allows practical use of the toughening effects of high austenitizing treatment without the adverse effects of grain coarsening on the tensile ductility and ductile-brittle transition behavior. More fundamentally, the results affirm that the influence of high austenitizing treatment on sharp-crack toughness is independent of grain size while the blunt-notch toughness and tensile ductility are grain-size sensitive.

The density of the consolidated RSP material was found to be 99.9% of full density, and metallography revealed occasional voids which were several microns in size. It is reasonable to expect better fracture properties after more complete consolidation. A similar level of porosity was found in the M2 matrix steel of Fig. 2. Although this steel did not undergo any significant improvement in toughness with high austenitizing treatments, the finer grain RSP material showed some advantage in both K_{IC} and C_v energy relative to the conventional material after high temperature austenitizing [6]. Efforts to obtain toughness improvements in similarly processed RSP 4340 and 300M steels have so far been hampered by higher levels of porosity and powder contamination which severely limit the fracture properties in these high strength materials [5]. While the results of the 4Mo-0.25C steel demonstrate the potential of RSP steels, it is evident that consistent and reliable methods of powder consolidation must be perfected to achieve reproducible results.

Oxidation Behavior

The fine inclusion dispersion and grain-coarsening resistance of RSP steels can also improve oxidation behavior, as demonstrated by cyclic oxidation kinetic experiments on the RSP 303 stainless steel of Table 1 [14]. The rate of weight change with 20 hour cyclic exposures to pure

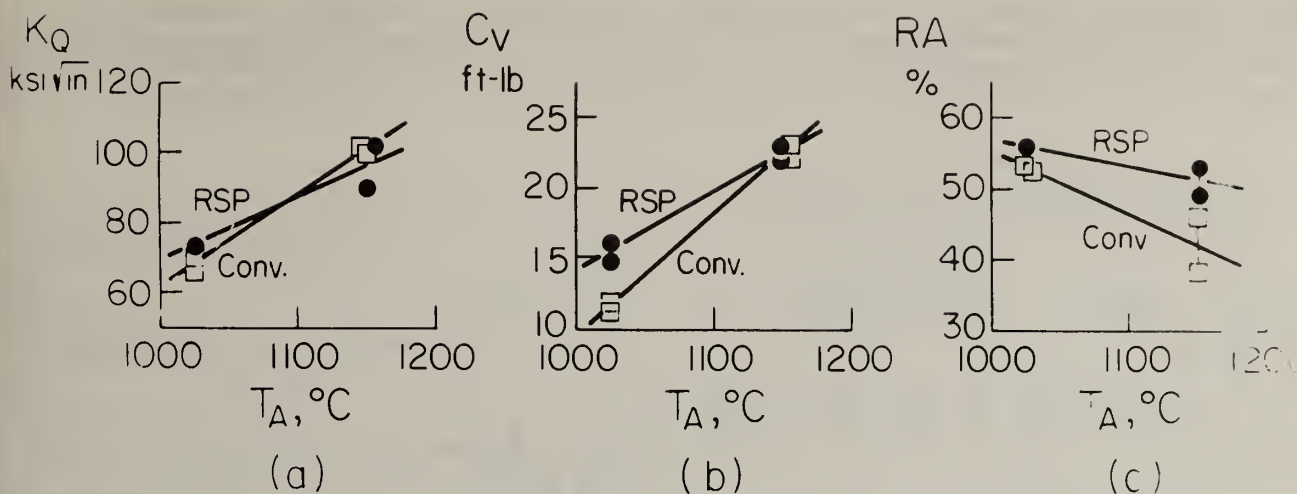


Fig. 3 Influence of austenitizing temperature on room-temperature fracture properties of 4Mo-0.25C steel, 150°C temper; (a) sharp-crack K_Q toughness, (b) Charpy impact energy, (c) tensile reduction in area [5].

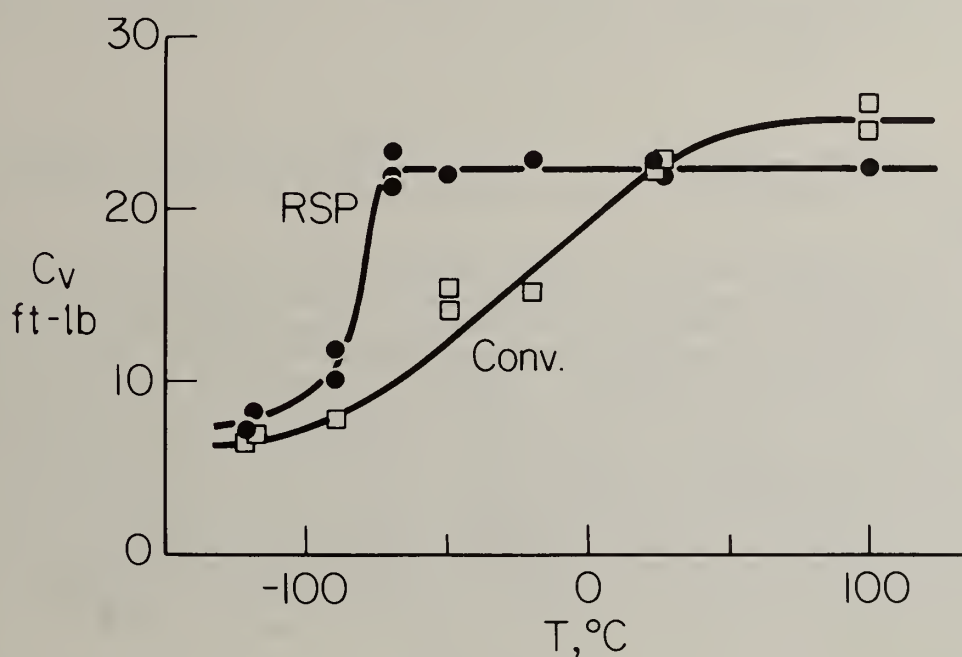


Fig. 4 Charpy ductile-brittle transition curves for RSP and conventional 4Mo-0.25C steel after 1150°C austenitizing, 150°C temper [5].

TABLE 3

Mechanical Properties of 4Mo-0.25C Steel [5]

	Aust. Temp.	Hardness, R_c	σ_y , ksi	UTS, ksi	%RA	CVN, ft-lb	K_Q , $\text{ksi}\sqrt{\text{in}}$
Conv.	1025°C	45.8	195	247	53	11.5	68
	1150°C	46.3	197	246	42	22.6	99
RSP	1025°C	46.0	183	227	56	15.3	73
	1150°C	44.7	181	229	51	22.4	95

oxygen at 900°C was compared with that of chemically-equivalent conventionally processed 304 stainless steel. Both materials were initially annealed for 6 hours at 1000°C, producing a grain size of 170 μm in the conventional 304 steel and 5.6 μm in the RSP 303 steel. STEM analysis of the RSP material after the 1000°C anneal revealed manganese sulfides of 0.2 to 0.5 μm diameter.

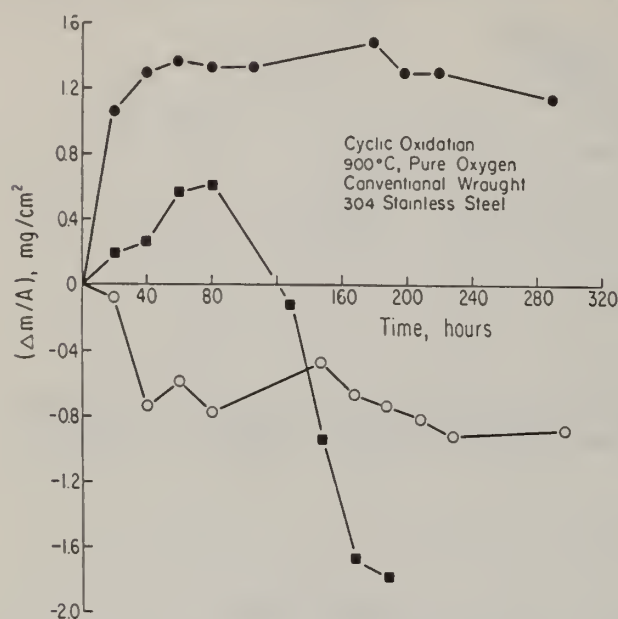


Fig. 5 Kinetics of cyclic oxidation of conventional 304 stainless steel [14].

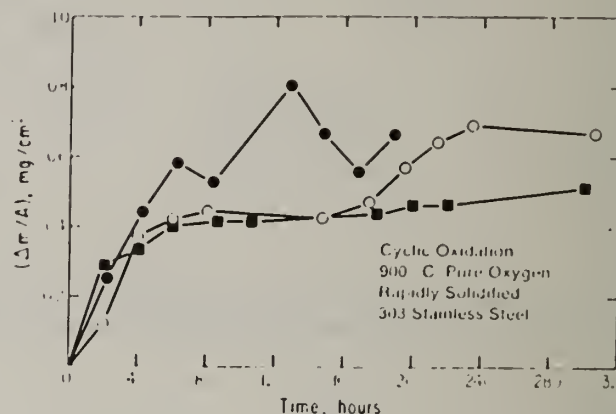


Fig. 6. Kinetics of cyclic oxidation of RSP 303 stainless steel [14].

The weight-change results obtained for three specimens of the conventional 304 steel are shown in Fig. 5. The kinetics of oxidation are quite variable, indicating both rapid weight gains and losses due to oxide spallation. Results for the identically treated RSP 303 steel are given in Fig. 6. The RSP steel demonstrated excellent oxidation resistance, showing consistent weight gains with no visual evidence of oxide-scale spallation. SEM analysis of the oxide films indicated that the superior oxidation resistance was due to the formation and growth of protective Cr_2O_3 and SiO_2 scales, which were promoted by the sulfide dispersion and enhanced grain-boundary transport of Cr to the oxide due to the stable, fine grain size. There was also evidence of increased adherence of the scale by the formation of intrusions of SiO_2 from the external scale into the alloy, which formed around the sulfides and along the closely-spaced grain boundaries, and which acted to key the scale mechanically to the base alloy. The overall oxidation kinetics were equivalent to a conventional 310 stainless steel containing considerably higher Cr and Ni. These results suggest that RSP inclusion refinement and grain-coarsening resistance can be employed either to improve the oxidation behavior of high-Cr alloys or to obtain equivalent behavior at lower Cr contents.

Conclusions

A primary benefit of RSP in hot consolidated steels is the achievement of fine dispersions of stable inclusion phases. The low solubility of these phases in the austenite imparts an unusual coarsening resistance to the dispersed particles such that they act as effective grain-boundary pinning dispersions at very high austenitizing temperatures. As demonstrated for a 4Mo-0.25C martensitic steel, the resulting grain-coarsening resistance allows substantial improvement of sharp-crack fracture toughness through the use of high austenitizing treatment without the reduction of blunt-notch toughness and tensile ductility that usually accompanies excessive grain coarsening. While both the RSP and conventional steels show an improvement of K_{IC} with high austenitizing, the finer-grained RSP material displays a 60°C lower ductile-brittle transition temperature. Obtaining consistent properties, however, requires reproducible methods of achieving full consolidation of the RSP powders. The fine inclusion dispersions and grain-coarsening resistance also provide improved oxidation resistance in RSP stainless steels through enhanced grain-boundary transport of Cr to the protective oxide together with mechanical keying of the oxide at the dispersed inclusions and closely-spaced grain boundaries.

Acknowledgements

This research is sponsored by the Office of Naval Research under Contract No. N00014-81-K-0013 and by fellowships from the AMAX Foundation. The martensitic steels were supplied by the Climax

Molybdenum Company, converted to powder by Pratt & Whitney Aircraft, Government Products Division, and consolidated at Wright-Patterson Air Force Materials Laboratories. Results reported here are based on thesis research at MIT by J.L. Goss, C.Y. Hsu, and P.M. Fleishman, and an undergraduate research project by D. Eisen.

References

- [1] T.F. Kelly and J.B. Vander Sande, Proc. 2nd Intl. Conf. Rapid Solidification Processing: Principles and Technologies, R. Mehrabian, B.H. Kear, and M. Cohen, eds, (Claitor's, Baton Rouge, 1980) p. 100.
- [2] G.B. Olson, H.C. Ling, J.S. Montgomery, J.B. Vander Sande, and M. Cohen, in Rapidly Solidified Amorphous and Crystalline Alloys, B. Giessen, B.H. Kear, and M. Cohen, eds. (North-Holland, NY, 1982) p. 355.
- [3] M. Suga, J.L. Goss, G.B. Olson, and J.B. Vander Sande, Proc. 2nd. Intl. Conf. Rapid Solidification Processing: Principles and Technologies, R. Mehrabian, B.H. Kear, and M. Cohen, eds. (Claitor's, Baton Rouge, 1980) p. 364.
- [4] J.L. Goss, Austenitic Grain Growth and Precipitation Strengthening in Rapidly-Solidified Alloys, M.S. Thesis, MIT, Cambridge, MA, Sept. 1980.
- [5] P.M. Fleishman, Fracture Toughness of Rapidly Solidified Martensitic Steels, M.S. Thesis, MIT, Cambridge, MA, Sept. 1982.
- [6] C.Y. Hsu, doctoral research in progress, MIT, Cambridge, MA.
- [7] T. Gladman, Proc. Roy. Soc. A (1966) 294, p. 298.
- [8] T. Gladman and F.B. Pickering, J. Iron Steel Inst. (1967) 205, p. 653.
- [9] G.Y. Lai, W.E. Wood, R.A. Clark, V.F. Zackay, and E.R. Parker, Met. Trans. (1974) 5, p. 1663.
- [10] W.E. Wood, Eng. Fract. Mech. (1975) 7, p. 219.
- [11] J.L. Youngblood and M.R. Raghavan, Met. Trans. A (1977) 8A, p. 1439.
- [12] R.O. Ritchie and R.M. Horn, Met. Trans. A (1978) 9A, p. 331.
- [13] R.O. Ritchie, B. Francis, and W.L. Server, Met. Trans. A (1976) 7A, p. 831.
- [14] G.J. Yurek, D. Eisen, and A. Garratt-Reed, Met. Trans. A (1982) 13A, p. 473.

STRUCTURE AND PROPERTIES OF RSP COPPER-BASED ALLOYS

I.E. Anderson, R.A. Masumura, B.B. Rath and C.L. Vold

Physical Metallurgy Branch, Material Science and Technology Division
Naval Research Laboratory, Washington, DC 20375

ABSTRACT

The benefits of rapid solidification processing (RSP) for fabrication of Cu-Mn based alloys for acoustic damping applications were examined. When these alloys are processed by conventional casting or hot working techniques, the products exhibit either heavily-cored dendritic or coarse banded microstructures. In this investigation pre-alloyed RSP powders were consolidated by hot extrusion to produce high damping alloys with increased homogeneity. The compositions selected for rapid solidification processing correspond to commercial damping alloys containing 58Cu-40Mn-2Al and 37Cu-55Mn-4Al-3Fe-1Ni, in weight percent. The microstructures and properties of the powder extrusions were compared to the ingot metallurgy products. These results permit an assessment of the potential advantages of RSP and advanced consolidation techniques for damping alloy development.

INTRODUCTION

The damping of elastic stress waves in solids in the acoustic frequency range (20 to 5000 hz) can be used to control unwanted noise and vibration. The decrease in amplitude with time can be the result of several different types of loss mechanisms. One such mechanism involving magneto-elastic interaction has been commercially exploited. During the past several years, this development of the basic Cu-Mn alloy has lead to two types of high damping materials [1]. The first is a cast alloy, known as "Sonoston" with composition, 55Mn-37Cu-4Al-3Fe-1Ni (wt.%) developed by Stone Manganese Marine, Ltd. The other is a wrought alloy, known as "Incramate" with composition, 58Cu-40Mn-2Al (wt.%) developed by the International Copper Research Association. Based upon the Cu-Mn binary system, damping in these alloys is dependent upon the interaction between an elastic wave and microtwin domain walls formed by the antiferromagnetic Mn-rich regions when given a specific thermal treatment [2-4]. The physical properties of these two alloys, "Sonoston" (Mn-rich) and "Incramate" (Cu-rich) have been characterized and documented. These compositions were selected to examine the effect of RSP on acoustic damping and to compare the RSP alloys with those fabricated by ingot metallurgy processes.

Powder metallurgical methods have been employed in two previous studies of the Cu-Mn system [5,6]. In both cases, elemental powders were consolidated by die compaction and sintering. After sintering, the densities ranged from 90 to 95% of the theoretical values indicating a high degree of porosity which is known to improve damping at the expense of strength and toughness. To obviate these difficulties, the present approach was to produce rapidly solidified powders from pre-alloyed stock and to consolidate the particles by extrusion at 50-150°C below the solidus. Using pre-alloyed RSP process has the advantage of producing an homogeneous and fine grained microstructure which should lead to improved corrosion resistance, ease of fabrication and increased damping properties.

POWDER CHARACTERIZATION

Ingots of the Cu-rich and Mn-rich alloys were made with compositions corresponding to their commercial counterparts. Rapidly solidified alloy powders were generated by centrifugal atomization and quenched in flowing helium gas at the Pratt and Whitney facility at West Palm Beach. Particle cooling rates were estimated to be near 10^5 °C/sec. [7]. Chemical analyses of the two powders yielded compositions to within 1% of that required.

The powders were screened by the producer to remove debris and non-typical particles larger than 80 mesh before consolidation. Particle size analysis showed that the powder samples closely followed a log-normal distribution with a maximum size of about 200 μm . The mean particle diameter for the Mn-rich alloy was 46 μm ; larger than the Cu-rich alloy powder, whose mean diameter was 29 μm . These distributions appear to match the typical characteristics of a centrifugally atomized powder [8].

Optical metallography of individual powder particle sections permitted an examination of the solidification structure of the individual particles. Figure 1 shows primarily dendritic solidification with a secondary dendrite arm spacing of about 0.5 μm for the Mn-rich alloy particles. Similarly, the Cu-rich alloy also exhibited a fine microstructure that appears to be cellular [8], with a cell size of about 1 μm . Internal porosity was observed in some of the Cu-rich and Mn-rich alloy particles. These types of pores may result from entrapped quenching gas or gas dissolved in the molten alloy which then form internal bubbles on solidification as shown in Figure 1. The impingement of molten particles on solidified particles may cause "splats" as can be seen in Figure 1.

X-ray diffraction measurements of both alloy powder samples showed a retained fcc structure at room temperature. The ternary Cu-Mn-Al isothermal section for 20°C [8] shows a $\gamma(\text{fcc}) + \alpha\text{-Mn}$ two phase mixture for the Cu-rich alloy. The Mn-rich alloys contains a significant amount of Fe and Ni (4 wt.% total) in addition to the Cu, Mn and Al, and the equilibrium phases are only known empirically. Due to line broadening and weak high-angle reflections, the lattice parameters of the fcc phases could not be calculated accurately. Generally, the unit cell of the Mn-rich alloy appears to be slightly larger than that of the Cu-rich alloy which is consistent with the similar atomic volumes of Cu and Mn.

EXTRUSION

The powders were consolidated at the Experimental Metals Processing Laboratory at Wright-Patterson AFB. The screened powders were placed originally into stainless steel containers, evacuated, and sealed under vacuum. The cylindrical containers were pre-heated to 800°C for 2 hours prior to extrusion. The Cu-rich powder sample was used in the initial extrusion attempt at 800°C with a cross section reduction of 12:1 and a final desired diameter of 1". Unfortunately the stainless steel can ruptured, exposed the billet to the atmosphere, and resulted in an irregular extrusion with a reduced diameter. As a consequence, the Mn-rich powder sample was recanned in a copper container with improved co-reduction properties and a successful extrusion was produced at 800°C with 12:1 ratio. The measured densities relative to the commercial alloys were 99.6% for the Mn-rich and 99.1% for the Cu-rich alloys. The microstructures of the as-extruded alloys are shown in Figures 2 and 3. Both extruded alloys show an equiaxed structure with grain sizes of about 10 μm and about 1-2 μm for the Cu-rich and Mn-rich alloys, respectively.

HEAT TREATMENT

The first step in the thermal schedule for the powder extrusions was an homogenization anneal. Since the γ -phase (fcc) is required for damping in Cu-Mn based alloys, the high temperature anneal was intended to minimize any microsegregation in the as-extruded microstructure. Encapsulated Cu-rich alloy samples were annealed at 800°C for one hour and water quenched. This is consistent with the recommended treatment for the commercial wrought product. The homogenization anneal promoted abnormal grain growth in the Cu-rich alloy microstructure, resulting in large grains, about 500 μm in diameter, with occasional clusters of small grains, about 20 μm in diameter, as shown in Figure 2. The grain interiors showed some evidence of dispersed stringers, presumably oxide, but appeared to be free of precipitates while some grain boundary regions exhibited isolated precipitate particles. X-ray diffraction measurements indicated that the structure was primarily single phase fcc.

The Mn-rich alloy responded to the high temperature anneal by forming a duplex microstructure. An annealing temperature of 900°C ($0.95 T_{\text{solidus}}$) was chosen. This is similar to the normalized temperature selected for the Cu-rich alloy anneal. Solidus temperatures were measured by differential thermal analysis with powder samples, where $T_{\text{solidus}}(\text{Cu-rich}) = 870^\circ\text{C}$ and $T_{\text{solidus}}(\text{Mn-rich}) = 955^\circ\text{C}$. Encapsulated Mn-rich samples were annealed at 900°C for 1 hour and water quenched. The resulting duplex microstructure, shown in Figure 3, consists of dark contrast phase regions of about 8-10 μm in diameter in a light contrast matrix. The dark phase appears as equiaxed particles and phase boundaries or precipitates are not apparent in the matrix.

Because X-ray diffraction measurements of the annealed and quenched structures of the Mn-rich alloy revealed primarily fcc reflections, other microanalytic techniques were utilized to identify the phase regions. Electron channelling patterns revealed the fcc structure of the dark phase regions. A (110) pole pattern of the "particle" phase region shown in relief can be seen in Figure 4. The erose surface condition of the interparticle region produced by electropolishing prevented the determination

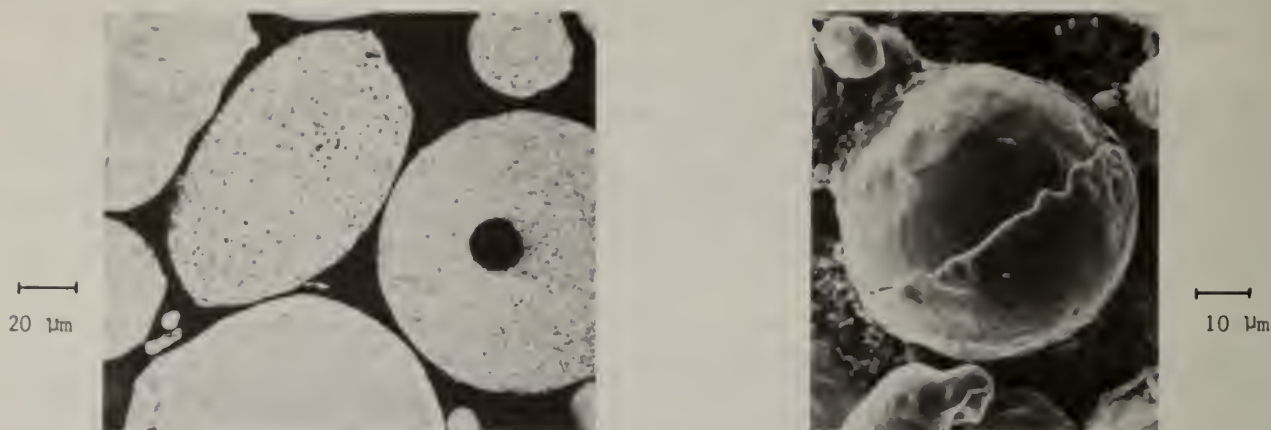


Figure 1. Mn-rich alloy powder cross-section and splat impingement

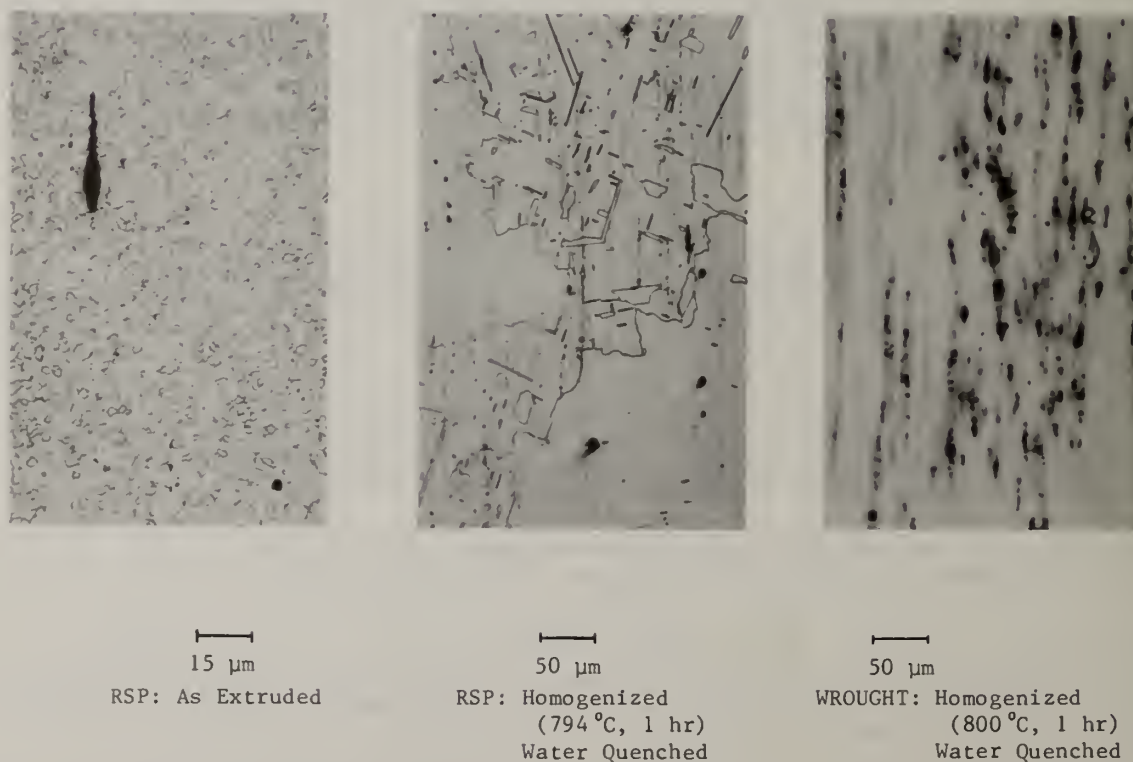
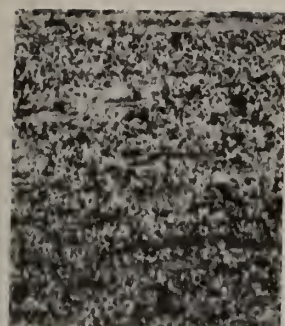
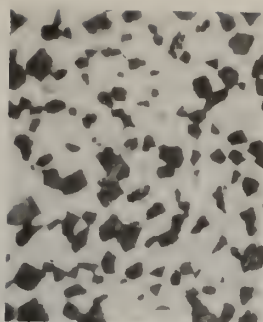


Figure 2. Microstructure of Cu-rich alloy.



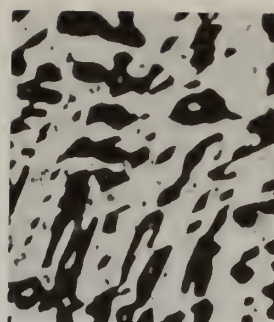
20 μm

RSP: As Extruded



20 μm

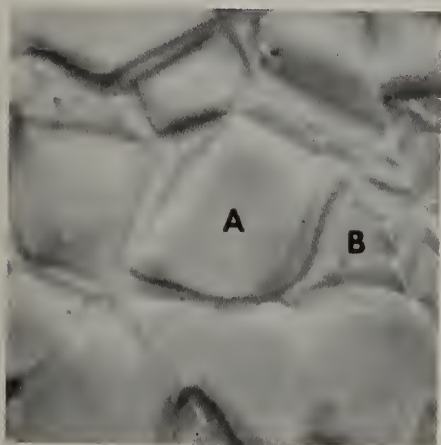
RSP: Homogenized
(900 °C, 1 hr)
Water Quenched



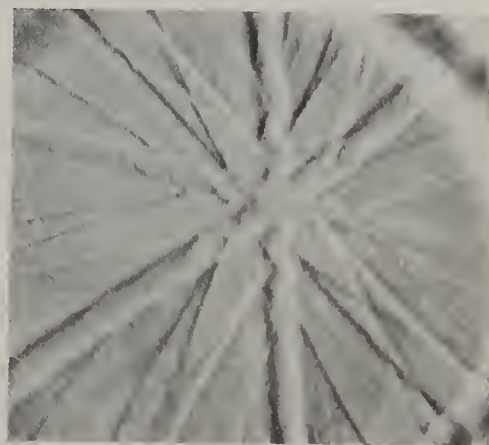
60 μm

CAST: Homogenized
(843 °C, 1 hr)
Air Cooled

Figure 3. Microstructure of Mn-rich alloy



Back Scattered Image



(110) fcc Channelling Pattern from
Grain A

CHEMISTRY (wt%)

	Mn	Cu	Al	Fe	Ni
"A"	54.8	36.4	2.8	4.7	1.3
"B"	46.0	46.7	3.8	2.2	1.3
nominal	55.0	37.0	4.0	3.0	1.0

Figure 4. Crystallography and Chemistry of Mn-rich alloy.

of the matrix phase structure, denoted as "B" in Figure 4, by electron channelling. Further development of thin foil preparation methods is planned to identify the phases with electron diffraction. The results of an electron microprobe analysis of the phase regions, are given Figure 4. The particle phase composition, A, is similar to the initial alloy composition, although lower in Al and higher in Fe. A significant composition shift between the particle phase and the matrix, B, was observed in the microprobe results. The apparent matrix composition suggests that other phases may exist in the microstructure which have not been resolved by this method. The cast microstructure [11] was described as essentially a two-phase mixture of a γ -phase (fcc) and a β -phase (bcc). A third phase, an inter-metallic compound, $\text{Cu}_3\text{Mn}_2\text{Al}$, was also indicated in the report as associated with the β -phase. While the heavily cored microstructure of the casting is distinct from the equiaxed, duplex structure of the extrusion, the identification of the phases [11] is consistent with the microanalytical results of this study.

The aging treatment selected for these alloys was based on the binary Cu-Mn alloy behavior [10] and commercial recommendations. An aging treatment is required to establish an optimum morphology for acoustic damping. The desired morphology contains a coarsened "tweed-like" structure of localized Cu-rich zones, separated by less than 1000 angstroms, in an antiferromagnetic Mn-rich matrix within each grain. The Mn-rich matrix should consist of randomly oriented microdomains. Acoustic energy dissipation is related to elastic wave interaction with the domain walls where the wall motion is impeded by the Cu-rich zones. Implicit in this microstructural model is that the aging treatment should be terminated prior to significant precipitation of the α -Mn phase, which would deplete the antiferromagnetic species.

The response of hardness and damping to aging treatments is summarized in Table I. The acoustic damping measurements were performed using the band-width technique of a cantilever beam in forced resonance [12]. This method for determining the loss factor, a measure of the damping, was used because it can cover a wide range (~100 to 4000 Hz) of frequencies. Values presented in Table I are averaged over the frequency spectrum. Based upon X-ray diffraction results, α -Mn precipitation occurs after an increase in the hardness of the alloy [10]. Thus hardness can be used to monitor, at least in a qualitative sense, the α -Mn precipitation and, hence, to select an aging treatment. Table I lists the loss factor and hardness (DPH), as a function of aging time. It is clearly evident that the initial rise in hardness (0 to 3 minutes) is the critical aging time in contrast to the recommended aging times of 8 hours for the Cu-rich alloy and 4 hours for the Mn-rich alloy [11,13]. The accelerated aging response of the Mn-rich alloy may be caused by the enhanced solute migration kinetics of fine grained materials due to grain boundary diffusion. In the Cu-rich alloy, the rapid α -Mn precipitation may be related to the high density of the oxide inclusions acting as nucleation sites, as evident in the longitudinal section of Figure 2.

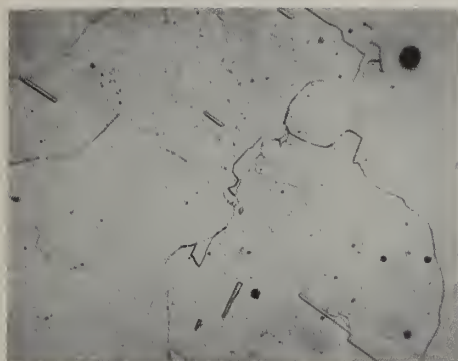
The comments in Table I on the microstructural evolution during aging are based on the results of an optical metallography study. A series of four micrographs, shown in Figure 5 was selected to illustrate the aging sequence of the Cu-rich alloy. In that figure, after 10 minutes of aging, the grain boundaries are decorated with precipitates, presumably α -Mn. Precipitation of α -Mn occurs in the grains after 180 minutes and continues well beyond 600 minutes.

For the Mn-rich alloy, three major aging steps are illustrated in Figure 6. Higher magnification was used to show the detail of the evolution of additional phases during the later stages of aging. The microstructural features of the Mn-rich alloy that was aged for 5 minutes, shown in Figure 6, appear unchanged from the as-quenched state in Figure 3. Solute migration and the presence of an unidentified, fine-scale phase mixture between the grains can be observed after 30 minutes of aging. The overaged condition, represented by the micrograph of the 1080 min. aged sample, is characterized by a continuous grain boundary phase and uniform contrast grains. The apparent light-contrast zone which surrounds the overaged grains may be an etching artifact.

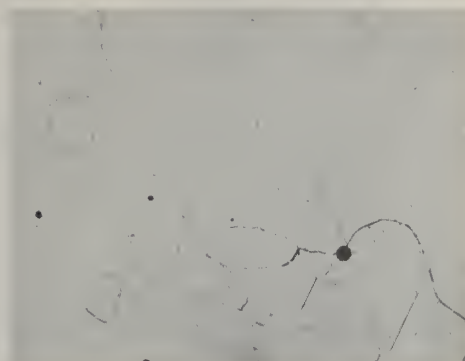
DISCUSSION

Rapid solidification processing of high damping Cu-Mn based alloys results in general microstructural refinement and increased alloy homogeneity. The microstructures of the conventionally processed versions of these alloys are often highly segregated, which can contribute to stress corrosion cracking and low fracture toughness. A marked improvement in these properties is expected to result [7] from the increase in homogeneity realized by the RSP approach used in this study.

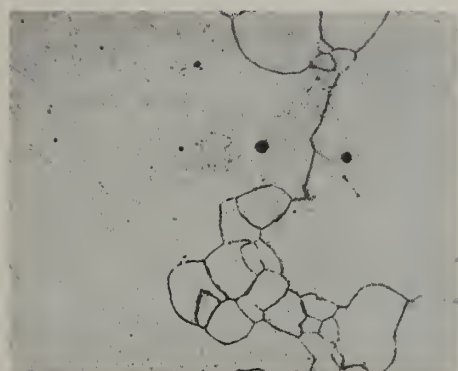
Consolidated specimens of the RSP powders displayed an accelerated response to aging treatments. In contrast to more typical RSP applications where a continuous precipitate arrangement is desirable, the optimum morphology of a Cu-Mn damping alloy should be developed upon aging prior to precipitation from a metastable solid solution [10]. Some factors that contribute to the rapid aging effect in the extruded samples are the small grain size in the Mn-rich alloy, and the presence of fine inclusions in



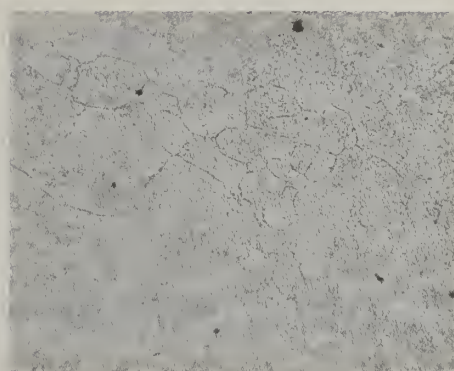
5 minutes



10 minutes



180 minutes



600 minutes

20 μm

Figure 5. Cu-rich alloy homogenized at 800° for 1 hour and aged at 400 °C.

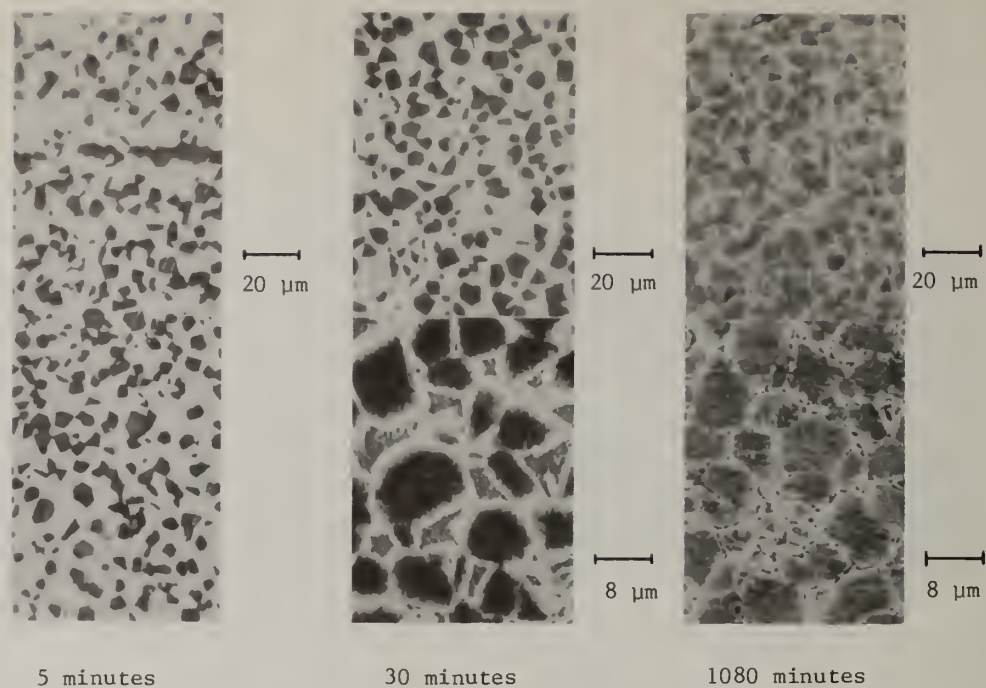


Figure 6. Mn-rich alloy homogenized at 900 °C for 1 hour and aged at 450 °C.

TABLE I: AGING RESPONSE RESULTS

Cu-rich alloy (Homogenized 800 °C, 1 hr; Aging Temperature 400 °C)				
<u>Aging Time</u>	<u>Loss Factor x 10⁻⁴</u>	<u>Hardness</u>	<u>Comments</u>	
(min)		(DPH)		
0	5.2	140	Pronounced Grain Growth	
3	---	155		
5	8.2	151	Apparent α-Mn in Grain Boundaries	
10	---	152		
20	2.8	159		
300	---	168	General Precipitation	

Mn-rich alloy (Homogenized 900 °C, 1 hr; Aging Temperature 450 °C)				
<u>Aging Time</u>	<u>Loss Factor x 10⁻⁴</u>	<u>Hardness</u>	<u>Comments</u>	
(min)		(DPH)		
0	4.3	159	Duplex Microstructure	
3	6.0	178		
5	4.5	187		
15	---	192	Solute Migration	
30	---	191		
45	---	189	Apparent α-Mn in Grain Boundaries	
200	---	200	General Precipitation	

the Cu-rich alloy. To establish convenient peak aging treatments and to enhance the thermal stability of the RSP alloys, the over-aging reaction associated with α -Mn precipitation must be suppressed. The results suggest a strategy to achieve this goal that includes high temperature annealing to encourage grain growth, improved consolidation processing to reduce the inclusion content, and alternative alloy selection to stabilize a single phase microstructure during the high temperature anneal. Clearly, the design of the commercial alloys used in this feasibility study was restricted by conventional ingot metallurgy practice. However, the enlarged composition range accessible to an RSP approach can allow alloy selection based primarily on damping property improvement.

CONCLUSIONS

Relative to the conventionally processed materials, the microstructure of the rapidly solidified and extrusion processed alloys have significantly increased homogeneity. The fine grained structure of RSP extruded products can contribute to a rapid aging response which may limit thermal stability. However, the results suggest a strategy to achieve a homogenous microstructure and an extended service life in RSP high damping Cu-Mn alloys. The RSP approach can be used to select improved alloy compositions without many of the limitations of conventional processing techniques.

ACKNOWLEDGEMENTS

We wish to thank Dr. R.A. Meussner of this Laboratory for his valuable work in preparing the micrographs and D. A. Gerard of Michigan Technological University for his assistance during the preliminary phases of this investigation.

REFERENCES

1. L. Mc. Schetkey and J. Perkins, Machine Design, 50(1978), 202.
2. J.A. Hedley, Metal Science Journal, 2(1968), 129.
3. R.J. Goodwin, Metal Science Journal, 2(1968), 121.
4. D. Birchon, D.E. Bromley, and D. Healey Metal Science Journal, 2(1968), 41.
5. J.L. Holman and L.A. Neumier, Modern Developments in Powder Metallurgy, 10(1976), 259.
6. P.W. Taubenblat, W.E. Smith, and R.L. Bieniek, Modern Developments in Powder Metallurgy, 10(1976), 241.
7. M. Cohen, B.H. Kear, and R. Mehrabian, Proc. of the Second Int'l. Conf. on Rapid Solidification Processing, (1980), pp 1-23.
8. J.E. Smugeresky, Met. Trans., 13A, (1982), 1535.
9. Y.A. Chang, J.P. Neumann, A. Mikula and D. Goldberg, "Phase Diagrams and Thermodynamic Properties of Ternary Copper-Metal Systems," INCRA Monograph VI, The Metallurgy of Copper, International Copper Research Association, Inc., New York, (1979).
10. J.M. Vitek and H. Warlimont, Metal Science, 10(1976), 7.
11. J.M. Langham, Stone Manganese Marine Limited Tech. Paper, no. 6 (1968).
12. R. Plunkett, "Measurement of Damping" in Structural Damping, (J.E. Ruzicka, editor), ASME, New York, 1959.
13. INGRAMUTE Technical Data Sheet, International Copper Research Association, Inc.

FUNDAMENTALS OF RAPID SOLIDIFICATION PROCESSING IN NICKEL-BASE SUPERALLOYS

E.H. Aigeltinger*, A.F. Giamei** and D.M. Dimiduk***

*Pratt & Whitney Aircraft, West Palm Beach, FL 33402

**United Technologies Research Center, E. Hartford, CT 06108

***AFWAL/MLLM/Wright-Patterson Air Force Base, OH 45433

ABSTRACT

A general overview will be given of the benefit currently derived from Rapid Solidification Processing (RSP) of nickel-base superalloys and what may be expected in the future. The discussion is focussed on powder RSP as this is the predominant method of production of RS nickel-base superalloys today. Some microstructural features of nickel-base superalloy powder, which can be produced by RSP, and of consolidated material are presented. Two categories of nickel-base superalloys are discussed: those processed at temperatures higher than the γ' solvus temperature and intended for high temperature use (above about 1800°F) and those processed at temperatures lower than the γ' solvus temperature and intended for low temperature use (lower than about 1500°F). The influence of RSP on the microstructure of both types of materials is discussed and possible avenues for further RSP exploitation of nickel-base superalloys are presented.

I. INTRODUCTION AND HISTORICAL PERSPECTIVE

The application of Rapid Solidification Processing (RSP) to nickel-base superalloys has been interesting, innovative and technologically effective. As the hardener content, volume fraction γ' and strength levels rose during the fifties and early sixties, superalloys underwent serious decreases in ingot homogeneity and workability. Detrimental macrosegregation occurred in large ingots with low cooling rates and long freezing times. Homogenization was out of the question based on the adverse economics of smoothing out fluctuations of relatively slow diffusers over distances of 0.01-0.10m [1]. The alloys also became more difficult to heat treat with only a small gap between the solution and incipient melting temperatures. At the same time, alloy costs began to rise and turbine disks were designed to higher levels of complexity, which increased the demands on workability.

The dilemma was solved by the sequential development of superalloy Powder Metallurgy (P/M) and hot, isothermal, low strain rate forming (GATORIZING®) [2]. The P/M approach started with a homogeneous liquid alloy, produced by Vacuum Induction Melting (VIM), which was then atomized using a gas pressure differential. The powder was canned and consolidated by extrusion (and more recently by HIP) below the γ' solvus temperature. The "blow" of a homogeneous melt with a cooling rate of 10^3 - 10^4 °C/S, vs. 10^{-2} °C/S for an ingot, combined with a powder particle volume of 10^{-13} m³, vs. an ingot volume of 1 m³, led to elimination of macrosegregation due to solute convection. Any residual microsegregation (due to dendritic growth) was eliminated during hot working and/or heat treatment.

The real benefit derived from P/M of nickel-base superalloys resulted from the 1-5 μ m grain size produced during powder consolidation by extrusion or HIP. This fine grain size imparted superplastic behavior to these alloys in that the strain rate sensitivity was high, allowing uniform flow and good fill of complex dies [3]. This coupled with low superplastic flow stresses made forging (GATORIZING) of large turbine disks feasible with presses of reasonable tonnage capacity.

At the same time, material utilization was improved by the application of sonic or near-net shape processing which reduced the required amount of input material. P/M was a technological success for turbine disk application.

In the late seventies, interest turned to even higher cooling rates, namely 10^4 - 10^6 °C/S in processes such as Rapid Solidification Rate [4] and 10^5 - 10^6 °C/S for Laserglaze [5]. In the first process rotary (centrifugal) atomization is carried out in flowing helium and in the second process a thin surface layer is first melted and then resolidified. In these processes convective gas and/or conductive cooling accelerate cooling of the melt. The objective was to obtain high undercooling

resulting in extended solid solubility and cellular or amorphous structures. Potential applications of RSP include low strategic metal content superalloys, higher temperature turbine blade alloys, related, specialized fabrication schemes [6] and hardened surface layers to resist erosion. To date the turbine blade alloys have shown significant promise and will be considered in some detail here.

The turbine material of interest was [111] textured and based on the NiAlMo ternary system. The RSP procedure plus extrusion for texture control plus conditioning heat treatment plus directional recrystallization (DR) led to a columnar-grained or single crystal material with a strong [111] axial texture. It was clear that the final texture and microstructure were strongly dependent upon both alloy composition and starting RSP microstructure.

In the following sections some microstructural features of these alloys, from powder particles to material for blade application, will be presented. Features associated with the outstanding high temperature properties will be emphasized.

II. MICROSTRUCTURAL FEATURES

Powder particles produced by rotary disk atomization have either a dendritic or a microcrystalline morphology, as shown in the particle cross-sections in Figures 1(a) and 1(b), respectively. The microcrystalline morphology is found in the smaller, more rapidly cooled particles and may be produced by homogeneous nucleation in the supercooled liquid. Concentration profiles across interdendritic regions and cell boundaries are shown in Figure 2 [7]. Segregation is very low in the microcrystalline particles indicating they are solidified at an extremely rapid rate. Segregation in the dendritic particles is considerably greater, however, it is substantially less than that found in cast materials. The reduced segregation results in a significant increase in incipient melting point for consolidated powder compared to cast material as shown for several alloys in Figure 3. This is important for subsequent processing as shown below.

For high temperature application transverse grain boundaries in the consolidated RSP alloys can be eliminated in the solid state by directional recrystallization. This consists of passing the material through a furnace hot zone with a temperature profile illustrated schematically in Figure 4.

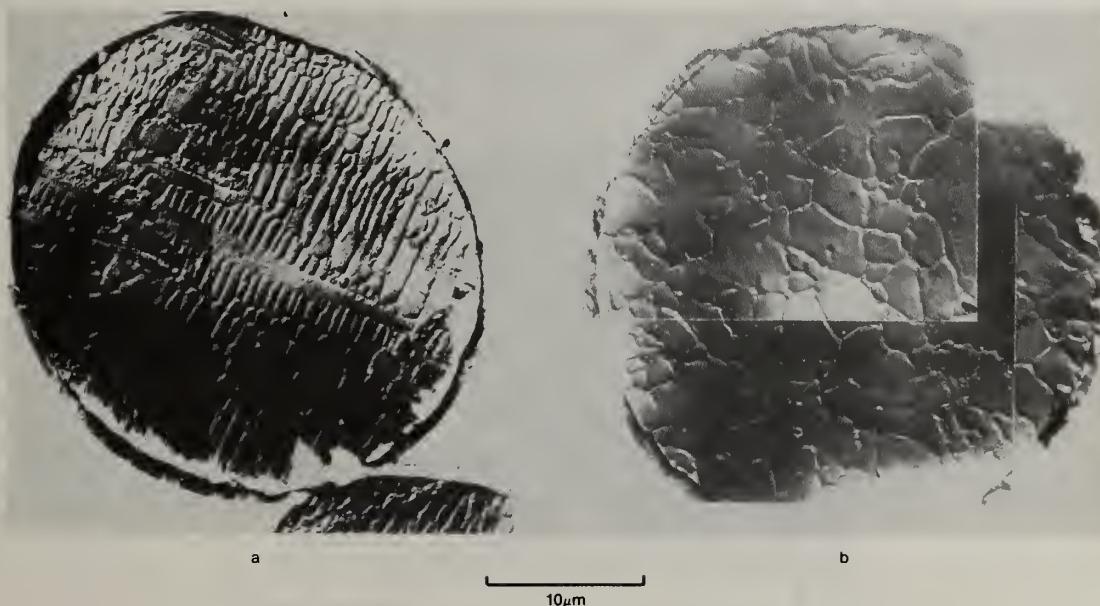


Figure 1: Dendritic (a) and microcrystalline (b) powder particle cross-sections

The DR process is driven by reduction in grain boundary energy (area) associated with the fine-grained consolidated powder structure. The grain boundaries are pinned by γ' until the γ' solvus temperature is reached and γ' dissolves. At this temperature the grain boundaries become mobile and one or several grains across the sample cross-section grow to a single crystal or columnar-grain structure, respectively as the material moves into the temperature gradient. Figure 4 illustrates why the RSP produced increase in incipient melting temperature is beneficial and sometimes essential

for DR processing. The higher incipient melting point case allows a larger difference between the γ' solvus and incipient melting temperatures through which the material must pass in order to achieve DR. A higher incipient melting point also results in a higher thermal gradient at the γ' solvus temperature which generally produces faster DR rates and lower defect content (twins and retained grains) in the DR'd material.

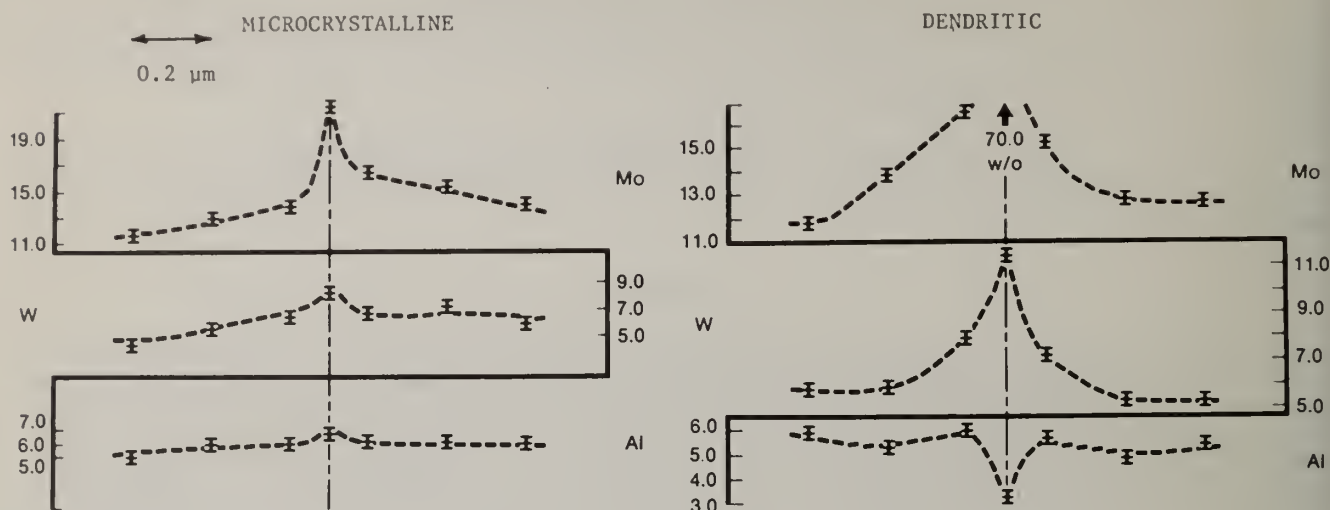


Figure 2: Concentration profiles (weight percent) across interdendritic and cell interfaces in dendritic and microcrystalline powder particles, respectively.

Any features of the as-consolidated microstructure which influence grain boundary motion can influence DR response in terms of DR rate, resulting grain orientation or defect content of the resulting material. For example, initial grain size, primary γ' geometry and dissolution kinetics, primary carbide and α (BCC) precipitate geometry, etc. all influence DR response. These features are all affected to some extent by RSP and subsequent TMP prior to DR processing.

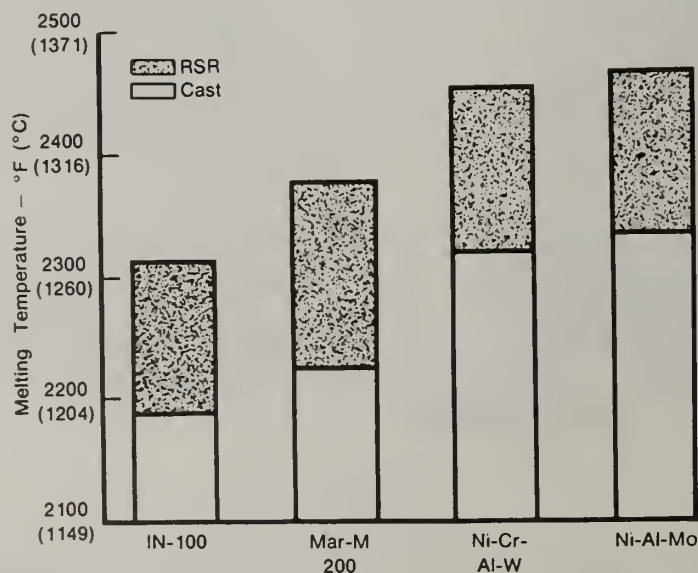


Figure 3: Comparison of RSR and cast incipient melting temperatures for several Ni-base superalloys.

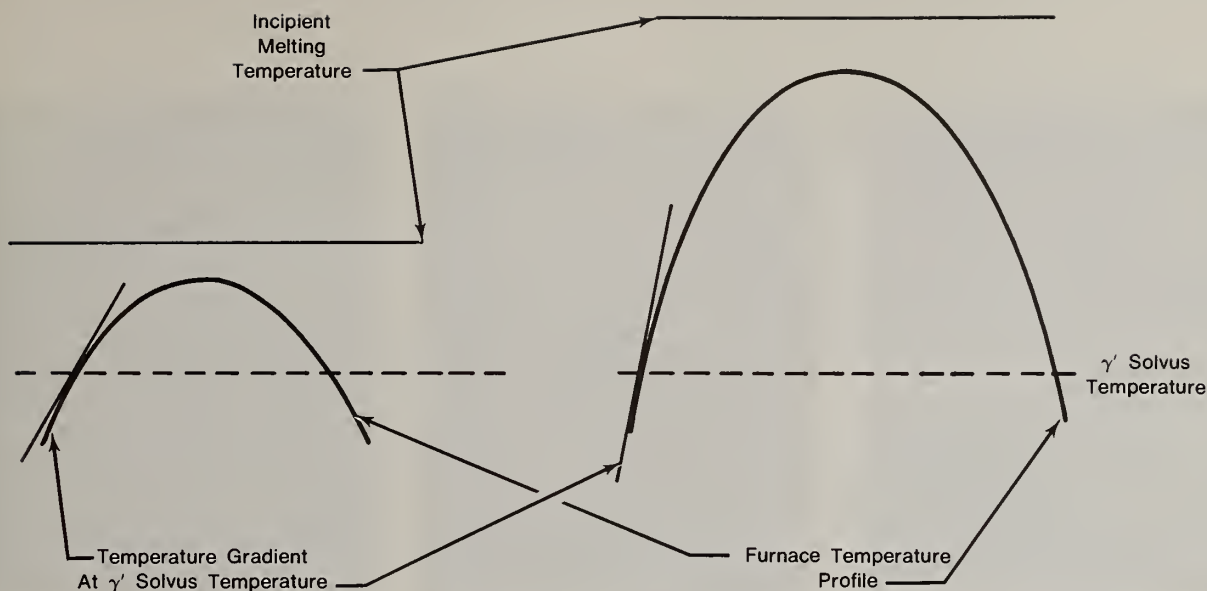


Figure 4: Illustration of temperature profiles and DR conditions for two different incipient melting - γ' solvus temperature "windows".

A representative as-consolidated microstructure is shown in Figure 5. Powder consolidation is typically done by extrusion at temperatures about 50°F below the γ' solvus temperature. The resulting structure is generally fine grained, the structure shown in Figure 5 having a grain size of 1-2 μm . The featureless grains in Figure 5 are γ' while the remaining grains have a γ matrix with a fine, cooling γ' precipitate. The latter grains consisted of γ phase at the extrusion temperature and the γ' precipitate formed on cooling from this temperature. This fine-grained structure provides the driving force for grain boundary motion in the DR thermal gradient, resulting in the columnar or single crystal grain structures produced by DR.

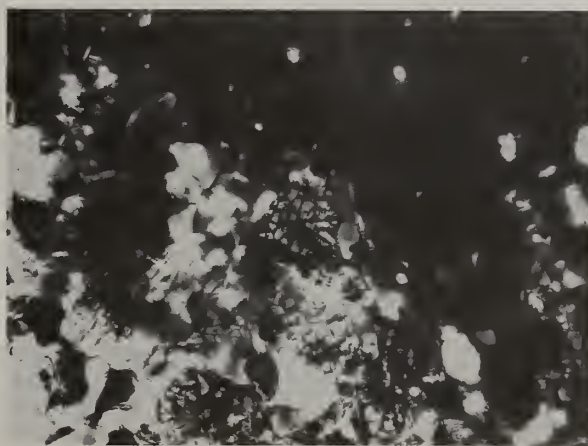


Figure 5: RSR, NiAlMo-base superalloy, as-extruded structure shown in TEM bright field.

If the crystals produced by this RSP-DR, solid-state processing are compared with those produced from the melt by directional solidification (DS), at least two microstructural features are found which are significantly different. Shrinkage voids formed during DS are not found in crystals produced by DR processing. These voids may weaken a cast material as they provide sites for initiation of cracks, especially under fatigue and/or creep conditions. Another microstructural difference is that DS crystals contain an array of low angle boundaries, Figures 6(a) and 6(b) while crystals

produced by DR are defect-free in this regard, Figure 6(c). The substructure density of cast crystals is a function of both crystal orientation and growth conditions.

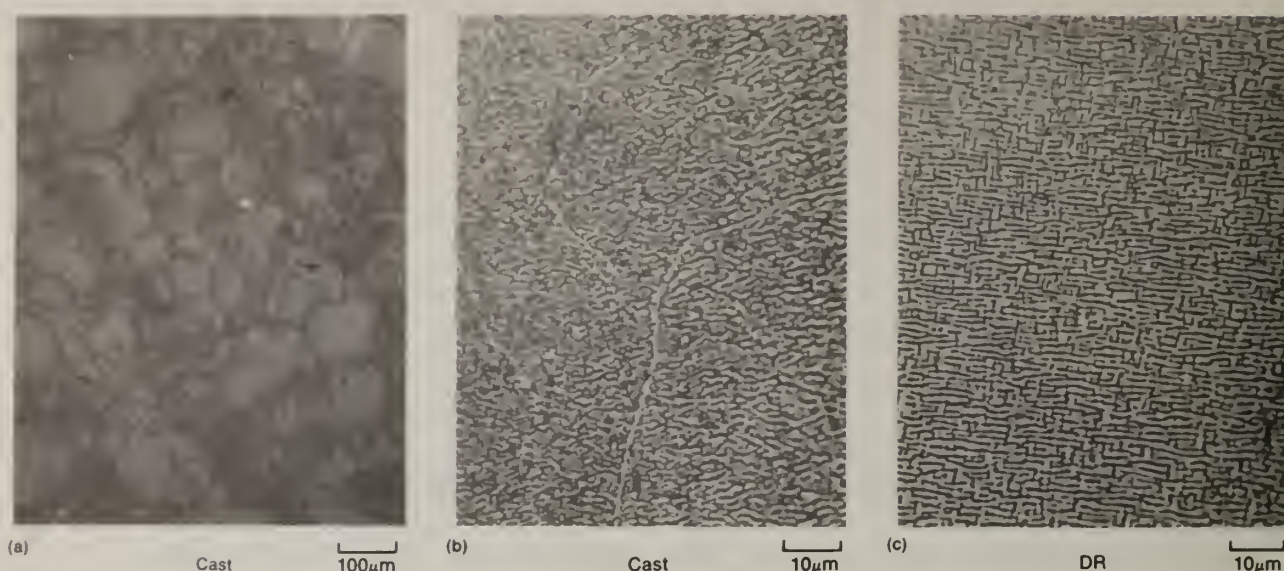


Figure 6: Cast, (a), (b) and DR, (c) microstructures after solution heat treatment.

Another difference between crystals produced by DS and DR processing is that of which crystallographic orientations can be readily produced by these processes. At the present time the [112] orientation of the NiAlMo-base alloys is of interest for its desirable balance of mechanical properties (see Mechanical Properties Section). This orientation can be obtained by DR processing while it cannot be produced by current DS practice because rotation away from [112] occurs during DS crystal growth. This demonstrates how RSP-P/M processing can be used to achieve homogeneous, fine-grained material essential for subsequent processing to a desired structural morphology.

The NiAlMo-base alloys, in the DR'd grain morphology, have stress-rupture capability about 150° better than that of MAR-M200 at high temperatures (see Mechanical Properties Section). The unique compositional requirement for these alloys is saturation in Mo at a temperature above the intended application temperature. This ensures Mo supersaturation at the application temperature, resulting in a number of important microstructural effects, as described in the following.

Mo partitions strongly to the γ matrix phase in preference to the γ' precipitate phase. A concentration of about 20-25 atomic percent Mo is reached in the γ matrix which expands the γ lattice so that at saturation the γ - γ' lattice mismatch, Δa_0 , is about 1%, with the lattice of γ larger than that of γ' . This is the reverse of the sign of misfit in most superalloys. The lattice parameters of the Ni-Mo binary and the approximate lattice parameter of γ' are shown in Figure 7 as a function of Mo content [8]. The lattice parameter of γ' does not change significantly with Mo content while that of γ increases dramatically as shown. The two are equal at some intermediate Mo content. As Mo increases to saturation, Δa_0 increases to its maximum value of about 1%.

This is shown experimentally in Figure 8 where Δa_0 is plotted as a function of saturation level for a number of alloys. The as-solutioned data show a continuous increase in Δa_0 to about 1% with increasing saturation level, because Mo is quenched in solution in both the γ and γ' phases on air cooling from the solution heat treatment temperature of 2400°F. The standard heat treatment consists of an additional four hours at 1975°F after the 2400°F solution heat treatment. This allows Mo present in excess of saturation to precipitate leaving the Mo concentration in solution constant for supersaturated compositions. After such an equilibration heat treatment, Δa_0 increases with Mo content until saturation is reached and then remains nearly constant with further increase in Mo content.

This relatively large value of γ - γ' lattice mismatch for a Ni-base superalloy is accommodated at the γ - γ' interface by formation of an array of interfacial dislocations, as shown in Figure 9 which should

provide a substantial barrier to dislocation motion during deformation. It is expected that these interfacial dislocations are associated with the high strength of the Mo-saturated NiAlMo-base superalloys.

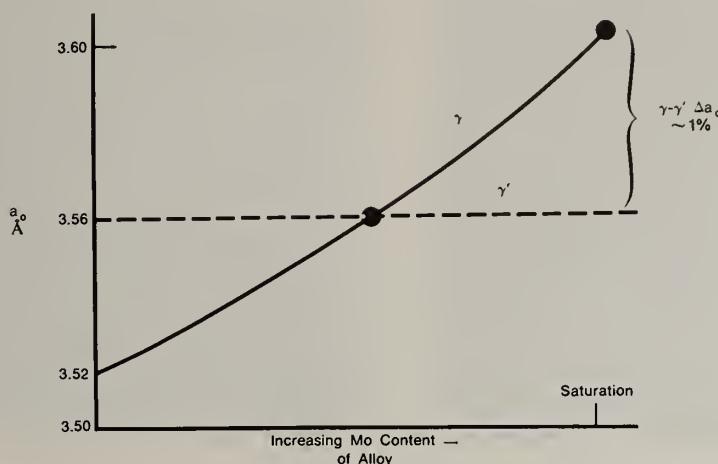


Figure 7: γ and γ' lattice constants as a function of Mo content.

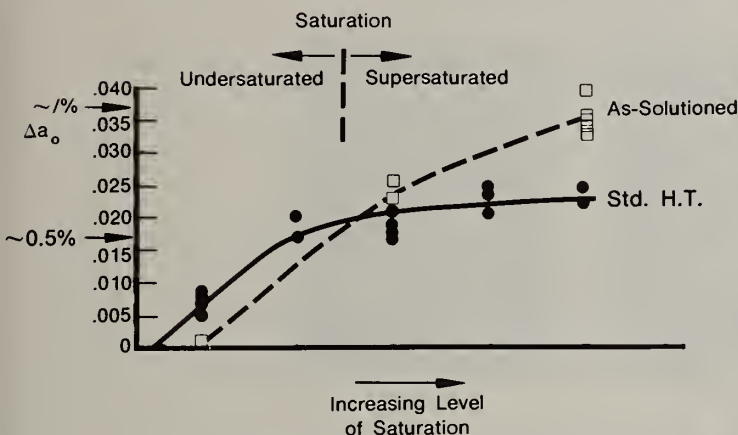


Figure 8: Lattice mismatch, Δa_o , as a function of alloy saturation level.



Figure 9: Bright-field TEM photomicrograph showing interfacial dislocations in NiAlMo alloy after solution heat treatment for two hours at 1316°C (2400°F) followed by 10 hours at 816°C (1500°F).

Despite the relatively high γ - γ' interfacial dislocation content, and hence interfacial energy, the γ' precipitate structure exhibits excellent thermal stability. This is in contrast to the poor γ' thermal stability and associated decrease in strength generally found in Ni-base superalloys when Δa_o deviates from zero by more than about 0.1 percent [9].

A possible basis for this excellent thermal stability is the influence of Mo on the diffusivity of Al in the γ matrix phase. Figure 10 shows the diffusivity of Al in binary Ni-Cr and Ni-Mo alloys as a function of Cr and Mo content. The curves show that both Mo and Cr produce a decrease in Al diffusivity but that Mo has a much stronger effect than Cr. Mo at saturation in Ni produces an order of magnitude decrease in Al diffusivity which is equivalent to about a 250°F increase in temperature capability in terms of resistance to γ' coarsening at Mo saturation compared to that at low Mo content.

This reduced Al diffusivity may account for the excellent diffusion controlled creep resistance of the NiAlMo-base superalloys through both improved γ' thermal stability and reduced dislocation mobility.

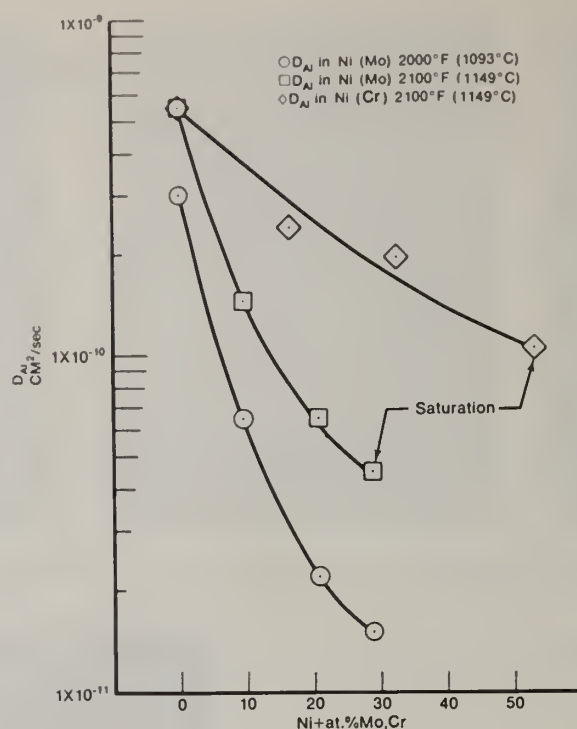


Figure 10: Diffusivity of Al in Ni-Mo and Ni-Cr binary alloys as a function of Mo or Cr content at 1093°C (2000°F) and 1149°C (2100°F) [10].

Additional evidence which supports a low value of Al diffusivity in the Mo-saturated alloys can be found in their inherent grain boundary instability in the form of cellular coarsening. The fact that grain boundary cellular coarsening is severe indicates a high driving force for coarsening exists, apparently as a consequence of the high γ - γ' lattice mismatch. So, when a path for rapid diffusion is present, in the form of a grain boundary, microstructural degradation or cellular coarsening, occurs. However, single crystals exhibit excellent microstructural stability, despite the high driving force for γ' coarsening.

At temperatures below about 1600°F, another significant strengthening mechanism is found in the NiAlMo-base alloys. At these temperatures, several types of Ni-Mo precipitate particles form in the γ matrix phase, in addition to the γ' precipitate phase. The precipitates have the general microstructural appearance shown in Figure 11. These precipitates are present as one or more of the phases: metastable Ni_2Mo (body-centered orthorhombic), metastable Ni_3Mo (D022) and equilibrium Ni_4Mo ($D1_a$). The strengthening effect associated with these precipitates, in combination with large negative lattice mismatch, is substantial at temperatures below about 871°C (1600°F) (as shown in the Mechanical Properties Section).

To this point, consideration has been given only to microstructural features of alloys heated to temperatures above the γ' solvus at some time during processing, as the nature of the DR process necessitates exposure to these high temperatures. As mentioned, a number of microstructural features of the consolidated material play a part in DR response, however, the mechanical properties of the resulting material do not appear to depend, to any significant extent, on microstructural features established directly by RSP. In contrast, processing at temperatures below the γ' solvus allows features influenced by RSP to be retained in the final microstructure to a much greater extent. Structures in this condition have not been considered during the DARPA/AFML/PWA blade alloy development program, consequently mechanical property data are not available. However, a range of microstructural features can be obtained and some of these are briefly presented below.

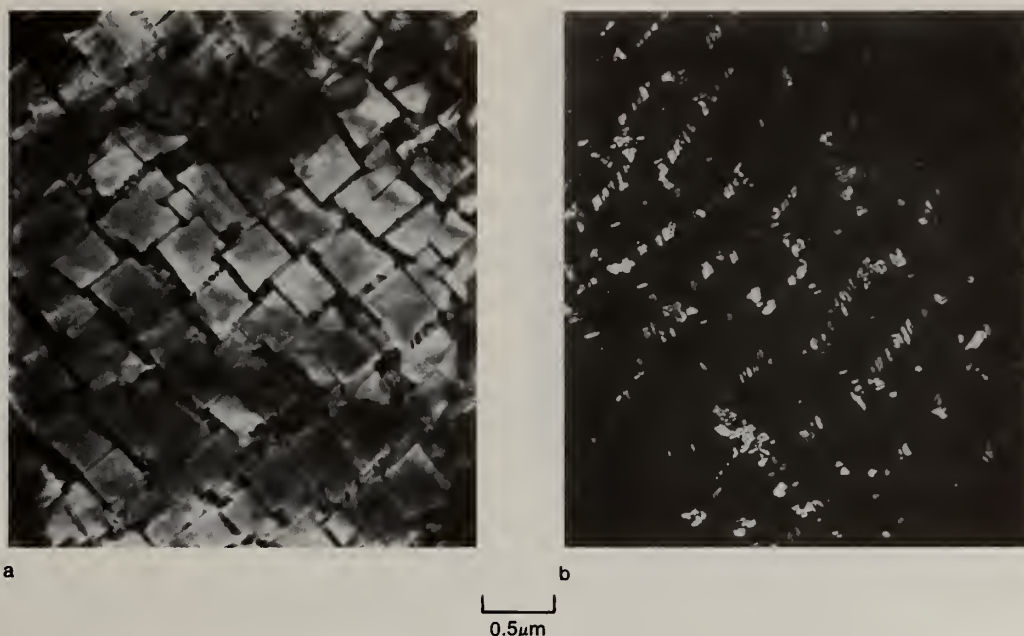


Figure 11: Ni_3Mo precipitate structure in a NiAlMo -base alloy after solution heat treatment for 2 hours at 1316°C (2400°F) followed by 100 hours at 760°C (1400°F). Bright field (a) and dark field (b) TEM images.

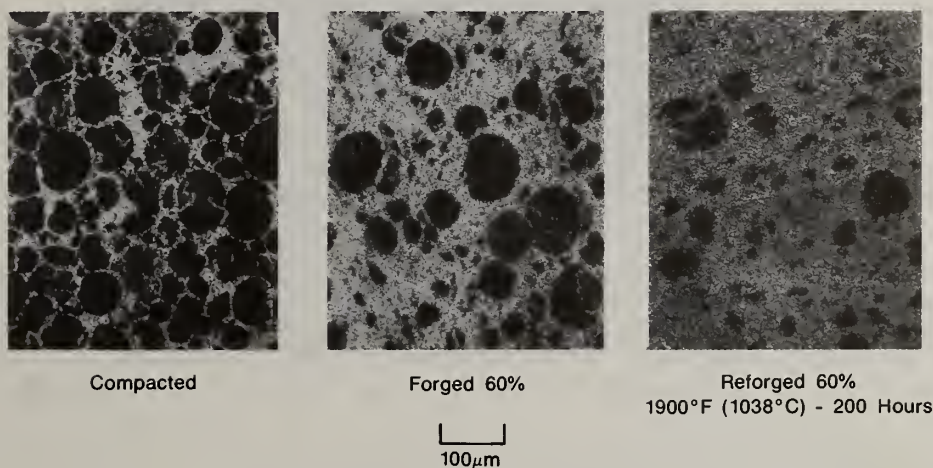


Figure 12: Various volume fractions of unrecrystallized particles in a recrystallized matrix produced by compaction and forging of NiAlMo -base superalloy RSR powder.

For example unrecrystallized powder particles can be retained, with various geometries and volume fractions, in a recrystallized matrix, as shown in Figure 12. The precipitate morphology in the recrystallized matrix and unrecrystallized particles can also be controlled by RSP and TMP. Figure 13 shows unrecrystallized particles in a recrystallized matrix consisting of fine grains of γ and γ' . These unrecrystallized particles have a very fine-scale morphology as shown in Figures 13(b) and 14. The unrecrystallized area shown in Figure 14 has a γ' matrix with some isolated areas of γ and α -BCC, Mo-rich precipitate particles. The morphology of these unrecrystallized powder particles is established by the RSP response of the material. In addition the areas of γ phase will develop the Ni_xMo ($x = 2, 3, 4$) precipitates discussed above on heat treatment at temperatures below about 871°C (1600°F).

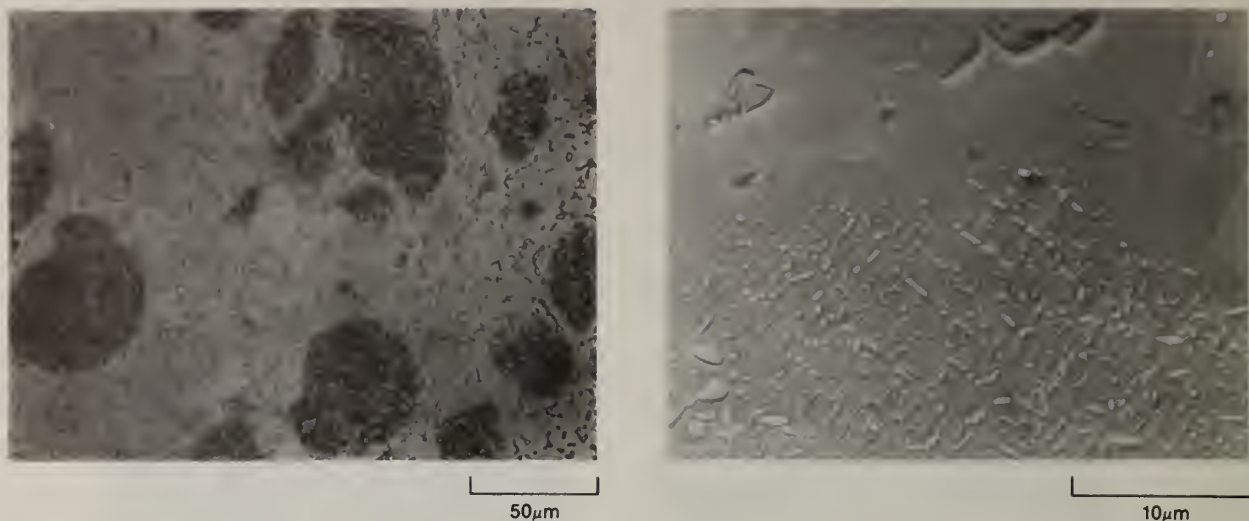


Figure 13: Optical (a) and TEM replica (b) photomicrographs of vacuum-hot compacted NiAlMo-base superalloy powder showing unrecrystallized particles in a recrystallized matrix.

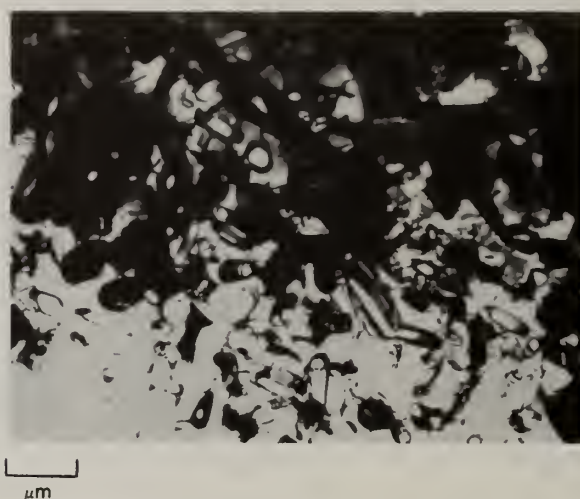


Figure 14: TEM bright field image showing detail of unrecrystallized NiAlMo alloy powder particle.

It is apparent that a variety of microstructures can be produced by RSP followed by suitable TMP. However, correlation of these microstructures with mechanical properties, in most instances even in general terms, is not possible at present.

III. MECHANICAL PROPERTIES

The NiAlMo-base superalloys have an advantage of approximately 83°C (150°F) in stress-rupture capability over MAR-M200 at high temperatures, as shown in Figure 15. This curve represents data for a number of alloys, such as alloy 185, having the composition: Ni-14Mo-7Al-6W-0.04C in weight percent. The curve is essentially the same for material tested in the [112] or [111] crystallographic orientations. These orientations have nearly the same stress-rupture capability and are both anomalously strong in these orientations compared to MAR-M200.

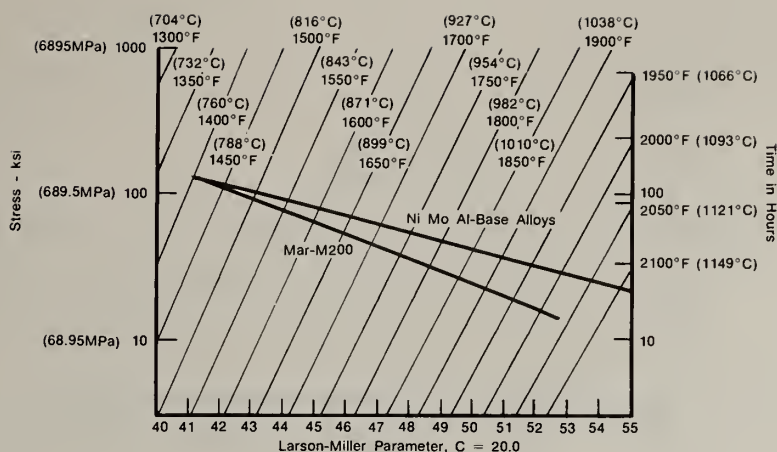


Figure 15: Larson-Miller plot comparing stress-rupture life behavior of NiAlMo-base alloys and Mar-M200.

The [112] orientation has a better combination of mechanical properties for turbine blade application in that the elastic modulus is lower than for the [111] orientation (36 vs. 42 X 10⁶ psi) which results in better LCF capability. Directional recrystallization processing is essential for producing the [112] orientation because, as mentioned in Section II, this orientation cannot be produced by current directional solidification processing practice.

Another property of importance, which is strongly influenced by solidification rate, is environmental resistance associated with low concentrations of reactive elements. During single crystal production by DS the slow rates inherent in this process combine long mold-metal reaction times with large melt/mold surface-to-volume ratios. The combination of such favorable conditions for mold/metal reaction(s) with considerable dendritic segregation makes it difficult to maintain reactive element concentrations at desired levels or to maintain uniform concentration throughout a casting. These difficulties are not encountered in RSP-DR produced material and uniform reactive element concentrations can be obtained in crystals made by this process.

Little mechanical property data are available for alloys processed and tested at low temperatures (less than 871°C (1600°F)), however a peak in hardness is observed on heat treatment at about 760°C (1400°F) after a sub-solvus partial solution at 1246°C (2275°F) for two hours. The hardness profile spanning temperatures from about 593°C (1100°F) to 982°C (1800°F) for a time of 20 hours is shown in Figure 16. This peak is associated with formation of Ni-Mo precipitate phases in the γ matrix phase, as described in the preceding section.

The yield strength of this alloy at 760°C (1400°F) after heat treatment for 50 hours at 760°C (1400°F) is 1240 MPa (178,000 psi). This compares favorably with IN100, on a strength-to-weight basis, which has a yield strength of 1040 MPa (150,000 psi) at 704°C (1300°F).

In summary, the high temperature strength capability of these alloys is excellent. There also appears to be potential for application at temperatures below about 871°C (1600°F), provided further development of these alloys is undertaken with this objective in mind.

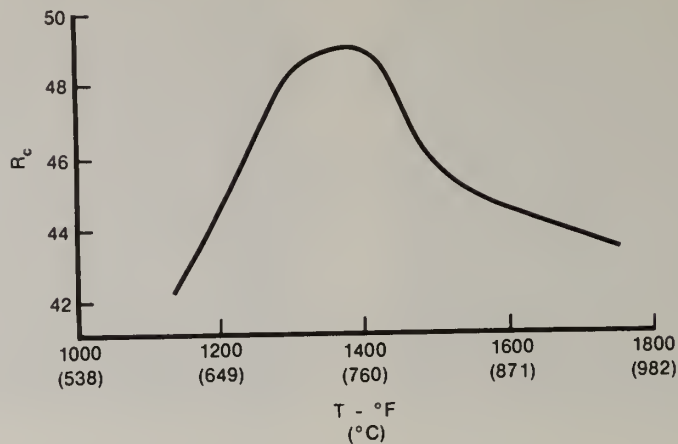


Figure 16: Rockwell C hardness profile of NiAlMo alloy powder consolidated by extrusion and heat treated for 2 hours at 1246°C (2275°F) followed by 20 hours at the indicated temperatures.

IV. FUTURE DIRECTIONS

For high temperature structural applications of crystals grown in the solid state by DR processing, it will be important to control, reduce or eliminate defects such as growth twins or retained grains in the directionally recrystallized product. The frequency of these defects is known to depend on alloy composition and TMP conditions. Additionally, it may become possible to favorably modify the grain boundary/stacking fault energy ratio to reduce twin fault probability. Alternatively, it should be possible to control the prior and final crystal orientations and growth velocities to minimize formation of growth twins and to better define the TMP conditions and textures to avoid formation of large numbers of twin-related grains during deformation. These improvements should lead to enhancement of creep resistance, stress-rupture life, stress-rupture ductility and fatigue capability.

Alloy development will focus more on undercooling and its relationship with microstructure, rather than cooling rate per se. Melt thermal history, minor elements in the alloy and ceramic environment (if any) will be important areas of effort. Clean melting will be a major thrust area. It will almost certainly become possible to specify and control the level and distribution of reactive elements in the final part. This combined with uniform distribution of major alloying elements, should lead to significant improvement in oxidation/corrosion resistance of RSP materials.

Considerable effort will be directed at preservation of RSP microstructural features (e.g., by Laserglasing or dynamic compaction) through consolidation and TMP, in order to derive the maximum RSP benefit. Production of finer particles or generally faster cooling rates will result in greater undercooling and the opportunity to obtain a wider range of useful microstructures. This will also provide the opportunity for exploitation of the superplastic deformation behavior of microcrystalline structures produced by RSP. Finally, development of dispersion strengthened structures and extended solid solutions remain essentially unexplored areas of considerable potential in nickel-base superalloys produced by RSP.

V. SUMMARY AND CONCLUSIONS

Current interest in RSP evolved from the expected benefit to be derived from rapid cooling rates and successes achieved by the combination of conventional P/M and the GATORIZING process. The RSR process, in combination with TMP including DR processing, when applied to NiAlMo-base alloy compositions, resulted in exceptionally strong Ni-base superalloys for high temperature application. The basis for this strength lies in the detailed nature of microstructural effects produced by Mo saturation including large values of γ - γ' lattice mismatch and low Al diffusivity in the γ matrix. Considerable potential remains for the application of these alloys at temperatures up to 871°C (1600°F).

Future effort will be directed at a number of areas such as reduction of defect content in solid-state, DR-processed crystals, optimization of reactive element distribution for improved environmental resistance, clean melting and exploitation of the deformation behavior of microcrystalline structures. Finally, preservation of RSP-produced microstructural features through consolidation and TMP, in order to maximize the direct benefit of RSP, will be an area of considerable future interest.

REFERENCES

1. M.C. Flemings, "Solidification Processing," McGraw-Hill, New York, 1974.
2. J.B. Moore and R.L. Athey, Design News, January 1970, p. 17.
3. N.E. Paton and C.H. Hamilton, "Superplastic Forming of Structural Alloys," AIME, Warrendale, PA, 1982.
4. A.R. Cox, J.B. Moore and E.C. van Reuth, Proc. of Third International Symposium on Superalloys, Claitor's, Baton Rouge, LA, 1976, p. 45.
5. E.M. Breinan, B.H. Kear and C.N. Banas, Physics Today, November 1976, p. 44.
6. B.H. Kear and E.R. Thompson, Science, Volume 208, May 23, 1980, pp. 847-856.
7. R. Field and H. Fraser, private communication.
8. W.B. Pearson, "Lattice Spacing and Structures of Metals and Alloys," Pergamon Press, New York, 1958.
9. I.L. Mirkin and O.D. Kancheev, Met. Science Heat Treat., nos. 1 and 2, 1967, pp. 10-13.
10. E. Aigeltinger and P. Reynolds, unpublished research.

ACKNOWLEDGEMENTS

The views and conclusions contained in this paper are those of the authors and should not be interpreted as necessarily representing the official policies, either expressed or implied, of the Advanced Research Projects Agency of the U.S. Government.

THE MECHANICAL BEHAVIOR OF RSPD MATERIALS

M.R. Jackson
General Electric Corporate Research and Development
Schenectady, New York 12301

R.W. Smashey
General Electric Aircraft Engine Group
Evendale, Ohio 45215

L.G. Peterson
General Electric Gas Turbine Division
Schenectady, New York 12345

ABSTRACT

A number of Ni, Fe and Co-base alloys have been evaluated in structures formed by rapidly solidified plasma deposition processing. Alloys have included both conventional superalloy compositions and experimental compositions. Tensile and rupture behavior have been evaluated for some alloys in orientations within the plane of the deposit. Results of tests to evaluate thermal fatigue resistance are described.

Introduction

Rapid solidification has received considerable attention in the past five years for metal processing (1,2). The technique offers the possibility of achieving unique mechanical properties through microstructural control. Ultrafine microstructures free of macrosegregation are produced in compositions developed for more conventional metals processes. More useful, potentially, is the increased range of compositions that can be generated and the metastability that can be produced in terms of extended solubility and non-equilibrium phase formation.

Plasma spraying in a low-pressure environment has been used to produce structural alloys by rapid solidification plasma deposition (RSPD) (3,4). Ultrafine microstructures free of microsegregation have been produced in thick deposits of nearly full density. For the past year, a program has been directed at examining the usefulness of the RSPD process for application of high-temperature superalloy materials (5). Areas being addressed have included the technology associated with the process, detailed physical descriptions of the plasma gun, plasma-powder interactions, and the materials technology.

The present discussion will describe some of the effort dealing with the materials technology. Specifically, mechanical behavior and modulus of elasticity have been evaluated for a variety of compositions. Possible influence on behavior due to unmelted powder particles incorporated into the RSPD structure has been investigated. Chemistry effects on intermediate temperature (750-950C) ductility have been considered. Bond strengths have been measured for RSPD materials deposited on non-RSPD substrates of the same composition. Finally, the resistance of RSPD materials to thermal fatigue exposure has been determined. Structures produced using a variety of plasma facilities were sectioned so that thermal stresses would be maximized either parallel to or perpendicular to the plane of plasma deposition.

Experimental Procedure

Powders of alloys to be deposited were gas atomized by Alloy Metals, Inc., Troy, MI, or Special Metals Corp., Ann Arbor, MI, or were vacuum atomized by Homogeneous Metals, Inc., of Herkimer, NY. All powders used for spraying had been sieved to recover the -400 mesh fraction, that is, particles $37\mu\text{m}$ and smaller in diameter. Gas analyses were performed on all the powder lots.

Depositions were performed in a low-pressure environment using plasma guns manufactured by two manufacturers. Conditions used during deposition are listed in Table I. Substrates were steel or copper plates, .3 cm thick and approximately 7 cm by 15 cm. The transverse direction between gun and substrate was parallel to the long axis of the plate. Total powder feed of as much as 2.3 kg was performed after the plate had been preheated to ~850C using the plasma as the heat source. Pre-heating and deposition generally were complete within 20 minutes.

TABLE I
SELECTED RSPD PARAMETERS

	A	B
Plasma Gun		
Plasma Gas Parameters	Ar 1.4 l/sec He .3 l/sec	Ar .84 l/sec H ₂ .14 l/sec
Gun Voltage	55V	52-53V
Gun Amperage	1300A	900A
Chamber Pressure	60 torr	40 torr
Powder-Feed Rate	2.9 g/sec	1.25 g/sec
Powder Injection	Internal, 20° angle	External
Carrier Gas	Ar .12 l/sec	Ar .025 l/sec
Gun-to-Substrate Distance	25-33 cm	39 cm
Traverse Rate	15-20 cm/sec	5 cm/sec

Test bars for tensile, stress rupture, elastic modulus, and oxidation resistance were normally produced with the test bar axis in the plane parallel to the substrate surface. Slugs were heat treated prior to machining to test bar geometry. In general, tensile tests were performed in an inert atmosphere or vacuum using a strain rate of .04/min. Tests were conducted over a range of temperatures from 20C to 1060C. Rupture testing was done in air at temperatures of 610C to 1060C.

Thermal fatigue behavior was measured in a simulated engine thermal shock (SETS) facility. Specimens ~5.1 cm in length were machined as a wedge tapering at a 15° angle from .51 cm wide at the base over a distance of 1.52 cm. The narrow end of the wedge was machined to a .064 cm radius. Wedges were machined from a cylindrical shell deposit (Figure 1) such that the sample was oriented in a longitudinal or short transverse relation to the shell deposit. Again, samples were cut as blanks, heat treated, and then machined. The SETS test consisted of heating the wedges end-on in gas burners from 425C to 1040C within a time period of 10 seconds, holding at 1040C for 40 seconds, cooling to 480C in 10 seconds, and further cooling to 425C in another 10 seconds. The initiation of cracking is monitored by periodic visual inspection. Crack growth rates can be measured after initiation.

Bond strength was measured using a test bar similar to that in the other mechanical test programs. Material for test bar blanks was electrodischarge machined from a thick deposit on a thick substrate so that the center of the gage to one end of the machined bar was RSPD material. Tensile strength and rupture resistance of the bond test bars were measured.

Results and Discussion

Alloy Selection

A study to determine what components within advanced jet engines would combine substantial performance or cost benefits with rapid production implementation indicated that stationary components in the hot section of the engine were high priority candidates. Initial design studies predicted that part life might be increased two- to four-fold by use of a composite structure in place of current monolithic structures. The composite would use materials with low thermal expansion coefficient on the hot side, and high thermal expansion coefficient on the cool side. This ordering of materials would effectively lower thermal strains produced by thermal gradients. The desired improvement in part life would be achieved with little change in mechanical properties of the individual layers of the composite relative to properties of the present monolithic alloys.

Based on the composite analysis, seven compositions were chosen for RSPD which compositionally are identical to commercially available cast or wrought materials. They were chosen on the basis of mechanical properties and thermal expansion behavior of conventionally produced materials. The alloys included powder compositions equivalent to the compositions of Rene' 80, Rene' 120, Udimet 700, Hastelloy-X, Mar M-509, A-286, and FeCrAlYT_i material. These compositions are listed in Table II.

In addition, six experimental compositions were chosen for RSPD. These compositions, designated C1 through C6, are also listed in Table II. Several considerations entered into selection of these alloys. It had been observed previously that many of the strong γ' superalloys, such as Rene' 80 or IN-738, showed a loss in ductility at about 900C when tested as RSPD material. An alloy simulating the composition of the γ phase of Rene' 80 showed good tensile ductility, while alloys with γ' content equal to or greater than that of Rene' 80 showed poor ductility (see Figure 2). One consideration for the alloys chosen was to determine whether other strong alloys would show the poor ductility, such as those strengthened by γ'' (C1 based on IN-718), or by a Ti-rich γ' (C6 based on A-286 or U-212). Another consideration related to the expectation that composites at

TABLE II
NOMINAL COMPOSITION OF EXPERIMENTAL ALLOYS

Alloys	Weight Percents													
Designation	Ni	Fe	Cr	Mo	Cb	Ti	Al	Si	Mn	C	B	Co	W	
René 80	59.7	.2	14.0	4.0	—	5.0	3.0	0.2	0.2	0.17	0.015	9.5	4.0	0.03 Zr
René 120	59.2	.2	9.0	2.0	—	4.0	4.3	0.1	0.1	0.17	0.015	10.0	7.0	3.8 Ta 0.07 Zr
Hastelloy-X	46.3	18.5	22.0	9.0	—	—	—	1.0	1.0	0.10	—	1.5	0.6	
Mar-M509	10.0	1.5	22.5	—	—	—	—	0.4	0.1	0.60	0.01	60.89	—	3.5 Ta 0.5 Zr
A-286	26.0	52.8	15.0	1.3	—	2.1	0.3	0.7	1.5	0.04	0.005	—	—	0.3V
FeCrAlYT _i	—	72.8	21.6	—	—	.5	4.6	—	—	—	—	—	—	.5Y
Udimet 700	52.1	<1.0	15.0	5.0	—	3.5	4.5	0.2	0.15	<.06	0.03	18.5	—	
C1	61.91	9.5	12.38	3.26	9.48	1.63	1.15	0.29	0.28	0.08	0.04	—	—	
C2	54.95	18.06	12.39	4.90	7.10	1.22	0.69	0.29	0.28	0.08	0.04	—	—	
C3	51.98	18.24	16.98	6.60	3.99	0.82	0.70	0.29	0.28	0.08	0.04	—	—	
C4	48.94	18.43	21.67	8.33	0.81	0.42	0.70	0.29	0.29	0.08	0.04	—	—	
C5	39.88	33.50	17.43	5.07	0.81	2.11	0.48	0.30	0.29	0.09	0.04	—	—	
C6	30.52	49.05	13.05	1.72	0.83	3.86	0.24	0.30	0.30	0.09	0.04	—	—	

high temperature might show significant metallurgical instabilities at interfaces due to interdiffusion. For this reason, concentrations of many elements in the alloy series were held nearly constant to minimize the diffusional effects. Alloy C4, which is similar to Hastelloy-X, includes small amounts of Al, Cb, and Ti to minimize interdiffusion with the other alloys. Alloys C1 through C4 make up one series, with C2 and C3 having compositions intermediate between C1 and C4, while alloys C4 through C6 make up a second series. The end point compositions were based on commercial alloys and were chosen to be consistent with the preliminary design analysis. A final consideration in the choice of experimental alloys was the intention of minimizing strategic element content, including Co, Cr, and Ta.

Structure Characterization

Oxygen and nitrogen analyses of the powders are shown in Table III. As can be seen, oxygen for the -400 mesh particles is in the range of 200-300 wppm for most of the alloys, regardless of manufacturer. These values are typical of laboratory scale (20-80 kg) atomizer production. Nitrogen appears to be more dependent on source, being below 60 wppm for C1 through C6. Whether these lower values are due to processing or melt stock is not known.

Particle size was measured in a particle analyzer. Despite the large range of compositions represented by the six alloys, C1 through C6, the particle size distributions of the -400 mesh fraction are nearly identical. Figure 3 shows the value of the particle diameter for which 90%, 50%, or 10% of the particles are smaller. The average values for the six alloys are: 90%/43.2 μm , 50%/25.9 μm , 10%/12.8 μm . The analyses shown here are also typical of analyses for the commercial alloy compositions. Figure 4 shows a typical -400 mesh powder fraction. There is a contradiction between SEM observations of particle size and those indicated by the particle analyzer. The analyzer indicates 10% of the particle volume is in particles larger than 43 μm ,

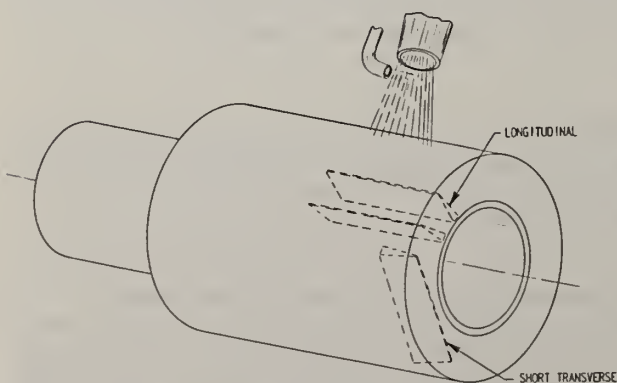


Figure 1. RSPD SETS wedge configuration.

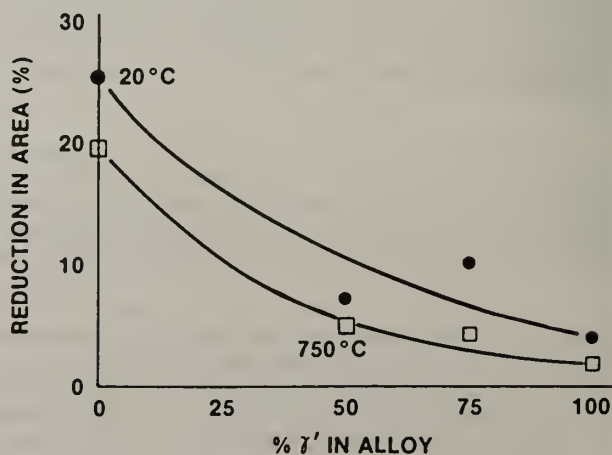


Figure 2. Tensile ductility in RSPD Ni alloys.

TABLE III GAS ANALYSIS OF -400 MESH POWDER

Alloy	Content (wppm)		Alloy	Content (wppm)	
	O	N		O	N
C1	184	38	A-286	790	142
C2	253	21	Hastelloy-X	587	231
C3	252	14	Rene' 80	306	182
C4	269	16	Rene' 120	180	76
C5	286	56	FeCrAlYTi	673	120
C6	310	12	Mar M-509	321	153
			U-700	141	30

TABLE IV GAS ANALYSIS OF RSPD DEPOSITS

Alloy	Content (wppm)		Alloy	Content (wppm)	
	O	N		O	N
C1	341	57	A-286	540	867
C2	380	43	Hastelloy-X	196	125
C3	401	26	Rene' 80	299	161
C4	395	30	Rene' 120	276	115
C5	345	67	FeCrAlYTi	1887	632
C6	317	25	Mar M-509	79	211
			U-700	116	65

yet particles larger than $40\mu\text{m}$ are almost never seen. The analyzer results are useful on a relative basis, however. If the measured "10% smaller" diameter moves below about $10\mu\text{m}$, the powder tends to feed poorly in the powder feeders and through the powder-injection ports.

Gas analyses for deposits shown in Table IV indicate oxygen pick-up following deposition ranges from near zero to as much as ~ 200 wppm. For the alloys shown, the degree of pick-up appears to be related to Al content of the alloy. Pick-up presumably occurs on the heated deposit surface while the plasma is on adjacent regions.

Densities of as-sprayed materials were generally above 97% of the theoretical full density values. This is shown in Table V, together with the results of density measurements on heat treated samples. High temperature heat treatments produce essentially full density structures, as shown in Figure 5.

Microstructures of as-deposited materials have been discussed elsewhere in the conference proceedings (6,7). The heat treated microstructures depend strongly on alloy chemistry. Alloys with low γ' solvus temperatures, or no γ' at all, can undergo significant *in situ* grain growth following deposition while the structure is still hot. Grain sizes of $50\text{--}100\mu\text{m}$ result in these materials after heat treatment at $1200\text{--}1250^\circ\text{C}$. The γ' strengthened alloys are fine grained ($\sim 1\mu\text{m}$) after deposition, and grow to only $25\text{--}50\mu\text{m}$ grain size during isothermal annealing.

TABLE V EFFECT OF HEAT TREATMENT ON DEPOSIT DENSITY

Alloy	Density (g/cm ³) after 1 h dry H ₂ treatment at				
	As-Deposited	960C	1060C	1160C	1260
C1	8.10	8.14	8.10	8.32	8.33
C2	8.04	8.00	8.01	8.12	8.35
C3	8.09	8.08	8.06	8.10	8.20
C4	8.09	8.11	8.13	8.19	8.24
C5	7.90	7.97	7.96	8.02	8.15
C6	7.95	7.91	7.89	7.97	7.96

	Density (g/cm ³) after 4 h treat at					
	As-Deposited	982C	1093C	1149C	1204C	
Rene' 80	8.11	8.11	8.11	8.14	8.19	8.22
Rene' 120	8.39	8.39	8.41	8.41	8.44	8.44
Hastelloy-X	8.22	8.25	8.30	8.30	8.30	8.30
Mar M-509	8.80	8.83	8.83	8.86	8.86	8.83
A-286	7.75	7.75	7.83	7.86	7.86	7.89
FeCrAlYTi	6.92	6.95	7.0	7.03	7.03	7.06

O - MEAN DIAMETER (VOLUME DISTRIBUTION)

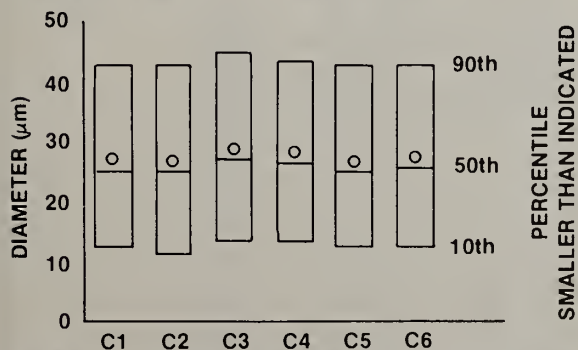


Figure 3. Particle size analysis of -400 mesh powders of alloys C1-C6.

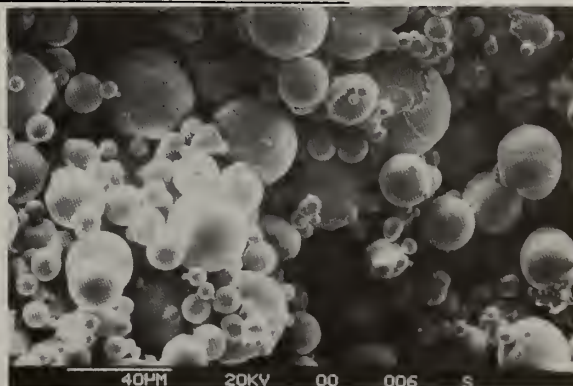


Figure 4. Scanning electron micrograph of -400 mesh Mar M-509.

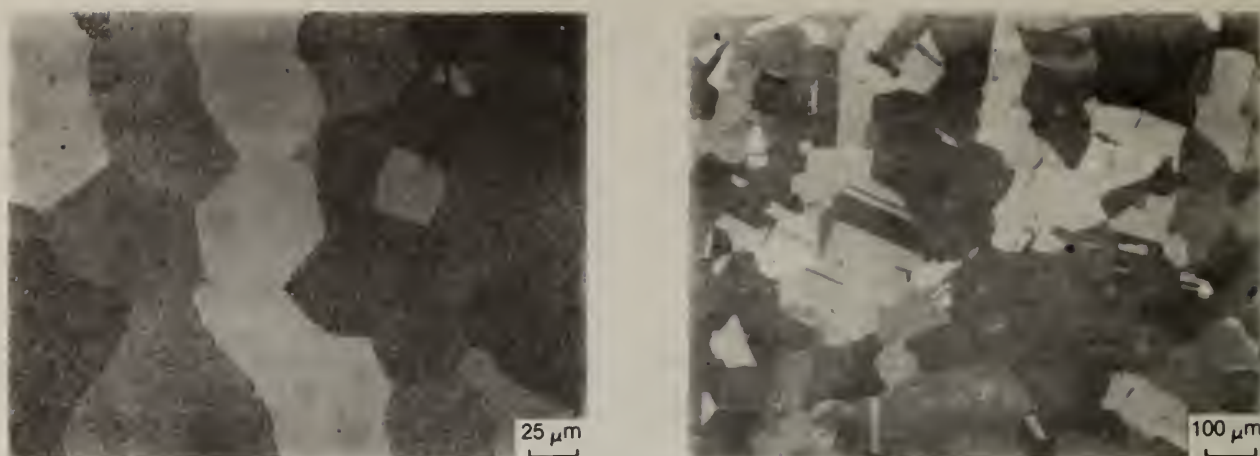


Figure 5. Transverse micrographs of RSPD U-700 after 1250 C/4h + 1080 C/4h + 843 C/24h + 760C/16h.

Mechanical Behavior

Tensile results for the RSPD conventional alloys are shown in Table VI. All alloys were solution treated at 1250C/4h, except A-286 and Hastelloy-X, which were solution treated at 1205C/4h. Commercial aging treatments were given for A-286, Rene' 80, Rene' 120, and U-700. To compare these alloys to their conventionally processed counterparts, the following observations can be made. RSPD versions of Rene' 80, Rene' 120, and Mar M-509 are stronger than conventionally processed materials from room temperature to 650-750C, they are nearly equal in strength over the range 750C to 950C, and are somewhat weaker at higher temperatures. Both Hastelloy-X and A-286 are weaker in RSPD form than conventionally processed over the entire test range.

Properties of hot isostatically pressed (HIP) powder processed versions of these alloys are shown in Table VII. These data provide an estimate of the effect of unmelted powders on the mechanical behavior of RSPD materials, since HIP powder provides an essentially unmelted particle structure. Tensile strength variations between HIP and RSPD are not large, although RSPD versions of Rene' 80 and Rene' 120 are greater than HIP at high temperature. More significant, however, is the trend for tensile ductility of the RSPD material to be greater than for HIP material. A severe unmelted particle structure may be expected to approach the HIP behavior.

TABLE VI
HEAT-TREATED RSPD CONVENTIONAL
ALLOY TENSILE PROPERTIES

Alloy	Test Temp		0.02% Yield Strength (ksi)	0.02% Yield Strength (MPa)	0.02% Yield Strength (ksi)	0.02% Yield Strength (MPa)	Ultimate		Elong (%)	Reduction of Area (%)
	(°F)	(°C)					Tensile Strength (ksi)	Tensile Strength (MPa)		
A-286	72	22	83.5	575.7	95.1	665.7	144.2	994.2	22.5	42.7
	1200	649	63.2	435.7	79.2	546.0	105.9	730.4	20.3	36.6
	1400	760	49.0	337.8	60.0	413.6	63.7	439.2	12.8	35.3
	1600	871	12.7	87.5	14.6	100.6	16.1	111.0	41.3	71.6
	1800	983	4.0	27.5	4.6	31.7	10.4	71.7	38.2	50.0
FeCrAlY	72	22	49.3	399.9	53.5	368.8	79.5	548.1	20.2	59.0
	1200	649	31.3	214.4	36.1	248.9	37.0	255.1	50.7	86.3
	1400	760	11.1	76.5	14.7	101.3	16.7	804.6	74.3	94.1
	1600	871	5.7	39.3	6.7	46.2	8.5	58.6	73.2	91.2
	1800	983	2.5	17.2	3.8	26.2	4.4	30.3	80.3	74.5
Mar-M509	72	22	56.3	388.1	68.9	475.0	162.6	1121.0	24.3	22.3
	1200	649	69.2	477.1	72.7	501.2	149.5	1030.7	22.1	20.2
	1400	760	26.0	179.2	36.5	251.6	77.4	533.6	30.8	27.9
	1600	871	32.4	223.3	38.7	266.8	47.0	324.0	19.2	20.2
	1800	983	19.4	133.7	23.8	164.0	28.3	195.1	6.2	6.7
Hastelloy-X	72	22	48.8	336.4	54.3	374.4	110.5	761.8	44.8	52.0
	1200	649	18.3	126.2	22.8	157.2	71.3	491.6	48.6	41.6
	1400	760	30.8	212.3	36.7	253.0	56.9	392.3	27.0	34.0
	1600	871	23.0	158.5	31.2	215.1	37.2	256.4	17.3	18.0
	1800	983	12.0	82.7	15.7	108.2	17.4	119.9	2.9	3.0
René 80	72	22	127.6	879.8	138.8	957.0	210.7	1452.7	12.7	16.3
	1200	649	90.3	622.6	115.8	798.4	183.2	1263.1	9.8	15.3
	1400	760	96.0	661.1	113.1	779.8	140.9	971.5	4.3	7.0
	1600	871	57.0	392.9	71.6	493.6	88.9	612.9	3.4	2.5
	1800	983	17.7	122.0	29.0	199.9	46.0	317.2	4.6	2.0
René 120	72	22	105.2	725.3	125.0	861.8	180.2	1242.4	5.4	5.9
	1200	649	113.2	780.4	133.1	917.7	178.9	1233.4	9.6	13.7
	1400	760	110.3	760.5	135.8	936.3	151.0	1041.1	6.6	9.8
	1600	871	72.5	499.8	93.8	646.7	111.9	771.5	5.5	6.3
	1800	983	30.0	206.8	44.5	306.8	53.5	368.8	5.4	3.0

TABLE VII

HEAT-TREATED HIP POWDER TENSILE PROPERTIES

Alloy	Test Temp		0.02% YS		0.2% YS		UTS		Elong. (%)	R. of A. (%)
	(°F)	(°C)	(ksi)	(MPa)	(ksi)	(MPa)	(ksi)	(MPa)		
A-286	72	22	66.1	455.1	74.8	515.7	113.9	785.3	20.2	43.6
	1600	871	12.7	87.5	17.6	121.3	19.1	131.6	28.9	39.2
	1800	973	6.9	47.5	8.8	60.6	10.0	68.9	37.1	36.6
FeCrAlY	72	22	51.3	353.7	56.4	388.8	80.3	553.6	21.6	54.4
	1600	871	5.1	35.1	6.8	46.8	11.6	79.9	88.8	94.9
	1800	983	3.4	23.4	3.8	26.2	4.2	28.9	60.9	75.0
Mar-M509	72	22	85.6	590.2	107.9	743.9	170.8	1177.6	8.1	10.9
	1600	871	21.2	146.1	34.5	237.8	39.5	272.3	10.5	12.0
	1800	983	14.0	96.5	18.0	124.1	22.8	157.2	5.5	6.9
Hastelloy-X	72	22	50.3	346.8	59.6	410.9	115.7	797.7	28.4	35.3
	1600	871	21.3	146.8	24.8	170.9	25.2	173.7	5.7	5.9
	1800	983	7.5	51.7	10.6	73.1	11.5	79.2	5.5	4.9
René 80	72	22	117.8	812.2	126.9	874.9	161.5	1113.5	5.7	4.8
	1600	871					---no test---			
	1800	983	14.8	102.0	22.3	153.7	26.5	182.7	2.2	1.9
René 120	72	22	120.6	831.5	131.4	906.0	197.1	1359.0	7.1	9.8
	1600	871	32.2	222.0	52.4	361.3	70.3	484.7	3.9	2.0
	1800	983	18.2	125.4	28.3	195.1	39.8	274.4	7.1	7.0

*Specimens repeatedly fail in threaded section

Tensile properties of the experimental RSPD alloys C1 through C4 are shown in Figure 6. All alloys were heat treated 1220C/1h + 900C/4h + 760C/12h. Alloy C4 is chemically similar to Hastelloy-X and alloy C5 to A-286, with C5 being intermediate in chemistry between C4 and C6. The figure compares the experimental alloys to RSPD and conventional versions of A-286 and Hastelloy-X.

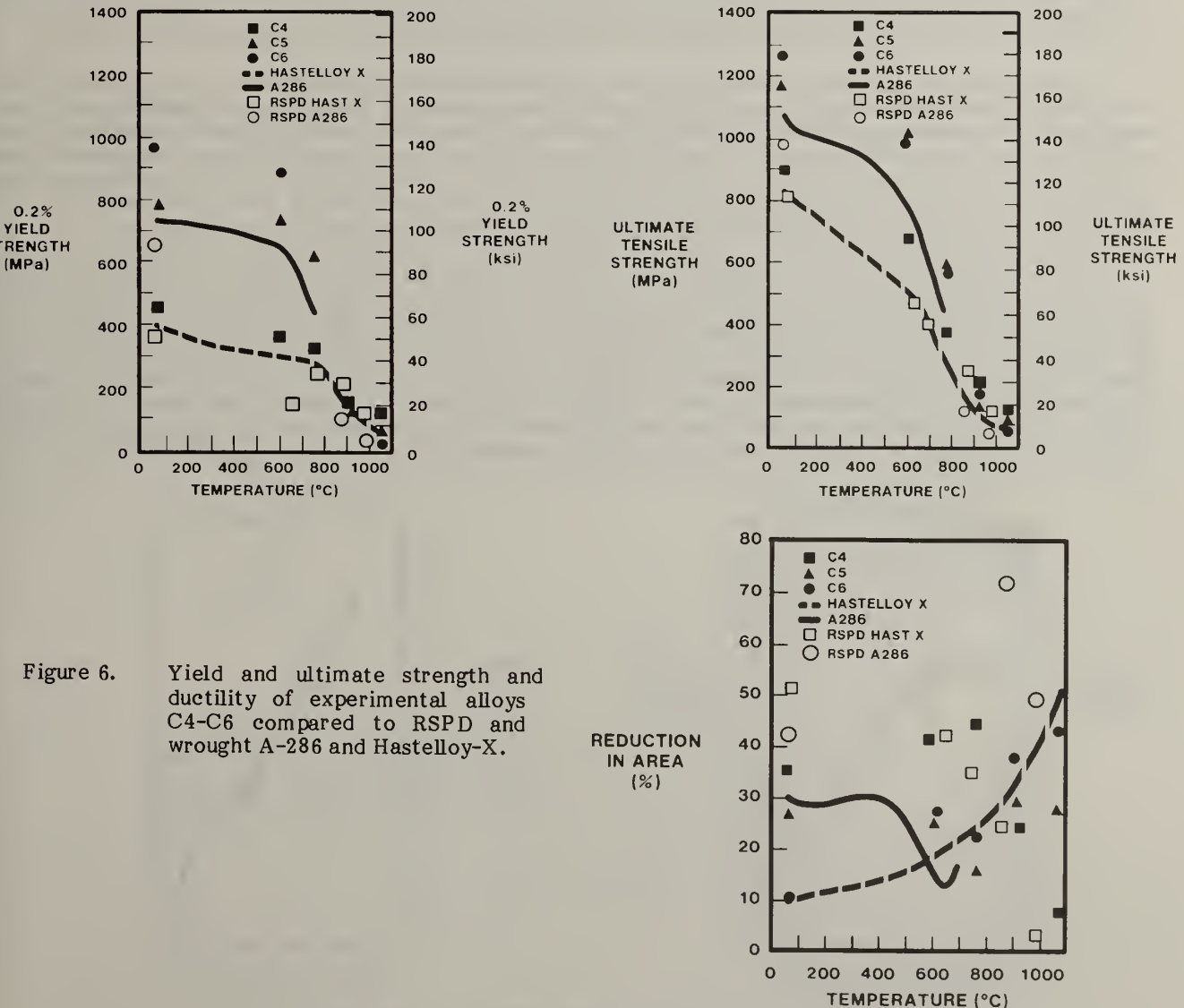


Figure 6. Yield and ultimate strength and ductility of experimental alloys C4-C6 compared to RSPD and wrought A-286 and Hastelloy-X.

On the basis of yield strength, both C5 and C6 are considerably stronger than conventional wrought A-286 or RSPD A-286. At elevated temperatures, C5 is as strong or slightly stronger than C6, even though the concentration of precipitation strengthening elements is much greater in C6. Presumably, this is due to the greater Ni content of C5 and its enriched solid solution strengthening (Mo, W, and Cr). Alloy C4 is stronger than conventional Hastelloy-X over the entire temperature range. It is stronger than RSPD Hastelloy-X below ~850C, and equivalent to it above that temperature. The pattern of ultimate tensile strength (Figure 6b) behavior for these alloys, compared to conventional and RSPD versions of Hastelloy-X and A-286, is identical to that for yield strength. In both figures, it can be seen that above 900C, alloy C4 is stronger than both C5 and C6.

Ductility, as represented by reduction in area in tensile tests, is shown in Figure 6c. The experimental alloys show reasonable ductility over the entire temperature range. Both C4 and RSPD Hastelloy-X show considerable reduction in ductility with increasing temperature, but the loss is less severe for C4. No strong ductility minimum is observed for any of the experimental alloys.

Similar comparisons can be made for rupture testing of the experimental RSPD alloys, as shown in Figure 7. All data for C1 through C4 are for the high temperature solution treatment. There is a smooth progression in properties with composition for C2 through C4, but C1 is markedly stronger than the others. Alloy C1 compares favorably with IN-718, the conventionally wrought alloy on which the C1 composition is based. Also shown for comparison is a curve describing conventional Hastelloy-X. At the highest test temperature, C4 is approximately 2.5 parameters (R,h) below wrought Hastelloy-X. The shortfall in rupture life decreases with decreasing temperature or increasing stress. An extrapolation of the data suggests C4 may be more rupture resistant than wrought Hastelloy-X at stresses greater than about 70 MPa (10 ksi).

A similar plot is shown in Figure 7 for alloys C4 through C6. Alloy C6 is nearly one parameter better than wrought A-286, and alloy C5 continues in that same trend, being stronger than A-286 over the entire test range, and stronger than wrought Hastelloy-X above 60 MPa (9 ksi). The rupture results for C5 and C6 are consistent with tensile behavior. However, C4 is stronger in tension than C5, but is weaker in rupture.

These same three alloys, C4 through C6, are compared to the RSPD versions of A-286 and Hastelloy-X in Figure 8. The experimental alloys are 1.0 to 2.3 (R,h) parameters better than the RSPD conventional compositions over the range of test conditions where comparisons can be made. This corresponds to a three- to ten-fold improvement in time-to-failure. Also shown in the same figure is a curve representing the average properties reported for RSPD Rene' 80 and RSPD Rene' 120. The data for the experimental alloys suggest that compatible composition series between alloys like Rene' 80 or Rene' 120 and alloys like Hastelloy-X or C4 may result in properties useful in high temperature composite components.

Stress rupture results for the RSPD version of conventional alloys are shown in Table VIII. In stress rupture, the RSPD materials are consistently weaker than comparable cast or wrought materials. RSPD Rene' 80 and Rene' 120, high γ' , average about 1.6 (R,h) parameters lower than cast in the lower temperature test range, and this difference becomes much greater at the high temperature end of the test range. RSPD Hastelloy-X (no γ') is about the equivalent of wrought Hastelloy-X at 760C (1400F) but degrades to about 4 (R,h) parameters less than wrought at 980C (1800F). RSPD Mar M-509 varies from five to seven (R,h) parameters weaker than cast, the difference becoming greater with increasing temperature. At 760C (1400F) RSPD A-286 approaches the stress rupture strength of wrought A-286, however, at 870C (1600F), it is much

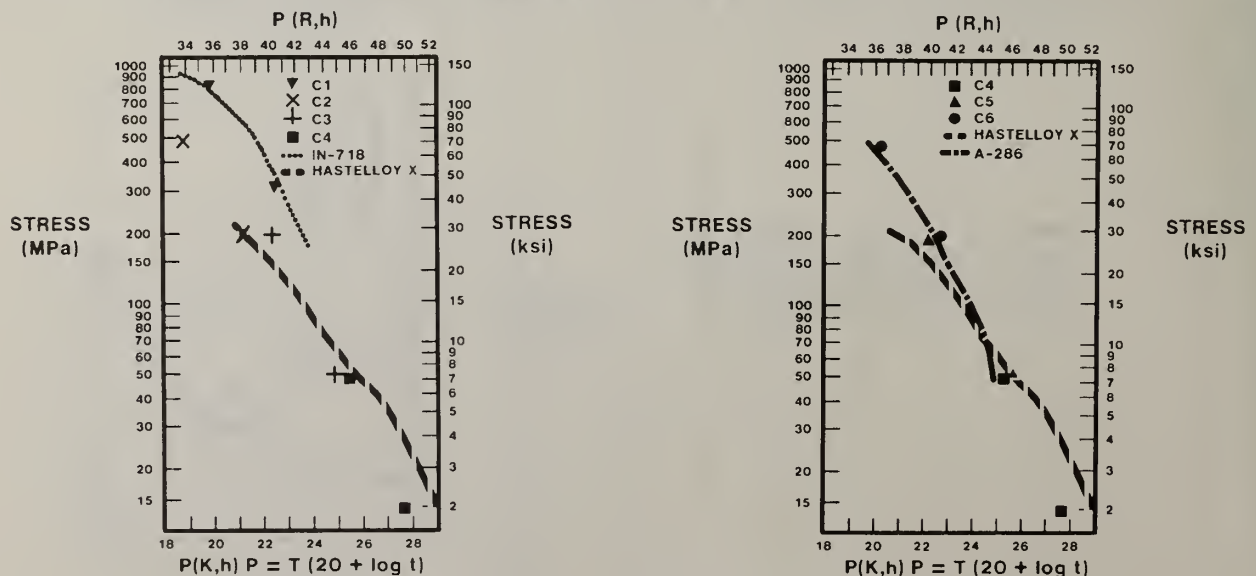


Figure 7. Stress rupture behavior of RSPD and wrought alloys.

TABLE VIII

HEAT-TREATED RSPD CONVENTIONAL ALLOY STRESS RUPTURE PROPERTIES

Alloy	Test Temp. (°F)	Test Temp. (°C)	Stress (ksi)	Stress (MPa)	Life (h)	P (C=20) (K,h)	P (C=20) (R,h)	Elong. (%)	R. of A. (%)
A-286	1400	760	25.0	172.3	31.3	22.2	40.0	9.1	10.7
	1600	871	6.0	41.3	43.8	24.8	44.6	60.7	63.3
	1800	983	2.0	14.1	1289.6	29.4	53.0	—	47.1
FeCrAlY	1400	760	5.0	34.4	58.7	22.4	40.4	89.1	89.2
	1600	871	3.0	20.6	32.1	24.6	44.3	44.5	40.8
	1800	983	1.5	10.6	0.1	23.8	42.9	79.8	89.2
Mar-M509	1400	760	20.0	140.6	2058.6	24.1	43.3	5.6	1.8
	1600	871	16.0	110.3	28.5	24.6	44.2	3.5	3.6
	1750	955	7.5	51.7	64.3	26.8	48.2	4.3	1.9
	1760	960	8.5	58.6	13.5	26.0	46.8	—	2.9
	1800	983	5.0	34.4	43.7	27.2	48.9	0.54	0.9
	1800	983	9.5	65.5	2.2	23.0	41.4	3.5	1.0
Hastelloy-X	1400	760	20.0	140.6	69.9	22.6	40.6	13.6	13.6
	1490	811	10.0	68.8	185.5	24.1	43.4	4.1	5.2
	1600	872	5.0	34.4	208.6	25.5	45.9	1.2	5.1
	1600	871	6.0	42.2	38.8	24.7	44.5	4.2	2.2
	1800	983	3.0	21.1	7.2	26.2	47.1	—	3.4
René 80	1600	871	34.0	239.1	7.6	23.9	43.0	9.4	8.6
	1750	955	7.5	51.7	197.8	27.3	49.2	39.1	34.1
	1760	961	8.5	59.8	79.3	27.0	48.6	24.4	26.3
	1800	983	5.0	35.2	737.2	28.7	51.6	*	45.7
	1800	983	12.0	84.4	12.2	26.4	47.6	12.5	17.1
René 120	1400	760	70.0	492.3	64.8	22.6	40.6	7.4	5.5
	1600	871	34.0	239.1	25.4	24.5	44.1	11.3	7.6
	1750	955	7.5	51.7	78.4	28.1	50.6	61.9	62.5
	1760	961	8.5	58.6	63.1	26.9	48.4	69.6	49.6
	1800	983	5.0	34.4	70.2	27.4	49.4	134.7	60.6
	1800	983	12.0	84.4	7.6	26.2	47.2	55.2	40.1

*Threads broke off on one end after test

weaker than wrought Hastelloy-X. FeCrAlY also is much weaker in stress rupture than Hastelloy-X sheet. The stress rupture strengths of all six RSPD conventional alloys is a reflection of their very fine grain size which has been shown by many others to be detrimental to good-high temperature stress rupture and creep strength.

Of special interest is the very high rupture ductility of the high γ' alloys, René 80 and René 120, in the 960C (1760F) to 980C (1800F) test range. An RSPD René 120 sample tested in 980C (1800F) tensile yielded elongation and R of A ductilities of 5.4% and 3%, respectively. The same material, sample geometry, and in the same heat treated condition yielded elongation and R of A stress rupture ductilities of 134.7% and 60.6%, respectively, an increase of about 25X. RSPD René 80, although somewhat less ductile than René 120, showed a similar behavior. Visual examination of the failed stress rupture bars showed the entire gauge length to be uniformly elongated, with the actual failure occurring without significant localized necking. This behavior shows the RSPD high γ' alloys to be very deformation rate sensitive, a property which may be utilized in subsequent forming operations. It also suggests that the ductility minimum observed to occur in this type of alloy during tensile tests may not be of significance in regard to actual component part performance since most components in actual operation are more rupture or creep limited than tensile limited.

Figure 8. Comparison of stress rupture behavior of RSPD alloys René 80, René 120, A-286, and Hastelloy-X to RSPD experimental alloys C4-C6.

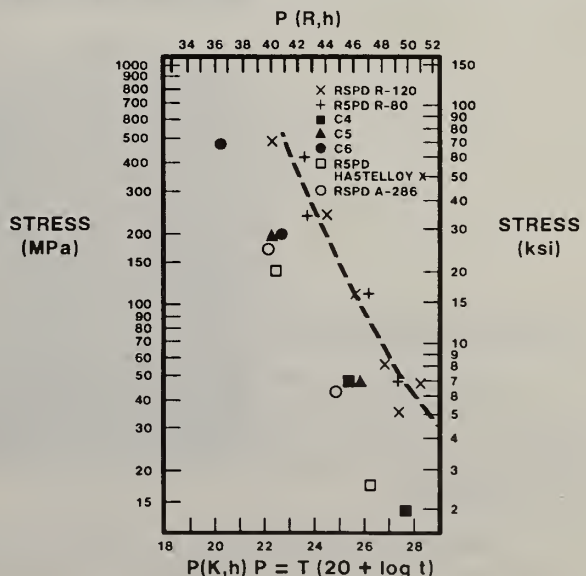


TABLE IX

RSPD/NON-RSPD HASTELLOY-X, TENSILE PROPERTIES

Sample	Test Temp.		0.02% YS		0.2% YS		UTS		Elong. (%)	R. of A. (%)
	(°F)	(°C)	(ksi)	(MPa)	(ksi)	(MPa)	(ksi)	(MPa)		
RSPD Hastelloy-X	72	22	48.8	336.4	54.3	374.4	110.5	761.8	44.8	52.0
	1200	649	18.3	126.2	22.8	157.2	71.3	491.6	48.6	41.6
	1400	760	30.8	212.3	36.7	253.0	56.9	392.3	27.0	34.0
	1600	871	23.0	158.5	31.2	215.1	37.2	256.4	17.3	18.0
	1800	982	12.0	82.7	15.7	108.2	17.4	119.9	2.9	3.0
Bond A	72	22	37.3	257.2	—	—	75.8	522.6	11.7	10.7
	1200	649	22.3	153.8	26.5	182.7	49.5	341.3	8.0	7.0
	1400	760	22.9	157.9	28.8	198.6	49.5	341.3	8.4	10.0
	1600	871	20.4	140.7	26.6	183.4	36.4	251.0	4.4	4.9
	1800	982	13.8	95.2	18.3	126.2	20.0	137.9	1.3	2.9
Bond B	72	22	37.9	261.3	—	—	95.3	657.1	25.8	29.1
	1200	649	22.3	153.8	29.4	202.7	54.5	375.8	10.0	18.7
	1400	760	22.6	155.8	28.3	195.1	58.2	401.3	19.4	18.0
	1600	871	22.5	155.1	27.8	191.7	36.9	254.4	7.3	7.0
	1800	982	14.5	100.0	18.5	127.6	20.1	138.6	4.5	1.0

Bond A — Grit Blast, 60 Grit, SiC + Vaporhane + Single Pass RTA Clean

Bond B — Surface Ground + Vaporhane + Triple Pass RTA Clean

(All samples heat treated 1205°C (2200°F)/4 h/HeQ)

The bond strength between an RSPD material and the substrate on which it is deposited has been evaluated for Hastelloy X, shown in Table IX. Reverse-transferred arc (RTA) cleaning, using single or triple pass cleaning was performed prior to deposition. Without such a cleaning process, bond strength is generally so low that test bars cannot be produced. The strengths observed at room temperature are equivalent to those seen in tests of RSPD to cast IN-738 (4).

Results of the comparisons indicate:

- 100% RSPD Hastelloy-X is stronger than RSPD Hastelloy-X to non-RSPD Hastelloy-X bonded material below 870°C (1600°F); this difference becomes insignificant at and above 870°C (1600°F).
- RTA cleaning apparently has a beneficial effect on RSPD Hastelloy-X bond strength. The strength of the bond made after the triple RTA cleaning pass is superior to that after a single pass.
- RSPD Hastelloy-X to non-RSPD Hastelloy-X bond ductilities are much lower than that of 100% RSPD Hastelloy-X up to 870°C (1600°F).
- All types of RSPD Hastelloy-X deposited from an external powder injection gun, bonded or not, have a ductility minimum beginning about 870°C (1600°F), which is not typical of conventional sheet.
- Triple RTA cleaning enhances bond ductility significantly when compared to single pass cleaning.

The results of stress rupture testing of wrought Hastelloy-X/RSPD Hastelloy-X binary composite samples are given in Table X. The 760°C (1400°F) and 810°C (1490°F) test points are about the equivalent of monolithic RSPD Hastelloy-X; the 870°C (1600°F) point is a particularly low value suggesting some interface problem. Of special significance are the low rupture ductility values measured on all three samples tested under the same condition.

TABLE X

HEAT-TREATED WROUGHT HASTELLOY-X/RSPD HASTELLOY-X
(METCO DEPOSITS) STRESS RUPTURE PROPERTIES

Specimen No.	Test Temp (°F)	Temp (°C)	Stress		Life (h)	P1m C=20	Elong. (%)	R. of A. (%)
			(ksi)	(MPa)				
578	1400	760	20	137.9	55	40.4	7.5	7.0
579	1490	810	10	68.9	126	43.7	1.9	2.0
580	1600	871	5	34.4	6.2	42.8	0.3	2.6

Thermal Fatigue Resistance

The behavior of RSPD materials when subjected to thermal fatigue conditions is of special interest when selecting component applications, including the potential advantages of multi-metal RSPD fabricated designs. The behavior of fine grain material typical of that produced by RSPD requires evaluation. Accordingly, it is the objective of this task to provide additional insight into the thermal fatigue behavior of RSPD materials.

A test matrix was selected to evaluate the thermal fatigue resistance of several RSPD monolithic and multi-metal material combinations via Simulated Engine Thermal Shock (SETS) testing which included the

following comparisons:

- RSPD Rene' 80 wedges produced using different vacuum plasma deposition system vs. conventionally cast Rene' 80.
- RSPD Rene' 80 wedges oriented in the longitudinal and short transverse directions relative to the original spray direction.

Longitudinal (SETS I) and short transverse (SETS II) oriented standard SETS wedge samples were cut from RSPD cylinders made using three different processes. The longitudinal RSPD samples were compared to equiaxed Rene' 80 in SETS I. The short transverse samples were compared to equiaxed Rene' 80 in SETS II. Both SETS I and II were run to a total of 10,000 cycles, respectively, rather than the 5,000 cycles originally planned. This extended testing was necessitated due to the failure to produce cracking in any of the RSPD samples during the first 5,000 cycles of either test. The thermal profile used for the first 5,000 cycles consisted of a 10 sec heating period from 415C to 1040C, a 40 sec hold at 1040C, cooling to 480C in 10 sec and further cooling to the original 415C in another 10 sec. With this cycle, cracking was induced in the conventional Rene' 80 samples of SETS I before the completion of the first 250 cycles. In SETS II, one of the conventional Rene' 80 samples cracked before 250 cycles and the second cracked before accumulating 500 cycles. At the end of the first 5,000 cycles in both SETS I and II, none of the RSPD samples had yet cracked. Edge views of each wedge after 5,000 cycles are shown in Figure 9. This confirms previous thermal fatigue results for RSPD Rene' 80 (4).

In order to induce cracking in all the wedges so that some estimate of relative crack propagation rates might be obtained, the thermal cycle for the next 5,000 cycles for both SETS I and SETS II was modified. In the modified cycle, the temperatures at the end of each period were held constant; however, the hold time for each period was reduced from 10 sec to 5 sec, thereby cutting the entire cycle time in half and increasing the relative heating and cooling rates. With this more severe cycle, all the longitudinal SETS samples developed cracking before 6,000 cycles (less than 1,000 cycles at the more severe conditions). Under the selected conditions and parameters the short transverse samples of SETS II showed one of two wedges made using the external injection systems to have cracks before 5,300 total cycles and the second wedge cracked before 5,600 cycles. One of two wedges made by the internal injection Low-Mach process also cracked before 5,600 cycles, the second cracked before 6,000 cycles. The Hi-Mach internal injection wedges lasted the longest, but were found to have cracked before they went through a total of 7,000 cycles.



Figure 9. Edge-on view of SETS wedges after 5000 cycles to 1040C.

The results of SETS I and II lead to the following conclusions:

- There was little difference in the relative ability of longitudinal and short transverse orientated Rene' 80 to withstand thermal shock.
- The various RSPD microstructures produced by different RSPD equipment and process controls had little effect on thermal fatigue resistance.
- Without exception, RSPD Rene' 80 had greater than 10X improvement over conventionally cast Rene' 80 with respect to cumulative cycles to crack initiation.

SUMMARY

Rapid solidification by plasma deposition (RSPD) produces a simultaneous RS process and consolidation to nearly full density. The process can be applied to superalloys with Ni, Fe and Co bases to produce low oxygen (generally ≤ 400 ppm), homogenous fine-grained structures. Heat treatment can result in full densification.

Excellent combinations of tensile strength and ductility result for the RSPD structure. For some compositions, RSPD is significantly better than conventionally processed material. The tensile ductility minimum at 750-950C previously observed for γ' strengthened alloys Rene' 80 and IN-738 has been found to be present principally in higher strength materials.

The low ductility in tensile tests is not observed in stress rupture, suggesting that its importance in component applications may not be great. Rupture resistance in general is lower than for conventionally produced material, primarily due to the fine grain size. However, for many applications alloys that cannot be conventionally processed to particular geometries can be produced by RSPD.

Bond strength and ductility are improved by reverse-transferred arc cleaning. Ultimate strength at 20C for RSPD to conventional Hastelloy-X is 655MPa (~ 95 ksi), essentially equivalent to earlier results for IN-738.

In thermal fatigue exposure, RSPD Rene' 80 was uncracked in 5,000 simulated engine thermal shock exposures, while the cast Rene' 80 cracked before completion of the first 250 cycles. Increasing the severity of the thermal shock exposure did lead to cracking of the RSPD alloys. Whether stresses were maximized parallel or transverse to the deposition plane had no effect on the behavior. Also, RSPD structures produced in a variety of gun types behaved nearly identically.

Acknowledgement

This program has been funded by DARPA, through the offices of Lt. Col. L.A. Jacobson, with H.L. Gegel of AFML serving as technical monitor. The authors wish to acknowledge the aid and support of P.A. Siemers, M.G. Benz, A.M. Johnson, J.R. Rairden, R.L. Mehan, R.W. Smith, J.S. Smith, L. Stoffer and D. Rigney, all of General Electric Company, and H. Lipsitt of AFML.

References

- (1) D.J. Looft and E.C. vanReuth, "Rapid Solidification Processing: An Overview," Proc. of the Int. Conf. on Rapid Solidification Processing, Reston, Va., p. 1, 1977.
- (2) R.J. Patterson, II, A.R. Cox and E.C. vanReuth, "Rapid Solidification Rate Processing and Application to Turbine Engine Materials," J. of Metals, p. 34, Sept. 1980.
- (3) M.R. Jackson and J.R. Rairden, "Thermal Fatigue Resistance of Plasma Sprayed Thick Superalloy Deposits," Fall Meeting Program, TMS-AIME, Pittsburgh, p. 74, Oct. 1980.
- (4) M.R. Jackson, J.R. Rairden, J.S. Smith and R.W. Smith, "Production of Metallurgical Structures by Rapid Solidification Plasma Deposition," J. of Metals, p. 23, Nov. 1981.
- (5) P.A. Siemers, "Rapid Solidification (RSPD) for Fabrication of Advanced Aircraft Gas Turbine Components," Contract F33615-81-C5156, Interim Report, Jan. 15, 1982, Apr. 15, 1982, July 15, 1982, Air Force Systems Command, AFWAL, Wright-Patterson Air Force Base, Ohio 45433.
- (6) T.L. Cheeks, M.E. Glicksman, M.R. Jackson and E.L. Hall, "Temperature Effects on Plasma Deposition of Ni-Base Materials," this conference proceedings.
- (7) A.M. Ritter and M.R. Jackson, "Microstructural Characterization of RSPD Structures," this conference proceedings.

NOTCHED TENSILE PROPERTIES OF RAPIDLY SOLIDIFIED AND INGOT-BASED ALUMINUM ALLOYS

Shinhoo Kang and Nicholas J. Grant

Massachusetts Institute of Technology
Cambridge, MA 02139

ABSTRACT

In the development of high-strength aluminum alloys, the focus has been on alloy toughness as well as on strength, stiffness, fatigue behavior, corrosion, etc. In this paper, tension properties (σ_{UTS} , σ_{YS} , elongation) of various rapidly solidified (RS) and ingot-based aluminum alloys were examined and correlated with their notched tensile properties. Compiled data have shown that a linear relationship exists between the yield strength (σ_{YS}) and the notch yield ratio (σ_{NTS}/σ_{YS}); there is a poorer correlation between the ductility and the notch yield ratio. On the basis of Linear Elastic Fracture Mechanics (LEFM), the linear relationship is extended to relate σ_{YS} with K_{IC} . Under a given set of processing parameters, the extended equation, $K_{IC} = f(\sigma_{YS})$, could be utilized to indicate whether the toughness of an alloy (taking into account the related processing steps) in any way encourages or discourages further development.

Overall results indicate that RS materials are not better than I/M alloys in terms of toughness, and raise the question of "why." One possible reason may be the presence of excess oxide in the form of continuous stringers in the inadequately worked RS-PM alloy. Tests are planned to attempt to evaluate the oxide issue.

I. Introduction

In alloy development for aircraft structural components, fracture toughness of the alloys has been getting more attention along with strength and other properties than before. In order to determine alloy toughness, various testing methods are being used. Of these methods, the plane strain compact test is indicated to be one of the most accurate ways to measure K_{IC} of lower ductility alloys such as the high-strength aluminum alloys. Unfortunately, not only is the preparation and testing of the compact specimens costly and time-consuming, but it is not easy to obtain valid K_{IC} results with respect to test specifications.

Sharp notch tension testing has been proposed to measure the fracture behavior of thick sections under plane strain conditions. This test is recognized as an inexpensive and quick method to determine alloy toughness, using a reasonable notch radius ($\rho \leq 0.0007"$). A circumferential notch is not the same as an infinitely small crack radius; however, a well-established stress concentration factor concept minimizes the difference between the two approaches. Even though there are many remaining problems in notch tension testing, including the alignment of the specimen, the notch radius, etc., this method seems very convenient to obtain a fast, inexpensive idea regarding a material's toughness, with a reasonable accuracy.

II. Results and Discussion

Compiled data of the tensile properties of many aluminum alloys [1-5] revealed interesting relationships with the notch yield ratio ($NYR = \sigma_{NTS}/\sigma_{YS}$). Kaufman and Johnson [6] had shown that the ratio of sharp-notch strength to yield strength is more indicative of an alloy's toughness than is the ratio of notch strength to ultimate tensile strength in comparing a variety of aluminum alloys. Figures 1 through 3 show typical relationships between NYR and tensile properties of I/M Al-Li-Zr alloys [4]. It should be noted that σ_{YS} and σ_{UTS} show a linear behavior with respect to the NYR, whereas the elongation values are not very sensitive to the change of the NYR, particularly when the ratio is less than one. Figures 4 and 5 are summaries of the alloy systems studied in this program. The following observations are warranted:

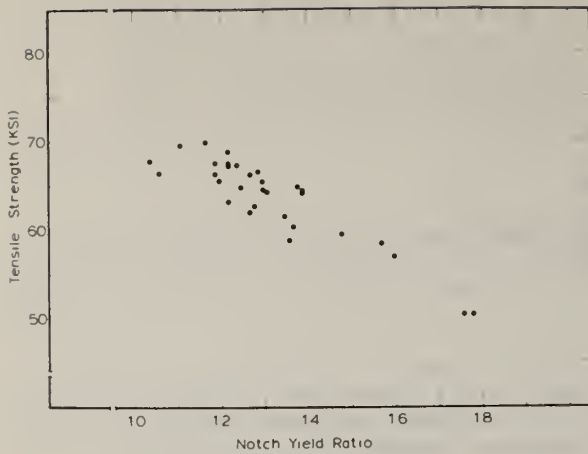


Fig. 1. σ_{UTS} vs. NYR for I/M Al-Li-Zr Alloy.

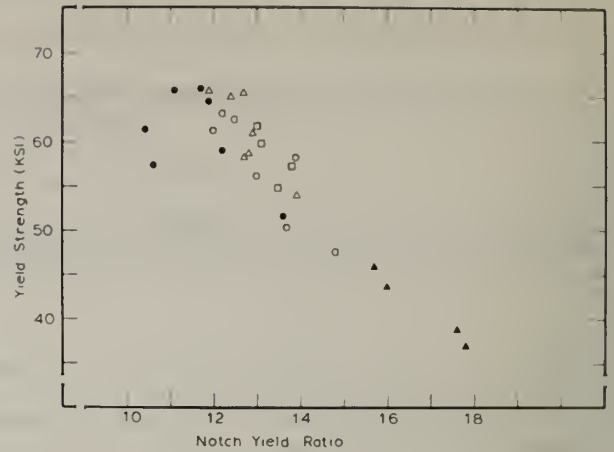


Fig. 2. σ_{YS} vs. NYR for I/M Al-Li-Zr Alloy.

- Ext. * + S.T. ** + W.Q. (R.T.) + 200°C (V.T.) ***
 - △ Ext. + S.T. + W.Q. (200°C) + 200°C (V.T.)
 - Ext. + S.T. + W.Q. (275°C) + 225°C (V.T.)
 - ▲ Ext. + S.T. + W.Q. (275°C) + 275°C (V.T.)
 - No Ext. + S.T. + W.Q. (R.T.) + 200°C (V.T.)
- Ext. * = Extrusion after casting
 S.T. ** = S.T. at 552°C (0.5 h)
 V.T. *** = Various Time

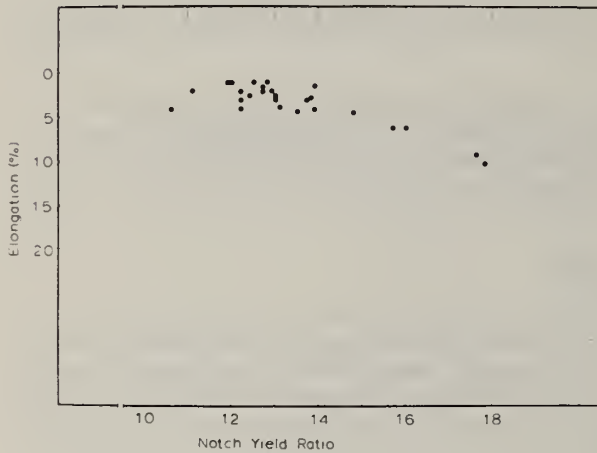


Fig. 3. Elongation vs. NYR for I/M Al-Li-Zr Alloy.

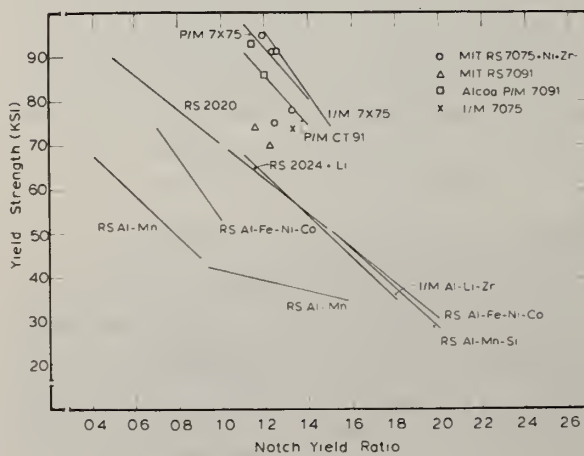


Fig. 4. σ_{YS} vs. NYR for Various Aluminum Alloys.

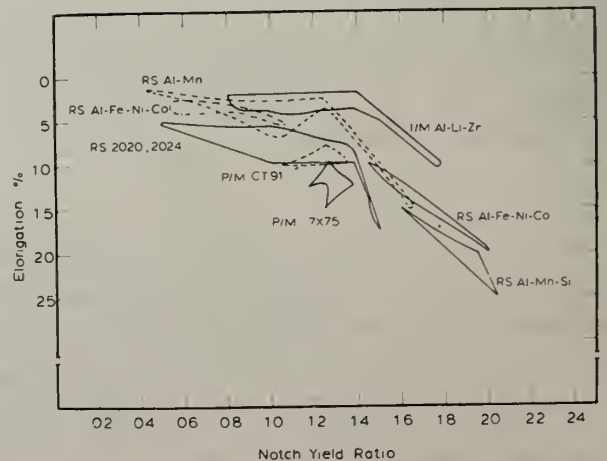


Fig. 5. Elongation vs. NYR for Various Al Alloys.

- 1) a linear relationship exists between σ_{YS} (or σ_{UTS}) and the NYR,
- 2) relatively low-strength alloys, with high NYR values, show a less steep slope than do the relatively higher strength alloys with low values of the NYR,
- 3) rapidly solidified aluminum alloys do not show any advantage relative to the σ_{YS} -NYR relationship as compared to the I/M aluminum alloys, and
- 4) elongation values are not good indicators of NYR values.

It has been commonly observed that rapid solidification processes result in higher volume fractions of oxides than that found in ingot alloys. When the oxides are present in the form of relatively continuous stringers, after comparatively small amounts of hot reduction of small billets by the extrusion process, grain boundary decohesion associated with the oxide stringers can be enhanced greatly, resulting in lower fracture resistance. The frequently observed highly delaminated fracture surfaces of some RS aluminum alloys are good examples of longitudinal grain boundary decohesion. Changes in powder-size distribution, oxide content, extrusion ratio and subsequent hot and cold work (based on the powder compact diameter) and other processing variables should result in improvement in the fracture patterns and behavior.

On the basis of Linear Elastic Fracture Mechanics, the relationship between σ_{YS} and NYR was extended to explore the relationship between σ_{YS} and K_{IC} , using presently existing equations. A relationship between σ_{NTS} and K_{IC} , using a 50% notched cross sectional area, was derived by Irwin [7] and later modified by Tada et al [8] on the basis of the stress intensity factor; the relationship follows:

$$K_{IC} = 0.454 \sigma_{NTS} [D]^{1/2} \quad (1)$$

where D is the major diameter of the notched tensile specimen. This equation has given reasonable estimates of K_{IC} for values of $\sigma_{NTS}/\sigma_{YS} \leq 1.1$ even without a plastic zone correction. However, for an alloy which shows sufficient plasticity, the plastic zone correction, with an extended notch depth, must be taken into account. According to the elastic stress field solution, the size of the plastic zone around the crack is

$$r_{YS} = \frac{1}{2\pi} \left(\frac{K_I}{\sigma_{YS}} \right)^2 \quad (2)$$

For the plane strain condition, the normal stress on the $\theta = 0$ plane can be as high as $3\sigma_{YS}$. If the effective yield stress in plane strain is $3\sigma_{YS}$, the plastic zone correction becomes

$$r_{YS}^* = \frac{K_I^2}{2\pi(3\sigma_{YS})^2} = \frac{K_I^2}{18\pi\sigma_{YS}^2} \quad (3)$$

Practically, plane strain does not exist at the specimen surface (crack tip). As a consequence, the average effective yield stress is much lower than $3\sigma_{YS}$. Irwin [9] used $1.68\sigma_{YS} (\sqrt{2}\sigma_{YS})$ as the effective yield stress, which modified equations 2 and 3 to:

$$r_{YS}^* = \frac{K_I^2}{2\pi(\sqrt{2}\sigma_{YS})^2} = \frac{1}{2\sqrt{2}} \cdot \frac{K_I^2}{2\pi\sigma_{YS}^2} = \frac{r_{YS}}{2\sqrt{2}} \quad (4)$$

A first-order correction by Irwin [9] for r_{YS}^* ($= r_{YS}/2\sqrt{2}$) as the effective increase of notch depth leads to:

$$\frac{\sigma_{NTS}}{\sigma_{YS}} = \frac{x}{0.233} \left(1 - \frac{x^2}{2} \right)^2 \quad (5)$$

where

$$x = \frac{K_{IC}}{\sqrt{\pi D} \cdot \sigma_{YS}}$$

Further corrections by Tata et al [8] result in:

$$\frac{\sigma_{NTS}}{\sigma_{YS}} = 4x \left(1 - \frac{x^2}{2} \right)^2 \quad (6)$$

where

$$x = \frac{K_{IC}}{\sqrt{\pi D} \cdot \sigma_{YS}}$$

On the other hand, a linear relationship between σ_{YS} and NYR can be expressed below with reasonable accuracy:

$$\sigma_{YS} = a(NYR) + b = a(\sigma_{NTS}/\sigma_{YS}) + b \quad (7)$$

where a is the slope and b is the intercept on y axis. By combining equations 1, 6 and 7, the following equations are obtained:

For an alloy with $\sigma_{NTS}/\sigma_{YS} \leq 1.1$,

$$K_{IC} = \frac{0.454\sqrt{D}}{a} (\sigma_{YS}^2 - b \sigma_{YS}) \quad (8)$$

For an alloy with $1.1 \leq \sigma_{NTS}/\sigma_{YS} \leq 1.7$,

$$K_{IC}^5 = c\sigma_{YS}^6 - c \cdot b\sigma_{YS}^5 - d\sigma_{YS}^4 K_{IC} + e\sigma_{YS}^2 \cdot K_{IC}^3 \quad (9)$$

where

$$c = \frac{(\pi D)^{5/2}}{a}, \quad d = 4(\pi D)^2, \quad \text{and } e = 4\pi D.$$

Figures 6 and 7 were obtained from equations 8 and 9 after computer computations. Hahn and Rosenfield [10] derived a relationship based on crack opening displacement:

$$K_{IC} \approx \left[2\sigma_{YS} E \left(\frac{\pi}{6} \right)^{1/3} D \right]^{1/2} f_c^{-1/6} \quad (10)$$

where E is the elastic modulus, f_c is the total volume fraction of second-phase particles and D is the diameter of cracked particles. As pointed out in their work, equation 10 cannot explain the fact that the K_{IC} value decreases with an increase in σ_{YS} at constant volume fraction of secondary phases. However, the cross-hatched areas in Figs. 6 and 7, which have practical applicability, are instructive of this fact. It is also to be noted that the left side of the inflection points in Fig. 7 must be out of LEFM (Linear Elastic Fracture Mechanics) range, which is the basis of compact and sharp notch tension testing.

In order to understand the relationship between the elongation values and the NYR (or toughness), as a first approximation, the elongation is expressed as follows:

$$\sigma_{YS} = \frac{\alpha}{\epsilon} + \beta \quad (11)$$

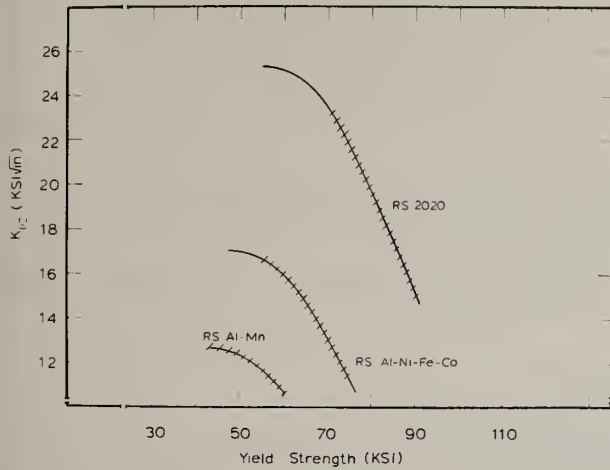


Fig. 6. Predicted K_{IC} vs. σ_{YS} for Aluminum Alloys with $NYR \leq 1.1$.

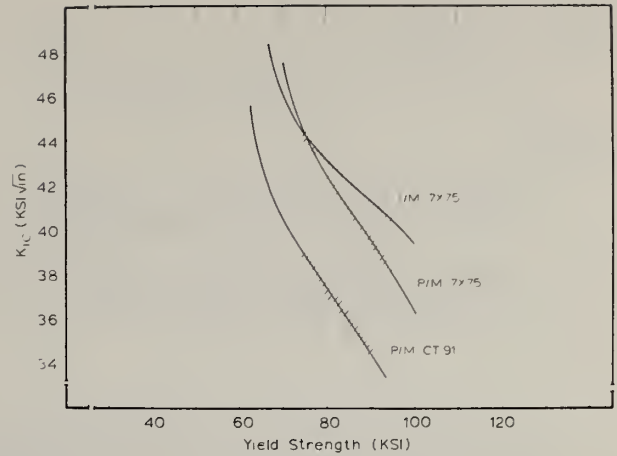


Fig. 7. Predicted K_{IC} vs. σ_{YS} for Aluminum Alloys with $1.1 \leq NYR \leq 1.7$.

where ϵ is elongation and α and β are constants. Equations 7 and 11 lead (if one lets $NYR = x$) to:

$$x = NYR = \frac{1}{a} \left(\frac{\alpha}{\epsilon} + \beta - b \right) \quad (12)$$

Therefore,

$$\epsilon = \frac{\alpha}{ax - (\beta - b)} = \frac{\alpha/(-a)}{(\beta - b)/a - x}$$

where a (the slope) < 0 and $\alpha > 0$. Hence, the final form of equation 13 will be:

$$\epsilon = \frac{B}{A - NYR} \quad (14)$$

where $A = (\beta - b)/a > 0$ ($b \gg \beta$ in most cases) and $B = \alpha/(-a) > 0$. The plot of equation 13 is shown in Fig. 8; the hatched area of Fig. 8 corresponds to the elongation-nonsensitive-region with respect to

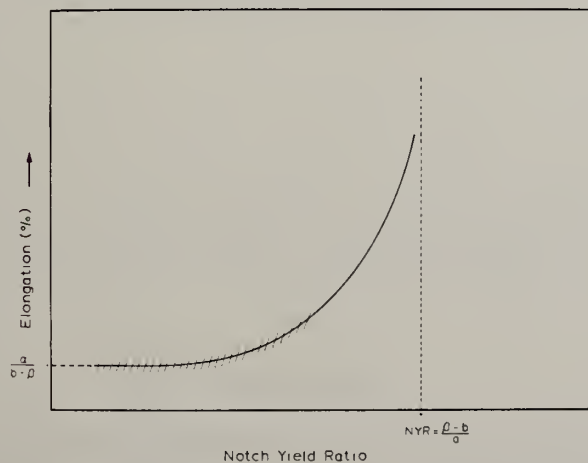


Fig. 8. Elongation Behavior with Respect to NYR.

NYR. It is to be noted from equations 7 and 11 that the elongation behavior, i.e., equation 13, is directly related to equation 11. Therefore, the elongation behavior (i.e., elongation values are not indicative of alloy toughness: [NYR]) is consistent with the fact that a linear relationship exists between σ_{YS} and NYR, as far as the first approximation, equation 11, holds. Typical example of the elongation behavior with respect to the NYR can also be found in reference 11.

The derived relationships between σ_{YS} and K_{IC} (equations 8 and 9) can be used for the following purposes:

- 1) getting a fast idea about a material's toughness (K_{IC}) along with strength values, not by compact testing, but by several notch tension tests at relatively low cost,
- 2) knowing about a material's limits in terms of strength and toughness for further development of an alloy system or for comparison between competing alloys.

III. References

- [1] D. P. Voss, "Correlation of Processing Parameters, Microstructure, and Mechanical Properties of High Strength Powder Metallurgically Produced Aluminum Alloys," Eng. Doctor Thesis, Rheinisch-Westfälischen Technischen Hochschule, Aachen, Germany, Nov. 1979.
- [2] S. Kang and N. J. Grant, Unpublished work.
- [3] H. G. Paris, F. R. Billman, W. S. Cebulak and J. I. Petit, Proc. of the 2nd Int'l Conf. on Rapidly Solidified Processing and Tech., Reston, Va., March 23-26, 1980, p. 331.
- [4] T. H. Sanders, Jr., "Factors Influencing Fracture Toughness and Other Properties of Al-Li Alloys" Final Report, Naval Air Development Center Contract No. N62269-76-C-0271, June 14, 1979.
- [5] O. R. Singleton, "High Strength, P/M, Al Mill Products," Reynolds Metals Co., 2nd Interim Report 4/1/80 - 6/30/80, Contract No. F 33615-79-C-5161.
- [6] J. G. Kaufman and E. W. Johnson, Proceedings, ASTEA, Am. Soc. Testing Mats., Vol. 62, 1962, pp. 778-793.
- [7] G. R. Irwin, "Onset of Fast Crack Propagation in High Strength Steel and Aluminum Alloys," Report No. NRL 4763, Washington, D.C., Naval Research Laboratory, 1956.
- [8] H. Tada, P. Paris and G. Irwin, The Stress Analysis of Cracks Handbook, pp. 2.6-2.7, Hellertown, Pa., Del Research Corporation, 1973.
- [9] G. R. Irwin, "Plastic Zone Near a Crack and Fracture Toughness," Proc. of the 7th Sagamore Materials Research Conf., Syracuse, N.Y., Syracuse University Research Institute, 1960.
- [10] G. T. Hahn and A. R. Rosenfield, Met. Trans., Vol. 6A, 1975, p. 653.
- [11] W. Wang, "Advanced Lithium-Containing Aluminum Alloys Made from Ultrasonically Gas Atomized Particulates," Sc.D. Thesis, M.I.T., Cambridge, MA, 1982, p. 131.

RAPIDLY SOLIDIFIED O.D. IN-100: STRUCTURE AND PROPERTIES

Charles H. Smith

General Electric Company
Corporate Research and Development
Schenectady, NY 12301

and

Nicholas J. Grant

Massachusetts Institute of Technology
Cambridge, MA 02139

ABSTRACT

An oxide dispersion stabilized IN-100 with 2 vol. % of 10 to 40 nm Y_2O_3 particles added was processed from fully alloyed rapidly solidified powders. Excellent dispersion of the oxides viz. Al_2O_3 , Y_2O_3 and $YAlO_3$ was obtained, resulting in a particle diameter of 21 to 79 nm and an IPS less than 0.2 μm . Full characterization revealed the as-extruded bar to have submicron equiaxed grains with a substructure that was highly worked and strained, containing a high dislocation density with extremely high room-temperature strength. The optimum structure was achieved by using a solid-state crystal growing process named ZAP (Zone Aligned Polycrystals). Large columnar grains with (100) fiber texture and a high grain aspect ratio (GAR) were produced. The optimum 100-hour rupture strength was 152 MPa (22 ksi) at 1093°C (2000°F) and 172 MPa (25 ksi) at 982°C (1800°F). Rupture elongations varied between 2 and 9%.

1. Introduction

Oxide dispersion stabilized (ODS) superalloys offer great promise as advanced high-temperature materials. The ability to combine the benefits of oxide dispersion stabilization for high temperatures and γ' strengthening for low and intermediate temperatures was demonstrated using the mechanical alloying process [1]. Since the first reported successes in 1970 by INCO, the mechanical alloying technique for preparing OD superalloys has been applied by a number of investigators [2-4]. The process is a high energy dry milling process in which a mixture of metal powders and premelted master alloy powders or particulates and very fine oxide particles is subjected to continuous deformation agglomeration, fracturing and rewelding in an appropriate grinding mill and ball charge in an inert atmosphere. Usually the powders are then consolidated by hot extrusion. The consolidation is followed by zone annealing (ZAP) above the γ' solvus to accomplish oriented recrystallization by formation of large elongated grains.

Although these alloys have exhibited the best mechanical properties and alloy stability at high temperature to date, the high cost of processing restricts their use considerably.

The purpose of this work was to develop a process and to fully characterize selected oxide dispersion stabilized Ni-base alloys. Full characterization involved determining the oxide (and γ') volume fractions and their respective interparticle spacings; the grain size, shape and texture; and the nature of the (intragranular) structure. The relationships between structure and properties were investigated.

2. Experimental

Rapid solidification via powder metallurgy eliminates large scale segregation common in cast structures; each powder particle is in effect a micro-ingot containing the full complement of alloying elements in the correct proportions. Processing [5] was accomplished by starting with atomized pre-alloyed powders; vacuum atomized powders and RS, inert powders (Osprey Metals) were examined in this

study. The chemical compositions are given in Table 1. The powders were manufactured from master re-melt cast ingots. Subsequent processing to incorporate the fine (10 to 40 nm) Y_2O_3 particles by inert gas ball milling was accomplished as described elsewhere [5]. The powder conglomerates after such a process are irregularly shaped, Fig. 1. Table 2 lists the consolidation treatments which were applied.

Table 1. Compositions (Weight Percent) of Alloys Studied

Alloy		Ni	Co	Cr	Mo	Al	Ti	W	Ta	C	B	Zr	Fe	Y_2O_3
N-2	(1)	bal	20	20	10	0.5	-	-	-	-	-	-	-	1.18
N-3	(1)	bal	20	20	10	0.5	-	-	-	-	-	-	-	2.76
N-4	(2)	bal	14	10	3	5.5	4.6	-	-	0.16	0.012	0.04	0.1	-
N-5	(2)	bal	14	10	3	5.5	4.6	-	-	0.16	0.012	0.04	0.1	1.2
IN853	(3)	bal	-	20	-	1.2	2.4	-	-	-	0.007	0.07	-	1.3
MA6000 E	(3)	bal	-	15	3.5	4.5	2.0	4.0	2.0	-	0.01	0.15	-	1.1

- (1) Solid solution strengthened: Homogeneous Metals Co.
(2) IN-100 type; γ - γ' with about 60 v/o γ' : Osprey Ltd.
(3) Mechanically alloyed M-MO materials: Benjamin et al [4,6,12]

Table 2. Processing Parameters - Evacuation and Extrusion

Evacuation				Extrusion		
				Temp ($^{\circ}C$)	Maximum Force (tons)	
Alloy	Temp ($^{\circ}C$)	Time (h)	Pressure (μm)		Upset	Running
N-2	650	24	0.5	1066	290*	280
N-3	650	24	0.5	1149	290*	280
N-4	650	4	30.0	1149	330*	275
N-5	650	4	30.0	1149	300*	270

* 300-ton press

3. Results and Discussion

As-Extruded Structures

Table 3 lists important structural characteristics of the alloys. The grain sizes of the extruded bars were of submicron dimensions and essentially equiaxed. Some reports [6,7,12] have claimed that mechanically alloyed ODS alloys recrystallize after extrusion to submicron, equiaxed grains while retaining a high dislocation density. It is difficult to conceptualize a recrystallized structure with a high dislocation content. The TEM micrographs of Figs. 2 to 4 show highly deformed structures with dislocation substructures. The dislocation content was estimated to be greater than 10^9 cm/cm³. These alloys did not recrystallize during extrusion. It is the authors' opinion that recrystallization could have occurred during the time when the canned alloy is at the extrusion temperature (1 hour) prior to extrusion. Grain sizes, as measured by the linear intercept method, yielded about 0.4 μm for N-2, N-3, and N-5, and 0.6 μm for N-4.

Transverse to the high angle grain boundaries in alloys N-2, N-3 and N-5 are bands of dislocation tangles which define a cellular type of structure. Cell sizes vary as follows: N-2 and N-3, 0.013 to 0.042 μm ; and N-5, 0.009 to 0.039 μm . Figure 4 demonstrates that the cell walls along a grain's high angle boundary are thin and well defined, while the cell walls across the grain width are thick and irregular. Like most ODS alloys, the processing of the alloys in this work had a major effect on the oxide particle distribution and on the structure of the matrix. The range of particle sizes is shown in Fig. 5. A typical particle size distribution measurement is shown graphically in Fig. 6.

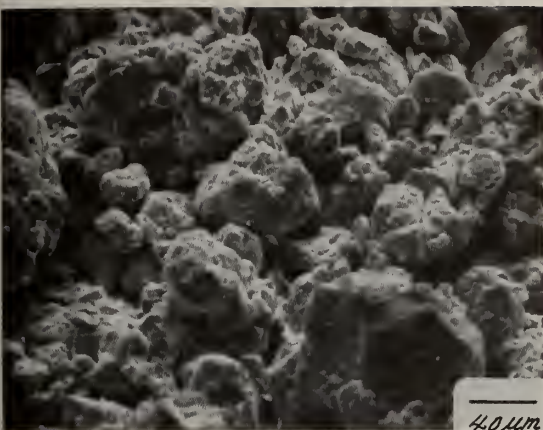


Fig. 1. Appearance of ball mill blended alloy N-5 with Y_2O_3 .

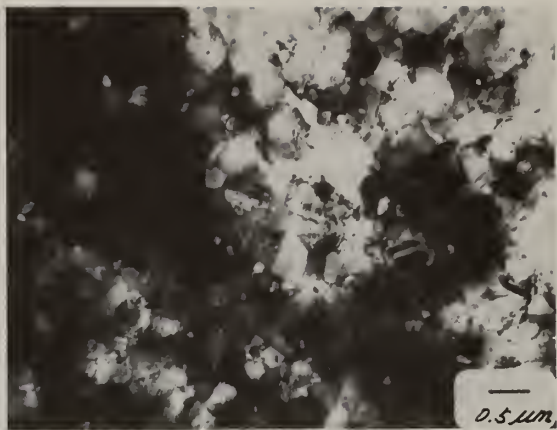


Fig. 2. TEM micrograph of alloy N-2; as extruded, transverse view.



Fig. 3. TEM micrograph of alloy N-5; as extruded, longitudinal view.

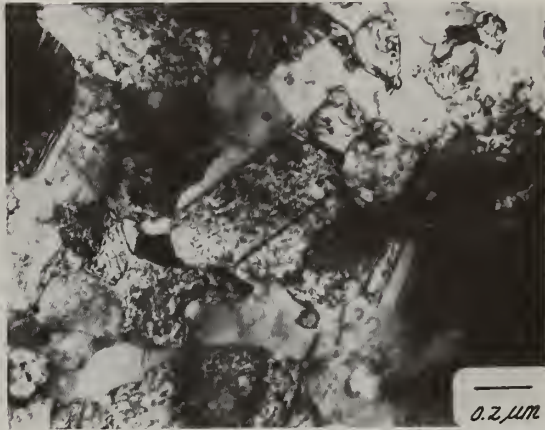


Fig. 4. TEM micrograph of as-extruded N-5 showing cell structure.

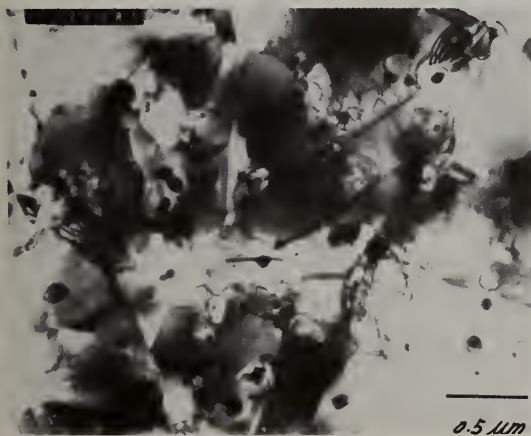


Fig. 5. TEM micrograph of as-extruded alloy N-2 showing fine Y_2O_3 oxide dispersion.

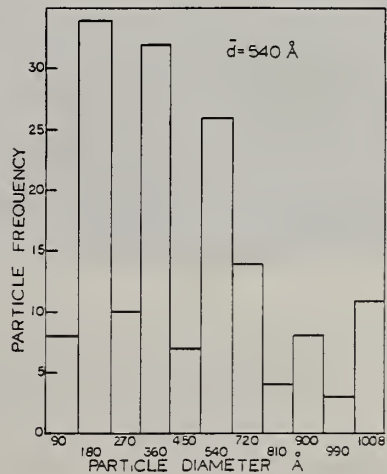


Fig. 6. Typical oxide particle size distribution for alloy N-3.

Table 3. Structural Characteristics of Nickel-Base Alloys (As Extruded)

	N-2	N-3	N-4	N-5
Ext. Temp. (°C)	1066	1149	1149	1149
Ext. Ratio (Area)	20:1	16:1	16:1	16:1
Theoretical Density (g/cc)	8.42	8.33	7.75 ^{***}	7.75
Measured Density (g/cc)	8.51	7.82	7.92	7.99
% Theoretical Density	101	94	102	103
Volume % Y ₂ O ₃ (added)	2.0	5.0	-	2.0
Avg. Grain Size (μm)	0.41	0.36	0.62	0.43
Avg. Oxide Particle Size (μm)	0.079	0.034	0.112 [*]	0.021
Grain Aspect Ratio (GAR)	1-2	1-2	1-2	1-2
IPS (μ) ^{**}	0.319	0.121	-	0.105

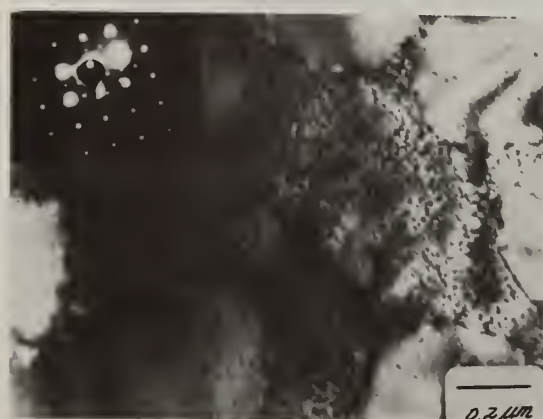
^{*} Oxide particles from surface oxidation, primarily in the form of Al₂O₃.

^{**} $IPS = [(A - n \bar{a}_p)/n]^{1/2}$, where $\bar{a}_p = [(\pi \bar{d})/4]^2$, \bar{d} = mean oxide particle size, A = area on micrograph, and n = number of oxide particles in A.

^{***} Density of IN100 (cast).

Phase Extraction and Analysis

Following methods outlined in the literature [8], separations of the oxides and γ' from the alloys were made. For alloy N-5, γ' precipitates were extracted from a sample heat treated as follows: (1260°C/2h/AC + 1232°C/0.5h/AC + 954°C/2h/AC + 843°C/24h/AC). The analyzed w/o oxide values for N-3 and N-5 are 2.96 and 2.65, respectively. The γ' content for N-5 was determined to be about 59%. TEM studies revealed coarser precipitates varying in size from 0.1 to 0.4 μm dispersed throughout the matrix; they in turn are surrounded by hyperfine 200A γ' particles. Both types of γ' appear to be spherical and are readily seen in Fig. 7. Both fine and hyperfine γ' precipitates are coherent; these L1₂ ordered structures introduce superlattice reflections in the selected area diffraction patterns. This is shown by the diffraction pattern insets in Fig. 7 for a (100) zone pattern. The precipitates have also been identified in dark field using a (100) γ' superlattice reflection.



(A)



(B)

Fig. 7. TEM micrograph (A) of γ' precipitates in N-5 after ZAP treatment; corresponding (100) zone SAD pattern, inset, showing γ' superlattice reflections. (B) Dark field using a (100) γ' superlattice reflection.

Stability Studies

The structural stabilities of the processed, as-extruded alloys were assessed by Rockwell "C" hardness (at 20°C) versus temperature profiles; see Fig. 8. Alloys N-2, N-3 and N-5 maintain hardness

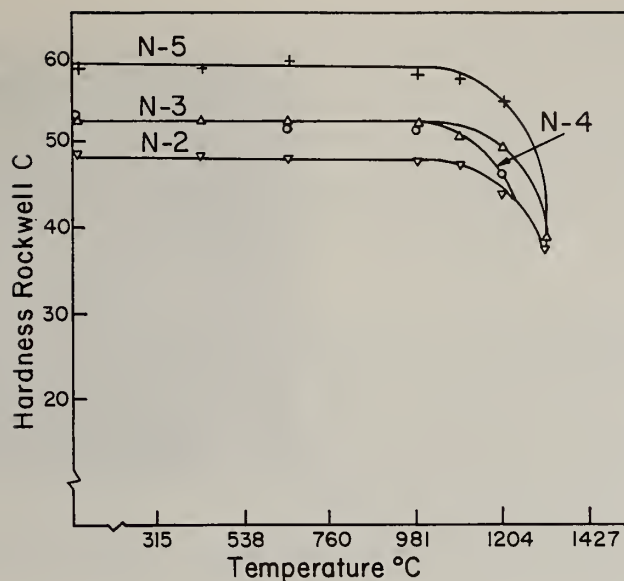


Fig. 8. Rockwell C hardness (at 20°C) versus annealing temperature for alloys N-2 to N-5.

stability to 1093°C (2000°F) and above but at different hardness levels, based on dislocation, cell boundary and grain boundary pinning by the fine oxide dispersions. Recovery, followed by partial recrystallization, are responsible for the drop in hardness at the higher temperatures.

Room-Temperature Tensile Tests

The room-temperature tension properties for the several alloys are listed in Table 4, along with data on the several mechanically alloyed OD materials. It was determined that the strength of ODS alloys increased generally with increasing volume fraction of oxide [9,10]. Hence the increases in strength of alloys N-2 and N-3 with 2 and 5% additions of Y_2O_3 , respectively, were expected. The exceedingly high strength value of as-extruded N-5 was the result of its combined volume fraction of γ' (59%) and Y_2O_3 (2%) added. The tensile behavior of these alloys is typical of that of the more complex ODS Ni-base alloys in which the yield strength approaches the ultimate strength, indicating less plastic yielding. Of importance in understanding this behavior is the state of the final material struc-

Table 4. Room-Temperature Tensile Data

Alloy	Condition	Ref.	Yield Strength ksi (MPa)	UTS ksi (MPa)	Elong. (%)	R.A. (%)
N-2	As Ext.		207 (1427)	209 (1441)	2	4
N-3	As Ext.		239 (1648)	246 (1697)	2	3
N-3	As Ext. + ZAP 3"/h at 1300°C		114 (789)	135 (926)	3	3
N-4	As Ext.		223 (1539)	223 (1539)	2	4
N-5	As Ext.		326 (2253)	326 (2253)	1	2
N-5	As Ext. + ZAP 3"/h at 1260°C + HT*		189 (1302)	201 (1389)	2	4
N-5	As Ext. + 1243°C/2h/AC + HT		156 (1076)	174 (1198)	3	4
IN853	As Ext. at 1066°C		295 (2037)			
IN853	As Ext. + 10h at 1177°C	6	176 (1212)			
IN853	As Ext. + 10h at 1260°C	6	100 (689)	146 (1007)	12	16
MA6000E	As Ext. at 1038°C	13	186 (1284)	188 (1294)	2.5	3.0
MA6000E	As Ext. at 1010°C then hot rolled at 1010°C	13	185 (1275)	186 (1284)	2.0	6.0

* HT = 1232°C/0.5h/AC + 954°C/2h/AC + 843°C/24h/AC

ture which results from the effects of such variables as the temperature for hot extrusion, the deformation strain and the strain rates which are responsible for the level and distribution of the stored energy of deformation. The severe cold working which results from the high strain rate extrusion at the extrusion temperature leads to a submicron grain size and a high level of residual strain energy stored within the substructure. Tensile data after ZAP and recovery heat treatments are also included in Table 4 for N-3 and N-5. Annealing at temperatures greater than 1093°C caused a drop in the yield/tensile ratio and an increased work hardening response. Clearly any strength increase derived through particle dislocation interactions was lost due to recovery, recrystallization and grain growth processes.

Recrystallization and Elevated Temperature Stress-Rupture Strength

A large grain size is required for optimum high-temperature strength. The recrystallization temperature of the alloys was the most important variable of the starting materials. The recrystallization response for alloys N-3 and N-5 was studied and found to be different. For N-5, the response was delayed and optimized at 1243°C. For N-3 the best response was at 1316°C. Alloy N-3 exhibited a response that was entirely dependent upon the material's prior thermomechanical history. In contrast, the delayed response of N-5 is attributed to the higher level of stored energy present and the presence of a large volume content of precipitates which must first be solutionized before there can be any response. A fine, uniform distribution of oxides proved essential for the desired storage of energy.

Using a solid-state crystal growing technique called Zone Aligned Polycrystal (ZAP), large columnar grains were developed for alloys N-3 and N-5.

The maximum ZAP rate is thought to be controlled by the mobility of the interface between the recrystallized and the as-worked material. For N-3 the interface temperature was >1300°C and specimen movement varied from 7.6 cm (3.0 inch)/hour to 15.2 cm (6.0 inch)/hour; for N-5, the interface temperature was >1260°C and motion rates varied from 3.8 cm (1.5 inch)/hour to 7.6 cm (3.0 inch)/hour.

Evaluation of ZAP treated material showed that the dispersoid size was not affected by the treatment. Dislocations were virtually absent and strong (100) recrystallization textures were developed.

The mechanism by which a very coarse-grained, elongated textured structure is produced from another textured, highly cold-worked structure is unknown, but two factors are postulated as influencing grain-boundary mobility, namely, 1) the orientation of the grain boundary with respect to the crystallographic orientation of the growing grain, and 2) the directional effects of the dispersoids. The combination of these two effects yields not only irregular shaped grains but also a preferred recrystallization texture (Fig. 9).

Stress-rupture behavior of N-5 is shown in Figs. 10 and 11. The stress for a 100-hour life at 1093°C is 22 ksi (152 MPa); the curves show the classical flat slopes of OD alloys. Figure 12 demonstrates that this alloy has comparable strength properties to the best previously reported alloys (IN853 and MA6000E). Alloy N-5 has 59% γ' while MA6000E is reported to have 39% γ' [13], with a 100-hour rupture stress of 24 ksi at 1093°C.

With a stress for 100-hour rupture life at 1093°C of 22 ksi, alloy N-5 has exhibited high-temperature strength values second only to MA6000E. Its strength exceeds that of some of the best superalloys reported to date, namely DS MAR-M 200, DS eutectics ($\gamma/\gamma'-\delta$) and single crystal alloys (PWA 1409). See Table 5 and Fig. 12. The very simple method of processing [5] employed for N-5 makes the method worthy of serious consideration.

Table 5. Comparison of Stress for 100-Hour Rupture Life for Several Superalloys

Alloy	100-Hour Rupture Strength, ksi (MPa)			
	Ref.	982°C (1800°F)	1038°C (1900°F)	1093°C (2000°F)
Mar-M 200 (DS)	14	29 (200)	20 (138)	-
MAR-M 200 (Cast)	14	26 (179)	16 (110)	9 (62)
IN100 (Cast)	14	25 (172)	18 (124)	-
MAR-M 509 (Co-base)	14	15 (103)	12 (83)	8 (55)
PWA 1409 (Mono crystal)	15	30 (207)	-	-



Fig. 9. The grain structure of N-5 test bar after ZAP treatment (7.6 cm/h at 1260°C) plus heat treatment.

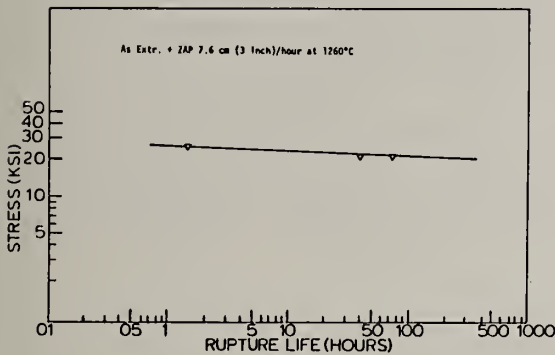


Fig. 11. Log stress versus log rupture time for alloy N-5 (ZAP treatment) at 1093°C.

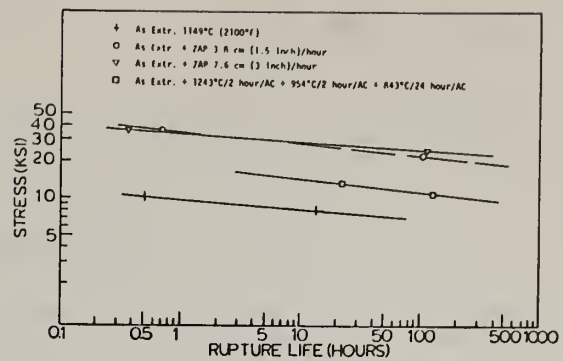


Fig. 10. Log stress versus log rupture time for Alloy N-5 at 982°C.

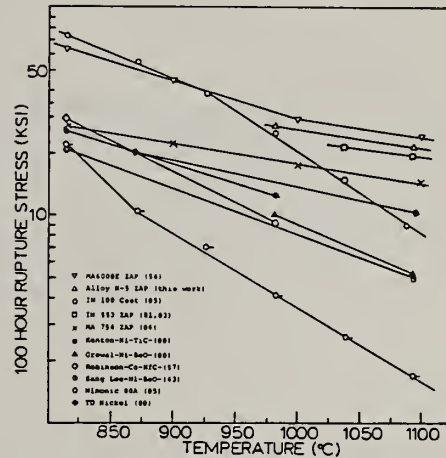


Fig. 12. Comparison of stress values for 100h life versus temperature for a variety of Ni-base alloys.

4. References

1. Benjamin, J. S., "Dispersion Strengthened Superalloys by Mechanical Alloying," Met. Trans., 1, 2943 (1970).
2. Gessinger, G. H., "Mechanical Alloying of IN-738," Met. Trans., 7A, 1203 (1976).
3. Kramer, K. H., "Dispersion Strengthened Superalloys," Powder Metallurgy International, 9, 105 (1977).
4. Merrick, H. F., Burwick, L. R. and Kim, Y. G., "Development of Oxide Dispersion Strengthened Turbine Blade Alloy by Mechanical Alloying," NASA CR-135150, January, 1977.
5. Smith, C. H., "Process Development and Characterization of an ODS Nickel Base Superalloy," Ph.D. Thesis, MIT (1982).
6. Cairns, R. L., "Effect of Annealing on Structure and Properties of a Dispersion Strengthened Superalloy, IN-853," Met. Trans., 5, 1677 (1974).
7. Sellars, C. M. and Petkovic-Luton, R. A., "Creep of Dispersion-Strengthened Alloys," Materials Science and Engineering, 46, 74 (1980).
8. Kriege, O. H. and Sullivan, C. P., "The Separation of Gamma Prime from Udimet 700," ASM Trans. Quarterly, 61, 278 (1968).

9. Zwilsky, K. M. and Grant, N. J., "Dispersion Strengthening in Copper-Alumina System," Trans. AIME, 22, 371 (1961).
10. Zwilsky, K. M. and Grant, N. J., "Copper-Silica and Copper-Alumina Alloys of High Temperature Interest," Trans. AIME, 209, 1197 (1957).
11. Smith, C. H. and Grant, N. J., to be published.
12. Cairns, R. L., Curwick, L. R., and Benjamin, J. S., "Grain Growth in Dispersion Strengthened Superalloys by Moving Heat Treatment," Met. Trans., 6A, 179 (1975).
13. Merrick, H. F., and Kim, Y. G., "Characterization of an Oxide Dispersion Strengthened Superalloy, MA6000E, for Turbine Blade Applications," NASA CR-159493, May, 1979.
14. The International Nickel Co., Inc., "High Temperature, High Strength Nickel Base Alloys," Third Ed., N. Y. (1977).
15. Ver Snyder, F. L. and Shank, M. E., "The Development of Columnar Grain and Single Crystal High Temperature Materials Through Directional Solidification," Material Science and Engineering, 6, 213-247 (1970).

5. Acknowledgements

The authors are pleased to acknowledge support by DOE under Contract No. EG-77-S-02-4466 and by Howmet for a fellowship which permitted completion of this research study.

THE MICROSTRUCTURE OF TOOL STEELS PROCESSED FROM RAPIDLY SOLIDIFIED POWDERS

S. Kumar, A. Lawley and M. J. Koczak

Drexel University, Philadelphia, PA

ABSTRACT

A detailed microstructural examination has been made of T15 tool steel processed from rapidly solidified powders. Gas atomized powders were screened into four size fractions ($\leq 840\mu\text{m}$; $250\text{--}840\mu\text{m}$; $44\text{--}100\mu\text{m}$; $\leq 44\mu\text{m}$), hot isostatically pressed to full density and heat-treated. Two HIPing temperatures, two austenitizing temperatures and three tempering temperatures were included in the study. Atomized and consolidated powders were characterized by means of optical and electron microscopy, x-ray diffraction and hardness. Cubic and hexagonal MC carbides are present in each size fraction of the atomized powder in the form of interconnected carbide networks. Carbide size decreases and particle hardness increases with decreasing particle size. MC, M_6C and M_{23}C_6 carbides are present after HIPing in the form of individual particles in a matrix of α -ferrite. The volume fractions of MC carbides ($\sim 16\%$) and M_6C carbides ($\sim 17\%$) are essentially independent of prior particle size and HIPing temperature. For both types of carbide and for each powder size fraction, the carbide size distribution is skewed to higher values with an increase in HIPing temperature. At a given HIPing temperature, carbide size distribution is broader for the coarser size fractions. M_{23}C_6 carbides can go completely into solution during austenitizing and do not reprecipitate on tempering. No new carbide-types form on tempering. The final volume fraction of M_6C is a function of austenitizing and tempering temperatures.

INTRODUCTION

Powder metallurgy (P/M) high speed tool steels have been a commercial reality for over a decade. Compared to their ingot metallurgy (I/M) counterparts, the P/M tool steels exhibit superior alloying homogeneity coupled with fine grain size and a uniformity and fineness of carbide dispersions that cannot be achieved by conventional casting and working processes. The microstructural characteristics of the P/M material are reflected in improved grindability, bend strength, tool life, and consistent machinability. In addition, a smaller out-of-roundness occurs during heat-treatment compared to the I/M product; this is a consequence of the relatively isotropic microstructure of the P/M tool steels.

Commercial P/M tool steels are consolidated from gas atomized powder covering a broad particle size range, typically $< 1200\mu\text{m}$. Hence, a range of cooling rates is inherent in the as-atomized powder prior to consolidation, with the finer particle sizes falling in the rapid solidification regime. A primary purpose of the present study is to examine the possible role of powder particle cooling rate on the microstructure and properties of high speed tool steels. To this end, gas atomized powders have been screened into specific size fractions and evaluated in powder form and after consolidation to full density. Microstructural observations on T15 are presented here.

EXPERIMENTAL PROCEDURE

T15 tool steel powder of weight composition 1.52% C , 4.67% Cr , 5.22% Co , 12.19% W , 4.85% V , 0.31% Mn , 0.46% Si , 0.0063% O_2 , 0.1% N_2 , balance Fe was atomized in nitrogen. The four powder size fractions studied were $\leq 840\mu\text{m}$, $250\text{--}840\mu\text{m}$, $44\text{--}100\mu\text{m}$ and $\leq 44\mu\text{m}$. Bars of each size fraction were HIPed at 1195°C or 1130°C . The higher temperature is that used by Crucible, Inc. for its commercial P/M high speed tool steels. The lower temperature was used as a possible means for controlling grain size and carbide size during densification. Heat-treatment studies of pieces cut from the HIPed bars included two austenitizing temperatures (1176°C and 1225°C) and three tempering temperatures (538°C , 552°C and 565°C). The HIPing, austenitizing and tempering temperatures are coded in Table I.

An initial appreciation for overall powder shape and surface condition was obtained utilizing SEM. High resolution SEM of polished and etched powder cross-sections was used for carbide characterization. Two-stage replicas of the etched powder cross-sections were also examined by means of TEM. Carbide

Table I: Coding System for Powder Consolidation and Heat Treatment

Code	Interpretation
H1	Hot Isostatically Pressed at 1130°C
H2	Hot Isostatically Pressed at 1195°C
A1	Austenitized at 1176 C for 4 mins. and oil-quenched
A2	Austenitized at 1226 C for 4 mins. and oil-quenched
T1	Tempered for (2 + 2 + 2) hrs. at 538°C
T2	Tempered for (2 + 2 + 2) hrs. at 552°C
T3	Tempered for (2 + 2 + 2) hrs. at 565°C

phases in the powder were identified by means of x-ray diffraction. For purposes of identification, carbides were chemically extracted from the powder or consolidated material (1). Carbide volume fractions, sizes and size distributions were determined by means of a combination of selective etching (1) and quantitative metallography.

RESULTS AND OBSERVATIONS

1. Atomized Powders

The powder particles are generally spherical in shape with small satellites present in each size fraction. Debye-Scherrer diffraction patterns of extracted carbides from each size fraction are consistent with the presence of cubic and hexagonal MC carbides. Powder cross-sections corresponding to three size fractions are shown in Figures 1, 2 and 3. A transition from cellular to a dendritic solidification mode is evident with decreasing particle size. In the cellular mode, carbides exist as interconnecting networks. Martensite needles are visible in the coarse powder, Figure 1.

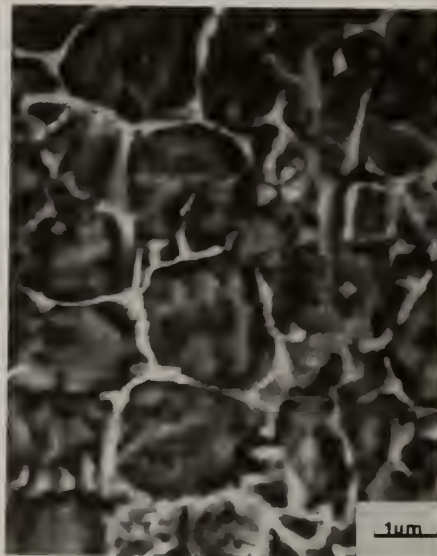


Figure 1: Atomized powder particle cross-section (SEM) from 550-700µm screen fraction. Etch: Kalling's reagent + HCl/Picral.

Figure 2: Atomized powder particle cross-section (SEM) from 110-130µm screen fraction. Etch: Kalling's reagent + HCl/Picral.

Figure 3: Atomized powder particle cross-section (SEM) from <37µm screen fraction. Etch: Kalling's reagent + HCl/Picral.

2. HIPed Material

Micrographs (SEM) of polished and etched samples corresponding to the coarsest and finest size fractions are shown in Figures 4 through 7. The carbides are coarser following HIPing at the higher



Figure 4: HIPed material (H1) from 250-840 μ m screen fraction. Etch: Kalling's reagent. SEM.

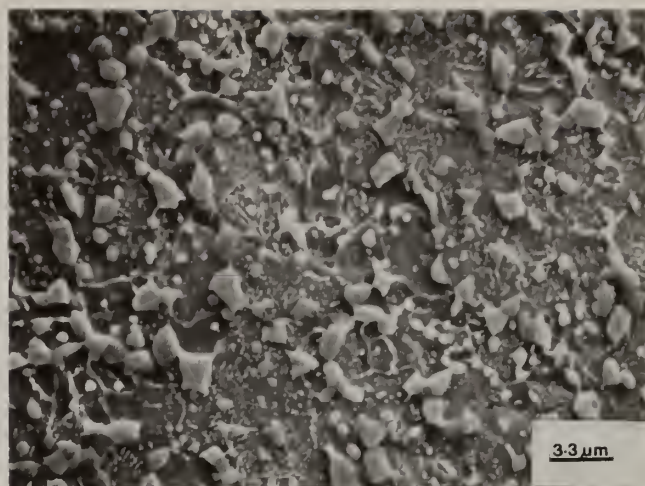


Figure 5: HIPed material (H2) from 250-840 μ m screen fraction. Etch: Kalling's reagent. SEM.

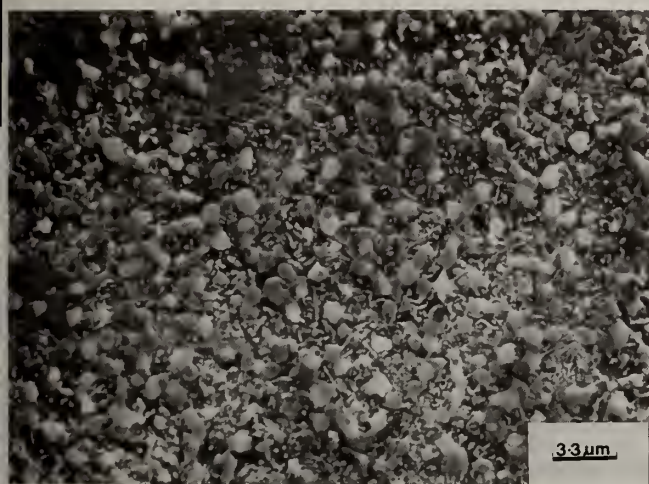


Figure 6: HIPed material (H1) from -44 μ m screen fraction. Etch: Kalling's reagent. SEM.

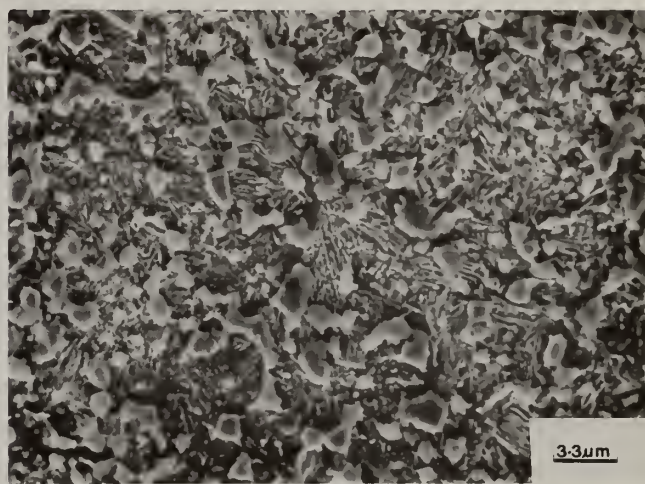


Figure 7: HIPed material (H2) from -44 μ m screen fraction. Etch: Kalling's reagent. SEM.

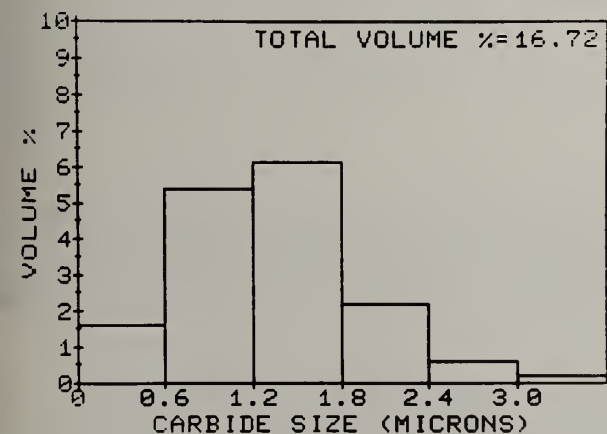


Figure 8: Size distribution for M_6C in HIPed (H1) material; 250-840 μ m screen fraction.

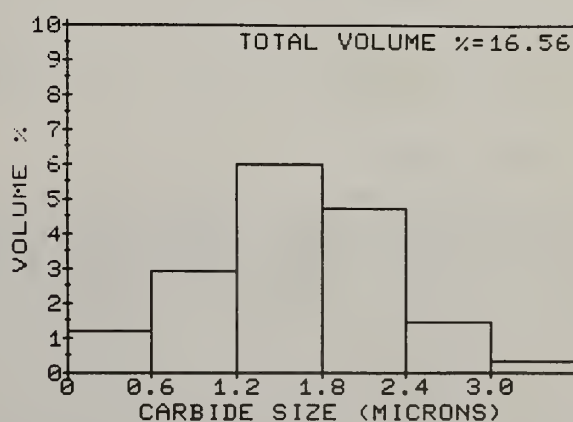


Figure 9: Size distribution for M_6C in HIPed (H2) material; 250-840 μ m screen fraction.

temperature (H2). For a given HIPing temperature (H1 or H2), the carbide size is essentially independent of prior particle size fraction. The matrix is α -ferrite and the carbides of the type MC, M_6C , and $M_{23}C_6$, in all cases. Carbide volume fractions are summarized in Table II, as a function of particle size fraction and HIPing temperature. For MC and M_6C carbides, the volume fraction is not a sensitive function of size fraction and HIPing temperature, Table II. However, the size distribution is skewed to higher carbide sizes with an increase in HIPing temperature, Figure 8 and 9. For a given HIPing temperature, the carbide size distribution is dependent on the prior particle size fraction; it is broader for coarser size fractions. No selective etching technique exists for the unambiguous identification of $M_{23}C_6$.

Table II: Carbide Volume Fraction as a Function of Powder Size Fraction and HIPing Temperature

	Size Fraction	H1	H2
MC	250-840 μ m	0.162	0.179
	$\leq 44\mu$ m	0.144	0.141
M_6C	250-840 μ m	0.167	0.166
	$\leq 44\mu$ m	0.175	0.152

3. HIP + Heat-Treated Material

Representative micrographs (SEM) of the T15 tool steel after austenitizing (quenching) and austenitizing + tempering are compared in Figures 10 and 11, respectively. Martensite is visible in the quenched condition. MC and M_6C carbides are present at each stage of heat-treatment; in addition, $M_{23}C_6$ is retained after austenitizing at A1. After austenitizing at A2, all the $M_{23}C_6$ carbides are dissolved and they do not reprecipitate during tempering. No new carbide-types form on heat-treatment. Volume fraction data for M_6C carbides are given in Table III. A significant fraction of M_6C goes into solution during austenitizing and then reprecipitates on tempering. As expected, more M_6C goes into solution at A2 than at A1. The volume fraction of M_6C increases with increasing tempering temperature, and the size distribution is skewed to coarser particle sizes, irrespective of the prior particle size fraction. A similar evaluation of the effect of heat-treatment on the volume fraction of MC is currently in progress.

Table III: Volume Fraction of M_6C as a Function of Heat Treatment

Size Fraction	A1	A1+T1	A1+T2	A2	A2+T1	A2+T2
250-840 μ m(H2)	0.0667	0.0721	0.0865	0.0543	0.0611	0.0752
$\leq 44\mu$ m (H2)	0.0688	--	0.1032	--	0.045	0.072

DISCUSSION

1. Atomized Powders

In gas atomization, a stream of liquid metal is broken-up by means of a high pressure gas stream. The resulting liquid droplets spheroidize in free fall before solidification due to surface tension. Particle collisions can occur before and/or after solidification (2) and this is responsible for satellite formation. Cubic MC and hexagonal γ -MC carbides have been identified in all the powder size fractions examined. γ -MC is not present in the HIPed material. This implies that γ -MC is not an equilibrium phase but is present in the atomized powder due to the high cooling rate and that γ -MC carbide goes back into solution when thermal energy is supplied to the powders. A transition from a cellular to a dendritic mode of solidification with decreasing particle size can be explained in terms of the cooling rate T , the thermal gradient G , and the solid/liquid interface velocity R . Similar observations have been reported by Smugeresky (3). Levi and Mehrabian (4) have pointed out that as the droplet size decreases, the time for the start and completion of solidification decreases, the interface velocity at equivalent fractions solidified increases and the G to R ratio decreases. Consequently, as the droplet size and the G to R ratio decreases, a change from a cellular to a dendritic structure can be expected.

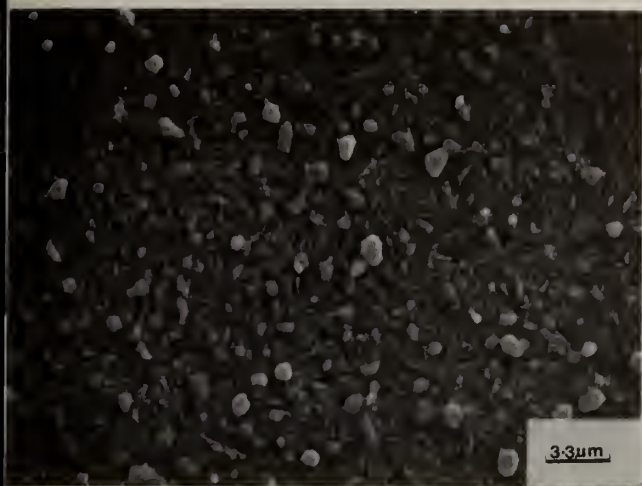


Figure 10: HIPed (H2) + austenitized (A2) material from 250-840 μ m size fraction. Etch: Kalling's reagent. SEM.

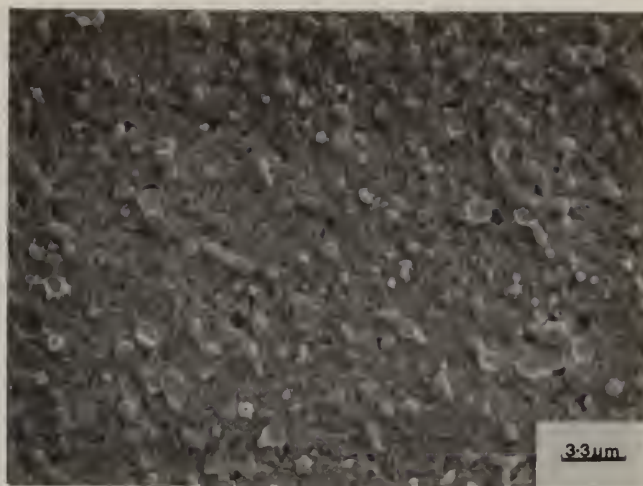


Figure 11: HIPed (H2) + heat-treated (A2+T3) material from 250-840 μ m size fraction. Etch: Kalling's reagent. SEM.

Needles of martensite are visible in the coarsest size fraction but are not evident in the finer powder particles. This can be explained in terms of the high degree of supersaturation of the austenite associated with increasing cooling rates (2).

2. HIPed Material

After HIPing, MC, M_6C and $M_{23}C_6$ carbides are present. This is to be expected since the slow cooling inherent in the HIP cycle leaves the consolidated material in the annealed condition. These carbides are known to be present after annealing (1).

No appreciable dependence of volume fraction of MC and M_6C with HIPing temperature and prior powder particle size exists. This implies that the equilibrium level of solubility is achieved. A comparison of Figures 4, 5, 6 and 7 shows that for a particular HIPing temperature, the carbides are approximately the same size. Further, the carbides are coarser following HIPing at the higher temperature.

A close examination of the size distribution for M_6C carbides shows that for a given HIPing temperature (H1 or H2), the 250-840 μ m powder size fraction exhibits a wider spread of carbide sizes than does the $\leq 44\mu$ m powder screen. For similar volume fractions, these observations imply that the rate of carbide nucleation was higher in the finer size fraction. This is probably related to (i) the higher surface area per unit volume, (ii) the larger number of particle-particle contact points per unit volume, (iii) the finer distribution of the carbide network and (iv) the higher degree of supersaturation with decreasing particle size. These four structural differences may affect nucleation rate separately or in combination. A similar comparison of the MC carbide distribution shows that the $\leq 44\mu$ m powder has a narrower size spread and a smaller average carbide size than the 250-840 μ m screen.

Only MC carbides are present in the atomized powder. Assuming that the volume fraction of MC present in the powder decreases with increasing cooling rates, then during HIPing, a higher nucleation rate should exist in the finer size fraction. This follows from the higher degree of supersaturation of the matrix and the surface area enhancement in the fine powders. In the coarser powder particles, existing MC carbides can serve as sites for precipitation, thereby enhancing growth.

3. HIP + Heat-Treated Material

The presence of $M_{23}C_6$ in the consolidated tool steel after austenitizing at A1 confirms that this temperature is not high enough to dissolve all this type of carbide which was present after HIPing. Therefore maximum strengthening of the matrix requires a higher austenitizing temperature, e.g. A2, at which all the $M_{23}C_6$ is dissolved. At A2, about 10% of the M_6C present after HIPing is dissolved in the matrix, cf. Tables II and III. M_6C starts to reprecipitate out on tempering, and this accounts for the increase in volume fraction. This carbide coarsens with increasing tempering temperature, with the resulting skew in the carbide size distribution curve to larger carbide sizes.

CONCLUSIONS

1. Cubic MC and hexagonal γ -MC carbides are present in the four size fractions of atomized powder examined. γ -MC is shown to be metastable.
2. HIPing temperature is important in dictating the size and size distribution of carbides; it has a stronger influence than the prior powder particle size.
3. The volume fractions of MC carbides ($\sim 16\%$) and M_6C carbides ($\sim 17\%$) are essentially independent of prior particle size and HIPing temperature.
4. A powder processing cycle, namely H1 + A2 + T2, has been selected for tool steel powder consolidation and heat-treatment as a precursor to evaluation of tool steel properties and performance.

ACKNOWLEDGMENT

This research is supported by the Office of Naval Research. The authors wish to thank Dr. B.A. MacDonald and Dr. D.E. Polk for their interest and involvement in the program.

REFERENCES

1. Blickwede, D.J., Cohen, M. and Roberts, G.A., "The Effect of Vanadium and Carbon on the Constitution of High Speed Steels", ASM Trans., p. 1161, Vol. 42, 1950.
2. Fischmeister, H.F., Ozerskii, A.D. and Olsson, L., "Solidification Structure of Gas-Atomized High-Speed Steel Powders", Powder Metallurgy, p. 1, Vol. 25, No. 1, 1982.
3. Smugeresky, J.E., "Characterization of a Rapidly Solidified Iron-Based Superalloy", Metall. Trans. A., p. 1535, Vol. 13A, Sept. 1982.
4. Levi, C.J. and Mehrabian, R., "Heat Flow in Atomized Metal Droplets", Metall. Trans B., p. 21, Vol. 11B, March 1980.

STRUCTURE AND PROPERTIES OF A POWDER-PROCESSED HIGH-CHROMIUM IRON

S. Mohan*, A. Lawley*, L. R. Woodyatt** and K. S. Brosius***

*Drexel University, Philadelphia, PA

**Bethlehem Steel Corporation, Bethlehem, PA

***Crucible Research Center, Pittsburgh, PA

ABSTRACT

Microstructure-property relationships have been developed for a powder-processed high chromium iron alloy (Fe-20%Cr-1.5%Mo-2.5%C) with particular interest vested in the possible effects of rapid solidification of the powder on final properties. The alloy was gas atomized, screened into three size fractions (119 to 213 μm ; 74 to 107 μm ; $\leq 44 \mu\text{m}$), hot isostatically pressed (HIPed) to full density, and heat-treated (HT) to give a structure consisting of M_7C_3 carbides in tempered martensite. Microstructures were characterized in the powder form, after HIPing and HIP + HT. Properties evaluated were hot hardness, hot compressive strength, fracture toughness and abrasive and adhesive wear resistance. Comparisons were made with a chill cast alloy of similar composition. Each of the above properties was relatively insensitive to powder particle size. The strength and temperature dependence of strength of the powder-processed and cast forms were similar but there were significant differences in fracture toughness and wear resistance between the powder-processed and cast forms of the alloy. The level of fracture toughness in the powder metallurgy material was significantly lower than that of the cast material. In terms of abrasive wear, the powder-processed material was inferior to the cast material at low stress levels but was comparable at high stress levels. Resistance to adhesive wear was marginally superior in the powder-processed material compared to the cast material. These property differences have been analyzed and interpreted in terms of the constituents, scale and morphology of the associated microstructures.

INTRODUCTION

High chromium white cast irons are used extensively in the mining industry due to their high level of abrasion resistance coupled with adequate toughness [1]. These alloys are also used as the roll material in rolling mill rolls, particularly in continuous hot plate and strip mills. Conventional casting of these highly alloyed materials results in both microscopic and macroscopic segregation of alloying elements, with attendant problems in heat-treatment, with property levels and in the uniformity of properties. Since alloying flexibility, chemical homogeneity and fine-scale microstructures are inherent in powder-processed alloys, this approach could offer a technically and economically viable alternative.

In this study, detailed relationships between microstructure and properties have been established for a powder-processed high-chromium iron. Particular interest was vested in the possible role of powder particle cooling rate, including the rapid solidification regime, on hot strength, fracture toughness, abrasive and adhesive wear. Microstructure and property comparisons were made on a cast alloy of similar composition.

EXPERIMENTAL PROCEDURE

Powder of weight composition Fe-20.6%Cr-1.48%Mo-2.44%C-0.5%Mn-0.41%Si-0.007% O_2 -0.12% N_2 was nitrogen gas atomized and screened into three size fractions, 119 to 213 μm , 74 to 107 μm , and $\leq 44 \mu\text{m}$. These size fractions are designated A, B and C, respectively and reflect approximate cooling rates of 10^4°C/s , 10^5°C/s and $5 \times 10^5^\circ\text{C/s}$ respectively. Powder characteristics, microstructure, and constitution were identified utilizing SEM and x-ray diffraction.

Blended and screened powders from each size fraction were HIPed to full density at 1121°C . HIPed material was soaked at 1010°C for 3 hours, air cooled, and tempered at 575°C for 3 hours.



Figure 1(a). Atomized powder; 119 to 213 μm size screen. Arrows point to austenite dendrites. SEM.

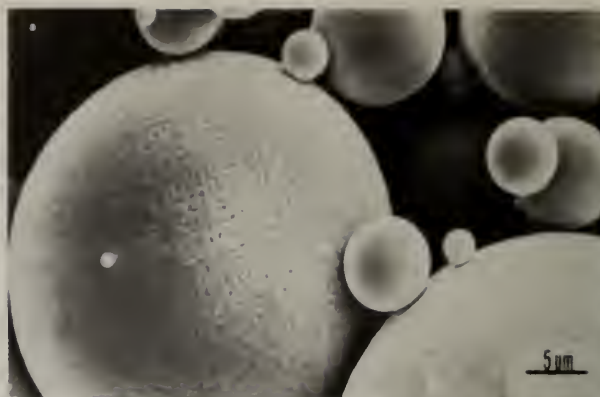


Figure 1(b). Atomized powder; $\leq 44 \mu\text{m}$ size screen. SEM.

Consolidated material was characterized by means of high resolution SEM and x-ray diffraction.

Hot hardness, hot compressive strength and static fracture toughness (ASTM E399-78a) were determined for the HIPed + heat-treated material. Abrasive wear resistance was measured by means of the dry sand-rubber wheel test (ASTM G65-80) at two stress levels [2]. Resistance to adhesive wear was evaluated by means of the crossed-cylinder test.

A chill cast alloy (code D) of similar composition to that of the P/M material was heat-treated to the same hardness level as that of the P/M material. The microstructure and properties of this material were evaluated as described above.

RESULTS AND OBSERVATIONS

1) Powders

Representative micrographs (SEM) of powder from the coarsest and finest size fractions examined are compared in Figure 1. Particles are generally spherical in shape with relatively smooth surfaces. At each size fraction, small satellites are attached to the larger particles. Dendritic-type solidification structures are evident. Dendrites were identified (EDAX) as being austenitic. M_7C_3 -type carbides are present in each particle size range.

2) HIPed and Heat-Treated Material

Representative micrographs (SEM) of two of the size fractions are illustrated in Figure 2. The scale of the microstructure is similar in Figures 2(a) and 2(b) and consists of eutectic carbides



Figure 2(a). HIPed and heat-treated material; 119 to 213 μm size screen. A = eutectic carbides, B = area showing secondary carbides in tempered martensite. SEM.



Figure 2(b). HIPed and heat-treated material; $\leq 44 \mu\text{m}$ size screen. SEM.

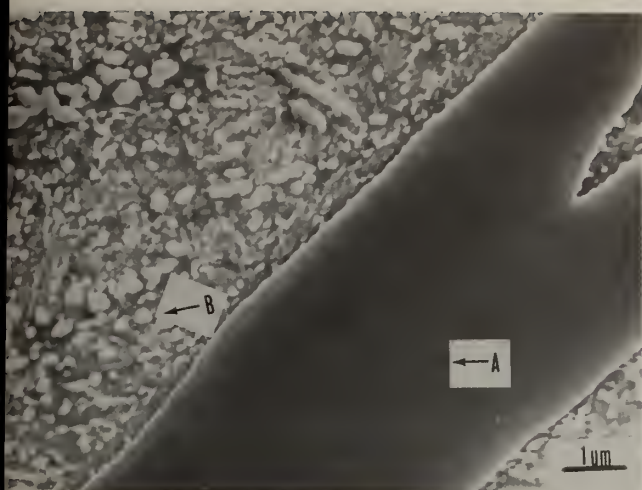


Figure 3. Chill-cast material. A = eutectic carbides, B = secondary carbides. SEM.

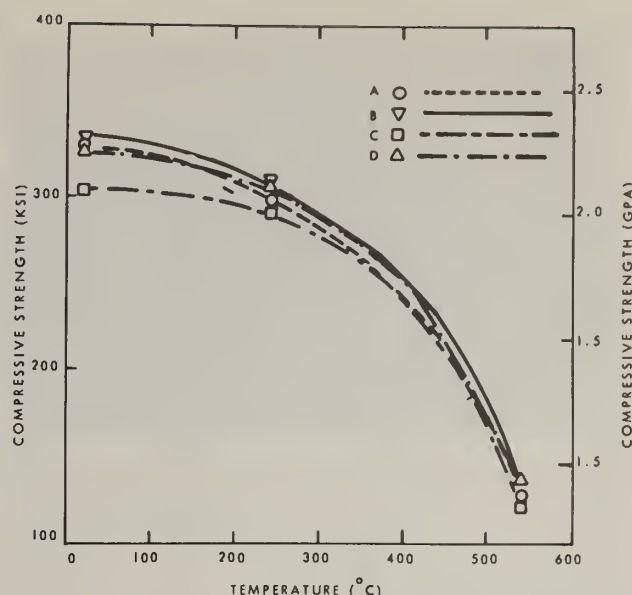


Figure 4. Hot compressive strength as a function of temperature for P/M (A,B,C) and chill-cast (D) material.

and secondary carbides in a matrix of tempered martensite. For comparison, a representative micrograph (SEM) of the chill cast and heat-treated material is shown in Figure 3; coarse eutectic carbides and smaller secondary carbides are present in a matrix of tempered martensite.

3) Hot Strength

Results of the hot compressive tests are shown in Figure 4. The temperature dependence of strength, and strength level at a given temperature, are similar in each of the three powder size fractions and the cast materials. Hot hardness shows a similar dependence on temperature.

4) Fracture Toughness

Fracture toughness levels for the P/M and chill cast material are compared in Figure 5. For the HIPed + heat-treated P/M material, fracture toughness is largely independent of prior powder particle size. The fracture toughness of the cast alloy is about twice that of the P/M-processed material. For tool steels, when toughness is measured by means of the Charpy test, P/M processed material is generally superior to the cast and wrought product [3].

5) Wear Resistance

Low stress abrasive wear resistance, measured in terms of the wear factor, for the P/M and cast materials is compared in Figure 6. Under these conditions, the P/M material is less resistant to wear than the cast form. In high stress tests, the level of abrasive wear resistance is similar in the two forms of material. No effect of prior powder particle size was detected.

Under conditions of adhesive wear, the P/M-processed material exhibits a wear resistance slightly higher than that of the cast alloy. No significant dependence of adhesive wear resistance on prior powder particle size was observed.

DISCUSSION

1) Microstructure

The matrix of the chill cast alloy consists of highly supersaturated (retained) austenite which is destabilized during austenitizing. Thus, fine-scale secondary carbides are precipitated. In comparison, after HIPing, the P/M material has a ferritic matrix low in alloying elements so that secondary carbides do not precipitate when the material is austenitized. This is substantiated by

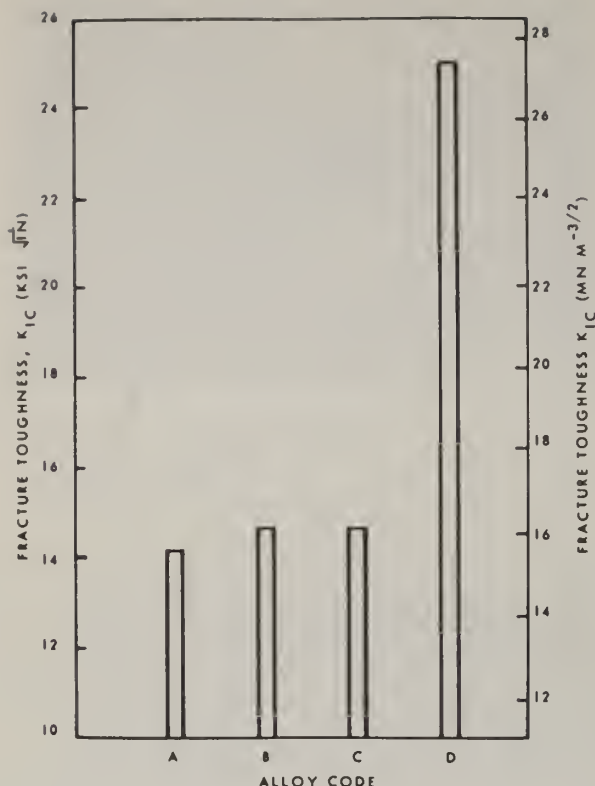


Figure 5. Fracture toughness of P/M (A,B,C) and chill-cast (D) material.

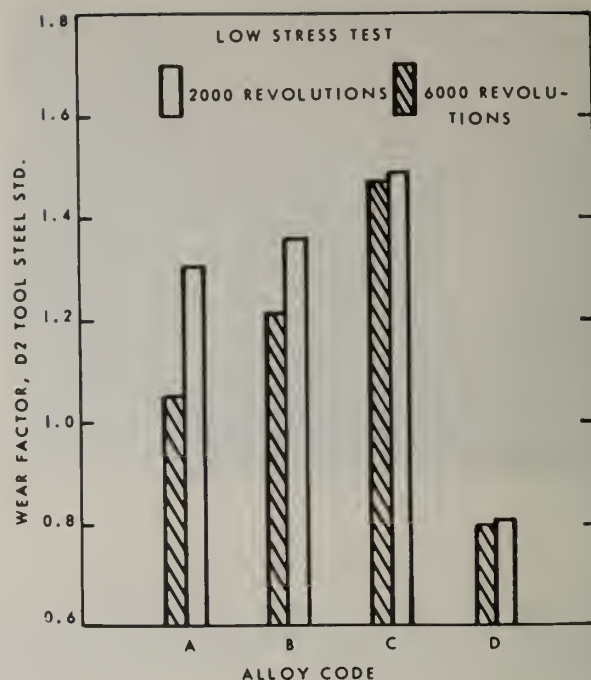


Figure 6. Low stress wear data for P/M (A,B,C) and chill-cast (D) material.

the observation that the volume fraction of carbides (~ 0.23) is similar in the HIPed P/M material before and after heat-treatment. The spherical secondary carbides in the P/M material, formed during HIPing, remain after heat-treatment. In the chill-cast material, the carbide volume fraction increases from 0.19 to 0.29 after heat-treatment. The P/M-processed material has a much finer microstructure than the cast form, for each of the prior particle screen sizes.

2) Properties

It is the size and shape of the eutectic carbides that differ most in the P/M and cast materials. This difference is primarily responsible for the observed differences in properties and wear response between the two forms.

A. Hot Strength

The level of hardness and compressive strength and their dependence on temperature are similar in both the P/M processed and cast material. Since the size and shape of the eutectic carbides are significantly different in the two materials, strength and hardness must be controlled primarily by the matrix phase. The loss in compressive strength and hardness at elevated temperature is associated with matrix softening. Depletion of carbon from the martensitic matrix leads to softening of the matrix phase. Softening also results from growth and/or coalescence of the carbide particles.

B. Fracture Toughness

Qualitatively, the superior fracture toughness of the cast alloy compared to the P/M-processed material is understood in terms of the corresponding fracture surface morphologies, Figure 7. Extensive fine-scale microvoid coalescence and fine cleavage are evident on the fracture surfaces of the P/M-processed material. Microvoids develop around the small carbides with little

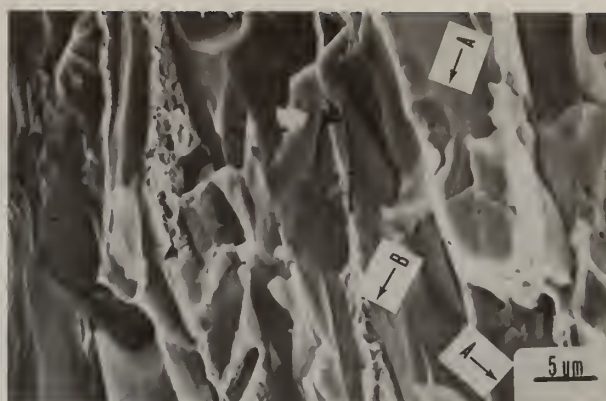
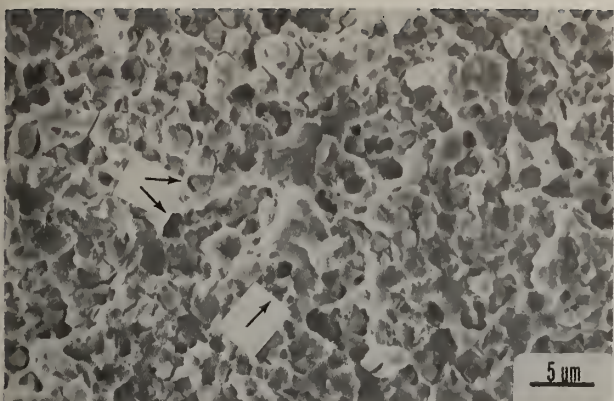


Figure 7(a). Overload fracture surface of HIP + heat-treated P/M material (119-213 μm size screen). Arrows point to microvoids. SEM.

Figure 7(b). Overload fracture surface of chill-cast + heat treated material. A = cleaved carbides; B = dimpled rupture.

associated shear. Other fine features appear to be the flat facets which occur in clusters adjacent to the dimples; these are related to the fine-scale structure of the matrix. Crack initiation takes place at carbide-matrix interfaces and this is followed by microvoid coalescence. In the cast material, the relative absence of fine carbides eliminates sites for microvoid initiation. The crack propagates primarily through the matrix between the coarse network of eutectic carbides, with some associated cleavage of the coarse (eutectic) carbides.

C. Wear

In the low stress abrasion testing of the P/M material, silica particles (size 212-300 μm ; hardness 900 KHN) can readily gouge out the small carbides (size $\sim 2 \mu\text{m}$; hardness 1700 KHN) from the martensitic matrix (hardness 700 KHN). Thus these small carbides make only a small contribution to abrasive wear resistance. In comparison, the larger elongated clusters of carbides in the cast form are more resistant to gouging. Removal requires cutting and/or chipping of the carbides.

In the high stress test, the small eutectic carbides in the P/M processed material are readily removed from the wear surface by spalling under the influence of the Al_2O_3 abrasive particles (size 212 to 300 μm ; hardness 2000 KHN). Thus, the carbides are only partially effective in reducing material loss. The Al_2O_3 particles are able to cut through both the matrix and the carbide clusters in the cast alloy with relative ease. Optical metallography of wear surface cross-sections and SEM of wear surfaces confirm the above differences in the mechanisms of abrasive particle - wear specimen interactions.

In terms of adhesive wear the P/M material is marginally superior to the cast material. This is due primarily to the higher surface area density of the carbides in the P/M material compared to that of the cast material. Thus, the mean free path of the intervening matrix is smaller in the P/M alloy than in the cast material. This results in an increased contact area between the tungsten carbide cylinder and the M_7C_3 carbides in the P/M material.

ACKNOWLEDGMENT

This work was supported by Bethlehem Steel Corporation. The authors are indebted to Dr. John M. Chilton for his advice and interest in this program.

REFERENCES

- [1] F. Maratray, "Choice of Appropriate Compositions for Chromium-Molybdenum White Irons", Climax Molybdenum S.A., Paris, France (1971).
- [2] F. Borik, Rubber Wheel Abrasion Test, SAE Preprint 700687. Society of Automotive Engineers, 1970.
- [3] A. Kasak and E. J. Dulis, Powder Met., Vol. 21 (2), p. 116, 1978.

THE EFFECT OF POWDER COOLING RATE AND THERMAL EXPOSURE
ON THE TENSILE PROPERTIES OF A RAPIDLY SOLIDIFIED
NICKEL BASE SUPERALLOY

D. B. Miracle, K. A. Williams, and H. A. Lipsitt

AFWAL Materials Laboratory
Metals and Ceramics Division
Wright-Patterson AFB OH 45433

ABSTRACT

Although much work has been conducted in the area of rapid solidification, little has been done to correlate the structure/property relationships of a material with differences in the cooling rates of the starting powders. This study was designed to investigate the influence of powder cooling rate, within the range of 10^4 to 10^6 °C/sec, on stock extruded from rapidly solidified superalloy powder. Powder particle sizes ranged from less than 53 microns to approximately 250 microns, representing a change in cooling rate of approximately one order of magnitude. The effect of long time exposure at high temperatures on mechanical properties of the consolidated alloy was also determined. The results showed no effects on properties due to differences in cooling rate. Long time exposure at high temperature was found to degrade the properties of equiaxed material tested at room temperature and 1400°F mainly because of phase changes, Ostwald ripening of the γ' , and grain boundary cellular coarsening.


Introduction

In the mid-1970's, a program was begun to develop a new family of turbine blade materials with the increased temperature capabilities necessary for advanced high-performance engines. The program was conducted by the Government Products Division of Pratt and Whitney Aircraft, under the sponsorship of the Defense Advanced Research Projects Agency and the AFWAL Materials Laboratory. The Ni-Al-Mo system was chosen as a base, and alloys were produced by the Rapid Solidification Rate (RSR) powder metallurgy process, utilizing cooling rates between 10^4 and 10^6 °C/sec [1]. These high quench rates have been shown to be beneficial in other alloy systems [2], but little was known about the effects of rapid cooling in nickel-base superalloys. A project was thus initiated at the AFWAL Materials Laboratory to assess the role that this range of cooling rates played in the tensile properties of one of the alloys produced--Alloy 185, a γ' strengthened Ni-base superalloy which contained 73.8% Ni, 15% Al, 9% Mo, 2% W and 0.2% C (atomic percent).

Conventional powder-making techniques, with cooling rates in the range of 10^2 - 10^4 °C/sec, have essentially eliminated the problem of macrosegregation associated with conventional casting techniques. Microsegregation persists, however, on the order of the secondary dendrite arm spacing. As the cooling rate of the powders increases, the secondary dendrite arm spacing (DAS) becomes smaller, and the material becomes more homogeneous. In the limiting case, at very high quench rates, homogeneous nucleation may occur and microsegregation may effectively be eliminated. This has been shown previously with conventional superalloy powders produced by the RSR technique, where the volume fraction of homogeneously nucleated, or "micro-crystalline," powders increases as the quench rate increases (particle size decreases) [3]. It has also been shown that at very high quench rates, an amount of solute in excess of the equilibrium quantity may be quenched in solution during the solidification process. This excess quantity may precipitate during subsequent thermal or thermomechanical treatment with such a size and distribution as to be effective as another precipitation strengthening phase. These were possible effects of cooling rate on tensile properties to be investigated by this study.

Any candidate material for high temperature application must exhibit a microstructure that is stable at its use temperature for extended periods of time. Some of the microstructural instabilities upon long-term exposure at 1700°F for 250 hours have been documented for Alloy 185 [4], but the effect of these instabilities on mechanical properties had not been established. The documentation of the effect of these instabilities upon the tensile properties was also an objective of this program.

Table I
Mesh Fractions

<u>MESH SIZE</u>	<u>PARTICLE SIZE (μ)</u>	<u>QUENCH RANGE</u>
- 60/+ 80	250-177	$\sim 10^4$ °C/sec
- 80/+100	177-149	
- 80	< 177	
-140/+170	105-88	
-140	< 105	
-270	< 53	
		$\sim 10^5$ °C/sec

Procedure

The effect of cooling rate was isolated as follows: powder runs of Alloy 185 were precision-sieved to several powder mesh size distributions. In general, a different average cooling rate was associated with each of the sieved mesh sizes. Since the surface-to-volume ratio increases as particle size decreases, the smaller particles experience a higher quench rate. This has been verified experimentally for other superalloys and is shown in Figure 1 for MAR-M 200 by plotting secondary DAS as a function of particle size [5]. Six mesh size distributions were used and are given in Table 1, along with the predicted range of cooling rates associated with each distribution. The powder was placed in stainless steel cans, hot outgassed, and then extruded at 2000-2300°F with reductions in area of 26:1. The extrusions were then de-canned and machined into tensile specimens. The specimen geometry has been used by this Laboratory before and appears in the literature [6]. Half of each of the extrusions was heat-treated for 250 hours at 1700°F prior to machining. The exposures were done in a Lindberg box furnace in a flowing Ar atmosphere.

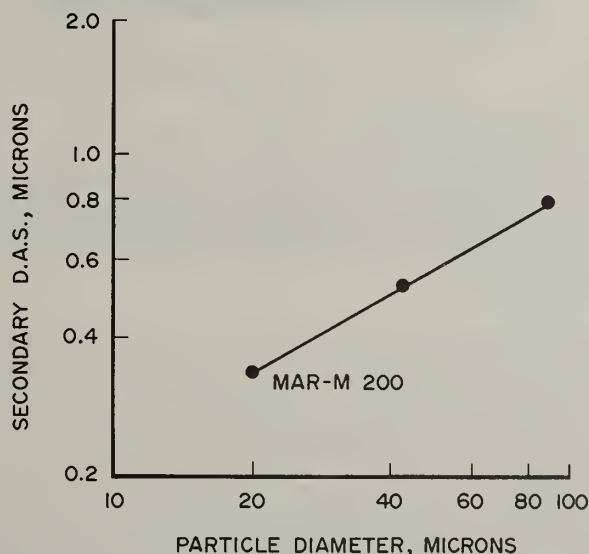


Figure 1. Variation of Secondary Dendrite Arm Spacing with Particle Size.

The tensile tests were conducted on an Instron tensile machine using a strain rate of 0.016 cm/cm per min. Strain was measured with a linear variable differential transformer (LVDT). A majority of the tests were done at room temperature, 1400°F, and 1800°F, although a small number of DR'ed specimens were tested at 1600°F. Temperature was controlled to $\pm 10^\circ\text{F}$ in all cases. All tests were run in air.

Microstructural characterization was done with the aid of an ETEC SEM and a Philips 300 TEM. Specimens were polished using standard metallographic techniques and etched with a glyceresia etch.

TEM thin foils were produced with a Fischione polishing unit using a methanol-butanol-perchloric acid solution as the electrolyte and utilizing voltages of approximately 20-25 volts at temperatures from -20 to -50°C.

Results and Discussion

A representative photomicrograph of the as-extruded material is shown in Figure 2. The material appears to be fully recrystallized and exhibits a grain size in the range of 16-20 μm . A coarse incoherent γ' surrounds grains of nominally semi-coherent γ' precipitates in a γ matrix. Other phases (apparent at this scale of magnification) have been identified by TEM studies and electron-probe microanalysis as an α -Mo precipitate and carbides. Electron diffraction in the TEM revealed the presence of two other phases residing between the γ' --a phase that has been identified as a Pt_2Mo isotype (nominally Ni_2Mo) and a phase with the DO_{22} structure (nominally Ni_3Mo). No microstructural variations were apparent for different mesh sizes.



Figure 2. Microstructure of As-Extruded Material.

Tensile properties are shown in Figure 3. Approximately ten to twenty tensile tests were made at each temperature, including specimens from all powder mesh sizes. Differences in powder mesh size produced no systematic variation in either the stress or strain levels achieved. Thus, it appears that any cooling rate effects that may have been present in the powder (i.e., supersaturation, microcrystallinity, etc.) have been lost after conventional processing, that the effects were too small to measure, or that the effects manifest themselves under different circumstances (i.e., low cycle fatigue or oxidation, for instance).

Post-consolidation processing does have an effect on the microstructure and properties. Material which was directionally recrystallized (DR-ed) and heat treated subsequent to extrusion is slightly weaker than the as-extruded equiaxed material. The properties are shown in Figure 4. The equiaxed material has a mild $\langle 111 \rangle$ (high elastic modulus) texture with a mean γ' size of 380-400 nm. The grains in the DR'ed material are completely aligned in the high modulus orientation, the mean γ' size is much larger (500-600 nm), and it has no Pt_2Mo or DO_{22} type precipitates. In a precipitation-strengthened material, the increase in flow stress is a function of the size and distribution of the strengthening phase. In the DR'ed and the equiaxed materials, the effects of the variations in the modulus and the size and distribution of the strengthening precipitates almost offset one another such that the flow strength of the DR'ed material is only slightly weaker than that of the equiaxed material.

Equiaxed 185 exhibits a mid-range ductility minimum. This has been seen in other superalloys and has been attributed to a variety of mechanisms [7,8]. In this case, one additional possible explanation is strain localization and subsequent premature fracture. The strength of the alloy is seen to decrease only slightly from room temperature to 1400°F. However, γ' experiences a dramatic increase in strength in this range with a maximum around 1400°F [9]. Because the strength differential between the γ and γ' is greatest around 1400°F, the potential for strain localization is also the greatest. Indeed, strain localization at precipitate-free regions at the grain boundaries of precipitation-strengthened alloys has been documented as the mechanism for premature fracture in Al

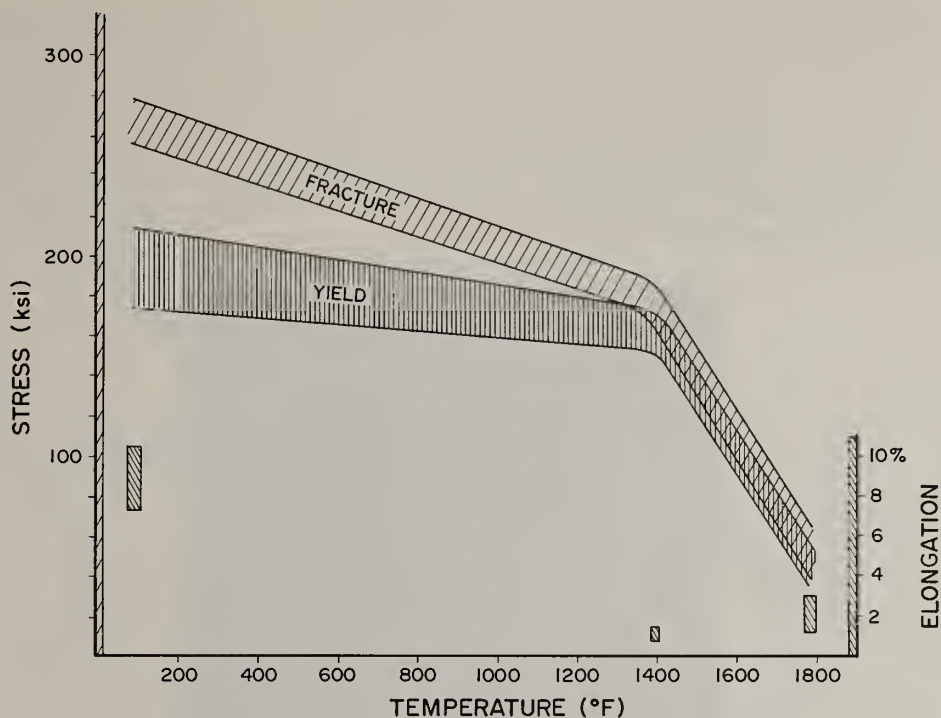


Figure 3. Tensile Properties of As-Extruded Material.

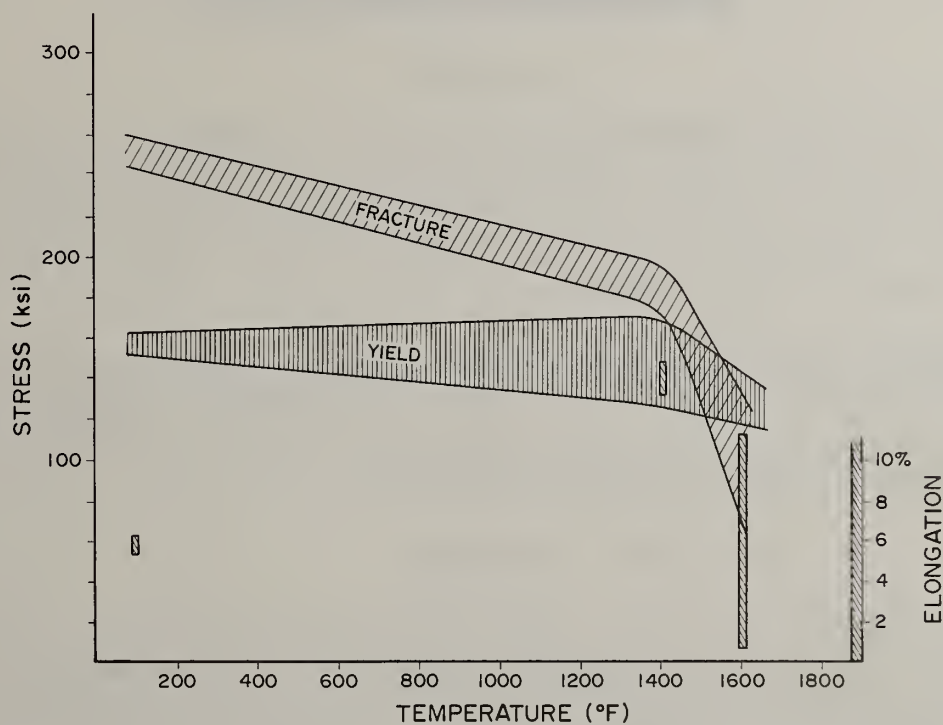


Figure 4. Tensile Properties of Directionally Recrystallized Material.

alloys and steel [10]. It should be noted that a ductility maximum is seen in the DR'ed material at 1400°F.

The microstructural response of the equiaxed alloy to an exposure of 1700°F for 250 hrs is shown in Figure 5. The most dramatic change is the occurrence of a discontinuous precipitation reaction at the grain boundaries, resulting in a drastic coarsening of both the γ and γ' phases. This coarsened region is up to 10 μm in width and represents a significant loss in material strengthened by fine γ'

precipitates. The matrix γ' is seen to coarsen somewhat from an average γ' size of 380-400 nm to 670-700 nm--often by "linking up" with adjacent particles of γ' . This is possible because the very fine Pt_2Mo and DO_{22} type precipitates previously residing in the regions between the γ' have gone into solution. The solution temperatures for these phases is between 1550-1650°F [11]. Therefore, at 1700°F, they solution rapidly, thus no longer providing a barrier to the γ' coarsening. The solutioning of the Pt_2Mo and DO_{22} type precipitates provides an excess of Mo in the matrix which precipitates as large, randomly distributed particles with various morphologies. These precipitates have been previously identified as α -Mo [12]. None of the high aspect ratio phases previously seen and tentatively identified as NiMo were seen in significant quantities. This has been attributed to variations in actual 185 composition [13].

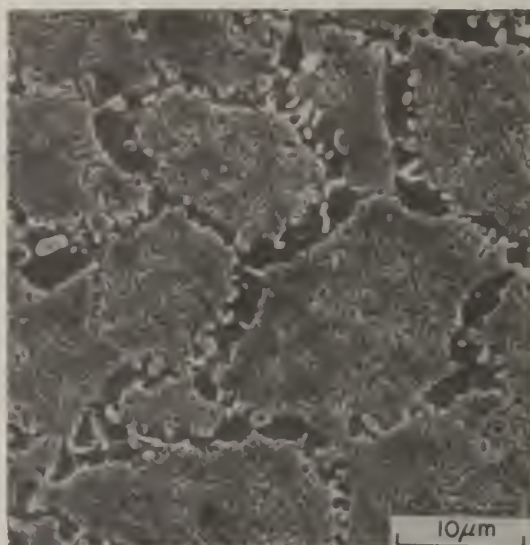


Figure 5. Microstructure After 1700°F/250 Hours.

The effect of the elevated temperature exposure on the tensile properties of Alloy 185 is shown in Figure 6. A drastic drop in yield, ultimate, and fracture stress levels was noted at room temperature and 1400°F, with little change in the material's behavior at 1800°F. A slight decrease in room temperature ductility was also observed. The strength degradation appears to result from many factors including, but not limited to, Ostwald ripening of the γ' and cellular coarsening at the grain boundaries. The overriding factor, however, may be the loss of precipitate strengthening by the very fine Pt_2Mo and DO_{22} type precipitates.

At 1800°F, the alloy exhibited the same level of strength, irrespective of its previous microstructural condition. It was observed, after testing at 1800°F, that the microstructures were now equivalent. Thus, during heat up, all material experienced the following: the loss of the very fine ordered precipitates and the subsequent precipitation of the excess Mo as α -Mo; the coarsening of phases at the grain boundaries due to a discontinuous reaction; and partial solutioning of the γ' particles, resulting in a mean size of approximately 430 nm.

Conclusions

From this investigation, no effect of cooling rate on the tensile properties of Alloy 185 was noted (after consolidation) for the range of powder particle sizes studied. The alloy exhibited a slight decrease in strength from room temperature to 1400°F and a sharp decrease between 1400°F and 1800°F. A mid-range ductility minimum was seen at 1400°F in the equiaxed material. A mid-range ductility maximum was seen at 1400°F in the directionally recrystallized material. A long-term exposure of 1700°F for 250 hours resulted in a significant degradation of the equiaxed tensile properties.

Acknowledgments

The authors are grateful to the Rapid Solidification Processing Group at the Government Products Division, Pratt & Whitney Aircraft Company, for supplying the material for this project and for directionally recrystallizing the needed bar stock. Mr. Attwell M. Adair, of our laboratory, is the Program Manager for the rapid solidification rate (RSR) research and development program.

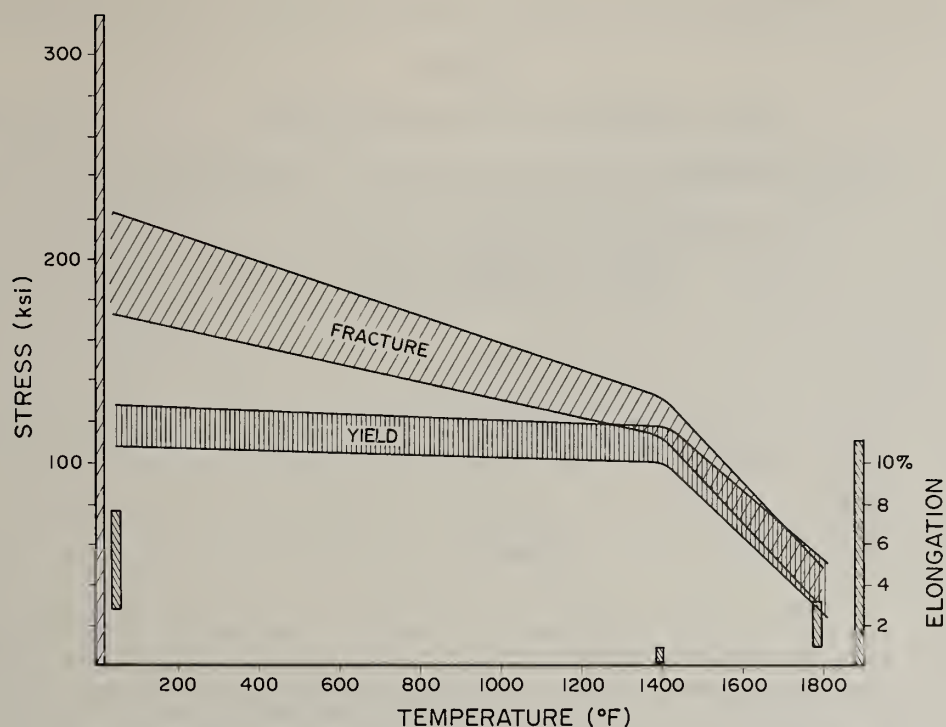


Figure 6. Tensile Properties After 1700°F/250 Hours.

References

- [1] M. R. Glickstein, R. J. Patterson II, and N. E. Schockey, Rapid Solidification Processing, p. 46, edited by R. Mehrabian, B. H. Kear, and M. Cohen, Claitor's, 1978.
- [2] C. M. Adam, R. G. Bourdeau, and J. W. Broch, Application of Rapidly Solidified Alloys, AFWAL-TR-81-4188, February 1982.
- [3] P. R. Holiday, A. R. Cox, and R. J. Patterson II, Rapid Solidification Processing, p. 246, edited by R. Mehrabian, B. H. Kear, and M. Cohen, Claitor's, 1978.
- [4] K. A. Williams, D. B. Miracle, and H. A. Lipsitt, Rapid Solidification Processing: Principles and Technologies, II, p. 129, edited by R. Mehrabian, B. H. Kear, and M. Cohen, Claitor's, 1980.
- [5] P. R. Holiday, A. R. Cox, and R. J. Patterson II, Rapid Solidification Processing, p. 246, edited by R. Mehrabian, B. H. Kear, and M. Cohen, Claitor's, 1978.
- [6] H. A. Lipsitt, D. Shechtman, and R. E. Schafrik, Met. Trans. A, **6A**, p. 1991, 1975.
- [7] D. A. Woodford, Met. Trans A, **12A**, p. 299, 1981.
- [8] D. A. Woodford and R. H. Bricknell, Superalloys 1980, p. 633, edited by J. K. Tien, S. T. Wlodek, H. Morrow III, M. Gell, and G. E. Maurer, ASM, 1980.
- [9] P. H. Thornton, R. G. Davies, and T. L. Johnston, Met. Trans, **1**, p. 207, 1970.
- [10] E. Hornbogen and H. Kreye, J. Mater. Sci., **17**, p. 979, 1982.
- [11] P. L. Martin and J. C. Williams, private communication.
- [12] P. L. Martin and J. C. Williams, private communication.
- [13] Unpublished research by High Temperature Materials Research Group, AFWAL Materials Laboratory.

TENSILE BEHAVIOR OF RSR IRON-ALUMINIDES

M. G. Mendiratta, S. K. Ehlers, and D. K. Chatterjee

Systems Research Laboratories, Inc.
2800 Indian Ripple Road
Dayton, OH 45440-3696

H. A. Lipsitt

AFWAL Materials Laboratory
Wright-Patterson Air Force Base, OH 45433

ABSTRACT

Ordered binary alloys in the composition range Fe-25 to -50 at% Al have been fabricated by blending and hot extruding prealloyed RSR powders. The tensile properties were determined from room temperature to 700°C. Alloys containing up to 40 Al were found to possess a good combination of room-temperature tensile strength and ductility. The stoichiometric FeAl underwent a brittle-to-ductile transition at ~450°C. In the DO₃ alloys, the strength decreased significantly with temperature, presumably due to the approaching DO₃ → B2 transformation in the vicinity of 540°C; however, the single-phase B2 alloys exhibited good strength retention at high temperature. The slip systems, dislocation configurations, and fracture modes have been determined. Deformation mechanisms governing the tensile flow and fracture behavior of these alloys are presented.

Introduction

Two ordered structures, one having DO₃ crystal lattice (based upon Fe₃Al composition) and the other the B2 crystal lattice (based upon FeAl), exist on the iron-rich side of the Fe-Al phase diagram. At room temperature, the DO₃ and B2 orders are maintained in the composition range ~ 23.8 to 34.8 Al and ~ 35 to 51 Al, respectively. These ordered alloys are considered to be highly oxidation-resistant [1,2]; and, therefore, have potential for high-temperature structural applications. A number of studies have been conducted to determine the slip systems in these materials [3-6]; however, very limited effort has been expended on the tensile behavior [7-9]. Although the operative slip of {110} <111> provides more than a sufficient number of independent systems for polycrystalline ductility, these materials are generally thought to be extremely brittle and difficult to fabricate. Previous studies on these ordered alloys have been carried out on materials prepared by conventional ingot-metallurgy techniques. In the present study, the tensile behavior of a number of powder-produced (P/M) alloys, covering a wide range of compositions from Fe-25 to -50 Al, has been investigated. The tensile flow and fracture properties of these P/M alloys were determined from room temperature to 700°C. In addition, extensive SEM fractography and thin-foil TEM were carried out in an attempt to understand the deformation mechanisms.

Experimental Procedures

Two lots consisting of spherical, prealloyed -140 mesh RSR powders (Pratt and Whitney) having compositions of Fe-25 and -50 Al were utilized to prepare alloys having nominal compositions of Fe-25, -35, -40, and -50 Al. The compositions Fe-35 and -40 Al were prepared by mechanical blending of appropriate quantities of the two powder lots. The Fe-25 Al powders were consolidated by hot extrusion at 900°C with an extrusion ratio of 16:1, while the Fe-35, -40 and -50 Al compositions were consolidated by hot-extrusion at 1000°C with the same extrusion ratio. The chemical analysis of the powder lots showed them to contain 0.03, 0.03, and 0.006 wt% carbon, oxygen, and nitrogen, respectively, and very small amounts of metallic impurities. The machined tensile specimens of all four alloys were subjected to a homogenization anneal of 900°/24 hr. The Fe-25 Al alloy was further heat treated at 500°C for 100 hr to produce a high degree of DO₃ order. The tensile tests were carried out in an Instron machine at a crosshead speed of 0.025 cm/min in air from room temperature to 700°C. For TEM, thin discs (~ 0.25-mm thick) were cut by precision low-speed diamond saws, mechanically ground to a thickness of ~ 0.125 mm, and electrolytically thinned utilizing the double-jet technique. The

electrolyte consisted of one part HNO_3 and two parts methyl alcohol by volume. The polishing was carried out at -40°C and 10 V. Fracture modes were examined by scanning electron fractography.

Results

Initial Microstructure

Metallographic examination of as-extruded-plus-heat-treated specimens of all the alloys revealed an equiaxed recrystallized grain structure with an average grain size of $\sim 50\ \mu\text{m}$ for Fe-25Al and $\sim 30\ \mu\text{m}$ for the remainder of the alloys. The prior powder-particle boundaries decorated by submicron-size impurity particles (presumably oxides, nitrides, or carbides) were also observed metallographically; however, in general, the recrystallized grain boundaries did not coincide with the prior powder boundaries. Electron-probe microanalysis carried out on several grains indicated that the blended alloys were homogeneous with regard to Al and Fe content. As observed by TEM, the $500^\circ\text{C}/100\ \text{hr}$ heat treatment produced in the Fe-25Al alloy thermal DO_3 -order domains (size $\sim 0.3\ \mu\text{m}$) having highly irregular boundaries. The size of the domains and the sharpness of the superlattice reflections in the electron-diffraction patterns indicated that a high degree of DO_3 order had been achieved. In contrast, electron-diffraction patterns in the Fe-35Al alloy showed sharp and intense superlattice reflections corresponding to the B2 order and extremely weak DO_3 reflections, indicating that this composition is in the B2 phase field very near the DO_3 -to-B2 boundary. TEM examination of Fe-40 and -50Al revealed the presence of the single-phase B2 order. In the three B2 alloys, no thermal anti-phase domain boundaries (APB) were observed, presumably due to the long-time homogenization at high temperature ($900^\circ\text{C}/24\ \text{hr}$).

Tensile Properties

Fe-25Al. Figure 1 shows the stress-strain ($\sigma - \epsilon$) curves for different test temperatures. At room temperature, this alloy exhibited a high yield strength, $\sigma_{0.2}$, of $\sim 103\ \text{ksi}$ and an elongation to fracture, ϵ_f , of 8%. It is apparent from the $\sigma - \epsilon$ diagrams that work-hardening rate increases with temperature up to 300°C , above which it decreases appreciably. The maximum ductility was exhibited at $\sim 540^\circ\text{C}$, above which it decreased slightly.

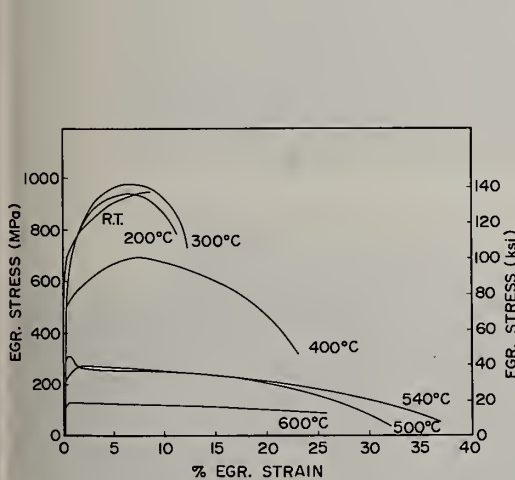


Fig. 1. Engineering stress-strain curves for different test temperatures for Fe-25Al.

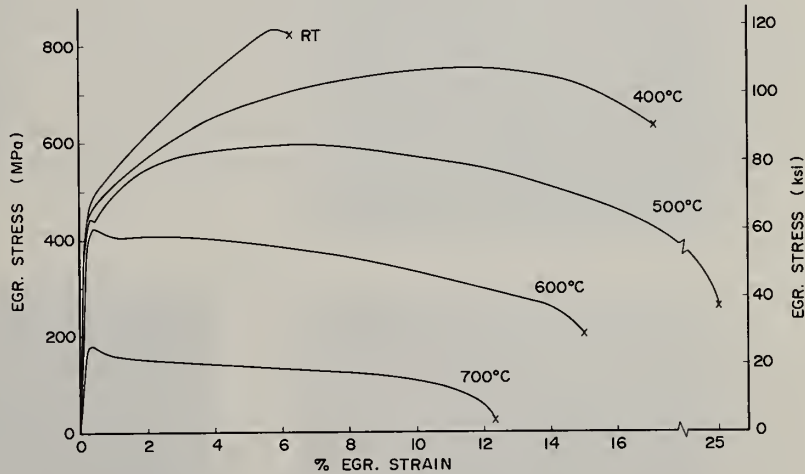


Fig. 2. Engineering stress-strain curves for different test temperatures for Fe-35Al.

Fe-35Al and -40Al. For Fe-35Al the $\sigma - \epsilon$ diagrams are given in Fig. 2. The $\sigma - \epsilon$ diagrams for Fe-40Al exhibited a similar trend to that for Fe-35Al and, hence, are not included here. At room temperature, $\sigma_{0.2}$ values of 70 and 92 ksi and ϵ_f values of 6 and 2.5% were obtained for Fe-35 and -40Al, respectively. Both alloys exhibited very high work-hardening rate at room temperature. Figure 3 shows the variation of $\sigma_{0.2}$, ϵ_f , and percent reduction in area, R.A., with test temperature for Fe-35Al. Up to 600°C , $\sigma_{0.2}$ decreases slowly with temperature; however, above this temperature it drops rapidly. A ductility maximum is observed at 500°C , above which both R. A. and ϵ_f decrease. A similar trend in the temperature dependence of $\sigma_{0.2}$, ϵ_f , and R.A. was also observed for Fe-40Al.

Fe-50 Al. Figure 4 shows the $\sigma - \epsilon$ curves for the stoichiometric FeAl. No ductility was observed up to 450°C; at this temperature the alloy exhibited some degree of plasticity. As in the case of Fe-35 and -40 Al, a maximum in ductility was exhibited at 500°C, above which the ductility decreased with temperature.

Figure 5 shows the variation of $\sigma_{0.2}$ with temperature for the four alloys investigated. For the Fe-25 Al alloy, a rapid drop in strength occurred above 200°C. However, in comparison, the Fe-35 and -40 Al alloys exhibited a significantly lower decrease in strength up to 600°C; at this temperature the yield strength was ~60 ksi, and above this temperature the strength decreased rapidly.

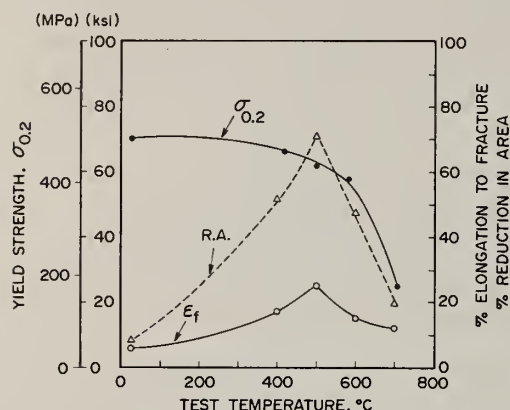


Fig. 3. Variation of yield strength, percent elongation to fracture, and percent reduction in area with temperature for Fe-35 Al.

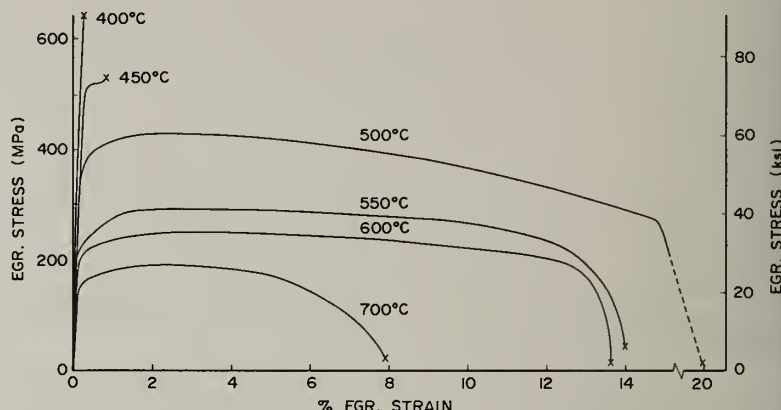


Fig. 4. Engineering stress-strain curves for different test temperatures for Fe-50 Al.

Fracture Modes

Fe-25, -35, and -40 Al alloys exhibiting ductility at room temperature fractured by the transgranular cleavage mode. The Fe-50 Al alloy with no ductility exhibited intergranular fracture. With increasing test temperature, increasing proportions of tearing and dimples were observed; and at 500°C, where a maximum in ductility occurred, the fracture surfaces consisted of a mixture of large and small transgranular dimples. With increasing test temperatures, a decrease in ductility was observed, and the fracture mode consisted of an increasing proportion of grain-boundary facets containing small cavities. Examples of this transition in fracture mode are given in Figs. 6(a) and 6(b) which show the room-temperature cleavage and high-temperature intergranular-cavity fracture for Fe-35 Al.

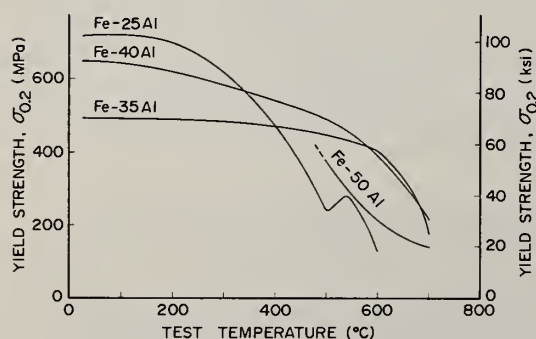


Fig. 5. Variation of yield strength with temperature for Fe-25, -35, -40 and -50 Al alloys.

Deformation Structures

Previous studies on single-crystal and polycrystal D_{03} and B2 Fe-Al alloys [3-6,10] have shown that at room temperature, the slip direction is $\langle 111 \rangle$. Slip occurs in the $\langle 111 \rangle$ direction either by

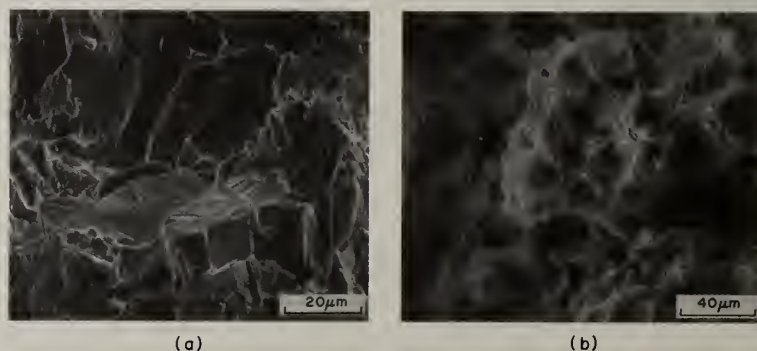
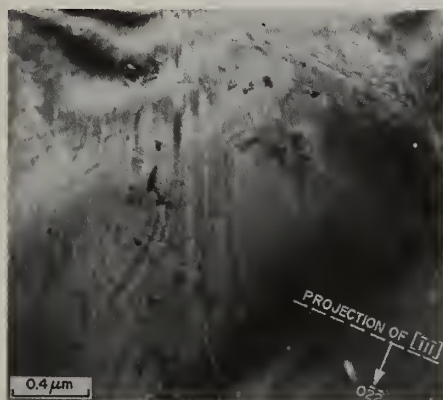


Fig. 6. Fracture-mode transition in Fe-35 Al a) transgranular cleavage at room temperature, b) intergranular cavities at 600°C.

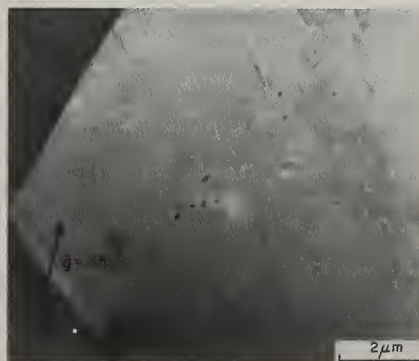
the movement of perfect superlattice dislocations or by their dissociation to produce APB trails. In the DO_3 lattice, the superlattice dislocations consist of four ordinary $a'/4 \langle 111 \rangle$ dislocations separated by nearest-neighbor (NN) and next-nearest-neighbor (NNN) APBs. a' is the lattice parameter of the DO_3 unit cell and is twice the length of that for the disordered BCC lattice. In the B2 lattice, the superlattice dislocation consists of two ordinary $a/2 \langle 111 \rangle$ dislocations separated by NNAPB. The ease or difficulty of glide of these superlattice dislocations and their imperfect variants governs the flow and fracture behavior in these alloys. Specific TEM contrast and diffraction conditions required to characterize these features have been reviewed by Marcinkowski [11]; and, in the present study, the same procedures have been followed.

Fe-25 Al. The room-temperature deformation in the Fe-25 Al alloy was accomplished by the movement of ordinary dislocations and the formation of NN and NNNAPBs; no coupled dislocations were observed in any grains. Figure 7(a) is a bright-field electron micrograph showing the $a'/4 \langle 111 \rangle$ ordinary screw dislocations; the general motion of these dislocations through the grain is indicated by the slip traces left behind. As can be seen, the slip traces are highly curved with a significant angular spread, indicating that the glide dislocations have cross-slipped extensively during deformation. The movement of the ordinary dislocations produces APB bands is shown in Fig. 7(b), which is a dark-field micrograph taken with the superlattice reflection (200). At 200 and 300°C, where higher work hardening was observed, TEM examination revealed the presence of coupled superlattice dislocations in a number of grains.

Fe-35 and -40 Al. For these alloys, room-temperature deformation occurred by movement of superlattice dislocations of the $a/2 \langle 111 \rangle$ Burgers vector, as can be seen in the electron micrographs of Figs. 8(a) and 8(b). Numerous paired dislocations can be observed; that these were superlattice



(b)



(b)

Fig. 7. TEM micrographs showing room-temperature deformation substructures in Fe-25 Al
a) bright-field micrograph showing cross-slip of ordinary dislocations, b) dark-field micrograph showing slip-induced NNAPBs.

Fig. 8. TEM micrographs showing superlattice dislocations in Fe-35 Al deformed at room temperature a) bright field, b) weak-beam dark field ($g/3g$).

dislocations was deduced from the constancy of the separation distance of the component dislocations under the g^+ and g^- diffraction conditions. Figure 8(b) is a weak-beam dark-field micrograph from which the separation distance of the dislocations in the screw orientation for the Fe-35 Al alloy was measured to be $\sim 50 \text{ \AA}$, which is in agreement with the value obtained by Ray, *et al.* [12]. Dark-field examination utilizing superlattice reflections $\{100\}$ did not reveal unambiguously the formation of slip-produced APBs. At all temperatures up to 700°C , the Burgers vector was found to be $\langle 111 \rangle$.

Fe-50 Al. At room temperature, slip occurred predominantly in uniformly distributed planar bands, Fig. 9(a). The standard $\bar{g} \cdot b = 0$ analysis revealed that most of the dislocations had a Burgers vector $\langle 111 \rangle$ and were in screw orientation. It was not possible to resolve the components of the superlattice dislocations by weak-beam dark-field observation, most probably due to the high APB energy of this alloy. Although the predominant slip direction was $\langle 111 \rangle$, a few dislocations of the $\langle 100 \rangle$ type were also observed. In contrast, at 500°C the predominant slip direction was found to be $\langle 100 \rangle$, with a few dislocations being of the $\langle 111 \rangle$ type. Figure 9(b) shows the 500°C dislocation structure, with $\langle 100 \rangle$ dislocations mainly in the edge orientation. Numerous loops and dipoles, characteristic of thermally assisted deformation, were also observed.

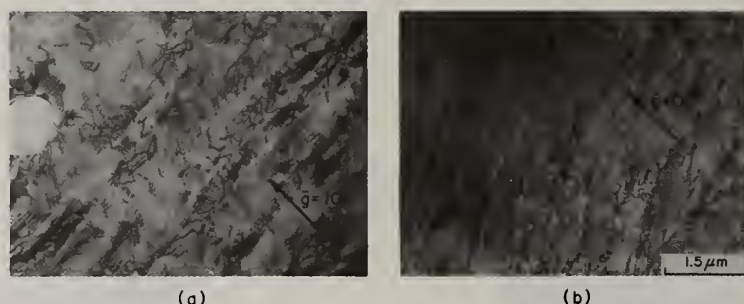


Fig. 9. Bright-field electron micrographs showing dislocation structures in Fe-50 Al a) specimen deformed at room temperature, b) specimen deformed at 500°C .

Discussion

Room-Temperature Flow and Ductility

The room-temperature ductility of the iron-aluminides from Fe-25 to -40 Al is due to the ability of the $\langle 111 \rangle$ dislocations to move freely. For the Fe-25 Al alloy, the values of NNAPB and NNNAPB energies (77 and 85 ergs/cm², respectively) are relatively low [12] and the nucleation of superlattice dislocations is difficult [13-15]; therefore, in this alloy the ordinary dislocations which create APB faults move and cross-slip freely. Such dislocation character is responsible for the observed parabolic low work hardening and a reasonably high ductility. Also, since the applied stress must overcome APB energies, the observed yield strength is quite high.

With increasing Al content in the B2 alloys, the NNAPB energy increases [12], and the nucleation of superlattice dislocations is energetically favored [14-15]. Thus, in Fe-35 and -40 Al alloys numerous paired dislocations and no slip-produced APBs were observed. The motion of superlattice dislocations produces very high work hardening presumably due to the Taylor-type locking of superlattice dislocations on neighboring parallel slip planes [16] and to the production of APB tubes at jogs [3,17]. Also, the equilibrium separation distance between the superlattice dislocations is sufficiently large ($\sim 50 \text{ \AA}$) to prevent easy cross-slip. These factors combine to decrease the ductility of these alloys with increasing Al content, although an increase in yield strength was observed.

Extrapolation of the $\sigma_{0.2}$ curve for the Fe-50 Al (Fig. 5) to room-temperature indicates that the alloy would have yielded at room temperature at a stress of $\sim 180 \text{ ksi}$. This value should be considered in the context of the reported value of critical resolved shear stress (CRSS) of $\sim 68 \text{ ksi}$ for dominant $\langle 111 \rangle$ $\{110\}$ slip [4]. This CRSS value is extremely high. Thus, the observed lack of ductility in the Fe-50 Al alloy at room temperature may be due to the yield strength exceeding the fracture strength, thereby causing premature fracture.

High-Temperature Properties

The yield strength drops rapidly in the Fe-25 Al alloy with temperature; while in the Fe-35 and

-40 Al alloys, the strength decrease is significantly more gradual (Fig. 5). The Fe-25 Al alloy undergoes a second-order $DO_3 \rightarrow B2$ phase transformation at a low temperature of 540°C; the approach to this transformation is thought to be responsible for the rapid drop in high-temperature strength. In contrast, the Fe-35 and -40 Al alloys are thought to be fully ordered up to their melting temperatures, thus exhibiting a less severe strength drop with temperature.

All iron-aluminides investigated exhibited a loss of ductility with increasing temperature above 600°C (e.g., Fig. 3). This loss of ductility was accompanied by a transition in fracture mode from transgranular-dimple formation to intergranular-cavity formation. Further experiments involving varying strain-rate tensile tests [18] have shown that this loss of ductility is both stress and diffusion enhanced. Generally the intergranular cavities form in engineering alloys which are subjected to creep deformation; during the creep process the impurities segregate to the grain boundaries and aid in cavity nucleation. In the present case the strain rate was significantly higher than that generally occurring during creep deformation; however, diffusion of some impurity species may be sufficiently rapid. The observed loss of ductility in the iron-aluminides indicates the presence of an instability which may have important engineering implications.

Conclusions

1. The RSR Fe-25 to -40 Al alloys are ductile at room temperature. Maximum ductility and yield strength are exhibited by Fe-25 Al. Ductility decreases with increasing Al content.

2. In Fe-25 Al, the room-temperature plastic flow is governed by the movement and cross-slip of ordinary dislocations creating APB bands. In contrast, with increasing Al content, the plastic flow occurs by the movement of superlattice dislocations.

3. The Fe-50 Al alloy is totally brittle at room temperature and exhibits a brittle-to-ductile transition at ~ 450°C.

4. The yield strength of the Fe-25 Al alloy drops rapidly with temperature, presumably due to the $DO_3 \rightarrow B2$ transformation at a low temperature of 540°C. In contrast, the Fe-35 and -40 Al alloys, showing no transformation, are reasonably strong up to 600°C ($\sigma_{0.2} = 60$ ksi).

5. All the alloys studied exhibited a high-temperature ductility loss and associated intergranular cavity fracture mode.

References

- [1] C. Sykes and J. W. Bampfylde, J. Iron Steel Inst. 130 (II), 389 (1934).
- [2] E. R. Morgan and V. F. Zackay, Met. Prog. 68, 129 (1955).
- [3] R. C. Crawford, Phil. Mag. 33, 529 (1976).
- [4] T. Yamagata and H. Yoshida, Mater. Sci. Eng. 12, 95 (1973).
- [5] Y. Umakoshi and M. Yamaguchi, Phil. Mag. A 41, 537 (1980).
- [6] Y. Umakoshi and M. Yamaguchi, Phil. Mag. A 44, 711 (1981).
- [7] G. P. Rauscher, Jr., F. C. Perkins, and J. F. Nachman, "Study of Factors Influencing Ductility of Iron-Aluminum Alloys," Technical Report under Contract AT(11-1)742 (U.S. Atomic Energy Commission, University of Denver, Denver, CO, 1961).
- [8] M. J. Marcinkowski, M. E. Taylor and F. X. Kayser, J. Mater. Sci. 10, 406 (1975).
- [9] G. Sainfort, P. Mouturat, P. Pepin, J. Petit, G. Cabane, and M. Salesse, Memoires Scientifiques Rev. Metallurg., LX 2, 125 (1963).
- [10] M. J. Marcinkowski and N. Brown, Acta Met. 9, 764 (1961).
- [11] M. J. Marcinkowski "Theory and Direct Observation of Antiphase Boundaries and Dislocations in Superlattices," in Electron Microscopy and Strength of Crystals (G. Thomas and J. Washburn, Eds.) (Interscience Publishers, N.Y., 1963), p. 333.
- [12] I. L. Ray, R. C. Crawford, and D. J. H. Cockayne, Phil. Mag. 21, 1027 (1970).
- [13] H. J. Leamy and F. X. Kayser, Phys. Stat. Sol. 34, 765 (1969).
- [14] H. J. Leamy, F. X. Kayser, and M. J. Marcinkowski, Phil. Mag. 20, 763 (1969).
- [15] H. J. Leamy, F. X. Kayser, and M. J. Marcinkowski, Phil Mag 20, 779 (1969).
- [16] M. J. Marcinkowski and G. Lakso, J. Appl. Phys. 38, 2124 (1967).
- [17] C. T. Chou, and P. B. Hirsch, Iss. Electron Microsc. Anal., 459 (1981).
- [18] M. G. Mendiratta, Systems Research Laboratories, Inc., Dayton, OH, work in progress under Air Force Contract F33615-81-C-5059.

MICROSTRUCTURE AND MECHANICAL PROPERTIES
OF RAPIDLY-SOLIDIFIED WHITE-CAST IRON POWDERS

Lawrence E. Eiselstein^{*}, Oscar A. Ruano^{**}
Oleg D. Sherby^{***}, and Jeffrey Wadsworth^{****}

^{*}Metallurgy Group, Poulter Laboratories, S.R.I.
International, Menlo Park, California 94025

^{**}Centro Nacional de Investigaciones-Metalurgica,
Av. de Gregoria del Amo, S/N, Madrid-3, Spain

^{***}Department of Materials Science and Engineering
Stanford University, Stanford, California 94305

^{****}Metallurgy Department, Lockheed Research Laboratory
Palo Alto, California 94304

ABSTRACT

Rapidly solidified white cast iron powders containing 2.4 and 3.0%C, as well as a 3.0%C alloy containing 1.5%Cr, were investigated. The as-quenched microstructures of these white cast iron powders consist of retained austenite, cementite, and a small fraction of martensite. Upon heating to 600°C the microstructure changes to a mixture of fine cementite ($\approx 1 \mu\text{m}$ diam.) and ferrite of grain size 1 to 3 μm .

It is shown that densification of compacts of the white cast iron powders can be enhanced by multiple phase transformations through thermal cycling. This transformation warm pressing at intermediate temperatures leads to dense compacts at low pressures and short times. Because the transformation temperature is low, ultrafine structures are found in the densified compacts.

The influence of these fine microstructures on the mechanical properties of the white cast irons was determined at intermediate and room temperatures by tension and compression tests. The white cast irons were found to be superplastic in the temperature range of 630–725°C. Maximum tension elongations of 1410% were found for the 3.0%C + 1.5%Cr material, 940% for the 3.0%C material, and 480% for the 2.4%C material (in all cases tested at 700°C at a strain rate of 1% per minute). Negligible cavitation was noted during superplastic deformation of these white cast irons. Under superplastic conditions, the white cast irons exhibited a high strain rate sensitivity exponent $m = 0.5$ and activation energies for plastic flow nearly equal to the activation energy for grain boundary diffusion. These values are in agreement with models for superplasticity based on grain boundary sliding accommodated by slip mechanisms adjacent to the grain boundary. Room temperature compression tests of the white cast irons revealed large strain-to-failure values in the order of $\epsilon = 0.25$. In tension tests, a ductility of over 7% was obtained in rapidly solidified 3.0%C white cast iron at room temperature in contrast to nil ductility for the as-cast material.

INTRODUCTION

Powders with a very fine microstructure can be obtained by the rapid solidification rate (RSR) process which makes use of advanced jet technology for their production [1]. Such fine microstructures are very attractive because of the potentially beneficial properties they can show in industrial applications. For such applications, however, the densified compacts must retain the fine microstructure of the individual powders. For this reason, the compacting methods should avoid coarsening of the microstructure.

In the present investigation, the microstructures and the annealing behavior of ferrous powders

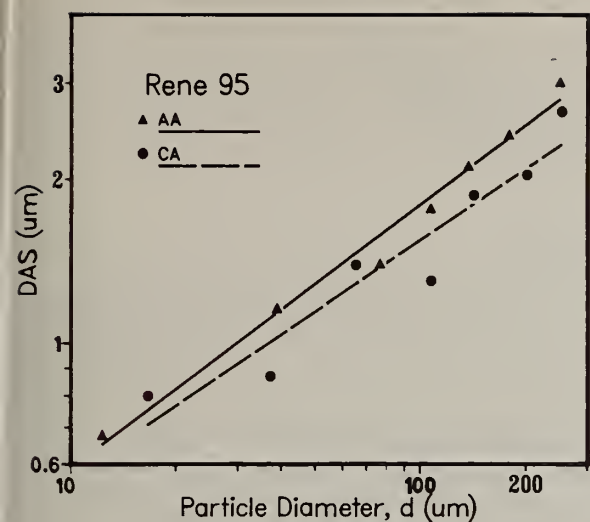


Figure 2. DAS vs. particle size. CA particles have smaller dendrites than AA particles, but both are in same order of magnitude.

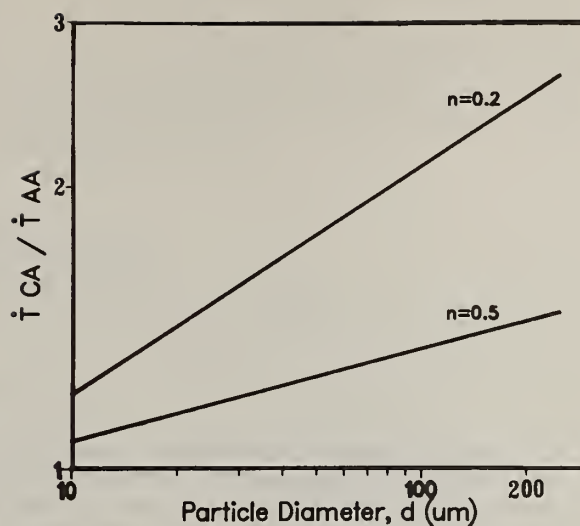


Figure 3. Relative cooling rate vs. particle size for reported extremes of the coefficient n used to calculate \dot{T} .

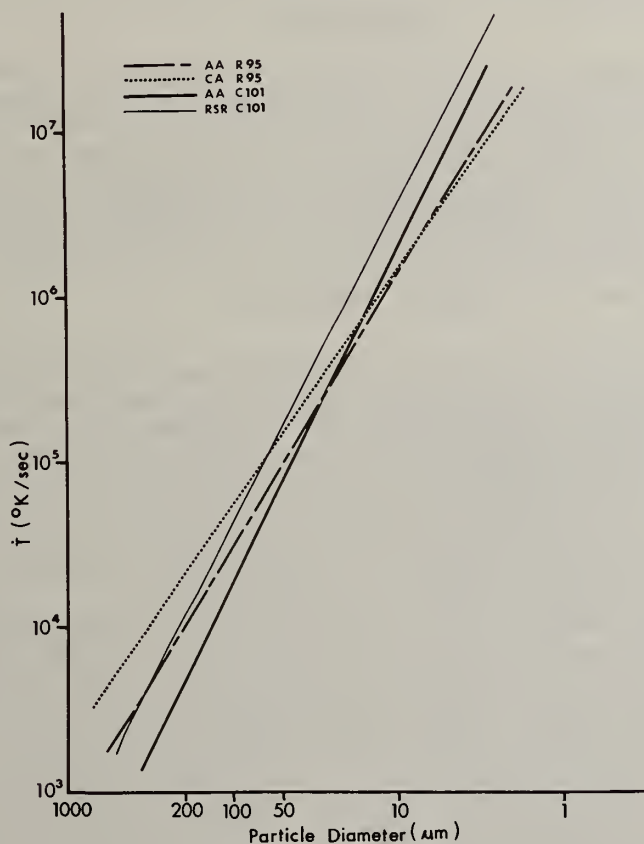


Figure 4. Approximate cooling rates vs. particle size. AA and CA R-95 are contrasted with AA and RSR C-101. (5)

RAPID SOLIDIFICATION STUDIES OF Ni₃Al ALLOYS*

C. C. Koch, J. A. Horton, C. T. Liu,
O. B. Cavin, and J. O. Scarbrough

Metals and Ceramics Division
Oak Ridge National Laboratory
Oak Ridge, Tennessee 37830

ABSTRACT

Rapidly solidified foils of Ni₃Al (24 at. % Al) with and without additions of boron (500 and 1000 ppm by weight) were prepared in an arc-hammer apparatus. The bend ductility, microhardness, and microstructure of the foils were studied as a function of solidification rate, which was defined by foil thickness. Boron-free Ni₃Al samples exhibited brittle behavior over the entire range of solidification rates used (foil thicknesses 20 to 100 μm). However, boron-containing samples, which were ductile for foil thicknesses greater than 45 μm showed a transition-to-brittle behavior in the range of thickness of 30 to 45 μm . The high hardness of the rapidly quenched foils (450 DPN) remained approximately constant in this transition range. Electron microscopy revealed a complex anti-phase boundary (APB) structure that could not be correlated to the mechanical behavior. The suppression of the beneficial boron segregation to grain boundaries is believed to be responsible for the ductile-to-brittle transition on increasing solidification rate.

Introduction

Intermetallic compounds, such as the iron or nickel aluminides (e.g., Ni₃Al, NiAl, Fe₃Al, FeAl), have unique properties that make them potential structural materials for elevated temperature applications. The ordered crystal structures in these materials reduce the atomic mobility at elevated temperatures resulting in good strength, stability, and creep resistance. Unlike conventional alloys, the static strength of many aluminides shows an increase rather than a decrease with increasing test temperatures [1,2]. The presence of aluminum provides an oxidation resistant Al₂O₃ film. However, the major problem with using aluminides as structural materials is their low ductility and brittle fracture [1,3], particularly at low temperatures. Because of poor fabricability and low-fracture toughness, the aluminides have not been considered as serious candidates for structural applications.

The nickel aluminide, Ni₃Al (γ'), is an important strengthening constituent of nickel-base superalloys. While single crystals of Ni₃Al (which has the L1₂ structure) exhibit extensive ductility [4], polycrystalline forms are extremely brittle, suggesting grain boundary embrittlement. The intergranular fracture observed supports the idea that weak grain boundaries — either due to their structure or impurity segregation — cause brittle fracture with little plastic deformation in the grains. While there has been research aimed at improving the ductility of intermetallic compounds like Ni₃Al for over 20 years, only recently has there been significant success in this area. Two approaches to this problem have provided solutions: (1) rapid solidification processing, and (2) microalloying. Rapid solidification processing of Fe₃Al (30 at. % Al) powders has provided fine-grained homogeneous alloys which exhibit useful ductility (5–8% elongation at room temperature) [5]. Recently, Inoue et al. [6] have reported improvements in ductility and strength of L1₂ compounds in Ni-Al-X (X = Cr, Mn, Fe, Co, or Si) alloys by rapid solidification using the melt-spinning technique. Elongations of 4 to 27% were achieved. It was suggested that this improvement in ductility was due to rapid solidification producing a lower degree of long-range-order, fine-grain-structure, and suppressing-grain-boundary segregation. Microalloying — the addition of small quantities of an element (<1%) for controlling the chemistry and cohesion of grain boundaries — has been found to dramatically ductilize Ni₃Al. Aoki and Izumi [7] first discovered that boron additions of 500 and 1000 ppm by weight imparted room temperature ductilities of 35%. Liu and Koch [8] later found that boron concentrations of 250 to 1000 ppm along with control of the thermal-mechanical treatment produced ductilities of greater than 50% elongation.

*Research sponsored by the Division of Materials Sciences, U.S. Department of Energy under contract W-7405-eng-26 with the Union Carbide Corporation.

As part of the goal of our present research program to understand the effects of boron on the mechanical behavior of Ni₃Al, we have prepared a series of Ni₃Al samples, with and without boron additions, by rapid solidification in an arc-hammer apparatus. We report here preliminary results of the ductility, hardness, and microstructure of these Ni₃Al alloys as a function of quench rate. Since boron diffusion to the grain boundaries must be necessary to provide its beneficial effects, this experiment was designed to see whether suppressing the segregation of boron would prevent its ductilizing effect and thus provide information on the mechanism responsible.

Experimental

Samples from the previous study [8] of Ni-24 at. % Al (referred to as Ni₃Al in this paper) containing 0, 500, or 1000 ppm of boron were cut into small pieces for rapid solidification in the arc-hammer apparatus. The solidification rate in the arc hammer is a function of hammer velocity, mass of the liquid alloy, as well as melt superheat. A model of the arc hammer [9] has provided estimates of solidification rates of 10⁶ to 10⁷ degrees per second for metallic glass foils typically 20 to 40 μ m thick. In this paper we shall use foil thickness as a measure of solidification/quench rate. The foils produced in the arc hammer for different hammer speeds and alloy masses were typically 1.5 to 3.0 cm in diameter by 20 to 100 μ m thick. The structure of the foils was determined by x-ray diffraction on a Philips automated diffractometer using copper K α x-radiation. The integrated intensity of pairs of fundamental and superlattice lines (200:100 and 220:110) were measured in an attempt to extract the long-range-order parameter, S.

The bend ductilities of rectangular strips cut from the foils were obtained by bending around progressively smaller cylinders until cracking and then fracture occurred. The fracture strain, ϵ^f , was calculated by

$$\epsilon^f = t/(2r + t) ,$$

where r = radius of the cylinder and t = thickness of the foil. The foil thicknesses were measured between the conical points of a dial gauge equipped with a slip clutch and accurate to about 1 to 2 μ m. If a foil could be bent 180° on itself so that r \approx 0, $\epsilon^f \approx$ 1, the material is considered to be quite ductile.

Microhardness measurements were made on the foils in a Wolpert-Griess hardness tester with a Vickers diamond indenter and a load of 100 g.

Approximately 3-mm-diam disks were cut from the foils and thinned electrolytically for examination by transmission electron microscopy. The thinned foils were examined in an analytical electron microscope, Philips EM 400T equipped with a field-emission gun.

Experimental Results

The crystal structure of all the rapidly solidified foils was found to be the ordered L1₂-type by both x-ray and electron diffraction. Well defined superlattice reflections were observed. X-ray diffraction and electron diffraction revealed a high degree of preferred orientation in the quenched foils with a (100) type texture. This preferred orientation prevented a straightforward determination of the long-range-order parameter, S, by the conventional technique [10]. However, Starke et al. [11] have developed a procedure for extracting S in heavily textured Cu₃Au (L1₂ structure). We are presently employing this procedure in our work and the results will be reported elsewhere. In any case, it was observed that even the fastest quench rates used in this study could not suppress the ordered-crystal structure which contains a substantial degree of long-range order.

The results of the bend tests are presented in Fig. 1 as a plot of fracture strain versus sample thickness; sample thickness being inversely related to quenching rate. Data for Ni₃Al samples which do not contain boron (represented by open circles) all exhibit brittle behavior with values of fracture strain less than 0.01. Conversely, Ni₃Al samples containing 500 and 1000 ppm of boron show completely ductile behavior for sample thicknesses greater than approximately 50 μ m. The foils can be bent 180° on themselves giving values for the defined fracture strain of one. However, for sample thicknesses between about 30 to 45 μ m, that is for faster quenching rates, a marked change in ductility is observed. Over this range of sample thickness (quenching rate) the fracture strain drops dramatically from $\epsilon^f = 1$ to $\epsilon^f < 0.01$. Within this transition range, ductile and brittle behavior was often observed within a given specimen. Cracks were seen to form from the edge of the bent specimen at very low strains (<0.01) but then stop. The specimen could then continue to be bent back upon itself. Parts of several samples which exhibited brittle fracture behavior could be bent 180° on themselves. The brittle fracture behavior appeared to be intergranular in nature. A scanning electron micrograph of the fractured surface of a 26- μ m-thick specimen containing 1000 ppm boron,

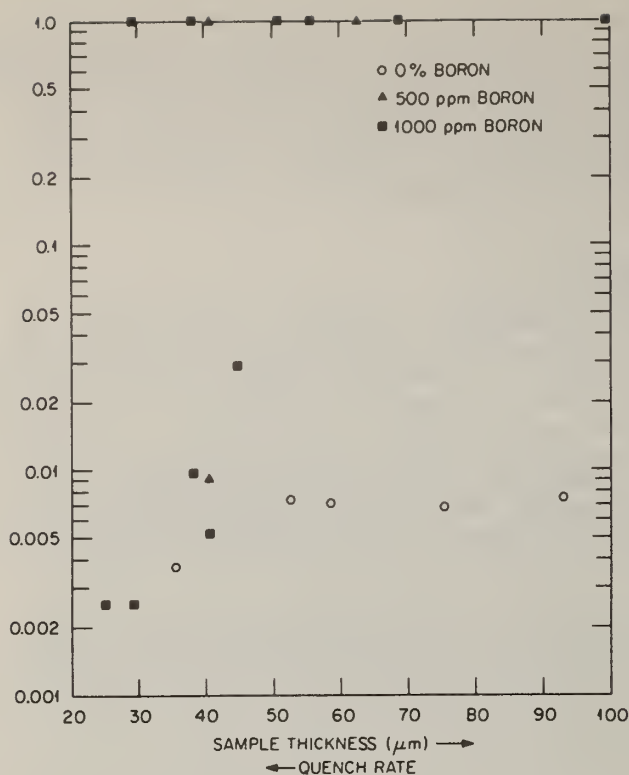


Fig. 1. Bend fracture strain, ϵ^f versus sample thickness. Boron-doped specimens showed a ductile-to-brittle transition around a thickness of 45 μm . All the specimens without boron additions exhibited brittle behavior.

presented in Fig. 2, indicates the grain boundary separation. Auger electron spectroscopy studies are in progress to define more precisely the nature of the grain boundary fracture.

Microhardness is plotted against specimen thickness (inverse quench rate) in Fig. 3. The bars on the data points represent plus or minus twice the standard deviation of at least ten measurements. The hardness of rapidly quenched specimens (thickness $\leq 60 \mu\text{m}$) is approximately 450 DPN. This magnitude has been obtained for heavily cold-rolled single crystals of Ni_3Al [12] and cold-rolled polycrystalline Ni_3Al containing boron additions [13]. The hardness decreases with specimen thickness, that is, with slower cooling rates. A 45- μm -thick foil was subsequently annealed at 1000°C for 15 min. The hardness dropped from 440 DPN to a value of about 240 DPN, comparable to the values for annealed, bulk Ni_3Al . It should be noted that the transition range of specimen thickness from

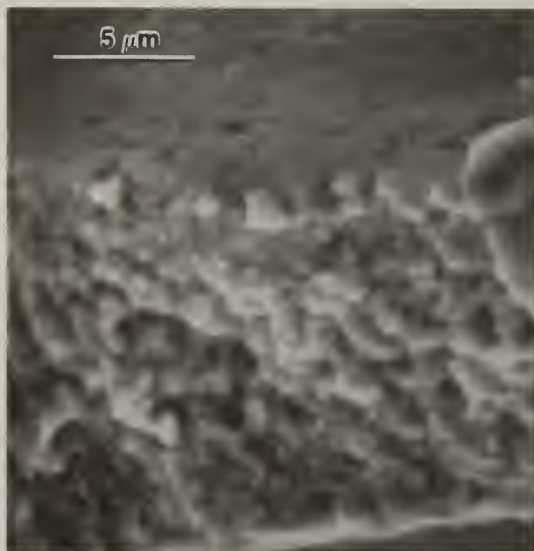


Fig. 2. Scanning electron micrograph of a brittle fracture surface of Ni_3Al containing 1000 ppm boron.

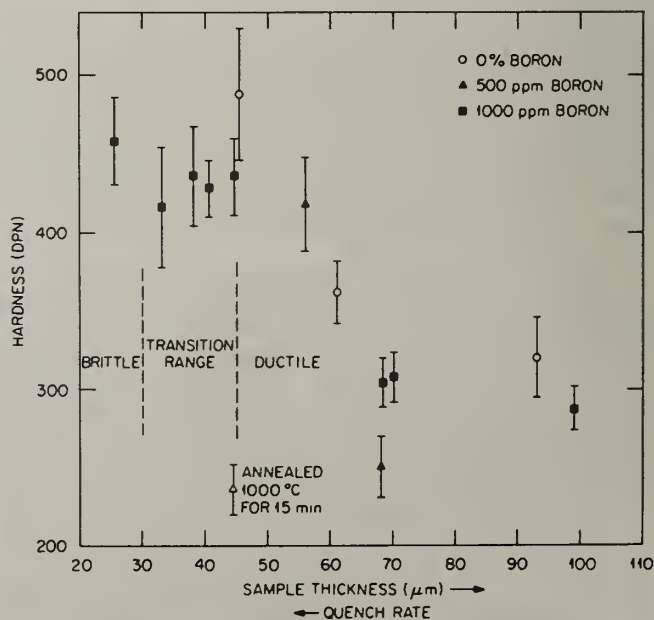


Fig. 3. Hardness versus sample thickness.

ductile-to-brittle behavior lies within the region where the hardness is essentially constant. Likewise, no obvious differences in hardness can be observed as a function of boron concentration. Thus, it would appear that the hardness of the rapidly quenched Ni_3Al samples is mainly affected by the bulk structure, over which boron concentration has little influence. However, the bend ductility is expected to be controlled by grain boundary properties, which are dramatically altered by the presence of boron.

The microstructures of the rapidly solidified Ni_3Al samples as revealed by transmission electron microscopy have the following features. The average grain diameters of the specimens varied from about 1.0 to 3.5 μm as measured by the linear intercept method. The more rapidly quenched specimens have the smaller grain size. For example, for Ni_3Al samples containing 1000 ppm B, a specimen 50 μm thick had an average grain size of 0.70 μm compared to a specimen 90 μm thick with an average grain size of 3.4 μm . There was no obvious dependence of grain size on boron concentration. The above grain sizes are for the center of the specimen cross sections. The grain size on the specimen surface of the 50 μm thick, 1000-ppm B specimen ranged between 0.25 and 0.50 μm which was about one-fourth to one-half the size of the grains in the center. This morphology of larger, textured grains in the bulk, and smaller grains on the surface of alloys solidified in the arc hammer has been observed previously [14] for $(\text{Fe},\text{Co})_3\text{V}$ alloys with the L1_2 structure. The main features within the grains are dislocations and APBs. The dislocation density is in general very low, some grains being completely free of dislocations. The APBs are readily observed in rapidly quenched Ni_3Al , as already noted by Inoue et al. [6] but in contrast to conventionally prepared material [15] in which APBs are rarely observed. In Fig. 4 a bright-field micrograph typical of the APB structure observed in the smaller grains is given. Curved APBs surrounding small domains are seen in the center of the grain, while straighter APBs, approximately normal to the grain boundary, separate larger domains. In the larger grains the APB structure illustrated in Fig. 5 is often observed. In this case there are several regions within the grain of the small curved APBs surrounded by larger domains, which are now not confined to the edge of the grains. The domain size was measured by the linear-intercept method with the number of intercepts increased by one third to account for the out-of-contrast APBs for micrographs made with $\langle 200 \rangle$ and $\langle 220 \rangle$ diffraction vectors. The domain size (small domains) for the boron-containing specimens is about 50 nm in diameter, essentially independent of solidification rate, while for the boron-free samples domain diameters of about 80 nm are observed. The domain size at the surface where the grains were smaller was approximately the same as in the center of the specimen. The tentative conclusion is that boron has reduced the diameter of the small domains by 30 to 40%. Annealing at 1000°C for 15 min increased the average grain diameter to 6.5 μm and removed all the



Fig. 4. Bright-field electron micrograph of a Ni_3Al sample containing 1000-ppm B; the APB structure in small grain. Foil normal and electron-beam direction near $[114]$.

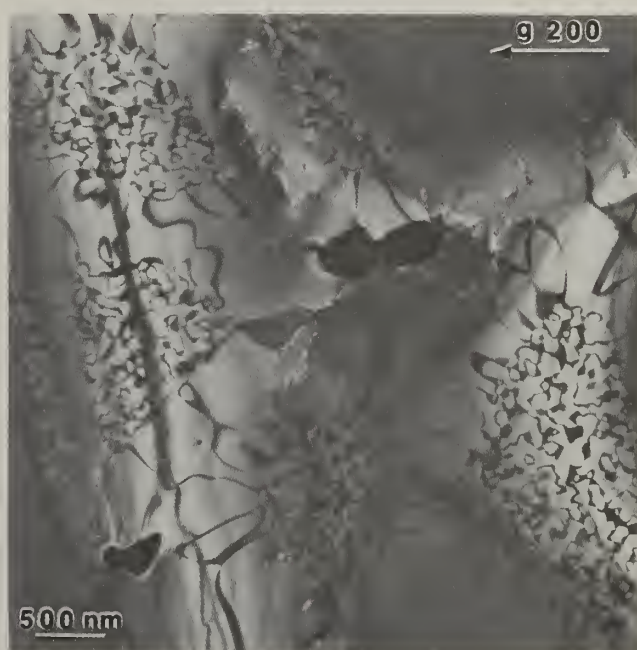


Fig. 5. Dark-field electron micrograph on the $[100]$ superlattice reflection of a Ni_3Al sample containing 1000-ppm B; the APB structure in large grain. Foil normal and electron-beam direction near $[001]$.

Discussion

While more research is required to clarify several of the experimental observations made in this preliminary study, some tentative explanations of the results can be given.

A simple rationalization of the solidification rate dependence of the ductile-brittle transition in boron-containing samples is that at sufficiently fast cooling rates the beneficial segregation of boron is suppressed leaving the grain boundaries brittle. If this explanation should hold, it implies that (1) harmful impurity elements (such as sulfur) can segregate to the grain boundaries faster than can boron, or (2) impurity segregation is not responsible for the weakness of grain boundaries in Ni_3Al but the weakness is an inherent property of the grain boundary structure. Clearly, experimental verification of this suggestion by, for example, Auger spectroscopy is needed.

Rapid solidification by the arc-hammer process has not increased the ductility of boron-free Ni_3Al in contrast to the melt-spinning study of Inoue et al. [6] on Ni-Al-X ($X = \text{Cr, Mn, Fe, Co, or Si}$) L_{12} materials. Their explanation for the ductilizing effects of rapid solidification is based on prevention of segregation to the grain boundaries and small domain size effects. They reported their grain sizes to range from 2 to 5 μm . Their domain sizes as measured from Fig. 1 [6] by the same technique as used here were 30 to 75 nm. The domain sizes reported here ranged from 50 to 80 nm which is similar to their domain sizes. The quench rates used here were probably faster as judged by specimen thickness (their 100 μm thick ribbons and wires as compared to 20 to 100 μm thick produced here) and as judged by grain size, their 2 to 5 μm compared to 0.7 to 3.4 μm produced here. In this study, rapid solidification by itself did not ductilize the pure Ni_3Al even though the solidification rate was faster.

Of the several possible mechanisms that might be responsible for the high hardness of our most rapidly solidified samples, dislocation density and anti-phase domain size must be dismissed. The dislocation density is low and similar for all specimens and the anti-phase domain size is also essentially independent of quenching rate over the range of samples studied. In addition, the domains observed in our Ni_3Al samples appear to be too coarse to produce any significant hardening [16]. The differences in grain size and the degree of long-range order remain as the likely variables to explain this hardness difference, but confirmation of this suggestion must await the results of our quantitative x-ray study.

The complex APB structure in rapidly solidified Ni_3Al revealed by transmission electron microscopy promises to provide additional information on the APB energy in this highly ordered alloy and thus on its mechanical behavior. A detailed structural study is in progress, utilizing the analytical and microdiffraction capabilities of the Philips EM 400T/FEG.

References

- [1] N. S. Stoloff and R. G. Davis, *Prog. Mater. Sci.* **13**(1), 1-34 (1966).
- [2] B. H. Kear, C. T. Sims, N. S. Stoloff, and J. H. Westbrook, eds., "Ordered Alloys — Structural Applications and Physical Metallurgy," in *Proc. 3rd Bolton Landing Conf.*, Claitor's Publishing Division, Baton Rouge, Louis., 1970.
- [3] H. A. Lipsitt, D. Shechtman, and R. E. Schafrik, *Metall. Trans. A* **11A**, 1369 (1980).
- [4] S. M. Copley and B. H. Kear, *Trans. AIME* **239**, 977 (1967).
- [5] S. K. Ehlers and M. G. Mendiratta, paper presented at the Annual TMS-AIME Meeting, Dallas, Texas, Feb. 14-18, 1982.
- [6] A. Inoue, H. Tomioka, and T. Masumoto, *J. Mater. Sci. Lett.* **1**, 377-80 (1982).
- [7] K. Aoki and O. Izumi, *Nippon Kinzoku Gakkaishi* **43**, 1190 (1979).
- [8] C. T. Liu and C. C. Koch, to be published in *Proceedings of Conference on Trends in Critical Materials Requirements for Steels of the Future, Conservation and Substitution Technology for Chromium*, Vanderbilt University, Oct. 4-7, 1982.
- [9] D. M. Kroeger, W. A. Coghlan, D. S. Easton, C. C. Koch, and J. O. Scarbrough, *J. Appl. Phys.* **53**, 1445-53 (1982).
- [10] B. D. Cullity, *Elements of X-Ray Diffraction*, Addison-Wesley Publishing Co., 1956, pp. 363-78.

- [11] E. A. Starke, Jr., J. C. Ogle, and C. J. Sparks, Jr., pp. 372-90 in *Advances in X-Ray Analysis*, 12 ed. C. S. Barrett, J. B. Newkirk, and G. R. Mallett, Plenum Press, New York, 1969.
- [12] E. M. Schulson, *The Role of Grain Size on the Brittle to Ductile Transition of the Strongly Ordered Alloy Ni₃Al*, Progress Report (DE-AC02-81ER10907) Thayer School of Engineering, Dartmouth College, Hanover, New Hampshire, March 1982.
- [13] C. T. Liu, unpublished research, Oak Ridge National Laboratory, 1982.
- [14] E. H. Lee, C. C. Koch, and C. T. Liu, "Rapidly Solidified Amorphous and Crystalline Alloys," pp. 375-79 in *Materials Research Society Symposia Proc. 8*, ed. B. H. Kear, B. C. Giessen, and M. Cohen, Elsevier Science Publishing Co., New York, 1982.
- [15] Y. Calvayrac and M. Fayard, *Acta Metall.* 14, 783 (1966).
- [16] R. G. Davis and N. S. Stoloff, *Trans. Metall. Soc. AIME* 230, 390 (1964).

MICROSTRUCTURAL CHARACTERIZATION OF RSPD STRUCTURES

A.M. Ritter and M.R. Jackson
General Electric Corporate Research and Development
Schenectady, New York 12301

ABSTRACT

When plasma deposition of melted particles is performed in a low-pressure environment, solidification occurs rapidly. For high-temperature Ni-base superalloy compositions, particles smaller than $37\mu\text{m}$ are injected into the plasma, accelerated and heated simultaneously, and flattened either against a substrate or against rapidly solidified plasma deposited (RSPD) material just deposited. Thickest splats seen in thin foils by transmission electron microscopy are generally $3\text{--}4\mu\text{m}$. Assuming these are discs created by flattening the largest particles, volume considerations indicate the discs are on the order of $100\mu\text{m}$ in diameter. Over a considerable range in deposit temperature, little variation in splat dimension is observed, but substantial change in the structures of grains and within grains is observed. For substrates heated to approximately 900°C before deposition, the solidification structures indicate a quench rate equivalent to that attained in melt-spun ribbon.

Introduction

Application of rapid solidification technology to Ni-base high-temperature superalloys has been in progress for a number of years (1,2). Powder atomization, self-quenching (laser or electron beam processing), and melt-spinning (3-5) have received the most attention because of the high cooling rate achievable and the relative ease of experimentation. Plasma deposition has also received some study, but most of this work was done at atmospheric pressure, either in air or an inert gas shroud (6,7). The structures formed tended to be low in density ($\sim 90\%$ of the theoretical density) and to have considerable oxide content (oxygen concentration of $\sim 1\text{ w/o}$). For low-pressure plasma spraying (LPPS), low oxide content and nearly full density were achieved in MCrAlY coatings. Deposition of structural alloys as free-standing bodies has been termed rapid solidification plasma deposition (RSPD) (8,9). Such deposits have been found to have excellent structural integrity and the process is being developed for potential high-temperature components (10).

Because of the interesting mechanical properties displayed by RSPD alloys, a study of as-deposited microstructure and control of that microstructure was initiated. A characterization of the as-deposited microstructure will be presented here.

Experimental Procedure

Alloys with chemistries near or equal to the following nominal composition were chosen: .14Cr, .095Co, .05Ti, .04Mo, .04W, .03Al, .0017C, .0003Zr, .00015B, and balance Ni, by weight fraction. Powders produced by both gas atomization and vacuum atomization were purchased sieved to pass through a 400 mesh screen, which results in a maximum particle size of $37\mu\text{m}$ for spherical powder. These powders were fed at approximately $10\text{--}20\text{ kg/h}$ into an Ar-He plasma (Electro-Plasma, Inc. gun) at 52V , 1300A , 60 torr tank pressure, or into an Ar- H_2 plasma (Metco gun) at 56V , 700A , 60 torr tank pressure. A deposit was formed on substrates of steel or copper located at a distance of $25\text{ to }45\text{ cm}$ from the gun. Deposits approximately 1 cm thick were made either with or without relative translation between gun and substrate.

Slices were cut with a diamond saw from deposits both parallel and perpendicular to the plane of the deposit. These were for light optical metallography or were mechanically and electrochemically thinned to perforation for transmission electron microscopy. The electrochemical thinning was a jet milling technique using a 20% perchloric acid/ 80% methanol electrolyte. Light optical metallography of polished mounted samples was sometimes complemented with platinum shadowed replica or extraction replica electron microscopy. Extraction was performed using a 10% Br/ 90% methanol solution.

Transmission electron microscopy was performed using an Hitachi H-600 or a JEOL JSEM-200 microscope. Bright field, dark field, and electron diffraction imaging were performed for phase analysis and crystal orientation observations.

Low-Temperature Deposition

Typical powder particles are shown in Figure 1. Although the largest particle passing through a 400 mesh screen is $37\text{ }\mu\text{m}$ in diameter, a very wide range of sizes actually is included in the powder fed to the gun. For both gas atomized and vacuum atomized powders, the particle size distribution includes 0.2 below $10\text{--}12\text{ }\mu\text{m}$, 0.5 below $25\text{ }\mu\text{m}$ and a mean size of $28\text{ }\mu\text{m}$, on a volume basis. The degree of segregation within these particles will depend on particle size, with dendritic segregation being most severe in the coarsest powders.

In the deposits from EPI plasma guns, particles are observed (Figure 2) which have a structure very similar to the dendritic structure of the as-atomized powder. Some appearance of shock deformation is seen in the large particle. The question arises as to whether these particles did not melt in the plasma, or whether they melted and re-solidified in transit. Experiments have been suggested, such as homogenizing particles before spraying so that no dendritic structure would exist (11). Any dendritic structure in spherical particles within the deposit would then be an indication of melting and re-solidification in transit. However, a consideration of segregation kinetics suggests such experiments will not answer the question.

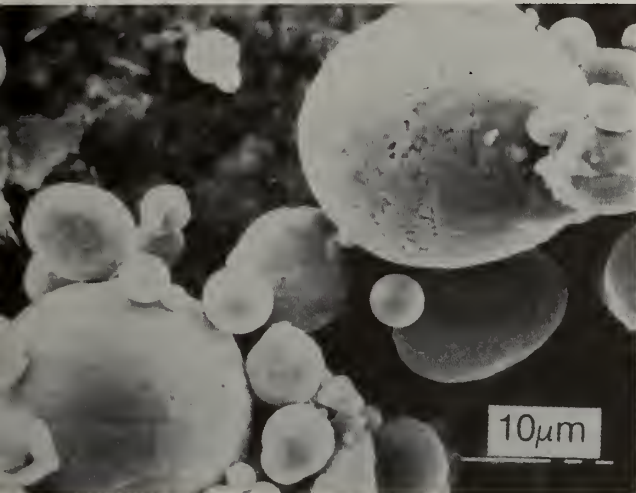


Figure 1. Micrograph of -400 mesh powder.

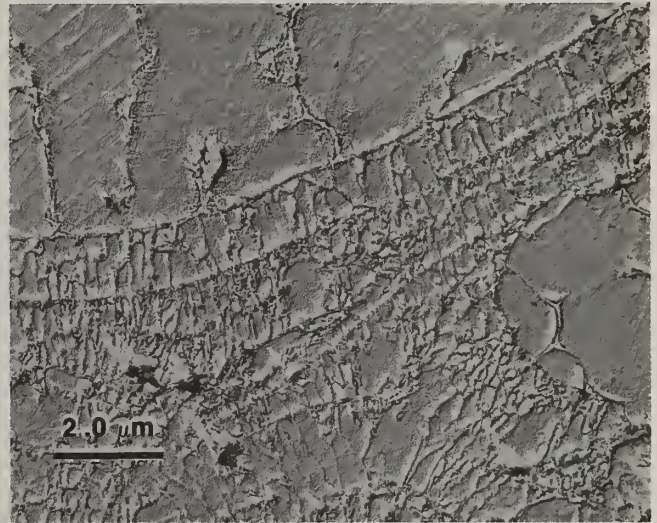


Figure 2. Spherical particles in RSPD alloy.

Homogenization in the liquid will occur over a distance approximated by \sqrt{Dt} , where D is the diffusivity and t is the diffusion time. The diffusivity in the liquid will be on the order of $10^{-5}\text{ cm}^2/\text{sec}$. Since the distance over which powder travels from gun-to-substrate is $\sim 3\text{ m}$ and the particle velocity is greater than 300 m/sec , the transit time is on the order of a millisecond. The homogenization region from \sqrt{Dt} will be on the order of $1\text{ }\mu\text{m}$. For a particle heated just above the liquidus and then re-solidified, its segregation pattern will be essentially identical to that which would exist if the particle never had melted. A similar argument could be made for the lack of segregation in an homogenized particle that was melted and re-solidified.

This simple analysis suggests such experiments will not clarify whether these particles ever melted. It is of interest, however, that the analysis also suggests particles arriving fully molten may be segregated liquids with compositional distributions essentially the same as in the atomized powder.

Similar questions arise for microstructures such as seen in Figure 3. The structure appears to consist of dendritic cores sheared on what was formerly interdendritic material. Most likely interpretations include a particle heated prior to impact to a temperature intermediate between the high melting point of the cores and the lower melting point of the interstices; or alternatively, a particle heated on impact by conversion of kinetic to thermal energy, again to just above the melting point of the interstices. Of course, re-solidification of a fully melted particle could have progressed partially prior to impact. A lower magnification view of an alloy more prone to the shearing behavior is seen in Figure 4.

No such question is raised for particles that were fully melted at impact. Transmission electron microscopy (TEM) is shown in Figure 5. A foil taken parallel to the plane of the deposit, Figure 5a, shows an equiaxed morphology with average grain size well below $1\text{ }\mu\text{m}$ in diameter. The structure, deposited at approximately 900°C , shows a very homogeneous grain size, no evidence of dendritic or cellular features, and infrequent occurrence of carbide particles. There is no $\delta\text{-}\delta'$ nodular eutectic at grain triple points, such as is observed in cast material. For the alloy carbon content of 0.15 w/o, a carbide volume fraction of about 0.015 is expected, if all the carbon were present as carbide. The apparent carbide fraction is considerably less than is seen in conventionally cast structures of the same composition. Most of the carbides observed in the RSPD

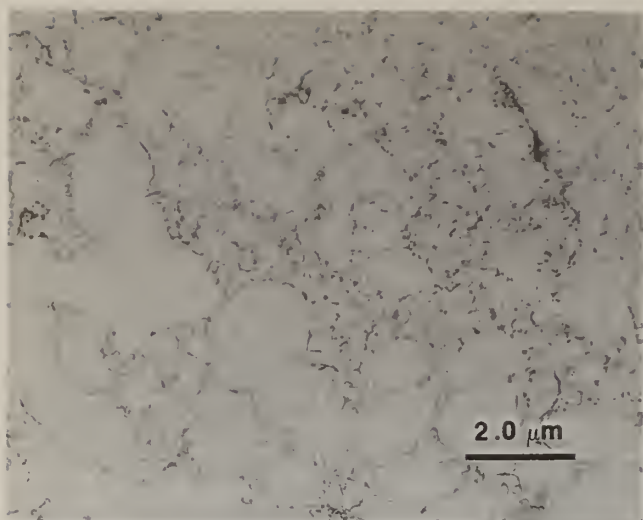


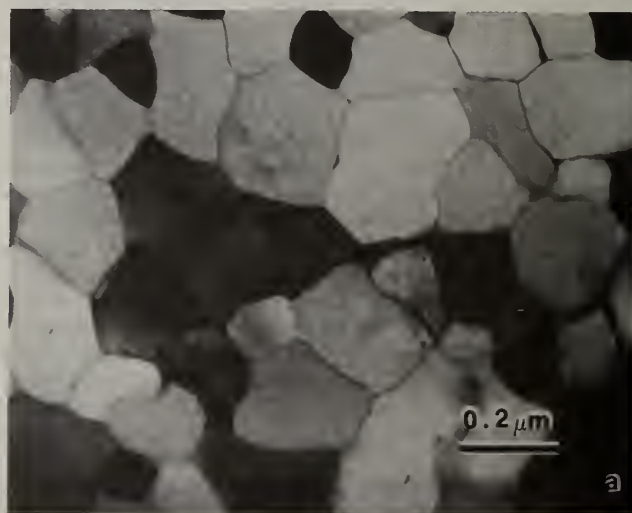
Figure 3. Melting between dendrite cores.

Figure 4. Transverse micrograph of RSPD alloy.



material produced at 900C are fine, on the order of $.01-.2\mu\text{m}$, and exhibit an electron diffraction pattern consistent with an M_{23}C_6 crystal lattice. Some of the very fine carbides may be MC. Occasionally a much larger carbide is observed, on the order of $5\mu\text{m}$. These exhibit an MC crystal lattice diffraction pattern, close to that of TiC. It is believed that these carbide particles are ones that were present in the atomized powder, and that the powder particles did not experience a sufficient time-temperature pulse to solution these carbides into the liquid. As noted earlier, transit times for powder particles from injection into the plasma to deposition on the substrate is of the order of a millisecond.

Figure 5. Transmission electron micrograph.
a) Parallel and b) tranverse-to-plane of low-temperature deposit.
c) Dark field view of b.



The distribution of the $M_{23}C_6$ carbide particles is displayed in Figure 5b, for a foil taken perpendicular to the plane of the deposit. Individual splatted discs show a demarcation of their interfaces with adjacent splats by the presence of the fine carbides. The splats vary in thickness, from a maximum of about $4\mu\text{m}$ to very thin discs. It is expected that the $4\mu\text{m}$ splats are produced by spreading of the largest powder particles ($37\mu\text{m}$), and that the thinner discs result from the entire range of molten droplets that reach the substrate. Of course, the very finest particles probably are vaporized by the plasma gases, while coarser fractions (still very fine) are not vaporized but are too small in mass to break free of the plasma jet as it is diverted around the substrate. The vaporized particles and the low-mass particles are lost to the deposition process.

Within the individual splat layers, a columnar grain morphology is observed, with the grain width corresponding to the equiaxed grain diameter seen in Figure 5a. Dark field microscopy indicates that for the $\sim 900^\circ\text{C}$ deposition temperature, grains grow from one splat layer through the next, sometimes extending over three splat thicknesses (Figure 5c). The structure within the splats again indicates a lack of segregation, with carbides only marking inter-splat interfaces.

The well-defined splat interfaces can be interpreted as evidence of a lack of general re-melting by a molten droplet spreading over a just-solidified splat. For particle sizes, powder-feed rates, and particle densities in the plasma, particles spreading across the surface cover any single location on that surface approximately 350 times per second. If arrival times from particle-to-particle were identical, this would require a solidification time $1/350$ sec, or .0029 seconds. Because of the statistical nature of the powder feeding and injection, the lack of re-melting suggests a much shorter solidification time.

Oxygen contents of -400 mesh powders for conventional Ni-base superalloys vary typically from 120-300 wppm. The lower value is for material in production lots where atomizing chambers are only infrequently opened to atmosphere, while the higher value is for material produced by a batch process, with an atomizer cleaning sequence immediately before production. If all the oxygen were on powder surfaces, these levels would correspond to the equivalent of 5-15 atom layers, depending on particle size distribution and the degree of roughness of the powder surfaces. During RSPD processing, another 50-150 wppm of oxygen is incorporated into the final deposit. This total corresponds to approximately 0.1 a/o oxygen, which would be expected to produce 0.2-0.3 v/o oxide in the microstructure. A first consideration might predict that the oxide would be at inter-splat interfaces, because these might correspond roughly to the outer surface of the original powder particles. However, droplet spreading on the rough RSPD surface (Figure 6) may involve considerable deformation and mixing of the droplet-oxygen layer boundary. This may produce a more general distribution of oxide particles. Observations of oxides in the fully melted and splatted structures is extremely infrequent. It is possible that some fraction of the oxygen is present in the carbide particles as oxy-carbides.

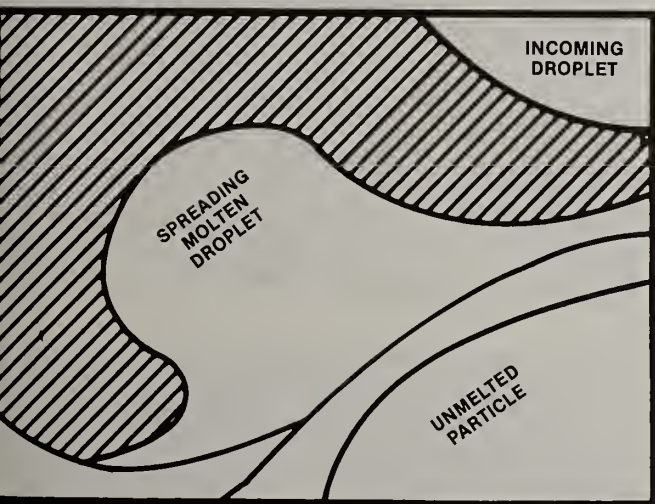


Figure 6. Schematic view of the roughness of the exposed RSPD surface.

High-Temperature Deposition

When a greater energy density is concentrated on the deposition surface, such as by decreasing the gun-substrate separation or by eliminating relative motion between gun and substrate, changes in microstructure can occur. *In situ* annealing can occur if temperatures are very great (12), but even at temperatures which do not significantly alter microstructure after deposition, considerable variations from those shown in Figure 5 can be produced. A deposit made using a Metco plasma gun with no translation of gun relative to substrate is shown in Figure 7. This is from a foil perpendicular to the plane of the deposit for a structure produced at $\sim 1150^\circ\text{C}$. The thickness of individual splats is similar to the lower temperature deposits, but the columnar

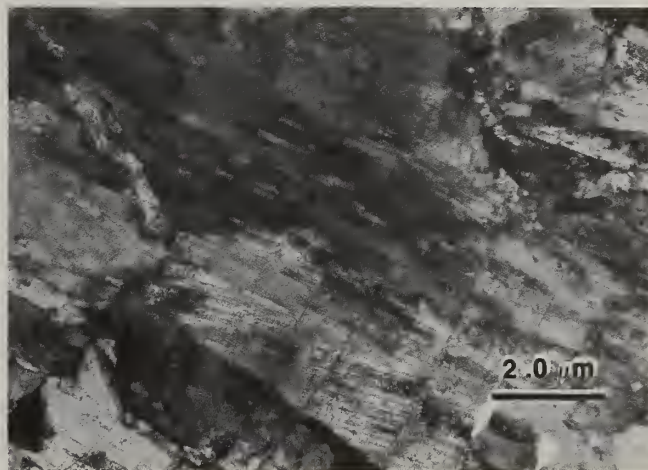


Figure 7. Transmission micrograph transverse-to-plane of high-temperature deposit.

grain size and the corresponding equiaxed grain size on sections parallel to the deposition plane is more than an order of magnitude greater than for the lower temperature deposits. Dark field microscopy indicated growth of individual columnar grains through as many as 10 splat interfaces. Again, carbides marked the splat interfaces, but the carbides were MC-type carbides, with unit cell dimensions close to TiC. Within the columnar grains was a considerable substructure shown in Figure 8. The structure appears to be cellular in nature, and this is also seen on the sections parallel to the deposition plane. Cell boundaries have a pronounced demarcation from small carbides as well. The γ' produced in the sample as the deposit cooled following termination of deposition at a temperature above the γ' solvus is evident in Figure 8.

Comparison to Other RS Processes

Powder atomization processes are generally rapid solidification methods for powders less than $\sim 100 \mu\text{m}$ in diameter. Even for much finer powders, cooling rates are such that dendritic structures frequently result. Cooling rates can be estimated from the spacing between secondary dendritic arms found in the powder particles. However, in the splat-quenched RSPD structures no evidence is seen of dendritic solidification in the low-temperature deposits, while a cellular solidification microstructure is observed for higher temperature deposits. This comparison to powder structures indicates a cooling rate greater than 10^5 K/sec .

A similar comparison can be made with structures from melt spun ribbon. A sample of an RSPD Ni-base superalloy was re-melted and rapidly solidified by a melt-spinning operation, and the resulting ribbon was examined by TEM. A fine, equiaxed structure was observed in foils prepared parallel to the plane of the ribbon (Figure 9). Replica electron microscopy of sections polished transverse to that plane showed that the majority of the ribbon thickness consisted of columnar grains. The equiaxed structure seen in TEM was essentially identical to that observed in the RSPD material, with a grain size for the equiaxed structure of less than $0.5 \mu\text{m}$. The microstructural similarity for the same composition produced by RSPD and by melt-spinning suggests that cooling rates for the two processes are also comparable. A cooling rate of approximately 10^5 – 10^6 K/sec can be estimated for the RSPD structures from such a comparison. This is a reasonable rate compared to estimates made based on splat thickness, the maximum solidification interval and the thermal gradients imposed by the process.

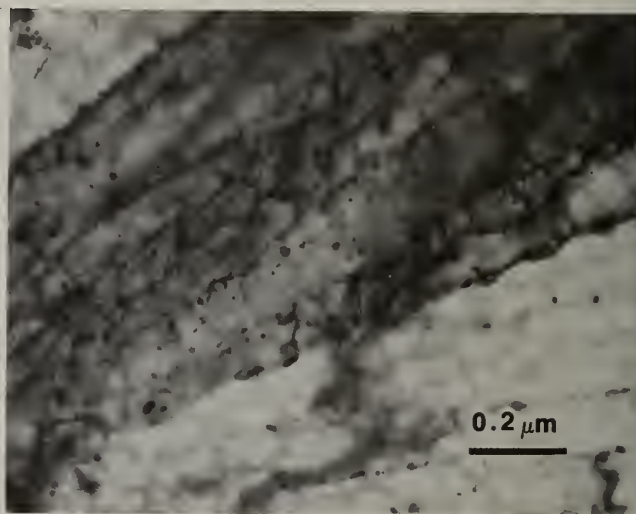
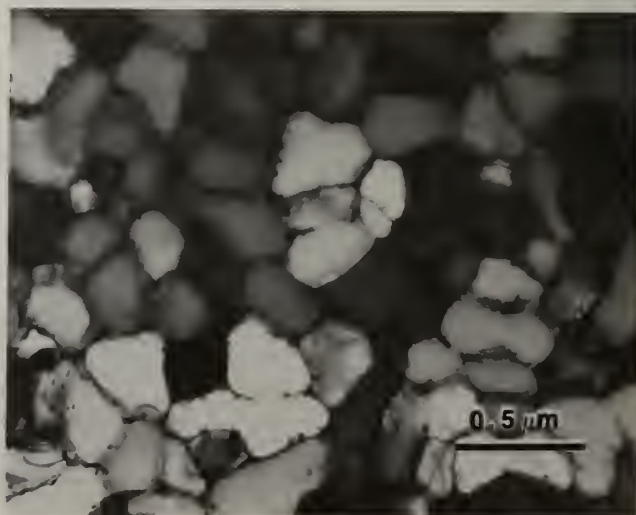


Figure 8. Transmission micrograph transverse-to-splat boundary and splat interior.

Figure 9. Transmission micrograph through the thickness of a melt-spun ribbon.



Summary

Microstructures of as-deposited RSPD Ni-base superalloys are characterized by a layered assembly of discs generally less than $3\text{ }\mu\text{m}$ in thickness, which formed as liquid droplets impacted the surface and spread prior to re-solidifying. Within the discs are columnar grains, with the long axis of the grains perpendicular to the plane of the disc. In the plane of the discs, the columnar grains are equiaxed. Grain growth occurs from splat-to-splat, with nucleation of new grains eliminating further growth in about three splat thicknesses at 900C deposition, and in about 10 splat thicknesses at 1150C deposition. The lower temperature depositions appear to have solidified in a planar mode, with splat boundaries marked by fine carbides. The higher temperature deposition shows a cellular microstructure, with both splat boundaries and cell boundaries marked by carbides. A fraction of the microstructure consists of spherical particles that appear to have arrived at the substrate without melting, and other particles that appear to be melted only along interdendritic interstices. Cooling rates in excess of 10^5 K/sec are expected.

Acknowledgement

The authors wish to note the technical discussions with J.R. Rairden, R.W. Smith and J.S. Smith (all of General Electric Company). Depositions were made by S.F. Rutkowski, W.A. Seaman and J.A. Resue. Metallographic preparation was performed by J.A. Resue.

References

- (1) D.J. Looft and E.C. vanReuth, "Rapid Solidification Processing: An Overview," Proc. of the Int. Conf. on Rapid Solidification Processing, Reston, Va., p. 1, 1977.
- (2) R.J. Patterson, II, A.R. Cox and E.C. vanReuth, "Rapid Solidification Rate Processing and Application to Turbine Engine Materials," J. of Metals, p. 34, Sept. 1980.
- (3) P.N. Ross and B.H. Kear, "Surface Segregation in Rapidly Solidified Powders," Proc. Int. Conf. on Rapid Solidification Processing, Reston, Va., p. 278, 1977.
- (4) P. Duwez and R. Willens, "Rapid Quenching of Liquid Alloys," Trans. AIME, 227, p. 262, 1963.
- (5) E. Breinan, B. Kear, C. Banas and C. Greenwald, "Surface Treatment of Superalloys by Laser Skin Melting," Proceedings of the 3rd Int. Sym. Superalloys: Metallurgy and Manufacture, Edited by Kear, et al, Claitors Publishing division, Baton Rouge, LA (1976) p. 435.
- (6) D.R. Mash and I. MacP. Brown, "Structure and Properties of Plasma Cast Materials," Matls. Engr. Quart., p. 18, Feb. 1964.
- (7) R.W. Cahn, "Rapid Solidification by Plasma Spraying," Proc. Int. Conf. on Rapid Solidification Processing, Reston, Va., p. 129, 1977.
- (8) J.R. Rairden, M.R. Jackson, M.F.X. Gigliotti, M.F. Henry, J.R. Ross, W.A. Seaman, D.A. Woodford and S.W. Yang, "Coatings for Balanced Environmental/Mechanical Behavior," Proc. Int. Conf. on High-Temperature Corrosion, NACE, San Diego, p. 72, 1981.
- (9) M.R. Jackson, J.R. Rairden, J.S. Smith and R.W. Smith, "Production of Metallurgical Structures by Rapid Solidification Plasma Deposition," J. of Metals, p. 23, Nov. 1981.
- (10) P.A. Siemers, "Rapid Solidification (RSPD) for Fabrication of Advanced Aircraft Gas Turbine Components," Contract F33615-81-C-5156, Interim Reports, Jan. 15, 1982, Apr. 15, 1982, July 15, 1982, Air Force Systems Command, AFWAL, Wright-Patterson Air Force Base, Ohio 45433.
- (11) H. Lipsitt, Materials Laboratory, AFWAL, Wright-Patterson Air Force Base, Ohio, private communication, 1982.
- (12) T.L. Cheeks, M.E. Glicksman, M.R. Jackson and E.L. Hall, "Temperature Effects on Plasma Deposition of Ni-Base Materials," this conference proceedings.

PRECIPITATION SEQUENCES IN A RAPIDLY SOLIDIFIED Ni-Al-Mo-W ALLOY

Dennis M. Dimiduk

AFWAL Materials Laboratory
Metals and Ceramics Division
Wright-Patterson AFB OH 45433

ABSTRACT

Rapid solidification P/M techniques have been used in developing nickel-base superalloys with high molybdenum content. Previous studies on these consolidated powders have shown that a sequence of precipitation reactions occurs which results in the formation of Ni₃Mo compounds in many of the Ni-Al-Mo-W alloys. The present study centers around the thermal stability of these Ni₃Mo phases and their effects on the stability of the γ' strengthening phase. Long-term aging at elevated temperatures has been performed in order to establish the dissolution temperatures of the Dl_3 , DO_{22} , Pt_2Mo and BCC stereotypical phases. The results of TEM observations on the heat-treated alloys, as well as the implications that these precipitate phases have for the design of Ni-Al-Mo base alloys, will be presented.

Introduction

One of the many fascinating areas of application for rapid solidification technology (RST) over the last five years has involved nickel-base superalloy development. In particular, P/M techniques have allowed the Ni-Al-Mo ternary base system to be explored over a much broader range of composition than that previously explored in the $\gamma/\gamma' - \alpha$ directionally solidified eutectics. RST has allowed homogeneous, equiaxed grain morphologies to be studied in addition to aligned grain structures. Recent studies of this alloy base have included a wide range of quaternary and higher-order elemental additions [1]. Cox, et al., in reporting mechanical test results of aligned grain forms of these alloys, demonstrated that a W-containing alloy, RSR 185, had very attractive high-temperature creep strength [1,2]. Martin, et al., in performing microstructural studies, indicated that after high-temperature extrusion and air cooling, the matrix of this alloy was not simply a solid solution of f.c.c. γ , but rather that a number of ordered precipitates of the class Ni₃Mo existed between the cuboidal particles [3]. In another study Pearson, et al., demonstrated that the presence of DO_{22} -type ($\text{Ni}_3(\text{MoTa})$) coherent precipitates had a favorable effect upon the creep properties of single crystals [4]. The composition which they studied was a Ta-containing version of a Ni-Al-Mo base alloy also investigated by Martin, et al. [3]. Kersker, et al., have recently shown in the same composition that the coherent DO_{22} -type precipitate can serve to stabilize the γ' , Ll_2 -type phase up to the disordering temperature of the DO_{22} [5].

In light of these observations, the present study was initiated to determine the critical ordering temperatures (T_c) of the various Ni₃Mo phases which form in the RSR 185 alloy. Additionally, the precipitation of the b.c.c. α -Mo phase was studied through the temperature of dissolution. The intent of these studies was to identify the temperature range over which the reported microstructural effects exist and consequently determine the maximum temperature at which the mechanical properties could be affected by the presence of these phases.

Experimental Procedure

The material investigated was prepared as powder by the rotary atomization process at Pratt and Whitney Aircraft and has a nominal composition of 72.6Ni-6.8Al-14.4Mo-6.2W-0.4C (wt. %). Powder of -140 mesh size was canned, out-gassed, and extruded with a 26:1 reduction ratio at 2300°F. Prior to heat treatment, the stainless steel can was removed from the extruded bars by machining. Slices (3 cm long) of the bars were prepared for heat treatment in air. Initial microstructural evaluation showed the extrusions to be consistent with those of previous studies [3]. Uniform grains having an ordered " γ matrix" of both the DO_{22} and Pt_2Mo (Ni_2Mo) isomorphous phases existed, with a uniform distribution of γ' and an M_6C -type carbide throughout the grains. All samples were given a γ'

solution heat treatment at 2390°F for 1 hr., followed by an ice-water quench. This treatment resulted in a very uniform distribution of γ' of about 0.1 μm edge length throughout the grains, with the γ' necklace entirely solutioned. Examination by TEM showed the matrix to be disordered.

A sequence of up-quenching experiments was chosen for the determination of T_c for each of the phases. A 3 cm bar of the alloy was placed in the furnace at the desired temperature for initiating the aging treatment. After 50 hr. the bar was water quenched, and a 5 mm slice was removed for preparation of TEM samples. The remainder of the bar was then inserted into a furnace at the next temperature of interest and aged for an additional 50 hr. This procedure was chosen so that if the ordering reactions for the Ni-Mo phases were very rapid and occurred upon cooling (as does the γ' reaction), the T_c could still be determined by the change in precipitate morphology which is expected to occur after solutioning and re-precipitation. The T_c of the Ni-Mo phases was determined by examining the temperature range 1350-1700°F in 50-deg. increments. Temperatures as high as 2300°F were required in studying the dissolution of the α -Mo phase. TEM examination was carried out in order to observe the ordered "matrix" phases, γ' morphology, and grain-boundary phases and morphology.

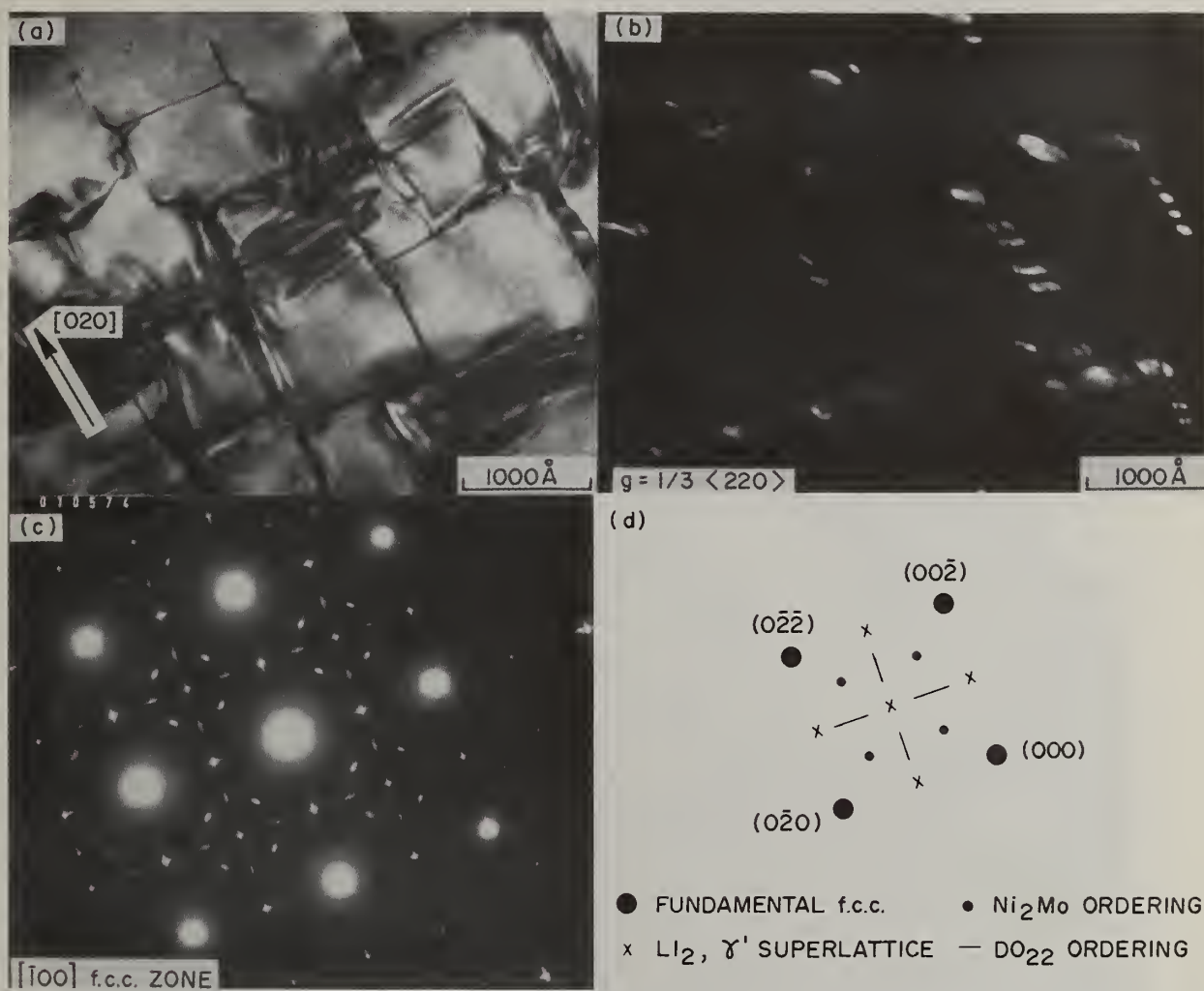


Figure 1 TEM micrographs and selected area diffraction patterns showing Ni_2Mo phase: (a) B.F., $g = (020)$ (b) D.F. using $1/3 (022)$ reflection (c) $[100]$ zone-axis pattern with DO_{22} and Ni_2Mo (d) indexed trace of (c)

Results/Discussion

Structural identification of the Ni-Mo-type phases by electron diffraction is most readily accomplished by examination of zone-axis patterns which contain $\langle 220 \rangle$ and, more importantly, $\langle 420 \rangle$ type reciprocal lattice vectors. Individual variants of these phases cause intensity peaks to occur at one-third, one-fourth, one-fifth of the unit $\langle 420 \rangle$ distances, depending upon the particular phase(s) present. These occurrences have been discussed in some detail in the literature and will not be discussed here [6-8]; however, it is these features of electron-diffraction patterns which were used to detect the Ni_xMo phases during these studies.

In this W-containing alloy, the DO_{22} - and Pt_2Mo -type phases develop during aging in the temperature range 1350-1500°F. The $D1_8$ -type (Ni_4Mo) structure was not observed in this alloy at any point during aging of the solution-treated and water-quenched samples. Separate studies of RSR-185 aged in the as-extruded condition did reveal the $D1_8$ phase when the alloy was aged below 1500°F. It is expected that this discrepancy can be accounted for by the non-equilibrium constitution of the matrix which exists both in the as-extruded and in the solution-treated-and-quenched samples. Figs 1(a) and (b) are bright- and dark-field micrographs, respectively, of the 1400°F-aged samples. The diffraction pattern and schematic trace in Figs 1(c) and (d) show that reflections from the DO_{22} phase exist along with those from the Pt_2Mo -type phase.

Further aging of the RSR-185 samples indicated that the DO_{22} had a solution temperature between 1500 and 1550°F, while the dissolution of the Ni_2Mo phase did not occur until 1600°F was reached. These results appeared to be consistent with those recently reported by Martin and Williams [9]; however, the non-coherent Ni_2Mo reported in their work was not observed here. A phase of similar morphology was observed above 1650°F; however, convergent-beam electron-diffraction studies indicate that this phase has a structure type and lattice parameter consistent with an M_{12} C-type carbide and that the orientation relationship and lattice parameter are such that some of the $\langle 220 \rangle$ and $\langle 420 \rangle$ reciprocal lattice vectors are divided into thirds, just as they are by the Ni_2Mo phase [10].



Figure 2 (a) One quadrant of $[100]$ zone with $(0\bar{1}1)$ satellites (b) D.F. using $(0\bar{1}1)$ and satellite spots (c) D.F. using $1/3 (022)$ (d) D.F. using $1/3 (022)$

Of potentially greater interest in this study are the observations made on the samples aged between 1600 and 1700°F. In this temperature range the Ni_2Mo is going into solution and, simultaneously, the b.c.c. α -Mo phase is precipitating throughout the matrix. Fig 2 shows an $\langle 001 \rangle$ diffraction pattern along with bright- and dark-field images of a microstructural feature which has been shown to be unique to the early stages of α -Mo precipitation. The high-aspect-ratio regions shown in Fig 2(b) give rise to the pairs of satellite reflections associated with the $(0\bar{1}1)$ reflections in Fig 2(a). These high-aspect-ratio features (referred to here as α' -Mo for discussion purposes) are

characterized by the satellite pairs on the $\{110\}$ -type reflections on all zones containing $\{110\}$. The exact nature of the α' -Mo is not yet understood and cannot be readily explained by those features which are known to cause satellite reflections in electron-diffraction patterns [11,12]. Particularly puzzling in this case is the fact that the satellite pairs occur only on the superlattice reflections and not on the fundamental reflections. Inspection of Figs 2(c) and (d) indicates that regions depleted in one variant of the Ni_2Mo phase exist adjacent to a single corresponding variant of the α' -Mo. This precipitation reaction remains the subject of further study.

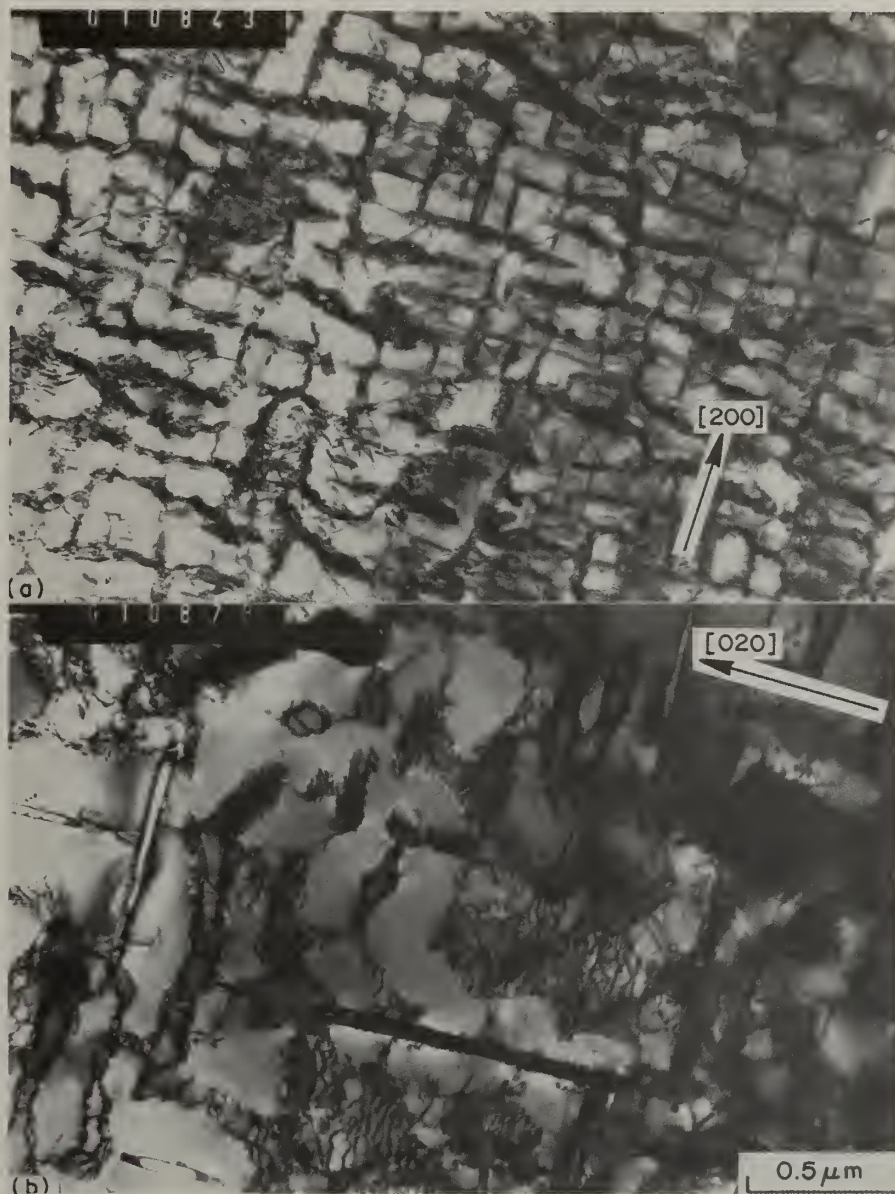


Figure 3 TEM B.F. micrographs of water-quenched RSR-185 after: (a) long-term aging at 1600°F (b) same sample after 50 hr. at 1650°F

Continued aging of the RSR-185 alloy at 1700°F results in complete precipitation of α -Mo in two different orientation relationships. These relationships were part of a separate study and were determined to be the Nishiyama-Wasserman and Pitsch orientation relationships for f.c.c.:b.c.c. systems [13]. It was determined that the α -Mo phase did not completely solution until the solvus temperature for the matrix γ' had been exceeded (about 2300°F).

Throughout this study the size and morphology of γ' was observed after each aging treatment. It is important to note that very little coarsening of the γ' occurs during aging through 1600°F or while the Ni_2Mo phases exist as a "matrix". Fig 3(a) is a bright-field micrograph of a sample aged in 50-deg. increments throughout the range 1350 to 1600°F for a total time at temperature of 300 hr. This image is compared with the same sample after an additional 50 hr at 1650°F. A marked change occurs in both the γ' size and morphology after the additional time at higher temperature. Although

the mechanistic evidence for Ni₃Mo phases restricting γ' coarsening has not yet been obtained, the evidence in Fig 3 indicates that coherent Ni₃Mo is an effective stabilizer of the γ' phase. In light of this evidence and the evidence put forth by Pearson, et al. [4], one would expect that alloys designed for use below 1600°F could incorporate such precipitates for microstructural and, thereby, property control. In the event that the Ni-Al-Mo system is explored as a polycrystalline alloy with Ni₃Mo precipitates, efforts would have to be devoted to finding ways of deterring the discontinuous precipitation reaction known to occur in the grain boundaries of these alloys. Several studies have shown that such reactions result in a drastic decrease in tensile and rupture ductility [1,14].

Summary

The critical ordering temperature for the Ni₃Mo phase in RSR-185 was found to be between 1500 and 1550°F, while the Ni₂Mo phase was found to be stable for about another 100 deg. or to 1600°F.

A microstructural feature (α' -Mo) which appears to be a precursor phase to the b.c.c. α -Mo was shown to precipitate after long times at 1600°F. This feature gives rise to paired diffraction intensity on the {110} superlattice reflections but not on the fundamental {220}-type reflections.

The γ' precipitate phase appears to be stabilized by the presence of coherent Ni₃Mo in the " γ " regions of the alloy. This stabilization appears to be effective to a maximum temperature equal to the T_c of Ni₃Mo (1600°F).

Acknowledgments

The author wishes to thank Dr P. L. Martin for many helpful discussions regarding this study. The assistance offered by Mr M. J. Kaufman and Professor H. L. Fraser, in performing convergent-beam electron-diffraction analysis, is also acknowledged.

References

- [1] A. R. Cox, R. G. Bourdeau, R. J. Patterson, E. H. Aigeltinger, R. E. Anderson, J. W. Broch, and T. D. Tillman, Application of Rapidly Solidified Superalloys, AFWAL-TR-80-4051, May (1980).
- [2] R. E. Anderson, A. R. Cox, T. D. Tillman, and E. C. van Reuth, Rapid Solidification Processing II, p. 416, edited by R. Mehrabian, B. H. Kear, and M. Cohen, Claitor's (1980).
- [3] P. L. Martin, H. A. Lipsitt, and J. C. Williams, Rapid Solidification Processing II, p. 123, edited by R. Mehrabian, B. H. Kear, and M. Cohen, Claitor's (1980).
- [4] D. D. Pearson, B. H. Kear, and F. D. Lemkey, Creep and Fracture of Engineering Materials and Structures, p. 213, edited by B. Wilshire and D. R. J. Owen, Pineridge Press (1981).
- [5] M. M. Kersker, E. A. Aigeltinger, and J. J. Hren, Proceedings from Thirty-Ninth Annual EMSA Meeting, p. 46, edited by G. W. Bailey, Claitor's (1981).
- [6] S. K. Das and G. Thomas, Phys. Stat. Sol. (a), vol. 21, p. 177 (1974).
- [7] M. Yamamoto, F. Shohno, and S. Nenno, Trans. JIM, vol. 19, p. 475 (1978).
- [8] E. Ruedl, P. Delavignette, and S. Amelinckx, Phys. Stat. Sol., vol. 28, p. 305 (1968).
- [9] P. L. Martin and J. C. Williams, "Microstructural Development During Aging of Ni-Mo-Al-X Alloys," International Conference on Solid-Solid Phase Transformations, ASM, (1982).
- [10] D. M. Dimiduk, Private Research (1982).
- [11] P. Hirsch, A. Howie, R. B. Nicholson, D. W. Pashley, and M. J. Whelan, Electron Microscopy of Thin Crystals, Butterworth and Co., London (1967).
- [12] G. Thomas and M. J. Goringe, Transmission Electron Microscopy of Materials, John Wiley and Sons, Inc., New York (1979).
- [13] D. M. Dimiduk, "Orientation Relationships between BCC Mo and FCC γ in a Ni-Al-Mo-W Superalloy," to be published in Met. Trans. A.
- [14] K. A. Williams, D. B. Miracle, and H. A. Lipsitt, to be published.

EFFECT OF THE RAPID-SOLIDIFICATION METHOD
ON MICROSTRUCTURES AND PROPERTIES OF Al-Li ALLOYS

P. J. Meschter, J. E. O'Neal, and R. J. Lederich

McDonnell Douglas Research Laboratories
St. Louis, Missouri 63166

ABSTRACT

Extrusions of the alloy Al-3Li-1.5Cu-0.5Co-0.2Zr have been prepared from vacuum-atomized powder, ultrasonically atomized powder, and roller-quenched flakes. The two powder-production methods yield extrusions of comparable microstructures and mechanical properties and are thus equally suitable for scale-up to produce large batches of Al-Li alloy powders. The roller-quenched flakes were difficult to consolidate to 100% density, and the ductility of the flake extrusion was adversely affected by interflake debonding. The microstructure and properties of Al-3Li-1.5Cu-0.5Co-0.2Zr were shown to be more sensitive to variations in alloy composition than to the particulate production method or rapid-solidification rate.

Introduction

Most of the numerous previous investigations of rapid-solidification processing of Al-Li alloys have concentrated on the influence of alloy chemistry, processing variables, and heat treatment on microstructure and properties. Rapidly solidified particulates have generally been produced by only one method in any one study, and few properties data exist on the same alloy prepared by different rapid-solidification (R/S) methods. The object of this investigation was to isolate the effect of the R/S method on the microstructure and properties of the low-density, high-modulus, high-strength alloy Al-3Li-1.5Cu-0.5Co-0.2Zr, and to develop criteria for deciding which R/S method is most suitable for production of large volumes of Al-Li alloy particulates.

Experimental Procedure

Rapidly solidified powder and flakes for this study were prepared by vacuum atomization (Homogeneous Metals, Inc., Herkimer, NY), ultrasonic atomization, and twin roller quenching (both performed at McDonnell Douglas Research Laboratories). Salient characteristics of the particulates produced by these three methods are summarized in Table 1. Average solidification rates were calculated using the correlation with dendrite arm spacing developed by Matyja et al.[1] Powders produced by vacuum atomization and by ultrasonic atomization are comparable in average particle size and dendrite arm spacing and hence have similar average solidification rates. The average solidification rate in the roller-quenched flakes is more uniform than in the powders and is approximately an order-of-magnitude larger.

Powders and chopped flakes were canned, cold consolidated, vacuum degassed at 400°C, and extruded into 1.25 cm diam axisymmetric extrusions at 400°C and an extrusion ratio of 16:1 by Nuclear Metals, Inc., Concord, MA. Chemical compositions of the extrusions are listed in Table 2. The two powder extrusions had comparable chemistries, while the flake extrusion was low in Li and Zr and thus had significantly lower strength levels. Samples from the extrusions were solution annealed at 530°C for 1 h. 190°C aging curves of all samples were similar and showed peak hardness after 4 h aging time.

TABLE 1
COMPARISON OF RAPID SOLIDIFICATION (R/S) METHODS

Characteristic of R/S Method	Vacuum Atomization	Ultrasonic Atomization	Twin Roller Quenching
Quench medium	Vacuum (expansion of pressurizing gas)	Argon at 8.3 MPa flowing at Mach 2, pulsed at ~ 80 000 Hz	Stainless steel rolls at 1725 rpm
Particulate shape	Spherical powder	Spherical powder	Flakes
Particulate dimensions	Avg. diam = 46 μm 80% of powder between 32 μm and 58 μm diam	Avg. diam = 59 μm 80% of powder between 38 μm and 89 μm diam	5 cm x 0.5 cm x 125 μm thick
Dendrite arm spacing (D.A.S.)	0.7-4 μm D.A.S. at average particle diam = 2.4 μm	0.7-5.5 μm D.A.S. at average particle diam = 2.9 μm	0.6-1.0 μm
Average solidification rate	$\sim 10^4$ K/s	$\sim 10^4$ K/s	$\sim 10^5$ K/s

TABLE 2
ANALYZED COMPOSITIONS OF Al-3Li-1.5Cu-0.5Co-0.2Zr EXTRUSIONS

Rapid Solidification Method	Analyzed Composition (wt%)			
	Li	Cu	Co	Zr
Vacuum Atomization	3.14	1.63	0.44	0.21
Ultrasonic Atomization	3.06	1.40	0.46	0.18
Roller Quenching	2.68	1.47	0.32	0.10

Microstructure and Properties

Microstructures of solution-annealed and of peak-aged Al-3Li-1.5Cu-0.5Co-0.2Zr extrusions produced from the three types of particulates are shown in Figures 1 and 2. The sizes and distributions of constituent particles, δ' precipitates, incoherent Co-containing dispersoids, and subgrains are similar for the two powder extrusions (Figures 1a, 1b, 2a, 2b, 2d, and 2e). The partial recrystallization in the flake extrusion (Figure 1c) is attributable to the smaller Zr concentration in this extrusion, and the smaller density of constituent particles in the flake extrusion is attributable to the lower Li concentration. Thus the rapid-solidification method and solidification rate ($> 10^4$ K/s) have little effect on the solution-annealed or peak-aged microstructures of the alloy.

Mechanical properties of solution-annealed and peak-aged extrusions are summarized in Table 3. The ductility of the alloy is low regardless of particulate type or heat treatment. Peak-aged strengths of extrusions made from vacuum atomized and ultrasonically atomized powders are virtually identical, in keeping with the similarity of the microstructures. The flake extrusion does not have a higher ductility than the powder extrusions even at a considerably lower yield strength level.

Fractographs of the peak-aged extrusions shown in Figure 3 reveal fracture largely along subgrain boundaries in all three types of extrusions. In addition, the vacuum-atomized powder extrusion shows relatively large cleaved regions (Figure 3a), which are not present in the fractographs of the other two extrusions. No convincing explanation for this effect exists at this time. The ultrasonically atomized powder extrusion shows some evidence of interparticle debonding (Figure 2b). The flake extrusion shows extensive interflake debonding, aggravated by the existence of occasional pre-existing voids on flake boundaries as a result of incomplete compaction in the original extrusion. Flake debonding adversely affected strength and ductility in the peak-aged alloy. Mechanical testing of a flake extrusion of a composition comparable to those of the powder extrusions is required to quantitatively determine the extent of mechanical properties degradation caused by flake debonding.

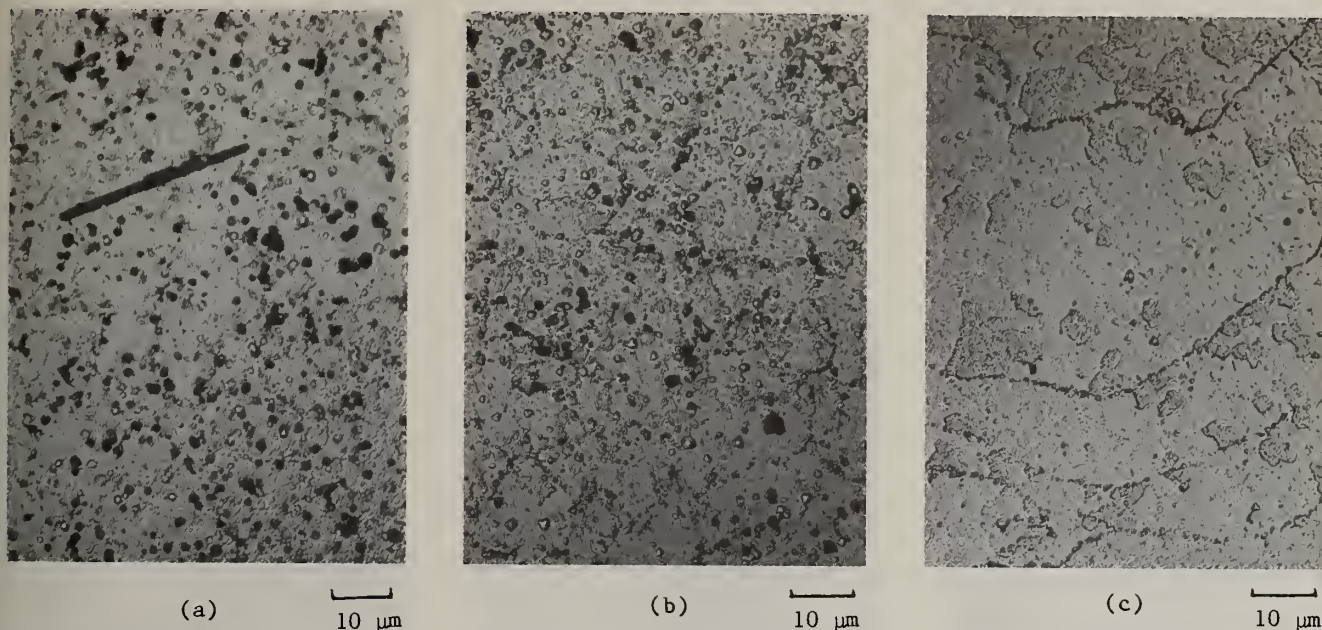


Figure 1. Optical microstructures of solution-annealed Al-3Li-1.5Cu-0.5Co-0.2Zr extrusions produced from a) vacuum atomized powder, b) ultrasonically atomized powder, and c) roller quenched flakes.

TABLE 3
MECHANICAL PROPERTIES OF Al-3Li-1.5Cu-0.5Co-0.2Zr EXTRUSIONS

Process	Solution-Annealed		Solution-Annealed and Peak-Aged	
	0.2% Yield Stress, MPa (ksi)	Elongation %	0.2% Yield Stress, MPa (ksi)	Elongation %
Vacuum Atomization	270 (39.2)	3.6	515 (74.6)	0.7
Ultrasonic Atomization	211 (30.6)	4.4	509 (73.5)	1.6
Roller Quenching	151 (21.8)	6.1	399 (57.9)	1.1

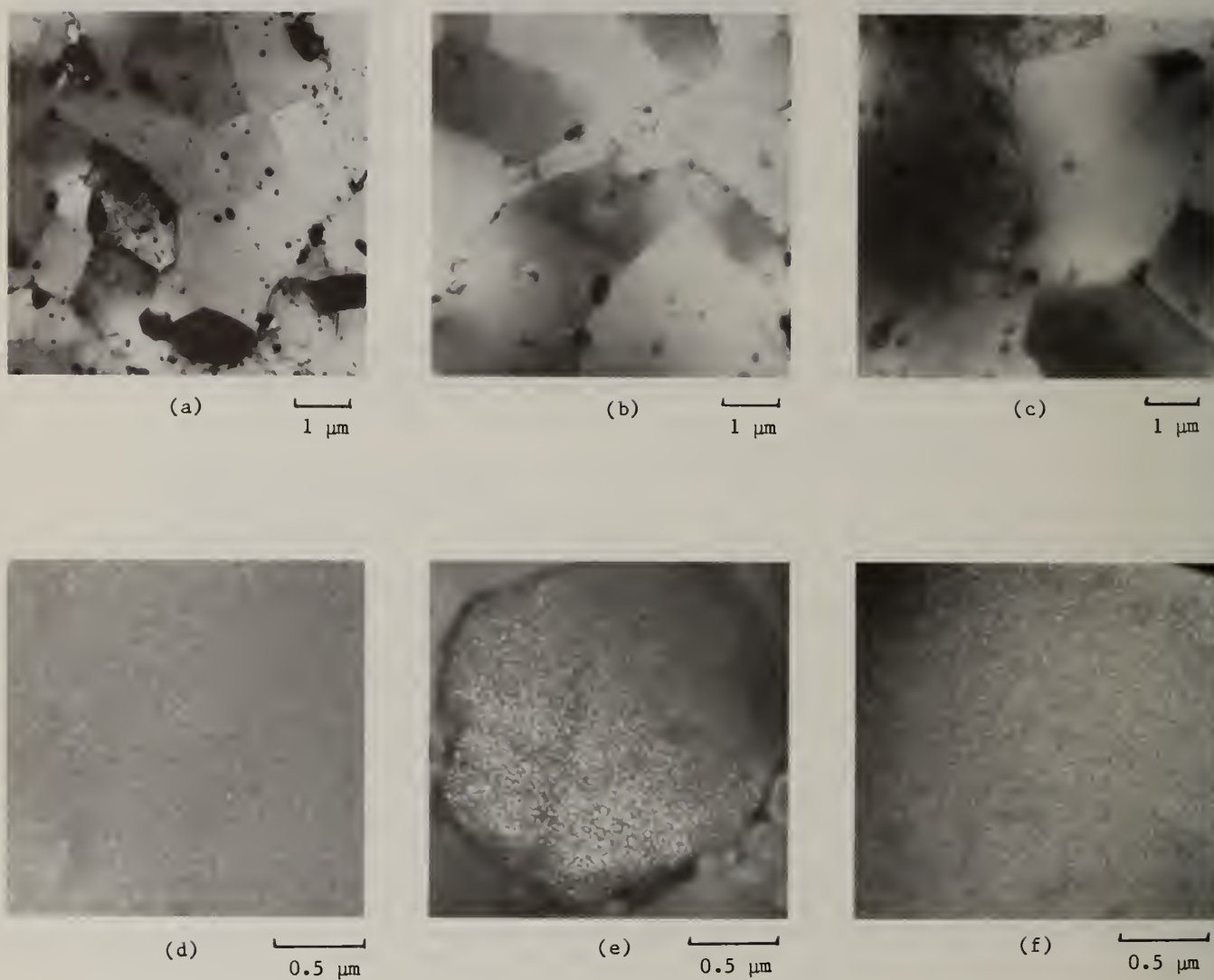


Figure 2. Microstructures of Al-3Li-1.5Cu-0.5Co-0.2Zr (a) - (c) solution annealed 530°C/1 h: (a) vacuum atomized powder, (b) ultrasonically atomized powder, and (c) roller quenched flakes. (d) - (f) 530°C/1 h plus peak-aged 190°C/4 h. Dark field, δ' reflection (d) vacuum atomized powder, (e) ultrasonically atomized powder, and (f) roller quenched flakes.

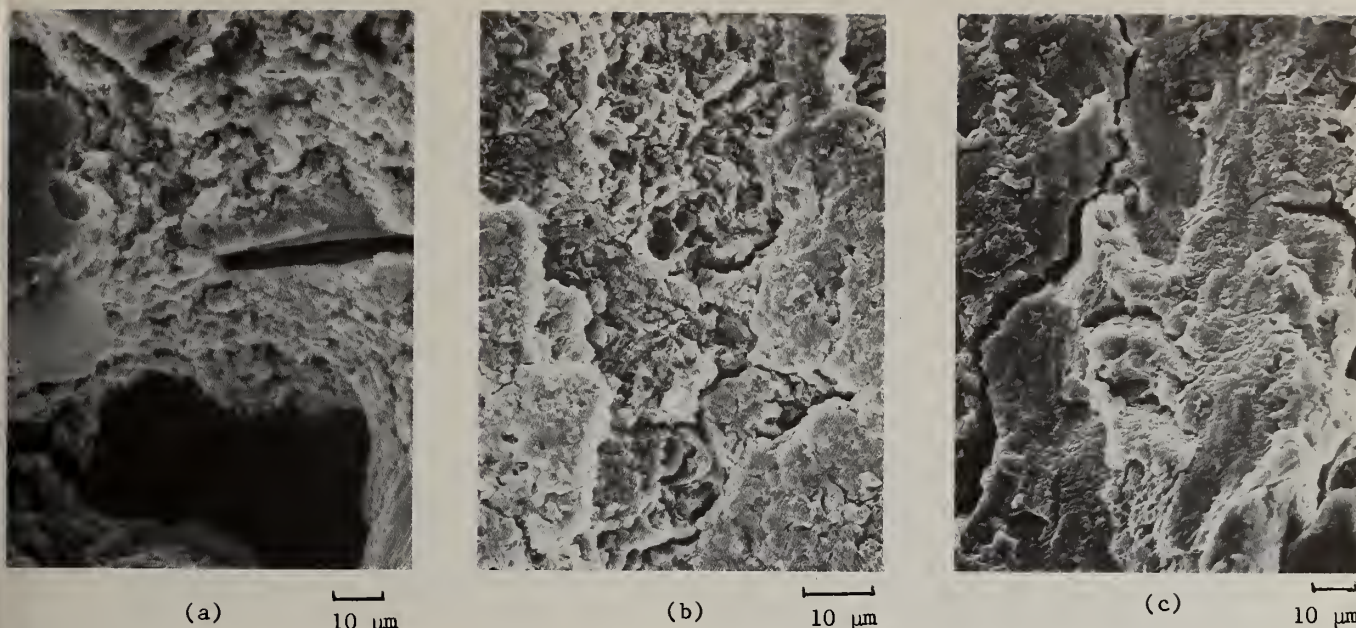


Figure 3. Microstructures of tensile fracture surfaces of peak-aged Al-3Li-1.5Cu-0.5Co-0.2Zr extrusions prepared from (a) vacuum atomized powder, (b) ultrasonically atomized powder, and (c) roller quenched flakes.

Conclusions

1) Vacuum atomization and ultrasonic atomization are methods of powder production of Al-Li alloys which yield powders of similar morphology, size range, and average solidification rate. Consolidated forms produced from the two types of powders have similar microstructures and properties. These two methods are thus equally suitable for scale-up to produce large quantities of powder.

2) Rapidly solidified powders are preferable to flakes or splats because they are more readily consolidated to 100% density and show superior interparticle bonding under comparable consolidation processing conditions.

3) Microstructures of solution-annealed and peak-aged Al-3Li-1.5Cu-0.5Co-0.2Zr extrusions are more sensitive to variations in chemistry, particularly Li and Zr levels, than to original particulate type or rapid solidification rate, provided that this rate is $\geq 10^4$ K/s.

4) The low ductility in peak-aged Al-3Li-1.5Cu-0.5Co-0.2Zr is not directly attributable to particulate type, except that interflake debonding adversely affects ductility. Current research on Al-Li alloys at McDonnell Douglas Research Laboratories centers on the specific effect of the precipitate-former Cu, high hydrogen levels, and the interaction between incoherent dispersoids and substructure, as alternative sources of low ductility in this alloy.

Acknowledgment

This research was sponsored by McDonnell Douglas Corporation Independent Research and Development (IRAD) program.

Reference

[1] H. Matyja, B. C. Giessen, and N. J. Grant. J. Inst. Metals 96, 30 (1968).

AGING BEHAVIOR OF DEVITRIFIED Ti RICH ALLOYS CONTAINING METALLOIDS

Sung H. Whang and Y.Z. Lu

NORTHEASTERN UNIVERSITY
Boston, MA 02115

ABSTRACT

Rapidly quenched Ti rich glassy alloys containing B and Si were made and devitrified as functions of temperature (550 - 950°C) and time. Different aging responses for $Ti_{70}Zr_{10}Ni_{10}B_{10}$ and $Ti_{70}Zr_{10}Ni_{10}Si_{10}$ were observed from the annealing experiments. For the former, initial modest aging response was followed by a strong second response after a long-hour annealing at 700°C while for the latter the first response only was detected. Also, the second aging in the Ti-Zr-Ni-B alloy develops very high hardness as well as a brittle phase.

Microstructure of heat treated $Ti_{68}Zr_{6}Al_{4}Ni_{10}B_{12}$ glass at 950°C for 2 hours shows that grain size remains within sub-micron range in diameter while precipitate grows into a half-micron size of acicular shape.

Introduction

Recently, a unique microstructure exhibiting high hot and cold strength has been synthesized via devitrification of glassy alloys containing metalloids [1][2][3]. Particularly, this group of alloys, in which sub-micron equiaxed metalloid dispersoid and metalloid-insoluble metal matrix form a network structure, gives rise to a microstructure stable at high temperature with unique mechanical properties. Similarly, a large quantity of metalloid elements (up to 20 at %) can be dissolved in Ti alloys via glass formation and later precipitated out by annealing. The following is a preliminary study of devitrified microstructure and mechanical properties of Ti rich glasses.

Experimental

An alloy button prepared in an arc furnace under inert gas atmosphere was splat-quenched using hammer and anvil technique. The sample foils were examined by x-ray diffractometer to determine amorphousness. Subsequently, the crystallization of the glassy alloy was studied by DSC-2 calorimetry with a heating rate of 80 K/min and a temperature range up to 1000 K. To study aging behavior the samples were wrapped in thin tantalum foil and sealed in quartz capsules under vacuum (10^{-3} torr) the capsules samples were heat treated in a furnace as functions of temperature and time. Hardness of the samples was measured by Vickers diamond pyramid tester using 50 and 100 g loads.

Results

a) Glassy State

Table 1 shows measured hardness (Hv) and crystallization temperatures (T_x) for some Ti-Zr-M-B (Si) alloys and as-quenched Ti-6Al-4V alloy, where M is Cr, Mo, Ni and Al. Young's modulus was estimated from a correlation between hardness and Young's modulus in glassy alloy [4]. Each alloy has more than one exotherm. The temperature at which the strongest peak occurs was indicated with an

Table 1
Properties of Ti-Rich Glassy Alloys Before and After Crystallization

Alloy	As-Quenched Structure	Microhardness Hv (GPa)	Estimated Young's Modulus (E) (GPa)	Crystallization Temperature (°C)	Aged; 750°C 2h, Hv (GPa)
Ti ₇₀ Zr ₁₀ Ni ₁₀ B ₁₀	Glass	6.31 (G)	~115	357, 452	9.7
Ti ₆₈ Zr ₆ Al ₄ Ni ₁₀ B ₁₂	Glass	6.27 (G)	~114	407, 477	9.6
Ti ₇₀ Zr ₁₀ Ni ₁₀ Si ₁₀	Glass	4.94 (G)	~87	413, 544*	8.8
Ti ₇₀ Zr ₁₀ Mo ₂ Cr ₄ Ni ₄ Si ₁₀	Glass	5.83 (G)	~106	419, 551*, 567	6.2
Ti-6Al-4V	Cryst.	4.28 (C)			

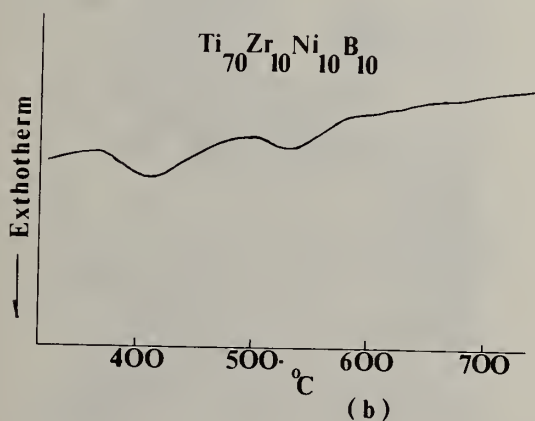
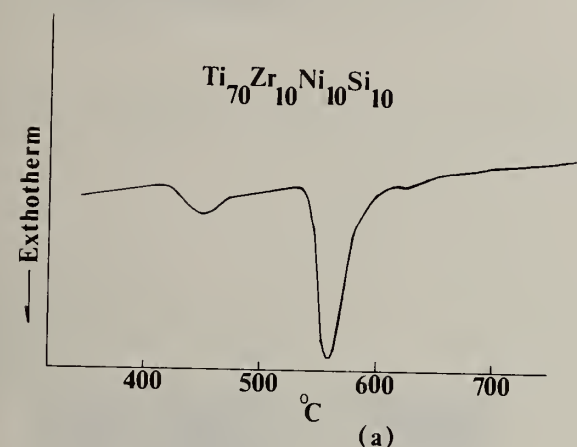
*Major exotherm

asterisk in the table. It is interesting to note that Ti₇₀Zr₁₀Ni₁₀B₁₀ does not exhibit any strong exothermal peak as shown in Fig. 1(b).

The crystallization temperatures of Ti₇₀Zr₁₀Ni₁₀Si₁₀ are similar to those of Ti₇₀Ni₂₀Si₁₀ glass (428°C, 539°C) [5]. The Ti alloys containing B show higher hardness in both glassy and crystalline states than the Ti alloys with Si. Overall, hardness values at aged state are as much as 10 - 80% higher than those at glassy state.

b) Heat Treatment

As-quenched glassy alloys were crystallized isochronally at a temperature range of 550 - 950°C for 2 hours. Measured hardness for Ti₇₀Zr₁₀Ni₁₀Si₁₀ and Ti₇₀Zr₁₀Ni₁₀B₁₀ alloys was plotted against annealing temperature as shown in Fig. 2. For both alloys lower temperature annealing gives rise to higher strength than higher temperature annealing, which is expected from the growth kinetics of grain and precipitate. The fact that in Ti₇₀Zr₁₀Ni₁₀B₁₀ hardness does not change in the range of 750 - 950°C may be indicative of insignificant microstructural change above 750°C. Isothermal annealing was conducted on Ti₇₀Zr₁₀Ni₁₀B₁₀ and Ti₇₀Zr₁₀Ni₁₀Si₁₀ at 700°C below β transus shown in Fig. 3. Initial aging response presumably comes from α -Ti and titanium-metalloid compound. However, the second aging response for the Ti-Zr-Ni-B alloy occurs after ten hour annealing. Also, it is interesting to point out that similar double aging was observed in Ti_{90-x}Zr₁₀B_x but not in Ti_{90-x}Zr₁₀Si_x, where x = 1-8 [6].



Figs. 1(a) and 1(b) One of two exotherms for the Ti-Zr-Ni-Si (a) is very strong in contrast with two weak peaks in the Ti-Zr-Ni-B (b).

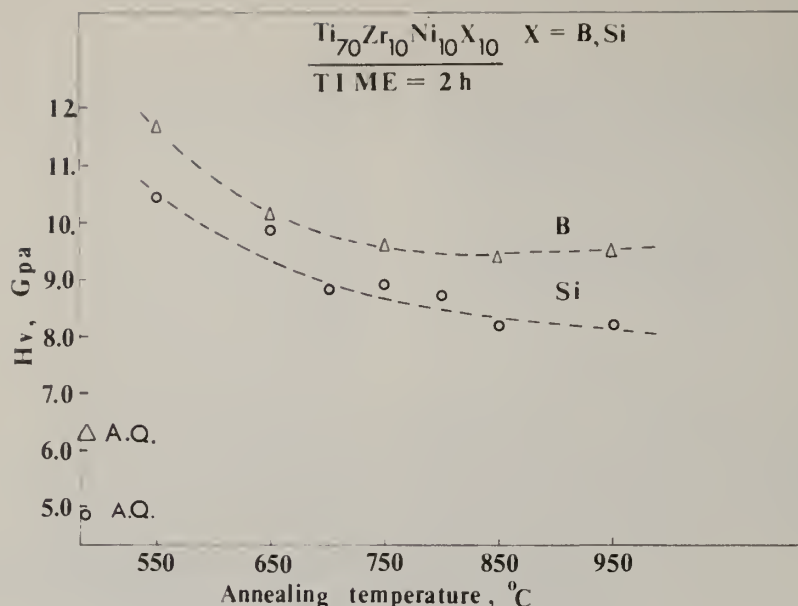


Fig. 2 Isochronal annealing (2h) at a temperature range of 550°C - 950°C for $\text{Ti}_{70}\text{Zr}_{10}\text{Ni}_{10}\text{B}_{10}$ and $\text{Ti}_{70}\text{Zr}_{10}\text{Ni}_{10}\text{Si}_{10}$.

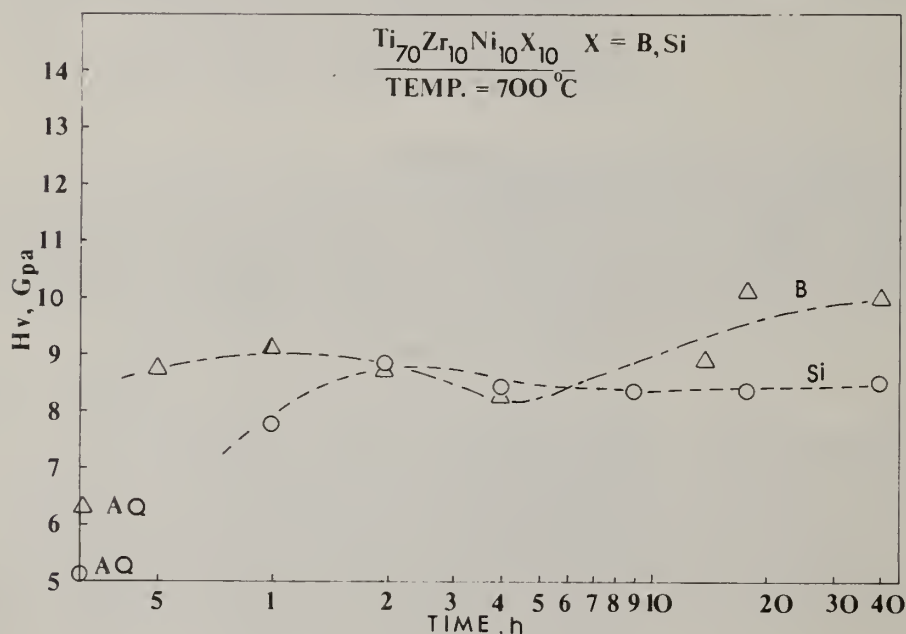


Fig. 3 Isothermal annealing at 700°C at a range of 0.5 - 40 h for $\text{Ti}_{70}\text{Zr}_{10}\text{Ni}_{10}\text{B}_{10}$ and $\text{Ti}_{70}\text{Zr}_{10}\text{Ni}_{10}\text{Si}_{10}$.

Microstructure

Bright field TEM micrograph of $\text{Ti}_{68}\text{Zr}_{6}\text{Al}_{4}\text{Ni}_{10}\text{B}_{12}$ alloy aged at 550°C for 4 hours shown in Fig. 4(a) exhibits very fine early stage crystallization and grain growth. The corresponding diffraction pattern shown in Fig. 4(b) also confirms the fact that grain size is indeed very small from the continuous first debye ring. A number of bright spots inside the first ring indicate the existence of precipitates having a larger cell size, probably borides.

In Figs. 5(a) and 5(b), microstructure of the Ti-Zr-Al-Ni-B alloy annealed at 950°C for 2 hours exhibits sub-micron grains and randomly scattered needle shape precipitates. From these micrographs grain growth in the devitrified Ti alloy is not serious even at the elevated temperature and the grain size remains within a sub-micron range while precipitate grows large enough to alter mechanical properties of the alloy.

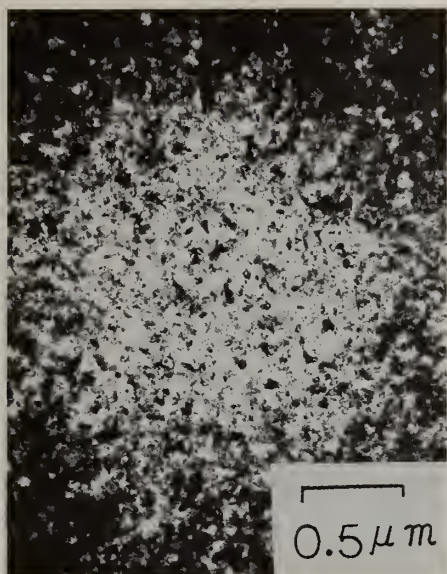


Fig. 4(a) Electron Micrograph of $\text{Ti}_{68}\text{Zr}_6\text{Al}_4\text{Ni}_{10}\text{B}_{12}$ aged at 550°C for 4 hours.

Fig. 4(b) Diffraction pattern of 4(a).

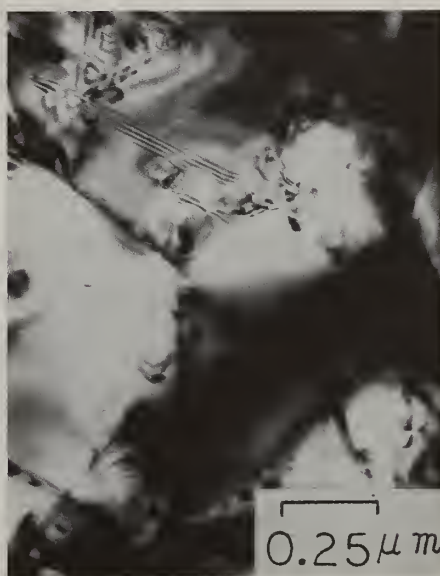
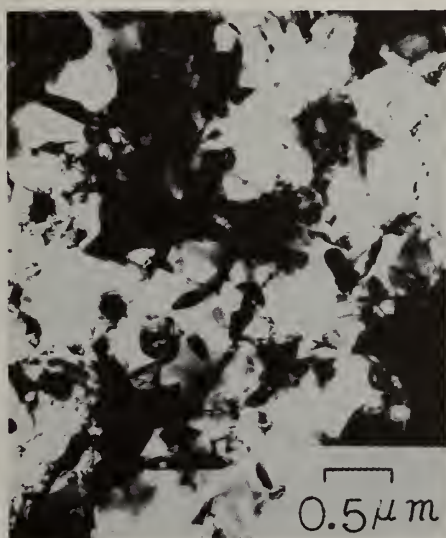


Fig. 5(a) Micrograph of the Ti-Zr-Al-Ni-B alloy annealed at 950°C for 2 hours.

Fig. 5(b) Higher magnification micrograph of 5(a).

Discussions

Glass forming ability of Ti alloy containing Si is superior to that of Ti alloy containing B. For example, glass forming was observed in binary Ti-Si but not in binary Ti-B. Also, $\text{Ti}_{74}\text{Zr}_{10}\text{Ni}_6\text{Si}_{10}$ alloy forms glass upon quenching while $\text{Ti}_{80-x}\text{Zr}_{10}\text{Ni}_x\text{B}_{10}$ alloys require full 10% Ni to go to glassy state.

It is speculated that precipitate reaction corresponding to the second aging response shown in the isothermal annealing of the Ti-Zr-Ni-B alloy may not be shown in the DSC-pattern as well as in the isochronal plot probably because of its high temperature and sluggish kinetics. The reason for the double aging in the Ti-Zr-Ni-B alloy may be as follows. For the initial age hardening, orthorhombic TiB or unknown (Ti, Zr)B type may be formed (based on phase diagram information). At the same time, the formation of hexagonal ZrB_2 or perhaps $(\text{Zr}, \text{Ti})\text{B}_2$ can be possible thermodynamically although nucleation and growth of this compound may be sluggish. Therefore, the second aging is believed to be associated with the precipitation of this compound. On the other hand, single aging response for the Ti-Zr-Ni-Si alloy is consistent with that for Ti-5Zr-1Si [7], in which $(\text{Ti}, \text{Zr})_5\text{Si}_3$ was identified as a G.P. zone precipitate instead of Ti_5Si_3 . The devitrified Ti alloys in this experiment are brittle except the Ti-Zr-Mo-Ni-Si. Furthermore, extensive brittleness develops in these alloys after long time annealing at a higher temperature. This is coincident with the microstructure of the annealed Ti-Zr-Al-Ni-B alloy in which acicular shape precipitates were found. However, for the Ti-Zr-Mo-Cr-Ni-Si alloy, a significant portion of ductility remains after devitrification and annealing at higher temperature (700 - 1000°C).

Acknowledgements

The authors wish to thank Mr. G. Mouchawar and K. Carlson for their assistance in carrying out this experiment. This work has been supported by the Office of Naval Research, Arlington, VA, which is gratefully acknowledged.

References

- [1] Ranjan Ray, J. Mat. Sci., 16 (1981) 2924.
- [2] Ranjan Ray, Proc. Mat. Res. Conf., Rapidly Solidified Amorphous and Crystalline Alloys, B.H. Kear, B.C. Giessen and M. Cohen, eds., 8 (1981) 435.
- [3] C.C. Wan, Proc. Mat. Res. Conf., Rapidly Solidified Amorphous and Crystalline Alloys, B.H. Kear, B.C. Giessen and M. Cohen, eds., 8 (1981) 441.
- [4] S.H. Whang, D.E. Polk and B.C. Giessen, Proc. 4th Int. Conf. on Rapidly Quenched Metals, Sendai Japan (1981) 1365.
- [5] D.E. Polk, A. Calka and B.C. Giessen, Acta Met., 26 (1978) 1097.
- [6] Y.Z. Lu and Sung H. Whang, TMS-AIME Fall 1982, St. Louis, MO, to be published.
- [7] H.M. Flower, P.R. Swann and D.R.F. West, Titanium Science and Technology, eds., Jaffee & Burte, 2 (1972) 1143.

DIRECTED ENERGY SURFACE PROCESSING OF METALS

T. R. Tucker and A. H. Clauer

Battelle's Columbus Laboratories
Columbus, OH 43201

Abstract

Lasers and particle beam generators have been employed to develop a variety of processes for improving the surface properties of metals. These processes include laser or electron beam transformation hardening, surface melting, cladding, alloying, ion implantation, and pulsed laser shock hardening. Consistent with the theme of this conference, only those processes involving melting and solidification are considered here.

All modifications involving fusion of either the base material or a surface alloying agent rely on the energy beam as a localized and directed source of heat input. The relative merits of lasers or electron beams depend on the degree of beam control and the efficiency with which the energy is coupled to the workpiece. For example, the electron beam can be scanned by pattern generators and efficiently absorbed by most metals to produce controlled surface melts. The introduction of a powder alloy to the process, however, presents problems for an electron beam but increases the coupling efficiency of a laser beam. Such trade offs are examined with reference to recently reported results.

The process speeds and melt depths involved in surface melting, cladding, and alloy mixing, insure that rapid solidification rates are achieved. Initially, much development was directed towards the production of glassy metallic surface layers by these techniques. In the last several years, progress has been reported in that regard, but problems associated with residual stress, thermal stability of microstructures, and thin sections persist. Of more engineering significance now are those processes which involve the more modest solidification rates ($<10^5$ °K/S). In general, metastable phases and/or refined microstructures can be expected. However, other important factors influencing properties are melt convection, epitaxial growth, oxidation tendency, and thermal shock resistance.

Introduction

The improvement of metallic surface properties by directed energy processing methods depend on the ability of the energy beams to rapidly heat a thin metallic surface layer in a controlled manner. The rapid process rate allows refined microstructures, enhanced alloy solid solubilities, and reduced or dispersed inclusions to be produced. Control of the applied energy is necessary to localize the heat pulse to as thin a surface layer as is practical and thereby reduce bulk property changes. Thermal input control is also necessary to maintain process consistency.

The two most prominent directed energy sources used in surface materials processing are the high-power continuous-wave laser and the electron beam. Both sources can be scanned, focused, or shaped to perform a variety of process functions, although the methods to accomplish these ends differ in the two cases. To the extent that the two energy sources can be made to provide an equivalent thermal input, they are interchangeable.

While lasers and electron beams can perform similar functions, each has advantages and disadvantages in particular applications. The e-beam is a more energy efficient source. A high percentage of the operating electrical power is produced as e-beam power. Moreover, the electrons are efficiently absorbed (80-90%) by most metals. The e-beam is easily focused and scanned over short distances by electromagnetic lenses and deflectors. On the negative side, e-beams generally require vacuum operation and cannot be effectively propagated long distances. In addition, e-beams are not suitable for processes involving powder streams because of the charging effects of isolated particulates in the beam.

TABLE I. LASER AND ELECTRON BEAM SURFACE PROCESSING GEOMETRIES

BEAM MODE	PART MOTION	E-BEAM	LASER	APPLICATIONS
Point	Fast Rotation and Linear		X	Skin melting, glazing
Defocused Point	2D Raster	X	X	Cladding, surface melting
Effective Line Source	Linear	X	X	Melting, cladding, consolidation
Square Patch	Stationary or Linear	X	X	Cladding, consolidation, transformation hardening
Lissajous Scan	Stationary or Linear	X		Cladding, consolidation, transformation hardening

By comparison, the laser is not as energy efficient. Operating electrical efficiencies of 5-10% are common. CO₂ laser wavelength absorption efficiencies are typically 10% for most metals. This disadvantage can be mitigated by use of absorption enhancers or in processes involving particulates. Offsetting the energy disadvantage for the laser are the following positive factors: operation in gaseous atmospheres, insensitivity to particles or magnetic fields or electrically insulating sample regions, long propagation distances, and the ability to be shaped to a uniform power distribution.

Process Geometries

A variety of process schemes for covering surface areas are possible depending on the desired depth of treatment, substrate geometry, beam characteristics and material additions required. Some of the more general approaches are outlined in Table I and illustrated in Figures 1 through 6. A combination of beam shaping and part motion are usually employed. The processes in the table go from the highest solidification rates at the top to the slower rate processes at the bottom.

The beam can be used at focus with a high speed relative to the sample surface to yield extremely high heating and cooling rates. This method is described in the next section. By applying the beam at or near focus and scanning the part in a raster fashion (Figure 1), area coverage can be achieved with overlapping beam passes. The raster coverage involves linear motion in one direction perpendicular to the beam axis and a slower translation (or stepping motion) in a mutually perpendicular direction. The two motions must be coordinated to result in the desired overlapping factor. Rotational motion can be substituted for linear translation to cover cylinders, shafts, or spiral surfaces.

A focused beam can be rapidly oscillated to generate an effective line source of energy. The e-beam is particularly suited to this type of treatment (Figure 2). By sweeping the beam with a high-frequency triangular waveform and combining motion perpendicular to the oscillation direction, surface areas can be covered in a manner analogous to the raster coverage pattern. Rapid oscillations in both the X and Y directions produce a rectangular patch of energy (Figure 3). This uniform energy pattern can be scanned across a sample or pulsed onto a specimen for a selected time interval.

Laser beams can also be rapidly scanned to produce line or uniform rectangular thermal inputs. However, the scanning mechanisms for laser beams are different from that of e-beams. Rotating or vibrating reflective optics are required for laser beams. Orthogonal rotating polygon mirrors (Figure 4) can be coordinated to yield a small rectangular raster scan pattern. The same coverage can be obtained with oscillating mirrors, but in this case motions are restricted to harmonic oscillations. The sinusoidal oscillations give rise to Lissajous patterns rather than uniform raster coverages.

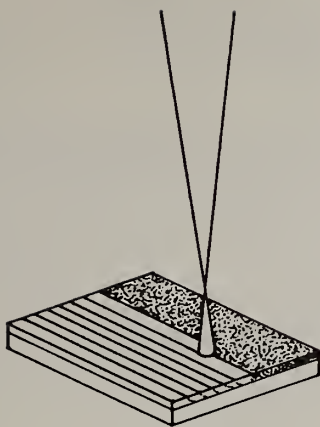


Figure 1. Area coverage of a flat sample by raster scanning

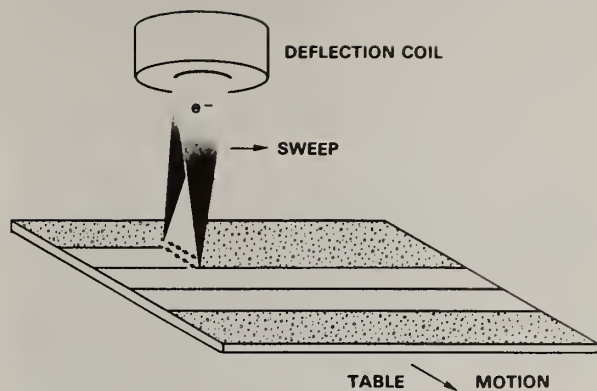


Figure 2. Oscillation of a focused e-beam to produce effectively a line source of energy input

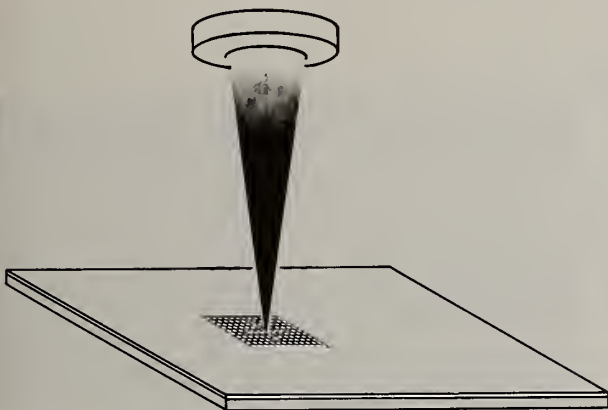


Figure 3. Rapidly scanned e-beam in two dimensions to input a uniform rectangular energy input

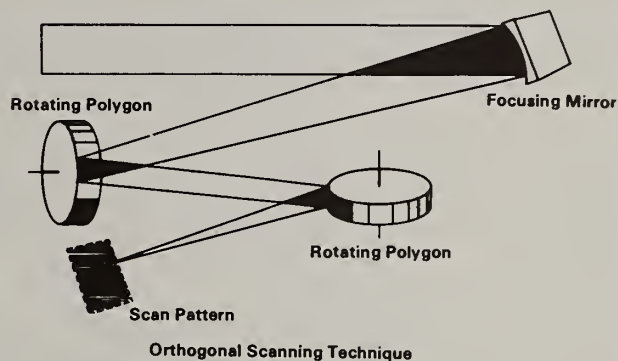


Figure 4. Formation of a uniform rectangular laser beam profile by use of rotating polygonal mirrors

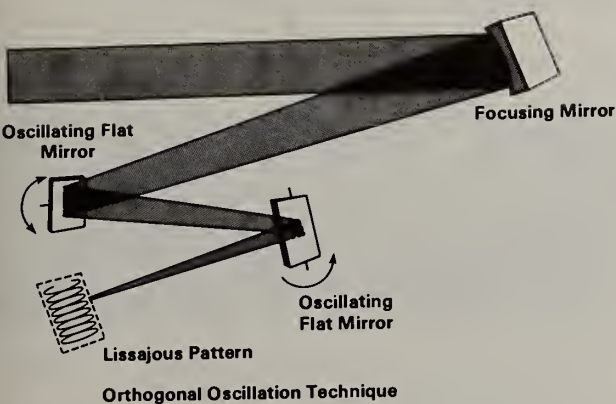


Figure 5. Formation of a rectangular laser beam profile by use of oscillating mirrors

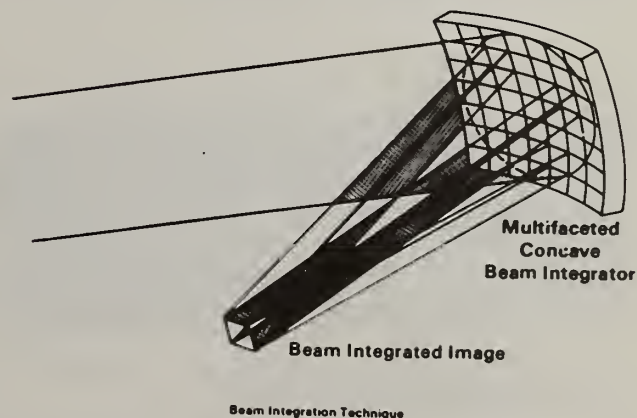


Figure 6. Formation of spatially averaged square beam profile by use of faceted optics

The laser beam can also be shaped to produce approximately uniform rectangular energy distributions without beam scanning. The use of segmented optics (Figure 6) provides for overlaying smaller segments of a single larger high-power beam. The integration of the original beam distribution averages its non-uniformities and generates a rectangular rather than round shaped cross section. These differences are important for some of the slower processes of interest such as homogenizing surface melts, coatings consolidation, and transformation hardening. Moreover, the integrated beam can be reimaged and manipulated to tailor the input beam distribution to the part dimension and geometry.

Amorphous Surface Layers

Early development of directed energy surface processing technology was concerned with the production of glassy metallic layers on crystalline substrates. The goal of this development was to derive the strength, ductility, and electrochemical advantages of amorphous metals on the surfaces of bulk parts to improve their resistance to corrosion, fatigue, and/or wear.

The first use of laser radiation to rapidly surface melt an alloy producing glassy material was reported by Breinan and coworkers in 1976 (1,2). The method, which they termed 'laser glazing', employed a stationary laser beam that was brought to focus in the plane of the specimen's top surface. The specimen was fastened to a turntable which translated under the laser beam as the rotary stage turned. The sample thereby received a spiral melt treatment analogous to the grooves in an audio recording.

Figure 7 shows the cross section of an individual melt pass in a glass forming alloy (NiCrSiBFe) glazed by the method described. The fusion zone exhibits the featureless behavior after etching, which is characteristic of glassy phases. This particular alloy along with the PdCuSi alloy reported in reference 1 are known to be relatively easy metallic glass formers.

Although the rapid surface melting of separated beam passes readily produces glassy stripes on surfaces of these alloy types, the production of an extended amorphous surface layer by this method is more difficult. The source of the processing difficulty lies in the overlapping pass geometry as in Figure 8. The fusion zone layer of this M2 tool steel sample, which was melted by a scanning e-beam, has no glassy phase present, but the edge of the melt zone of each overlapping beam pass is clearly visible. When glassy metal formers are skin melted, crystallization occurs along and just below these overlap zones.

To date, there have been two reports of continuous beam processed surfaces which have retained an amorphous microstructure - the first employing focused laser radiation and a specially prepared microcrystalline alloy coating, and the second using a scanned electron beam 'line' source.

Laser Processed Glassy Layer

Tucker and Ayers reported glassy overlapped laser melt passes on alloy AMS 4777 which had been prepared as a coating on a mild steel coupon (3). The alloy coating process was chosen so as to preserve alloy chemical composition and produce a fine-grained microstructure (4,5).

For the skin melting process, the applied laser power was high (9 kW) with a rapid rotational speed (600-900 cm/s). After 30 overlapping laser passes, an uncracked featureless surface layer was produced with an average melt depth of 25 μm . The totally glassy layer appeared to be about 10 μm deep.

The retention of glassy phase was attributed to the starting coating microstructure, the extremely rapid process rate, and the properties of the alloy employed. AMS 4777 has a relatively low quench rate threshold for glassy phase formation, high thermal stability, smooth flow characteristics, and good ductility in the amorphous state. It is likely that this combination of properties is necessary for the laser skin melt process to be successful.

E-beam Processed Glassy Surfaces

Bergmann and Mordike (6) modified the scanned line source electron beam surface treatment to produce noncrystalline surface layers. The effective line source beam, which was produced by oscillating a focused e-beam with a 10 kHz triangular wave form, was scanned at speeds of 20-40 cm/s across samples of FeCrBC and NiNb alloys (7). A beam size of 60 μm was reported.

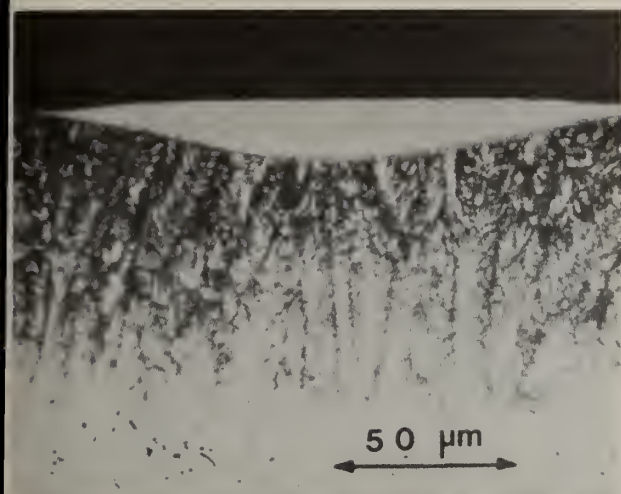


Figure 7. Cross-section of glassy-metallic laser surface melt zone in NiCrSiBFe alloy. (From Tucker & Ayers, Ref. 3)

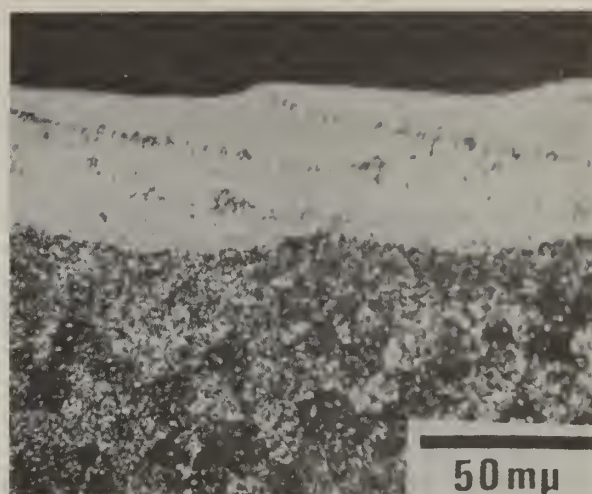


Figure 8. Overlapping e-beam melt passes on M2 tool steel (from Kurup et.al., Ref. 14)

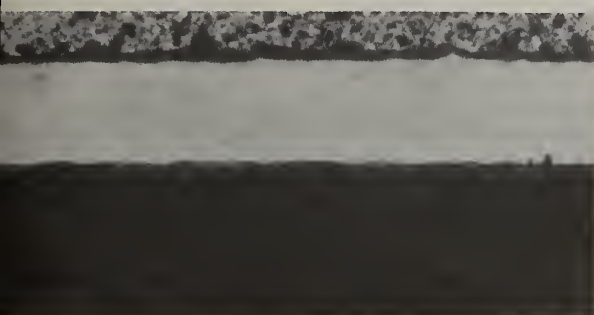


Photo 2 - Vibro laser cladding
(longitudinal cross-section x 15)

Figure 9. Surface smoothness of a laser clad layer of NiCr on mild steel substrate by concurrent vibration of specimen (from Powell & Steen, Ref. 15)

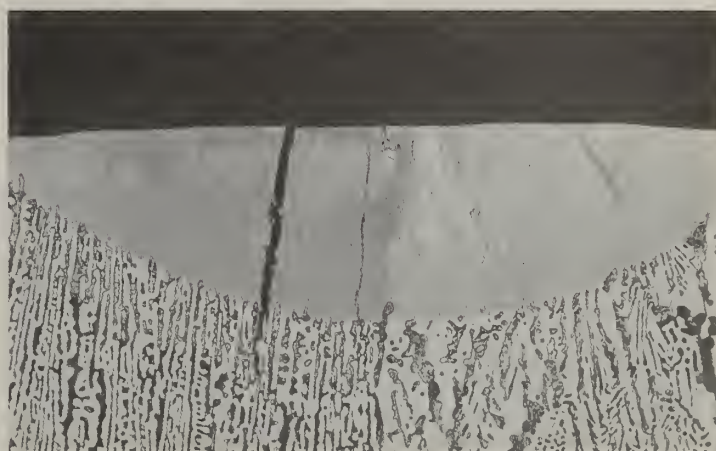


Figure 10. Epitaxial solidification on a laser surface melted track in white cast iron



Figure 11. Microstructural non-uniformity in laser surface melted MarM002 processed at 91 cm/s (from Lipscomb et.al., Ref. 17)

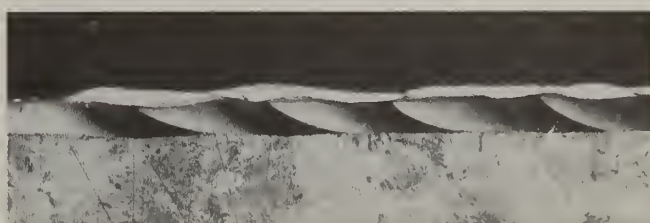


Figure 12. Overlapping heat-affected zones in laser melted FeC_{0.8} alloy

By employing the described process conditions with the appropriate beam power, a condition was reached whereby a region could remain molten over the time span of several line oscillations. Thus, a melt front would proceed along the line at the process speed, and no overlapping solidification layers need be produced. This method resulted in a beam interaction time over several line oscillations that was nearly as short as that of the laser skin melt process above but without the solidification between passes.

The principal advantage of the electron beam over the focused laser for glassy surface melting is its small spot size. CO₂ laser beams have sufficient power, time stability and line scan capability through the use of rotating polygon optics. Their diffraction-limited focused beam sizes, however, are simply too large to apply the line scan approach for this application. A laser beam of shorter wavelength would be more focusable, but such a beam is not practically available in high-power continuous mode at present.

Practical Considerations

While progress has been made in demonstrating the technical feasibility of using directed energy processing to produce glassy metal surfaces, there are several practical considerations inhibiting development of applications using this technology. The principal limitation imposed on the process is alloy suitability. The number of alloys that can be beam treated to a glassy state appears to be smaller than the set that can be produced by other rapid solidification methods.

Another limitation of glassy coatings is the thickness of the amorphous layer. It is unlikely that glassy zone thicknesses can exceed 20 μm in practice. This limit is more restrictive than that of melt spun ribbon for example. It is not possible to build up glassy layer thickness by repetitive treatments because subsequent tempering effects immediately below each rapid melt pass would crystallize the underlying layer. It is theoretically feasible to build up alternating layers of glassy and crystalline structures, but not bulk glassy material.

Another factor influencing performance of skin melted layers is the residual tensile stress distribution imposed by the processes. The shrinkage stresses arising from the cooling of the solidified layer on a cooler substrate can be quite large. Cracking is often a problem with either crystalline or glass-forming alloys. Thus, the ductility of the alloy in the glassy state is an important property as far as beam processing is concerned. An increased sensitivity to fatigue damage can also be assumed due to the residual stresses.

Taking these considerations together, it is clear that the materials combinations and useful applications to result from the beam processing approach would be highly specialized and restrictive. This is not to say that the development in this area to date has been unsuccessful, but rather that it will probably not have the general applicability that was initially expected.

Crystalline Surface Layers

Surface melting and surface alloying using directed energy beams have the advantages of providing control of chemistry, microstructure, and properties at the specimen surface different from that of the bulk material. Although surface melting alone does not usually change the alloy chemistry, the microstructural changes can benefit wear, erosion and corrosion properties. These benefits derive from refinement of the microstructure leading to higher hardness and smaller potential failure sites, and from the resolutioning and refinement of phases which are deleterious to corrosion or wear resistance. Many of the results of numerous studies on microstructure and processing are contained in various conference proceedings (8-11).

In any of the directed energy beam surface melting and alloying processes there are several major concerns. These are surface cracking, surface smoothness, porosity, and microstructural uniformity. The cracking is a result of residual surface tensile stresses created by solidification and thermal shrinkage on cooling after melting. Crack alignment in general occurs parallel, perpendicular and, at times, at 45 degrees to the beam traverse direction. The occurrence of cracking will depend on the solidification temperature range and hot strength of the alloy, the temperature differences developed between the substrate and the melt, the rate of cooling, the degree of plastic strain developed in the substrate layer, and the presence of any solid state transformations which may occur in either the cooling melt zone or the underlying heat affected zone. Minimizing the surface cracking tendency would considerably enhance the viability of surface melting processes as a material improvement process. This problem has received little attention from a basic research standpoint because its complex nature does not lend itself to simple modeling assumptions.

Surface smoothness is affected by the ripple effects (12,13) in surface melt tracks similar to the ripples observed in weldbeads. In addition to the surface ripples, there may be a trough formed in the center of the track or an undercut or overflow along the sides of the track. A minimum amount of as-treated surface roughness is desired to avoid or minimize any secondary machining of the surface. This is particularly important if more rapidly solidified, and therefore thinner, surface layers are desired for applications such as wear resistance which require smooth surfaces.

The degree of roughness can be addressed by modifying the laser or e-beam power, beam size, scanning rate and cover gas within the constraints of accomplishing the desired depth of melt and microstructural or property modification. Lower beam powers and more rapid beam scanning rates tend to enhance the surface smoothness but also develop thinner melt layers. E-beam melting also provides relatively smooth surfaces under certain conditions (14). Powell and Steen found that vibrating the substrate during laser surface alloying improved the surface smoothness, reduced porosity in fused powder coatings and reduced the cracking tendency (15). An example of a smoother surface profile from a surface cladding operation is shown in Figure 9. Similar effects should also apply to simple surface melting.

Pores in the melted layer are of less concern than are cracks, but nevertheless are best avoided if possible. The porosity is usually nominally spherical and therefore can be attributed to entrapped gas in the melt layer. One cause is residual gas from that originally present in the surface layer, e.g., in preplaced powder, plasma-sprayed coatings or in solution in the alloy (16). Another cause is the vaporization of a constituent of the alloy, or reaction of an alloy constituent with the atmosphere. Porosity attributed to oxidation of the carbon has been observed in laser surface melted cast irons with inadequately shielded melt regions. Also an increased tendency for porosity with increasing phosphorous content has been reported in laser surface melts of gray cast iron (16).

Uniformity of the microstructure and chemistry is of major importance to obtaining treated surfaces with acceptable, consistent properties. Variations in microstructure and chemistry are caused by variations in the temperature gradient, solidification rate, cooling rate, and the convective and mixing (e-beam) currents in and through the melt layer. There may be significant variations in the size and morphology of the microstructure and in distribution of the phases through the melt layer. Because of the variation in the temperature gradient and rate of solidification, the solidification structure often varies through some range of cellular to dendritic characteristics and shows a coarsening of the microstructure and increasing segregation from the bottom to the top of the melt zone. Another effect is that the presence of the substrate in intimate contact with the melt layer promotes epitaxial solidification relationships between the resolidified melt layer and the substrate. This is particularly evident in the laser surface melted white cast iron shown in Figure 10, where there is a clear correlation between the iron carbide dendrites in the melted layer and the carbide orientation in the underlying grains.

Another source of non-uniformity of microstructure is caused by the presence of convective currents in laser melted pools and this plus electromagnetic stirring in electron beam melted pools. These melt currents create local differences in temperature and therefore solidification conditions, which often show up as "swirl-like" patterns in metallographic cross sections of the melt zone. These effects have been observed in a number of alloys, but primarily in nickel-base superalloys (17,18). These swirl patterns originate from local variations in growth direction, size of dendrites or cells, phase distribution and segregation. A laser melt showing very noticeable variations of this type is shown in Figure 11. Alternating copper- and silver-rich bands have been observed in copper-silver alloys by Beck et al (19). The magnitude of these variations will depend on the alloy's solidification characteristics, the complexity of the microstructure, and the melting conditions such as melt depth, preheat, and super heat. Modification of these conditions could afford some degree of control over this convective or mixing affect.

Another cause of non-uniformity is the heat affected zone surrounding the melt layer. This not only affects the material below the melt layer, but with the overlapping passes used to obtain area coverage, it affects the surface material along the edge of each succeeding pass. A representative example is shown in Figure 12. The darker lines delineating each succeeding pass define the heat affected zones intersecting the surface. Although heat affected zones cannot be avoided, their effects can be minimized by modifying the process parameters, selection of alloy composition, and post surface melting heat treatment. The extent of the heat affected zone is decreased by decreasing beam power and interaction times; these conditions will also decrease the melt depth. Alloy compositions less sensitive to aging or tempering during rapid excursions to higher temperatures will also minimize this effect. Post-processing heat treatment may tend to make the melt layer more uniform in structure. The presence of a hardened heat affected zone may be desirable where improved support is useful to support a thin surface melted or alloyed layer against wear or erosion.

In surface alloyed melts, in addition to the above effects, there is also the need for uniform mixing of the surface deposited alloy addition into the melt layer. This mixing occurs by both diffusion and the convective and electromagnetic (e-beam) currents. It is also influenced by the melting conditions used. In surface alloying of mild steel with molybdenum an indication of these effects was observed (20). The surface alloying was accomplished by melting a molybdenum powder layer into the steel surface. Under rapid melting conditions, the beam power was high enough that the molybdenum layer melted first and was mixed with the melted steel below primarily by convective mixing. This resulted in swirl patterns as shown in Figure 13a which appear to consist of iron rich melt regions having been carried up into the melt layers. A similar effect was observed for chromium surface alloyed in steel via an EDAX elemental map of the chromium distribution in the melt layer (21). The mixing is not homogeneous, but in general appears to be satisfactory for most applications.

A different situation can be developed if the alloy coating has a higher melting temperature than the substrate. For example at a low enough laser beam intensity a plasma sprayed molybdenum layer on a steel substrate was heated above the melting temperature of the underlying steel before the molybdenum melted. Melting then began at the molybdenum-steel interface, favoring diffusion over convective mixing of both constituents from the initiation of melting. This resulted in a much more uniform appearing melt zone, Figure 13b, indicating a more uniform distribution of molybdenum. There was still not uniformity of composition; point EDAX analysis of molybdenum in the melt layer in Figure 13b gave top center and bottom analyses of 33.2, 27.2, and 28.7 weight percent molybdenum. Alloyed surface layers having the highest additive concentrations at the top of the layer have often been observed (22).

An example of the relative influence of convection and diffusion of alloying elements in a laser melt is shown in Figure 14. In this case, the beam interaction time, τ_i , was 5×10^{-5} seconds, and the surface melt time was $\tau_m \approx (2 \text{ to } 5) \tau_i \approx 2 \times 10^{-4}$ sec. Using these parameters, the convective flow distance, S_c can be estimated from

$$S_c \sim (\tau_m \eta / \rho)^{1/2} \quad (1)$$

where ρ is the material density and η is the melt viscosity, and the diffusion distance S_d from

$$S_d \sim (\tau_m D)^{1/2} \quad (2)$$

where D is the liquid diffusion coefficient. These relations give $S_c \sim 1 \times 10^{-3}$ cm and $S_d \sim 1 \times 10^{-4}$ cm, or $S_c \approx 10 S_d$. These distances are consistent with the mixing effects represented by the flow lines from the interdendritic zones in the left half of Figure 14. The convective flow lines of the material from the interdendritic regions do extend about 10 to 15 μm . In addition the amount of diffusional smearing of the existing compositional lamellae near the surface of the melt is consistent with a nominal 1 μm distance.

Since the effects of directed energy beam processing relate to the in-depth thermal effects in the material being processed, it is necessary for a thorough understanding of the observed affects and basic studies of microstructure and property modification to have an analytical or modeling method to calculate local temperatures and heating and cooling rates. A number of models have been developed (23-25) and used (26) for determining these quantities, but the agreements with the observed effects is not yet sufficiently accurate to be of use as an independent analytical technique. Better methods for including the amount of absorbed energy from the beam, convective flow in the melt, heats of fusion and temperature dependent thermal properties are required to improve the predictive capabilities of the modeling approach.

Properties

As more directed beam materials processing work is being accomplished, increasing attention is being paid to the resulting property changes. The properties of primary interest are wear, erosion and corrosion resistance - a direct result of the surface modification aspects of the process.

Several studies have provided encouraging results. Laser surface melting has produced enhanced corrosion resistance in Mg-Zn (27) Al-Fe (28) alloys. In the material not surface melted, large intermetallic particles created galvanic corrosion cells on the material surface. Surface melting and rapid solidification caused these phases to be dissolved and subsequently maintained in solution or highly refined in the resolidified surface layer, thereby reducing corrosive attack.

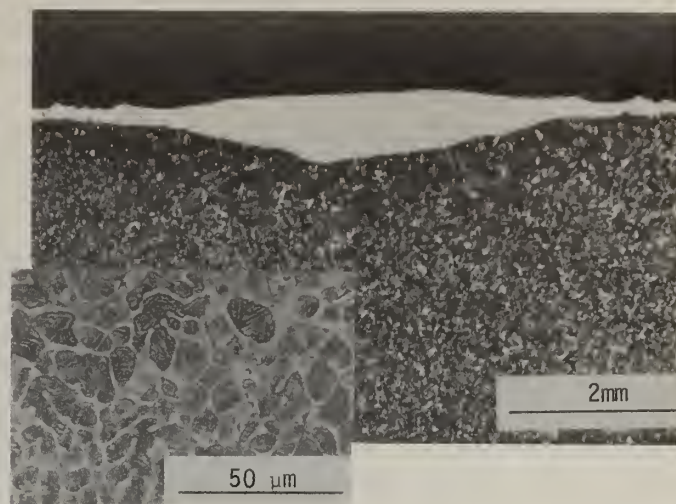
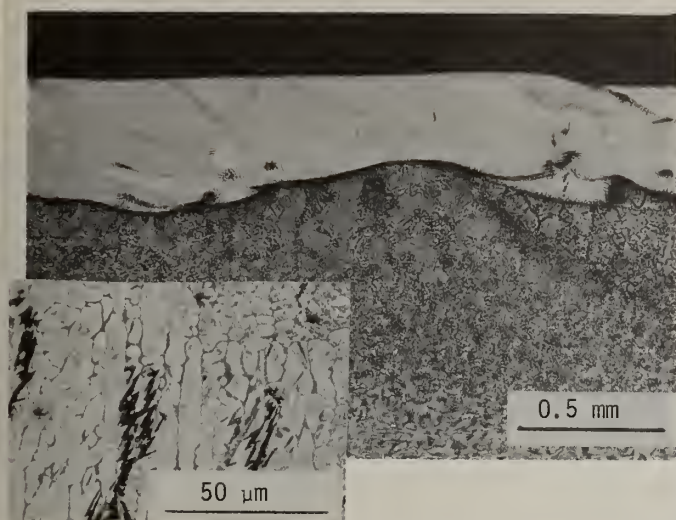
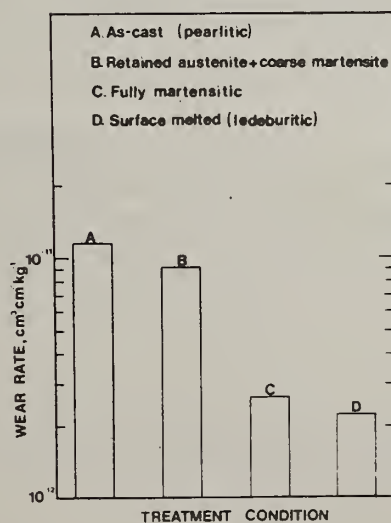


Figure 13. Appearance of laser melted steel coupons alloyed with molybdenum and carbon; (a) conditions favoring convective mixing, (b) conditions favoring diffusive mixing. Inserts show higher magnification views of alloyed zones.



Figure 14. Mixing patterns in a rapidly laser-surface melted layer of FeMoC alloy

Figure 15. Improvement in wear resistance of laser surface treated gray cast iron (from Bell, Ref. 30)



Cavitation erosion resistance of Al-Fe bronze was also increased by laser surface melting (29). The wear resistance of gray cast iron has been reduced by surface melting (30). In this case the surface melting develops a more rapidly solidified hard, white cast iron surface on a gray cast iron substrate. The improvements in wear are shown in Figure 15.

The use of surface melting or alloying in fatigue sensitive applications is limited by the residual tensile stresses developed during solidification of the surface layer. Laser surface melting of Ti-6Al-4V (31) significantly decreased its fatigue life. While the rapidly solidified microstructures contributed to this loss of fatigue strength, there is little doubt that the residual surface tensile stresses did also. The surface melted specimens contained numerous parallel surface cracks after fatigue testing whereas the unmelted specimens had single fracture origins.

For applications where residual tensile surface stresses will degrade the useful life, as in cyclic fatigue, fretting fatigue, stress corrosion cracking, hydrogen embrittlement, there may be benefits to be gained by application of a properly controlled alloy chemistry and microstructure. In addition to these effects, consideration of how to minimize or avoid the effects of residual tensile stresses must also be included in the process design and development.

Summary

Progress in the field of laser and e-beam surface processing of metals during the last 2 years can be summarized in the following conclusions.

In the case of glassy metallic surface layers by rapid surface melting, several methods have demonstrated success on small extended surface areas. However, the limited number of suitable alloys, thin amorphous case depths, and high residual tensile stresses limit the applicability of such glassy layers. These difficulties have decreased the interest in skin-melting processes in spite of the technical progress.

With respect to the microstructure encountered in rapidly solidified beam processed materials, metallurgical phases are comparable to those found in specimens prepared by other rapid quenching processes. That is to say, extended alloy solid solubilities, metastable phases, retention of high-temperature phases to room temperature, and glassy material can be produced. It is significant to note that no phases unique to beam processing have been reported to date.

While the crystallographic phases produced by beam processing are similar to other rapidly solidified materials, the microstructural arrangement of these phases can be different. For the most part these differences can be attributed to epitaxial solidification effects and melt convection inherent in the rapid heating rates employed.

In surface alloying, cladding and coatings consolidation, significant progress has been demonstrated in the areas of microstructural refinement, alloy mixing and metallurgical bonding of treated layers. Process development has extended coverage to somewhat larger areas and various sample geometries. Many of the effects inhibiting this development relate to surface smoothness, consistency over larger process areas, and thermal stresses.

Finally, the engineering, property data base for beam processed materials needs to be greatly improved. Data on wear and corrosion of surface melted and alloyed samples have recently appeared in the literature, but this data is insufficient to draw any general trends or make meaningful comparisons with competing technologies. Property evaluation should receive the most attention in this field in near term studies.

Acknowledgement

Portions of this work which were performed by the authors was supported by the Army Research Office, Research Triangle Park, North Carolina.

References

1. Breinan, E. M., Kear, B. H., and Banas, C. M., Physics Today, 29 (11), p. 44 (1976).
2. Breinan, E. M., Kear, B. H., Banas, C. M., and Greenwald, L. E., Superalloys, Metallurgy and Manufacture, Claitor's Publishing Div., Baton Rouge, Los Angeles (1976), p. 435.
3. Tucker, T. R. and Ayers, J. D., Met. Trans. A, 12A, p. 1805 (1981).
4. Tucker, T. R. and Ayers, J. D., Rapid Solidification Processing, Principles and Technologies II, Claitor's Publishing Div., Baton Rouge, Los Angeles (1980), p. 206.
5. Tucker, T. R., Ayers, J. D., and Schaefer, R. J., Laser and Electron Beam Processing of Materials, Academic Press, New York, New York (1980), p. 755.
6. Bergmann, H. W. and Mordike, B. L., J. Mat. Sci., (16), p. 863 (1981).
7. Mordike, B. L., and Bergmann, H. W., Rapidly Solidified Amorphous and Crystalline Alloys, Elsevier Science Publishing Co., New York, New York (1982), p. 463.
8. Laser and Electron Beam Processing of Materials, C. W. White and P. S. Peercy, ed., Academic Press, New York (1980), p. 747.
9. Lasers in Metallurgy, The Metallurgical Society of AIME, Warrendale, Pennsylvania (1981), p. 33.
10. Rapid Solidification Processing, Principles and Technologies II, Claitors Publishing Div., Baton Rouge, Los Angeles (1980), p. 221.
11. Rapidly Solidified Amorphous and Crystalline Alloys, Elsevier Science Publishing Co., (1982), p. 535.
12. Anthony, T. R. and Cline, H. E., J. Appl. Phys., 48, p. 3888 (1977).
13. Esquirel, O., Mazumder, M., Bass, M., and Copley, S., Rapid Solidification Processing, Principles and Technologies II, Claitors Publishing Div., Baton Rouge, Los Angeles (1980), p. 180.
14. Kurup, M., Lewis, B. G., and Strutt, P. R., Lasers in Metallurgy, The Metallurgical Society of AIME, Warrendale, Pennsylvania (1981), p. 33.
15. Powell, J. and Steen, W. M., Lasers in Metallurgy, The Metallurgical Society of AIME, Warrendale, Pennsylvania (1981), p. 93.
16. Mordike, B. L. and Bergmann, H. W., Rapidly Solidified Amorphous and Crystalline Alloys, Elsevier Science Publishing Co. (1982), p. 463.
17. Lipscomb, K., Steen, W. M., and West D. R. F., Rapid Solidification Processing, Principles and Technologies II, Claitor's Publishing Div., Baton Rouge, Los Angeles (1980), p. 189.
18. Draper, C. W., Preece, C. M., and Jacobsen, D. C., Laser and Electron Beam Processing of Materials, C. W. White and P. S. Peercy, ed., Academic Press, New York (1980), p. 721.
19. Beck, D. G., Copley, S. M., and Baas, M., Laser and Electron Beam Processing of Materials, C. W. White and P. S. Peercy, ed., Academic Press, New York (1980), p. 734.
20. Tucker, T. R., Clauer, A. H., and Ream, S. L., Rapidly Solidified Amorphous and Crystalline Alloys, Elsevier Science Publishing Co. (1982), p. 541.
21. Weinman, L. S., Devault, J. N., and Moore, P., Applications of Lasers in Materials Processing, American Society for Metals, Metals Park (1979), p. 245.
22. Gnanamuthu, D. S., Applications of Lasers in Materials Processing, American Society for Metals, Metals Park (1979), p. 177.
23. Cline, H. E. and Anthony, T. R., J. Appl. Phys., 48, p. 3895 (1977).
24. Sekhar, J. A., Mehrabian, R., and Fraser, H. L., Lasers in Metallurgy, The Metallurgical Society of AIME, Warrendale, Pennsylvania (1981), p. 207.

25. Chande, T. and Mazumder, J., Lasers in Metallurgy, The Metallurgical Society of AIME, Warrendale, Pennsylvania (1981), p. 165.
26. Tucker, T. R., Clauer, A. H., Walters, C. T., and Ream, S. L., Lasers in Metallurgy, The Metallurgical Society of AIME, Warrendale, Pennsylvania (1981), p. 53.
27. Kattanis, T. Z., Lasers in Metallurgy, The Metallurgical Society of AIME, Warrendale, Pennsylvania (1981), p. 1.
28. Draper, C. W., Vandenburg, Preece, C. M., and Clayton, C. R., Rapidly Solidified Amorphous and Crystalline Alloys, Elsevier Science Publishing Co. (1982), p. 529.
29. Draper, C. W., Lasers in Metallurgy, The Metallurgical Society of AIME, Warrendale, Pennsylvania (1981), p. 21.
30. Bell, T., Metallurgia, 49 (3), p. 103 (1982).
31. Bayles, R. A., Meyn, D. A., and Moore, P. G., Lasers in Metallurgy, The Metallurgical Society of AIME, Warrendale, Pennsylvania (1981), p. 127.

INTERFACE RESPONSE IN LASER-MELTED ALLOYS

S. M. Copley, D. Beck and M. Bass

University of Southern California
Los Angeles, CA 90089-0241

ABSTRACT

By scanning the surface of a metal or alloy with a focused CW-CO₂ laser beam, it is possible to melt and solidify it at high rates. In Ag-Cu alloys, we have shown that sufficient kinetic undercooling can be attained by this method to form the metastable extended solid solution. For a Ag-38.3 at pct. Cu alloy scanned at 34 cm s⁻¹ to produce the metastable solid solution, thermodynamic considerations indicate that an undercooling of at least 52°C was attained. Metallographic examination of melt trails revealed the presence of regularly spaced bands approximately marking sequential positions of a planar melt-solid interface. These bands correspond to fluctuations in concentration of at least 1.1 at pct. Their presence suggests that the interface may have an oscillating steady state motion. Implications of the banding phenomenon will be discussed with respect to mass and thermal transport at the melt solid interface and characteristics of the interface response function.

Introduction

The name rapid solidification processing (RSP) has been applied to solidification processes in which the cooling rate is greater than 100°Ks⁻¹ [1]. In such processes, it has long been recognized that equilibrium may not exist at the melt-solid interface. Deviations from equilibrium may occur for two reasons: (1) suppression of nucleation of the equilibrium phase(s) due to rapid cooling; and (2) kinetic undercooling due to high solidification rates.

We summarize here the results of an investigation of the rapid solidification of Ag-Cu alloys. Rapid solidification was attained by scanning the surface of Ag-Cu alloy specimens with a continuous wave, carbon dioxide laser beam. Two aspects of our research will be described: (1) estimation of melt-solid interface temperature; and (2) observations of variations in solute concentration along the direction of local interface motion (banding) and speculation as to its origin.

Laser Melting and Solidification

In our experiments, the specimen was mounted to a turntable and rotated under the laser beam. Single trails resulted from a single rotation. Multiple overlapping trails were produced by multiple rotations accompanied by a continuous translation of the turntable perpendicular to the laser beam.

The laser beam had a Gaussian spatial distribution of intensity and diameter (1/e²) of 196 μm. A flow of inert gas was maintained over the specimen surface. Absorption of the incident radiation was enhanced by a graphitic coating. Conduction of heat from the substrate to the turntable was increased by use of a conductive cement.

Viewed in a frame of reference that is stationary with respect to the laser beam, laser melting and solidification may be considered to be a quasi-steady-state process. Accordingly, the shape of the melt pool, which is shown schematically in Fig. 1, does not change with time and the local interface velocity is given by the equation

$$V = V_0 \cos \theta \quad (1)$$

where V_0 is the velocity of the specimen with respect to the laser beam and θ is the angle between the normal to the melt-solid interface and the specimen velocity. For the melt pool shown in Fig. 2, the interface velocity in the center plane varies from 0 at the bottom of the pool to 0.95 V_0 at the top.

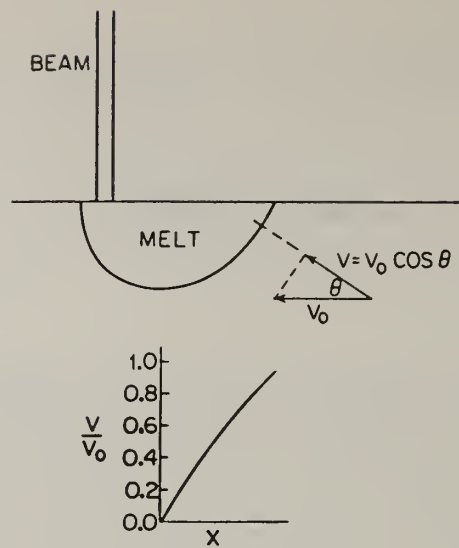


Figure 1 Interface velocity varies with angle θ along the back edge of the melt pool.



Figure 2 Melt pool sectioned perpendicular to the direction of specimen translation. (Marker indicates $7.5 \mu\text{m}$)

A photomicrograph of a melt pool sectioned perpendicular to the direction of motion is shown in Fig. 2. The specimen velocity was 34 cm s^{-1} and the incident beam power was 1090W. Both the Cu-rich phase (dark, dispersed) and the Ag-rich phase (light, continuous) can be seen in the unmelted region. It was not possible to dissolve the Cu-rich phase at a beam velocity of 34 cm s^{-1} . After laser melting and solidification, the composition in the melt trail was inhomogeneous as evidenced by decoration of the convection swirls on the left hand side of the melt pool. In order to attain a uniform composition in melt trails formed at 34 cm s^{-1} , a laser premelting step involving scanning the surface 10 cm s^{-1} using the same beam power was employed. This resulted in a uniform composition as can be seen at the right hand side of the melt pool, which overlapped a trail premelted at 10 cm s^{-1} .

It is clear by examination of Fig. 2 that the melt is in contact with both the Ag-rich and Cu-rich equilibrium phases during solidification. Thus, in laser melting and solidification, deviations from equilibrium must be the result of kinetic undercooling due to the high interface velocity rather than the suppression of nucleation due to the high cooling rate.

Melt-Solid Interface Temperature

The Ag-Cu equilibrium diagram shows two equilibrium phases, α (Ag-rich) and β (Cu-rich), which form from the melt by a eutectic reaction at 1052°K [2]. Both Ag and Cu are face centered cubic and years ago Duwez, Willens and Klement showed that metastable extended solid solutions could be formed across the α - β phase field by "splat cooling" [3]. In laser melting and solidification experiments, it is very difficult to measure directly the melt solid interface temperature. We have taken an indirect approach to determining the interface temperature which yields an upper bound. In our approach we determine $T_0(C)$, the maximum temperature at which it is thermodynamically possible to form the metastable extended solid solution from a melt of the same composition (C). We examine melt trails produced at different powers and velocities employing x-ray diffraction. If the metastable extended solid solution is detected, the melt-solid interface temperature must have been less than $T_0(C)$.

In order to determine $T_0(C)$, we must know the Gibbs free energy of mixing (ΔG_{mix}) as a function of composition for both the solid and liquid phases. We have calculated $\Delta G_{\text{mix}}^{\text{S}}$ for the solid phase employing the Lumsden solution model [4,5], and $\Delta G_{\text{mix}}^{\text{L}}$ for the liquid phase, extrapolating thermochemical measurements made at higher temperatures. Details of the calculations are published elsewhere [6].

Figure 3 is a plot of ΔG_{mix} for the solid and liquid phases calculated at 1003°K. Two points on the $T_0(C)$ curve (see Fig. 4) corresponding to 1003°K are established by noting the compositions where $\Delta G_{\text{mix}}^{\text{L}} = \Delta G_{\text{mix}}^{\text{S}}$. For $C < 0.381 \text{ a/o Cu}$ or $C > 0.676 \text{ a/o Cu}$, the Gibbs free energy decreases if liquid is transformed to solid of the same composition and thus such a transformation is possible. Points on the metastable solidi and liquid curves at 1003°K are determined by the common tangent rule.

Figure 4 shows a phase diagram for the Ag-Cu system. The equilibrium diagram is based on that of Hansen and Anderko [2]. The T_0 curve and metastable solidi and liquid curves were calculated previously by us [6]. Triangular and diamond shaped points on the diagram are used to indicate compositions where laser melting and solidification experiments have been carried out with the objective of producing and detecting the metastable phase.

Initial experiments involved scanning electron microscopic examination of trails laser melted at a scan speed of 0.7 cm s^{-1} in Ag electroplated with Cu. Primary Ag-rich dendrites and a very fine plate-like eutectic microstructure were observed throughout the melt zone [7]. Further experiments were conducted at a scan speed of 10 cm s^{-1} on alloy compositions indicated by the triangles in Fig. 4. The metastable extended solid solution was detected by x-ray in single trails for all three alloys [8]. Thus, the maximum possible interface temperatures were 795, 700 and 779°K for the Ag-25 at pct Cu, Ag-50 at pct Cu and Ag-75 at pct Cu alloys, respectively.

Still further experiments were carried out employing a scan speed of 34 cm s^{-1} with alloy compositions indicated by the diamonds in Fig. 4. In these experiments, the surface was covered by multiple overlapping trails. The metastable extended solid solution was detected by x-ray in the Ag-18 at pct Cu, Ag-28.2 at pct Cu and Ag-38.3 at pct Cu alloys. [6] Thus the maximum possible interface temperatures were 838, 771 and 727°C for these alloys, respectively. No metastable solid solution was detected at the compositions indicated by the open diamonds. It is believed that the metastable extended solid solution was probably present initially in the trails but decomposed to α and β due to additional heating associated with the multiple overlapping procedure.

Figure 5 shows the $\{111\}$ reflections from an x-ray scan of the laser melted and solidified layer for the Ag-38.3 at pct Cu alloy (eutectic composition). Four peaks were detected in the as-irradiated sample (0.0 sec) corresponding to the Ag-rich equilibrium solid solution (α), a Ag-rich meta-

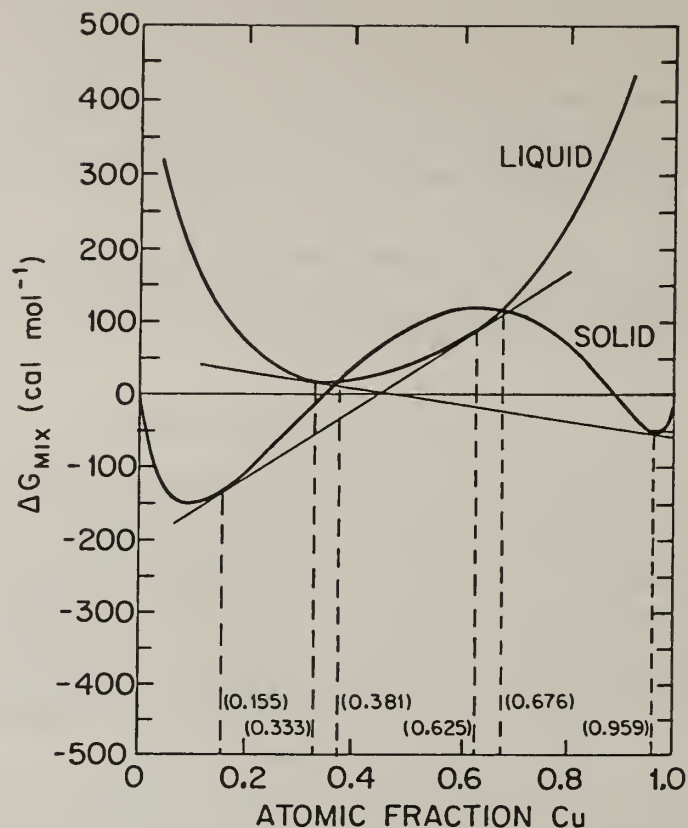


Fig. 3 ΔG_{mix} versus composition curves for solid and liquid phases at 1003°K illustrating determination of points for the T_0 -curve, metastable solidi curves and metastable liquid curves.

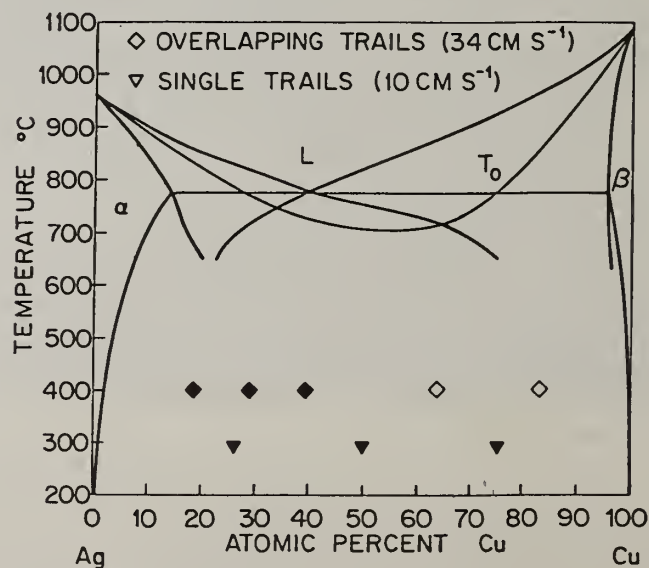


Fig. 4 Ag-Cu phase diagram showing T_0 -curve, metastable solidi curves and metastable curves. Diamonds and triangles indicate compositions investigated.

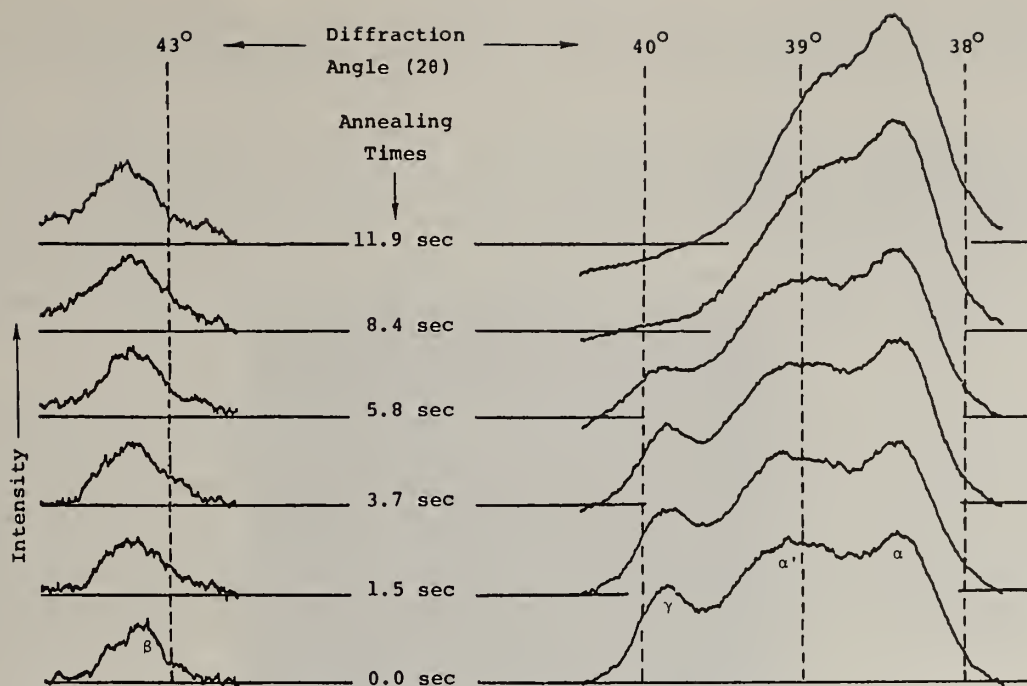


Fig. 5 The {111} diffracted intensity for an x-ray scan of a laser melted and solidified layer on a Ag-38.3 at pct Cu alloy.

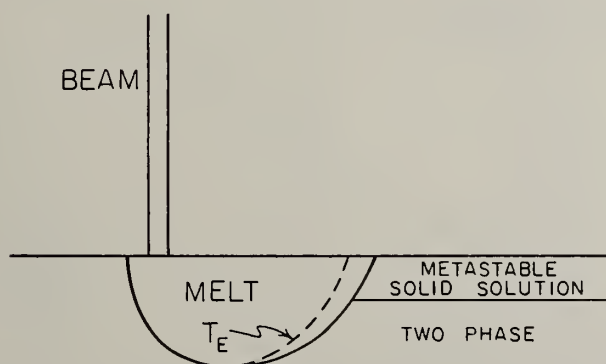


Fig. 6 Schematic drawing showing proposed structure of laser melted trail in Ag-38.3 at pct Cu alloy.

stable solid solution designated α' , the metastable extended solid solution having the same composition as the alloy (γ) and the Cu-rich equilibrium solid solution (β). Also shown in Fig. 5 is the effect of annealing at 420°C for various periods of time on diffracted intensity. As would be expected, the intensity of the γ -peak decreased while that of the α -peak increased with increasing annealing time.

The x-ray response of the Ag-38.3 Cu alloy can be understood if the upper region of the trails solidified as the metastable extended solid solution while the lower region solidified with the two-phase eutectic microstructure as shown schematically in Fig. 6. This arrangement phases is likely because the lower region solidified with a lower interface velocity and hence a higher interface temperature than the upper region. Such an arrangement should produce a strong γ -peak and broad α' -peak for the Ag-rich eutectic phase corresponding roughly to the metastable solidus. The α and β peaks were diffracted from regions where the metastable extended solid solution decomposed to form the equilibrium phases. No separate β' peak corresponding to the Cu-rich eutectic phase was detected because it was masked by the β peak owing to the steepness of the metastable β solidus.

The observed lattice parameters for α , α' , β and γ phases in the Ag-38.3 at pct Cu alloy are shown in parentheses in Fig. 7. The arrows labeled α_{\max} and β_{\max} indicate the lattice parameters of terminal solid solutions corresponding to the maximum solid solubility limit. The values of the lattice parameters observed for the α and β phase indicate that they were formed by solid state precipitation. The arrow for the γ phase is based on the work of Duwez et al. [3]. The lattice parameters of the γ phases in the Ag-38.3 at pct Cu alloy and the other alloys investigated are in good agreement with those predicted from Duwez et al.'s work. The lattice parameter of the α' phase is significantly smaller than that predicted from the metastable solidus indicating a more Cu-rich composition. This observation suggests that solute trapping may occur at the melt- α' interface during solidification.

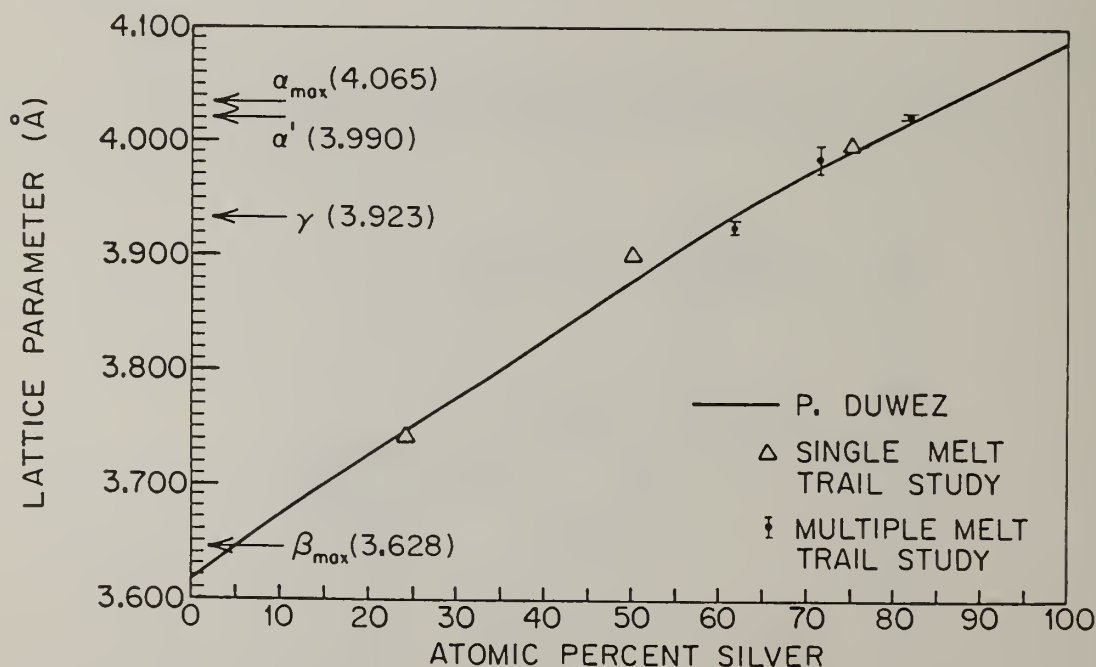


Fig. 7 Comparison of observed lattice parameters to those of Duwez et al.

Solute Banding

We have previously reported the occurrence of variations in solute concentration along the direction of local interface motion in laser melted and solidified trails [9]. These variations produce solute bands that approximately mark sequential positions of the melt-solid interface during solidification. Figure 8 shows such bands revealed by etching in a Ag-50 at pct Cu alloy. Statistical analysis of the results of an energy dispersive x-ray analysis of the compositions of the light and dark bands is given in Table 1 and showed that to the 99.9 confidence level they were different. The average atomic fraction of Ag was found to be at least 1.1 at pct greater in the light bands than the dark bands. Actually the difference was probably greater because the sampling volume was approximately 1 μm in diameter due to the depth of penetration, while the bands being studied are less than 1 μm in width.

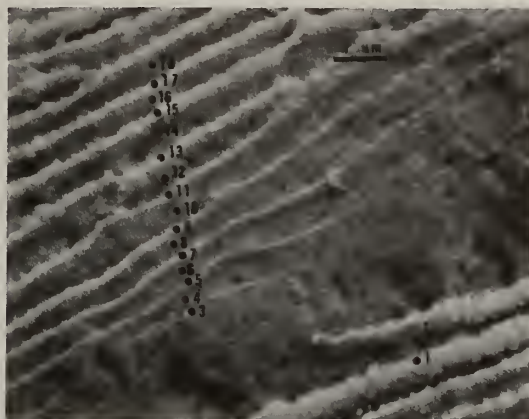


Fig. 8 Heavily etched bands - Cu 50 at pct Ag.

Table 1. Concentrations Found For Points in Figure 8

Pair Number (Points)	Ag Concentration	
	Light Band	Dark Band
1 (1&2)	80.3	78.6
2 (3&4)	71.0	70.1
3 (5&6)	71.8	70.1
4 (7&8)	71.6	70.2
5 (9&10)	69.7	69.3
6 (11&12)	70.0	70.0
7 (13&14)	71.2	69.9
8 (15&16)	71.7	69.9
9 (17&18)	69.9	69.2
10 (19&20)	79.4	78.1
(off picture)		

We have proposed that the solute bands observed in laser melted and solidified trails are evidence for planar, oscillating, steady-state interface motion. Further, we have suggested that such motion might be explained on the basis of heat and mass transport at an undercooled planar interface, if sufficient information regarding the interface response functions were known [6]. Although, neither kinetic theories nor experimental data are available which define these functions, thermodynamics places some limitations on them. These limitations can be conveniently described by a diagram developed by Baker and Cahn [10].

Figure 9 shows a Baker-Cahn type diagram, we have calculated for the Ag-Cu system. The range of solid compositions, C_S , that can form with a net decrease in free energy from a liquid of composition, C_L , at a specific interface temperature lie within or on the closed loop corresponding to that temperature. For steady-state solidification, C_S must equal the alloy composition, C_0 .

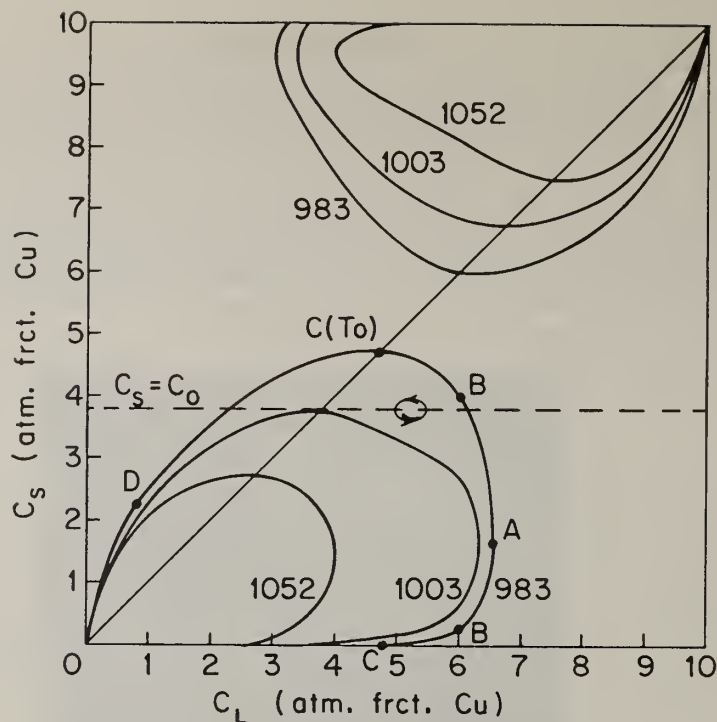


Fig. 9 The range of compositions that can form with a net decrease in free energy from a liquid of composition C_L . For steady-state solidification C_S must equal the alloy composition C_0 .

Consider, for example, steady state solidification of an Ag-38.3 at pct Cu alloy (eutectic composition). The diagram, Fig. 9, indicates three cases:

- (i) For interface temperatures greater than 1003°K, e.g. 1052°K, it is thermodynamically impossible for a metastable solid solution with the eutectic composition to form from a melt with any composition.
- (ii) For an interface temperature equal to 1003°K, a metastable solid solution with the eutectic composition can form but only from a melt with the same composition.
- (iii) For interface temperatures less than 1003°K, e.g. 983°K, it is possible for a metastable solid solution with the eutectic composition to form from melts with compositions ranging from Ag-24 at pct Cu to Ag-61 at pct Cu.

In case (iii), kinetics dictates which value of C_L lying within the allowed limits will occur.

With the appropriate interface response functions, it may be possible to find oscillating steady-state solutions for the coupled heat and mass transfer equations at the moving interface. We speculate that if such solutions exist, it might be possible to determine experimentally interface response functions through measurement of the spacing and concentration variation of solute bands. An oscillatory solution, which can be shown as a closed curve, see arrows in Fig. 9, may under certain circumstances lead to cellular interface breakdown through a diffusional instability described by Baker and Cahn [10]. For a melt composition approaching the limiting Cu-rich composition, a downward fluctuation in solid composition may cause the melt composition to move outside the range where steady state solidification is possible. In this case, the plane front interface would break down and lag back to a lower temperature. Evidence for such breakdown has been observed in laser melted and solidified eutectic melt trails (see Ref. 6, Fig. 12).

Acknowledgment

This work was supported in part by the National Science Foundation, Metallurgy Program, Grant No. DMR 78-07532.

References

- [1] M. Cohen, B.H. Kear and R. Mehrabian, "Rapid Solidification Processing - An Outlook" in Rapid Solidification Processing, edited by R. Mehrabian, B.H. Kear and M. Cohen. Claitor's Publishing Division, Baton Rouge, LA (1980).
- [2] M. Hansen and K. Anderko, Constitution of Binary Alloys, McGraw Hill Book Co., New York, NY, 1958, p. 18.
- [3] P. Duwez, R. H. Willens, and W. Klement, Jr., J. Appl. Phys., 1960, vol. 31, pp. 1136-37.
- [4] John Lumsden, Thermodynamics of Alloys, The Institute of Metals, London, 1952, p. 335.
- [5] B. E. Sundquist, Trans. TMS-AIME, 1966, vol. 236, pp. 1111-22.
- [6] D. G. Beck, S. M. Copley and M. Bass, Met. Trans. 13A, 1879-89 (1982).
- [7] S. M. Copley, M. Bass, E. W. Van Stryland, D. G. Beck, and O. Esquivel, "Microstructures of Surface Alloyed Ag-Cu Films Produced by Laser Melt Quenching," Proc. III Int. Conf. Rapidly Quenched Metals, vol. 1, pp. 147-50, The Metals Society, London, 1978.
- [8] D. G. Beck, S. M. Copley, and M. Bass, "Constitution and Microstructure of Ag-Cu Alloys Produced by Continuous Laser Melt Quenching," Laser and Electron Beam Processing of Materials, C. W. White and P. S. Peercy, Eds., pp. 734-39, Academic Press, NY, 1980.
- [9] D. G. Beck, S. M. Copley and M. Bass, Met. Trans. 12A, 1687-91 (1981).
- [10] James C. Baker and John W. Cahn, Solidification, ASM, Metals Park, OH, 1971, pp. 23-58.

INFLUENCE OF ELECTRON BEAM SCANNING PARAMETERS ON SURFACE MELTING AND HEAT TREATMENT CHARACTERISTICS

P. R. Strutt, M. Kurup and A. Taquir

Metallurgy Department, University of Connecticut,
Storrs, CT, 06268

1. Introduction

The unique feature of directed energy beam materials processing is the ability to form fully consolidated and perfectly bonded rapidly solidified layers on a surface. The actual energy source may produce electrons, ions, or photons, for instance, and in each case the particles may be focussed into a concentrated beam. This beam may then be rapidly deflected across a substrate surface by optical or electromagnetic means, thereby forming a rapidly solidified layer. Other rapid solidification processing methods, in contrast, cannot directly form such a layer, since the as-formed material is either produced as a powder or ribbon.

The particular advantages of using an electron beam as an energy source are (i) the high efficiency of energy coupling between the beam and material [1], and (ii) the facility with which the beam may be deflected electromagnetically [2]. Recent studies of "electron beam glazed" hard iron-base materials shows there to be a considerable enhancement in:

- (i) microhardness [3]
- (ii) wear resistance [4 and 5]
- (iii) resistance to chemical attack [5].

These specific features show the technological significance of the technique in increasing the performance of components used in cutting and machining and in applications requiring high wear resistance. A particular application would be in the development of mainshaft bearings used in high performance military engines capable of operation at speeds up to 3 million DN [6]; D is the diameter in millimeters and N the number of revolutions per minute. Presently there is a need for an inner-race with a surface that will withstand excessive bearing and wear forces, larger Hertzian stresses, and corrosion pitting [7]. However, the body of the race must possess good toughness and notch fatigue properties. Obviously, electron beam surface melting provides a method for producing the required dual properties. Using the technique it would thus be possible to develop an inner race with a surface possessing good rolling contact fatigue [6] and good corrosion resistance and a body combining moderate strength with good toughness and notch fatigue properties [6].

Naturally, the sophisticated application of "electron beam glazing" just discussed requires a precise knowledge of factors determining the homogeneity, morphological characteristics, tempering characteristics, and surface topography of wide surface melted traces. The present paper summarizes recent studies of these aspects and considers specific aspects in detail, such as, the circumstances in which a scanning beam either acts as a "linear heat source" or "moving point source".

2. Surface Area Melting

An electron beam may rapidly scan across a surface in a variety of ways either by two-axis electromagnetic deflection [2] or by single-axis electromagnetic deflection combined with a mechanical stage translation [8-11]. In essence however, all types of scanning may be characterized as being either of the (i) moving point source or (ii) linear heat source type, these two modes are now considered in some detail. A separate section on two-axis electromagnetic deflection is included, this, in essence, is an alternative form of point source melting.

2.1. Moving Point Source Melting

We envisage in Fig. 1 that a strip of rapid solidified material is formed by an oscillating electron incident upon a moving substrate surface. Constant velocity of the beam as it moves to and fro requires that the field in the electromagnetic deflection yoke responds linearly to an applied triangular waveform excitation voltage. This is achieved by employing a low inductance coil (in the microhenry range) driven by ultra-high rate response current amplifiers. Presently, a high degree of linearity is attainable at frequencies < 15 kHz using a triangular waveform excitation signal. Under these conditions a uniform depth of melting is obtained with no detectable dwelling of the beam at the amplitude maxima.

As the situation is depicted in Fig. 1 the movement of the specimen translation stage per cycle of beam oscillation is nearly equal to the beam diameter. Under this condition the entire strip of glazed material is formed with minimal overlap of successfully melted traces. Generally, however, any degree of overlap may be obtained simply by selecting appropriate values of oscillation frequency (f) and specimen stage velocity (V).

Figure 2 shows an actual processed surface formed by a scanning point heat source where the familiar surface ripple structure is well evident along the individual traces. The material in Fig. 1 is a high carbon (1.5 wt.%), low alloy (1.5 wt.% Cr) steel whose composition is given in Table I. In this particular instance the beam oscillation frequency is low (62.5 hertz) and beam has a power of 170 watts and a focussed diameter of 0.035 cm. The value of w , the width of the rapidly solidified strip, is ~ 2 mm; V is 1.7 cm.s^{-1} .

The successively overlapping zones of the strip of material seen in Fig. 2 are also shown in the corresponding longitudinal section in Fig. 3. The striking feature in Fig. 3 is the homogeneous appearance of the "as-glazed" martensitic structure throughout the entire surface melted region with no evidence of microstructural change where successive zones overlap. The homogeneous nature of the martensitic structure is further confirmed by careful examination at high magnification in the scanning electron microstructure, a typical field of view is shown in Fig. 4. Interestingly, this microstructure is similar in type to that formed in the same material by thermomechanical processing followed by cryogenic quenching [12]. The fact that the microstructure can be produced by a short duration-single step process is thus rather intriguing both from a metallurgical viewpoint and in terms of electron beam processing technology.

The absence of any change of the martensitic structure in the zone overlap regions indicates that the ambient temperature in a zone is above that for the $\gamma \rightarrow \alpha$ transition when the adjacent zone solidifies. It has been demonstrated that a significant delay time between the formation of adjacent zones results in appreciable microstructural modification where the zones overlap. These findings are serendipitous in that they show that an undesirable microstructural feature may readily be avoided when forming rapidly solidified surface layers.

2.2. Two-axis Electromagnetic Deflections

Surface scanning studies have shown that particularly smooth surface may be formed using a scanning pattern obtained by applying two triangular waveform signals of nearly equal frequency to the x and y axes of the beam deflection yoke. This mode has been used previously for generalized surface heating [2]. The succession of rectangular Lissajous figures traced out in this scanning mode are shown in Fig. 5 where x and y axis deflections of the spot on the substrate have maximum values of a and b respectively. The rectangular path results from the progressively increasing amount of phase lag between the two frequencies. As the beam sweeps diagonally across from point A (where the phase lag is zero) the path intercepts the line BC when the x axis deflection amplitude attains its maximum value: the intersection point is at a distance $(b\Delta f/f)/(1 + \Delta f/f)$ below point C. After this the path next intercepts line CD when the y axis amplitude attains its maximum value. The distance of this intercept point to the left-hand side of point C is $a\Delta f/f$. In proceeding in this way it is readily apparent how the successive rectangular type of scanning pattern is obtained. A simple consideration shows that the angle θ in Fig. 5 is given by

$$\tan \theta = \frac{b}{a} \frac{1}{1 + \Delta f/f} \quad (1)$$

Also by geometrical construction the spacing d between two adjacent diagonal traces is given by

$$d = \frac{2ab\Delta f/f}{\{a^2(1 + \Delta f/f)^2 + b^2\}^2} \quad (2)$$

It should be noted at this juncture that no mention has been made of the actual beam spot diameter w . When considering a beam of finite width the diagonal lines in the pattern will represent the path traced out by the center of the spot.

In considering the n th cycle, the beam path intercept on line BC is a distance y_n away from point C:

$$y_n = \frac{(2n - 1)(\Delta f/f)b}{1 + \Delta f/f} \quad (3)$$

Equation (3) can be used to find n , the number of cycle required to sweep out the entire area ABCD, simply by noting that y_n will then be equal (or almost equal) to b . The precise condition is given by

$$n > \frac{1}{2} \frac{\Delta f}{f} > n - 1 \quad (4)$$

It should be noted that, although the time to complete a frame is n/f , the line spacing is frequency independent and depends on the ratio $\Delta f/f$.

Typical micrographs showing sequential changes in topography in two-axis electromagnetically scanned surfaces are shown in Figs. 6 and 7, in this case the substrate material is M2 high speed steel, see Table I for the composition. Low magnification micrographs of regions glazed for a frequency of 60 Hz are shown in Fig. 6 where Fig. 6(a) shows part of successive glazed traces obtained for $\Delta f/f = 1/150$. With this value of $\Delta f/f$ the number of cycles per frame is 75 and the surface finish obtained after a complete frame is shown in Fig. 6(b). As is evident from eqn. (2), the effect of decreasing the ratio $\Delta f/f$ is to reduce the spacing distance d and as a result to produce overlapping of melting zones when $w > d$ where w is the beam diameter. An intriguing finding is the remarkable increase in surface uniformity as $\Delta f/f$ is progressively decreased. This became strikingly evident when Figs. 6(b), 6(c) and 6(d) were compared, for which the corresponding values of $\Delta f/f$ are 1/150, 1/450 and 1/600; in each case the value of f is 60 Hz. The experimental and calculated values of d are given in Table I for results obtained both at 30 Hz and at 60 Hz. Figures 7(a), 7(b) and 7(c) show the surface topographies of the specimens corresponding to Figs. 6(b), 6(c) and 6(d) at a higher magnification.

The overlapping of glazed zones is clearly seen in cross-sectional view, as shown in Fig. 6. It seems reasonable that the rather dramatic increase in surface uniformity achieved by repetitive melting and solidification arises from the dispersion or evaporation of surface contaminants. This cleansing promotes progressively better melting of the solid surface by molten liquid during each successive cycle. By examination of the micrographs it is evident that it is possible to eliminate the "ripple structure" and to obtain a surface with minimal periodic topographical variation.

2.3 Line Source Surface Melting

As previously discussed microstructural change due to transient heat flow from adjacent passes may be avoided by ensuring that the temperature in a zone exceeds that for the $\gamma \rightarrow \alpha$ transition when the neighboring zone solidifies. Another approach, however, is to wave a linear heat source across the entire width of the specimen, see Fig. 9. Such a source is conveniently produced by rapidly oscillating an electron beam and by slowly moving the substrate material. The analysis to be presented examines the range of parametric values required to area glaze in this particular mode; the parameters include power density, oscillation frequency, and translation velocity.

The requirement for a rapidly oscillating beam to act as a linear melting source is that in any one cycle the material at one extremity remains molten until the beam returns on completion of the cycle. In order to express this condition analytically we use the Greenwald heat transfer analysis [12]. On the basis of this particularly simple analysis the peak temperature attained at point on the surface, such as the reference extremum previously mentioned, is given by equation 5.

$$T_p = ab\tau^{1/2} + T_R \quad (5)$$

where T_R is the residual temperature due to the undissipated heat from previous cycles. Here we neglect the ambient chamber temperature T_0 since it is relatively small. The interaction time is τ and the parameters a and b are given by

$$a = (4\alpha/\pi)^{1/2}; \quad b = q_0/\kappa \quad (6)$$

In this equation α and κ are the thermal diffusivity and thermal conductivity and q_0 the incident beam power density (in watts per cm^2). If we assume that the actual spot oscillates in a perfectly linear manner across the surface at a frequency of f then τ is equal to $d/2wf$, where d is the spot diameter and w the width of oscillation as measured on the specimen surface. In substituting $d/2wf$ for τ in equation 5 we obtain equation 7 for the temperature difference ($T_p - T_R$);

$$(T_p - T_R) = ab(d/2w)^{1/2} \cdot (1/f)^{1/2} \quad (7)$$

The residual temperature T_R at the extremum may be determined by applying N number of iterations to an expression in ref. [13]. The result of this is given by equation 8.

$$T_R = \sum_1^N ab \{ (n/f)^{1/2} - (n/f - d/2wf)^{1/2} \}; \quad (8)$$

Equations 7 and 8 express the irradiation temperature ($T_p - T_R$) and the residual temperature T_R in terms of parameters, which include the number of cycles N ; their ratio is given by equation 9.

$$T_R/(T_p - T_R) = \frac{\sum_1^N n^{1/2} - \sum_1^N (n - d/2w)^{1/2}}{(d/2w)^{1/2}} \quad (9)$$

Now, for material at the reference position to remain molten when the beam returns there after a cyclic excursion the value of T_R must equal the melting point temperature T_m . It is now convenient to define the ratio $T_R/(T_p - T_R)$ by the parameter ξ , where T_R is equal to T_m ($\sim 1500^\circ\text{C}$ for iron). The condition that the vaporization temperature not be exceeded ($T_V \sim 2900^\circ\text{C}$) requires that $\xi > 1$, an alternatively that the irradiation temperature ($T_p - T_R$) be less than T_m . This now gives equation 10.

$$\sum_1^N n^{1/2} - \sum_1^N (n - d/2w)^{1/2} = \xi \cdot (d/2w)^{1/2} \quad (10)$$

The solution to the problem, therefore, is to determine the value of N satisfying equation 10. This value is, in effect, the number of cycles required to maintain a molten state on the substrate surface along the line of the oscillating incident beam. We may thus regard the quantity N/f the interaction time to produce a molten strip of material of width w . In envisaging the progressive movement of this strip across the entire substrate as a quasi-continuous process the translation velocity (V) is therefore equal to $(fd)/N$, see equation 11.

$$V = (fd)/N \quad (11)$$

The requisite parameters to produce a continuous rapidly solidified strip across a substrate surface of given width (w) with a beam diameter d are found by first iteratively solving equation 6 to find the value of N . The inverse of this is (from equation 11) the normalized translation velocity (V/fd) and Fig. 10 shows this parameter as a function of normalized width (w/d) for values of T_R of 1250, 1500, and 1750°C ; these temperatures correspond to values of ξ of 1.40, 1.00, and 0.71.

Once values of frequency (f) and beam diameter (d) have been selected to find the velocity V we then determine the value of the parameter b and hence q_0 , the power density from equations 5 and 6. For convenience this equation may be rewritten to give beam power P as a function of beam diameter, oscillated beam width and applied frequency, see equation 12,

$$P = \frac{\pi \kappa T_m}{a} (d/2)^{3/2} (wf)^{1/2}; \quad (12)$$

For an example we consider the required beam power and velocity V to produce a 1.25 cm wide track, it is assumed that d is 0.035 cm. In this particular case (w/d) is 35.71, calculation and graphical solution (Fig. 10) shows V/fd to be 0.01190, with $f = 1,000$ hertz the value of V is 0.42 cm.s^{-1} . Solution of equation 12 shows that P is 554 W.

Actual examples of wide zones formed in M2 high speed steel are shown in Fig. 11 where the width is 5-7 mm and the frequency 1000 hertz; in each case the beam diameter and power is 0.035 cm and 563 watts respectively. The shallow zone (Fig. 11a) is formed with a translation velocity V of 4.35 cm.s^{-1} and is seen to have a reasonable constant depth with a mean value of $62 \text{ } \mu\text{m}$, see Table II. The effect of reducing the translation velocity V to 1.75 then to 0.44 cm.s^{-1} is to significantly increase the melt depth to $510 \text{ } \mu\text{m}$ & $1,250 \text{ } \mu\text{m}$. The deep zones in Figs. 11b and c, nevertheless, are uniform and symmetrical in shape. The dimensions of the five width zones discussed are given in Table II, these include those shown in Fig. 11; the process parameters are also given. The parameter P^* is the threshold power to initiate the formation of a molten zone as calculated by the preceding analysis. For each value of P^* there is a corresponding calculated value of the peak temperature. It would seem reasonable to attribute a value exceeding 2900°C to penetration of the beam (or cavity formation).

In the case of the particularly wide zone (3.2 cm) shown in Table II a threshold power of 2292 watts is required to initiate wide molten zone formation at a beam oscillation frequency of 1000 hertz. Interestingly, a significant decrease in the peak temperature is obtained by increasing the frequency by an order of magnitude without any significant power change, i.e. 2106 as compared with 2290 watts. The physical consequence of the value of T_p below that for vaporization shows that "cavitation" can be avoided by applying a sufficiently high beam oscillation frequency.

3. Fluid Flow Effects

3.1 Compositional Homogenization

Previous studies of laser [14-17] and electron beam glazing [4] have shown that significant segregation of alloying elements may result from the connective flow within the melt zone. The case of the high speed steel M2 is particularly interesting, since the flow induced segregation is frequently sufficient to produce regions of differing phase upon subsequent solidification [17]. As a consequence a pattern of light etching austenite and dark etching ferrite within a cross-sectional view is clearly indicative of the familiar connective flow field [14]. This type of effect is not observed in similar alloys with carbon contents exceeding that corresponding to the peritectic composition. Nevertheless, the effect of connective flow induced segregation is still clearly discernible in these materials.

In the studies of singly melted zones in molybdenum-base tool steels the degree of compositional variation increased with increasing beam velocity. Interestingly, a similar effect is discernible in the wide zones in M7 high speed steel in Fig. 8. The "mottled" appearance of the zone in Fig. 8b as revealed upon etching shows a more complicated compositional variation than in the case of a single-pass "point source" melted zone. Nevertheless, the dark etching "swirls" are clearly indicative of a connective flow pattern. Such an effect is suggestive of the pattern of "connective cells" considered originally by Lord Rayleigh and later by Landau in the "rotons" in superfluidity theory, see Normand, Pomeau, and Velarde [18].

3.2 Surface Topography

In contrast to the familiar "ripple" pattern in Fig. 2, and the smooth surface effect produced by successive remelting [2], yet another topography is produced by linear heat source melting. These surfaces appear to be particularly smooth and have a "matt" appearance. Microscopic studies of such surfaces on M2 tool steel reveal a particularly intriguing topography consisting of a fairly uniformly distributed small "hillocks". In such an as-melted in Fig. 12 the "hillocks" are smooth in appearance and within the "valleys" there appears to be a fine filamentary eutectic-type structure. The effect of progressively polishing and etching the surface is revealed in Figs. 13a-d. In these micrographs the typical cellular structure is initially evident within the "hillocks" and eventually throughout as the "hillocks" are polished away. The filamentary structure quite clearly exists at, and very near to the surface. Systematic experiments now in progress reveal that the spacing between the "hillocks" decreases with increasing translation stage velocity V . An interesting explanation for the modulated "hillock" type appearance is that it results from fluid flow created by "connective cells" of the type just discussed [18]. A rigorous mathematical

physics analysis of this type of phenomenon reveals a result which is contrary to what might be intuitively anticipated [18]. Namely, that the valleys correspond to fluid "up-flow" from within the interior of the liquid body and the "hillocks" to fluid "down-flow". This phenomenon is part of a continuing study which is systematically considering the effects of the various processing parameters.

Acknowledgement

Appreciation is expressed to the Office of Naval Research for support of the current project under Contract N00014-78-C-0580 and to Dr. Bruce MacDonald for his interest and encouragement in the program.

References

- [1] P. R. Strutt, Mat. Sci. Eng., 44 (1980), 239.
- [2] P. R. Strutt, Mat. Sci. Eng., 49 (1981), 87.
- [3] Y. W. Kim, P. R. Strutt and H. Nowotny, Met. Trans., 10A (1979), 881.
- [4] B. G. Lewis and P. R. Strutt, Journal of Metals, Nov., 1982, p. 37.
- [5] A. W. Ruff and L. K. Ives, Wear, 75 (1982), 285.
- [6] B. L. Averbach, Metal Progress, Dec., 1980, p. 19.
- [7] T. V. Philip, Metal Progress, Feb., 1980, p. 52.
- [8] W. Gruhl, B. Grzemba, G. Ibe and W. Hiller, Aluminum, 53 (1977), 177.
- [9] R. Mayer, W. Dietrich and D. Sundermeyer, Weld. J. (Miami), 56 (1977), 35.
- [10] J. D. Ayers, T. R. Tucker and R. J. Schaefer, Proc. Second Int. Conf. on Rapid Solidification Processing, Claitor's Publishing Division, Baton Rouge, LA, 1980, p. 212.
- [11] T. R. Tucker, J. D. Ayers and R. J. Schaefer, "Laser and Electron Beam Processing of Materials", Academic Press, New York, 1980, p. 760.
- [12] H. Sunada, J. Wadsworth, J. Lin and O. D. Sherby, J. Mat. Sci. Eng., 38 (1979), 35.
- [13] L. E. Greenwald, E. M. Breinan and B. H. Kear, Laser-Solid Interactions and Laser Processing, Am. Inst. of Physics, NY, 1978, p. 189.
- [14] S. M. Copley, D. Beck, O. Esquivel and M. Bass, Laser-Solid Interactions and Laser Processing, Am. Inst. Physics, NY, 1979, p. 161.
- [15] R. Mehrabian, S. Kou, S. C. Hsu and A. Munitz, Laser-Solid Interactions and Laser Processing, Am. Inst. of Physics, NY, 1978, p. 129.
- [16] R. H. Kear, J. W. Mayer, J. M. Poate and P. R. Strutt, Metallurgical Treatises, AIME, 1981, p. 321.
- [17] P. R. Strutt, B. G. Lewis and M. Kurup, Electron-Beam Laser Glazing of Iron-Base Materials, Annual Process Report 1981, ONR Contract N00014-78-C-0580.
- [18] C. Normand, Y. Pomeau and M. G. Velarde, Rev. of Modern Phys., 49(3) (1977), 581.

TABLE I

Major Alloying Elements (wt%) in Hard Iron-Base Materials

	C	Cr	W	V	Mo	Co	Ti	Ni	Mn	Si	Fe
Ferro-TiC(SK)	5.0	3.5	-	-	3.0	3.0	21.0	0.5	-	-	64.0
M2	0.84	4.5	6.3	2.0	5.0	0.12	-	-	0.30	0.30	Bal
M42	1.09	3.7	1.4	1.2	9.6	7.9			0.24	0.40	Bal
M7	1.01	3.6	1.7	1.8	8.3	-			0.29	0.29	Bal
52150	1.48	1.34	-	0.01	0.02	-		0.02	0.56	0.07	Bal

TABLE II

P (watts)	P* (dV0)	f (hertz)	w (mm.)	V (cm.s ⁻¹)	d (μm)	T _D (°C)
563	310	1,000	6.8	0.44	1,240	2636
563	405	1,000	6.1	0.88	510	3069
563	611	1,000	6.2	1.75	220	3848
563	848	1,000	5.0	4.35	62	5143
3000	2292	1,000	32.0	1.00	250	5379
	2106	10,000	32.0	1.00		2627

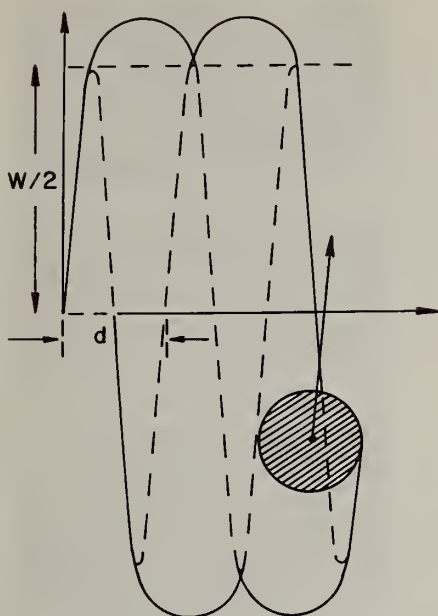


Fig. 1.

Schematic diagram showing a wide strip of rapidly solidified material being formed by an oscillating beam.



Fig. 2. Actual view of the surface of 52150 bearing steel formed by an oscillating beam ($f=62.5$ hertz).

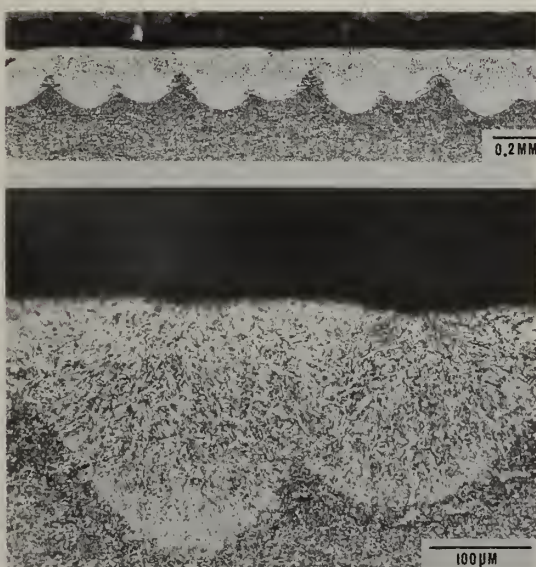


Fig. 3. Longitudinal section of the surface layer melted by an oscillating point source in 52150 bearing steel, note the absence of an "overlapping effect", frequency is 62.5 hertz.

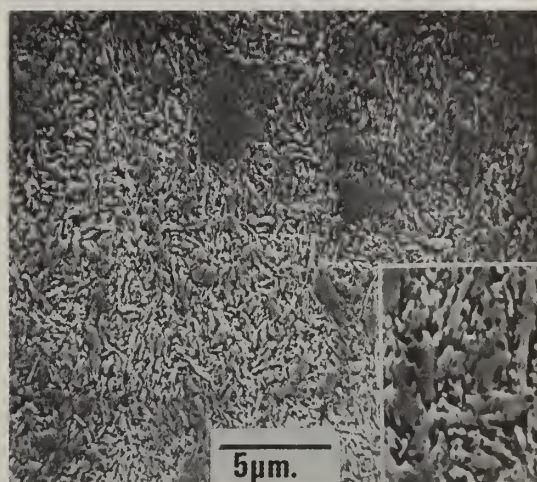


Fig. 4. Detailed microstructure in a section shown in Fig. 3.

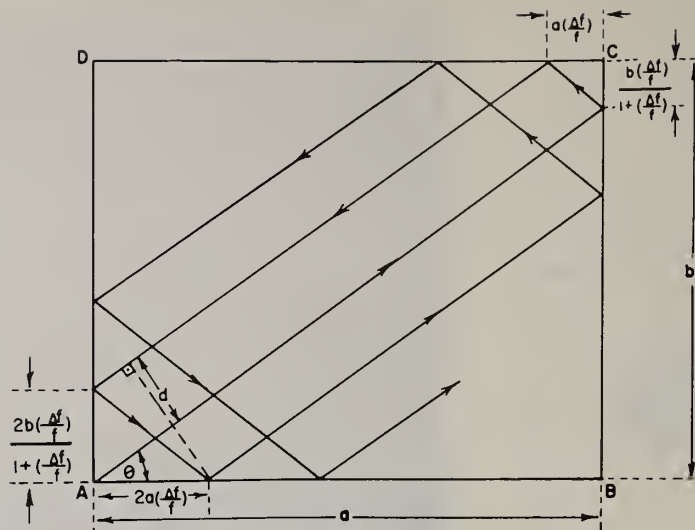


Fig. 5. Schematic diagram showing the x-y deflection pattern formed by two nearly equal frequency triangular waveforms.

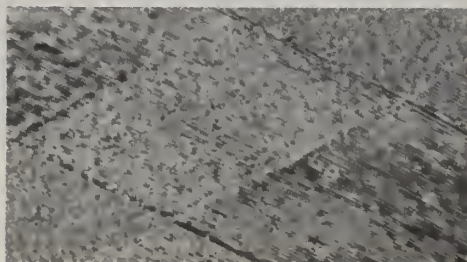
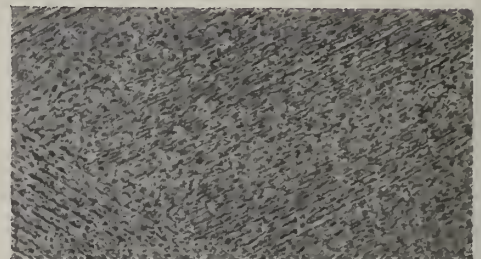
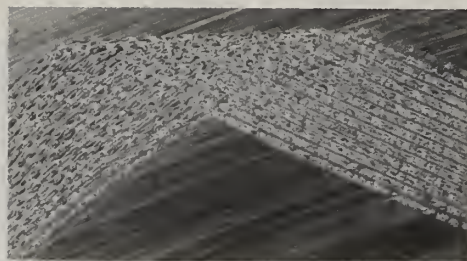


Fig. 6. Low magnification of "glazed" surfaces on M2 steel using the scanning mode illustrated in Fig. 5; conditions are given in text.

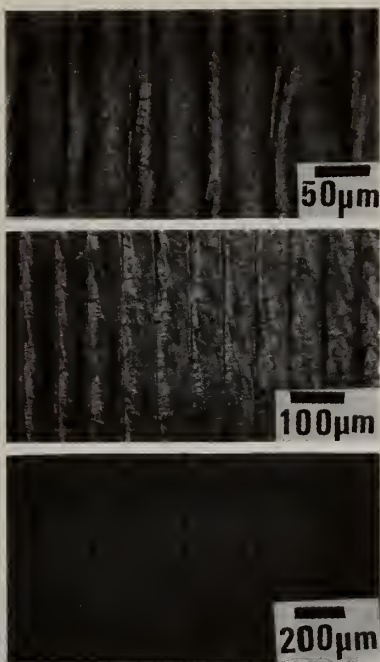


Fig. 8. Cross-sectional view of a surface layer shown in Fig. 7 showing zone overlapping.

Fig. 7.

Higher magnification micrographs of surface shown in Fig. 6.

Fig. 9. Schematic diagram of linear heat source melting.

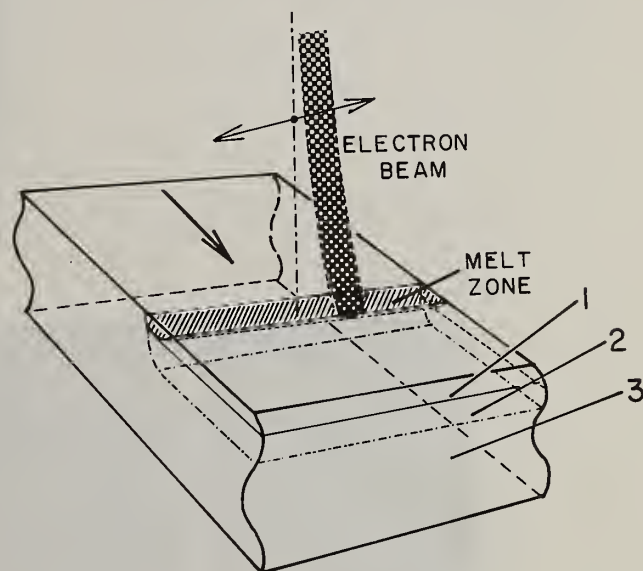
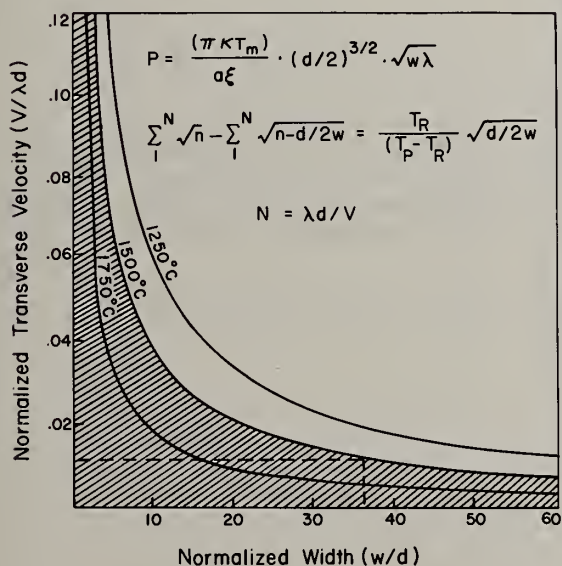


Fig. 10. Graph of Normalized Velocity as a function of Normalized Width for linear source scanning.



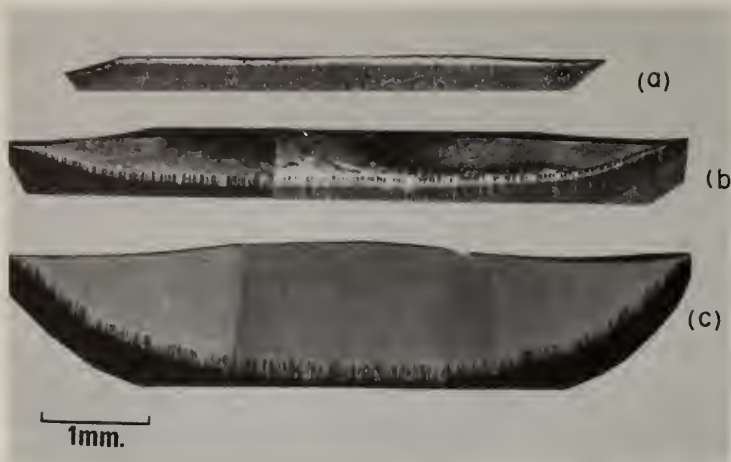


Fig. 11.

Cross-sectional views of wide zones in M7 steel formed by linear heat source melting. For conditions see text and Table II.

Fig. 12.

"As glazed" surface of material glazed using a linear heat source, material - M7 steel.

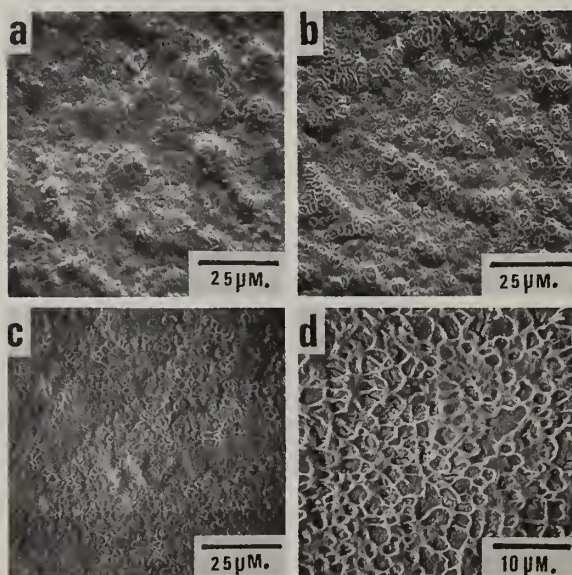
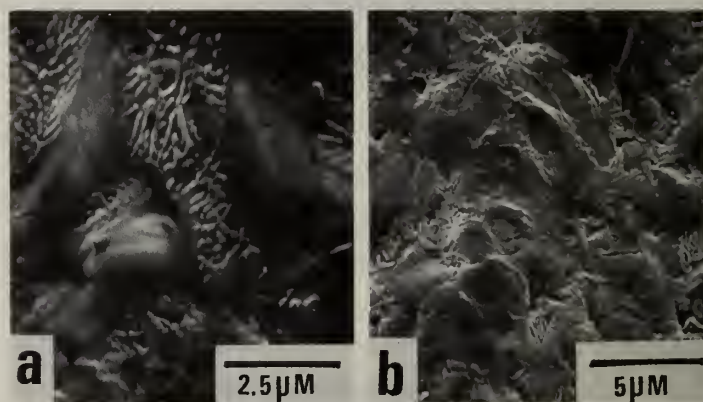


Fig. 13.

Surface topography and microstructure of similar areas as shown in Fig. 12 following successive amounts of light polishing and subsequent etching.

IMPROVED IRON BASE ALLOYS

MADE USING A RAPID

SOLIDIFICATION PROCESS

Ranjan Ray and Viswanathan Panchanathan

Marko Materials, Inc., North Billerica, MA

and

Saul Isserow

Army Materials and Mechanics Research Center

Watertown, MA

ABSTRACT

Initial results of investigation on selected iron base alloys using a Rapid Solidification Powder Metal Technology currently being developed at Marko Materials under a DARPA/AMMRC program are reported. The various alloys studied include commercial precipitation hardenable (PH) stainless steels, iron aluminide base alloys and high speed steels. These alloys were modified with specific amounts of boron and processed by melt spinning as rapidly solidified powders followed by hot extrusion. The consolidated alloys were subjected to various heat treatment procedures for optimum mechanical properties.

A 30-35% improvement in tensile strength combined with good ductility has been achieved in boron modified PH stainless steels compared to the conventional alloys.

Rapidly solidified Fe-Al-B alloys show high specific strength and modulus of elasticity in the temperature range 1000-1400°F. The other noteworthy attributes of the iron aluminide base alloys are outstanding oxidation resistance, good low cycle fatigue strength, and high thermal stability at elevated temperatures. Very high elongations, typically up to 280%, were achieved in these alloys at high temperatures (1600°F) indicating the possibility of superplastically hot deforming these materials into shaped objects.

A rapidly solidified boron modified tool steel showed significant improvement in tool life in cutting (turning) tests, compared to its commercial counterpart.

INTRODUCTION

During the past three years, Marko Materials has been engaged in the development of a rapid solidification powder metal technology to produce improved iron-based alloys containing certain specific amounts of boron. Rapid solidification processing of such boron-containing ferrous alloys produces generally a solidified alloy having a chemically homogeneous, metastable microcrystalline phase(s). Upon subsequent heat processing during hot consolidation, the metastable phase decomposes into an aggregate of stable phases including a fine dispersion of borides. The fine boride particles enable retention of an ultrafine recrystallized (matrix) grain structure and contribute to the microstructural stability and enhanced mechanical strength of the alloys at elevated temperatures. Marko practices its rapid solidification powder production process as follows: The alloys are produced by the method of melt spinning as chill cast thin ribbons which are brittle as a consequence of metastable phase formation; the chill cast (brittle) ribbons are readily pulverized into powders of desirable size ranges by a rotating hammer mill. Powders are consolidated into bulk forms by standard powder metallurgical techniques e.g. hot extrusion.

In August 1981, Marko began a DARPA/AMMRC program aimed at evaluating the suitability of the afore-said iron base alloys of different classes for potential defense hardware application (e.g. gas turbine engine parts). One major thrust of this program was to demonstrate the feasibility of scaling up Marko's powder production process to a pilot-plant size, thus providing a basis for a new manufacturing technology. This paper highlights some of the important results accomplished on three classes of alloys during the first year of the program.

PROCESS SCALE UP

Equipment has been designed, fabricated and installed to batch produce large quantities (150-300 pounds) of rapidly solidified powder. This equipment (Figure 1) is based on the principles of fabrication of multiple ribbons chill cast by melt spinning followed by in-line pulverization of the ribbons directly off the rotating substrate using hammer mill into powders. At the time of writing, the testing and debugging of the scaled-up powder production system have been initiated. The chief attributes of this process are anticipated to be (a) ability to manufacture all powder particles with uniform quench history, and (b) ability to produce economically a high yield (95%) of good quality powder quenched at a very high rate under the effect of conductive cooling.

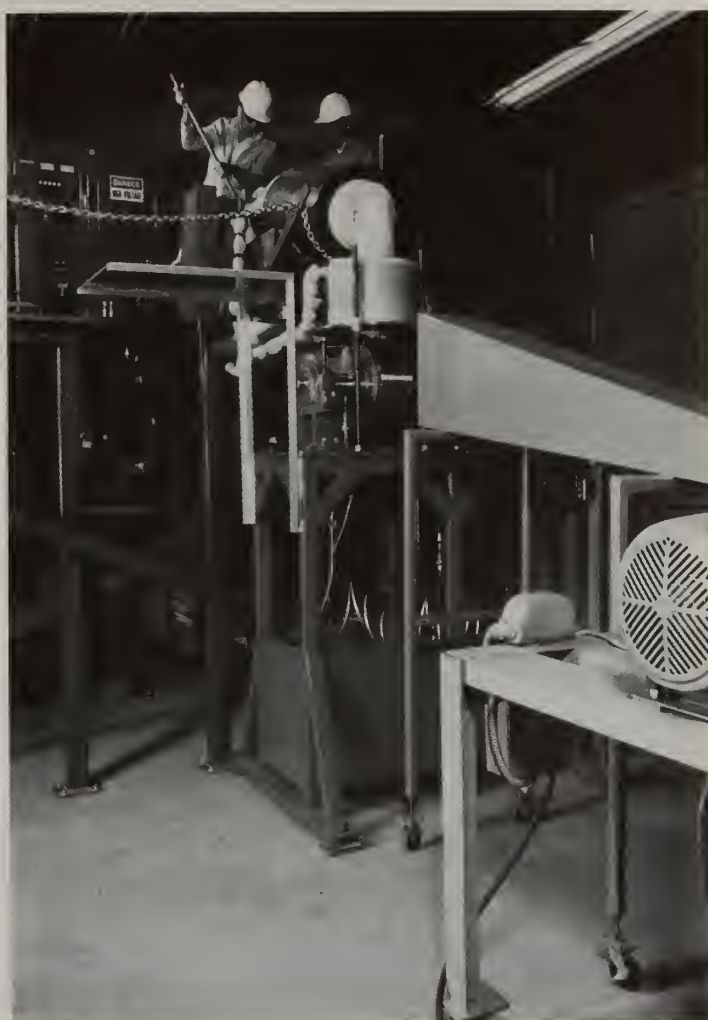
ALLOY STUDIES

Commercial iron-base alloys combining high strength with good oxidation/corrosion resistance at high temperatures are primarily the hardenable stainless steels or modifications based on them. The various martensitic stainless steels of the straight chromium grades (e.g. AISI 420, 440, etc.) as well as the semiaustenitic and martensitic precipitation hardenable (PH) stainless steels (e.g. 17-7 PH, AM 350, 17-4 PH, etc.) are useful to 900°F. Strengthening due to martensite formation or precipitation hardening in these steels decreases rapidly above 900°F due to tempering and overaging effects.

Austenitic precipitation hardenable stainless steels are an outgrowth of extensive compositional modification of austenitic stainless steels for retention of high strength above 900°F. These alloys are better known as iron-base superalloys and are considered to be forerunners of the more widely used nickel and cobalt base superalloys. These highest temperature commercial iron-base superalloys, with capabilities up to 1200°F, include Discaloy, A-286 and V-57. Most of these alloys in this system contain about 15% chromium to provide corrosion resistance, 25% nickel to stabilize the austenite structure, 1-2% molybdenum for solid solution strengthening and 2-3% aluminum plus titanium for precipitation hardening. Higher temperature conventional wrought alloys of this type appear unlikely to be accepted by industry because of a tendency towards phase instability as alloy content is increased. With increasing nickel content in these alloys (replacing iron), improved stability is achieved, but at a higher cost.

The major goal of the DARPA/AMMRC program is to optimize and evaluate selected iron base alloys of Marko via rapid solidification technology (RST) for potential high temperature structural applications in the intermediate temperature range of 800-1200°F. These new RST alloys will be specifically developed to evolve as potential replacements, on the basis of cost-effectiveness, superior properties and/or low contents of strategic metals (e.g. Cr, Co etc.) for conventional precipitation hardenable (PH) stainless steels, titanium alloys and iron base superalloys.

Figure 1. RST powder production
facility at Marko
Materials



MODIFIED PH STAINLESS STEELS

Alloys of one category which were undertaken for the present investigation are based on conventional PH stainless steels modified to contain 1.6-2.4 weight percent boron. Preliminary exploratory screening of a number of different PH stainless steels with different boron concentrations led to the selection of the two alloys for detailed studies as listed in Table 1.

TABLE 1
Nominal Chemistry of Boron Modified Precipitation
Hardenable Stainless Steels

Alloy No.	Composition (weight percent)
RST 1.1	PH 15-7 Mo containing 2.1% Boron [Bal Fe, 15.1 Cr, 7.1 Ni, 1.2 Al, 2.2 Mo, .07 C and 2.1 B]
RST 1.27	Custom 450 containing 2.2% Boron [Bal Fe, 15 Cr, 6 Ni, 0.8 Mo, 1.5 Cu, 0.27 Cb, 0.05 C, and 2.2 B]

The RST 1.1 alloy is a modification of a semiaustenitic PH stainless steel. Conventionally processed semiaustenitic PH steel (annealed or solution treated) exhibits microstructure consisting of austenitic matrix with an average grain size of 20 microns[1]. Transmission electron microscopic examination of thinned, electropolished sections of as solidified ribbons of RST 1.1 alloy parallel to the ribbon surface revealed microcrystalline structure consisting of equiaxed grains (Figure 2). There is no evidence of second phase precipitation at the grain boundaries. The size of the micro grains vary, but is typically 0.25 microns. Furthermore, the grains were in all cases subdivided into a cell structure. The cell diameter is very small, typically 300-500 Å. Boron has negligible solid solubility in steels. Precipitation of M_2B occurs above 58 p.p.m boron in commercial Fe-Cr-Ni base stainless steels [2]. Rapid quenching inhibits the diffusional processes which cause second phase precipitation and generated the present extremely homogeneous non equilibrium supersaturated solid solution phase with microcrystalline morphology. Wood et al obtained by rapid solidification of melt up to 1.0% boron in supersaturated metastable Fe-Cr-Ni base solid solution which decomposed upon aging at high temperatures forming complex $M_{23}B_6$ borides at the grain boundaries with no obvious crystallographic relationship with the matrix [3]. Figure 3 shows a transmission electron micrograph of RST 1.1 alloy ribbon heat treated at 1750°F for 2 hours followed by air cooling to room temperature. The resultant microstructure which grew from the original rapid solidification structure was still extremely fine. The primary matrix grains remained small, about 0.3 micron, perhaps due to the pinning effect induced by 0.1-0.3 micron sized boride crystals nucleated at grain boundaries (indicated by arrows in the micrograph). Additionally a very fine scale precipitate phase was observed within the grains. Although the as solidified ribbons were brittle, the heat treatment at 1750°F rendered them fully ductile to 180° bending.

PREPARATION OF BAR STOCK AND MECHANICAL PROPERTIES

Alloy powders of the two boron modified PH steels were prepared by the RST melt spinning-pulverization process. About 20 pounds of -80 +400 mesh sized powders of each alloy were hot dynamically out gassed and sealed off in 4 inch dia. mild steel cans for consolidation by extrusion. Extrusion was accomplished at 1975°F at a high reduction ratio (20:1) to ensure complete densification of powders.

The commercial PH 15-7 Mo alloy is a semiaustenitic stainless steel generally produced and used in flat rolled sheet and strip products. After fabrication, through a series of relatively simple low temperature heat treatments, it can be heat treated to a variety of strength levels depending on the design requirements. The heat treatment consists of three basic steps: (1) austenitic conditioning, (2) martensitic transformation, and (3) age hardening by formation of fine precipitates of Ni-Al intermetallic compound. The optimum heat treatment cycles of semiaustenitic PH steels are dependent on careful control of the interrelationship of austenite and ferrite forming constituents and their relationship to the total chemical balance of the system. It should be noted that the RST 1.1 alloy has a microcrystalline grain structure containing a fine dispersion of boride phase(s). It is very likely that the alloy chemistry of the matrix was disrupted as a result of addition of boron and hence the optimum heat treatment condition for RST 1.1 might be different than for commercial PH 15-7 Mo steel.

The heat treatments for the RST alloy were initially chosen based on the basic principles of physical metallurgy associated with the commercial PH steels. A reasonable wide latitude in the times and temperatures of the various heat treatment sequences is possible to obtain usable mechanical properties. However, the heat treatments employed in the present investigation were restricted to (a) austenite conditioning around 1600°F, (b) subzero treatment around -100°F for 8 hours and (c) precipitation hardening between 840°F and 1020°F. The precipitation hardening effect is a complex interplay of three separate and distinct reactions e.g. tempering of martensite, precipitation of an intermetallic compound and reversion of martensite to austenite. The degrees to which these reactions proceed depend on the times and temperatures. A careful analysis of the complex aging phenomenon will be required to develop the optimum mechanical properties of the present alloy. The effect of selected precipitation hardening treatments on the mechanical properties of the RST 1.1 alloy is shown in Table 2.

As illustrated in Figures 4 and 5, the RST 1.1 alloy in suitably heat treated condition possesses tensile properties (0.2% offset YS and UTS) about 25-30% higher than a fully heat treated commercial semiaustenitic (17-7 PH) stainless steel in the range from room temperature to 1000°F.

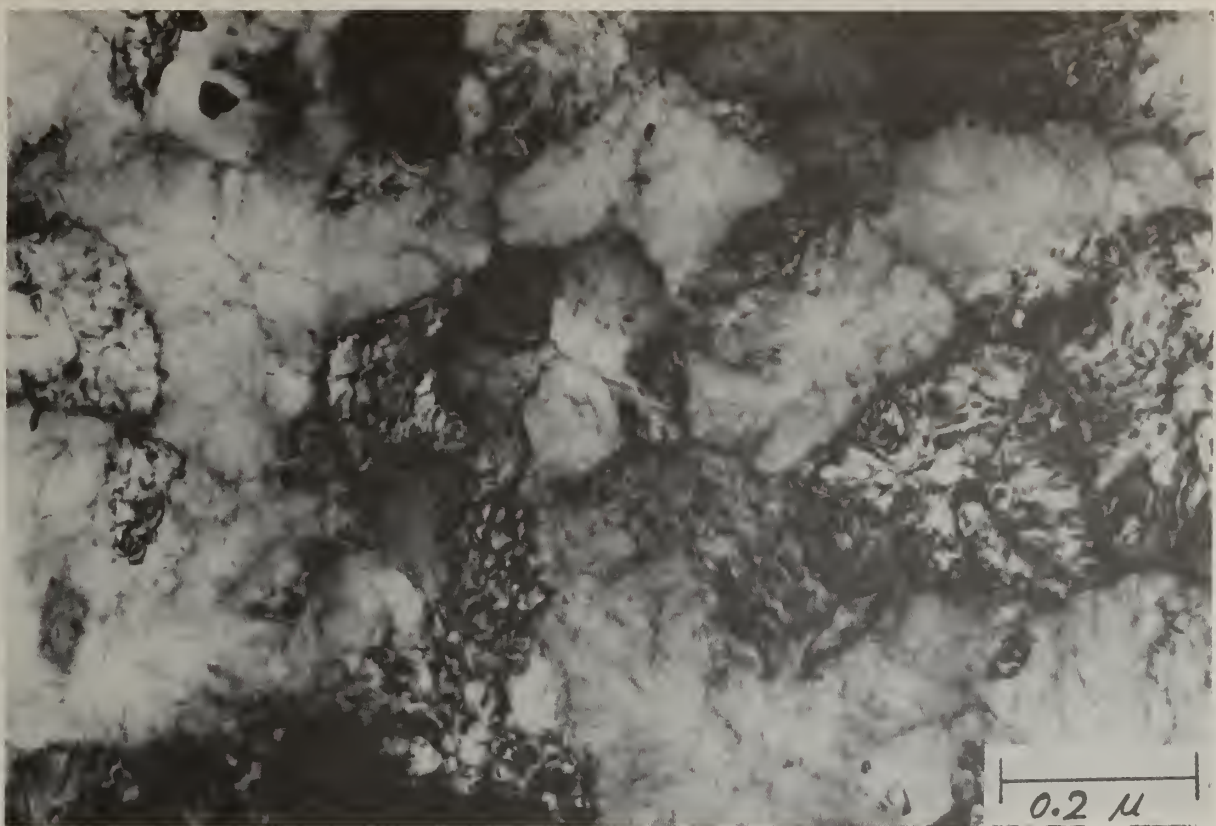


Figure 2. TEM picture of RST 1.1 alloy ribbon as quenched

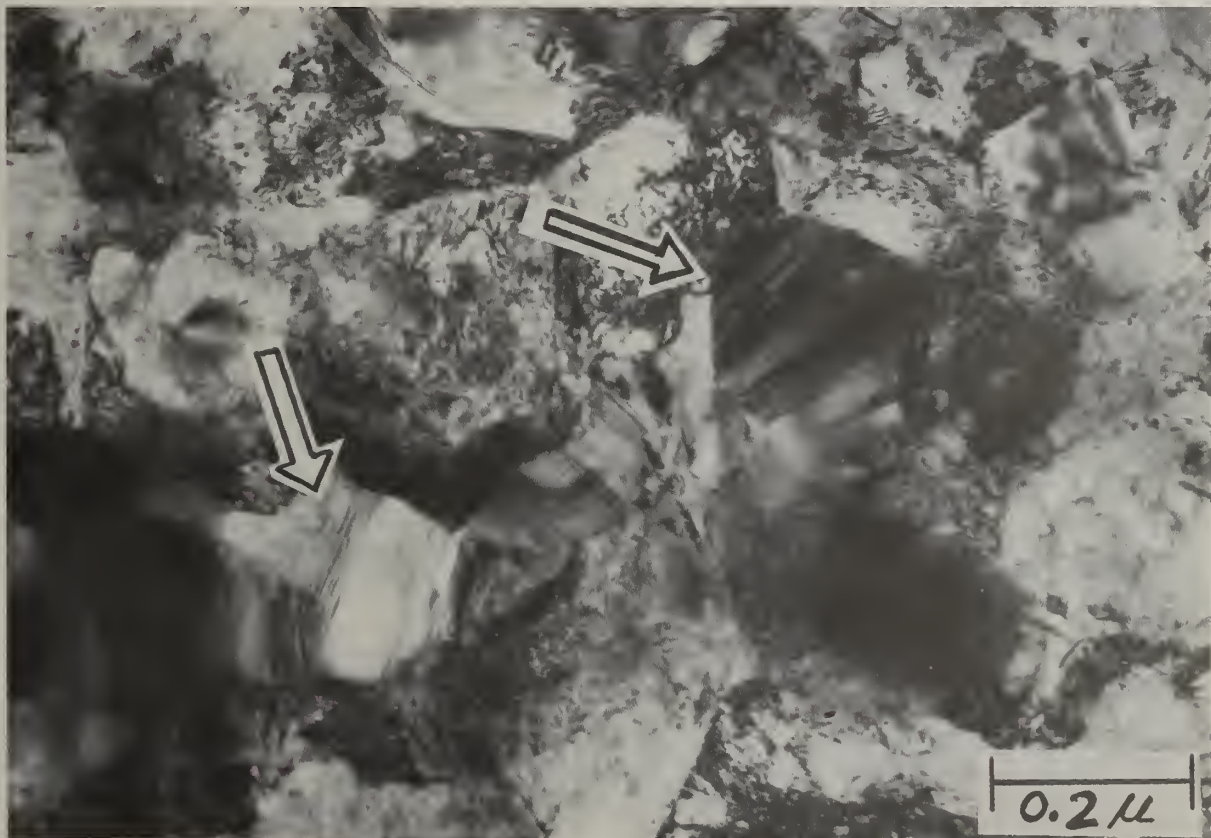


Figure 3. TEM picture of RST 1.1 alloy ribbon heat treated at 1750°F for 2 hours

TABLE 2

Room and Elevated Temperature
Properties of RST 1.1 Alloy

Aging condition following sub- zero treatment	Test Temperature °F	0.2% Offset Yield Strength		Ultimate Tensile Strength		% Elongation	% RA
		KSI	MPa	KSI	MPa		
24 hours at 840°F	75	255	1760	277	1911	0.4	0.6
	800	173	1184	180	1242	0.6	1.0
72 hours at 840°F	75	230	1586	250	1722	3	6
	800	173	1192	181	1248	3.6	4.5
24 hours at 1024°F	75	135	928	192	1325	11.4	12.1
	1000	100	692	122	842	15.3	18.1

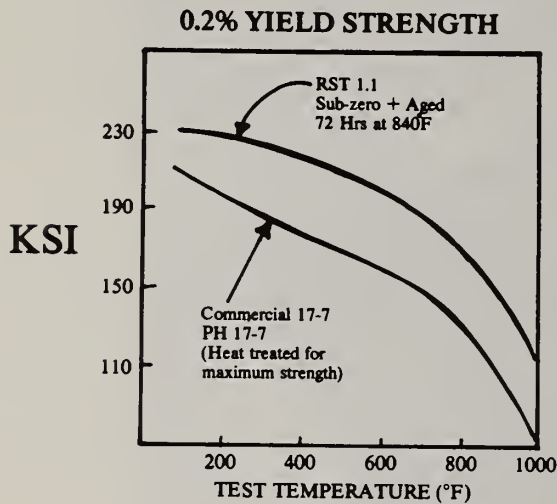


Figure 4. 0.2% yield strength of RST 1.1 alloy and commercial 17-7 PH steel as a function of test temperature.

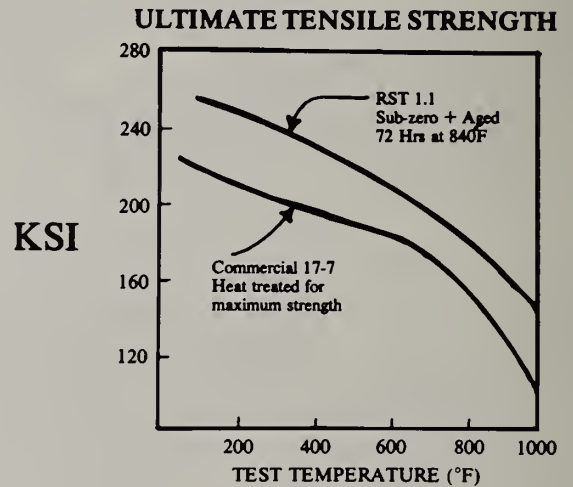


Figure 5. Ultimate tensile strength of RST 1.1 alloy and commercial 17-7 PH steel as a function of test temperature.

All of the commercial semiaustenitic stainless steels such as 17-7 PH, PH 15-7 Mo, Ph 14-8 Mo etc. are generally capable of developing approximately the same tensile strength [1] ranging from a low 175,000 psi (1206 MPa) to a high 240,000 psi (1655 MPa). However, fracture toughness and ductility of the semiaustenitic stainless steels all heat treated to the same tensile strength level are not the same. It is also known that fracture toughness is an excellent indicator of the stress corrosion resistance of these steels at room as well as elevated temperatures. Stress corrosion resistance is generally enhanced with increasing fracture toughness. Work has been planned, therefore, to determine the fracture toughness values of the present RST 1.1 alloy and compare them with the semiaustenitic stainless steels at the same tensile strength levels.

The RST 1.27 alloy of the present work is based on commercial Custom 450 alloy which is a martensitic precipitation hardenable steel. After high temperature solution treatment, the structure of this steel is martensitic. Additional strengthening is achieved by an aging treatment at 900-1100°F. The RST 1.27 alloy was prepared as bars similarly as the RST 1.1 alloy. Fine microstructural features were observed in the optical photomicrographs of the as extruded bars (Figure 6). The extruded bars were subsequently aged between 850 and 1020°F for different hours. Selected tensile data of the RST 1.27 alloy are given in Table 3 as a function of different age hardening treatments. The RST 1.27 alloy was found to exhibit greater than 25% improvement in tensile properties (0.2% offset YS and UTS) than Custom 450.

TABLE 3
Room and Elevated Temperature
Tensile Properties of RST 1.27

Condition	Test Temp. °F	0.2% Offset Yield Strength		Ultimate Tensile Strength		% Elong.	% RA
		KSI	MPa	KSI	MPa		
Aged at 840°F for 4 hours	RT	228	1571	251	1730	4.3	4.8
	600	187	1288	208	1433	7	10
	800	163	1123	188	1295	7.7	13
Aged at 1020°F for 4 hours	RT	212	1461	233	1605	7.2	11.5
	600	184	1268	198	1364	3.1	9.4
	800	164	1130	179	1233	12	12
	1050	111	765	122	841	11.3	24

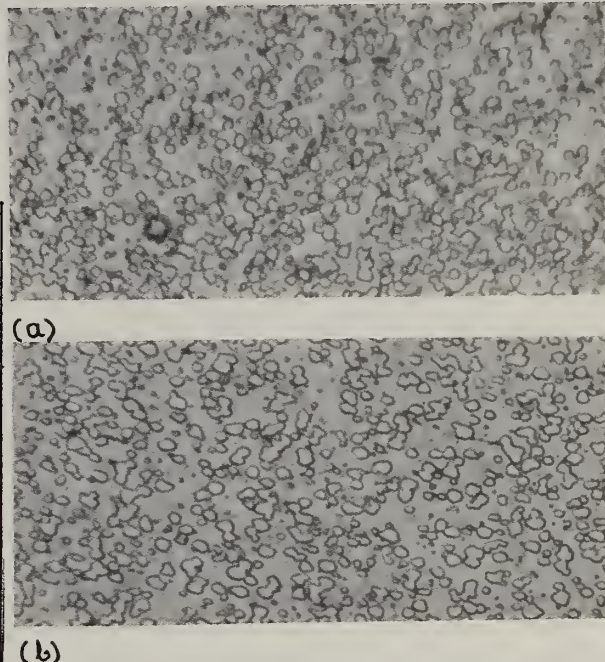


Figure 6. Optical photomicrographs (1000x) of as extruded RST 1.27 alloy bar (a) longitudinal section (b) transverse section.

Stress corrosion tests were carried out with tensile specimens of the RST 1.27 alloy in the age hardened condition in accordance with NACE TM-01-77. The environment used was distilled water solution of 0.1 percent NaCl, 0.5 percent acetic acid, saturated with H₂S gas. Time to failure was measured as a function of applied stress. The RST 1.27 alloy was found to have significantly superior sulphide stress corrosion resistance than Custom 450 (see Table 4).

TABLE 4
Stress Corrosion of Tensile Specimens in
0.1% NaCl + 0.5% Acetic Acid + H₂S

Alloy	Hardness Rockwell C	Applied Stress		Time to Failure
		KSI	MPa	
Custom 450	41	60	414	10 hours
RST 1.27	42	60	414	56 hours

Alloys based primarily on iron and aluminum, relatively inexpensive elements with abundant and more secure reserves, offer excellent alternative possibilities to the current heat resistant alloys containing chromium, nickel and cobalt. Iron-aluminum alloys containing 13 wt.% (24 at%) or higher contents of aluminum exhibit outstanding oxidation resistance and were considered as potential candidates for a wide variety of heat resistant applications as engineering components. Binary iron-aluminum alloys have a strong susceptibility to microcracking during the ingot casting operation due to low thermal conductivity and high thermal expansivity. This characteristic feature, coupled with large grain growth at high temperatures, renders hot working iron-aluminum alloys containing high aluminum contents difficult. Poor workability and room temperature brittleness of these alloys have retarded their applications. Furthermore, iron-aluminum alloys with about 13 wt.% or higher contents of aluminum have stress rupture properties less than adequate for high temperature applications. Some of these problems encountered in the iron-aluminum alloys can be circumvented by processing the alloys from pre-alloyed rapidly solidified powders of high purity. Recent efforts at Pratt and Whitney Aircraft generated improved strength and ductility combined with good oxidation resistance in Fe-Al alloys containing 13 wt.% aluminum, 1.5 wt.% titanium and 0.5 to 0.7 wt% boron which were compacted from rapidly solidified powders [4].

A new family of Fe-Al-B alloys was examined via RST at Marko under the present investigation. The primary rationale for addition of boron in certain critical concentrations to Fe-Al alloys was to render the alloy responsive to Marko's RST process (melt spinning-pulverization). Furthermore, boron was anticipated to generate microcrystalline structures stabilized by finely dispersed borides in the consolidated alloy. Strength and ductility are likely to benefit from such structures. Preliminary search for alloys which conformed to the RST processing constraint and displayed excellent high temperature oxidation resistance led to the formulation of the following optimum composition:

Bal Fe, 17-22 wt.% Al and 3-4 wt.% B

Additions of alloying elements such as Mo, W and V to the above alloys were explored for beneficial effects on creep strength and thermal stability via possible formation of stable borides. Table 5 lists the three alloys which were studied in greater details in the present program.

The Fe-Al base alloys were prepared as bars by hot extrusion of RST powders (-80 +400 mesh) at 1750°F using a reduction ratio of 14:1. The extruded rods were further given an annealing treatment at 1740°F for 3 hours prior to testing of various mechanical properties (e.g. tensile, stress rupture and low cycle fatigue). The alloy compositions of the present Fe-Al-B system are novel with little or no knowledge existent in the prior art about the various phase relationships in this ternary system. Henceforth, a detailed understanding of the microstructural features of these new RST alloys in the consolidated state was deferred pending full determination of their mechanical properties in the desired temperature range. An immediate goal in the current program was to find out the potential usefulness as well as the drawbacks of the present alloys.

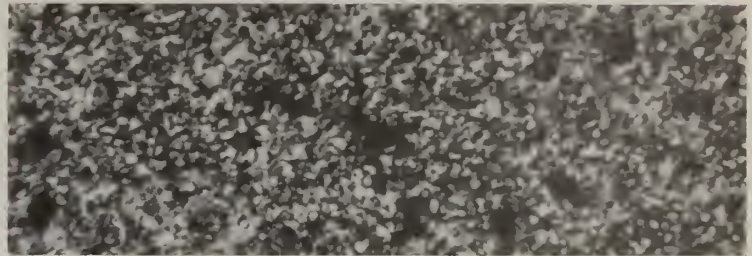
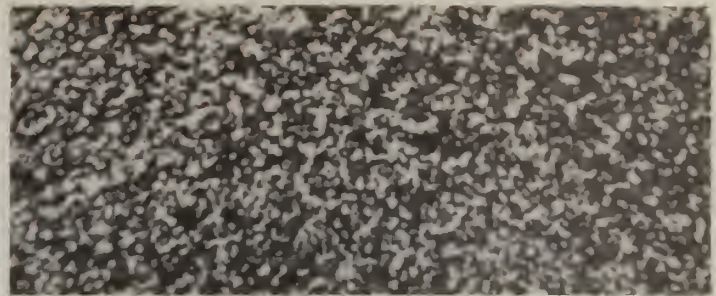
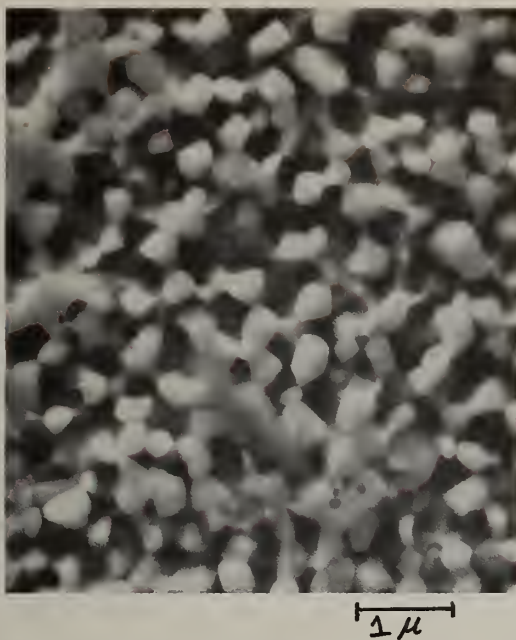
Elevated temperature tensile properties of the Fe-Al-B alloys are listed in Table 6.

Figure 6 shows the SEM micrograph of RST 4.2 alloy ribbon heat treated at 1750°F for 1 hour. The microstructure consists of a fine dispersion of a precipitate phase on a fine grained general matrix. The size of the multi-faceted precipitates is about 0.5 micron. Assuming boron to be partitioned entirely in the precipitate phase, EDX (Energy Dispersive x-ray) analysis revealed the precipitate to be an iron rich boride phase with a small amount of aluminum. The matrix composition, as a consequence of the formation of the iron rich boride phase, shifted close to the intermetallic FeAl₃ compound. Fine microstructural features were revealed in the optical photomicrographs of the RST 4.2 alloy in as extruded condition (Figure 8).

TABLE 5

Iron-Aluminum-Boron Alloys

Alloy	Composition, weight percent			
	Fe	Al	B	Other
RST 4.2	Bal	17.9	3.1	-----
RST 4.4	Bal	20.8	4.1	-----
RST 4.24	Bal	21.3	4.0	4.8 Mo 2.5 V



(b)

Figure 7. SEM photograph of RST 4.2 alloy ribbon heat treated at 1750°F for 1 hour.

Figure 8. Optical photomicrographs (1000x) of extruded bars of RST 4.2 alloy.

(a) longitudinal section

(b) transverse section

TABLE 6

Elevated Temperature Tensile
Properties of RST Fe-Al-B Alloys

Alloy	Test Temperature °F	0.2% Offset Y.S		Ultimate Tensile Strength		% Elongation	% RA
		KSI	MPa	KSI	MPa		
RST 4.2 [Fe-17.9 Al-3.1 B]	800	157	1082	177	1223	0.2	0.2
	1000	118	813	140	967	7.6	8.2
	1200	72	496	93	643	24.0	31.2
	1400	26	181	58	397	56	41.5
RST 4.4 [Fe-20.8 Al-4.1 B]	1000	118	813	144	992	5.4	7.9
	1200	79	547	101	693	18.2	24.2
	1400	23	157	60	411	49.4	37.2
	1600	9	60	14	97	280.8	71.7
RST 4.24 [Fe-21.3 Al-4.8 Mo-2.5 V-4 B]	1000	137	947	162	1118	2.5	4.1
	1200	78	538	115	793	8.1	11.6
	1300	51	348	94	646	5.1	8.9

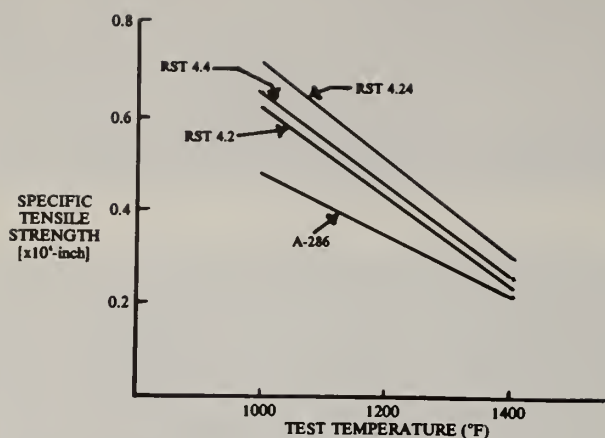


Figure 9. Specific tensile strength of RST Fe-Al-B alloys and A-286 as a function of test temperatures.

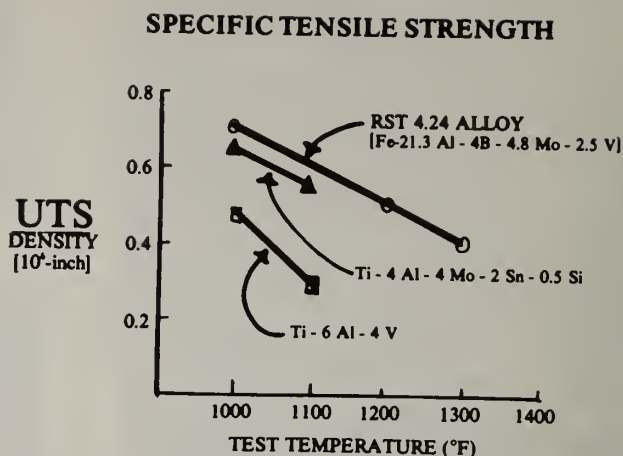


Figure 10. Specific tensile strength at elevated temperatures of RST 4.24 alloy and commercial titanium alloys.

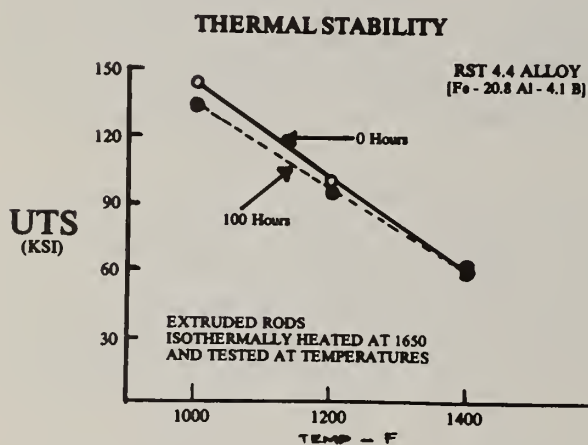


Figure 11. Effect of isothermal annealing at 1650°F on tensile strength of RST 4.4 alloy in the range 1000-1400°F.

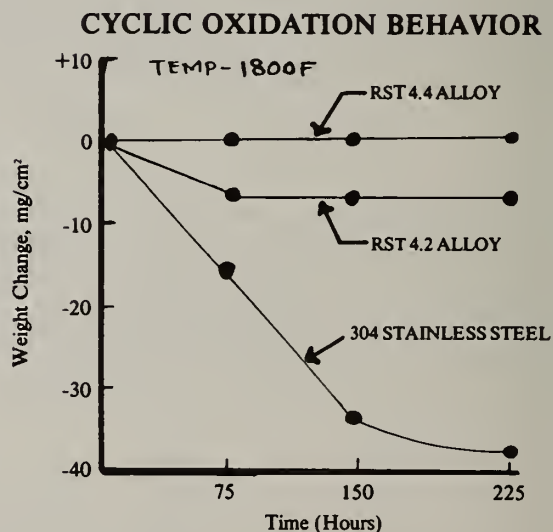


Figure 12. Cyclic oxidation behavior at 1800°F of RST Fe-Al-B alloys as shown compared to 304 stainless steel.

All the alloys were found to exhibit low ductility i.e. less than 1% elongation at temperatures below 800°F. At 1000°F or higher temperatures, the alloys exhibited reasonably good to excellent ductility combined with attractive tensile strength values.

The density values of the Fe-Al-B alloys range from 0.228-0.235 lb/inch³ (6.32-6.53 gm/cc) which are generally 20% lower than iron base alloys. In the temperature range of interest, i.e. 1000-1400°F, the present alloys exhibited significantly higher specific tensile strength values than iron base superalloy, A 286 as illustrated in Figure 9. The RST 4.24 alloy was found to have higher specific strength than two commercial titanium base alloys at high temperatures (Figure 10). Low temperature tensile properties are not satisfactory criteria for selecting a high temperature alloy. Such tests, made after an alloy has been exposed to higher temperatures, are indicative of the change in properties that may be expected due to high temperature exposure. Thermal stability of structures of alloys intended for long term uses at high temperatures is considered an important characteristic. The RST 4.4 alloy of this work showed excellent thermal stability as evidenced by little or no decrease in the ultimate tensile strength values in the range 1000-1400°F (Figure 11) after annealing the alloy at 1600°F for 100 hours.

Low room temperature ductility of the Fe-Al-B alloys might pose a problem during fabrication of parts by conventional machining. However, perhaps due to equiaxed grained structure stabilized by a large volume fraction of dispersoids e.g. borides, the RST Fe-Al-B alloys can be elongated at elevated temperatures to exceptionally large strains without risk of rupture. High elongations (to 280%) at 1600°F have been achieved with the RST 4.4 alloy (Table 6) indicating superplastic behavior. Superplasticity might allow forging of these alloys into complex shapes at relatively low stress.

A potential problem that needs to be addressed involves inadequate high temperature stress rupture strength values of the microcrystalline alloys. For example, at 1000°F, 100-hour specific creep strength of the RST 4.4 alloy is comparable to A 286 (see Table 7). However, with increasing temperatures, the stress rupture strength of the fine grained RST alloy deteriorates at faster rate than the conventional coarse grained A 286 alloy. The grain-boundary related creep rupture failure mechanism becomes a serious concern for fine grained materials. Control of grain size in the present RST alloys seems deemed important to enhance creep and rupture strength without excessively trading off tensile and yield strength properties. Judicious alloying with proper elements to improve creep resistance via decreased boundary diffusion offers an alternative option.

TABLE 7

Stress Rupture Properties

Alloy	100 Hour Specific Rupture Strength [inch x 10 ⁻³]		
	1000°F	1100°F	1200°F
RST 4.4	320	197	105
A 286	325	265	205

Cyclic oxidation between 70 and 1800°F was studied with two RST alloys, 4.4 and 4.2. The specimens were heated in static air environment to 1800°F for 50 hours and cooled to room temperature, and then reheated. The changes of weight as a function of exposure time are shown in Figure 12. When exposed in air at high temperatures, the Fe-Al-B alloys form thin, continuous and tightly adherent oxide skin over the entire specimen surface. The oxidation resistance of the present alloys was found to be excellent as compared to 304 stainless steel.

Low cycle fatigue testing at 1200°F with smooth bar specimens indicated reasonably good fatigue life of the RST 4.4 alloy. Some test data are given in Table 8.

TABLE 8

Low Cycle Fatigue Data of
RST 4.4 Alloy at 1200°F

Test Conditions				
Mode: Longitudinal Strain Control				
A Ratio: 1; Frequency: 0.50 Hz				
Wave Form: Triangle				
Maximum Engineering Stress, Max(KSI):	45.8	71.6	74.4	101.5
Minimum Engineering Stress, Min(KSI):	-50.0	-76.6	-79.8	-105.3
Measured Total Strain Range, (%)	0.37	0.70	0.80	2.00
Measured Plastic Strain Range, (%)	.02	0.11	0.24	0.81
Cycles to Failure:	55,587	3,635	2,549	118

The present Fe-Al-B alloys have very high modulus of elasticity over a wide range of temperatures (Figure 15). For example, the RST 4.4 alloy exhibits 50% higher specific modulus than A 286 alloy in the range from room temperature to 1200°F.

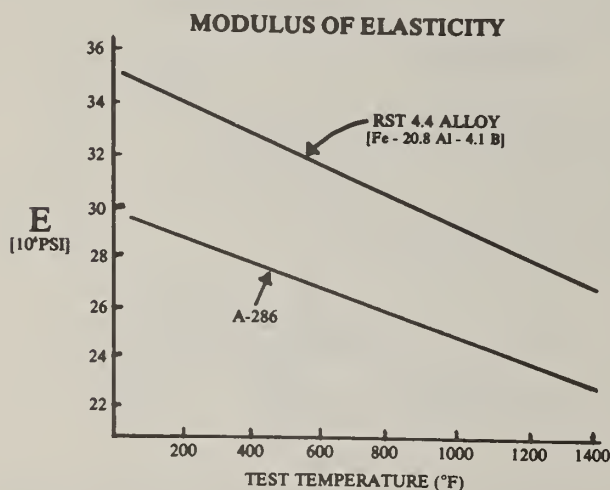


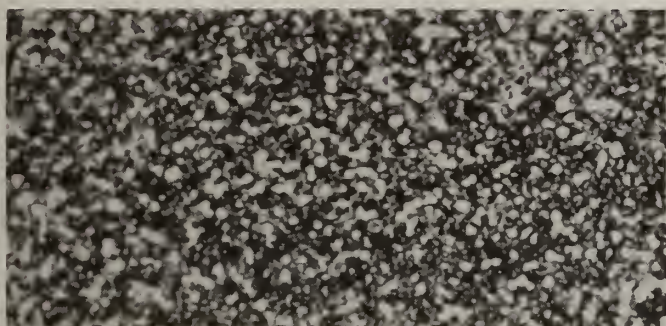
Figure 15. Modulus of elasticity of RST 4.4 alloy and A-286 as a function of test temperature.

BORON MODIFIED HIGH SPEED STEELS

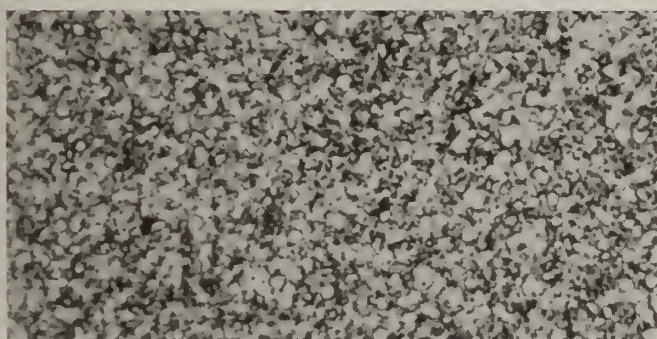
Powder metallurgical technologies have recently been applied to the production of tool steels [5,6]. Because of their finer grain size, more uniform dispersion of fine carbides and improved alloy homogeneity, high speed steels processed by such powder metallurgical techniques exhibit, compared to ingot cast materials, superior cutting performance, a better response to hardening heat treatments, improved

dimensional stability and improved grindability of cutting edges. In the present program, the principles of RST have been applied to the design of improved high speed steels. The alloys were formulated with compositions similar to conventional high speed steels modified to contain 0.45 to 1.35% boron. The addition of boron was intended to provide a fine dispersion of refractory metal borides in the martensitic matrix of the RST alloy after suitable heat treatments. These borides do not dissolve or deleteriously coarsen at elevated operating temperatures, giving enhanced hot hardness and high temperature strength.

One such alloy is RST 3.11 having composition similar to commercial M-4 high speed steel containing 0.65% boron. Its nominal composition is as follows: Bal Fe, 4.25 Cr, 4.0 V, 4.5 Mo, 5.75 W, 1.35 C and 0.65 B. The alloy was prepared as bars by hot extrusion of RST powders at 1975°F using a reduction ratio of 20:1. Its microstructure is very homogeneous and fine grained dispersed with fine boride particles (Figure 13). The consolidated alloy was austenitized at 2175°F followed by oil quenching to room temperature. RST 3.11 was fully heat treated to a hardness value of Rockwell C 66 and then tested as a single point lathe tool bit in a cutting (turning) operation using 4340 steel with a hardness of Rockwell C 35 as work material. The tool life versus cutting speed curve is shown in Figure 13. This figure also shows, for the sake of comparison, the cutting life of a widely used conventional M-2 high speed steel. M-2 and M-4 high speed steels are generally used for turning operations with a cutting speed of 50 to 75 ft/min. From Figure 14, it is estimated at a cutting speed of 60 ft/min., the RST 3.11 shows 70% improvement in tool life compared to M-2. Also, at 75 ft/min. cutting speed, the improvement in tool life of the RST alloy is 30% over M-2.



(a)



(b)

Figure 13. Optical photomicrograph of RST 3.11 alloy extruded bar.
Magnification: 1000x
(a) Longitudinal section
(b) transverse section

TURNING 4340 STEEL, ROCKWELL C 35

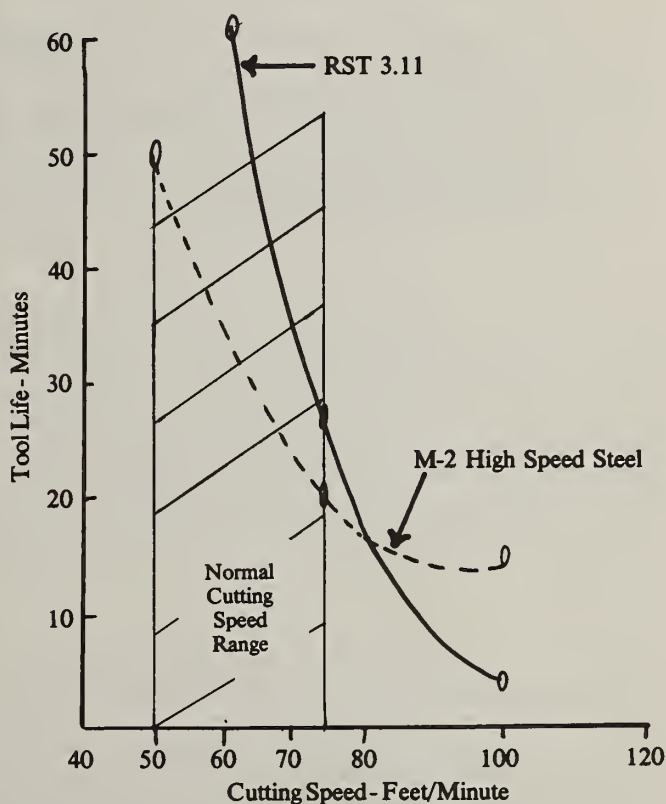


Figure 14. Tool life as a function of cutting speed of RST 3.11 alloy and a commercial M-2 steel.

CONCLUSIONS

It is believed from the work done in the initial phase of the DARPA/AMMRC program, the feasibility of applying Marko's rapid solidification powder metal alloy technology to synthesis of new and improved iron base alloys has been demonstrated. Although the first generation alloys investigated under this program cannot be considered as optimum, the results of the study are sufficiently encouraging to warrant further intensive development work.

ACKNOWLEDGEMENTS

The work is being sponsored by the U.S. Defense Advanced Research Projects Agency and monitored by the U.S. Army Materials and Mechanics Research Center, Watertown, Massachusetts under the contract No. DAAG 46-81-C-0062. The TEM and SEM photographic work was conducted by Dr. S. Sastri, Gillette Company, Boston, Massachusetts.

REFERENCES

1. D. Peckner and I.M. Bernstein, Eds., Handbook of Stainless Steels, McGraw-Hill, Inc. (1977)
2. H.J. Goldschmidt, J. Iron Steel Inst., 209, p. 900 (1971)
3. J.V. Wood and R.W.K. Honeycombe, Proc. Second International Conference on Rapidly Quenched Metals, N.J. Grant and B.C. Giessen, Eds., Section 11, M.I.T. Press, Cambridge, Mass., 107 (1976)
4. S. Das and E. Slaughter, Proc. Second International Conference on Rapid Solidification Processing, Eds., R. Mehrabian, B.H. Kear and M. Cohen, Claitors p.354 (1980)
5. T. Levin and R.P. Harvey, Metals Progress, vol 115, No. 6, p. 31 (1979)
6. A. Kasak, G. Steven and T.A. Neumeyer Society of Automotive Engineers, Automotive Engineering Congress, Detroit (1972)

S. C. Huang, K. M. Chang and E. L. Hall

General Electric Corporate Research and Development
P.O. Box 8
Schenectady, NY 12301

ABSTRACT

Melt spinning of superalloys has produced crystalline and in some compositions amorphous ribbons, which, upon heat treatment, yield unique microstructures. This paper reports our preliminary investigation of the opportunity for developing new superalloys through the melt-spinning, rapid solidification process. Two superalloys were chosen as the basis of our studies. One was a nickel-based superalloy into which various amounts of boron were added to change the solidification and precipitation behavior. When the boron addition was less than 1.0 wt.%, a crystalline cell structure developed with boride precipitation at cell boundaries. When the boron addition was greater than 1.0 wt.%, the as-cast ribbon contained small particles ($<200\text{\AA}$) of Ni-base solid solution embedded in an amorphous matrix. In the other studied alloy which contains 0.43 wt.% carbon, only one-third of the ribbon thickness (near the ribbon surface contacted with the casting wheel) developed a homogeneous solidification structure containing monocarbide precipitates less than 200\AA in size. The high-temperature stability of borides and carbides in the above systems will also be presented. These results have helped us to define guidelines for our future superalloy research using the rapid solidification technique.

Introduction

Alloys produced by rapid solidification usually develop microstructures unobtainable by conventional casting. These unique microstructural features include submicron grain size, extended solid solution, ultrafine precipitation, metastable phases, and in some cases metallic glasses can be produced [1]. Commercial alloys, originally developed using conventional processing, may exhibit improved properties when prepared by rapid solidification and consolidation. With few exceptions, however, alloy systems designed explicitly to take the full advantage of rapid solidification have yet to be explored [2-4].

Fine carbide and boride particles strengthen grain boundaries as well as the bulk material. Carbon and boron, however, tend to segregate during solidification, causing blocky precipitation at grain boundaries and thus give rise to suboptimal properties. Rapid solidification reduces solute segregation and is therefore capable of extending the domain of alloying. Studies of carbides and borides in iron-base alloys processed by rapid solidification techniques have been carried out [5-7]. The present paper reports on the boride and carbide dispersion produced by the melt-spinning process in nickel-base superalloys. In particular, the effects of boron and carbon on the ribbon castability, microstructure, phase stability and ductility have been investigated. A specific aim of the present studies is to demonstrate the capability as well as the limitation of rapid solidification processing in nickel-base superalloy development.

Experimental

One of the superalloys studied (alloy A) has a nominal composition as in Table 1. The gamma prime fraction is about 30% and the concentrations of the prime carbide and boride-forming elements are typical of most superalloys. Ribbons of alloy A and its variations with boron levels of 0.75, 1.45 and 3.0 weight percent were fabricated by the melt spinning technique in ambient air. The other superalloy studied (alloy B, Table 1) was originally designed for the unidirectional growth of γ/γ' - TaC eutectics. Ribbons of alloy B were melt-spun in a vacuum. The ribbon cross-sections were studied by optical metallography, the ribbon bottom-surface topography by microscopy using the Normarsky-interference contrast, and the ribbon top surface by scanning electron microscopy (SEM).

TABLE 1. Nominal Compositions of Alloys Studied (w/o)

Alloy	Ni	Co	Cr	Al	Ti	Nb	Ta	Mo	W	Re	C	B
A	balance	14.0	17.0	1.75	3.5	0.65	—	—	8.0	2.0	0.02	0.01
B	balance	3.80	3.84	5.34	—	—	11.37	3.01	4.33	6.44	0.43	—

These yielded information about the solidification structure and the ribbon-wheel contact characteristics. Furthermore, transmission electron microscopy (TEM) examinations of the ribbon microstructures were made on samples electrolytically thinned in the solution of 20% perchloric acid in methanol. For alloy B ribbons, microstructures at various positions through the ribbon thickness were studied by TEM on samples thinned from either one or both of the ribbon surfaces. Differential scanning calorimetry (DSC) and X-ray diffraction were performed on the ribbons based on alloy A to determine the ribbon structure and phase stability as influenced by boron content. The ribbon ductility, as cast and annealed at 900°C for 1 hour, was tested by bending.

Results and Discussion

A. Effects of Boron on Castability

Alloy A is in general difficult to cast into ribbon in air. The quench rate is too slow to prevent unacceptable oxidation of the ribbon surface, particularly at the beginning of each casting run. Observations are that the sticking distance of alloy A ribbons on the casting surface are too short to provide adequate secondary cooling. Additions of boron greater than 1.0 wt.% to alloy A drastically improve air castability, giving fast enough solidification and secondary cooling that little oxidation of the ribbons occurs. The ribbon-to-wheel sticking distance increases with boron additions greater than 1.0 wt.%, but the contact patterns [8] on the wheel-side surfaces of the ribbons fail to show any evidence of improved metal-wheel contact, Fig. 1. In fact, the alloy A ribbon shows near-perfect contact with the wheel in regions between extended air pockets, Fig. 1(a), while the ribbon of alloy A containing 3.0 wt.% boron shows uniform but poor contact with the wheel, Fig. 1(b). The beneficial effects of boron on the ribbon castability thus cannot be totally attributed to its modification of the liquid-metal fluidity or surface tension, which may influence the melt-wheel contact characteristics. Instead, it should be largely attributed to boron's effect on the thermal properties of the melt and the thermodynamics and kinetics of the solidification process [9].

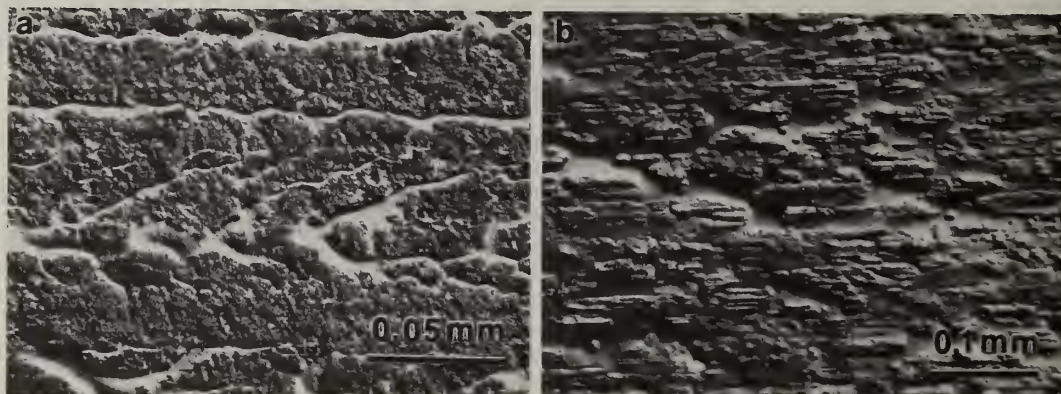


Fig. 1 The melt-to-wheel contact patterns observed on the wheel-side surfaces of the air-cast ribbons of (a) alloy A and (b) alloy A plus 3.0 w/o boron. The castings were in the horizontal direction.

B. Effects of Boron on Solidification Microstructures

The solidification structure developed in ribbons is most conveniently studied on the ribbon top surface where liquid metal is 'decanted'. Figure 2 compares the ribbon top surface structure as influenced by the boron content. For alloy A, which contains only a trace amount of boron, the surface dendrites are about 1 μm in length, and only a few ternary branches are visible, Fig. 2(a). Although the ribbon surface appears to have the [100] texture judging from the branching symmetry, the [100] dendritic crystals tend to have rotation mismatches with neighbors. A detailed study [10] has shown that the dendrites are, in fact, formed by independent nucleations and that every dendrite constitutes a separate grain. When the boron content is increased to 0.75 wt.%, the [100] dendritic structure is still maintained, Fig. 2(b). The dendrites are about 2 μm in length, and they tend to

be more intricately branched, having a ternary branch spacing of $\sim 0.2 \mu\text{m}$, compared to $\sim 0.5 \mu\text{m}$ in the low-boron ribbons. Furthermore, some neighboring dendrites of similar orientation seem to group together, being surrounded by the heavily segregated grain boundaries. The grains as conceivable in Fig. 2(b) are about $5 \mu\text{m}$ in diameter. When boron is further increased to beyond 1.0 wt.%, the dendritic structure no longer exists, Fig. 2(c). Instead, the ribbon becomes essentially structureless, decorated only by some unidentified surface striations.

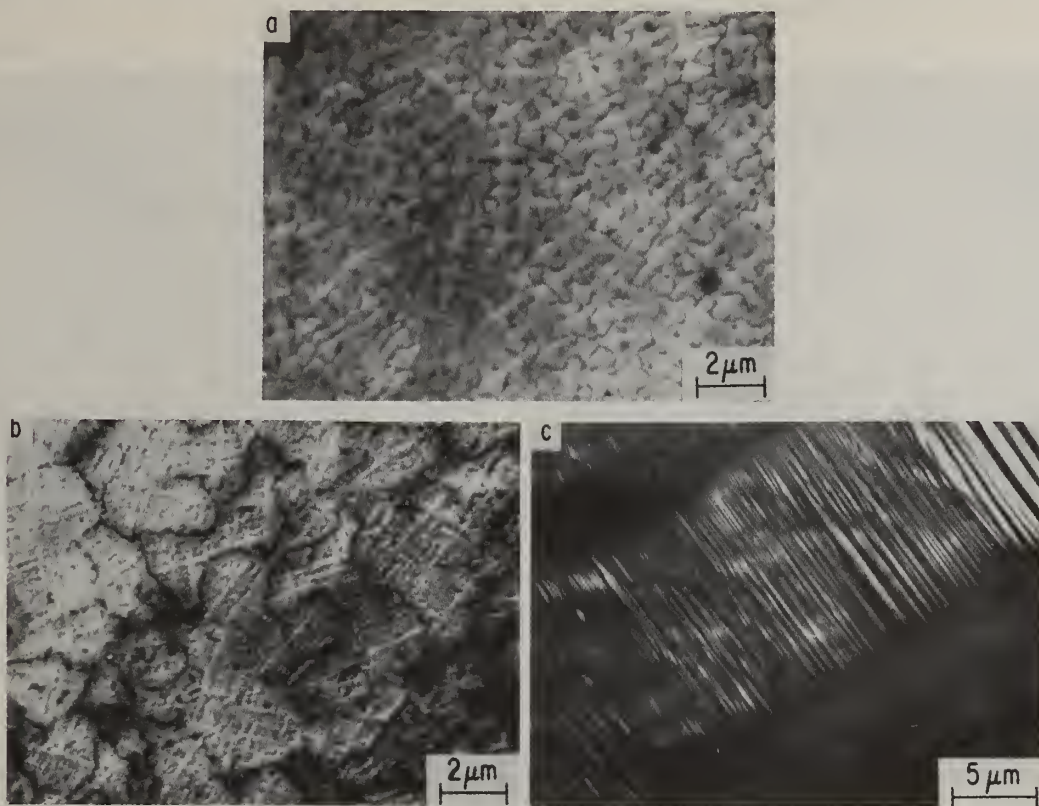


Fig. 2 The 'decanted' solidification structure on the top surfaces of superalloy ribbons having boron concentrations of (a) 0.01 w/o, (b) 0.75 w/o, and (c) 3.0 w/o.

A comparison of the ribbon cross-sectional structure dramatizes the effect of boron on the ribbon solidification, Fig. 3. As shown in Fig. 3(a), a segregated crystalline structure develops when $B < 1.0 \text{ wt.}\%$. Here, the solidification crystals nucleated at the wheel-side surface and grow unidirectionally toward the ribbon top surface, in the cellular morphology initially before a transi-

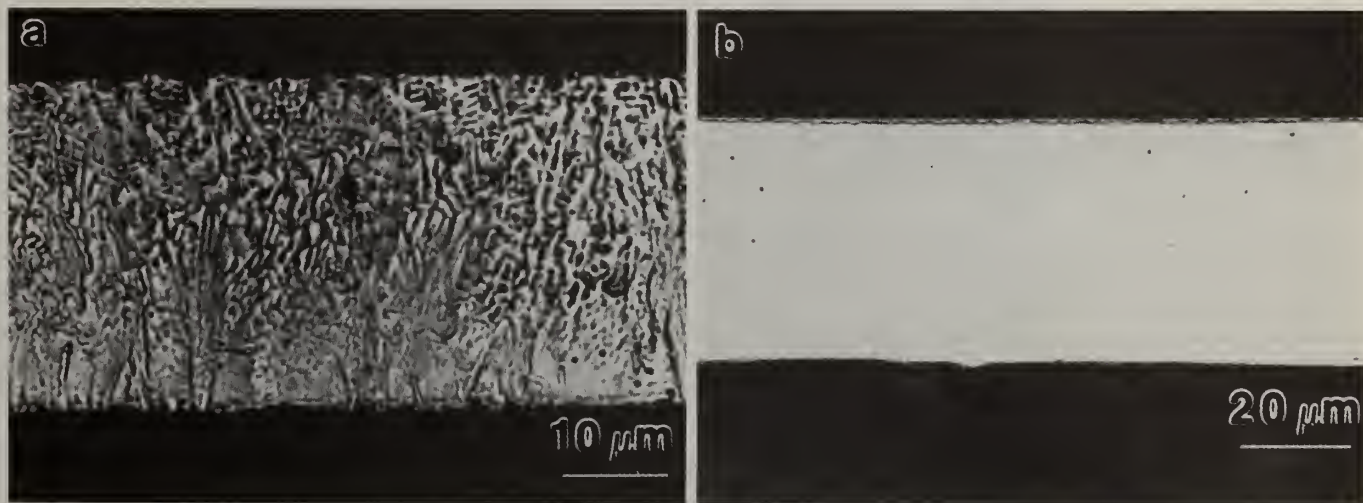


Fig. 3 The cross section micrographs of superalloy ribbons containing (a) 0.01 w/o and (b) 3.0 w/o of boron. The wheel-side surface is shown at bottom.

tion to the branched dendritic morphology beyond the center of the ribbon thickness. Small additions of boron refine the structural size-scale. When the boron content is increased to $B > 1.0$ wt.%, a planar-front solidification must have occurred, since the resultant ribbon structure is uniform without obvious segregation, Fig. 3(b). As discussed previously, this swift change in the solidification mode at the 1.0 wt.% boron level is not due to improvement in solidification heat transfer, but due to the reduced atom mobility at the solid-liquid interface. Boron has been known for its promotion of the formation amorphous phases [9].

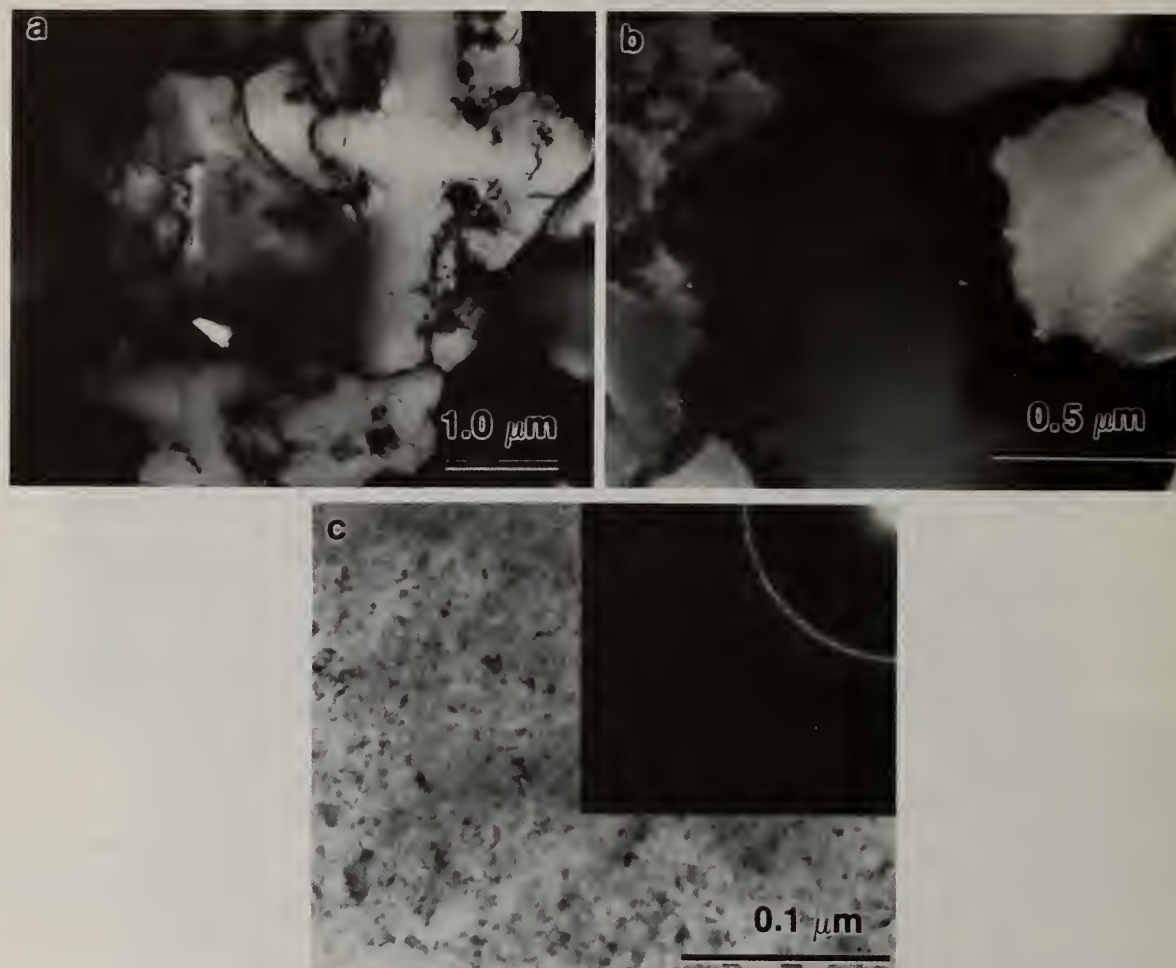


Fig. 4 TEM microstructure in superalloy ribbons containing (a) 0.01 w/o, (b) 0.75 w/o, and (c) 1.45 w/o of boron.

The microstructures of the superalloy ribbons containing various amounts of boron were further investigated at high magnifications by TEM. For $B < 1.0$ wt.%, boride particles precipitate essentially in the interdendritic regions, Fig. 4(a) and (b). Apparently, boron has segregated during the solidification process. The size, as well as the quantity, of the borides increases with increasing boron content, with the boride diameter being $\sim 0.01 \mu\text{m}$ in alloy A ribbons, Fig. 4(a), and $\sim 0.1 \mu\text{m}$ in the ribbon containing 0.75 wt.% boron, Fig. 4(b). The specific boride phase and composition are yet to be determined. Fig. 4(a) and (b) also show the refinement of the dendritic structure as observed in Fig. 3(a) and (b). Gamma prime precipitates cannot be resolved in the magnifications used, even though the superlattice diffraction spots can be detected. For $B > 1.0$ wt.%, the as-cast ribbons show a homogeneous structure containing small precipitates of less than 200\AA , Fig. 4(c). Electron diffraction reveals that the precipitates are nickel-base solid solution particles embedded in an amorphous matrix. This is in corroboration to the X-ray diffraction result of Fig. 5 that there are diffraction peaks of crystalline nickel phase overlapping with the broadened diffraction background due to the presence of an amorphous phase. Boron is believed to be entrapped during the nonequilibrium plane-front solidification, resulting in the amorphous phase without boride precipitation.

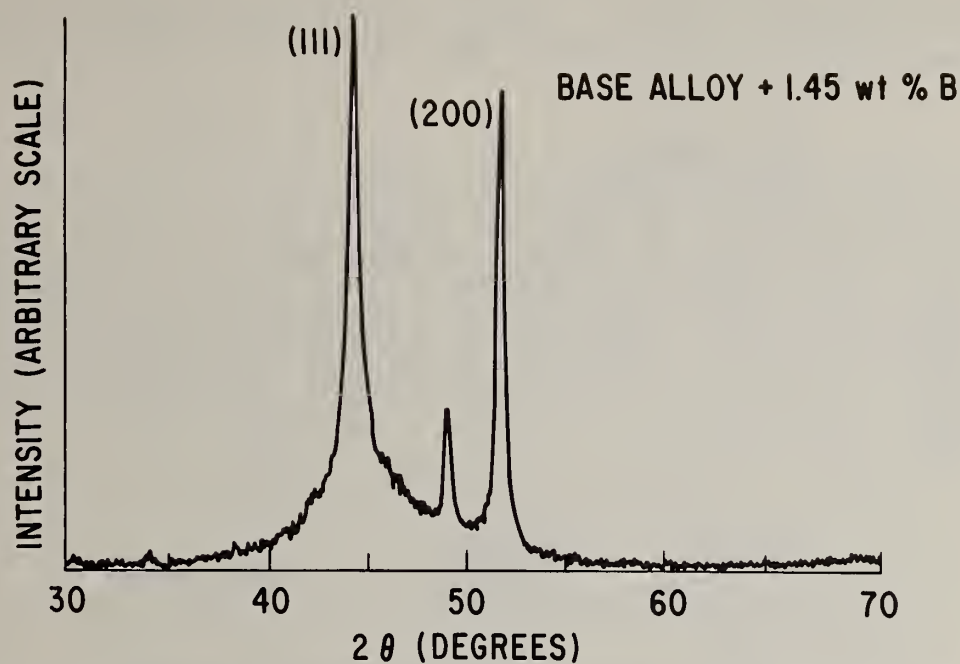


Fig. 5 X-ray diffraction pattern showing the coexistence of a crystalline and an amorphous phase in the as-cast superalloy ribbon containing 1.45 w/o boron.

C. Effects of Boron on the Annealed Microstructure

The ribbon of alloy A with 0.75 wt.% boron addition was annealed at 760°C for 24 hours. The resultant structure as in Fig. 6 shows a uniform distribution of coherent gamma prime precipitation about 0.03 μm in diameter. Compared to Fig. 4(b), the intercellular boride particles remain about 0.1 μm in diameter without significant coarsening. Neither the cell size nor the morphology is affected by this low temperature anneal. When the ribbon is annealed at 900°C for 1 hour, the resulting gamma prime precipitates are about 0.5 μm in diameter, and the boride particles coarsen to about 0.2 μm in diameter agglomerating to the grain boundary triple points. Coarsening of the grain structure seems to just begin, perhaps made easy by the redistribution of the grain boundary boride particles.



Fig. 6 Microstructure in the superalloy ribbon containing 0.75 w/o boron, annealed at 760°C for 24 hours.

The differential scanning calorimetry (DSC) study reveals two low temperature reactions, at $\sim 460^{\circ}\text{C}$ and $\sim 600^{\circ}\text{C}$, in those ribbons containing $\text{B} > 1.0 \text{ wt.}\%$, Fig. 7. The specific reaction temperatures vary slightly with boron concentration, but both reactions are absent in ribbons containing $\text{B} < 1.0 \text{ wt.}\%$. After annealing at 460°C for 1 hour, the ribbon with 3.0 wt.% boron exhibits a microstructure similar to Fig. 4(c). However, it generates electron diffraction rings additional to those from the nickel particles, indicating the possible precipitation of borides from the as-cast

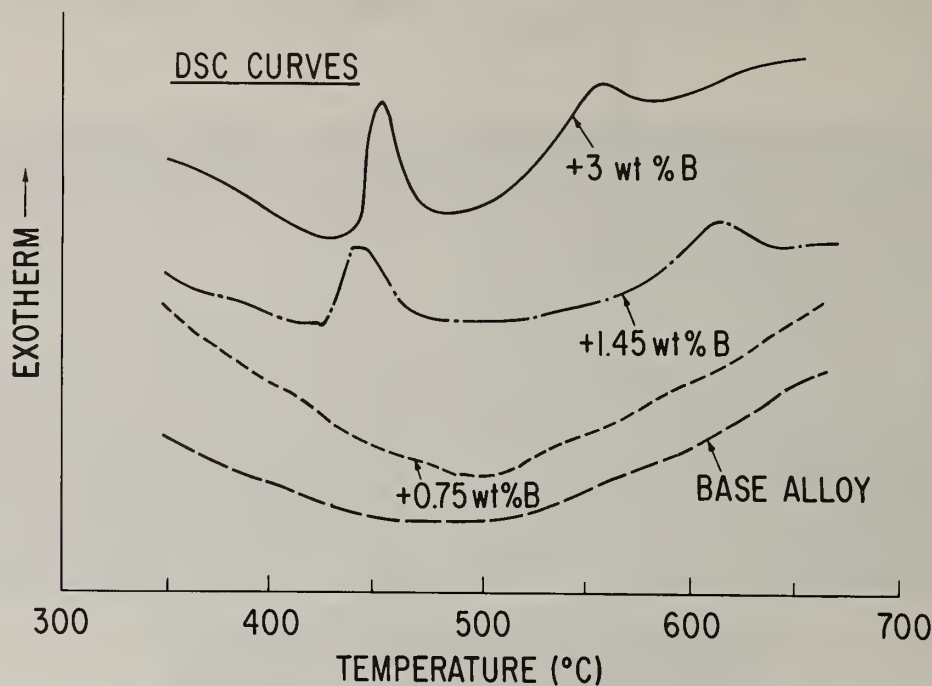


Fig. 7 DSC curves for superalloy ribbons of various boron concentrations, based on alloy A.

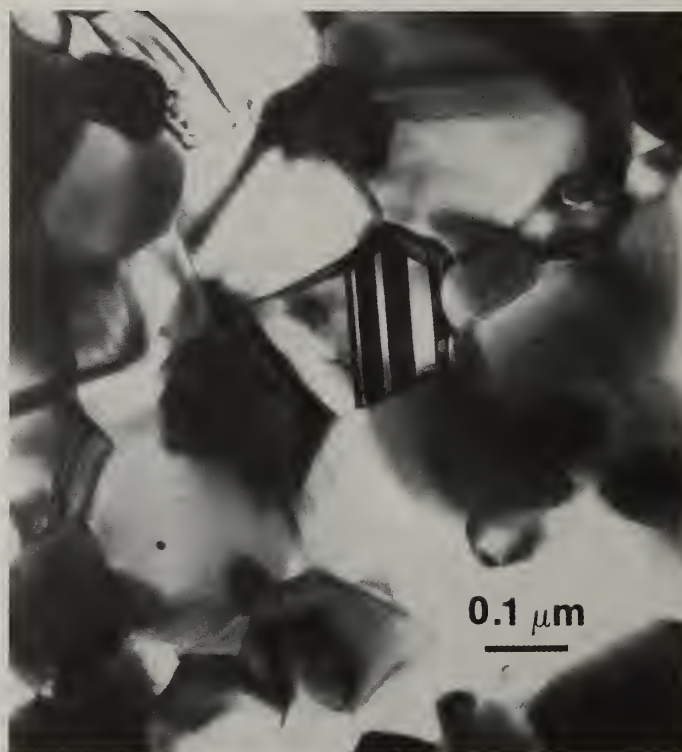


Fig. 8 Microstructure in the superalloy ribbon containing 3.0 w/o boron, annealed at 900°C for 1 hour.

amorphous matrix. Annealing at 600°C for 1 hour precipitates no additional new phase. The nickel and boride particles enlarge slightly to about 200Å, but the matrix phase remains homogeneous with no development of grain structure. Annealing at 900°C for 1 hour produces a unique microcrystalline structure having uniform grains of approximately 0.2 µm in diameter [3,4], Fig. 8. There is no obvious precipitation of gamma prime phase within grains and boride particles of about 0.1 µm precipitate at the grain boundary triple points. Preliminary analyses by electron diffraction suggests the boride is $M_{23}B_6$.

D. Effects of Boron on Ribbon Ductility

The ribbon ductility can be conveniently tested by bending to fracture. The fracture strain, e , is given by $e = h/(D+h)$, where h is the ribbon thickness and D is the bend diameter at which the ribbon fractures. The test results, Table 2, show that the ductility of the as-cast ribbons decreases with increasing boron content up to $B = 1.45$ wt.%. Further increase in boron improves the ductility, presumably due to the increase in the degree of amorphous state. After annealing at 900°C for 1 hour, the ribbon of 0.75 wt.% boron becomes ductile. Ribbons of higher boron concentrations, however, become further embrittled after annealing. This result is contrary to that of ref. [3] which showed an improved ductility when amorphous structure containing less than 2 wt.% boron was transformed to microcrystalline structure.

TABLE 2. Ribbon Bend-Fracture Strain

Composition	Strain to bend-fracture (as-cast)	Strain to bend-fracture (900°C/1 hr)
alloy A	1*	1*
A + 0.75 w/o boron	0.03	1*
A + 1.45 w/o boron	0.01	0.004
A + 3.0 w/o boron	0.04	0.006

*Bent 180 degrees without fracture.

E. Microstructure in Ribbons Containing Carbon

The microstructure of a longitudinal section (parallel to the casting direction) in an alloy B ribbon is shown in Fig. 9. As shown in this figure, the microstructure varies through the ribbon thickness, being homogeneous near the wheel-side surface, cellular at the ribbon center, and dendritic near the top surface. These structural variations are much more pronounced than in the boron-modified ribbons. Obviously, the microstructure developed in the carbon-modified alloys are more sensitive to the cooling rate.

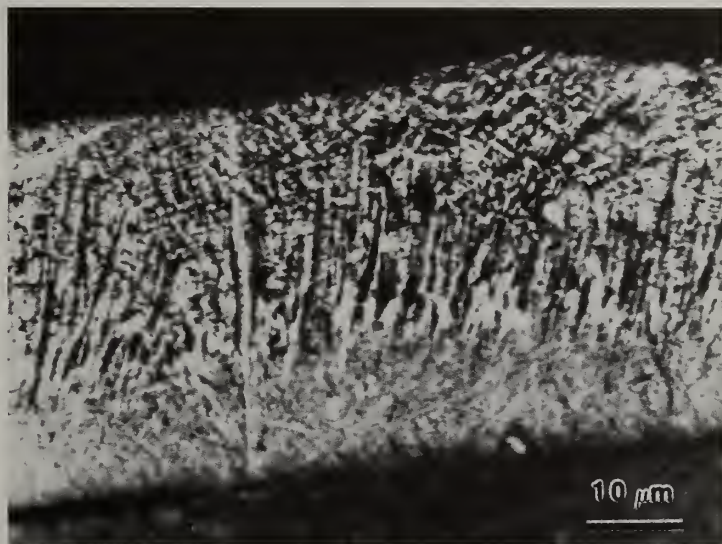


Fig. 9 Optical micrograph of a longitudinal section in an alloy B ribbon. The wheel-side surface is shown at bottom.

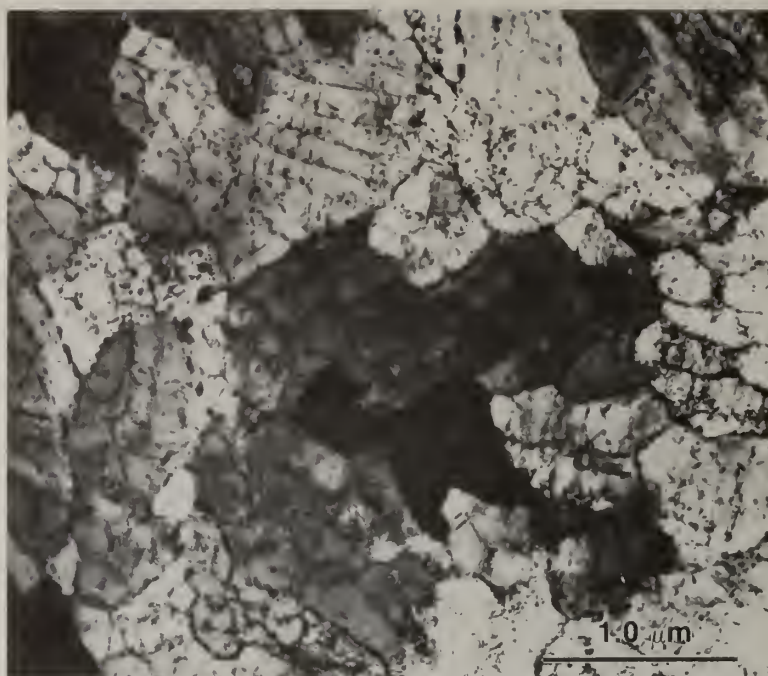


Fig. 10 TEM overall cell structure near the wheel-side surface of alloy B ribbon.

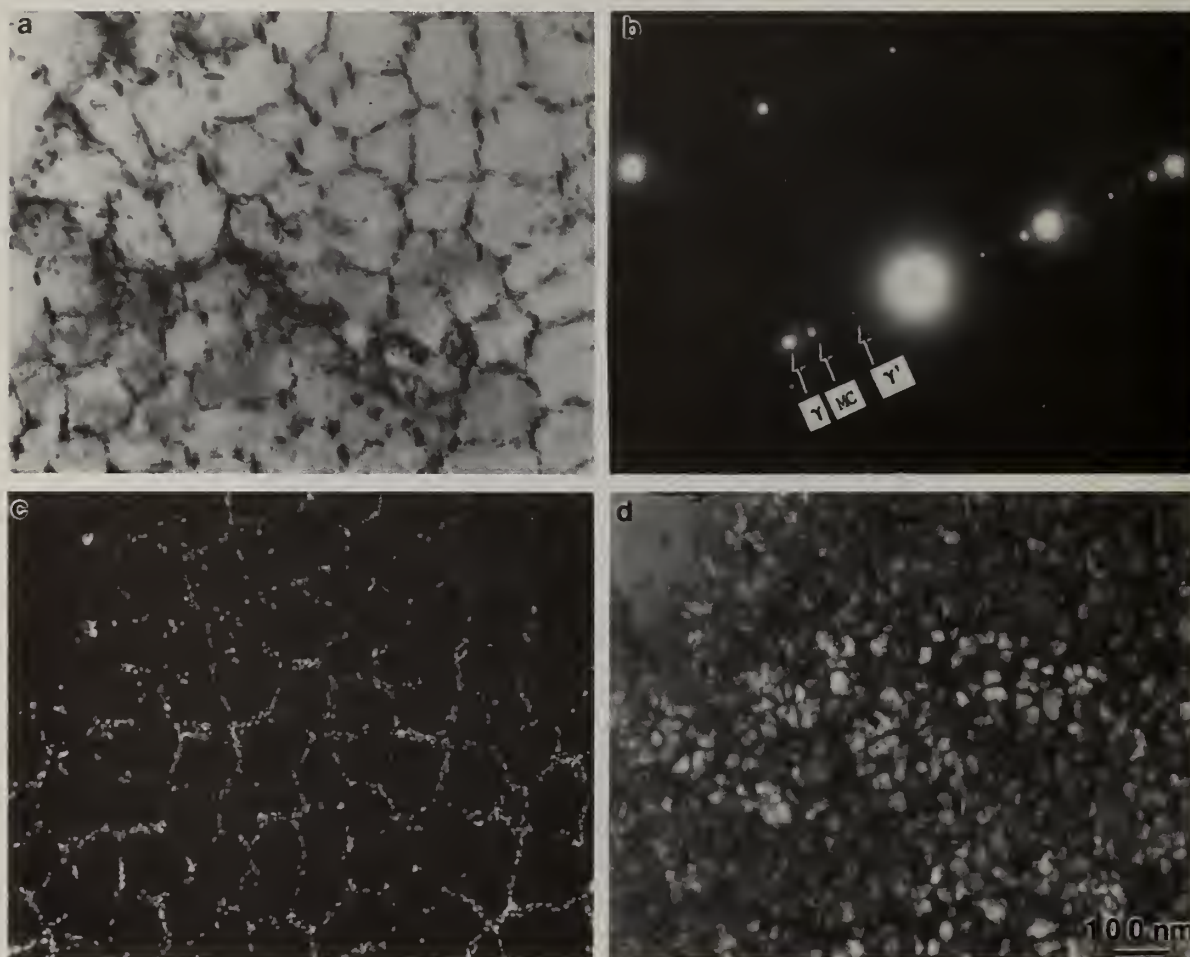


Fig. 11 The subcell structure observed near the wheel-side surface of alloy B ribbon: (a) bright field image, (b) the electron diffraction pattern, (c) dark field image using an MC carbide reflection, and (d) dark field image using a gamma prime reflection.

The overall microstructure at the wheel-side surface of the ribbon is shown in the TEM micrograph of Fig. 10. The structure consists of cells of varying sizes, generally 0.5 to 2.0 μm in diameter. The boundaries between these cells are decorated with particles less than 20 nm in diameter, Fig. 11(a). In addition, a large number of particles of similar size are seen inside the cellular grains, often forming a regular subcell structure. Both the boundary and sub-boundary particles can be shown by electron diffraction to have the MC-carbide structure, Fig. 11(b). X-ray spectroscopy further reveals that the particles are rich in tantalum. The lattice parameter measured for the carbide particles is approximately 0.426 nm (in comparison to 0.455 nm reported for the stoichiometric TaC), suggesting a carbide composition of $\text{Ta}_{0.55}\text{C}_{0.45}$.⁽¹¹⁾ Substitution of Ta for other carbide formers may also contribute to the reduced lattice parameter. It is also shown by dark field studies that within a single grain, all the TaC particles are of a single orientation, and have fully coherent relationships with the matrix, Fig. 11(c). The electron diffraction pattern also reveals the presence of gamma prime in the gamma matrix. The dark field image formed using the gamma prime reflection shows that the gamma prime is also fully coherent, with a cuboidal morphology and an approximate dimension of 30 nm, Fig. 11(d).

In the center of the ribbon, the size of the cellular grains has increased slightly, the mean gamma prime size is approximately 50 nm, and the carbide particles at both the grain boundaries and inside the grains are much larger, 50 to 100 nm in diameter. Furthermore, the amount of the intragranular carbide precipitation is notably decreased. Near the ribbon top surface, the centers of the primary cells are totally depleted of carbide, Fig. 12. The carbide particles which preferentially precipitate in the intercellular regions generally take an irregular shape. Some continuous precipitation along cell boundaries can also be observed.

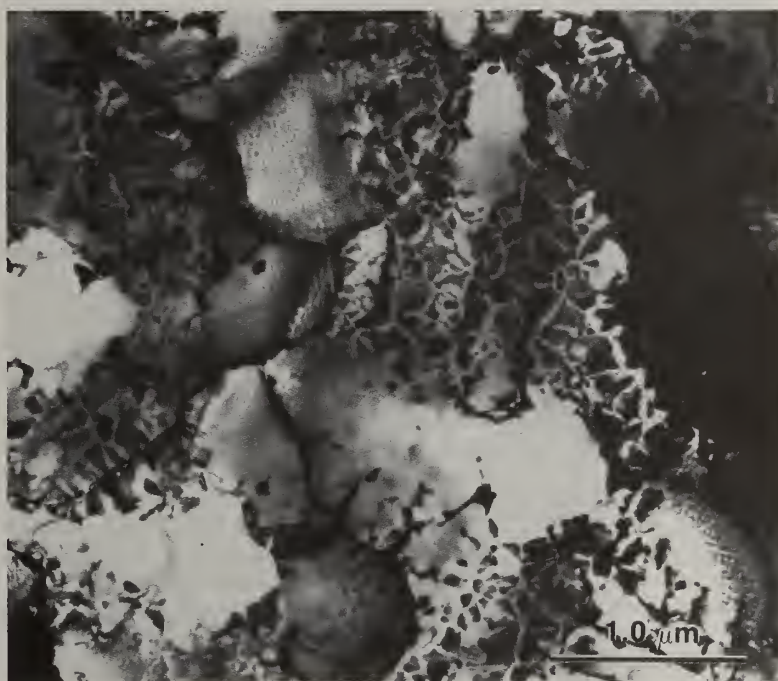


Fig. 12 TEM microstructure near the top surface of alloy B ribbon.

The alloy B ribbons have been annealed at 1000°C for 2 hours. The annealed structure near the center of the ribbon is shown in Fig. 13. The gamma prime precipitation is coarsened to about 0.1 μm in diameter, but the cell size remains unchanged, being stabilized by the cell boundary precipitation. It should be noted that the irregular carbide particles are stable under the present annealing condition, showing no signs of changes in morphology, distribution or size. There is, however, a second set of precipitation particles, which are rounded in shape, 0.02 to 0.1 μm in size, and primarily located at the cell boundaries. Preliminary analyses indicate that the latter particles are rich in rhenium and are precipitated and coarsened during the anneal.

Conclusions

Boron additions to a superalloy have demonstrated drastic modifications in the melt spinning castability, solidification structure, and heat treatment precipitation. More specifically, boron affects the liquid-metal thermal properties, and when B > 1 wt.%, a continuous ribbon can be readily

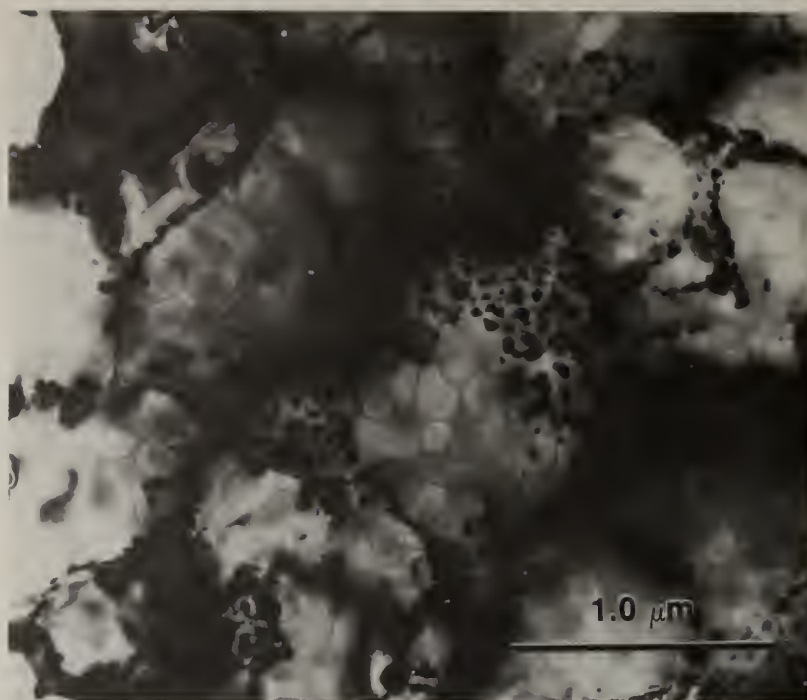


Fig. 13 Microstructure near the center of alloy B ribbon, annealed at 1000°C for 2 hours.

cast in air without excess surface oxidation. Boron also refines the dendritic structure and changes the solidification kinetics, and when $B > 1$ wt.%, a mixture of microcrystalline and amorphous phases can be obtained as is evident from DSC and X-ray diffraction. TEM studies further show that the high boron ribbons contain small particles <20 nm in diameter of Ni-base solid-solution embedded in an amorphous matrix. Annealing the ribbons at 600°C for 1 hour precipitates uniform borides smaller than 10 nm, and annealing at 900°C for 1 hour produces 0.2 μm microcrystalline cells, which are decorated with cell boundary precipitation of 0.1 μm borides. This unique microcrystalline structure, however, embrittled the high boron superalloy ribbons, giving a bend fracture strain less than 0.01.

A uniform microstructure in a superalloy containing 0.43 wt.% carbon can be produced only when the cooling rate is greater than 10^5 K/s. In the bottom third of the ribbon thickness near the wheel-side surface, the microstructure consists of uniform subcells of about 0.1 μm in diameter, having MC-carbide precipitation smaller than 20 nm at the subcell boundaries. With the reduced cooling rate toward the ribbon top surface, the subcell structure gradually diminishes and MC-carbides ranging from 50 to 100 nm in diameter precipitate only in the intercellular regions. The MC-carbides remain stable after annealing at 1000°C for 2 hours, but particles of a second phase precipitate and coarsen at the cell boundaries during the anneal. This unstable, rhenium-rich precipitation causes reduction in ductility and strength of the annealed ribbon.

Acknowledgments

We thank R. J. Zabala, R. P. Laforce, L. Perocchi, and the late A. C. Rockwood for their technical assistance. We also thank S. W. Yang, M. R. Jackson, B. Cantor, and L. A. Johnson for stimulating discussions.

References

- [1] P. Duwez, R.H. Willens, and W. Klement, *J. Appl. Phys.*, 31 (1960) 1136.
- [2] T.H. Sanders, Jr., J.W. Johnson, and E.E. Underwood, *Proc. 2nd Int. Conf. Rapid Solidification Processing*, Reston, Virginia, March 1980, Ed. R. Mehrabian et al., Claitor's Publishing, p. 141.
- [3] R. Ray, *Proc. MRS Meeting on Rapidly Solidified Amorphous and Crystalline Alloys*, Boston, November 1981, Ed. B.H. Kear et al., North-Holland, p. 435.
- [4] C.C. Wan, as in Ref. 3, p. 441.

- 1] J.V. Wood and R.W.K. Honeycombe, Mat. Sci. Eng., 38 (1979) 217.
- 2] E.R. Slaughter and S.K. Das, as in Ref. 2, p. 354.
- 3] J.J. Rayment and B. Cantor, Proc. 3rd Int. Conf. Rapidly Quenched Metals, Univ. of Sussex, July 1978, Ed. B. Cantor, The Metals Society, P. 110.
- 4] S.C. Huang and H.C. Fiedler, Met. Trans., 12A (1981) 1107.
- 5] I.W. Donald and H.A. Davies, Phil. Mag., A42 (1980) 277.
- 10] S.C. Huang and A.M. Ritter, to be published in the Proc. AIME Symposium on the Chemistry and Physics of Rapidly Solidified Materials, St. Louis, Missouri, September 1982.
- 11] E.K. Storms, The Refractory Carbides, Academic Press, 1967.

HIGH TEMPERATURE OXIDATION OF RAPIDLY SOLIDIFIED Ni-Al-Mo-W ALLOYS

G. H. Meier and F. S. Pettit

University of Pittsburgh
Pittsburgh, PA 15261

A. S. Khan

Pratt and Whitney Aircraft
West Palm Beach, FL 33402

ABSTRACT

The effects of Mo and W additions on the isothermal and cyclic oxidation behavior of Ni-Al alloys in the temperature range of 760 to 1200°C are reported. The presence of Mo and W was found to affect the selective oxidation of Al in two ways. At higher temperatures and in some concentrations these elements, particularly Mo, had the beneficial effect of promoting the formation of an external layer of protective Al_2O_3 in a similar manner to the well-known effect of Cr additions to Ni-Al alloys. Under other conditions these elements, particularly W, had the detrimental effect of promoting internal oxidation of the Al, apparently by decreasing the alloy interdiffusion coefficient. In the latter case the accumulation of MoO_3 and WO_3 in the reaction product produced catastrophic oxidation rates, particularly at the higher temperatures. Extensive spalling and large weight losses in cyclic oxidation were observed wherever significant amounts of Mo- and W- oxides formed. The modification of the alloys with additions of several percent Cr and Ta and a few tenths of a percent Y and Hf promoted the formation of an adherent, protective Al_2O_3 scale over the temperature range studied with corresponding excellent resistance to both isothermal and cyclic oxidation.

Introduction

The major emphasis of this study is on the effect of Mo and W on the selective oxidation of Al from Ni-Al alloys to form a continuous external Al_2O_3 scale and the extent to which Mo and W can promote catastrophic oxidation. Therefore, a brief discussion of these phenomena will be presented.

The formation of a continuous external film of an oxide such as Al_2O_3 as opposed to its formation as internal oxide particles is essentially determined by a balance between the outward flux of Al through the alloy and the inward migration of the internal oxidation front. The formation of an external scale is favored by increased Al concentration, a higher alloy interdiffusion coefficient and lower oxygen permeability which can result from decreased p_{O_2} in the atmosphere and the presence of other elements in the alloy which form oxides of high O_2 stability (e.g. Cr in Ni-Cr-Al alloys). An additional factor favoring formation of a continuous Al_2O_3 film is a slow growth rate of the other surface oxides (transient oxides).

The critical Al content in binary Ni-Al alloys for external Al_2O_3 formation has been determined (1) and found to decrease with increasing temperature. For example, Ni-6Al is a NiO-former at 900°C but forms an external Al_2O_3 film at 1200°C. The addition of Cr to Ni-Al alloys is known to enhance external Al_2O_3 formation at smaller Al concentrations but there are no studies of the effect of Mo or W on Al_2O_3 formation. However, several studies have been reported for the effect of W on Cr_2O_3 formation on Ni-Cr alloys. El-Dahshan, et al., (2) found that additions of 40 wt.% W to Ni-10Cr promoted external Cr_2O_3 formation at temperatures between 900 and 1000°C, presumably due to W acting as an "oxygen getter" in the same manner as Cr in Ni-Al. It was observed, however, that the W additions resulted in ultimate breakdown of the Cr_2O_3 due to W causing a marked decrease in the alloy interdiffusion coefficient so that the flux of Cr to the scale/alloy interface was not sufficient to maintain the Cr_2O_3 layer. Similar effects were reported by Espevik, et al., (3) for W additions to Ni-22Cr.

The oxidation literature contains several examples of catastrophic attack induced by high refractory metal contents in Fe- and Ni- base alloys. Leslie and Fontana(4) found that Mo-containing Fe-25Ni-16Cr alloys underwent catastrophic oxidation at 900°C in static air even though the oxidation resistance was good in flowing air. Brenner (5) found that binary Ni-Mo and Fe-Mo alloys containing as much as 30% Mo did not oxidize catastrophically at 1000°C. Pizzini, et al., (6) obtained similar results for Ni-Mo alloys. Brenner, (7) however, found that a number of Fe-Ni-Mo and Fe-Cr-Mo alloys did undergo catastrophic attack. This attack was ascribed to the accumulation of liquid MoO₃ at the scale/alloy interface. Peters, et al., (8) found that Ni-15Cr-Mo alloys had good oxidation resistance in flowing atmospheres but Mo contents in excess of 3% caused catastrophic attack in static atmospheres. A Mo-rich oxide was observed at the scale/alloy interface suggesting the importance of MoO₃ accumulation. Relatively little work has been done on the effect of Mo or W on the oxidation of α -Al₂O₃-forming alloys, although catastrophic hot corrosion of such alloys is well documented (9). It appears that the Mo and W play an important role in causing this type of degradation.

This paper presents the results of a study of the effects of Mo and W on the oxidation of Ni-Al alloys prepared both by conventional casting and consolidation of rapidly solidified powders. Results for the oxidation behavior of similar alloys modified by small additions of Cr, Ta, Y, and Hf are also presented.

Experimental

The compositions of the alloys studied are listed in Table 1. These include alloys prepared by conventional drop casting and by consolidation of rapidly solidified powders. Specimens were cut,

Table 1 Nominal Alloy Compositions

Concentrations (Weight Percent)

<u>Alloy</u>	<u>Ni</u>	<u>Al</u>	<u>Mo</u>	<u>W</u>	<u>Cr</u>	<u>Ta</u>	<u>Y</u>	<u>Hf</u>	<u>Preparation Technique</u>
Ni-Al	Bal.	6	-	-	-	-	-	-	Drop Cast
A	Bal.	7	11	-	-	-	-	-	Drop Cast
B	Bal.	7	14	-	-	-	-	-	Drop Cast
C	Bal.	7	17.5	-	-	-	-	-	Drop Cast
JG-185	Bal.	6.8	14.4	6.1	-	-	-	-	Drop Cast
RSR-185	Bal.	6.8	14.4	6.1	-	-	-	-	Rapid Sol.
RSR-467	Bal.	7.1	11.4	6.3	-	-	-	-	Rapid Sol.
Modified-467	Bal.	6.7	11	6	3 to 4	1.5	0.1	0.1 to 0.2	

polished through 600 grit SiC, ultrasonically cleaned in ethanol, and dried. The oxidation experiments were carried out in flowing air at temperatures between 760 and 1200°C in either a continuously-weighing microbalance or an automatic thermal cycling apparatus. The oxidation morphologies were examined by optical and scanning electron metallography and X-ray diffraction.

Results and Discussion

The composition of the alloys was found to influence their oxidation behavior to a greater extent than the preparation technique. Figure 1 compares the rates of oxidation at 1150°C in flowing air. These curves are characteristic of the behavior of the alloys in the highest temperature range studied (1100-1200°C). The rates for RSR-185 and JG-185 are initially rapid and then level off. However, this plateau is partially due to the evaporation of MoO₃ from the specimens as evidenced by condensation of MoO₃ crystals in cooler parts of the reaction tube. After times on the order of fifty hours the curves bend up sharply giving oxidation rates faster than those for an NiO forming alloy such as Ni-6Al. The corrosion morphology typical of RSR-185 and JG-185 is shown in Figure 2 for JG-185 exposed for 30 minutes at 1200°C. The scale is composed of a dense outer NiO layer beneath which is a 5 μ m thick layer containing only Ni and Mo and which is indicated by X-ray diffraction to be NiMoO₄. Beneath this layer are the fragmented remnants of a layer which is an intimate mixture

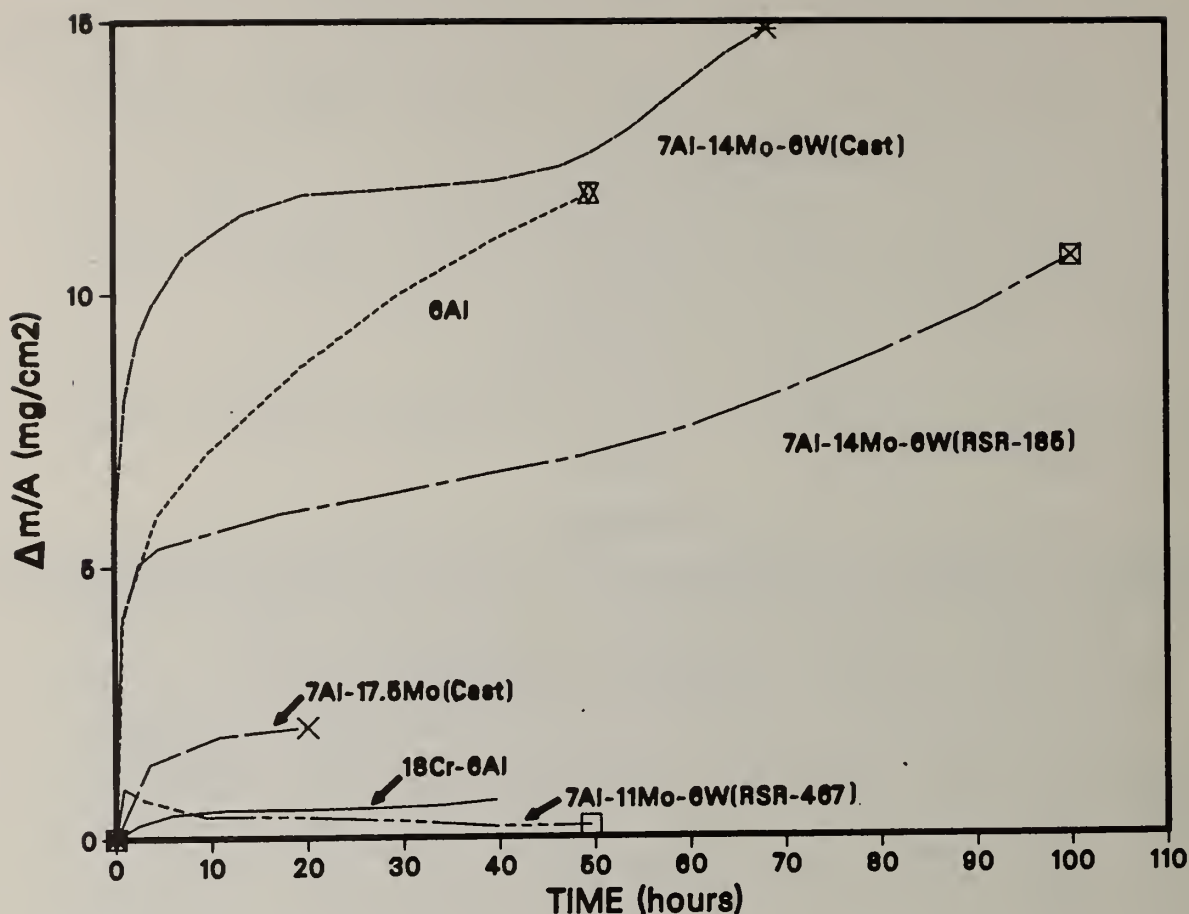


Figure 1 Oxidation rates for several cast and RSR alloys in air at 1150°C.

of Al_2O_3 , $NiAl_2O_4$, $NiMoO_4$, $NiWO_4$, NiO and, perhaps, MoO_3 . The dark internal oxides are Al_2O_3 and the bright layer at the scale/metal interface is rich in Mo and contains significant amounts of Al. After 1 hour (Fig. 3) it is seen that the growth of the external scale has consumed the internal oxidation zone leaving a ragged scale/metal interface. The X-ray maps of Figure 3 indicate the formation of an Al_2O_3 film over some portions of the scale/metal interface. This layer is not able, however, to completely seal the surface and the corrosion sequence repeats itself. Observation of specimens exposed for longer times indicates that this repetition continues to occur.

The preceding metallographic results suggest the mechanism presented in Figure 4 for the degradation of RSR-185 and JG-185 in the temperature range above 1100°C. Initially, (t_1) an external NiO scale forms with internal Al_2O_3 precipitates in the alloy. As indicated by the approximate values of the equilibrium oxygen partial pressures, the dioxides of Mo and W can form below the NiO but the trioxides are unstable. With continued reaction (t_2) the dioxides of Mo and W react with the NiO to form $NiMoO_4$ and $NiWO_4$. At this stage the external scale is analogous to that found on binary Ni-Mo alloys. (5,6) However, for the Al-containing alloys the trioxides of Mo and W form (t_3) producing a liquid oxide. This, of course, requires the p_{O_2} at the scale/alloy interface to exceed the dissociation pressures of NiO. The evaporation of MoO_3 was observed in the present experiments indicating that the outer NiO scale cracks since the NiO scales formed on binary Ni-Mo alloys are apparently impermeable to MoO_3 . (5,6) This cracking could be the cause of the p_{O_2} becoming high enough to form the liquid trioxides. On the other hand, if the Ni activity below the scale decreases much below 0.1 the trioxides could become stable. In this case the liquid formation could be the cause of the scale disruptions. Once the liquid forms the subsequent corrosion is similar to that observed in some hot corrosion reactions. The liquid preferentially attacks the Al_2O_3 or the interface between the Ni and Al_2O_3 . This leads to the incorporation of the internal Al_2O_3 particles and islands of Ni into the liquid corrosion product (t_4). At the same time some areas of the alloy are forming continuous Al_2O_3 films and the outer $NiMoO_4$ layer is consumed by MoO_3 evaporation.

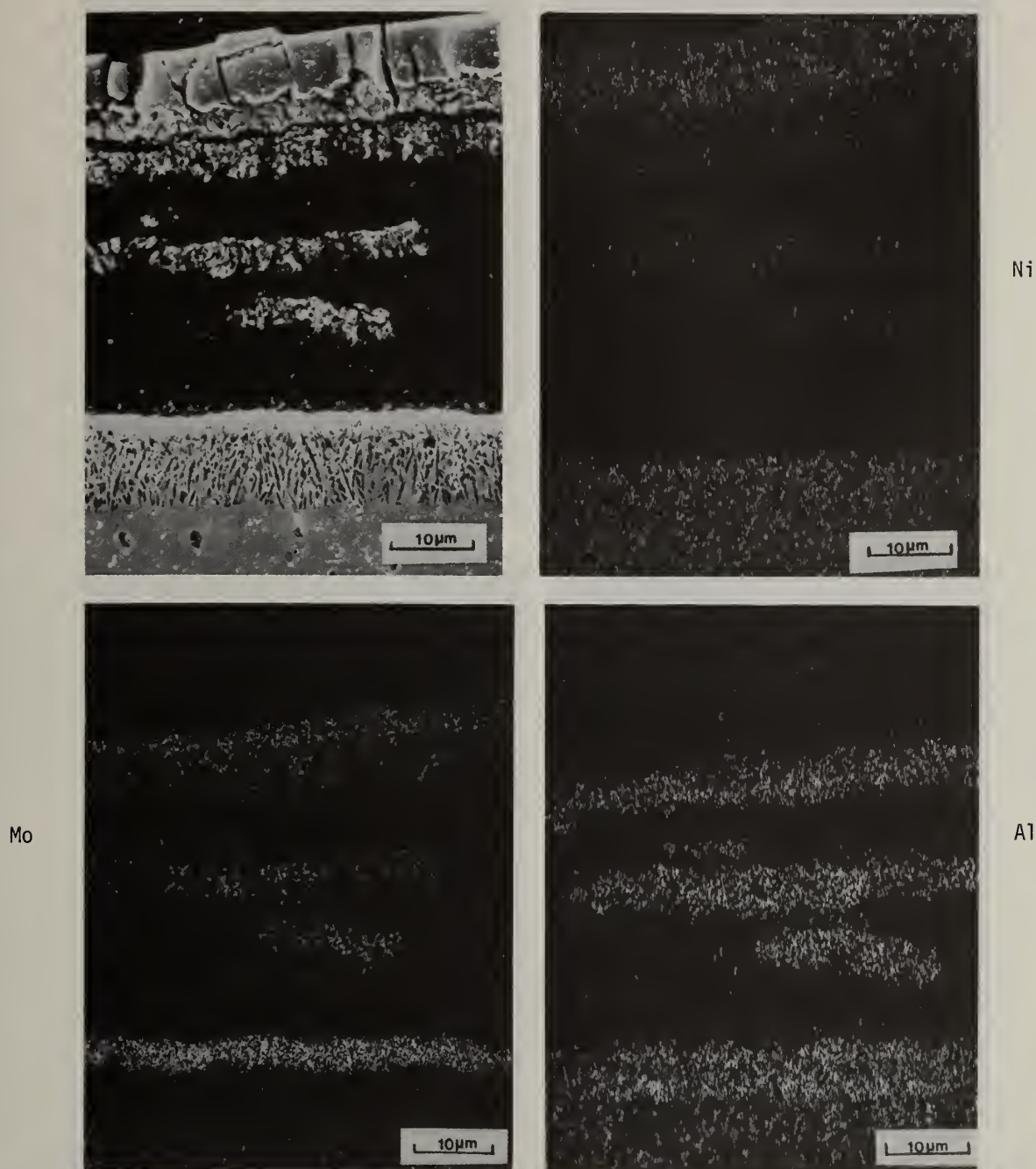


Figure 2 Cross-section of cast Ni-7Al-14Mo-6W exposed for 30 minutes in air at 1200°C.

The Al_2O_3 films are never able to become complete and are continually stripped and incorporated into the liquid corrosion product (t_5). At this stage the outer scale is NiO and below this is a layer of NiO which contains Al_2O_3 and NiAl_2O_4 . This layer forms by the evaporation of MoO_3 from the liquid corrosion product. Below the NiO layers is a layer containing NiO, Al_2O_3 , NiMoO_4 , and NiWO_4 , and NiO being formed by the oxidation of the Ni islands. At this stage the internal oxides of Al again form in the alloy substrate and the above mechanism goes through another cycle. The more rapid oxidation rate for the cast alloy compared to the RSR alloy is believed due to a less homogenous distribution of Mo and W in the former.

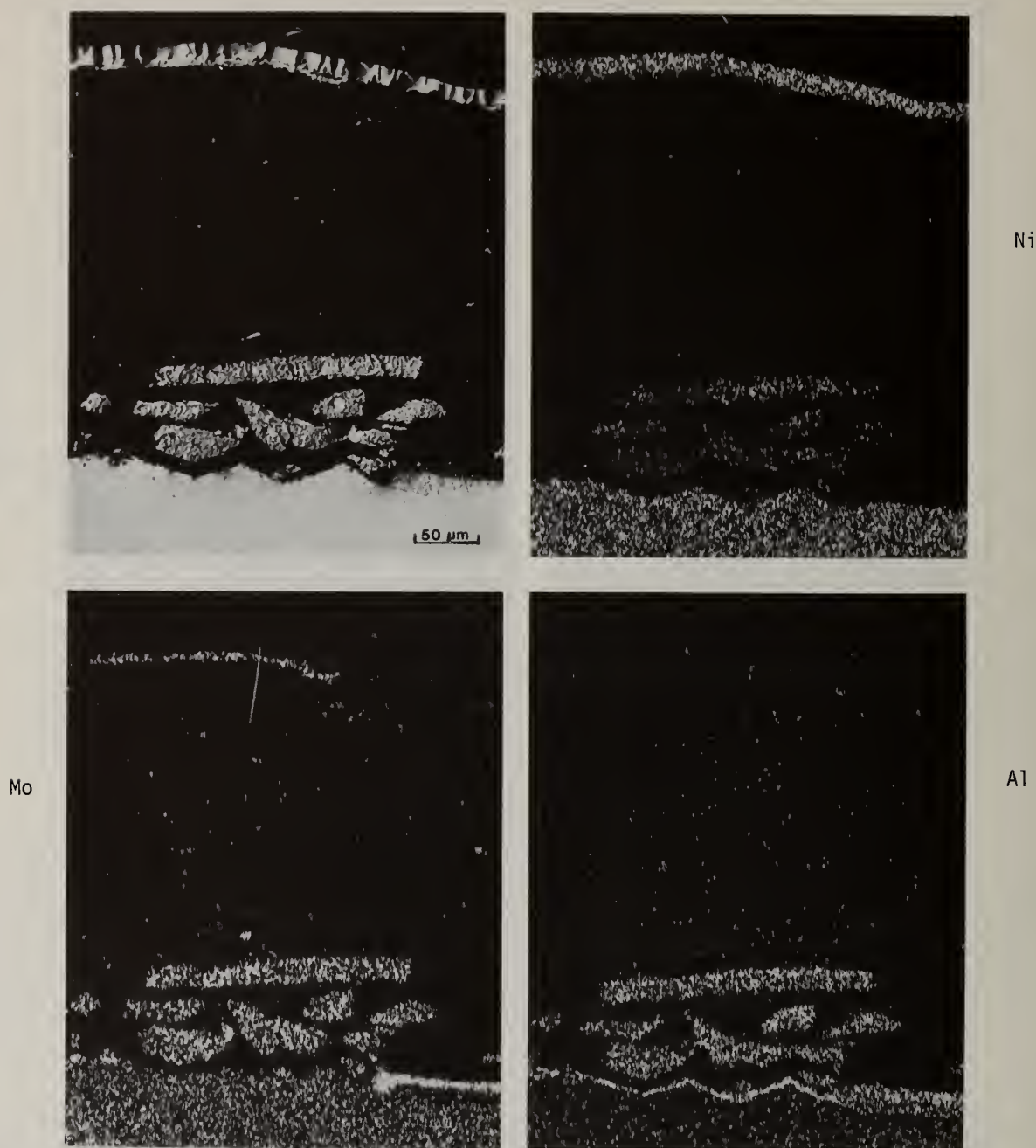


Figure 3 Cross-section of cast Ni-7Al-14Mo-6W exposed for 1 hour in air at 1200°C

Several additional observations support the above mechanism. One specimen of RSR-185 was exposed at 1150°C in argon in which the residual oxygen partial pressure was approximately 10^{-6} atm. The reduced oxygen pressure caused the NiO to grow much slower than in air and allowed a protective layer of Al_2O_3 to seal the surface and prevent the formation of significant amounts of Mo-oxides. A similar effect was observed when 6 weight percent Cr was added to the alloy, even for exposures in air. In this case the Cr acted as a "secondary getter" and allowed a protective Al_2O_3 scale to seal the surface.

Another supporting observation is the slow oxidation rate of the lower-Mo RSR-467 (Fig. 1). This alloy develops a thin Al-rich scale and exhibits an oxidation rate comparable to Ni-18Cr-6Al. Apparently, the Mo and W behave as oxygen getters in a manner similar to Cr to promote an Al_2O_3 scale while the lower Mo concentration prevents sufficient accumulation of Mo-oxides to initiate

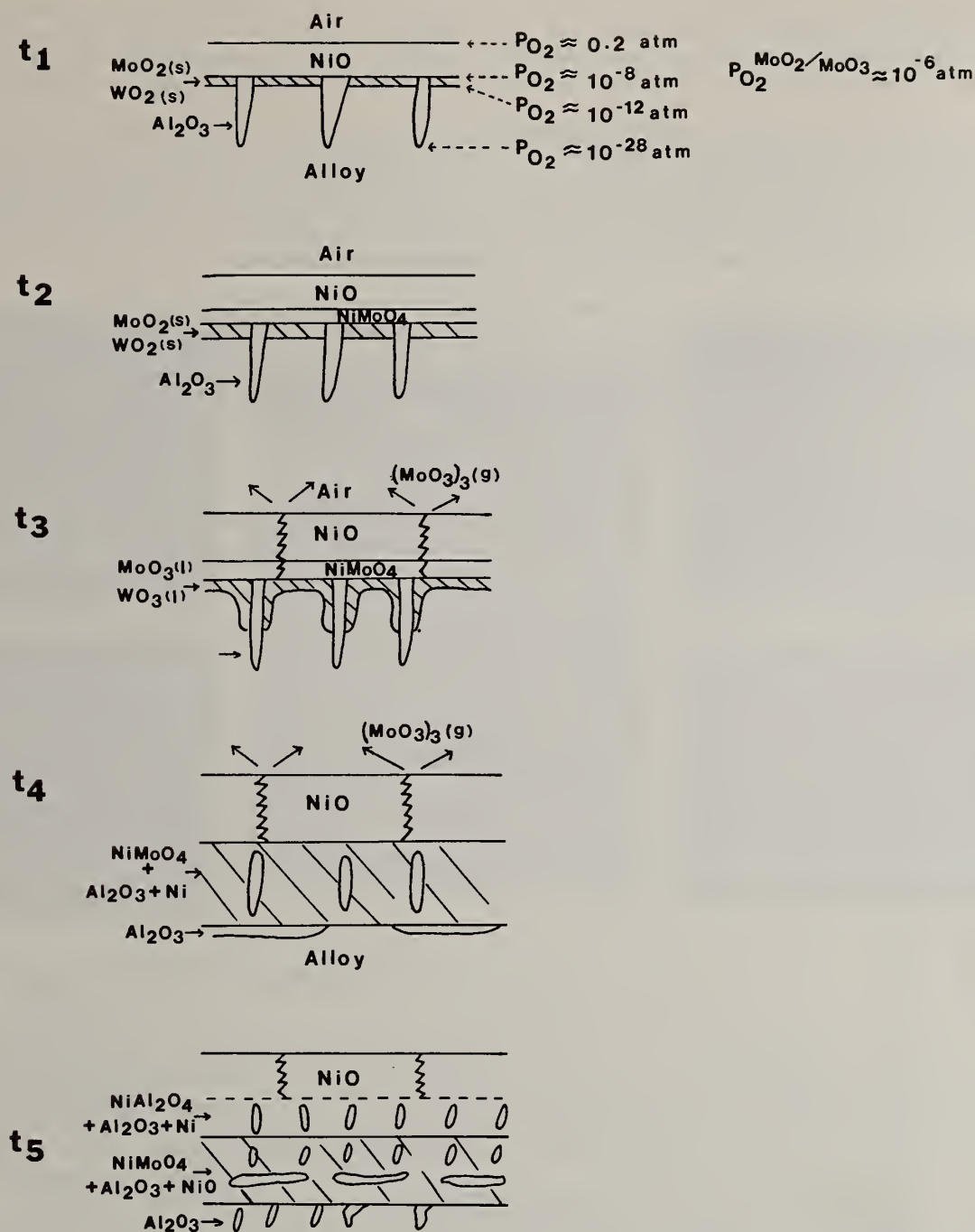


Figure 4 Model for the rapid oxidation of Ni-Al-Mo-W alloys

the rapid attack observed for RSR-185. Once the Al_2O_3 layer becomes continuous the p_{O_2} below the scale remains too low for the oxidation of Mo or W. The maximum in the weight p_{O_2} change for RSR-467 after 1 hour is due to the evaporation of transient Mo-oxides after the Al_2O_3 layer has covered the alloy surface.

The exposure of ternary Ni-Al-Mo alloys has indicated a difference in the behavior of Mo and W. For example, the Ni-7Al-17.5Mo alloy has the same total refractory metal content (in terms of mole fraction) as the Ni-7Al-14Mo-6W alloys but shows much slower oxidation rates (Figure 1). This alloy was also observed to form a continuous (or nearly continuous) Al_2O_3 scale. Thus it appears that Mo can effectively act as a secondary getter to promote external Al_2O_3 formation since it forms oxides with stabilities lying between those of NiO and Al_2O_3 . The stabilities of the oxides of W are similar to those of Mo which indicates W could also promote external Al_2O_3 formation. The reason that it does not is believed to be a reduction in the alloy interdiffusion coefficient.

Diffusion data are not available for Ni-Al-W system but the interdiffusion coefficient in binary Ni-W alloys decreases with increasing W concentration. (10,11) The diffusion coefficient of Al in Ni-Mo alloys has been observed to decrease slightly with increasing Mo concentration (12). However, the effect of Mo on the diffusion coefficient is apparently less than that of W.

An additional feature regarding the oxidation mechanism is that although considerable MoO_3 evaporation was observed this evaporation does not seem to have either beneficial or detrimental effects on the rapid oxidation process as the corrosion appears to be flow-rate independent. Experiments run with inverted Al_2O_3 crucibles covering the specimens produced the same amount of attack as those run in flowing gas. This observation is different from that for Ni-Cr-Mo (8) where severe corrosion was only observed in stagnant atmospheres.

The oxidation behavior of the Mo-containing alloys was somewhat different at temperatures below 1000°C . The rates of oxidation at 850°C are compared in Figure 5. All of the Mo-containing alloys are NiO-formers and oxidize more rapidly than the Al_2O_3 -former Ni-18Cr-6Al, included in Figure 5 for comparison. RSR-467 and Ni-6Al oxidize at comparable rates and, exhibit similar oxidation morphologies consisting of an external NiO scale and internal Al_2O_3 precipitates which form continuous films in some locations.

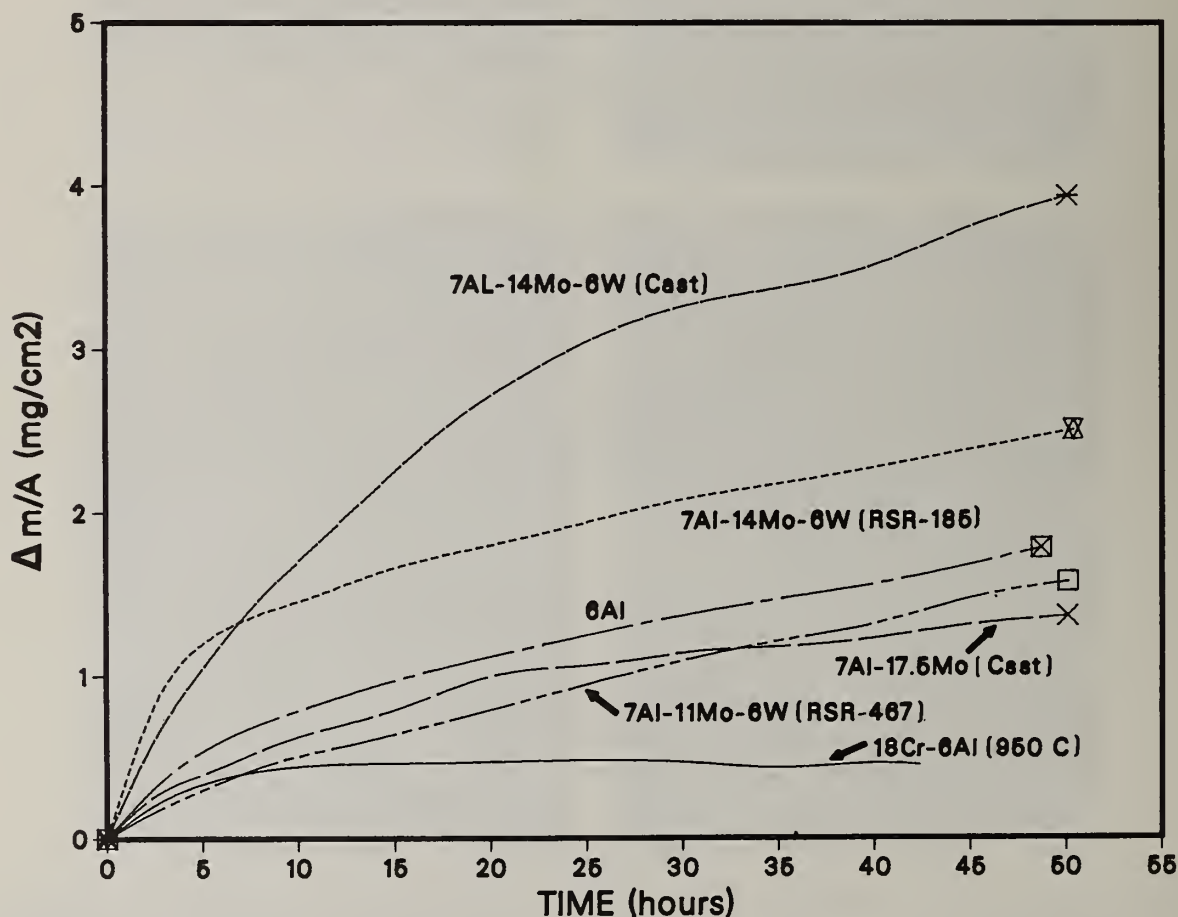


Figure 5 Oxidation rates for several cast and RSR alloys in air at 850°C

The cast alloy JG-185 and RSR-185 oxidized significantly faster than Ni-6Al. This is due primarily to profuse internal oxidation of these alloys as indicated in Figure 6. A significant difference from the high temperature behavior of the same alloys is that the internal oxides are rich in Mo and W as well as Al at low temperatures. These oxides form continuous networks allowing rapid ingress of oxygen into the alloy. The oxides of Mo eventually begin to concentrate at the scale/alloy interface during lower temperature exposures, as indicated in Figure 6, and once NiMoO_4 begins to form significant spalling of the scale occurs on cooling. This is a significant observation since the scales remain adherent in essentially all cases where NiMoO_4 does not form.

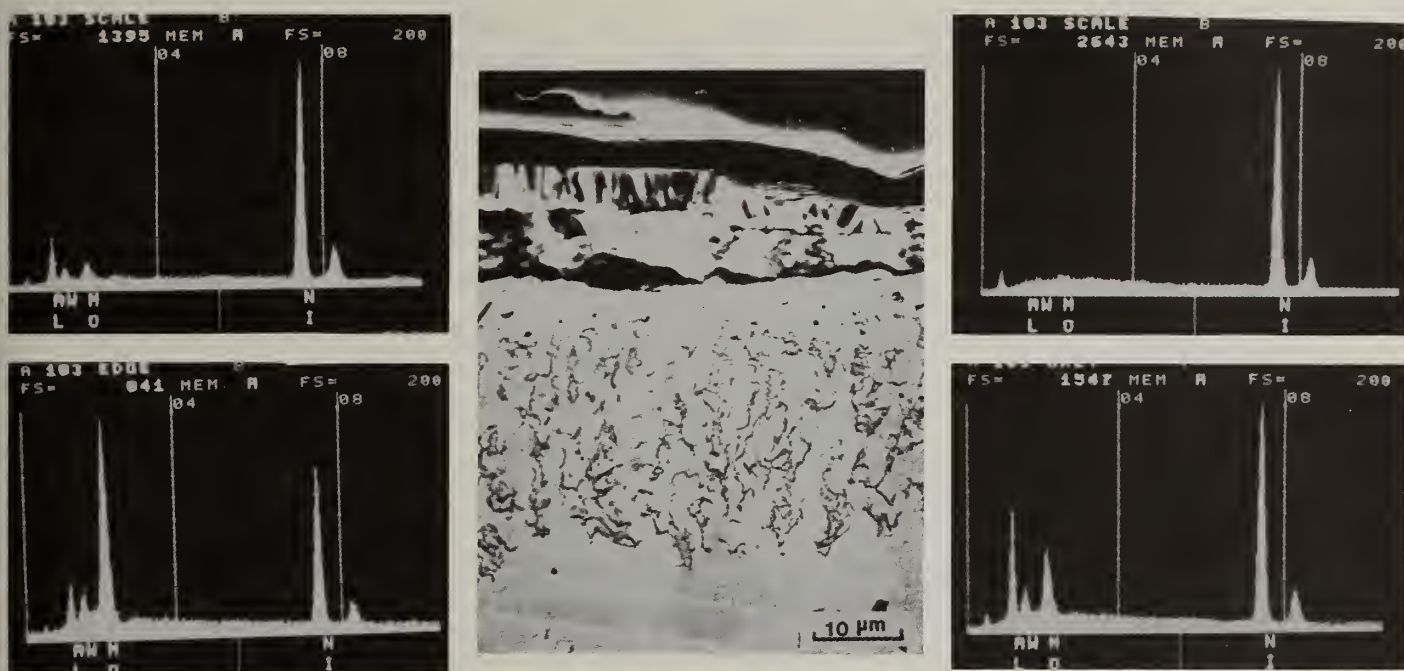


Figure 6 Cross-section of cast Ni-7Al-14Mo-6W exposed for 12 hours in air at 850°C.

The reason that this phase promotes spalling is the occurrence of a phase transformation at about 650°C with an accompanying large volume change (5,6) which promotes shattering even in bulk NiMoO_4 . (This effect was also observed in the current work when NiO and MoO_3 were heated together and formed NiMoO_4). Therefore, it is clear that alloy compositions or coatings which preclude the formation of NiMoO_4 must be used for this class of alloy to have resistance to cyclic oxidation.

Figure 7 shows the cyclic oxidation behavior of RSR-185 over a range of temperatures. The alloy shows significant weight losses at the higher temperatures whereas at 760°C it has continued to gain weight after 100 hrs. However, even at this temperature, extending the time of oxidation or shortening the cycle length will produce weight losses. Figure 8 is a typical microstructure of a cycled specimen showing significant internal oxidation and Al-depletion.

Thermal cycling also has a significant effect on the oxidation behavior of the more resistant alloys such as RSR-467 as indicated in Figure 9. After about 150 hours weight losses are observed which increase with increasing exposure time.

Modification of RSR-467 by small additions of Cr, Ta, Y and Hf results in an alloy which forms an adherent Al_2O_3 layer over the entire temperature range studied. This is illustrated in Figure 9 for 850°C and in Figure 10 for 1150°C.

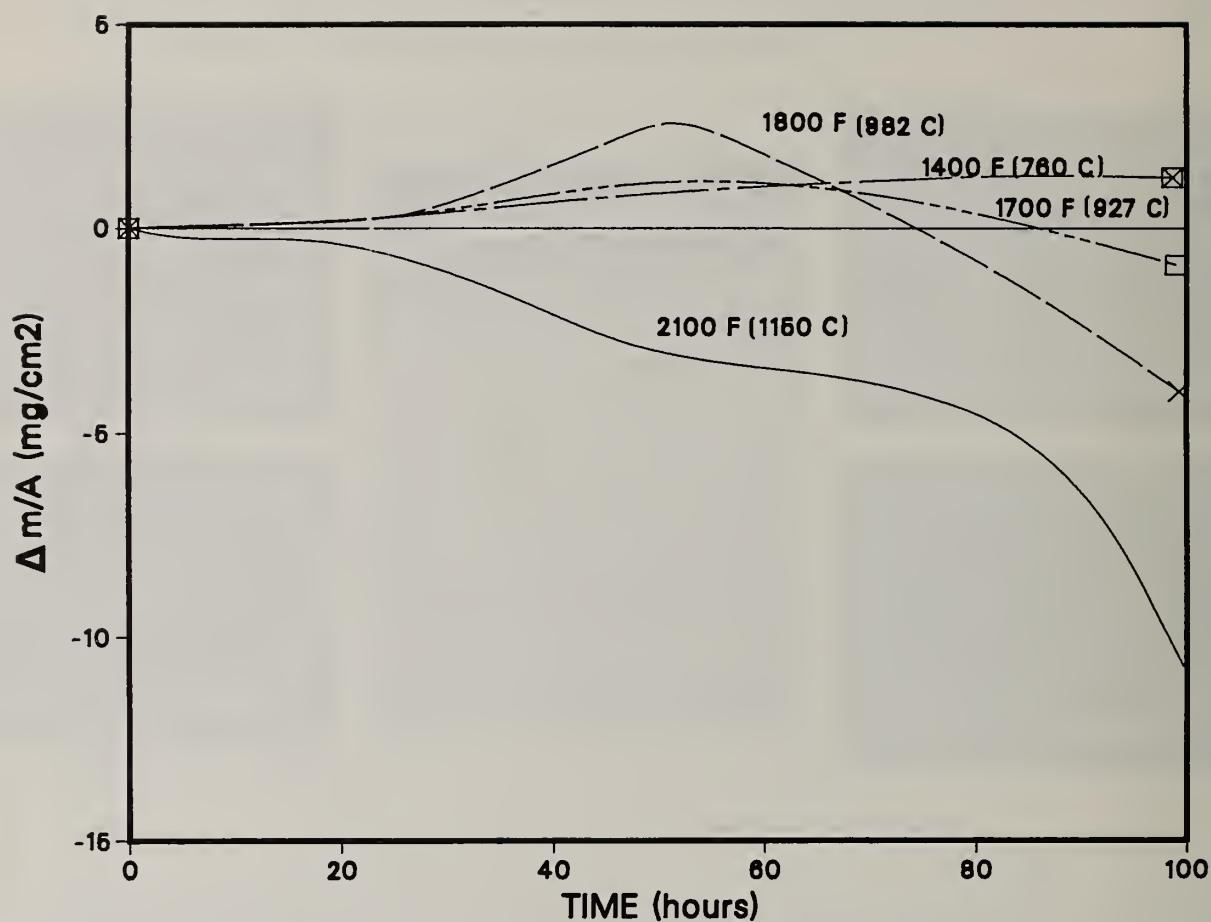


Figure 7 Cyclic oxidation of RSR-185 in the temperature range 760 to 1150°C. Cycles consist of 25 hours heating, 1 hour cooling.

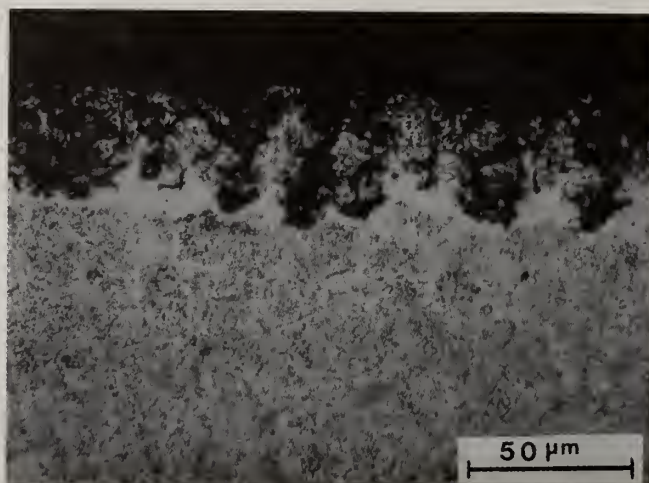


Figure 8 Cross-section of RSR-185 exposed in cyclic oxidation for 200 hours at 870 °C.

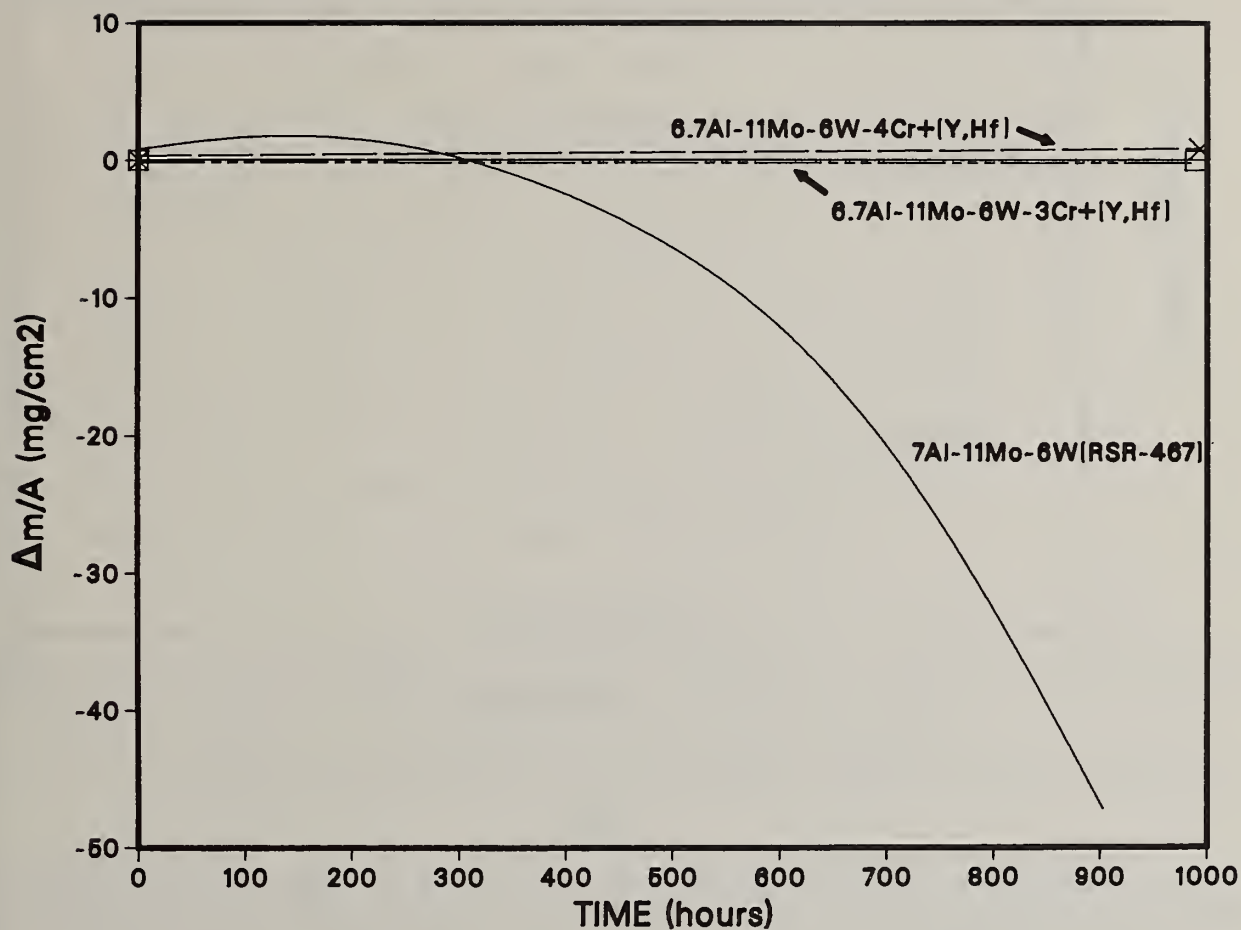


Figure 9 Cyclic oxidation of RSR-467 and modified -467 alloys at 850°C . Cycles consist of 50 minutes heating, 10 minutes cooling.

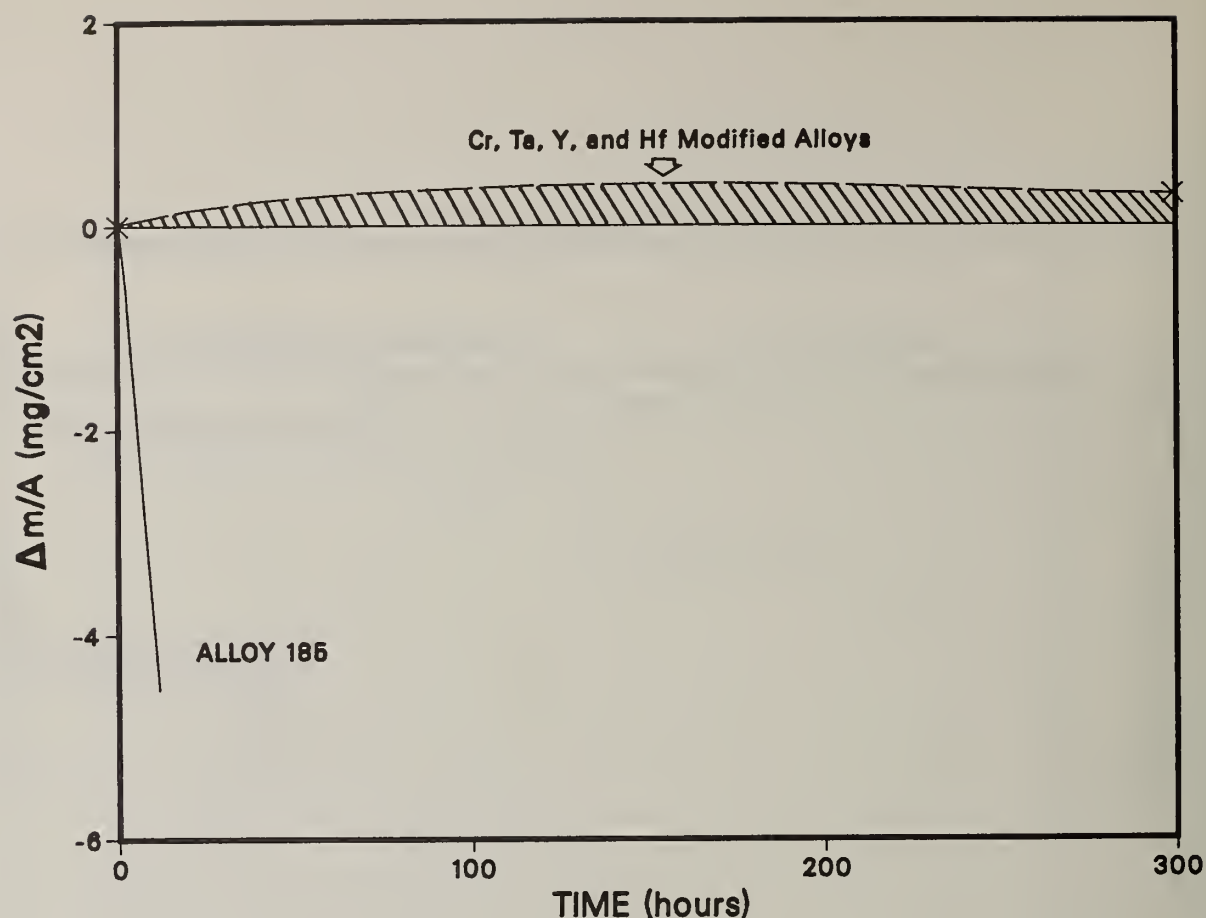


Figure 10 Cyclic oxidation of modified 467 alloys and RSR-185 at 1150° C.

Summary

The oxidation behavior of several Mo- and W-containing Ni-Al alloys has been studied over a range of temperatures. It was found that for temperatures above 1100°C the presence of Mo and W can promote the formation of a protective Al_2O_3 scale in a manner similar to Cr additions. However, if the Mo concentration exceeds a critical value the formation of liquid oxides results in rapid corrosion. This critical concentration lies between 11 and 14 wt. percent for rapid solidified alloys containing about 7 percent Al and 6 percent W. However, this value is probably lower for less homogeneous, cast alloys and is lower if the alloys are exposed under cyclic conditions. The mechanism for the rapid corrosion has been described. The oxidation of W-free alloys has indicated that Mo concentrations in excess of 17 wt. percent can be tolerated under isothermal conditions without producing severe degradation. The detrimental influence of W is believed to be due to a reduction in the alloy interdiffusion coefficient.

At temperatures less than 900°C all of the unmodified Ni-Al-Mo-W alloys were NiO formers. Apparently, the decreased alloy interdiffusion coefficient due to the W in solution negates the oxygen-gettering effect of W and Mo and prevents the formation of a continuous Al_2O_3 scale. The alloys containing the higher Mo concentration oxidize faster than Ni-6Al due to the profuse formation of internal oxides of Al, Mo, and W. The scales remained adherent on cooling until $NiMoO_4$ was formed. When this occurred extensive weight losses were observed during cyclic oxidation.

The addition of Cr to Ni-Al-Mo-W alloys was observed to promote the formation of protective Al_2O_3 films. The modification of the Ni-Al-Mo-W alloys with additions of Cr, Ta, Hf, and Y resulted in the formation of adherent, protective Al_2O_3 scales which provided excellent cyclic oxidation resistance over the entire temperature range studied.

References

1. F. S. Pettit, Trans. AIME, 239, 1296 (1967).
2. M. E. El-Dahshan, D. P. Whittle, and J. Stringer, Corr. Sci., 16, 83 (1976).
3. S. Espevik, R. A. Rapp, P. L. Daniel, and J. P. Hirth, Oxid. Met., 14, 85 (1980).
4. W. C. Leslie and M. F. Fontana, Trans. A. S. M., 41, 1213 (1949).
5. S. S. Brenner, J. Electrochem. Soc., 102, 7 (1955).
6. S. Pizzini, E. Ruedl, and L. Merletti, "Oxidation of Nickel-Molybdenum Alloys: Thermogravimetric and Structural Analysis" in Metal-Slag-Gas Reactions and Processes, Z. A. Foroulis and W. W. Smeltzer, eds., Electrochem. Soc., Princeton, N. J., 1975, p. 448.
7. S. S. Brenner, J. Electrochem. Soc., 102, 16 (1955).
8. K. R. Peters, D. P. Whittle, and J. Stringer, Corr. Sci., 16, 791 (1976).
9. J. A. Goebel, F. S. Pettit, and G. W. Goward, Met. Trans., 4, 261 (1973).
10. J. M. Walsh and M. J. Donachie, Met. Sci. J. 3, 68 (1969).
11. V. N. Pimenov and V. E. Ugaste, Fiz. Metal. Metalloved., 35, 590 (1973).
12. J. E. Bridge and G. N. Maniar, Met. Trans., 3, 1006 (1972).

ACKNOWLEDGEMENTS

The authors gratefully acknowledge the contributions of D. Meikle, K. Andrew, E. Hewitt and C. Martin in performing the experiments done at the University of Pittsburgh. The authors also wish to thank R. J. Hecht and J. A. Miller for their constructive discussions and support.

This work is jointly sponsored and monitored by the U.S. Defense Advanced Research Projects Agency and the Air Force Wright Aeronautical Laboratories.

The views and conclusions contained in this paper are those of the authors and should not be interpreted as necessarily representing the official policies, either expressed or implied, of the U.S. Defense Advanced Research Projects Agency, U.S. Air Force, or the U.S. Government.

RAPIDLY SOLIDIFIED CARBIDE POWDERS PRODUCED BY SPARK MACHINING OF Ti AND Zr

C. S. Pande and J. D. Ayers

Physical Metallurgy Branch, Naval Research Laboratory, Washington, DC 20375 USA

ABSTRACT

Fine rapidly solidified TiC and ZrC powders were obtained from commercial purity Ti and iodide processed Zr by spark machining in kerosene, the carbide being formed because of a reaction between the metal and carbon from kerosene. Powders produced by this process were studied by x-ray diffraction, and by scanning (SEM) and transmission electron microscopy (TEM). Results from these studies show that depending on the processing condition in spark machining, the resultant powders are either single phase carbides or contain, in addition, unreacted metal or free graphite. Examination of the spark machined surfaces by x-ray diffraction and by SEM revealed that they were covered by a carbide layer and that the degree of carburization correlated with the carbon concentration of the spark generated powders.

Single phase TiC-ZrC alloy powders were also produced by spark machining of the metallic alloys. Heat treatment of these single phase powders produced a phase separation into TiC and ZrC rich phases both with NaCl structure but with different lattice parameters.

This study has thus demonstrated that equilibrium and metastable structure carbide powders ranging in size from about 40 μm down to submicron sizes can be produced by this technique. The rate of powder production was only a few grams per hour, but the unique microstructures produced may make these powders technologically interesting.

Introduction

It is well known that rapid solidification processing may result in materials with microstructure and chemical homogeneity very different from that obtained by conventional means. The novel properties are determined largely by the transport processes occurring at the liquid/solid interface. However, a detailed study of the basic mechanism of solidification and its correlation with resultant microstructure is needed to fully utilize the potential benefits.

It was realized as early as 1924 [1] that spark machining generates carbide, oxide or nitride layer resulting in a surface hardening effect. This effect has also been employed commercially. However, the nature of the materials removed by the spark machining has received much less attention. If the dielectric is a hydrocarbon, the reaction products are metal carbides. These carbides are produced not only on the metal surface, but are ejected from the surface into the dielectric. They are usually in the form of fine roughly spherical powders, of the size ranging from less than a micron in diameter to up to 40 μm . These carbide powders are obviously produced by a solidification mechanism similar to that in other rapid solidification processing. The detailed technique of the formation of such metal powder carbides have been published elsewhere [2]. The present paper is concerned mostly with the microstructure obtained by this technique.

Formation of Carbide Powders

The conditions under which these powders were produced are given in Table 1. After machining with a graphite tool with kerosene as the dielectric, carbide powders were collected from the dielectric, and washed to remove organic residue. The powders so obtained were examined by x-ray

diffraction and by scanning (SEM) and transmission electron microscopy (TEM). Energy dispersive x-ray analysis and electron energy loss analysis has been used to analyze Ti (and Zr) and carbon content, respectively.

Table 1

Metals used in this study:	Commercial purity Ti; Iodide processed Zr
Electrical discharge instrument:	AGIE Type AB 30H which generates a square wave of variable frequency
Frequency of electric discharge:	400 to 25000 hertz using a 50% duty cycle
Dielectric:	Kerosene
Cutting tool:	Graphite (rotating)
Polarity of the discharge:	Workpiece both positive (conventional) and negative
Voltage of the discharge:	220 Volts

Further details are given in reference 2.

Results

Titanium Carbide Powders

A low magnification micrograph obtained by scanning electron microscope (SEM) is shown in Fig. 1. The metal powders were seen to be nearly spherical, though a few particles did show odd geometries. The size ranged from submicron to up to about 40 μm . X-ray examination of these powders showed strong TiC peaks (with NaCl structure) as expected, but it also contained weak lines which were identified as due to a small amount of α phase Ti. How is Ti distributed in a given TiC particle? This was investigated by etching the powders for several minutes or longer in Kroll's reagent (5 parts HF, 10 parts HNO_3 rest water) which dissolves Ti and Zr but not their carbides. The etchant attack is very slow, due to the fact that the outer layer of the particles are more likely to be TiC, or coated with TiC. However, where the attack was deep enough, the Ti metal was etched away revealing a TiC dendritic structure (see Fig. 2). It was indicated that individual powder particles have probably different volume fraction of TiC.

These powders were then examined in TEM. For this purpose the powders had first to be thinned. The following technique of thinning gave consistently good results. The metal powders were sandwiched between two thin sheets of vanadium (~5 mil thick) and cold-rolled. 3 mm disc were then punched out and thinned in the middle using ion thinning (argon ions at 5 KV) till perforation. Carbide particles were found to be electron transparent near the perforation. Fig. 3 is the TEM micrograph TiC particle showing the various grains inside a single TiC powder. Many micrographs indicated that the outer edge of the particle is titanium carbide; inside the particle, however, metallic Ti is present. The SEM and TEM, and x-ray results were thus consistent.

Attention was next given to producing TiC powders which have much less metallic inclusions. This led to the use of the 'reversed polarity' for producing these powders. Spark machining is normally done with the workpiece positive relative to the tool, because electron bombardment of the metal in this mode leads to faster cutting rate. If the polarity is reversed the metal will be bombarded with positive ions (carbon ions if kerosene is used as a dielectric). This should lead to better carburization as was borne out by the experiments. The TiC powders, obtained by the reversed polarity were not attacked visibly by the etchant. More significantly, the measured lattice parameter indicated it to be almost pure TiC. Finally, TEM again showed that these particles were probably pure TiC. A few of them were found to be single crystals (see Fig. 4).

The other processing variable is the frequency of the spark discharged. This parameter was varied and the TiC content of the specimens were ascertained using x-rays. The amount of α phase Ti found in these powders decreased with decreasing frequency.

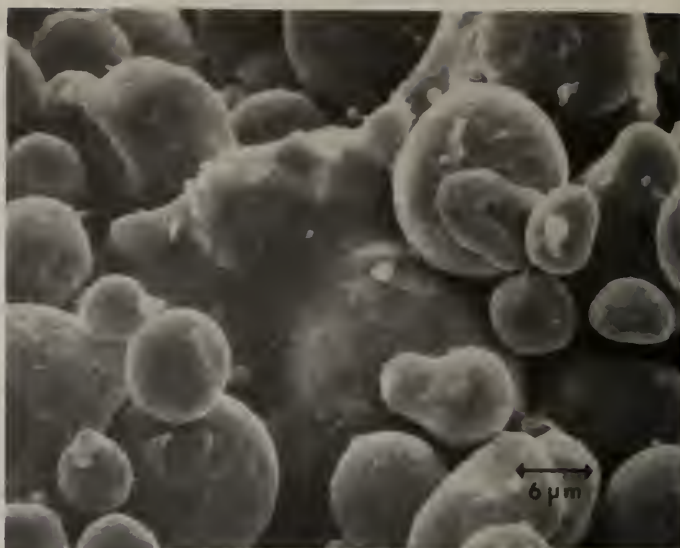
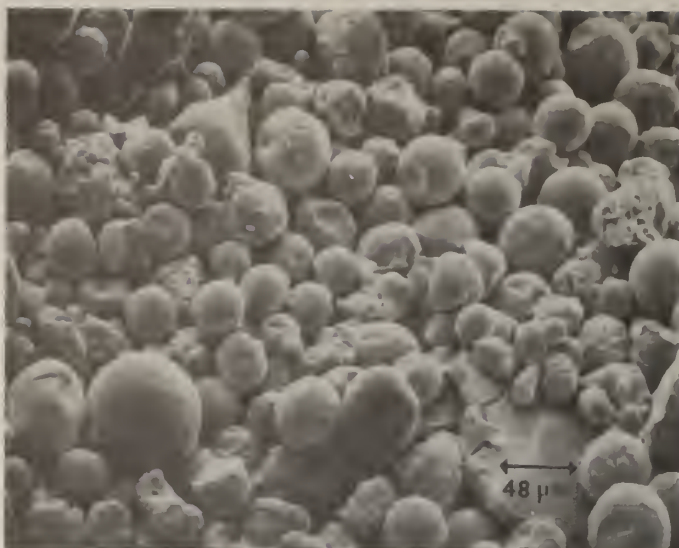


Figure 1. Titanium carbide powder prepared by spark machining of Ti in kerosene.

(a)
Powder obtained at 6000 Hertz with normal
polarity.

(b)
Powder obtained at 12000 Hertz with
'reverse' polarity.

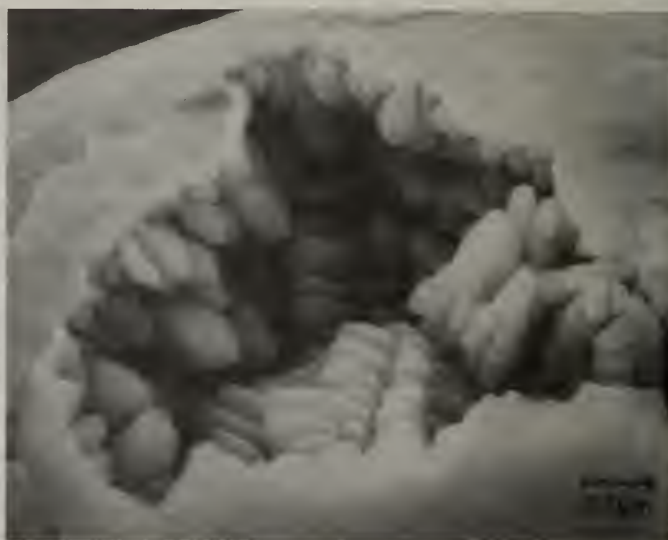


Figure 2(a). A titanium carbide powder produced by machining Ti with normal polarity at 6000 Hertz and then etched in Kroll's reagent which attacked Ti but not TiC. Metallic titanium has been removed revealing TiC dendrites.

Figure 2(b). A titanium carbide powder obtained under the same processing conditions as (a), and etched similarly. The dendrites in this case are coarser, indicating a higher carbon content.



Figure 3. A TEM micrograph of a TiC particle obtained with normal polarity showing grains in the particle and some free Ti.

Zirconium Carbide Powders

As is expected from the similarity of Ti-C and Zr-C phase diagrams the electron machining behavior of Zr was similar to that of Ti. Many ZrC particles showed surface structure similar to TiC. Some particles exhibited a typical surface morphology. TEM revealed that those surface features (many small irregular patches) are each the base of elongated grains growing inward in the powder particle.

TiC-ZrC Alloy Powders

The technique of using these powders has been extended to powders of alloys of titanium and zirconium also. Single phase TiC-ZrC has been produced. Heat treatment of these single phase alloy leads to a phase separation into TiC and ZrC rich phases, both with NaCl structure but with different lattice parameters.

Conclusions

Spark machining was found to be a simple and convenient tool to study rapid solidification processes in metal carbides. With suitable processing conditions (reversed polarity and low frequency discharge), single phase TiC can be produced. This study has also demonstrated that spark machining provides a convenient tool for investigating the basic mechanism of rapid solidification in metal carbides.

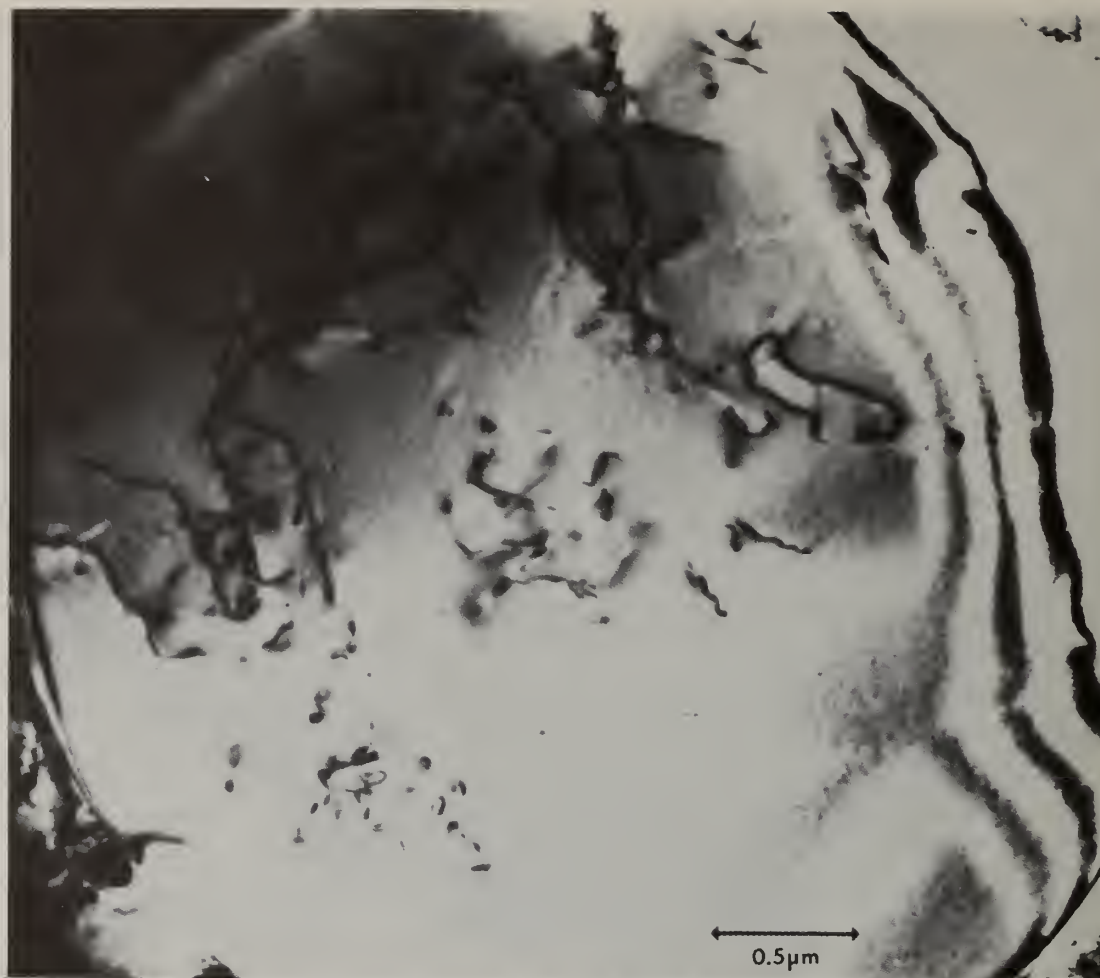


Figure 4. A TEM micrograph of a TiC particle obtained with reverse polarity showing a single crystal TiC particle. The dislocation densities in these particles rarely exceeded $10^6/\text{cm}^2$.

Acknowledgments

The authors are grateful to Miss Kathy Moore and Mr. Steve Smith for their contribution to this work.

References

- [1] Rawdon, H. S., AIME Trans., Vol. 70, 1924, p. 37 (Discussions).
- [2] Ayers, J. D. and Moore, K., (to be published).

PROCESSING, MICROSTRUCTURE AND PROPERTIES OF MELT
SPUN AND CONSOLIDATED SUPERALLOYS

R.H. VanStone*, J.R. Hughes**, R.E. Maxwell***,
H.H. Liebermann****, and R.G. Rowe**

*General Electric Aircraft Engine Business Group, Cincinnati, Ohio 45215

**General Electric Corporate Research and Development, Schenectady, NY 12301

***General Electric Corporate Research and Development, Schenectady, NY 12301

currently with General Electric Lamp Glass and Components, Cleveland, OH 44110

****Allied Corporate Technology, Parsippany, New Jersey 07054, formerly with General
Electric Corporate Research and Development, Schenectady, NY 12301

ABSTRACT

The single roller chill block melt spinning process, commonly used to produce amorphous alloy ribbons, was modified to produce rapidly solidified 20-30 micrometers thick ribbon of the nickel-base superalloys Rene'95 and the developmental alloy 1200/19. These ribbons had cellular or columnar microstructure which were devoid of branched dendrites. Scanning transmission electron microscopy analysis showed no significant microsegregation. Several pounds of narrow and 11 mm wide ribbon were produced.

Compacts of randomly packed narrow ribbon and wound spools of wide ribbon were hot isostatically pressed to full density. The randomly packed ribbon compacts were extruded to improve their toughness. After both HIP compaction and HIP plus extrusion, the prior ribbon boundaries contained a relatively high density of aluminum and zirconium oxides and MC-type carbides.

The mechanical properties of consolidated Alloy 1200/19 were evaluated in both the HIP plus heat treated condition and the HIP plus extruded plus heat treated condition. The tensile, creep, rupture and fatigue crack growth properties of the HIP plus extruded ribbon were similar to those obtained for rapidly solidified, helium atomized HIP-compacted powder of the alloy.

INTRODUCTION

The continuing demand for improved performance in aircraft gas turbine engines having longer operating lives and improved reliability has encouraged the development of new turbine disk alloys which are capable of operating at higher stresses and higher temperatures than conventional alloys. A major advancement in enhancing the temperature capability of such alloys was the development of nickel-base superalloys which are manufactured by powder metallurgy (PM) methods⁽¹⁻⁴⁾. This technology allows more efficient material utilization and reduces mechanical property variations resulting from compositional segregation and difficult forging operations associated with conventionally cast and wrought superalloys. The reduction of segregation in γ - γ' superalloys has permitted the use of higher γ' volume fractions and higher levels of solid solution strengthening elements.

The next logical step in the quest for performance of superalloy disks is through the use of more advanced rapid solidification technology. One such rapid solidification process is chill block melt spinning (CBMS), which has been used to fabricate amorphous alloy⁽⁵⁻⁷⁾ and superalloy^(8,9) ribbons. The CBMS process, shown schematically in Figure 1, consists of a thin stream of liquid alloy which is ejected under pressure from a nozzle onto a rapidly rotating substrate wheel which removes heat by conduction. The simultaneous mass and heat transfer produces thin, nickel-base superalloy ribbon solidified at rates in excess of those obtainable using conventional gas atomization. This process provides high yields of rapidly solidified material with uniform thickness and more uniform microstructures than material obtained in rapidly solidified powders⁽¹⁷⁾.

This paper describes the development of melt spinning process parameters and compaction procedures used for the production of advanced nickel-base superalloys. Selected mechanical properties of the compacted CBMS materials were also determined. These studies were performed using Rene'95 and experimental Alloy 1200/19. Rene'95 is an advanced γ - γ' alloy which has been used in aircraft engine disks and other high temperature, high stress applications. Alloy 1200/19 is a developmental alloy designed to simultaneously increase temperature capability and cyclic defect tolerance⁽¹¹⁾. The compositions of these alloys are listed in Table 1. Alloy 1200/19 has a γ' content of 38 percent compared to 45 percent for

Rene'95. The γ' content of Alloy 1200/19 was reduced primarily by reductions in aluminum and columbium. To offset the loss in tensile, creep, and rupture strength associated with lower γ' content, the amount of solid solution strengthening was increased by raising the tungsten content and adding rhenium.

Table I. Nominal Compositions of Rene'95 and Alloy 1200/19

	Alloy Composition (Weight Percent)											
	<u>Co</u>	<u>Cr</u>	<u>Mo</u>	<u>W</u>	<u>Re</u>	<u>Al</u>	<u>Ti</u>	<u>Cb</u>	<u>Zr</u>	<u>C</u>	<u>B</u>	<u>Ni</u>
Rene' 95	8.0	13.0	3.5	3.5	--	3.5	2.5	3.5	0.05	0.05	0.01	Balance
Alloy 1200/19	14.0	17.0	---	8.0	2.0	1.75	3.5	0.65	--	0.02	0.01	Balance

Melt Spinning of Superalloy Ribbons

Davies, et. al.⁽⁸⁾ and Wood, et. al.⁽⁹⁾ used chill block melt spinning to produce relatively small volumes of nickel-base superalloys. The CBMS process used to fabricate the large volumes of ribbon required for the mechanical property evaluation of the percent investigation was described in previous publications^(11,12) and will be summarized here.

The quench rates achieved during rapid solidification are controlled primarily by the thickness of the sample and the nature of interfacial contact between the wheel and the specimen^(13,14). Calculations by Ruhl⁽¹⁵⁾ have shown that the average quench rate varies inversely with the square of specimen thickness for ideal cooling or inversely with specimen thickness for Newtonian interface-controlled cooling. Therefore, careful control of the ribbon thickness is required to produce uniform rapidly solidified microstructures. Ribbon thickness is primarily controlled by the liquid flow rate through the nozzle, the ribbon width, and the wheel surface velocity. Liebermann, et. al.⁽¹⁰⁾ demonstrated that the fluid-ribbon thickness relationships developed for amorphous alloys also apply to superalloys. Subsequent experiments determined ribbon thickness as a function of wheel surface velocity for fixed mass flow rates. The variation ribbon thickness as a function of substrate velocity is shown in Figure 2 for Rene'95 melt spun on OFHC cooper and 304 stainless steel wheels. Ribbon thickness is strongly dependent on substrate velocity (V_s) at low values of V_s ; however, attempts to obtain ribbon thickness significantly smaller than 20 microns by increasing wheel velocity will probably not be effective, as shown in Figure 2. Similar CBMS ribbon thickness-wheel velocity data have been obtained for amorphous alloys⁽¹⁶⁾ and Alloy 1200/19⁽¹²⁾.

The microstructures of Rene'95 CBMS ribbons were characterized using optical metallography and scanning transmission electron microscopy (STEM). Direct evidence for the decreasing solidification rate with increasing specimen thickness is shown in Figure 3, which shows Nomarski interference micrographs of ribbons with thicknesses of 16 and 52 microns. In these micrographs, the ribbon surface which was in contact with the rotating wheel is shown at the bottom of each micrograph. Figure 3a shows the presence of branched, secondary dendrites near the free surface of the thicker ribbon. This is direct evidence of reduced solidification rate with increasing ribbon thickness. The microstructure of the 16 micron thick ribbon as shown in Figure 3 b is devoid of these branched, secondary dendrites. It was concluded from several such observations that ribbon thicknesses less than 30 microns were sufficient to suppress the branched dendritic microstructure for the CBMS process used in this investigation. As shown in Figure 2, this thickness can be readily obtained using the melts spinning process. All materials produced for evaluation of mechanical properties were sufficiently thin to suppress the formation of secondary dendrite arms.

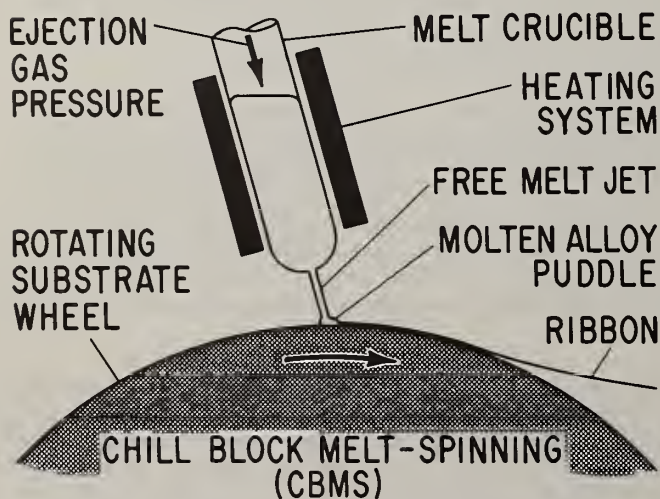


Figure 1. Schematic Diagram Showing the Chill Block Melt Spinning (CBMS) Process

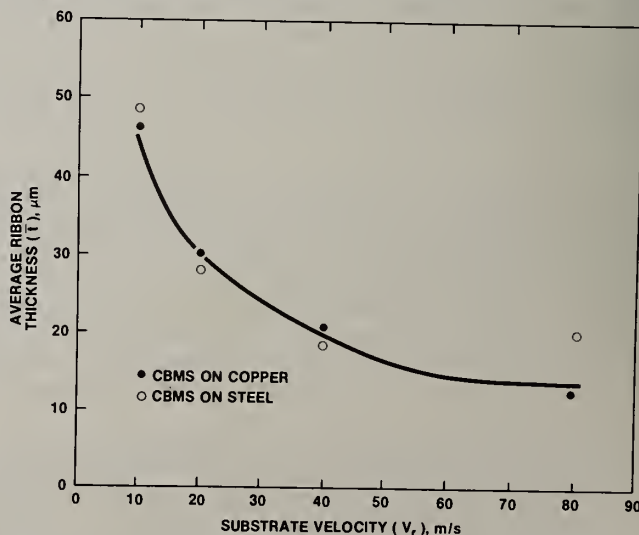


Figure 2. Variation of CBMS Rene'95 Average Ribbon Thickness with Substrate Surface Velocity

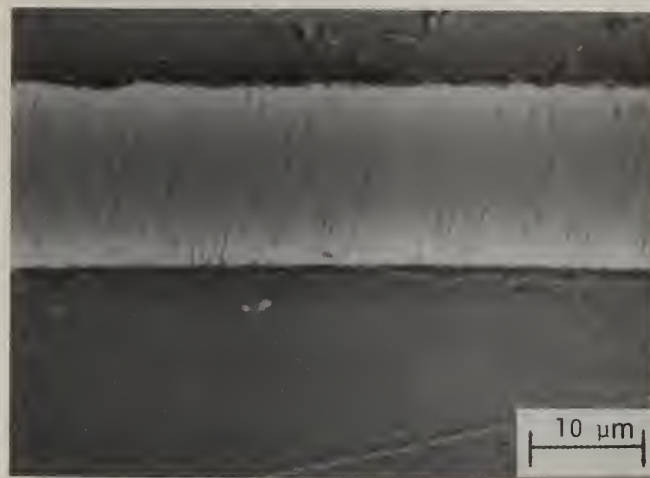
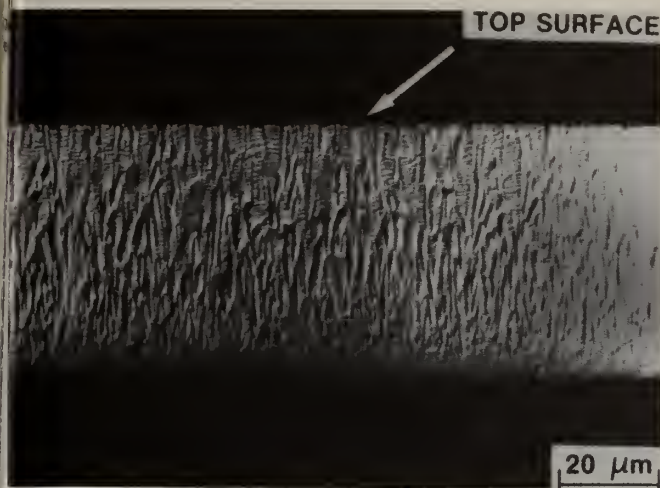


Figure 3. Optical Micrographs of (a) 52 Micron^(a) and (b) 16 Micron Thick CBMS Rene'95 Ribbon^(b)

STEM was used to study phases and segregation in CBMS ribbons having several different thicknesses. A bright field TEM micrograph from the midplane of a 30 micron thick ribbon is shown in Figure 4a. This microstructure consists of small, equiaxed grains 0.2 to 0.6 microns in diameter separated by high angle boundaries containing second phase particles. These high angle boundaries are not the low angle boundaries usually associated with cellular instability of the liquid-solid interface. This observation suggests that cellular solidification instabilities were suppressed in this region. Selected area diffraction of grain boundary regions was used to identify the grain boundary particles as MC-type carbides. Figure 4b shows a dark micrograph of the region shown in Figure 4a imaged with a MC carbide diffraction spot confirming their identification. STEM analyses of the carbide suggests that these carbides are primarily (Cb, Mo, Ti) C⁽¹²⁾.

It should be noted that other areas of this ribbon showed a tendency towards a more cellular microstructure⁽¹²⁾. In these regions, the grains tended to be larger; this presumably resulted because the columnar grains were farther from their nucleation sites and therefore wider. Cell boundaries within the grains also contained MC carbides.

Microsegregation near cell, grain and dendrite boundaries was evaluated using STEM. All measurements were performed using a Hitachi H-600-1 electron microscope operating at 100 KV. Analysis of cell wall and dendrite arm segregation was performed using beam spot sizes of approximately 100 Å and 200 Å, respectively. Due to scattering in the matrix and stage drift, the actual size of the regions analyzed

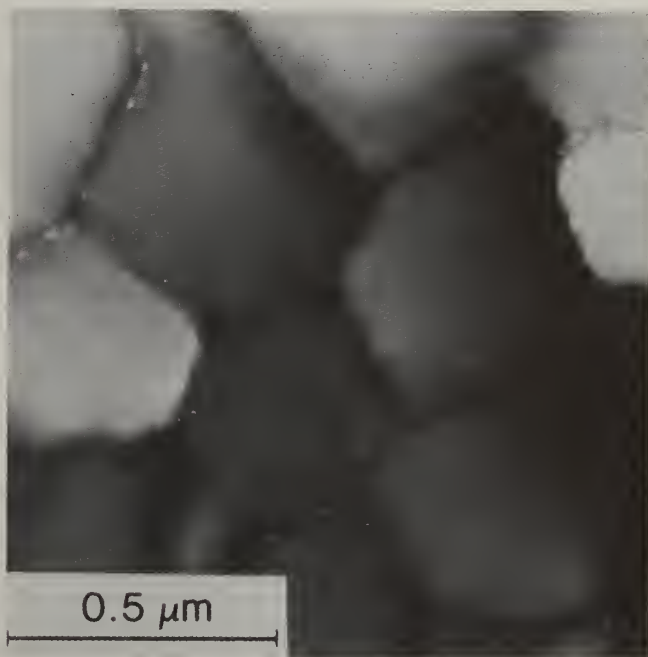
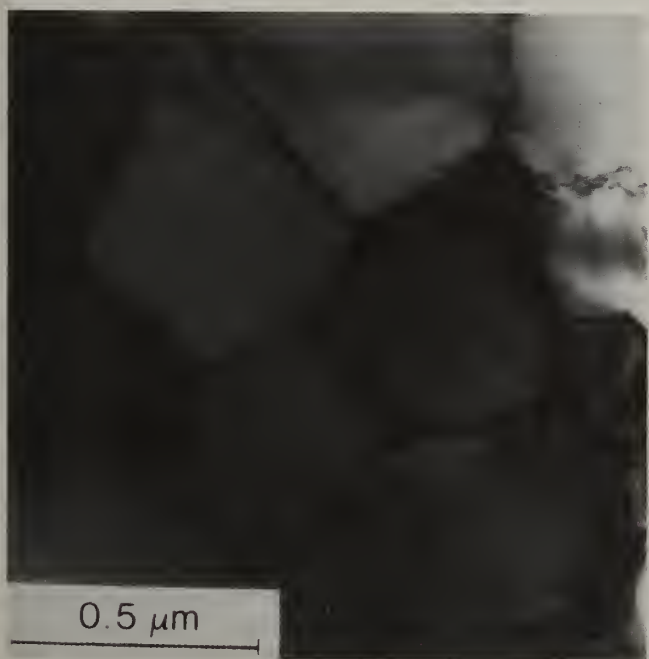
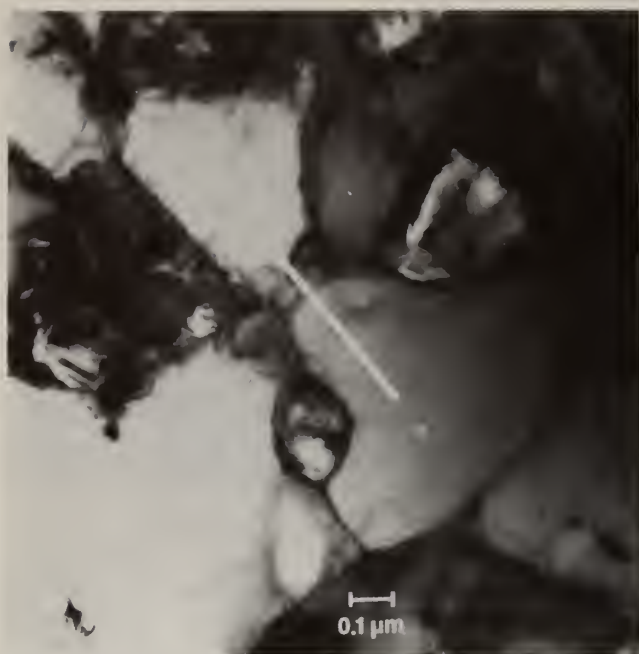
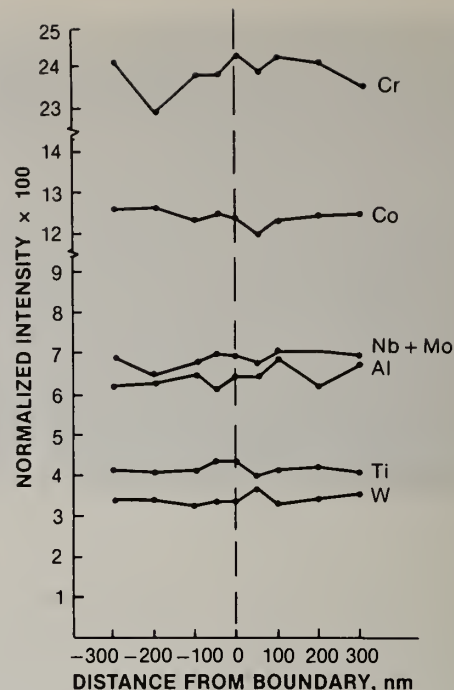


Figure 4. Thin Foil TEM micrographs of CBMS Rene'95 Showing (a) Bright Field, (b) Dark Field^(a) of a Region of Equiaxed Grains.^(b)



(a)



(b)

Figure 5. Results of STEM Compositional Profile (b) Across Grain Boundary (a) in CBMS Rene'95.

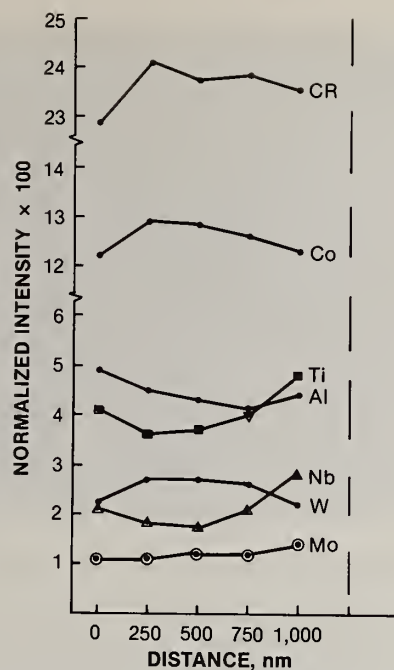
were approximately 250 Å and 400 Å, respectively. Variations in STEM specimen thickness, the absence of exact multi-component standards, and differences in absorption characteristics make identification of exact local compositions in complex superalloys like Rene'95 extremely difficult. As a result, the spectra will be presented as intensities normalized to $\text{NiK}\alpha$ for a qualitative indication of composition. No attempts were made to further quantify the results.

The results of a STEM profile across the boundary between grains of a 15 micro thick sample are shown in Figure 5. This foil was taken near the free surface of the ribbon, the most slowly cooled portion of the material. The superimposed line on the electron micrograph in Figure 5a shows the location where the STEM trace was performed. The results of the STEM analysis are shown in Figure 5b. There was little observable segregation on the scale of the STEM probe.

Results of other probes occasionally showed increases in columbium, molybdenum, and titanium, the strong carbide-forming elements, along the grain or dendritic boundaries. This result is presumably due to MC carbides in the boundaries, such as those shown in Figure 4. No conclusive evidence of segregation was observed in specimens with thicknesses up to 37 microns. A 100 micron thick Rene'95 ribbon was melt spun to evaluate the amount of segregation present in interdendritic regions. This ribbon has a dendritic microstructure with a secondary dendrite arm spacing of approximately 1 micron. The results of the STEM analysis of this sample are shown in Figure 6. The electron micrograph of the region analyzed is shown in Figure 6a. The dashed line is the interdendritic boundary inferred from the carbide distribution and the solid line shows the location of the STEM scan. The STEM results are shown in Figure 6b, where the dashed line is the position of the inferred interdendritic boundary. The titanium and columbium contents show a much larger increase than that previously shown in Figure 5. The gradient, shown in Figure 6, extended over a distance of approximately 0.75 micron and the segregation level is expected to be approximately two times that of the bulk composition. Previous diffusion calculations⁽¹⁷⁾ for Rene'95 have shown that during 1800°F HIP compaction, chemical segregation can be homogenized over a distance of approximately 1.75 microns. The increased compaction temperatures used to produce the mechanical test specimens in the present study and the reduced ribbon thickness which prevented formation of branched dendritic microstructures would reduce the amount of segregation present even further. These STEM results confirm that ribbon with thicknesses less than 30 microns will have extremely limited micro-segregation in the matrix.

HIP Compaction of CBMS Ribbon

Two different forms of CBMS ribbon were compacted using a hot isostatic press (HIP) cycle. The first form consisted of a narrow ribbon which was approximately 3 mm wide and 12.5 to 25.0 cm long. The narrow ribbon segments were randomly packed and pressed into HIP containers. The other form of CBMS ribbon studied in this program was approximately 11 mm wide having lengths ranging from 0.02 to 25 m. These segments were spot welded together and subsequently would under light tension around a mandrel and placed in a HIP container.



(a)

(b)

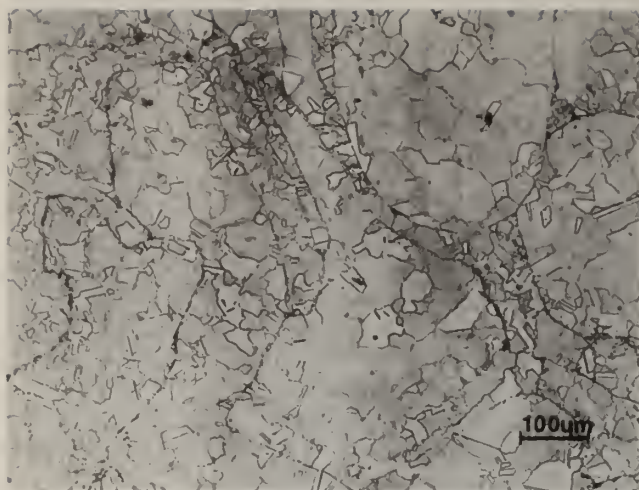
Figure 6. Results of (b) STEM Compositional Profile in a (a) Region of CBMS Rene'95 with Dendritic Microstructure.

The HIP containers of both forms of CBMS material were degassed and sealed. The HIP cycle selected for the Rene'95 ribbon was a 3-hour, 2200°F exposure at 15 ksi. This temperature is approximately 65°F above the γ' solvus temperature of Rene'95. This type of HIP cycle increases the healing of voids by creep and diffusion bonding. Super γ' solvus temperature have been shown to enhance the cyclic defect tolerance for Rene'95^(18,20) and AF15⁽¹⁸⁾. A total of 15 Rene'95 containers were HIP compacted during this program to densities equivalent to those obtained for PM Rene'95⁽¹²⁾. Another important measure of the quality of HIP compaction is thermally induced porosity (TIP). TIP is the porosity generated within the compacted material from entrapped gases during elevated temperature exposure. The TIP values of the CBMS ribbon compacts as measured by a change in density after the thermal exposure fell within the normal limits for PM Rene'95⁽¹²⁾.

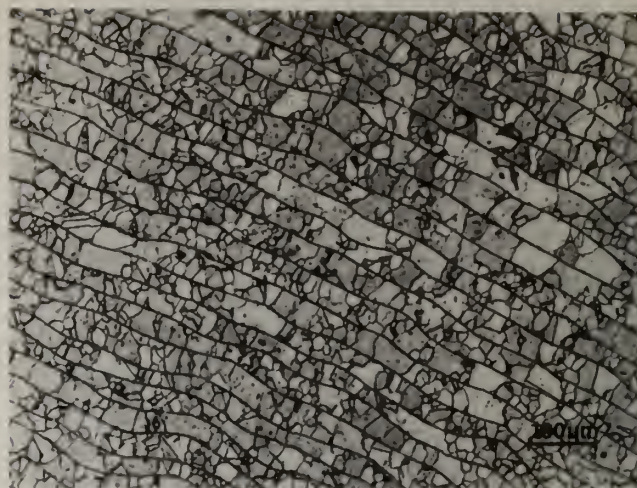
The microstructures of both the narrow, randomly packed and the wide, wound ribbons were characterized using optical metallography and transmission electron microscopy (TEM). Figure 7 shows optical micrographs of both product forms taken from metallographic sections perpendicular to the axis of the HIP container. Both materials have a grain size of approximately 25 microns and show no evidence of lack of bonding; however, the prior ribbon boundaries are very heavily decorated in these microstructures. Comparison of the micrographs suggest that the ribbon thickness in the randomly packed specimen was significantly greater than the wound ribbon, but this was not the case. In the compact containing randomly packed ribbon, the ribbon thickness direction will tend to be aligned perpendicular to the metallographic surface in Figure 7a. Thus, a metallographic plane would section the ribbon width resulting in a large apparent spacing. In the wound ribbon micrograph in Figure 7b, the metallographic plane is perpendicular to the ribbon width resulting in transverse viewing the ribbon so that the minimum ribbon thickness is observed.

The low magnification micrographs in Figure 7 appear to indicate that grain growth is impeded by the prior ribbon boundaries. This was generally the observed situation, but higher magnification optical metallography and thin foil TEM has shown occasional grain growth across prior ribbon boundaries (PRB).

The nature of PRB regions in Rene'95 CBMS ribbon were studied using TEM extraction replicas. A PRB region of HIP-compacted CBMS Rene'95 is shown in Figure 8. The PRB region consists of second phase particles and coarse γ' . The second phase particles were identified, using electron diffraction techniques, as aluminum oxides, zirconium oxides, and MC carbides. Similar observations have been made for Alloy 1200/19 CBMS ribbons. The source of these oxides is not fully known at this time. Eight oxygen content measurements of the Rene'95 compacts were in the range from 67-227 ppm. Two of these measurements were outside the specification limits (150 ppm) of Rene'95 PPM product. Ritter and Henry⁽²¹⁾ have documented oxide and carbide precipitation on prior particle boundaries (PPB) in HIP-compacted PM Rene'95, but the density of boundary decoration in PPB was much lower than that shown in Figure 7 and 8 in CBMS ribbon.



(a)



(b)

Figure 7. Optical Micrographs of (a) Randomly Packed and (b) Wound CBMS HIP-Compacted Rene'95.

The tensile properties of HIP-compacted CBMS Alloy 1200/19 ribbon were measured at 1000°F. This material was HIP-compacted in a three hour, 2050°F HIP cycle at 15 ksi, solution treated at 1925°F for one hour, cooled with a helium purge, and aged at 1250°F for 8 hours. This processing was identical to that used on the PM version of Alloy 1200/19⁽¹¹⁾. The γ' solvus temperature of this alloy is approximately 2000°F, so the HIP temperature was above the γ' solvus temperature while the solution temperature was below it. The results of individual tensile tests on Alloy 1200/19 are shown in Table II for randomly packed CBMS ribbon and PM Alloy 1200/19. The major differences between the materials are the extremely low tensile ductilities in the CBMS conditions relative to the PM product. The specimens with low ductilities also have low tensile strengths due to specimen failure before necking occurred. Fractography of the failed CBMS tensile specimens showed that the fracture occurred along PRB. The lower tensile ductility in the longitudinally oriented specimen of the CBMS Alloy 1200/19 most likely resulted from the applied stress being perpendicular to a majority of prior ribbon boundaries. A lower number of PRB were perpendicular to the axis of applied stress in transverse specimens. In an attempt to improve the ductility of CBMS Alloy 1200/19, the HIP'ed compacts were extruded.

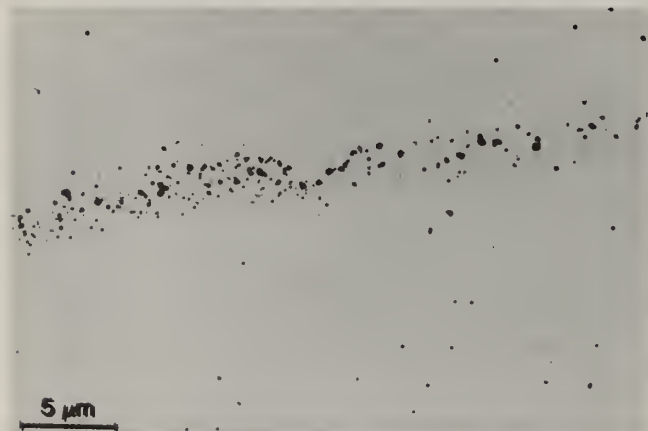
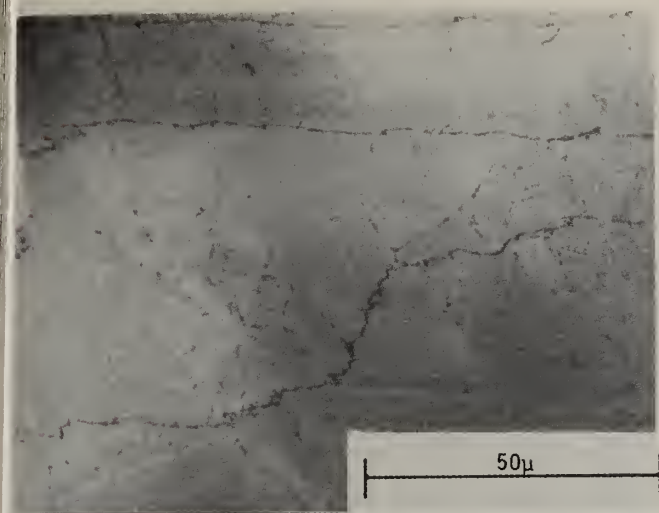


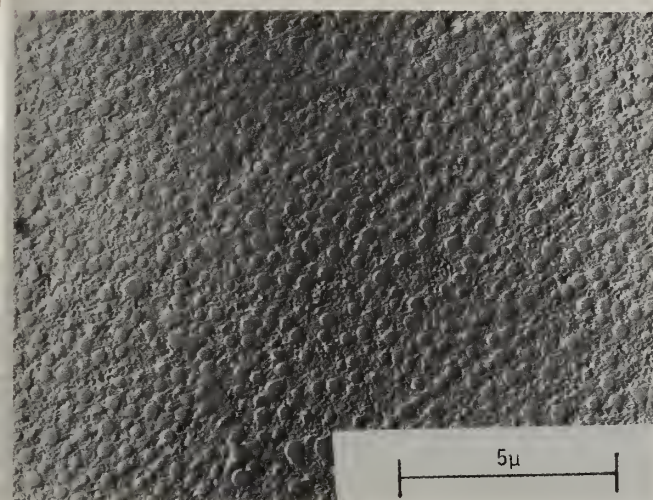
Figure 8. TEM Extraction Replica of HIP Compacted CBMS Rene'95 Ribbon Showing Second Phase Particles Along Prior Ribbon Boundaries.



(a)



(b)



(c)

Figure 9. Optical Micrograph (a), TEM Extraction Replica (b), and TEM Replica (c) of extruded CBMS Alloy 1200/19.

Table II. Tensile Properties of HIP-Compacted PM and CBMS Alloy 1200/19

Material Condition	Temperature (F)	0.2% Offset Yield Strength (Ksi)	Ultimate Tensile Strength (Ksi)	Elongation (%)	Reduction in Area (%)	Specimen Orientation Relative to Axis of HIP-
PM	75	158.0	217.0	32.0	32.7	Longitudinal
	1000	142.4	199.8	23.3	28.8	Longitudinal
	1200	138.2	203.0	18.3	20.0	Longitudinal
CBMS	1000		93.1	0.0	2.0	Longitudinal
	1000		158.9	0.06	2.0	Longitudinal
	1000	160.8	168.4	1.6	5.0	Transverse
	1000	162.2	189.7	5.6	12.5	Transverse

*Sample Failed Before Reaching 0.2% Plastic Strain.

Extrusion was used to simultaneously impart more shear deformation and elongate the spacing between adjacent second phase particles along prior ribbon boundaries. The randomly packed ribbon form was used for the HIP'ed extrusion billet instead of wound ribbon in order to obtain sufficient billet length for test specimen evaluation.

Approximately 0.8 kg of Alloy 1200/19 CBMS ribbon was loaded into a 2 in. dia. HIP container and HIP'ed at 2050°F. The container was subsequently machined into 1.75 inch diameter extrusion billet, loaded into an extrusion can and extruded at 1960°F with an extrusion ratio of 8:1. The Alloy 1200/19 portion of the resulting extrusion was approximately 0.6 inch in dia. and 11.5 inches long. The extrusion temperature was below the γ' solvus temperature of this alloy and resulted in the extrusion having a fine grain size. The extrusion was given a double solution treatment; a three hour, 2050°F cycle followed by a one hour, 1925°F treatment. The first cycle was intended to restore the microstructure to the grain size observed in the material HIP'ed at 2050°F. The second solution treatment and the subsequent aging cycles were the same as that used for the HIP-compacted CBMS ribbon in order to form the same γ' distribution.

The microstructure of the extruded CBMS Alloy 1200/19 material was studied using optical metallography and TEM replicas. Figure 9a shows that the grain size is similar to that previously shown in Figure 7 for HIP compacted Rene'95. Even after extrusion, the PRB regions were still decorated, as shown in Figure 9a. Figure 9b shows a TEM extraction replica of a PRB region in the extruded material. The PRB particles in these boundaries have a spacing approximately twice that observed in HIP'ed CBMS Rene' 95. This probably results from the lower reactive element content of Alloy 1200/19 relative to that of Rene' 95 and hence a lower oxide particle density. The increased oxide spacing may also result from the extrusion process. Figure 9c shows the γ' distribution of this material as revealed in a TEM replica. This γ' distribution is similar to that obtained in HIP-compacted helium atomized Alloy 1200/19 powder which received the same heat treatment⁽¹¹⁾. The large amount of primary γ' resulted from the final solution treatment being 75°F below the γ' solvus temperature.

The tensile, creep, rupture, and cyclic defect tolerance properties of extruded CBMS Alloy 1200/19 were determined in axisymmetric specimens with uniform gage lengths. The gage diameter of the creep/rupture specimen was 0.2 inch, while all other specimens had a 0.25 inch diameter gage section. Tensile tests were performed at room temperature, 1000°F, and 1200°F. These data are plotted in Figure 10 along with previous results on the HIP-compacted PM Alloy 1200/19 and the average tensile properties of PM Rene' 95. The yield and ultimate tensile strengths of both forms of Alloy 1200/19 are very similar, but both are approximately 15 percent lower than that of PM Rene' 95. Alloy 1200/19 was solution treated approximately 75°F below its γ' solvus temperature, while the curve for Rene' 95 was determined for material solution treated only 30°F below its γ' solvus temperature. The strength of Alloy 1200/19 could probably be substantially increased by increasing the solution treatment temperature^(18,20). This would reduce the volume fraction of primary γ' and allow a larger fraction of the γ' to be used for precipitation hardening. The tensile ductilities of the extruded CBMS Alloy 1200/19, as measured by the elongation and reduction in area, are inferior to those of the PM version of this alloy but are substantially greater than those shown in Table II for the HIP-compacted CBMS Alloy 1200/19. Previously, the lower tensile ductilities in the extruded CBMS Alloy 1200/19 relative to those of the PM version of this alloy were caused by the higher density of oxides and carbides along prior particle boundaries in the extruded material. The difference in ductilities between Rene' 95 and Alloy 1200/19 is most likely due to their differences in strength⁽¹⁸⁾. The good ductilities observed in the extruded CBMS superalloy are quite encouraging because this is the first time that mechanical properties of relatively large volumes of a melt-spun superalloy have been reported.

Figure 11 shows scanning electron micrographs of CBMS tensile specimens fractured at 1000°F. The HIP-compacted CBMS ribbon specimen shown in Figure 11a failed almost entirely along prior ribbon boundaries. Higher magnification observations showed that most of the fracture surface was covered by small dimples which apparently nucleated at the oxides and carbides within the PRB regions. Other studies on cast and wrought product forms have shown this general type of intergranular dimple rupture⁽²²⁻²⁴⁾. The extruded CBMS specimen also failed by dimpled rupture; however, the fracture path is not totally along the PRB regions. This apparently is the cause for the large improvement in tensile ductility. Further reduction in the frequency of oxide and carbide in PRB regions may result in ductilities equivalent to those of PM Alloy 1200/19 shown in Figure 10.

A single combined creep/rupture test was performed on the extruded CBMS Alloy 1200/19 at 1200°F with an initial stress of 125 ksi, which is 87% of its 0.2 percent yield strength at 1200°F. This specimen had a 0.2 percent creep life of 1220 hours and a rupture life of 5146.6 hours. These properties are shown using a Larson-Miller normalization in Figure 12. The solid lines in this plot indicate the 0.2 percent creep and rupture properties of Rene' 95. The arrow on the PM Alloy 1200/19 creep data point indicates that the terminal creep strain was less than 0.2 percent⁽¹¹⁾. These results show that both PM and extruded CBMS Alloy 1200/19 have creep and rupture capabilities

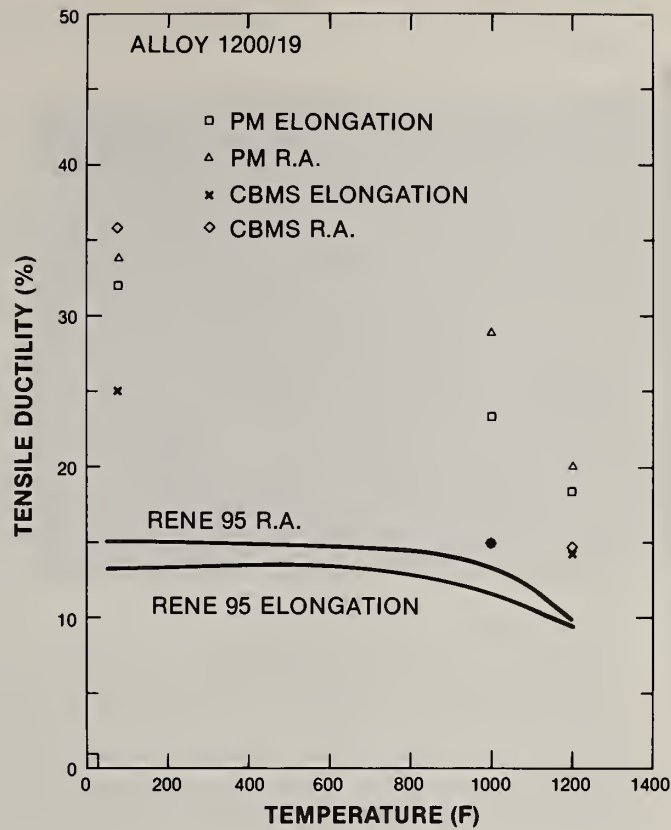
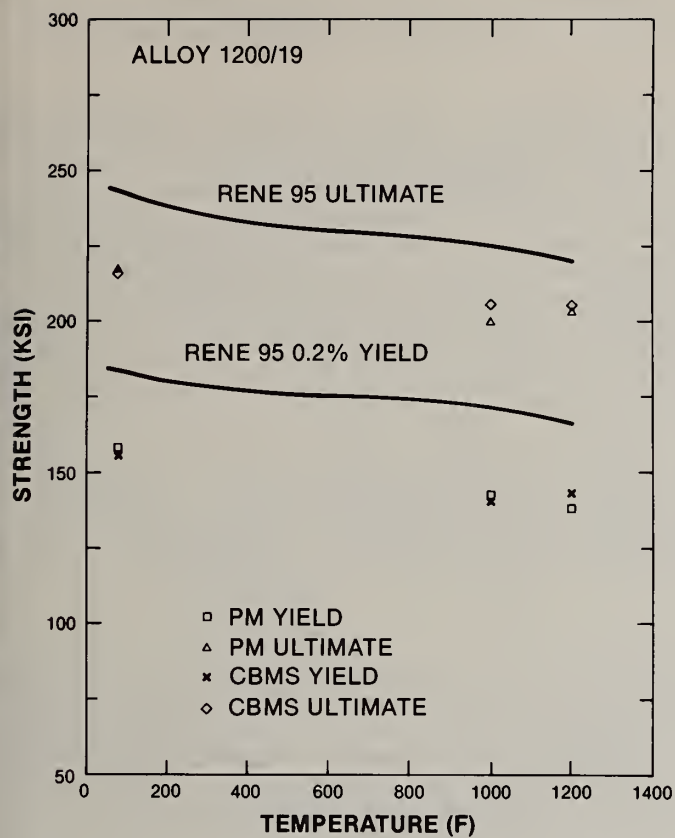


Figure 10. Variation of the (a) Strengths and (b) Tensile Ductilities of Alloy 1200/19 With Temperature.

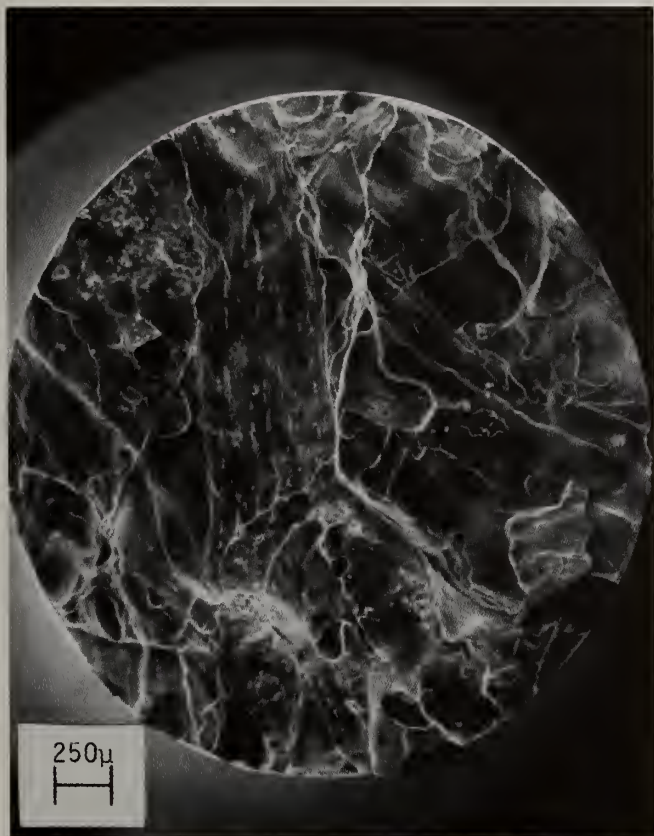


Figure 11. SEM Fractographs of Tensile Specimens of (a) HIP-Compacted & (b) HIP'ed Plus Extruded CBMS Alloy 1200/19.

which exceeded those of Rene' 95. The creep and rupture capabilities of Alloy 1200/19(12) are similar to those of AF115 (2, 25), a PM disk alloy with a 650°F creep and rupture capability improvement over Rene' 95.

The fatigue crack growth rates were determined using the DC potential drop techniques developed by Gangloff^(26, 27) and VanStone, et. al. ⁽²⁸⁾ for axisymmetric specimen geometries containing 0.1 mm deep electrical discharge machined notches. The cyclic defect tolerance evaluations included both strain controlled tests on specimens with 0.1 mm radius semicircular defects and load-controlled tests on specimens with 0.1 mm chord-shaped defects identical to those used in other investigations on nickel-base superalloys (11, 18, 19, 20, 26, 28). The crack growth rate data determined in 1000°F 0.33 Hz (20 cpm) crack growth rate tests were analyzed in the form of a linear elastic fracture mechanics fatigue growth curve where fatigue crack growth rate (da/dN) is plotted against the range in stress intensity factor (ΔK). Figure 13 shows the fatigue crack growth curve for HIP'ed PM and HIP'ed plus extruded CBMS Alloy 1200/19. The solid line in these curves is the baseline curve constructed by VanStone and Gangloff⁽¹⁹⁾ for the PM Rene' 95. Both sets of data show that Alloy 1200/19 has lower fatigue crack growth rates than Rene' 95 at 1000°F.

The similarity of properties between PM and CBMS Alloy 1200/19 indicates that this alloy has a wide range of processability. The high creep and rupture properties suggest that this type of low α , high solid solution strengthened alloy has potential as an advanced disk material. In addition, the low γ' volume fraction and high ductility may permit heat treatments which refine γ' size and possibly retard the fatigue crack growth rates relative to those shown in Figure 13⁽²⁰⁾.

Discussion

This investigation has shown that CBMS process can be used to produce relatively large volumes and high yields of rapidly solidified superalloys which are free of microsegregation and branched dendritic microstructures. These ribbons can be compacted to full density using several techniques, including the winding of ribbon around a mandrel to fabricate axisymmetric shapes. This approach was used to fabricate the six inch diameter HIP-compacted ⁽²⁹⁾ shape shown in Figure 14. This process has many of the advantages summarized by Breinan, et. al. ⁽²⁹⁾ for layer glazing and avoids the thermally induced cracking problems associated with layer glazing.

The primary technical barrier issue for the use of CBMS products for structural applications is the extensive PRB decoration which occurs in HIP-compacted material which results in low tensile ductilities. In this study, it was demonstrated that extrusion substantially improved these properties to a level where they approached those of PM product forms. This approach cannot be easily used to solve the ductility problems in large wound HIP-compacted shapes due to the large diameters of such part. Thus, it is imperative to develop the melt-spinning and compaction procedures which can eliminate or substantially reduce the PRB decoration to more fully utilize the potential advantages of rapidly solidified CBMS materials.

Acknowledgements

The authors acknowledge the financial support of the Defense Advanced Research Projects Agency (DARPA) which funded portions of this investigation and the guidance of Dr. E.C. VanReuth of DARPA and Mr. A.M. Adair and Mr. W.T. O'Hare of the Air Force. We would also like to thank Mr. E.C. Nagy, Mr. R.J. Zabala, and Mr. L.C. Perocchi of General Electric Corporate Research and Development, Mr. R.W. Smashey of the General Electric Aircraft Engine Group, and Mr. F.J. Rizzo of the Crucible Compacted Materials Operation for their assistance in producing and compacting the CBMS ribbon. Mr. L.T. Duvelius and Mr. E.D. Deaton were instrumental in conducting the mechanical property evaluations. Dr. E.N. Hall performed the STEM microanalysis. The authors are deeply indebted to Mr. A.M. Johnson and Dr. D.C. Williams for their encouragement, support and many helpful suggestions during this investigation.

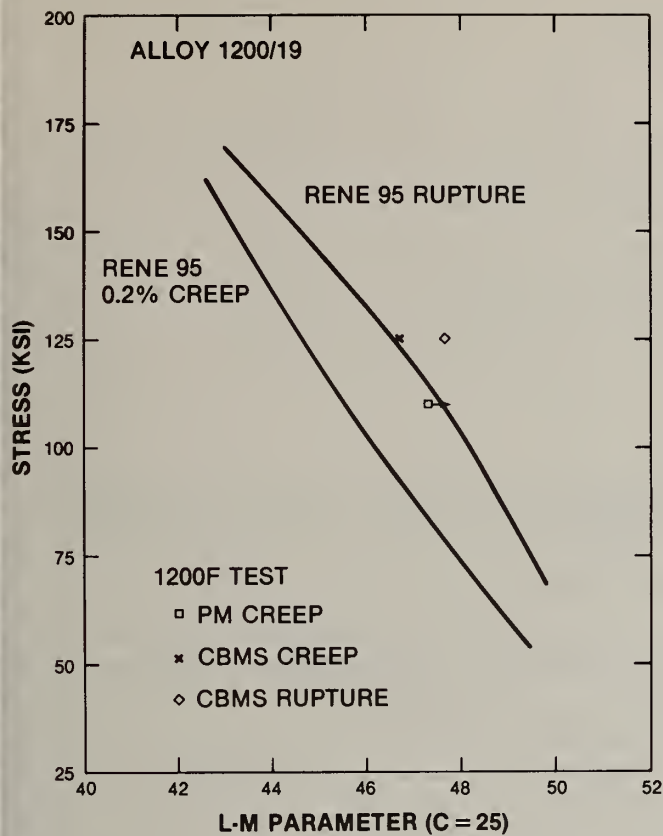


Figure 12. Larson-Miller Plot of the Creep and Rupture Properties of CBMS and PM Versions of Alloy 1200/19 Relative to Those of Rene'95

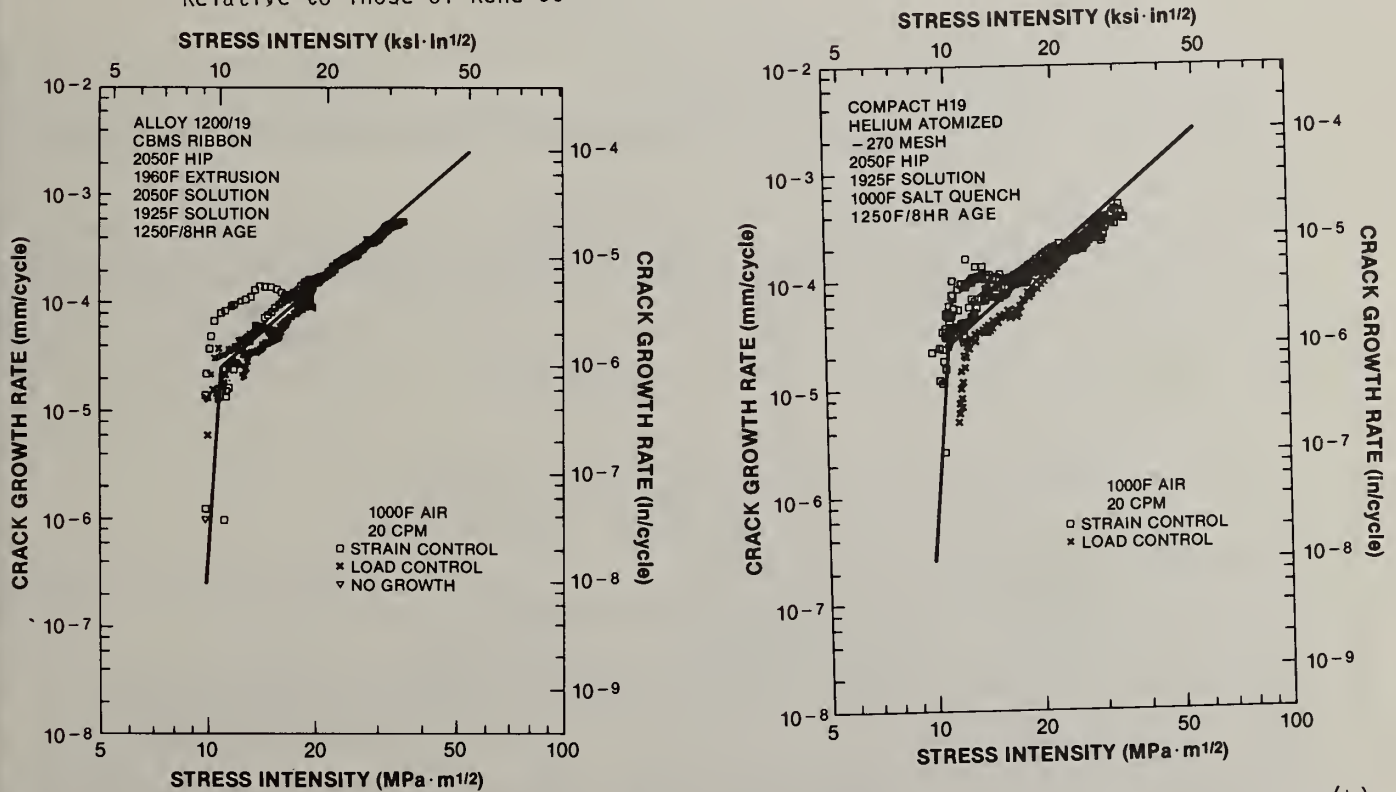


Figure 13. Comparison of the Fatigue Crack Growth Rate Curves of the CBMS (a) and PM (b) Versions of Alloy 1200/19.



Figure 14. Photograph of Six Inch Diameter Wound CBMS Alloy 1200/19 Shape

REFERENCES

1. P.S. Mathur and J.L. Bartos, USAMRDL-TR-76-30, May 1977.
2. J.L. Bartos, AFML-TR-74-187, December 1976.
3. R.D. Eng and D.J. Evans, NASA-CR-135409, March 1978.
4. R.D. Eng and D.J. Evans, NASA-CR-165549, May 1982.
5. D.F. Polk and B.C. Giessen, Metallic Glasses, ASM, Metals Park, Ohio, 1978, p.1.
6. R.W. Cahn, Contemp Phy, 21⁽¹⁾, 1980, p.43.
7. C. Sury and Rayanna, Suppl. Sci. Rep. RITU, A-7.
8. H.A. Davies, N. Shohoji, and D.H. Warrington, Rapid Solidification Processing Principles and Technologies II, Claitor's, Baton Rouge, 1980, p. 153.
9. J.V. Wood, P.F. Mills, A.R. Waugh, and J.V. Bee, J. Mat. Sci., 15, 1980, p. 2709.
10. H.H. Liebermann, R.E. Maxwell, R.W. Smashey, and J.L. Walter, "Process and Structural Aspects of Melt Spun Rene'95 Nickel-Base Superalloy Ribbons", Submitted to Metallurgical Transaction.
11. R.H. VanStone, AFWAL-TR-82-4032, Vol. II, Cincinnati, Ohio, June 1982
12. R.H. VanStone, H.H. Liebermann, J.R. Hughes, J.L. Walter, H.A. Davies, and R.W. Smashey, AFWAL-TR-82-4032, Vol. III, June 1982.
13. H. Jones, Rep. Prog. Phys., 36, 1973, p. 1425.
14. H. Jones, Rapid Solidification Processing Principles and Technologies, Claitor's, Baton Rouge, 1978, p.28.
15. R.C. Ruhl, Mat. Sci. Eng., 1, 1967, p. 313.
16. H.H. Liebermann, Mat. Sci. Eng., 43, 1980, p. 203.
17. R.H. VanStone, F.J. Rizzo, and J.F. Radavich, Rapid Solidification Processing Principles and Technologies II, Claitor's, Baton Rouge, 1980, p. 317.
18. R.H. VanStone, "Long Life Disks From Rapidly Solidified Materials: Volume I, Rene'95 and AF115 Process Development", AFWAL-TR-82-4032, Vol. I, June 1982.
19. R.H. VanStone and R.P. Gangloff, Rapid Solidification Processing Principles and Technologies II, Claitor's, Baton Rouge, 1980, p. 317.
20. R.H. VanStone, M.F. Henry, and A.M. Ritter, Final Report, Contr. No. N00019-79-C-0695, Dec., 1980
21. A.M. Ritter and M.F. Henry, General Electric Corporate Research & Development, Schenectady, N.Y. 12301, Unpublished Research.
22. I. Kirman, Met. Trans., 2, 1971, p. 1761
23. Jack Nutting, Physical Chemistry in Metallurgy, 1976, p. 489-495.
24. Gerald M. Ludtka and David E. Laughlin, Met. Trans., 13A, 1982, p. 411.
25. D.M. Carlson, AFWAL-TR-81-4078, August 1981.
26. R.P. Gangloff, Fatigue of Engineering Materials and Structures, 4, 1981, p.15.
27. R.P. Gangloff ASTM STP 738, ASTM, Philadelphia, PA., 1981, p. 120.
28. R.H. VanStone, D.D. Krueger, and L.T. Duvelius, "Use of DC Potential Drop Crack Monitoring Technique in the Development of Defect Tolerant Disk Alloys, to be published in ASTM STP 791, ASTM, Philadelphia, PA., 1983.
29. E.M. Breinan, D.B. Snow, C.O. Brown, and B.H. Kear, Rapid Solidification Processing Principles and Technologies II, Claitor's, Baton Rouge, 1980, p. 440.

S. C. Huang*, E. L. Hall*, and T. K. Glasgow**

*General Electric Corporate Research and Development
P.O. Box 8
Schenectady, NY 12301

**NASA Lewis Research Center
Materials Division
Cleveland, OH 44135

ABSTRACT

Superalloys with various levels of M_3B_2 boride have been studied by the melt-spinning rapid solidification process. The alloy compositions studied were chosen using the formula (matrix)_{100-x}(boride)_x, where the matrix atom composition was (Ni_{0.85}Cr_{0.13}Mo_{0.02})_{0.85}(Al_{0.7}Ti_{0.3})_{0.15}, the boride was (Ni_{0.1}Cr_{0.3}Mo_{0.5}Ti_{0.1})_{0.6}B_{0.4}, and the boride fraction $x = 0.15, 1.5$ and 7.5 . It was found that the boron content in the range of the present study did not significantly affect the ribbon castability. Increasing boride level decreased the bend ductility of the as-cast ribbons, but the ductility was drastically improved after the step anneal of $1080^\circ\text{C}/4$ hrs and $900^\circ\text{C}/10$ hrs. TEM studies of an as-cast ribbon showed uniform gamma prime precipitates of about 10 nm in diameter in crystalline cells which were less than 1 μm in size. The cell boundaries were decorated with boride particles smaller than 50 nm in diameter. Also studied was the annealed ribbon microstructure, particularly in regard to the grain and boride coarsening, boride-matrix coherency, and the boride chemistry. The boride composition was determined after electrolytic extraction. Finally, the incipient melting temperatures of the rapidly solidified ribbons were determined by DTA.

Introduction

Small boron additions, around 0.01 w/o have been found to improve the creep properties of polycrystalline nickel base superalloys [1]. This improvement is generally attributed to boron fitting atomically into small holes in the grain boundaries. Significantly larger amounts of boron, around 1 w/o, form discrete boride phases (such as M_3B_2) which may also improve superalloy mechanical properties.

The present paper reports on our investigation of the M_3B_2 boride using the rapid solidification, melt-spinning process. In particular, preliminary results on the boride chemistry, ductility, structure, and volume fraction, along with some ribbon microstructure, as-cast and annealed, will be presented. Incipient melting as influenced by boride fraction and rapid solidification will also be discussed.

Experimental

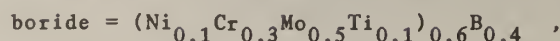
Three alloys have been studied. The compositions were based on formula

$$(\text{matrix})_{100-x} (\text{boride})_x ,$$

where the M_3B_2 - boride atom fraction, x , was 0.15, 1.5 or 7.5. The atomic composition of the matrix was chosen as

$$\text{matrix} = (\text{Ni}_{0.85}\text{Cr}_{0.13}\text{Mo}_{0.02})_{0.85}(\text{Al}_{0.7}\text{Ti}_{0.3})_{0.15} ,$$

representing approximately 50% gamma prime, and that of the boride was



selected according to the M_3B_2 chemistry reported in Ref. (3) and (4). Alloy compositions in weight percent are listed in Table 1. Ribbons of the alloys were fabricated in vacuum by the rapid-solidification, melt-spinning process. Ribbon surface topography was studied by optical metallography and scanning electron microscopy (SEM). This yielded information about the ribbon-wheel contact, solidification structure and the ribbon fracture characteristics. Further detailed microstructural examination was conducted using analytical electron microscopy (AEM). The analytical electron microscope has transmission imaging and electron diffraction capabilities, and is equipped with an energy dispersive X-ray spectrometer for chemical analysis with ~10 nm rated resolution. Samples were prepared by jet-electropolishing in a solution of 20% perchloric acid in methanol. Boride particles, after being extracted electrolytically in a 15% HCL-methanol solution, were studied by X-ray diffraction, electron diffraction, energy dispersive X-ray spectroscopy (EDS), to determine their structure and chemistry. Finally, differential thermal analysis (DTA) was performed on the as-cast ribbons. The DTA conditions were: sample weight ~80 mg, heating rate 10°C/min., and the argon flow rate 150 cc/min.

Table 1 - Nominal Compositions of Alloys Studied (w/o)

alloy number	M_3B_2 fraction	Ni	Cr	Mo	Al	Ti	B
70	0.15	77.34	10.50	3.05	5.16	3.94	0.012
71	1.5	76.49	10.60	3.73	5.10	3.96	0.12
72	7.5	72.69	11.07	6.75	4.82	4.07	0.60

Results and Discussion

(A) Ribbon Formability and Ductility

The three compositions studied were cast into ribbons having uniform dimensions and smooth surfaces. No consistent variations in the ribbon-to-wheel sticking distance or in the wetting pattern observable on the ribbon wheel-side surface [5] could be found as a function of the boride levels. Ribbons of all three compositions were obtained in fragments 2 to 20 cm long, presumably fractured in flight after separation from the casting wheel surface or upon impact with the vacuum chamber walls. A scanning electron micrograph of the fracture surface in alloy-71 ribbon shows the intercellular fracture characteristics, Fig. 1. Hot tearing or intermediate-temperature embrittlement might have contributed to the ribbon fracture during casting.

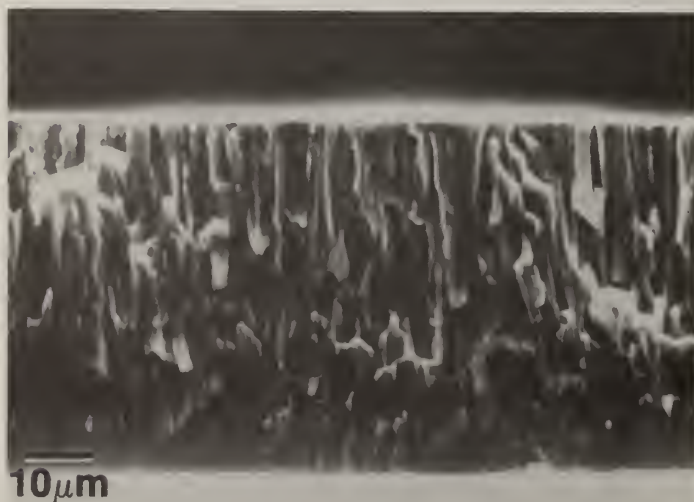


Fig. 1 An SEM micrograph showing a cross-sectional surface in the alloy-71 ribbon, exposed by ribbon fracture during casting. The ribbon top surface is shown at top.

Preliminary tests have demonstrated that the bend ductility of the as-cast ribbons decreases with increasing boron content, but the ductility can be significantly improved after a step anneal of 4 hours at 1080°C and 10 hours at 900°C.

(B) Microstructure in Alloy-71 Ribbon

The solidification morphology developed in alloy-71 ribbon is also revealed in Fig. 1: cellular near the wheel-side surface and dendritic near the top surface [6,7]. An extremely fine nucleation structure is barely perceptible at the wheel-side surface of the ribbon [7]. It has been further found that the alloy-70 ribbon is predominantly cellular while the alloy-72 ribbon becomes more pronounced in dendritic structure. Increasing boride level generally decreases the ribbon solidification size-scale. In alloy 71 ribbon, the fiber crystals growing unidirectionally from the bottom to the top surface have an average diameter of ~1 μm in the cellular region and ~2 μm in the dendritic region, Fig. 1.

Alloy-71 microstructure in an area near the middle of the ribbon thickness has been studied by analytical electron microscopy (AEM). The AEM sample geometry was such that the transverse section of the fiber crystals were examined. Preliminary results on the as-cast ribbon show a uniform grain (or cell) structure with a grain size of about 0.5 μm , Fig. 2. Also clearly shown in this figure are particles along grain boundaries, ranging in size from 20 to 100 nm. These particles, as revealed by energy dispersive X-ray spectroscopy (EDS), are rich primarily in Cr and secondarily in Mo, with slight enrichment in Ti. Significant amounts of Ni are also found, but the majority of it is attributable to the interference from matrix which overlaps the particles. Accordingly, the grain-boundary particles may correspond to the $(\text{Cr,Ni})_2(\text{Mo,Ti})\text{B}_2$ boride [4]. Further characterization of the as-cast boride will be carried out. Finally, Fig. 2 also displays in the grain interior a mottled contrast which corresponds to a uniform distribution of gamma prime precipitates which are about 20 nm in diameter. In dark field images formed using a gamma prime reflection, some coarse γ' , up to 50 nm in diameter, is observed along the grain boundaries.

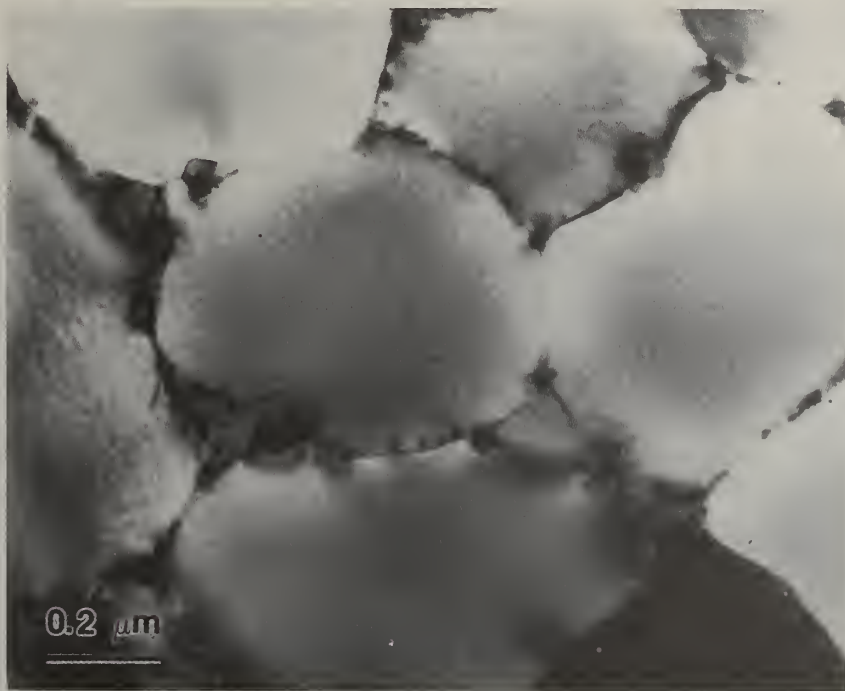


Fig. 2 Microstructure near the center of the alloy-71 ribbon, as cast.

The overall structure in alloy-71 ribbon, annealed in two steps at 1080°C for 4 hours and at 900°C for 10 hours, is shown in Fig. 3. It can be seen that the grains are on the order of a few microns in diameter and that the spheroidal borides are from 0.2 to 0.6 μm in diameter, both of which have coarsened in size significantly from the as-cast structure shown in Fig. 2. Most of the coarsened grains have an internal dislocation structure, and in many cases dislocation tangles outline the gamma prime particles. Some of these may be misfit dislocations; some others may be the as-cast grain-boundary dislocations not completely removed in the anneal process. Boride particles can be found at the grain boundaries as well as in the grain interior. The intragranular borides, generally smaller in size, mark some previous boundaries.

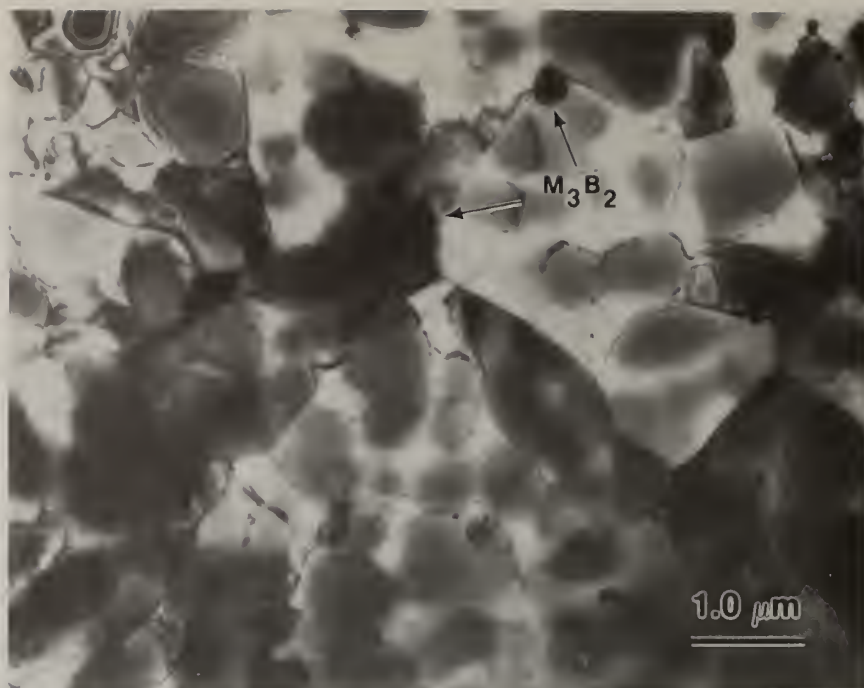


Fig. 3 The overall microstructure near the center of the alloy-71 ribbon, step-annealed 1080°C/4 hrs. and 900°C/10 hrs.

Figure 4 is a bright field/dark field pair showing the gamma prime particles in the annealed alloy 71 ribbon. In Fig. 4(b), a gamma prime reflection has been used to form the image, and thus the γ' particles appear bright. In addition to the large γ' particles which average 0.5 μm in diameter, small spherical γ' can be observed formed either during cooling from or at the lower heat treatment temperature. Furthermore, in Fig. 4(a) apparent misfit dislocations can be seen at the interfaces between the boride particles and the matrix. In Fig. 4(b) some boride particles are

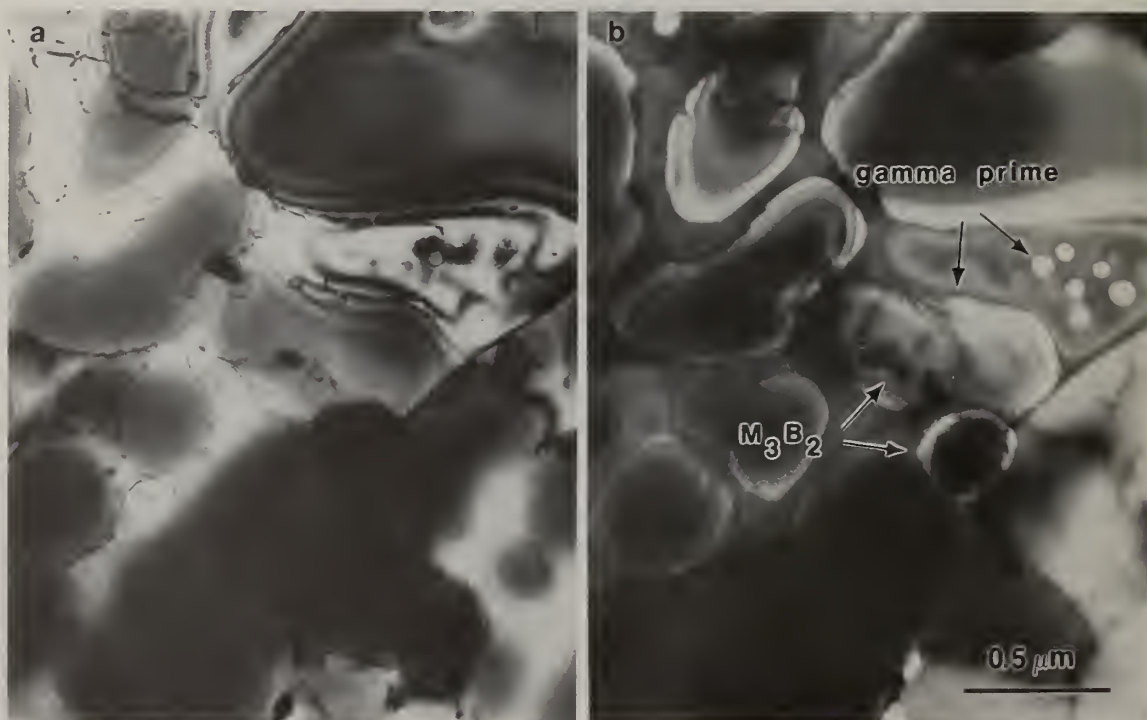


Fig. 4 A bright field/dark field pair of TEM micrographs showing detailed microstructure in the annealed alloy-71 ribbon.

brightened along with the γ' particles since a boride reflection has occurred near to the γ' reflection used to form the image. Electron diffraction studies indicated that the boride/matrix orientation relationship is

$$\begin{array}{ccc} (001)_{\text{matrix}} & || & (001)_{\text{boride}}, \\ [001]_{\text{matrix}} & || & [001]_{\text{boride}}, \\ & \text{and} & \\ [100]_{\text{matrix}} & || & [310]_{\text{boride}}. \end{array}$$

The spheroidal annealed boride particles have been identified by electron diffraction as M_3B_2 , having a tetragonal structure, $a = 5.71$ and $c = 3.07\text{\AA}$. An EDS of the annealed boride shows the enrichment of primarily Mo and secondarily Cr — in reverse order to that found in as-cast boride. Nickel and titanium also appear in the spectrum. The above results are consistent with the molybdenum-rich $(\text{Mo,Ti})_2(\text{Cr,Ni})\text{B}_2$ boride as reported in Ref. (4).

(C) Borides in Alloy-72 Ribbon

Efforts to characterize the alloy-72 ribbon structure were concentrated on the boride particles, extracted from ribbons as-cast or step-annealed 4 hours at 1080°C and 10 hours at 900°C . The extracted as-cast boride, as shown by SEM, was fine in size, ranging from 0.006 to $0.6\text{ }\mu\text{m}$ in diameter. During annealing, the size became much larger, mostly between 0.2 and $0.5\text{ }\mu\text{m}$. These results are similar to those in alloy 71, suggesting that the boride size is quite independent of the boron level. The boride particles in alloy 72 are thus conceivably larger in number and can be expected to stabilize the grain structure more effectively. SEM study further shows clearly the spheroidization of the boride particles due to the heat treatment.

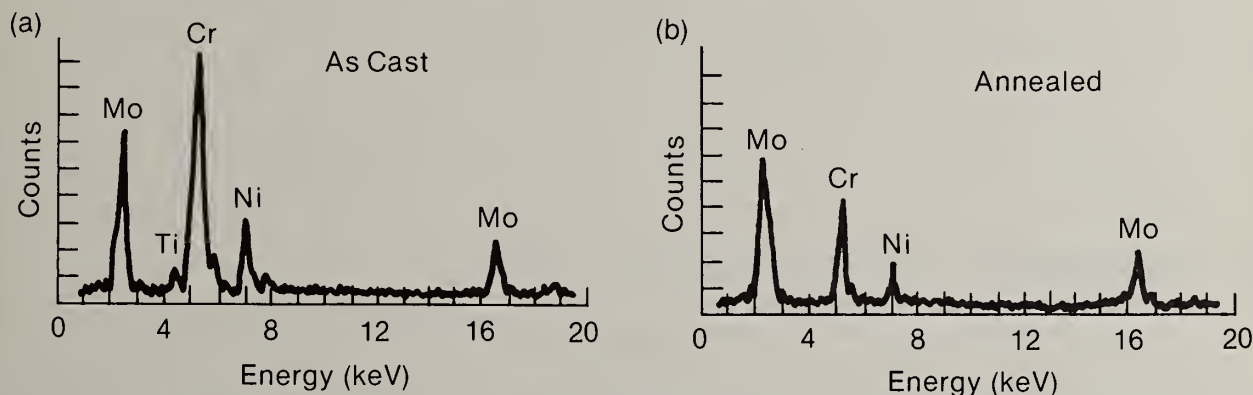


Fig. 5 The energy dispersive X-ray spectra of borides extracted from (a) as-cast, and (b) annealed alloy-72 ribbon.

For alloy 72, the as-cast boride has a tetragonal structure with $a = 5.67$ and $c = 3.05\text{\AA}$, as determined by X-ray diffraction. An energy dispersive X-ray spectrum of the boride, Fig. 5(a), shows strong Cr, medium-strong Mo, medium Ni, and weak Ti peak. These results suggest the as-cast boride being of the chromium-rich, low-parameter $(\text{Cr,Ni})_2(\text{Mo,Ti})\text{B}_2$ type [4]. On the other hand, electron diffraction of the annealed boride yields lattice parameters of $a = 5.8$ and $c = 3.1\text{\AA}$, and EDS shows strong Mo, medium Cr, weak Ni, and barely perceptible Ti peaks, Fig. 5(b). These results suggest the annealed boride being of the molybdenum-rich high-parameter $\text{Mo}_2(\text{Cr,Ni})\text{B}_2$ type [4]. A similar boride composition change has been found in the as-cast and annealed ribbons of alloy 71.

(D) Ribbon Thermal Analysis

Results of the differential thermal analysis (DTA) on ribbons of all three compositions studied are compared in Fig. 6. In general, each on-heating thermogram exhibits two endothermal peaks: a high-temperature peak corresponding to the melting of the matrix, and a low temperature one corresponding to melting of the chromium-rich, as-solidified boride [4,8]. As shown in Fig. 6, with the boron content increasing from 0.012 to 0.60 w/o, the liquidus temperature decreases from 1354 to 1285°C . More significantly, incipient melting of the boride phase occurs at 1223°C for the rapidly-solidified alloy-70 and 71 ribbons, with the boron content of the latter being larger by an order of magnitude. For the alloy-72 ribbon, containing 0.6 w/o boron, an additional five-fold increase, the incipient melting temperature decreases only slightly to 1212°C . These compare to an incipient

melting temperature decreases only slightly to 1212°C. These compare to an incipient melting temperature of 1201°C reported for the conventionally-cast B-1914 alloy which contains 0.1 w/o boron [8]. As also shown in Fig. 6, the intensity of the incipient-melting peak increases with boron level, in proportion to the quantity of the boride phase formed during the rapid ribbon quenching.

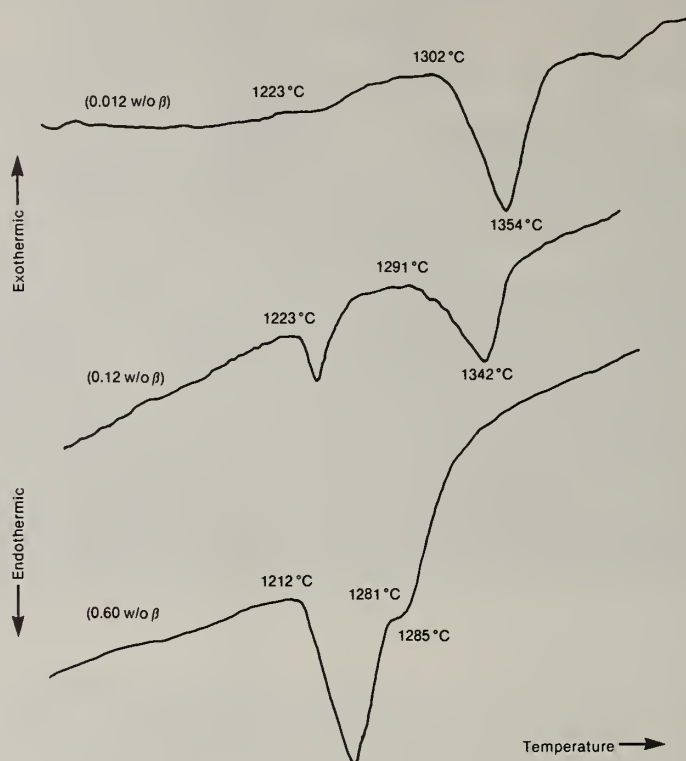


Fig. 6 DTA thermographs of the alloy-70, 71 and 72 ribbons.

Conclusions

Superalloy ribbons with M_3B_2 boride levels up to 7.5 atom fraction can be fabricated quite readily by the rapid-solidification melt-spinning process. The ribbons, however, tend to fracture during casting, perhaps due to hot-tearing or intermediate-temperature embrittlement. The as-cast boride is identified as $(Cr,Ni)_2(Mo,Ti)B_2$, and after a step-anneal, becomes $(Mo,Ti)_2(Cr,Ni)B_2$, richer in molybdenum. The annealed boride has a semicoherent relationship with the matrix: $(001)_{\text{boride}} \parallel (001)_{\text{matrix}}$, $[001]_{\text{boride}} \parallel [001]_{\text{matrix}}$, and $[310]_{\text{boride}} \parallel [100]_{\text{matrix}}$. The step-anneal also coarsens the grains and the boride particles. The size of the as-cast and annealed boride, however, seems to be unaffected by the boride level. While the bend ductility of the as-cast ribbons decreases with increasing boride fraction, the ductility can be improved by the heat treatment. Finally, the incipient melting temperature is 1223°C for alloy-70 and 71 ribbons and 1212°C for alloy-72 ribbon.

Acknowledgments

We thank R.J. Zabala, L.C. Perocchi, R.P. Laforce, and P.C. Irwin for technical assistance. We also thank H.R. Gray and L.A. Johnson for stimulating discussions. This research is partially supported by the NASA Lewis Research Center.

References

- [1] R.F. Decker and J.W. Freeman, Trans. AIME, 218 (1960) 277.
- [2] D.H. Maxwell, J.F. Baldwin, and J.F. Radavich, Metall. Met. Forming, Oct. 1975, p. 332.

- [3] J.R. Mihalison, in Reviews on High-Temperature Materials, Ed. J.B. Newkirk, Freund Publishing, Tel-Aviv, Israel, Vol. II, No. 3, 1974, p. 244.
- [4] W.J. Boesch and H.B. Canada, J. Met., April 1968, p. 46.
- [5] S.C. Huang and H.C. Fiedler, Met. Trans. A, 12 (1981) 1107.
- [6] H.A. Davies, N. Shohoji, and D.H. Warrington, Proc. 2nd Int. Conf. Rapid Solidification Processing, Ed. R. Mehrabian et al., Reston, Virginia, 1980, p. 153.
- [7] S.C. Huang and A.M. Ritter, to be published in Proc. Symp. Chem. Phys. Rapidly Solidified Materials, TMS-AIME Fall Meeting, Oct. 1982, St. Louis, Missouri.
- [8] C.J. Burton, in Proc. 3rd Int. Symp. Superalloys: Metallurgy and Manufacture, Ed. Kear et al., Claitor's Publishing, Seven Springs, Pennsylvania, Sept. 1976, p. 147.

PREPARATION OF METALLIC GLASSES WITH SECOND PHASE PARTICLES

D.G.Ast and P.G.Zielinski

Materials Science and Engineering
Cornell University
Ithaca N.Y. 14853

ABSTRACT

Ni[75]Si[8]B[17] metallic glasses with varying fractions of WC and TiC second phase particles were prepared using two different techniques. In the first method, the second phase particles were added to the melt before the latter was extruded. In the second method, the particles were injected immediately after extrusion into the still liquid melt puddle. The volume fraction of second phase particles incorporated into the cast ribbon and their spatial distribution were studied as a function of the preparation parameters by optical microscopy of sectioned specimens.

In ribbons prepared with the first method, the spatial distribution of second phase particles depended critically on the geometry of the melt puddle. As the volume fraction of second phase particles increased, the particles tended to agglomerate in periodically spaced clumps along the center plane of the ribbon.

In ribbons prepared with the second method, the distribution of the second particles was homogeneous and independent of volume fraction.

The mechanical properties of the dispersed alloys and of undispersed control specimens were studied by tensile and bending tests, and by scanning electron microscopy observations of shear bands formed during deformation. In ribbons with homogeneously distributed second phase particles, yield stress and Youngs modulus increased relative to undispersed control specimens. Ribbons containing agglomerated particle clumps, on the other hand, had fracture stresses lower than undispersed control specimens.

1. Introduction

Dispersion of second phase particles is commonly used to modify important mechanical properties of materials such as yield strength (metals) or fracture toughness (ABS polymers, zirconia dispersed ceramics). In metals, second phase particles are usually formed by precipitations and this limits the chemical composition of the strengthening phases. Powder metallurgical methods can overcome this restriction (e.g. TD Nickel) but these alloys have not been commercially successful.

The properties of metallic glasses containing (externally added) second phase particles have not been studied in detail. However, observations on partially crystallized alloys [1] indicate that the yield strength should improve.

Allied Chemical has filed a patent on the preparation of metallic glasses with second phase particles [2] and a preliminary report on the preparation and

properties of a Ni based metallic glass containing WC particles has been published by Kimura et al [3]. The latter report that the yield strength improves relative to undispersed matrix material.

The mechanical properties of dispersed materials depend critically on the spatial distribution of particles. In the ribbons prepared by chill block casting, the distribution of particles is controlled by the fluid flow in the melt puddle which, under certain operation conditions, can be turbulent [4]. In such a case, particles added to the melt prior to extrusion tend to agglomerate in the center of vortexes which are shed periodically into the cast ribbon. This difficulty can be overcome by adding the particles after extrusion but before solidification.

This paper discusses the microstructure of ribbons prepared by these two different preparation techniques and their mechanical properties.

2. Preparation techniques

In order to achieve satisfactorily results in a system in which second phase particles are introduced into the liquid state, the following conditions must be met: i) the density difference between the particles and the matrix should be small to avoid segregation by gravity ii) the particles should be wetted by the matrix and should not dissolve in the melt before solidification iii) the particles should not act as nuclei for the crystallization and iv) fluid flow should be laminar in order to avoid segregation in turbulent flows. Obviously, many of these conditions are easier to meet in a system which minimizes the time of contact between the fluid and the particle.

In our apparatus, density differences are usually not a serious problem, even when the particles are added to the melt before extrusion since stirring by the RF field of the heating coil keeps the particles suspended. A more serious problem is the commencement of matrix crystallization at the corners of second phase particles which was occasionally observed in [3]. Thus, high quenching rates are required for the matrix material. High quench rates require a good heat transfer to the wheel. An analysis shows that the direct influence of particles (i.e. rule of mixing contribution to the thermal conductivity and heat capacity of the matrix) on heat transfer is small [5] compared to the surface condition of the wheel which can influence heat transfer up to >60% [6]. However, investigations of the contact of the liquid solid interface [7] show that the true area of contact depends critically on the surface morphology of the solid, and that the liquid contacts the solid continuously only when a critical wetting condition is satisfied. A consequence of this condition is that the presence of particles which are not wetted by the matrix can change this critical wetting condition and thus indirectly greatly reduce heat transfer from the matrix to the quenching surface.

Ni[75]Si[8]B[17] was chosen as the matrix material. This alloy is a good glass former which can be prepared in ribbons as thick as 225 μm [8]. The second phase particles were WC and TiC, which are wetted well (contact angle about 0° (WC) and 32° (TiC)) by liquid Ni [9].

Ingots of Ni[75]Si[8]B[17] were prepared by arc melting of high purity (4N) nickel, nickel boride and silicon. Ribbons were prepared by chill block casting using a quartz crucible with a slit orifice (0.2 mm) positioned close (0.5-0.7 mm) to a rotating copper wheel (290 mm diameter, surface speed 21 m/sec). The second phase particles were introduced either by adding the powders to the crucible prior to heating (method 1), or by blowing the particles into the melt puddle during the extrusion process (method 2) using an arrangement similar to a small sand blasting gun [10]. The He operating the gun served simultaneously as a conventional quench stabilizer of the liquid.

In either case, the resulting ribbons were 30 - 60 μm thick and 4 - 7 mm wide. The amorphous structure of the matrix material was confirmed by x-ray diffraction and transmission electron microscopy.

3. Results

3.1 Particle distribution

The distribution and volume fraction of second phase particles was determined by optical microscopy of surfaces polished parallel either to the surface or to the

edge of the ribbon. This polishing process was continued until the center of the ribbon was reached in order to determine the three dimensional particle distribution.

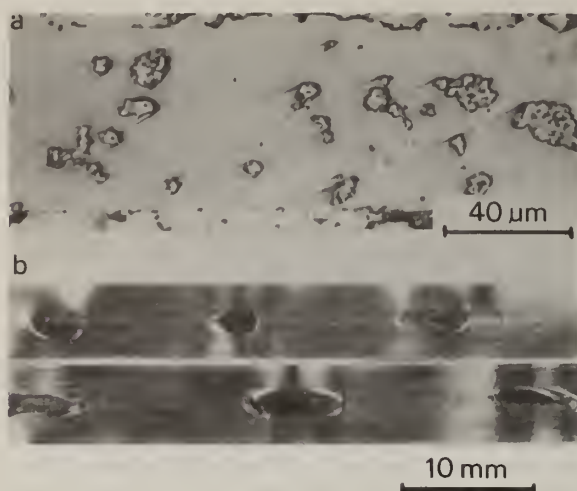


Fig. 1
Cross section (a) and surface (b) of Ni[75]Si[8]B[17] ribbons containing various fractions of WC particles (Preparation method 1).

Fig. 1 shows an optical micrograph of the cross section and the surface of ribbons prepared by method 1 (i.e. addition of particles to the crushed ingot prior to melting). At low volume fractions (Fig. 1a) the WC are nearly homogeneously distributed, with the occasional formation of a particle agglomerate. As the volume fraction of WC increases large and periodically distributed particle agglomerates are observed along the ribbon (Fig. 1b). A ribbon with an average volume fraction of 6% WC was selected for mechanical testing in order to evaluate the influence of these agglomerates on the mechanical properties.

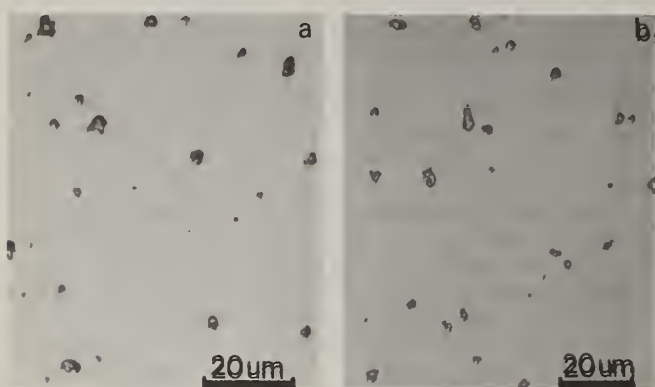


Fig. 2
Homogenous distribution of second phase particles [WC - (a), TiC - (b)] in Ni[75]Si[8]B[17] ribbons prepared by method 2.

Ribbons prepared by method 2 (i.e. post extrusion addition) contained a homogeneous distribution of second phase particles at all volume fractions investigated. A typical cross section is shown in Fig. 2. The volume fractions were estimated from several micrographs and averaged over the length of the ribbon. For the samples shown in Fig. 2 the volume fractions are 4.5% WC (Fig. 2a) and 6.4% TiC (Fig. 2b).

3.2 Mechanical properties

Ribbons prepared by method 1 were shaped into tensile specimens with reduced cross sections and polished edges. All tensile specimens fractured in the linear regime of the stress strain curve. The fracture stresses calculated from the load at failure and the measured cross sections are shown in Table 1. Inspection of this table shows that the yield strength of dispersed ribbons prepared by method 1 is lower than that of undispersed ribbons. Scanning electron microscopy (SEM) fractography was carried out in a JEM 35 B and the results are indicated in Fig. 3. The failure pattern of the undispersed material (Fig. 3a) is typical for metallic glasses and shows the vein pattern characteristic of shear-tearing. Inspection of Fig. 3b suggests that the agglomerates act as the initial site for decohesion. Since in a metallic glass, in the absence of work hardening, failure in shear occurs at the weakest cross section a very small fraction of agglomerates can cause premature failure in a tensile specimen.

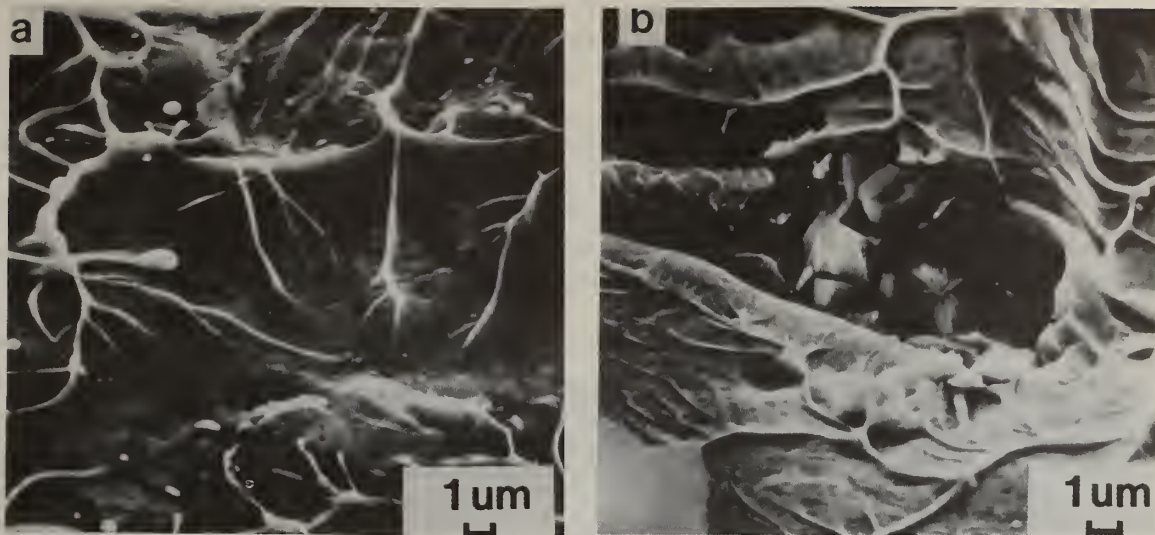


Fig. 3. Fracture surfaces of undispersed (a) and dispersed (b) Ni[75]Si[8]B[17] with 6 vol.% of WC prepared by method 1.

Ribbons prepared by method 2 were difficult to polish (because of the presence of hard transition metal carbides) and were therefore investigated in bending. In this test a ribbon is bent into a hairpin configuration, inserted between two parallel platens, and then slowly compressed. The force exerted on the platens by the ribbon is recorded as a function of the platen separation D , in an Instron testing machine. Typical results of such tests are shown in Fig. 4 for an undispersed ribbon (curve A) and for two ribbons containing second phase particles.

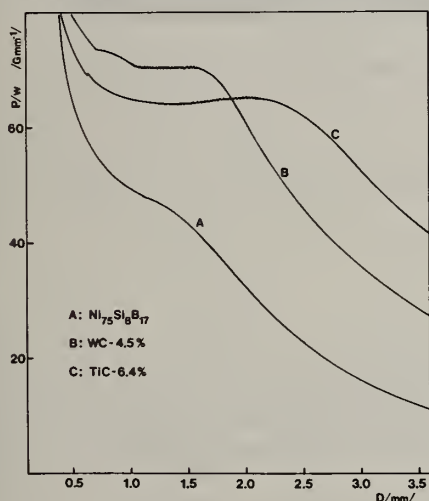


Fig. 4. Load corresponding to unit width of the ribbon (P/w) vs separation distance (D) as recorded for undispersed (A) and dispersed ribbons (B,C) in bending test.

Inspection of this figure shows marked differences in the mechanical behavior of the three ribbons. The dispersed ribbons show a serrated plateau (see curves B, C) which is absent in the non dispersed ribbon. Since metallic glasses behave very close to ideal elastic - plastic solids, bending tests can be analyzed quantitatively to obtain the flow stress and the elastic modulus of the ribbon under test [11,12]. The results obtained are generally in good agreement with those obtained in tensile tests which require a more demanding specimen preparation (reduced cross section, carefully polished edges) in order to achieve reliable results. Table 1 lists the the yield strength and Youngs modulus of undispersed and dispersed metallic glasses prepared as a function of the preparation and testing conditions. Note the good agreement between tensile and bending tests in the undispersed case.

Table 1 indicates that ribbons prepared by method 2 have a significantly increased yield stress and a high σ_y/E ratio of about 1/40. In order to examine the influence of the second phase particles on the plastic deformation process, i.e. the formation a propagation of shear bands, both undispersed and dispersed materials were bent into a hairpin configuration and examined inside a scanning electron microscope at decreasing platen spacings (see Fig. 5).

Table 1: Mechanical properties of Ni[75]Si[8]B[17] metallic glasses with second phase particles.

Volume fraction	Preparation method	σ_y (GPa)	E(GPa)	Test
0	standard	1.59	-	tension
0	"	1.57	81.5	bending
6% WC	Method 1	1.35	-	tension
4.5% WC	Method 2	2.15	107.5	bending
6.4% WC	Method 2	2.65	107.6	bending

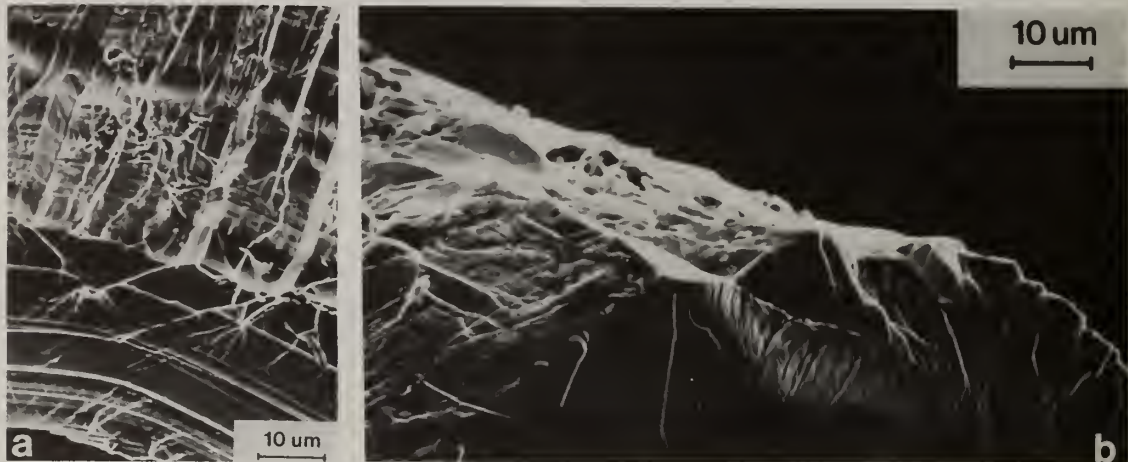


Fig. 5. SEM micrographs of shear bands formed during bending of undispersed (a) and dispersed (b) [4.5 vol.% WC] Ni[75]Si[8]B[17] ribbons (Method 2).

The character of the shear bands observed on polished cross sections differed markedly indicating that the presence of second phase particles significantly changes the microscopic deformation mechanism.

4. Discussion

The formation of undesirable particle agglomerates in ribbons prepared by method 1 can be explained in a semiquantitative fashion by the boundary layer instability [4]. A large shear gradient exists in the melt puddle since fluid elements in the vicinity of the melt nozzle have zero tangential velocity whereas those in the vicinity of the wheel surface move with high velocity (about 20m/sec). A qualitative evaluation shows that the Reynold number is such that turbulent flow and boundary layer separation can occur. In the latter case the particle accumulate in regions of low rotational flow. Periodic vortex shedding releases the clumps of particles "down stream" where they are frozen in into the ribbon cross section as shown in Fig. 1b. These agglomerates, which were observed already at very low volume fractions are weak centers in the center of the ribbons and degrade the mechanical properties of the glasses investigated.

Ribbons prepared by method 2 contain a homogeneous distribution of second phase particles. Although the detailed mechanism of the elastic and plastic deformation in the presence of these particles is very complex, one can try, in a zero approximation to model these materials as composites. In such materials it is frequently found that Youngs modulus obeys the rule of mixture, i.e.

$$E = E_p V_{fp} + E_n V_{fn} \quad (1)$$

where E_p and E_n represent Youngs modulus of the particle and matrix material and V_{fp} and V_{fn} their respective volume fractions. Taking $E = 440$ GPa (TiC) and 660 GPa (WC) [13], relation (1) is plotted in Fig. 6. A comparison with the experimental data shows good agreement with the predictions of the rule of mixture. Thus, it appears that the elastic properties of these reinforced glassy materials are in agreement with the behavior of composites.

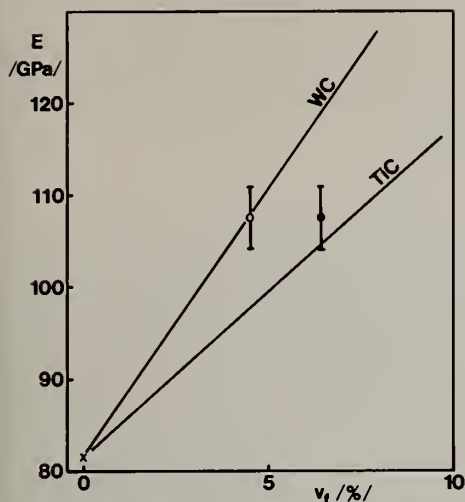


Fig. 6. Young modulus of dispersed Ni[75]Si[8]B[17] glasses as a function of volume fraction of second phase particles. Solid line is the prediction of eq. (1).

The plastic deformation requires a more detailed discussion. When an undispersed Ni[75]Si[8]B[17] metallic glass is tested in a hairpin configuration, the load vs platen separation curve contains typically three stages. At large platen separations (2.1 to 1.4 mm) the material deforms homogeneously without formation of any shear bands. Below 1.4 mm, the deformation proceeds via the formation of shear bands which are formed in a spatially homogeneous manner such that the radius of curvature at the tip of the hairpin is roughly given by half of the platen separation. At distances below about 1.1 mm, the deformation proceeds only in a few shear bands close to the apex of the ribbon (kinking) until fracture occurs or the material is doubled back on itself. These three stages of deformation in bending are discussed in more detail in ref [14].

The plateau in the load vs distance curves (Fig. 4) which develops with increasing amount of second phase particles corresponds to stage II, i.e. to the formation and propagation of shear bands. The serrations reflect the interactions of the shear bands with the second phase particles. These interactions include delocalization of shear bands, cutting processes of particles, and nucleation of shear bands at particles. The deformation mechanism is complex and requires further investigations. From the technological point of view, the formation of the plateau indicates an extended plastic deformation range, i.e. a desirable feature in metallic glasses.

Acknowledgments

This research was sponsored by ONR under contract NR 039-151. Additional support was provided through the use of central facilities of the Materials Science Center at Cornell, which in turn is supported by NSF.

References

1. H. Kimura a T. Masumoto, Acta Metall. 28(1980)1677
2. M. Narasimham - US Patent 4 330 027 (1982)
3. H. Kimura, B. Cunningham a D. G. Ast - Proc. IV Int. Conf. Rapidly Quenched Metals, Eds. T. Masumoto, K. Suzuki (The Japan Inst. Metals, Sendai 1982) V. II, p.1385
4. P. G. Zielinski a D. G. Ast, submitted to Scripta Met.
5. P. G. Zielinski a D. G. Ast, submitted to Metall. Trans.
6. S. Huang a C. Fiedler - Metall. Trans A 12(1981)1107
7. R. S. Timsit - Appl. Phys. Lett. 40 (1982) 379
8. M. Hagiwara, A. Inoue a T. Masumoto - Metall. Trans. A 12(1981)1027
9. G. V. Samsanov - Handbook of High Temperature Materials, no 2 (Plenum Press, New York 1964)
10. P. G. Zielinski a D. G. Ast - patent pending
11. D. J. Krenitsky a D. G. Ast, J. Mat. Sci. 14(1979)275
12. L. Bresson, J. P. Chevalier a M. Fayard, Scripta Met. 16(1982)499
13. L. E. Toth - Transition Metals and Nitrides (Academic Press, New York 1971)
14. P. G. Zielinski a D. G. Ast - to be published

The Effect of Solidification Velocity
on the Microstructure of Ag-Cu Alloys

W. J. Boettinger, R. J. Schaefer, F. Biancaniello

Metallurgy Division
National Bureau of Standards
Washington, DC 20234

and

D. Shechtman*

Center for Materials Research
The Johns Hopkins University
Baltimore, MD 21218

ABSTRACT

Electron beam surface melting and resolidification passes have been performed on a series of Ag-Cu alloys between 1 wt.% Cu and the eutectic (28.1 wt.% Cu) at speeds between 1.5 and 400 cm/s. At low growth rates conventional dendritic or eutectic structures are obtained. At high growth rates microsegregation-free single phase structures are obtained for all compositions. The velocity required to produce this structure increases with composition for dilute alloys and the values agree with the predictions of absolute stability of the liquid-solid interface with equilibrium partitioning. For alloys between 15 and 28 wt.% Cu, the velocity required to produce the microsegregation-free extended solid solution decreases with composition and is related to nonequilibrium trapping of solute at the liquid-solid interface. At intermediate growth rates for alloys with 9 wt.% Cu or greater, a structure consisting of alternate bands of cellular and cell-free material is obtained. The bands form parallel to the local interface.

Introduction

Rapidly solidified crystalline alloys are well known to exhibit a refined scale of microsegregation and interdendritic second phase particles. In some cases this microsegregation and the interdendritic phases can be completely eliminated by rapid solidification. These microsegregation-free structures can occur in alloys with compositions greater than the equilibrium solubility of the primary phase. Such structures provide an ideal starting microstructure for subsequent thermomechanical processing. However, the solidification velocities required to produce these structures are not well known.

The classic splat-quenching experiments of Duwez, Klement, and Willens [1] showed by x-ray diffraction that complete solubility of Ag and Cu in the solid state at all compositions could be obtained despite the presence of a solid miscibility gap and eutectic reaction in the phase diagram. Boswell and Chadwick [2] showed later by TEM examination that splat quenched Ag-Cu solidified from the melt as a single solid phase free of microsegregation. Surface melting and resolidification experiments using lasers or electron beams permit better control over solidification velocity than other rapid solidification techniques. Such experiments involve no bulk undercooling due to the presence of the alloy substrate and nucleation processes do not therefore play an important role. Also, because the liquid is contained in its own solid, a knowledge of heat transfer coefficients is not required. Elliott, Gagliano, and Krauss [3] using a pulsed laser, and Copley et al. [4-6] using a scanned CW laser, showed that supersaturated solid solutions of Ag-Cu could be formed by surface melting and resolidification experiments. The solutions however, contained a rather unique structure consisting of bands formed parallel to the local solidification interface. In these papers no structures are reported which are free of the bands and the velocities at which the transitions of microstructure occur are not described.

*Guest Worker, Metallurgy Division, National Bureau of Standards.

In the present paper, a series of electron-beam surface melting experiments has been performed on Ag-rich, Ag-Cu alloys. These experiments determine the transition velocity for changes from dendritic or eutectic growth to microsegregation-free solidification. This information permits the evaluation of existing rapid solidification models and points to areas where new models are required. The results and discussion in this paper appear in more detail elsewhere [7].

Experiments

Alloys were prepared by induction melting of 99.99 percent pure components in a graphite crucible and chill casting under argon in a carbon-coated copper slab mold. Ingots were cold-rolled to 3 mm thick sheets. For the surface melting experiments, the substrate must be prepared with either no microsegregation or microsegregation fine enough to ensure complete mixing during surface melting. Alloys containing 1 and 5 wt.% Cu were homogenized for 20 h at 750 °C. Alloys containing 9, 15, and 23 wt.% Cu were surface melted using overlapping electron-beam passes to a depth of ~ 0.5 mm at a scan speed of 3 cm/s. This produces a dendrite arm spacing less than 1 μ m. Alloys containing 28.1 wt.% Cu (the eutectic composition) required no pretreatment. Wet chemical analysis of the six alloys yielded compositions of 1.07, 5.49, 9.23, 15.25, 23.50, and 28.61 wt.% Cu respectively. Rapid solidification experiments were performed by single, one-dimensional sweeps of a focused 21 keV, ~ 50 mA, ~ 1 mm diameter electron beam at speeds between 1.5 and 400 cm/s across the surface of a prepared alloy substrate which was attached to a water-cooled copper block.

Significant effects arise from the change in weld puddle shape as the scan rate is increased. The local solidification velocity is equal to the product of the scan velocity with the cosine of the angle between the scan direction and the local growth direction. Because of this factor, growth velocities even at the top center of the weld puddle for high scan speeds may differ from the scan speed. By examining longitudinal sections through the weld centerline by optical microscopy and assuming that grain boundaries propagate parallel to the growth direction, the angle, θ , between the electron beam scan direction and the growth direction at the top of the weld was measured. For scan speeds below 30 cm/s, the growth velocity near the weld surface usually differs from the scan speed by 15 percent or less. At velocities of 200 cm/s, the measurements indicated that the growth rate is about one-half of the scan speed.

Results

Figure 1 shows a summary of the microstructures observed at the center of the weld zone near the free surface as a function of the electron beam scan velocity and alloy composition for all experiments performed. The figure is divided into four regions exhibiting four general types of microstructure: (a) dendritic (cellular), (b) eutectic, (c) banded, and (d) microsegregation-free. The detailed results will be described by alloy composition.

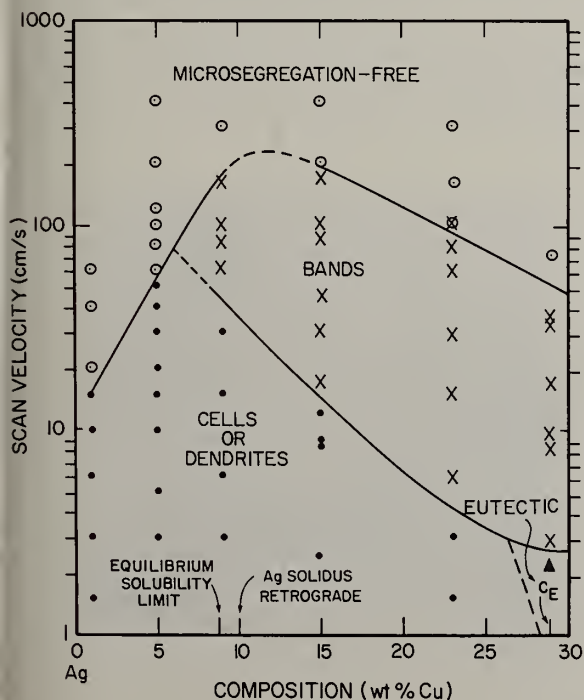


Fig. 1 Summary of microstructures observed in Ag-Cu alloys as a function of composition and electron-beam scan velocity.

Dilute alloys exhibit a transition from segregated to microsegregation-free structures at velocities which increase with alloy composition. These velocities agree within a factor of two with the theoretical predictions of absolute stability of the liquid-solid interface as described in another paper in these proceedings [8].

Ag-9 wt.% Cu, -15 wt.% Cu, and -23 wt.% Cu.

These alloy compositions are beyond the equilibrium solubility limit (8.8 wt.% Cu) of Cu in Ag at the eutectic temperature. The 9 wt.% Cu alloy does not exceed a calculated [9] Ag-solidus metastable retrograde composition however. As seen in figure 1, the microstructure of each of these alloys changes with increasing velocity from dendritic to banded and from banded to microsegregation-free.

The refinement of the primary arm spacing with scan velocity for Ag-9 wt.% Cu alloy is shown in figure 2. The rate of change of spacing with the actual solidification velocity may however be somewhat different due to changes in weld puddle shape as discussed previously. TEM examination of a Ag-15 wt.% Cu melt trail scanned at 2.5 cm/s showed a cellular microsegregation pattern with a relatively small volume fraction of eutectic in some areas and no eutectic in other areas (fig. 3). The maximum velocity at which dendritic growth is observed decreases with alloy composition from 30 cm/s for Ag-9 wt.% Cu to 4 cm/s for Ag-23 wt.% Cu (fig. 1).

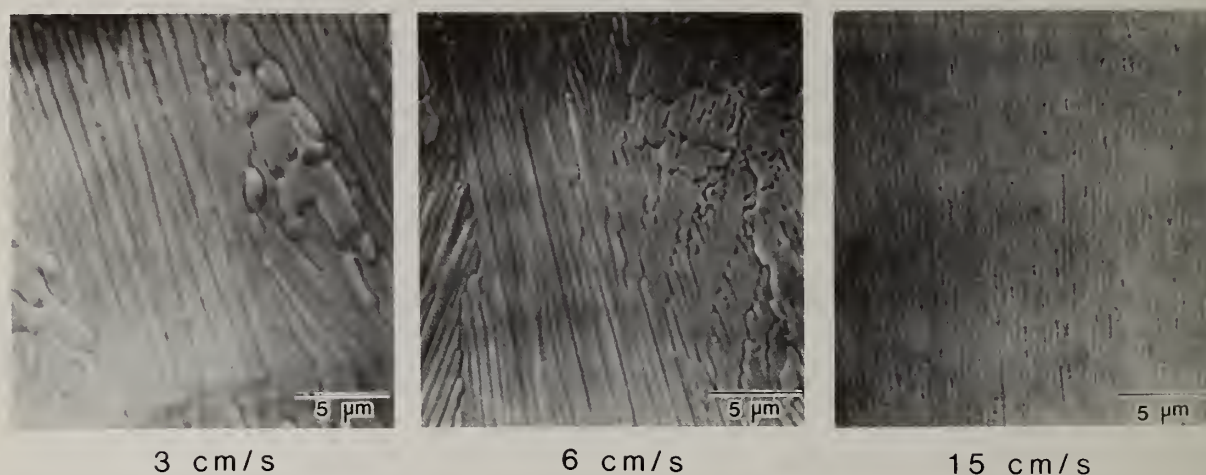


Fig. 2 Refinement of primary dendrite arm spacing with scan velocity for Ag-9 wt.% Cu alloys. SEM.

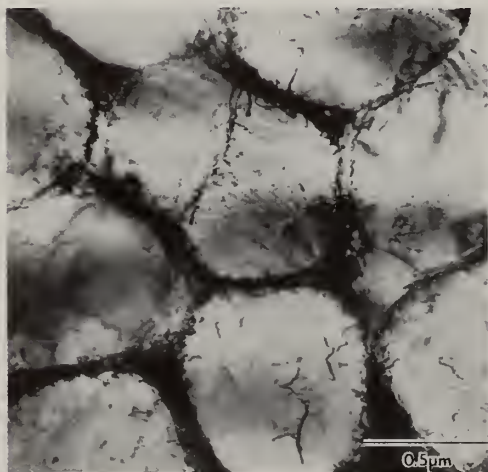


Fig. 3 Cellular microsegregation pattern observed in Ag-15 wt.% Cu alloy at a scan velocity of 2.5 cm/s. TEM.

A structure consisting of light and dark etching bands or striations is observed in the intermediate velocity range shown in figure 1. Figure 4 shows a transverse and a longitudinal section through the weld centerline for a 15 wt.% Cu alloy scanned at 30 cm/s. The lower part of the melted region, where the solidification velocity is lowest, is dendritic. The upper part of the melted region is banded. As seen in figure 4b the bands are parallel to the expected shape of the trailing edge of a melted zone. A transition from dendritic to banded structure, observed in the same sample suggests strongly that the origin of the banding phenomenon is growth related rather than an artifact of nonsteady beam power [3] or melt convection [5].

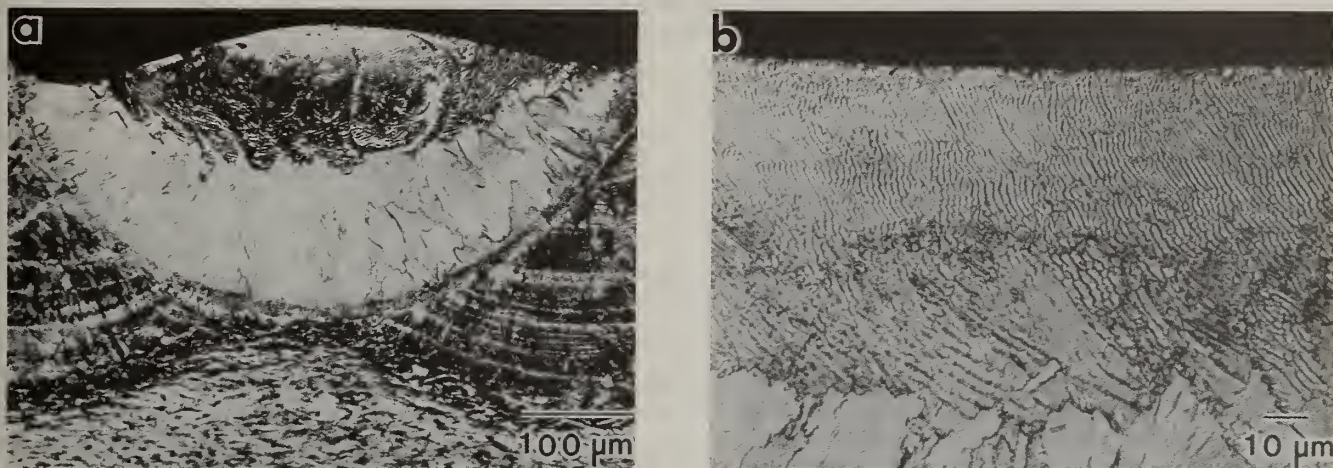


Fig. 4 (a) Transverse and (b) longitudinal sections of a Ag-15 wt.% Cu alloy scanned at 30 cm/s, showing transition from (unresolved) dendritic structure to the banded structure. Optical microscopy. The scan direction is to the right in (b).

TEM examination of the banded structure (fig. 5) in a 23 wt.% Cu alloy scanned at 17 cm/s revealed alternate layers of cellular and cell-free alloy. Evidently the dark etching material seen in optical micrographs of the banded structure corresponds to the cellular layer. X-ray fluorescence measurement in the STEM with a probe size just large enough to average over the entire width of an individual layer ($\sim 0.4 \mu\text{m}$) revealed no statistically significant difference in average composition between the cellular and the cell-free layers. Clearly microsegregation does exist however within the cellular layers. Care was taken in the preparation of the TEM sample to document the growth direction. The cellular layer appears to originate microstructurally from an interface instability occurring in the cell-free layer. The cellular structure then propagates for a short distance until a layer of solute marks the cell fronts. The continuity between the cell-free layer and the subsequently formed cellular region is seen clearly in the isolated subgrain (dark grain). For higher scan velocities the widths of the cellular layers decrease compared to the widths of the cell-free layers, until at high velocity the cellular layers disappear and the banded structure is absent. In eutectic alloys, the banded structure is identical with the exception of a finer cell size.

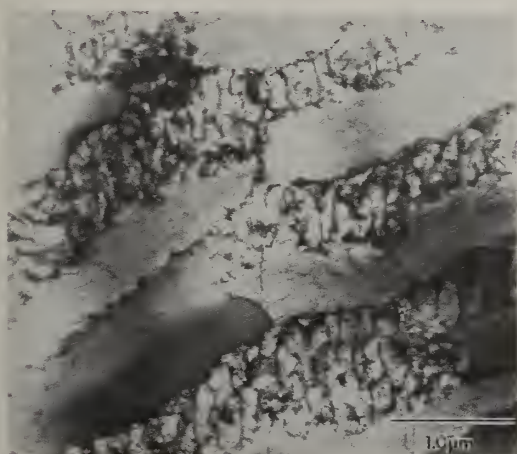


Fig. 5 High magnification view of the banded structure. The growth direction is from lower right to upper left. TEM.

The 9 wt.% Cu, 15 wt.% Cu, and 23 wt.% Cu alloys are free of the banded structure at velocities of 300, 200, and 157 cm/s and above (fig. 1). As discussed in a previous section, actual growth rate may differ from the scan velocity because of changes in weld puddle shapes at scan velocities over 100 cm/s. Clearly however, the banded structure can be suppressed by high scan velocities to produce a microsegregation-free structure. Furthermore, this velocity decreases with increasing concentration. Figure 6 shows micrographs of a 23 wt.% Cu alloy scanned at 157 cm/s. The transition from a banded structure at the bottom of the melted region, where the growth rate is low, to a band-free structure at the top of the melted region, where the growth rate is high, is seen in figure 6b. TEM micrographs of this sample (fig. 6c) confirm the absence of bands but show significant solid state (spinodal) decomposition of the microsegregation-free structures produced from the melt.

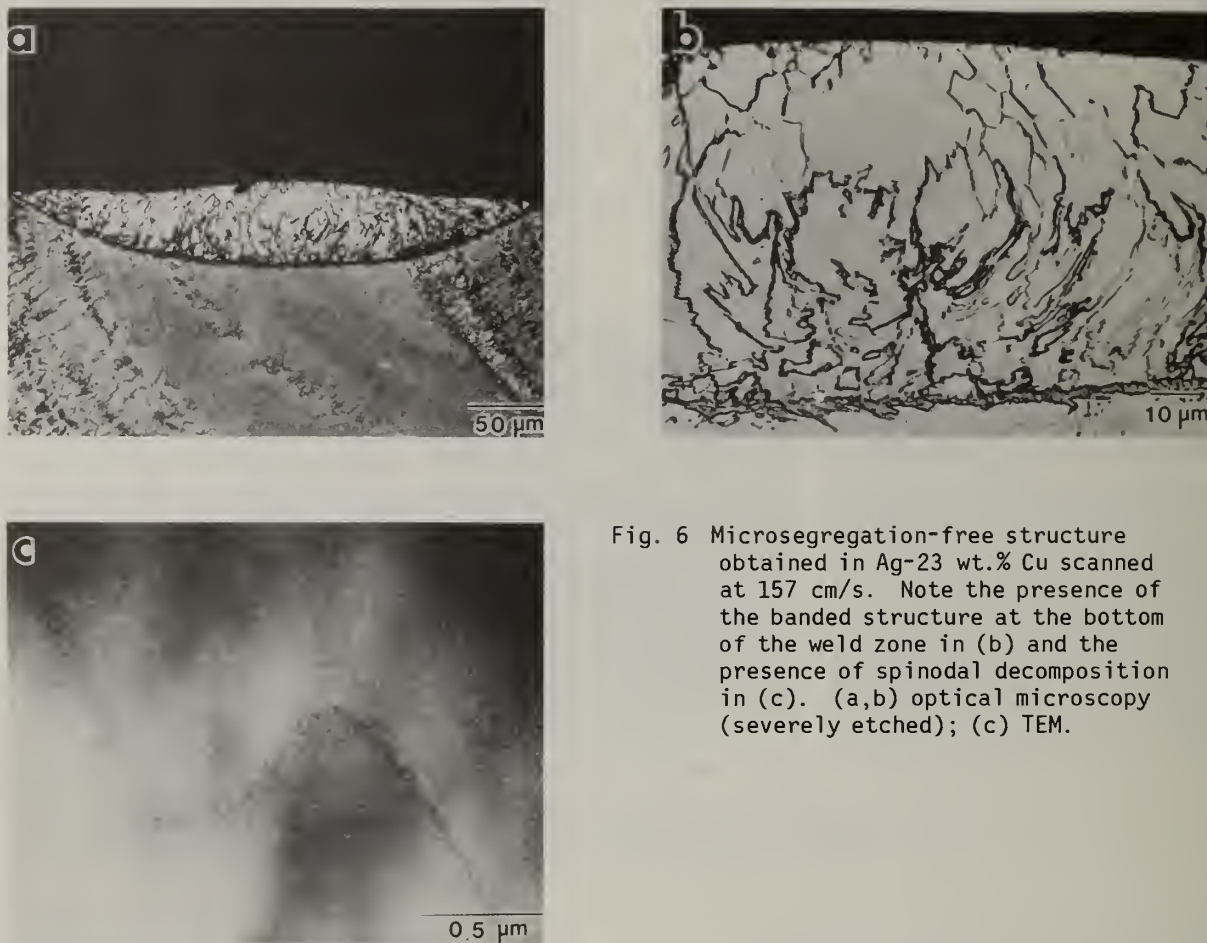


Fig. 6 Microsegregation-free structure obtained in Ag-23 wt.% Cu scanned at 157 cm/s. Note the presence of the banded structure at the bottom of the weld zone in (b) and the presence of spinodal decomposition in (c). (a,b) optical microscopy (severely etched); (c) TEM.

Ag-28 wt.% Cu.

The eutectic composition, when electron beam melted at 2.5 cm/s, consists of a fine eutectic structure with a spacing of ~ 200 Å. The electron diffraction pattern from the eutectic yields lattice parameters of 4.05 Å and 3.65 Å for the two phases. These values are close to those obtained [10] for Ag and Cu at their respective limits of equilibrium solid solubility at the eutectic temperature. Above 2.5 cm/s the eutectic composition does not solidify by a coupled growth mechanism. The microstructure consists of the same banded structure observed for noneutectic alloys. Above 70 cm/s the eutectic composition forms a structure without segregation similar to those shown in figure 6.

Coupled Growth.

The maximum observed growth rate for the Ag-Cu eutectic in the present work is ~ 2.5 cm/s with a spacing of ~ 200 Å. Cline and Lee [11] have directionally solidified the Ag-Cu eutectic up to a growth rate of 0.27 cm/s with an average lamellar spacing of ~ 950 Å. In their experiments growth at higher velocities was prevented by the limitations of heat extraction in their solidification furnace. They found the lamellar spacing λ and the growth velocity, v , to be related by

$$\lambda^2 v = 1.4 \times 10^{-11} \text{ cm}^3/\text{s}. \quad (1)$$

In the present experiments, the heat extraction rate is not limited by a furnace. Extending their relation to a growth velocity of 2.5 cm/s predicts a lamellar spacing of 237 Å. This compares quite favorably with the eutectic spacing seen in the present work.

The present results strongly suggest that there should exist a theoretical limit on the rate at which coupled eutectic growth can occur. One theoretical limit can be found from the inclusion of a temperature dependent diffusion coefficient in eutectic growth theory [12]. The results of Eq. (1), phase diagram information and diffusion data [13] can be used to show that for slow growth, $v = 3.5 \times 10^{-4} (\text{cm s}^{-1} \text{ K}^{-2}) \Delta T^2$, where ΔT is the difference between the interface temperature and the eutectic temperature. Incorporating the temperature dependence of D to extend this relation to large undercooling, yields a maximum velocity of ~ 4.9 cm/s at a spacing of 78 Å. These estimates compare to the experimentally determined values of 2.5 cm/s at 200 Å. Possible reasons for this discrepancy and other theoretical limits on the eutectic growth rate are discussed elsewhere [7].

It should be emphasized that the temperature dependence of the diffusion coefficient becomes important in the present analysis only because of the relatively large undercoolings required to accomplish the solute redistribution and surface area creation necessary for eutectic growth. For dilute alloys the temperature dependence is much less important.

It is also interesting to note that the finest spacing seen by Boswell and Chadwick [2] in splat quench alloys was ~ 300 Å. This observation was used by them to assess the growth rate imposed by the splat quench on the foil. Because this eutectic structure occurred only in small regions adjacent to the metastable extended solid solution, it seems more likely that a maximum growth rate for the eutectic was reached locally in the small regions and surpassed in most of the foil to form the metastable structure.

Dendritic Growth in Concentrated Alloys.

To be consistent with the idea that a temperature dependent diffusion coefficient leads to a maximum rate for coupled growth of a eutectic, a maximum rate for dendritic growth of concentrated alloys must also exist. Although the theory of dendritic growth is continually being refined, especially for high rate [14], a simple expression formulated by Burden and Hunt for controlled growth [15] with the inclusion of a temperature dependent diffusion coefficient demonstrates the qualitative features of this maximum. The calculated maximum velocity [7] increases for increasing deviation from the eutectic composition. The maximum thus parallels the experimental data for the boundary between dendritic and banded microstructure. The calculated values are a factor of 2 to 4 higher than the experimental data, consistent with the disparity between the calculated and observed maxima for eutectic alloys. For very dilute alloys this maximum is irrelevant because it occurs at velocities above those at which the planar interface is stable.

Microsegregation-Free Structure.

For Ag-1 wt.% Cu and -5 wt.% Cu alloys, microsegregation-free structures are produced by planar growth at velocities predicted by absolute stability theory with equilibrium partitioning [8]. For concentrated alloys beyond the solidus retrograde composition, equilibrium partitioning is not a possible mechanism to produce a microsegregation-free structure. The transition from banded structure to microsegregation-free structure for concentrated alloys is most likely related to the onset of complete solute trapping. The upper velocity boundary of the banded region (fig. 1) when extrapolated to pure Ag suggests a velocity for solute trapping of ~ 5 m/s for dilute alloys. This velocity is consistent with data obtained for solute trapping in dilutely doped Si [16]. The fact that the

eutectic composition can be produced as a single phase microsegregation-free material at lower growth rates than, for example, 9 and 15 wt.% Cu alloys suggests a significant composition dependence for the onset of solute trapping.

Banded Structure.

The origins of the banded structure are difficult to determine with certainty. Beck, Copley, and Bass [6] have recently suggested that the bands are due to an instability proposed by Baker and Cahn [17] related to growth with solid composition and interface temperature above the solidus. However the observation of band-free structures in alloys for alloy composition beyond the solidus retrograde, where single phase growth can never occur below the solidus, seems to negate this idea.

The preceding discussion has suggested that the lower velocity boundary of the banded region in figure 1 is caused by a limitation of the maximum growth rate of dendritic and eutectic growth in concentrated alloys. The discussion also has suggested that the upper velocity boundary of the banded region in figure 1 is caused by significant deviation from interfacial equilibrium and the concomitant increase of the partition coefficient to unity. Clearly the microscopic events which occur during the formation of the banded structure must be related to these two phenomena. These microscopic events are discussed in more detail elsewhere [7].

Acknowledgment

The authors appreciate support from DARPA for this research. We also thank S. R. Coriell for many helpful discussions.

References

- [1] P. Duwez, R. H. Willens, and W. Klement, Jr., J. Appl. Phys. 31, 1136 (1960).
- [2] P. G. Boswell and G. A. Chadwick, J. Mat. Sci. 12, 1879 (1977).
- [3] W. A. Elliott, F. P. Gagliano, and G. Krauss, Met. Trans. 4, 2031 (1973).
- [4] S. M. Copley, M. Bass, E. W. Van Stryland, D. G. Beck, and O. Esquivel, Proc. III Int. Conf. Rapidly Quenched Metals, 1, p.147, The Metals Society, London (1978).
- [5] D. G. Beck, S. M. Copley, and M. Bass, Met. Trans. A 12A, 16 (1981).
- [6] D. G. Beck, S. M. Copley, and M. Bass, Met. Trans. A 13A, 1879 (1982).
- [7] W. J. Boettinger, R. J. Schaefer, F. Biancaniello, and D. Shechtman, Met. Trans. A., to be published.
- [8] W. J. Boettinger, S. R. Coriell, and R. F. Sekerka, these proceedings.
- [9] J. M. Murray, Met. Trans. A, (1983) to be published.
- [10] R. K. Linde, J. Appl. Phys. 37, 934 (1966).
- [11] H. E. Cline and H. Lee, Acta Met. 18, 315 (1970).
- [12] W. J. Boettinger, in Rapidly Solidified Amorphous and Crystalline Alloys, B. H. Kear, B. C. Giessen, and M. Cohen, Eds., Elsevier, p. 15 (1982).
- [13] T. Yamamura and T. Ejima, J. Jap. Inst. Met. 37, 901 (1973).
- [14] R. Trivedi, to be published.
- [15] M. H. Burden and J. D. Hunt, J. Cryst. Growth 22, 109 (1974).
- [16] M. J. Aziz, J. Appl. Phys. 53, 1158 (1982).
- [17] J. C. Baker and J. W. Cahn, in Solidification, ASM, Metals Park, p. 23 (1971).

NONDESTRUCTIVE CHARACTERIZATION OF RAPIDLY SOLIDIFIED Al-Mn ALLOYS

R. J. Schaefer*, M. Rosen**, J. J. Smith**, D. Shechtman** and R. Mehrabian*

*National Bureau of Standards
Washington, DC 20234

**The Johns Hopkins University
Baltimore, MD 21218

ABSTRACT

Supersaturated Al-Mn alloys were prepared by melt spinning and by electron beam surface melting of bulk samples. The samples were evaluated by several methods, in the as-prepared condition and after annealing for several different times at 450° C. The measurements gave consistent indication of the high degree of supersaturation attained in the rapidly solidified materials, and showed the changes of several properties as precipitation progressed. At low supersaturation the precipitates were localized at the grain boundaries and the supersaturation of the lattice disappeared only slowly, whereas at higher manganese concentrations the precipitates were abundantly dispersed throughout the matrix and the lattice supersaturation decreased more rapidly.

Introduction

Nondestructive methods are needed to characterize the modified layers which can be generated by the action of directed energy sources on the surface of metals. The information generally required includes the depth of the layer and its microstructural character. In many cases the surface layer will not differ in composition from the bulk material, i.e. no surface alloying is present, and the surface layer is detected through the effect of the modified microstructure on the probing signal.

Manganese has a maximum equilibrium solid solubility in aluminum of approximately 1.55 wt.% at the eutectic temperature [1], which is only slightly below the melting temperature of aluminum. It has long been known [2], however, that this solubility can be increased by rapid solidification to compositions far beyond the eutectic (2%) between Al and Al₆Mn. In response to heat treatment, precipitation may occur as either the equilibrium orthorhombic Al₆Mn or other phases [3] depending upon the temperature and impurity content. Nondestructive evaluation of the state of precipitation may either detect some direct influence of the precipitates or it may primarily detect the decrease of Mn in solid solution as the process progresses.

Results and Discussion

Sample Preparation

Melt-spun ribbons with Mn concentrations of 0.1, 1, 2, 3, 7, 9, 12, and 15 wt.% Mn were prepared from 99.999% Al and 99.95% Mn. The ribbons were typically 2 mm wide and 20 μ m thick. For annealing, the ribbons were sealed in borosilicate glass ampoules with 1/2 atmosphere of helium. Annealing was at 450°C for 5 minutes, 1 hour and 3 hours.

A sample of Al-7 wt.% Mn was prepared for electron beam surface melting by chill casting, rolling at 600°C to a thickness of 9 mm, and annealing for 1 hour at 450°C. Surface melting was carried out by electron beam scans along the length of the sample at a velocity of 50 cm/s, with successive scans offset 0.4 mm laterally and with a time delay of 15 seconds between scans to allow cooling. In this way a rapidly solidified surface layer 8 cm long, 2 cm wide and 0.2 mm deep was formed.

Sample Evaluation

The melt-spun ribbons were evaluated by measurements of lattice parameter, electrical resistivity, and sound velocity, and by transmission electron microscopy. The measurements indicated that

Electrical Resistivity of Al-Mn Alloys

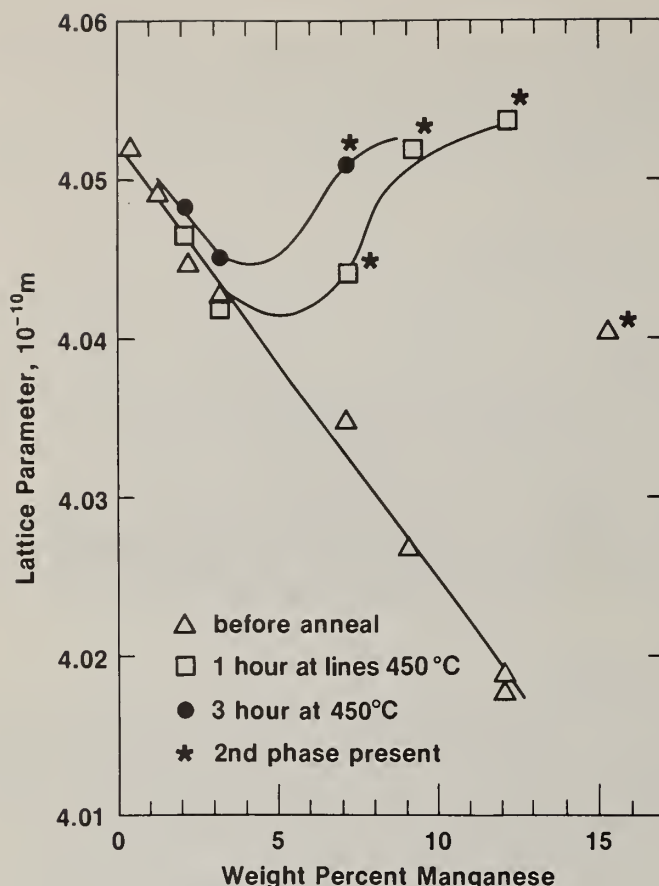


Fig. 1. Variation of the lattice parameter of the Al phase as a function of Mn concentration in the as-spun and annealed conditions.

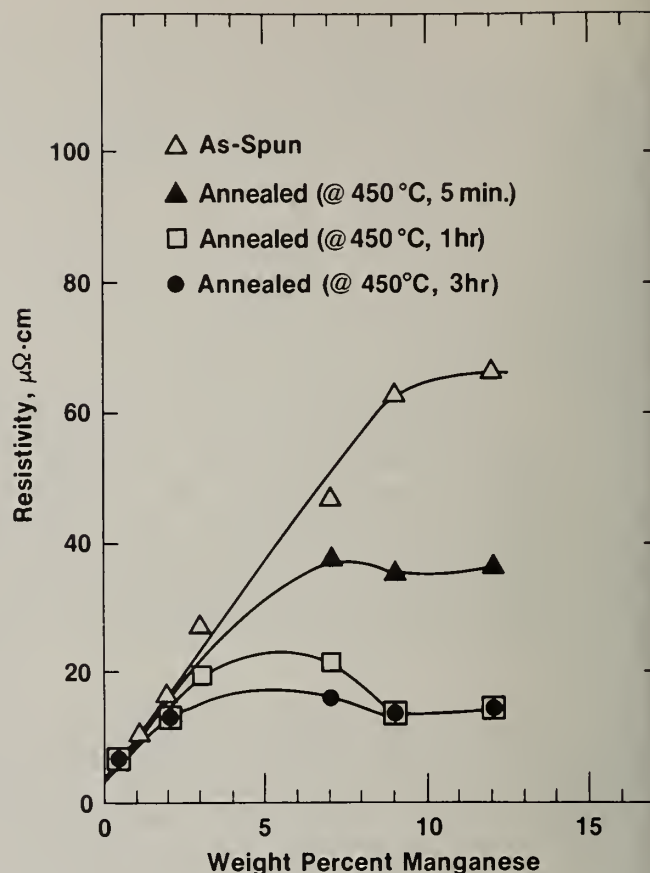


Fig. 2. Variation of the electrical resistivity in Al-Mn alloys as a function of Mn concentration in the as-spun and annealed conditions.

at concentrations up to 12 wt.% most of the manganese was in solid solution in the as-spun ribbons. At 450°C, precipitation occurs heterogeneously at the grain boundaries at low Mn concentrations but at many more locations throughout the sample at high concentrations. As a result, the supersaturation of manganese in the aluminum lattice diminishes rapidly in the high concentration samples but more slowly in the more dilute alloys where longer-range diffusion is required.

Lattice Parameter Measurements

Lattice parameters were measured on an X-ray diffractometer using $\text{CuK}\alpha$ radiation, plotting calculated values for individual peaks against $\psi = (\cos^2\theta/\sin\theta)$ and extrapolating to $\psi = 0$. In the as-spun ribbons, diffraction peaks were seen only from the aluminum phase at compositions up to 12 wt.% Mn, and the lattice parameter (Fig. 1) decreased linearly with increasing Mn content, with a slope in agreement with prior measurements [2,3]. At 15 wt.% Mn, additional peaks, not corresponding to the equilibrium Al_6Mn phase, appeared in the pattern and the lattice parameter of the Al phase indicated a composition of approximately 4 wt.% Mn in solution. Measurements of the top and bottom surfaces of the 12% alloy showed essentially identical results, indicating that the supersaturated phase was present throughout the thickness of the ribbons.

Annealing of the Al-7 wt.% ribbon for 1 hour at 350°C showed little change in the diffraction pattern. After 1 hour at 450°C however, Al_6Mn was present and the peaks from the aluminum phase were significantly broadened, with the average value of the aluminum lattice parameter having increased approximately one half of the way to its equilibrium value at that temperature. At 9 and 12

wt.% Mn, the 1 hour 450°C anneal gave an aluminum phase lattice parameter close to the equilibrium value but at 3 wt.% Mn or less the same anneal gave no perceptible change in the lattice parameter. Annealing for 3 hours brought the lattice parameter of the 7wt.% Mn sample close to its equilibrium value and also caused significant changes in the low composition samples.

The diffraction chart of a 9 wt.% Mn sample annealed for 5 minutes at 450°C showed extreme line broadening with a line shape indicating that much of the aluminum phase was still close to its original composition but that localized regions had already become significantly depleted in manganese.

The Al-7 wt.% Mn sample prepared for surface melting showed initially a lattice parameter for the aluminum phase indicating only a small concentration of Mn in solution, and strong Al₆Mn peaks. After electron beam surface melting, only a single faint peak indicative of a second phase was present and the measured lattice parameter of the aluminum phase lay well below the line for as-spun ribbons in Fig. 1. The value of the lattice parameter in this case, however, may have been seriously affected by the large residual stresses which are inevitably present in such surface melted layers. The surface layer showed a pronounced orientation texture as revealed by the complete absence of the (111) and (222) peaks in the diffraction pattern.

Electrical Resistivity

The electrical resistivity of the ribbons (Fig. 2) was determined by means of a standard four probe potentiometric method with an accuracy of about 1 part in 10⁵. Considering the overall uncertainty in the geometrical shape factor of each sample, the estimated error in the absolute resistivity values is about ±5%. The as-spun ribbons exhibit a strong increase in electrical resistivity with increasing manganese content. An apparent leveling of the resistivity is observed at concentrations above 9 wt.% Mn. Annealing at 450°C for even short periods (5 minutes) has a large effect on the electrical resistivity of the higher concentration alloys. By means of a nucleation and diffusion controlled process, Al₆Mn particles are precipitated out of the aluminum matrix, thus denuding the lattice of effective scatterers of electrons. This "purification" process is apparently responsible for the observed decrease in electrical resistivity relative to the supersaturated, as-spun, alloy. The difference in the absolute values of the electrical resistivity between the as-spun and annealed condition, $\Delta\rho$, increases with increasing manganese concentration up to 9 wt.% Mn, and subsequently levels off. The electrical resistivity of the annealed 12 wt.% Mn alloy is almost identical to that of the 2 wt.% Mn alloy, indicating that the contribution of the fully grown, and incoherent, Al₆Mn precipitates to the measured total resistivity is almost negligible. Such a behavior is expected from relatively large isolated precipitates, about 5×10^{-7} m in size, in a continuous matrix phase, in which case the resistivity of the sample is determined primarily by the resistivity of the matrix.

Electron Microscopy

The microstructures of as-spun and annealed ribbons of the 3 wt.% and 9 wt.% Mn alloys are shown in Fig. 3. The 3 wt.% Mn alloy shows only dislocations in the as-spun condition, and after 1 hour at 450°C it shows a few Al₆Mn precipitates localized at grain boundaries. In the Al-9 wt.% Mn alloy, the as-spun alloy consists of a cellular structure with very fine precipitates at the cell boundaries. It is conjectured that the fine precipitates were formed in the solid state during rapid cooling after solidification. It is not clear whether the fine precipitates are direct precursors of the large ones that form upon annealing at 450°C. After 1 hour at this temperature, the 9 wt.% Mn sample shows abundant Al₆Mn precipitates throughout.

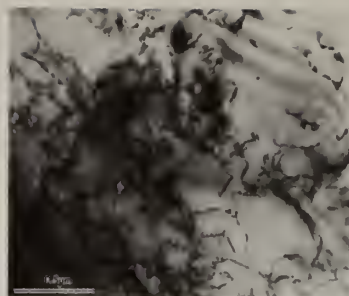
X-ray, TEM and electrical resistivity observations all indicate that at high supersaturations precipitation progresses most rapidly because of the large number of nuclei formed and the correspondingly short diffusion distances. The leveling of the electrical resistivity at concentrations above 9 wt.% Mn may be the result of the presence of the cellular structure. It is suggested that the concentration of Mn in the Al lattice adjacent to the cell boundaries is very low, and in this case these regions would act as a continuous network of low-resistivity material which would decrease the electrical resistivity of the sample to a larger extent than a simple volume fraction would indicate. The x-ray diffraction peaks of the Al-12 wt.% Mn ribbons have distinct tails on the low angle side, confirming that some aluminum is present with considerably less than 12 wt.% Mn in solution.

Sound Wave Velocity

The velocity V_e of ultrasonic extensional waves is $(E/\rho)^{1/2}$, where E is the Young's modulus and ρ is the density. The velocity of such waves propagating along the ribbon was determined by measuring the transit time of a single pulse generated by a laser and detected by a piezoelectric transducer. The detector was about 200 mm from the spot on the ribbon irradiated by the Q-switched Nd:YAG laser (Fig. 4). The transit time of the extensional sound wave propagating along the ribbon

Al-3 Wt. % Mn

No segregation is observed in the as-spun ribbon. Following heat treatment, large Al_6Mn precipitates form at the grain boundaries.



As-Spun Ribbon



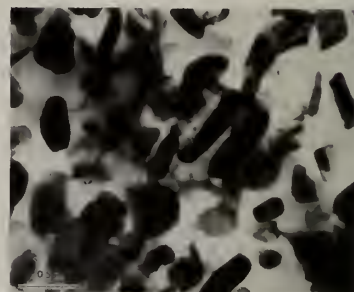
Heat Treated 450°C-1h

Al-9 Wt. % Mn

Fine particles of metastable compound form at the grain boundaries of as-spun ribbon. Following heat treatment, precipitation of Al_6Mn is observed.



As-Spun Ribbon



Heat Treated 450°C-1h

Fig. 3. TEM of Al - 3 wt.% Mn and Al - 9 wt.% Mn in the as-spun and annealed conditions.

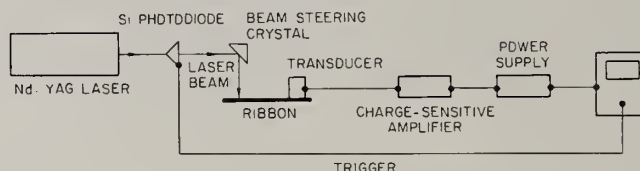


Fig. 4. Laser generation and piezoelectric detection of ultrasonic waves in thin ribbons.

could be determined to within one part in 10^5 . The separation between the impinging laser pulse and the quartz receiver was determined to within ± 0.2 mm. The total estimated error in the calculated value of the sound velocity was $\pm 0.1\%$. The measurements were carried out at room temperature in the as-spun condition and after the ribbons were subjected to the appropriate heat treatments.

The propagation velocity of Rayleigh surface waves was used to characterize the supersaturated solid solution generated by electron beam surface melting of the slab of Al-7 wt.% Mn. The Rayleigh velocity in the electron beam melted and rapidly solidified layer was found to be 3039 m/s. On the untreated side of the slab, the microstructure of which consisted of Al_6Mn precipitates in an aluminum phase matrix, the Rayleigh wave velocity was 3091 m/s, substantially higher than the velocity in the supersaturated solid solution. This behavior was expected since the specific sound velocity of the Al_6Mn particles is substantially higher than that of the aluminum matrix. A similar behavior was observed in Al-Cu alloys after aging [5].

Figure 5 shows the variation of the sound velocity in Al-Mn alloys as a function of Mn content for both as-spun and annealed alloys. The salient feature in Fig. 5 is the fact that the sound velocity, and thus the Young's modulus, of the heat treated alloy is always higher than that of the

Sound Velocity vs. Wt % Mn in Al-Mn Alloys

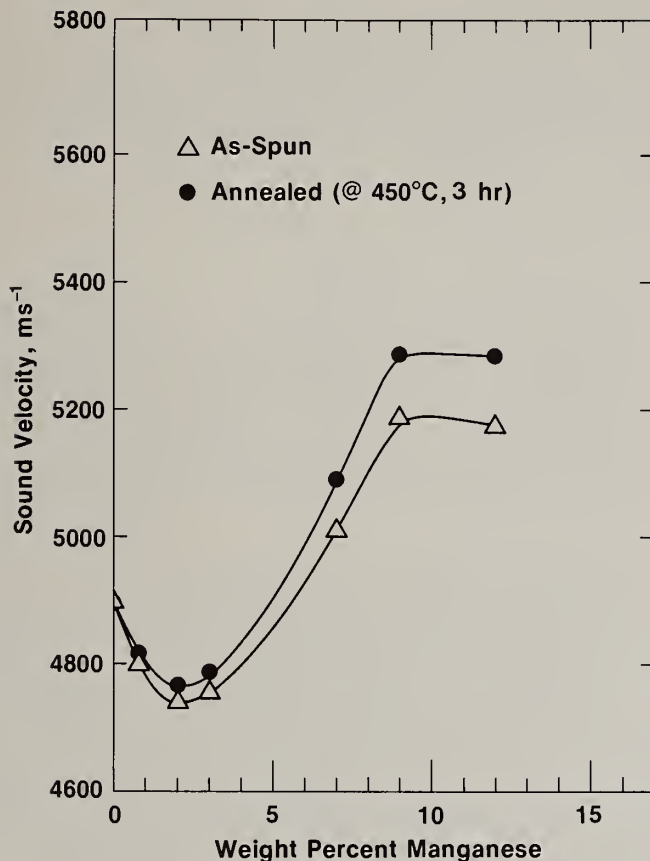


Fig. 5. Variation of the extensional sound wave velocity in Al-Mn alloys as a function of Mn concentration in the as-spun and annealed conditions.

as-spun state. The difference between the as-spun and the annealed conditions increases with increasing Mn concentration, up to 9 wt.% Mn. This relatively large difference is significant when nondestructive techniques are considered for monitoring on-line and in real-time the progress of the metallurgical process leading to a rapidly solidified single-phase supersaturated alloy.

The extensional sound wave velocity initially decreases with increasing Mn content up to about 2 wt.% Mn. Subsequently the velocity increases, followed by a plateau starting at 9 wt.% Mn. The density, based on the measured lattice parameters of the as-spun ribbons, is expected to be a linear function of composition. Reported values of the static elastic modulus as a function of composition [6] show a slight suggestion of nonlinearity, but not enough to account for the pronounced minimum in sound velocity seen here. It is thus apparent that either the density of the melt-spun ribbons differs from the value derived from X-ray measurements, or the elastic modulus of the ribbons differs from that measured statically on bulk samples.

CONCLUSIONS

Nondestructive ultrasonic and electrical resistivity measurements were found to be feasible for in-process dynamic monitoring and determination of the supersaturation range of rapidly solidified alloys. Up to 12 wt.% Mn can be incorporated into an Al lattice by rapid solidification, and the subsequent precipitation can be monitored by any of several methods.

ACKNOWLEDGEMENTS

The authors thank F. S. Biancaniello for sample preparation and C. Bechtold for consultation on X-ray diffraction. Thanks are also due to DARPA for financial support.

REFERENCES

- [1] F. A. Shunk, Constitution of Binary Alloys, Second Supplement, McGraw-Hill, New York (1969)
- [2] G. Falkenhagen and W. Hofman, Z. Metallkunde 43, 69 (1952)
- [3] R. Hoier, S. E. Naess, and E. Nes, Z. Metallkunde 64, 640 (1973)
- [4] I. Obinata, E. Hata, and K. Yamagi, J. Japan Inst. Met. 17, 496 (1953)
- [5] M. Rosen, E. Horowitz, S. Fick, R. Reno and R. Mehrabian, Mater. Sci. Eng. 53, 163 (1982)
- [6] N. Dudzinski, J. R. Murray, B. W. Mott, and B. Chalmers, J. Inst. Metals 74, 291 (1948)

EXPERIMENTAL STUDIES OF THE DYNAMICS OF RAPID SOLIDIFICATION USING ACOUSTIC EMISSION

R. B. Clough, H. Wadley, and R. Mehrabian
Center for Materials Science
National Bureau of Standards
Washington, DC 20234

ABSTRACT

One- and two-dimensional heat flow models for rapid melting and resolidification of metallic substrates subjected to high energy laser and electron-beam sources are now available, including both stationary and moving heat sources. Methods are accordingly needed for monitoring these processes in real time during solidification. In this paper we discuss the use of acoustic emission methods to monitor rapid solidification of precisely controlled electron beam surface melts of commercially pure aluminum and 2219 aluminum alloy. These results are discussed in relation to heat flow calculations and resolidification microstructures.

The driving forces for the emission are the density changes due to phase transformations and the stresses induced by thermal contraction during and after solidification. For a restricted range of values of the product qa , heat flux times the radius of the circular region over which it is absorbed, steady-state thermal profiles and melt depths are established. Increasing this product results in increased melt depth and increased amounts of acoustic emission on resolidification when the beam is switched off. The amount of emission is in addition much greater in the 2219 aluminum alloy than in the commercially pure 1100 aluminum. Micrographs show that the 2219 aluminum alloy exhibits extensive hot tearing while the 1100 aluminum has no cracks, so that we attribute part of the enhanced signal to hot tearing in the 2219 aluminum alloy. Additional experiments in which the substrate microstructure was varied were found to have small effect upon solidification cracking but a significant effect upon acoustic emission. This suggests both plastic deformation and hot heating generate detectable acoustic emission in 2219 aluminum alloys.

Introduction

Directed high energy sources (laser and electron beams) are currently being evaluated for rapid surface melting and resolidification of a range of engineering alloys [1]. In these processes, the bulk substrate, in intimate contact with the molten surface layer, acts as the quenching medium resulting in high solid/liquid interface velocities and short solidification times during cooling. These rapidly solidified alloys exhibit enhanced wear and corrosion resistance, arising, it is believed, from improved chemical homogeneity and the fine scale of microstructure. Such materials offer promise for applications such as bearing surfaces, cutting tool faces, and corrosion resistant parts.

At present, critical process variables such as solid/liquid interface velocity or the cooling rate can only be deduced using one- and two-dimensional heat flow models for melting and resolidification. Experimental methods to measure, in situ, process variables are required so that confirmation of microstructure-process variable relationships may be made. Furthermore, surface modification of some alloys is severely limited by the occurrence of cracking during solidification.

In this work, we report the use of acoustic emission techniques to monitor rapid solidification of electron beam surface melted 1100 commercially pure aluminum and a 2219 aluminum alloy in several different heat treated conditions. Heat flow theory has been used to set up controlled experiments in which shallow melts were formed at the surface of the aluminum plates. After attainment of steady state conditions, the energy source was terminated, resulting in rapid solidification for which the acoustic emission response was measured. Effects of varying both the substrate composition and electron beam parameters on the acoustic emission response have been investigated and linked with post-mortem metallographic observations of microstructure to deduce the origin of the elastic waves.

The problem considered was the rapid melting and resolidification of an alloy substrate subjected to a high-intensity stationary heat source over a circular region on its bounding surface. The numerical solutions were developed for an Al-4.5 wt.% Cu alloy which is close to the composition of the 2219 aluminum alloy (whose principle solutes were 6.6 wt.% Cu, 0.34 wt.% Mn) used in the experiments reported in this paper. It was assumed that the substrate had previously been subjected to conventional solidification--it segregated and precipitated a weight fraction of eutectic calculated from the Scheil equation [2].

The generalized two-dimensional heat flow model and solution technique developed in an oblate coordinate system [3] can readily take both space and time variations of the heat flux into consideration. For the purpose of this paper, it is reasonable to assume that a step function heat flux is applied at time zero with a uniform circular distribution. The shape and location of the "mushy" zone, bounded in space by the liquidus and solidus isotherms, are then calculated for various combinations of process variables. Special emphasis is placed on conditions that result in steady state heat flow. That is, conditions under which the total amount of heat absorbed at the surface circular region is exactly offset by the conduction of heat into the substrate interior. This results in a steady-state thermal field with a maximum temperature at the center of the circular surface region. This enables a quiescent condition (i.e., with static stresses) to be established prior to solidification. Two dimensionless variables are used to describe heat flow:

$$k (T(0,0) - T_0)/qa \quad \text{and} \quad a/\sqrt{4\alpha_s t} \quad (1)$$

where k is thermal conductivity, $T(0,0)$ is the temperature in the center of the circular region; T_0 is initial substrate temperature, q and a are absorbed heat flux and radius of the circular region, respectively. $a/\sqrt{4\alpha_s t}$ denotes dimensionless inverse time, α_s is thermal diffusivity of the solid, and t is time. Values of the variables are given in table I.

Table I
Properties of Al-4.5% Cu Alloy Used in Calculations [4,5]

Notation	Name	Value
k_s	Thermal conductivity of solid	180.6 Wm ⁻¹ k ⁻¹
k_l	Thermal conductivity of liquid	100.8 Wm ⁻¹ k ⁻¹
α_s	Thermal diffusivity of solid	7.6 x 10 ⁻⁵ m ² s ⁻¹
T_E	Solidus temperature	821 K
T_L	Liquidus temperature	923 K
T_v	Vaporization temperature	2744 K

In order to account for the release of heat of fusion, the first term of expression (1) was enlarged to:

$$(k_l(T(0,0) - T_L) + \Delta\zeta + k_s (T_E - T_0))/qa \quad (2)$$

where the subscripts l and s denote liquid and solid, respectively and T_L and T_E are the liquidus and solidus temperatures, respectively. $\Delta\zeta$ is an equivalent term accounting for heat conduction in the "mushy" region and is calculated to be $\sim 6.2 \times 10^4$ W/m for the Al-4.5 wt.% Cu alloy [4].

It has been verified that for a given value of expression (2) all isotherms in the alloy substrate are located at the same dimensionless distance for identical dimensionless times. Figure 1 shows a plot of results obtained from computer calculations relating the two dimensionless variables noted above. A number of important facts are deduced from this figure. First, there is a minimum value of the product qa required if the center of the circular region is to reach a given temperature $T(0,0)$, e.g. the liquidus T_L or the vaporization T_v temperatures, of the alloy. That

is, when the power is maintained for long times (for small values of $a/\sqrt{4\alpha_s t}$) the vertical axis approaches unity--steady state conditions then prevail if $T(0,0) < T_V$. The sum of the second and third terms in the numerator of the ordinate $\Delta\zeta + k_s(T_E - T_0) \cong 1.56 \times 10^5 \text{ W/m}$, where T_0 is ambient temperature. Therefore, for the Al-4.5 wt.% Cu alloy, a minimum value of the product $qa \sim 1.56 \times 10^5 \text{ W/m}$ is required if the center of the circular region is to reach the liquidus temperature of the alloy, $T(0,0) = T_L$. Similarly, $k_s(T_V - T_L) \sim 1.84 \times 10^5 \text{ W/m}$, a minimum value $qa \sim 3.4 \times 10^5 \text{ W/m}$ is deduced for $T(0,0) = T_V$. The temperature at the center of the circular region for any dimensionless time can also be readily deduced from Figure 1. For example, for a heat flux of $q = 2.7 \times 10^8 \text{ W/m}^2$ absorbed over a circular region of radius $a = 10^{-3} \text{ m}$ ($qa = 2.7 \times 10^5 \text{ W/m}$) temperatures of $T(0,0) = 1384 \text{ K}$ and $T(0,0) = 2054 \text{ K}$ are reached in $t \sim 9.2 \text{ ms}$ ($a/\sqrt{4\alpha_s t} \sim 0.6$) and $t = 52.7 \text{ ms}$ ($a/\sqrt{4\alpha_s t} \sim 0.25$), respectively. Note that for $t > 52.7 \text{ ms}$ ($a/\sqrt{4\alpha_s t} < 0.25$), the plot in Figure 1 approaches unity on the vertical axis, and steady state conditions are obtained, i.e. a maximum temperature $T(0,0) = 2054 \text{ K}$ is reached. Therefore, for products $1.56 \times 10^5 \leq qa \leq 3.4 \times 10^5 \text{ W/m}$, $a = 10^{-3} \text{ m}$, and times $t \geq 52.7 \text{ ms}$ temperatures are likely to be in the range $T_L \leq T(0,0) \leq T_V$ and steady state conditions are expected to prevail for the Al-4.5 wt.% Cu alloy substrate.

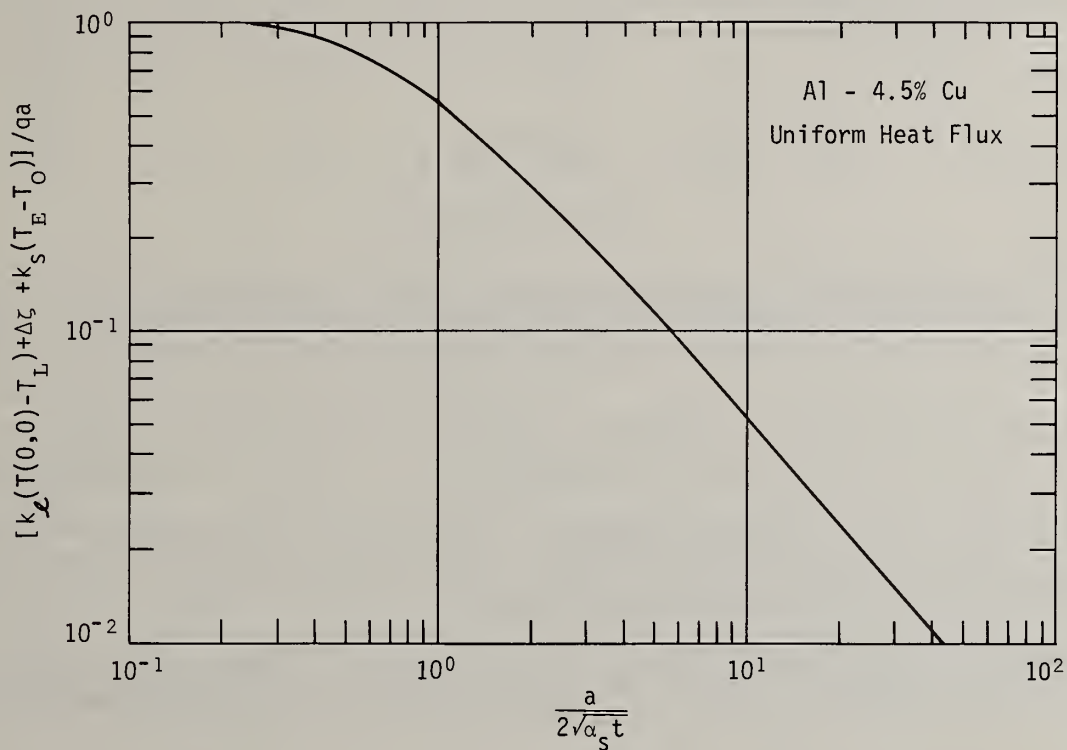


Figure 1. Temperature at the center of the circular region during melting of a semi-infinite Al-4.5 wt.% Cu alloy substrate as a function of uniform absorbed heat flux, radius of the circular region and time [4].

Figure 2 shows the location of the "mushy" zone (the region bounded by liquidus and solidus isotherms) during the approach to steady-state conditions, followed by rapid solidification. The isotherms here represent the situation in which heat was applied until almost a steady-state condition was achieved, the solidus isotherm reached a plateau, at which point beam power was turned off resulting in rapid solidification. The vertical distance between the two curves denotes the size of the "mushy" zone. Upon attainment of a steady-state condition the "mushy" zone extended $\sim 1/4$ of the maximum melt depth $z/a = 0.4$ or ~ 0.1 . Loss of superheat and shallower temperature gradients during solidification result in significantly larger "mushy" zone sizes. For example, when the substrate surface reaches the liquidus temperature, the solidus isotherm is at approximately $z/a \sim 0.3$ --the size of the "mushy" zone is three times larger than when solidification started.

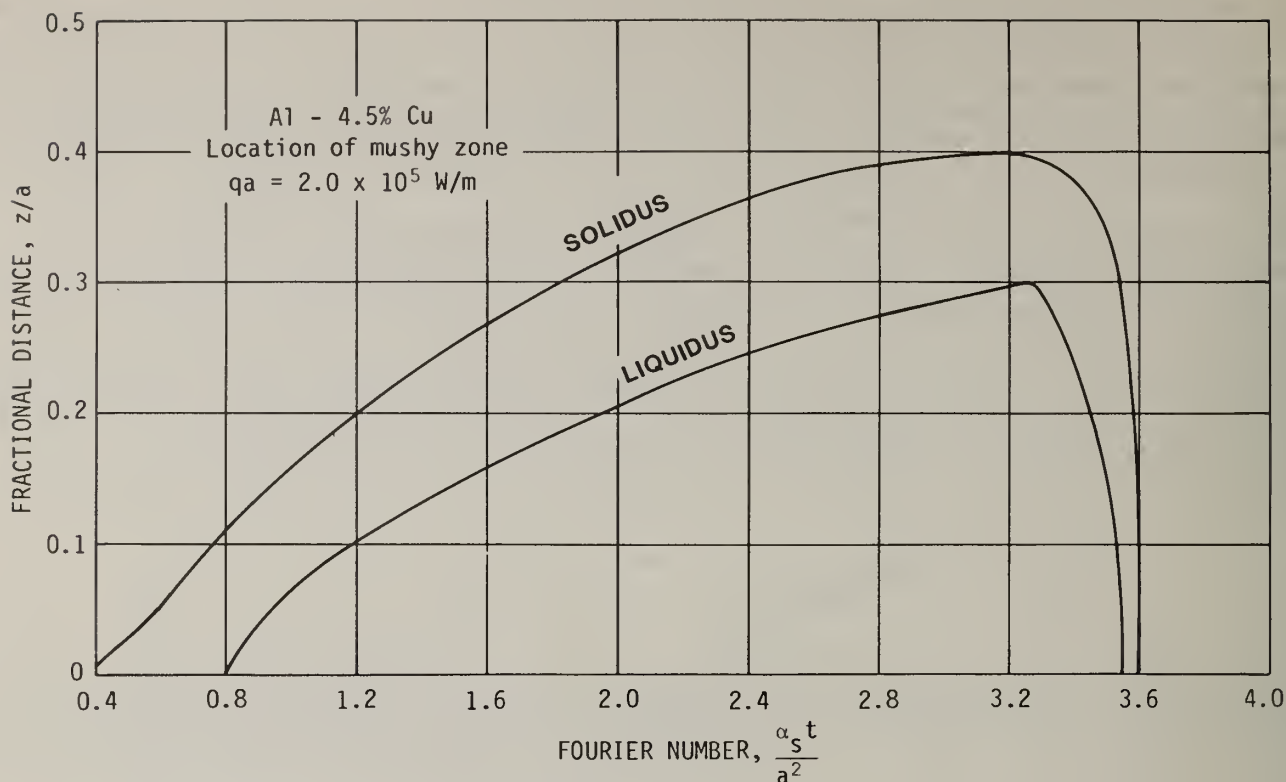


Figure 2. The dimensionless size and location of the "mushy" zone along the z -axis versus time for product $qa = 2.0 \times 10^5 \text{ Wm}^{-1}$. T_{923} and T_{821} denote the locations of the liquidus and solidus isotherms, respectively [4].

Average solidus and liquidus interface velocities and solidification times can be readily calculated from the data shown in Figure 2. Assume that $\underline{a} = 10^{-3} \text{ m}$, $\underline{q} = 2 \times 10^8 \text{ W/m}^2$. Δt for the liquidus and solidus to move from their maximum depths, $z_L = 3 \times 10^{-4} \text{ m}$ and $z_s = 4 \times 10^{-4} \text{ m}$, to the surface are $\sim 3.7 \text{ ms}$ and $\sim 4.75 \text{ ms}$, respectively. This translates into average liquidus and solidus velocities of $8.1 \times 10^{-2} \text{ m/s}$ and $8.5 \times 10^{-2} \text{ m/s}$, respectively. Note that while the two average interface velocities are almost equivalent, initially the solidus moves much slower than the liquidus resulting in the large "mushy" zone size noted above.

The steady-state shapes and locations of the "mushy" zone, liquidus and solidus isotherms as a function of both dimensions r and z are readily obtained from the computer calculations. In Figure 3, we show the positions of the steady-state "mushy" zones for two values of the product qa .

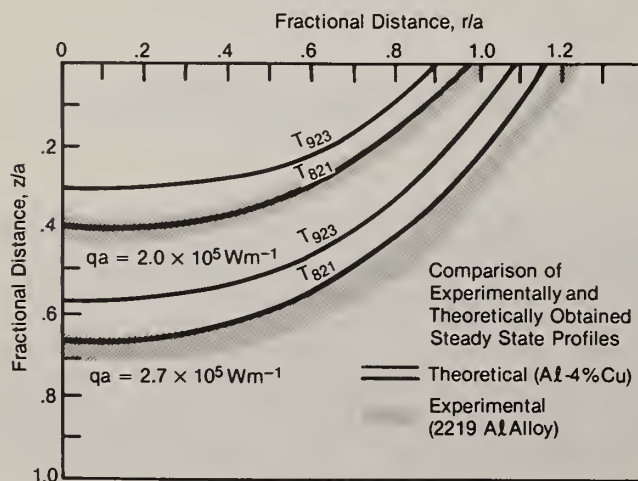


Figure 3. Comparison of predicted and experimentally measured steady-state melt profiles for aluminum-copper alloy at two values of qa .

Both values are within the range noted above for which $T_L \leq T(0,0) \leq T_V$. While the theoretically calculated size of the "mushy" zone does not change significantly with increasing value of q_a , from 2×10^5 to $2.7 \times 10^5 \text{ Wm}^{-1}$, Figure 3 shows that the melt depth almost doubles. Experimental melt profiles of the 2219 aluminum alloy are plotted on the same figure for comparison. Detailed experimental procedures are described in a later section. Agreement between the two is reasonably good considering the various assumptions of the calculations including a slightly different alloy composition, and constant but different thermophysical properties for the solid, the "mushy" zone, and the liquid. The calculations are based on complete absorption of the incident energy by the substrate. This is a reasonable assumption for electron beam surface melting.

Acoustic Emission Theory

Acoustic emission is the elastic radiation from changes of stress in a body. Such changes may be either positive (e.g., elastically constrained thermal expansion during absorption of a laser pulse) or negative (e.g., the growth of a crack through an already stressed region). The propagation of elastic waves through an observation point within/on the body results in transient elastic displacements of the point. These are the basic physically observable quantities in an acoustic emission experiment.

Calculations [6-8] using dynamic elasticity are able to predict acoustic emission waveforms. To demonstrate the calculations, the transient displacement vertically above four point sources, a vertical dipole, a horizontal mode I loaded crack, a thermal expansion (dilatation), and an inclined shear loop are shown in Figure 4 [9]. If such waveforms due to actual sources are measured, the dynamics and other source properties can be deduced [11].

Experimental

Materials

In the present investigation the acoustic emission from two aluminum alloys has been simultaneously studied. One alloy was 1100 aluminum, a 99.0 percent commercial purity aluminum. The second alloy studied was 2219 aluminum containing 6.6 wt.% Cu, 0.08 wt.% Si, 0.3 wt.% Mn, and 0.104 wt.% Zr. The 2219 aluminum alloy was in the -T87 condition. Rectangular plate samples were cut from each alloy with dimensions of $4.0 \times 1.5 \times 0.4 \text{ cm}$.

Electron Beam Facility

Samples were mounted in the facility shown in Figure 5 and placed in an electron beam heating unit. To insure attainment of steady-state conditions, the samples were heated with a 100 ms duration stationary electron beam pulse with a circular cross section having a 1 mm radius a . The electron beam was accelerated through 25 kV and the beam current deduced from the voltage developed across a resistor placed in series with the line to ground. The heat flux was calculated for each pulse, and the current varied so that heat flux could be investigated as an experimental variable. The product q_a was systematically varied between $\sim 1.6 \times 10^5$ and $3.4 \times 10^5 \text{ W/m}$ to produce steady-state melt profiles at the long times $t \sim 100 \text{ ms}$ noted above.

Acoustic Emission Measurements

A schematic diagram of the acoustic emission instrumentation is shown in Figure 6. A piezoelectric transducer was used to convert the elastic displacements of the acoustic emission into a voltage signal that could subsequently be electronically processed. To optimize sensitivity (signal-to-noise ratio) signals were bandpass filtered between 0.02 and 1 MHz and a transducer with high sensitivity in this passband (see inset in Fig. 6) was used to measure emission. The gradual build-up of stress could activate rapid stress drops of $\pm 1 \text{ ms}$ risetime accompanying deformation and fracture events. The coarse sampling interval required to follow the more gradual contraction stress results in effectively only random discrete sampling of the fast risetime (high frequency) signals. In effect, the bandwidth is limited by a 5 μs sampling rate to about 100 kHz. Studies showed, by varying the low pass filter, that approximately half the typical signal was below 100 kHz. Much of this can be attributed to the filtering effect of the transducer; its sensitivity (Fig. 6) drops about 40 dB between 100 kHz and 1 MHz. Signals were amplified 50 dB for the 2219 aluminum alloys and 70 dB for 1100 aluminum.

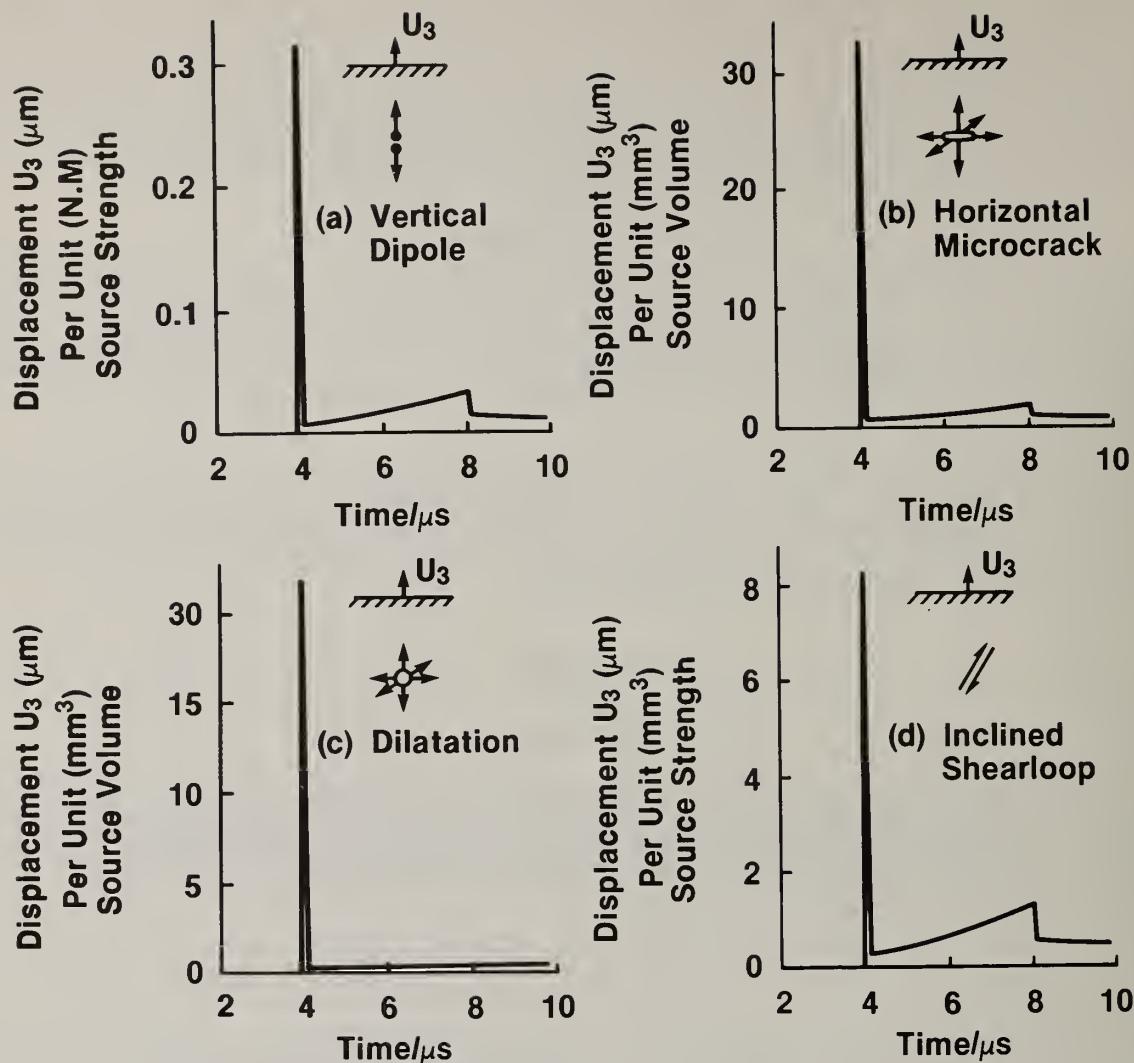


Figure 4. Transient epicenter vertical displacements above four point sources: (a) Vertical dipole; (b) Horizontal microcrack; (c) Dilatation; and (d) Inclined shear loop [9].

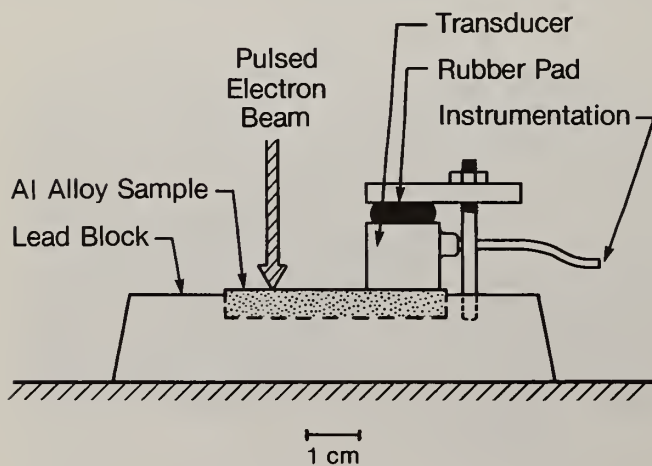


Figure 5. Schematic diagram of the experimental facility to measure acoustic emission during the rapid solidification of electron beam surface melted aluminum alloys.

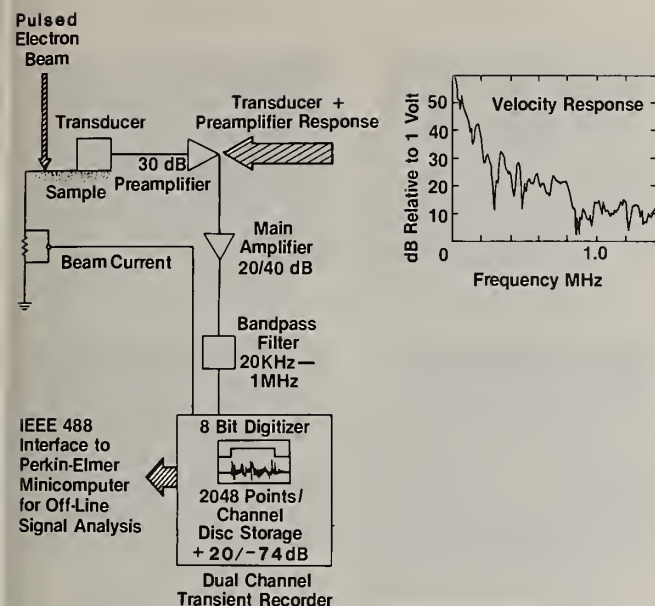


Figure 6. Schematic diagram of acoustic emission instrumentation together with the transducer plus preamplifier response determined by the breaking capillary method. (Transducer calibration by F. Breckenridge).

The acoustic emission signal and the beam current were digitally recorded on separate channels of a 2-channel 8-bit transient recorder. For the examination of emission throughout the entire pulse, a coarse sampling interval of 200 μ s (giving a record length of 400 ms) was used for a few pulses on each alloy. In this study our interest was focused on the acoustic emission during solidification and for the majority of measurements, digitization was performed at 5 μ s intervals (10 ms record) from just prior to the moment the electron beam was cut off. The digitized data was temporarily stored on floppy diskettes at the remote electron beam installation and transferred, off-line, to a 1.5M Byte minicomputer for data analysis. In these experiments we are not attempting to deduce dynamic source information. Wave propagation within the sample is too complex to allow this at present. Rather, we are attempting to follow the kinetics of solidification through the temporal variation of acoustic emission activity. This "activity" was arbitrarily (but in a rigorously standardized manner) measured by computing the mean square voltage of the emission as a function of time and then integrating this over time until the signal became lost in noise. This provided a useful single number (related to acoustic emission energy) with which to describe the relative "activity" of the different electron beam pulses/samples.

Results

Microstructure

The effect of increasing the product qa , absorbed heat flux q (Wm^{-2}) times radius of the circular region a , upon melt size and microstructure is shown in Figure 7 for both the 1100 aluminum and the 2219 aluminum alloy. Figure 3 shows a comparison between the calculated and experimentally measured depth profiles for the 2219 aluminum alloy. Agreement is good considering various assumptions of the heat flow model including constant thermophysical properties for the alloy. The size of the melted region for qa values in the steady-state regime increased with qa . For the same qa , the alloy, with its lower liquidus temperature, had a slightly deeper melt depth. The 2219 alloy also had a less clear interface between the rapidly solidified region and the unmelted substrate. This is marked the "mushy" zone in Figure 8. It denotes a partially melted region between the melt pool and the unmelted substrate. Figure 9 shows the effect of qa upon melt profile for qa values in the vaporization regime. Deep penetration can be observed in both alloys.

Detailed metallographic observations indicate considerable plastic deformation to accompany melting and resolidification, and, in the case of the 2219 alloy, considerable hot tearing also occurred (see Fig. 8 for example). The effect of qa upon melt depth along the z-axis for both alloys is shown in Figure 10. Melting occurred at slightly lower qa values for the 2219 alloy and, for a given qa , melt depths were always greater for 2219.

Figure 7. Optical micrographs of 1100 and 2219 aluminum alloys showing the effect of qa upon melt profile and ensuing microstructures in the "steady state" region.

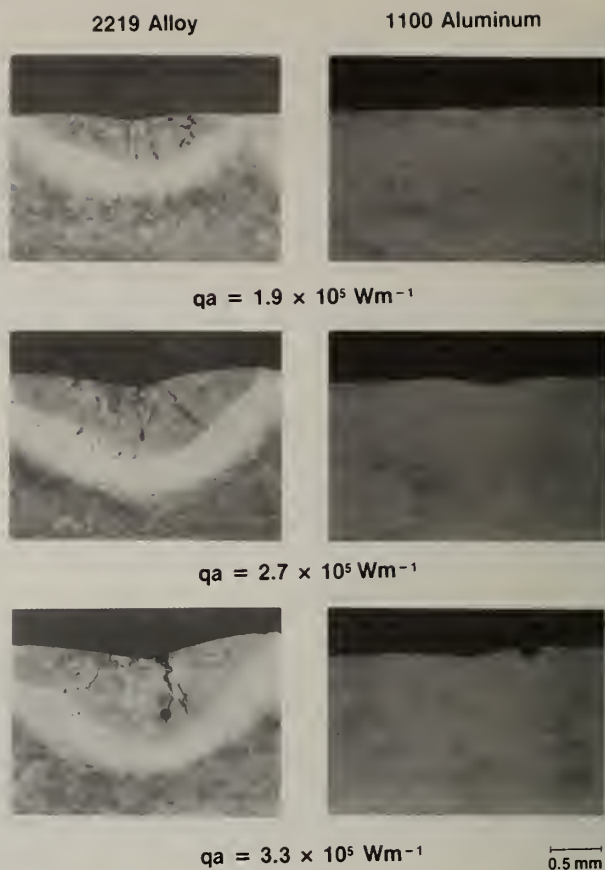
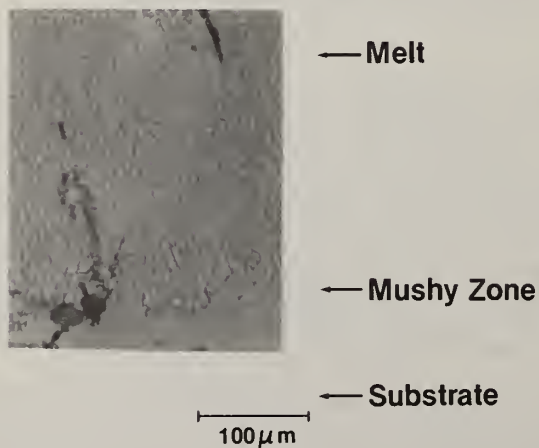
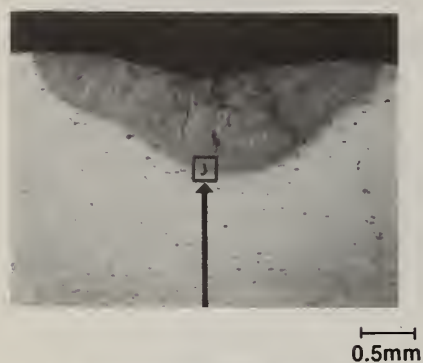


Figure 8. Optical micrographs of 2219 aluminum alloy surface melted at $qa = 2.7 \times 10^5 \text{ Wm}^{-1}$ showing detailed microstructure of the region of the "mushy" zone at the bottom of the melt pool.

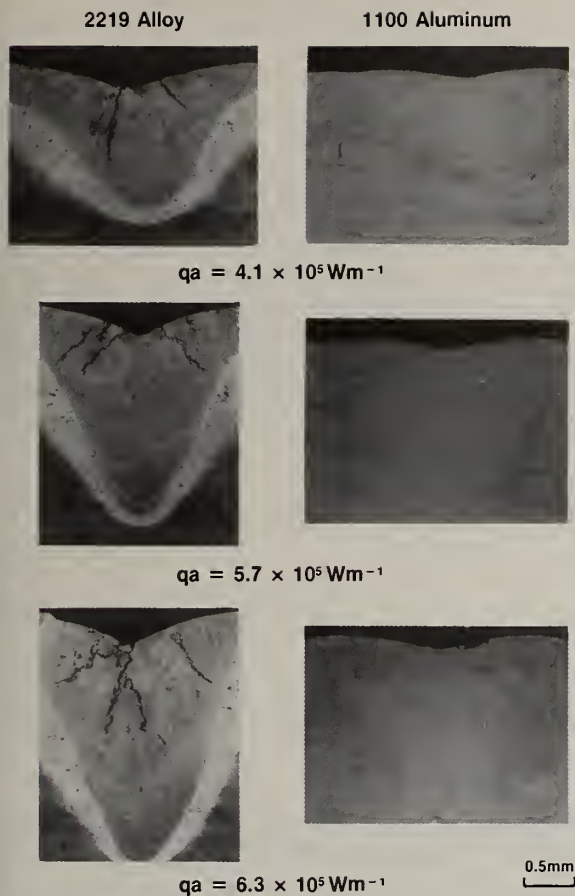


Figure 9. Optical micrographs of 1100 and 2219 aluminum alloys showing the effect of q_a upon melt profile and ensuing microstructure of q_a such that $T[0,0] > T_v$.

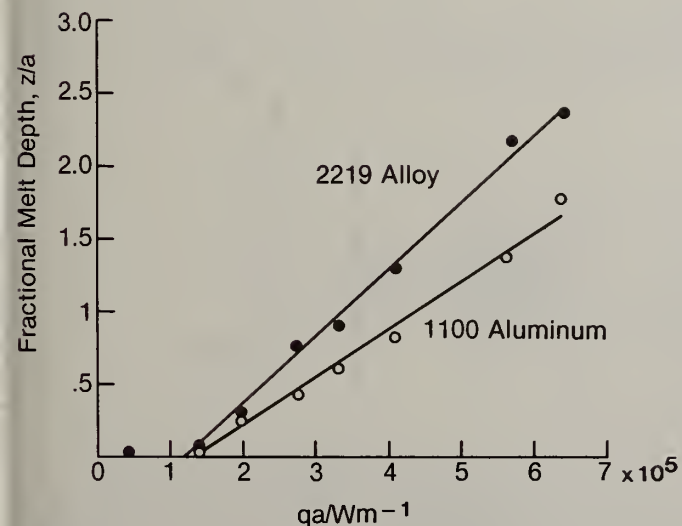


Figure 10. The effect of q_a upon melt depth for 1100 and 2219 aluminum alloys. Melt depth is measured from the liquidus isotherm to the substrate surface for the 2219 alloy.

Acoustic Emission

The temporal behavior of the acoustic emission signal, together with absorbed heat flux, are shown in Figure 11 for $q_a = 2.7 \times 10^5 \text{ Wm}^{-1}$ for both metals over the entire beam pulse. It can be

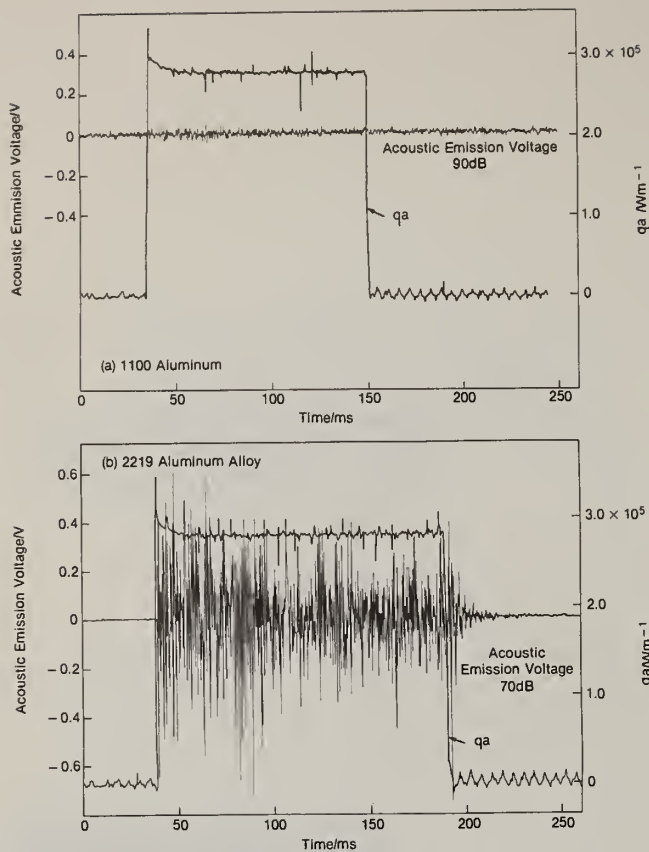


Figure 11. Acoustic emission generation during pulsed electron beam heating ($q_a = 2.7 \times 10^5$ W/m) and subsequent cooling of 1100 and 2219 aluminum alloys. Note that 1100 aluminum measurements were made at a 10x higher gain, but even so generated orders of magnitude less emission.

seen that very much more acoustic emission is observed from the 2219 alloy than from 1100 aluminum both while melting was occurring and during rapid solidification after beam cut-off.

The acoustic emission energy during the period of solidification (during and after beam cut-off) is shown, as a function of q_a , in Figure 12. Figure 12(a) and (b) focuses on the AE behavior of 2219 material in a -T87 condition in the thermoelastic region, where no melting occurs, (12(a), $q_a = 1.36 \times 10^5$ W/m) and the melt region (12(b), $q_a = 2.70 \times 10^5$ W/m), showing the beam current (dotted line) and AE response (solid line). Note that melting in this case often produces an extra pulse of AE during solidification. In Figure 13 the cumulative energy of the AE signals during solidification is shown for both the 2219 and 1100 materials. Each of the data points are the average of 15 separate electron pulses on three different, but nominally similar samples. It can be seen that the acoustic emission is typically a hundred times more energetic in the 2219 aluminum alloy.

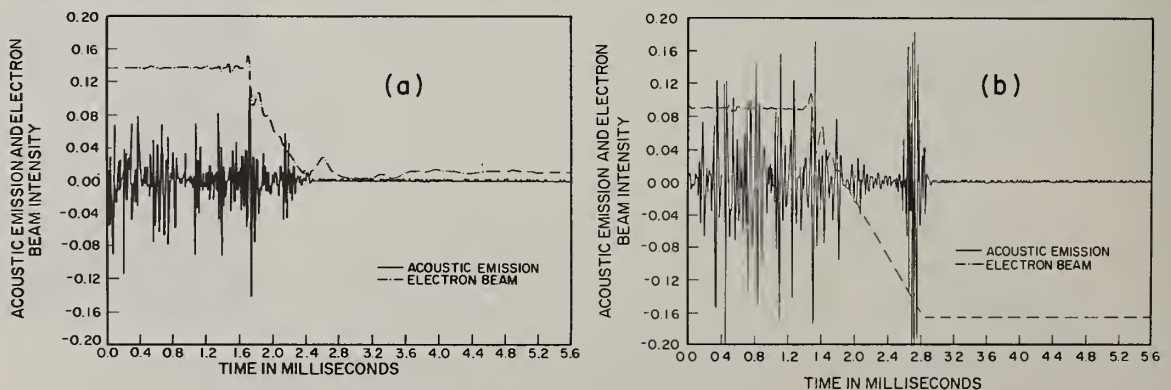


Figure 12. Effect of q_a level on the type and quantity of AE during rapid solidification of 2219 aluminum. (a) $q_a = 1.36 \times 10^5$ W/m. (b) $q_a = 2.70 \times 10^5$ W/m.

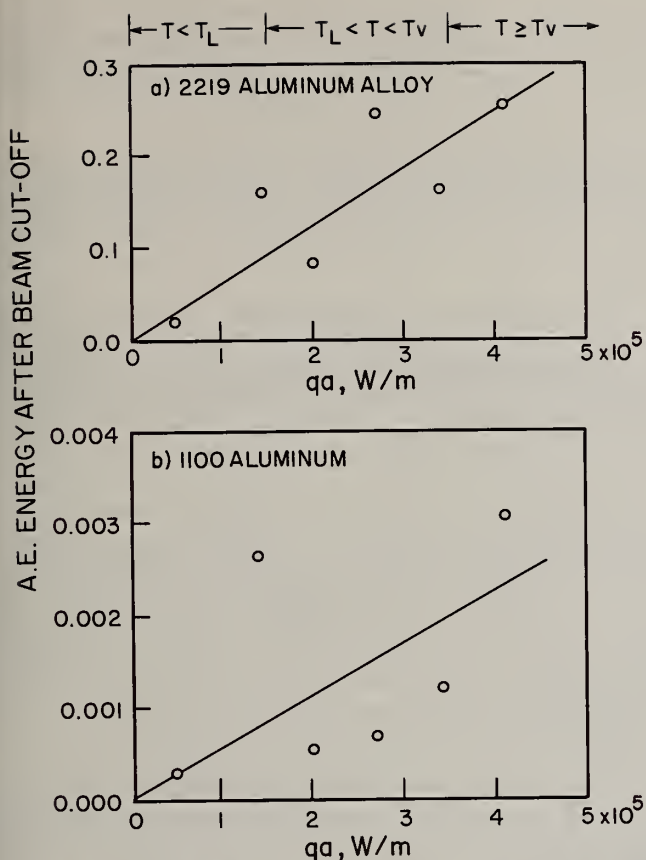


Figure 13. The effect of qa upon acoustic emission after electron beam cut-off for steady-state conditions in (a) 2219-T87 and (b) 1100 aluminum alloys. Note the different scales for the two alloys.

Acoustic emission during solidification was measured from samples with different substrate microstructures. Table II shows that the amount of AE during rapid solidification is dependent on the microstructure of the substrate. In this experiment, 2219 aluminum was tested in the solutionized condition (75 min. at 535 °C, ice water quench), and -T6 conditions (aged to peak hardness at 177 °C for 18 hours). The grain size was 50 μm . The table indicates that the T6 condition emitted the greater AE.

Table II

Acoustic Emission After Beam Cut-off as Affected by Substrate Material Condition

Material Condition	Rockwell B Hardness	Energy (Relative Units)		
		$qa \leq 1.5 \times 10^5 \text{ W/m}$	$qa > 1.5 \times 10^5 \text{ W/m}$	Total
2219-Solutionized	39	0.008	0.013	0.021
2219-T6	77	0.056	0.117	0.173

Discussion

During electron beam heating and subsequent cooling, both 1100 and 2219 aluminum alloys generate detectable levels of acoustic emission but that from the 2219 alloy is 1 to 2 orders of magnitude greater in intensity (Fig.11). Here, we would like to deduce the physical origin of this emission. To do this we shall use our understanding of the differences in the behavior of the two alloys during solidification, in conjunction with elementary elastodynamic calculations, to deduce the stress change mechanisms that generate detectable signals.

Every change in stress radiates elastic waves. Due to noise and to sensitivity limitations not every stress change generates detectable elastic waves. Many of the stress changes occurring during solidification of the 2219 aluminum alloy are clearly detectable, while very few in 1100 aluminum are of sufficient strength to satisfy detectability criteria. To develop this argument further, it is essential to elucidate the detectability criterion for this system. That is, what is the relation between the measured acoustic emission energy and the source stress change?

We have devised a rather simple method for this calibration in which we use the predictable thermal stress induced by the absorption of a short duration laser pulse to generate elastic waves at the natural source position. For the experiments we used a 25 ns duration 12 mJ energy Nd:YAG pulse from a Q-switched laser as the artificial source.

This source generated a signal whose energy, when measured using the same conditions as for the 2219 aluminum alloy experiments, was 0.30 units. From this, since the smallest detectable energy was about 0.0005 units, we estimate the smallest detectable dipole source to be about 1 μNm [7]. Differences in the radiation patterns of various sources are likely to be reduced because of the multiple paths of reflected rays that contributed to measurements.

Origin of Acoustic Emission During Cooling

From above, it is clear that only those stress changes for which $D_{ij} \geq 1 \mu\text{Nm}$ will give detectable acoustic emission in these experiments. During the electron beam treatments on 1100 aluminum we have observed very weak acoustic emission signals: presumably, the stress changes accompanying melting/resolidification here have dipole components $< 1 \mu\text{Nm}$. The 2219 aluminum alloy has generated intense acoustic emission signals: the addition of 6.6 wt.% Cu has resulted in many stress changes during processing for which $D_{ij} \gg 1 \mu\text{Nm}$. We can use these differences to aid our deduction of the acoustic emission sources.

Since the solidification interface velocity, cooling rate, and thermal constants do not vary appreciably between the two alloys we would expect the development of thermoelastic contraction stress to be similar in both alloys. Since little or no acoustic emission was observed from the 1100 alloy it is reasonable to assume this potential acoustic emission is undetectable in these experiments. Very high contraction stresses undoubtedly develop, but in solidification from a steady state condition the cooling rate is presumably too slow to generate detectable elastic waves above 20 kHz frequency. The more rapid cooling of short duration, high flux density laser pulses might be measurable however.

The maximum potential thermal stress that could develop upon cooling can be estimated from the relation:

$$\Delta\sigma = (\lambda + 2/3\mu)\beta\Delta T$$

where ΔT is the temperature drop, about 600 °C in aluminum. This results in a stress of ~ 900 MPa, many times the yield strength of both alloys. Thus, during cooling, we expect plastic deformation to relax the thermal stress. Each dislocation that slips will radiate elastic waves and could be a detectable emission source.

Suppose a unit of slip consists of the simultaneous expansion of n dislocation loops each expanding over an area dA on the same slip plane. Then the dipole matrix [8] is given by

$$\begin{aligned} D_{ij} &= n C_{ijkl} b_k dA_\ell \\ &\cong n\mu b dA \end{aligned}$$

For detectability this must exceed 1 μNm leading to the criterion $ndA \geq 0.13 \text{ mm}^2$.

Previous studies reviewed in reference [10] have indicated the fraction of slip events during uniaxial plastic deformation able to generate detectable signals is highly sensitive to composition and microstructure. For grain sizes below about 100 μm it is unlikely the 1100 aluminum alloy could generate detectable signals because n would have to be unrealistically large to satisfy the detectability criterion. In the alloy, during solidification a spectrum of microstructures exist ranging from hot solid solution to the peak hardness precipitate distribution. Previous studies have indicated that deformation of aluminum alloys containing small ($\leq 100 \text{ \AA}$) diameter shearable precipitates generates intense acoustic emission due to cooperative slip phenomena. Variation of the substrate microstructure, which we expect to have only a small effect upon processes other than

plastic deformation, resulted in large changes in acoustic emission. The most active sample condition (T6) was the one containing a mixture of θ'' and θ' precipitates. Thus, for $qa \geq 1.56 \times 10^5 \text{ Wm}^{-1}$ a part, at least, of the extra acoustic emission from the 2219 aluminum could be due to plastic deformation. While for $qa < 1.56 \times 10^5 \text{ Wm}^{-1}$ (for which no melting occurred) probably all the emission is from plastic deformations.

For $qa \geq 1.56 \times 10^5 \text{ Wm}^{-1}$ melting resulted, and upon subsequent resolidification hot tearing occurred raising the possibility of an extra emission source. The dipole strength for formation of a circular microcrack under mode I stress σ is approximately given by

$$D_{ij} = (\lambda + 2\mu) 2(1-\nu^2) \frac{\sigma r^3}{E} \pi$$

where ν = Poisson's ratio, r = crack radius, and E = Young's modulus. Substituting physical property values for aluminum and assuming $\sigma = 100 \text{ MPa}$ yields the detectability criterion $r \geq 1 \mu\text{m}$. Many cracks clearly satisfied this criterion. For these cracks to generate detectable signals they should also propagate at speeds greater than 1 ms^{-1} . Data on the micromechanisms of crack extension during hot tearing are sparse. Metallographic evidence indicates cracks have propagated beyond the prior melt boundary into unmelted material suggesting fast fracture may indeed have occurred. However, such evidence is far from conclusive and, because of the pronounced substrate effect, for the moment, we may only speculate that a part of the emission from samples for which $qa \geq 1.56 \times 10^5 \text{ Wm}^{-1}$ was from cracking.

Acknowledgments

We are grateful for the advice and assistance of R. Schaefer, C. Brady, J. Chang, F. Breckenridge, and C. Turner and the financial support of the Defense Advanced Research Projects Agency under DARPA Order No. 4275.

REFERENCES

- [1] R. Mehrabian, Int. Metals Rev., 1982, 27(4), 185.
- [2] M. C. Flemings, Solidification Processing (McGraw Hill, New York, NY, p. 142, 1974).
- [3] S. C. Hsu, S. Kou, and R. Mehrabian, Metall. Trans., 1980, 11B, 29.
- [4] J. A. Sekhar, S. Kou, and R. Mehrabian, accepted for publication Metall. Trans.
- [5] S. C. Hsu, S. Chakravorty, and R. Mehrabian, Metall. Trans., 1978, 9B, 221.
- [6] J. A. Simmons and R. B. Clough, "Theory of Acoustic Emission," Dislocation Modeling of Physical Systems, J. Hirth and M. Ashby, Eds., Acta/Scripta Metallurgica, Pergamon Press (1981).
- [7] H. Wadley, C. Stockton, J. Simmons, M. Rosen, S. Ridder, and R. Mehrabian, "Quantitative Acoustic Emission Studies for Materials Processing," DARPA/AFML Annual Review of Quantitative NDE, held in 1982.
- [8] H. N. G. Wadley, C. B. Scruby, and J. E. Sinclair, Phil. Mag., 1981, 44, pp. 249-274.
- [9] C. B. Scruby and H. N. G. Wadley, Accepted for publication in J. Phys. D, 1983
- [10] H. N. G. Wadley and R. Mehrabian, to be published.
- [11] H. N. G. Wadley, C. B. Scruby, and G. Shrimpton, Acta Met. 1981, 29, 399.

CRYSTALLIZATION KINETICS OF AMORPHOUS ALLOYS BY ULTRASONIC MEASUREMENTS

M. Rosen*, E. Horowitz*, H. N. G. Wadley**, and R. Mehrabian**

*The Johns Hopkins University, Baltimore, MD 21218 and
the National Bureau of Standards, Washington, DC 20234

**The National Bureau of Standards, Washington, DC 20234

ABSTRACT

The crystallization kinetics in amorphous PdCuSi and CuZr ribbons, prepared by the melt spinning technique, were determined from ultrasonic wave propagation measurements, microhardness and optical metallography. Ultrasonic waves were generated using a laser pulse. The waves were piezoelectrically detected after propagation over a predetermined distance. From the variation of the elastic moduli with crystallization time at isothermal holding temperatures the activation energies and the growth laws of the processes were determined. The elastic moduli of the alloys increase by about 40% during the transition from the amorphous to the crystalline state. Furthermore, the sound velocity and the elastic moduli were found to be sensitive to structural relaxation processes occurring in the disordered amorphous state prior to crystallization. The structural relaxation is accompanied by a significant increase in hardness, as revealed by microhardness measurements. It is conjectured that the frequency dependence of the ultrasonic attenuation, as interpreted within the framework of the theory of viscoelasticity, may explain the hardening process in the amorphous state. Metallographic examination showed that the crystallization process in the ribbons proceeds by rapid nucleation at the free surfaces followed by frontal linear growth of the crystallized phase towards the center of the ribbon. In the interior, however, random nucleation and growth occur. The observed growth kinetics are in agreement with theoretical considerations. The effect of composition on the Young's moduli of the amorphous and crystalline states has been investigated in the Zr-Cu system. In contrast to the crystalline structure the amorphous state exhibits a smooth S-curve in the variation of the moduli with copper content. The inflection point at 50% Cu is interpreted as the point of maximal configurational entropy of the amorphous alloy with respect to the Cu-Zr atom pairs.

Introduction

Formation of metallic glasses through rapid solidification techniques and their subsequent crystallization upon heating has been the subject of numerous investigations. The extensive interest in the materials is due to their unusual mechanical, physical and chemical properties. While some practicing engineers are vigorously pursuing new alloys and processing techniques to develop commercially attractive amorphous products for use in electronic and power industries, others are recrystallizing specific alloys through selected heat treatments into microcrystalline structures which exhibit high coercivities or lend themselves to consolidation into bulk products. Characterization of the range of microstructures thus produced using nondestructive techniques is an attractive proposition both in terms of its contribution to the understanding of the kinetic phenomena at play during the various transformations, as well as its ultimate commercial utilization for on-line feedback control of process variables.

Metallic glasses are not thermodynamically stable, and they tend to structurally relax and finally crystallize upon appropriate heat treatment. Waseda et al. (1) showed that annealing metallic glasses increased the short-range order. Egami (2) used energy-dispersive methods to confirm the log-time kinetics of the relaxation process. His work indicated that the activation energy for relaxation continuously increased with time, which may correspond to the removal of quenched-in defects. The process of crystallization into a stable state involves drastic variations in the properties of the material

Although changes in density and electronic structure associated with the crystallization process are rather minute (3), appreciable variations were observed in several physical properties, including the elastic moduli (4-6). The crystallization behavior of metallic glasses was examined by several workers (7-10). It was found that small additions of noble metals (Cu, Ag) to Pd-Si greatly stabilizes the amorphous phase, and particularly in $\text{Pd}_{0.775}\text{Cu}_{0.06}\text{Si}_{0.165}$ glass (11) which became the subject of numerous investigations. The effect of isothermal annealing on the crystallization kinetics of $\text{Pd}_{0.775}\text{Cu}_{0.06}\text{Si}_{0.165}$ was determined by differential scanning calorimetry (11).

Associated with relaxation and crystallization of metallic glasses are variations in the elastic and mechanical properties. Young's modulus E and shear stiffness μ generally increase by 20-40%, but the bulk modulus K by only about 7% upon crystallization (5). Kursumovic and Scott (12) found that E for $\text{Cu}_{60}\text{Zr}_{40}$ increased by about 10% due to structural relaxation and another 15% upon crystallization. In contrast, the density of glassy metals is generally only 0.3-1.5% less than the corresponding crystalline structures. As-quenched metal glasses contract approximately 0.5 volume percent upon relaxation. Freed and VanderSande (13) found that after aging $\text{Cu}_{46}\text{Zr}_{54}$ at 375°C, the tensile fracture stress σ_f and Knoop microhardness numbers (KHN) rose to a maximum from the as-spun state and then fell to a minimum before finally increasing again. They ascribed the initial "humps" in σ_f and KHN to be due to structural relaxation, and the final increases to crystallization. Davis (14) used the simple relation $H_y = 3\sigma_y$, where H_y is the Vickers microhardness and σ_y is the yield stress, to estimate strengths of metallic glasses. He found that observed H_y/σ_y values for $\text{Ni}_{49}\text{Fe}_{29}\text{P}_{14}\text{B}_6\text{Si}_{12}$ (MetglasTM 2826B) and $\text{Pd}_{0.775}\text{Cu}_{0.06}\text{Si}_{0.165}$ agreed reasonably well with theory.

Straightforward elasticity and wave propagation theories enable one to calculate E (15). For one-dimensional extensional wave propagation in a homogeneous, isotropic, linearly elastic solid, Young's modulus is given by $E = v_E^2 \cdot \rho$ where v_E is the extensional wave velocity and ρ is density.

Objectives

The objectives of the present investigation were as follows:

- Determination of the isothermal transformation kinetics from the amorphous to the crystalline state by means of monitoring changes in sound wave velocity (elastic modulus)
- Calculation of the kinetic parameters: activation energies and crystallite growth regime. Comparison with experimental evidence.
- Information about the relaxational changes occurring in the amorphous state, prior to crystallization.
- Corroboration with optical and electron microscopy, x-rays and microhardness concerning the relationship between microstructure and properties.

Experimental

Metallic glass ribbons were prepared using the melt-spinning technique (16). A quartz shooter with 0.5 mm diameter nozzle, contained a PdCuSi or CuZr crystalline button. An induction coil melted the button, and the shooter was then pressurized with helium to 70 KPa to inject the molten alloy onto a balanced oxygen-free, high-conductivity copper disk spinning at 7,000 rpm. A 2 mm wide, 30 μm thick ribbon was produced. Ultrasonic, x-ray, and STEM examinations indicated that the ribbon was completely amorphous. The as-spun ribbon was cut into 200 mm sections and placed into Vycor tubes. After evacuating the tubes to approximately 5×10^{-6} torr, they were sealed. The encapsulated ribbons were then heat-treated in a forced-air convection furnace. For each isothermal heat treatment, the temperature was held constant to within $\pm 20^\circ\text{C}$. Three heat treatment temperatures were chosen. The first was near the crystallization temperature T_c , the second near the glass transition temperature T_g , and the third intermediate temperature T_i . The experimental technique, Fig. 1, for measuring v_E , and thus E , has already been described elsewhere (17).

The velocity of the ultrasonic extensional wave V_E ($V_E = (E/\rho)$, where E is the Young modulus and ρ is the density) propagating along the ribbon was determined by measuring the transit time of a single pulse generated by a laser and detected by a piezoelectric quartz-crystal transducer located at a distance of about 200 mm from the spot on the ribbon irradiated by the laser. The transient load was applied by rapid deposition of energy from a single-pulse of a Q-switched neodymium glass laser with a wavelength of 1.06 μm . The laser-pulse duration was 15 ns, and the pulse energy, for this specific series of measurements, was about 20 mJ. The deposition of the laser energy onto the

absorbing specimen produces a state of unbalanced compressive thermal stress as the locally heated material tends to expand but is restrained initially by its own mechanical equilibrium. The elastic stress wave propagates along the specimen and may be detected by a piezoelectric transducer. The laser pulse was line-shaped to produce a nearly plane wave. A photodetector was used to trigger a transient pulse recorder as the laser pulse was generated. Thus, the transit time of the extensional sound wave propagating along the ribbon could be determined to within better than 1 part in 10^4 . The separation (about 200 mm) between the impinging laser pulse and the quartz receiver was determined to within ± 0.2 mm. The total estimated error in the calculated value of the Young modulus was $\pm 0.2\%$. The sound velocity measurements were carried out at room temperature.

Laser Generation and Piezoelectric-Sensor Detection of Ultrasonic Waves in Thin Ribbons

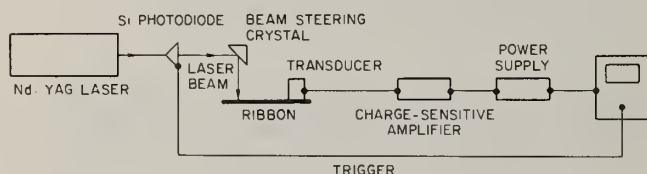


Fig. 1 Laser generation and piezoelectric detection (PZT transducer) of ultrasonic waves in thin ribbons.

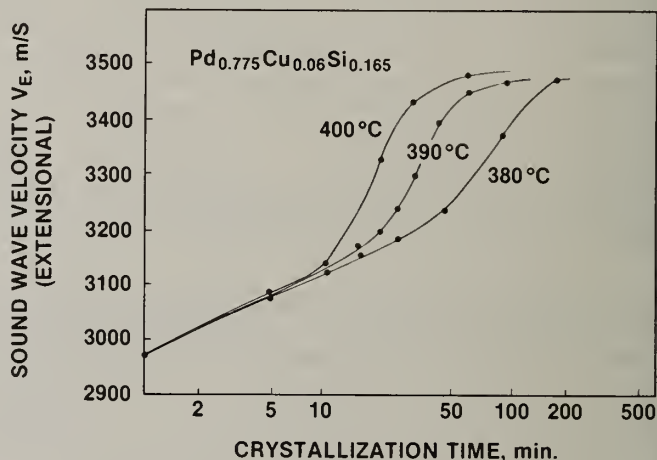


Fig. 2 Variation of the extensional wave velocity, V_E , in PdCuSi ribbons as a function of crystallization time at 380, 390 and 400°C.

In this work, ultrasonic extensional waves were detected using a National Bureau of Standards conical PZT transducer having a flat response between DC and 2 MHz. Signal amplification was provided by an EMI 6306 charge-sensitive amplifier powered by an EMI Power Supply Type 6396*. A silicon photodiode triggered a Nicolet Explorer III digital oscilloscope so that the elastic wave could be recorded and transit times read directly from the screen of the oscilloscope.

Finally, small sections of each heat treated specimen were mounted in epoxy for Knoop microhardness number (KHN) measurements. To minimize anvil effects and to ensure the KHN values were taken on the bulk material, each specimen was cut perpendicular to its length vector, and then was mounted with its cut face exposed. After polishing the mounted ribbons to 0.05 μm alumina, KHN values were determined using a 10g load and averaging four symmetrical indentations.

Results and Discussion

Fig. 2 shows the variation of the extensional wave velocity, V_E , as a function of crystallization time at three isothermal holding temperatures, 380, 390, and 400°C. The initial sound-wave velocity, in the amorphous state, was found to be 2970 m.s^{-1} , whereas in the fully crystallized state it reached an asymptotic value of 3490 m.s^{-1} . Taking 10.52 and 10.69 g.cm^{-3} as the density (ρ) of the amorphous and crystalline $\text{Pd}_{0.775}\text{Cu}_{0.06}\text{Si}_{0.165}$, respectively, the Young moduli could be calculated. They were found to be 9.28 MPa for the amorphous state and 13.0 MPa for the crystalline state, i.e. ΔE of about 40%. The present values of V_E and E for the amorphous state are somewhat higher than those quoted by Davis *et al.* (18) for Pd-Cu-Si.

Fig. 2 exhibits a relatively sharp increase in the sound velocity during the first 5 minutes of the isothermal holding. Subsequently, typical sigmoidal curves are developed, depicting the crystallization kinetics.

*All references to commercial equipment in this paper are for identification purposes only and in no way constitute any endorsement or evaluation of the relative merits of such equipment.

The initial increase in the extensional sound velocity, of about 3.7%, i.e. 7.4% in the Young modulus, appears to be related to a structural relaxation that precedes the crystallization process in the amorphous state (19). Structural relaxation was found to be particularly enhanced in glasses obtained at high quenching rates, where greater structural disorder is to be expected. The lower elastic stiffness in the glassy state has been attributed to the interatomic displacements inherent in a disordered structure (20). The elastic stiffness should, therefore, increase with increased local ordering as a consequence of the structural relaxation. This is compatible with the increase in the sound velocity, as shown in Fig. 2. Within the framework of the present investigation, the variables of this thermally-activated relaxation process were not studied in detail.



Fig. 3 Crystallization sequence of amorphous PdCuSi as a function of time at a constant temperature, by optical metallography.

The crystallization process in Pd-Cu-Si involves a thermally-activated nucleation and growth process dominated by the frequency of nucleation, and a diffusional growth. Turnbull (21) adopted the classical nucleation theory (22) for glass formation and crystallization in the amorphous state. Formation of critically-sized stable nuclei capable of further growth is characterized by a series of concentration fluctuations. A steady state nucleation rate can be expressed as $I = ke^{-(Q+A)/RT}$, where k is a constant, A and Q are activation energies of formation and growth, respectively. In terms of the reciprocal rate theory $\ln t = (K + Q/RT + A/RT)$ or $\frac{\partial \ln t}{\partial (1/T)} = \frac{Q}{R} + \frac{A}{R} + \frac{1}{RT} \frac{\partial A}{\partial (1/T)}$. By assuming $Q \gg A$, then $\frac{\partial \ln t}{\partial (1/T)} = \frac{Q}{R}$. Thus, if t is the crystallization time for a specific fraction of volume

transformed from the amorphous into the crystalline state ($\ln t$) vs. $(1/T)$ gives a value proportional to the activation energy of the process. The activation energy for 50% crystallization of amorphous $\text{Pd}_{0.775}\text{Cu}_{0.06}\text{Si}_{0.165}$, obtained from the ultrasonic measurements, Fig. 2 was found to be 232 kJ/mole.

This value is significantly lower than 400 kJ/mole determined by calorimetry (10), but is in rather close agreement with values of activation energies for recrystallization in other glasses (23.)

Optical metallography indicates, however, that the crystallization process in Pd-Cu-Si ribbons is not homogeneous in the bulk. Fig. 3 is a view from the thin edge of a ribbon heat treated for various times at 390°C. Two coexisting growth processes are apparent. One is rapid nucleation on the free surfaces, followed by a frontal growth from the external surface of the ribbon towards the interior. The other growth process involves nucleation of crystallized regions in the bulk, followed by spherical growth. The growth rate was determined from the metallographic observations. It was found that the frontal growth is linear with respect to crystallization time, in agreement with theoretical considerations due to Cahn (24). It should be mentioned in this context that the ultrasonic measurements detect the kinetics of the bulk growth, rather than the specific linear growth of the advancing front, as was determined by metallography. Furthermore, this study demonstrates the importance of the specimen geometry in the analysis of the crystallization kinetics in thin ribbons. The Johnson-Mehl analysis (25) should be used with care by considering the possibility of simultaneous operation of different nucleation and growth processes that exhibit different reaction kinetics. Therefore, experiments specifically designed to isolate nucleation and growth processes are necessary for a better understanding of the contribution of each to the total crystallization process.

Figure 4 shows the effect of copper content on the Young's modulus of Zr-Cu alloys in the crystalline and amorphous state. The lowest value of the Young's modulus is for pure crystalline zirconium. A maximum and a minimum are found for alloys with compositions near the intermetallic compounds Zr_2Cu and $ZrCu$, respectively. The variation of the Young's modulus with composition of the amorphous alloys, between 30 and 70% copper, is a smooth S-curve with an inflection point at 50 a/o copper. It is conjectured that the amorphous state can be interpreted in terms of the Bragg and Williams approximation for short range order where the mixing pairs Zr-Zr, Cu-Cu and Cu-Zr are of equal probability at the composition of 50 a/o Cu. The inflection point on the Young's modulus versus composition curve will then represent the point for maximal configurational entropy of the amorphous alloy. The theoretical model should be corroborated by appropriate X-ray analysis in order to establish its validity.

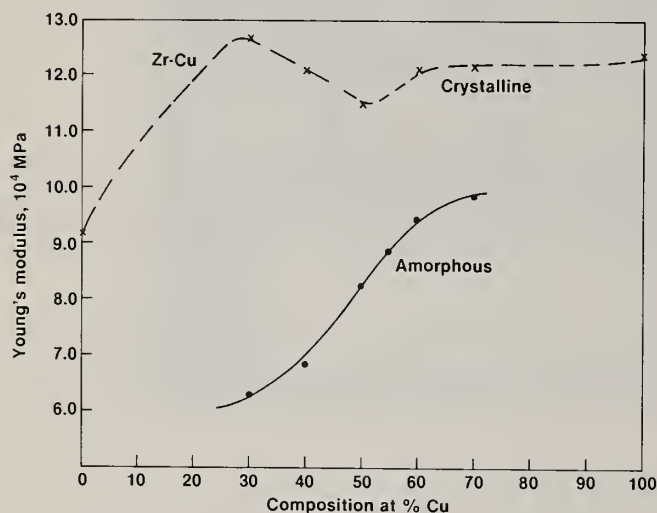


Fig. 4 Variation of Young's modulus with copper content of amorphous and crystalline Zr-Cu alloys.

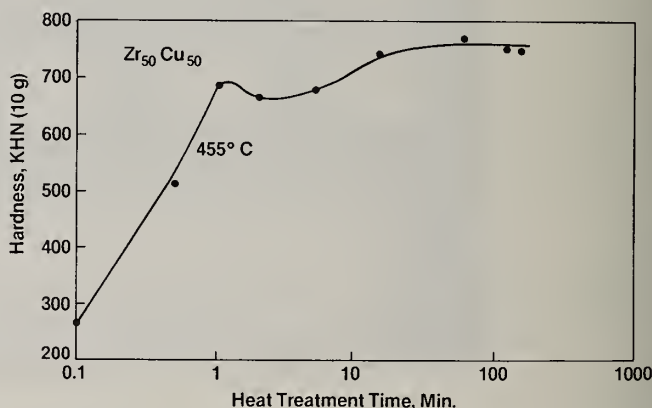


Fig. 5 Variation of microhardness during crystallization of amorphous $Zr_{50}Cu_{50}$ alloy at a constant temperature.

The initial increase in the extensional sound velocity, of about 7.4% in the Young modulus of PdCuSi and a similar increase in the Zr-Cu amorphous alloys, appears to be related to a structural relaxation that precedes the crystallization process in the amorphous state. Structural relaxation was found to be particularly enhanced in glasses obtained at high quenching rates, where greater structural disorder is to be expected (26). The lower elastic stiffness in the glassy state has been attributed to the interatomic displacements inherent in a disordered structure (20). The elastic stiffness should, therefore, increase with increased local ordering as a consequence of the structural relaxation. This is compatible with the increase in the sound velocity, as shown in Fig. 2.

Microhardness measurements, Fig. 5, on the ribbon edge, perpendicular to the length vector of the ribbon, revealed that while in the amorphous, precrystallization state, the material undergoes some significant changes in its mechanical properties. Fig. 5 depicts a plot of KHN (Knoop Hardness Numbers) vs log-time for Zr₅₀Cu₅₀ heat treated at 455°C. This isothermal treatment significantly alters the hardness of the amorphous alloy before crystallization ensues. In agreement with Freed and VanderSande (13) for Zr₅₄Cu₄₆ ribbons, microhardness first increased from the as-spun value to a relative maximum of 88%. With continued aging, Knoop microhardness fell to a shallow minimum before rising to a final asymptotic value of approximately 720 kg. mm⁻². This last point contrasts results by Freed and VanderSande in that their KHN values continued rising even after 600 minutes at 375°C (15°C below T_g). Using DSC and TEM, they determined that the volume fraction of crystalline material was between 0.80 and 0.90 after 600 minutes. The asymptotic Knoop hardness values found in this work, however, represent the fully crystalline state.

The embrittlement mechanism in the amorphous alloy can be related to the removal of the quenched-in free volumes (vacancy clusters). Initially, the amorphous alloy has a disordered packing of the constituent atoms. The reduced coordination of the atom complexes, due to the present of excess free volumes, allows shear transformations to be sustained. The free volumes are analogous to dislocation core segments. Consequently, the material is very ductile in the disordered amorphous state.

Heat treatment in the amorphous region at temperatures below the glass transition temperature, T_g, or for relatively short periods of time at temperatures above T_g causes structural and compositional relaxation. The free volumes are redistributed by short range shuffling of the atoms, thus a more rigid close packed atomic distribution of high coordination is achieved. The dense random packing of hard spheres (Bernal structure) leads to a significant embrittlement of the amorphous phase.

The topological and compositional relaxation processes occurring in the amorphous state can be investigated by analyzing the behavior of the shear and compressional components of the ultrasonic attenuation, and their frequency dependence. From the theory of viscoelasticity, for a shear relaxation:

$$\mu = \mu_{\infty} \frac{\omega^2 \tau_s^2}{1 + \omega^2 \tau_s^2} + i \mu_{\infty} \frac{\omega \tau_s}{1 + \omega^2 \tau_s^2} \quad \text{where, } \mu \text{ and } \mu_{\infty} \text{ are the relaxed and unrelaxed shear moduli, respectively, } \omega \text{ is the vibration frequency, and } \tau_s \text{ is the shear relaxation time.}$$

$$\tau_s = \eta_s / \omega \quad \text{and} \quad \eta_{\omega} = \frac{\mu_{\infty} \tau_s}{1 + \omega^2 \tau_s^2} \quad \text{where, } \eta_{\omega} \text{ and } \eta_s \text{ are frequency dependent and frequency independent shear viscosities, respectively.}$$

In addition, the compressional viscosity can be expressed in terms of the relaxation time for a compressional process, τ_c , the relaxation time for a shear process τ_s , and the bulk modulus, B, of the material: $\eta_c = \frac{B \tau_c}{1 + \omega^2 \tau_s^2}$

The compressional and shear viscosities of the medium, η_c and η_s , respectively, are related to the experimentally determined attenuation, α , in the following manner: $\alpha = \left(\frac{\omega^2}{2\rho v^3} \right) \left(\eta_c + \frac{4}{3} \eta_s \right)$

where v is the sound velocity and ρ is the density of the amorphous material.

Thus, from the frequency dependence of the ultrasonic attenuation, obtained by means of the dual-laser interferometer, the behavior of the bulk and shear viscosities can be characterized. Consequently, it is possible to establish the functional relationship between the appropriate relaxation times and the diffusional reactions leading to topological and compositional changes in the amorphous state. This specific phase of the investigation is currently in progress. It can be realized through the capability of the laser generation-laser interferometric detection of propagating sound waves, and the subsequent analysis of their frequency dependence (27).

Summary and Conclusions

- Structural relaxation and crystallization processes, induced by isothermal heat treatment above the glass transition temperature in CuZr and PdCuSi amorphous alloys was studied by means of ultrasonics, microhardness and metallography.

- Sound wave velocity versus log-time of isothermal heat treatment exhibited isokinetic sigmoidal behavior. Young's modulus increased by about 40% when the alloys transformed from amorphous to crystalline state.
- Structural relaxation, before the crystallization process ensues, is manifested by an increase in Young's modulus and by a drastic increase in microhardness.
- The eutectic-like decomposition of the amorphous phase in melt-spun ribbons occurs by rapid nucleation and linear growth at the free surfaces, and by homogeneous nucleation and linear growth in the bulk of the ribbon.
- The activation energies for crystallization were for PdCuSi and Zr₅₀Cu₅₀ were found to be 232 and 360 kJ/mole⁻¹, respectively.

Acknowledgments

The authors are thankful to F. Biancaniello for preparation of the specimens. Fruitful discussions with S. Fick are greatly appreciated. Support from Defense Advanced Research Projects Agency (DARPA) under DARPA Order No. 4275 is gratefully acknowledged. Technical monitor of this contract was Lt. Col. L. A. Jacobson.

References

1. Y. Waseda, H. Okazaki and T. Masumoto, J. Mat. Sci. **12**, 1927 (1977).
2. T. Egami and T. Ichikawa, Mat. Sci. Eng. **32**, 293 (1978).
3. H. S. Chen and J. T. Krause, Scripta Met. **11**, 761 (1977).
4. H. S. Chen, M. J. Leamy and M. Barmatz, J. Non-Crystalline Solids **5**, 444 (1971).
5. B. Golding, B. C. Bagley and F. S. L. Hsu, Phys. Rev. Letters **29**, 68 (1972).
6. H. S. Chen, J. Appl. Phys. **49**, 3289 (1978).
7. P. Duwez, R. H. Willens and R. L. Crewdson, J. Appl. Phys. **36**, 2267 (1965).
8. J. J. Burton and R. P. Ray, J. Non-Crystalline Solids **6**, 393 (1971).
9. T. Matsumoto and R. Maddin, Acta Met. **19**, 725 (1971).
10. B. G. Bagley and E. M. Vogel, J. Non-Crystalline Solids **18**, 29 (1975).
11. H. S. Chen and D. Turnbull, Acta Met. **17**, 1021 (1969).
12. A. Kursumovic and M. G. Scott, Appl. Phys. Letters **37**, 620 (1980).
13. R. L. Freed and J. B. VanderSande, Met. Trans. A **10**, 1621 (1979).
14. L. A. Davis, Scripta Met. **9**, 431 (1975).
15. K. F. Graf, Wave Motion in Elastic Solids, Ohio State University Press, Columbus, OH (1975).
16. H. A. Davies, Rapidly Quenched Metals III I, p. 1, Proc. Third Internat. Conf. Rapidly Quenched Metals, The Metals Society, London, ENGLAND (1978).
17. M. Rosen, H. N. G. Wadley and R. Mehrabian, Scripta Met. **15**, 1231 (1981).
18. L. A. Davis, C. P. Chou, L. E. Tanner and R. Ray, Scripta Met. **10**, 937 (1976).
19. A. Kursumovic, M. G. Scott, E. Girt and R. W. Cahn, Scripta Met. **14**, 1303 (1980).
20. D. Weaire, M. F. Ashby, J. Logan and M. S. Weins, Acta Met. **19**, 799 (1979).

21. D. Turnbull, Contemp. Phys. 10, 473 (1969).
22. R. Becker and W. Döring, Ann. Phys. 24, 719 (1935).
23. T. Matsumoto and R. Maddin, Acta Met. 19, 725 (1971).
24. J. W. Cahn, Acta Met. 4, 449 (1956).
25. W. A. Johnson and R. F. Mehl, Trans. AIME 135, 416 (1939).
26. H. S. Chen, Rep. Prog. Phys. 43, 355 (1980).
27. H. Palmer, S. Fick and M. Rosen (in press).

OXIDATION RESISTANCE OF A FINE-GRAINED RAPIDLY SOLIDIFIED 18-8 STAINLESS STEEL

G. J. Yurek

The H. H. Uhlig Corrosion Laboratory
Massachusetts Institute of Technology
Cambridge, MA 02139

ABSTRACT

A fine-grained, rapidly solidified 18-8 stainless steel (AISI 303) exhibited superior resistance to oxidation under both cyclic and isothermal conditions compared with a conventional wrought alloy of the same composition. The enhanced resistance to oxidation is attributed to three factors: (1) the formation and growth of protective scales is promoted by the fine alloy grain size ($\leq 10\mu\text{m}$) and by the presence of a dispersion of fine MnS precipitates in the steel matrix, (2) scale adherence is increased by the formation of intrusions of oxide from the external scale into the alloy, which form along closely-spaced alloy grain boundaries and probably around the dispersed phase, and which act to key the scale mechanically to the alloy, and (3) growth stresses in the scales are reduced by the formation of scales of uniform composition, which are promoted by the uniform composition of the alloy. Modification of the microstructures of 18-8 stainless steels through rapid solidification processing appears to allow an increase in operating temperature of at least 25°C under cyclic oxidation conditions and about 75°C under isothermal conditions.

INTRODUCTION

Resistance of an alloy to oxidation at elevated temperatures requires the development of a protective scale on the alloy surface. A protective scale is one that provides an effective barrier between the alloy and its environment. To be an effective barrier requires that solid-state diffusion of cations and anions through the scale be very slow. Because scales that meet the latter requirement usually comprise Cr_2O_3 , Al_2O_3 or SiO_2 , many structural alloys and coating compositions are designed to form surface scales of these oxides at elevated temperatures. A second requirement that must be fulfilled for an oxide scale to be protective is that it adhere tightly to the alloy substrate both during isothermal exposure to a high-temperature environment and under conditions wherein the temperature is cycled between low and high temperatures.

Although most studies of the oxidation behavior of alloys focus on the effects of the environment and alloy composition on oxidation resistance, the structure of an alloy can also play a very important role in the development of protective scales. As described in a recent paper [1], the combination of a stable, fine alloy grain size, a fine, uniform dispersion of nonmetallic or intermetallic inclusions and a uniform alloy composition, all of which may be achieved through rapid solidification processing, should provide an excellent microstructure for oxidation resistance. The objective of this paper is to describe the oxidation resistance of a fine-grained solidified 18-8 stainless steel that contained a dispersion of fine nonmetallic precipitates.

EXPERIMENTAL

A rapidly solidified 303 stainless steel powder, which is designated 303RS in this paper, was prepared by Pratt & Whitney Aircraft by forced convective cooling in He of centrifugally atomized droplets. Particles that were -140 mesh were consolidated by hot extrusion at 900°C with a 10:1 reduction in area. Samples of the consolidated bar were prepared for oxidation experiments by annealing for 6h at 1000°C to stabilize the microstructure. The same heat treatment was given to specimens of conventional, wrought 304 and 310 stainless steels (designated herein as 304W and 310W). The composition of the three alloys are given in Table 1.

Table 1. Compositions of Steels Employed in this Investigation

Steel	Composition, Wt Pct										
	C	Mn	P	S	Si	Ni	Cr	Mo	Co	Cu	N
304W	0.04	1.62	0.033	0.016	0.13	8.78	18.28	0.32	0.19	0.26	0.045
303RS	0.059	1.60	0.028	0.34	0.62	8.68	17.31	0.37	0.15	0.78	0.032
310W	0.06	1.64	0.028	0.006	0.52	19.90	25.0	0.18	0.16	0.16	0.074

After annealing, the specimens were polished through 6 μ m diamond paste. Cyclic oxidation experiments were conducted by inserting the specimens into a furnace at 900°C in pure oxygen for 20h, quenching the specimens to room temperature in air, measuring the change in weight (Δm) and reinserting the specimens into the furnace. Isothermal oxidation tests at 900°C in pure oxygen were conducted using a thermogravimetric apparatus that employed an Ainsworth semi-microbalance as the weighing unit.

ALLOY MICROSTRUCTURES

The 303RS after the 1000°C anneal had a fine grain size (5.6 μ m average grain size) and contained a uniform dispersion of fine MnS precipitates (0.2 to 0.5 μ m diameter). The 304W and 310W alloys had grain sizes of 170 and 19 μ m, respectively. After 300h at 900°C, the 303RS had an average grain size of 8 μ m, which indicates considerable resistance to grain coarsening. The size and distribution of the MnS precipitates were virtually unchanged.

OXIDATION RESULTS

Results of the cyclic oxidation experiments for the three alloys are shown in Figs. 1-3 as plots of the weight change per unit area ($\Delta m/A$) versus time. Three separate experiments were conducted for each alloy.

The results in Fig. 1 for 304W appear quite variable; however, each specimen exhibited considerable spallation during these tests. Hence, the specimens that showed no apparent weight change after about 40h of exposure actually lost weight by spallation and regained weight upon subsequent oxidation. All specimens exhibited a decrease in cross-sectional thickness, which is perhaps a better indication of the degradation of the alloy by oxidation. The variability of the results presented in Fig. 1 is probably due to inhomogeneities in the 304W.

The 303RS exhibited considerable resistance to cyclic oxidation. Very little spallation was observed during cycling, thereby demonstrating that the plots in Fig. 2 yield a true indication of the oxidation resistance of this alloy; i.e., the oxidation rate decreased as time increased.

Data for the 310W alloy are shown in Fig. 3. Although the 310W contains more Cr and Ni than 303RS, the latter alloy exhibited similar, if not better, resistance to cyclic oxidation.

Data for the isothermal oxidation tests, which were obtained only for 303RS and 304W, are shown in Fig. 4. The test temperatures were 800, 900, 1000 and 1100°C. There was little difference in oxidation resistance at 800 and 900°C. Both alloys exhibited relatively good resistance to oxidation at these temperatures, although the 304W did exhibit some oxide breakdown at 900°C. At 1100°C, both alloys oxidized rapidly. Although the 304W also oxidized rapidly at 1000°C, the 303RS exhibited good resistance to oxidation at this temperature (the latter result was reproducible; the curve shown in Fig. 4 for the 303RS at 1000°C represents the fastest oxidation kinetics observed for this alloy under these conditions).

The maximum recommended operating temperature for an 18-8 stainless steel under cyclic conditions is usually specified to be 875°C[2]. The 303RS alloy used in this study exhibited excellent resistance to cyclic oxidation at 900°C, and thus, it appears that the maximum operating temperature of an 18-8 stainless steel under cyclic conditions can be increased by at least 25°C through modification of the alloy microstructure. The maximum recommended operating temperature for an 18-8 stainless steel under isothermal conditions is usually specified to be 925°C. The 303RS steel exhibited very good resistance to oxidation under isothermal conditions up to 1000°C, which is an increase of 75°C in the maximum operating temperature.

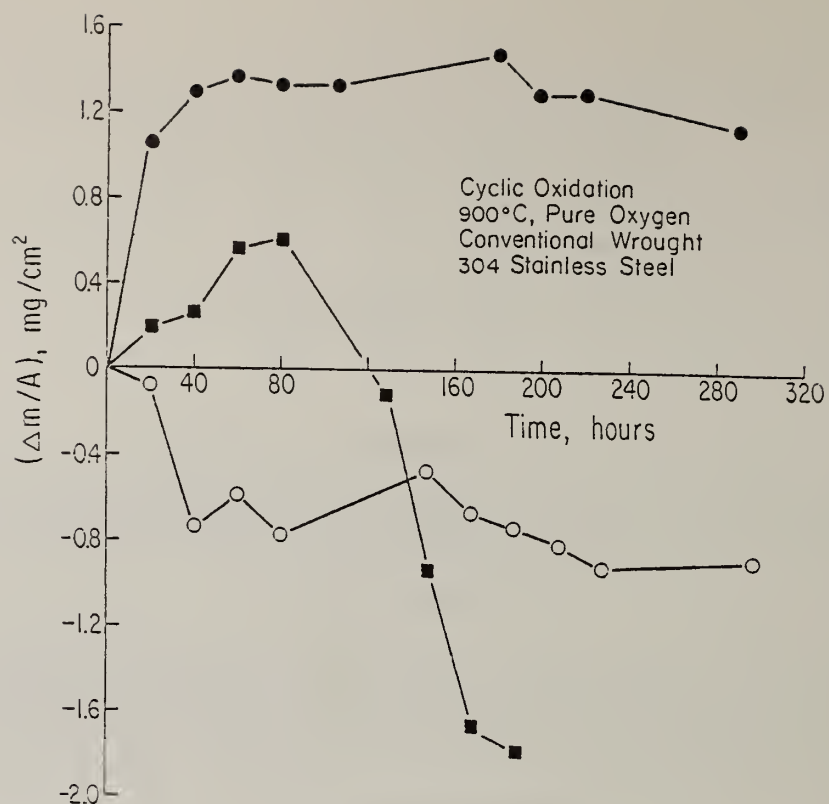


Figure 1. Kinetics of the cyclic oxidation of a 304 stainless steel. Data for three separate experiments are depicted.

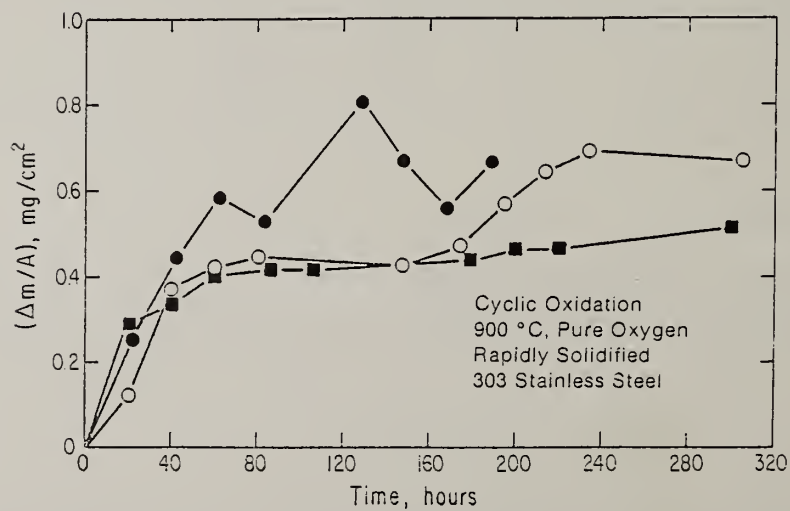


Figure 2. Kinetics of the cyclic oxidation of a fine-grained, rapidly solidified 303 stainless steel. Data for three separate experiments are depicted.

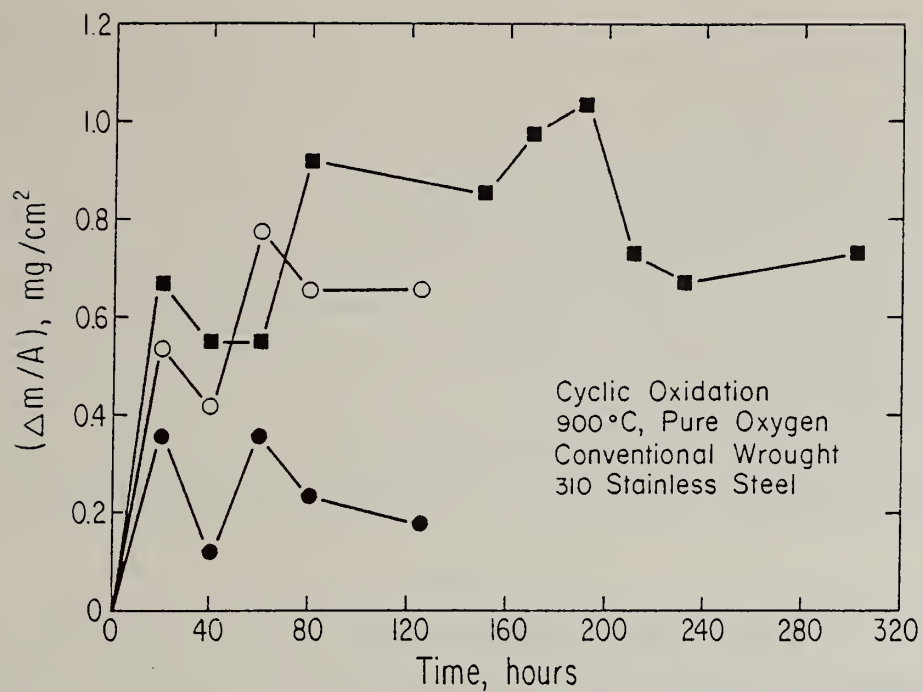


Figure 3. Kinetics of the cyclic oxidation of a 310 stainless steel. Data for three separate experiments are shown.

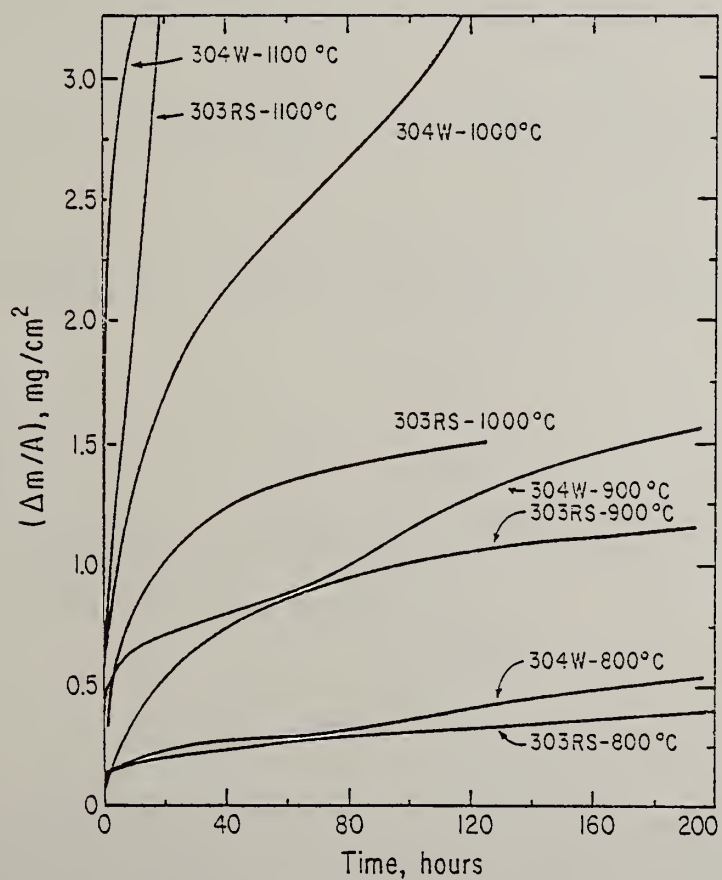


Figure 4. Isothermal oxidation kinetics for 304W and 303RS stainless steels.

The mechanisms of the oxidation of the 303RS were discussed in detail in a recent paper [1]. In brief, the fine grain size of this alloy appears to promote the formation of protective, Cr_2O_3 -rich scales by preferential formation of Cr_2O_3 over grain boundaries and by rapid grain boundary diffusion of Cr from the interior to the surface of the alloy. Although the alloy contains only 0.6wt% Si, SiO_2 forms in a relatively short time along the alloy/scale interface, which acts as a secondary barrier between the alloy and the gas phase. The SiO_2 also forms as intrusions from the external scale into the alloy along the closely spaced alloy grain boundaries. These oxide intrusions may act to mechanically key the oxide scale to the alloy surface, thereby explaining the very good adherence of the oxide scale to the alloy. The major role played by the MnS precipitates is probably pinning of the alloy grain boundaries which stabilizes the fine grain size at high temperatures. The MnS may also contribute to scale adhesion by helping to promote a convoluted alloy/scale interface over alloy grains. Finally, the uniform composition of the alloy appears to promote formation of external scales of uniform composition, which would tend to decrease stresses and stress gradients in the scale, thereby enhancing the ability of the scale to resist spallation.

ACKNOWLEDGEMENTS

This work was supported by a NASA grant (contract #NSG-7645) through the Materials Processing Center at M.I.T.

REFERENCES

- [1] G.J.Yurek, D.Eisen and A.Garratt-Reed, Met Trans A, 1982, vol. 13A, p. 473.
- [2] L.A.Morris, Handbook of Stainless Steels, D. Peckner and I.M.Bernstein, eds., McGraw-Hill, N.Y., 1977, p. 17-1.

L. V. Meisel, P. J. Cote, and D. M. Quinn

U.S. Army Armament Research and Development Command
 Large Caliber Weapon Systems Laboratory
 Benet Weapons Laboratory
 Watervliet, NY 12189

ABSTRACT

Methods are described for preparing fine powders of amorphous and other metastable alloys by rapid deposition from electroless baths. Five different alloys have been prepared by these methods and characterized by means of x-ray diffraction, SEM, and DTA techniques. The properties and transformation kinetics of these alloys are described. In particular, some features of non-isothermal transformation kinetics and incubation effects are discussed.

Introduction

One of the principal areas of interest in the field of rapid solidification processing is the preparation of metastable phase alloy powders and their consolidation into bulk components. A. Wurtz [1] in 1844 was apparently the first to report on the preparation of metastable phase powders; his method involved the chemical reduction of nickel ions in aqueous solutions of sodium hypophosphite. Later work on sodium hypophosphite solutions by Brenner and Riddell [2] at NBS led to the development of the electroless plating process; related work on electrolytic plating by Brenner et al [3] led to the preparation of the first metallic glass, NiP. Electroless deposition of nickel, cobalt, copper, and palladium is now routine in the plating industry. Commonly used reducing agents include hypophosphite, formaldehyde, hydrazine, borohydride, and amine borane.

In this paper we describe some characteristics of powders which we prepared by inducing decomposition of a variety of electroless baths. Five different metastable alloy powders were obtained in this manner: amorphous and crystalline phases of NiP, and crystalline phases of NiWP, CoP, CoWP, and NiB.

Our most extensive results concern the transformation kinetics of NiP alloy powders using differential scanning calorimetry. Isothermal transformation data are in excellent agreement with Johnson-Mehl-Avrami (JMA) theory [4]; i.e., the degree of reaction $x(t)$ at time t is given by

$$x(t) = 1 - \exp[-(k(T)t)^n] \quad (1)$$

where the rate constant $k(T)$ at temperature T is given by

$$k(T) = A \exp(-E/RT), \quad (2)$$

with A constant, $E = RT$ is an activation energy for the transformation process, R is the gas constant, and the JMA exponent n is determined by the details of the transformation process.

Constant heating rate results are well described by

$$x(T) = 1 - \exp[-W^n] \quad (3)$$

where

$$W(T) \cong W_0 + \frac{k(T)T^2}{T\dot{\theta}} \left[1 - 2 \frac{T}{\theta} + 6 \left(\frac{T}{\theta} \right)^2 \right] \quad (4)$$

with $T = T_0 + \dot{T}t$, \dot{T} is the (constant) heating rate, $W_0 = [-\ln(1 - x(T_0))]^{1/n}$ which is zero if no reaction has occurred at $t = 0$. Equations (3) and (4) are deduced in Reference [5] for systems governed by JMA theory in the isothermal case and where the degree of reaction is determined by the number of atom movements; equivalent results were obtained by Henderson [6] on the assumption that the reaction rate in the general case is given by the JMA isothermal theory. The Kissinger equations, which form the basis of the Kissinger method [7], can also be deduced from Eqs. (3) and

(4). Thus, References [5] and [6] provide a theoretical basis for the analysis of constant heating rate transformation kinetics in many systems and, in particular, for the powders analyzed here.

Interesting incubation effects, apparently unrelated to the formation of critical nuclei, are observed in the isothermal and constant heating rate transformation of metastable crystalline NiP powders, while no such effects are apparent in the transformation of the a-NiP powders.

Experimental

Sample Preparation

Powder samples of NiP [2], NiB [8], CoP [9], NiWP [10], and CoWP [11] were prepared from solutions based on standard electroless baths operated under conditions which produce spontaneous decomposition (i.e., deposition throughout the entire volume of the bath). The concentration of the reducing agent was doubled relative to standard baths, high bath temperatures were maintained ($T > 96^\circ\text{C}$) and additions of bath stabilizers were omitted in the electroless baths.

Powder samples of the same alloys were also prepared by seeding the baths with low concentrations ($\sim .001\text{ M}$) of PdCl_2 following the method of Randin et al [12]. The seeding process apparently results in a colloidal suspension of palladium metal from the reduction of palladium ions by the hypophosphite, which in turn leads to rapid deposition throughout the entire bath, as with spontaneous decomposition. We find that this deposition can be interrupted by filtering out the palladium suspension. No significant differences were found between samples prepared by either method.

Structural Characterization

Sample compositions were determined by standard wet chemistry methods. Debye-Scherrer x-ray analysis was used to determine alloy phases. Powder morphology was examined by scanning electron microscopy.

Transformation Kinetics

The kinetics of the phase transformations were studied using isothermal and constant heating rate differential scanning calorimetry (DSC) employing a Dupont 990 Thermal Analysis System. Aluminum sample pans and an argon atmosphere were used in all runs. An empty sample pan served as a reference.

The isothermal transformation kinetics data were obtained from the time dependence of the DSC output for a series of temperatures. The DSC output is assumed to be proportional to the reaction rate dx/dt ($I_{\text{DSC}} = cdx/dt$, $c = \text{constant}$) so the degree of reaction $x(t)$ is given by $x(t) = s(t)/S$ where $s(t) = \int I_{\text{DSC}} dt = c[x(t) - x(0)]$ and $S = s(\infty)$. The technique for extracting the time exponent n and $k(T)$ in an isothermal experiment described by Eq. (1) is to plot $\ln[-\ln(1 - s(t)/S)]$ vs. $\ln t$ so that n is given by the slope and $k(T) = t_0^{-1}$ where $\ln t_0$ is the $\ln t$ intercept.

The constant heating rate data were analyzed by the Kissinger method based on Eqs. (3) and (4) as described in References [5] and [6]. Thus, the activation energy for the transformation process is given by the slope of the plot of $\ln(T/\dot{T}_M)$ vs. \dot{T}_M^{-1} where \dot{T} is the heating rate and T_M is the temperature at the maximum reaction rate. Corrections are required to account for incubation effects and to account for thermal lag effects which are inherent with this method. The thermal lags were established empirically using the Curie temperature of Ni and the melting point of Sn.

Results and Discussion

Structural Characterization

Sample compositions for the powders prepared from electroless baths are given in Table 1.

Table 1. Compositions in at% for powders prepared from electroless baths. a-NiP and x-NiP refer to amorphous and metastable crystalline phases, respectively. The other as-prepared powders are in metastable crystalline phases.

a-NiP	x-NiP	NiWP	CoWP	NiB	CoP
Ni:80 P:20	Ni:85 P:15	Ni:84 W:5 P:11	Co:92 W:3 P:5	Ni:80 B:20	Co:92 P:8

We find that the compositions of the NiP powder samples are extremely uniform and can be controlled by maintaining constant bath pH. A measure of the uniformity in composition is given by the positions of the DSC transformation peaks which are the same for all NiP samples from a given bath. In addition, the width of the DSC peaks are close to the theoretical widths, which further reflects the homogeneity of the powder compositions. (Examples of DSC peaks are shown in Figure 5.) On the other hand compositions of the other powders were not precisely controlled by bath pH so that inhomogeneous powders, which exhibit complex DSC traces, were obtained frequently.

X-ray diffraction data indicate that, except for a-NiP, the as-deposited powders are metastable solid solutions of the various constituents. The as-deposited nickel and cobalt alloys are found to have fcc and hcp crystal structures, respectively.

Scanning electron microscopy (SEM) reveals that the powders have similar morphology; being comprised of clusters of attached spheres with diameters ranging from $\sim 1 \mu$ to 10μ , and having a wide distribution of cluster sizes, ranging from individual spheres to clusters with overall dimensions up to $\sim 100 \mu$. Figures 1 and 2 show samples of amorphous and metastable crystalline NiP powders which are typical of all the powders and were taken from the samples that were used for the detailed studies of transformation kinetics.



Figure 1. SEM micrograph of amorphous NiP powder sample prepared from an electroless bath.



Figure 2. SEM micrograph of metastable crystalline NiP powder sample prepared from an electroless bath.

Figure 3 is an optical micrograph showing sections of typical x-NiP spheres. There are laminations evident within the spheres. Such features are characteristic of alloy deposition from aqueous baths although no satisfactory explanation yet exists to their origin [13]. This may be due in part to the fact that the detailed structure of the laminations varies widely from one alloy to another. As noted earlier, the compositions of the NiP powders appear remarkably uniform which seems to rule out composition fluctuations as the origin of the laminations. Changes in crystallographic orientation, on the other hand, offer a consistent explanation for the observed features in these powders.

Figure 4 is a SEM micrograph of a section x-NiP spheres which was etched with modified Fry's etchant (HNO_3 , HCl , and CuCl_2). The boundaries between the laminations shown in Figure 3 appear to have been completely dissolved. This suggests that a thin impurity layer, possibly containing hydroxides or hydrated oxides, are present at the interface of the laminations, since such impurities are commonly found in electrodeposits and are soluble in acids.



2000X

Figure 3. Optical micrograph showing sections of metastable crystalline NiP spheres.

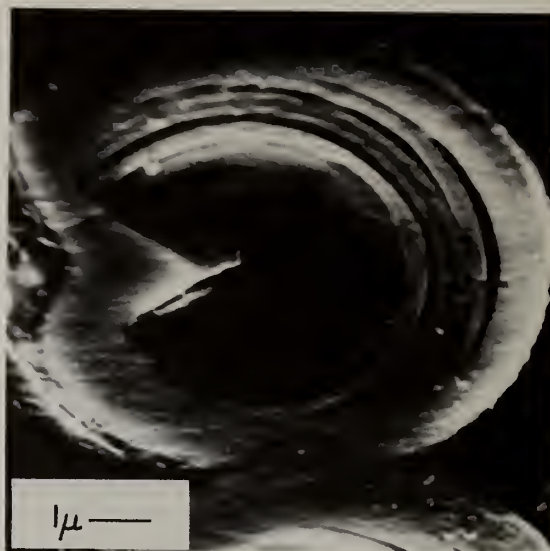


Figure 4. SEM micrograph of etched section of a metastable crystalline NiP sphere.

Transformation Kinetics

Isothermal and constant heating rate studies of transformations in amorphous and metastable crystalline NiP powders were performed using DSC methods. The isothermal data are well described by the JMA equation, deduced from Eqs. (1) and (2). The constant heating rate data are well described by Eqs. (3) and (4) and were analyzed by the Kissinger method. Activation energies, preexponential factors, and JMA exponents n describing the transformation of a-NiP, as-prepared x-NiP, and preannealed (as described later) x-NiP powders, deduced from isothermal and constant heating rate DSC studies, are summarized in Table 2.

Table 2. Kinetic parameters for amorphous (a-NiP), as-prepared metastable crystalline NiP (x-NiP), and preannealed powders, obtained from isothermal and constant heating rate DSC measurements. \bar{n} represents the mean value of the JMA exponent.

Sample	Isothermal			Constant \dot{T}	
	E (kcal/mole)	$\ln A$ (A in sec^{-1})	\bar{n}	E (kcal/mole)	$\ln A$ (A in sec^{-1})
a-NiP	38.6	30.4	2.3	40.7	32.5
x-NiP	52.7	39.2	3.09	55.5	41.0
Preannealed x-NiP				54.2	40.4

A feature of transformations in the as-prepared x-NiP powders which is not observed in the a-NiP powders is an incubation time, t_{inc} , representing a time delay before any indication of a transformation is observed in an isothermal anneal. We find that t_{inc} is apparently controlled by an activation process with activation energy $E = 66.6$ kcal/mole for x-NiP.

In the isothermal experiments, the DSC output (dx/dt) is zero for $t \leq t_{\text{inc}}$ and increases from zero for $t > 0$, proceeds through a maximum, and returns to zero. Following standard procedures, the DSC traces for a series of temperatures were integrated and yield straight lines over most of the range in plots of $\ln [-\ln(1-s/S)]$ vs. $\ln(t-t_{\text{inc}})$. The n values range from 2.8 to 3.2 with a mean \bar{n} of 3.09 in the x-NiP powders and range from 2.1 to 2.5 with a mean \bar{n} of 2.3 in the a-NiP powders.

In the constant heating rate experiments, we found that a modification of the standard Kissinger method is required to account for the effects of incubation times. A demonstration of these effects in the crystalline NiP powders is given in Figure 5 which is a plot of the DSC output vs. temperature for a heating rate of 50K/min. The theoretical curve was obtained from Eqs. (3) and (4) with values for the parameters E , $\ln A$, and \bar{n} obtained from the isothermal measurements. The difference between the theoretical curve and the data on the as-prepared powders is substantial. The data show a maximum transformation rate at $T_M = 636\text{K}$ and a full width at half maximum (FWHM) of approximately 8K while the corresponding theoretical values are 631K and 11.7K.

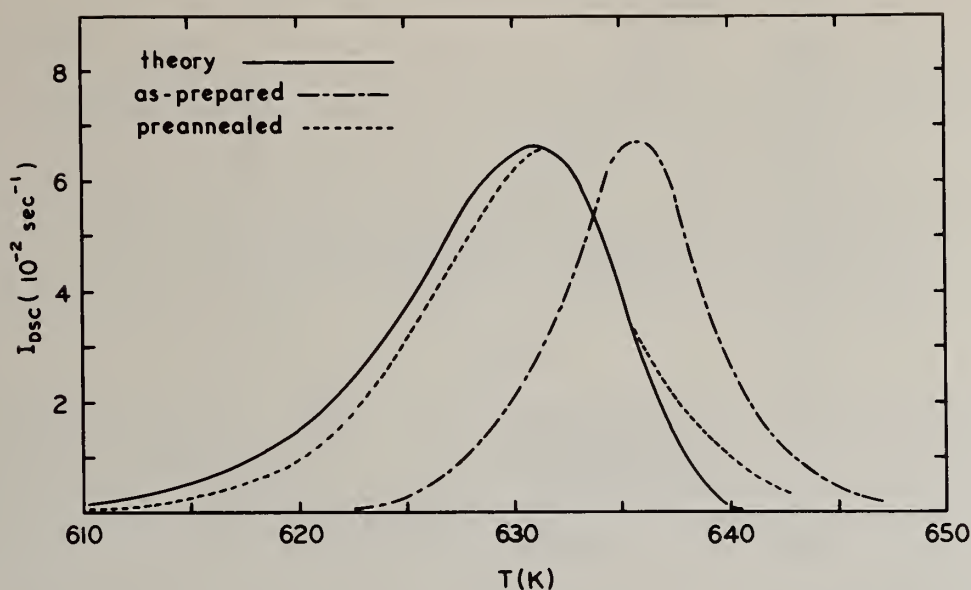


Figure 5. Experimental and theoretical DSC trace at 50K/min for metastable crystalline NiP powders. Parameters used in the theoretical curve were obtained from isothermal data. Area of theoretical curve is normalized to unity. Peak heights of experimental curves were scaled to match the theoretical curve.

The small observed value for FWHM reflects a high degree of uniformity in sample composition as we suggested earlier. The fact that the FWHM is actually less than predicted and T_M higher than predicted suggests that incubation effects are responsible since they act to delay the onset of the transformation. The isothermal data are routinely corrected for the incubation process while no such corrections are made in the standard Kissinger method. We found that if we preannealed x-NiP samples at $T = 568K$ for 15 minutes (i.e., the incubation time at 568K) before a constant heating rate study, incubation effects were eliminated, i.e., the data on the preannealed x-NiP sample are seen from Table 2 and Figure 5 to be in excellent agreement with the theoretical predictions. The elimination of incubation effects in the constant heating rate runs by means of isothermal preanneals suggests that the standard model for the formation of critical nuclei [14] cannot explain incubation in the x-NiP powders.

Another illustration of incubation effects is given in Figure 6 which shows Kissinger plots of data from as-prepared and preannealed samples. The parameters E and $\ln A$ were obtained from least squares fits to the data. It can be seen from Table 2 that preannealing through t_{inc} leads to improved agreement with the isothermal parameters.

The kinetic parameters of the NiP powders reveal considerable differences in the nature of the transformations of the amorphous metastable crystalline phases. The JMA exponent of the crystalline powders is near 3 which is associated with activated rate spherical growth on pre-existing nuclei [15]. The JMA exponent is closer to 2.5 in the amorphous powders, which is associated with diffusion controlled spherical growth with activated non-zero nucleation rate [15].

Besides yielding consistent values of the kinetic parameters describing the transformation of amorphous and metastable crystalline NiP, the excellent agreement between the results of the analyses by the isothermal method and the Kissinger method provides evidence of the appropriateness of the generalized form of the JMA theory as given in References [5] or [6] to non-isothermal heterogeneous reactions. Greer [16] obtained similar results in a detailed study of transformation kinetics in a-FeB; the basic assumptions in his numerical analysis are equivalent to those used in the generalization of JMA theory given in Reference [5]. A more complete presentation of the experimental results in x-NiP as well as an alternative derivation of Henderson's equations describing non-isothermal solid state reactions with more general starting assumptions are given in Reference [5].

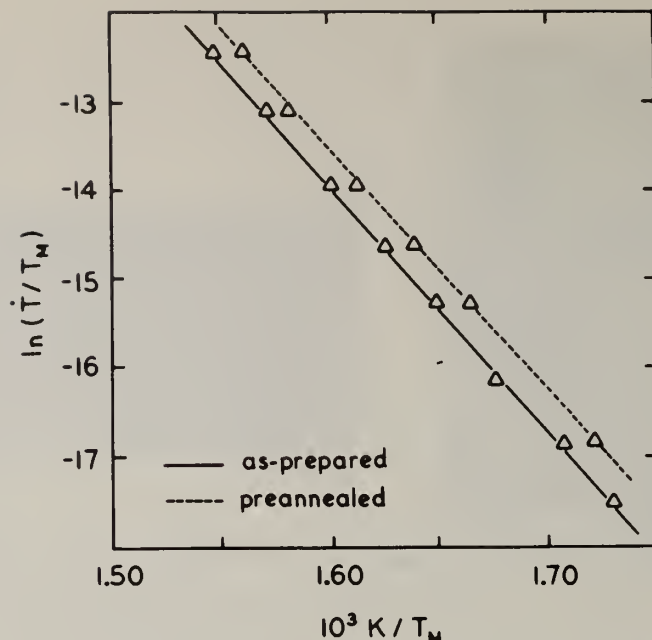


Figure 6. Kissinger plots for as-prepared and preannealed x-NiP powders. T unit is $Ksec^{-1}$ and T_M is in K.

Acknowledgements

We wish to thank many of our colleagues for their generous assistance: Mr. G. Capsimalis obtained the x-ray data, Mrs. T. V. Brassard, Mr. L. McNamara and Mr. C. Rickard obtained the micrographs; Drs. E. Chen and F. K. Sautter provided many helpful discussions on electrodeposition; and Ms. E. Fogarty was instrumental in the timely completion of the manuscript.

References

- [1] A. Wurtz, *Compt. Rend.* **18**, 702 (1844); **21**, 149 (1845).
- [2] A. Brenner and G. E. Riddell, *J. Res., Natl. Bur. Std.* **37**, 1 (1946).
- [3] A. Brenner, D. F. Couch, and E. K. Williams, *J. Res., Natl. Bur. Std.* **44**, 109 (1950).
- [4] W. A. Johnson and R. F. Mehl, *Trans. AIME*, **135**, 416 (1939) and M. Avrami, *J. Chem. Phys.* **7**, 1103 (1939).
- [5] L. V. Meisel and P. J. Cote, *Acta Met.*, to be published.
- [6] D. W. Henderson, *J. Non-Crystalline Solids* **30**, 310 (1979).
- [7] H. F. Kissinger, *J. Res. Natl. Bur. Std.* **57**, 217 (1957); *Anal. Chem.* **29**, 1702 (1957).
- [8] T. Watanabe and Y. Tanabe, *Mat. Sci., and Eng.*, **23** 97 (1976).
- [9] A. Brenner and G. E. Riddell, *J. Res., Natl. Bur. Std.* **39**, 385 (1947).
- [10] F. Pearlstein and R. Weightman, *J. Electrochem. Soc.* **6**, 427 (1968).
- [11] F. Pearlstein and R. Weightman, *Plating*, **54** 1 (1967).
- [12] J. P. Randin and H. E. Hintermann, *Plating*, **54**, 523 (1967).
- [13] A. Brenner, *Electrodeposition of Alloys*, Academic Press, New York, (1963), Chapter 7.
- [14] J. H. Holloman and D. Turnbull, *Prog. Metal. Phys.* **4**, 333 (1953).
- [15] See for example, V. Raghavan and M. Cohen in *Treatise on Solid State Chemistry*, Ed. N. B. Hannay, Plenum Press, New York (1975).
- [16] A. L. Greer, *Acta Met.*, **30**, 171 (1982).

PREPARATION OF GLASSY METALS AS POWDERS VIA HYDROGEN EMBRITTLEMENT*

B.C. Giessen, S.H. Whang and F. Dabkowski

Materials Science Division, Institute of Chemical Analysis
and Department of Chemistry
Northeastern University, Boston, MA 02115

ABSTRACT

Preparation of metallic glasses by melt spinning readily yields metastable materials in the form of a homogeneous product; however, the alloy ribbons are frequently ductile and are thus not directly amenable to the pulverization process required to produce powders suitable for further P/M processing. Extending the well-known metals processing technique of pulverization by reversible hydrogen embrittlement to metallic glasses (and probably other RSR produced metastable alloys), such alloys can be prepared as powders by loading them with hydrogen at pressures of 5-20 MPa in an autoclave or high pressure ball milling chamber. Hydrogen charging is generally done at elevated temperature to provide activation while comminution is carried out at room temperature. The sample is then unloaded by evacuation of hydrogen before exposure to air. Particulates are screened and studied by XRD, DSC and microscopy. This approach has also been used and described in a recent paper by Maeland and Libowitz. The paper describes preliminary results on the pulverization of glassy $\text{Fe}_{78}\text{B}_{12}\text{Si}_{10}$.

Introduction

Glassy alloys can be prepared in ribbon form as well as in the form of atomized powders using rapid liquid quenching techniques. RSR processing by solid-substrate quenching methods such as melt spinning is generally preferable to quenching methods which utilize heat conduction by gases, such as quench-atomization, due to the higher cooling rates and greater product homogeneity which distinguish the former techniques over the latter; ribbon material tends to have a more uniform microstructure than powders which have microstructures with wide qualitative and quantitative differences, depending on the droplet size and other aspects of their quenching history [1].

However, in order to reap the benefits of melt spinning while at the same time being able to apply well-established P/M techniques to the consolidation of melt spun ribbon alloys, the quenched material must first be converted to powder without destroying its desirable properties such as ductility and toughness. To accomplish this and to pulverize ductile metallic glasses or other ductile, RSR processed alloys into powders with unchanged mechanical properties appears to be a problem that, at present, is still solved only incompletely.

The high bend ductility of many RSR alloys makes it very difficult to pulverize them into fine particulates via a mechanical treatment unaided by embrittlement. The following methods are therefore candidates for a solution to this problem:

- a) Melt spinning into small particles, e.g., by quenching on a profiled substrate configured to produce flake shaped particles. It is not clear whether a large scale preparation facility based on this principle is viable on a long-term operation basis.
- b) Cutting or other size reduction by shearing action. An approach to prepare alloy flakes by this method is under study.
- c) Pre-comminution embrittlement by physical means. Low temperature embrittlement is an obvious candidate method; however, it is not known which ductile glasses, if any, can be embrittled enough to permit sufficient size reduction.
- d) Reversible chemical embrittlement by hydrogenation. This method, patterned after the well known process for producing powders of ductile metals such as tantalum by reversible hydrogenation, is a major candidate for powder production and its application is discussed here.

Attempts at comminution in hydrogen atmosphere are based on the prior observation that some Fe based glassy alloys become brittle when charged cathodically with hydrogen [2, 3] and on many studies of hydrogen absorption in glassy metals [4, 5] where reversible embrittlement was reported. However, in these studies [5] it was also found that even in hydride forming glassy alloys such as Zr-Ni there is no pressure plateau in the pressure-concentration isotherms similar to that in hydride-forming crystalline metal-hydrogen systems. In addition, Fe based alloys do not form equilibrium hydrides at low pressures. As a result, the concentrations of hydrogen in Fe base glassy metals that are needed for embrittlement require application of high hydrogen equilibrium pressures. Recently, embrittlement of Fe base glassy metals by low hydrogen concentrations added before melt spinning has been reported [6]; also, Maeland and Libowitz [7] have demonstrated that several Fe based glassy alloys could be pulverized under high hydrogen pressures (10-15 MPa). In the following, we will describe a similar experiment conducted in this laboratory in an effort to produce powders from glassy ribbon material.

Experiments

Figure 1 shows the laboratory scale hydriding system used for comminution experiments. It consists of a commercial autoclave with a magnetically activated hammer (originally intended in this system for use as a stirrer), a vacuum system and a hydrogen pressurizing system. The autoclave can be operated at a maximum pressure level of 5000 psi (34.5 MPa) at 343°C and at correspondingly lower pressures at higher temperatures. Glassy metal samples are charged with hydrogen in the autoclave by a series of cyclic heatings under high pressure. Samples activated and hydrogenated at high temperature are subsequently comminuted at room temperature. After comminution, hydrogen is removed from the samples by evacuating the autoclave. Following removal from the autoclave the powders are screened using graduated sieves. Parameters and typical results are presented in the next section.

Results and Discussions

A small amount (about 0.5g) of glassy $\text{Fe}_{78}\text{B}_{12}\text{Si}_{10}$ alloy ribbons was cut into pieces 0.5 to 1.5cm in length and placed in the autoclave. (Only small quantities were used as the hammer system presently used becomes clogged by larger sample quantities.) At the start of each thermal cycle hydrogen with pressures of about 1000 psi (6.9 MPa, as measured at room temperature) was admitted and the temperature was then raised to 400°C (i.e., to 127°C below the glass transition temperature which is 527°C for this alloy [8]). Two or three thermal cycles, each lasting about 30 minutes, were then made. Starting during the last cycle and continuing after cooling, the sample was comminuted for a specified time, typically of the order of 20 hrs.

To test whether the resulting embrittlement was indeed due to hydrogenation, similar cyclic heatings were carried out under vacuum or, alternatively, under argon gas, using the same loading conditions; no alloy embrittlement was found in the ribbons after these treatments. This rules out the possibility of embrittlement being due to partial crystallization or structural relaxation during the cyclic heating and demonstrates the need for the presence of hydrogen during the embrittlement heating cycles. It can be assumed that cyclic heating in hydrogen generates microcracks and hence produces fresh surfaces and facilitates hydrogen absorption.

The powders produced were checked by X-ray diffraction and found to be amorphous. After screening with standard sieves the powders exhibited the size distributions shown in Table 1. It was noted that this size distribution is not Gaussian but that alloy fraction quantity is related to sieve size by a simple linear relationship. This unusual size distribution was also found by Maeland and Libowitz [7], and appears to be independent of the hydrogen pressure which was 7-10 MPa in the present work, i.e., lower than that used by these workers (12-15 MPa) [7]. This unfavorable size distribution is assumed to be due to the relatively soft hammering mechanism used which is clearly insufficient; a ball milling system operating under high hydrogen pressure can be expected to permit the production of RSR materials in larger quantities and hopefully, with better size distributions of the RSR powders (such a system is now under construction).

It appears that Fe alloy glass powders of small particle sizes adequate for P/M work can be prepared by this method; the major question remaining to be answered is how the toughness and ductility of metallic glasses thus pulverized and subsequently consolidated compares with the corresponding properties of the original, as-spun materials. This study must await the availability of adequate amounts of powdered material.

Acknowledgements

We are grateful for support of this work by the Army Research Office, Durham, Contract DAAG-29-80-0088 under subcontract with M.I.T.

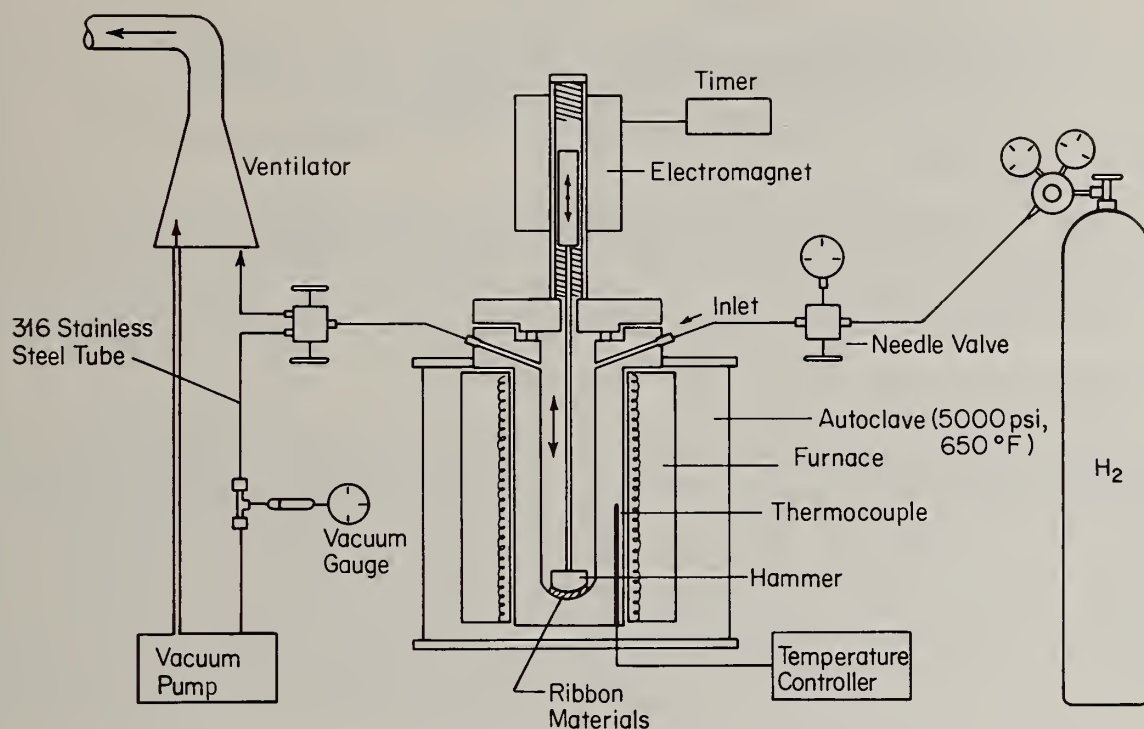


Fig. 1 Schematic diagram of system used for hydrogenation and comminution of Fe-based amorphous ribbons.

Run No.	+250(μm)	$\frac{-250}{+125}$	$\frac{-125}{+63}$	$\frac{-63}{+45}$	$\frac{-45}{+38}$	-38
1	54.7	30.7	9.9	2.8	0.7	1.2
2	56.9	27.7	9.6	2.9	2.9	---

Table 1

Size distribution (in wt%) of $\text{Fe}_{78}\text{B}_{12}\text{Si}_{10}$ glassy metal powders after hydrogen charging at 1000 psi at 400°C and comminution for 20 hrs.

References

- [1] R.H. Patterson, II, in Rapidly Solidified Amorphous and Crystalline Alloys, MRS Symposia Proceed. Vol. 8, B.H. Kear, B.C. Giessen and M. Cohen, Eds., North-Holland N.Y. (1982) p. 123.
- [2] M. Nagumo and T. Takahashi, Mat. Sci. Eng., 23 (1976) 257.
- [3] S. Ashok, N.S. Stoloff, M. Glicksman and T. Slavin, Scripta Met., 15 (1981) 331.
- [4] F. Spit, K. Blok, E. Hendriks, G. Winkels, W. Turkenburg, J.W. Drijver and S. Radelaar, Proc. 4th Int. Conf. on Rapidly Quenched Metals, Sendai, Japan, 2 (1981) 1635.
- [5] K. Aoki, A. Horata and T. Masumoto, Proc. 4th Int. Conf. on Rapidly Quenched Metals, Sendai, Japan, 2 (1981) 1649.
- [6] H. Shahani, H. Soderhjelm and M. Nygren, Rapidly Solidified Amorphous and Crystalline Alloys, MRS Symposia Proceed., Vol. 8, B.H. Kear, B.C. Giessen and M. Cohen, Eds., North-Holland, N.Y. (1982) p.289.
- [7] A.J. Maeland and G.G. Libowitz, Mater. Lett., 1 (1982) p.3.
- [8] I.W. Donald and H.A. Davies, Phil. Mag. A42 (1980) 423.

*Communication No. 150 from the Institute of Chemical Analysis, Northeastern University, Boston, MA 02115

AN ARC FURNACE MELT SPINNER FOR THE RSR PROCESSING OF REFRACTORY AND REACTIVE ALLOYS*

S. H. Whang and B. C. Giessen

Materials Science Division, Institute of Chemical Analysis
and Department of Chemistry
Northeastern University, Boston MA 02115

ABSTRACT

Melt spinning is a convenient method for the preparation of RSR processed alloys; however, its most common forms use oxide crucibles such as quartz which introduces melting temperature limitations due to the softening temperature of the crucible material and crucible-melt reactions.

Cold hearth techniques are very desirable for the RSR processing of molten refractory or highly reactive elements. Following a design described in the literature, we have found arc melting to be convenient for small sample quantities. A two-chamber system has been built, with a small, non-consumable electrode arc melter in the upper chamber and a rotating copper quenching wheel located in the lower chamber directly underneath the cold hearth which is provided with an appropriate hole of small bore. After melting the alloy, a pressure differential is produced between the top and bottom chambers by a ballast tank and a thin stream of molten metal is quenched into a ribbon upon impingement on the wheel. Among alloys prepared as ribbons by this technique have been alloy glasses with high titanium content and $\text{Nb}_3(\text{Nb},\text{Si})$ alloys prepared as the metastable A15 type phase. Possible modifications of the basic design are discussed, including the use of alternative heat sources such as energy beam or induction melting.

Introduction

Melt spinning has become the technique of choice for the continuous production of rapidly solidified metals and alloys in ribbon form, and in the last decade melt spinning technology has substantially advanced in accordance with increasing requirements concerning the quality of ribbon or sheet materials. The basic melt spinning technique goes back to the method of Strange and Pim [1] in which a molten jet impinges onto a cold, rotating disk; most alloys of interest in RSR technology can be spun by this technique. An important component of the melt spinning system is the crucible; various crucible materials are in use depending on alloy properties. The preferred crucible material is silica; graphite, alumina, zirconia etc. have also been used. However, reactive alloys such as alloys rich in Ti and Zr or alloys with very high melting temperatures such as refractory alloys containing Nb, Ta, Mo, W, Re, Ru, Os, Rh, Ir, etc. cannot be readily melted and superheated using these crucible materials. Problems associated with these crucible limitations can be solved using a water cooled copper hearth as a crucible. Such a cold copper hearth and a rotating quenching wheel were first combined into an operational arc furnace melt spinner by Tutzauer et al. [2]. Use of cold-hearth arc melting of small alloy pellets combined with quenching by the hammer-and-anvil method as a way of avoiding crucible contamination has been described by Wang [3] and was subsequently used and discussed [4]; such a unit, provided with a pressure driven piston for alloy quenching, has been in continuous operation in our laboratory for a number of years. The following is a description of an arc furnace melt spinner constructed and in experimental use in this laboratory and a review of some experiments carried out with this unit.

Design Features and Operation

The Arc Melt Spinner

Figure 1 shows a schematic diagram of the laboratory scale arc melt spinner constructed at Northeastern University. The spinner system is made up of a main chamber, a vacuum system, inert gas supply system, a D.C. power system and an A.C. motor. The main chamber consists of two compartments: the top compartment, i.e., the melting section, contains an inert gas plasma arc electrode, a removable copper crucible, a gas inlet and a vacuum outlet. The bottom compartment includes a spinning disk made of copper or molybdenum, a ribbon guide pipe, a gas inlet and a vacuum outlet.

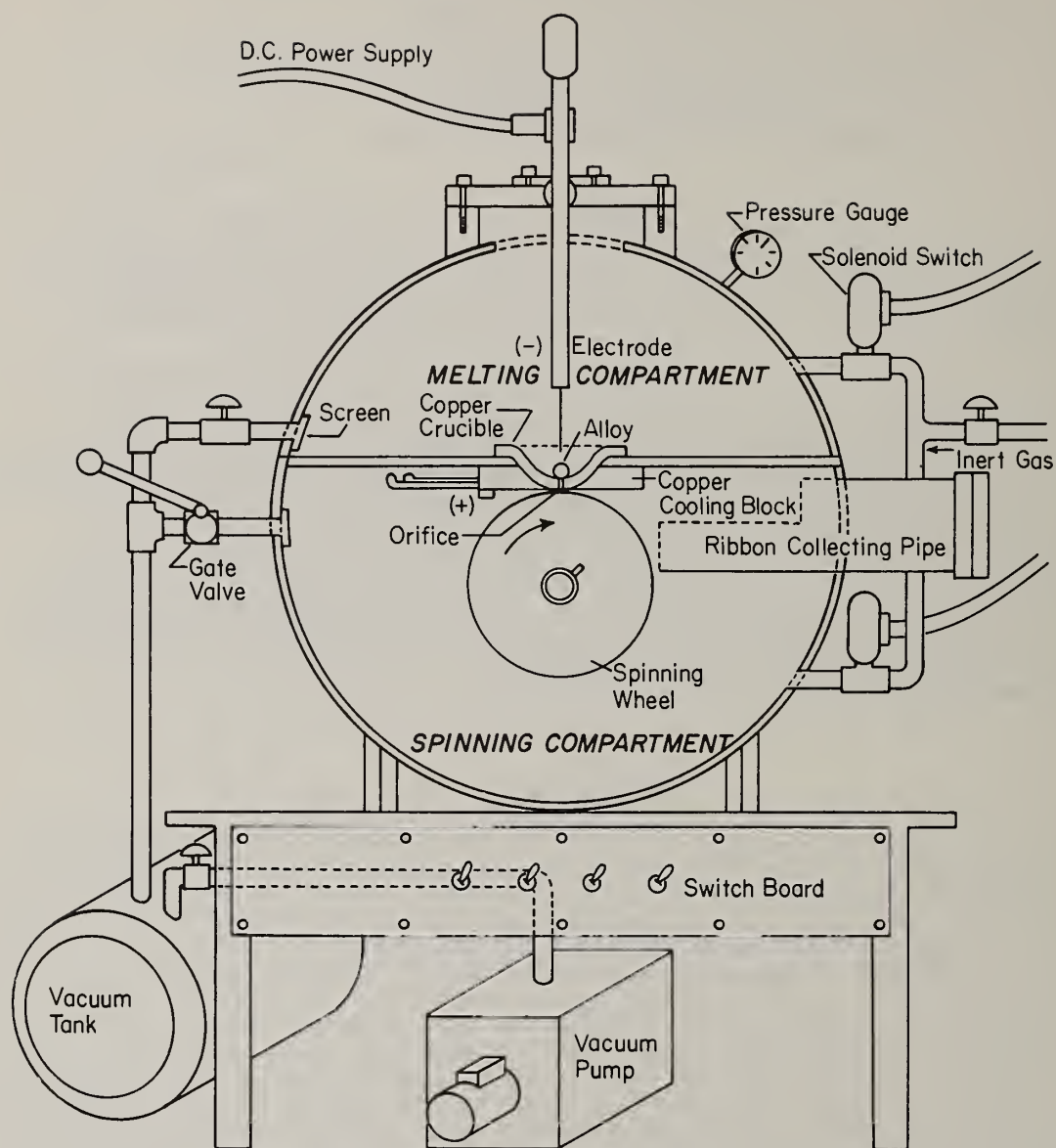


Fig. 1 Schematic diagram of the arc furnace melt spinner constructed at Northeastern University. A motor which drives the spinning wheel is located behind the main chamber.

Melting

A premelted alloy button ($\sim 0.5g$) is placed at the bottom of the copper crucible such that it covers the orifice centered in the crucible as shown in Fig. 1 and is melted using the arc electrode while both compartments are kept under argon atmosphere at equal pressures. The molten alloy is superheated to facilitate formation of a fine molten jet. This is particularly important for refractory alloys where the surface tension at the melting temperature is still too high to allow formation of a fine melt stream.

Spinning

The superheated melt is formed into a fine molten jet flowing through the orifice of the copper crucible by a pressure differential applied between the two compartments, either by rapidly pressurizing the melting compartment or depressurizing the spinning compartment. A stationary pressure gradient can be maintained during spinning as the molten alloy "plugs up" the orifice which is the only opening between the two compartments. In the design shown in Fig. 1 the spinning compartment is rapidly depressurized by opening a gate valve connecting an evacuated ballast tank to the spinning compartment. Spinning proceeds at that point and the spun ribbon is caught in a retrieving pipe dimensioned such that impingement of the ribbon on the back wall does not affect the quenching process.

Crucial Components and Dimensions

The operation of this system is determined by the same parameters critical in a melt spinning system: flow rate (determined for a given material by the orifice size and the pressure differential between the two chambers), wheel speed, crucible-to-wheel distance, angle of impingement and degree of superheating. Additional parameters specific to an arc melting system are the shape of the copper hearth and the ratio of the length to width of the orifice; this aspect ratio must be kept below a critical value to prevent freezing of the melt to the cooled orifice wall.

Experiments

To date many Ti rich alloys have been spun into ribbon material using this unit. The quenched compositions include alloys from the binary systems Ti-Fe, Ti-Cu and Ti-Ni and the ternary systems Ti-Ni-Si [5], Ti-Zr-B(-Si), Ti-6Al-4V, etc. For these alloys the following spinning parameters were used: orifice diameter, 0.4mm; pressure differential, about 10 psi; disk surface speed, ~ 20 m/sec, angle of impingement, 90° . The resulting ribbons had a thickness of $20\mu m$. The ribbons spun from Ti-Cu, Ti-Ni and Ti-Ni-Si were amorphous as checked by X-ray diffractometry. In another experiment $Nb_{82}Si_{18}$ having a high melting temperature ($\sim 2000^\circ C$) was successfully spun by this technique using an increased melting current of $\sim 75A$ and a higher pressure differential of 18 psi. According to X-ray analysis, the spun ribbon consisted predominantly of a textured A-15 structure (as found earlier [6] for arc furnace quenched [4] foils of Nb-Si alloys). However, the ribbon was narrow and thick, probably as a result of the high surface tension of the melt.

Discussion

Current Status

The reported results show that this method is promising for its intended purpose; however, in its present experimental form, the unit has some operational drawbacks. Thus, the reproducibility of the spun ribbons is not yet satisfactory since melting, superheating and timing of pressurization for spinning rely on the operator's skill and reactions. Also, prolonged heating of a small alloy button in the arc may result in vaporization of a significant amount of volatile component from the alloy. It should be noted that the arc spinning technique is not favorable for alloys having a very high thermal and electrical conductivity such as alloys rich in Al or Cu; the fact that their melt - crucible interface resistance to heat loss as well as the thermal gradient in the alloy are low makes it difficult to superheat them sufficiently for ready flow.

Further Developments

Looking beyond the present, we believe that this technique can be upscaled and modified to produce RSP refractory materials in the amounts needed for alloy development and processing and, ultimately, production. This will require, in the first place, a means of supplying adequate amounts of alloy materials in a continuous fashion. This can be accomplished by continuously providing feed material to the melt pool from a reservoir in particulate form, e.g., as small pellets or a coarse powder. If discontinuous operation is acceptable, use of a consumable electrode prepared from the alloy under study may be considered; however, this approach is less economical considering the higher manufacturing cost of such electrodes. In view of the control problems inherent in cold-hearth arc furnace operation (which are aggravated by the need of keeping the orifice size constant, i.e.,

of avoiding any freezing) one may also consider (or re-consider) alternative forms of heating, e.g. by induction or laser as discussed in the following.

An induction heated cold hearth system making use of an rf field concentrator coil and a slitted silver hearth with a central orifice has been described by Willens and Buehler [7] (reviewed in Ref. [8]). Although this unit was intended for use with a "gun" type splat cooling unit (i.e. using atomization and particle acceleration by shock wave) combined with a stationary copper substrate, it could be adapted to melt spinning by use with a gas pressure system and a copper wheel to provide a thin stream of metal flowing onto a rapidly rotating substrate.

Turning to laser heating, use of this energy source to melt pellets of materials prior to quenching by the hammer-and-anvil method has been described [9]; with a sufficiently powerful laser, it would be possible to maintain a melt pool fed by a continuous supply of pellets (as described above) and drained by a continuous stream through an orifice onto a quenching wheel.

Acknowledgement

Support of this work by the Army Research Office, Durham, under Contract DAAG29-80-C-0147 is gratefully acknowledged. The authors also thank Y.Z. Lu and Y.Q. Gao for their assistance.

References

- [1] Strange, E.H., and Pim, C.A., 1908, U.S. Patent No. 905758.
- [2] Tutzauer, H., Esquinazzi, P., De La Cruz, N.E., and De La Cruz, F., Rev. Sci. Instrum. 51 (1980) 546.
- [3] Wang, R., Rev. Sci. Instrum., 41 (1970) 1233.
- [4] Fischer, M., Polk, D.E., and Giessen, B.C., Rapid Solidification Processing, Principles and Technologies, Mehrabian, R., Kear, B.H., and Cohen, M., eds., Claitor's Publishing Division, Baton Rouge (1978) 140.
- [5] Polk, D.E., Calka, A., and Giessen, B.C., Acta Met., 26 (1978) 1097.
- [6] Waterstrat, R.M., Haenssler, F., and Müller, J., J. Appl. Phys., 50 (1979) 4763.
- [7] Willens, R.H., and Buehler, E., Met. Trans. TMS-AIME 236 (1966) 171.
- [8] Giessen, B.C. and Willens, R.H., in Phase Diagrams, Alper, Allen M., ed., Vol. III (1970) 103.
- [9] Krepski, R., Swyler, K., Carleton, H.R. and Herman, H., J. Mat. Sci. 10 (1975) 1452.

*Communication No. 149 from the Institute of Chemical Analysis, Northeastern University, Boston, MA 02115

A NEW HIGH STRENGTH NICKEL-BASE MICROCRYSTALLINE
ALLOY VIA RAPID SOLIDIFICATION TECHNOLOGY

V. PANCHANATHAN

Marko Materials, Inc.
No. Billerica, MA 01862

S. SASTRI and S. HAHN

The Gillette Company
Boston, MA 02106

ABSTRACT

A new high strength nickel-base alloy with microcrystalline microstructure has been developed by the rapid solidification technique. The composition of the alloy designated as Markomet 8 is as follows (weight percent):

Bal Ni, 21.8 Cr, 2.8 Fe, 8 Mo, 9.3 W, 1.5 Cb, 0.7 C, and 0.7 B

The method of melt-spinning-pulverization was used to prepare powders which were consolidated into bar stock by hot extrusion. The alloy exhibits excellent oxidation resistance at elevated temperatures upto 1800°F. Typically, at 1800°F the oxidation rate is 1.37 mg/cm². The alloy also has excellent corrosion resistance in nitric acid, formic acid, and phosphoric acid. The mechanical properties (tensile and stress rupture strength values) of the consolidated microcrystalline alloy at different temperatures are reported. Typical ultimate tensile strength values are:

175 KSI (1205 MPa) at room temperature and 97 KSI (667 MPa) at 1400°F.

The microstructural features of the alloy investigated by TEM and SEM are reported.

INTRODUCTION

Rapid solidification processing (RSP) has been recognized in recent years as having outstanding prospects for creation of new engineering alloys with improved service performance characteristics. The major R & D efforts on RSP alloys in the past several years have been geared towards enhancement of mechanical properties and high temperature capabilities suitable for many aerospace/defense oriented hardware application [1,2,3]. One field where RSP can make significant contribution is in the development of new alloys having high corrosion resistance combined with superior mechanical strength. These improvements in corrosion resistance and mechanical properties are anticipated to result from one or more of the following characteristics of these rapidly quenched materials:

- (1) unique chemical compositions and novel microstructures, and
- (2) excellent chemical homogeneity and uniformity of structures.

Recent research efforts at Marko Materials led to the development of a new family of rapidly solidified nickel base alloys possessing high strength and excellent corrosion resistance suitable for potential technological applications. The present paper describes the structure and properties of one alloy belonging to the aforesaid category.

ALLOY-COMPOSITION, PREPARATION TECHNIQUES & STRUCTURES

The new alloy was designed based on nickel for general corrosion resistance. It contains as primary constituents, chromium for oxidation resistance and molybdenum for pitting corrosion. The alloy is designated as Markomet 8 and has the following composition in wt.%.

BalNi, 21.8 Cr, 2.8 Fe, 8 Mo, 9.3 W, 1.5 Cb, 0.7 C, and 0.7 B

Markomet is the registered trade mark of Marko Materials Inc.

The alloy was produced by the method of melt spinning as rapidly solidified ribbons, typically .002 inch thick and .06 inch wide. Incorporation of certain critical amounts of metalloid elements [e.g. B and C] as alloying elements enables the alloy to be rapidly quenched into single crystalline solid solution phase with fCC structure as revealed by x-ray diffraction analysis. The as quenched structure consists of an extremely fine grain structure with grains, subgrains or crystallites typically ranging 100-200 Å in size as evidenced by TEM examination (Fig. 1).

The as quenched ribbons were found to be hard [~1100 DPN] and brittle. The brittle ribbons were readily pulverized into powders under 100 mesh by a standard hammer mill. The powders were subsequently consolidated into bars by hot extrusion at 2100°F using an extrusion ratio of 12:1.

A hot-extruded bar specimen (3/8" dia.) was cut, polished, and electrolytically etched in 10% oxalic acid solution for SEM study of the microstructure. A Hitachi S-700 field emission scanning electron microscope was used with operating conditions as follows: 20 KeV acceleration voltage, 20° specimen tilt, 5mm W.D. SEM micrographs of the specimen (Fig. 2) show a fine dispersion of second phase precipitates on the general matrix. The size of these multi-faceted precipitates vary from 0.5µm to 3.0µm. Larger precipitates, however, consist of two or more precipitates, i.e. precipitates of lighter and darker contrasts. An optical micrograph (Fig. 3) taken at 2,000X does not show this difference in contrast, which arises from the atomic number difference.

EDX (Energy Dispersive X-ray) analysis of these precipitates show that the lighter contrast precipitates contain very high concentration of Mo and W, while the darker precipitates contain much higher Cr concentration than that of the matrix. The matrix composition has been found by EDX analysis to be as follows:

65.38 Ni, 17.7 Cr, 5.4 Fe, 0.66 Cb, 3.72 Mo, and 5.74 W

MECHANICAL PROPERTIES:

Table 1 lists the tensile properties of the as extruded alloy at room and elevated temperatures.

TABLE - 1
ROOM AND ELEVATED TEMPERATURE TENSILE PROPERTIES

Temperature		Ultimate tensile Strength		0.2% Offset yield Strength		% Elongation
°F	°C	MPa	KSI	MPa	KSI	
75	24	1205	175	1059	154	8
600	316	1072	155	933	135	9
800	427	1052	152	891	129	9
1200	649	951	138	886	128	10
1400	760	667	97	638	93	18
1600	871	369	54	296	43	44

A study of the table indicates that this alloy has good mechanical properties at room and elevated temperatures. It is of interest to compare the properties of this alloy with a conventional Alloy 625 (Bal Ni, 20-30 Cr, 8-10 Mo, 5(max) Fe, 3.15 Cb and Ta). Alloy 625 has got UTS of 138.8 KSI at room temperature and 88.4 KSI at 1400°F. [4]. The rapidly solidified alloy shows nearly 25% higher tensile strength at room temperature and 10% at 1400°F.

Table 2 lists the stress to cause rupture in 100 hrs. at high temperatures. It is nearly 60% of the yield strength at 1200°F and drops to 25% at 1400°F. The stress rupture values are slightly lower compared to Alloy 625 (71 KSI at 1200°F and 27 KSI at 1400°F).

TABLE - 2
STRESS TO CAUSE RUPTURE IN 100 HRS.

Test Temperature		Rupture Strength	
°F	°C	MPa	KSI
1200	649	413	60
1400	760	158	23
1600	871	48	7

CORROSION BEHAVIOR:

Immersion corrosion testing was carried out in different solutions and Table 3 lists the corrosion rate of Markomet 8 alloy in various solutions. A study of the Table indicates its good corrosion resistance in various acid media.

TABLE - 3
CORROSION BEHAVIOR

Solution	Concentration (weight percent)	Test Temperature		Test Time, hours	Corrosion Rate, mils per year
		°F	°C		
Nitric Acid	50	176	80	48	2.6
	65	212	100	48	10
Formic Acid	20	158	70	48	0.1
	40	158	70	48	0.1
Phosphoric Acid	70	212	100	48	6
Sulfuric Acid	10	158	70	48	2
Hydrochloric Acid	5	158	70	48	157

The corrosion rate of this alloy is comparable to Alloy 625 in all the acids excepting hydrochloric acid.

OXIDATION BEHAVIOR:

Table 4 lists the oxidation behavior of Markomet 8 alloy. The sample was heated to the desired temperature and cooled to room temperature every 50 hrs. and then reheated. From the weight changes, the oxidation rate was determined after 250 hrs. The oxidation resistance is excellent as evidenced by less oxidation rate on prolonged exposure. However Alloy 625 on exposure at 1600°F for 250 hrs. had an oxidation rate of 0.85 mg/cm², indicating superior oxidation resistance of Markomet 8 alloy compared to Alloy 625.

TABLE - 4
OXIDATION BEHAVIOR

Test Temperature		Exposure Time, hours	Oxidation Rate, mg/cm ²
°F	°C		
1600	871	250	0.38
1800	982	250	1.37
2000	1093	250	2.16

SUMMARY:

A new bulk microcrystalline nickel-base alloy, designated Markomet 8, has been developed by Marko Materials, Inc. using rapid solidification technology and powder metallurgical consolidation. This alloy is characterized by high strength room and elevated temperature properties in combination with good corrosion and oxidation resistance. The microstructural features of the alloy investigated by TEM and SEM are reported.

REFERENCES:

- [1]. Rapid Solidification Processing II, R. Mehrabian, B.H. Kear, and M. Cohen, Eds, Claitors Publishing Division, Baton Rouge, Louisiana, 1980.
- [2]. Rapidly Quenched Metals III, 3rd International Conference, Vols. 1 and 2, Ed, B. Cantor, The Metals Society, London, 1978.
- [3]. Rapid Solidification Processing, R. Mehrabian, B.H. Kear, and M. Cohen, Eds., Claitors Publishing Division, Baton Rouge, Louisiana, 1978.
- [4]. Bulletin Cabot Alloy 625, Published by Cabot High Technology Materials Division.



.05 μm

Fig. 1a



Fig. 1b

Fig. 1: a) Transmission Electron Micrograph of Markomet 8 and
b) The Corresponding SAD Pattern

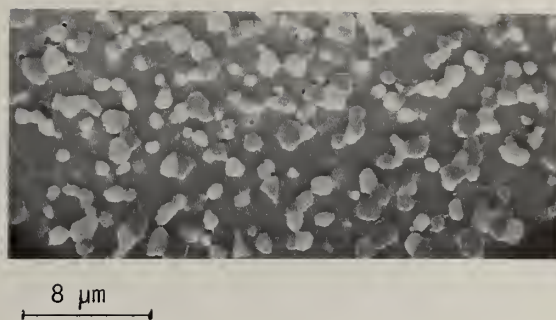
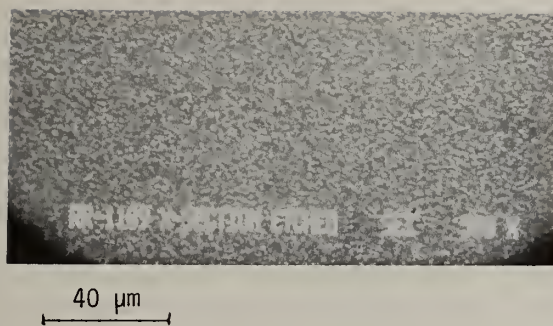


Fig. 2: Scanning Electron Micrographs of Markomet 8

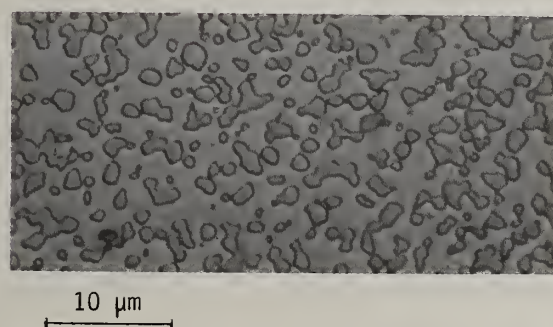


Fig. 3: Optical Micrograph of Markomet 8

R.P.I. Adler and S.C. Hsu

GTE Laboratories, Inc.
Waltham, MA 02254

ABSTRACT

A key to better understanding and control of Rapid Solidification Processing is the characterization of the dynamic wetting interaction and the solidification behavior that takes place between the liquid metal supply and the moving heat sink. The approach taken has been to design simple screening procedures which reduce the experimental effort but still allows the identification of significant parameters for the dynamic interaction between the solidifying liquid, a gas boundary layer, and a solid-heat removing substrate without evaluating every process combination for this coupled mass/heat transfer phenomena. A simple dynamic contact test procedure is now being used to generate phenomenological information and empirical results on the wetting and solidification of a droplet having a glancing impact with a metallic surface in a vacuum. The present methodology of impacting fixed volume droplets from a series of metals and alloys near their respective melting points can discriminate between the limiting dynamic wetting classes as well as systematic trends as a function of impact angle within each grouping.

Introduction

The objective of this study is to identify the significant operational variables and thermo-physical parameters that control the efficiency of the melt spinning process. This involves understanding the dynamic interaction between a solidifying liquid, a gas boundary layer, and a solid heat removing substrate.

Attention has been paid to the dynamics of the solid-melt-gas interaction [1-5]. The effect of surface free energy (liquid-vapor, solid-vapor, and liquid-solid) on the wetting/spreading of liquid on a solid substrate has been well established through the conventional stationary (sessile drop) wetting experiments [6,7]. The influence of substrate roughness, temperature and vibration, and interfacial tension and liquid-solid mutual solubility on wettability has been reported for these experiments [8-10]. There have also been several investigations in which a metal/alloy was rapidly quenched onto a moving substrate. The evaluations have separately considered the effects of: substrate roughness [2,4,11,12]; increased substrate temperature [13] (using a heated substrate to improve spreading); and liquid nitrogen cooled substrates for enhancing cooling rates [14] or related to the increased solidification rate [15]. Others studied the influence of liquid characteristics such as the effect of : superheat on the foil width [16,17]; the impact forces on wetting [4,17]; and the involvement of quenching stress [18] on the foil structure. Finally, discussions about gas entrapment between the liquid and substrate leading to reduced effective areas of thermal contact and thus lower heat extraction rates [2-4, 19-23] for the liquid, as well as the dependency on alloy composition [2] have been reported.

Since the spatial transients for this unique combination of phenomena are complex, this multiphase interaction has been difficult to comprehend and then correlate with the structure and morphology of the resulting product. However the systematic classification of the variants of this kind of transient phenomenon not only could provide fundamental information but can also be usefully applied to optimizing productivity for the melt spinning process. In essence then we are trying to develop empirical tests and then generate predictive guidelines that can be used to indicate appropriate combinations of material and process conditions for any desired melt spun product.

Experimental

The experimental approach for this program involves developing a simplified dynamic wetting system that allows the screening of a range of materials in a consistent manner. Essentially a falling, molten metal droplet is made to impact on an inclined substrate; by running experiments in a vacuum environment it is possible to isolate the primary phenomenon from effects that may be induced by a gas boundary layer as illustrated in Figure 1.

Initial activity has been directed at evaluating whether the Falling Droplet/Inclined Substrate

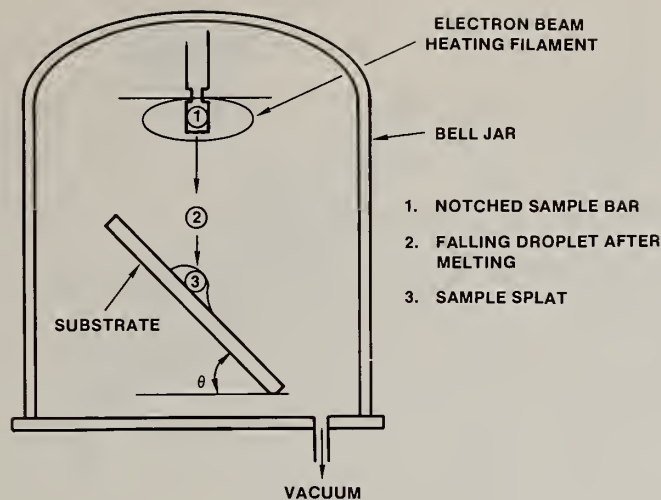


Figure 1. Experimental Setup

Plane test produces results than can identify differences in dynamic wettability between various material combinations of melt and heat extracting substrate. In this test a fixed volume liquid metal droplet (0.23 inch diameter) having a constant impact velocity of 66 in/sec strikes an inclined plane of a "standard" OFHC copper with a surface prepared with 320 grit emery paper. These substrates have reproducible surface roughness values of 16 micro inches CLA and normally had a 280°C surface temperature.

Results

Observations of the impact phenomena and any solidification that occurs were made using high speed cinematography. The substrate inclination angle (θ) was the primary experimental variable for a representative group of five melt compositions having a wide range of melting temperatures and surface tension values. The initial impact and spreading phenomena at any given inclination angle were surprisingly independent of melt composition. Thus each impacting molten metal sphere spreads into a tear drop shaped disc with a maximum width that was inversely proportional to $\sin \theta$.

The subsequent phenomena could be classified as splat solidification or droplet recollection. There were systematic dimensional trends that represented various types of dynamic wetting behavior. As will be demonstrated, these effects would not be evident using classical, sessile drop wetting procedures.

The characteristic of forming solidified splats during dynamic droplet testing has been used to identify the wetting class of materials (Cu, Zr, and Al). The solidified splat width, taken as the largest lateral dimension, is usually upwards of twice the droplet diameter but tends to fall off as θ is increased (Figure 2). The elongated length of the splat tends to increase faster than the respective width decreases for increasing values of θ so that the aspect ratio (Table 1) also increases with θ . Comparatively the magnitude of these effects are more pronounced for Cu, followed by Zr, and least for Al.

Even though impacting droplets of the non-wetting class of materials also form a spreading liquid film on impact, dominant restraint forces cause this film to retract into a droplet that rebounds away. Experiments using greater inclination angles ($\theta=70^\circ$) were useful in reducing the thickness and doubling the aspect ratios of the primary splats of most materials. However for Ni - 20% Cr rebounding droplets formed even at $\theta=70^\circ$ because a sufficiently thin liquid film was not produced so that solidification could prevent droplet formation. On the other hand there is a transition in the wetting behavior of the AMS 4778 alloy (Ni-2.8% B-4.5% Si) droplets as indicated on Figure 2. At inclination angles below 40° there is a characteristic non-wetting behavior while at angles of 45° and above the wetting behavior is intermediate between Zr and Al.

The systematic differences between materials exemplified by the trends in Figure 2 can not be exclusively related to the relative magnitudes of the respective surface tensions. More significantly the transitional behavior of the nickel-base brazing alloy (AMS 4778) may be important because this alloy can be readily melt spun on a copper substrate wheel. Further testing, analysis, and correlations are required to substantiate these results and correlative inferences to "melt spinnability", but certainly the designed test procedure appears to have the resolution to discriminate between vari-

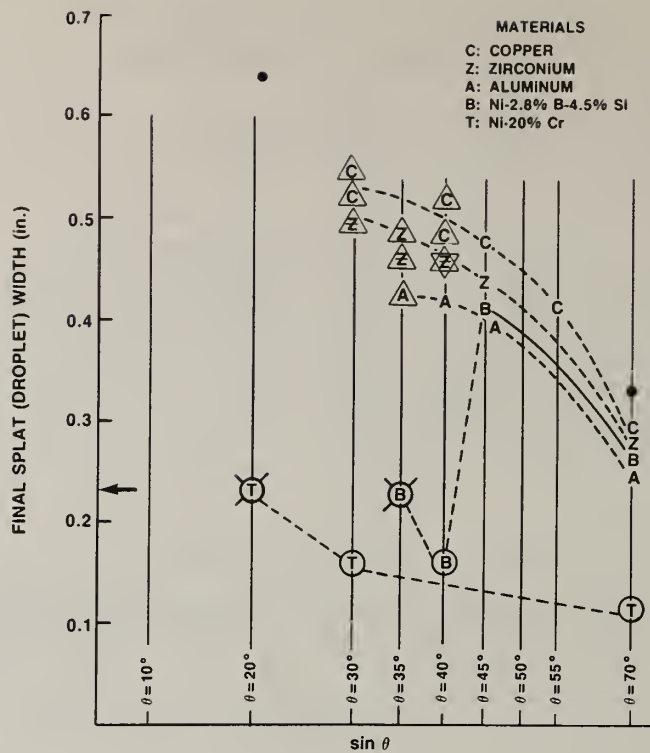


Figure 2. Relationship Between Final Splat Width and Inclination Angle θ

MATERIAL	ASPECT RATIO AT		
	$\theta=30^\circ$	$\theta=45^\circ$	$\theta=70^\circ$
Cu	1.3	2.1	4.9
Zr	1.2	1.8	4.5
Al	1.0	2.1	4.6
AMS 4778	DROPLET	1.7	4.0

Table 1. Systematic Dimensional Relations for Solidified Splats

ous classes of dynamic wetting behavior.

Conclusions

- 1) Splat dimensions represent balance between:
 - spreading/solidification phenomena
 - retractive surface energy forces.
- 2) Molten droplet/inclined substrate test discriminates between dynamic wetting classes.
- 3) This procedure to identify positive/negative classes of melt/substrate combinations for RSP remains viable.

Acknowledgment

The authors would like to thank the Office of Naval Research for the support of this research under contract N000014-82-0434. The technical assistance of Walter Allen and Neil Schauder is also appreciated.

References

1. T.R. Anthony and H.E. Cline, J. Appl. Phys. 50 (1), 239 (1979).
2. C.E. Mobley, R.E. Maringer and L. Dillinger, Proc. International Conference Rapid Solidification Processing: Principles and Technologies, R. Mehrabian, B.H. Kear and M. Cohen, eds., Claitor's Publishing Division, Baton Rouge, LA, p. 222 (1977).
3. J.V. Wood and R.W.K. Honeycombe, J. of Materials Science 9, 1183 (1974).
4. S.C. Huang and H.C. Fiedler, Conf. Proc. "Continuous Casting of Small Cross Sections," Y.V. Murty, F.R. Mollard, eds., The Metallurgical Society of AIME, p. 127 (1980).
5. R.B. Pond, R.E. Maringer and C.E. Mobley, New Trends in Materials Processing, C.S. Hartley, T.E. Tietz and B.H. Kear, eds., American Society for Metals, Metals Park, OH, p. 124 (1976).
6. Lawrence E. Murr, Interfacial Phenomena in Metals and Alloys, Addison-Wesley Publishing Company, Reading, MA (1975).
7. Arthur W. Adamson, Physical Chemistry of Surfaces, Interscience Publishers (1967).
8. S.J. Hitchcock, N.T. Carroll and M.G. Nicholas, J. Materials Science 16, 714 (1981).
9. J.F. Oliver and S.G. Mason, J. Materials Science 15, 431 (1980).
10. R.J. Klein Wassink, J. of the Institute of Metals 95, 38 (1967).
11. H. Jones, Material Sci. Eng. 5, 1 (1969).
12. P.J. Wray, Met. Trans 12B, 167 (1981).
13. K. Togano, H. Kumakura and K. Tachikawa, Appl. Phys. Lett. 40 (1) (1982).
14. D. Pavuna and D. Hainsworth, J. Non-Crystalline Solid 37, 417 (1980).
15. P.H. Shingu and R. Ozaki, Met. Trans 6A, 33 (1975).
16. F.E. Luborsky and H.H. Liebermann, Materials Sci. Eng. 49, 257 (1981).
17. C.A. Williams and H. Jones, Materials Sci. Eng. 19, 293 (1975).
18. A.R. Yavari, P. Desre and P. Hicter, Scripta Metallurgica 15, 503 (1981).
19. Ranjan Ray, Carl F. Cline, D.E. Polk and L.A. Davis, U.S. Patent 4,154,283, (May 1979).
20. M.C. Narasimhan, U.S. Patent 4,142,571 (March 1979).
21. Davor Pavuna, J. Materials Science 16, 2419 (1981).
22. Makoto Matsuura, M. Kikuchi, M. Yagi and K. Suzuki, Japanese Journal of Applied Physics 19, 9, 1781 (1980).
23. H.H. Liebermann, Proc. Third International Conference on Rapid Quenched Metals, B. Cantor, ed., The Metals Society, Vol. I, p. 34 (1978).

RAPID-SOLIDIFICATION PROCESSING OF TITANIUM ALLOYS

T. C. Peng, S. M. L. Sastry, and J. E. O'Neal

McDonnell Douglas Research Laboratories
St. Louis, Missouri 63166

ABSTRACT

Rapid-solidification processing (RSP) of titanium alloys was investigated using surface melting, splat quenching, and spin atomization techniques. Rapidly solidified 0.05-0.25 mm thick flakes, and 100-500 μm diameter spherical powders were produced, and the dependence of cooling rate on flake thickness and powder diameter was determined. Microstructures of several commercial Ti-alloys and novel Ti-alloys produced by RSP were determined. Novel alloy compositions and beneficial microstructures that can be obtained by RSP of Ti alloys were determined.

Introduction

Rapid solidification processing (RSP) of titanium alloys results in fine, homogeneous metastable microstructures in the as-solidified state [1-3]. These microstructures may correspond to desirable property combinations, or they may be decomposed in a controlled manner by heat treatment to produce microstructures desirable for improved properties [4,5]. Although RSP has had a major impact on the metallurgy of nickel-, iron-, and aluminum-based alloys [6-9], there has not been wide application of RSP to Ti-alloy metallurgy. Recent studies on the rapid solidification of Ti, modified by the additions of rare-earths or boron, as well as titanium/high-aluminum alloys containing rare-earths, indicated that significant microstructural refinement can be achieved by RSP technology [10,11]. Preliminary studies of these systems indicated the persistence of the microstructural refinement during subsequent heat treatment and suggested a correlation between this refined microstructure and significant increases in strength and hardness of the alloys. The results obtained indicate promise of RSP titanium alloys with higher modulus, strength, and creep resistance. The effectiveness of different RSP techniques for producing the desired high cooling rates and unique microstructures in Ti-alloys was determined in this investigation.

Experimental Procedure

The methods used for RSP were laser surface melting [3,12], electron-beam-melting/splat-quenching and laser-melt/spin-atomization.

Laser surface melting was used principally for determining the dendrite-arm-spacing/cooling-rate correlation for Ti-alloys [13,14] and for screening large numbers of potential compositions during the development of new RSP Ti alloys. Prealloyed Ti alloys produced by arc-melting as well as Ti-substrates coated with different alloying elements were used as the starting materials for determining microstructural refinement and novel-alloy formation.

Electron-beam-melting/splat-quenching illustrated in Figure 1(a) was used to produce 50-500 g lots of Ti-alloy flakes for microstructural examination by transmission electron microscopy and mechanical property evaluation. The electron beam is focused onto a prealloyed Ti-alloy rod. The molten drops hit a rotating copper disk, and the centrifugal force stretches the droplets into thin flakes. The melt-drop size and drip rate are controlled by varying the power into the alloy rod. The flake thickness (and hence the cooling rate) are controlled by varying the rotational speed of the copper disk.

In the laser-melt/spin-atomization technique, illustrated in Figure 1(b), a continuous-wave CO_2 laser beam with an incident power of 6.2 kW was used to melt the top surface of a cylindrical, prealloyed titanium rod rotating at 10 000-30 000 revolutions per minute. The molten droplets expelled by the centrifugal force from the circumference of the rod are cooled by a helium gas flow.

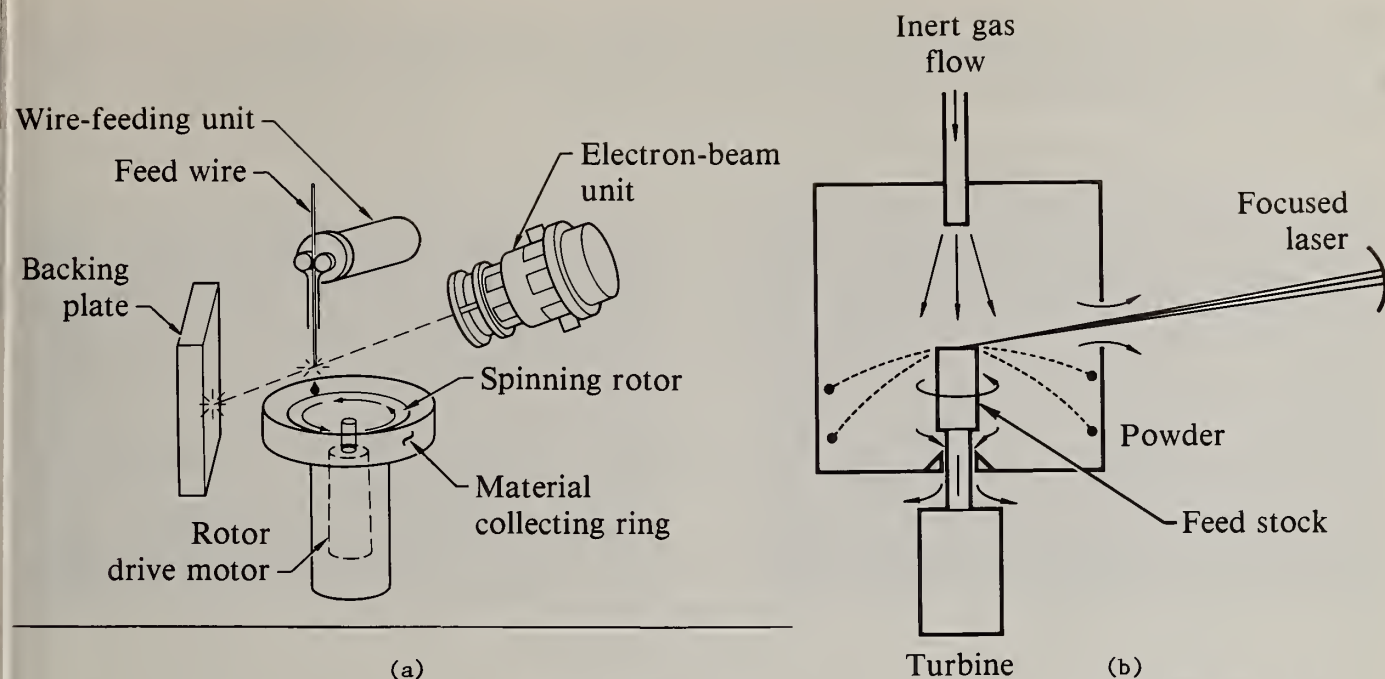


Figure 1. Schematic diagrams of (a) electron-beam-melting/splat-quenching and (b) laser-melt/spin-atomization methods for rapid solidification processing of titanium alloys.

The RSP Ti-alloys were analyzed by optical microscopy and scanning and transmission electron microscopy to characterize the microstructural modifications effected by rapid solidification.

Results and Discussion

Morphologies and Cooling Rates of Rapidly Solidified Ti Alloys: The morphologies of rapidly solidified Ti alloys produced by electron-beam-melting/splat-quenching and laser-melt/spin-atomization are shown in Figures 2(a) and 2(b). The dendrite-arm/cell spacings in the rapidly solidified alloys were 1-10 μm corresponding to cooling rates of 10^7 - 10^4 K/s. Although laser surface melting is not readily

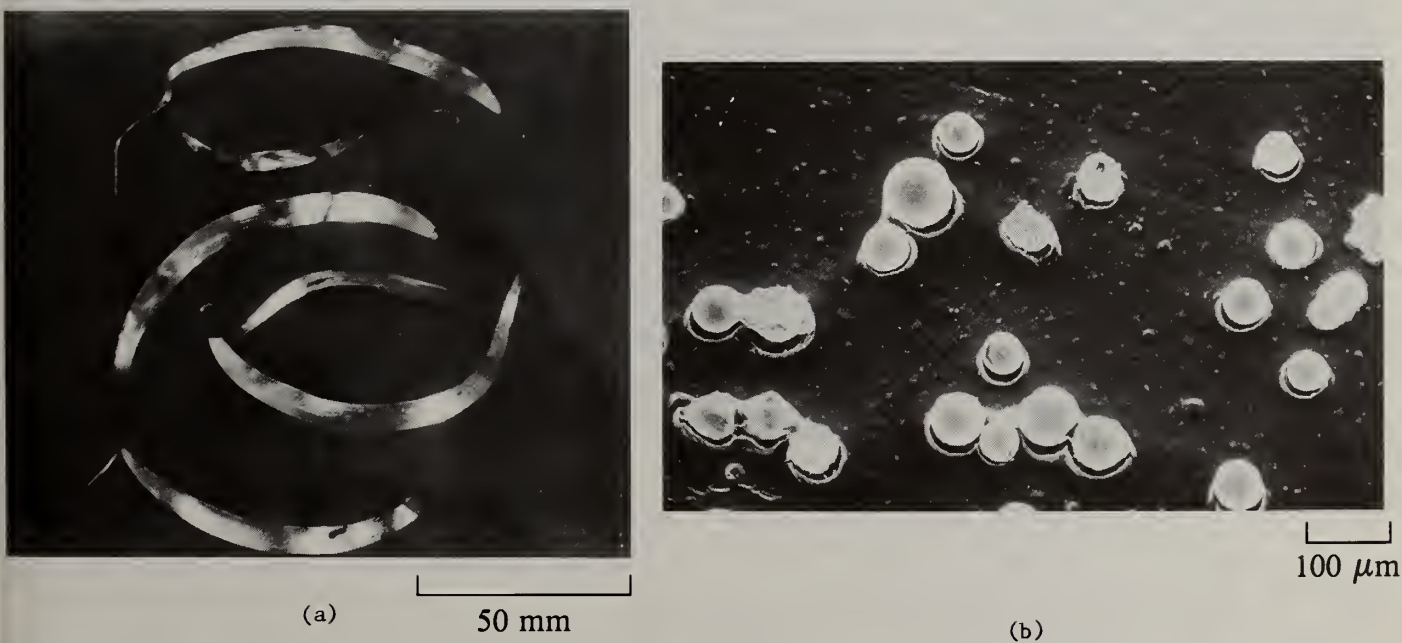


Figure 2. Particulate morphologies of rapidly solidified titanium alloys produced by (a) electron-beam-melting/splat-quenching and (b) laser-melt/spin-atomization.

adaptable for bulk production of material, it is an effective technique for producing high cooling rates, and it is a rapid and inexpensive means for screening large numbers of potential alloy compositions. The electron-beam-melted and splat-quenched flakes are particularly suitable for a detailed study of as-rapidly-solidified microstructures and microstructural evolution upon subsequent annealing.

The success of the laser-melt/spin-atomization technique for the production of fine ($< 100\text{ }\mu\text{m}$ diam) spherical powders with cooling rates $> 10^4\text{ K/s}$ indicates promise of solving some of the problems which hitherto impeded titanium rapid-solidification technology. The reactivity of molten titanium with crucible materials and the high affinity of Ti for interstitial elements such as carbon, nitrogen, and oxygen have been the major obstacles in producing rapidly solidified Ti-alloy powder. These problems are overcome in the laser-melt/spin-atomization technique. Furthermore, sporadic and local overheating, sputtering, electrode contamination, and preferential vaporization of low-melting components of Ti-alloys encountered in spin-atomization using electric arc-discharge and electron-beam melting are significantly reduced in the laser-melt/spin-atomization technique.

Microstructures of Rapidly Solidified Ti Alloys: The novel Ti-alloys that can be obtained by rapid solidification processing include dispersion-strengthened Ti alloys, intermetallic compound forming alloys, eutectoid formers, and fine-grained conventional Ti alloys.

Dispersion Strengthened Ti Alloys: Homogeneously distributed, fine, incoherent dispersoids were obtained in Ti-rare earth alloys. Figures 3(a)-3(c) show microstructures of conventionally processed, rapidly solidified, and annealed Ti-2.0Er. The conventionally cast alloy has coarse, equilibrium, constituent particles (Figure 3(a)) which produce low ductility and toughness. Rapid solidification results in single-phase microstructures consisting of $0.2\text{--}0.5\text{ }\mu\text{m}$ martensite plates (Figure 3b). Although the equilibrium solubility of Er in both $\alpha\text{-Ti}$ and $\beta\text{-Ti}$ is low [15], the single-phase microstructure in rapidly solidified Ti-2.0Er alloy indicates large increases in solubility by rapid solidification. Annealing the splat-quenched flakes at $700\text{--}800^\circ\text{C}$ produces homogeneously distributed fine ($< 0.1\text{ }\mu\text{m}$) incoherent dispersoids (Figure 3(c)). Similar results were obtained in the other Ti/rare-earth alloys. The incoherent dispersoids produce significant improvements in room- and elevated-temperature tensile strength and creep resistance [16].

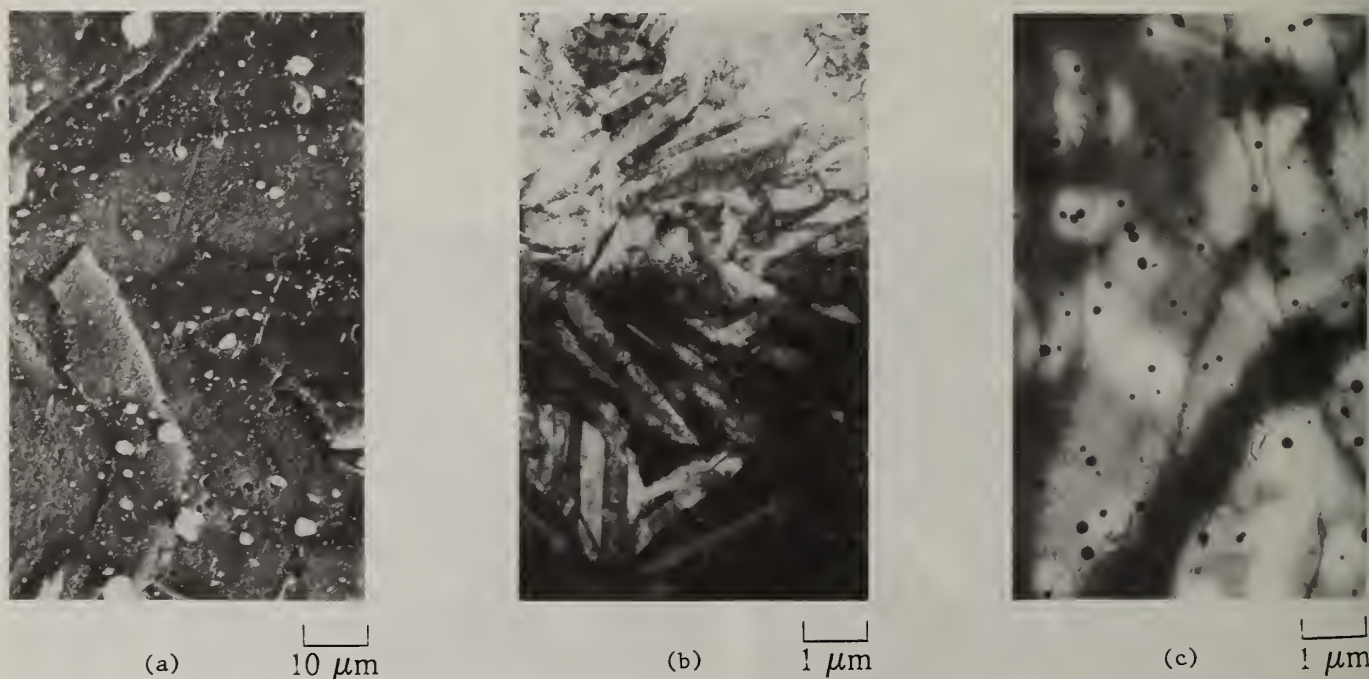
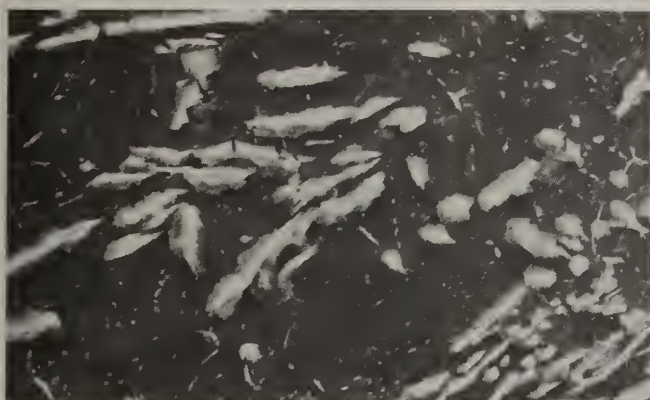


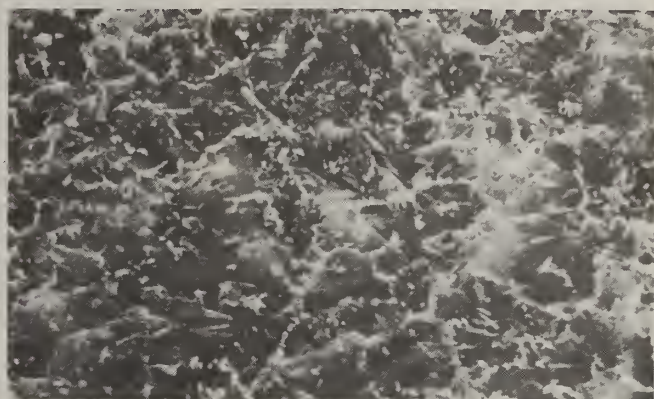
Figure 3. Microstructures of Ti-2.0Er alloy: (a) conventionally processed, (b) rapidly solidified and, (c) rapidly solidified and annealed at 700°C for 100 h.

Compound Formers: Boron and carbon additions to conventionally processed Ti result in coarse titanium boride and titanium carbide dispersions (Figures 4(a), and 5(a)). However, rapid solidification of Ti-1.0B and Ti-1.0C alloys results in significant grain refinement and large volume fractions of fine dispersoids (Figures 4(b) and 5(b)). The presence of such dispersions have been shown to increase the strength by 100% and modulus by 30% of titanium [11].



(a)

10 μm



(b)

1 μm

Figure 4. Microstructures of (a) conventionally processed and (b) rapidly solidified Ti-1.0B alloy.



(a)

10 μm



(b)

1 μm

Figure 5. Microstructures of (a) conventionally processed and (b) rapidly solidified Ti-1.0C alloy.

Eutectoid Formers: The segregation at grain boundaries of eutectoid forming elements such as Ni, Cu, and Fe in conventionally processed Ti alloys has hampered their development for high-strength application. The microstructures of rapidly solidified Ti-3Ni and Ti-7Ni alloys in Figures 6(a) and 6(b) demonstrate the fine-scale homogeneous microstructures that can be produced by rapid solidification processing. Ti-3Ni exhibits a fine martensitic structure, while Ti-7Ni has a retained-beta cellular microstructure with fine Ti_2Ni at the cell boundaries. Annealing of Ti-3Ni at 700°C for 16 h resulted in growth of the alpha phase from the martensite and the formation of Ti_2Ni at the boundaries of impinging alpha grains. The fine-grained microstructure consisting of homogeneously distributed Ti_2Ni precipitates is conducive to increased strength. The results demonstrate that rapid solidification processing of Ti-alloys containing eutectoid formers allows greater flexibility in controlling the entectoid decomposition products.

Combined Precipitation- and Dispersion-Strengthened Alloys: In rapidly solidified Ti-alloy systems such as Ti-8Al-2.0Er a combination of shearable, coherent, ordered Ti_3Al (α_2) precipitates and incoherent erbium-containing dispersoids can be produced. These microstructures are particularly effective for increasing the room-temperature tensile strength and high-temperature creep resistance.

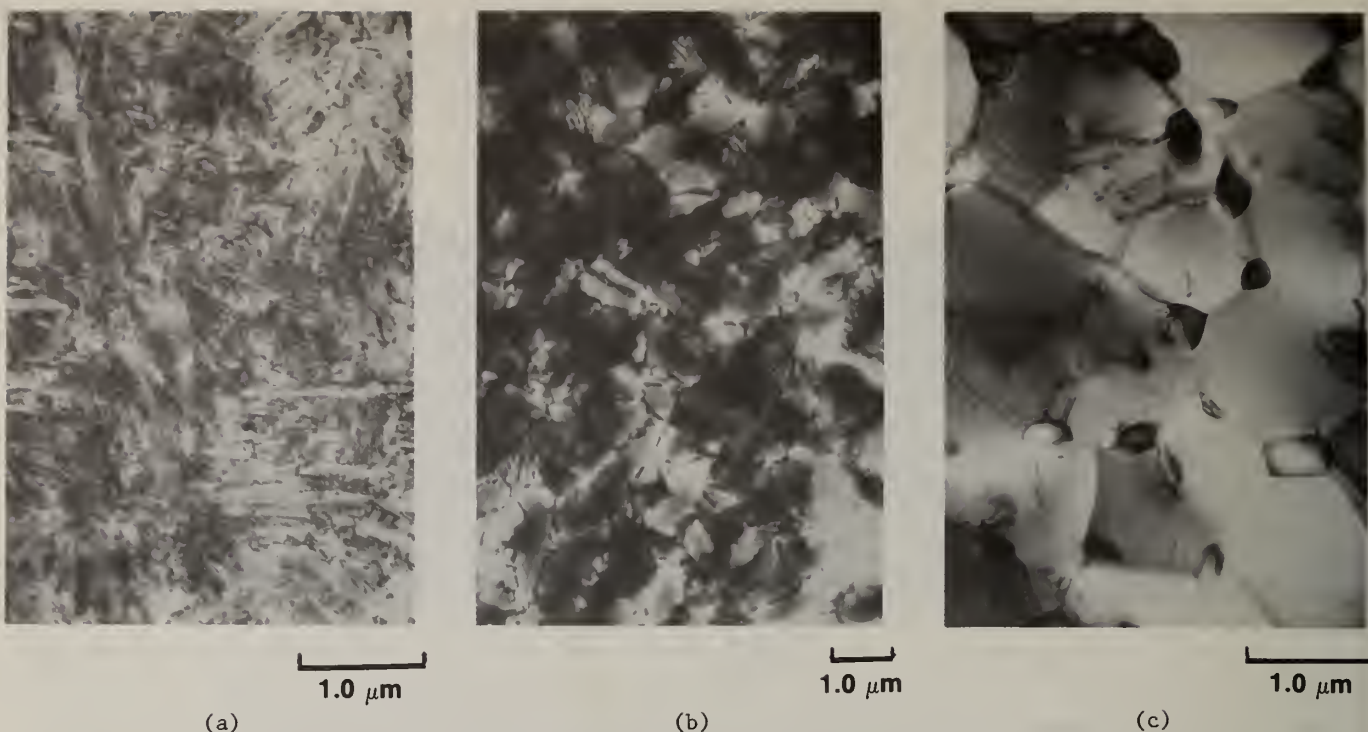


Figure 6. Microstructures of rapidly-solidified (a) Ti-3Ni, (b) Ti-7Ni and, (c) Ti-3Ni annealed at 700°C for 16 h.

Fine-Grained, Conventional Ti Alloys: Rapid solidification processing of conventional near-alpha and alpha-beta titanium alloys such as Ti-8Al-1Mo-1V, Ti-6Al-4V, and Ti-6Al-2Sn-4Zr-2Mo produces martensitic structures (Figure 7(a)) containing dislocation substructures. Annealing these alloys at 800-1000°C results in equiaxed, fine-grained microstructures (Figures 7(b) and 7(c)). Alloys having such equiaxed, fine-grained microstructures have superior room-temperature mechanical properties and high-temperature superplastic formability.

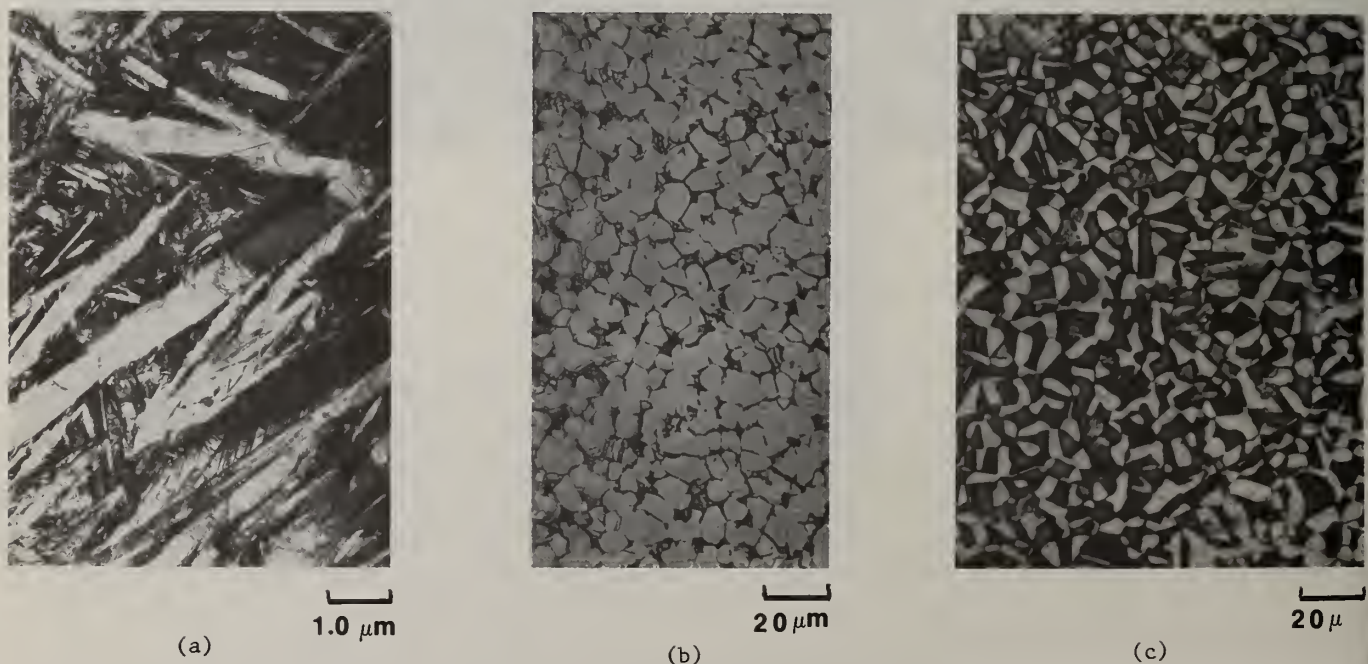


Figure 7. Microstructures of rapidly solidified (a) Ti-6Al-4V, (b) Ti-6Al-4V annealed at 900°C for 2 hours and, (c) Ti-6Al-4V annealed at 1000°C for 1 h.

Acknowledgements

This research was conducted in part under the McDonnell Douglas Independent Research and Development program and in part under the Office of Naval Research Contract No. N00014-76-C-0626.

References

- [1] S. M. L. Sastry, J. E. O'Neal, and T. C. Peng, Dispersion Strengthening and Rapid Solidification Processing of Titanium Alloys, 110th AIME Meeting, Chicago, IL, 22-26 Feb 1981.
- [2] J. E. O'Neal, T. C. Peng, and S. M. L. Sastry, Microstructural Studies of Laser-Melted Titanium-Rare Earth and Titanium-Boron Alloys, in Proc. Electron Microscopy Soc. Amer., ed. by G. W. Bailey (Claitor's Publ. Div., Baton Rouge, LA, 1981), p. 66.
- [3] T. C. Peng, S. M. L. Sastry, and J. E. O'Neal, Exploratory Studies of Laser Processing of Titanium Alloys, in Annual AIME Meeting, Chicago, IL, 22-26 Feb 1981.
- [4] R. E. Maringer, C. E. Mobley, and E. W. Collings, Preparation and Properties of Compacts of Melt Extracted Staple Fibers of Ti-6Al-4V Alloy, AIChE J. **180**, 111, (1978).
- [5] S. M. L. Sastry, T. C. Peng, J. E. O'Neal, and L. P. Beckerman, Dispersion Strengthening of Titanium Alloys, TMS-AIME Fall Meeting, 26-28 Oct 1982, St. Louis, MO.
- [6] M. Cohen, B. H. Kear, and R. Mehrabian, Rapid Solidification Processing - An Outlook, in Proc. of 2nd Int. Conf. on Rapid Solidification Processing, ed. by R. Mehrabian, B. H. Kear, and M. Cohen (Claitor's Publ. Div., Baton Rouge, LA, 1980), p. 1.
- [7] J. J. Rayment and B. Cantor, The Rapid Quenching of Steels, in Proc. of 2nd Int. Conf. on Rapid Solidification Processing, ed. by R. Mehrabian, B. H. Kear, and M. Cohen (Claitor's Publ. Div., Baton Rouge, LA, 1980), p. 165.
- [8] A. R. Cox, J. B. Moore, and E. C. Van Reuth, On the Rapid Solidification of Superalloys, in Superalloys: Metallurgy and Manufacture, ed. by B. H. Kear, D. R. Muzyka, J. K. Tien, and S. T. Wlodek (Claitor's Publ. Div., Baton Rouge, LA, 1976), p. 45.
- [9] V. Anand, A. J. Kaufman, and N. J. Grant, Rapid Solidification of Modified 7075 Aluminum Alloy by Ultrasonic Gas Atomization, in Proc. of 2nd Int. Conf. on Rapid Solidification Processing, ed. by R. Mehrabian, B. H. Kear, and M. Cohen (Claitor's Publ. Div., Baton Rouge, LA, 1980), p. 273.
- [10] P. J. Meschter, J. E. O'Neal, and S. M. L. Sastry, Characteristics and Thermal Stability of Dispersed Phases in Rapidly Solidified Titanium-Rare Earth Alloys, TMS/AIME Meeting, St. Louis, MO, 24-28 Oct 1982.
- [11] T. C. Peng, S. M. L. Sastry, and J. E. O'Neal, Microstructures and Mechanical Properties of Rapidly Solidified Ti-B and Ti-6Al-4V-B Alloys, TMS-AIME Annual Meeting, Atlanta, GA, 6-10 March 1983.
- [12] E. M. Breinan, B. H. Kear, and C. M. Banas, Processing Materials with Lasers, Physics Today, **29**, 44 (1976).
- [13] H. E. Cline and T. R. Anthony, Heat Treating and Melting Material with a Scanning Laser or Electron Beam, J. Appl. Phys. **48**, 895 (1977).
- [14] T. C. Peng, S. M. L. Sastry, and J. E. O'Neal, A Correlation Between Dendrite-Arm-Spacing and Cooling Rate for Laser-Melted Ti-13V-3Al-3Sn-3Cr, Int. Conf. on Application of Lasers in Materials Processing II, Los Angeles, CA, 24-26 January 1983.
- [15] R. P. Elliott, Constitutions of Binary Alloys, (McGraw Hill, New York, 1965) 1st Supp.
- [16] S. M. L. Sastry, T. C. Peng, J. E. O'Neal, and L. P. Beckerman, Consolidation, Thermomechanical Processing, and Mechanical Properties of Rapidly Solidified Dispersion-Strengthened Titanium Alloys, Third Conf. on Rapid Solidification Processing, Gaithersburg, MD, December 6-8, 1982.

THE MICRO-PARTICLE PROCESSOR TO PRODUCE FINE POWDERS AND COATINGS*

Julius Perel, John F. Mahoney, Scott Taylor, Zef Shanfield**, and Carlos Levi†

Phrasor Scientific, Inc.
Duarte, California 91010

ABSTRACT

The Micro-Particle Processor has been fabricated at the Phrasor Scientific Laboratory after extensive research and development of the Electrohydrodynamic (EHD) technique of producing very fine droplets of various alloy metals. The Processor produces small quantities of liquid metal droplets for use in studies of rapid solidification processes and in the production of coatings. EHD has been used to produce tiny spheres of alloys that are amorphous, single crystalline, bi-crystalline, etc. Adhesive coatings have been produced such as aluminum on titanium and silicon on graphite. The Processor could be used to produce small quantities of fine powders for material science studies and for low volume applications. The method provides for rapid coating rates and stoichiometric coatings because the coatings are made by impinging droplets rather than atoms.

EHD produces fine droplets ($<30\text{\AA}$) by the application of an intense electric field to a liquid surface. The liquid is produced by the heating of alloy metals in an alumina reservoir and delivered to an alumina capillary nozzle held at high potential. Heating of the droplet source, control of high voltage and all the other operations are performed by a micro-processor via a video terminal. The software contains the sequence of operations that automatically controls the production and collection of sub micron powders. The operator inputs parameters specific to the alloy tested by means of a keyboard.

The Micro-Particle Processor was fabricated and tested at the Phrasor Laboratory then partially dismantled and shipped to the National Bureau of Standards. The Processor was in operation a few days after being uncrated by both Phrasor and NBS personnel. Several minor modifications were made after delivery to allow for rapid turn around. The Processor is being used at the NBS to further studies of fundamentals of rapid solidification, extended solubility and new alloy designs, such as, Al-Mn and Al-Fe combinations. Results of these tests will be presented by the NBS.

* This work was sponsored by DARPA and monitored by ONR under contract #N00014-77-C-0373.

** Present address: Northrop Research and Technology, Palos Verdes, California

† Present address: Mexico City

1. INTRODUCTION

In May 1982, Phrasor Scientific, Inc. delivered a Micro-Particle Processor (μ PP) to the National Bureau of Standards, thus completing the Table Top Powder Generator Program supported by ARPA and monitored by ONR. The program was initiated to (1) develop the method of high temperature Electrohydrodynamics (EHD), (2) apply this technology to rapid solidification and other materials-oriented areas, and (3) produce a unique laboratory instrument capable of generating micron and submicron particles of various alloy systems (Ref.1-5). Before the initiation of this contract little, if any, technical information existed in the field of high temperature EHD to draw upon the experience of previous research of state-of-the-art development. This program has succeeded in introducing into Materials Science a unique material processing and research tool based on advances made in the understanding and construction of molten metal EHD devices during the past few years. The integration of these two very distinct and separate technologies, EHD and Materials Science, for rapid solidification studies has stimulated interests in such diverse applications as nucleation studies, magnetic properties of fine powders, powders composed of refractory metal and ceramic materials, rare earth and precious metal applications, copper powders for dispersion in inks used with hybrid circuits, photovoltaics, novel coatings and others. The capability of the EHD process to deposit thin films and

coatings has been evaluated as a process that could produce low-cost polycrystalline silicon sheet for solar photovoltaic applications (Ref. 6).

The main objective of this program was the development of an automated Micro-Particle Processor, capable of producing rapidly solidified powders in laboratory quantities for use by material scientists. This work was motivated by the possibility of processing new material structures and compositions by rapid solidification. Amorphous powders and new alloy compositions were originally anticipated and have been produced by EHD.

Much more work in metallurgy is required to increase our understanding of the inter-relationship between various process variables involved in rapid solidification. These variables, such as alloy composition, cooling rate, microstructure, etc. can only be obtained through careful experimentation and imaginative theoretical considerations. The Micro-Particle Processor is able to provide controlled and reproducible scientific experimentation affordable in a relatively small research laboratory. It also provides a means for producing submicron droplets of both low and high temperature alloys which are rapidly quenched in flight or by deposition on various substrates (conductive cooling).

The EHD technique, initially developed to produce charged liquid droplets of glycerol for space propulsion applications, requires the application of an intense electric field to a liquid surface. The intense field is obtained by applying high voltage to the tip of a capillary nozzle to which the liquid is transported. The electric field draws the liquid out to a spike releasing charged droplets which are further accelerated by the field. These charges can be as small as atomic ions and can be as large as twice the capillary inner diameter, depending upon the electric field and the liquid flow rate. For the rapid solidification application, alloy metals heated in an alumina crucible are delivered by gas pressure to an alumina capillary nozzle, entirely operated under high vacuum conditions (10^{-5} torr). The droplets cooled by radiation and solidified to powders, are collected by various substrates for examination by electron microscopy. Powders ranging from 30nm to 100 μ m have been observed with estimated cooling rates by radiation alone ranging from 10^3 K/s to 10^8 K/s. When coatings are made the conditions are arranged so that the droplets remain molten when they impinge upon the collecting substrate.

2. CAPABILITIES AND ACCOMPLISHMENTS

Capabilities of the Micro-Particle Processor

The capabilities of EHD to produce rapidly quenched metallic powders for the materials scientist are listed below:

- ° Solidification studies relating average cooling rate, prior to solidification, and particle size to the formation of amorphous and crystalline structures.
- ° Rapid solidification studies performed to determine the effect of particle size and cooling rate on increases in solute solubility of alloyed elements.
- ° Rapid solidification and heat transfer studies on extremely fine crystalline and glass metal powders.
- ° Production of electron transparent metal powders. The direct observation using TEM of a complete casting is a unique capability heretofore not available.
- ° Nucleation studies that relate particle size to the number of crystals (number of nuclei) in each particle.
- ° Electron diffraction study of fine powders to establish the sequence of formation of stable and metastable phases in a given alloy system as a function of cooling rate.
- ° The electron transparency of the fine powders produced permits studies of the growth morphology (plane front, cellular, or dendritic) during solidification. Effects of particle size, cooling rate, and solute content upon liquid-solid interface morphology can be studied.

The above listed capabilities have been demonstrated in several publications (Ref. 2, 3, 4, 7).

Results of Powder Studies

In the course of developing the μ PP, several materials were used to extend the EHD technique to higher temperatures and to include a wider variety of material types. The major differences between the alloys experienced in EHD involved such liquid parameters as melting point, surface tension and wetting angle between liquid and nozzle. Table I lists the pure elements and alloy combinations tested at Phrasor. The work at NBS extends this list even further. These studies resulted in observations of amorphous, single crystalline, bi-crystalline and tri-crystalline powders. Studies of extended solubility segregation, nucleation and metastable phases were made, greatly aided by the fact that the powders were sufficiently small to be electron transparent.

A few examples of the powders produced by the EHD technique and analyzed by TEM are shown here. They illustrate interface breakdown due to segregation and nucleation behavior producing bi-crystals in smaller powders and micro-crystals in larger ones.

The Al-6% Si powders below 200nm solidify in a plane front mode without segregation even for Si content as high as 6% when the solubility is 1.65%. This extended solubility indicates the achievement of large undercoolings prior to nucleation. In the larger particles, there was usually a transition from plane-front to cellular (segregated) growth as the droplet size increased and the achievable undercooling was consequently decreased. Fig. 1 shows an example of the interface break-down due to segregation in an Al-6% Si powder.

A large fraction of the powders in the range of 200nm or smaller are bi-crystals as shown in

TABLE I

LIST OF ELEMENTS AND ALLOYS SPRAYED

Elements	Binary	Amorphous Alloys
Pb	Pb-60% Sn	Fe-15% Si-10% B
Sn	Al-4.5% Cu	Fe-40% Ni-14% P-6% B
Al	Al-28% Cu	Al-30% Ge
Cu	Al-3% Si	
Ge	Al-6% Si	
Si	Al-12% Si	
	Al-25% Fe	
	Al-1% Mn	
	Al-30% Ge	

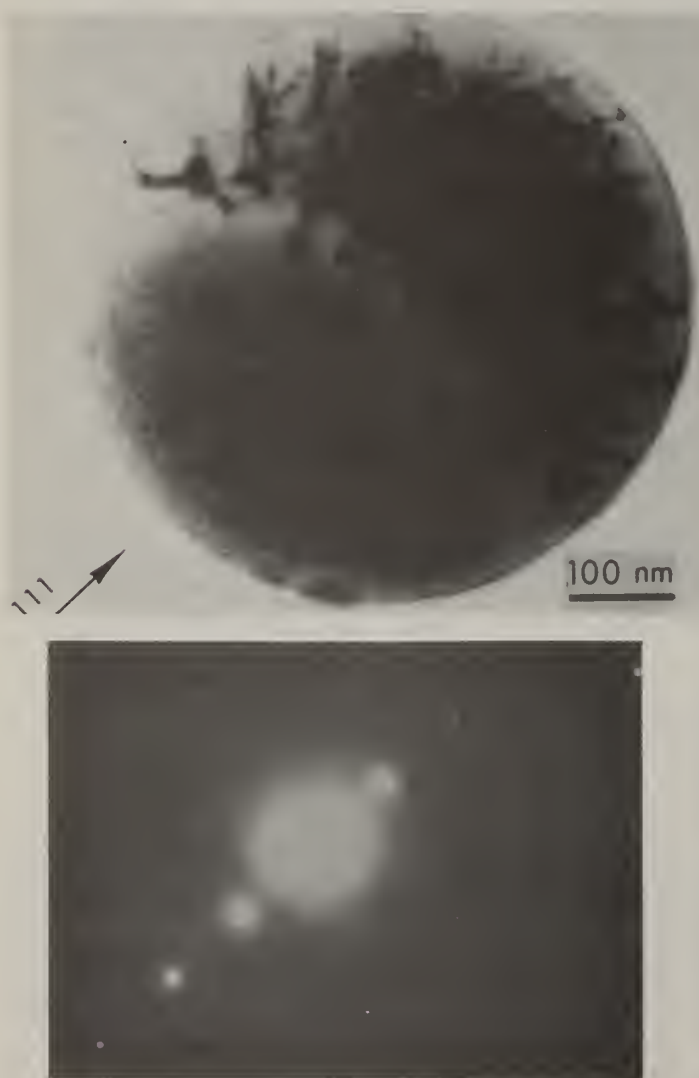


Figure 1. TEM image and diffraction pattern of an Al-6%Si powder, showing the transition between plane front and cellular growth modes due to segregation.



Figure 2. Examples of a bicrystal in Al-Ge eutectic powders.



50 nm

Figure 3. Typical structure of powders above 100nm in diameter of Al-30% Ge.

Figure 4. Photograph of the Micro-Particle Processor Delivered to NBS.

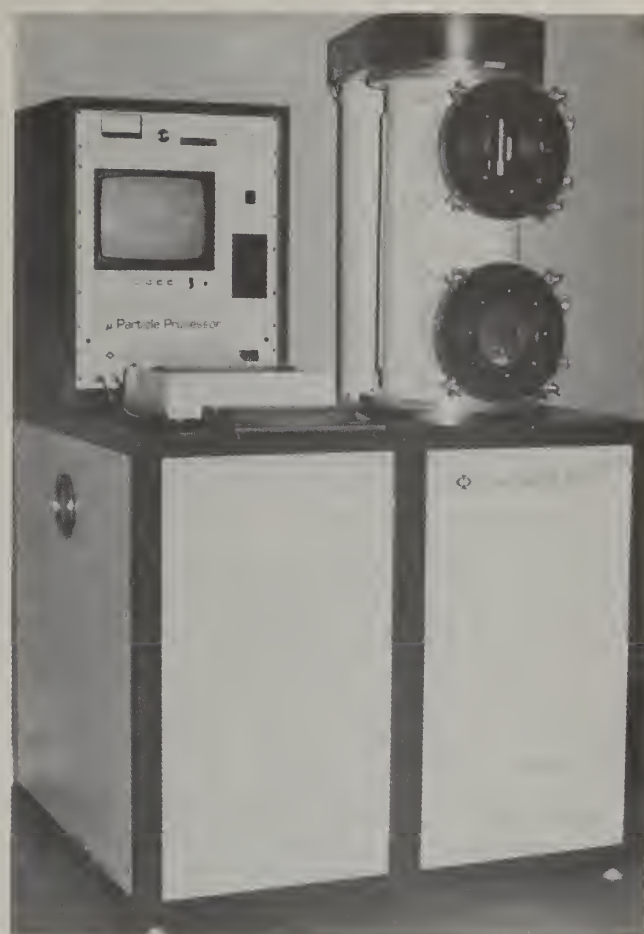


Fig. 2. Some preliminary diffraction and micro-chemical information suggests that one of the crystals may be Al-rich and other, Ge-rich but this is not conclusive.

Most of the larger powders, above 100nm, have a structure similar to that in Fig. 3 where a large number of crystals in the range of 10nm can be distinguished by diffraction contrast. Some of the powders that could be properly tilted in the TEM revealed a microstructure reminiscent of that produced by the plane-front to cellular transition in Fig.1.

3. RESULTS AND APPLICATIONS

A micro-structure study was made by Levi and Mehrabian (Ref.6) using the electron transparent sub-micron aluminum alloy powders produced at Phrasor Scientific by the EHD process. Various micro-structures of several hundreds of powder samples were observed including homogeneous plane-front solidified single crystals, cellular crystals, block segregates, multiple grains and twins. With the aid of thermodynamic concepts, thermal history and solidification modes were deduced. It was found that segregation decreased with smaller particle sizes. This presumably was caused by the greater undercooling experienced by the smaller particles. Nucleation studies also showed that larger undercooling promotes multiple nucleation and the occurrence of twins. These and other observations were made showing how electron transparent powders generated by EHD are very useful in fundamental solidification studies.

Among the most interesting applications of EHD produced powders are their use as Analytical Electron Microscopy standards and their suitability for re-melt and re-solidification experiments in the electron microscope (Ref.4 and 8). These uses are made possible because of the small size of the EHD particles and because they are generally spherical in shape.

The capability of the EHD generation method to produce and control charged liquid droplets leads to a wide range of applications in materials Science. Some of the important features of EHD useful in these applications involve: copious production of submicron droplets, the high speed to which they can be accelerated, the vacuum or gas environment selected, the choice of selecting that either droplets or powders can be impinged upon the substrate. Different uses considered for applications of powders include micron sized copper powders for conductive inks, silicon spheres for photovoltaics and

special chemical compounds produced by the projection of molten droplets through carbide, nitride or hydride producing atmospheres. Fine metal (or non-metal) flakes can be produced by splat impingement on a non-adhering surface.

Surface properties can also be altered by coatings to increase hardness, prevent corrosive contact, retard oxidation, increase wear resistance, and in general provide a coating which lowers the overall cost of the raw material or production such as the production of solar cells (Ref.6). Spongy coatings have been produced. Special coatings on a reactive substrate may be obtained that is not achievable in a bath or gaseous atmosphere.

4. THE MICRO-PARTICLE PROCESSOR

The production of the Micro-Particle Processor was the final goal of the DARPA/ONR Program (Table-top Powder Generator)(Ref.9). The Processor is able to produce about 20 grams of alloy material in about two to three hours. This limitation is due to the size of the reservoir volume (as listed in Table II, Specifications) in this particular model. It is possible to increase powder yields by using a larger reservoir or by operating multi-nozzle droplet sources. The production rate increases nearly linearly with the number of nozzles. Table II also lists some of the other μ PP specs.

A photograph of the μ PP delivered to NBS, is shown in Figure 4 and a diagram showing its dimensions are given in Figure 5. Within the Main Console are the vacuum pump system, the high voltage system, the source heater controls, and the electrical control relay system. On the left side on top of the Main Console is the Computer Console containing the computer, floppy disc drive, video screen and the vacuum gauge (controller). In front of the Computer Console is the printer and the control keyboard. On the right side in the vacuum chamber which contains the EHD source visible through the top view port and the powder (sample) collector which can be observed through the bottom view port. Behind the vacuum chamber is a cylindrical column routing the high voltage and source heater cables to the top of the chamber. These cables are shielded by the High Voltage Cover on top of the column and the chamber. Figure 6 shows a close-up photograph of the Computer Console and the chamber showing the EHD source operating at high temperature. The video screen is shown displaying parameters of the experimental run. Figure 7 shows the video screen in the Standby Mode, as it appears when the μ PP is first turned on. It provides the date and time, inserted by the operator, and describes the states of the various vacuum valves, the pumps, the pressure, whether the cooling water is on and whether the view ports are open or closed. The different modes of the μ PP, shown on the screen determine the sequence of the operation that is all computer controlled. The modes of operation are listed below:

- | | | |
|-------------------|-----------------------|------------------------|
| 1. Standby Mode. | 3. Start Vacuum Pumps | 5. Heat up & Operation |
| 2. Set Parameters | 4. Pumpdown Chamber | 6. Shutdown |

TABLE II
SPECIFICATIONS

SOURCE:

Voltage.....1 to 20kV
Current.....0 to 3mA
Nozzle Heater Power.....500W Max.
Reservoir Heater Power...500W Max.
Operating Temperature....To 1350°C (2462°F)
Reservoir Pressure.....To 2000 Torr Max.
Reservoir Volume.....0.3in³ (4.8cm³)
Nozzle Orifice.....002" DIA (.005cm)

MATERIALS:

Reservoir.....High Purity Alumina
Nozzle.....High Purity Alumina
Source Gasket.....GRAFOIL(graphite)
Extractor......030" Graphite
Nozzle Heater.... .020" Ta
Reservoir Heater. .020" Ta
Thermocouple.....Type K (Chromel-Alumel)

CONSOLES:

Main Console.....40" high by 47" wide
by 40" deep (101 x 119 x 101cm)
Computer Console....27" high by 21" wide by
21" deep (68x53x53cm)
Vacuum Chamber.....12" i.d. x 27.5" high
(30 x 70cm)

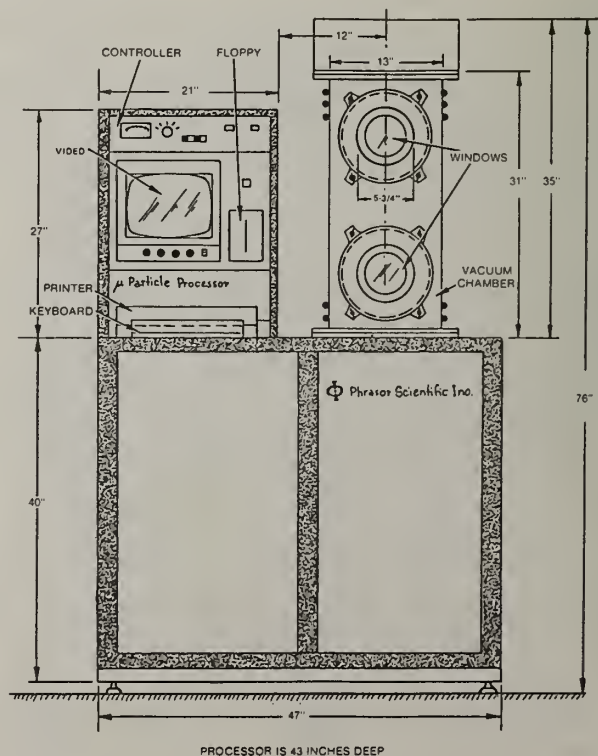


Figure 5. Diagram of the Micro-Particle Processor.

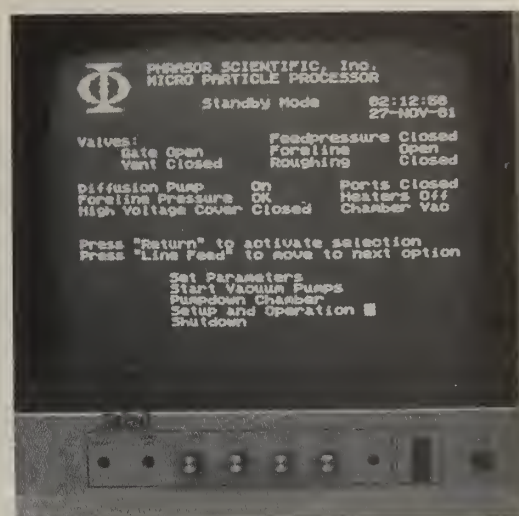
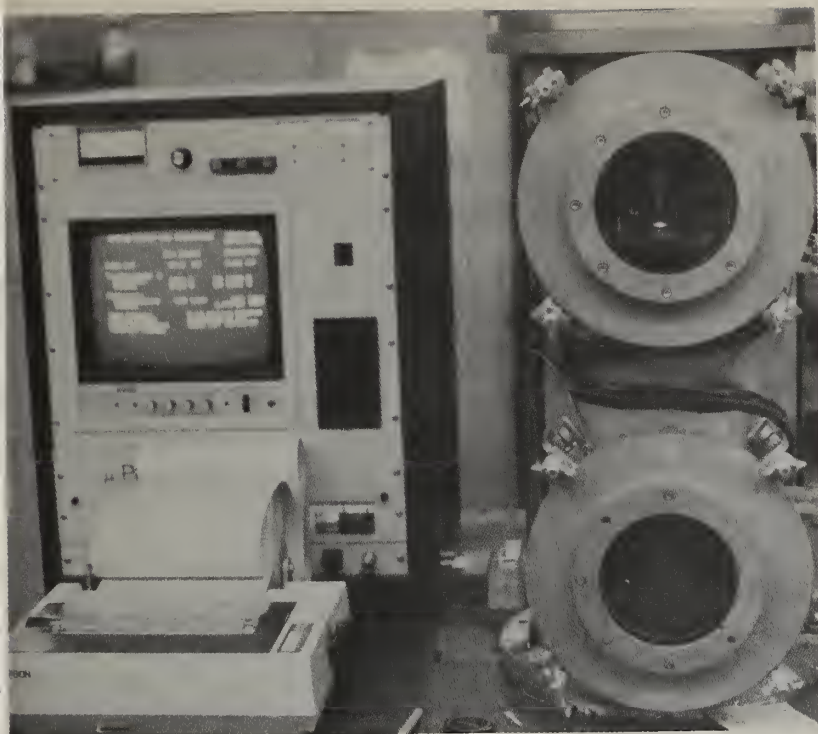


Figure 7. Close up of the Standby Mode on the Video Screen.

Figure 6. Photograph of the Computer Console and the Vacuum Chamber.

When the Set Parameter Mode is selected, the screen changes to display all the important parameters to identify the particular run such as date, time, operation, alloy, temperatures, etc. After these are complete, the display returns to the Standby Mode with the cursor on the next mode in the sequence. When Start Vacuum Pumps is selected, the operator can turn on the pumps and open the proper valves. The computer program also prevents the operator from making mistakes such as turning on the vacuum pump and opening the gate valve while a view port is open. The next mode allows for the chamber pumpdown. The Heatup and Operation Mode is the one in which the alloy is sprayed. After completion of the run, the Shutdown steps are sequenced.

The Micro-Particle Processor produced on the ARPA/ONR Program was delivered to the National Bureau of Standards in May 1982. In a co-operative effort between Phrasor Scientific and the Bureau, the μ PP was put into operation in a few days and the Al-Fe alloys were processed. The NBS Solidification Program using the μ PP includes fundamental studies of extended solubility, new alloy design, comparisons of theory with experiment and development of predictive models of micro-structure formation. Results from the initial experiments on the μ PP as part of the extensive NBS program are reported by Shechtman and Ridder in this Third Rapid Solidification Processing Conference (Ref.10).

ACKNOWLEDGEMENTS

The authors are grateful for the support provided by Dr. E.vanReuth and Lt.Col.L.Jacobson of DARPA and Dr.B.MacDonald of ONR. Dr.Pol Duwez, well known in Rapid Solidification, was extremely helpful.

REFERENCES

1. J.F.Mahoney, J.Perel, Z.Shanfield and B.E.Kalensher, "Development of a Tabletop Model for the Generation of Amorphous/Microcrystalline Metal Powders", Interim Tech.Report #80-1, ONR, Arlington, VA (1980).
2. J.Perel, J.F.Mahoney, B.E.Kalensher, K.E.Vickers & R.Mehrabian, Rapid Solidification Processing: Principles and Technologies, edited by R.Mehrabian, B.H.Kear, M.Cohen (Claitor's Pub.Div., Baton Rouge, LA, 1978).
3. J.Perel, J.F.Mahoney, B.E.Kalensher & R.Mehrabian, Advances in Metal Processing, edited by J.J.Burke, R.Mehrabian & V.Weiss, (Plenum Pub.Corp.1981), p.79.
4. J.Perel, J.F.Mahoney, S.Taylor, Z.Shanfield & C.Levi, Amorphous and Crystalline Alloys, B.H.Kear, B.C.Giessen and M.Cohen, editors, (Elsevier Science Pub.Co., North Holland 1982), p.131.
5. J.F.Mahoney, "Tiny Particles Aid Research on Microstructures", Indus.Res.&Dev., 24, 150 (January 1982).
6. J.F.Mahoney & J.Perel, "Electrostatic Spray of Silicon for Photovoltaic Applications", IEE/IAS 1981 Annual Meeting, Philadelphia, PA, (5-9 October 1981).
7. G.C.Levi & R.Mehrabian, "Microstructures of Rapidly Solidified Aluminum Alloy Submicron Powders", Metallurgical Trans., 13A, 13, (1982).
8. H.Fraser, University of Illinois, private communication.
9. J.F.Mahoney, J.Perel, Z.Shanfield, B.E.Kalensher & S.Taylor, "Development of a Table Top Model for the Generation of Amorphous/Microcrystalline Metal Powders", Final Technical Report #82-1, ONR (1982).
10. D.Shechtman, S.D.Ridder, & R. Mehrabian, "Microstructural Studies on Supercooled Sub-Micrometer Powder Particles." Third Conference on Rapid Solidification Processing: Principles & Technologies, NBS, Gaithersburg, MD (6-8 December 1982).

RAPID SOLIDIFICATION SURFACE TREATMENT
OF
DISCS AND RINGS BY ELECTRON BEAM PROCESSING

M. TULI

Pilgrim Materials Corp. South Windsor, Ct. 06074

P.R. STRUTT

Uni. of Connecticut, Storrs, Ct.

ABSTRACT

The technological requirement of surfaces with enhanced wear and rolling contact fatigue resistance frequently involves treatment of cylindrical surfaces. As a consequence, the electron beam surface melting technique has been applied for treating discs and rings with various dimensions. The technique has been successfully applied for the microstructural modification of hard materials.

INTRODUCTION

Methods for producing hard, wear and corrosion resistance facings on materials are important in terms of:

1. Improved performance
2. Cost reduction
3. Rejuvenation of high technological components.

For this reason various types of plasma deposited coatings are being used to a ever increasingly scale in variety of industrial applications.

Directed energy beam processing now provides a unique approach to forming surface layer having an unusual degree of microscopic refinement and homogeneity (1,2). Most frequently, these layers are perfectly bonded to the substrate material. This particular aspect can be of extremely importance in specific application where the lack of perfect bonding in the case of plasma deposited layer is frequently regarded as a significant draw-back.

Electron beam processing is a particularly versatile technique since the beam may be readily programmed to treat large area of complex geometry (3).

EXPERIMENTAL TECHNIQUES AND RESULTS

In laser/electron beam glazing momentary melting and ensuing rapid solidification proceed as the high energy beam traverses the material surface. This results either in the formation of microcrystalline or amorphous layer. The fact that some alloys undergo transformation into the amorphous state has led to the term "laser glazing" and "electron beam-glazing". The actual cooling rates achieved and the thickness of the rapidly solidified layer critically depends upon the power density and the velocity of the beam relative to the substrate material. In contrast to other rapid solidification techniques the cooling rate may be varied over a particularly wide range, from 10^4 to 10^8C.s^{-1} , for example, with melt depths ranging from 2mm to a micron (4).

Rapidly solidified surface layers of high dimensional tolerance and homogeneity are attainable using ultra-rapid beam deflection system specifically developed by Pilgrim Materials Corporation. Precision control of electron motion is achieved by use of a low inductance/high current deflection yoke driven by an ultra-rapid response

current control amplifier. This circuit is designed so that the beam can follow any type of oscillation voltage waveform.

Fig. 1a shows the actual current triangular waveform through the coil and Fig. 1b shows the actual input voltage waveform which is produced by current feed-back circuitry. Negligible disturbance of triangular current waveform is maintained up to a frequency of 15KH. The complete circuitry involved in this application is contained within a single unit, as shown in Fig. 2. A cylindrical bar (M-42 tool steel) $\frac{1}{2}$ " diameter, was treated using electromagnetically oscillated beam generated by this unit (Fig. 3).

Topographical and Microstructural Characteristics

Fig. 4a and b are low and medium magnification micrographs of a longitudinal view of a 1.25 inch (3.18 cm) wide zone produced by an electron beam laterally oscillated at 1000 hertz. Clearly evident in these figures is the uniform thickness of the rapidly solidified layer; the melt depth is approximately 250 μ m. In addition, the actual surface is particularly smooth and does not display any evidence of ripple structure. The entire zone etches in a homogeneous manner, which is indicative of a uniform microstructure and an absence of significant segregation of alloying elements.

In Fig. 4c the zone thickness seems to taper-off very smoothly at the edge. Obviously, this highly desirable feature results from an almost instantaneous reversal of the electron beam at the maximum amplitude.

Finally, a high magnification scanning electron micrographs in Fig. 5 shows a homogeneous cellular solidification structure in the rapidly solidified M2 high speed steel. This structure is typical of the hard martensitic/austenitic microstructure observed both in laser and electron beam glazed M2 high speed steel. (6).

CONCLUSIONS

This study shows that a much higher quality, homogeneous electron beam glazed surface (1 micron) can be formed on a cylindrical/disc surface using "line heat source".

An important industrial application of the technique just described is for the surface treatment of high performance bearing used in gas-turbine jet.

REFERENCES

1. P.R. Strutt, H. Nowotny, M. Tuli and B. Kear, Mat. Sci. & Engr. 36, 217 (1978)
2. P.R. Strutt, Metal. Forum, 4 117 (1981)
3. M. Tuli, P.R. Strutt, Materials Research Society Annual Meeting (1981)
4. R.J. Schaefer, T.R. Tucker and J.D. Ayers, Laser/E.B. Processing of Materials, Academic Press, N.Y. 749 (1980)
5. P.R. Strutt, Mat. Sci. & Engr. 44, 239 (1979)

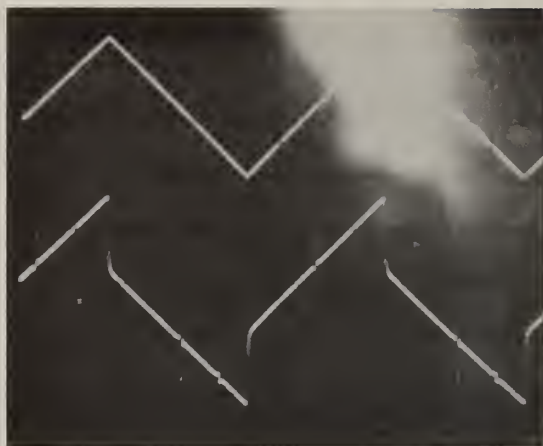


Fig.1.

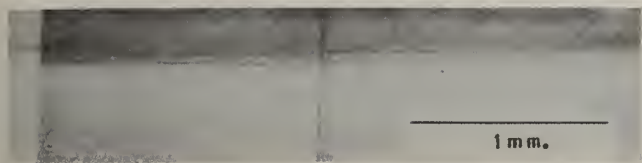
- a. Shows the actual current triangular waveform through the coil.
- b. Shows the actual voltage waveform which is produced by current feed-back circuitry.



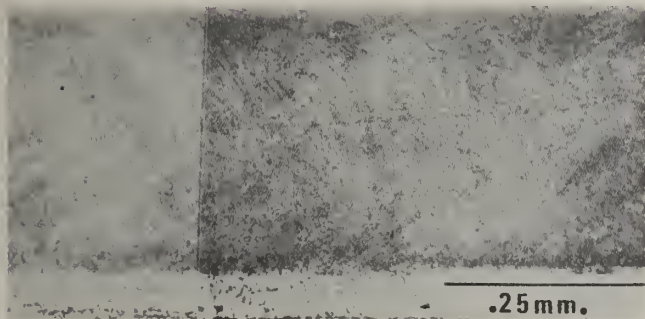
Fig.2. Single unit with complete circuitry.



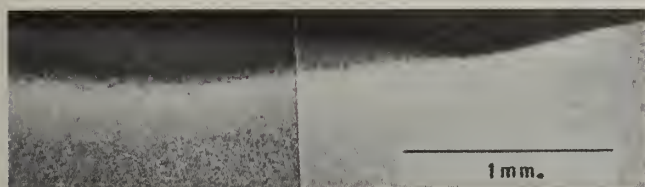
Fig.3. A cylindrical bar (M-42 tool steel) was treated using electromagnetically oscillated beam generated by unit shown in fig.2.



(a)



(b)



(c)

Fig.4.
a&b are low & medium magnification micrograph of a longitudinal view of a 1.25 inch (3.18 cm) wide zone produced by an electron beam laterally oscillated at 1000 hertz. Melt depth is approximately 250um.

In 4c the zone thickness seems to taper-off very smoothly at the edge.



Fig.5.
Shows a homogenous cellular solidification structure in the rapidly solidified M2 high speed steel.

PLASMA DEPOSITION EFFECTS ON STRUCTURES AND PROPERTIES OF RSPD SUPERALLOYS

R. W. Smith

General Electric Gas Turbine Division
Schenectady, NY

D. V. Rigney, J. S. Smith

General Electric Aircraft Engine Group
Evendale, OH

J. R. Rairden

General Electric Corporate Research and Development
Schenectady, NY

ABSTRACT

The low pressure plasma deposition process has evolved from research and development to manufacturing during the past six years for the application of environmentally resistant coatings to superalloy components. Recently, research and development studies have extended this technology to the fabrication of rapidly solidified plasma deposited (RSPD) structural bodies. This report documents the results of a coordinated study, funded by DARPA, (Project 4289) in three organizational components of GE to evaluate several commercially available plasma spray systems for deposition of superalloy components.

Introduction

The low pressure plasma deposition process has evolved from research and development to manufacturing during the past six years for the application of environmentally resistant coatings to superalloy components. Recently, research and development studies have extended this technology to the fabrication of rapidly solidified plasma deposited (RSPD) structural bodies. [1] This is a progress report on the results of a coordinated study to evaluate and further develop several commercially available plasma guns for deposition of superalloy components.

Three important factors in plasma spray deposit quality are: the plasma jet, powder distribution/injection, and environment.

These factors control the heat content of the gases, the heat transfer to the powder particles, the location of the particles in the jet, the particle velocity, and the environmental reactions. Therefore, the degree of particle melting, the deposition pattern, the deposit density, the deposit efficiency, and the extent of deposit inclusions are determined by the processing factors. The arc gas flow rate and composition, the nozzle design (manufacturer or manufacturer model), and the power level contribute most to the energy content of the gas. The nozzle design and the jet pressure ratio (P_0/P_{chamber}) will determine how the energy is distributed in the plasma jet, either in heat content (enthalpy, H) or velocity (V) and determine the exit Mach number (Ma #). Powder injection parameters, such as powder size distribution, injection gas flow rate, powder flow rate (P.F.R.), injection location and injection angle, will all affect powder particle velocities and trajectories. Hence, how well powder particles will be melting become controlled by the plasma jet and the powder injection.

The intent of this paper is to present a progress report on a coordinated study, under contract to DARPA, to evaluate several commercially available plasma guns, operated in accordance with manufacturer's instructions and modifications discussed with the manufacturer. These evaluations were conducted on two Ni-base superalloy deposits, Rene 80 and Hastelloy Alloy X, in an effort to determine plasma deposition parameters.

Experimental

Different vendors' guns were studied as a function of processing parameters i) power level ii) arc gas composition iii) arc gas flow rate iv) nozzle design v) powder injection location, internal and external vi) pressure ratio (chamber pressure) vii) and relative gun/substrate motion. A γ ' strengthened superalloy, Rene 80 and a non- γ ', solid solution/carbide strengthened superalloy, Hastelloy Alloy X were selected as the candidate alloys for this study. The initial processing conditions used were either those recommended by the gun vendor or those which had been developed in-house prior to the start of the project. Table 1 summarizes the parameter ranges evaluated for each of the plasma gun designs.

TABLE 1: PLASMA DEPOSITION PARAMETER RANGES

Anode	Power (kw)	Arc Gas Flow			Chamber Pressure (torr)	Powder Feed Rates (g/min)	Powder Injection			TA (KW)	Spray Distance (mm)
		Ar (slm)	He	H ₂			Flow (slm)	Location	Angle		
Vendor A Ar/He											
Mach 3 (std)	40-80	108-180;	28-140;	--	14 - 120	100	15	Int. & Ext.	20°	0-3	400
Mach 2 (new)	50-72	90-120;	23-64;	--	20 - 300	100	4-15	Int. & Ext.	20°	0	400
Vendor A Ar/H ₂	74	169	--	23	60	190-380	17	Int.	20°, 25°, 30°	1	381-457
Vendor B Ar/H ₂	40-56	50	--	6-9	30 - 235	76	0.7-2.9	Ext. 8 - 22mm	-2°	0	260-410

Stationary (sweet spot) or traversing deposits were made onto 150 x 150 mm plates in thicknesses from 3mm to 15mm for deposition times from 1 1/2 to 30 minutes, depending on the particular evaluation or specimen requirement.

The alloys, Rene 80 and Hastelloy-X, were selected for study because they are used extensively in gas turbines. RSPD data can be compared with a large data base for both alloys as conventionally processed.

Results and Discussions

Evaluations of deposits made during processing parameter studies were spray pattern (sweet spot and traversing), deposit efficiency, as-deposited density, heat treated density, as-deposited metallography, heat treated metallography, and selected tensile testing.

Spray Pattern

The deposit spray pattern is a measure of the particle trajectories in the plasma jet measured at the substrate. The spray patterns, in general, are characterized by bell shaped mounds which build up during deposition. The patterns have been found to be affected by the gun/substrate motion, spray distance, chamber pressure powder size distribution, nozzle design, and powder feed injection parameters (i.e. location, number of ports, injection angle, etc.). The spray pattern spreads, shrinks, shifts axis, or changes thickness distribution with these process variables. The thickest, central region of the deposit is the most dense, however, the periphery of the deposit rapidly decreases in density. This drop off in density has been attributed to a "fringe" of the plasma jet where powders are heated less efficiently and may be completely unmelted yet become entrained in the deposit. The "fringe" region has also been found to be sensitive to the aforementioned process variables.

In general the spray pattern has been found to increase in diameter and become more distributed with i) decreasing chamber pressure ii) increasing power iii) increasing spray distance (S.D.), while the "fringe" becomes larger with i) decreasing power ii) increasing chamber pressure iii) increasing arc gas flow rates iv) and gun/substrate motion.

Deposit Density

The as-deposited density is a measure of the melting efficiency of the plasma jet and as such is a good indication of the process variables effects on deposit quality. The density has been

found to be quite sensitive to deposit location (center vs. fringe) and substrate/gun motion where the "fringe" of the plasma jet has to be included over the entire deposit, unlike "sweet spots" where the fringe is not included in the deposit center.

The deposited structures have all been heat treated from 1200°C to 1250°C for one or more hours to complete the consolidation process, in accordance with the results reported in Ref 2. Density improvements from 1 to 3 percentage points were observed by heat treatment. For this study, all specimens received a 2 hour 1250°C densification heat treatment in vacuum or argon before the final alloy heat treatment.

Table 2 shows the range of as-deposited and heat treated deposit densities over a wide range of processing parameters measured under the conditions of this evaluation for the Rene 80 and Hastelloy-X sweet spot and traversing deposits. It was found that densities varied from 94.0 to 100.4 as-deposited to 98.9 to 100.8[±] for heat treated samples.

TABLE 2: DENSITY OF DEPOSITS

Gun	% Density* Rene 80		Hastelloy-X**	
	As Deposited	Heat Treated @ 1250°C	As Deposited	Heat Treated @ 1250°C
Vendor B, Ar/H ₂ Large Plates	96.5 - 100.5	99.1 - 100.9	97.6 - 100.5	99.8 - 101.5
	96.1 - 98.4	99.4 - 100.6	97.0 - 99.5	99.3 - 100.7
Vendor A, Ar/He Large Plates	96.3 - 99.9	98.9 - 100.3	94.4 - 99.7	96.3 - 99.8
	94 - 98.7	N/A	95.4 - 97.7	N/A
Vendor A, Ar/H ₂ Large Plates	95.9 - 99.3	99.4 - 100.6	96.7 - 99.6	99.1 - 100.3
	97.8 - 98.5	99.4 - 100.8	96.1 - 99.4	98.4 - 100.6

*For Rene 80, 100% density = 8.17 gm/cm³

**For Hastelloy X, 100% density = 8.23 gm/cm³

Microstructure - As-Deposited

The as-deposited microstructures of Rene 80 and Hastelloy-X were most affected by RSPD processing variables. The deposits are formed by a rapid succession of powder particle impacts built up on top of one another. The impacting powder particle population has been found to be in various stages of melting and/or solidification. Hence the deposits include features of unmelted particles, partially (interdentritically) melted powder particles, smaller pieces of larger dendritic powder particles, or completely melted particles which splat out into thin lamellae. Figures 1 thru 4 are examples of these microstructures. It has been found that the plasma jet enthalpy level most controls the as-deposited microstructures described above, but other variables can also effect microstructure. The plasma jet heat flux and high substrate temperature was found to induce directional grain growth mostly in the Hastelloy-X, coarsen γ' , or precipitate M₂₃C₆ carbides in Rene 80. These changes occurred both through the thickness (function of time vs. temperature) or radially. The radial changes in microstructure were attributed to both heat flux and the degree of entrainment of unmelted powder particles from the plasma jet "fringe". Figure 1a illustrates the typical unmelted particulate nature of the "fringe" area Rene 80 deposit.

Figures 1a through 1c illustrate the range of deposit microstructures of Rene 80. Figure 1a microstructure represents low enthalpy deposits made (either low power or high gas flow). Figure 1b shows a typical microstructure of Rene 80 or other high γ' nickel-base superalloy showing a moderate volume fraction of unmelted (spherical with dendrites or cells from atomization) or partially melted particles in a melted matrix. These type deposits were obtained from the recommended plasma jet parameters from Vendor A Mach 3+ conditions. Vendor B jets or further changes by lowering the Vendor A jet Mach number while keeping the power high have higher enthalpy "hotter" jets which produce more complete melting seen in the deposit microstructure 1c. The sweet spot deposit has very few unmelted particles, has a high density, and also 1-3 μ m thick "splats" showing very good melting.

Selected jet conditions were chosen for spraying the Hastelloy-X, and Figures 2a and 2b show the representative microstructure of the deposits. It can be seen that in all cases recrystallization has occurred, removing any of the "splat" microstructure. It is believed that the low alloy content and lack of γ' or any other precipitate in these Hastelloy-X deposits has removed the barrier for grain growth that in most cases maintained the splat nature of the Rene 80 deposits. The "sweet-spot" deposit plasma jet heat flux or substrate temperature in all cases was enough to induce grain growth in all the Hastelloy-X deposits. Relative differences in density

[±]Note: Greater than 100 percent density values probably result from compositional difference from reported values.

and uniformity of grain size across the deposits can be used to judge the optimum plasma jet for depositing Hastelloy-X. Again, the higher enthalpy jets produced the densest, most uniform Hastelloy-X deposits.

Traversing of the plasma jet has been found to reduce the grain growth that occurs in the Rene 80, and more substantially, the Hastelloy-X deposits. In addition, traversing the substrate forming deposits which include the "fringe" has been found to cause interpass layering of most deposits.

Figure 3 shows the typical structure of a traversing Vendor A Mach 3+ Rene 80 RSPD deposit in this evaluation. A layer line is seen in these deposits and its origin lies in the traversing of the plasma jet over an area larger than a sweet spot. Note the high unmelted particle content of the layer lines in Figure 3. It is believed that during the traversing, the fringe of plasma jet deposits both less than ideally melted particles and condensed vapor from vaporized powder on to the deposit surface.

Figure 4 is an example of the interpass layering that also occurred in this evaluation with the Vendor B plasma deposits. The structures are well melted; however, bands every 30-45 μ m delineate pass interfaces.

In summary, under the condition of this evaluation, plasma nozzle design, arc gas composition and flow rate, and power level varied the jet enthalpy the most. Hence, most of the as-deposited major structural differences resulted from these changes. Chamber pressure, which changes the nature of the jet expansion and powder feed (location and feed rate) can affect the as-deposited microstructure, density, and degree of melting. The balance of parameter changes, spray distance, and transferred arc did not significantly change the structure of these deposits, except where heat flux to the deposits may have induced grain growth. The larger traversing deposit plates produce a very uniform deposit along the centerlines and variations in deposit location are sensitive to deposit condition or alloy composition. Large deposits are also sensitive to interpass layer lines believed to be entrapment of fringe "debris" (unmelted or vaporized and condensed powder particles).

Microstructure - Heat Treated

The most important processing aspect of the heat treatment on microstructure is the influence that the as-deposited microstructure has on the final-heat treated structure. The effect of plasma processing on the as-deposited microstructure has been discussed previously. Features in the Rene 80 deposits were more varied than in the Hastelloy-X and include porosity, completely unmelted (possibly resolidified) deformed particles, fine grain melted matrix, interpass lines, lamellar structure from splatting of particles, and recrystallized grains. The Hastelloy-X deposits showed mostly recrystallized structures and the other features observed in Rene 80 were not typically discernible.

Figures 5a and 5b illustrate the range of microstructures observed for the heat treated (1250°C/2 h FC + 1204°C/2 h RQ + 845°C RQ) Rene 80 deposits. One example shows a fine grained structure (2 to 20 μ m) with limited grain growth being possibly controlled by the volume fraction of unmelted particles; in fact, the prior particles are decorated similar to P/M alloys. Another example shows better grain growth with equiaxed grains, more uniform size (25 to 75 μ m) and no prior unmelted particles.

In summary, it has been found that for the highly alloyed γ' strengthened, Rene 80 grain sizes were limited to maximum 50-75 μ m, with high heat treat temperatures, while for the simpler non- γ' strengthened alloy Hastelloy-X, grain growth was not as limited resulting in uniform structures. It is believed the stable MC carbide distribution in the Rene 80 is controlling grain size and that the as-deposited structure of the deposit will determine this carbide distribution either along particle, splat interfaces or interpass interfaces.

Tensile Tests

Tensile tests for both Rene 80 and Hastelloy-X sweet spot and large plate deposit produced over a wide range of processing conditions are in progress. Results to date for tests conducted at 910°C on small pin loaded flat tensile specimens, machined from these sweet spot deposits, are shown in Table 3. Prior to machining, the deposits were given a high temperature heat treatment (1250°C - 2 hrs) to further densify the deposits and increase grain size.

TABLE 3: 910°C TENSILE PROPERTIES SUMMARY SHEET
SPECIMENS MACHINES FROM SWEET-SPOT DEPOSITS

Process	Rene 80			Hastelloy-X		
	0.2% YS (MPa/ksi)	UTS (MPa/ksi)	Elongation (%)	0.2% YS (MPa/ksi)	UTS (MPa/ksi)	Elongation (%)
Vendor B Gun Ar/H ₂	<u>268-436</u> 38.8-63.3	<u>492-568</u> 71.4-82.4	0.5 - 3.5			
Vendor A Ar/He Gun Sweetspot	<u>331-527</u> 48.0-76.4	<u>405-582</u> 58.8-84.4	1.6 - 3.4	<u>119-172</u> 17.3-24.9	<u>154-190</u> 22.3-27.6	30.3 - 39.6
Vendor A Ar/H ₂	<u>324-428</u> 47.1-56.6	<u>337-428</u> 49.0-62.2	0 - 1.0	<u>159-179</u> 23.1-26.0	<u>168-188</u> 24.4-28.5	11.0 - 50.2
Avg Conv. * processed	<u>430.9</u> 62	<u>604.7</u> 87	13	<u>162.3</u> 23.5	<u>185.6</u> 26.7	42.0

The 910°C test temperature was selected because it has been reported^[1] that a significant ductility loss was observed in this range for γ' alloys in their study. This study then evaluated the effect processing variables may have had on this ductility minimum.

As can be seen from Table 3 the low ductility of Rene 80 was not strongly affected by variations in processing. The yield strengths and ultimate tensile strengths observed in this evaluation for Rene 80 ranged from 267 MPa/38.8 ksi - 528 MPa/76.4 ksi and 338 MPa/49.0 ksi - 581 MPa/84.4 ksi, respectively. The upper end of these test results compare favorably with those attained for conventionally cast Rene 80. The variation in yield strength was found to correlate with the as-deposited density, with the lower strength specimens corresponding to deposition conditions which resulted in lower density deposits.

The Hastelloy-X tensile properties exhibited much less variation than was observed for the Rene 80. This tensile property insensitivity to process variables for Hastelloy-X was also seen in the deposited microstructures for this alloy. These property levels, including ductility, are comparable to those observed for wrought Hastelloy-X sheet.

The conclusions from these tensile tests is that large variations in deposition parameters can influence the tensile strength results for Rene 80. The same variations show relatively little effect on Hastelloy-X, as was observed in both the as-deposited and heat treated microstructures.

Summary

This paper presents a progress report on the continuing evaluation of the plasma spray process for producing rapidly solidified alloys. The authors have made a sensitivity study of two superalloys, Rene 80 and Hastelloy-X. It has been found that the plasma jet enthalpy as function of equipment or by selection of operating parameters most affects the deposited structure of these materials. However, deposition parameter effects for Hastelloy-X are largely normalized by post deposition heat treatment as reflected in negligible differences in microstructure and tensile properties. For Rene 80, a more complex γ' strengthened alloy, a more restrictive range of parameters are required to achieve similar results. Tests are continuing to further evaluate the effect of some of the other features introduced by the processing variables such as substrate size or gun/substrate motion. Other deposit parameters such as powder feed variables, and chamber pressure, most affect deposit shape and efficiency with no discernable difference in "sweet spot" structure. Finally, substrate temperature and plasma jet heat flux were found to control grain growth and/or grain orientation while deposit structure (i.e. splat vs. unmelted) dictated carbide or other stable phase alignment or location.

The advantage of using high enthalpy processing conditions to improve deposit density has been demonstrated. It was shown that the control of powder injection is particularly important in using the Vendor B Ar/H₂ gun.

In order to increase the density of bodies formed using gun and/or substrate motion, improved guns which minimize or eliminate the fringe region in the spray patterns will be required.

*Conventionally cast Rene 80 or wrought sheet Hastelloy-X

Acknowledgements

The research reported herein was sponsored by DARPA Project 4289, Lt. Col. L. Jacobson and the authors and Air Force Project Monitor Dr. H.C. Gegel. We would also like to thank the General Electric Co. for their support and the many people there who have contributed to this effort.

References

- [1] M.R. Jackson, J.R. Rairden, J.S. Smith, R.W. Smith, J. of Metals, Nov. 1981.
- [2] J.R. Rairden, M.R. Jackson and M.F. Henry, To be published in the Proceedings of the 10th International Conference on Thermal Spraying, Essen, FRG, May 1983.

WP1008/C326/2072A

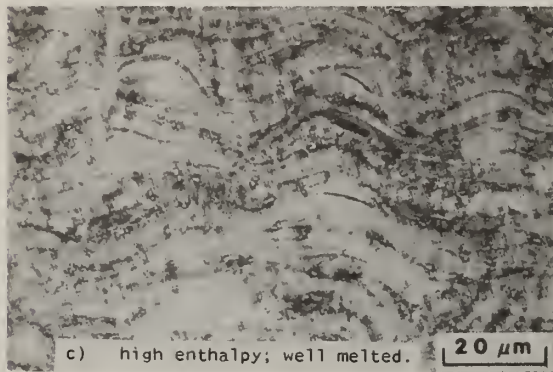
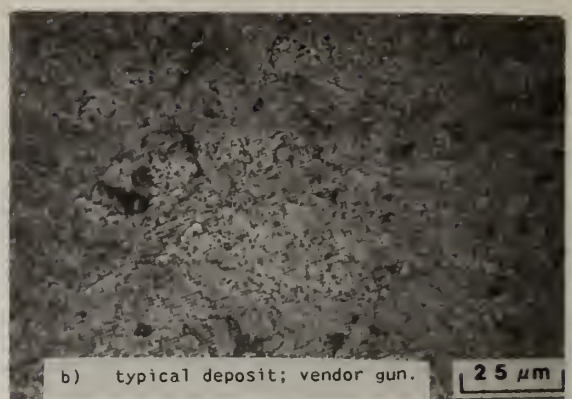
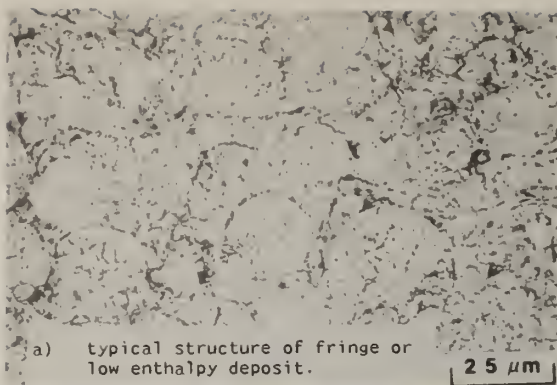


Figure 1 Typical as-deposited microstructures of RSPD Rene 80; (etched).

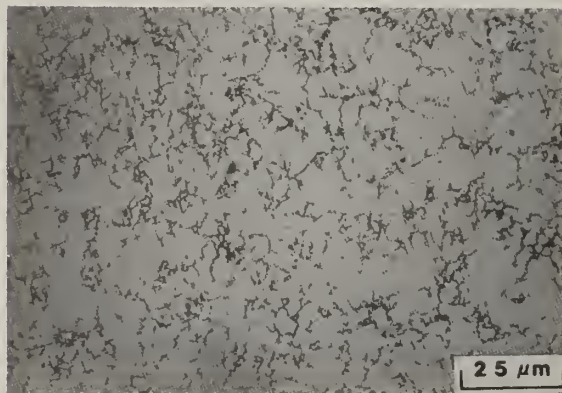


Figure 2 Typical as-deposited microstructures of RSPD Hastelloy Alloy X; (etched).

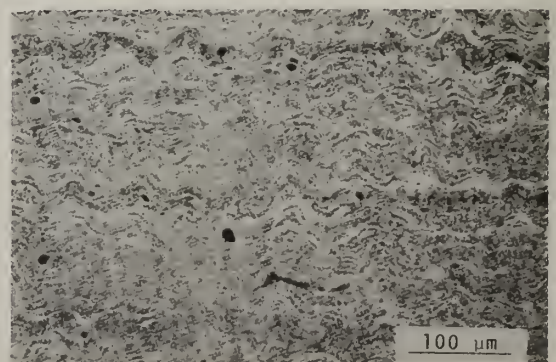
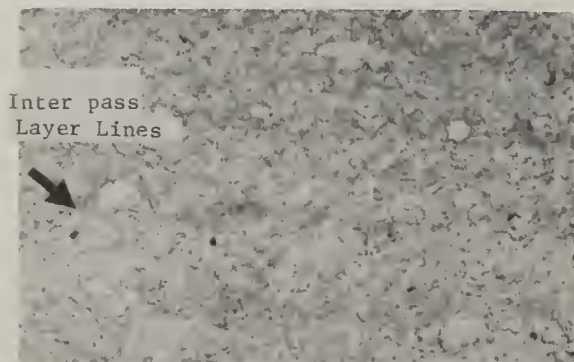
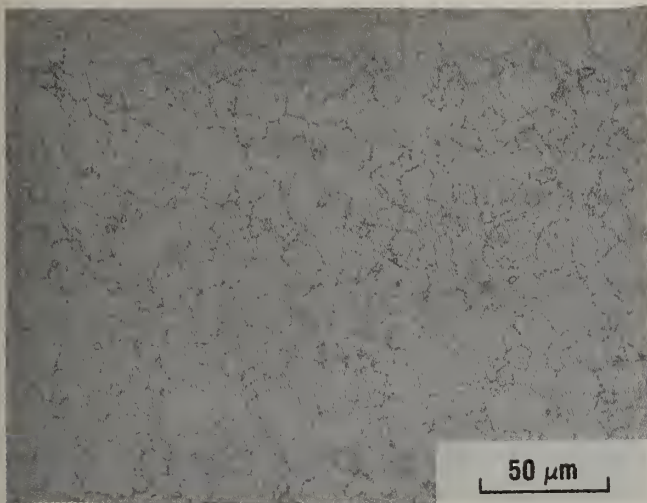
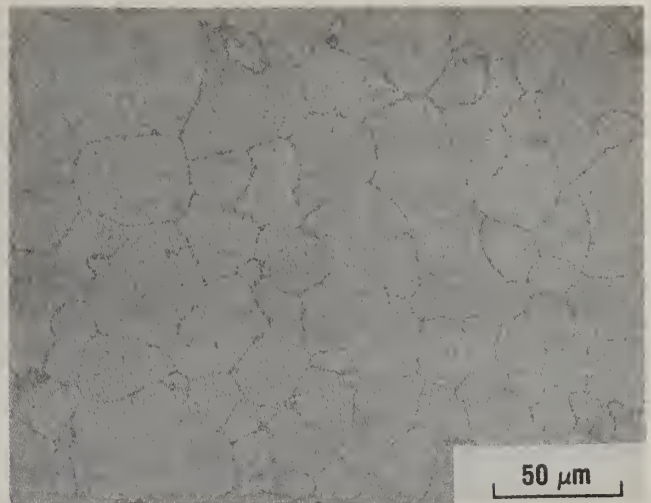


Figure 3 Mach 3 large traversing deposit microstructure of RSPD Rene 80.

Figure 4 High enthalpy large traversing deposit microstructure of RSPD Rene 80.



a) high unmelted content deposit.



b) well melted deposit.

Figure 5 Heat treat microstructure of RSPD
Rene 80 deposits.

THE MICROSTRUCTURE OF RAPIDLY SOLIDIFIED NiAl-Cr QUASIBINARY EUTECTIC

D. Shechtman*, T. Z. Kattamis⁺, F. S. Biancaniello⁺⁺ and W. J. Boettinger⁺⁺

*Center for Materials Research
The Johns Hopkins University
Baltimore, MD 21218

⁺Dept. of Metallurgy
University of Connecticut
Storrs, CT 06268

⁺⁺Metallurgy Division
National Bureau of Standards
Washington, DC 20234

ABSTRACT

The microstructure of melt-spun ribbon of the NiAl-Cr quasibinary eutectic composition has been characterized by optical and transmission electron microscopies. The eutectic composition is Ni-38.5wt%Cr-19.4wt%Al and is of interest because of the similarity of crystal structures (CsCl for β -NiAl and BCC for α -Cr) and lattice parameters of the two phases in the eutectic. The rapidly quenched microstructure consists of 0.5 μ m diameter columnar grains of the β -NiAl phase supersaturated with chromium to the eutectic composition. Between these grains a fine rod-type eutectic structure of the β -NiAl and α -Cr phases is observed with eutectic spacings as fine as 12 nm. The composition of the phases in the eutectic portion of the microstructure were found to be close to the equilibrium solubilities for these phases. A rationale for the appearance of a supersaturated β -NiAl phase at the eutectic composition, rather than a supersaturated α -Cr phase, will be presented based on the T_0 curves for this alloy system.

Introduction

The directional solidification of NiAl-Cr quasibinary eutectic alloy (Ni-33at%Al-34at%Cr) was previously investigated by Walter, et al. [1-4], who saw in it potential for high temperature applications. The eutectic consists of fine, nonfaceted fibers of α -Cr BCC phase embedded in a β -NiAl matrix, which is an ordered BCC phase (CsCl-type) containing some chromium in solid solution. From previous work by Kornilov, et al. [5], the NiAl-Cr quasibinary eutectic temperature is 1445 °C. The α -Cr phase at 1200 °C contains 20.6 mole% NiAl and, hence, has a composition of 17.1at%Ni-17.1at%Al-65.8at%Cr. The β -NiAl at 1200 °C phase contains 84.5 mole% NiAl, hence has a composition of 45.8at%Ni-45.8at%Al-8.4at%Cr. The volume fraction of fibers is about 0.34. In the directionally solidified eutectic all directions and planes of the two phases are parallel. The solidification microstructure consists of eutectic colonies of α -fibers of circular cross-section embedded in $\langle 100 \rangle$ -oriented columnar grains of β -NiAl and parallel to the growth direction, except near the cell boundaries where they are inclined to this direction. Despite this inclination the crystallographic relationship between fibers and matrix remains the same [1]. Both cubic phases are crystallographically related with only a small lattice mismatch, as evidenced by the large distance between dislocations observed at the interphase interface.

Walter, et al. [2] studied the effect of growth velocity on inter-fiber spacing. They quantitatively established the decrease in cell size and inter-fiber spacing with increasing growth velocity. They also investigated the effect of alloy additions on microstructural changes, in particular the rod-to-plate transition [3].

It appeared interesting to extend the study of solidification microstructures of the NiAl-Cr quasibinary eutectic to those achieved by rapid solidification, anticipating that the small difference in lattice parameter between the two phases would lead to substantial extension in solid solubility. Melt-spinning was used in this investigation. The growth rates achieved in this process are difficult to quantify, because of the possibility of bulk undercooling and an imprecise knowledge of the interface heat transfer coefficient. However, melt-spinning provides a simple way to assess

the alloy's response to rapid solidification processing.

Results of the work on microstructure of melt-spun ribbon of NiAl-Cr quasibinary eutectic alloy are reported herein and are also included in another publication [6].

Experimental Procedure

Rapidly solidified ribbons of NiAl-Cr quasibinary eutectic were melt-spun on a room temperature wheel in a helium atmosphere. Ribbons of about 25 μm thick and 2.5 mm wide were obtained at a linear velocity of 24 m/s. The ribbons were studied by optical microscopy, X-ray diffraction and analytical electron microscopy. Specimens for electron microscopy were electropolished and studied in a scanning transmission electron microscope equipped for nondispersive X-ray fluorescence analysis. The composition of the phases in the foil was evaluated by using the nominal composition of the specimen as standard. The Cliff-Lorimer coefficients were determined by using the intensities obtained from a thin area representing the general microstructure with a probe size of about 1 μm . Analysis of individual phases was then conducted in the same area of similar thickness. The C-L coefficients were redetermined for each set of analyses in different regions of the foil. This procedure eliminates the need for additional corrections of the measured X-ray intensities.

Results

The microstructure of an arc-melted chill-cast cylindrical specimen, 6.3 mm in diameter is illustrated in Figure 1. The rod-like α -Cr-rich phase is revealed as the dark etching phase.

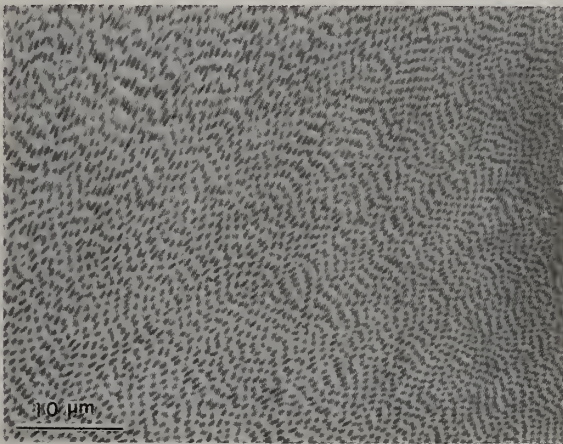


Figure 1: As-cast microstructure of arc-melted NiAl-Cr quasibinary eutectic (optical microscopy).

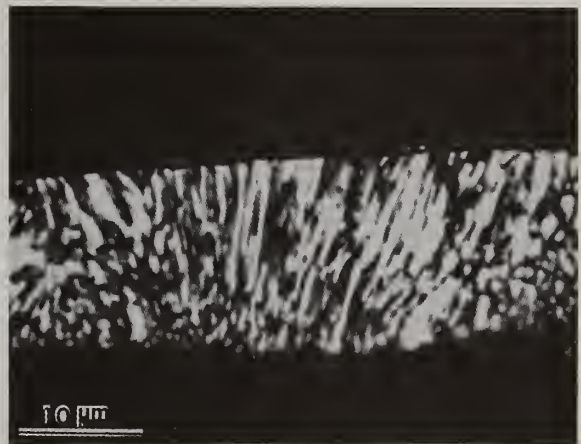


Figure 2: Columnar grains in melt-spun ribbon, edge-on section (optical microscopy).

The cast microstructure of the ribbons consists mainly of a columnar zone with columnar grains parallel to the heat flow direction. The intergranular spaces were not optically resolved. The average columnar grain width increased slightly with distance from the chill, Figure 2, from about 0.5 to 1.3 μm . The average columnar grain width also increased slightly with ribbon thickness.

The microstructure of the ribbon as observed by electron microscopy is shown in Figure 3, which represents cross-sections of columnar grains that grew perpendicular to the ribbon surface. The columnar grains average 0.5 μm in diameter and are surrounded by a fine eutectic. The boundary between a columnar grain and a region of particularly fine eutectic is shown at a higher magnification in Figure 4. The columnar grain is decomposed into a fine microstructure typical of conditional spinodal decomposition [7] with an average wavelength of 10 nm (lower right, Figure 4). The eutectic rods grow roughly perpendicular to the columnar grain and their spacing ranges from 12 nm, Figure 4, to 60 nm, Figure 3. The microstructure is not uniform and in some areas the volume fraction of the columnar grains by far exceeds that of the eutectic, Figure 5. In other regions of the same foil the volume fraction of the eutectic is much higher, Figure 6. These variations may correspond to different distances from the heat sink, however this was not confirmed in the present study.

A large proportion of columnar grains are single ordered domains. However, some of them contain two or more domains. Anti-phase domain boundaries are shown in Figures 3 and 7. These APBS run across the grain and in most cases end in a chromium-rich rod of the eutectic. The significance of these APBS to the understanding of the solidification process will be discussed later in this paper.

A diffraction pattern taken from a columnar grain, Figure 8, identified the structure as CsCl (B2). A diffraction pattern taken from a columnar grain and its surrounding eutectic, Figure 9, shows no extra reflections besides the CsCl. This indicates that both phases in the eutectic and

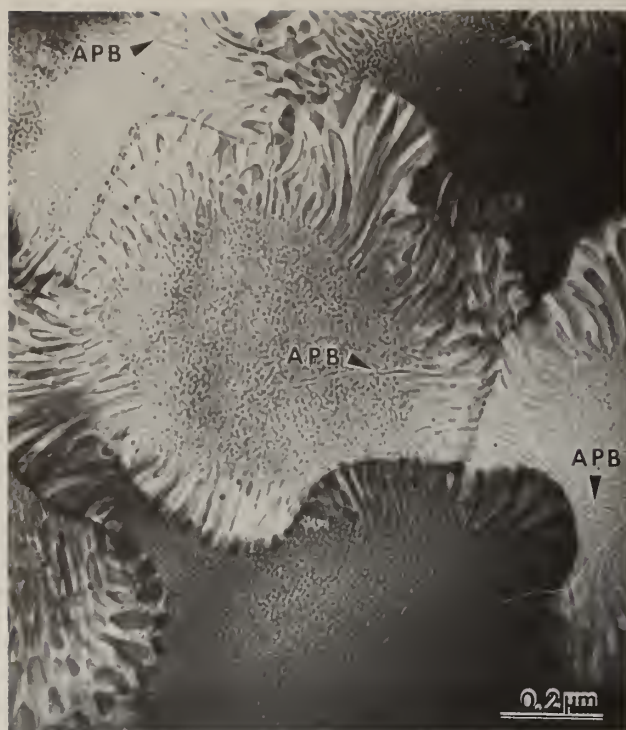


Figure 3: Transverse section of columnar grains and surrounding eutectic in melt-spun ribbon (TEM). Note APBS in center grain.

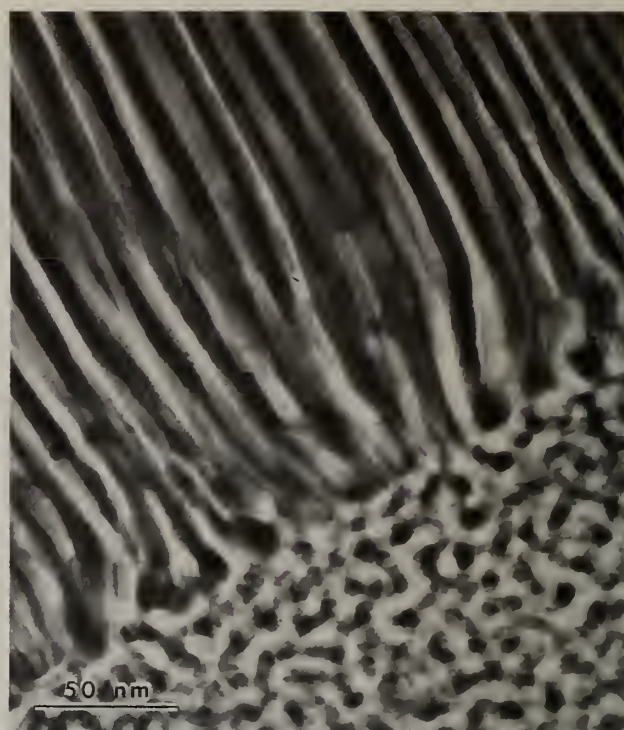


Figure 4: Columnar grain-eutectic interface. Inter-rod eutectic spacing: 12 nm (TEM).



Figure 5: Region of foil consisting primarily of columnar grains (TEM).



Figure 6: Region of foil consisting primarily of eutectic (TEM).

the columnar grain have the same orientation and almost identical lattice parameters. An X-ray diffraction scan taken from the ribbon shows that the reflections from the CsCl lattice and those from the BCC lattice are indistinguishable. Lattice parameter measurements resulted in a figure of $a = 0.28882$ nm. Microdiffraction patterns were taken from a rod and the adjacent matrix of the eutectic, as shown in Figure 10. The rod is identified as BCC, Figure 10a, the matrix as CsCl structure, Figure 10b.

A composition analysis of the columnar grain cores has shown that they have the same composition

as the original alloy, Figures 11a and b. They are, therefore, β -NiAl supersaturated with chromium to the eutectic composition. The BCC phase in the eutectic was also analyzed, Figure 11c and was found to be composed mainly of chromium of near equilibrium composition at the eutectic temperature (13.9 at%Ni and 7.5 at%Al). The CsCl phase in the eutectic was not analyzed due to experimental difficulties, but based on an estimated volume fraction of the phases in the eutectic the phase is estimated to contain about 13 at% chromium, i.e. near the expected equilibrium composition for the β -NiAl phase at the eutectic temperature.



Figure 7:

High magnification illustration of APBS

Discussion

Two features of this rapidly solidified structure are unique and will be discussed separately: The columnar grains of spinodally decomposing alloy with the β -NiAl structure and with composition near the eutectic, and the fine rod-type eutectic structure. It is important for the analysis of rapid solidification processes to establish whether the β -NiAl phase was a direct product of solidification or whether it has ordered in the solid state from a supersaturated α -Cr phase.

Columnar Grains

Because of the extension of solubility required for the formation of the columnar grains, an examination of the possible T_0 curves for the NiAl-Cr system is in order. Figure 12 shows the stable phase diagram as solid lines [5] and a possible schematic set of metastable extensions of the solvus curves (dashed) and the T_0 curves (long-short dashed). The figure assumes that the two solvus curves meet at a metastable tricritical point above which the transition from the BCC phase to the CsCl phase is second order. This transformation can be second order according to the symmetry restrictions of Landau [8]. This metastable extension upward to the tricritical point, where the crystal structures differ by an ordering reaction, is formally similar to the metastable extension of the solvus curves between identical crystal structures (FCC) in the Ag-Cu system upward to an ordinary critical point. The proposed metastable tricritical point is thermodynamically identical to the stable tricritical point in the Fe-Al system where the ordering is between Fe (BCC) and FeAl (B2) [7]. The schematic free energy curves for the solid phases shown in Figure 12 are identical to those proposed by Allen and Cahn [7]. With the addition of the liquid free energy curve to generate the stable eutectic phase diagram the structure of the T_0 curves becomes apparent. In this figure we have assumed that the tricritical temperature is relatively low due to the similarity in the lattice parameters of β -NiAl and α -Cr. The lattice parameters would be identical above the tricritical point. In Figure 12 the dotted curve is the metastable extension of the second order phase transition below the tricritical point and is the locus of points where the free energy curves of the disordered and ordered phases join tangentially. This curve is generally thought to lie much closer to the solvus for the disordered phase rather than that for the ordered phase [7]. The T_0 curve for the disordered phase is seen to split into two branches when it crosses this dotted line. The lower branch is the continuation for the disordered phase, while the upper branch is for β -NiAl phase. This upper branch continues to the NiAl side of diagram where it is the normal T_0 curve for β -NiAl. The relatively small depression of the T_0 curve for β -NiAl below the eutectic temperature is a



Figure 8: Selected area diffraction (SAD) pattern of a columnar grain.



Figure 9: Diffraction pattern taken from a columnar grain and its surrounding eutectic.

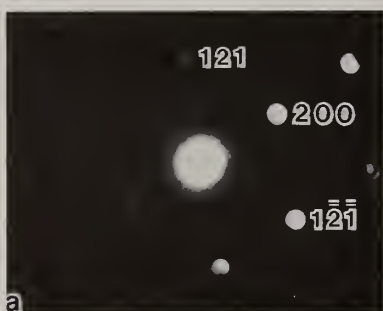


Figure 10: (a) Microdiffraction from rod in eutectic.
(b) Microdiffraction of matrix in eutectic.

consequence of the relatively low tricritical temperature. This fact again is formally similar to the T_0 curve for Ag-Cu.

This diagram leads to two important conclusions which are consistent with the experimental results. First, the T_0 curve for β -NiAl phase at the eutectic composition occurs at a higher temperature than the T_0 curve for the α -Cr phase. Second, if the β -NiAl phase was formed with the eutectic composition directly from the melt, it would undergo subsequent solid state spinodal decomposition into ordered and disordered phases. This type of spinodal has been termed a conditional spinodal [7]. Typical decomposition structures of FeAl by conditional spinodal show coarse anti-phase domains of the FeAl along with a fine scale compositional separation into disordered Fe and ordered phase.

The structure of the columnar grains in the present work is identical to the above mentioned structure. The grains contain coarse antiphase domains and fine spinodal structure. This strongly suggests that the columnar grains solidified from the melt as supersaturated β -NiAl rather than supersaturated α -Cr. No antiphase domain boundaries would be visible, if the supersaturated Cr phase had solidified from the melt. The solidification of the ordered phase directly from the melt is also suggested by the fact that at the eutectic composition T_0 for the ordered phase is higher than for the disordered phase. Hence, at the eutectic composition partitionless solidification of the β -NiAl phase can occur with less undercooling than that required for the partitionless solidification of the Cr phase.

Eutectic Structure

The solidification of the ribbon is envisioned in two steps. First, the formation of the columnar grains of supersaturated β -NiAl by partitionless solidification followed by the formation of a fine rod eutectic structure in the regions between the columnar grains by near equilibrium solidification. This eutectic solidification would presumably result from the reduction in growth rate caused from the evolution of latent heat during growth of columnar grains. The nucleation of the BCC

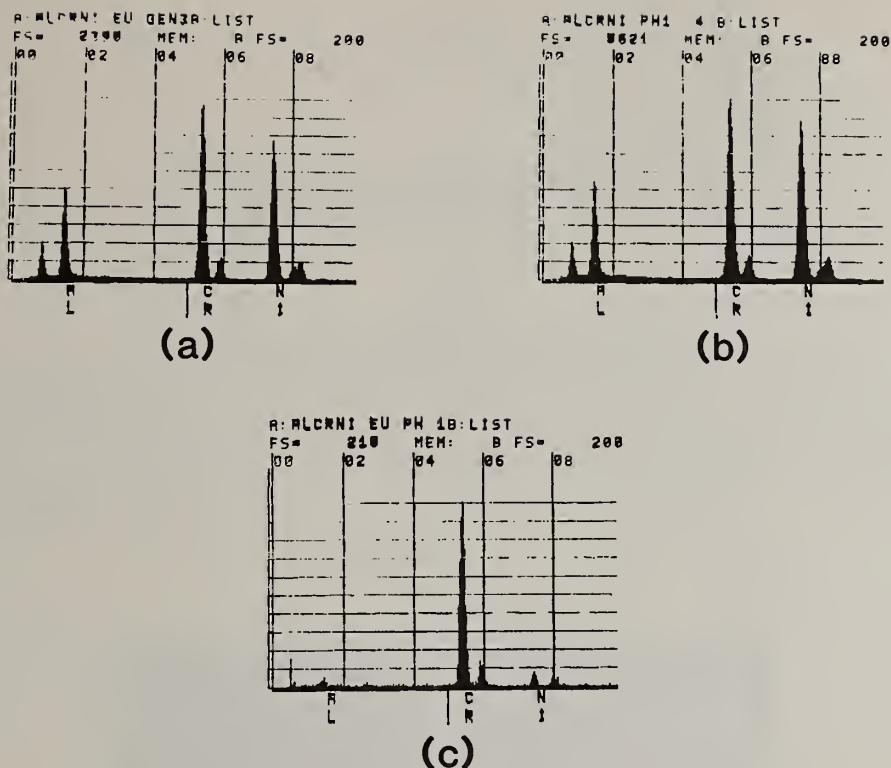


Figure 11: (a) General composition of the ribbon (used as standard). Composition of a columnar grain (b) and of a Cr rod in the eutectic (c).

phase from the CsCl phase seems to be difficult and is demonstrated by the fact that in most cases the eutectic originating from one columnar grain impinges directly upon an adjacent columnar grain. Only rarely do eutectics originating from adjacent grains meet. Once the eutectic has nucleated it rapidly consumes the liquid that remains between the two columns.

The eutectic solidification apparently occurs with near equilibrium compositions for the two solid phases. Although a wide variety of eutectic spacings are seen ranging from 60 nm down to 12 nm the minimum spacings are of particular interest. As described by Boettinger [9] the temperature dependence of the liquid diffusion coefficient leads to a predicted maximum solidification rate for eutectics typically around 10 cm/s. In Ag-Cu eutectic alloys the maximum observed growth rate is 2.5 cm/s with a eutectic spacing of about 20 nm [10]. Hence, the present observation of 12 nm spacing is very interesting. Cline and Walter [2] have measured the rod spacing, λ , as a function of solidification velocity, v , up to 0.021 cm/s. They found these parameters to be related by $\lambda^2 v = 7 \times 10^{-12} \text{ cm}^3/\text{s}$, deduced from their graph. The value of the $\lambda^2 v$ constant for NiAl-Cr is smaller than for Ag-Cu ($1.4 \times 10^{-11} \text{ cm}^3/\text{s}$) and for most other eutectics [11], presumably because of the low interface energy between β -NiAl and α -Cr phases, that can be attributed to the strong orientation relation and similarity of lattice parameters of the two phases in the eutectic. An experimental determination of the maximum growth rate of the NiAl-Cr eutectic structure will be performed in the future, using electron beam melting experiments.

Acknowledgments

Thanks are due to Dr. Frank Lemkey for pointing out to WJB the similarity of phases in this alloy system and to Dr. John W. Cahn for interpretation of ordered structures. The authors acknowledge the support of DARPA.

References

- [1] J. L. Walter, H. E. Cline and E. F. Koch, Trans. TMS-AIME, 245 (1969) 2073.
- [2] J. L. Walter and H. E. Cline, Met. Trans., 1 (1970) 1221.
- [3] H. E. Cline and J. L. Walter, Met. Trans., 1 (1970) 2907.

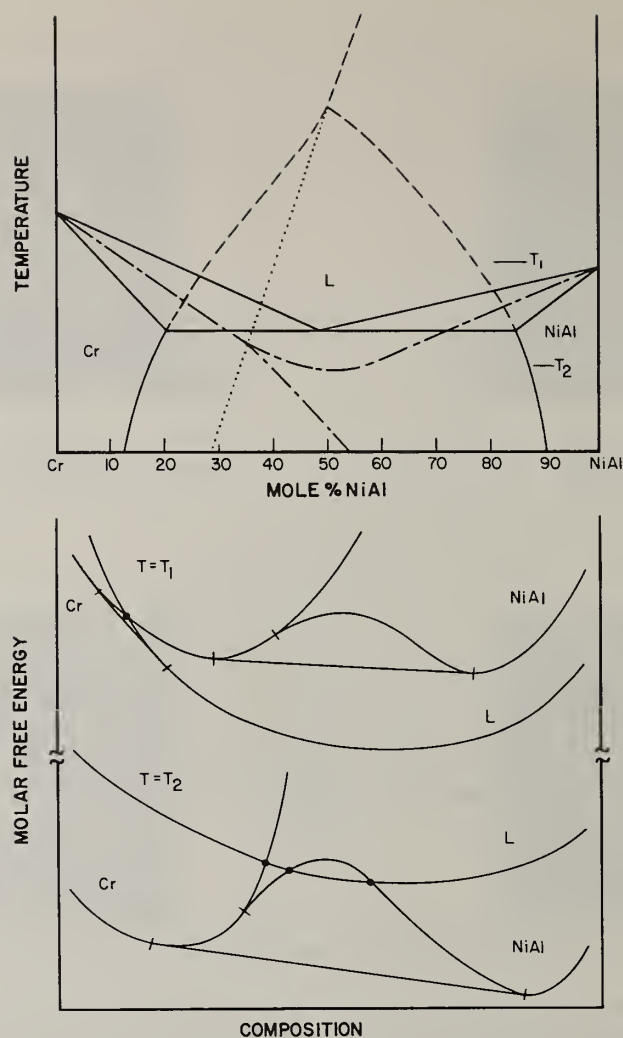


Figure 12: (a) NiAl-Cr phase diagram (solid lines), metastable extension of solvus curves (dashed) to tricritical point and T_0 curves for α -Cr and β -NiAl. (b) Schematic free energy vs composition curves for NiAl-Cr system.

- [4] J. L. Walter and H. E. Cline, *Met. Trans.*, 4 (1973) 33.
- [5] I. I. Kornilov and R. C. Mintz, *Dokl. Akad. Nauk USSR*, 94 (1954) 1085.
- [6] D. Shechtman, T. Z. Kattamis, F. S. Biancaniello and W. J. Boettinger, to be published, *J. Mater. Sci.*
- [7] S. M. Allen and J. W. Cahn, *Acta Met.*, 24 (1976) 425.
- [8] L. D. Landau and E. M. Lifshitz, *Statistical Physics*, Pergamon Press, London, 1958, p. 434.
- [9] W. J. Boettinger, *Rapidly Solidified Amorphous and Crystalline Alloys*, B. H. Kear, B. C. Giessen and M. Cohen, ed., Elsevier Publishing Company, 1982, p. 15.
- [10] W. J. Boettinger, R. Schaefer, F. Biancaniello and D. Shechtman, these Proceedings.
- [11] W. Kurz and D. J. Fisher, *International Metals Reviews*, Nos. 5 and 6 (1979) 177.

WEAR PROPERTIES OF RAPIDLY SOLIDIFIED SURFACES
OF A PSEUDO-BINARY Fe-TiC ALLOY

P. R. Strutt*, B. G. Lewis*, S. F. Wayne*, S. L. Rice*, B. H. Kear**

*University of Connecticut, Storrs, CT

**Exxon Research and Engineering Co., Linden, NJ

ABSTRACT

The wear behavior of the steel-base cemented carbide material Ferro-TiC (SK) has been studied following electron beam glazing and tempering treatments. A distinction is made between wear of SK against a moderately hard martensitic stainless steel (17-4PH), and a hard molybdenum-base high speed steel (M42). The effect of glazing is to produce a three-fold increase in the wear life in tests performed using a fully hardened M42 high speed steel counterface material.

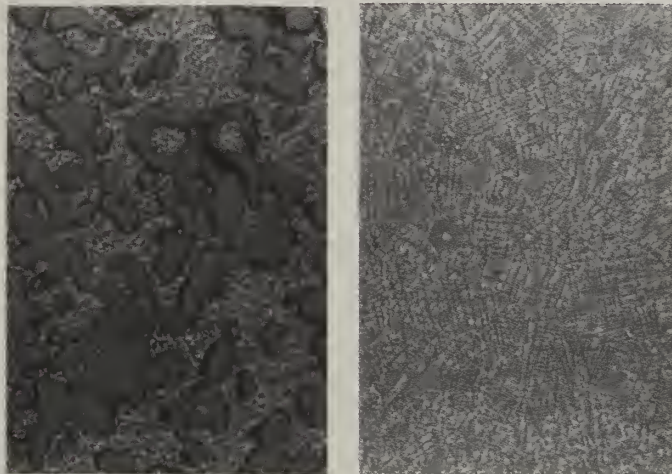


FIG. 1. Microstructure of Fe-TiC Alloy (a) As Sintered, (b) After e.b.-Glazing, Showing Refined Dendritic Structure

Introduction

When the cemented carbide Ferro-TiC, otherwise known as SK, is subjected to a rapid solidification electron-beam surface melting (glazing) treatment, the original blocky TiC carbides are transformed into a highly refined dendritic structure [1,2], Figure 1. This feature coupled with a high hardness suggests a possible benefit in terms of improved wear properties. The present study was undertaken to test this proposition. As will be shown, under appropriate conditions, significant improvements in wear resistance due to e.b.-glazing can be achieved.

Specimen Preparation

Wear-pin specimens of SK material were glazed using a Carl Zeiss electron beam unit. A beam power density of 10^5 watts/cm² was achieved by setting the power level at 300 watts and by adjusting the focusing to give a measured spot diameter of 0.3 mm. Under these conditions, and with a beam scanning rate of 100 cm/sec, a narrow glazed band about 100 μ m in depth was obtained, which experienced an average cooling rate of 5×10^6 °C/sec. Continuous surface coverage of glazed material was attained by

applying two nearly equal frequency signals to the X and Y deflection coils, so as to trace out a series of overlapping Lissajous figures [3], Figure 2. This particular scanning mode was originally developed for the purpose of solid state transformation hardening of steels, without actual melting [4].

All the material used, whether it was subsequently tested in the unglazed or glazed conditions was initially austenitized at 1050°C for 5 min., and then quenched into oil at 50°C. Following this treatment, a few samples were doubled tempered at 450°C for 1 hr.

Table 1. Major Alloying Elements (Wt.%)
in M42, 17-4PH, and SK (Ferro-TiC)

	Fe	Cr	W	V	Mo	Co	Ti	Mn	Si	C	Ni	Cu	P	Nb/Ta
M42	Bal	3.70	1.36	1.12	9.62	7.88	-	0.24	0.40	1.09	-	-	-	-
17-4PH	Bal	16.5	-	-	-	-	-	0.06	1.0	0.05	4.0	4.0	0.04	0.35
SK	Bal	3.5	-	-	3.0	3.0	21.0	-	-	5.0	0.5	-	-	-

All other elements <0.01 wt.%

Wear Testing

Wear tests were carried out in a standardized test machine [5], in which the end of a small cylindrical SK wear pin (3mm dia.) both impacted and slid across a steel counterface. Tests were performed using two different counterface materials - a moderately hard (400 DPN) martensitic stainless steel (17-4PH), and a hard (930 DPN) molybdenum-base high speed steel (M42), Table 1. In all tests, the transverse sliding velocity was 8 m. sec⁻¹ and the nominal maximum impact stress was 69 MPa at a repetition rate of 800 cycles/min. To determine the extent of wear, pins and counterface samples were weighed before and after testing. Wear pins of SK material in both the unglazed (500 DPN) and glazed (950-1000 DPN) conditions were tested against the two different counterface materials at ambient temperature.

Wear Against a Moderately Hard Steel

Figure 3 shows the general appearance of the microstructure of a glazed SK wear pin after testing. The surface is covered with a thin layer of counterface material (Zone A), which has been transferred onto the pin during testing. Below this layer is a much thicker dendritic carbide region (Zone B), which represents the full extent of the homogeneous glazed material. Zone C is a transition zone of partial glazing, involving melting and re-solidification of the steel matrix only i.e. without complete dissolution of the original blocky carbides. Zone D is representative of the unmelted parent material. Close inspection of Zone B reveals that it is separable into an upper heat-affected (tempered) deeply etched region 3-4 μ m below the surface, and a lower more evenly etched dendritic carbide structure. These microstructural features were rather typical of all glazed and tested wear pins.

Figure 4 compares the microstructures of unglazed and glazed SK wear pins after testing against 17-4PH. The surface of the unglazed sample is rough, Figure 4(a), and there is evidence for patchy regions of transferred counterface material. Below this there is a region of intense plastic deformation in the sliding direction, which contains small fragmented carbides. The actual amount of plastic strain is estimated from measurements on several micrographs to be >50 pct. In complete contrast, in the glazed sample, Figure 4(b), there is a much greater amount of visible transferred material, but no evidence for significant plastic deformation in the upper part of Zone B. In both cases, there is evidence for cracking in the surface layers, arrows in Figure 4. These are limited to the transferred material in the unglazed sample, whereas in the glazed sample they extend into Zone B, terminating near its base. Post-glaze tempering treatments to increase martensite ductility did not reduce the propensity for crack formation in the glazed material.

No significant weight changes were recorded for glazed and unglazed pins. On the other hand, metallographic examination provided indirect evidence for more wear of unglazed pins than glazed pins. This is deduced from Figure 4(a), where carbide particles have clearly worked their way into the adhered material (Zone A). In contrast, the corresponding counterface materials (impact discs) underwent substantial wear, as determined by actual weight losses. Thus, the overall situation can be described as essentially 'one-body wear'. Figure 5 shows plots of the actual experimental weight change data. For completeness, the effect of tempering the glazed pins is included. Tempering reduces the wear rate of the counterface material, which may be the result of more material adhering to the tempered pin.

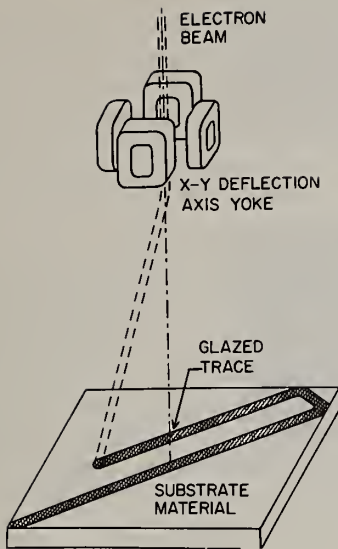


FIG. 2. Schematic of Electron Beam Glazing, Utilizing Electromagnetic Beam Deflection

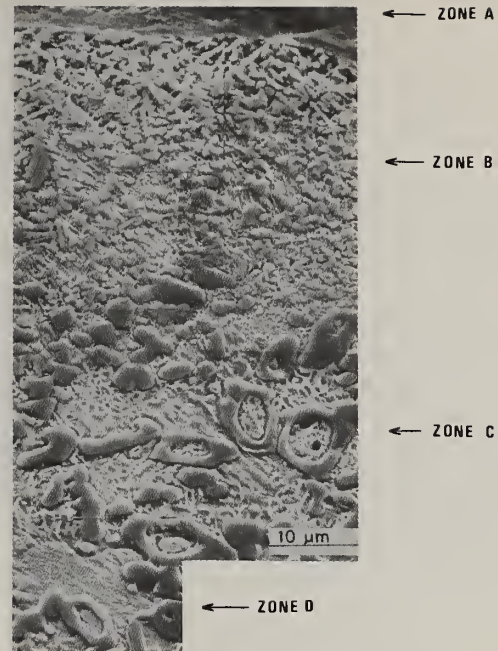


FIG. 3. Electron Beam Glazed Ferro-TiC(SK) Wear Pin Sectioned Parallel to the Sliding Direction, Showing Adhered Counterface Material (Zone A), and Sub-Surface Zones of Fully Glazed (Zone B), Partially Glazed (Zone C), and Unmelted Substrate (Zone D)



FIG. 4. Comparison of the Surface Microstructures of Unglazed (a) and Glazed (b) Ferro-TiC (SK) Wear Pins, After Wear Against a Moderately Hard 17-4PH Steel Counterface

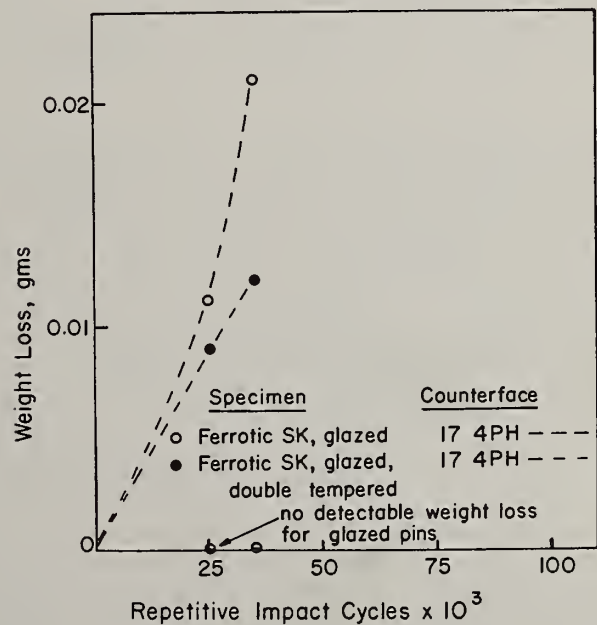


FIG. 5. Weight Loss Data for Glazed Ferro-TiC (SK) Worn Again 17-4PH

Figure 6 compares the microstructures of unglazed and glazed SK wear pins, after testing against M42 high speed steel. The unglazed sample, Figure 6(a), exhibits some of the features characteristic of wear against the softer 17-4PH material, Figure 4(a), such as surface roughness, and near-surface plastic deformation and carbide fragmentation, but there is no indication of pick-up of counterface material. On the other hand, the glazed sample exhibits quite distinctive features, not previously seen in the 17-4PH case. As shown in Figure 6(b), the wear surface is smooth, contains no detectable counterface material, and there is no evidence for cracking of the glazed material. Careful examination reveals a small amount of carbide fragmentation, limited to the top 2-3 μm of the glazed region.

Figure 7(a) shows that wear of unglazed SK pins against M42 produces significant weight losses for both pin and counterface materials, i.e. two-body wear, in contrast to the one-body wear characteristic of 17-4PH. Both tempered and untempered samples wear at a similar rate up to 50,000 cycles, beyond this there is a continued weight loss only for the untempered material. A possible explanation for this behavior is that a greater amount of M42 counterface material adheres to the tempered wear pin, which gives rise to wear of M42 against M42 in the later stages of testing. A similar two-body wear is found also in the case of the glazed material, Figure 7(b), except that to obtain a weight loss equivalent to that of unglazed material, Figure 7(a), it is necessary to increase the test time by a factor of 2.5 (i.e. to 250,000 cycles). In other words, e.b.-glazing in this case increases wear life by 2.5x.

Discussion

The present work shows that electron-beam glazing is capable of improving the wear resistance of a hard cemented carbide material. Although the underlying mechanisms are imperfectly understood, it is believed that the most important factors contributing to improved performance are (i) the high degree of homogeneity of the rapidly solidified material, and (ii) the high yield strength of the ultra-refined microstructure.

Before considering wear of glazed material, it is instructive to consider the degradation process of untreated material. The microstructure of unglazed SK material, Figure 4(a), after wear against a 17-4PH steel counterface, is indicative of a situation where fragmented carbide particles tend to align themselves along curved flow lines within a plastic deformation slip field produced by shear along the wear direction. X-ray diffraction analysis of wear debris confirms that small TiC particles are indeed carried from the SK material into the adhered layer.

Observations during actual wear tests indicate that an adhered layer of 17-4PH forms at an early stage on the wear-pin surface. It is the continual breakaway and renewed build-up of this layer that produces the wear debris. The 17-4PH readily shears from the counterface due to the plastic softening resulting from localized heating during sliding and impact. When, however, a sufficiently thick layer has been transferred to the wear-pin the adhered zone exhibits a hardness of about 800 DPN. The increase in hardness arises from a combination of precipitation hardening, mechanical mixing of alloy phases and oxides, and the presence of untempered martensite formed as a result of wear test induced heat treatments. In addition to being hard, microstructural observation of severe cracking shows Zone A structures to be rather brittle. Interestingly, the cracks in the adhered 17-4PH layer do not propagate into the cemented carbide material. Presumably this is because the matrix phase readily accommodates the intensified stress field at the crack tip by plastic deformation. Although there are no detectable cracks within the near-surface region of the SK material, a small amount of SK nevertheless is removed. Presumably, this arises from the small amount of near surface material, which is firmly bonded to the fragments of adhered 17-4PH, detaching itself during the wear process.

From the experimental observations, and the preceding considerations, it is evident that glazing is advantageous in improving wear resistance provided that an appreciably thick, brittle and tenacious adherent layer does not form. Such a conclusion is well supported by the wear experiments using a hardened M42 steel counterface. Little or no detectable adhered layer is formed, presumably because the good hot hardness prevents plastic shearing. In this case, the material degradation process appears to be surface abrasion involving the continued removal of fine particles. The creation of such particles must involve surface microcracking, but such cracks are highly localized since they do not penetrate the glazed surface layer. This type of wear process occurs on both the SK wear pin and the M42 counterface. In the glazed condition the fine particle fragmentation is reduced, thus showing the beneficial effect of electron beam glazing in reducing wear.

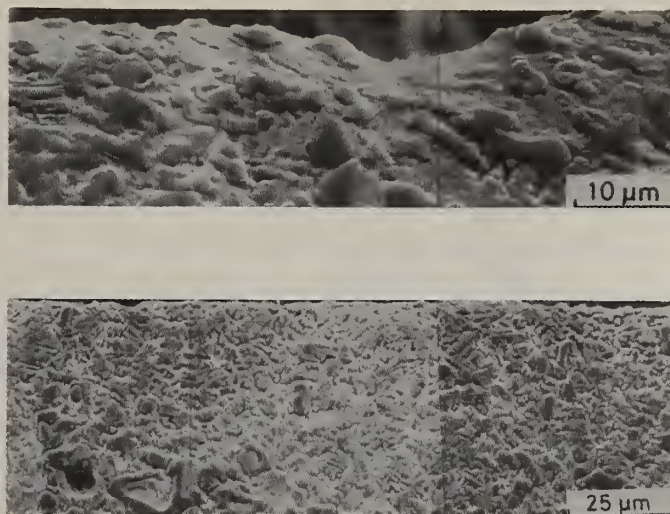
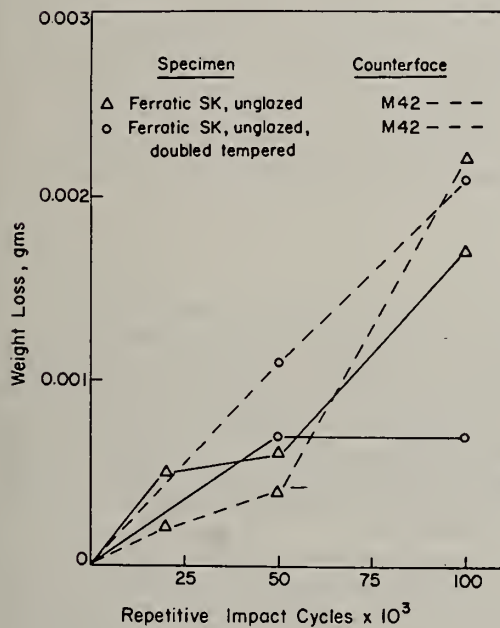
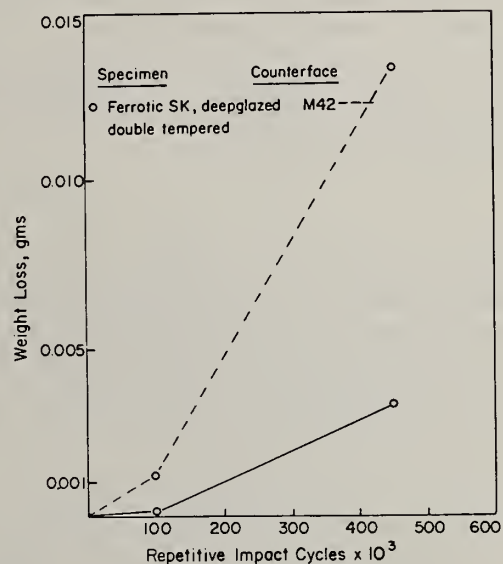


FIG. 6. Comparison of Surface Microstructures of Unglazed (a) and Glazed (b) Ferro-TiC (SK) Worn Against a Hard M42 High Speed Steel Counterface



(a)



(b)

FIG. 7. Weight Loss Data for Unglazed (a) and Glazed (b) Ferro-TiC (SK) Worn Against M42

References

1. Lewis, B. G., Gilbert, D. A. and Strutt, P. R. (1980). Laser and Electron Beam Processing of Materials (eds. C. W. White and P. S. Peercy), Academic Press, 747.
2. Strutt, P. R. (1977). Metals Forum, Pergamon Press, 117.
3. Strutt, P. R. (1981). *Mat. Sci. & Eng.*, **49**, 87.
4. Mayer, R., Dietrich, W. and Sundermeyer, D. (1977). *Weld. J.*, **56**, 35.
5. Rice, S. L. (1979). *Wear*, **54**, 291.

FABRICATION OF ORIENTED SINGLE CRYSTAL WAFER STOCK FROM Ni-Al-Mo-X ALLOY POWDERS

R. E. Anderson, H. A. Chin and S. E. Hughes

PRATT AND WHITNEY AIRCRAFT/GPD
WEST PALM BEACH, FLA 33402

B. B. Rath

NAVAL RESEARCH LABORATORY, WASHINGTON, DC

ABSTRACT

Utilizing a rotary atomization device to produce prealloyed, rapidly-cooled, metal powder, P&WA has developed alloys which exhibit uniaxial creep strength significantly greater than that of the best available directionally solidified nickel-base superalloy. However, the grain boundary strength of this material is poor necessitating a single crystalline approach to allow application of this class of materials in many advanced gas turbine airfoils. An extensive effort has been undertaken to optimize alloy composition and processing parameters for producing bulk quantities of seed oriented single crystalline sheet stock of Ni-Al-Mo-X compositions (X representing W, Ta, Cr, Hf, Y, C) for use in subsequent turbine blade application. The properties of the alloy as it is currently configured will be reviewed. Further, a description of the processing sequence as it is currently arranged, and the effects of the various processing steps on the microstructure and texture of the material will be presented. Furthermore, the influence of the varying microstructural parameters on the relative perfection and growth selectivity of the crystals grown in the solid state are discussed.

INTRODUCTION

The efficiency of a gas turbine engine is directly tied to the maximum gas stream temperature. The need for further increases in turbine inlet temperature has not abated. Before the findings of recent programs at P&WA, the point of diminishing returns was being reached in terms of conventional airfoil materials and cooling technology. The conclusion was reached that a radical departure from established turbine airfoil materials and design approaches would have to be taken if further gains in airfoil operating temperature capability and hence, engine performance were to be attained. To meet this challenge, P&WA in conjunction with the Defense Advanced Research Projects Agency (DARPA) and the Air Force undertook a program aimed at applying the principle of rapid solidification to nickel base superalloys in general and to turbine airfoils in particular. This program, reported on previously ^{1,2,3}, was aimed at developing an alloy with creep and rupture capability 100°F higher than the best available production airfoil material of that time. This effort was so successful that it was mated with the radial wafer cooling concept in an attempt to produce an airfoil with the potential for withstanding a 250°F increase in turbine inlet temperature in a device like the P&WA F100 turbine engine.

The fabrication effort aimed at producing prototype airfoils was also discussed previously. ⁴ This effort led to a brief, but successful, engine test two years ago. Since that time, P&WA, the Air Force, and DARPA have been aggressively pursuing a follow on program aimed at (1) producing these types of airfoils at a reasonable cost, (2) further improving the durability of these components through design and process modifications, and (3) substantially improving the material environmental resistance and thermal stability through compositional modifications. A significant portion of this effort is associated with the adoption of a wrought, directionally recrystallized (D.R.) single crystalline component approach to enhance alloy and blade durability and properties. The technique for the fabrication and the properties of these single crystalline assemblies represent the topic of this discussion.

BACKGROUND

GENERAL

The potential benefit of an airfoil fabricated from radially oriented wafers made from a very high strength superalloy has been described previously.^{4,5,6} It has been speculated that such a component could lead to a 40% reduction in specific fuel consumption or to a 15 to 20% increase in thrust-to-weight ratio in an engine like the P&WA F100 turbofan. However, these airfoils (a total of 20 were made and two were engine tested) contained several non-optimal features. First, the cooling scheme lead to thermal inhomogeneities. Second, the alloy exhibited only marginal environmental resistance as well as thermal instabilities which made its strength time-dependent. Third, the traverse ductility of that material/component was marginal. Fourth, the cost of the assembly was extremely high. In short, the concept needed a significant amount of optimization to reach the level of excellence needed to be considered as a prime candidate for the airfoil system in production turbine engines.

One of the most serious problems to be solved was the inherently poor transverse strength of the grain boundaries in directionally recrystallized alloy 185 (Ni-14.5Mo-6.8Al-0.04C-6.1W). This strength in this direction was so low that it eliminated the material from consideration for use in some of the more advanced applications. One solution to this problem was simple: eliminate all grain boundaries.

WHY RAPID SOLIDIFICATION?

To maximize the high temperature capability of nickel base superalloys, the matrix phase is commonly strengthened with large additions of compatible refractory elements such as tantalum and tungsten. The theoretical limits of solubility for the various additions is set by the phase equilibria, beyond which deleterious phases such as σ and μ are rejected. In practice, the solubility limits of the alloying elements are significantly lower than the theoretical limits because of the sluggish kinetics of conventional solidification processing.

At the time this effort was initiated, the most advanced production airfoil material was directionally solidified alloy MAR-M200+Hf, (nominal composition Ni-9Cr-10Co-2Ti-5Al-12.5W-2Hf-1Cb-0.14C-0.015B). Several flight airfoils of this material were found to exhibit Laves - phase precipitation but only in the dendrite cores of the castings. Microprobe analyses of these cored regions indicated tungsten concentration in excess of 40% even though the nominal composition of the airfoils was within specification.

The implications of these findings were twofold. An inordinate amount of tungsten was being concentrated in the dendrite cores by the relatively long range segregation associated with the slow directional solidification process used in casting complex turbine airfoils. The suppression of this precipitation could only be accomplished by suppressing solidification induced segregation. Now, since the refractory alloying elements were being rejected from the γ phase at the current level of alloying, further alloying additions aimed at additional strengthening would be totally frustrated by the rejection of these additions culminating in further deleterious third phase precipitation.

The simplistic idea of adding refractory elements to superalloys until saturation is reached to strengthen them is an appealing one because it is a relatively straight-forward approach. It is easy to speculate on what the creep strength of MAR-M200+Hf would be if the composition of the dendrite cores was the uniform composition of the alloy. Obviously, some of the effectiveness of this approach would be lost on a self-loaded high speed rotation part like a turbine airfoil because the density (and hence, the airfoil stress) would increase as the alloy's nominal refractory element content increased. If most of the tungsten is in the dendrite cores, then little is in the interdendritic regions leaving these areas relatively weak in creep and stress rupture loading, where elements like W, Ta, and Mo etc., show their biggest beneficial effect on superalloys.

There are two obvious methods for reducing constitutional segregation: reducing solidification induced segregation by increasing the solidification rate, and homogenizing the structure through the use of long-time, high-temperature solutioning cycles. The effectiveness of the solutioning cycle is an obvious function of the maximum temperature as well as the time. The maximum temperature is, however, also a function of the solidification rate because it is limited by the incipient melting point, a temperature which is developed in the structure by the solidification induced segregation of low melting point alloying phases and elements to the grain boundaries and interdendritic regions. With MAR-M200 and normal directional solidification techniques, this temperature (circa 2175°F) was so low that full homogenization without local melting would require solutioning for inordinately long times (weeks or months).

It is possible to produce simple geometry cast test bars with a fairly uniform composition by increasing the directional solidification rate (typically mold withdrawal rate). This approach would allow both shorter homogenization times to complete the task (because of the higher homogenization temperatures usable without melting) and/or the use of higher effective strengthener contents. However, in complex airfoil castings where solidification rates must be reduced (withdrawal rate reduced) to improve mold fill and grain structure, this approach too is frustrated. Consequently, while it may be possible to improve uniformity and, hence, strength in test bars (and perhaps in simple airfoil castings) these gains are not translatable to high performance geometries with more highly alloyed compositions using production directional solidification techniques.

Recognizing that uniformity in alloying element distribution can enhance strength in the metals needed to make the turbine's most performance limiting component, it became necessary to develop a technique to use this approach to allow the practical fabrication of hardware. P&WA chose the most rapid solidification technique which was available at the time for producing bulk quantities of homogeneous material, the powder metallurgy approach. Theoretically, the interdendritic distances in a powder particle are so short that even if dendritic solidification were the primary solidification mode atomistic uniformity in composition could be reached by high temperature homogenization in a reasonable engineering time. It was speculated that if MAR-M200 could be made uniform by the powder metallurgy technique then sufficient tungsten could be added to drive the temperature capability up by well over an effective 100°F without either exceeding the solubility of tungsten or raising the density beyond reasonable limits.

Using commercially available powder from Special Metals Corporation, this theory was tested. Alloy MAR-M200 powder was procured, consolidated by extrusion, forged to a pancake shape, DR'ed, and tested in creep and rupture. Although the alloy was found to D.R. to a $\langle 110 \rangle$ orientation, a relatively weak orientation for superalloys, this material was found to be clearly superior to the directionally solidified alloy in 1% creep strength and roughly equivalent to the cast material in stress rupture resistance. Furthermore, the powder metallurgy approach appeared a viable technique for producing strong airfoil materials. What was needed to fuel the development process was a source of large quantities of segregation free, or at least segregation suppressed, powdered material on which to do alloy content and optimization studies.

THE POWDER RIG

To supply large quantities of rapidly solidified powder, P&WA built the rotary atomization device discussed previously.³ Rotary atomization was selected because this method seemed to offer the best probability of producing a controlled particle size distribution. Helium gas quenching was selected for simplicity of handling, high heat extraction capability, and inertness. Conventional metal melting and powder handling equipment was used whenever possible to minimize complexity.

The powder making device now has the capability of pouring 300 or more pounds of powder per atomization run. A recirculator has been added to reduce the helium consumption, and the turbine now has the capability of turning at 35,000 rpm (thus producing a finer, more uniform droplet distribution). This device has been used to produce in excess of 20 tons total of rapidly solidified metal powder in assorted nickel, aluminum, copper, and iron based alloy systems.

ALLOY MODIFICATION

The alloy developed in the previous program, directionally recrystallized alloy 185 (Ni-6.8Al-14.4Mo-6.0W-0.02C), although inordinately strong in high temperature creep and rupture loading, exhibited several deficiencies. The columnar grained structure of the DR alloy possessed inadequate rupture strength across high energy boundaries. The base composition is supersaturated in Mo and W and rejects the excess as α -Mo, W. The oxidation resistance of alloy 185, particularly at high temperatures, leaves much to be desired. Finally, alloy 185 in its most creep resistant orientation ($\langle 111 \rangle$ axial) exhibits poor strain controlled and thermal fatigue resistance. This is a fundamental characteristic of the relatively high elastic modulus of nickel based alloys in this orientation ($\cong 44 \times 10^6$ psi at R.T. for the $\langle 111 \rangle$ as opposed to $\cong 18 \times 10^6$ psi for the $\langle 100 \rangle$ orientation).

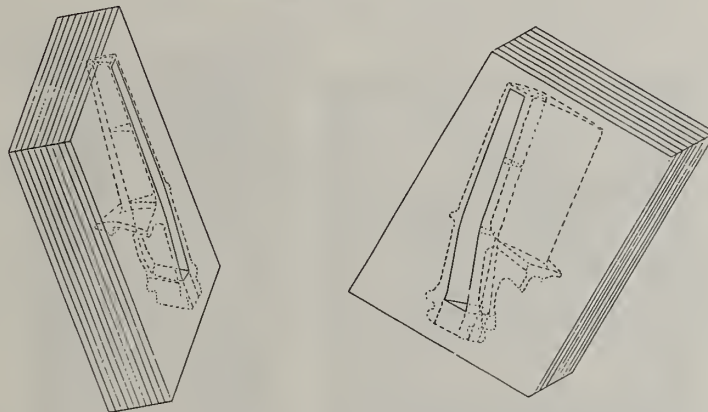
A major alloy and process development effort has been conducted during the last two years in an attempt to solve these problems. The phase instability problem was essentially eliminated by reducing the Mo level from 14.5 weight percent to 10.0 or less. The high temperature oxidation problem was resolved through the addition of minor alloying elements (most importantly Yttrium). The problem of fatigue resistance and grain boundary strength has been resolved through an oriented single crystalline approach. This effort has led to the development of PWA 1121 (single-crystalline, directionally recrystallized Ni-6.8Al-3.0Cr-10.0Mo-6.0W-1.5Ta-0.15Hf-0.02C-0.1Y).

Oriented single crystals can improve fatigue life because of the inherent anisotropy of the nickel based superalloy system. It was discovered early in the effort that the $\langle 112 \rangle$ crystallographic direction in the Ni-Mo-Al system exhibits nearly as much creep and rupture strength, and substantially more rupture ductility, than the $\langle 111 \rangle$ orientation. Furthermore, this orientation has a characteristic elastic modulus which represents a compromise between the two prime orientations ($E_{\langle 112 \rangle} \cong 34 \times 10^6$ psi at RT.) Consequently, the strain controlled low cycle fatigue resistance of single crystals of this material, oriented in the $\langle 112 \rangle$ direction, also should exhibit a compromise. Test results have recently substantiated this premise. However, $\langle 112 \rangle$ D.R. crystal growth is not readily producible from material consolidated by high temperature extrusion, the technique used previously for consolidating Ni-Mo-Al-X powder. Apparently, D.R. orientation is a complex function of the input material deformation and microstructure texture as described elsewhere in this conference.⁷ Consequently, the technique most appropriate for producing a texture with a $\langle 112 \rangle$ direction in a useful dimension of the material appears to be a combination of hot and cold rolling.

THE COMPONENT AND THE DEFORMATION SEQUENCE

Early experiments indicate that consolidation of Ni-Mo-Al powder by extrusion at high temperatures (circa 2300°F) produces a $\langle 111 \rangle$ fiber texture. If this material is subsequently rolled to sheet stock by cross rolling techniques, a $\{110\}\langle 112 \rangle$ sheet type texture is produced. This texture is compatible with $\langle 112 \rangle$ D.R. growth parallel to the primary working direction. Obviously, the product of this process is sheet stock. This is fortuitous because the component being used as a demonstration vehicle for this alloy is a radial wafer concept turbine blade which uses sheet stock (wafers) exclusively for its input material as shown in Figure 1. The design of this component has been upgraded to improve the cooling effectiveness and to make it compatible with the projected properties of the material.

FIGURE 1
FINAL BONDED ASSEMBLY OF SINGLE CRYSTAL RADIAL WAFER BLADE



FD 254151
621211
26428

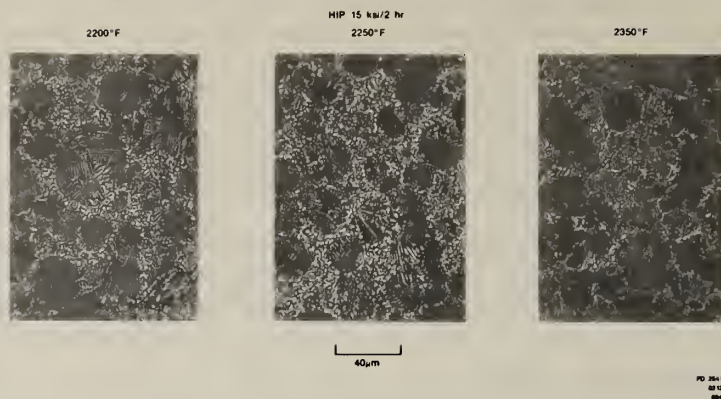
STATEMENT OF THE PROBLEM

Having solved most of the problems associated with the use of this material from a theoretical standpoint, all that remained was to produce single crystalline stock from prealloyed rapidly solidified powder of the appropriate composition. Described below are the steps taken in consolidating the material, shaping it, D.R.ing the subcomponents, and fabricating the final assemblies. Many of the techniques are similar to those described previously,* while others have had to be changed significantly. What is discussed are the critical steps in the sequence and some of the rationale for their choice.

FABRICATION SEQUENCE

The remelt stock for atomization was produced at PWA/GPD by conventional vacuum melting techniques. However, since the atomization device has grown in capacity to a current level of 300 lbs, the 100 lb capacity laboratory melting facility has been outstripped. Consequently, commercial vendors such as Special Metals are now producing the remelt stock for this effort. The material under consideration here came from a 4,000 lb Special Metals master heat of the composition listed previously as PWA 1121.

FIGURE 2
CONSOLIDATION TEMPERATURE EFFECTS ON THE AS-HIP MICROSTRUCTURE OF PWA 1120 BILLETS

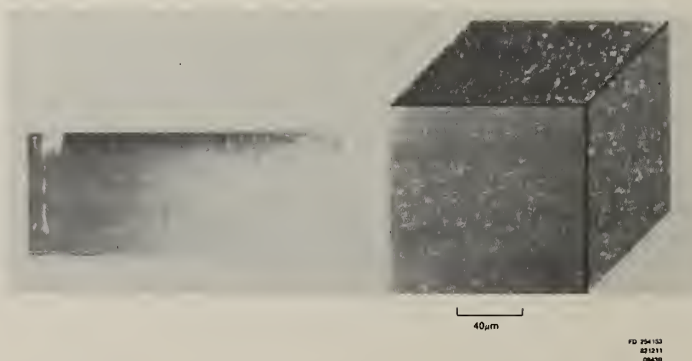


This material was atomized in the GPD powder device in heats ranging in sizes from 250 lb. to over 300 lbs. The heats were cross blended in an attempt to normalize any unforeseen anomalies such as undetected leaks in the atomization system, spot cleanliness problems, etc. Each step of the atomization sequence, sizing, storage and canning was all accomplished under either vacuum or positive helium pressure in an attempt to all-inertly handle the powder. Immediately prior to canning, the powder was passed through the GPD hot dynamic outgassing system into Inconel 600. Typical pressures during canning and sealing were in the 10^{-5} torr range at 1000°F. The cans for this effort ranged in capacity from 145 to over 300 lbs. Inconel 600 is used as can stock because it also doubles as a hot rolling can.

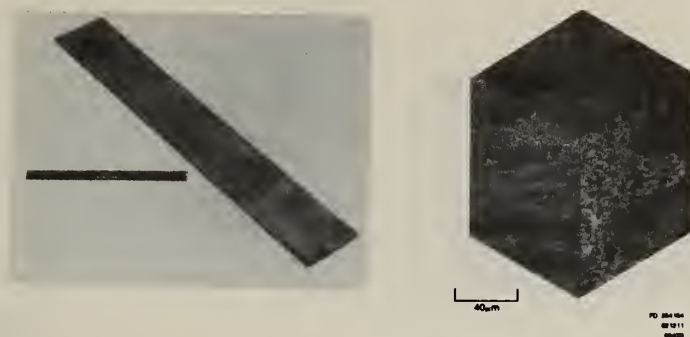
Consolidation of the powder was accomplished at IMT in Boston, Mass. The powder was consolidated to full density at all temperatures studied above 2100°F. Consolidation at the temperatures studied led to a 50% or greater level of recrystallization as shown in Figure 2. Subsequent formability was found to increase with percent recrystallization so that HIP temperatures were kept intentionally high. However, hypersolvus ($T_{HIP} > T_{\gamma' solvus} \cong 2325^\circ\text{F}$) cycles were found to lead to reduced formability resulting from excessive grain growth. Consequently, 2250° was used for the bulk of the material processed in this effort.

Hot rolling was accomplished at Cabot, Cyclops, AMAX, and GPD. Rolling schedules were designed to yield a final decanned product of approximately 0.400 in. thick using a reduction of 5% initially increasing to 20% per pass with reheats at 2250°F on every pass. A typical hot rolled and decanned billet is shown in Figure 3. Losses due to edge cracking, tearing, etc. were minimal with the total yield through hot rolling approaching 85%. The hot rolled plates were subjected to a normalization heat treatment comprised of a two hour isothermal anneal at 2275°F followed by controlled cooling to fully recrystallize the structure and normalize the γ' (second phase) morphology.

FIGURE 3
HOT ROLLED AND DECANNED PWA 1120 BILLET ILLUSTRATIVE MACRO- AND MICROSTRUCTURES



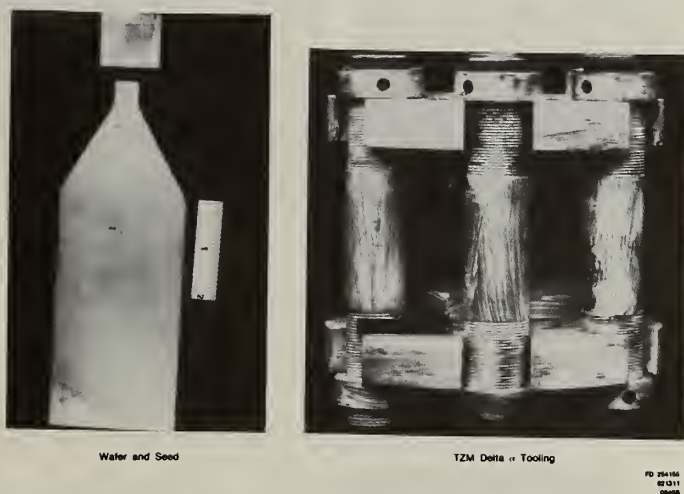
Following hot rolling, normalization, and decanning (either chemically or mechanically) the billets were cold rolled to final thickness. The schedules were adjusted to yield a final thickness of nominally 0.145 in. using a 65% total reduction, the final 25% of which was accomplished in the cross rolling direction. Reductions were taken at 1% per pass with 2200°F/10 min/AC anneals applied after each 5% initial to 15% final reduction. Typical cold rolled products from these operations are shown in Figure 4. The yields through cold rolling, after trimming, approximated 80% of theoretical.



Following rolling and trimming to size, the wafers were subjected to surface preparation for diffusion bonding. This operation was generally accomplished by mechanical lapping. Sufficient material was removed to clean the surface and size the wafer to the proper thickness. In instances where large quantities of material had to be removed (for example when an 0.080" final thickness was desired) the wafers were double disk ground to rough size, and lapped to finish dimensions.

Since a multiple piece assembly was required as the final product, two processing sequences were evaluated in component fabrication. The first technique involved the assembly of pregrown single crystalline stock. Alternatively, it was shown feasible to diffusion bond fine grained stock and then, to directionally recrystallize the monolithic assembly. Both techniques were demonstrated in this effort, and since both have unique advantages (and disadvantages), both will be outlined here.

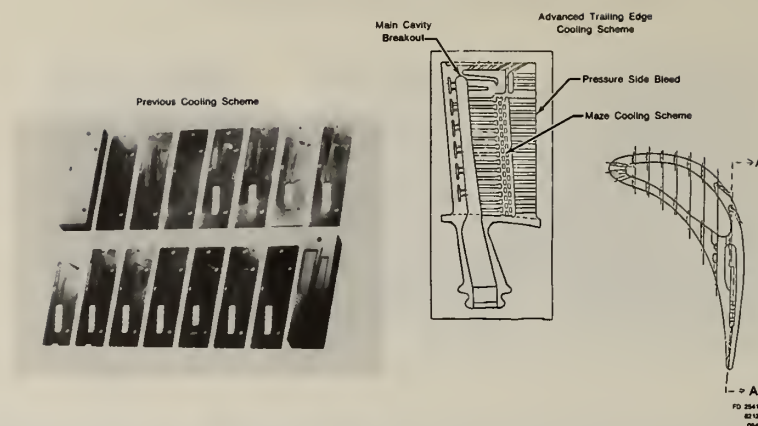
FIGURE 5
WAFER AND TOOLING DESIGNED FOR ORIENTATION CONTROLLING SEED BONDING PRIOR TO DIRECTIONAL RECRYSTALLIZATION



To produce a pregrown assembly, the fine grained and lapped wafers were trimmed to the shape shown in Figure 5 to facilitate the attachment of an orientation controlling seed crystal. The joining operation was accomplished using differential expansion tooling in vacuum during heating to 2050°F. The lapped surfaces were carefully cleaned, electropolished, and loaded into the TZM tooling and placed under a 2 Ksi preload. The assembly was then placed into a vacuum furnace, and the chamber was evacuated and heated to the appropriate bonding temperature. Typically, three (3) samples were bonded in each die stack per load. Bonding pressures varied, and successful bonds were produced with pressures as high as 10^{-2} torr. Bonding yields were very high with 90% of the seeded stock exhibiting grain transferral across the lap bond joint.

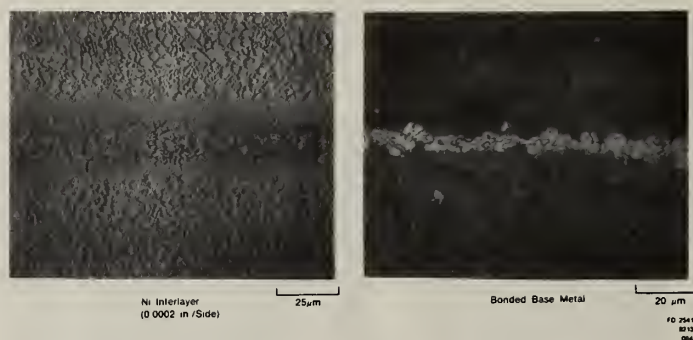
After bonding, the preseeded fine grained samples were trimmed to remove any potential grain nucleating sharp edges and submitted for D.R. The D.R. heat treatments were conducted in the GPD vacuum induction gradient furnace. The samples were loaded into the furnace either one, two, or three at a time and grown to a point where sufficient material remained unheat affected to generate seed stock. Vacuum levels were maintained sufficiently low to minimize graphite hot zone and sample oxidation but high enough to minimize sample chromium and aluminum depletion. Traverse rates ranged from 1/8 to 3/4 in/hr with gradients measured at the γ' solvus temperature approximating 2500°F/in. The yield of single crystals from this approach was found to be highly orientation dependent but was above 50% on an overall basis.

FIGURE 6
COOLING PATTERNS FOR TWO TYPES OF RADIAL WAFER DESIGNS



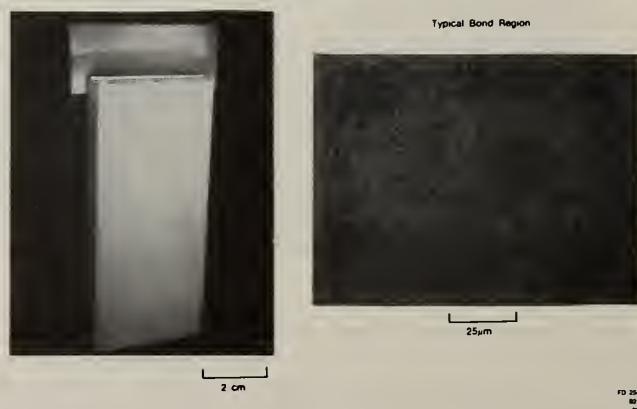
The D.R.'ed single crystals were finish machined and transferred to assembly bonding. To facilitate ready bond closure around the somewhat intricate internal airfoil passages of the type shown in Figure 6, a compliant layer of pure nickel was applied to each mating face. This layer (typically 0.0005 thick) was applied by either sputtering (the preferred method) or plating. Bonding was accomplished in a vacuum hot press at pressures above 15 Ksi. Upsets were held below the 1% level to guarantee bond closure without inducing sufficient strain to recrystallize the assembly upon subsequent full solution heat treatment.

FIGURE 7
MICROSTRUCTURE OF BOND REGION OF PREGROWN SINGLE CRYSTAL ASSEMBLIES



The final assembly (previously shown in Figure 1) contained typical bond interfaces illustrated metallographically in Figure 7. These assemblies were to be final heat treated prior to delivery for final machining by a variety of conventional and non-conventional machining techniques.

FIGURE 8
MACRO AND MICROSTRUCTURE OF A BONDED ASSEMBLED WAFER STACK



To produce a prebonded block, the processing sequence was reversed. The as-rolled stock was precision machined to the final thickness plus a bonding upset tolerance of 1%. The passages were then machined into the wafers which were then electropolished and delivered directly to bonding without the application of an interlayer.

Bonding was accomplished in a vacuum hot press at 2050°F. Stop blocks were used to control deformation, and since the material is inherently highly superplastic, applied stresses were typically in the 1 to 3 Ksi range. An assembled prebonded block is shown in Figure 8.

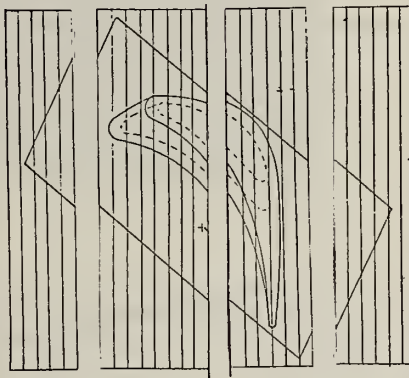
These blocks also need a seed to control D.R. grain growth direction. This seed was applied by differential expansion diffusion bonding in a manner similar to that described previously. The full width seeds were generated from the end croppings of the pregrown wafers described above. The doubly bonded blocks were then trimmed to regular cross-sectional geometries and D.R.'ed at conditions similar to that described for the pregrown wafers. A sample from this technique is illustrated in Figure 9. For blade fabrication, a series of these blocklets (four in all) will subsequently be bonded together to produce the full airfoil cross section (shown schematically in Figure 10) and machined to final shape.

FIGURE 9
MACRO- AND MICROSTRUCTURE OF DR HEAT TREATED PREBONDED BLOCK



FD 254161
881211
88-08

FIGURE 10
BLOCKLETS TO BE BONDED TO PRODUCE THE FULL AIRFOIL CROSS SECTION

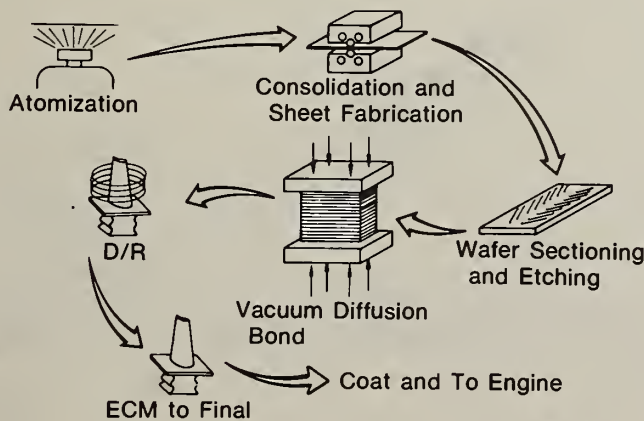


FD 254161
881211
88-08

DISCUSSION

The complexity of the radial wafer blade brings the engineer immediately to the problem of process economics. This is doubly true if the required component must be single crystalline in nature. The early radial wafer blades were made by slicing oversize extrusions, machining the radial cooling passages into the slices, diffusion bonding the assembly, and D.R.'ing the block. This sequence is illustrated in Figure 11. This approach was simple from a technical standpoint but led to an apparently poor material utilization factor. Furthermore, when the base alloy was found to be grain boundary weak, some technique for minimizing or eliminating grain boundaries or grain boundary angles was required. The process economics are also strongly effected by yield factors which, for this application, are largely controlled by heat treatment (D.R.) response.

FIGURE 11
MANUFACTURING SEQUENCE FOR RSR RADIAL WAVER BLADE

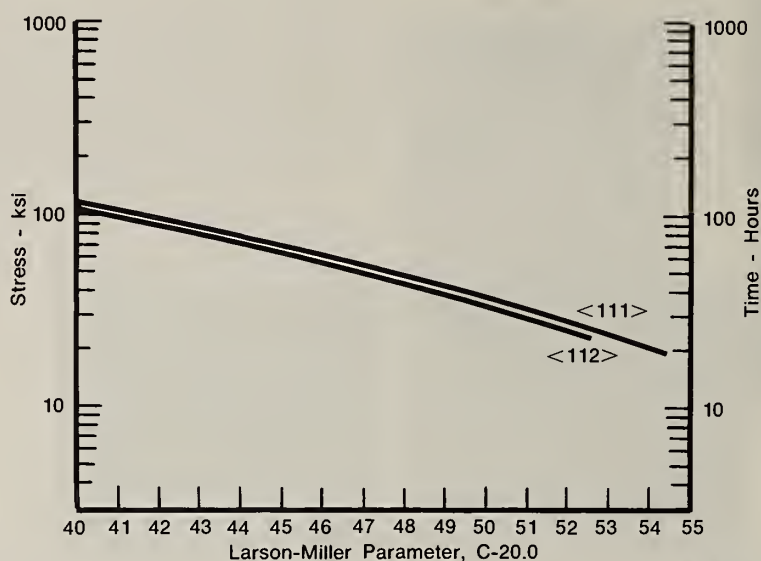


FD 254161

It was discovered early in the program that strong textures greatly enhance D.R. growth response. Early data also indicated that deformation textures controlled D.R. orientation. Furthermore, since the properties of the alloy under consideration are anisotropic, it appeared feasible to control the final properties of the fabricated assembly by controlling the processing/deformation sequence. Finally, if D.R. orientations were controlled by deformation texture, a singular texture would, of necessity, produce an effectively single crystalline structure.

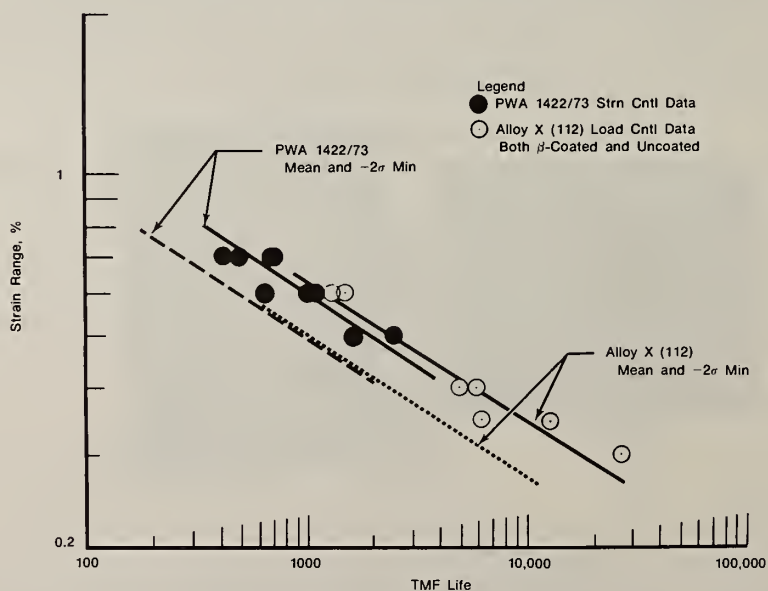
A comparison of the properties of alloy X as a function of orientation indicated the following: the $\langle 111 \rangle$ orientation is superior to all other orientations in creep loading; the $\langle 001 \rangle$ orientation offers the best strain-controlled low cycle fatigue resistance because of its inherently low elastic modulus; and the 112 orientation seems to offer the best combination of the above mechanical and physical properties extremes for use in the radial wafer design. Figures 12, 13, and 14 compare the most relevant properties for turbine airfoil as a function of orientation (where appropriate for this material). Because of these orientation property variations, the $\langle 112 \rangle$ orientation was selected for blading applications.

FIGURE 12
STRESS RUPTURE DATA AS A FUNCTION OF ORIENTATION FOR ALLOY PWA 1121



FD 254162
821311
0945B

FIGURE 13
LOAD CONTROLLED THERMAL MECHANICAL FATIGUE DATA OF ALLOY PWA 1121



FD 254163
821211
0952B

FIGURE 14
STATIC OXIDATION BEHAVIOR OF UNCOATED ALLOY-185 AND ALLOY PWA 1120
Cycle 2100° F/1 Hr/AC



FD 254-165
82 12 11
00029

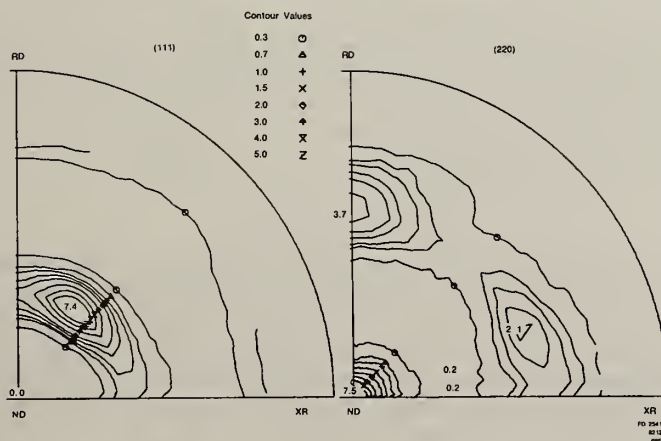
With the $\langle 112 \rangle$ having been selected as the prime axial airfoil direction and with the need for strong texture to enhance directional grain growth, cold cross-rolling was selected as the prime material finish forming technique. Cold rolling appeared to offer the potential for developing the strongest deformation texture, and cross rolling offered the potential for developing a truly singular $\{110\} \langle 112 \rangle$ texture. Early cold cross rolling yields were less than satisfying (Figure 15). However, recent experience has been far more enjoyable with rolling yields approximately approaching 90% of theoretical. The texture produced by these operations is depicted in Figure 16.

FIGURE 15
EFFECT OF TECHNIQUE ON COLD-CROSS ROLLING YIELDS

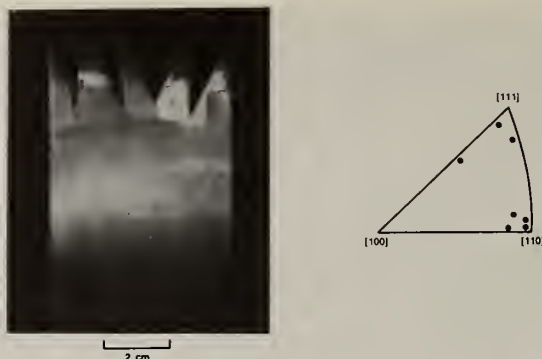


FD 254-165
82 12 11
00029

FIGURE 16
X-RAY DIFFRACTION POLE FIGURES MEASURED ON COLD CROSS ROLLED PWA 1120



FD 254-165
82 12 11
00029



This material was exposed to the D.R. cycle with no intentional anneals after rolling. As stated above, early studies indicated that texture steered grain growth. Apparently, however, texture intensities of the level developed here are insufficient to fully control growth orientation. A sampling of the D.R. orientations developed when as-rolled material is directionally recrystallized parallel to the primary working directions is illustrated in Figure 17. Note that the texture seems to preclude the appearance of random orientations rather than to guarantee the presence of selected orientations. Furthermore, since the $\langle 110 \rangle$ direction appears with such frequency, it appears that this is the preferred growth direction in this alloy system, and this habit growth will overcome the effects of texture of this level of strength. Again, it is speculated that a stronger texture may offer the potential for greater orientation control, but to date, testing of this hypothesis has not been possible.

An alternate technique is required, therefore, to control orientation. Two techniques were tried. The first technique was statistical in nature and involved initiating a large number of grains at the top of the plate, selecting an appropriately oriented grain (if possible) by Laue' back diffraction techniques, and isolating and propagating the selected grain through the wafer. This method was found too tedious for general applicability but, in fact, was used to generate seed material. The more preferred method, and the technique used for the growth of most of the crystals in this effort, was to bond on a growth directing seed crystal.

Initial attempts at bonding a truly single crystalline seed onto the fine grained stock gave spotty results. It was not found feasible using the techniques described above to drive a grain with an inappropriate orientation through the pre-established texture. Grain growth would cross the bond plane, terminate, and new appropriately oriented grains would nucleate, grow, and consume the fine grained stock. Even with appropriately oriented seeds, grain growth would often not continue from the seed through the matrix. The reasons for these growth breakdowns are unclear, but the "hard seed technique" was abandoned because of its low success ratio.

The success ratio of the "soft-seed technique" has been more than adequate. The superplastic, fine-grained region of the soft seed apparently complies well with the fine grained sample, allowing local bond joint oxide disruption and/or grain boundary migration/recrystallization during joining. Whatever occurs, subsequent growth down the seed, across the joint, and into the matrix is enhanced. Seed transferral using this method and differential expansion loading to mate the surface is well above 90%. Using this method, growth orientation control resolves down to mechanically aligning the appropriate seed orientation with the desired primary growth axes of the plate. To date this alignment has been easily held to within about 8 degrees of the nominally required orientation. A level which has been somewhat arbitrarily selected as adequate for mechanical property predictability.

There appears to be preferred growth directions in the NiMoAl X alloys evaluated as cross rolled plate. The $\langle 110 \rangle$ orientation has exhibited growth in this system at greater than $3/4$ "/hr. The growth rate of the $\langle 112 \rangle$ orientation has, at times, approached this rate but generally seems to exhibit a growth limit nearer $1/2$ "/hr. The $\langle 111 \rangle$ direction seems to exhibit a ceiling near $3/8$ "/hr. Normally, when one of the higher index grains breaks down, the new grain which replaces it is oriented such that a $\langle 110 \rangle$ type axis is parallel to the principal rolling direction with the (100) plane in the plane of the sheet (cube on face, rotated 45° texture). This orientation unfortunately does not exhibit outstanding creep or fatigue strength and has been the secondary grain orientation which has claimed most of the rejected samples.

A final statement will be made concerning the economics of the technique as outlined above. The current technique calls for approximately 7 lbs of powder to be consolidated to yield each pound of actual airfoil block material. This relatively low material utilization factor results from the need to roll oversized product to protect dimensions and finished surfaces and the apparent need to cross roll to enhance texture strength. Various schemes have been advanced to raise this ratio including straight, bright finish rolling to 0.005" over finish thickness. Such an improvement in yield (to about 30% overall) appears technically feasible, but not without a large amount of technical effort to guarantee that the final product will be appropriately heat treatment responsive. A large percentage of the cost of this component is associated with the grain growth yields and with the material utilization factor. If both of these factors can be improved through improved rolling technique designed to enhance texture strength and improve material utilization then a substantial reduction in the cost of these components (several hundreds of dollars per component) could be realized.

CONCLUSION

The feasibility of producing single crystal stock out of NiMoAl X alloys for use in radial wafer turbine blade fabrication has been demonstrated using a variety of processing routes. Rolling to produce directly heat treat responsive material has also been shown to be a viable approach. "However, reliance on texture to control grain growth orientation has been found unfeasible, and a supplemental orientation controlling technique (solid-state crystal seeding) has been shown necessary. The properties of the single crystals produced by these techniques fully meet expectations and represent an excellent compromise between strength and durability. Effort should continue, however, to improve the economics of the approach.

REFERENCES

1. Bourdeau, R. G. and J. B. Moore, Thermomechanical Processing of RSR Superalloy Powders, in Proceedings of the International Conference on Rapid Solidification Processing, Reston, Va, Nov. 1977, 334-346.
2. Cox, A. R., J. B. Moore and E. C. van Reuth, Rapidly Solidified Powders, Their Production, Properties and Potential Application, AGARD Conference Proceedings No. 256, 1978.
3. Holiday, P. R., A. R. Cox and R. J. Patterson, II, Rapid Solidification Effects on Alloy Structures, Proceedings of the International Conference on Rapid Solidification Processing, Reston, VA, Nov. 1977, 245-257.
4. Anderson, R. E., et. al., Use of RSR Alloys for High Performance Turbine Airfoils, Proceedings of the Second International Conference on Rapid Solidification Processing, Reston, VA, 1980, 416-428.
5. Cox, A. R., and R. J. Ondercin, Manufacture of Advanced Turbine Airfoils Using RSR Powder Alloys, Manufacturing Technology Advisory Group (MTAG), Phoenix, AZ, 1979.
6. George, D. B., B. T. Brown, and A. R. Cox, The Application of Rapid Solidification Rate Superalloys to Radial Wafer Turbine Blades, AIAA/SAE/ASME 15th Joint Propulsion Specialist Conference, Las Vegas, Nevada, 1979.
7. Chin, H. A., S. E. Hughes, J. S. Andrus and J. L. Larson, On the Texture Development-Directional Recrystallization Interaction of Rapidly Solidified Ni-Mo-Al-W and Ni-Cr-Al-W Alloys, paper presented at the International Conference on Rapid Solidification Processing, Reston, VA, December 6-8, 1982.

ACKNOWLEDGEMENTS

This work is jointly sponsored and monitored by the U.S. Defense Advanced Research Projects Agency and the Air Force Wright Aeronautical Laboratories.

The views and conclusions contained in this paper are those of the authors and should not be interpreted as necessarily representing the official policies, either expressed or implied, of the U.S. Defense Advanced Research Projects Agency, U.S. Air Force, or the U.S. Government.

DEFECT ANALYSES OF P/M SUPERALLOYS

W. H. Chang, H. M. Green and R. A. Sprague

General Electric Co., Evendale, OH 45215

ABSTRACT

This paper discusses the characteristics of manufacturing defects in a typical high-strength P/M superalloy, Rene 95. The nature, origin and size range of four types of defects found in the as-HIP material are described and their influence on the LCF behavior analyzed. Isothermal forging of the HIP material is shown to improve the LCF behavior considerably. The improvement is attributed to dispersion of large defects, especially of the PPB (Prior Particle Boundary) type. As a result of defect dispersion, the LCF life of the forged material is also benefited by a greater tendency toward internal fatigue initiation and initiation by crystallographic cracking or from small voids.

INTRODUCTION

The need for high-performance aircraft-engine disks has during the past decade spurred the development of P/M superalloy technology. Among the challenges accompanying this development, none are more critical than first, the availability of high-quality powders or billets and second, the design and management of engine components for safe and reliable service introduction. P/M superalloys can be consolidated by hot isostatic pressing (HIP), HIP followed by forging, or other combinations of compaction and working. Depending on the powder cleanliness and processing procedure, each type of material can contain defects differing in nature, size and distribution. A thorough knowledge of the defect characteristics is a prerequisite to predictability of material behavior and hardware performance.

This paper discusses the defects which have been found or induced in specimens of a typical high-strength P/M disk alloy, Rene 95, both in the as-HIP condition and after isothermal forging. Rene 95 in P/M form has a nominal composition (in wt %) of 0.065C, 13Cr, 8Co, 3.5Al, 2.5Ti, 3.5Cb, 3.5Mo, 3.5W and balance Ni. It normally consists of coarse, medium and fine gamma prime in a highly-alloyed gamma matrix which also contains a fine dispersion of Cb, Ti-rich carbides. Unless indicated otherwise, the materials discussed in this paper were produced from -150 mesh powders by argon atomization. The heat treatments consisted of 2065F/1 hr, oil quench, 1600F/1 hr, A.C. and 1200F/24 hrs, A.C. for the as-HIP condition and 2055F/1 hr, A.C. and 1400F/16 hrs, A.C. for the HIP and isothermally forged (H+F) condition.

Defects in As-HIP Material

Defect Characteristics

Table 1 summarizes the characteristics of four types of defects identified at the failure initiation sites of as-HIP Rene 95 LCF specimens. Representative appearances of these defects are illustrated in Figure 1. Types 1 and 2 are ceramic inclusions which exist as discrete and often chunky particles (Type 1, Figure 1A) or as agglomerates of fine particles (Type 2, Figure 1B). Both types apparently originate from the melting crucible, pouring tundish or the atomizing nozzle during powder production. Aluminum is usually the major metallic element with Zr, Mg or Ca also present in various amounts depending on the particular ceramics involved. The sizes of Type 1 and Type 2 defects are limited by the screening opening through which the powders have been sieved and are not altered significantly by reaction during the HIP cycle. As indicated in Table 1, the ceramic defects average about 10 mils² with very few reaching 50-100 mils².

In direct contrast to Type 1 and Type 2 which are "condensed" defects, Type 3 or the PPB (Prior Particle Boundary) defects are "diffused" in that they generally spread over a larger volume of material. As shown in Figure 1C, Type 3 defects are characterized by a semi-

continuous network of fine oxide or carbide particles around the host powder surfaces. A residual core of the initial defect-forming source may or may not be present at center of the affected area. Figure 1C illustrates an example of PPB defect with a core of refractory remaining. Formation of Type 3 defects appears to require a source of oxygen or carbon which reacts with powder surfaces during the HIP cycle. Potential sources of PPB defects include refractories containing water glass (sodium silicate) as binder, organic contaminants inadvertently introduced during powder handling (e.g. Buna N and vacuum grease), mill scale (rust) and leakage during powder canning. Depending on the nature and amount of the contaminant and the rate of powder consolidation during the HIP process, PPB defects can range from a few mils² to several orders of magnitude larger than the maximum (250 mils²) shown in Table 1. The PPB defects are thus potentially the most detrimental to P/M superalloys.

Since the powders are produced by argon atomization, argon is unavoidably entrapped in some of the powders, giving rise to voids or Type 4 defects in the consolidated product. Individual voids seldom exceed 2 mils². Clusters of voids, however, often exist to yield substantially larger combined sizes as indicated in Table 1.

Effect of Defects on LCF

Defects are of major concern to P/M superalloys primarily because of their adverse effect on LCF. The total LCF life (N_t) of high-strength disk alloys can be considered to consist of three parts: life spent in crack initiation (N_0), life in Stage-1 propagation (N_I) and life in Stage-2 propagation (N_{II}) which ends essentially in final failure. Within certain temperature and strain ranges, the sum of $N_0 + N_I$ can consume over 90% of total LCF life. Yet microstructurally, $N_0 + N_I$ corresponds to but a very small crack size or area. This means that defects whose sizes exceed the corresponding $N_0 + N_I$ crack size would reduce LCF life drastically by depriving the material of resistance to crack initiation and Stage-1 propagation. Figure 2, for example, shows the effect of EDM holes of prescribed sizes intentionally introduced to the gage section of LCF specimens made from as-HIP, CAP (Consolidated at Atmospheric Pressure) and rolled, and cast and wrought Rene 95, tested at 1000F, $A=1$, and $\Delta\epsilon_t=0.66\%$. In the absence of significant defects, the intrinsic LCF life is well over 100,000 cycles. Induced surface defects exceeding 5 mils², however, are sufficient to reduce life to less than 10,000 cycles by eliminating $N_0 + N_I$.

Defects affect LCF life to a degree which varies with both defect size and location of failure initiation. This is illustrated in Figure 3 for as-HIP Rene 95 at 1000F, $A=1$ and $\Delta\epsilon_t=0.66\%$. The data shown were obtained from specimens which contained surface or internal defects sufficiently large to permit only Stage-2 crack propagation. Within this range, the LCF life is linearly related to defect area on a log-log basis. Note that for a given size, a defect is much less detrimental when situated internally than when it is located at the surface. The less severe effect of internal defects is due in part to the reduced stress range intensity amplification but in a large measure probably results from the absence of adverse environmental interactions. Since surface failures are less likely the fewer the number of defects, Figure 3 reinforces the simple concept that the LCF life of as-HIP P/M alloys can be improved to the extent the defects are reduced both in number and in size. This concept is particularly pertinent to PPB type defects.

Table 1: Major Defects in As-HIP Material

Major Type	Description	Typical Elements	Size, Mils ² (*)	
			Avg.	Max.
1	Discrete, chunky ceramic	Al, Mg, Zr, Ca, O	8	50
2	Ceramic agglomerates	Al, Si, Mg, Ca, O	10	110
3	Reactive agglomerates forming PPB	Al, Zr, Cr, Ca, O, C, Ca, (Fe)	15	250
4	Voids	Ar	6	10

(*) Based on defects at initiation sites of LCF test specimens made from -150 mesh powder.

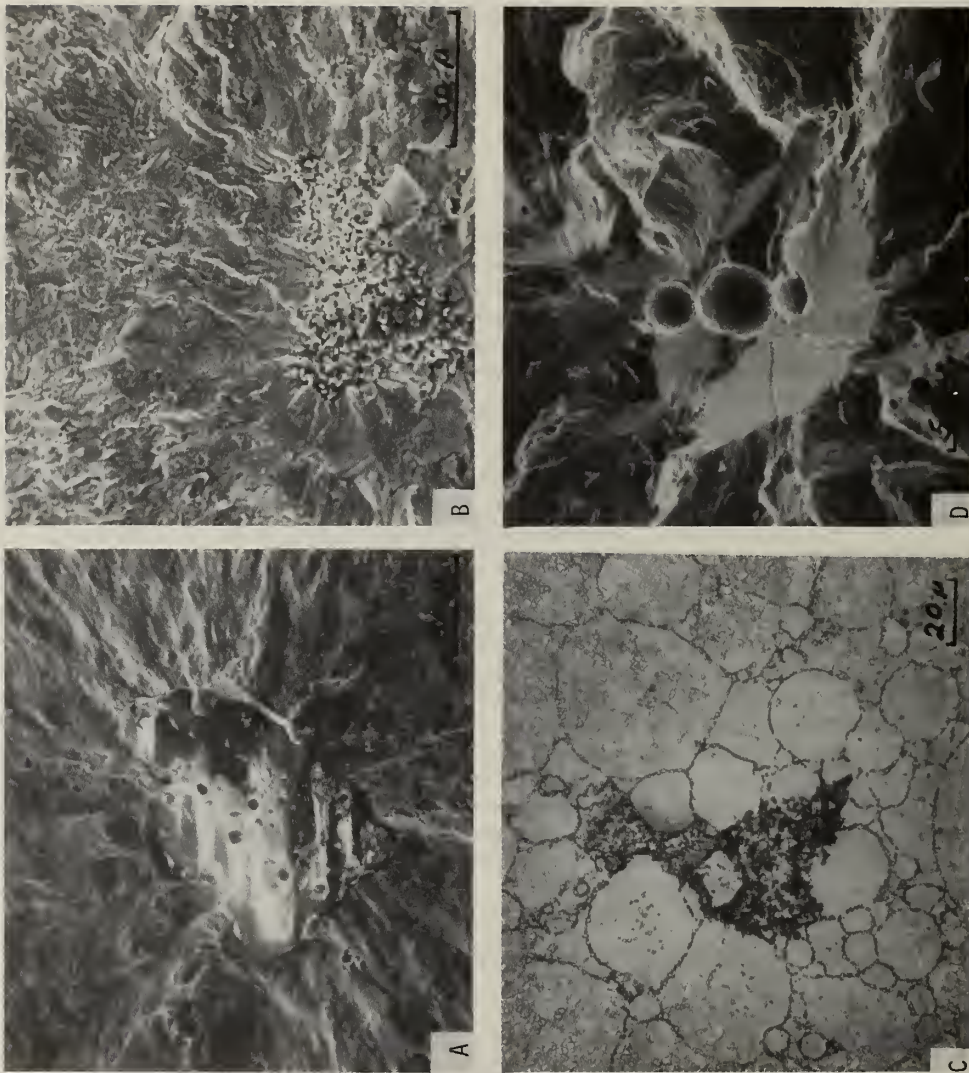


Figure 1: Defects in As HIP Rene 95: A, B, C and D Represent Types 1, 2, 3 and 4, Respectively (See Text)

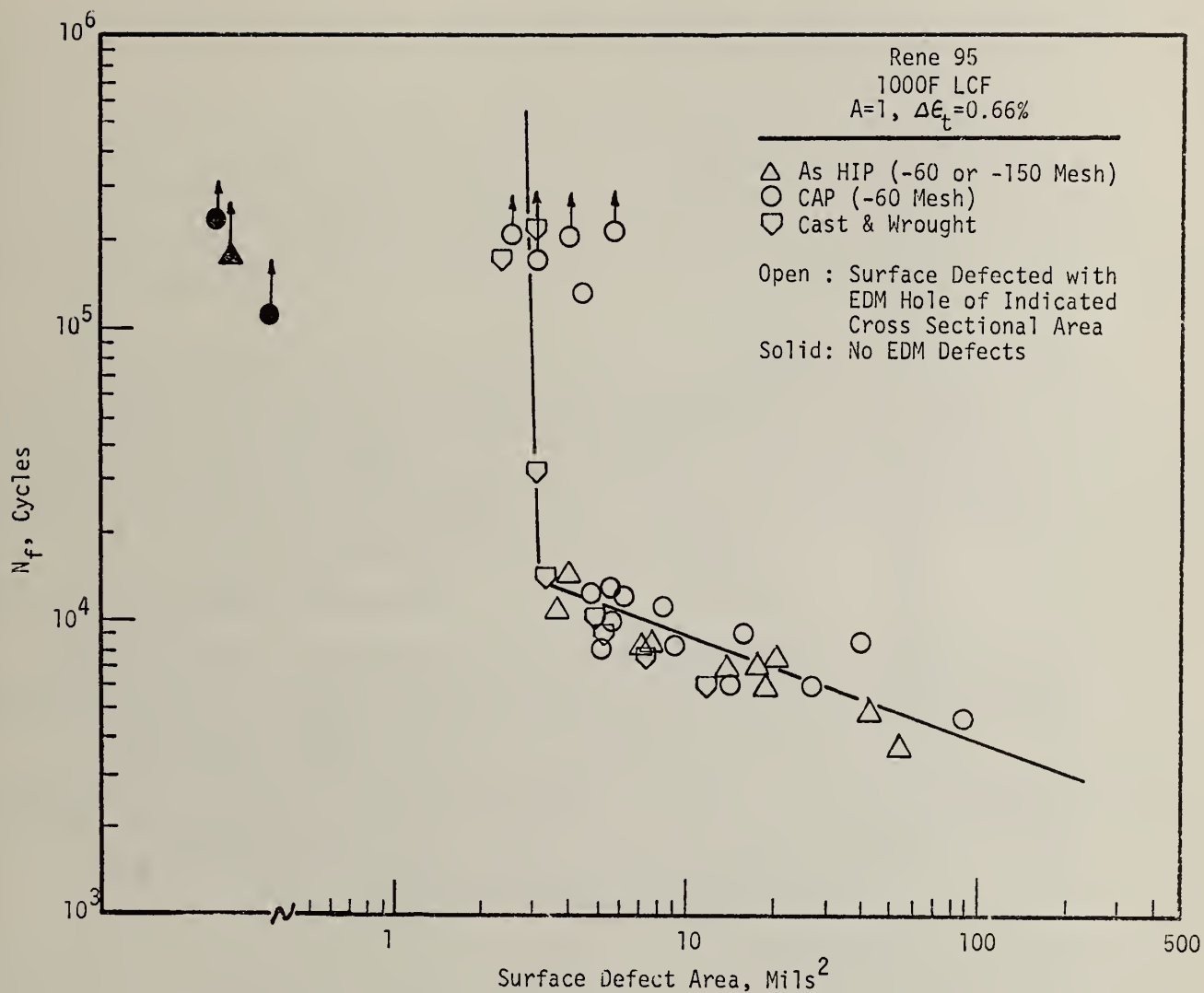


Figure 2: Effect of Surface Defect Size on LCF Life of Various Types of Rene 95

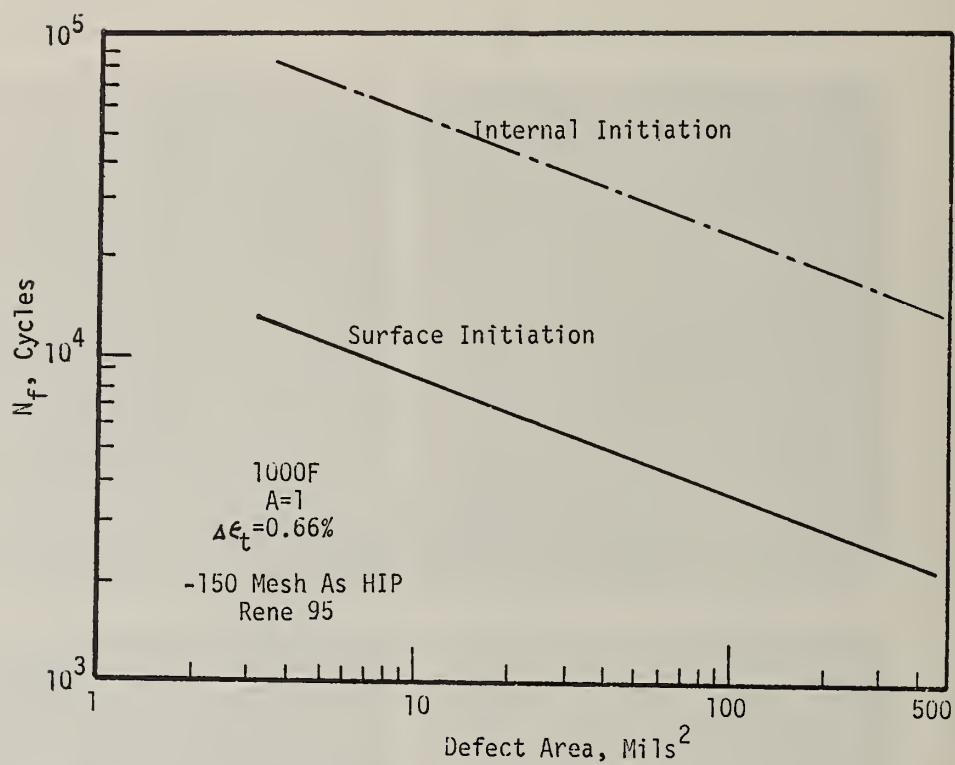


Figure 3: Effect of Defect Size and Failure Location on LCF Life

Defect Modification by Isothermal Forging

Results on Doped Material

The potential of isothermal forging in defect modification was initially assessed by doping Rene 95 powders with Type 1 (chunky ceramic) and Type 3 (PPB) defect formers. The dopants selected were Al_2O_3 (Type 1, -60+80 mesh, 1,000 particles per pound of Rene 95), Buna N (O ring material, Type 3, 500 particles per pound) and vacuum grease (Type 3, 1 cc per pound). Both doped and undoped materials, after HIP at 2050F, were isothermally forged at 2050 for 0 to 80% reduction. Figure 4A shows that forging had little effect on Al_2O_3 , other than occasional fracturing. The larger PPB defects, on the other hand, were greatly reduced in size, generally to stringer or cigar shapes, lying randomly in the forging plane (Figure 4, B and C). Consistent with these characteristics of defect modification, there were corresponding changes in mechanical properties. Table 2 shows that both tensile ductility and LCF life of doped Rene 95 were improved by the forging operation. Further, the improvements were much more pronounced in materials doped with Type 3 than with Type 1 defects.

While as-HIP materials (doped or undoped) invariably initiated LCF failure at one of the four types of defects described previously, some forged specimens failed by crystallographic cracking without impurity-related defects. An example is shown in Figure 4D. The initiation was usually associated with one or more somewhat larger grains which are designated as Type G "defects". Note that since the forged structure generally had very fine grain sizes ($<10\mu$) and that even occasional larger grains seldom exceeded 30μ , Type G failures preserved their initial processes of crack initiation and Stage-1 propagation, as evidenced by the small facets delineating the initiation site in Figure 4D. Consequently, Type G failures were generally associated with long LCF lives.

Effect of Forging on Undoped Material

Defect Type and Size Distribution: Based on examination of initiation sites of LCF specimens, Table 3 compares the defect type, defect size and location of failure between as-HIP and H+F (HIP+isothermally forged, 60-80% reduction) Rene 95. Several trends are discernible pertaining to the influence of forging on defect modification:

1. The forged specimens were much less prone to surface initiation, being almost immune at 1000F (Table 3, Column D). Under conditions more conducive to surface initiation (750F/0.7% $\Delta\epsilon_t$), the frequency of such failure was 33% vs. 75% for the as-HIP specimens.

Table 2: Effect of Isothermal Forging on Ductility and LCF Life of Seeded Rene 95

Material	RT/1200F Tensile El., %	1000F/0.66% $\Delta\epsilon_t$ LCF Life, Cycles	
		\bar{X}	\bar{X} -3S
1. As-HIP (Unseeded)	17/15	36,840	11,800
2. H+F (Unseeded)	20/22	128,848	-
3. As-HIP (Al_2O_3 Seeded)	10/5	3,411	1,758
4. (3) + F	14/15	8,219	4,101
5. As-HIP (Buna N Seeded)	10/3	2,561	1,200
6. (5) + F	19/19	134,001	22,241

*All -150 mesh powder. Forging reduction: 80%

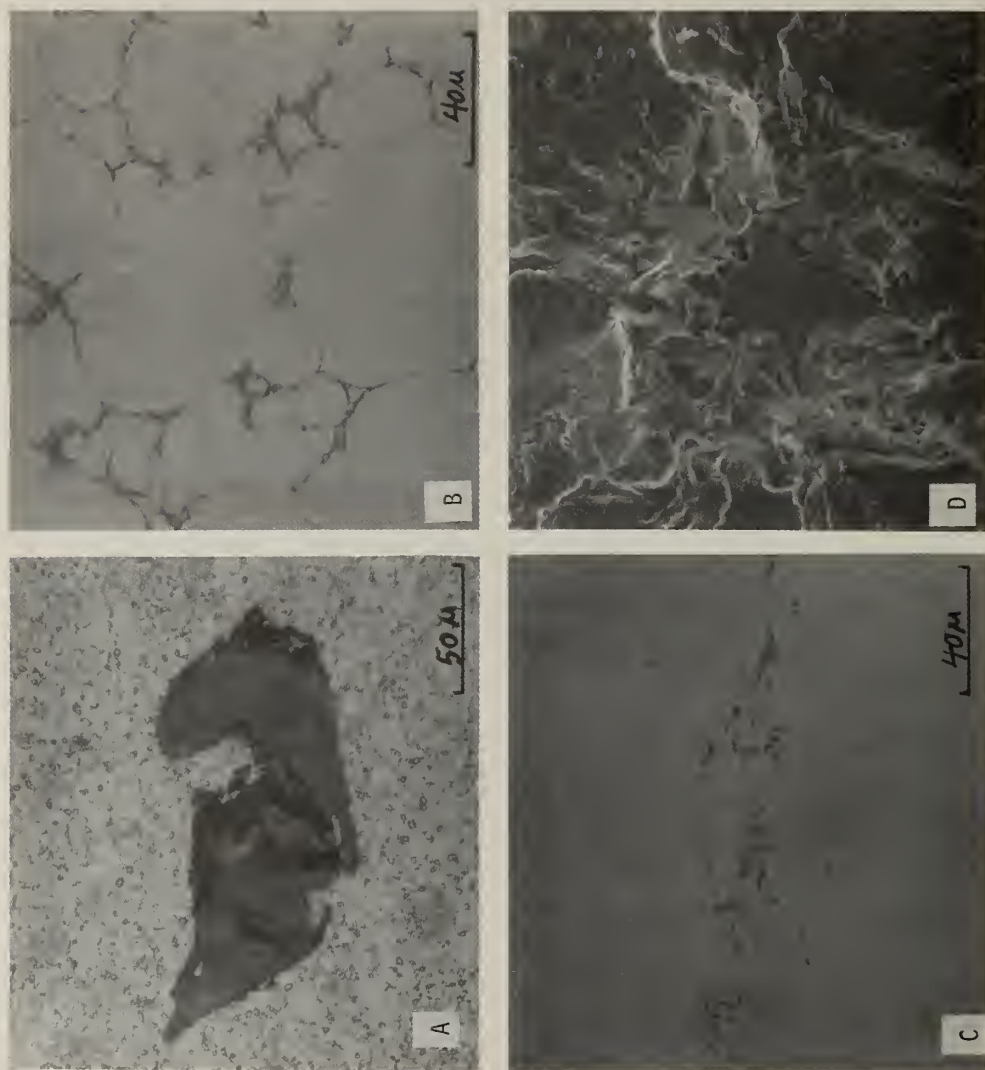


Figure 4: Effects of Isothermal Forging on Defects and LCF Failure Initiation:
 (A) Alumina Inclusion in H+F, (B) Vacuum Grease Induced PPB in As HIP,
 (C) PPB Defect in (B) Modified by 80% Isothermal Forging Reduction,
 and (D) LCF Initiation in H+F by Crystallographic Cracking Without
 Impurity-Related Defects

Table 3: Comparison of Defect Type and Size at LCF Initiation Site - As HIP vs H+F

A	B	C	D	E					F	G			
Temp oF	$\Delta\epsilon_t$ %	Material	Overall Surface Failure %	Frequency of Defect Type*					Defect Type	Defect Size, Mils ²			
										As HIP		H + F	
										Ave.	Max.	Ave.	Max.
				1	2	3	4	G					
1000	0.78	As HIP	76	21	74	4	1	0	1	6.7	36	5.3	16.0
			5	66	5	0	0	29	2	9.5	50	6.1	11.3
		H+F							3	18.7	242	None	None
									4	6.3	10.3	None	None
	0.66	As HIP	31	15	77	7	1	0	1	11.2	50	3.9	12.0
			5	29	28	3	14	26	2	13.1	111	4.8	13.0
		H+F							3	19.3	83.6	4.2	4.5
									4	5.3	6.8	0.8	1.4
	0.70	As HIP	75	33	58	9	0	0	1	7.5	9.1	6.4	13.7
			33	13	24	0	30	33	2	8.6	13.1	4.2	9.3
		H+F							3	-	6.4	None	None
									4	None	None	1.1	1.5

* Type G represents crystallographic cracking without impurity-related defects

2. In contrast to as-HIP specimens which invariably failed from impurity-related defects (Types 1 through 4), a substantial number (26 to 33%) of H+F specimens failed from Type G defects (Column E). Of these, about 5% at 1000F and about 50% at 750F were surface related, constituting a major source of surface failures at the lower temperature. As explained before, Type G failures, even when initiated externally, were associated with long LCF lives.

3. Types 1 and 2 ceramic inclusions constituted the most frequently observed defects in both materials. The average size of each type (5-10 mils²) did not differ significantly between the two materials although the maximum sizes (especially Type 2) appear to be somewhat smaller in the H+F specimens (Column G), suggesting that the Type 2 defects may have been dispersed by the forging reduction.

4. Although Type 3 (PPB) defects were only infrequently found in both materials, the frequency of occurrence was consistently higher in the as-HIP specimens (4, 7 and 9% vs. 0, 3 and 0% for H+F, under the three testing conditions, Column E). Further, both the average and especially the maximum sizes found in the H+F specimens (4.2 and 4.5 mils², respectively) were considerably smaller than those found in the as-HIP specimens (19 and 242 mils², respectively).

5. Void-induced (Type 4) failures became much more frequent in H+F specimens, reaching 14% at 1000F/0.66% $\Delta\epsilon_t$ and 30% at 750F/0.7% $\Delta\epsilon_t$, as compared with 1% or less for the as-HIP material. The lack of Type 4 failures in the latter case is not surprising since the relatively small voids would be bypassed as initiation sites in favor of larger defects which were present. Once the larger defects had been dispersed by forging, then the most abundant and uniformly distributed small defects would be favored for crack initiation, especially those located at or near the surface. These conditions were fulfilled by voids in the H+F material, thus accounting for the propensity toward Type 4 failures in the H+F material, from voids located only slightly below surface. Note from Table 3, Column G that the voids in the H+F specimens were very small (≤ 1.5 mil²), with correspondingly minor detrimental effect on LCF life.

Effect of Forging on LCF Life: The preceding comparisons indicate that through its effects in eliminating or modifying large defects (especially PPB), isothermal forging facilitates (a) internal crack initiation, (b) initiation by crystallographic cracking and (c) void-induced initiation. As shown in Figure 5 and Table 4, these characteristics in concert resulted in several fold improvement in LCF life (both average and -3S) over as-HIP Rene 95. The improvement was consistent with that shown previously in Table 2 for doped materials.

Table 4: LCF Life Comparison Between As-HIP and HIP+Isoforged Rene 95

Temp. °F	$\Delta\epsilon_t$ %	Material	N _f , Cycles	
			\bar{X}	\bar{X} -3S
750	0.70	As-HIP	21,003	3,920
		H+F	104,148	34,103
1000	0.78	As-HIP	11,676	1,564
		H+F	61,693	12,961
	0.66	As-HIP	37,000	4,500
		H+F	181,052	70,752

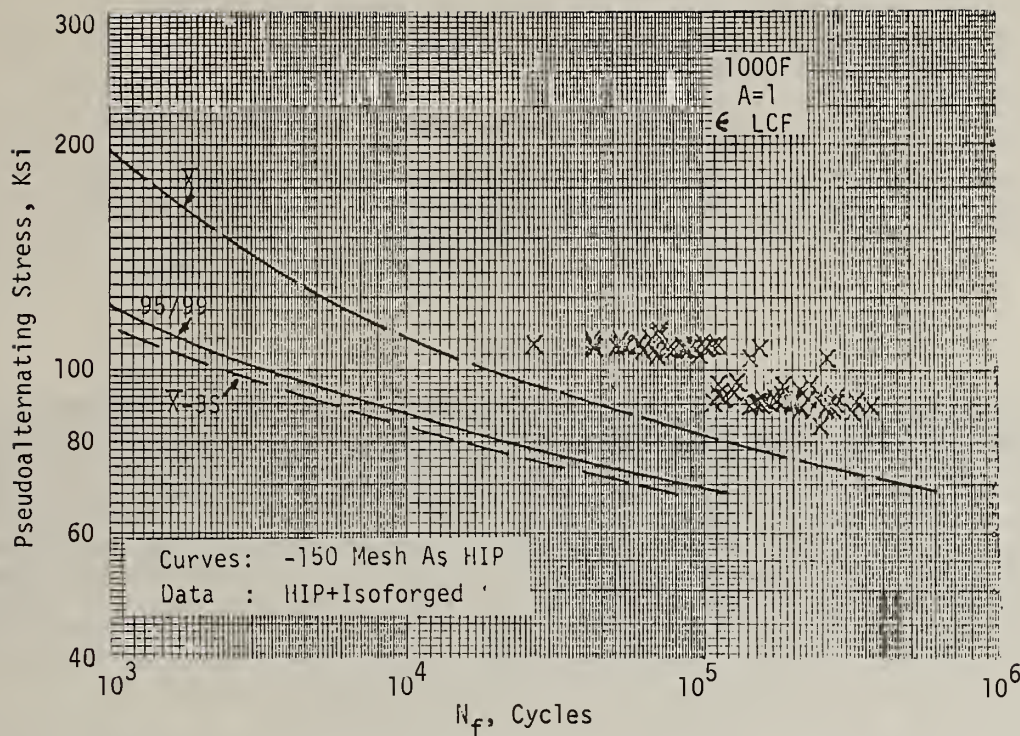


Figure 5: Overall LCF Life Comparison at 1000F
(As HIP vs H+F)

Concluding Remarks

Given clean powder and manufacturing care, the as-HIP process is capable of producing high-quality components. The results presented in this paper indicate that further improvement in LCF behavior can be achieved by isothermal forging through defect modification. The fine-grained structure effected in a forged product provides an additional advantage in overall defect control by allowing more discriminating nondestructive inspection. The benefits of forging reported in this paper, while based primarily on laboratory specimens, are achievable in engine components provided, again, a high degree of powder cleanliness and manufacturing care is maintained.

Acknowledgments

The authors are indebted to the following individuals of the General Electric Company: Cliff Shamblen for his work on defect characterization on USAF Contract F33615-78-C-5225, David Mourer for his contribution in isothermal forging evaluation and Ken Wright for reviewing the manuscript.

INTERPRETIVE REVIEW OF COMPARATIVE MICROSTRUCTURES OF
POWDERS AND CONSOLIDATES OF P/M SUPERALLOYS PRODUCED
BY MODERN ATOMIZATION PROCESSES*

Robert D. Kissinger and John K. Tien

Henry Krumb School of Mines
Columbia University
New York, NY 10027

ABSTRACT

This paper reviews in a comparative manner cooling rates, powder morphology and consolidated microstructure and some properties of superalloys produced by the commercial and the new processes. The review strategy will be to give preference to the comparison of the same alloy produced by different atomization techniques. For example, the surface morphology of the RSR powder is smooth with occasional fracture, whereas the AA powder surfaces are connected to many small satellite powders. Depending on powder size, the AA powders have approximately twice the number of particles containing gas pores as the RSR powder. From secondary dendrite arm spacing (DAS) measurements, it was estimated that argon atomized superalloy powders show a cooling rate with the same order of magnitude as the RSR superalloy powders. Comparisons and conclusions involving other atomization processes will also be presented and discussed, as will some mechanical properties.

* An invited review paper

Introduction

Commercial production of superalloy powders is primarily by inert (usually argon) gas atomization (AA) and vacuum, or soluble gas, atomization (VA). A third commercial process, the rotating electrode process (REP), has been used to produce superalloy powders, but has found greater success in titanium powder production. Still in the developmental stage are the rapid solidification rate (RSR) and the ultrasonic atomization (UA) processes. A detailed description of the above atomization processes can be found in the literature [1] and will not be discussed in this compacted review dealing mainly with powder metallurgy (P/M) superalloy microstructures. Emphasis will be given to comparisons of the same alloy produced by different atomization processes and, more specifically, to a comparative study of VA, AA, and RSR superalloy powders currently in progress at Columbia University. For this comparative study, RSR and AA powder material of IN 792 (AA material only), IN 792 + Hf (C101), and IN 792-boron, carbon modified (B1925) produced from the same ingot material were supplied by Pratt & Whitney Aircraft through DARPA contract AF 33615-76-C-5136 and Special Metals Udimet Powder Division, respectively. UA modified IN 100 was supplied by Homogeneous Metals, Inc.

Powder Size Distribution

Typical powder size distributions [2] of similar superalloy powders produced by VA, AA, and RSR processes are given in Fig. 1. The RSR process apparently produces a narrower size distribution of powder particles as compared to the broader distributions of the VA and AA processes. Although mean particle diameters of the RSR and VA powders are slightly smaller than the AA powders, these values can be varied to some extent by changing certain processing parameters. For example, increasing the speed of the rotating disk in the RSR process [3] or increasing the relative gas to liquid velocity [4,5], or changing the nozzle configuration in the AA process will result in a decrease in the mean particle diameter. For the REP process, powder size is, on the average, coarser than the above processes with the powder particles usually falling within a narrow size range.

Surface and Interior Power Structures

An example of superalloy powders produced by AA, RSR, and VA is shown in Fig. 2. Although the three atomization processes yield relatively spherical particles, there are slight differences in surface morphology. The majority of RSR powders are smooth with occasional fractures caused by particle-particle or particle-apparatus wall collisions. Both AA and VA powders exhibit small satellite particles connected to powder surfaces. All three types of powders occasionally show particles enveloped by metal shells, occurring when a liquid droplet impinges on and surrounds an already solidified particle. The RSR powders generally show the greatest percentage of these splat cooled structures. Not shown in Fig. 2 are REP powders, which are characterized by smooth, satellite-free particles similar in surface character to the RSR powders.

Analysis of sectioned AA, RSR, and VA powders reveals the presence of porosity in the form of entrapped gas. A simple qualitative calculation determining the percentage of particles containing gas pores shows that at least twice as many AA powder particles contain gas pores as do RSR powders of the same particle diameter (Fig. 3). For the one VA superalloy powder studied, the percentage of powder particles containing gas pores was similar to AA powders.

Individual powder particles can be considered as small castings with cellular, dendritic, and/or microcrystalline microstructures characteristic of each particle's thermal history. While cooling microstructures of atomized powders differ for different powder particle sizes, powder particles of the same diameter also exhibit varying cooling microstructures. For example, Fig. 4 shows both a dendritic and a microcrystalline microstructure for two 12 μm -diameter AA C101 powder particles.

Relative Cooling Rates and Retained Carbon in Solution

For those particles which are dendritic, it is possible to measure secondary dendrite arm spacings (DAS) and correlate these measurements with particle diameter. It is found that DAS varies with particle diameter according to the empirical relationship [6]:

$$\text{DAS} = A d^m \quad (1)$$

where d is the particle diameter. Table I lists values of A and m calculated for similar superalloy powders produced by VA, AA, and RSR. In graphical form (Fig. 5) the data show that for the same alloy and average particle diameter, the AA process produces a coarser average DAS as compared to the RSR process. Data for VA IN 100 are included in Fig. 5 for comparison with the AA and RSR IN 792-type superalloys.

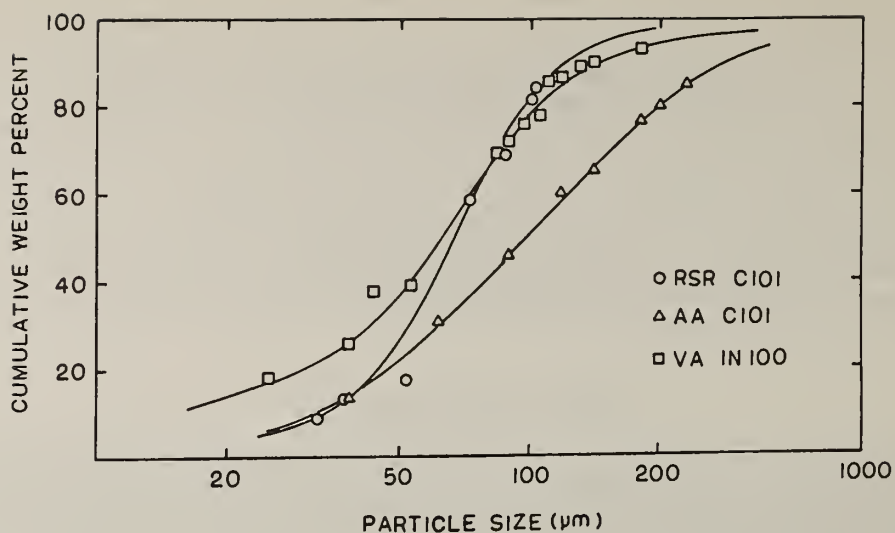


Fig. 1. Powder size distributions for RSR C101, argon atomized (AA) C101 and vacuum atomized (VA) IN 100. (Ref. 2.)

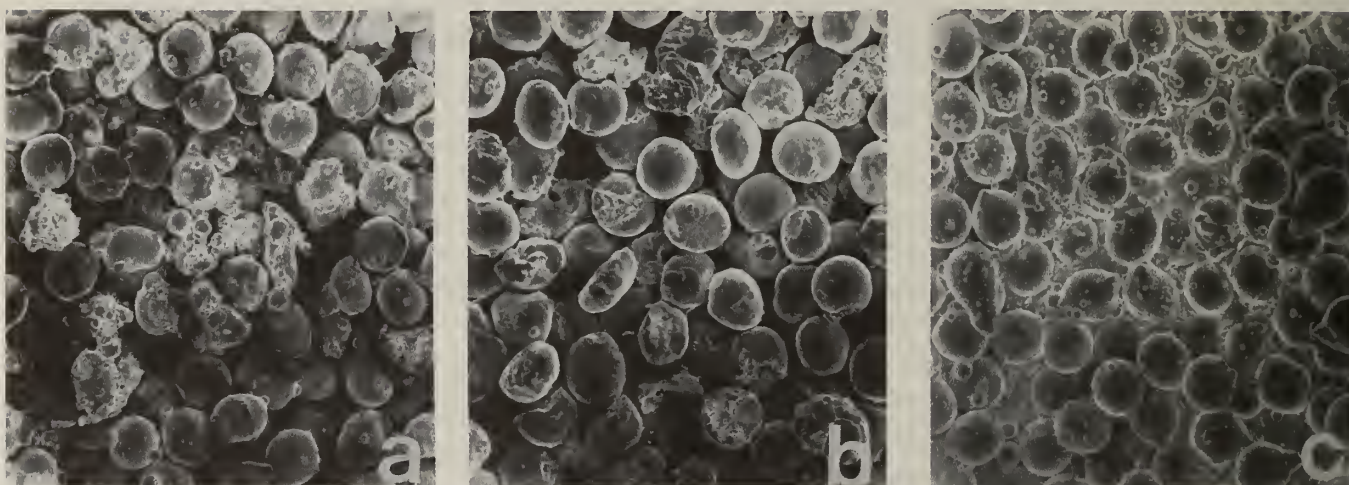


Fig. 2. Superalloy B1925 powders produced by (a) argon atomization and (b) RSR and (c) Superalloy IN 100 produced by vacuum atomization. (-140+150 mesh powders)

TABLE I

Secondary Dendrite Arm Spacing vs. Particle Diameter

$$DAS = Ad^m$$

<u>Process</u>	<u>Alloy</u>	<u>A</u>	<u>m</u>
VA	IN 100	0.225	.525
AA	IN 792	.164	.545
AA	C 101	.130	.605
AA	B 1925	.159	.540
RSR	C 101	.116	.574
RSR	B 1925	.105	.512

DAS has also been shown to vary with cooling rate according to the empirical relationship:

$$DAS = B\dot{T}^{-n} \quad (2)$$

where \dot{T} is the local cooling rate. Unfortunately, experimental values of B and n have been determined for only a few alloy systems within a restricted range of cooling rates. However, it is possible to calculate approximate relative RSR/AA cooling rates by coupling Equation (2) with Equation (1). If the ratio of DAS_{RSR}/DAS_{AA} is calculated for the same alloy from data listed in Table I, and the constant B in Equation (2) is considered only alloy dependent, the relative cooling rate, $\dot{T}_{RSR}/\dot{T}_{AA}$, can be expressed as:

$$\frac{\dot{T}_{RSR}}{\dot{T}_{AA}} = \frac{DAS_{RSR}}{DAS_{AA}}^{-\frac{1}{n}} \quad (3)$$

Calculated relative cooling rates for RSR and AA B 1925 and C101 as a function of particle diameter are shown in Fig. 6 for $n = 0.3$, which is the experimental value determined for a Maraging 300 steel from data spanning four orders of magnitude up to 10^{30}C/sec [7]. For both alloys the AA powders surprisingly show cooling rates within the same order of magnitude as the RSR powder cooling rates, which are quoted to be on the order of 10^{50}C/sec for superalloy particles in the $100\text{ }\mu\text{m}$ range [8].

With these extremely high cooling rates available for superalloy powder production, it is possible to extend the solid solubility limits of various alloying elements. For example, a detailed analysis of carbon partitioning in AA René 95 [9] has shown that as particle size decreases (and cooling rate increases), the percent of total carbon in the powder present as MC type carbides decreases. Figure 7 shows the hyperbolic nature of the carbide partitioning function.

Consolidated Microstructures

The most common consolidation techniques used in P/M superalloy processing are hot isostatic pressing (HIP) and hot extrusion. Early attempts at P/M superalloy consolidation resulted in the deleterious precipitation of carbide films at prior particle boundaries (PPB), as well as the formation of precipitates at PPB's due to oxygen and nitrogen gas adsorption on powder particle surfaces. These problems have been solved to some extent by alloy modifications, inert handling of powders, and changes in consolidation heating cycles. For example, carbon levels of P/M superalloys reduced to 0.02 weight percent [10,11] and the addition of strong carbide formers [12,13,14], e.g., Hf, Nb, and Ta, have reduced or eliminated PPB carbides and/or modified the type and distribution of carbides. Table II lists the composition of modern P/M superalloy chemistries, which makes use of one or more of the above composition modifications. With the combination of alloy redesign, improved powder handling, and appropriate heat treating schedules, the integrity of as-HIPed P/M superalloys has dramatically increased, as witnessed by a recent Pratt & Whitney Aircraft report [15], which states that as-HIPed VA and AA MERL 76 can be used for commercial jet engine disks with considerable saving in weight and machining costs.

The response of superalloy powders to HIP has been reported to vary with respect to the atomization process. Centrifugally atomized (RSR) iron-nickel base powders have shown a greater tendency, as compared to AA powders produced from the same piece of bar stock, to retain the as-solidified powder structure during HIP [16]. We have also found this to be the case for as-HIPed and HIP + heat treated RSR and AA B1925 and C101. A comparison of consolidated microstructures of alloy C101 is

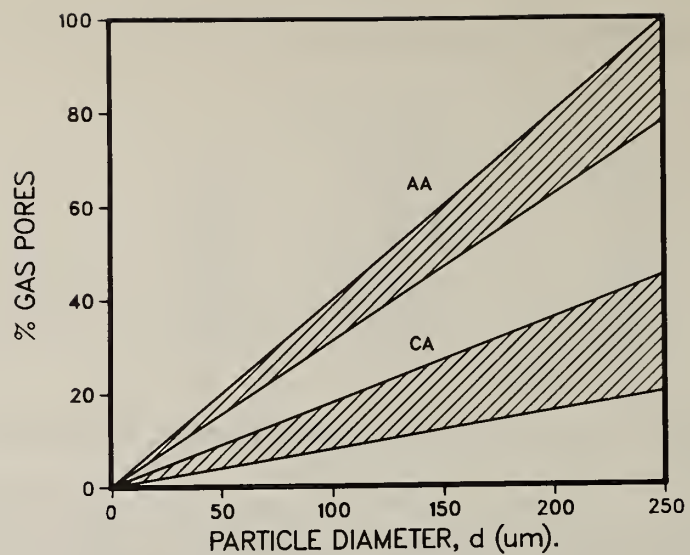


Fig. 3. Percent of argon atomized (AA) and centrifugally atomized (CA) powder particles containing entrapped gas pores as a function of particle diameter.

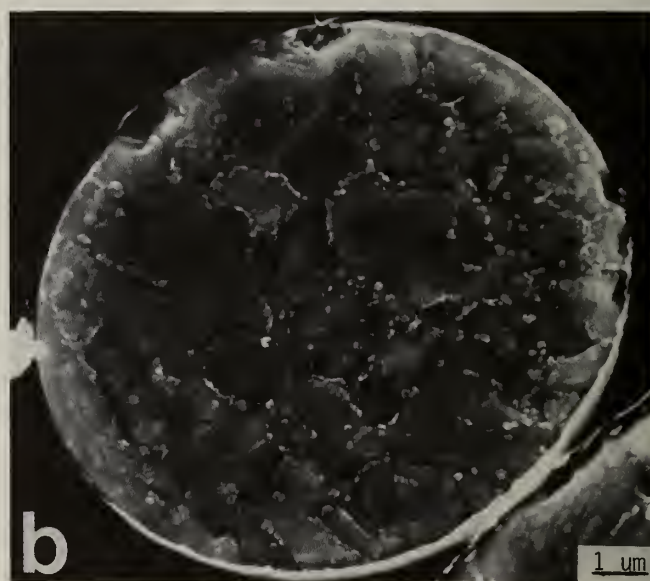


Fig. 4. Two 12 μm -diameter argon atomized C101 powder particles exhibiting (a) dendritic and (b) microcrystalline microstructures.

TABLE II

Nominal P/M Superalloy Compositions (Wt. Percent)

<u>Alloy</u>	<u>Ni</u>	<u>Cr</u>	<u>Co</u>	<u>Mo</u>	<u>W</u>	<u>Cb</u>	<u>Al</u>	<u>Ti</u>	<u>C</u>	<u>B</u>	<u>Zr</u>	<u>Hf</u>	<u>Other</u>
Astroloy	55.4	15	17	5	-	-	4.0	3.5	.06	.03	-	-	-
IN 100	54.5	12.4	18.5	3.2	-	-	5.0	4.3	.07	.012	1.0	-	1.0 V
René 95	62.4	13	8	3.5	3.5	3.5	3.5	2.5	.06	.01	.05	-	-
IN 792	60.7	12	9	1.9	3.8	-	3.4	4.0	.11	.016	.08	.79	4.1
B 1925	60.3	11.6	8.7	1.7	5.1	-	3.4	4.0	.01	.10	-	-	5.1
C 101	59.7	12	9	1.9	4.3	-	3.4	4.0	.10	.017	.06	1.1	4.4 Ta
MERL 76	54.5	12.5	18.5	3.2	-	1.4	5.0	4.4	.02	.02	.06	.4	-
AF 115	55.3	10.7	15	2.8	5.9	1.7	3.8	3.9	.05	.02	.05	.75	-

René is a trademark of the General Electric Company

MERL 76 is an improved turbine disk alloy developed by Pratt & Whitney Aircraft

AF 115 is also an advanced turbine disk alloy developed by the General Electric Company for the Air Force

shown in Fig. 8. The $-104\text{ }\mu\text{m}$ (-150 mesh) RSR material seems to retain more of the pre-HIP powder structure, with the average γ' precipitate size in the large particle interiors remaining much smaller than the γ' precipitate size in the interparticle regions, even after heat treatment. There also appears to be a higher percentage of thermally induced porosity (TIP) in the $-230\text{ }\mu\text{m}$ (-60 mesh) AA HIP + heat treated material.

The as-HIPed RSR and AA consolidated materials were studied using transmission electron microscopy, and it was found that the RSR material had a tendency to retain not only original grain size within the larger prior particles, but also to retain the smaller scale DAS microstructure, as shown in Fig. 9a. This tendency was not observed nearly as often in the AA material (9b) and is thought to be related to the slightly higher cooling rate, and accompanying increase in homogeneity, of the RSR superalloy powders as compared to the AA powders.

Conclusion

Following HIP or hot extrusion consolidation, P/M superalloys are generally hot forged or rolled. These P/M materials show excellent hot working characteristics due to their small grain size, and the lateral flow of material associated with forging or rolling improves low and intermediate temperature mechanical properties by breaking up PPB's and the larger gas pores. Unfortunately, available mechanical property data for P/M RSR nickel base superalloys are limited to creep rupture test results [17,18], making comparisons with other P/M atomization processes, of which there are large inventories of stress rupture and tensile data, very difficult. Comparisons must therefore be limited to commercially produced as-HIP, HIP + forge, cast, and cast + wrought materials. The literature shows that as-HIP and HIP + forge P/M superalloy mechanical properties are as good, if not better, than the cast and wrought versions [19,20,21].

Improved low cycle fatigue (LCF) resistance of P/M superalloys has been obtained by screening out the larger non-metallic particles introduced during atomization. Consolidated materials still contain P/M processing related defects, however, which consist primarily of the smaller non-metallic inclusions and thermally induced porosity (TIP). The effect of these defects on LCF properties of P/M superalloys has been well documented [20,22,23]. Despite the unpredictable nature of these defects, P/M superalloys have shown good LCF properties [24,25,26] and, in some cases, equal or surpass cast and wrought alloys.

P/M processing of superalloys has achieved the benefits of increased chemical homogeneity and improved workability. Still to be fully realized is the ability to produce reliable near net shape as-HIPed superalloy components with the accompanying savings in materials and cost. This will require a better understanding in, and control over, the atomization and consolidation processes in P/M superalloy production, e.g., minimizing or eliminating entrapped gases in powder particles and maximizing material flow of all powder particles during HIP.

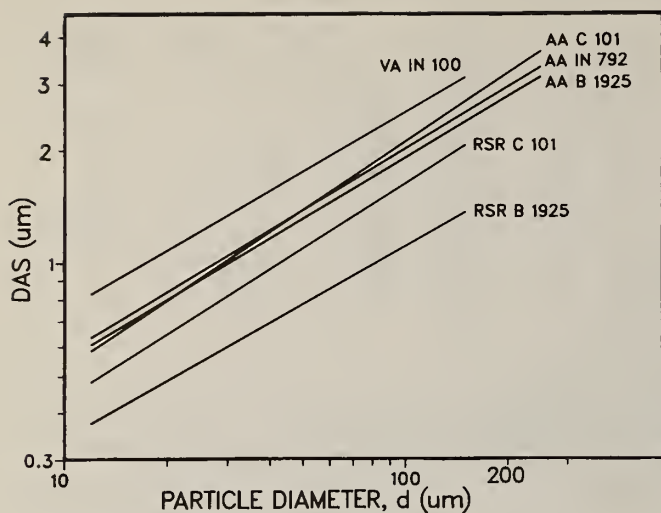


Fig. 5. Secondary dendrite arm spacing (DAS) vs. particle diameter for similar nickel base superalloys.

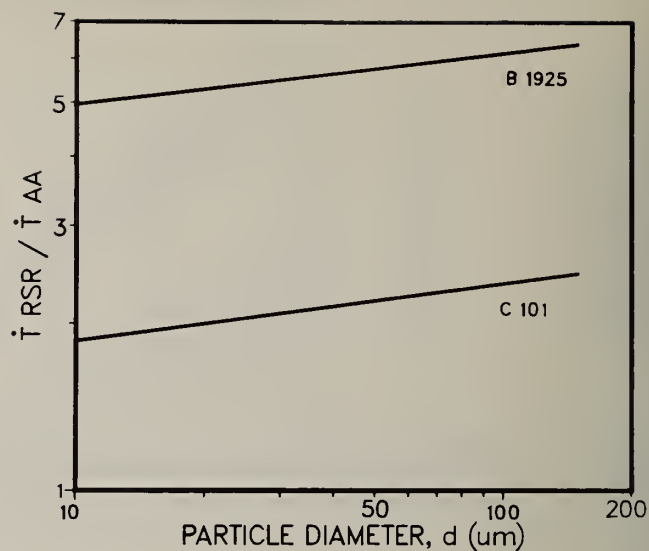


Fig. 6. Relative cooling rates for RSR and argon atomized (AA) Superalloys B1925 and C101.

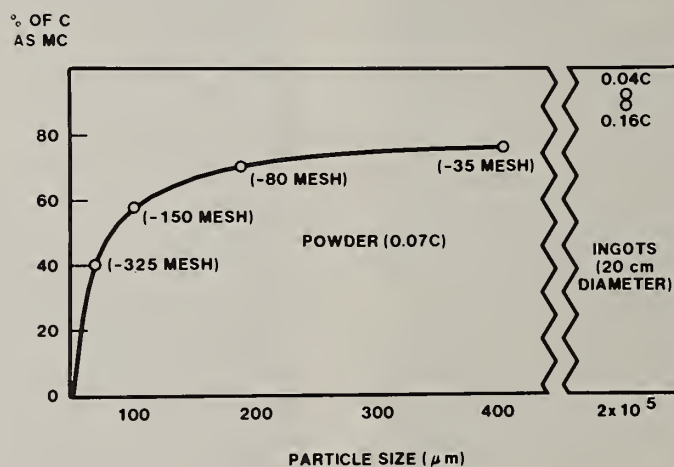


Fig. 7. Percent carbon as MC-type carbide as a function of particle diameter for René 95. (Ref. 9).

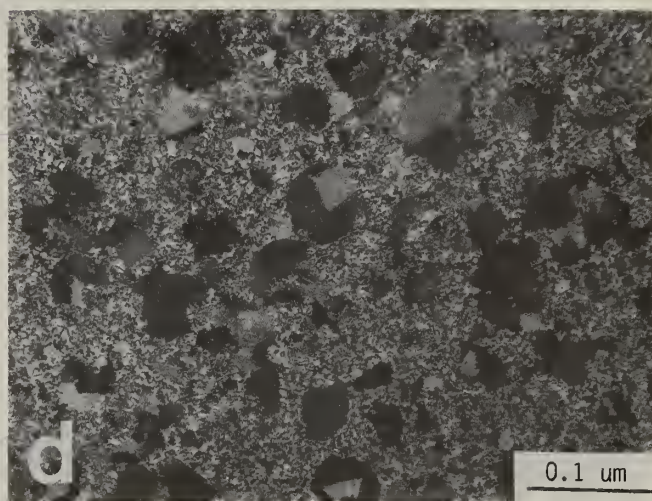
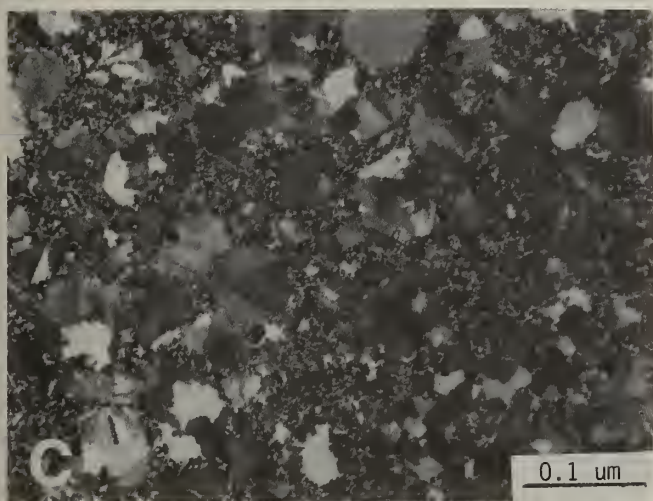
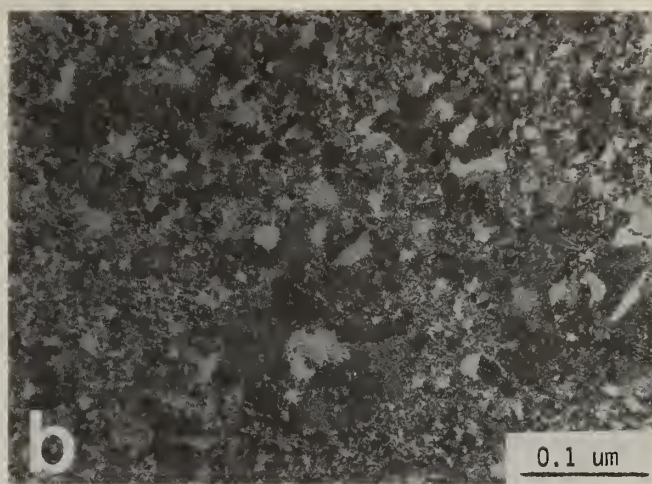
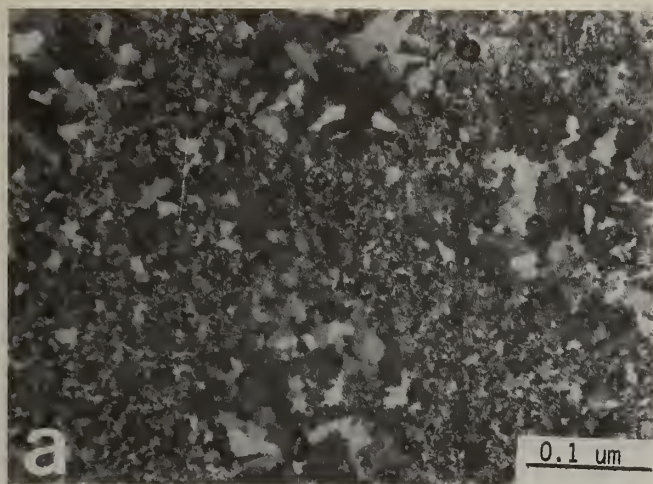


Fig. 8. Consolidated microstructures of superalloy C101: (a) -60 mesh as-HIP argon atomized, (b) -60 mesh HIP + heat treated argon atomized, (c) -150 mesh as-HIP RSR and (d) -150 mesh HIP + heat treated RSR.

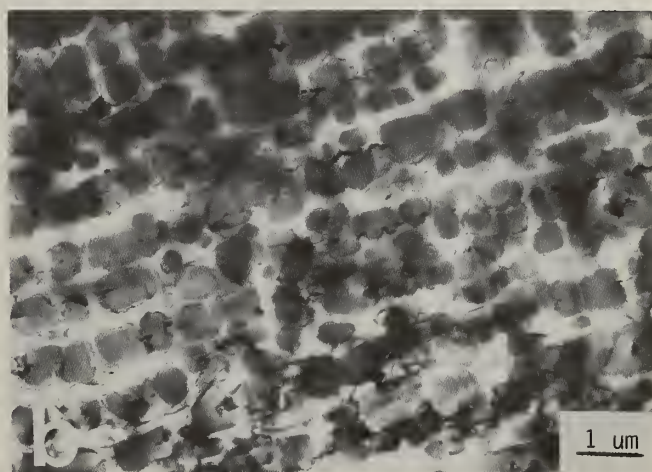
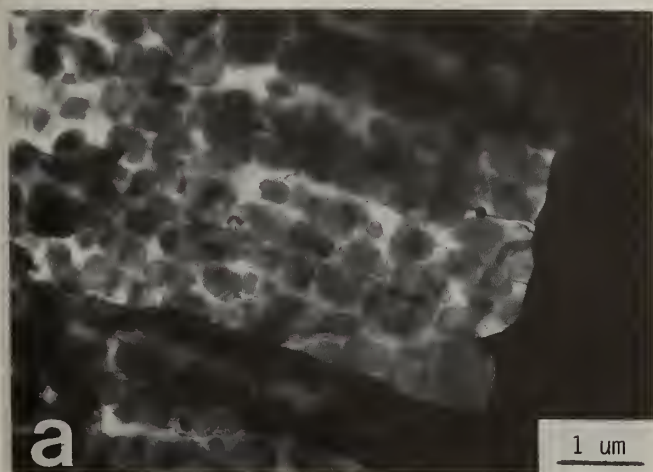


Fig. 9. (a) Retained secondary dendrite arm microstructure in as-HIP RSR Superalloy C101. (b) Typical microstructure of the interior of a prior particle of as-HIP argon atomized Superalloy C101.

Acknowledgment

The authors wish to acknowledge sponsorship of this research by a grant from the Air Force Office of Scientific Research, monitored by Dr. Alan Rosenstein.

References

1. N.J. Grant: Advances in Powder Technology, 1981 ASM Materials Science Seminar, G.Y. Chin, ed., ASM, Metals Park, Ohio, 1982, Ch. 1.
2. J.K. Tien and T.E. Howson: *ibid*, p. 161.
3. S.J. Friedman, F.A. Gluckert and W.R. Marshall, Jr.: Ch. Eng. Prog. 48, No. 4, (1952) 181.
4. K.Y. Kim and W.R. Marshall: *AIChE J.* 17, No. 3, (1971) 575.
5. D. Bradley: *J. Phys. D.: Appl. Phys.* 6, (1973) 1724 and 2267.
6. P.A. Joly and R. Mehrabian: *J. Mat. Sci.* 9, (1974) 1446.
7. R. Mehrabian: Rapid Solidification Processing--Principles and Technology, Proc. Int. Conf. on Rapid Solidif. Processing, R. Mehrabian, B.H. Kear and M. Cohen, eds., Claitors, Baton Rouge, 1978, p. 9.
8. A.R. Cox, J.B. Moore and E.C. van Reuth: Superalloys: Metallurgy and Manufacture, Proc. Third Int. Symp. on Superalloys, B.H. Kear, D.R. Muzyka, J.K. Tien and S.T. Wlodek, eds., Claitors, Baton Rouge, 1976, p. 45.
9. J.A. Domingue, W.J. Boesch and J.F. Radavich: Superalloys 1980, Proc. Fourth Int. Symp. on Superalloys, J.K. Tien, S.T. Wlodek, H. Morrow III, M. Gell and G.E. Maurer, eds., ASM, Metals Park, Ohio, 1980, p. 335.
10. L.N. Moskowitz, R.M. Pelloux and N. Grant: Superalloys--Processing, Proc. Second Int. Symp. on Superalloys, MCIC Report 72-10, 1972, p. Z.
11. S.H. Reichman and J.W. Smythe: *Mod. Dev. in Pow. Metall.* 5, (1971) 73.
12. R.D. Eng and D.J. Evans: Superalloys 1980, Proc. Fourth Int. Symp. on Superalloys, J.K. Tien, S.T. Wlodek, H. Morrow III, M. Gell and G.E. Maurer, eds., ASM, Metals Park, Ohio, 1980, p. 491.
13. G.J. Lewis, D.M. Parkin and F.A. Thompson: *Proc. Conf. on Forging and Props. of Aerospace Mats.*, Metals Soc., London, 1978, p. 399.
14. M.J. Blackburn and R.A. Sprague: *ibid*, p. 350.
15. R.D. Eng and D.J. Evans: NASA Report #N82-26439, May 1982.
16. J.E. Smugeresky: *Met. Trans.* 13A, No. 9, (1982) 1535-1546.
17. A.R. Cox and E.C. van Reuth: Rapidly Quenched Metals III, Proc. Third Int. Conf. on Rapidly Quenched Metals, Vol. 2, B. Cantor, ed., The Metals Soc., 1978, p. 225.
18. R.J. Patterson II, A.R. Cox and E.C. van Reuth: *J. Metals* 32, No. 9, (1980) 34.
19. J.K. Tien, W.J. Boesch, T.E. Howson and W.B. Castledine: *Mod. Dev. in Powder Metall.*, Vols. 12-14, MPIF, Princeton, 1981.
20. J.L. Bartos: *Proc Conf. on Powder Metall. in Defense Technology*, Vol. 5, MPIF, Princeton, 1980, p. 81.
21. W. Betz, B. Borchert and W. Track: Superalloys 1980, Proc. Fourth Int. Symp. on Superalloys, J.K. Tien, S.T. Wlodek, H. Morrow III, M. Gell and G.E. Maurer, eds., ASM, Metals Park, Ohio, 1980, p. 643.
22. D.A. Jablonski: *Mats. Sci. Eng.* 48, (1981) 189.
23. R.V. Miner and R.L. Dreshfield: *Met. Trans. A* 12A, (1981) 261.
24. M.M. Allen, R.L. Athey and J.B. Moore: *Met. Eng. Q.* 10, No. 1, (1970) 20.
25. D.J. Evans, D.N. Duhl and R.B. Slack: *Mod. Dev. in Pow. Metall.* 8, (1974) 473.
26. J.F. Barker and E.H. Van Der Molen: Superalloys--Processing, Proc. Second Int. Symp. on Superalloys, MCIC Report 72-10, 1972, p. AA.

CONSOLIDATION AND FORMING OF P/M POROUS BILLETS

H. L. Gegel, J. S. Gunasekera, S. M. Doraivelu, J. C. Malas, J. T. Morgan, and L. E. Matson

AFWAL Materials Laboratory
AFWAL/MLLM
Wright-Patterson Air Force Base, OH 45433

ABSTRACT

The success of powder metallurgy (P/M) and processing depends strongly upon the ability to produce economically a near-net-shape (NNS) part having a required set of service properties. These properties are generally controlled by the final microstructure which evolves through billet-preparation schedules and subsequent metal-working operations. Quality billets must be produced to have optimum aggregate properties which are controlled by the fundamental characteristics (composition, microstructure, size, hardness, and surface properties) of the particles and their size distribution in the matrix. These characteristics are controlled to a large extent by the average and discrete quenching rates and, hence, by the particular RSR powder-making process. Therefore, in this paper the powder making processes, consolidation, and plastic working are considered as a total system and discussed with emphasis on the plasticity theory for porous materials, analytical process modeling of various metal-working processes, and applications of process-modeling techniques for controlling the metal-flow pattern and achieving required microstructure and shape. Experimental data on constitutive equations and deformation-process modeling for X7091 Al, 2024 Al-20 vol% SiC, and Ti-6242 alloy systems are presented along with the discussions.

INTRODUCTION

Powder Metallurgy (P/M) is a relatively new area of process engineering. Over the past 25 years, most of the information in the literature has been devoted to studies of powder-making processes for difficult-to-form materials, cold compaction techniques for producing near-net-shape compacts, and the sintering process. The recent development of P/M alloys and the advent of Rapid Solidification Technology (RST), however, has demanded hot-consolidation and subsequent plastic working to insure the required shape and mechanical properties. Therefore, the P/M process--as it is understood today--can be divided into three general areas: (1) powder making, (2) preform or blank making (consolidation), and (3) plastic working of blanks or preforms. Although this is a simplistic breakdown of a complex process (aside from the final operations), it is sufficient to provide an overall perspective. An issue in P/M technology that can be influenced by these processing steps leading to the finished part is economics. Each step in the P/M process is important because defects which occur during these steps generally cannot be removed by sintering or heat treatment. Therefore, the objectives of this paper are (1) to examine P/M processing from the vantage point of a vendor (forging or extrusion industry) considering the above areas as a total system as shown in Fig. 1, and (2) to present some recent results of deformation process modeling which was conducted for the purpose of improving the properties of RST P/M materials in a finished part.

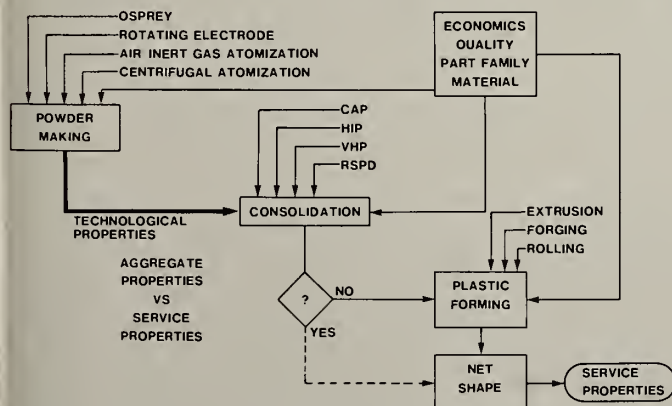


Fig. 1. P/M process perspective.

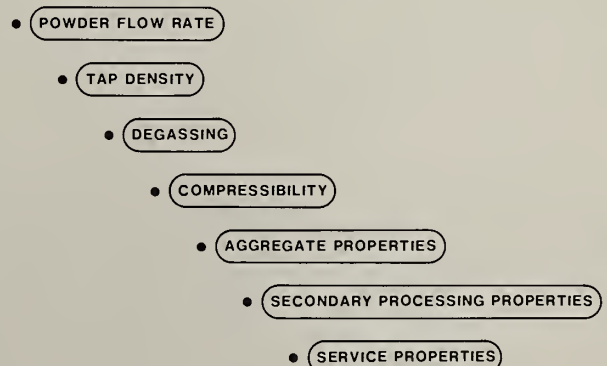


Fig 2. Technological properties.

In the P/M process, the powder-making step is of the utmost importance because the fundamental powder characteristics of the individual particle such as composition, size, shape, microstructure, and surface structure are controlled by the particular process used to produce the particles. These powder characteristics, in turn, control the technological properties, especially the aggregate properties of the consolidated material which are listed in Figs. 2 and 3. Several popular powder-making processes which are being investigated as possible methods for making RST powders are: air atomization, centrifugal atomization plus forced convection helium-gas cooling, the rotating electrode process, and the Osprey process. Although other processes exist, they will not be discussed here. The powder produced by each of these processes has its own distinct characteristics. Two of the factors most strongly influencing the subsequent sequences of any P/M process are (1) the particle size distribution and (2) the environment which controls the average cooling rate and--as shown in Fig. 4--the particle shape, particle contamination, surface layer, and specific surface area. The particle size distribution controls the discrete cooling rate of each particle and, hence, determines which of the particles will be quenched to the microcrystalline and which to the dendritic structure. Therefore, the particle size controls the hardness, composition gradient, surface layer, and microstructure. A range of microstructures is usually found for the alloy powders produced by the various processes. It has been observed that the centrifugal-atomization process usually produces a more narrow size range, as shown in a study conducted by Hildeman [1] on the Al-Ni-Fe alloy system (see Fig. 5). This can be an advantage in cases where it is necessary to have a controlled-microstructure distribution.

SERVICE PROPERTIES

- YIELD STRENGTH
- ULTIMATE TENSILE STRENGTH
- DUCTILITY
- TOUGHNESS
- LOW CYCLE FATIGUE
- HIGH CYCLE FATIGUE
- HIGH TEMPERATURE PROPERTIES

PLASTIC WORKING PROPERTIES

- INTERPARTICLE BOND STRENGTH
- RELATIVE DENSITY
- CONSTITUTIVE RELATIONS
- WORKABILITY

Fig. 3. Aggregate properties.

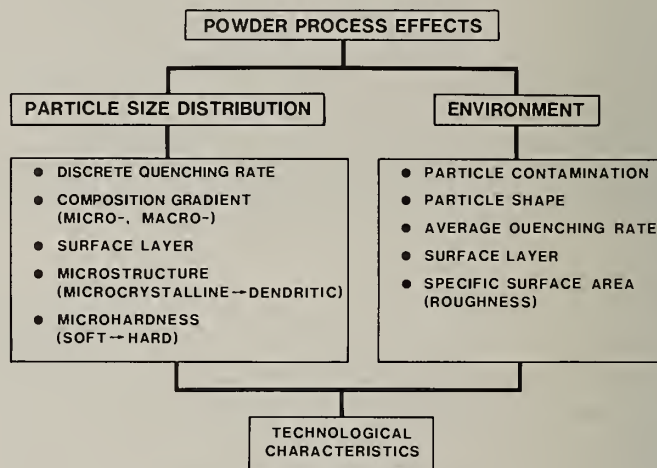


Fig. 4. Powder process effects.

Alloy systems, designed for high-temperature applications, which contain strong intermetallic compounds present some unique difficulties because of the wide range of microstructures which develop as a result of the discrete quenching rate for each particle associated with a particular particle size distribution. A large difference in the temperature dependence of the microhardness value is expected for particles having the microcrystalline structure and those having the dendritic structure. From studies to investigate the LCF behavior of nickel-base P/M materials, it is known that the interfaces of coarse particles of dendritic structure are sites for fracture initiation. It has been observed that some critical strain is required to ameliorate the difficulties associated with the coarse powders and foreign matter introduced by powder handling. Overcoming these effects is a metalworking problem which could be simplified if one were working only with powder having a homogeneous microstructure as well as chemical composition. The coarse dendritic particles retain their hardness with increasing temperature; therefore, they behave as rigid bodies, moving with the metal flow pattern. They do not shear and often agglomerate, which exacerbates the problem. The metalworking problem then is to control the distribution and strengthen the matrix to permit the transfer of stress and strain into the dendritic particles. The latter is required to condition the particles in such a way that they will be energetically favorable for recrystallizing during subsequent processing steps.

The surface layers of metal-alloy powders are enriched with impurities; and therefore, the physical properties may differ considerably from those of the base material. This layer may be enriched with some solute element, an oxide layer, a hydrated oxide layer, a metallic carbide, an intermetallic compound, or a combination of these, e.g., an oxide layer plus an intermetallic compound. The surface composition is controlled by the size and shape of the particle since both affect the specific surface area. As an example, Hildeman, Lege, and Vasudevan [1] showed the variation of oxygen content with surface area for angular, flake, and spherical Al-Ni-Fe alloy powder (see Fig. 6). The powder-making process controls the nature of the surface layer and the physical properties of the base material. The surface layer is an important part of the particle structure since it accepts the

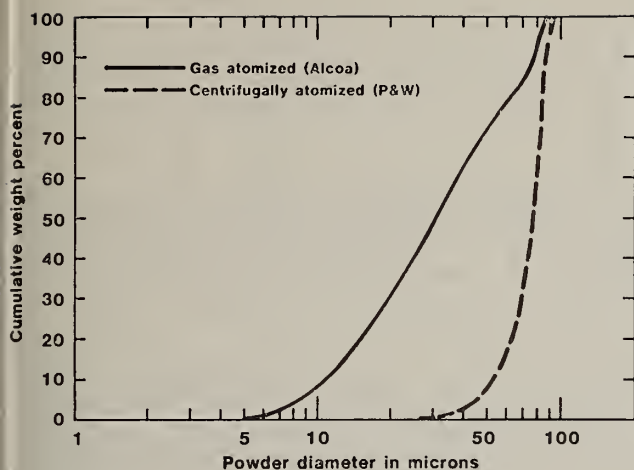


Fig. 5. Coulter counter particle size distribution of Al-3.7 Ni-1.5 Fe powders.

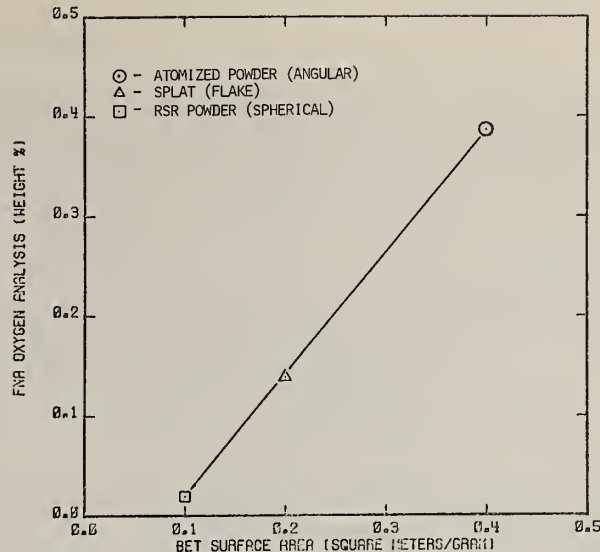


Fig. 6. Percentage of oxygen versus surface area.

contact load when the powder is poured into the mold. The contact pressures on the surface layer, due to the small surface area or particle contact area, become so great that plastic deformation or local fracture of the particle occurs. The stress state of the particle is always at some limiting or critical value, and the surface layer in the contact zone will either plastically deform or fracture. The most general case of a contact load during the compaction process is a combination of normal and tangential loads. The surface layer is always perturbed by the inter-particle contact loads. Surface layers with hydrated oxide films are of particular importance to aluminum alloys made by air atomization using RST. These layers must be converted to some stable-oxide form before subsequent processing steps can be initiated. During this conversion process, the volatile components are liberated over different temperature ranges as shown by MSA and TGA studies. The results are presented in Figs. 7 and 8 for X7091 aluminum powder.

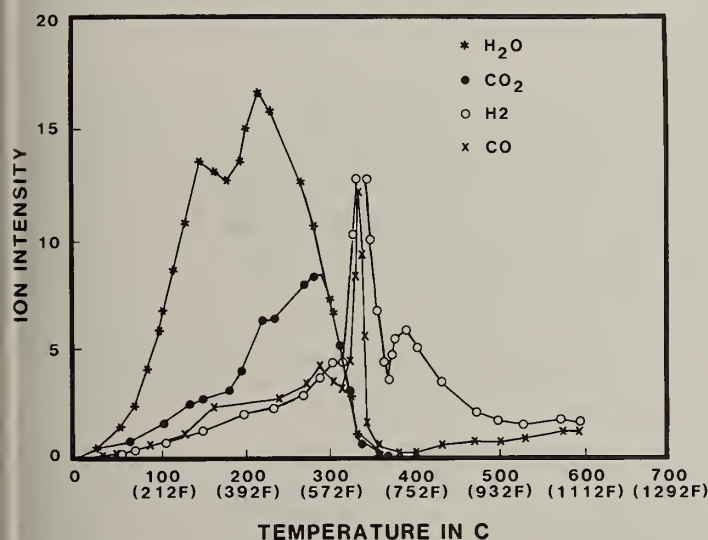


Fig. 7. Plot of ion intensity versus temperature for CT-91 green compact (data obtained by MSA).

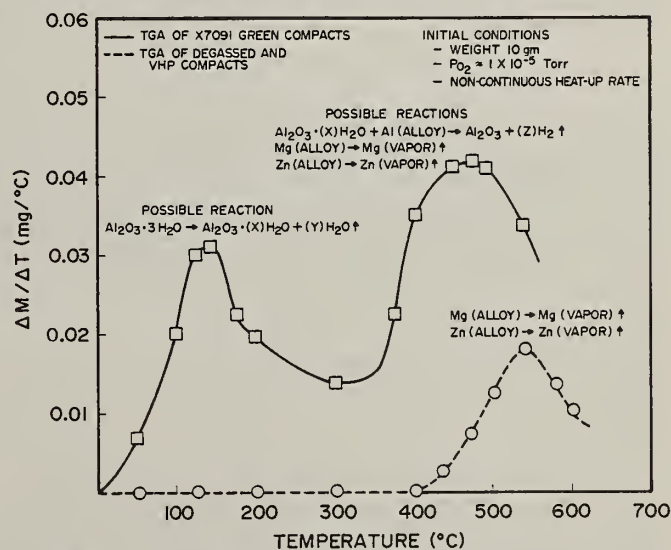


Fig. 8. $\Delta M/\Delta T$ versus temperature (data obtained by TGA).

Failure to make this conversion will lead to a phenomenon known as blistering which occurs when the above volatile components are liberated during subsequent thermal exposures. This problem can be solved for certain aluminum powders by subjecting them to a suitable degassing treatment. In Fig. 8, degassed and VHP compacts show little liberation of any volatile matter up to 400°C. However, around 500°C, Mg and Zn are volatilized and liberated. Therefore, a proper degassing temperature should be selected to avoid loss of these elements for this particular alloy. Details on degassing kinetics and selection of degassing temperature are given in another paper [2] by the present authors. Nickel-base alloys, in contrast, should not be allowed to form a stable oxide on their surface because this acts as a site for heterogeneous nucleation of a γ' surface for these alloy systems. Inert powder-making and -handling systems should be used for this class of alloy system.

The preform or blank-making process is controlled to a large extent by the powder-making process and by the physical properties of the individual particles. A powder compact before application of external pressure consists of many physical particles which are more or less uniform in composition. The particles range in size from fine to coarse, and their corresponding microstructures range from microcrystalline to coarse dendritic. At tap density, these powders usually retain their shape, and they can exert pressure on the surrounding medium. However, they cannot resist tensile stresses. The compact at tap density occupies a position somewhere between a liquid and a solid. The technological characteristics of this powder, as listed in Fig. 2, depend upon the resistance of the individual particles to compression, shearing, and bending. The high-temperature RST aluminum and nickel-base P/M alloys have considerable resistance to these types of loading. The higher the hardness of the particle and the greater its surface roughness, the lower the tap density of the powder compact. Correspondingly, the punch must travel a greater distance in the case of low tap density, which results also in higher tool wear.

The properties of this compact continuously change during pressing. The individual particles are linked together by different bonds which depend upon the dimensions of the particles. The bonds are usually between individual particles in contact with other particles and the bonding is due to adhesion at the contact surfaces. Particles which are soft and plastic form strong adhesion bonds during cold compaction, while those which are hard and less ductile do not. A practical comparison can be made between the cold compaction of X7091 which is a soft, ductile aluminum alloy and the cold compaction of Al-8Fe-4Ce which is a high-hardness alloy. The latter composition cannot be ejected from a simple cylindrical mold when cold compacted without severely cracking, while the former material develops excellent green strength and can be ejected as a cylinder under similar conditions.

The compacting pressure tends to cause the particles to shift and occupy the most stable geometric position; this is accompanied by contact distortion and shearing of the particles. The basic particle shape tends to remain undistorted. Angular particles, relative to spherical particles, do not form better green-strength compacts since green strength is principally controlled by the strength of local adhesion. Vacuum hot pressing or hot isostatic pressing must be used to densify a compact when the particles are hard and resist compression. The aggregate properties of the compacts produced by VHP or HIP should be equivalent to the service properties of the components. Otherwise, these compacts demand subsequent forming operations which are explained in detail in the following section. In this case, the aggregate properties of the billet should be at least equivalent to the plastic-working properties.

PLASTIC WORKING

Plastic working of P/M preforms is being used increasingly in powder metallurgy as a means of shaping and strengthening the finished part. Plastic working has been observed to improve markedly the properties and microstructures of finished shapes by decreasing the residual porosity, increasing the strength of the matrix, and imparting a better surface finish. Additionally, controlled plastic working of preforms or billets is now being considered as a means of strengthening and increasing their workability. This additional working is also thought to be essential for controlling the properties in the finished shape. The results of many empirical observations indicate that a critical strain is required to overcome the effect of large particles and foreign debris which are introduced during powder handling. Parts forged directly from an untreated preform or billet often do not receive sufficient plastic work for production of good second-tier mechanical properties. Failure to achieve sufficient plastic deformation and proper strain distribution often leads to increased scatter and reduced values of these critical mechanical properties.

Plastic working is essential for overcoming powder-making defects such as discrete foreign particles and size-distribution-related defects. To perform proper plastic working on P/M material, it is essential to obtain a good understanding of the material behavior during plastic shaping. This understanding necessitates construction of a plasticity model for porous bodies which satisfactorily describes the experimental results. While the problems involved in the plastic working of P/M materials have much in common with those of conventional alloys, a number of differences exist which are the direct result of the discrete nature of the individual powder particles. One important feature of the plastic deformation of a porous body is that it undergoes a permanent change in volume, which affects its Poisson's ratio [3-4]. Another characteristic is that the mechanical strengthening experienced by a porous solid during plastic deformation is brought about not only by a change in porosity but also by a strengthening of the matrix.

A continuum-mechanics approach is being used for modeling different P/M metalworking processes using the finite-element method (FEM) for obtaining solutions. This requires a plasticity theory applicable to porous materials and constitutive equations with density as one of the parameters for studying densification during deformation, as explained below.

The design of billet-consolidation processes and of the dies used to forge or extrude porous P/M materials to full density requires a special yield function for development of the plasticity analysis. The plastic-flow behavior of porous P/M materials is more complicated than that of ingot materials because the hydrostatic component of stress influences the onset of plastic flow. The effect of hydrostatic stress is taken into account by considering a yield function of the form

$$AJ_2' + BJ_1^2 = Y_R^2 = \delta Y_0^2. \tag{1}$$

Here J_2' is the second invariant of the deviatoric stress, and J_1 is the first invariant or the hydrostatic component of stress. Y_0 and Y_R are the yield stresses of fully dense and partially dense materials, respectively. A , B , and δ are functions of relative density.

Many researchers have determined these constants through heuristic arguments and the use of experimental results. Green [5] presented an analytical method which considered a uniform cubic array of spherical voids in a solid under states of stress corresponding to pure shear and hydrostatic compression. The results for these two stress states allowed determination of the two variables A and B . He assumed the stress distribution to be uniform in two directions through the minimum section of the array and the effect of the voids on the stress in the third direction to be negligible on the planes midway between the voids. Oyane, Shima, and Kono [6] determined A and B using more stringent assumptions. They found poor agreement between their theoretical and experimental results and, therefore, reported experimentally determined values in a later paper. Shima and Oyane [7] abandoned this analytical approach entirely and, instead, refined empirical relations obtained for their experimental values. Kuhn and Downey [8] also presented experimentally obtained values for these two variables. However, in the present study, the authors derived these variables taking into account the distortion energy due to the total stress tensor. The final equation obtained is

$$(2 + R^2)J_2' + \frac{(1-R^2)}{3} J_1^2 = (2R^2-1) Y_0^2 \tag{2}$$

Theoretical curves along with experimental results for the uni-axial state of stress are shown in Fig. 9 for X7091 Al alloy. This figure not only shows good agreement between the theoretical and experimental results but also explains the influence of hydrostatic stress at various density levels. When full densification is achieved, the function automatically becomes the von Mises yield function. Using this yield function, effective stress- and effective strain- relative density relationships have been derived and compared with the experimental results for the uni-axial state of stress for the same alloy. Excellent agreement has been observed between theoretical and experimental results, as shown in Figs. 10 and 11. The theory is also applied to various P/M processes such as frictionless closed-die forging, frictionless plane-strain compression, and hydrostatic compression. These results are presented in Figs. 12 and 13. The results show that beyond 95 percent of theoretical density, it is difficult to obtain full densification in hydrostatic and closed-die forging by application of pressure alone since the pressure required for full densification increases beyond that obtainable by commercial presses. Therefore, this suggests that pressings should be made at a temperature and strain rate which will accelerate diffusion to permit full densification to be obtained.

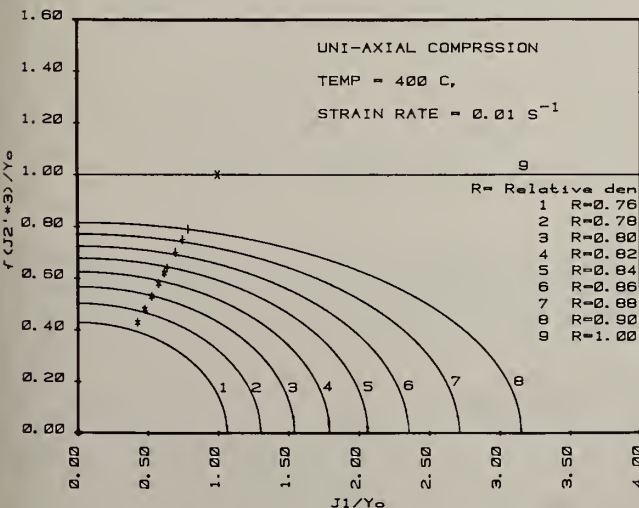


Fig. 9. Yield surface in J_1 and J_2 space.

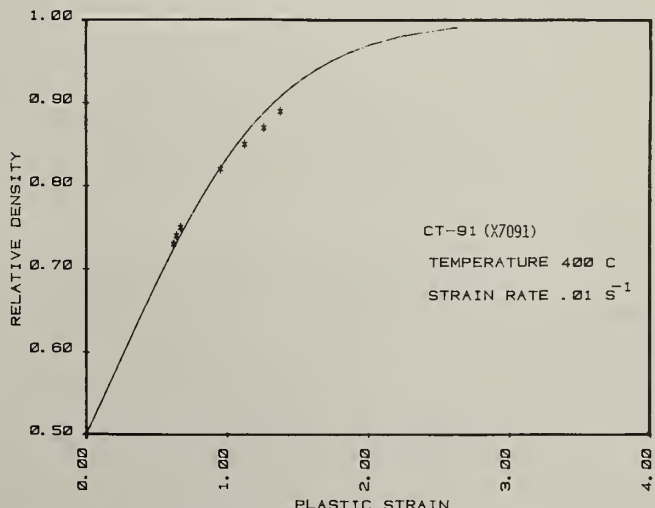


Fig. 10. Relative density versus plastic strain.

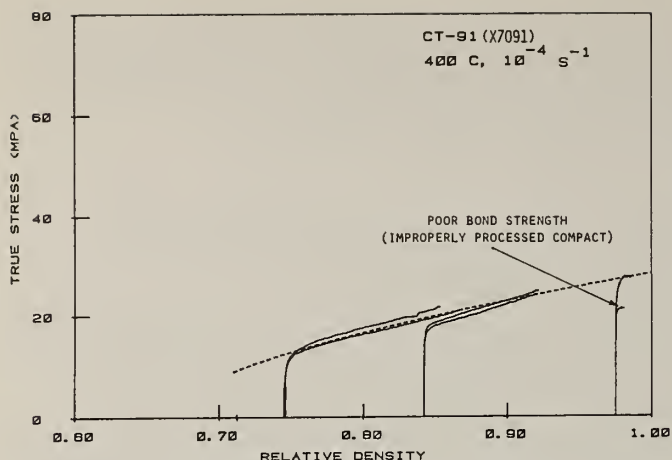


Fig. 11. True stress versus relative density for uni-axial state of stress.

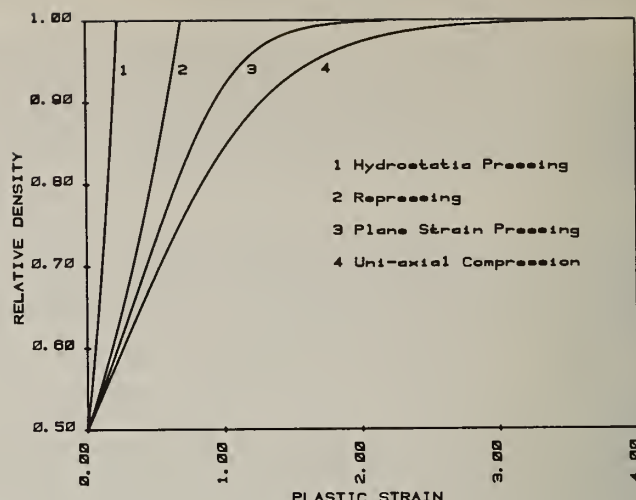


Fig. 12. Relative density versus plastic strain for different processes.

In order to study the effect of strain rate upon densification during hot working, a constitutive model has been developed by the present authors for CT 91 (X7091) Al alloy. Uni-axial compression tests have been conducted at different temperatures and strain rates, as shown in Fig. 11; and using these results, the hot-working temperature has been selected. The values of flow stress are plotted in three-dimensional coordinates as a function of density and strain rate using the computer, as shown in Fig. 14. This data base has been used in the model for studying geometric strain hardening (densification) during various metal-forming operations for X7091 Al alloy.

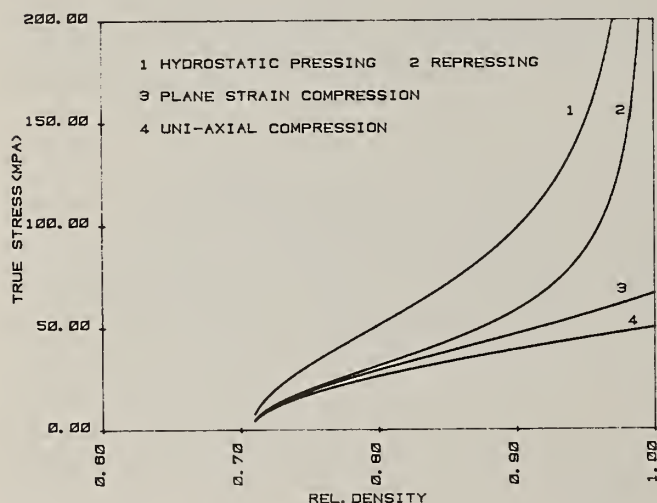


Fig. 13. True stress versus relative density for different processes.

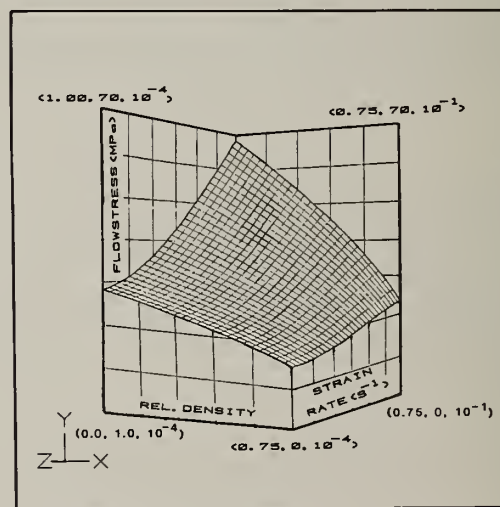


Fig. 14. Constitutive behavior model for X7091 Al alloy.

Analytical Modeling

Several methods are available for the analytical modeling of metal-working processes. However, the FEM has become popular for the solution of metal-working problems due to the rapid development of computers and numerical methods. Many studies have been conducted to solve various metal-working problems using this method. These were reviewed and discussed in detail by the present authors in another paper [9]. In all these studies the von Mises yield criterion has been used since the material under consideration is always fully dense; however, for P/M applications the influence of hydrostatic stress must be taken into account. In the current study the method developed by Kobayashi and Oh [10] has been used for predicting the metal flow through streamlined extrusion and disk forging since the starting billets are fully dense material. However, a program called ALPID will be modified to incorporate the yield function presented above for future studies which may consider the use of porous billets. From this point of view, the relevant equations required for modification are summarized below.

Equilibrium conditions, neglecting body forces:

$$\sigma_{ij,j} = 0 \quad (3)$$

where σ_{ij} is the stress tensor and $,j$ denotes particle differentiation with respect to j .

Compatibility conditions:

$$\begin{aligned} \dot{\epsilon}_{11} &= 1/2 \left(\frac{\partial V_1}{\partial x_1} + \frac{\partial V_1}{\partial x_1} \right) \\ \dot{\epsilon}_{12} &= 1/2 \left(\frac{\partial V_1}{\partial x_2} + \frac{\partial V_2}{\partial x_1} \right) \\ \dot{\epsilon}_{ij} &= 1/2 (V_{i,j} + V_{j,i}) \end{aligned} \quad (4)$$

Mass is constant, $\dot{\epsilon}_v \neq 0$

Constitutive relations:

$$\sigma_1 = \frac{Y_R}{\dot{\epsilon} (2 + R^2) (1 - R^2)} [2(1 - R^2) \dot{\epsilon}_i + 3R^2 \dot{\epsilon}_v] \quad (5)$$

Boundary conditions:

$$\begin{aligned} \sigma_{ij} n_i &= F_j \text{ on } S_F \\ v_i &= V_i \text{ on } S_V \end{aligned} \quad (6)$$

and $|f_s|$ = frictional stress with the proper sign, where n_i is the unit vector normal to the surface.

Equations (3) - (6) can be put into the variational principle as

$$\begin{aligned} \sigma &= \int_V Y_R \left\{ \frac{2}{3(2 + R^2)} [(\dot{\epsilon}_1 - \dot{\epsilon}_2)^2 + (\dot{\epsilon}_2 - \dot{\epsilon}_1)^2 + (\dot{\epsilon}_3 - \dot{\epsilon}_1)^2] + \frac{1}{3(1-R^2)} \dot{\epsilon}_v \right\}^{1/2} \\ &+ \int_{S_F} m \frac{Y_R}{\sqrt{3}} \Delta V - \int F_i V_i dS. \end{aligned} \quad (7)$$

Application - Extrusion OF P/M 2024 Al-20 vol% SiC

A new type of P/M aluminum alloy is being developed which incorporates SiC whiskers into the powder agglomerate for the purpose of increasing the modulus of elasticity and the strength properties of aluminum alloys. These alloys have many attractive properties, but they are difficult to fabricate by metalworking processes. A number of applications exist for these materials in aerospace structural components if they can be extruded or forged into complex geometries without fracturing the whiskers and changing their aspect ratio. The strength properties are strongly dependent upon this ratio, while the effective modulus of elasticity is less strongly influenced by it beyond an aspect ratio of ≈ 12 . Figure 15 shows the change in aspect ratio of SiC whiskers as a function of processing steps, and Fig. 16 shows the dependence of the modulus of elasticity upon the aspect ratio.

The standard shear dies commonly used to extrude aluminum alloys by industry are not satisfactory for extruding this new class of materials. The internal shearing and turbulence of the material caused by the die geometry fractures the SiC whiskers and forces them to be agglomerated. The distribution of the SiC whiskers and their fracture can be controlled through the use of streamlined extrusion dies.

A streamlined extrusion die, by definition, is one whose material velocity profile remains constant during the reduction from the billet inlet to the die to the material exit. Friction between the workpiece and the die surface in actual practice prevents "ideal" metal flow from occurring; therefore, the metalworking problem is to find a practical compromise in die design and in the process parameters (temperature, strain rate) in order to achieve the goal of approximating streamlined flow. Through process modeling this goal can be achieved with a minimum number of trial-and-error iterations. The rigid-viscoplastic FEM discussed above was used to simulate the

process on the computer and to select the proper die geometry and processing conditions. The die geometry was modeled by means of a method developed by Gunesechera, *et al.* [9]; and this model, in turn, was used to formulate the FEM model.

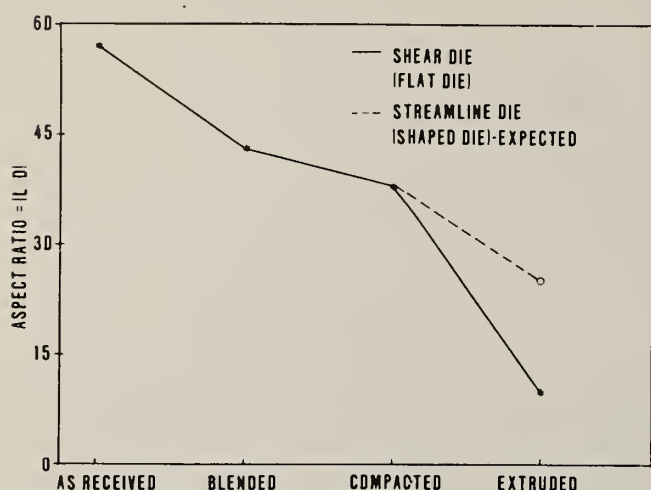


Fig. 15. Aspect ratio versus various processing steps.

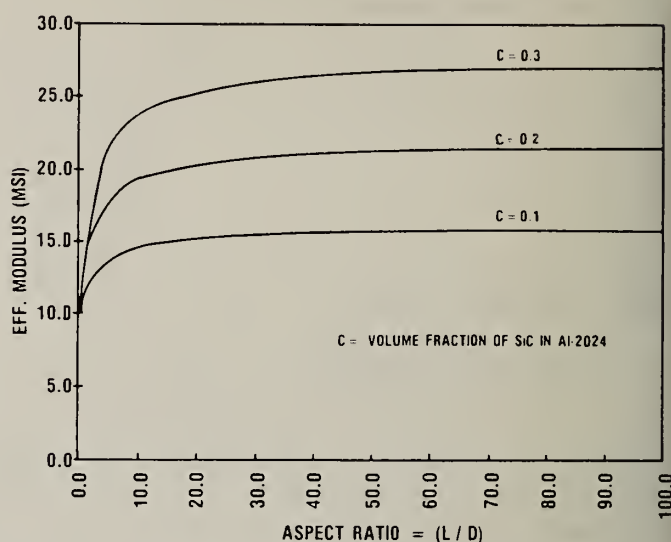


Fig. 16. Effective modulus versus aspect ratio.

Constitutive relations were developed for the 2024 Al-20 vol% SiC whisker material by compression testing small cylindrical specimens as a function of temperature and strain rate. A MoS₂ lubricant was used to assure homogeneous deformation at a strain rate around $\sim 0.50 \dot{\epsilon}$ and temperatures of 400°C to 550°C. The results are shown in Fig. 17 for a strain rate of 10^{-2} /sec. Information concerning the billet-processing steps will now be introduced in order to provide a fuller appreciation of the importance of billet conditioning. The 2024 Al-20 vol% SiC whisker material is first properly degassed to remove the water attached to the powder surface layer and blended to achieve good mixing of the powder particles and whisker material--an important step. The mixture is then vacuum hot pressed to a density of $\sim 97\%$ or greater. The material workability after vacuum hot pressing is insufficient for subsequent metalworking operations such as forging and complex extrusion. Therefore, this billet is thermomechanically processed by streamlined extrusion to improve the workability. The constitutive data shown in Fig. 17 were obtained from this material. The SiC whiskers in the powder compact are essentially random or possess discrete random orientation and become oriented in the plane normal to the compressive axis in accordance with the laws of classical mechanics. However, the SiC whiskers after being extruded again develop a discrete random orientation somewhat similar to that developed after the blending step. The fiber orientation after this billet-conditioning step is determined by the material point velocity-field. The area-reduction ratio should be based upon the degree of fiber orientation desired. The random orientation of the SiC whiskers is desirable for additional hot working by either extrusion or forging.

The die length for approximating streamlined flow was determined from the FEM analysis using the constitutive relations developed for the 2024 Al-20 vol% SiC whisker material. A die length was selected, and a die was manufactured. Another, shorter die was produced in order to approximate the metal-flow pattern of a shear die. The point-velocity field for a typical shear die, a short conical die, and the streamlined die is shown in Figs. 18 and 19. Analysis also shows that increasing the die length beyond the optimum length provides no additional benefit. Isothermal extrusion at 475°C (880°C) was carried out for both the optimum-length streamlined die and the short die.

Microstructures for the two cases are shown in Figs. 20 and 21. The optimum-length streamlined die produced the desired effect. The SiC whiskers were not fractured and were oriented parallel to the axial direction. The short die caused the SiC whiskers to fracture in the regions where turbulent flow occurred. This is in agreement with the velocity-field predictions in Fig. 15 for these dies. It should also be noted in Fig. 15 that the 180-deg. shear die produces a more turbulent flow condition.

This case history clearly shows that process analysis is a valuable tool in determining the proper processing conditions and die geometries for producing a finished shape having controlled microstructures and properties.

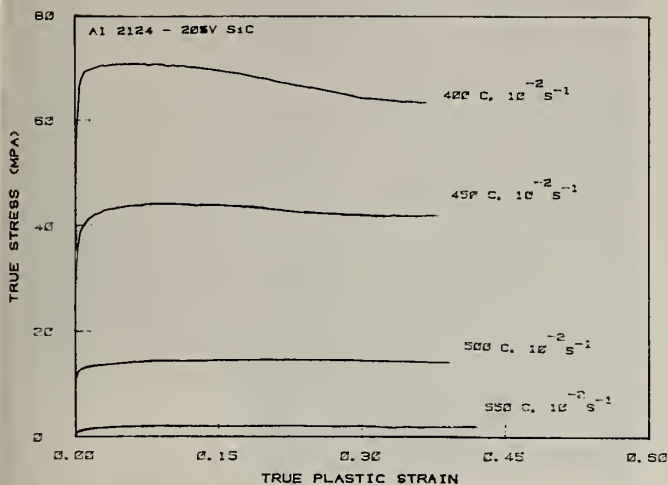


Fig. 17. True stress versus true strain curves for 2024 Al-20 vol% SiC.

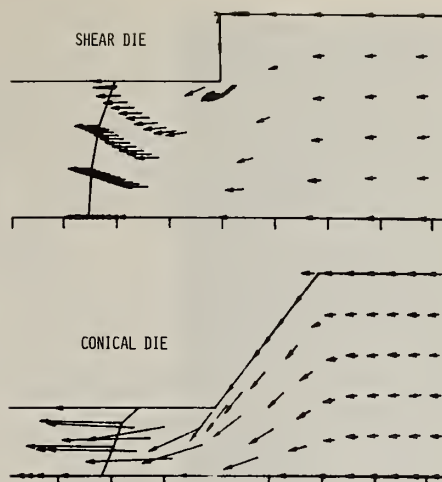


Fig. 18. Velocity field during extrusion using shear and conical dies.

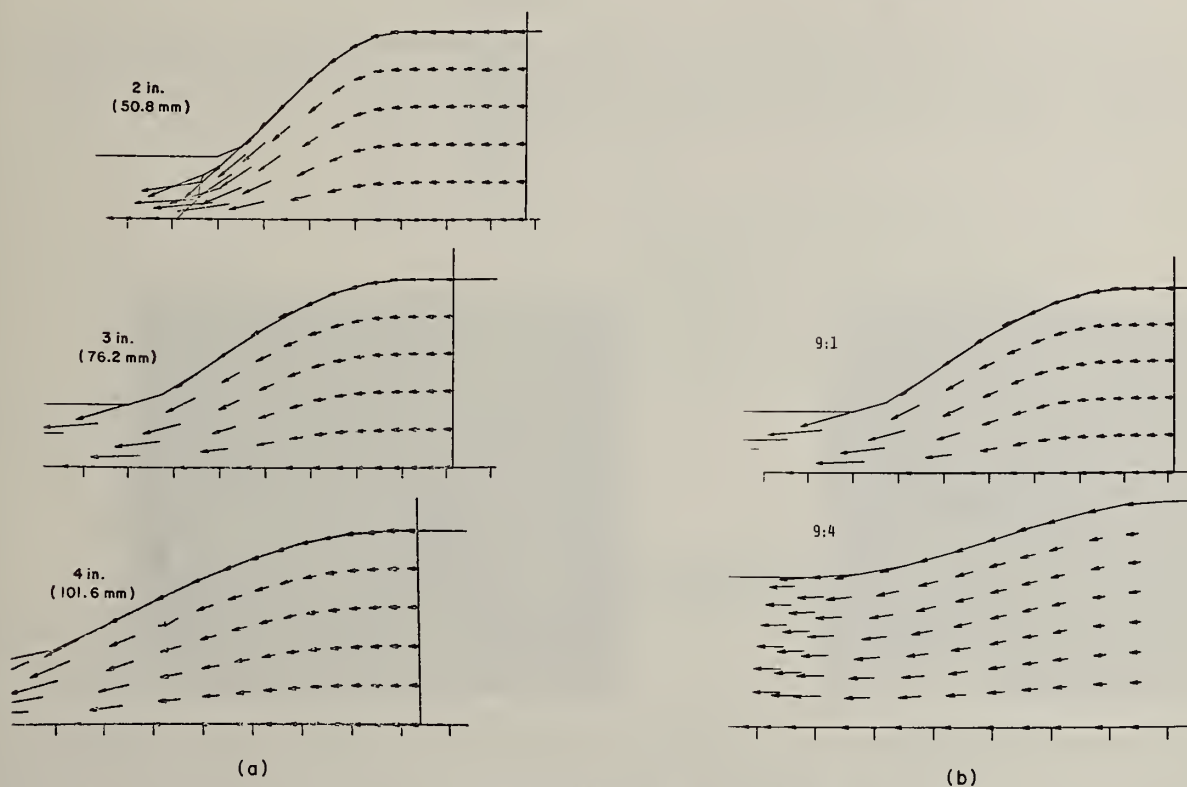


Fig. 19. (a) Effect of die length upon metal flow during streamlined extrusion (extrusion ratio 9:1)
(b) Effect of extrusion ratio upon metal flow [streamlined die length, 3 in. (76.2 mm)].

Application - Design of an Advanced Turbine Disk Having Superior LCF Properties

Considerable service experience has been accumulated by the aerospace industry to conclude that the most probable site for LCF failure initiation is at the interface of large powder particles which are essentially undeformed. The microstructures for nickel-base alloys (Alloy-X) hot worked by extrusion [11], high-temperature aluminum (Al-8Fe-4Ce) alloys after forging [12], and REP Ti 6-4 alloy after HIPing and heat treatment [13] have many particles which remain undeformed, even after severe plastic deformation, as shown in Figs. 22-24. Metallurgical examination clearly indicates that these particles are much harder than those of the continuous matrix material. Since both of these alloy systems derive their high-temperature strength from intermetallic compounds, it can be deduced that these powder particles contain intermetallic compounds whose hot hardness decreases more slowly with increasing temperature than that of the matrix material. Thus, these particles behave as rigid bodies and flow in the same pattern as the surrounding material. Figure 18 shows that the metal-flow pattern can cause these rigid bodies to accumulate in certain areas to form



Fig. 20. Microstructure of extruded product through streamlined die of 3-in. length.



Fig. 21. Microstructure of extruded product through streamlined die of 2-in. length.

a larger site for LCF failure initiation. Therefore, it can be conjectured that conventional extrusion with shear-type dies is not effective in completely breaking up the coarse, hard particles and that it can, in fact, cause larger failure sites to be created by the metal-flow pattern. This observation suggests the following approach for improving P/M materials.

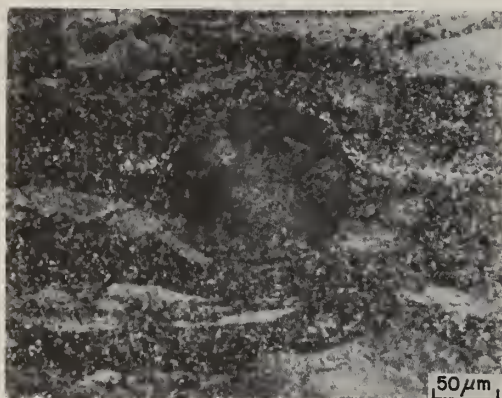


Fig. 22. RSR nickel-base alloy after extrusion.

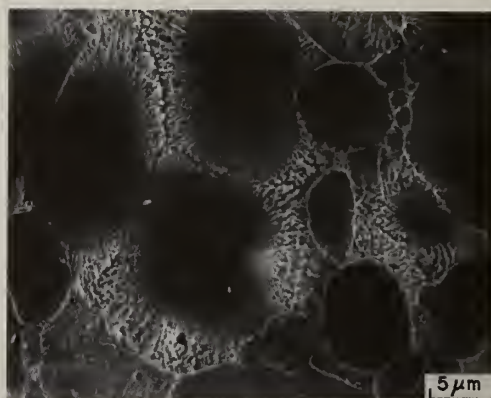


Fig. 23. Al-Fe-Ce alloy powder after forging.

Hot isostatically pressed material should be thermomechanically treated by extruding the billet material through streamlined dies. This step will improve the workability and strength of the workpiece material while maintaining a favorable distribution of the larger and harder coarse particles. The purpose of this step is to change the nature of the flow curve from one which exhibits flow softening to one which does not. An example of this behavior is shown in Fig. 25 for the case of Ti-6242 alloy. The significance of this material behavior, as exhibited by the titanium alloy, is that the two curves approach each other at a true strain of ~ 1.0 . When the curves touch, both specimens have essentially the same microstructure and improved hot workability. Once this material behavior has been achieved, the material can be hot worked at a lower temperature. The streamlined extrusion die required to produce this effect, i.e., the area-ratio reduction, can be determined by this test. For the case of Ti-6242, the extrusion ratio would be $\sim 9:4$, which would produce an effective strain of ~ 1.0 . The actual extrusion ratio is thus based upon the effective true strain after the completion of work softening.



Fig. 24. REP Ti 6-4 alloy after HIPing and heat treatment.

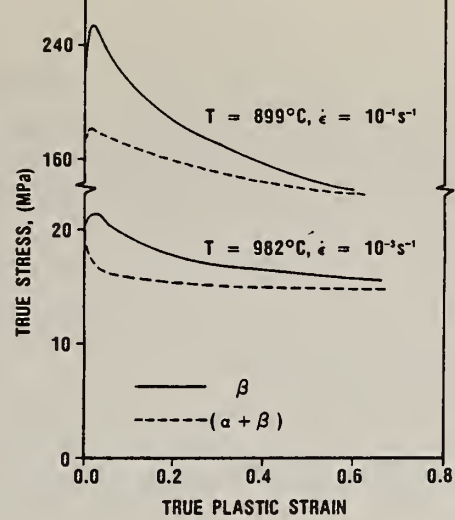


Fig. 25. Flow curves for β and $\alpha + \beta$ Ti-6242 alloy.

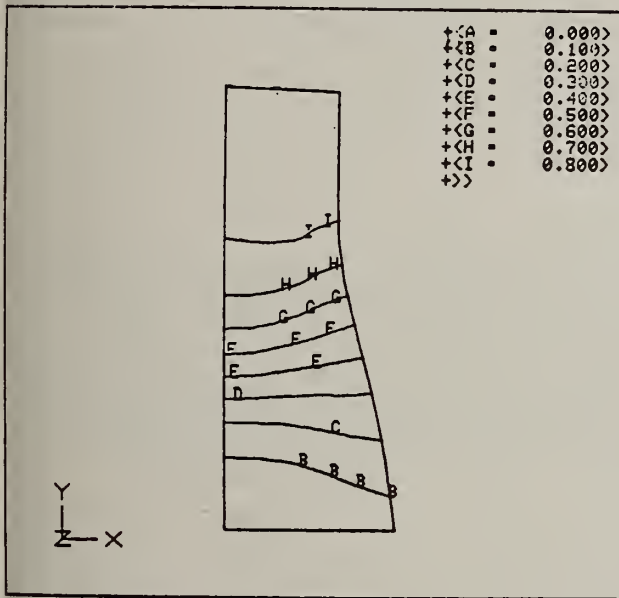


Fig. 26. Effective strain contour during streamlined extrusion.

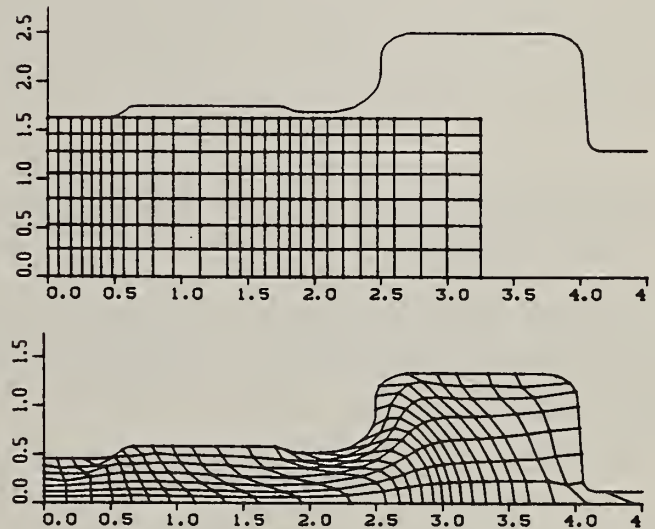


Fig. 27. Ti disk forging.

After thermomechanical treatment the material can be used as the preform for the hot die or the isothermal forging process required to produce the disk. Designing the forging process requires an understanding of the manner in which shear stresses and strains are partitioned from the matrix material into the harder, coarser particles remaining after billet conditioning. Recalling the process for extruding the SiC whisker material described above, the metalworking problem with titanium and nickel-base alloy systems is the reverse. In order to prevent the SiC whiskers from fracturing, it was necessary to extrude the material at 475°C--just below the solidus temperature where the flow stress of the matrix material is significantly less than the fracture stress (approximately equal to its yield strength) of the SiC whiskers. However, it is necessary to increase the flow stress of the matrix material of the P/M nickel-base alloys such that it is greater than the flow stress of the coarse, dendritic-like powder particles. In this way, the matrix material can partition energy into the coarse powder particles. This situation can possibly be achieved by thermomechanically conditioning the as-HIPed billet in the manner previously described. The increased workability which accompanies billet conditioning allows the forging process to be carried out at a lower temperature where the flow stress of the matrix phase is close to that of the coarse particles.

The effective strain distribution for a streamlined die which was designed for conditioning these RST P/M materials is shown in Fig. 26. This uniform effective strain distribution assures that: (1) all material will receive the same amount of plastic work in a practical sense, and (2) the larger and harder particles will not cluster into a larger failure site. The FEM model allows the extruded product to be fully characterized with respect to its processing history. This processing history in terms of its plastic strain can be transferred to the FEM model for forging the disk.

Figure 27 shows a typical simulation of an isothermal disk-forging process. The strain distribution can be easily observed by the grid distortions and also by plotting the effective strain contours. Other field quantities such as the temperature or velocity can be displayed, since they are always computed by the model. However, it is necessary to display only the field quantity which is pertinent to the process-modeling objective.

Different preform geometries can be tested in the computer by a series of iterations, and the optimum preform geometry which yields the effective strain distribution and microstructure can be selected. Immariageon [14], for example, has developed a constitutive-equation form which allows both the effective strain and grain-size distribution to be predicted for the 713 nickel-base alloy. Process modeling allows the designer to be innovative and to create new processing possibilities. For example, he can address the possibility of using process control as another means of guaranteeing quality assurance, thus permitting him to forge closer to net shape beyond the sonic envelope.

Plasticity analysis also can be used to gain new insight into the goals of powder making. The current goal of powder making appears to be biased in the direction of producing mostly fine powder particles having a microcrystalline microstructure. The justification for this objective is based upon the observation that (1) this type of microstructure responds differently to heat treatment than the coarser, dendritic microstructures, and (2) 100% microcrystalline powder particles do not contain any sites (other than possibly foreign ceramic particles) for LCF failure initiation. However, a study by Buzzanell and Lherbier [15] to investigate specifically the effect of varying structural conditions and powder size upon the LCF behavior of these materials showed that -60 mesh powders exhibited significantly better LCF behavior than powders having microcrystalline microstructures. This consistent observation in the LCF behavior could not be explained. Their materials were consolidated by CAP-plus-isothermal forging.

The micromechanical plasticity analysis in the present study suggests that one should consider producing powders which have a constant microhardness from particle to particle in the powder compact. Practically speaking, it is unlikely that 100% microcrystalline material can be produced, implying that a certain volume fraction of LCF failure sites will always be present in the form of coarse, dendritic particles. Manipulation of the powder-making process to control the particle-size distribution such that uniform microhardness values are produced should be a goal in addition to that of producing 100% microcrystalline material. The most probable explanation for the coarse particles producing significantly better LCF properties than the microcrystalline material [15] is the manner in which the load during forging is transferred from particle to particle. A rigid matrix can transfer stress and strain homogeneously, making it possible to reduce the defect size below a critical value.

CONCLUSIONS

1. The plastic working of P/M material represents an increasing trend toward improvement of the service properties of components.
2. A yield function of the form $(2 + R^2) J_2 + J_1^2 (1 - R^2)/3 = (2R^2 - 1)Y_0^2$ is required for the development of plasticity theory and analytical process modeling of porous materials.
3. Plasticity theory for porous materials suggests that beyond 95% densification, application of pressure alone is insignificant in the case of hydrostatic and repressing processes. To achieve full densification, proper control of temperature and material is required.
4. Analytical process modeling provides the ultimate capability of achieving the full advantages of materials produced by RST.
5. More attention should be given to understanding the powder-making process in order to permit the size distribution and the average quenching rate to be adjusted systematically for controlling the physical properties of the powders.
6. The goal of achieving a uniform chemical distribution should be extended to the control of the microhardness distribution. The latter can have a profound effect in controlling the LCF behavior of a P/M material.

ACKNOWLEDGEMENT

The authors would like to thank Mr. A. M. Adair, AFWAL/MLLM, WPAFB, OH, for providing many technical reports which were useful in writing this paper. Drs. Gunasekera and Doraivelu wish to acknowledge the NRC-AFSC Research Associateship Program and Universal Energy Systems, Dayton, OH, for financial support during the course of this investigation. Thanks are also due to Mrs. M. Whitaker and Mrs. H. L. Henrich (Systems Research Laboratories, Inc.) for editorial assistance and preparation of this manuscript.

REFERENCES

- [1] G. J. Hildeman, D. J. Lege, and A. K. Vasudevan, "Fundamentals of Compaction Processes for Rapidly Quenched Prealloyed Metal Powders," Alcoa Technical Center, PA, Oct. 1982.
- [2] J. T. Morgan, H. L. Gegel, S. M. Doraivelu, L. E. Matson, I. A. Martorell, and J. F. Thomas, "Consolidation of Metal Working Preform of X7091 (CT-91) Aluminum Powder," presented at the TMS-AIME Annual Meeting, Dallas, TX, Feb. 1982.
- [3] G. M. Zhdanovich, "Theory of Compacting of Metal Powders," Translated from Teorize Pressovaniye Metzillchaskikli Poroshkov, pp. 1-262, 1969, by The Foreign Technology Division, WPAFB, OH, June 29, 1971 (Translation No. FTD-HCC-23-775-70).
- [4] H. A. Kuahn, "Deformation Processing of Sintered Powder Metals," Chap. 4 in Powder Metallurgy Processing: New Techniques and Analysis (Academic Press, NY, 1978), P. 99.
- [5] R. J. Green, Int. J. Mech Sci. 14, 215 (1972).
- [6] M. Oyane, S. Shima, and Y. Kono, Bull. JSNE 16, 1254 (1973).
- [7] S. Shima and M. Oyane, Int. J. Mech. Sci. 18, 285 (1976).
- [8] H. A. Kuhn and G. L. Downey, J. Eng. Mat. Tech. 41 (1973).
- [9] J. S. Gunasekera, H. L. Gegel, J. C. Malas, S. M. Doraivelu, and G. Griffin, "Computer Aided Engineering Approach to Metal Forming," in Proc. 2nd Int. Computers in Engineering Conf., Vol. 1 (ASME, NY, Aug. 1982), pp. 1-6.
- [10] S. Kobayashi, "Thermoviscoplastic Analysis of Titanium Alloy Forging," AFWAL-TR-81-4130 (Air Force Wright Aeronautical Laboratories, Wright-Patterson AFB, OH, 1981); S. I. Oh, "Finite Element Analysis of Metal Forming Processes with Arbitrarily Shaped Dies," Int. J. Mech. Sci. (to be published).
- [11] J. A. Miller, "RSR Powder Processed Blades and Vanes," PWA/GPD FR-16247 (DARPA, Arlington, VA, 30 Apr. 1982); A. Adair (AFWAL/MLLM), WPAFB, OH 45433, Private communication, 1982.
- [12] S. D. Kirchoff and W. M. Griffith (AFWAL/MLLS), WPAFB, OH 45433, Private communication, 1982.
- [13] P. R. Smith, (AFWAL/MLLS), WPAFB, OH 45433, Private Communication, 1982.
- [14] J. P. Imangeon, D. Murphy, and A. K. Koul, "Plastic Flow Behavior of Powder Processes Nickel-Base Superalloys During Isothermal Forgings," presented at the Metal Congress during TMS-AIME Annual Meeting, St. Louis, MO, Oct. 1982.
- [15] J. P. Buzzanell and L. W. Lherbier, "Processing Effects on the Properties of P/M René Near-Net Shapes," in Proc. 4th Int. Symp. on Superalloys (ASM, Metals Park, OH, 1980), pp. 149-158.

PROCESSING OF P/M ALUMINUM ALLOYS X7090 AND X7091

F. R. Billman, J. C. Kuli, Jr., G. J. Hildeman, J. I. Petit and J. A. Walker

Alcoa Laboratories, Alcoa Center, PA 15069

ABSTRACT

The role of various processing sequences during both the consolidation of P/M aluminum alloy billets, from rapidly quenched ($>10^5$ °C/sec) commercially atomized powders, and their subsequent fabrication to wrought product shapes is discussed. Beginning with effective techniques for hot degassing of initial powder particle surfaces, the judicious usage of common time-temperature-deformation parameters is the key to development of premium quality aircraft structural materials.

Hot die consolidation of the original powder into the intermediate billet stage introduces shear-type deformation strains within an evacuated porous metal compact so as to simultaneously achieve 100% density and intimate particle-to-particle bonding. Residual porosity and improperly dispersed powder particle surface films act as impediments to metallurgical bonding, causing affected billets to exhibit poor ductility and fracture toughness. Metal temperatures must be chosen with due consideration to: powder surface outgassing characteristics, elevated temperature flow stresses, and each P/M alloy's sensitivity to microstructural coarsening.

Once properly consolidated, P/M billets are readily fabricable by conventional aluminum alloy extrusion, forging and rolling processes. Exemplary influences of various extrusion process variables will be described to demonstrate X7090 and X7091 P/M alloy structure/process/property correlations.

INTRODUCTION

Premium Properties from Preferred Structures

The successful development of commercial 7XXX type aluminum alloy powder metallurgy (P/M) products for high strength, "high technology" applications is based on the metallurgical premise that premium properties are achieved through the controlled evolution of preferred microstructural features. Such preferred microstructures are usually finer and more homogeneous than can be developed in competitive ingot metallurgy (I/M) products. Metallurgical characteristics of P/M products are developed through control of the initial powder particle solidification process, the thermal and deformation practices used to consolidate the powder into the final wrought component shape, and final heat treatments used to achieve the desired balance of strength, toughness and corrosion resistance.

A schematic overview of Alcoa's commercial aluminum alloy Wrought P/M Process is shown in Figure 1. Process sequences have been developed over the past 33 years, with careful attention being given to the interdependence of specific alloy compositions and process parameters. [Refs. 1-16] This presentation will focus primarily on manufacture of heat treatable 7XXX type P/M extruded products to describe current commercial P/M structure/process/property correlations.

Table I compares nominal chemical compositions of current 7XXX type P/M alloys with some of their I/M counterparts. Alcoa's commercial X7090 and X7091 alloy compositions and three experimental compositions being studied by Kaiser are shown. In contrast to the I/M alloys, P/M compositions usually incorporate alloying additions of cobalt to yield Co_3Al_9 type dispersoid particles within the aluminum alloy matrix. Chromium, zirconium, manganese, iron, nickel and other dispersoid-forming ingredients can also be readily utilized with or without cobalt in P/M alloys; often in amounts significantly greater than is feasible for commercial ingot products. [Refs. 9, 10, 12, 13]

Faster Melt Quenching Provides Finer As-Cast Structures

The ability to effectively utilize novel alloying additions and extended amounts of conventional I/M alloying ingredients through increasingly rapid melt quench rates has been widely explored and publicized. [Ref. 17-23] A generalized relationship for aluminum alloys, illustrated here by Figure 2, predicts the capability for achieving progressively finer microstructural features with increasingly rapid liquid \rightarrow solid melt quenching techniques. The plot shown here intentionally suggests overlap between coarse and fine powders and between fine powder and splat-quenched materials (flakes, ribbon, wire, etc.). Specific quenching rate boundaries of these rapid solidification processes, particularly the various powder atomization methods, can vary quite significantly as a function of atomized droplet size, the manner in which such droplets are created and the relative amount of undercooling achieved within the molten droplets.

Convectively quenched droplets (i.e. Alcoa's gas atomized and gas quenched powders or PWA's centrifugally atomized and gas quenched powders) of a given size will exhibit significantly finer microstructural features in a given alloy than will similarly-sized powders produced in a closed batch-type atomization chamber wherein a relatively small volume of gas is used to achieve the dual function of droplet formation and droplet quenching. For a given alloy composition, beneficial effects of droplet undercooling on the as-cast powder particles have been reported. [Refs. 24-27]

Recent investigations have also shown that measured dendrite cell sizes, for a given melt quenching process, can vary significantly as a function of alloy type and composition. [Refs. 28-32] Also, the relative melt quenching rate actually obtained in both atomized powder and splat-quenched materials is strongly influenced by conditions at the melt/quenchant interface where surface films and static gas layers will inhibit optimum heat transfer. Because of these alloy/process quench rate/structure complexities, plots like Figure 2 can only serve as a generalized illustration of the metallurgical incentive for using rapidly solidified powder relative to conventionally cast ingots.

Fine Powder Structures Retained in Wrought Products

Figure 3 contrasts the measured sizes of three metallurgical features (grain size, dendrite cell size and interparticle spacing) in 7075 alloy extrusions manufactured from two grades of gas atomized powder and from two sizes of conventionally cast direct chill (DC) ingot. As-cast structural advantages of the original, more rapidly solidified powders have been retained through the various billet consolidation and wrought product manufacturing sequences. [Ref. 33] Under such controlled processing conditions, the relative sizes of other microstructural features in comparable I/M and P/M products are shown in Table II. Both I/M and P/M materials are fully dense in their commercial wrought product forms as a consequence of using sufficient hot deformation to close and heal original ingot shrinkage porosity and initial P/M compact or billet porosity. Hot deformation effectively fragments and disperses prior powder particle surface oxide films in a manner rather analogous to the refinement of as-cast ingot grain boundaries.

RAPIDLY SOLIDIFIED POWDER PRODUCTION

Atomized powders exhibit size distribution ranges according to the specific (and usually proprietary) atomizing practices used, as illustrated in Figure 4. [Ref. 34] Similar size distributions in both irregular and "regular" powder shapes can often be achieved by gas atomization techniques. Less reactive atomizing gas mixtures (i.e. those having significantly lesser amounts of air, oxygen, moisture, CO_2 , etc.) enable the newly atomized droplet to reach a "regular" and more energetically favorable shape before the outer oxide skin is sufficiently established to fix the particle morphology, whereas surface oxide formation in more highly

FIGURE 1

SCHEMATIC FLOW CHART OF ALCOA'S
COMMERCIAL ALUMINUM ALLOY WROUGHT P/M PROCESS
(Refs. 1-16)

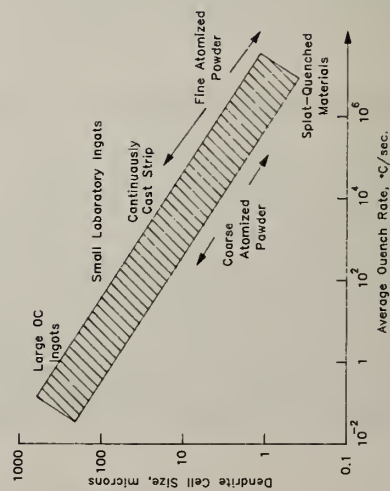
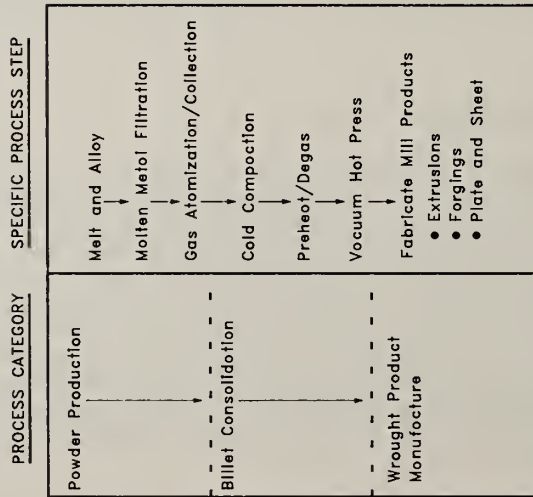


FIGURE 2

GENERALIZED RELATIONSHIP FOR ALUMINUM ALLOYS

TABLE I
NOMINAL CHEMICAL COMPOSITION FOR HIGH STRENGTH 7XXX ALLOYS

	Weight Percent (Balance is Aluminum)						
	Zn	Mg	Cu	Cr	Zr	Mn	Ti
I/M Alloys							
7050	6.2	2.25	2.3	.04	.12	<.10	-
7075	5.6	2.5	1.6	.23	-	<.30	-
7150	6.4	2.35	2.2	.04	.14	<.10	-
7175	5.6	2.5	1.6	.23	-	<.10	-
7178	6.8	2.8	2.0	.26	-	<.30	-
7475	5.7	2.25	1.6	.22	-	<.06	-
P/M Alloys							
X7090 (1)	8.0	2.5	1.0	-	-	1.5	<.5
X7091 (1)	6.5	2.5	1.5	-	-	.4	<.5
15198 (2)	7.4	2.4	2.1	.3	-	-	<.5
MR61 (2)	8.5	2.5	1.5	-	.2	-	<.5
MR64 (2)	7.4	2.4	2.1	.2	.2	-	<.5

NOTES: (1) X7090 and X7091 are registered with the Aluminum Association and are protected by U.S. Patents 3,544,394 and 3,637,441 assigned to Alcoa.

(2) 15198, MR61 and MR64 are Kaiser's experimental alloy designations.

TABLE II
RELATIVE SIZES OF TYPICAL MICROSTRUCTURAL FEATURES
IN 7XXX ALLOY WROUGHT PRODUCTS

Feature	I/M Product	P/M Product
Constituent Particles (Fe, Si types)	2-100 microns	<0.5 micron
Nonmetallic Inclusions (Common limits of Melt Filtration Technology)	<10	<10
Dispersoid Particles	0.01-0.5 (Zr, Cr, Mn types)	0.01-0.5 (Zr, Cr, Mn, Fe, Ni, Co types)
Age Hardening Precipitates	0.002-0.008	0.002-0.008
Oxide Film Thickness on Powder Particle	-	~0.01
Individual Oxide Particle After Hot Deformation	-	~0.01
Random Oxide Clusters After Hot Deformation	-	~0.05

reactive atomizing gas mixtures occurs so rapidly as to better preserve the highly irregular molten droplet shapes initially created by the atomization process itself. [Ref. 35]

All Aluminum Powders Have Surface Oxides

The generation of an aluminum powder particle without the presence of a continuous surface oxide film is extremely improbable in any commercially feasible environment since even the solid state oxidation reaction to form Al_2O_3 thermodynamically requires an oxygen partial pressure of only 10^{-53} atmospheres. [Ref. 35-37] Aluminum alloys containing Mg or Li are even more reactive.

For a given type of alloy, and a given type of powder, air-atomized irregular Al-Mg-X powder for instance, oxygen content is a linear function of the mean particle diameter as shown in Figure 5. "Regular" and truly spherical powder shapes will still exhibit this linear relationship, but their data bands will be displaced to lower total oxygen contents as indicated. The reason for such displacement is suggested by the Figure 6 plot of oxygen content versus powder surface area for an Al-Ni-Fe alloy composition where the three significantly different types of rapidly solidified particulate are characterized with regard to their respective surface areas. [Ref. 38-39] The linear relationship in Figure 6 implies a similar oxide thickness and composition for all three types of particulate produced in the same alloy composition. Expected shifts in this relationship for different alloy compositions having either more or less reactivity with the atomization and quenching environments are noted.

Pertinent characteristics of some aluminum alloy powders are given in Table III. Additional data on the three Al-Ni-Fe particulates is included here to verify that the oxide film thickness is, in fact, virtually identical for all three types. Note also the measured differences in average dendrite cell sizes. In dispersion-hardened nonheat treatable aluminum alloys, the progressively finer and more homogeneous microstructural features associated with increasingly rapid melt quenching rates often provide direct strength and ductility improvements in the final wrought product. As an example, room temperature tensile properties of forgings identically fabricated from the three different Al-3.7Ni-1.5Fe powders described in Figure 6 and Table III were reflective of their original melt quenching rates:

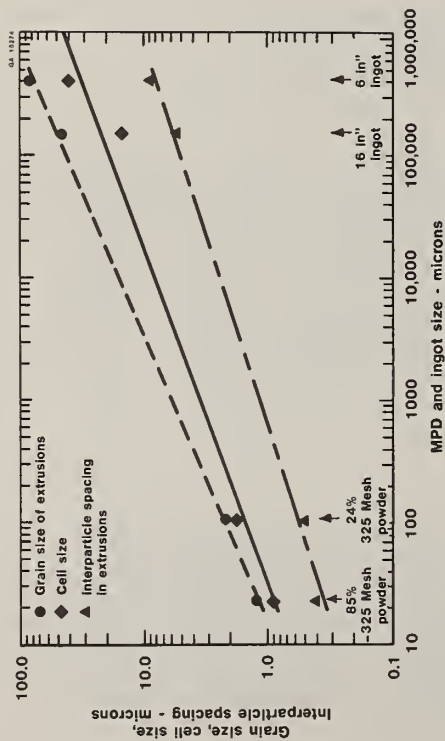
Most Rapid → Alcoa Splat - 350 MPa UTS, 276 MPa YS, 16.2% EL, 38% RA;
Rapid → Alcoa Irregular Powder - 335 MPa UTS, 244 MPa YS, 15.2% EL, 34% RA;
Least Rapid → PWA RSR Powder - 295 MPa UTS, 214 MPa YS, 10.2% EL, 16% RA.
[Ref. 38-39]

For heat treatable 7XXX aluminum P/M alloys any initial microstructural advantage of splat-quenched materials over fine, irregular powders can be substantially normalized during the inherently high temperature billet consolidation sequences and/or during final solution heat treatments. Further discussion of commercial 7XXX P/M products is therefore directed toward the use of atomized powder. The remainder of the loose powder data in Table III characterizes 7XXX type alloy powders produced by Alcoa, Reynolds and Kaiser using a variety of gas atomization techniques. [Refs. 34-35, 38-40] Average powder sizes and total bulk oxygen contents vary widely as a consequence of the atomizing nozzle parameters and gas environments used; but, oxide thickness measurements are relatively comparable. Similar data would be expected for 7XXX alloy spherical RSR powder.

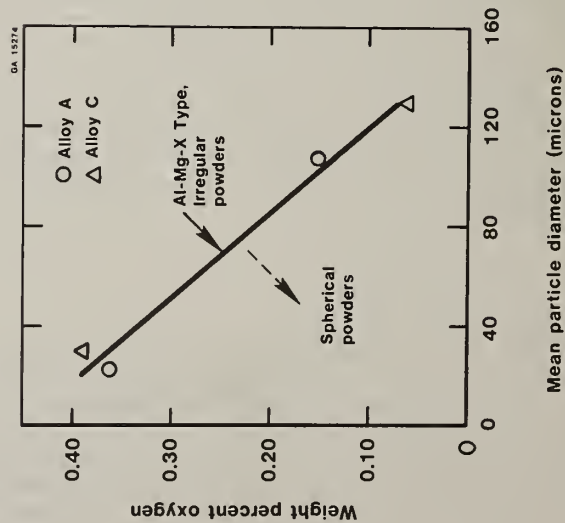
Outgassing of Aluminum Powder

In addition to their surface oxide films most, if not all, aluminum powder surfaces also contain hydroxides. For Mg and Li bearing alloy compositions, reaction with even trace amounts of moisture (i.e. - 90°F dewpoint gas environments) is a virtual certainty. When either pure aluminum or aluminum alloy powders are heated, gaseous by-products are evolved. Adsorbed surface moisture can be vaporized and chemically combined hydroxides can decompose. Figure 7 is a generalized illustration of the principal outgassing events possible. [Refs. 8, 15, 40-56] The exact reaction mechanisms have not been fully defined; but a growing appreciation of the various possible by-products is being evidenced in the technical literature.

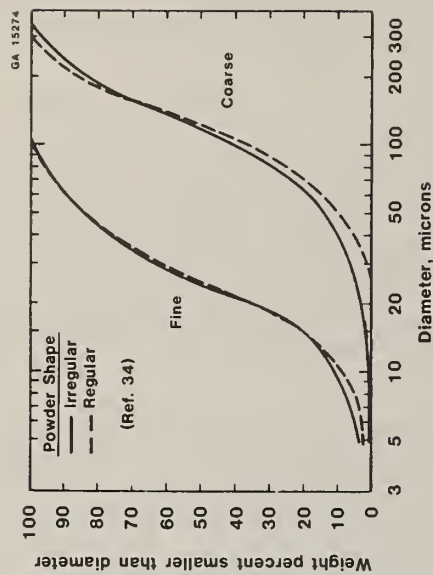
Discrepancies among the various investigations with regard to whether hydrogen or water vapor is the predominant outgassing species are believed to reflect variations in (1) powder or compact density and cross-section, (2) heating rate and thermal gradients across the compact cross-section and (3) differences in the relative degassing efficiencies of the various flowing inert gas and vacuum systems used. The total amount of gas liberated should be a function of the powder alloy, the powder particle surface area, the powder atomizing and handling environments and the maximum preheat/degassing temperature used. Zn and Mg vaporization losses do occur at the highest solid



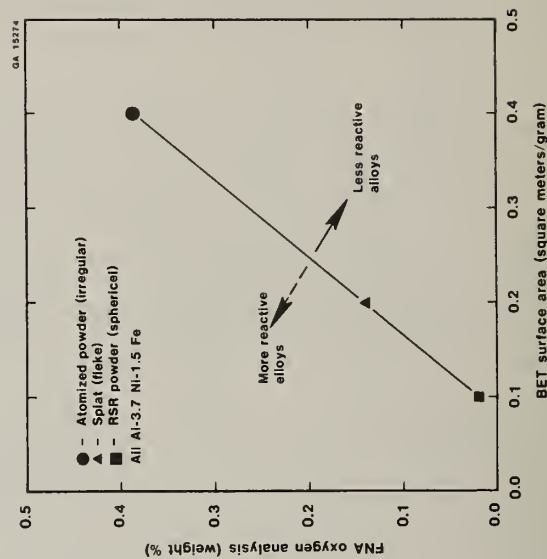
Effect of Mean Powder Diameter (MPD) and Ingot Size on the Structure of Alloy 7075 (Ref. 33)
Figure 3



Effect of Powder Size on Oxygen Content of Extrusions (Refs. 38-39)
Figure 5



Particle Size Distributions of Al-6.4 Zn-2.2 Mg-1.5 Cu Alloy Powders
Figure 4



Surface Area vs. Oxygen Content Characteristics for Various Particulate Morphologies (Adapted from Refs. 38-39)
Figure 6

Pertinent Characteristics of Some Aluminum Alloy Powders
Table III

Alloy	Powder Type	Particle Size ⁽¹⁾	Dendrite Cell Size	FMA Oxygen Content ⁽²⁾	Oxide Thickness ⁽³⁾
Al-Ni-Fe (Refs. 38-39)	PWA-RSR spherical	77 microns median	~1 micron	0.020 wt. %	42 angstroms
	Alcoa splat flakes	~6/4200 mesh	<0.5	0.139	30
	Alcoa air atomized	31 microns median	~0.5	0.386	35
Al-Zn-Mg-Cu X7091 By Alcoa (Ref. 35)	Flue gas atomized ⁽⁴⁾	15 microns APD	—	0.230	50-100
	Air atomized	13	—	0.369	50-100
	Air atomized	28	—	0.204	—
Al-Zn-Mg-Cu By Alcoa (Ref. 34)	Air atomized	24 microns APD	—	0.295	—
	Argon atomized	27	—	0.145	—
	Air atomized	115	—	0.083	—
	Argon atomized	116	—	0.056	—
Al-Zn-Mg-Cu (Ref. 40)	Alcoa X7091	11 microns	1.2	0.55	67
	Air atomized	Linear APW	—	0.50	123
	Reynolds X7091	13	—	—	—
	Air atomized	16	1.6	0.42	150
	Kaiser M864	29	2.0	0.16	101
	Flue gas ⁽⁴⁾ atomized	61	3.5	0.22	102

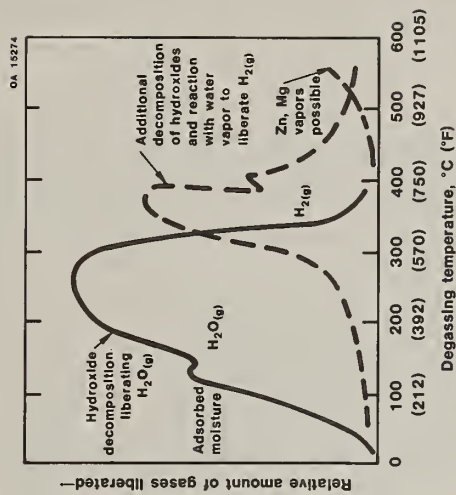
Notes: (1) of variety of available methods, powder particle size data above represent:

- Coulter counter median diameter
- U.S. Standard mesh size. Flakes were ~20 microns thick.
- Fisher sub-sieve sizer APD
- SEM image analyzer, linear elliptical APW

(2) All values are test neutron activation determinations of total oxygen content (oxides, hydroxides, moisture, etc.).

(3) Powder oxide thicknesses are determined by Auger Electron Spectroscopy with argon sputtering technique.

(4) Synthetic flue gas has an approximate composition of 0.0% oxygen, 2% hydrogen, 12.6% CO₂, 0.6% CO, balance nitrogen.



*Peaks can vary in location, magnitude and sharpness as a function of:

- Powder alloy composition
- Atomizing/handling environment
- Bulk powder or compact density and cross-section
- Heating rate
- Degassing efficiency of flowing inert gas or vacuum system

Generalized Illustration of Principal Aluminum Alloy Powder Outgassing Events*
(Refs. 40-56)

Figure 7

state degassing temperatures, but result in only very modest losses at the extreme compact surfaces unless very long, hard vacuum exposures are used.

CONSOLIDATION OF FULLY DENSE BILLETS

For both safety and process efficiency reasons Alcoa preconsolidates its fine aluminum alloy powders into a 70-80% dense compact using conventional cold isostatic pressing technology. These compacts are then preheated for degassing prior to vacuum hot pressing into 100% dense billets.

Compact Preheating and Degassing

Table IV outlines the important features of an efficient P/M compact degassing and P/M billet vacuum hot pressing methodology. Figure 8 illustrates how a 7XXX alloy preheat temperature versus time cycle can vary as P/M compacts increase from <25 cm (10 in.) in diameter to >76 cm (30 in.) in diameter. For the smaller compacts, typical of Alcoa's commercial 50 kg (110 lb) P/M billets, a dynamic vacuum heatup and 1 hour soak cycle can be achieved in 7 hours. For the much larger compacts necessary for consolidation of ≥ 1545 kg (3400 lb) P/M plate billets heatup is accomplished more rapidly under Ar atmosphere (static or hot flowing argon) with a 1 hour evacuation period at the end of the ~ 30 hour cycle. Actual soak times at the $\sim 510^\circ\text{C}$ (950°F) maximum degassing temperature will vary appreciably from ~ 24 hours at the outer periphery of a large compact to only 1 hour at the compact's center. [Ref. 16, 57] Optimum degassing temperatures should be both below a particular alloy's solidus temperature and in a time-temperature regime where microstructural coarsening is minimized. For nonheat treatable aluminum P/M alloys, degassing temperatures are usually $\leq 399^\circ\text{C}$ (750°F). [Refs. 30, 39, 58-60]

Vacuum Hot Pressing the Billet

Alcoa's standard P/M billet process involves the use of a welded aluminum alloy canister to maintain a relatively gas-free environment within the interconnected pores of the 70-80% dense compact while it undergoes hot deformation to full density. Canister wall thickness, welded end-cap designs and compact/canister/cylindrical die geometries must be matched to preclude rupture of the deforming canister and loss of vacuum.

Recently Alcoa has also developed several canless techniques for vacuum hot-die consolidation of P/M billets or fully dense forged preforms, depending on the size and shape of the hydraulic press die cavity used. Simple P/M compacts are first preheated and outgassed in a dry argon furnace and then quickly loaded into the appropriate hot die cavity. Special vacuum sealing methods permit the evacuation of the hot die chamber and the hot P/M compact within a 5-15 minute period, following which the press ram or punch is continuously advanced so as to deform the canless hot compact into a 100% dense article. Three process variants are possible: Canless P/M Billets can be consolidated and then ejected from a tapered-diameter cylinder for subsequent fabrication into extruded or forged components; canless billets can be consolidated in a straight-walled cylinder followed by immediate substitution of an extrusion die for the blind die, and renewed ram motion to fabricate a Direct P/M Extrusion; and fully dense forged preform shapes can be produced from simple P/M compacts in the Direct P/M Forging process. [Refs. 61, 62] As in Alcoa's standard canned billet process, the introduction of significant amounts of shear-type hot deformation strains within the evacuated porous metal compact serves to fragment and disperse original powder particle surface oxide films during the densification process.

The necessity for preventing long time, high temperature exposures to either nitrogen or air has been confirmed in these Direct P/M processes. Both nitrogen and air react with the hot P/M compacts to form nitrides and oxides along the channels of interconnected porosity. Consequently, fracture toughness levels in the subsequent wrought products can be degraded by 50-70%. [Ref. 61-62]

Toughness as Billet Quality Indicator

In Alcoa's experience the room temperature notch tensile/yield strength ratio indicative of fracture toughness is a sensitive evaluator of 7XXX P/M billet quality. Thus P/M billet slices are routinely taken, heat treated to the appropriate -T7 temper and both smooth and notched tensile tests are performed. The resultant NTS/YS ratio is used, along with other room temperature tensile properties, as ACCEPT/REJECT criteria for billet release. NTS/YS and other typical characteristics of Alcoa's X7091 and X7090 alloy billets, in sizes of 27 kg (60 lb) to

TABLE IV

COMPACT DEGASSING AND P/M BILLET VACUUM HDT PRESSING CONSIDERATIONS

Temperature/Time Selections

- Achieve Adequate Degassing
- Afford Practical Flow Stress
- Minimize Structural Coarsening

Evacuated Environment

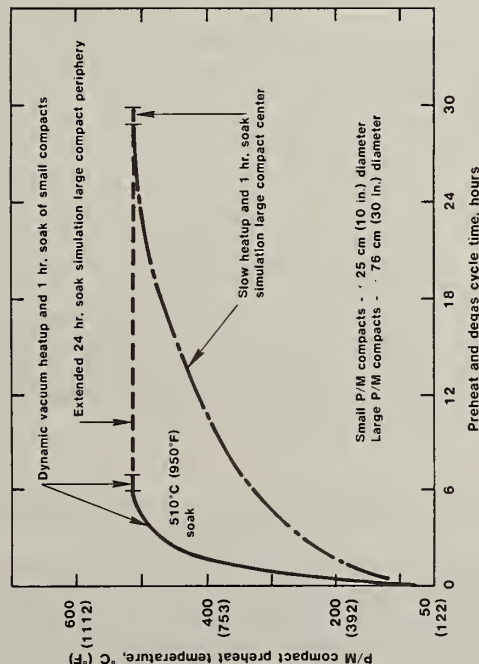
- Minimize Gas-Stabilized Porosity
- Minimize Metallic Vapor Losses
- Use Practical System/Cycle

Hot Pressing Pressure/Dwell

- Adequate to Achieve Full Density
- Practical Production Rate/Cost

Deformation Path

- Simultaneous Densification and Bonding
- Fragment and Disperse Powder Particle Surface Films



Comparative Small vs. Large Billet Process Simulations (Refs. 16, 57)
Figure 8

TABLE V

REPORTED CHARACTERISTICS OF
ALCOA'S X7091 AND X7090 BILLETS
27kg (60 lb) to 1545 kg (3400 lb) sizes

A. POWDER	X7091	X7090
Particle Size, microns Fisher APD ⁽¹⁻⁴⁾	12.6-14.2	12.4-14.1
Oxygen Content, FNA Wt. % ⁽¹⁾	.582-.618	.595-.621
B. BILLET		
(1) Oxygen Content		
Small Billet - Std. Alcoa Process ⁽¹⁾	.311-.318	.333-.356
- Alcoa Conless ⁽²⁾	.350-.445	-
Medium Billet - Std. Alcoa Process ⁽³⁾	.339-.365	.386-.411
Large Billet - Alcoa 3400 lb ⁽⁴⁾	.416-.437	.322-.416
- Simulated Periphery ⁽¹⁾	.339-.347	.354-.363
- Simulated Center		
(2) Hydrogen Content, fusion ppm		
Small Billet - Std. Alcoa Process	.96-1.3	1.51-1.71
- Alcoa Conless	3.2-5.8	-
Medium Billet - Std. Alcoa Process	1.95-2.22	1.77-2.04
Large Billet - Alcoa 3400 lb	5.4-5.8	-
- Simulated Periphery	6.5 avg.	5.8 avg.
- Simulated Center	5.9 avg.	7.1 avg.
(3) NTS/YS - Tested T7E69 or T7E70		
Small Billet - Std. Alcoa Process	> 1.0	>0.8
- Alcoa Conless	1.0	-
Medium Billet - Std. Alcoa Process	> 0.9	1.0
Large Billet - Alcoa 3400 lb	-	-
- Simulated Periphery	> 1.0	>0.8
- Simulated Center	> 0.9	>0.7

NOTES: (1) Reference 57 (3) Reference 63
(2) Reference 61 (4) Reference 16

1545 kg (3400 lb), are listed in Table V. Bulk oxygen contents of both the original powder and resultant billet materials are given here to demonstrate the reduction in total oxygen content achieved through removal of H₂O vapor during the compact preheat/degassing step. [Refs. 16, 40, 57, 61, 63] Although an oxygen content of <0.5 weight percent has been specified for X7090 and X7091 wrought products (see Table I), there is no direct correlation between oxygen content and billet or product properties.

Bulk hydrogen contents also decrease from >30 ppm in fine atomized 7XXX alloy powder to <10 ppm in the billet. With the exception of the extremely low hydrogen contents (<.2ppm) reported by Voss for his 7075 alloy P/M extrusions fabricated from small laboratory compacts which had been rigorously degassed in a 90 hour cycle incorporating relatively hard vacuum levels (10⁻³ Pa), other investigators invariably measure hydrogen contents in P/M billets and mill products which are 10-100 times more than is considered acceptable in a 7XXX ingot. [Refs. 52, 53] Part of this P/M versus I/M difference is due to the fact that only gaseous hydrogen is believed to exist in commercial quality ingots whereas high temperature hydroxides (and perhaps other chemically combined species) do reside in P/M materials.

As an example, three adjacent metal samples were taken from the 1545 kg (3400 lb) billet material described in Table V. Two samples were analyzed by the standard 800°C ITHAC fusion extraction technique which resulted in total hydrogen gas evolution from the molten alloy of 5.41 and 5.81 ppm. The third 9 mm diameter x 40 mm long sample was subjected first to hot vacuum solid state extraction for 4-1/2 hours at 500°C to yield 1.62 ppm of evolved gas, and was then heated to 800°C liberating an additional 3.91 ppm of gaseous by-products. Total gas liberated from this third sample was 5.53 ppm -- in substantial agreement with the other two fusion determinations. The conclusion to be drawn from such data is that a large portion (~70% here) of the total gas evolved during fusion extraction of aluminum P/M materials probably does not exist in a detrimental gaseous form in the solid state article. [Ref. 57] This may help to explain why P/M billet and P/M product properties, including fracture toughness, seem relatively insensitive to fusion extracted hydrogen levels <10 ppm.

FABRICATION OF P/M EXTRUSIONS

Billet Properties Improved by Additional Hot Deformation

Although the vacuum hot pressed P/M billets are 100% dense and relatively well bonded their strength, ductility and toughness levels are all improved with additional hot deformation as represented schematically in Figure 9. For a given 7XXX alloy, powder type and billet size/configuration, increasing amounts of hot deformation strain serve to develop relative "property plateaus". Ultimate tensile strengths seem to stabilize first, then the tensile yield strength and ductility parameters, and finally the NTS/YS or K_{IC} toughness values. [Refs. 57, 64]

Billet to Product Quality Correlation

With controlled thermal and deformation processing, a billet-quality to extruded product-quality relationship can be demonstrated using their respective toughness indices as shown in Figure 10. Excellent extruded P/M product properties have been verified for all three Alcoa processes (Standard scalped canned P/M billet → extrusion, Canless P/M billet → extrusion, Direct P/M billet/extrusion) as shown in Table VI.

Strong Toughness versus Strength and Orientation Relationships

Variations in good quality billet and extruded product toughness levels usually reflect minor shifts in chemical composition within a given alloy's composition limits. As shown by Figure 11, a strong relationship exists between room temperature toughness and tensile yield strength values in 7XXX P/M products. Note also the similar correlation but displaced toughness versus yield strength trend for the three different test orientations within the same extruded bar shape. Such reduced toughness levels in the transverse planes are also common to 7XXX I/M products and are reportedly associated with elongated grain shapes, grain boundary orientations and deformation textures. [Refs. 65-75] Precise resolution of metallurgical structure in P/M products is most challenging because of the extremely uniform and small features present, but fracture surfaces within good quality wrought products exhibit ductile-dimple failure in all three planes.

Influences of Dispersoid Coarsening and Extrusion Parameters on Toughness

In a recent Alcoa study, billets processed by all three preheat/degas cycles shown in Figure 8 were extruded into three different bar shapes at three different extrusion billet temperatures. [Ref. 57] Resultant room temperature tensile properties of a given alloy were all measured to be virtually constant for all extrusion conditions but NTS levels were influenced as shown in Table VII. NTS in the long-transverse (LT) test orientation were most affected in both alloys, but longitudinal NTS values in X7090 alloy extrusions could also be significantly influenced. Extrusion ratio and extrusion billet temperature were the most influential variables.

Co₂Al₉ dispersoid coarsening in the richer X7090 alloy (1.5 weight percent Co) was measured as a consequence of the 24 hour soak at ~510°C (950°F) cycle and NTS values were decreased 6-7% in both L and LT failure planes as a consequence of increased amount of Co₂Al₉ particles in the 0.2-0.8 micron size range. Earlier Alcoa investigators reported strong toughness degradation with Co₂Al₉ particle coarsening in the 0.4-1.4 micron size range. [Refs. 11, 28]

Figure 12 provides a visual illustration of the influences of both extrusion ratio and extrusion billet temperature on the NTS/YS toughness indices of X7090-T7E71 extruded bars. Yield strength was essentially constant for all conditions. Extrusion ratios >12:1 and 589K (600°F) billet temperatures provided the best L and LT toughness characteristics.

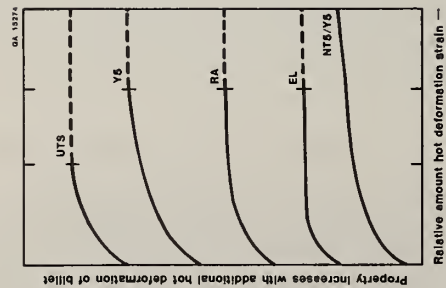
Actual K_{IC} compact-tension type fracture toughness tests were performed on 12:1 extrusion ratio products fabricated from P/M billets having been preheated/degassed with the short (1 hour) and the long (24 hour) soak cycles at ~510°C (950°F). As shown in Figure 14 the usual NTS/YS versus K_{IC} relationship exists for all processing conditions except where toughness was degraded by coarsened Co₂Al₉ particles present in X7090 alloy. The benefits of lower billet extrusion temperature are dramatically evidenced for both alloys. And, the relative insensitivity of NTS/YS to extrusion practice variables in X7091 is explained by the very shallow slope of the NTS/YS versus K_{IC} toughness curve for NTS/YS ratios >1.3. In such high toughness regimes, the material's actual fracture toughness performance must be judged on the basis of K_{IC} results.

Although this same study also included the use of several strain rates (ram speeds) for each set of extrusion conditions, no direct effect of strain rate could be discerned on any of the mechanical properties measured. In light of the initial billet temperature effect, one might question why increased adiabatic heating within the more rapidly strained billets did not also create measureable toughness differences. Because these laboratory tests involved short billet lengths, and the length of billet extruded at any given ram speed was quite short (L/D ~1), adiabatic heating influences might have been inadvertently minimized. Ram speed (strain rate) influences on toughness of production extrusions (where extrusion billet L/D >4) must still be considered possible.

The extrusion ratio parameter ($R = \text{Area of Cylinder} \div \text{Area of Product}$) alone does not adequately quantify the strain history of the wrought shape. Aspect ratio ($A = \text{Product Width} \div \text{Product Thickness}$) can also be an important descriptor. The longitudinal strength advantage in highly deformed, axisymmetric (low aspect ratio) extrusions is relatively well known. [Refs. 30, 65] Other effects can be more subtle. In 7050 alloy I/M extrusions, for example, product aspect ratio does have a significant effect on strength, toughness and stress corrosion properties, with the optimum overall property combinations in all test orientations being developed in extrusions fabricated with both high extrusion ratios and high aspect ratio. [Ref. 66] Experimental studies are currently underway at Alcoa Laboratories to explore the independent influence of aspect ratio (at constant extrusion ratios) in 7XXX alloy P/M extrusions. [Ref. 76]

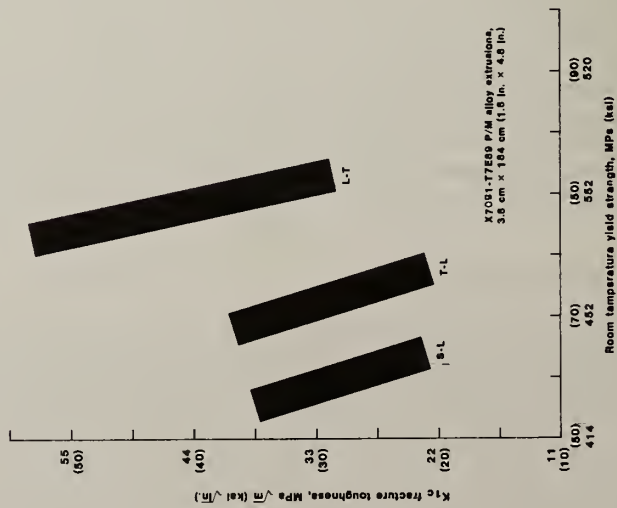
Structural Observations

In addition to the metallographic finding that long time, high temperature degassing cycles did measurably coarsen Co₂Al₉ dispersoid particles in the Co-enriched X7090 alloy, various other structural investigations sought to identify microstructural or macrostructural reasons for the significant influence of extrusion billet temperatures on resultant wrought product fracture toughness properties. Results are summarized in Table VIII. Subtle evidence of finer grain and subgrain sizes was found in the higher toughness, low temperature extruded, products. The predominant failure mode, for all extrusion conditions, was ductile-dimple fracture wherein dimple size and spacing was in relative agreement with dispersoid size and spacing. Co₂Al₉ dispersoid particles were often seen within individual dimples. [Refs. 57, 77]



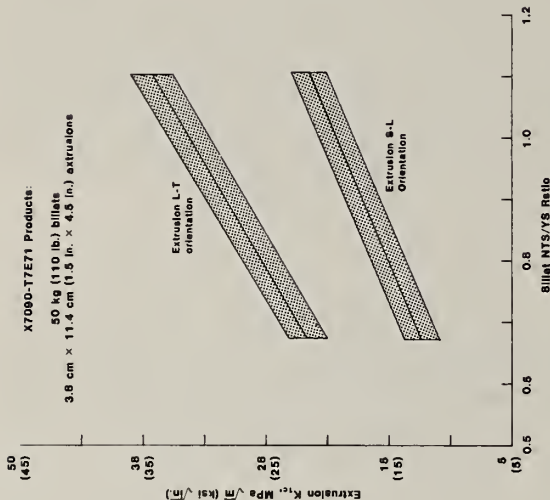
Use of Additional Hot Deformation to Increase Property Levels of XXXX P/M Billets (Refs. 57, 64)

Figure 9



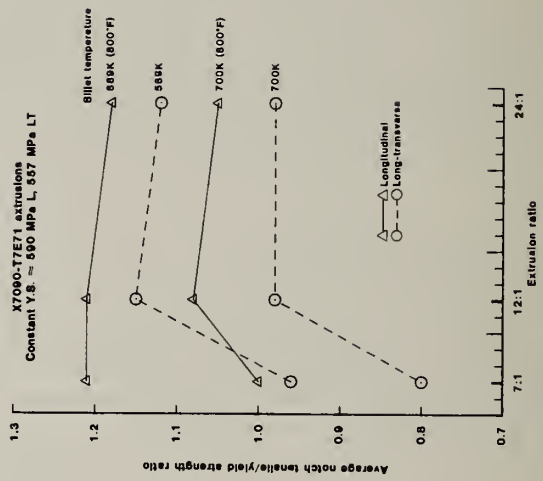
Trans Line Relationships Among Yield Strength, Failure Plane and K_{1c} Fracture Toughness

Figure 11



Trend Line Correlations of Alcoa P/M Billet and Extruded Product Toughness Levels

Figure 10



Influence of Extrusion Ratio and Extrusion Billet Temperature on NTS/YS Toughness Indicator (Ref. 57)

Figure 12

TABLE VI

TENSILE PROPERTIES OF SEAT TRACK EXTRUSIONS FABRICATED BY ALCOA'S STANDARD AND NEW CANLESS P/M BILLET PROCESSES [Ref. 61]

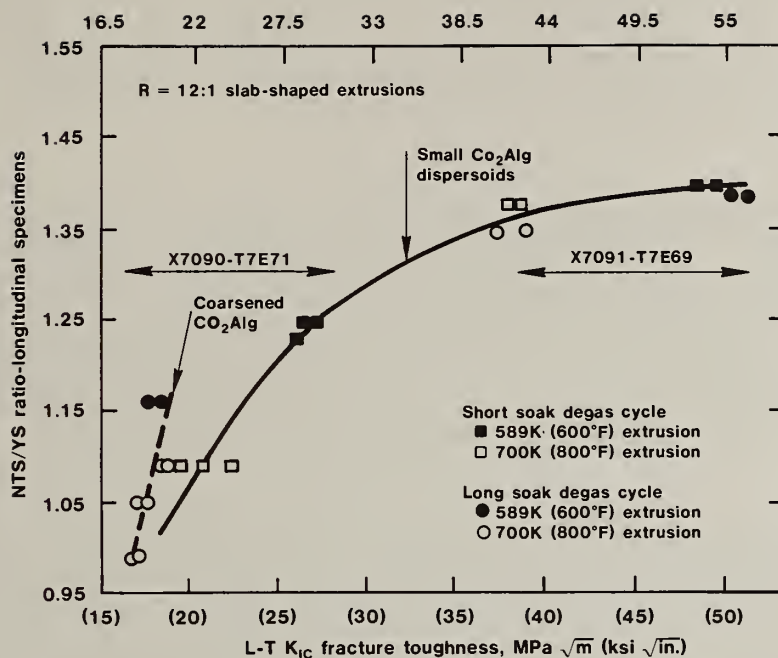
Alloy-Temper	Process	Longitudinal-Room Temperature			
		UTS	YS	EL %	No. Tests
X7091-T7E192	Standard	612	563	10.8	6
	Canless P/M	633	590	9.5	6
	Direct P/M	622	576	10.3	24
X7091-T7E69	Standard	588	553	9.1	6
	Canless P/M	596	562	9.2	6
	Direct P/M	590	554	8.5	24
X7090-T6E192	Direct P/M	666	636	7.8	9
X7090-T7E71	Standard (Plant Data)	620	580	8.6	9
	Direct P/M	636	606	8.0	8

TABLE VII

SUMMARY OF PROCESSING EFFECTS ON NOTCHED TENSILE STRENGTHS OF P/M EXTRUSIONS [Ref. 57]

Process Variable*	X7090-T7E71		X7091-T7E69	
	L	LY	L	LY
Hot Press Preheat/DeGas Cycle	+41 (6%)	+39 (7%)	MPa	No Effect Noted
Extrusion Ratio	+16 (3%)	+116 (27%)	MPa	- +83 (14%)
Extrusion Billet Temperature	+97 (16%)	+71 (16%)	MPa	+19 (3%) +29 (5%)
	~25% ~50%		~3% ~19%	

*Maximum influence of particular process variable is computed. Analysis assumes optimum process of short preheat/degas cycle, >12:1 extrusion ratio and 589K (600°F) extrusion billet temperature.



Correlation of NTS/YS and K_{IC} Fracture Toughness (Ref. 57)
Figure 13

TABLE VIII

EFFORTS TO IDENTIFY STRUCTURAL REASONS FOR DEFORMATION
TEMPERATURE VERSUS TOUGHNESS EFFECTS IN X7090 AND X7091
P/M ALLOY EXTRUSIONS [Ref. 57, 77]

Structural Evaluation	Comparative Results As P/M Billet Extrusion Temperature Reduced From 700K(800°F) to 589K(600°F)
Optical Metallography	Both grain and subgrain size was subtly finer. All interior grain sizes >ASTM10. Surface recrystallized grain depth increased; but maximum depth ≤ 0.250 mm (0.01 in.) in X7091. Depths shallower and intermittent in X7090.
X-Ray Pinhole Patterns	Ring Spotliness (Possible Coarsening) \rightarrow Clear.
Guinier X-Ray Phase Analysis	$M' \rightarrow M$ and CO_2Al_9 present in same amounts for all extrusion temperatures.
SEM-Measurement of Grain and Subgrain Boundary Intercepts in 3 Dimensions	Calculated Boundary Area per Unit Volume (S_v - mm^2/mm^3). As extrusion temperature decreased, S_v increased by $\sim 15\%$ in X7090 and 3-20% in X7091.
SEM Fractography	All tensile and toughness failures by dimple frac- ture with dispersoid particles within dimples. Large dimple size/spacing in the lower-dispersoid containing X7091.

Plant trials have confirmed the benefits of reduced extrusion billet temperatures on measured fracture toughness properties, but the verification of definitive Cause and Effect relationships among the observed X7090 and X7091 P/M microstructural features is a continuing challenge. The deleterious effect of large (≥ 1 micron) second phase particles seems firmly established and loose powder or P/M compact degassing practices must be designed to minimize such dispersoid coarsening reactions. This is especially important in the consolidation of large P/M billets for plate and sheet product fabrication. Complimentary studies are underway to better define the interactive roles of second phase Co_2Al_9 dispersoid particles with deformation texture, recrystallization characteristics, and fracture toughness and corrosion resistance. [Ref. 78]

SUMMARY

Commercial manufacture of X7090 and X7091 alloy Wrought P/M extrusions and forgings is already underway using Alcoa's patented alloy/process combinations. Fine, irregular-shaped, and very rapidly solidified powder is continuously atomized in a 60 million pound per year plant facility. Degassed and vacuum consolidated billets up to 159 kg (350 lb) weights are then routinely produced for subsequent fabrication of extrusions or forgings in Alcoa's various production facilities. 1545 kg (3400 lb) billets have been experimentally produced and ≥ 3636 kg (8,000 lb) billet capability is being pursued for manufacture of full scale P/M alloy plate and sheet products before 1986. Enroute to achieving these production capabilities, extensive R&D studies have outlined common processing needs for 7XXX and other types of aluminum alloy P/M products.

Production of high quality powder is followed by outgassing of the original oxide-coated powder particle surfaces and vacuum consolidation into fully dense billets. Oxide film thickness of aluminum powders is a function of the alloy composition but is virtually the same for different atomizing processes, whether they involve air or "inert" gas atomizing/collection environments. Oxygen content is a direct function of the surface area/volume ratio for the various powder morphologies. Bulk oxygen contents of the billet and wrought product materials are usually lower than oxygen contents of the as-atomized powders themselves, in verification of effective hot degassing techniques for removal of adsorbed and chemically reacted moisture from the surface oxide films. Hydrogen contents measured in high quality 7XXX alloy P/M billets usually fall within a 1-10 ppm range when measured by fusion extraction techniques, but a significant portion of this hydrogen is only released as a gas after melting has occurred. Consequently, the actual amount of detrimental hydrogen gas in optimally processed solid state P/M products may be comparable to the ≤ 0.3 ppm levels of similar I/M materials.

Room temperature tensile and notch tensile testing of P/M billets can be used to develop ACCEPT/REJECT lot release criteria which enables significant billet-quality to product-quality correlations. Property levels in high quality, well-bonded billets are still further improved by subsequent hot deformation enroute to the final wrought component shape. Fracture toughness levels are particularly sensitive to the relative amount and type of deformation strains incurred. Strength and toughness properties are sensitive to variations in actual lot to lot chemical compositions, to test orientation, to the presence of relatively coarse second phase dispersoid particles, and to other conventional 7XXX process/property relationships.

ACKNOWLEDGEMENTS

The continued contractual R&D support of the U.S. Army Armament R&D Command, the U.S. Air Force Systems Command and the Defense Advanced Research Projects Agency (Department of Defense) is gratefully acknowledged. Equally important to the active development and commercial implementation of Wrought P/M Aluminum Alloys is the strong desire of the Materials Users to embrace this technology, and the dedicated commitment of the Aluminum Company of America's Laboratory and Corporate Management. Similarly, the interest and contributions by the Operating and Metallurgical personnel of Alcoa's commercial Powder and Fabricating Plants are most appreciated.

REFERENCES

1. Alcoa-Unpublished Work, 1949-1960.
2. Towner, R. J., U.S. Army Contract DA-36-034-ORD-3559RD, Prog. Rept. 7-62-AP59-S, Oct. 1962.
3. Haarr, A. P., op. cit., Prog. Rept. 7-63-AP59-S, Oct. 1963.
4. Lyle, J. P., Jr., op. cit., Final Rept.-Section I, Sept. 1966.
5. Haarr, A. P., op. cit., Final Rept.-Section II, Dec. 1965.

6. Haarr, A. P., op. cit., Final Rept.-Section III, May, 1966
7. Lyle, J. P., Jr., Aluminum, Vol. I, 1967.
8. Lyle, J. P., Jr. and Towner, R. J., U.S. Patent 3,544,392, Dec. 1970.
9. Lyle, J. P., Jr. and Towner, R. J., U.S. Patent 3,544,394, Dec. 1970.
10. Lyle, J. P., Jr. and Towner, R. J., U.S. Patent 3,563,814, Feb. 1971.
11. Cebulak, W. S. and Truax, D. J., U.S. Army Contract DAAA25-70-C0358, Phase I Final Report, March 1971.
12. Ibid., Phase II Final Report, June 1971.
13. Lyle, J. P., Jr. and Towner, R. J., U.S. Patent 3,637,441, Jan. 1972.
14. Cebulak, W. S., Contract DAAA25-70-C0358, Phase III Final Report, Sept. 1972.
15. Cebulak, W. S., Contract DAAA25-72-C0593 Phase IVA Interim Reports-Oct. 1972, Jan. 1973, June 1973.
16. Cebulak, W. S., op. cit., Phase IVB Final Report FA-TR-76067, Apr. 1977.
17. Duwez, P., Willens, R. H. and Klement, Jnl. Applied Physics, Vol. 31, 1960.
18. Spear, R. E. and Gardner, G. R., Trans. Amer. Foundryman's Soc., Vol. 71, 1963.
19. Duwez, P. and Willens, R. H., Trans. Met. Soc. AIME, Vol. 227, 1963.
20. Bardes, B. P. and Flemings, M. C., Trans. Amer. Foundryman's Soc., Vol. 74, 1966.
21. Matyja, H., Giessen, B. C. and Grant, N. J., Jnl. Inst. Metals, Vol. 96, 1968.
22. Furrer, P., VDI-Zeitschrift, Vol. 116, No. 16, 1974.
23. Jones, H., Aluminum, Vol. 54, 1978.
24. Hirth, J. P., Met. Trans., Vol. 9A, 1978.
25. Mehrabian, R., Rapid Solidification Processing-Principles and Technologies, 1978.
26. Perepezko, J. H. and Rasmussen, D. H., Met. Trans., Vol. 9A, 1978.
27. Gill, W. N., Chem. Eng. Commun., Vol. 12, 1981.
28. Lyle, J. P., Jr. and Cebulak, W. S., Met. Trans., Vol. 6A, Apr. 1975.
29. Billman, F. R., Granger, D. A. and Fujioaka, T., Unpublished Alcoa Research, 1976-78.
30. Lewis, R. E. et. al., DARPA/AFWAL Contract F33615-78-C-5203 Phase I Final Report, 1982.
31. Trivedi, R., Verhoeven, J. D. and Mason, J. T., Proceedings AIME/ASM Symposium on Crystallization of Nonequilibrium Structures, Dallas, Feb. 1982.
32. Paris, H. G., Sanders, T. H. and Mullins, J. W., Proceedings AIME/ASM Symposium on High Performance Aluminum Powder Metallurgy, Dallas, Feb. 1982.
33. Lyle, J. P., Jr. and Cebulak, W. S., Powder Metallurgy for High Strength Applications-Syracuse Univ. Press, 1972.
34. Lyle, J. P., Jr., Cebulak, W. S. and Buchovecky, K. E., Progressing Powder Metallurgy, Vol. 28, 1972.
35. Otto, W. L., Jr., U.S. Air Force Contract F33615-74-C-5077, Final Report AFML-TR-76-60, May 1976.
36. Richardson, F. D. and Jeffes, J. H. E., J. Iron Steel Inst., Vol. 160, 1948.
37. Darken, L. S. and Gurry, R. W., Physical Chemistry of Metals-McGraw Hill, 1953.
38. Hildeman, G. J., Lege, D. J. and Vasudevan, A. K., Proceedings AIME/ASM Symposium on High Performance Aluminum Powder Metallurgy, Feb. 1982.
39. Hildeman, G. J. et. al., U.S. Air Force Contract F33615-79-C-5037, Final Report AFWAL-TR-82-4156, Oct. 1982.
40. Bohlen, J. W., Roberts, S. G. and Chanani, G. R., Naval Surface Weapons Center Contract N60921-80-C-0238, Final Report NOR82-4, June 1982.
41. Dromsky, J. A. and Lenel, F. V., Trans. Met. Soc. AIME, Vol. 230, Oct. 1964.
42. Culleiton, C. J., Wilkinson, O. E. and Toussaint, R. F., Unpublished Alcoa Rept. I-66-6, 1966.
43. Wefers, K. W. and Bell, G. M., Alcoa Laboratories Technical Paper No. 19, 1972.
44. Cebulak, W. S., Unpublished Alcoa Research (AP250), 1972.
45. Arbuzova, L. A., Tyul'pakova, R. V. and Chernykh, N. Ye., Tekhnol. Legk. Splavov, No. 8, 1975.
46. Roberts, S. G., U.S. Patent 3,954,458, May 1976.
47. Arbuzova, L. A., Dunilkin, V. A. and Kunin, L. L., Poroshkovaya Metallurgiya, No. 9, Sept. 1976.
48. Zirkovic, Z. D. and Dobovisek, B., J. Thermal Anal., Vol. 12, 1977.
49. Roberts, S. G., U.S. Patent 4,104,061, Aug. 1978.
50. Danilkin, V. A., et. al., Poroshkovaya Metallurgiya, No. 8, Aug. 1978.
51. Leyko, J., Maciejewski, M. and Szuniewicz, R., J. Thermal Anal., Vol. 17, 1979.
52. Voss, D. P., U.S. Air Force AFOSR Grant 77-3440, Progress Report #1, May 1978.
53. Ibid., Final Report EORD-TR-80-1, Oct. 1979.
54. Singleton, O. R., AFML Contract F33615-79-C-5161 Interim Report, May 1980.
55. Hildeman, G. J., Unpublished Alcoa Report 56-81-AP353, May 1981.
56. Morgan, J. T., Gegel, J. L., Doraivelu, S. M. and Matson, L. E., Proceedings AIME/ASM Symposium on High Performance Aluminum Powder Metallurgy, Feb. 1982.
57. Billman, F. R., Petit, J. I., Sanders, R. E., Jr. and Paris, H. G., U.S. Army Armament R&D Contract DAAK-10-79-C-0193, Final Report-Draft, Aug. 1981.

58. Sanders, R. E., Jr. and Hildeman, G. J., U.S. Air Force Contract F33615-77-C-5086, Final Report AFWAL-TR-81-4076, Sept. 1981.
59. Denzer, D. K., Billman, F. R. and Paris, H. G., DARPA Contract MDA903-81-C-0415, Final Report, Mar. 1982.
60. Langenbeck, S. L. et. al., AFWAL Contract F33615-81-C-5096, Interim Report, Apr. 1982.
61. Kuli, J. C., Jr. and Billman, F. R., Contract F33615-79-C-5053.
62. Pishko, R., AFWAL Contract F33615-77-C-5129, Final Report Draft, Oct. 1982.
63. Kuli, J. C., Jr. and Billman, F. R., U.S. Army Armament R&D Contract DAAK10-81-C-0186, Final Report in preparation.
64. Billman, F. R., Unpublished Alcoa Research, 1978.
65. Van Horn, K. R., Trans. ASM, Vol. 47, 1955.
66. Staley, J. T. and Sawtell, R. R., WESTEC Presentation, March 1977.
67. Kawabata, T. and Izunui, O., Jnl. Materials Science, Vol. 13, 1978.
68. Starke, E. A., Jr., Materials Science and Engineering, Vol. 29, 1977.
69. Staley, J. T., AIME-IMD Spring Meeting Presentation, May 1974.
70. Staley, J. T., ASTM Symposium on Properties Related to Toughness, Montreal, ASTMSTP 605, 1976.
71. Kirman, I., Met. Trans., Vol. 2, Jul. 1971.
72. Hahn, G. T. and Rosenfield, A. R., Met. Trans., Vol. 6A, Apr. 1975.
73. Sanders, T. H. Jr. and Staley, J. T., Proceedings ASM Conference on Fatigue and Microstructure (Oct. 1978-St. Louis), 1979.
74. Garrett, G. G. and Knott, J. F., Met. Trans., Vol. 9A, Sept. 1978.
75. Starke, E. A., Jr., Jnl. of Metals, Jan. 1970.
76. Petit, J. I., Unpublished Alcoa Research, 1982.
77. Sanders, R. E. and Billman, F. R., Unpublished Alcoa Report 56-80-AP336, Nov. 1980.
78. Walker, J. A. and Paris, H. G., U.S. Air Force Contract F33615-80-C-5098, Final Report in preparation.

POST RSPD PROCESSING EFFECTS ON GRAIN GROWTH

R.A. Amato, M.R. Jackson and P.A. Siemers

General Electric Corporate Research and Development
Schenectady, New York 12301

ABSTRACT

Rapid solidification plasma deposition (RSPD) is a process by which material is built up by layers onto a substrate to form a near net shape component. Materials fabricated by plasma spray deposition have structures characteristic of the rapid solidification processes. Recent studies have indicated that these structures can provide enhanced properties at low and intermediate temperatures. This study focuses on attempts to increase the grain size of RSPD materials in order to optimize the mechanical properties over a broader temperature range.

An evaluation of grain growth resulting from a broad range of post deposition treatments has been conducted on a number of Ni and Ni-Fe base alloys, along with variation in tensile and stress rupture properties. The techniques studied include isothermal or thermal gradient annealing, strain and isothermal or thermal gradient annealing, hot rolling, and forging.

Grain coarsening has increased to sizes approaching those of cast alloys following strain and anneal processing. Other techniques are, in general, unsuccessful in producing large grains. As expected, high temperature mechanical properties increase with the grain size in RSPD material.

INTRODUCTION

The fabrication of near net shape structures by the rapid solidification plasma deposition (RSPD) process has evolved from coatings technology and early flame spraying techniques(1,2). The process involves the injection of fine powders into a high energy plasma jet where they melt and are directed towards a substrate. Upon impacting the substrate, the material is rapidly solidified. The ability to build up layers of metal on a substrate in low pressure has lead to sound structures requiring little subsequent working and/or machining(3). The technique is especially attractive when using materials for which casting and further processing are difficult. Rapidly solidified materials (4,5) have ultra-fine grain sizes with excellent strength at low and intermediate temperatures and chemical homogeneity manifested by an increase in solidus temperatures over cast or wrought material.

While nearly full densification results from high temperature isothermal annealing, grain sizes have been limited to 25-50 μm in some Ni and Ni-Fe based alloys. Poor high temperature strength and stress rupture life are due to the abundant grain boundary area. Difficulty in achieving grain coarsening is not exclusive to the RSPD process. For superalloy components made by conventional powder metallurgy, limited coarsening is attributed to MC and M_{23}C_6 carbides, oxides, and even γ' (Ni_3Al) particles impeding grain boundary motion(6,7). Superalloy material typically contains significant quantities of these phases, and the thick RSPD structures deposited in low pressure have oxygen levels in the 300-500 wppm range.

Nucleation and growth considerations lead to two possible grain growth techniques. By raising the total free energy of a specimen sufficiently, for example as strain energy, recrystallization and subsequent grain growth upon annealing can be promoted. Alternatively, eliminating the phases pinning boundaries will increase mobility and promote larger grains. These basic concepts, reviewed by Burgers and Aust (8,9), suggest that grain growth can be achieved in RSPD materials by prior deformation or by controlling composition.

This investigation sought to increase the grain size of RSPD materials through techniques employing both deformation and heat treatments. Specifically these techniques included: strain followed by isothermal or thermal gradient annealing, hot rolling and forging, and chemistry studies using Rene' 80 and experimental Ni-Fe base alloys. In addition, the effect of thermal gradient annealing on material in the as-sprayed condition was tested.

These attempts to increase grain sizes were intended to improve high temperature mechanical properties. To measure this effect in RSPD alloys, mechanical properties were determined at various temperatures on materials exhibiting increased grain size.

EXPERIMENTAL PROCEDURE

Deposition Processing and Alloy Selection

All deposits were made in a low pressure plasma spray facility. The vacuum chamber pressure was reduced to below 0.33 kPa (2.5 torr) prior to back-filling with plasma gases to 8 kPa (60 torr). An EPI Model 03CA gun, with an anode having a 20° powder feed port angle, was operated at 55 volts and 1300 amps. Argon and helium plasma gases had inlet flow rates of 1.40 liters/sec (179 scfh) and 0.36 liters/sec (46 scfh), respectively. All gases were of commercial purity (99.99% pure, <10 ppm moisture, <20 ppm O₂).

Metal powder was fed into the gun using two Plasmadyne Roto-Feed Hoppers at a combined mass flow rate of 10.5 kg/hr (4.7 rpm at feeder). The Ar carrier gas had a volume flow rate of 0.12 liters/sec (15 scfh). Powders sieved to -400 mesh and having the composition listed in Table 1 were supplied by either Alloy Metals, Inc. of Troy, MI, or Homogenous Metals, Inc. of Herkimer, NY. Rene' 80 is a γ' (Ni₃Al) precipitation hardened Ni-base alloy containing the titanium carbide (MC) which breaks down into M₆C and M₂₃C₆ grain boundary carbides during subsequent heat treatment(10). The 47 v/o γ' phase is in solution at temperatures above 1150 °C. The six experimental alloys are strengthened by either a Ti-rich γ' or a Cb-rich γ'' precipitation phase(11). A sequence was chosen to gradually vary the volume fractions of the matrix and strengthening phases. An 1150 °C anneal was found to be sufficient to drive the precipitates into solution for all six alloys. The Rene' 80 and Hastelloy X are the standard compositions available commercially. The experimental alloys, designated C1-C6, have compositions similar to IN 718, Hastelloy X and U- 212.

Powder was deposited onto 15cm x 15cm (6 in x 6 in) steel plates that were grit blasted and degreased in Freon prior to coating. The gun traveled at a velocity of 15° cm/sec (6 in/sec), 30.5 cm (12 in) above the substrate. The gun was perpendicular to the substrate for a 90° impingement angle.

TABLE I
Nominal Compositions of Alloys
Atomic Percent

Alloy	Ni	Fe	Cr	Mo	Cb	Ti	Al	Si	Mn	C	B	W
C1	62	10	14	2	6	2	2.5	0.6	0.3	0.4	0.2	-
C2	55	19	14	3	4.5	1.5	1.5	0.6	0.3	0.4	0.2	-
C3	51.5	19	19	4	7.5	1	1.5	0.6	0.3	0.4	0.2	-
C4	48	19	24	5	0.5	0.5	1.5	0.6	0.3	0.4	0.2	-
C5	38.5	34	19	3	0.5	2.5	1.0	0.6	0.3	0.4	0.2	-
C6	29	49	14	1	1.5	4.5	0.5	0.6	0.3	0.4	0.2	-
Rene' 80	66.8	-	16	2.5	-	6	6.5	-	-	0.8	0.1	1.3
Hastelloy X	46.9	19.3	24.6	5.5	-	-	-	1.0	0.5	0.5	-	0.2

Post Deposit Processing

Plate deposits were sectioned to provide 3.5 cm x 1.5 cm x 0.15 cm (1.4 in x 0.6 in x 0.06 in) coupons whose faces were perpendicular to the plane of deposit and whose longitudinal direction was parallel to the direction of gun motion. Each slice was subsequently surface ground to make parallel coupon faces.

Thermal gradient treatments, similar to those used to align grains in dispersion strengthened superalloys, were performed by passing Rene' 80 specimens through a water cooled Cu chill inserted into a vertical tube furnace. The specimens were driven through the system at a rate of 2.5 cm/hr (1 in/hr). Temperature gradients of 100 °C/cm at γ' solvus temperatures were measured by a series of thermocouples mounted on a test specimen. Thermal gradients decreased as the specimen moved away from the Cu chill. A thermal gradient of 80 °C/cm was measured at the maximum furnace temperature of 1245 °C located 4.5 cm from the Cu chill.

Specimens that were to be strained prior to annealing were first given a high temperature solution anneal in order to achieve their full density and maximize the grain size. Rene' 80 specimens received a 2 hour solutioning treatment at 1220 °C which in some cases was followed by an additional hour at 1240 °C. This increased the starting grain size to 25 μ m. The Ni-Fe base alloys were given solution anneals for 1 hour at 1220 °C with the exception of Alloy C1, which showed evidence of incipient melting at temperatures as low as 1170 °C. This alloy was annealed at 1150 °C. All isothermal anneals were done in a 1.33×10^{-6} kPa (1 x 10⁻⁵ torr) vacuum furnace.

The solution annealed coupons were further sectioned into specimens 1.0 cm x 0.5 cm x 0.15 cm (0.40 in x 0.20 in x 0.06 in) and cold rolled on a two-high 6 x 6 rolling mill. The specimens were subsequently recrystallized for 1 hour, at the same temperatures used for solutioning, and the resulting grain size determined.

Specimens were selected for the strain and thermal gradient anneal study based on response to strain and isothermal anneal treatments. Alloys C2 and C4 were cold rolled 4% and 22%, respectively, following the solution annealing procedure previously described. The specimens were driven into the thermal gradient furnace at 2 cm/hr (0.8 in/hr) and 10 cm/hr (4 in/hr) and the resulting grain sizes determined.

Hot rolling specimens, 2.5 cm x 1.5 cm x 0.3 cm (1 in x 0.6 in x 0.12 in) were sliced from plate deposits of alloys C2, C3, C5, Hastelloy X, and Rene' 80 as previously described. The coupons were packed in 304L stainless steel after being coated with a thin layer of MgO to prevent bonding. The packs were heated in a Muffle furnace and reduced in a single pass on a two-high Birdsboro Mill at the conditions listed in Table 2.

Hot forging was done on a hammer forge on 2 cm x 3 cm x 3 cm specimens heated to 1200°C. A single stroke deformation of 27% reduction in thickness was followed by reheating and a second stroke of 30% reduction.

TABLE 2
SINGLE PASS HOT ROLLING CONDITIONS

Alloy	Temp. (°C)	% Reduction
C2	1220	52
C2	1220	26
C3	1220	51
C3	1220	27
C5	1220	50
C5	1220	27
Hastelloy-X	1230	53
Hastelloy-X	1230	26
René 80	1230	50
René 80	1230	23

Material Evaluation

The effect of grain size on the mechanical properties of RSPD alloys was determined for critically strained and isothermally annealed 3.5 cm x 1.5 cm x 0.15 cm (1.4 in x 0.6 in x 0.06 in) coupons prepared as described in a previous section. The large grained specimens were tensile and stress rupture tested at various conditions. The flat test specimens had a 0.63 cm (0.25 in) gage length. A strain rate of 0.08 min⁻¹ was used on Rene' 80 specimens while a rate of 0.04 min⁻¹ was used on the other specimens. Tensile tests were done in vacuum while stress rupture tests were done in argon and air, for Rene' 80 and the experimental alloys, respectively. The Ni-Fe base experimental alloys were heat treated 4 hrs at 900°C and 12 hrs at 760°C to precipitation strengthen the alloys.

Metallographic investigations were done to determine the grain size that resulted from the different processing techniques. The specimens were sectioned and mounted to reveal the three orthogonal planes of rolling. Grain sizes were determined utilizing a line intercept method with 12-30 measurements averaged to give grain sizes and error bands indicating the 90% confidence limits.

RESULTS

Microstructures

Strain and Isothermal Anneal: The effects of strain and anneal processing on RSPD materials was first investigated using Rene' 80. The extent of grain coarsening due to deformation and annealing, 1 hour at 1250°C, is shown in Figure 1. These results indicate that at very low reductions in thickness, i.e. less than 3%, no increase in grain growth is achieved. In the 3-6% deformation range large grains on the order of 100-150 μm are produced. The typical microstructure which developed after the 3-6% deformation and subsequent anneal is shown in Figure 2 along with the microstructure developed after a solution anneal. The primary recrystallized grain size decreased at deformations greater than the critical amount. Grain sizes were uniform through the thickness of the specimens in all cases.

The six experimental alloys along with Hastelloy X were subjected to a similar series of deformation and anneal heat treatments. The results of these tests are presented in Figures 3 and 4. The alloys show a similar behavior to Rene' 80, having a critical deformation range below which no increase in grain growth is observed but within this range large grain sizes can be found. Alloy C1 was an exception which showed only a slight increase in grain size.

The microstructures developed in alloys C2, C4, and Hastelloy X after critical strain and annealing, along with the microstructures characteristic of the materials given an isothermal anneal treatment only, are given in Figures 5-7. Alloy C2 had the largest increase in grain size of the experimental alloys and after just a 3% deformation and anneal grew grains to over 400 μm , see Figure 5. While grain growth proceeds through the individual pass layers, there is a tendency for the grain boundaries to become aligned with these layers. The increase in grain size of alloy C4, Figure 6, after the critical strain and anneal process compared to the isothermally annealed RSPD material is characteristic of alloys C3-C6 and commensurate with the increase found for Rene' 80. Hastelloy X responded most favorably to the strain and anneal treatments with recrystallization and grain growth resulting in 500 μm grains after just 2% reduction in thickness.

Beyond the critical deformation range the primary recrystallized grains decrease in their ability to grow beyond the 25 μm levels which developed without pre-straining. The recrystallized grain sizes found after the 14% reductions are characteristic of the results following larger deformations. Large secondary recrystallized grains, however, were found in alloys C4, C5, and Hastelloy X after 18-25% deformation and subsequent anneals, see Figure 8.

Grain boundary phases, which can cause inclusion-inhibited growth and can lead to secondary recrystallization, were extracted from alloy C4 and inspected by transmission microscopy. They have been determined to be rich in Cr and Mo with some Fe and Ni additions. The FCC structure has a lattice parameter of 10.8 \AA which suggests either a M_{23}C_6 or M_6C type carbide.

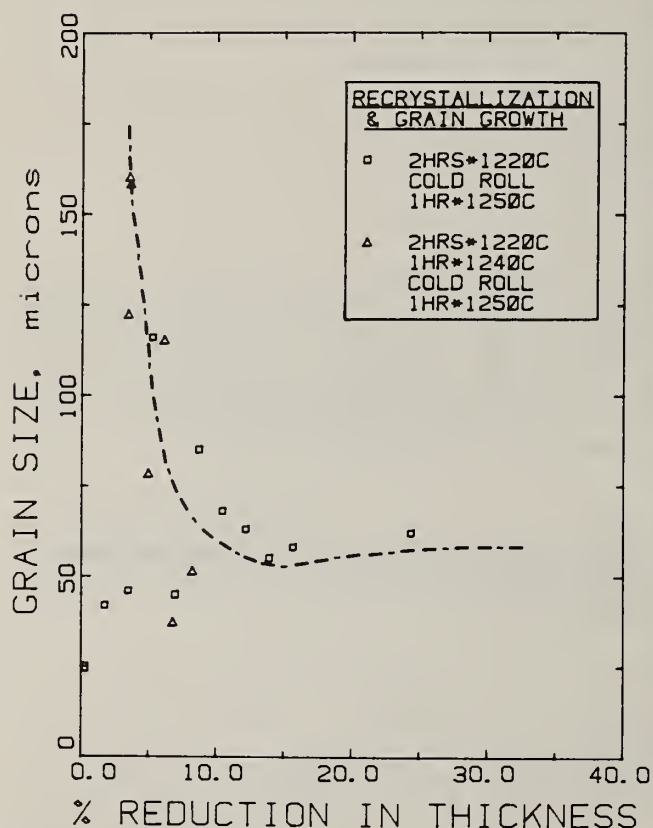


Fig. 1. Grain growth behavior of plasma-sprayed Rene' 80 as a function of the amount of cold rolling.

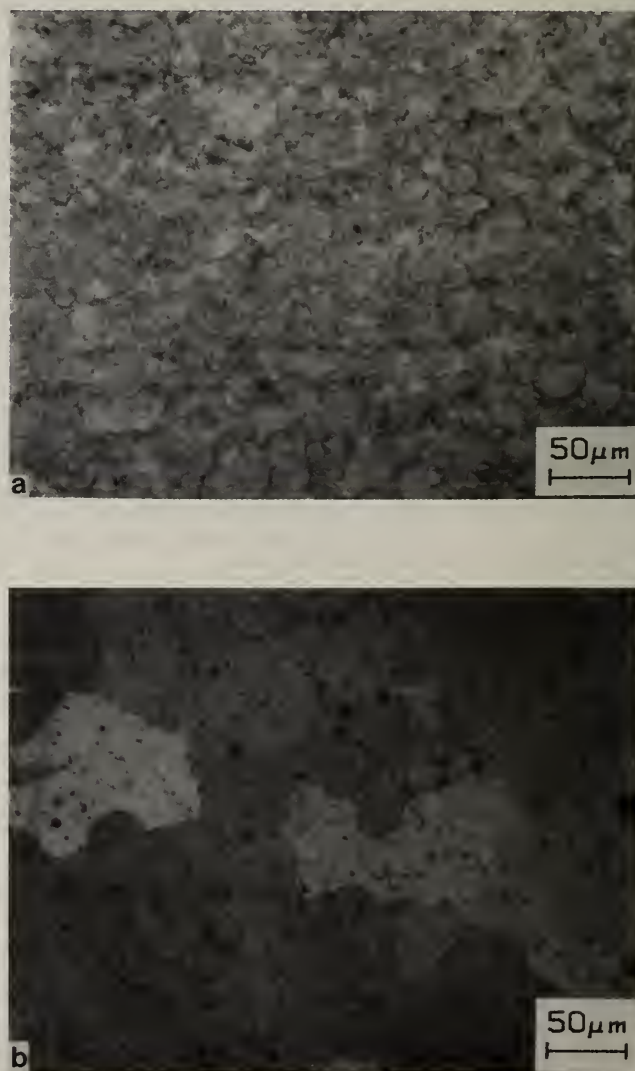


Fig. 2. Typical grain sizes developed in RSPD Rene' 80 following (a) an isothermal anneal were 25 μm while those resulting from (b) critical strain (3-6% reduction in thickness) and anneal processing were 100-150 μm .

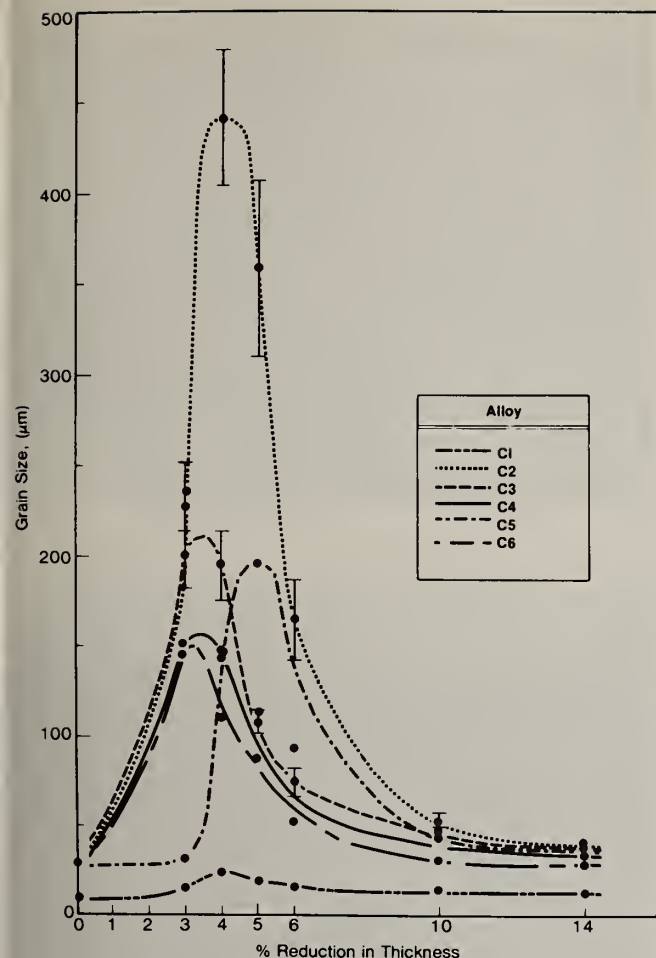


Fig. 3. Variation in grain size with deformation following recrystallization anneal heat treatment. Experimental alloys C2-C6 were annealed 1 hr. at 1220°C while alloy C1 was annealed 1 hr. at 1150°C. Error bars indicate 90% confidence limits.

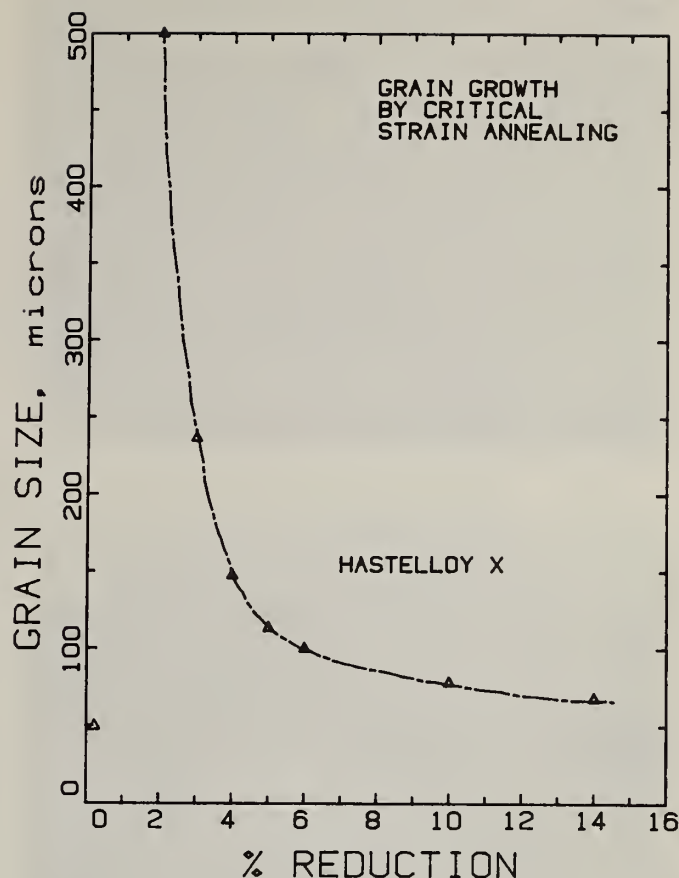


Fig. 4. Grain growth as a function of reduction in thickness following recrystallization anneal at 1220°C for 1 hr.

Strain and Thermal Gradient Anneal: For thermal gradient annealing studies, the furnace temperature profiles could be varied. In the present work, the profiles were controlled to achieve a 100°C/cm thermal gradient at the location where the γ' solvus temperature, 1150°C, was first exceeded. For Rene' 80 samples in the as-deposited condition, no increase in grain size was observed compared to isothermal annealing.

Alloys C2 and C4 showed a propensity to grow large primary or secondary recrystallized grains after reductions in thickness of 4% and 22%, respectively. The alloys were tested in these conditions to determine the effect that a 100°C/cm thermal gradient anneal would have on grain growth. Neither alloy C2 nor C4 grew elongated grains due to their exposure to a thermal gradient. Microstructures were characteristic of those resulting from an isothermal anneal rather than from a directional recrystallization process.

Hot Deformation: As an alternative to cold rolling with subsequent anneal treatments, a study was conducted to determine the feasibility of hot rolling RSPD superalloys to control grain size. Typical microstructures developed during hot deformation are shown in Figures 9 and 10. Similarities to the as-sprayed material exist with evidence of unmelted particles and a fine grain size. Rene' 80 seen in Figures 9(a) and (b) may have undergone dynamic recrystallization as the grain morphology remained equiaxed after 50% reduction in thickness. The Ni-Fe base alloy C2 may have undergone a similar effect as these grains are also equiaxed while unmelted particles have become elongated in the rolling direction, see Figure 10(a). A subsequent anneal again produced grains 25 μ m in size as seen in Figures 10(b) and (d). The observations from hot forming confirmed these results.

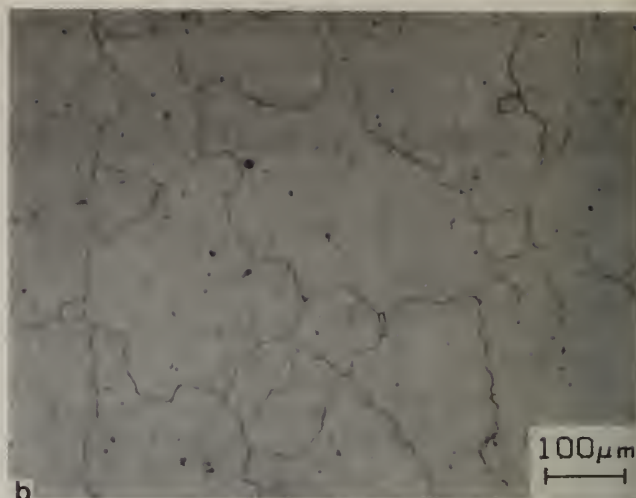
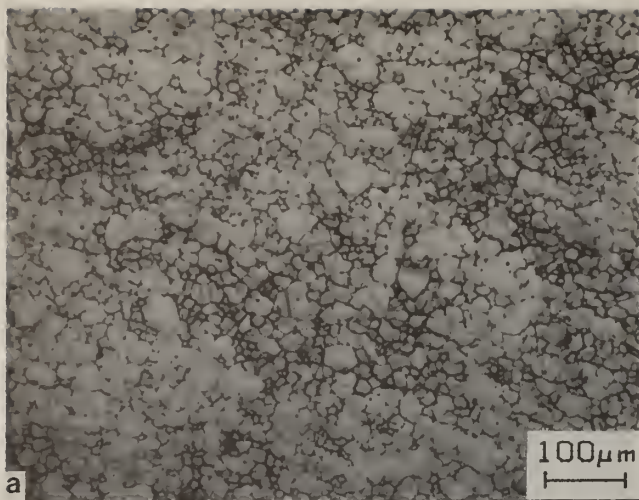


Fig. 5. Typical grain sizes developed in RSPD experimental alloy C2 following (a) 1 hr. at 1220°C were 25 μm while those resulting from (b) critically straining 3% (reduction in thickness) before annealing averaged 230 μm.

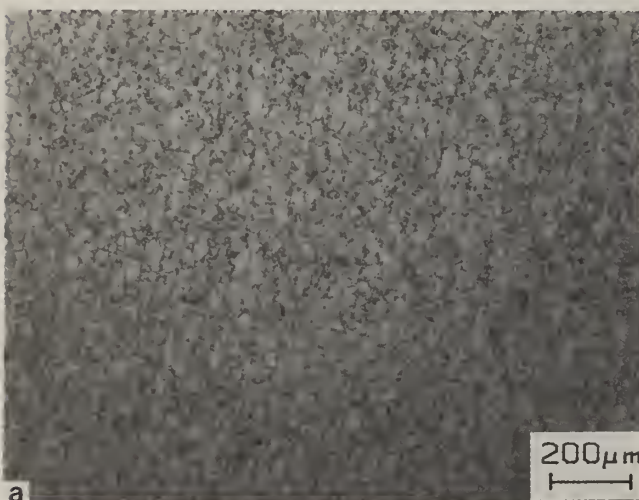


Fig. 6. Typical grain sizes developed in RSPD experimental alloy C4 following (a) 1 hr. at 1220°C were 25 μm while those resulting from (b) critically straining 4% (reduction in thickness) before annealing averaged 150 μm.

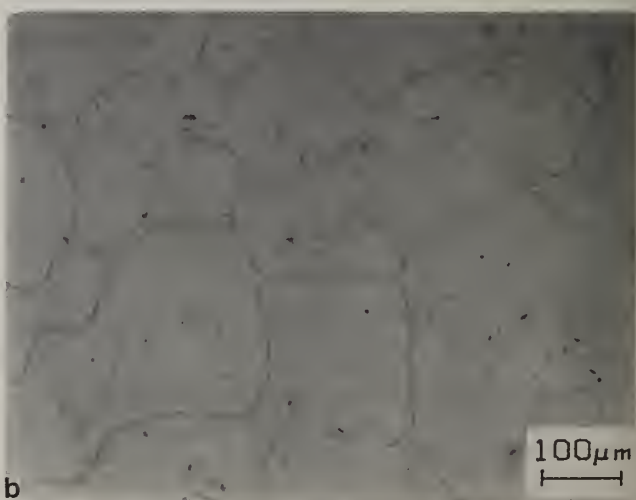
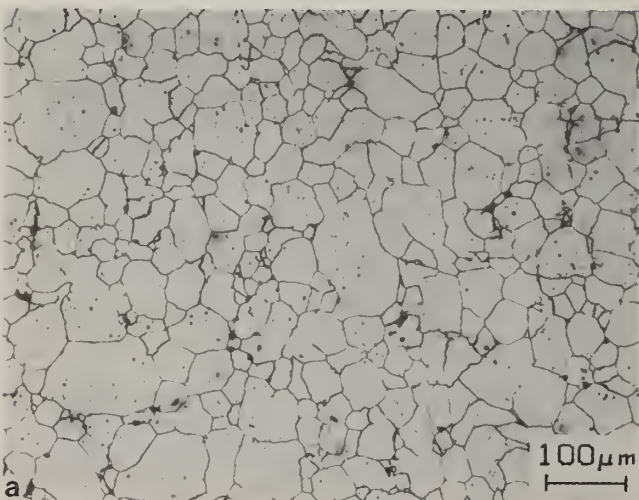


Fig. 7. Typical grain sizes developed in RSPD Hastelloy X following a) 1 hr. at 1220°C were 50 μm while those resulting from (b) critically straining 3% (reduction in thickness) before annealing averaged 240 μm.

Fig. 8. Secondary recrystallization is apparent in the RSPD alloys C4, C5, and Hastelloy X. This micrograph shows the rolling plane of experimental alloy C4 after 1 hr. at 1220°C, cold rolling 22%, and 1 hr. at 1220°C.

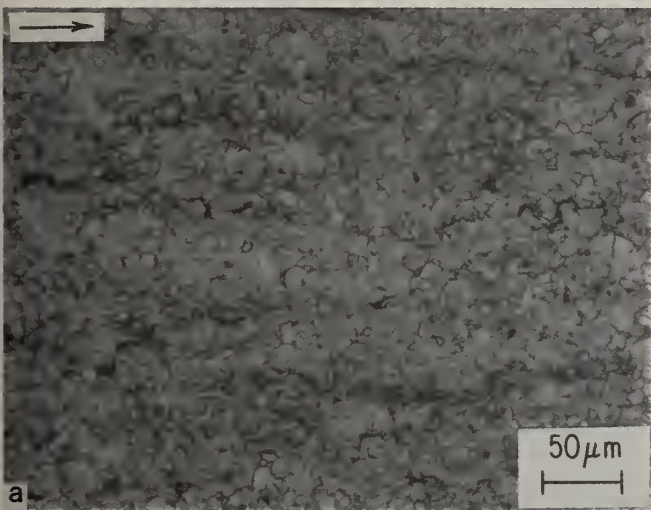
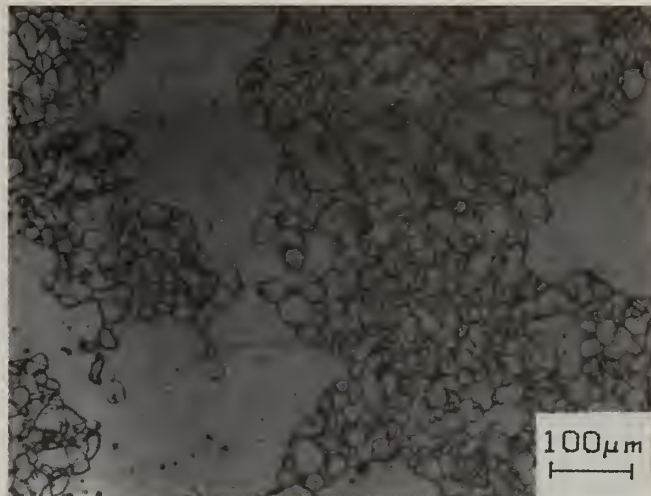


Fig. 9. Hot-rolled RSPD Rene' 80, reduced 50% in thickness at 1230°C, appeared to have undergone dynamic recrystallization as equiaxed grains 10 μm in diameter resulted. Micrographs taken (a) of the rolling plane and (b) perpendicular to the rolling plane.

An interesting observation regarding the microstructures of hot rolled and annealed RSPD material is the evidence of grain boundary motion beyond unmelted prior particle boundaries. It can be seen in Figure 11 that the grain boundary has advanced beyond the unmelted particle boundary which is decorated by fine carbides.

Material Properties

To determine the effect of grain coarsening on the high temperature properties of the RSPD alloys, critically strained and isothermally annealed specimens were tensile and stress rupture tested at various conditions. The results of these tests, along with data for the isothermally annealed RSPD material, are presented in Table 3 for Rene' 80 and Table 4 for the experimental alloys. Hastelloy X was not tested after strain and isothermal anneal treatments.

The major trends which are found when comparing isothermally annealed RSPD material to critically strained and annealed RSPD material are: an increase in high temperature strength, a decrease in low temperature strength and ductility, and an increase in stress rupture life. Rene' 80 tensile strengths at 1000°C increased from 213 MPa to 432 MPa as the grain size changed from 20 μm to 80 μm. The experimental alloys (alloy C1 is omitted from the comparison since it did not show a marked increase in grain size after processing, and the anomalous room temperature tensile data of isothermally annealed alloy C3 is not used in the comparison) did not show as significant an effect at high temperature as was found for Rene'

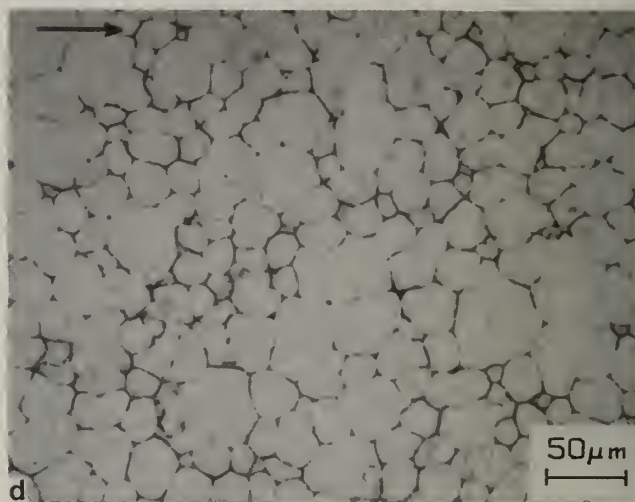
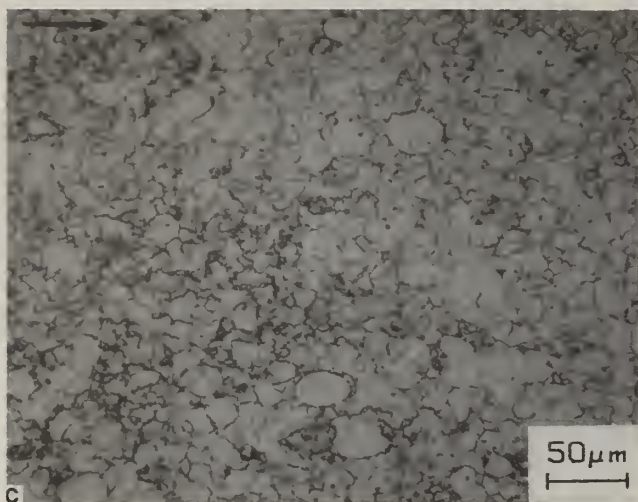
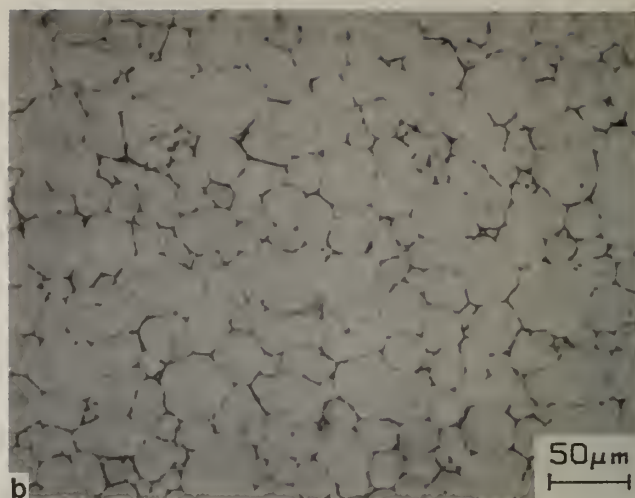


Fig. 10. Typical structures of RSPD alloys following hot deformation. Alloy C2 hot rolled 20% reduction in thickness at 1220°C. (a) rolling plane as deformed, (b) rolling plane deformed and post annealed, (c) longitudinal section as deformed, (d) longitudinal section as deformed and post annealed. Etchant: glycergia.

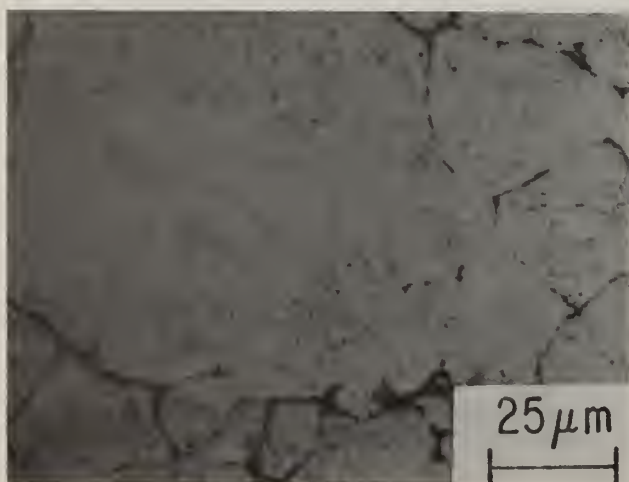


Fig. 11. Example of grain growth beyond unmelted particle boundary. Rolling plane of Alloy C2 rolled 20% reduction in thickness at 1220°C. Etchant: glycergia.

80. The exception to this was alloy C2 which increased from 64 MPa to 180 MPa, at 1060°C, when the grain size went from 25 μm to over 400 μm . The increases in grain size of alloys C5 and C6 did not result in an increase in the high temperature tensile strengths. The room temperature tensile strength and reduction in area of Rene' 80 decreased from 1330 MPa and 17% to 1280 MPa and 8.3% as the grain size increased. The experimental alloys were in general decreased by 10% in tensile strength and twice that in ductility at low temperatures. The results of the stress rupture tests indicate that the time to failure for Rene' 80 increased by 100% and for the experimental alloys increased by nearly one Larson-Miller parameter with larger grains.

Critically strained and annealed RSPD Rene' 80 material was compared to cast and fully heat treated material. The plasma sprayed material had strengths (1280 MPa at 20°C, 772 MPa at 850°C, and 432 MPa at 1000°C) that were equal to or greater than the cast material (1030 MPa at 20°C, 750 MPa at 850°C, and 345 MPa at 1000°C). The low temperature elongation of the plasma sprayed material, 8.3%, was slightly greater than that found in the cast material, 7.0%. At high temperatures, the ductility of the plasma sprayed material was significantly less than was found for the cast material: 3.9% compared to 23.0% at 850°C. The RSPD material was 2-3 Larson-Miller parameters below the cast and fully heat treated material.

DISCUSSION

There is a lack of normal grain coarsening behavior in certain RSPD materials following isothermal anneal heat treatments. This indicates that the energy necessary for grain boundary motion is greater than is generated by a reduction in grain boundary area. For similar reasons, the application of a temperature gradient to plasma sprayed Rene' 80 was unsuccessful in promoting grain boundary motion beyond that found after isothermal anneals.

Grain growth of RSPD materials can be achieved, however, by straining and annealing. The largest amount of grain growth occurs following a small but critical amount of deformation. The strain and anneal process has previously been successful in promoting grain growth in powder metals consolidated by extrusion (7,12). The small amount of deformation provides enough energy to nucleate a few recrystallized grains, and their subsequent growth results in large sizes.

Grains in Rene' 80, which grow on an average to 25 μm after an isothermal anneal, grow to 100-150 μm after a 3-6% critical strain and anneal. The six experimental alloys had grain sizes 25 μm or less after an isothermal anneal yet developed grains to 150-200 μm by the critical strain and anneal process. Alloy C2 grew the largest grains, averaging over 400 μm in diameter. This may be a result of a eutectic reaction, involving the carbide particles, that this alloy undergoes at temperatures only slightly above the anneal temperature. A reaction of this type could significantly affect the diffusion characteristics of the carbides and increase the grain boundary mobility. Alloy C1 after being critically strained and annealed grew grains that were only slightly larger than those developed by an isothermal anneal. The occurrence of a low temperature melting reaction, however, required a 70°C decrease in this alloys heat treating temperature. Hastelloy X had grain sizes that increased by an order of magnitude over the 50 μm size from an isothermal anneal following 2% deformation and a subsequent anneal.

TABLE 3

GRAIN GROWTH AND MECHANICAL PROPERTIES OF RENÉ 80

TENSILE TEST RESULTS

Alloy Preparation	Temperature (°C)	Grain Size (μm)	0.2 % Yield Stress (MPa)	Ultimate Tensile Strength (MPa)	Reduction In Area (%)
RSPD,	20	70	910	1280	8.3
2 h at 1220°C	850	100	705	772	3.9
1 h at 1240°C		(nonuniform)			
Cold Roll 5.0%	1000	80	425	432	2.9
1.5 h at 1250°C	1000 ⁽¹⁾	70	296	381	10.7
RSPD,	20	20	827	1330	17
2 h at 1250°C ⁽²⁾	850	20	524	723	12
	1000	20	186	213	9
As-Cast,	20	400-800	860	1030	7.0
Fully Heat Treated ⁽³⁾	850	400-800	560	750	23.0
	1000	400-800	<275	345	20.8

STRESS RUPTURE RESULTS

Conditions		Time to Failure (h)		(As-Cast, Fully, Heat Treated) ⁽¹⁾
Temperature (°C)	Stress (MPa)	RSPD ⁽⁴⁾	(RSPD, Isothermal Anneal 2 h at 1145°C, 4 h at 870°C) ⁽²⁾	
871	345	4.3	2.33 1.91 (at 262 MPa)	100
982	138	6.1	3.17 (at 117 MPa)	100

⁽¹⁾Additional 0.5 h at 1250°C during alloy preparation.

⁽²⁾M.R. Jackson

⁽³⁾Aerospace Structural Metals Handbook, for conventionally cast René 80

⁽⁴⁾2 h/1220°C, 1 h/1240°C, 5% cold rolling, 1.5 h/1250°C

TABLE 4

TENSILE BEHAVIOR OF EXPERIMENTAL ALLOYS
(Strain rate: 0.044/min)

	T(°C)	Full Heat Treatment ⁽¹⁾					Strain & Heat Treatment ⁽²⁾				
		YS(MPa)	UTS(MPa)	e_{ML}	e_f	RA	YS(MPa)	UTS(MPa)	e_{ML}	e_f	RA
C1	20	1103	1203	1.8	1.8	7.0	900	1390	18.5	18.7	16.6
	610	974	1176	2.8	2.8	5.4	800	1139	10.8	16.8	14.0
	760	647	688	1.2	4.0	3.1	600	645	2.8	6.8	6.0
	910	214	232	1.2	5.4	5.6	259	274	1.2	7.2	4.0
	1060	28	39	2.8	29.0	21.0	70	73	2.2	13.8	6.0
C2	20	596	963	28.0	36.0	45.0	273	714	50.5	54.8	34.4
	610	383	696	24.0	38.0	39.0	219	536	50.1	54.0	28.0
	760	369	379	7.2	22.0	22.0	232	376	13.1	53.7	34.7
	910	134	135	0.5	25.0	30.0	128	146	7.5	65.3	65.3
	1060	63	64	0.4	12.3	12.1	167	180	2.8	53.4	32.0
C3	20	272	352	3.0	3.0	8.6	299	735	55.4	64.1	41.3
	610	304	647	41.0	49.0	36.0	266	579	47.2	52.1	30.0
	760	389	444	4.0	26.0	22.0	297	403	7.1	48.4	33.3
	910	183	188	0.6	20.0	17.8	152	160	4.5	44.9	26.0
	1060	58	62	1.0	17.8	13.5	63	69	3.5	11.3	7.8
C4	20	446	906	28.0	34.0	36.0	347	808	40.2	48.2	37.9
	610	359	676	26.0	43.0	42.0	397	561	10.2	14.0	13.7
	760	314	382	7.8	58.0	45.0	No Test	—	—	—	—
	910	155	172	4.8	23.0	25.0	159	172	3.7	80.0	40.0
	1060	59	62	1.5	8.0	8.3	66	73	1.7	11.8	5.9
C5	20	787	1179	18.8	24.0	28.0	542	1006	22.3	23.8	20.7
	610	734	1016	14.2	22.0	26.0	541	856	20.1	32.1	29.4
	760	620	638	0.8	17.8	16.3	466	512	10.0	27.7	23.5
	910	130	132	0.4	30.0	30.0	124	134	15.7	69.2	39.2
	1060	54	55	4.5	31.0	28.0	46	51	16.9	28.2	18.0
C6	20	967	1265	9.7	9.7	10.7	829	946	2.1	2.1	2.7
	610	880	992	5.2	15.8	27.0	750	878	9.2	9.9	12.2
	760	592	615	1.2	19.2	23.0	562	589	5.6	15.1	14.0
	910	128	143	4.0	30.0	38.0	120	138	6.0	48.7	31.9
	1060	41	48	3.7	49.0	43.0	35	36	4.2	24.3	28.6

T —test temperature

YS —yield strength

UTS —ultimate tensile strength

 e_{ML} —strain at maximum load (%) e_f —strain at failure (%)

RA —reduction in area (%)

(1) 1 h/1220°C*, 4 h/900°C, 12 h/760°C, M.R. Jackson

(2) 1 h/1220°C*, cold roll 2–6%, 1 h/1220°C*, 4 h/900°C, 12 h/760°C

*except Alloy C1 which used 1150°C anneals

Note: All alloys deposited in EPI Ar-He plasma

Stress Rupture Properties in Air for Experimental Alloys

Alloy	Condition*	Test Temp. (°C)	Stress (MPa)	Life(h)	P(K,h)	Elong. (%)	R.in A. (%)
C1	1	610	827	3.1	13.1	3.4	5.9
	2	—	—	—	—	—	—
	1	760	310	1.0	20.7	3.0	3.2
	2	760	310	3.3	21.2	0.8	0.4
C2	3	610	483	14.0	13.7	10	12
	4	610	483	17.5	18.8	29	41
	3	760	193	4.1	21.3	15	14
	4	760	193	190.9	23.0	18	24
C3	3	760	193	26.9	22.1	13	12
	4	760	193	110.2	22.8	19	23
	3	910	48	11.5	24.9	51	32
	4	910	48	52.9	25.7	31	21
C4	3	910	48	31.5	25.4	27	27
	4	910	48	95.9	26.0	29	19
	3	1060	14	4.8	27.6	32	19
	4	1060	14	54.2	29.2	29	6.0
C5	3	760	193	58.3	22.5	4.1	6.6
	4	760	193	237.2	23.1	6.8	6.5
	3	910	48	41.4	25.6	35	28
	4	910	48	229.8	26.5	16	8.7
C6	3	610	483	572.6	20.1	4.5	7.4
	4	610	483	1143.9	20.4	(unloaded)	—
	3	760	193	81.6	22.6	14	13
	4	760	193	180.1	23.0	4.4	0

*Condition: 1 - 1 h/1150°C solution, M.R. Jackson
 2 - 1 h/1150°C, cold roll to critical strain, 1 h/1150°C
 3 - 1 h/1220°C, solution, M.R. Jackson
 4 - 1 h/1220°C, cold roll to critical strain, 1 h/1220°C
 (All had 4 h/900°C & 12 h/760°C final anneals)

The difference in the grain sizes of alloy C4 and Hastelloy X both before and after critical strain and anneal treatments is surprising since the alloys have basically the same chemistries. Alloy C4 (along with all the other alloys tested in this study except Hastelloy X) contains minor additions of Cb, Ti and Al. It appears that the lack of these major γ' , oxide and carbide forming elements in Hastelloy X resulted in much more mobile grain boundaries than are in the experimental alloys and Rene' 80. In addition, the evidence of grain growth through the individual pass layers after critically straining and annealing implies that the interfaces have good bonding and are not responsible for impeding grain boundary motion. It is more likely caused by solute atoms or phase(s) which can be abundant at these locations.

The smaller grain sizes developed as deformation increased beyond the critical strain regime are a result of the large number of nuclei forming throughout the lattice. This limits the extent each new grain can coarsen. The primary recrystallized grain size behavior of the alloy investigated in this study is typical of the effect of prior cold work on recrystallized grain size. Examining the microstructure produced after these large deformations and subsequent anneals revealed some large grains (over 100 μm) in Rene' 80, experimental alloys C4 and C5, and Hastelloy X. Secondary recrystallization resulted in these grains being significantly larger than the surrounding primary recrystallized grains.

Directional recrystallization of RSPD alloys, by a thermal gradient anneal, was not found to be successful in materials that demonstrated exaggerated grain growth during isothermal anneals. The conditions for critical strain annealing and secondary recrystallization, as demonstrated in this report, involve relatively small deformations. Post deposit treatments of these types are of interest since RSPD is meant to be a near net shape process.

Hot deformation processes produced microstructures which retained characteristics of the as-sprayed material treated isothermally at the working temperatures. Equiaxed grains, limited to 5-10 μm in diameter, developed in Rene' 80 specimens after 50% reduction in thickness at 1230°C. Similar sizes were observed in the experimental alloys and Hastelloy X. The 25 μm grain sizes produced by a subsequent anneal were typical of the structure developed following an isothermal anneal of unworked material. The results from forging operations coincide with the observations that grain growth was not enhanced by hot deformation.

The major mechanical property effects observed after an increase in grain size on RSPD material were a decrease in low temperature strength and elongation, an increase in high temperature strength, and an increase in stress rupture life. These effects were observed in both Rene' 80 and the experimental alloys, when critically strained and annealed material was compared to isothermally annealed material. The decrease in low temperature strength as grain size increases is predicted by the Hall-Petch relationship. The decreasing elongation is a result of less uniform slip as the grain size gets larger. The increase in high temperature strength and stress rupture life is expected with the decrease in grain boundary area.

The small decrease in strength at low temperatures compared to a large increase at high temperatures in Rene' 80 indicates that the amount of strengthening from grain boundaries is relatively small in this alloy. The experimental alloys, however, which show larger decreases in low temperature strength would appear to be more dependent on grain boundary strengthening. The increase in high temperature strength of alloy C2 after the critical strain and anneal process confirms the grain size effect in these alloys. The lack of overall agreement of the strength data is probably a result of the alloys having relatively low high temperature strength. The alloys do, however, concur with the trend based on the stress rupture results, increasing by nearly one Larson-Miller parameter with larger grain sizes.

The results clearly show that developing larger grains in RSPD Rene' 80 was sufficient to give the plasma sprayed material equal high temperature strength to that of the cast and fully heat treated material. The stress rupture life, however, appears to be more heavily dependent on grain size, and the RSPD material (80 μm grain diameter) is 2-3 Larson Miller parameters below the cast material (400-800 μm grain diameters).

CONCLUSIONS

An evaluation of grain growth resulting from a broad range of post deposition treatments has been conducted on a number of Ni and Ni-Fe base alloys, along with the variation in tensile and stress rupture properties. The principle findings and conclusions are:

- (1) The most successful method for achieving grain growth in RSPD material was straining with a subsequent recrystallization anneal. Grains were increased, to sizes approaching those typically found in cast materials, after a small but critical amount of cold rolling followed by an anneal treatment.
- (2) Grain growth was not increased by a thermal gradient anneal beyond the 25-50 μm size developed during an isothermal anneal.

- (3) Directional recrystallized of RSPD alloys, by a thermal gradient anneal, was not achieved in materials that demonstrated exaggerated grain growth during isothermal anneals.
- (4) Hot deformation processing was ineffective in promoting grain growth. Hot rolled specimens have microstructures characteristic of the as-sprayed material: unmelted prior particle boundaries and a fine grain size. Subsequent heat treatments increase these grains to the size found after isothermally annealing unworked material.
- (5) Coarsening the grain sizes of RSPD materials by critically straining and annealing resulted in improved high temperature mechanical properties. The extent to which this affected the tensile properties of an alloy was dependent upon the materials inherent high temperature strength and the relative importance of grain boundary strengthening.
- (6) Rene' 80 material that was plasma sprayed before critically straining and annealing had strengths that were equal to or greater than the cast and fully heat treated material.
- (7) Carbides or oxides formed after additions of certain elements, appear to be possible impediments to grain growth. Thus, the alloy compositions of interest for RSPD are such that some resist grain growth during annealing.
- (8) Some alloys show a tendency for secondary recrystallization during annealing following cold rolling. Secondary grains grew an order of magnitude larger than the uncoarsened matrix grains, but secondary recrystallization was never complete.

ACKNOWLEDGEMENTS

This program has been funded by DARPA (Contract No. F33615-81-C-5156), through the offices of Lt. Col. L.A. Jacobson, with H.L. Gegel of AFML serving as technical monitor. The authors would like to thank S. Rutkowski who prepared the plasma sprayed deposits along with T. Douglas, R. Laing, and P. Martiniano who did the rolling operations. In addition we would like to thank A. Ritter who identified the carbide particles by transmission electron microscopy.

REFERENCES

- (1) T.A. Roseberry and F.W. Boulger, "A Plasma Flame Spray Handbook", Report No. MT-043, Naval Sea Systems Command, Dept. of the Navy, 1977, March.
- (2) W.E. Ballard, Metal Spraying and Sprayed Metal, Charles Griffin and Company, London, 1948.
- (3) M.R. Jackson, J.R. Rairden, J.S. Smith, and R.W. Smith, "Production of Metallurgical Structures by Rapid Solidification Plasma Deposition", J. of Metals, 1981, November, 23.
- (4) D.J. Looft and E.C. van Reuth, "Rapid Solidification Processing: An Overview", Proc. of the Int. Conf. on Rapid Solidification Processing, Reston, Va., 1977, 1.
- (5) R.J. Patterson, II, A.R. Cox, and E.C. van Reuth, "Rapid Solidification Rate Processing and Application to Turbine Engine Materials", J. of Metals, 1980, September, 34.
- (6) L. Winberg and M. Dahlen, "Recrystallization in a Powder Metallurgy Nickel-Base Superalloy", J. of Mat. Sci., 1978, 13, 2365.
- (7) M. Dahlen and L. Winberg, "Grain Coarsening of PM Nickel-Base Superalloy by Critical Strain Annealing", Metal Sci., 1979, 13, 3 and 4, 163.
- (8) W.G. Burgers, "Principles of Recrystallization", in The Art and Science of Growing Crystals, J.J. Gilman ed., J. Wiley and Sons, NY, 1963, 416.
- (9) K.T. Aust, "Large Crystals Grown by Recrystallization", in The Art and Science of Growing Crystals, J.J. Gilman ed., J. Wiley and Sons, NY, 1963, 452.
- (10) E.W. Ross, "Rene' 80: A Cast Turbine Blade Alloy", Metal Progress, 1971, March, 93.
- (11) M.R. Jackson, "RSPD for Fabrication of Advanced Aircraft Gas Turbine Components", P.A. Siemens ed., DARPA Contract F33615-81-C-5156, Interim Report 1982, January.
- (12) M. Dahlen and H. Fischmeister, "Grain Size Control in PM Superalloys", European Symp. on PM VI, Stockholm, Sweden, 1978, June 149.

Ni-Mo-B ALLOYS: METALLIC GLASS TO DUCTILE CRYSTALLINE SOLID

S. K. Das, L. A. Davis, J. R. Y. Wang* and D. Kapoor*

Allied Corporation
Materials Laboratory
Corporate R & D
P.O. Box 1021R
Morristown, NJ 07960

ABSTRACT

The microstructures and mechanical properties of a series of rapidly solidified Ni-Mo-B alloys, containing from 20 to 30 at%Mo and 10 to 20 at%B, have been investigated using analytical electron microscopy and hot hardness testing. The as-cast metallic glasses are quite brittle and can be readily pulverized to powder and consolidated into bulk crystalline solids by hot isostatic pressing (HIP) or other means. The consolidated bulk samples show fine dispersions of borides (Mo_2NiB_2) which contribute to the strengths and hardnesses of the materials. Mechanical behavior is strongly influenced, also, however, by the matrix composition; when the Mo/Ni ratio in the matrix exceeds 0.25 the hot hardness is enhanced, as the matrix is strengthened through the presence of ordered phases (Ni_4Mo , Ni_3Mo and Ni_2Mo depending on composition and heat treatment). When Mo/Ni \leq 0.25 hot hardness is reduced, even when the B content is as high as 20 at%. Concurrently, room temperature toughness is enhanced in the absence of ordered phases.

INTRODUCTION

The formation of metallic glasses by rapid solidification processing and their application as magnetic materials is now well known [1]. To date, however, metallic glasses have found little application as structural materials [2]. In contrast rapid quenching of crystalline alloys for structural applications has become a field of considerable activity [3]. The goal, usually, is to produce consolidated bodies from powder/particulate, which, itself is microcrystalline in the as quenched state. Relatively little attention has been given to structural applications of crystalline alloys obtained by devitrification from the glassy state. Recent work at Allied Corporation has shown that devitrified metallic glasses of certain compositions, when consolidated into bulk compacts, exhibit outstanding properties [4]. As an example, in the present paper we report certain unique microstructural features of a class of Ni-Mo-B alloys which have attractive strength, hot hardness and wear resistance properties.

EXPERIMENTAL

The compositions of the alloys investigated in the present study are listed in Table 1. The alloys were rapidly quenched from the melt into continuous ribbons using either jet casting or the Planar Flow Casting (PFC) process [2]. The recrystallization temperatures and the incipient melting points of the alloys were determined from differential scanning calorimetry and differential thermal analysis of the as cast ribbons and are also listed in Table 1. The ribbons were consolidated into bulk compacts by pulverizing to -35 mesh powder and subsequent HIPping at 1100°C and a pressure of 15,000 psi. Thin foils suitable for transmission electron microscopy were prepared by a combination of electrolytic jet thinning and ion milling. The foils were examined in a Phillips EM400T scanning transmission electron microscope (STEM) equipped with an energy dispersive x-ray analytical system.

* Consolidated Metal Products Department, Allied Technologies Company, Allied Corporation.

RESULTS and DISCUSSION

The as cast ribbons were examined by x-ray diffraction analysis and appeared to be amorphous for all the compositions listed in Table 1. However, transmission electron microscopy revealed the presence of extremely small crystallites in jet cast ribbons of alloys containing 10% B (Fig. 1).

Table 1. Nominal compositions of the Ni-Mo-B alloys.

ALLOY NO.	COMPOSITION (atomic%)				RECRYSTALLIZATION TEMPERATURE (°C)	INCIPIENT MELTING POINT (°C)
	Ni	Mo	Fe	B		
1	54	26	-	20	-	-
2	49	31	-	20	561	1235
3	62	23	-	15	-	1245
4	60	30	-	10	574	1238
5	56.5	23.5	10	10	521	1250
6	66.5	23.5	-	10	535	1235

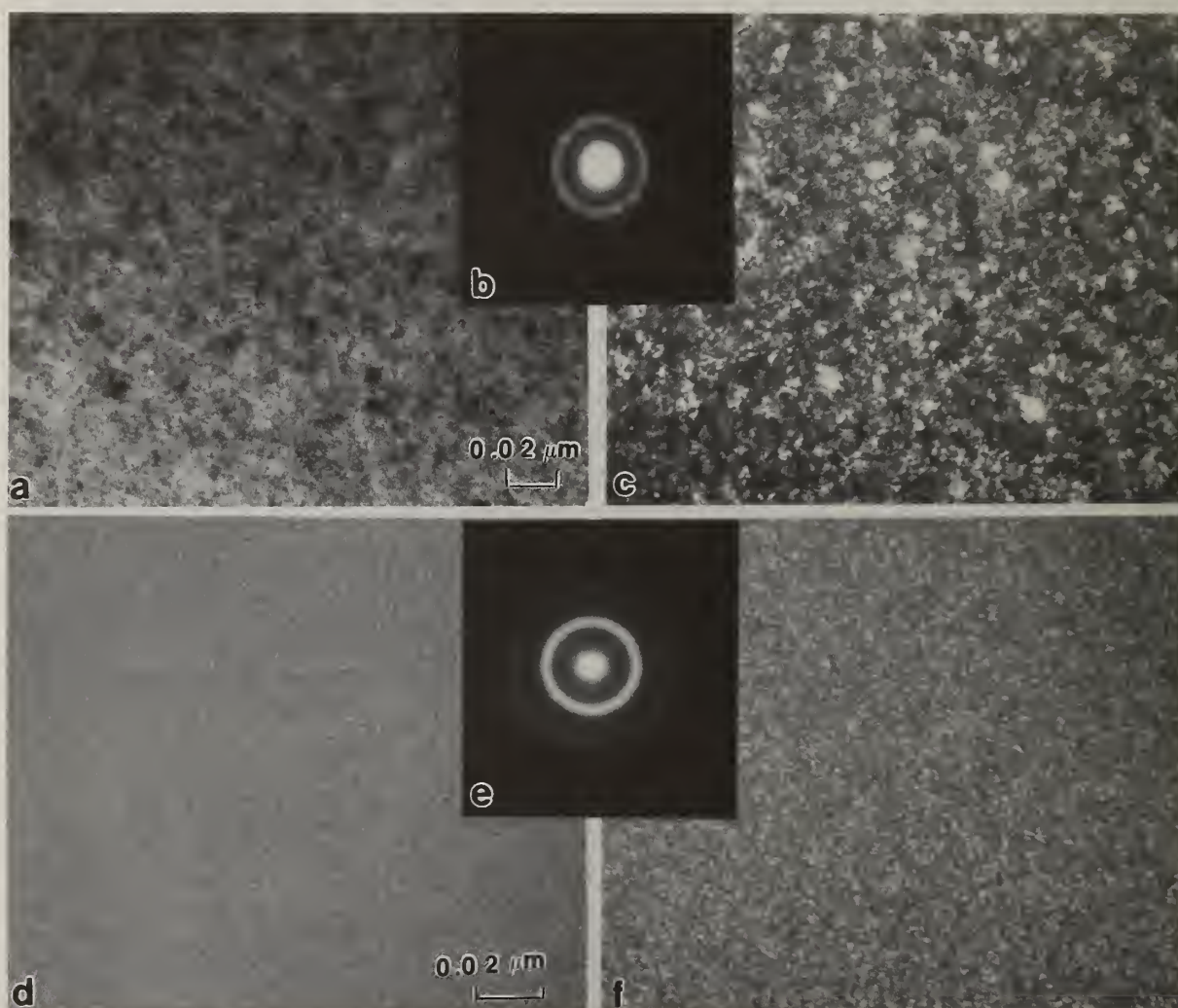


Fig. 1 Transmission electron micrographs of as cast ribbons of $\text{Ni}_{60}\text{Mo}_{30}\text{B}_{10}$ alloy using (a) - (c) jet casting and (d) - (f) the Planar Flow Casting technique; (a) and (d) are bright field micrographs, (b) and (e) are corresponding microdiffraction patterns and (c) and (f) are corresponding dark field micrographs.

The dark patches seen in Fig. 1(a) are indeed crystallites as evidenced by the microdiffraction pattern (Fig. 1b) and the dark field micrograph (Fig. 1c). The same alloy when cast using the PFC process does not show any detectable crystallites (Fig. 1d). No discrete spots can be seen in the microdiffraction pattern (Fig. 1e). The spotty contrast seen in the dark field micrograph (Fig. 1f) taken using the amorphous ring, can result from statistical density fluctuations even in a completely amorphous matrix [5]. These results show that a somewhat higher cooling rate can be obtained in the PFC process as compared to jet casting. The microstructures of the as cast ribbons of the alloys containing 15 and 20% B are similar to those shown in Fig. 1(d) - 1(f). Whether small crystallites are present or not the as cast ribbons are brittle and readily pulverized into powder and consolidated to full density by HIPping using the conditions specified above.

A typical microstructure of as HIPped $\text{Ni}_{54}\text{Mo}_{26}\text{B}_{20}$ alloy is shown in Fig. 2. It consists of a fine grained nickel-base matrix together with a dispersion of boride platelets (some are marked B in Fig. 2a). The boride phase was identified by electron diffraction (Fig. 2b) and x-ray diffraction to be orthorhombic Mo_2NiB_2 , which is isostructural with Mo_2CoB_2 . The chemistry was further confirmed by quantitative x-ray microanalysis (Fig. 2c) which gave a Ni:Mo ratio of $\sim 0.6:1$ in the boride particle. This ratio was found to hold for most of the alloys studied (see Table 2); the alloy containing 10% Fe was an exception in that a small amount of Fe substituted for Ni. It was found, in addition, that the matrix composition varied with the alloy-composition (Table 2). Also alloys that had a Mo:Ni ratio ≥ 0.25 in the matrix, exhibited ordering reactions in the matrix, as shown in Fig. 3 for $\text{Ni}_{60}\text{Mo}_{30}\text{B}_{10}$ and $\text{Ni}_{49}\text{Mo}_{31}\text{B}_{20}$ alloys. In the sample quenched in iced brine from 1100°C the matrix exhibits short range order (s.r.o.) as seen in the $[100]$ diffraction pattern (Fig. 3b) where diffuse scattering is observed at $\{1\frac{1}{2}0\}$ positions. The presence of $\{1\frac{1}{2}0\}$ s.r.o. diffuse scattering has been observed in binary Ni-Mo alloys containing 20 - 25at% Mo [6,7]. Upon annealing at 700°C fine ordered domains (50-100Å) can be identified in the matrix as shown in the dark field micrograph in Fig. 3(c). From the electron diffraction pattern (Fig. 3d) the domains can be identified as Ni_4Mo . In addition to the reflections from two variants of Ni_4Mo there are some additional spots (marked by the arrow in the diffraction pattern in Fig. 3d), which are due to the presence of a small volume fraction of Ni_2Mo phase; this phase has been observed as a metastable phase during early stages of ordering of binary Ni-Mo alloys [8]. On prolonged annealing metastable Ni_2Mo phase disappears and Ni_4Mo domains grow as shown in Figs. 3(e) and 3(f) for $\text{Ni}_{49}\text{Mo}_{31}\text{B}_{20}$ alloy. The same samples annealed at 800 and 850°C for 5-50 hours show fully ordered equilibrium Ni_3Mo phase (not shown here).

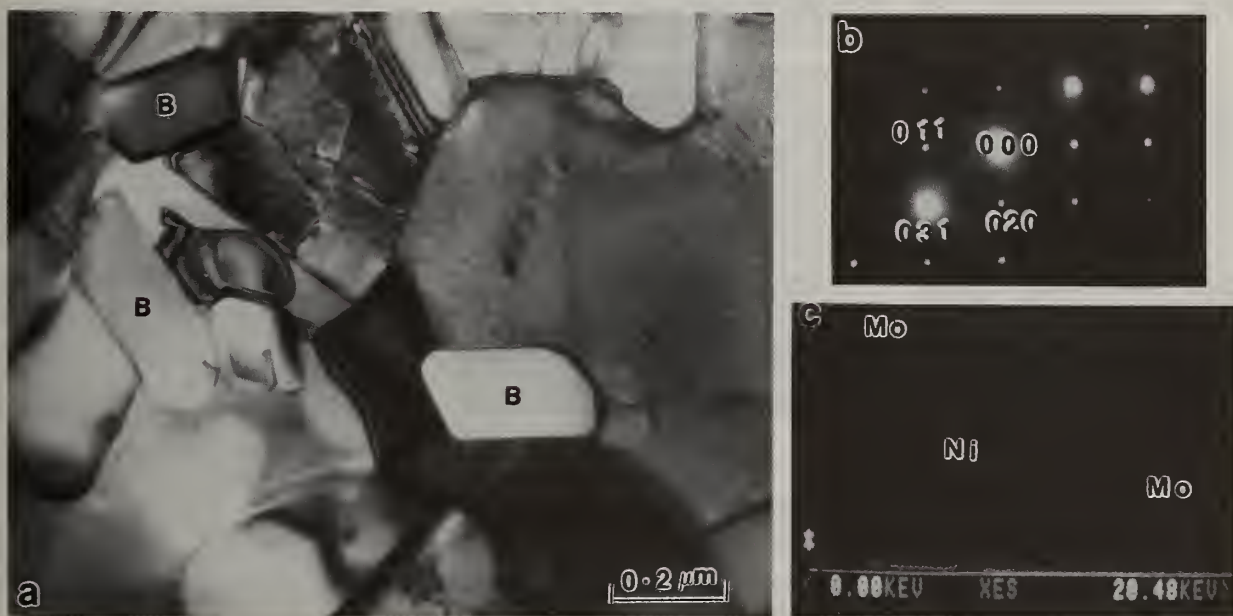


Fig. 2 Bulk microstructure of as HIPped $\text{Ni}_{54}\text{Mo}_{26}\text{B}_{20}$ alloy. (a) Bright field TEM, (b) selected area diffraction pattern and (c) x-ray microanalysis of one of the boride particles.

Table 2. X-ray Microanalysis of Ni-Mo-B Alloys

ALLOY NO.	NOMINAL BULK COMPOSITION (Atomic%)	MICROANALYSIS OF		ORDERED PHASES PRESENT IN MATRIX
		MATRIX Ni:Mo:Fe	BORIDE Ni:Mo:Fe	
1	Ni ₅₄ Mo ₂₆ B ₂₀	1:0.2:-	0.6:1:-	No
2	Ni ₄₉ Mo ₃₁ B ₂₀	1:0.27:-	0.6:1:-	Yes
3	Ni ₆₂ Mo ₂₃ B ₁₅	1:0.2:-	0.6:1:-	No
4	Ni ₆₀ Mo ₃₀ B ₁₀	1:0.3:-	0.6:1:-	Yes
5	Ni _{56.5} Mo _{23.5} Fe ₁₀ B ₁₀	1:0.28:0.2	0.55:1:0.08	No



Fig. 3 Effect of heat treatment on microstructure of (a) - (d) Ni₆₀Mo₃₀B₁₀ alloy and (e) - (f) Ni₄₉Mo₃₁B₂₀ alloy. (a) Bright field TEM of sample quenched in iced brine from 1100°C, (b) [100] SAD of matrix in (a), (c) Dark field using a Ni₄Mo spot in (d) from a sample aged at 700°C for 20h, (d) [100] SAD of matrix in (c), (e) Dark field of Ni₄Mo spot in (f) from a sample aged at 700°C for 50h, (f) [100] SAD of matrix in (e).

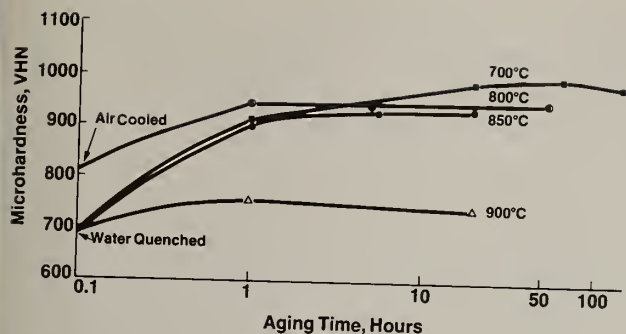


Fig. 4 Isothermal aging curves for $\text{Ni}_{60}\text{Mo}_{30}\text{B}_{10}$ alloy. The samples were annealed at 1100°C for 1 hr prior to aging. Hardness measurements made at 23°C .

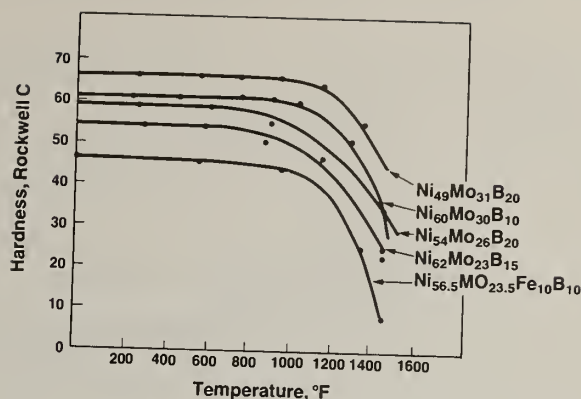


Fig. 5 Hot hardness of as HIPped Ni-Mo-B alloys.

These microstructural observations on matrix ordering correlate well with the mechanical properties of these Ni-Mo-B alloys. Figure 4 shows typical isothermal aging curves for the alloy $\text{Ni}_{60}\text{Mo}_{30}\text{B}_{10}$ which exhibits ordering reaction in the matrix. The degree of ordering in the matrix increases with increasing time as can be seen by the increase in microhardness with increasing annealing time for temperatures up to 850°C . On annealing at 900°C the matrix disorders and the microstructure is similar to the one shown in Fig. 3(a) which gives a lower hardness (Fig. 4). Hot hardness measurements show that for the same boron content the alloys exhibiting matrix ordering are harder than those that do not have an ordered matrix (Fig. 5). For example, the alloy $\text{Ni}_{49}\text{Mo}_{31}\text{B}_{20}$, that shows the ordered Ni_4Mo phase in the matrix, has higher hot hardness than the alloy $\text{Ni}_{54}\text{Mo}_{26}\text{B}_{20}$ which does not show long range ordering, even though these alloys have the same boron content and hence a similar volume fraction of borides. In addition to having good hot hardness the bulk solids made from these alloys are quite ductile.

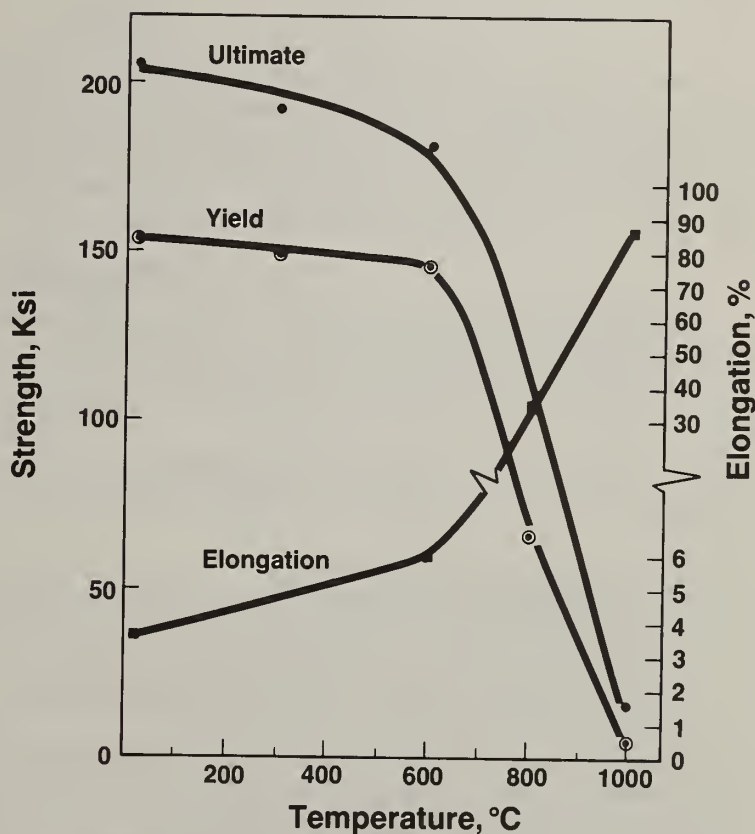


Fig. 6 Tensile properties of as HIPped $\text{Ni}_{56.5}\text{Fe}_{10}\text{Mo}_{23.5}\text{-B}_{10}$ alloy as a function of temperature.

Figure 6 shows hot tensile properties for the alloy $\text{Ni}_{56.5}\text{Mo}_{23.5}\text{Fe}_{10}\text{B}_{10}$. At higher temperature ($> 800^\circ\text{C}$) the material becomes superplastic due to its extremely fine grain size. This alloy has a room temperature transverse rupture strength of 490 Ksi and charpy impact (unnotched) strength of 50 ft. - lbs. The alloys that exhibit ordered phases have somewhat lower ductility than the ones that do not. However, by proper choice of heat treatment the degree of ordering in the matrix and the domain size can be varied, which in turn affects the toughness. The effect of such heat treatments on impact toughness is shown in Table 3. The as HIPped material is fully ordered due to the slow cooling from the HIPping temperature and exhibits an impact strength of only 4.0 ft.-lbs. On quenching from 1100°C the matrix is short range ordered (Fig. 3a) and the impact strength increases to 21.5 ft.-lbs. (Table 3).

Table 3. Effect of Heat Treatment on Room Temperature Impact Strength (unnotched) of Ni₆₀Mo₃₀B₁₀ Alloy.

No.	HEAT TREATMENT	IMPACT STRENGTH (ft-lb.)	ROOM TEMPERATURE HARDNESS, Rc
1	As HIPped	4.0	62
2	Annealed 1100°C/2h→ quenched in iced brine	21.5	53
3	As in 2) + aged at 600°C for 1h	11.0	57
4	As in 2) + aged at 650°C for 1h	10.0	56
5	As in 2) + aged at 700°C for 50h	4.0	61

In addition to the good mechanical strength the fine dispersion of borides in a fine grained matrix gives excellent wear resistance properties, a discussion of which is beyond the scope of this paper.

SUMMARY

The results presented here show that rapidly solidified Ni-Mo-B metallic glasses can be fabricated into bulk crystalline solids with useful engineering properties, e.g. high tensile strength, and high hot hardness. These properties are derived from their unique microstructural features such as fine boride dispersions with good high temperature stability and the presence of ordered phases in a fine grained matrix. This class of alloys has great promise for use as hot working tools and dies and in other wear resistance applications.

ACKNOWLEDGEMENTS

The authors are grateful to Ms. E. Musso for her experimental assistance and Mr. R. St. Amand for generating some of the mechanical property data.

REFERENCES

1. L. A. Davis and R. Hasegawa, Metallurgical Treatises, p. 301, Conference Proceedings, eds. J. K. Tien and J. F. Elliot, The Metallurgical Society of AIME, Warrendale, Pennsylvania, (1981).
2. L. A. Davis, N. J. DeCristofaro, C. H. Smith, "Metallic Glasses: Science and Technology", p. 1, Vol. 1, Conference Proceedings, eds. C. Hargitai, I. Bakanyi and T. Kemeny, Central Res. Inst. for Physics - Budapest (1981).
3. e.g. Rapid Solidification Processing, Principles and Technologies, II, eds. R. Mehrabian, B. H. Kear and M. Cohen, Claitor's Publishing Division, Baton Rouge, Louisiana (1980).
4. R. Ray, Proceedings of 4th International Conference on Rapidly Quenched Metals, p. 1515, eds. T. Masumoto and K. Suzuki, The Japan Institute of Metals, Sendai, Japan (1982).
5. J. M. Cowley, Proc. 13th Annual EMSA Meeting, p. 560, ed. C. J. Areeanaux, Claitor's Publishing Division, Baton Rouge, Louisiana (1972).
6. P. R. Okamoto and G. Thomas, Acta Met. 19, 825 (1971).
7. S. K. Das, P. R. Okamoto, P. M. J. Fisher and G. Thomas, Acta Met. 21, 913 (1973).
8. S. K. Das and G. Thomas, Phys. Stat. Sol (a) 21, 177 (1974).

MICROSTRUCTURAL MODIFICATION OF ALUMINUM-SILICON ALLOY
POWDERS DURING DYNAMIC CONSOLIDATION*

W. H. Gourdin

Lawrence Livermore National Laboratory
Livermore, CA 94550

J. E. Smugeresky

Sandia National Laboratories, Livermore
Livermore, CA 94550

ABSTRACT

We describe the preliminary results of a study of the dynamic consolidation of a rapidly solidified aluminum-6% silicon alloy powder. The distinctive microstructure of this alloy, which consists of a dispersion of silicon precipitates at the boundaries of essentially pure aluminum grains, provides an excellent grid against which to observe the changes induced by shock compaction. Examination of recovered specimens, shocked with either explosives or high velocity projectiles, shows that at low stress, high density is achieved without substantial interparticle bonding, and the microstructure is essentially that of the starting powder. For stresses between 1.7 and 2.6 GPa we observe increasing compact integrity, and the appearance of regions of altered microstructure at the interfaces between powder particles. Above 4.0 GPa, such modified material is a distinctive feature of the microstructure, and compacts are well bonded. Increasing the stress serves not so much to increase the density as to increase the amount of energy deposited in the specimen. Bonding is the result of the local deposition of energy at particle interfaces during the passage of the shock. This energy may be calculated from the measured Hugoniot (shock compression) curve of the powder. We suggest that through proper choice of stress level, structurally sound compacts can be formed with limited modification of the powder microstructure.

Introduction

Recent studies have shown that shock waves can be used to densify metal [1-4] and ceramic [5-8] powders at high stress in times of the order of microseconds. Such consolidation avoids the thermally activated changes which accompany conventional thermo-mechanical processing. As such, the technique is ideally suited to the processing of rapidly solidified metal powders which possess unique or metastable microstructures.[9]

In this paper, we report the preliminary results of a study of the dynamic consolidation of a rapidly solidified aluminum-6% silicon alloy powder. Our observations suggest that the bonding of consolidated material is a result of energy deposition at powder particle interfaces, which produces localized melting and rapid resolidification. The amount of energy deposited can be determined from the measured Hugoniot of the powder. Through proper choice of stress level, structurally sound compacts can be formed with limited modification of the initial powder microstructure.

Experimental

The as-received, ultrasonically gas atomized Al + 6% Si powder[†] was put through a 60 mesh sieve to remove very coarse material. The properties of the resulting -250 μ m powder are given in Table 1.

*This work was supported in part by the Army Research Office and performed under the auspices of the U.S. Department of Energy by the Lawrence Livermore National Laboratory under contract No. W-7405-Eng-48.

[†]Prepared by P. Domalavage and N. J. Grant of MIT.

Table 1

Al + 6% Si Ultrasonically Gas Atomized Powder: Characteristics

Packing density: 1.78 gm/cc
Theoretical density: 2.691 gm/cc

Specific area: 1450 cm²/gm
Eutectic temperature, T_m : 577°C

Size distribution: % Less than size	Size (μ)
100	250
75	70
50	34
25	23

The size distribution was determined using standard sieve analysis and the surface area was measured by the BET method. The microstructure, shown in Figure 1, is cellular with silicon precipitates at cell boundaries. A eutectic structure is also found in some particles. Lattice parameter analysis shows the aluminum matrix to be essentially pure. We have found no evidence for supersaturation within individual particles. However, splat caps (Figures 1, 5) at the surface of some particles show no precipitation, even though electron microprobe analysis shows approximately the same average Si content as the phase-segregated particle. This suggests that these regions may be supersaturated with respect to silicon, presumably because they cooled more rapidly than the particles themselves. As discussed below, thermally modified regions observed following dynamic consolidation have a microstructure similar to that of these splat caps.

Specimens were compacted using both high explosives and high velocity projectiles. In all cases, the geometry was planar, ensuring that passage of at least the first shock occurred under conditions of one-dimensional strain. The compaction assembly used in the gas gun is shown schematically in Figure 2. Impact of the aluminum projectile at speeds of 200-750 meters/sec generates a shock which propagates through the powder. Carbon piezo-resistive sensors, placed at the front and rear of the powder, were used in the determination of the Hugoniot. A massive stainless compaction chamber was used to contain the sample for later recovery.

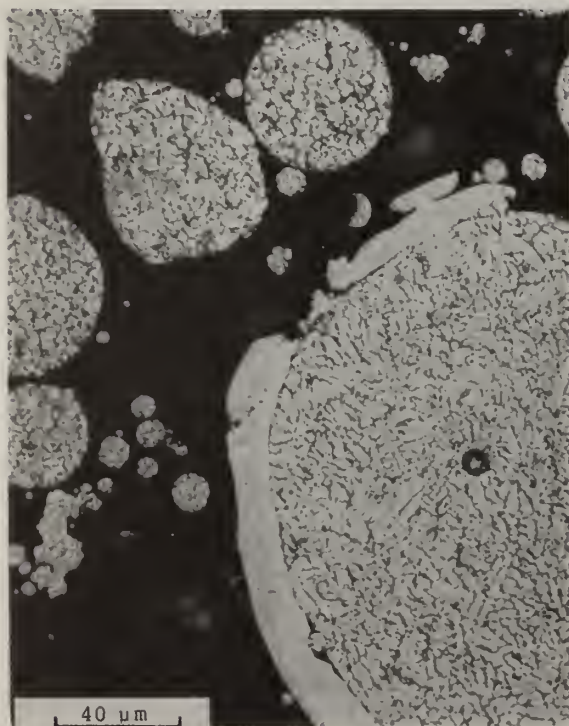


Figure 1. Microstructure of the as-received Al + 6% Si ultrasonically gas atomized powder. Note the "splat cap" on the larger particle.

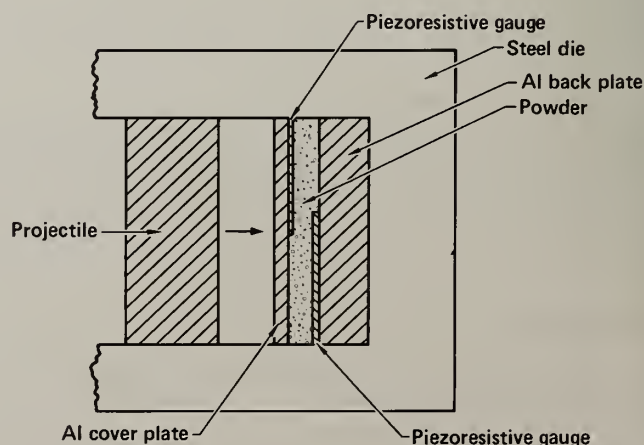


Figure 2. Schematic illustration of the assembly used in gas gun experiments.

The fixture used in explosive experiments is shown in Figure 3. A plane wave lens, 5.6 cm in diameter, was used to generate a plane detonation wave in the explosive. This impinged on a copper cover plate, which transmitted a shock into the powder, contained in a massive mild steel block. The stress delivered to the copper cover was measured for each of three different explosives, PETN 0.88 gm/cc, PETN 0.95 gm/cc and HMX 1.1-1.2 gm/cc. These stresses are in good agreement with those calculated from the equations of state for these explosives.[10,11] The stress delivered to the powder is calculated from the known stress in the copper.

Results

In this paper, we consider several specific experiments, spanning 1.3-4.0 GPa, which are representative of a range of powder response and compact structure. The details of these experiments are summarized in Table 2, and their position on the powder Hugoniot is indicated in Figure 4.

Low Stresses

The microstructure of experiment 71 (1.25 GPa) is shown in Figure 5. The overall microstructure is essentially that of the starting powder and the compact has little strength despite its high density (Table 2). We find no evidence of structural modification from the shock consolidation, other than material flow.

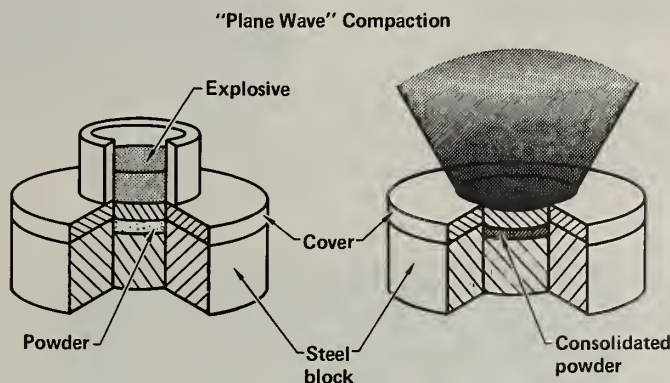


Figure 3. Plane wave compaction using explosives.

Table 2

Al + 6% Si Dynamic Compaction Experiments

Expt.	Type	Stress(GPa)*	Final Density [†]	E(10 ⁹ erg/gm)	T _{av} (°C)	Comments
71	Gun	1.25	98%	0.95	90	No bonding Al proj., 527 m/sec
95	Gun	1.65	99.6	1.51	144	Al proj., 660 m/s
7P	Expl.	1.8	97	1.56	148	PETN, 0.88 gm/cc
94	Gun	2.0	100	1.92	183	Al proj., 754 m/s
11P	Expl.	2.6	98	2.47	235	PETN, 0.95 gm/cc
15P	Expl.	4.0	98	3.96	377	HMX 1.1-1.2 m/cc Well bonded compact

*Stress of the first shock in the powder.

[†]Mercury porosimeter.

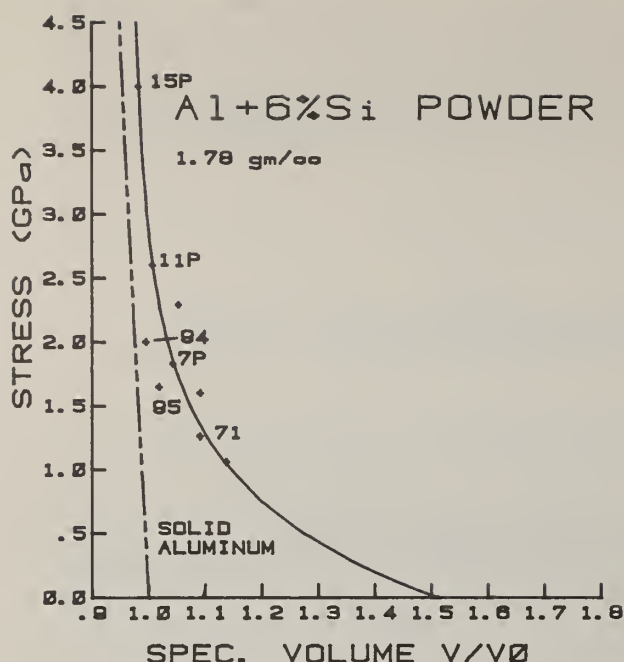


Figure 4. Stress-volume Hugoniot measured for the Al + 6% Si powder. Stresses for the explosive experiments were determined from the known stresses in the copper cover plate.

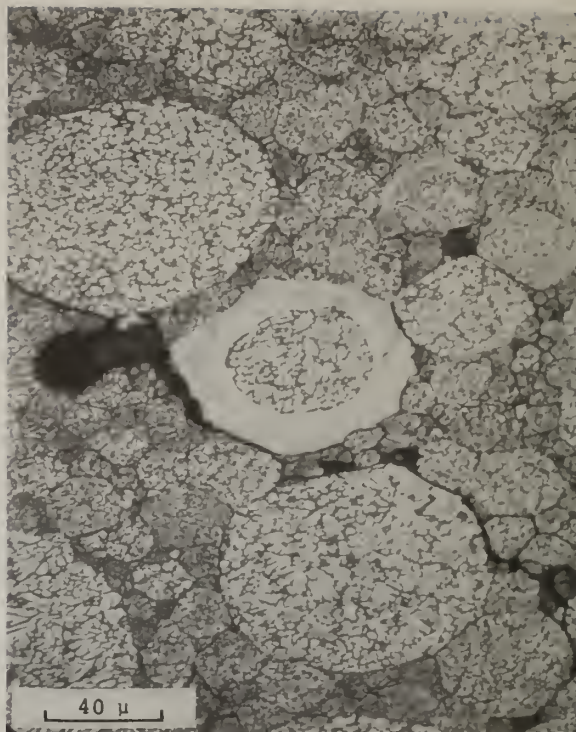


Figure 5. Microstructure of gas gun experiment 71. Note the residual splat cap surrounding a particle in the center of the photograph.

The featureless region surrounding one grain in Figure 5 is a splat cap, found in the starting powder. Numerous cracks in the sample result from tensile waves generated during release to ambient pressure.

Intermediate Stress

Between 1.7-1.8 GPa (Figure 6a) and 2.6 GPa (Figure 6b) regions of modified microstructure appear at particle interfaces in increasing numbers. Although most of specimens 94, 95 and 7P resemble Figure 5, some particle interfaces have the structure shown in Figure 6. The featureless areas bear a strong resemblance to the splat caps mentioned above, but their turbulent appearance is in marked contrast to the structure of Figure 5. Some fine precipitates are visible in the interfacial region, but the general appearance and the presence of unaltered surrounding grains suggests that the material has undergone local thermal modification. Smaller powder particles are no longer distinct. The compacts themselves become increasingly well bonded in this stress range, and can be handled without difficulty.

High Stress

For stresses ≥ 4.0 GPa (15P) considerable modification of the microstructure is evident, as shown in Figure 7. Altered material now forms a nearly continuous phase between and around powder particles and only the larger particles retain a semblance of their original microstructure. Modified regions show a dispersion of fine precipitates and a generally coarser structure than at intermediate stresses (Figure 6). Some areas show severe deformation. Despite large ruptures resulting from late-time distortion of the compaction fixture, sample 15P could be broken only with difficulty.

Discussion

The contrast with the original powder microstructure as well as the similarity to the splat caps suggests that the modified microstructures are a result of thermal alteration which occurs during the passage of the shock wave. Such modification is apparently local, occurring primarily at

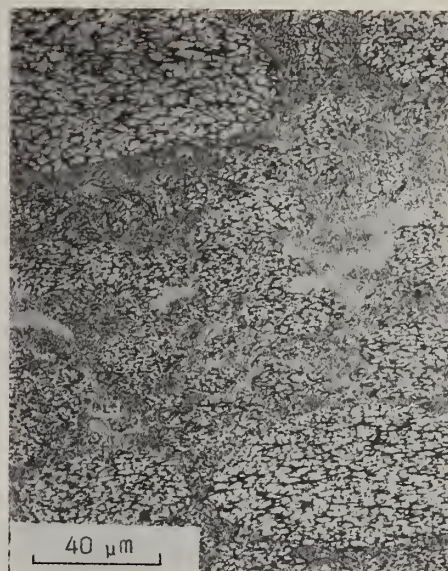
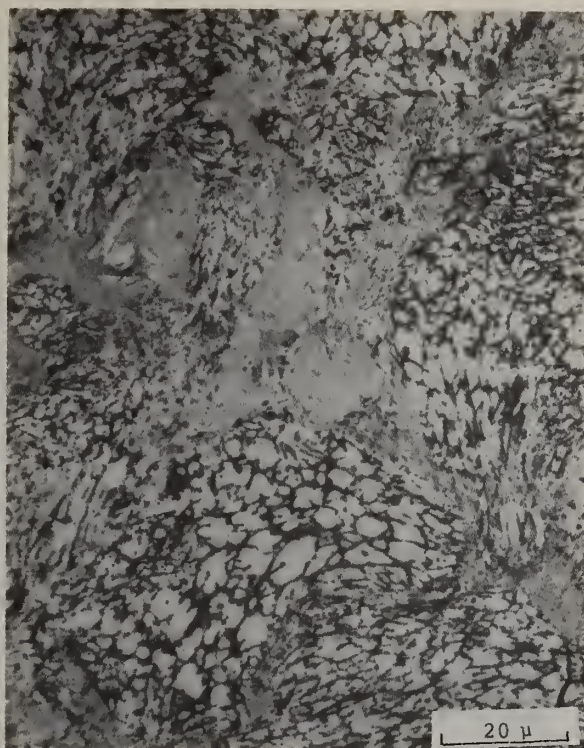


Figure 6. Microstructures of compacts formed in the intermediate stress region, 1.7-2.6 GPa: (a) 7P, formed with PETN explosive, 0.88 gm/cc; (b) 11P, formed with PETN, 0.95 gm/cc.

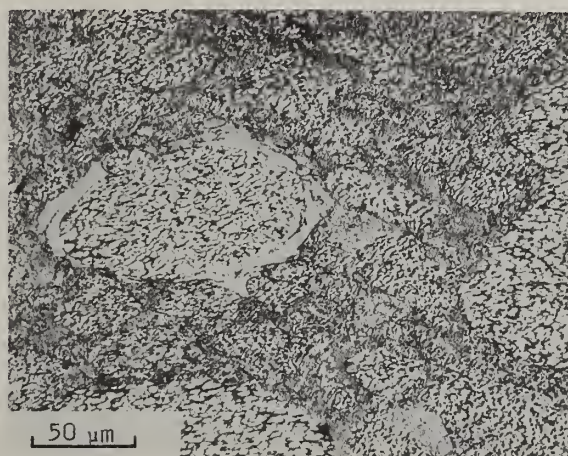


Figure 7. Microstructure of compact 15P, formed at 4.0 GPa using HMX explosive, 1.1 gm/cc.

powder particle interfaces. If the observed effects are indeed thermal, the energy deposited into the powder by the shock is of particular interest. From the Hugoniot of Figure 4, we can estimate that the density behind the first shock is close to solid in all experiments. Subsequent shocks deposit substantially less energy into the compact. Under such circumstances the energy deposited in the powder is just:

$$E = E_s - E_r \quad (1)$$

where E_s is the energy of the initial shock,

$$E_s = (1/2) P (V_0 - V) \quad (2)$$

and E_r is the energy regained upon release. Because the powder is close to solid density, E_r is generally small when compared with E_s , but may be estimated from the Hugoniot of solid aluminum. The approximate energies E , for each of the experiments shown in Figure 4, are collected in Table 2. Apparently energies in excess of $\sim 2 \times 10^9$ ergs/gm are required to produce the observed microstructural changes. This is significantly less than the energy required to heat and melt the entire mass, $\sim 9 \times 10^9$ ergs/gm, and the average temperature rise (Table 2) is substantially less than the eutectic, T_m (Table 1). However, if we imagine that this energy is deposited primarily through the particle surfaces, as a result, for example, of frictional heating as the particles deform around each other, the surface temperature can easily exceed T_m , producing a layer of molten material at the interface. A simple model for calculating the surface temperature of a typical powder particle has been recently developed and has been found to provide a satisfactory explanation of local microstructural changes observed in 4330V steel compacts.[12] Application of this model to the Al + 6% Si powder studied here shows that surface temperatures are expected to exceed T_m at a stress of 2.25 GPa, for which $E = 1.96 \times 10^9$ ergs/gm. These values define a critical state, above which interfacial melting begins. The correspondence between our observations and the results of the model calculation suggest that microstructural changes and bonding in the compacts are due primarily to localized melting followed by rapid resolidification. If the molten layer is thin, we can expect cooling to be rapid, much like a splat cap. As the energy input increases, the average temperature rises (Table 2), more material will melt and the cooling rate will decrease. The fine precipitates and generally coarser structure of sample 15P relative to 11P may reflect this.

The surface temperature achieved during the passage of the shock wave depends not only on the thermal properties of the material, but upon the characteristics of the powder as well.[12] Different powders, even of the same material, will, in general, begin to show interparticle melting at different stress levels. Similarly, at a given stress level, the final density of different powders may differ. Density and bonding are thus separate, though related, issues in dynamic consolidation. One can achieve high density in the absence of bonding, as demonstrated by the microstructure of shot 71 (Figure 5). However, above a critical value, a stress can be chosen so as to obtain both high density and adequate bonding in a compact while minimizing alteration of the initial powder microstructure.

Summary/Conclusions

We have found that at low shock stresses, $\lesssim 1.3$ GPa, dynamically consolidated Al + 6% Si powder has a high density but very little strength. The microstructure is essentially the same as that of the powder. As the stress is increased to 1.7-2.6 GPa, interparticle bonding begins to occur, and for stresses in excess of 4.0 GPa the compact has substantial strength. Bonding of the compacts apparently results from melting and rapid resolidification at the surfaces of powder particles. Such modified material begins to appear at intermediate stresses, and for high stresses $\gtrsim 4.0$ GPa, forms essentially a continuous feature. The energy deposited at the interfaces can be calculated from the measured Hugoniot of the powder.

From this work, we conclude the following:

- 1) The bonding in a dynamically consolidated specimen results from rapid energy deposition at powder particle interfaces. It is distinct from, but related to, the compact final density.
- 2) For the Al alloy powder studied here, bonding begins to occur between 1.7 and 2.6 GPa. Stresses in this range or in excess of 2.6 GPa are required to produce structurally sound, high density material.
- 3) A critical stress level appears to be necessary to achieve both high density and adequate cohesion.

Acknowledgments

The authors wish to thank P. Curtis for preparing the metallographic specimens and S. L. Weinland and T. Sullivan for performing the gas gun experiments. F. Helm performed the explosive experiments.

References

- [1] D. Raybould, D. G. Morris, and G. A. Cooper, J. Mat. Sci., 14:2523 (1979).
- [2] D. Raybould in Shock Waves and High-Strain-Rate Phenomena in Metals, M. A. Meyers and L. E. Murr, Editors, Plenum Press, New York, 1981.
- [3] D. Raybould, J. Mat. Sci., 16:580 (1981).
- [4] D. G. Morris, Metal Sci., March 1981, p 116-124.
- [5] R. A. Prummer, Ber. Dt. Keram. Ges., 50:75 (1973).
- [6] C. L. Hoenig and C. S. Yust, Amer. Cer. Soc. Bull., 60:1175 (1981).
- [7] W. H. Gourdin, C. J. Echer, C. F. Cline, and L. E. Tanner in Proc. 7th International Conf. on High Energy Rate Fabrication, University of Leeds, 1981, p 233-241.
- [8] W. H. Gourdin, S. L. Weinland, C. J. Echer, and S. L. Huffsmith, to be published.
- [9] D. G. Morris, Metal Sci., June 1980, p 215-220.
- [10] B. M. Dobratz, LLNL Explosives Handbook: Properties of Chemical Explosives and Explosive Simulants, Lawrence Livermore National Laboratory UCRL-52997.
- [11] E. L. Lee, private communication.
- [12] W. H. Gourdin, to be published.

MICROSTRUCTURE OF RAPIDLY SOLIDIFIED STAINLESS STEEL AND SUPERALLOY POWDERS: A COMPARISON OF POWDER-MAKING TECHNIQUES

John E. Smugeresky

Sandia National Laboratories
Livermore, CA 94550

ABSTRACT

Several complex ferrous alloys (I-903, JBK-75, HP-9-4-20, and maraging steel) in the form of either Inert Gas Atomized (IGA) or Centrifugally Atomized (CA) powder have been characterized and compared. Powder particle size, microstructure, morphology and packing density were used for the characterization. Definite differences in particle size and microstructure are generally observed, while particle morphology and packing densities are similar. Particle sizes can be separated and/or normalized by mechanical separation and differences in microstructure are also observed for differences in powder particle size for each technique. The microstructures are those of rapid solidification and are compared to those of slower conventional ingot metallurgy solidification. Because of the rapid solidification of atomization, the microstructure of the powder particles are metastable and consequently are easily transformed by the thermomechanical process of consolidation. The relation between powder-making techniques, powder characteristics, and properties in the consolidated condition are summarized.

Introduction

Complex alloys containing many elements are often prone to compositional variation caused by solute segregation during solidification, especially in large commercial ingots. This phenomenon, commonly known as "coring," occurs by solute rejection, which leaves solute-rich regions between dendrite arms. Subsequent homogenization can in some cases minimize the segregation but it usually is accompanied by undesirable excessive grain growth. Consequently, additional thermomechanical processing to achieve recrystallization is required to obtain smaller grain sizes.

Alternatively, reducing the size of the ingot or providing chilled molds to enhance heat extraction can reduce solute segregation at dendrite interstices by increasing the cooling rate. Atomization techniques for making metal powders can in effect reduce the "ingot" size to less than 250 μm by producing molten droplets that solidify in the absence of a mold, and are thought to provide cooling rates in excess of 10^4 K/sec. Thus, rapid solidification by atomization can provide significant improvements in compositional homogeneity of complex alloys (see Fig. 1).

Inert gas atomization (IGA) and centrifugal atomization (CA) are two rapid solidification powder making techniques which are believed to provide sufficiently different cooling rates and/or powder characteristics such that differences in properties of the consolidated powder should be observed. In this investigation, four iron-base complex alloys were atomized by IGA and CA to compare the techniques.

Experimental

The compositions of the alloys are given in Table I. IGA was done either by Udimet Powder Division of Special Metals or by Alloy Metals using argon gas. These powders were subsequently screened to remove particles larger than 250 μm . CA was done by Pratt & Whitney. These powders were screened to remove particles larger than 177 μm . Particle size distributions were determined by a screen analysis while apparent and tap densities were determined using ASTM techniques B212-76 and B527-70. Powders were consolidated by hot isostatic pressing (HIP) in evacuated and sealed stainless steel containers at 900 and 1200°C and 103 MPa for three hours. Since these alloys are precipitation hardened, post-HIP treatments were utilized prior to mechanical property measurements.

Table I. Nominal Alloy Composition

	JBK-75	I-903	HP 9-4-20	250 Maraging
Cr	15	-	<1	-
Ni	30	38	9	18
Ti	2	1.4	-	0.3
Al	0.2	0.7	-	0.04
C	0.02	-	0.2	0.02
Co	-	15	4	8.4
Mo	1.3	-	1	4.5
Fe	Bal	Bal	Bal	Bal
Nb	-	3.0	-	-

Results

In the space provided here, it is not possible to include all of the results to date. However, I will highlight the data to summarize the general characteristics of the powders so that a comparison can be made between IGA and CA. Powder characteristics are listed in Table II. The IGA powders have a wider particle size distribution containing significantly more particles less than 37 μm than the CA powders. Although the apparent densities depend on the technique used, the tap densities are not. The strengths of compacted powders HIP at 1200°C are generally similar to those of ingot metallurgy (I/M) processed material and independent of powder technique except for I-903, while ductility, as measured by RA, is similar to I/M material except for I-903 and compacts of 250 maraging steel made from CA powder. The as-solidified microstructure of the powders (Figs. 2-5) is dendritic for CA powder but is cellular for IGA powder. The smaller the powder particle is the finer its microstructure. For the IGA JBK-75 powder the finer particles show evidence of dendrites.

In all cases, the as-solidified structure was transformed during HIP at 1200°C and post-HIP heat treatment to that similar to conventional I/M products except for a slightly finer but more uniform grain size and prior powder particle boundary (PPPB) precipitate decoration (Figs. 6-8). These PPPB precipitates have been identified as TiC in JBK-75,¹ M₃C in HP 9-4-20,² and Ti, Ni, Mo rich precipitates in 250 grade maraging steel.³ However, for JBK-75 the use of lower HIP temperatures has resulted in microstructures and mechanical properties that depend on powder technique. Figure 9 summarizes the yield strengths, ductility, and density while Figure 10 summarizes the microstructure.

Discussion

The microstructure of rapidly solidified powders is affected by cooling rate ($\Delta\dot{T}$), thermal gradient (G), and solidification rate (R) in a manner described previously^{1,4,5}. Decreases in particle size generally result in finer microstructure but not necessarily a change from cellular to dendritic, suggesting that the G to R ratio remains constant for all particle sizes. However, the G to R ratio is lower for CA than for IGA as evidenced by the dendritic structures of the CA powder versus the cellular structure of the IGA powder. Dendrite arm spacing of the CA powder is significantly smaller than that of an ingot (see Fig. 1). This suggests that the G to R ratios of CA and conventional castings are similar, but the $\Delta\dot{T}$'s are dramatically different. Although extrapolation of dendrite arm spacing versus cooling rates for conventional castings to that for powders is a tempting approach for estimating the cooling rate in the powder, the extrapolation range is too large to expect the estimate of cooling rate to be any better than that using a random number generator.

The metastable character of the as-solidified structures is demonstrated by the transformed microstructures of HIP samples. Temperatures in the 1200°C range have routinely been used to ensure adequate interparticle bonding during densification.^{2,6-10} In these cases, all evidence of the as-solidified structure has been wiped out, and microstructures of HIP samples cannot be used to distinguish powder-making techniques. Fractography of HIP samples confirms that true metallurgical

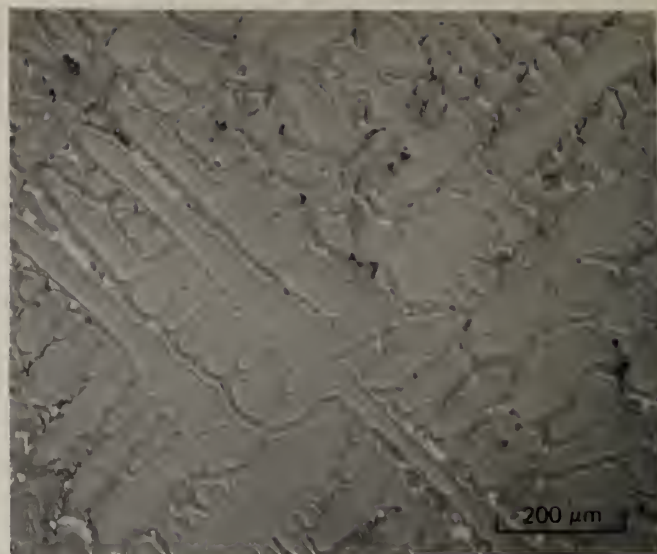
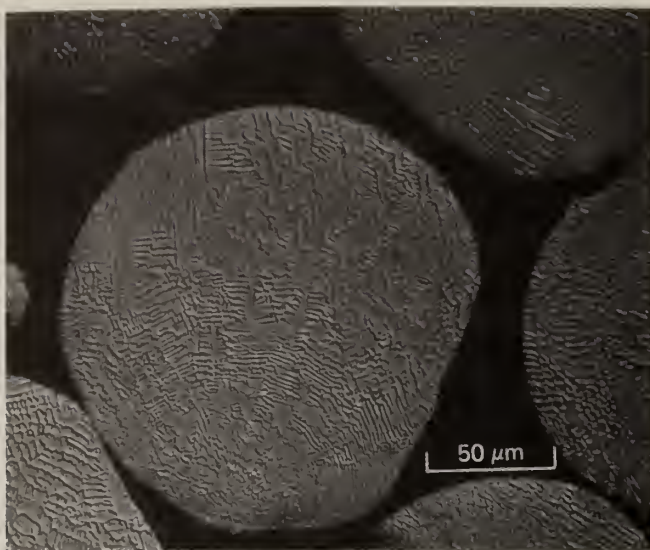


Figure 1. Comparison of As-Solidified Structure in (a) Conventional Ingot and (b) Centrifugally Atomized Powder Particle "Ingot"



Figure 2. Microstructure of JBK-75 (a) IGA Powder (b) CA Powder

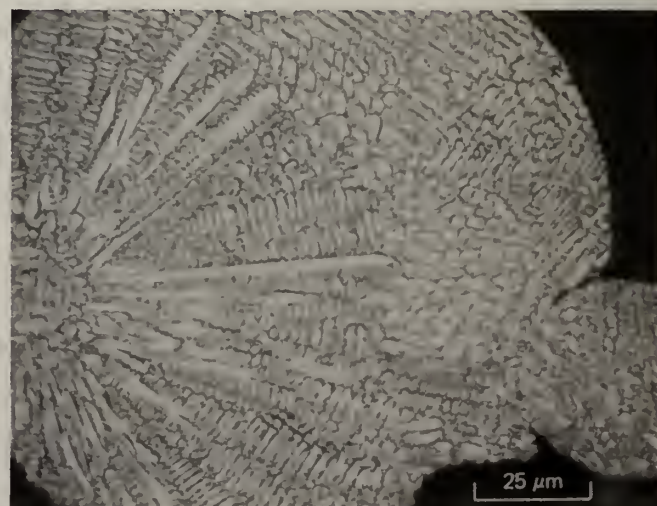
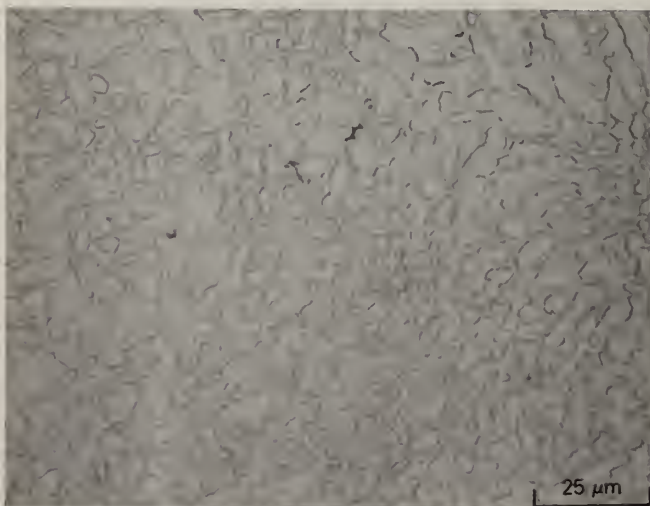


Figure 3. Microstructure of I-903 (a) IGA Powder (b) CA Powder

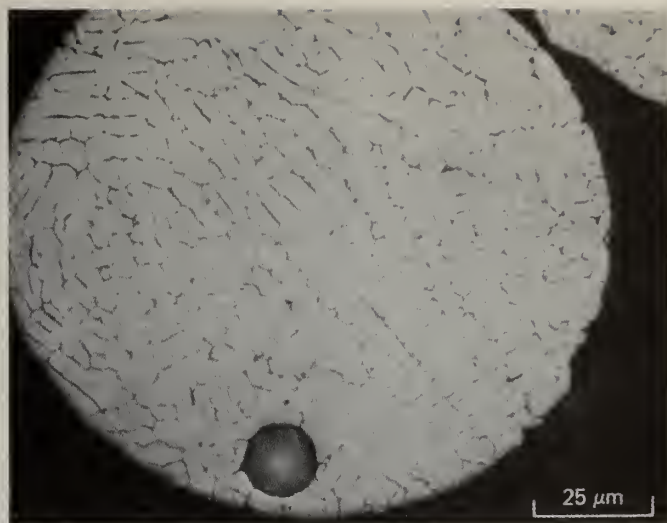
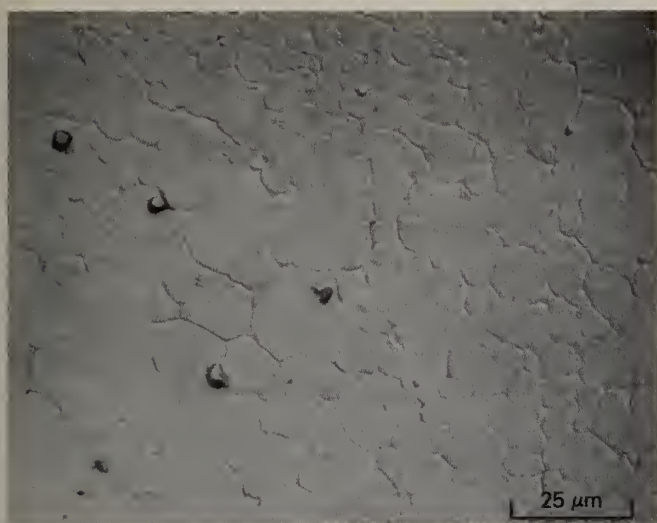


Figure 4. Microstructure of HP-9-4-20 (a) IGA Powder (b) CA Powder

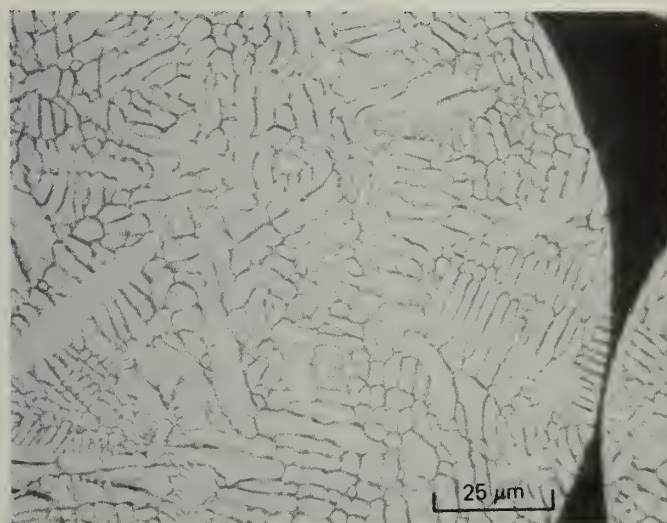
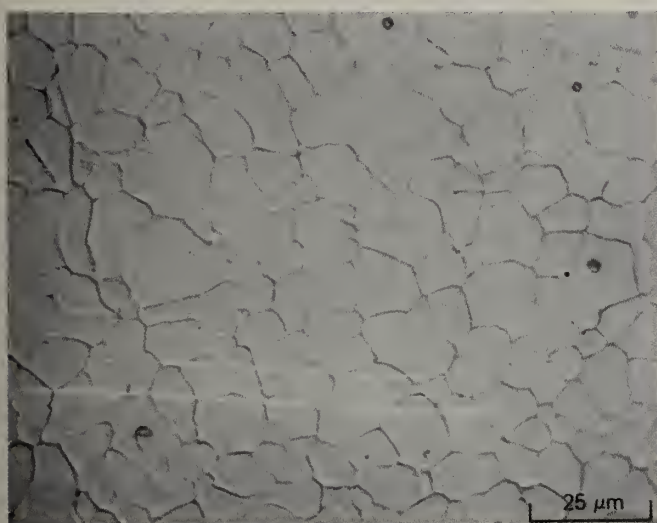


Figure 5. Microstructure of 250 Grade Maraging Steel: (a) IGA Powder (b) CA Powder

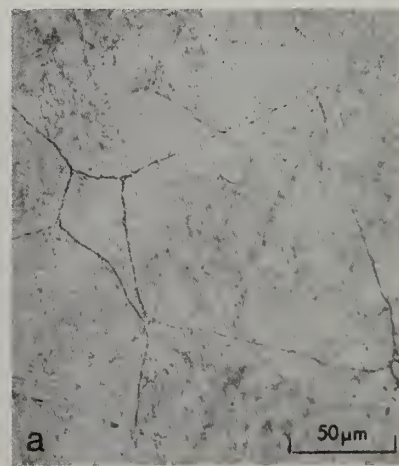
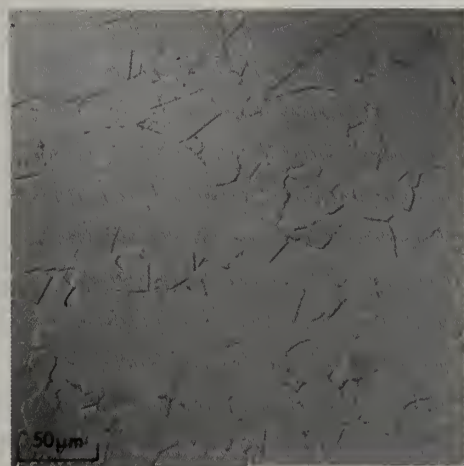
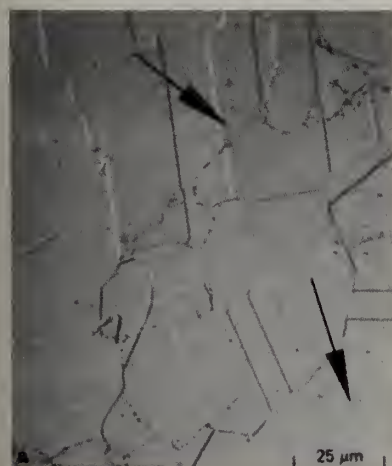


Figure 6 (Left). JBK-75 After Consolidation at 1200°C. Microstructure is similar to that of ingot metallurgy material except for prior powder particle boundary precipitates (arrows). Figure 7 (Middle). I-903 After HIP at 1200°C. Figure 8 (Right). 250 Grade Maraging Steel After HIP at 1200°C.

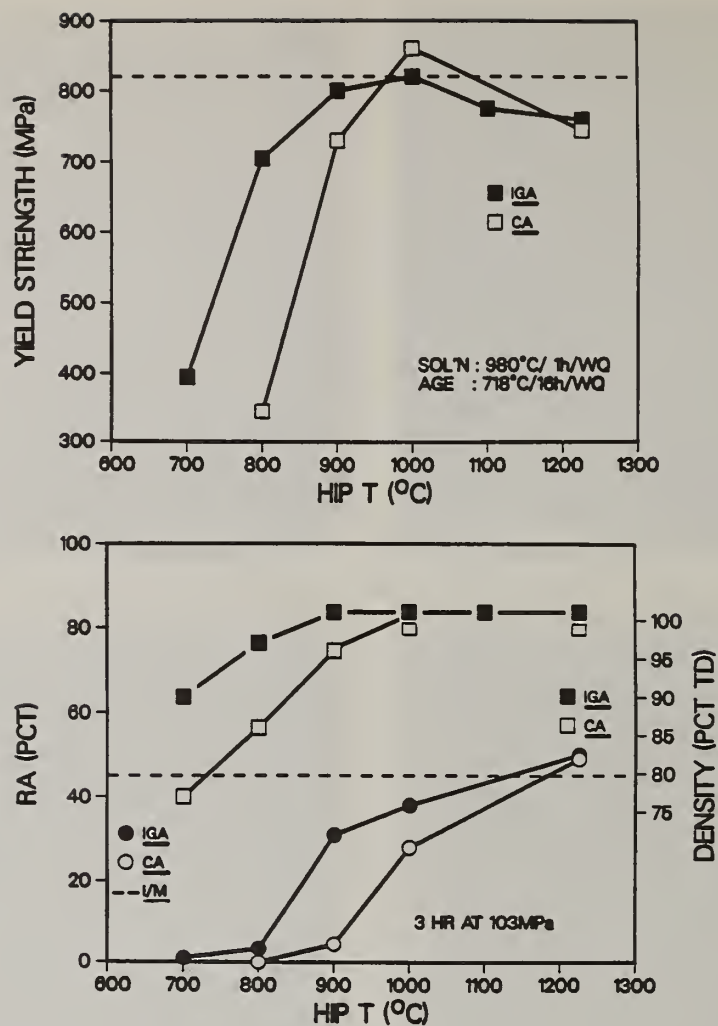


Figure 9. Yield Strength (a), Density (b, top curves), and Density (b, bottom curves) of Compacts of JBK-75 in the Solution Treated and Aged Condition as a Function of HIP Temperature.

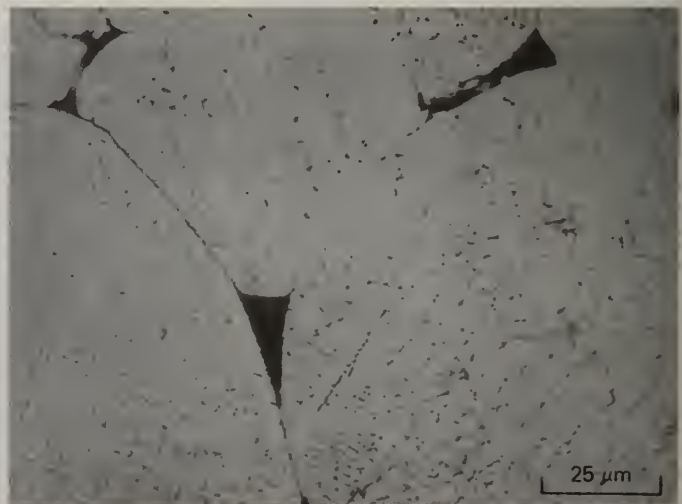
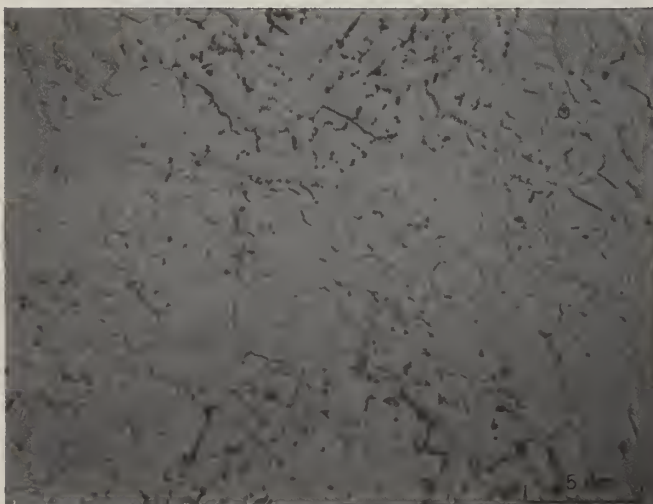


Figure 10. Microstructure of JBK-75 After HIP at 900°C. (a) IGA Material. Note evidence of both the as-solidified structure and transformed fine grain structure of this fully dense compact. (b) CA Material. Note the presence of porosity and the as-solidified structure as well as the absence of movement of prior powder particle boundaries.

TABLE II

Powder Characteristics

	JBK-75		I-903		HP-9-4-20		250 Grade Marage	
	IGA	CA	IGA	CA	IGA	CA	IGA	CA
Max. Particle Size (μm)	250	177	250	180	250	212	250	212
Avg. Particle Size (μm)	90	75	70	97	100	85	96	96
Amt. Powder (<37 μm (pct)	15	3	21	1	18	1	12	1
Morphology*	SPH+SAT	SPH	SPH+SAT	SPH	SPH+SAT	SPH	SPH+SAT	SPH
Apparent Density (% T.D.)	49	59	53	57	41	58	49	60
Tap Density (% T.D.)	64	65	66	65	55	65	58	68

*SPH = Spherical

SPH+SAT = Spherical with satellites

TABLE III

Powder Compact Properties*

	JBK-75			I-903			HP-9-4-20			250 Grade Marage		
	IGA	I/M	CA	IGA	I/M	CA	IGA	I/M	CA	IGA	I/M	CA
UTS (MPa)	1130	1135	1116	1185	1410	-	1315	1440	-	1720	1750	1655
YTS (MPa)	758	820	744	955	1200	-	1220	1245	-	1710	1680	1550
e _T (Pct)	24	22	25	7	14	-	13	16	-	N/A	14	4
RA (Pct)	50	45	49	12	38	-	55	63	-	52	62	14

*After HIP at 1200°C and heat treatment

bonding occurs when transparticle-transgranular fracture is observed. After HIP at lower temperatures, interparticle fracture is observed in some cases.^{3,7} Although interparticle fracture is at first glance faceted like intergranular fracture, the facets usually consist of "planar" ductile dimpled fracture characterized by very small, very closely spaced dimples. In several cases the dimples are associated with fine precipitates which form either on the powder surface prior to interparticle contact or at the interface during consolidation.⁷ In cases where the prior powder particle boundary becomes a migrating grain boundary, interparticle failure is generally not observed. Consequently, control of precipitation at PPPB's during consolidation and control of grain boundary migration are important in obtaining desirable properties and/or fracture mode in rapidly solidified and powder processed material.

In contrast, using lower HIP temperatures for JBK-75 demonstrates that powder-making techniques which provide quite different microstructures can provide consolidated material with quite different properties and microstructure. For example, HIP at 900°C provides good strength and ductility in compacts made from IGA powder, but provides reduced strength and negligible ductility in compacts made from CA powder. The difference is not only due to differences in density (98% theoretical density for CA and 100% theoretical density for IGA) but also to a lack of metallurgical bonding between CA powder particles. The dendritic structure of the CA powder is apparently stronger and more stable than the cellular structure of the IGA powder. Being stronger, the CA powder does not compress to full density during HIP at 900°C, and less than fully dense compacts have lower properties. However, such a drastic drop in ductility (from 32 to 3% RA) with only a 2% drop in density indicates the lack

of metallurgical bonding between powder particles. As seen in Fig. 10a, the PPPB's are still very evident in CA powder compacts, but quite difficult to detect in IGA powder compacts (Fig. 10b). In the latter case, the PPPB's are no longer individual grain boundaries, but have probably transformed into a series of small grains such that a trace of the PPPB passes through the interior of the grains rather than at the grain boundaries. Thus, regions that were formerly boundaries are actually interiors of single grains and thus represent truly metallurgically bonded material. Since this is not the case for CA powder compacts, they lack evidence of true metallurgical bonding.

Despite the transformation of the metastable as-solidified cellular structure, we see in Fig. 10b evidence of how to take advantage of rapidly solidified powders. In general the transformed structure contains very fine grains (approximately 5 to 10 times smaller than for powder HIP at 1200°C). By stopping the transformation at this time instead of allowing grain growth to occur, grain size strengthening is possible. Quenching from the HIP temperature can provide additional metastability of a supersaturated solid solution in precipitation strengthened alloys such as this so that subsequent aging using nonconventional heat treatments can provide increased strength. This hypothesis for exploiting rapidly solidified powders is presently under investigation.

Summary/Conclusions

Despite differences in microstructure of several ferrous alloy powders dependent upon rapid solidification powder making techniques, use of high temperatures during HIP wipes out all remnants of the as-solidified structures, and results in compacts with similar properties. Use of lower HIP temperatures, compacts are obtained with microstructures and properties dependent upon powder-making technique. IGA powders provided higher strength, ductility, and density after HIP at 900°C than CA powders. Although the microstructure in all cases transforms during HIP, the resulting structures for low temperature HIP are much finer than those of I/M material.

It is hypothesized that by combining HIP and post-consolidation heat treatments to control grain size and precipitate characteristics, rapidly solidified powder structures can be exploited to take advantage of differences in cooling rate between powder-making techniques.

Acknowledgements

This work was sponsored by DOE contract #DE-AC04-76DP00789; the CA powders were provided through DARPA.

References

1. J. E. Smugeresky, Met. Trans A, 13A (1982), 1535.
2. T. F. Klimowicz, SAND81-8229, June, 1981.
3. R. M. German and J. E. Smugeresky, Met. Trans A, 9A (1978), 405.
4. M. Cohen, B. H. Kear and R. Merabian, in "Rapid Solidification Processing, Principals and Techniques, II," Claitor's Publishing Division, 1980, pg. 1.
5. S. R. Coriell and R. F. Sekerka, ibid, pg. 35.
6. J. E. Smugeresky and R. M. German, Mat. Sci. & Eng. 36 (1978), 222.
7. J. E. Smugeresky and R. M. German, Met. Trans A, 9A (1978), 253.
8. J. L. Bartos and P. S. Mathur, in "Superalloys: Metallurgy and Manufacture," Proceedings of Third International Conference, September, 1976.
9. R. H. Van Stone and R. D. Gangloff, Reference 4, pg. 317
10. C. C. Law and M. J. Blackburn, Modern Developments in Powder Metallurgy, Vol. 14, APMI, Princeton, NJ, 1980, pg. 93.

CONSOLIDATION, THERMOMECHANICAL PROCESSING, AND MECHANICAL PROPERTIES OF
RAPIDLY SOLIDIFIED, DISPERSION-STRENGTHENED TITANIUM ALLOYS

S. M. L. Sastry, T. C. Peng, and J. E. O'Neal

McDonnell Douglas Research Laboratories
St. Louis, Missouri 63166

and

L. P. Beckerman

Air Force Wright Aeronautical Laboratories
Dayton, Ohio 45433

ABSTRACT

The feasibility of using rapid solidification processing techniques to produce dispersion-strengthened titanium alloys for use at temperatures up to 700°C was investigated. Titanium alloys containing large volume-fractions of fine (< 100 nm diam), incoherent dispersoids were produced by splat quenching electron-beam-melted Ti-Er and Ti-Nd alloys. The splat-quenched flakes were consolidated by vacuum hot pressing at 800–850°C at stresses of 56 MPa (8 ksi) and 70 MPa (10 ksi). The consolidated alloy disks were thermomechanically processed by rolling at 25–700°C and annealing at 500–700°C. The microstructures, hardness values, and tensile properties of thermomechanically processed alloys were determined. Significant increases in tensile and creep strength were observed in dispersoid-containing alloys. The effects of dispersoids on recrystallization, grain growth, and tensile and creep properties were determined.

Introduction

Dispersion strengthening is an effective method for increasing the useful service temperature of an alloy system. Production of dispersion-strengthened Ti alloys by conventional ingot casting and processing methods has been only partially successful [1–3] because additions of large amounts of dispersoid-forming elements result in small volume-fractions of coarse, equilibrium, constituent particles, which are ineffective for dispersion strengthening.

The solubility of potential dispersoid-forming elements in Ti can be increased significantly by increasing solidification rates to above 10^4 K/s, and the solid solutions can be annealed subsequently at suitable temperatures to obtain incoherent dispersoids [4–6]. Binary Ti-Er and Ti-Nd alloys were evaluated for the production of fine, incoherent dispersoids by rapid solidification. The thermal stability of dispersoids at 700–1000°C (1292–1832°F) and the effects of dispersoids on deformation, recovery, and recrystallization, and strengthening of Ti were determined.

Experimental Procedure

5-kg ingots of Ti-1.5Nd and Ti-1.0Er and 5 kg of 12.5-mm (0.5 in.) diam rods of Ti were procured from RMI Co. The Ti-Nd and Ti-Er alloy ingots were made from high-purity titanium (maximum oxygen concentrations of 0.08 wt%) and erbium and neodymium chips supplied by Research Chemicals, Inc. Each alloy was doubly melted by consumable-electrode arc melting, first in vacuum and then under argon gas pressure. The ingots, 7.5-cm (3.0 in.) diam and 40-cm (16 in.) long, were extruded to 12.5-mm (0.5 in.) diam rods by RMI Co. The extruded rods were used as feed stock for the production of rapidly solidified flakes by electron-beam melting and splat quenching [7]. The rapidly solidified flakes, which were 75–150 μ m thick and had cooling rates of $\approx 10^4$ K/s, were reduced by a rotary sheet-metal cutter to 2 x 2 mm particulates. The particulates were cleaned with acetone and a chem-mill solution consisting of hydrofluoric acid, nitric acid, and water, and consolidated into 50-mm (2.375 in.) diam and 90–120 mm (0.36–0.5 in.) thick disks by vacuum hot pressing at 800–850°C at stresses of

70-84 MPa (10-12 ksi) for 2-16 h. The consolidated disks were examined for complete densification by density measurements and optical metallography and scanning electron microscopy of through-thickness sections.

The consolidated Ti-alloy disks were isothermally forged at 800°C to obtain 4.0-mm (0.16-in.) thick plates suitable for further rolling. The high temperature and slow strain rates of deformation used in the isothermal forging operation produced fully recrystallized microstructures. The 4.0-mm (0.16-in.) thick plates were rolled at 25, 500, and 700°C with 10, 20, 30, 40, and 50% thickness reductions. The thickness reductions and temperatures selected were intended to establish the dependences on strain and temperature of the degree of recrystallization and the recrystallized grain size.

Tensile properties at 25-700°C (77-1292°F) and creep properties at 482°C (900°F), 600°C (1112°F), and 700°C (1292°F) were determined using test specimens 62.4-mm (2.5-in.) long having a 1.5 x 4.1 mm (0.06 x 0.16 in.) reduced-gauge section.

Results and Discussion

Dispersoids in Ti-Er and Ti-Nd Alloys

Typical dispersoid distributions in rapidly solidified Ti-1.0Er and Ti-1.5Nd alloys annealed at 700°C for 2 h and 100 h are shown in Figures 1 and 2. Whereas the ingot-processed alloys contained coarse ($> 0.5 \mu\text{m}$) particles, the rapidly solidified and annealed alloys contained 40-100 nm diam dispersoids with interparticle spacings of 90-200 nm. The Ti-1.5Nd alloy also had a small volume-fraction of coarse ($> 0.1 \mu\text{m}$ diam) disperseoids with interparticle spacings greater than $1 \mu\text{m}$. Rapid solidification refines the dispersoids by at least an order of magnitude in the alloys.

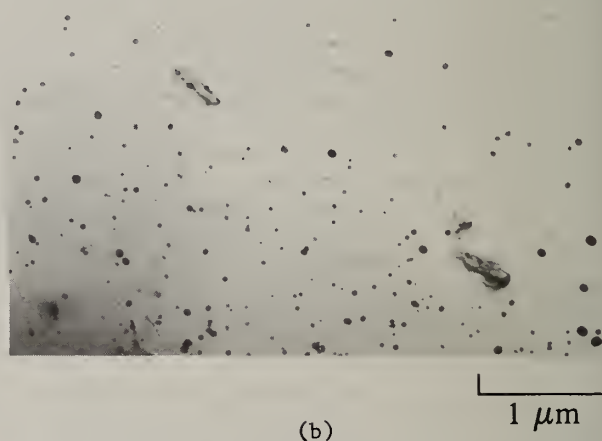
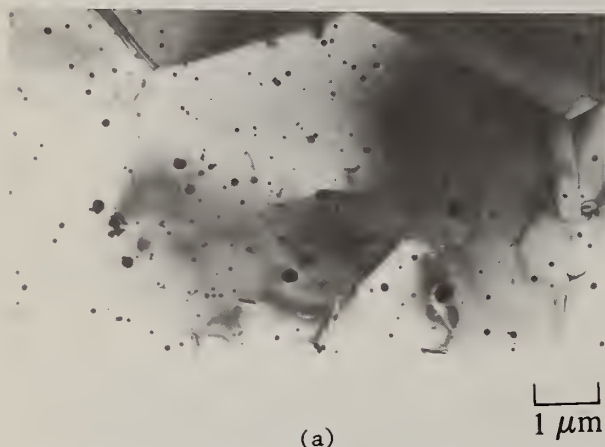


Figure 1. Microstructures of rapidly solidified Ti-1.0Er annealed at (a) 700°C for 2 h and (b) 700°C for 100 h.

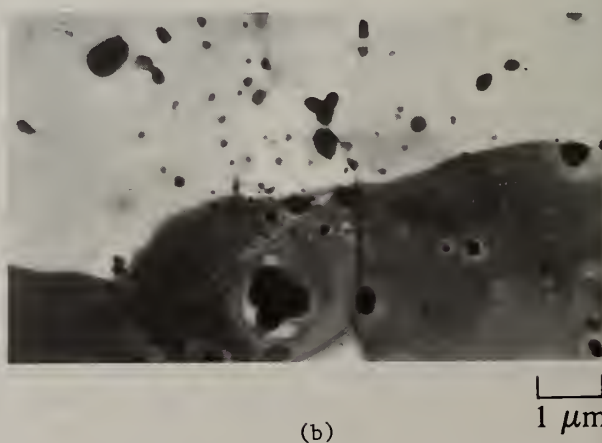
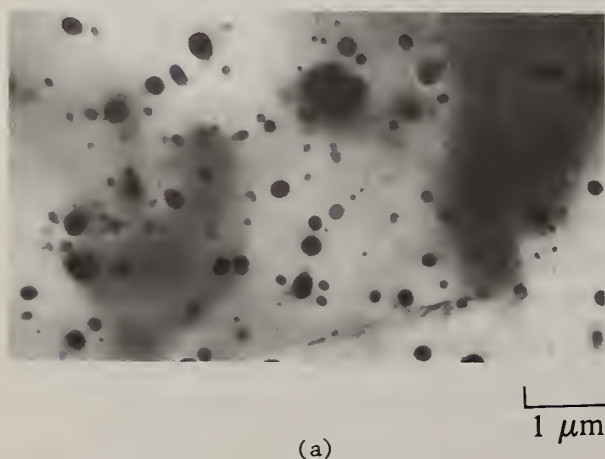


Figure 2. Microstructures of rapidly solidified Ti-1.5Nd annealed at (a) 700°C for 2 h and (b) 700°C for 100 h.

Effects of Dispersoids on Recrystallization and Grain Growth of Ti

The Ti-1.0Er and Ti-1.5Nd alloys rolled at 25°C with a 10% thickness reduction were partially recrystallized upon annealing; all other processing and annealing conditions resulted in complete recrystallization. The partially recrystallized Ti-1.0Er alloy had a dislocation cell structure with a cell size of $\approx 1\ \mu\text{m}$. The 700°C annealing of differently processed alloys resulted in complete recrystallization with smaller recrystallized grain sizes in Ti-Er and Ti-Nd alloys than in Ti.

To produce partially recrystallized or unrecrystallized microstructures by rolling and annealing Ti-1.0Er and Ti-1.5Nd, the amount of deformation should be $\approx 10\%$ and the annealing temperature should be $\approx 600^\circ\text{C}$. Higher reductions and annealing temperatures result in complete recrystallization. Because of the success of retaining the partially recrystallized microstructure in Ti-1.0Er by rolling at 25°C with 10% strain and annealing at 600°C, the Ti and Ti-1.0Er specimens were subjected to four cycles of cold rolling at 25°C and annealing at 600°C and 650°C. Ti-1.0Er specimens subjected to the cyclic cold-rolling and annealing have elongated dislocation cells (Figures 3) with the short dimension of the cells $\approx 1\ \mu\text{m}$. The unrecrystallized fibrous-grain structure typically found in dispersion-strengthened nickel and aluminum alloys could not be produced in rolled and annealed dispersion-strengthened Ti-1.0Er and Ti-1.5Nd alloys.

Effects of Dispersoids on Tensile and Creep Properties

Tensile properties at 25°C of differently processed Ti, Ti-1.0Er, and Ti-1.5Nd alloys are shown in Figures 4a-4c.

Specimens cold rolled with 10% thickness reduction have a substantial amount of internal energy in the form of dislocation tangles and cells. Specimens annealed at 600°C have recovered dislocation substructures with finer cell sizes in Er- and Nd-containing alloys than in Ti. Specimens annealed at 650 and 700°C have fully recrystallized grains. Annealing at 700°C for 100 h was performed to determine the effect on tensile properties of dispersoid coarsening that may occur at temperatures and times encountered in service use of this class of alloys. Under all processing and annealing conditions, the Ti-Er and Ti-Nd alloys have significantly higher yield strengths and ultimate tensile strengths than in Ti. The strength increments are greatest in the fully recrystallized specimens.

The magnitudes of the strength increments depend on concentration of the rare-earth alloying element and the thermomechanical processing schedule. The numbers above each bar in Figure 4a are the strength increments observed in Ti-Er and Ti-Nd alloys expressed as percentages of the unalloyed Ti values. The Ti-Er and Ti-Nd alloys annealed at 700°C for 100 h have the highest strength increments, but the ductilities in this case are significantly lower (Figure 5c). Annealing at 700°C for 2 h produces the best combination of strength and ductility in Ti-Er and Ti-Nd alloys. Annealing at 700°C for 2 h produces 402 MPa (66.1 ksi) yield stress and 25.1% total elongation in Ti-2.0Er (a 76% increase in strength and 7.7% decrease in ductility compared with Ti) and 553 MPa (79.4 ksi) yield stress and 18.4% total elongation in Ti-3.0Nd (111% increase in strength and 43% decrease in ductility compared with Ti).

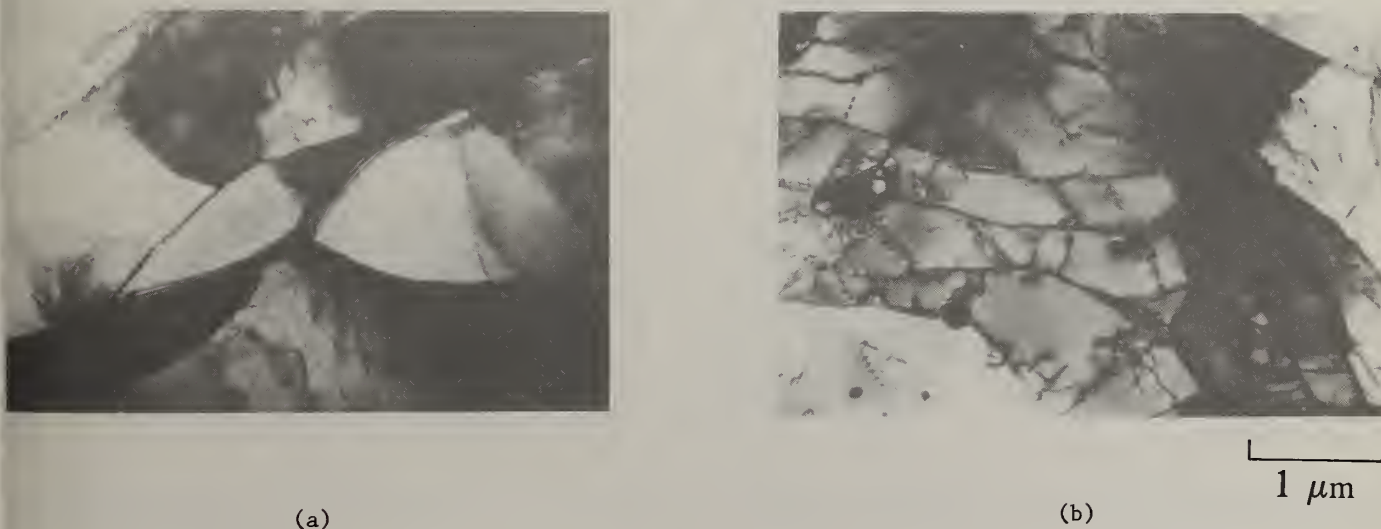


Figure 3. Dislocation cell structure in rapidly solidified (a) Ti and (b) Ti-1.0Er subjected to repeated 10% cold rolling and 650°C annealing cycles.

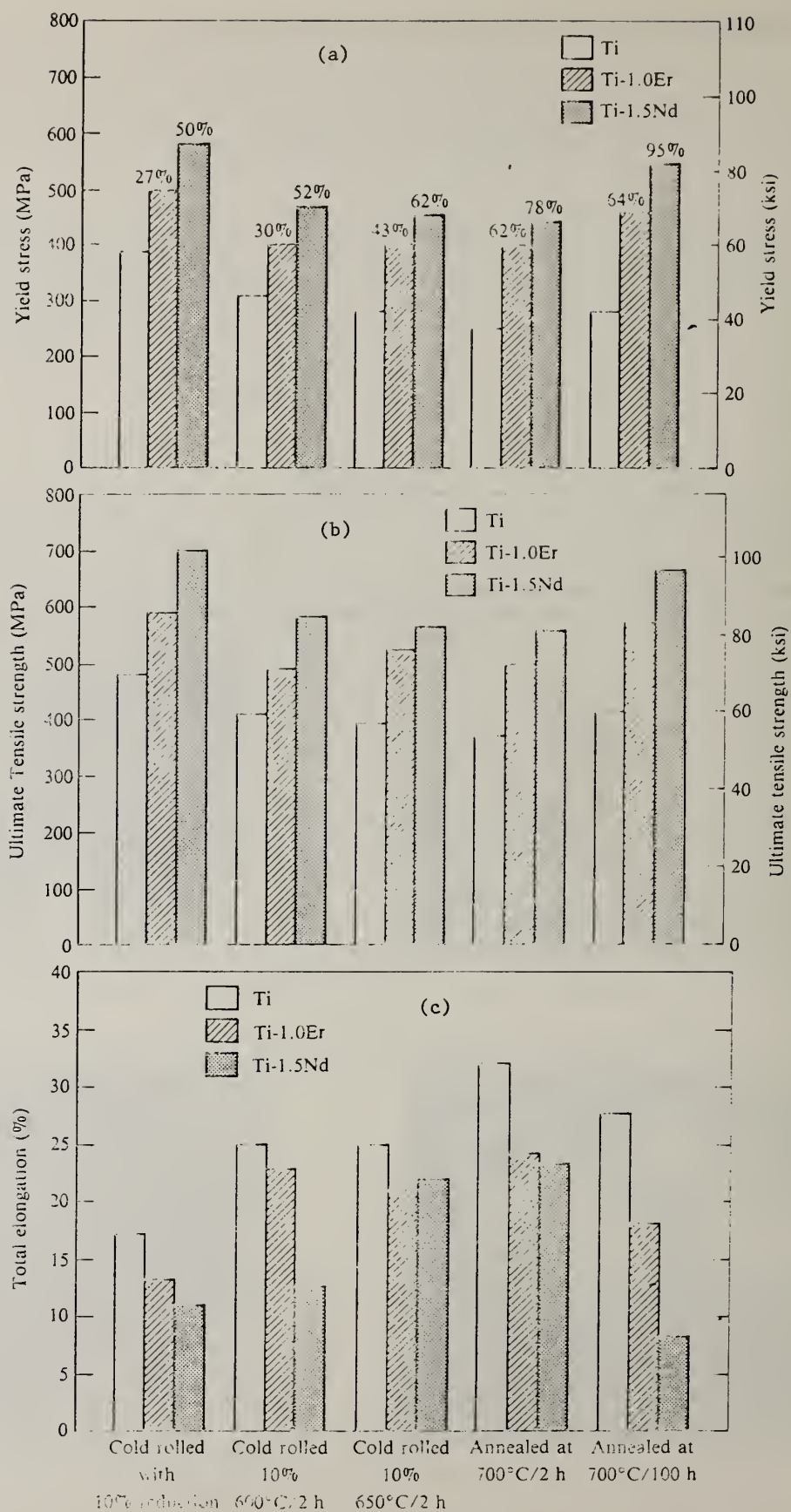


Figure 4. Effect of thermomechanical processing on (a) yield stress, (b) ultimate tensile strength, and (c) ductility of rapidly solidified Ti, Ti-1.0Er, and Ti-1.5Nd.

The steady-state creep rate and stress rupture lifetimes of Ti-1.0Er and Ti-1.5Nd alloys are shown in Figures 5 and 6. The Ti-1.0Er and Ti-1.5Nd alloys have significantly lower creep rates than titanium, with the effect being more pronounced at 700°C than at the lower temperatures. Of the three alloys, Ti-1.0Er has the lowest creep rate at all temperatures and stresses investigated. The dispersoid-containing alloys have order-of-magnitude longer stress-rupture lifetimes than Ti (Figure 6). For example, upon creep deformation at 600°C and 19 MPa (28 ksi), dispersoid-free titanium failed in 12.5 h whereas Ti-1.5Nd sustained 68 h and Ti-1.0Er sustained 288 h before fracture. Similar improvements were observed at 482 and 700°C. The proximity of plots of stress-dependence of stress-rupture time of Ti-1.0Er at 600°C (1112°F) and Ti at 700°C (1292°F) in Figure 6 clearly demonstrates the 100°C (200°F) increase in service temperature capability obtained by dispersions in Ti.

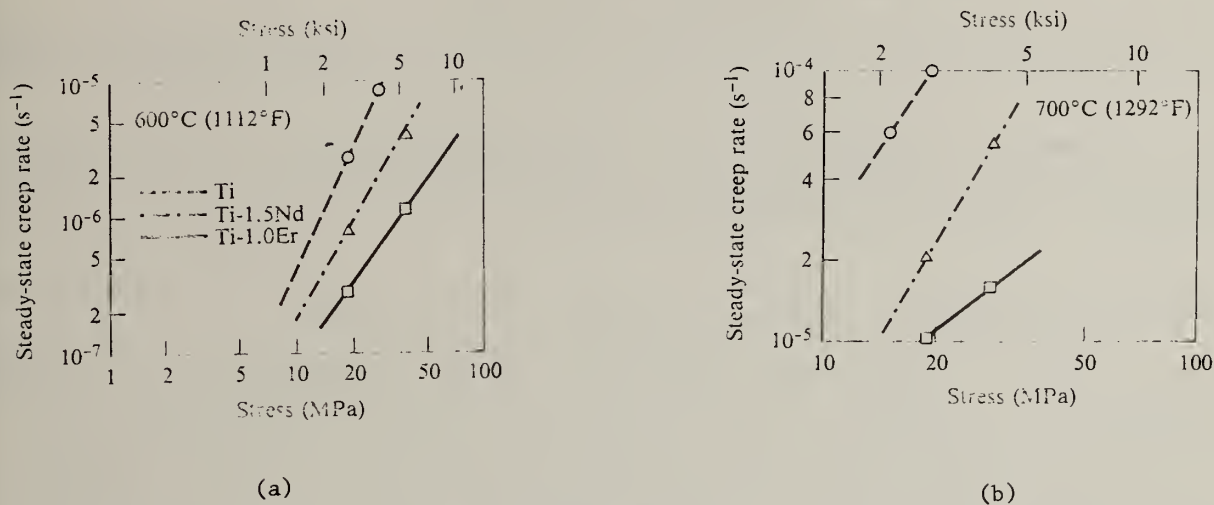


Figure 5. Effect of dispersoids on steady-state creep rate of Ti at (a) 600°C and (b) 700°C.

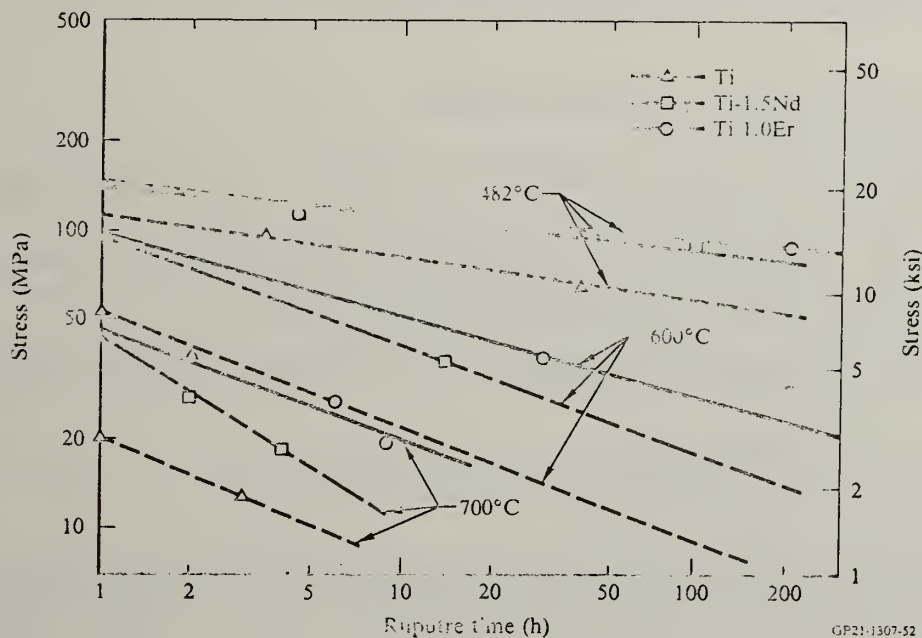


Figure 6. Effect of dispersoids on stress-rupture lifetimes of rapidly solidified Ti, Ti-1.0Er, and Ti-1.5Nd.

Conclusions

1. Rapid solidification at cooling rates $> 10^4$ K/s produces nonequilibrium, supersaturated, solid solutions and fine (< 100 nm) dispersoids in Ti-1.0Er and Ti-1.5Nd alloys.
2. The equilibrium, coarse, constituent particles, which are generally observed in conventionally cast Ti alloys containing 1-2 wt% Er and Nd, are totally absent in rapidly solidified alloys.
3. Compacts with $> 99\%$ theoretical densities are produced by vacuum hot pressing rapidly solidified particulates at 820-840°C and stresses > 70 MPa (10 ksi).
4. Thermomechanical processing by rolling at 25-500°C and annealing at 600-700°C does not produce fibrous-grain microstructures typically found in dispersion-strengthened nickel-base and aluminum-base alloys.
5. Annealing at 600°C of rolled Ti-1.0Er and Ti-1.5Nd alloys results in partially recrystallized microstructures with 1- μ m dislocation cells. Upon annealing above 650°C, the alloys readily recrystallize to equiaxed-grain microstructures with finer grain sizes in Ti-Er and Ti-Nd than in titanium.
6. The incoherent dispersoids in Ti-Er and Ti-Nd alloys increase by 40-110% the yield strength and ultimate tensile strengths of Ti with no significant loss in ductility.
7. At 700°C (1292°F), the target service temperature for dispersion-strengthened Ti, the dispersoid-containing alloys have 40% higher yield strength and ultimate tensile strength than dispersoid-free titanium.

Acknowledgements

This research was conducted under Air Force Contract No. F33615-81-C-5011.

References

- [1] F. R. Morral, Dispersion Strengthening of Metals, Batelle Columbus Laboratories MCIC Report MCIC-77-30 (1977).
- [2] C. F. Dixon and H. M. Skelly, Dispersion Strengthening Titanium with Refractory Oxides, Canadian Met. Quart. 11, 491 (1972).
- [3] M. J. Buczek, G. S. Hall, S. R. Seagle, and H. B. Bomberger, Grain Refinement of Titanium Alloys, AFML-TR-74-2557 (Nov 1974).
- [4] J. E. O'Neal, T. C. Peng, and S. M. L. Sastry, Microstructural Studies of Laser Melted Titanium-Rare Earth and Titanium-Boron Alloys, in Proc. Electron Microscopy Soc. Amer., ed. by G. W. Bailey (Claitor's Publ. Div., Baton Rouge, LA, 1981), p. 66.
- [5] S. M. L. Sastry, T. C. Peng, J. E. O'Neal, and L. P. Beckerman, Dispersion Strengthening of Titanium Alloys, TMS-AIME Fall Meeting, St. Louis, MO, 24-28 October 1982.
- [6] P. J. Meschter, J. E. O'Neal, and S. M. L. Sastry, Characteristics and Thermal Stability of Dispersed Phases in Rapidly Solidified Titanium-Rare Earth Alloys, TMS-AIME Fall Meeting, St. Louis, MO, 24-28 October 1982.
- [7] T. C. Peng, S. M. L. Sastry, and J. E. O'Neal, Rapid Solidification Processing of Titanium Alloys, Third Conf. on Rapid Solidification Processing, Gaithersburg, MD, 6-8 December 1982.

EFFECT OF AGING ON THE MICROSTRUCTURE OF RAPIDLY COOLED Ti-5Al-2.5Sn WITH Si ADDITIONS

A. G. Jackson*, T. F. Broderick**, F. H. Froes** and J. Moteff***

* Systems Research Laboratories, Inc.
2800 Indian Ripple Road
Dayton, OH, 45440

** Air Force Wright Aeronautical Laboratories
Materials Laboratory (AFWAL/MLLS)
Wright-Patterson Air Force Base, OH, 45433

*** University of Cincinnati
Cincinnati, OH, 45221

ABSTRACT

The structure of splat-cooled Ti-5Al-2.5Sn with Si additions was characterized as-produced and in various heat treated conditions. Additions of 0.5 or 1.0 wt.pct. Si produce a martensitic structure, while a cellular structure is produced with 5 wt.pct. Si. After heating at 535°C (1000°F) for 5, 10, 20, and 40h, the microstructural changes observed in the 0.5 wt.pct. Si alloy were a transformation of the martensite to alpha, grain growth, and a small amount of precipitation. In the 5 wt.pct. Si alloy similar heat treatments produced a decomposition of the cellular structure to a dispersion of small precipitates. Electron diffraction and EDS analysis indicated that the precipitates were probably Ti_5Si_3 . Similar alloys prepared by pendant drop melt extraction show a more dendritic microstructure in the as-produced condition. The results are discussed in terms of the solidification and cooling rate characteristics of the two processes used.

I. INTRODUCTION

In contrast to aluminum-based materials and superalloys, titanium powder metallurgy (PM) has been driven by cost considerations rather than improved performance (1). This situation is now changing, however, with PM/Rapid Solidification Technology (RST) of Ti alloys receiving attention because of the potential improvements in mechanical properties due to characteristics such as increased solubility and/or improved homogeneity. This should be particularly true for strengtheners such as Si, for which the equilibrium solubility is low. In the present paper, microstructures of splat-cooled and pendant drop melt extraction (PDME) (2-5) Ti-5Al-2.5Sn with additions of Si will be presented. The Ti-5Al-2.5Sn base alloy was chosen since it is a simple alpha alloy; the Si additions, since this element is a potent alloy strengthener particularly for high temperature applications.

II. EXPERIMENTAL PROCEDURES

The Ti-5Al-2.5Sn alloy containing 0.5% silicon is very close to the eutectoid composition and, consequently, evidence of a eutectoid decomposition would be expected. The structure of this alloy in the as-received condition is illustrated in Fig. 1a. The structure contains a very fine martensite, characterized by a high dislocation density within the grains. The corresponding diffraction pattern is shown in Fig. 1b, the zone being identified as $[1\bar{2}1\bar{6}]$. No precipitates are evident, indicating that the silicon is all in solution. On aging the material in vacuum for periods of up to 40h, the microstructure changes considerably. Precipitates present after 40h are shown in Fig. 2. No definitive diffraction pattern has been obtained yet, but Energy Dispersive Spectrometry (EDS) data indicates that the precipitates are Si-rich. Thus, the precipitates are tentatively identified as Ti_5Si_3 .

Fig. 3a shows the general morphology observed in the alloy containing 1 wt.pct. Si in the

as-received condition. The microstructure appears to consist of an extremely fine martensite with no specific orientation and a high dislocation density. No precipitates were observed even though the 1% Si level is hypereutectoid. The diffraction pattern, using a relatively large selected area aperture, shown in Fig. 3b, consists of partially formed ring patterns indicating that a wide range of orientations are present. This fine microstructure is typical of Ti alloys which have been rapidly cooled. Aging of this alloy initially yields a Si-rich eutectoid structure, which after 40h at 535°C (1000°F) has decomposed to a dispersion of Ti_5Si_3 precipitates (Fig. 4).

The microstructure present in the 5 wt.pct. Si produced by splat-cooling, is cellular with evidence of a very fine martensite within the cells. The cell boundaries are poorly formed and appear to contain many dislocations. This structure is interpreted to be the cellular structure expected as a result of a eutectic decomposition. A eutectic structure is not observed, indicating that solidification was sufficiently rapid to suppress its formation, but not sufficiently rapid to suppress the formation of the cell structure. In addition to the poorly formed cell structure, very small precipitates can be seen in the matrix (<10nm). Attempts to obtain diffraction patterns from the cell boundary structure were not successful, but the diffraction patterns from the general area indicated an HCP structure (Fig. 5a), with a [0111] zone axis. Examination of a portion of the boundary near the edge of the foil revealed a fine structure present within the boundaries. At 40h aging, the cell structure has broken up into irregularly-shaped precipitates, as shown in Fig. 6, which is a Si x-ray area scan of a portion of a STEM foil.

The PDME material was expected to solidify at a slower rate than the splat-cooled alloys. Microstructural differences due to this cooling rate variation, would be large if the variation covers the critical rate for formation of metastable phases, dendrites, etc. Evidently, the cooling rates in the PDME were above the critical rate, since the microstructures observed are essentially the same as observed in splat-cooled alloys. Fig. 7 shows the microstructure for the 0.5 wt.pct. Si alloy. Again, martensite is evident, but the lath size is slightly larger than in the base material. The absence of any precipitate particles is as expected, since at this concentration, the Si is in solid solution. A major change in microstructure is apparent in Fig. 8, which shows the 5 wt.pct. Si alloy produced by the PDME method. Examination of the microstructures suggests that the cooling of this fiber was not uniform. The fine structure around the outer edges is associated with a rapid quench, while the larger, more well developed structure in the interior indicates a slower quench rate. Some martensite is also present in the matrix, but it is not well developed. EDS x-ray analysis of the cells and cell boundaries indicated that the concentration of Si was significantly higher in the boundaries than in the matrix.

III. DISCUSSION OF RESULTS

The splat-cooled material exhibits a fine grain size as-cooled. An apparent increase in solid solubility in the 0.5 wt.pct. Si alloy was sufficient to suppress formation of the eutectoid, producing a metastable condition. The 1 wt.pct. alloy showed similar behavior. Such extensions in solubility have been seen in Al alloys and superalloys and Ti alloys appear to follow the same behavior. The cellular structure seen in the 5 wt.pct. Si alloy indicates that the solubility extension is less than this level of solute. Since the eutectic is at about 8 wt.pct., a strong eutectic formation is expected in this alloy, but this is not seen. The cellular structure indicates a high interface velocity and a high thermal gradient sufficient to produce a metastable structure in which the eutectic is suppressed (6).

The PDME material shows similar effects (5). Low-solute solid solubility is extended, and the eutectic is suppressed in the high solute case (5 wt.pct.). In this process, the liquid/solid interface velocity and related cooling rate (liquid temperature to solid temperature) is slower than in the splat-cooled method. The effect of the interface velocities on the microstructure appears to be the same for both processes. That is, the only effect is on the size of the structures produced; the splat-cooled structures being finer. During both processes, solidification in alloys containing less than 5 wt.pct. Si occurs fast enough for solute rejection to be minimized, suppressing the eutectoid. For alloys containing 5 wt.pct. Si, rejection of solute occurs during cooling, giving a cellular structure. Subsequent cooling after initial solidification results in further modification of the microstructure by diffusion mechanisms and metastable phase transformations.

For each process, there are at least two distinct temperature regimes which can significantly influence the final microstructure*: one spanning the transformation from liquid to solid, the other

* It is recognized that other temperature ranges may also contribute to the microstructures developed. For example, super-heating can completely destroy all nearest neighbor relationships resulting in a more random material than if quenching is carried-out from a temperature which is just above the liquidus.

after complete solidification has occurred. In the former temperature regime, the structure produced is strongly influenced by interface velocity and thermal heat transfer coefficient. The second temperature range, where the alloy has solidified, is characterized by a slower cooling rate. In titanium, the martensitic transformation occurs on rapid quenching, and such structures are observed in these alloys. The microstructure observed thus appears to develop in two stages. That is, at temperatures just above the liquidus, the short-range order present is frozen by the very high solid/liquid (S/L) interface velocity and the rapid removal of heat. This results in suppression of the eutectic and eutectoid decomposition, except in the high solute alloy (5 wt.pct.), where cells are formed. During the slower cooling after solidification, martensitic transformations take place, changing the initial metastable solidification structure, and producing the final martensite and cell structures observed.

IV. CONCLUSIONS

Production of rapidly-cooled Ti-5Al-2.5Sn, containing various levels of Si by splat-cooling and PDME methods, results in very fine grained martensitic material for low solute levels (up to at least 1 wt.pct.) and cellular structures for high levels of solute (5 wt.pct.). Aging of the splat-cooled alloys results in Ti_5Si_3 precipitation in the low solute alloys either as a dispersion or as a weakly formed eutectoid. The cellular structure present in the as-produced high solute alloys decomposes to a dispersion of irregularly-shaped Ti_5Si_3 . For both processes, there are two distinct temperature regimes (that span solidification and a lower temperature range in which the material is completely in the solid state) which together contribute to the final microstructures developed.

V. ACKNOWLEDGEMENTS

The authors gratefully acknowledge the assistance of R. Omlor and F. Deutscher in the portions of the TEM work and R. Bacon for his contributions to the SEM work. Helpful discussions with Dr. L. Beckerman are appreciated. This work was partially supported by Air Force Contract F33615-80-C-5079.

VI. REFERENCES

1. F. H. Froes, D. Eylon, G. E. Eichelman and H. M. Burte, JOM, Vol. 32, No. 2, Feb. (1980), p. 47.
2. A. G. Jackson, Ph.D. Thesis, University of Cincinnati, 1983.
3. A. G. Jackson, F. H. Froes, A. Clauer and R. Carbonara, TMS-AIME Fall Meeting, Louisville, October, 1981.
4. S. Sastry, T. Peng and J. O'Neal, TMS-AIME Fall Meeting, St. Louis, October, 1982.
5. A. G. Jackson, F. H. Froes, A. Clauer, and R. Carbonara, to be published.
6. R. Mehrabian, Int. Met. Rev., 27 (4), 185 (1982).

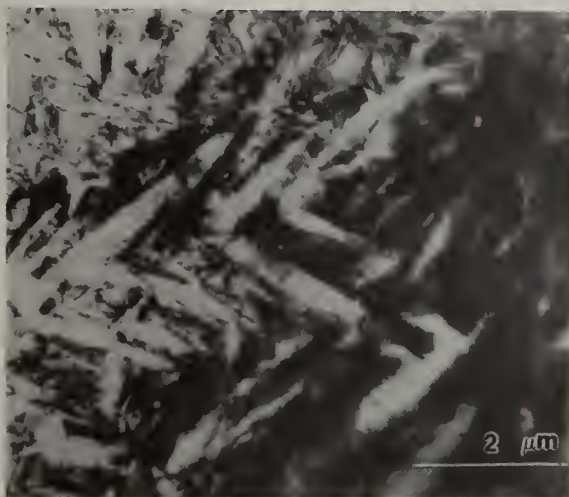


FIGURE 1(a): Microstructure of as-produced splat Ti-5Al-2.5Sn with 0.5 wt.pct. Si.

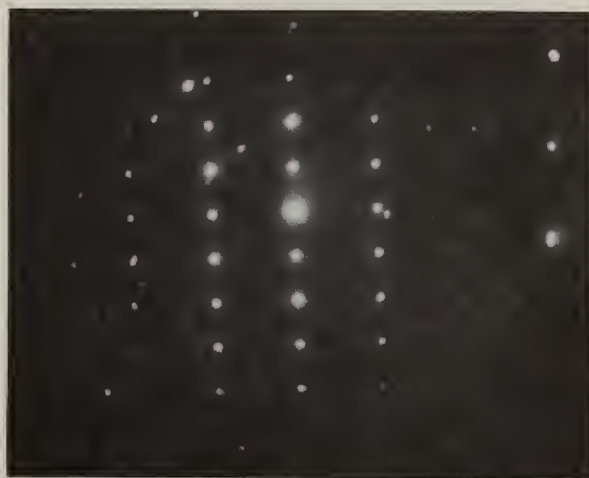


FIGURE 1(b): Diffraction pattern from the foil shown in Fig. 1(a). $\underline{B} = [1\bar{2}16]$.

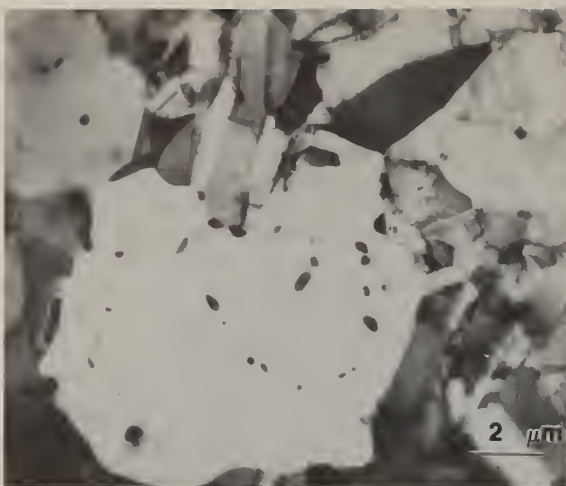


FIGURE 2: Same alloy as Fig. 1(a), aged 40h at 535°C, showing evidence of precipitation.

FIGURE 3(a): Microstructure of alloy with 1 wt.pct. Si.

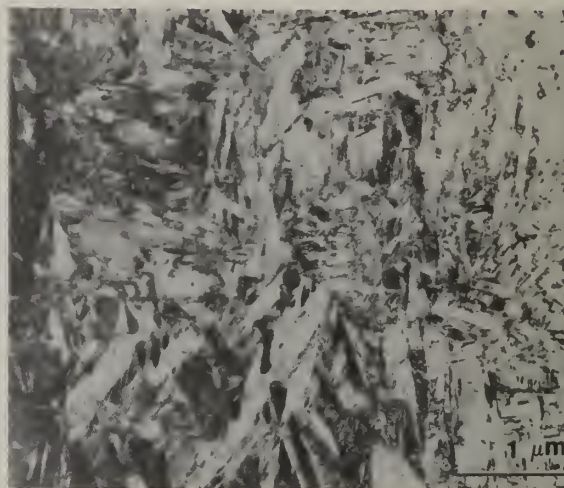


FIGURE 3(b): Diffraction pattern from area shown in Fig. 3(a).

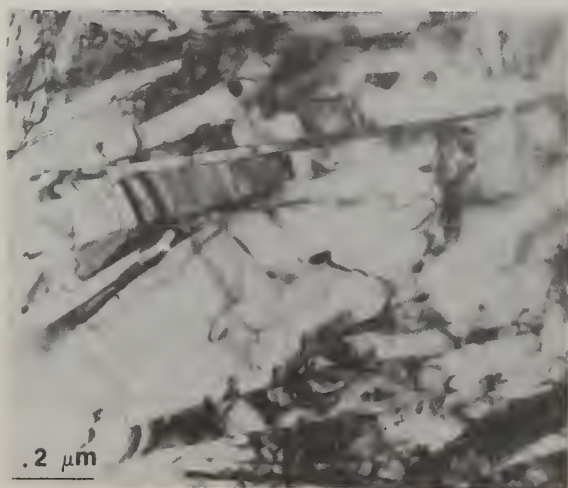
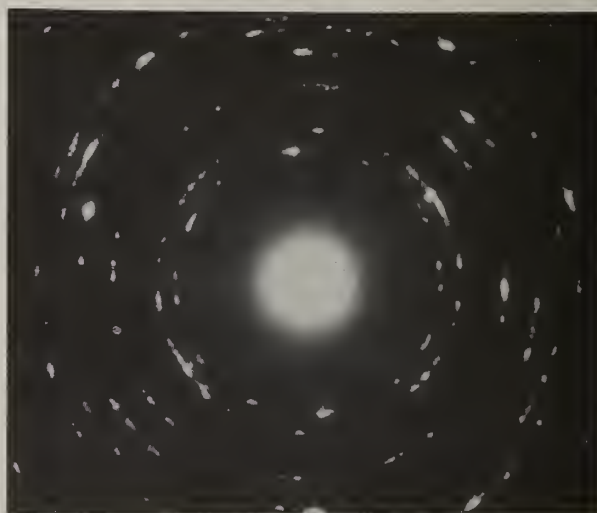


FIGURE 4: Same alloy as Fig. 3(a) aged 40h at 535°C.



FIGURE 5(a): Microstructure of alloy with 5 wt. pct. Si showing cellular microstructure.

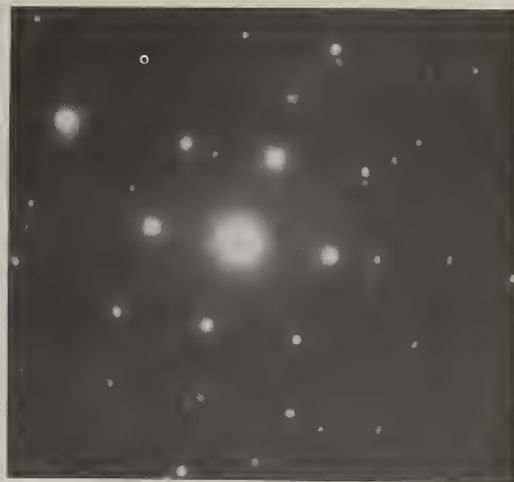


FIGURE 5(b): Diffraction pattern from area shown in Fig. 5(a), $B = [0\bar{1}1]$.



FIGURE 6: X-ray area scan (enhanced) showing the broken-up cell structure after aging 40h at 535°C. Same alloy as Fig. 5(a).

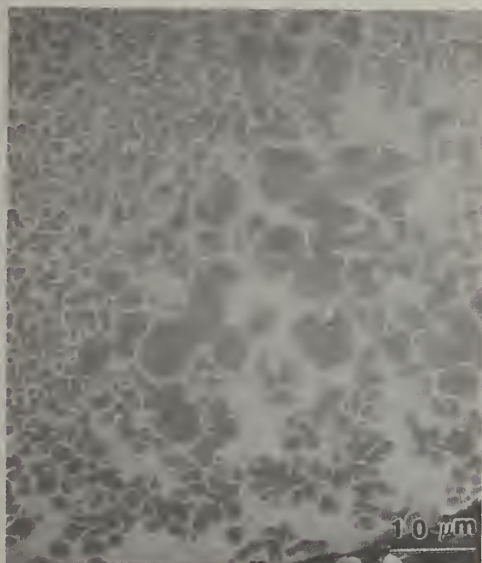


FIGURE 7: SEM micrograph of Ti-5Al-2.5Sn-0.5Si PDME material. Microstructure is similar to Fig. 1(a).

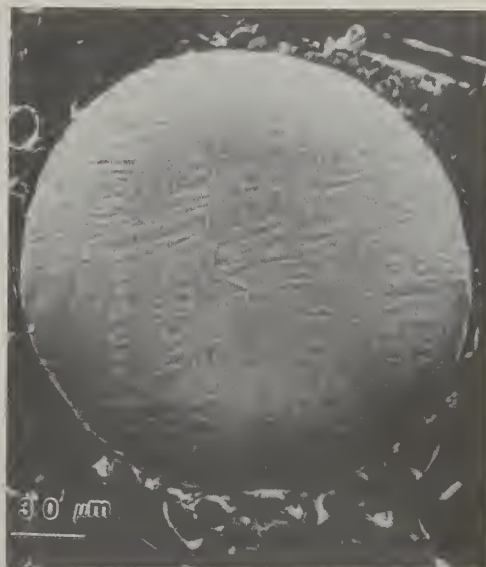


FIGURE 8: SEM micrograph of Ti-5Al-2.5Sn with 5Si. Microstructure exhibits a cellular structure.

ON THE TEXTURE DEVELOPMENT - DIRECTIONAL RECRYSTALLIZATION INTERACTION
OF RAPIDLY SOLIDIFIED Ni-Mo-Al-W AND Ni-Cr-Al-W ALLOYS

H. A. Chin, S.E. Hughes and J. S. Andrus

PRATT AND WHITNEY AIRCRAFT/GPD
WEST PALM BEACH, FLA 33402

J. L. Larson

UNIVERSITY OF ILLINOIS, URBANA-CHAMPAIGN, ILL 61801

ABSTRACT

Producing wrought single crystals from consolidated rapidly solidified powders will significantly increase the high temperature capability of nickel base superalloys. Through rapid solidification, Ni-Mo-Al-W and Ni-Cr-Al-W alloys were developed at PWA/GPD (under Government contract) which exhibited improvements in creep/stress rupture, oxidation resistance and fatigue over available cast alloys. Such improvements are due to a combination of (i) alloy design, (ii) RST processing to a metallurgically homogeneous condition, (iii) solid state directional recrystallization (DR) to single crystals, and (iv) thermo-mechanical process development to specific crystallographic textures for controlled orientation DR crystal growth.

This paper discusses the development of preferred orientation in rolled Ni-Mo-Al-W and Ni-Cr-Al-W alloys as a function of processing parameters. Rolled textures of both alloys are observed to be similar, exhibiting preferred orientations typical of intermediate to high stacking fault energy face-centered cubic alloys. Cold straight rolled product exhibited a texture centered at the $\{113\}\langle 332 \rangle$ with a spread in ideal orientations to $\{110\}\langle 112 \rangle$. By cross rolling, the texture spread was effectively converted to a singular texture centered at ideal orientation $\{110\}\langle 112 \rangle$. Intermediate annealing below the solvus of the alloy caused no change in the rolling texture though the rollability of the alloy is restored. Textures thus developed are observed to control the initiation and growth of specific crystal orientations on directional recrystallization. These texture-DR crystal orientation results are discussed and rationalized as a directional secondary recrystallization phenomenon.

INTRODUCTION

It is common knowledge that the most efficient means for increasing gas turbine engine performance is by increasing the turbine inlet gas temperature. However, since the engine environment of the Pratt and Whitney Aircraft/Government Products Division (PWA/GPD) F100 gas turbine already taxes current design and materials capabilities, further improvements require combinations of better materials and designs. For several years PWA/GPD has investigated the utility of wafer constructed airfoils having high cooling effectiveness. Concurrently, PWA/GPD pursued development of better materials for use in these wafer constructed airfoils. Envisioned was a stronger powder alloy composition which, when processed to single crystalline form, would represent an excellent material condition for high temperature creep loaded airfoils. Under joint funding from the Defense Advanced Research Projects Agency (DARPA) and the Air Force Materials Laboratory (AFML) two nickel base superalloys, 185 and 116, were developed for turbine blade and vane applications, respectively. Processing methods for generating single crystalline wafer stock from both alloys were developed. This paper presents the results of an investigation into the development of preferred orientation and how that preferred orientation affects crystallographically oriented directional recrystallization. Discussions on the development of deformation and annealing textures in f.c.c. metals are available in the literature [1-5].

The studies described in this paper examined the relationships between texture formation and hot isostatic pressing, extrusion, hot rolling, cold rolling and both hot and cold cross rolling for these alloys. Material processed by these methods was subjected to directional recrystallization (DR) heat

treatments to establish the relationships between deformation textures and both DR crystal orientation and growth rates.

The alloys used were developed at PWA/GPD under the combined sponsorship of DARPA and AFWAL. The alloy compositions are listed below:

	Composition, Wt%					
	Ni	Mo	Cr	Al	W	C
Alloy 185	bal	14.4	-	6.8	6.25	0.04
Alloy 116	bal	-	9.2	8.3	9.4	0.04

Both alloys utilized a high volume fraction of an ordered f.c.c. γ' - Ni₃Al phase, imparting high temperature strength through precipitation hardening. In addition, molybdenum was added to alloy 185 for solid solution strengthening, and chromium to alloy 116 for environmental resistance.

Both alloys were produced by a rapid solidification rate (RSR) powder process developed at PWA/GPD utilizing rotary atomization and forced convective cooling with helium gas under inert conditions [6 - 12]. Cooling rates attained were in excess of 1,000,000°C/second, which virtually eliminated macrosegregation. The powder particles produced were mostly in the 10 to 100 micron range and were spherical.

EXPERIMENTAL PROCEDURE

Alloy 185 and alloy 116 powders, produced by the PWA/GPD atomization rig, were placed in stainless steel consolidation cans immediately after hot dynamic outgassing at 1000°F and 10⁻⁴ torr pressure. Rectangular cans were used for hot isostatic pressing (HIP) consolidation and cylindrical cans for extrusion consolidation.

HIP was performed at 2250°F for 2 hours at 15 ksi pressure. The extrusion parameters investigated are listed in Table I. Both HIP and extrusion parameters resulted from earlier unpublished studies.

Hot rolling studies were conducted on canned alloys 185 and 116 consolidated by HIP. They were rolled using the parameters listed in Table II on a 12" diameter mill. Reductions per pass started at 5% and gradually increased to 20% as rolling progressed.

Cold straight rolling studies were conducted on extruded alloys 185 and 116. Extrusions 5E9, 5E19, 5E19, 5E21, 5E15, 6E7, 6E10 and 6E18 were all cold rolled to 15, 25, 35, 45 and 55% reductions. Annealing was performed every 5 to 10% in reduction for 5 minutes at 2200°F. Reductions per pass were on the order of 1%.

Cold cross-rolling studies were conducted on HIP plus hot rolled alloy 116 and 185 stock, and hot cross rolling studies were conducted on HIP alloy 116 and both HIP and extruded alloy 185. Parameters were as for above, except for total reductions and the inclusion of cross rolling. Cross-rolling was performed as either the final portion or an intermediate portion of the rolling. The cross-rolling and total reduction parameters are listed in Table III.

X-ray diffraction methods were used to determine texture orientation of the extrusion, HIP product and rolled strip. Plotting of the pole figures was accomplished using a computer and software written by Love [13].

TABLE I
EXTRUSION PARAMETERS AND RESULTING TEXTURES

I.D. #	ALLOY	EXTRUSION TEMPERATURE, °F	EXTRUSION RATIO	FIBER TEXTURE COMPONENTS
5E9	185	2000	15:1	<100>, <111> weak
5E19	185	2100	25:1	<100>, <110>, <111> weak
5E21	185	2250	15:1	<110>, <111> weak
5E15	185	2300	26:1	<111> weak
6E7	116	2100	15:1	<100> strong, <111> weak
6E10	116	2250	8:1	<111> strong
6E18	116	1900	8:1	<100>, <111> weak

TABLE II
HOT ROLLING PARAMETERS

ALLOY	ROLLING TEMPERATURE °F	TOTAL REDUCTION %
185	2275	90
185	2250	78
185	2100	75
185	2000	84
116	2250	75
116	2100	75

TABLE III
CROSS ROLLING PARAMETERS

ALLOY	ROLLING TEMPERATURE °F	TOTAL REDUCTION %	SR:XR (:SR) RATIO
185	70	85,78,73	60:40
185	70	73	70:30
185	70	85,78,67	75:25
185	70	78,73	80:20
185	70	71	34:48:18
185	70	71	42:42:16
185	70	71	60:25:15
116	70	67	65:35
116	70	67	75:25
185	2200	80	60:40
185	2100	91	70:30
185	2000	84	50:50
116	2300	91	65:35

Directional recrystallization heat treatments were performed on the processed alloys under vacuum (typically 10^{-3} torr) in a zone annealing furnace. A graphite susceptor, heated by induction, radiated heat onto the sample passing through. The gradient at the region of insertion into the susceptor provided the driving force for columnar grain growth. The measured thermal gradients at 2300°F ranged between 200°F/in and 300°F/in and insertion rates for smooth continuous grain growth varied from 1/8 inch/hour to 2 inch/hr. Furnace control was achieved with W/W-Re thermocouples imbedded in the susceptor such that the maximum specimen temperature peaked between the γ' solvus and incipient melting temperatures. Wafer stock from ten different rolling schedules was cut into 1/2 inch by 2½ inch strips with a wedge shaped leading edge for DR (the wedge increased the tendency toward single crystalline growth). Usually, columnar grains were grown to within 1/2 inch of the trailing edge and by back reflection Laue technique the crystallographic orientations of all major grains were recorded.

RESULTS AND DISCUSSIONS

CONSOLIDATION

The subsolvus HIP parameters were found to effect full consolidation of the powder billet. Pole figure analysis of the HIP product revealed a random distribution of crystal orientations or non-textured condition in both alloys.

For the extrusion parameters used, full consolidation of the powder billet resulted. Pole figure analysis of the extruded products revealed that the two classes of alloys, Ni-Mo-Al-W (185) and Ni-Cr-Al-W (116) developed extrusion textures typical of moderately high and low stacking fault energy fcc metals, respectively.

Alloy 185 developed four different textural conditions, as listed in Table I and predicted in Figure 1. Alloy 116 developed the three textural conditions also listed in Table I and predicted by Figure 1. The range of textures produced in both classes of alloys followed the changes expected in f.c.c. alloys from varying Stacking Fault Energy (SFE) and processing temperatures. The high temperature extrusions of both alloys appeared to occur above the γ' solvus (as single phase γ) due to adiabatic heating during deformation. Under this condition, alloy 185 exhibited the singular $\langle 111 \rangle$ fiber texture typical of higher SFE f.c.c. alloys undergoing a temperature related texture transition. Alloy 116 exhibited a singular $\langle 100 \rangle$ fiber texture typical of a low SFE f.c.c. alloy. Lowering the processing temperature resulted in a texture transition to the commonly observed duplex $\langle 111 \rangle + \langle 100 \rangle$ fiber texture for the moderate-to-low SFE f.c.c. alloys. The existence of the $\langle 110 \rangle$ fiber component found in alloy 185 processed in the intermediate temperature range has not been reported in the literature for f.c.c. metals. The development of that texture component is not understood at this time and requires further investigation.

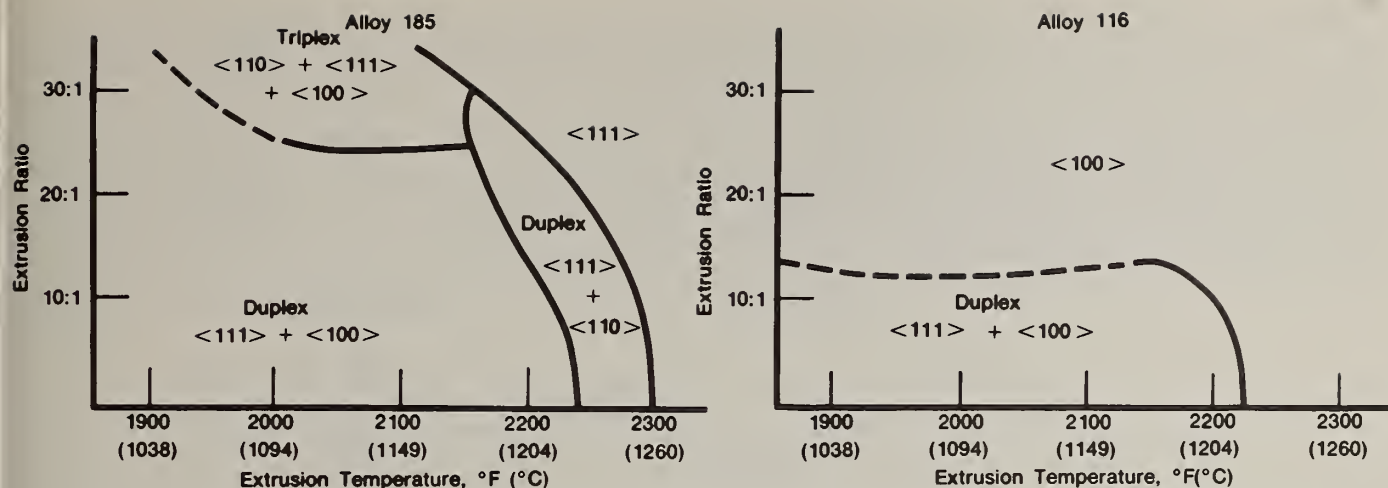


Figure 1: Fiber Textures in Alloys 185 and 116 as Influenced by Extrusion Ratio and Temperature.

ROLLING

Hot straight rolling was found to impart similar texture components to both alloys 185 and 116. Both exhibited a texture spread about the end orientations $\{113\}\langle 332 \rangle$ and $\{110\}\langle 112 \rangle$ with the most prominent component at $\{113\}\langle 332 \rangle$. The texture strengths were weak, typically at 2 times random. The texture strength was not significantly affected by the deformation temperature, although the alloy 185 strip rolled at 2000°F (the extreme lower hot rolling workability limit) exhibited a 3 to 4 times random texture strength.

The absence of a temperature-related texture transition in the hot rolled 116 and 185 was thought to be a result of heat losses during rolling. Thus, actual rolling temperatures were lower than for extrusion and texture transitions were insignificant, as with the lower temperature (2250°F) extrusions.

The low texture strengths of the hot rolled 185 and 116 are not fully understood. However, it is thought that at these high temperatures and low deformation rates these fine grained materials deform in part by grain boundary sliding and consequently lose texture strength.

Four different input textures of extruded alloy 185 and three of extruded alloy 116 were cold straight rolled. All responded in a similar fashion. Regardless of input texture, both alloys developed a weakly defined f.c.c. type sheet texture with as little as 9% reduction. With increased reduction, the sheet texture increased in definition (i.e. reduced spread) and strength. Textures could be described as a spread about the end orientations $\{113\}\langle 332 \rangle$ and $\{110\}\langle 112 \rangle$. The sheet textures were 2.5 x random at 25% reduction and 4 - 5x random at 36% reduction. Reductions greater than 35% resulted in even stronger and better-defined textures.

The deformation texture developed for both alloys was found to be unchanged by the many subsolvus (2200°F/5 min/air cool) intermediate annealing treatments used through the rolling schedule. Such behavior has been rationalized as crystallization *in situ*, whereby restoration occurs by subgrain rearrangement in the absence of movable recrystallization fronts. This was caused by the strong inhibitive effect of the ordered γ' phase on the growth of the classic f.c.c. $\{100\}\langle 001 \rangle$ annealing texture nuclei [5].

The texture development observed for both alloys appears to follow the trends reported in the literature for other f.c.c. metals and alloys. In the case of alloys 185 and 116, the end orientation $\{110\}\langle 112 \rangle$ is always present for the range of reductions studied. The major texture component, $\{113\}\langle 332 \rangle$, lies 10° off the $\{112\}\langle 111 \rangle$ by rotation about a $\langle 110 \rangle$ and is thought to be a product of the low to intermediate SFE alloys for the specific processing conditions. This is consistent with Dillamore's hypothesis [24] which characterizes the high SFE rolling texture as centered at the $\{4,4,11\}\langle 11,11,8 \rangle$, this component being a product of cross slip ($\{113\}\langle 332 \rangle$ lies 2° from the $\{4,4,11\}\langle 11,11,8 \rangle$). Theories for the characteristic plane strain rolling textures have been discussed extensively in the literature [2, 14 - 19].

Through cross rolling, both alloys 185 and 116 were observed to develop similar textures. The major effect of cross rolling was to change the straight rolling texture spread into a symmetric singular texture, centered at the $\{110\} \langle 112 \rangle$ component. The degree of textural singularity was observed to be dependent on the ratio of the straight to cross roll reductions, i.e. SR:XR. For alloys 185 and 116, a fair degree of singularity was achieved using SR:XR ratios within the bounds 80:20 and 60:40. Above and below these bounds the textures more closely matched those of straight rolled product, parallel to and 90° off the original (straight) rolling direction, respectively. Textural singularity also was observed in hot cross rolled product, centered at the $\{110\} \langle 112 \rangle$, although the texture strength was significantly lower. Figure 2 shows a pole figure of cold cross rolled Alloy 185.

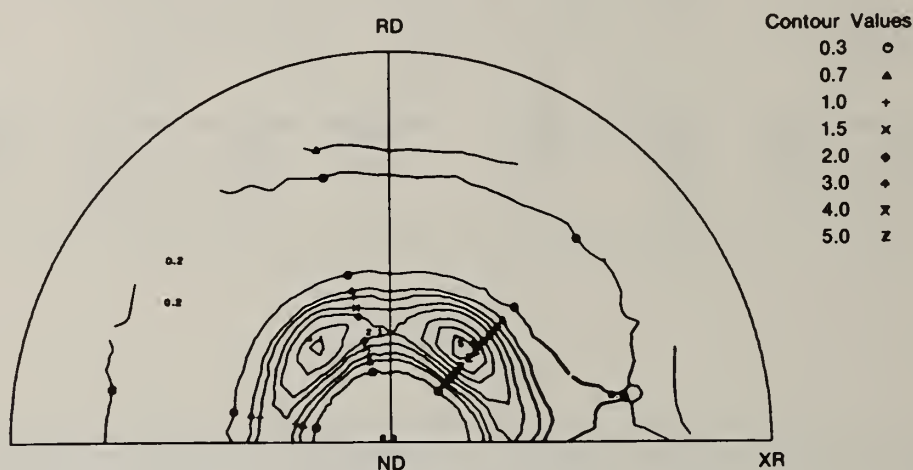


Figure 2: (111) Pole figure for cold cross rolled Alloy 185. 73% total reduction 70:30 SR:XR Ratio

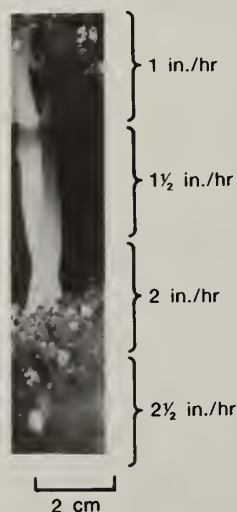


Figure 3: DR Rate Response of Cold Rolled Alloy 185.



Figure 4: Alloy 185 DR Strips Showing Wider Columnar Grains in the Cold-Cross Rolled Material (Left) Than the Straight Rolled Material (Right)

DIRECTIONAL RECRYSTALLIZATION

Hot rolled, cold straight rolled and cold cross rolled strips of each alloy were directionally recrystallized. The resulting grain growth patterns and orientations were documented.

In the as-rolled condition, only the cold rolled material responded to DR heat treatments. The cold rolled material exhibited continuous columnar grain growth from a maximum rate of 2 inch/hr down to 1/8 inch/hr, shown in Figure 2, whereas the hot rolled material exhibited only equiaxed grain coarsening. The as-rolled materials differed in texture strength (cold stronger than hot) and microstructure. Interrupted DR trials revealed that the cold rolled material, microstructure transformed during DR, producing grain boundary γ' necklaces. This transition, previously linked to positive DR response, was not found with the hot rolled material. However, a subsolvus conditioning heat treatment was developed for fine grain alloy 185 that established the necklace structure in previously non-DR responsive material. Hot rolled alloy 185 was condition heat treated to a necklace structure and subsequently exhibited columnar grain growth at insertion rates of 1/2 in/hr and slower. So it appears that both texture and microstructure significantly affected DR response. The desirable features of cold rolling versus hot rolling can be summarized as:

1. Stronger deformation texture
2. Finer and more homogeneous as rolled microstructure
3. DR response in the as-rolled condition
4. Continuous DR at insertion rates 4x faster
5. Greater propensity for single crystalline growth

The straight rolled material repeatedly grew narrower columnar grains than the cross rolled as shown in Figure 3. Cross rolling, with its singular texture, allowed fewer orientation combinations than straight rolled sheet. As the leading edge of a straight rolled sample underwent abnormal grain growth a larger number of allowed orientations grew resulting in narrower columnar grain widths.

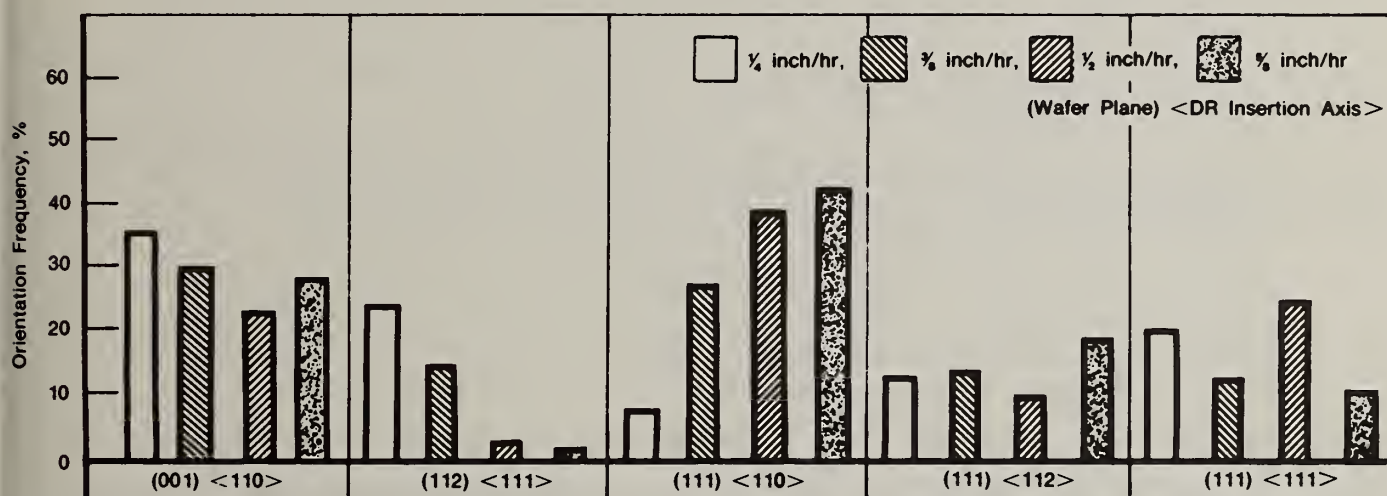


Figure 5: DR Grain Orientation Frequencies for Different Strip Insertion Rates Using Results From All Ten Rolling Schedules.

The columnar grain inspection and Laue data indicated that a strong cold cross rolling texture enhanced both single crystalline growth and orientation control. However, the effects of the cross rolling ratio variations were not discernable.

Repeated growth observations showed that the polycrystalline texture, though a necessary condition for allowed DR crystal orientations was not sufficient to guarantee a specific orientation (Frequencies of DR orientations for various growth rates are shown in Figure 4). However, by use of appropriate selection techniques (seeding, grain isolation, growth rates) any of the reported low index orientations could be produced as single crystals. In this respect, single crystal parts can be fabricated with selected mechanical properties compatible with service requirements.

The results of the study are consistent with previous studies on secondary recrystallization by Rosi et al [20], Aust [21] and Beck [22]. They reported that a few selected crystal orientations are promoted by the presence of a strong texture. The resulting crystals had a preference for specific orientation relationships to the matrix, the number of possible growth centers being limited by the existing texture such that other orientations are generally scarce. Further, the growth rate or mobility of a DR grain was strongly dependent on orientation. Previous studies showed similar results [20 - 23] where the $\langle 111 \rangle$ orientation exhibited the lowest mobility of all orientations, whereas crystals in the $\{111\}$ plane or zone exhibited the highest mobilities eg. $\langle 110 \rangle$ and $\langle 112 \rangle$.

The observations and the data presented represent an extensive evaluation of alloy 185. Admittedly the number of DR trials with similarly processed alloy 116 are fewer. However, the results of these trials with hot, cold straight, and cold cross rolled material duplicate those of alloy 185.

CONCLUSIONS

This study shows that, in general, deformation textures produced in alloys 116 and 185 follow the trends found for f.c.c. metals. Hot extrusion textures are dependent on alloy type, extrusion ratio and temperature, while hot rolling textures are virtually independent of rolling temperature, alloy type and seldom exceed 3 times random. Cold rolling texture types are relatively independent of alloy type, and texture strengths are higher and highly dependent upon percent deformation, with 35% reduction required to completely erase previous textures. Cross rolling imparts textural singularity upon both the hot and cold rolled material.

There is a strong correlation between crystallographic texture and both DR rate response and orientation control. Cold cross rolling produces the strongest, most singular textures, which promote the most rapid and most easily controlled DR. The DR crystal orientation control provided by the strongest textured material is not sufficient for production of DR single crystals, however, but must be supplemented with grain isolation techniques, furnace design, growth rate manipulation, and microstructural manipulation for growth of large single crystals. Studies investigating these parameters are underway.

ACKNOWLEDGEMENTS

The authors wish to thank O. B. Cavin (ORNL) and J. Umbach (PWA/GPD) for Pole figure generation, J. Zindel for the extrusion studies and R. E. Anderson and J. A. Miller for their constructive discussions and support.

This work is jointly sponsored and monitored by the U.S. Defense Advanced Research Projects Agency and the Air Force Wright Aeronautical Laboratories.

The views and conclusions contained in this paper are those of the authors and should not be interpreted as necessarily representing the official policies, either expressed or implied, of the U.S. Defense Advanced Research Projects Agency, U.S. Air Force, or the U.S. Government.

REFERENCES

- (1) H. Hu, Texture, 1974, Vol. 1, p. 233.
- (2) H. Mueller, Osterr. Akad. Wiss. Math Naturw. 1958, Vol. 7, p. 117
- (3) H. Hu and S.R. Goodman, Trans. Met. Soc. AIME., 1963 Vol. 227, p. 627
- (4) H. Hu and S.R. Goodman, *ibid*, 1963 Vol. 227 p. 1454
- (5) E. Hornbogen and H. Kreye, Proc. Intl. Symposium on Textures in Research and Practice, Clausthal - Zellerfeld, 1968, p. 274
- (6) A. R. Cox and E. C. VanReuth, Proc. 3rd Intl. Conf. Rapidly Quenches Metals, Univ. Surrey, U.K., 1978, p. 225
- (7) M.R. Glickstein, R.J. Patterson II, and N.E. Shockley, Proc. Intl. Conf. on Rapid Solidification Processing, Baton Rouge, LA, 1977, p. 46
- (8) P.R. Holiday, A.R. Cox and R.J. Patterson II, *ibid*, p. 246
- (9) R.G. Bourdeau and J.B. Moore, *ibid*, p. 334
- (10) D.B. George, J.B. Moore, and E.C. VanReuth AIAA/SAE/ASME Joint Propulsion Specialist Conf., Las Vegas, Nevada, 1979, p. 1
- (11) A.R. Cox, J.B. Moore and E.C. VanReuth, Proc. AGARD Conf #256, Adv. Fabrication Processes, Neuilly Sur Seine, France, 1978
- (12) R.E. Anderson, A.R. Cox, T.D. Tillman, and E.C. VanReuth, Proc. 2nd Intl. Conf. on Rapid Solidification Processing, Reston, VA, 1980, p. 416
- (13) G.R. Love, Oak Ridge National Lab. Tech. Memo, ORNL-TM-2018, 1968
- (14) I.L. Dillamore and W.T. Roberts, ACTA Met., 1964, Vol. 12, p. 281
- (15) I.L. Dillamore and W.T. Roberts, Met. Review, 1965, Vol. 10, No. 39, p. 271
- (16) I.L. Dillamore and H. Kato, Brit. Iron and Steel Res. Assoc. Report # MG/39/71, 1971
- (17) I.L. Dillamore and H. Kato, Metal Science, 1974, Vol. 8, p. 21
- (18) T. Kamijo, Trans. JIM, 1969, Vol. 10, p. 238
- (19) M. Hatherly, and I.L. Dillamore, J. Australian Inst. Metals, 1975, Vol. 20, p. 71
- (20) F.D. Rosi, B.H. Alexander and C.A. Duke, Tran AIME, 1952, p. 189
- (21) K.T. Aust, The Art and Science of Growing Crystals, J.J. Gilman, ed., John Wiley and Sons, 1963
- (22) P.A. Beck, Trans. AIME, 1951, Vol. 191, p. 475
- (23) B.B. Rath, and H. Hu, Trans. Met. Soc. AIME, 1966, Vol. 236, p. 1193
- (24) I.L. Dillamore, Met. Trans. 1970, Vol. 1, p. 2463

THERMAL STABILITY OF HIGH TEMPERATURE P/M ALUMINUM ALLOYS

Young-Won Kim*, M. M. Cook* and W. M. Griffith**

* Metcut-Materials Research Group
P.O. Box 33511
Wright-Patterson Air Force Base, OH, 45433

** Air Force Wright Aeronautical Laboratories
Materials Laboratory (AFWAL/MLLS)
Wright-Patterson Air Force Base, OH, 45433

ABSTRACT

Emerging high temperature aluminum P/M alloys have been characterized for thermal stability. The alloys selected are Alcoa aluminum powder alloys containing Fe (5.7 to 7.4 wt%) and a second alloying element (Ni, Ce, Co). These alloys are strengthened by finely dispersed intermetallic compounds that are formed during the melt atomization process. The materials' properties, especially strength, depend on the thermal stability of these compounds. A series of isochronal and isothermal experiments on vacuum hot-pressed material were conducted at temperatures between 316°C and 552°C. The annealing response was monitored by hardness measurements and microstructural changes were observed by SEM. The isochronal annealing experiments show that all the alloys have good stability up to 350°C and that the stability is rapidly lost at higher temperatures. The deterioration of stability differs in degree depending on the second alloying element, being the worst with Ce addition. The difference in the instability among alloys is further substantiated when the material is isothermally annealed. The coarsening of the intermetallic compounds is responsible for the decrease in stability and strength. Microstructural observations show the coarsening rates of the compounds vary from alloy to alloy.

I. INTRODUCTION

The need for stronger, lighter and more economical materials for aircraft structure and engine components has led to the development of new powder metallurgy (P/M) aluminum alloys (1,2,3). Aluminum P/M alloys for use at elevated temperatures are one such class of alloys. Characterized by a fine microstructure and a high volume fraction of thermally-stable intermetallic compounds, these alloys will compete with heavier steel and titanium alloys that experience service temperatures up to 330°C. The elevated temperature strength of the alloys depends on the thermal stability of these compounds. Optimum processing conditions have not been established for high temperature alloys in part because of the limited understanding of the thermal behavior of the strengthening compounds.

Three of the most promising alloys (Al-Fe-Co, Al-Fe-Ni and Al-Fe-Ce), currently under development by Alcoa, were selected for study. The thermal behavior for vacuum hot-pressed material was studied following isochronal and isothermal annealing. The coarsening of microstructure and strength change was monitored by SEM observations and hardness measurements.

II. EXPERIMENTAL

Several ternary alloys, based on Al-Fe, were supplied by Alcoa as alloy billets (1) that had been cold-compacted and then vacuum hot-pressed at 343°C. The compositions of three alloys selected for the present experiment are listed in Table I.

Table I. Alloy Compositions (wt%)(1)

Alloy	Alcoa No.	Fe	Ni	Co	Ce	Al
A	513671	5.70	----	6.20	----	Bal.
B	513670	5.70	6.10	----	----	Bal.
C	513672	7.40	----	----	3.40	Bal.

Small coupon specimens were prepared by sectioning the billets and polishing to 600 grit finish. Isochronal annealing experiments were conducted in air circulation furnaces, at temperatures between room temperature (RT) and 538°C and the annealing time was 1h. Two series of isothermal experiments were conducted in a salt bath at several temperatures selected from the isochronal annealing results. Changes of hardness values, after every annealing, were monitored by Rockwell B hardness measurements. Microstructural changes were observed by SEM of selected annealing conditions and for the starting material condition (as-hot-pressed).

III. RESULTS AND DISCUSSION

1. Isochronal Annealing

The three alloys were isochronally (1h) annealed at temperatures between RT and 538°C. The results are shown in Fig. 1 where RT hardness values, measured by Rockwell B (R_B), are plotted against annealing temperatures. The isochronal annealing responses of the alloys appear to be similar. Hardness values are relatively stable up to 350°C and they rapidly drop at higher temperatures. Further scrutiny, however, reveals observable differences in the annealing responses among the alloys, in addition to the differences in starting material's hardness. Alloy A (Al-5.7Fe-6.2Co) and C (Al-7.4Fe-3.4Ce) are very stable up to 350°C, showing hardness values virtually unchanged. Alloy B (Al-5.7Fe-6.1Ni), having a higher initial hardness value, exhibits some instability in this temperature range; however, this does not necessarily mean that Alloy B is unstable compared with the other two alloys. When Alloy B is heat-treated, for example, for 1h at 350°C to have R_B 92 and then isochronally annealed, the material exhibits the same stability as that of Alloy A or C (6,7).

At around 350°C, all the alloys begin to soften and at 538°C, a considerable fraction of hardness (from R_B 90 to 65) is lost. Coarsening of the strengthening intermetallic compounds is responsible for the loss. The rate of decrease with increasing temperature differs between alloys. Alloy A exhibits the slowest coarsening and Alloy C, the fastest, although the difference in the rate does not appear to be substantial. As will be shown, however, isothermal annealing substantiates the difference.

2. Isothermal Annealing

Using the results of the isochronal annealing experiments (Fig. 1), two series of isothermal annealing experiments were conducted over a wide range of elevated temperatures (316°C to 552°C).

a) In the first series of experiments, three temperatures (316, 349, 382°C) were selected around the critical temperature (350°C, Fig. 1), at which the stability to instability transition takes place for all the alloys. These temperatures bracket the maximum use temperature (goal) of the developing elevated temperature P/M Aluminum alloys. Accordingly, it is of engineering importance to characterize the thermal response of the alloys in the region. Three coupon specimen groups were prepared from as-hot-pressed billets for the three-stage isothermal annealing experiments.

The specimens of the first group were immersed in a salt bath at 316°C simultaneously. After a certain period of elapsed time, one specimen was removed and tested for hardness (Rockwell B scale, R_B). The longest annealing time at this temperature was 50h. The second and third groups of specimens were annealed at this temperature (316°C) for 50h. The second group of specimens was then isothermally-annealed at 349°C up to 33h. The third group of specimens were then given an additional annealing at 340°C for 33h and isothermal annealing experiments were conducted at 382°C up to 27h. The above annealing experiments thus provide continuous isothermal annealing curves at three intermittent temperatures. The results are shown in Fig. 2.

At 316°C, Alloys A and C exhibit an initial small hardness drop followed by fairly constant hardness values, whereas, Alloy B reveals constantly decreasing hardness values. This is consistent with the isochronal curve (Fig. 1) where Alloy B exhibits a similar trend. At 349°C, the isothermal annealing responses of the alloys are all similar; the hardness values constantly decrease. Up to this stage, it may not be unreasonable to say that the alloys have quite similar stability. When the isothermal annealing temperature is increased to 382°C, the annealing response becomes markedly different between alloys: Alloy C is the most unstable and Alloy A exhibits the highest stability. Alloy B, which was initially unstable at 316°C, now demonstrates a greater stability than Alloy C. It is worthwhile to point out, however, that the total decreases in hardness values are likely to be acceptable from the engineering viewpoint. When hot-pressed, Alloy B is extruded at a 20:1 ratio at 400°C, for example, the hardness value decreased to $R_B = 82$, but the tensile strength was 470MPa (67Ksi) (6,7). The hardness, $R_B = 82$, is compared with the final hardness ($R_B = 81.5$) of Alloy B, Fig. 2. This means that the material still retains the engineering strength after rather vigorous thermal treatments (Fig. 2).

b) In the second series of annealing experiments, five temperatures (380, 423, 470, 507, and 552°C) were selected from the later stage in isochronal annealing curves (Fig. 1). Isothermal annealing experiments at these temperatures have double purpose. Firstly, in the case that the material has to experience such high temperatures, for example, for degassing, it is important to know how the material loses the stability and thus, strength. Secondly, understanding the coarsening behavior at higher temperatures is of scientific importance. The experimental procedure was similar to that in the first series in that the isothermal annealing was continuously conducted at successively higher temperatures after an isothermal anneal. The results are plotted in Fig. 3.

At 380°C, the initial rapid decrease in hardness, shown by all the alloys, slows gradually. When the temperature is increased to 423°C after 12h at 380°C, the drop continues, however, no dramatic change is shown. A significant change occurs when the temperature is raised to 470°C. Alloy C exhibits a drastic decrease in hardness with time. While alloys A and B follow a similar trend, Alloy A is more stable. At higher temperatures, the difference in hardness changes between Alloy A or B and Alloy C is more obvious, indicating the coarsening of intermetallic compounds in Alloy C is occurring at a much faster rate. This will be shown, microstructurally, in the next section. One interesting feature in Alloy C is that the rate of decrease is not necessarily accelerated with increasing temperature. For example, the hardness decrease in Alloy C at 470°C is drastic and the decrease continues with time (see dotted line). At the next higher temperature (507°C), the initial decrease is significant but stability is quickly reached. At 552°C, however, the rapidly dropping rate is again observed to be continuous for a long period of time, although that trend is not shown to its conclusion in Fig. 3.

3. Microstructure

Microstructural observations were made for the as-hot-pressed condition and selected annealing conditions. All the observations were done by SEM after etching the specimens with Keller's etchant.

a) As-Hot-Pressed Material: There are distinguishable differences in microstructures between alloys, as shown in Fig. 4 where typical regions of the hot-pressed alloys are shown. In Alloys A and B, the typical microstructure is eutectic, with the eutectic nature more pronounced in alloy B, Figs. 4a and b. Both microstructures were taken from relatively large powder particles. The eutectic structure in Alloy A appears to be disturbed which is not understood clearly: either heat fluctuation during solidification or deformation during hot-pressing or both may be responsible. It is mentioned, however, that the disturbance is found infrequently. The eutectic is coupled in many cases, as shown in Fig. 4b, which also exhibits grain boundaries inside a powder particle. In contrast to Alloys A and B, Alloy C shows virtually no eutectic; instead, dendrite or cellular structure is predominant, Fig. 4c. It is likely that the addition of Ce in Al-Fe suppresses the formation of eutectic which is detrimental for material's ductility. In fact, Alloy C has shown the best ductility among the alloys after forging (2). It has been reported that improvement in the ductility of Alloys A and B can be achieved by destroying the eutectic structure using a severe deformation means such as extrusion (6,7).

It was also observed that Alloys A and B exhibit fairly uniform microstructure within a powder particle, while Alloy C exhibits a mixture of fine and coarse structures, Fig. 4c. However, overall microstructure in bulk material appears to be more uniform in Alloy C. Although, not shown here, Alloys A and B contain large powder particles having coarse intermetallic compounds in a dendritic form.

b) Heat-Treated Material: The SEM micrographs in Fig. 5 show the coarsening of

intermetallic compounds to which the hardness changes may be attributed. Overall, Alloy C exhibits coarse microstructure that probably is responsible for the low hardness values compared with other alloys, Fig. 1. When heat-treated at 398°C for 1h, Alloys B and C show some sign of slight coarsening, Figs. 5d, e and f. This is consistent with the corresponding hardness changes in Fig. 1. When heat-treated at a higher temperature (476°C) for 1h, there is a significant coarsening regardless of the alloy. Careful observation shows, however, that there is a considerable difference between alloys. Alloys A and B have fine microstructure regions that usually are within small powder particles. In contrast, Alloy C exhibits overall uniform coarse microstructure which makes the identification of powder particles difficult. This is, again, consistent with the observations that the hardness of Alloy C is decreased at a faster rate over the other alloys. It is noted that the intermetallic compounds generally become spherical after higher temperatures.

IV. CONCLUSIONS

1. All of the alloys investigated are isochronally (1h) stable up to 350°C. At higher temperatures, the hardness decreases linearly with increasing temperature, Al-Fe-Ce showing a slightly faster decrease.
2. Isothermal annealing experiments show that at 316°C, Al-Fe-Co and Al-Fe-Ce are quickly stabilized in hardness with time after initial small drops. Al-Fe-Ni shows constantly decreasing hardness although the drop is small. At higher temperatures, however, Al-Fe-Ce exhibits the least stability with time. Al-Fe-Co and Al-Fe-Ni behave similarly, but overall, Al-Fe-Co is more stable.
3. Al-Fe-Co and Al-Fe-Ni still maintain acceptable hardness after continuous annealing consisting of 316°C/50h, 349°C/33h and 382°C/27h. Al-Fe-Ce falls below acceptable hardness after a few hours at 382°C following the first two heat treatments.
4. The initial morphology of compounds differs between alloys. Al-Fe-Ce contains a dendritic or cellular type structure. In Al-Fe-Co and Al-Fe-Ni, eutectic structure predominates. The eutectic structure is detrimental to ductility. The rod-type compounds in eutectic become spherical after a high temperature annealing.

REFERENCES

1. W. L. Otto, Jr., "Metallurgical Factors Controlling Structure in High Strength P/M Products", AFML Technical Report, AFML-TR-76-60, May 1976.
2. R. E. Sanders, Jr. and G. J. Hildeman, "Elevated Temperature Aluminum Alloy Development", AFWAL Technical Report, AFWAL-TR-81-4076, Sept. 1981.
3. S. L. Langenbeck et.al, "Elevated Temperature Aluminum Alloy Development", Lockheed-California Co., AF Contract #F33615-81-C-5096, Interim Report, LR29977, Oct. 1981.
4. W. M. Griffith, R. E. Sanders, Jr., and G. J. Hildeman, "Elevated Temperature Aluminum Alloys for Aerospace Applications", Proceedings of High Performance Aluminum Powder Metallurgy (in press), Feb. 14-18, 1982, Dallas, TX.
5. S. D. Kirchoff, R. H. Young, W. M. Griffith and Y-W. Kim, "Microstructure/Strength/Fatigue Crack Growth Relations in High Temperature P/M Aluminum Alloys", Proceedings of High Performance Aluminum Powder Metallurgy (in press), Feb. 14-18, 1982, Dallas, TX.
6. Y-W. Kim and L. R. Bidwell, "The Effects of Thermomechanical Processing on Al-Fe-Ni P/M Alloy", TMS-AIME Annual Meeting, Feb. 22-26, 1981, Chicago, IL.
7. Y-W. Kim, L. R. Bidwell and W. M. Griffith, "The Effects of Microstructure on Tensile Properties of P/M Al-5.7Fe-6.1Ni", in preparation to publish in Met. Trans.

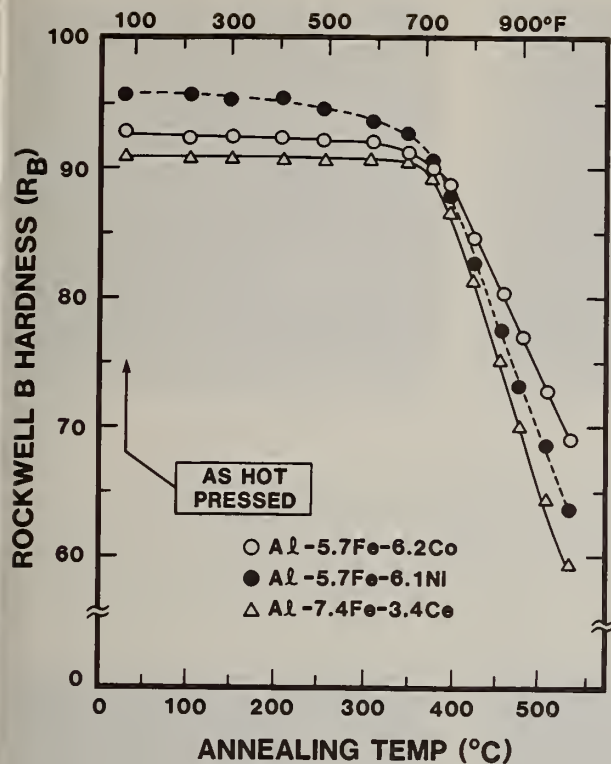


FIGURE 1

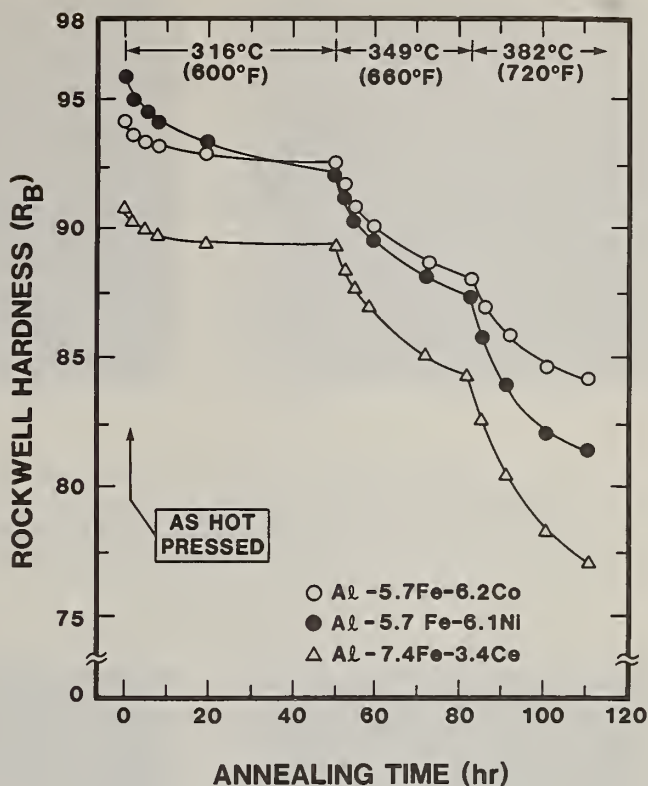


FIGURE 2

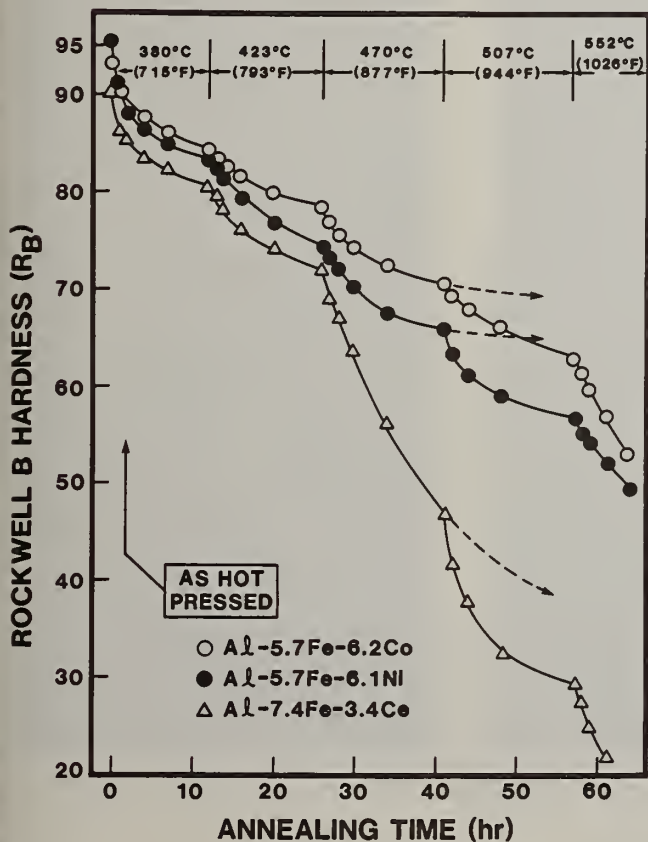


FIGURE 3

FIGURE 1: Isochronal annealing curves for alloys A (Al-5.7Fe-6.2Co), B (Al-5.7Fe-6.1Ni), and C (Al-7.4Fe-3.4Ce).

FIGURE 2: Isothermal annealing curves for alloys A (Al-5.7Fe-6.2Co), B (Al-5.7Fe-6.1Ni), and C (Al-7.4Fe-3.4Ce) near the critical temperature.

FIGURE 3: Isothermal annealing curves for alloys A (Al-5.7Fe-6.2Co), B (Al-5.7Fe-6.1Ni), and C (Al-7.4Fe-3.4Ce) at high temperatures.



FIGURE 4: Typical microstructures of as-hot-pressed alloys: a = Al-5.7Fe-6.2Co; b = Al-5.7Fe-6.1Ni; c = Al-7.4Fe-3.4Ce.

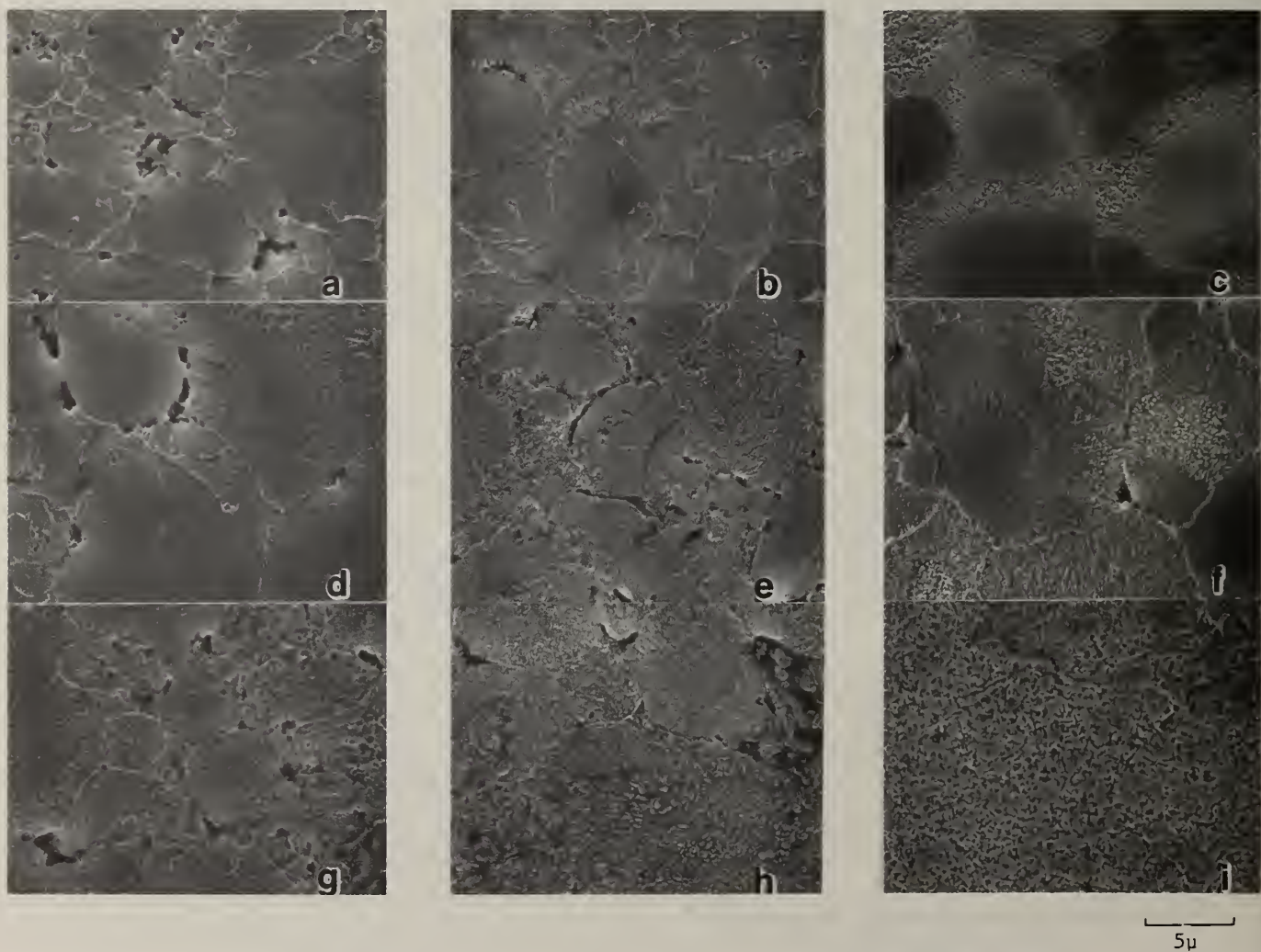


FIGURE 5: The effect of heat treatment on the microstructures of alloys A, B and C: a-c = as-hot-pressed; d-f = annealed, 398°C/1h; g-i = annealed, 476°C/1h.

EVALUATION OF VOIDS IN POWDER CONSOLIDATES USING LONG WAVELENGTH NEUTRONS

M. Fatemi and B. B. Rath

Physical Metallurgy Branch, Naval Research Laboratory, Washington, DC 20375

ABSTRACT

The capabilities of small angle neutron scattering method (SANS) have been shown to be unique in evaluating small defects in alloys fabricated by consolidating fine particulates. Potential applications in detecting small voids and precipitates either left in the alloy during fabrication or subsequently formed by nucleating and growth have been realized. The availability of high-flux research reactors, high speed, large capacity computers, and efficient position sensitive neutron detectors has made quantitative defect characterization possible. An analysis of radially averaged SANS profiles, obtained from area detector plots, provides information on the range and relative number of defects, such as microvoids in powder of relevant processing parameters. Results of a study on the detection of voids in powder compacted Ti-alloys and steels are described. Correspondence is established between SANS profiles and relative void size distributions with consolidation parameters such as pressure and temperature. It is shown that hydropressed Ti-6Al-4V powder exhibits a reduction in the number and size of voids with an increase in consolidation pressure from 60 ksi to 100 ksi. Similarly, hot-pressed stainless-steel powder shows a systematic decrease in porosity upon increase in compaction temperature from 800° to 1200°C. Results of the non-destructive evaluation by SANS, with supporting evidence from transmission electron microscopy, is presented.

Introduction

The application of non-destructive test methods to the problem of evaluating microstructural defects in materials has been a subject of ever increasing importance in materials science. To a large extent, this trend is due to the development of engineering materials of sophisticated composition aimed at higher durability and performance. It has been indicated (1-3) that, most non-destructive evaluation methods suffer from several limitations, particularly when the defects of interest are very small. Small-angle neutron scattering (SANS) is an appropriate method for flaw detection, where defects of interest are in a size range of approximately 100-1000Å. The neutron intensity profile scattered at small angles which generally decreases monotonically as a function of the scattering angle, contains information on the size and number density of the scattering centers in materials. The shape of the net scattering curve, obtained from the difference between the reference standard and the sample under investigation can be analyzed to evaluate a relative size distribution of the defects.

Methods for particle size distribution have been devised to obtain information, on the average size of defects and their distribution as a function of processing variables (4-7). These evaluations are based upon the assumption that the observed intensity is the integral of the product of the size-distribution function and the single-particle intensity function. Since there are no analytical forms that can be used in evaluating size distributions from various types of defects, numerical evaluation methods are utilized. Different algorithms have been used to derive size distributions of defects from SANS profiles (4-7), by numerically solving an integral equation of the type:

$$I(q) = K \int D(R) m^2(R) I_0(qR) dR \quad -(1)$$

which relates the number density, $D(R)$, of particles of radius R to the measured integrated intensity, $I(q)$. In the above equation $q = 4\pi \sin \theta / \lambda$, m is the excess nuclear scattering length density in the particle and $I_0(qR)$ is the single-particle scattering function which depends on the particle shape and dimensions.

However, if the sample contains a uniform dispersion of nearly similar particle sizes or the intensity data is limited in the q range, the Guinier method (8) may be employed which suggests that the natural logarithm of intensity, $\ln I$, proportional to the square of the wave-vector, q^2 , such that the:

$$\text{slope} = \frac{\Delta \ln I}{\Delta(q^2)} = \frac{R^2}{3} \quad -(2)$$

where R is the radius of gyration of the spherical particles. A straightline behavior $\ln I$ vs. q^2 over a significant portion of the scattered intensity is an indication of nearly uniform size. A trend of varying slopes indicates either particles of varying size and distribution or other complex scattering interactions. If the presence of a widely varying particle or void size distribution is recognized a more elaborate size distribution calculation is warranted. In the present investigation the analysis of the void sizes have been made using the Guinier method.

Powder consolidates of different metals and alloys, are known to contain a small volume fraction of voids, particularly if they have not been subjected to a post-consolidation hot working process. The source of these voids are due to: (1) a lack of complete densification which leaves unsintered regions in the final product, (2) shrinkage during solidification and (3) trapped gases within the powder particles. The characteristics of these cavities present in titanium alloy powders and powder consolidates have been described by Eylon et. al. (9). They have shown that the gas pores, present inside the powder particles do not close during the consolidation process. These cavities subsequently serve as the initiation sites for cracks (10). SANS provides a unique non-destructive method to quantitatively determine the void sizes in powder consolidates. The method can indeed be used to optimize processing variables to reduce the number density and size of voids in sintered or hot-isostatically pressed products.

Results and Discussion

A systematic study of porosity in powder consolidates of stainless steels HIPed at a constant 15 ksi pressure and varying temperatures and a Ti-6Al-4V alloy hydropressed at 1315°C at varying pressures has been conducted using SANS method. Electron microscopic examination of the samples provided supportive evidence of voids in these alloys systems.

Porosity in Powder Compacted Stainless Steels

Disks of stainless steel specimens prepared from gas-atomized powder (Fe-21Cr-6Ni-9Mn-.02C-.25N₂, wt%) from cylindrically extended rods were obtained from Sandia Corporation. Specimen designations with corresponding HIPing temperatures and final densities are listed in Table I.

A nominal thickness of 2.5mm was chosen for all samples, with surfaces polished on 400 and 600 paper, and finished with Linde A powder. A standardized sample preparation procedure was adopted to ensure uniformity and a minimization of surface strain, since minor variations in surface conditions have been shown to affect small-angle scattering profile (11).

Neutron scattering measurements were performed at the SANS facility of the Oak Ridge National Laboratory. After preliminary measurements, it was established that the significant part of the scattering was confined to very small angles ($q = .005$ to 0.015 \AA^{-1}). Therefore, the sample-to-detector distance was set at 16 meters for improved resolution on the 64 x 64 element

position-sensitive detector. The measurements were made in a vacuum of 10^{-5} mm of Hg. The scattering characteristics of a standard sample (wrought stainless steel) were measured and subtracted from each of the test samples to obtain a true measure of the scattering that is attributable to defects. Data processing included correction for background measurements and normalization of all data by the transmission and thickness factors.

TABLE I

Sample #	Temp., °C	Density*
B26	800	98.7
B28	800	98.9
B27	900	99.5
B33	1000	99.5
B34	1000	99.2
B36	1100	99.3
A5	1200	99.6
A6	1200	99.8
STD		100.0

*Nominal density is measured relative to wrought material as 100.0.

The Guinier plots from SANS measurements are shown in Fig. 1. For clarity in the display, two different scales are used; the lower set of curves for q^2 varying from 0 to 8×10^{-4} , \AA^{-2} , and the upper set of curves for q^2 varying from 0 to 2×10^{-4} , \AA^{-2} . The upper set shows the detailed variation in the maximum pore size, (corresponding to low- q values), while the lower set indicates the relative intensity of the smaller pores (related to higher- q values).

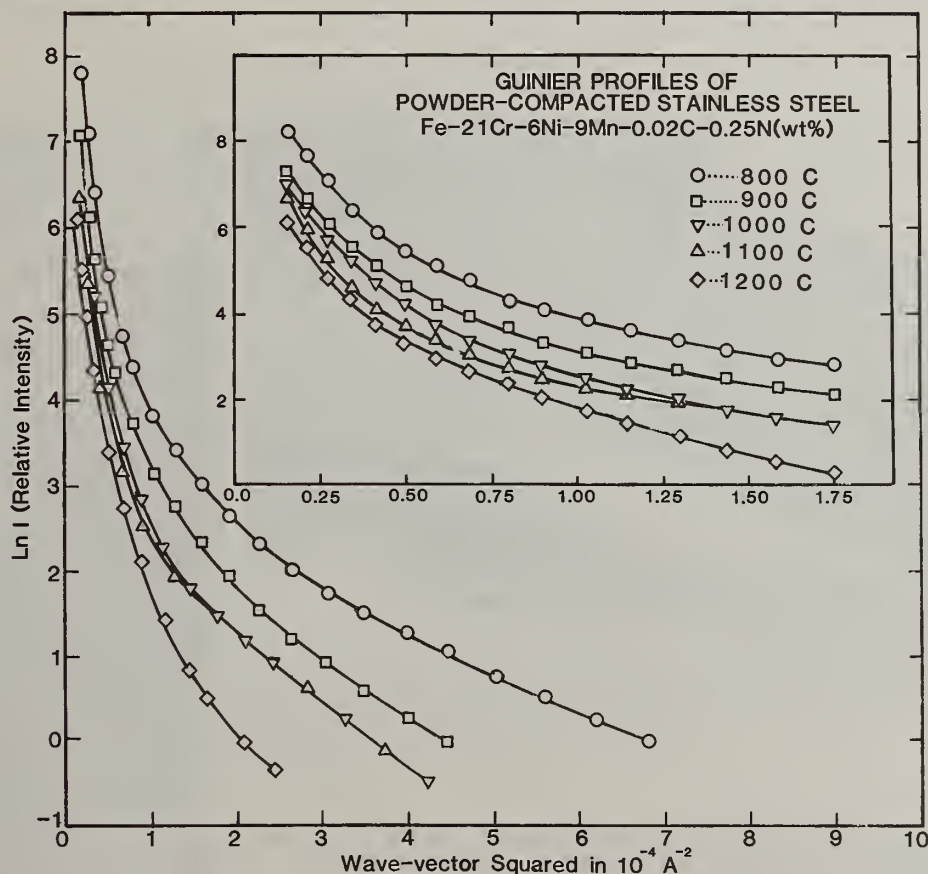


Figure 1 - Guinier plot of SANS profiles from (21-6-9) stainless steel, showing the relationship between intensities and compaction temperatures.

It is seen that the scattering decreases with increasing temperature. Similarly, the relative density quoted in Table I appears to be directly related to the temperature, the lowest temperature (800°C) corresponding to the lowest density (98.9%) and the highest temperature (1200°) to the highest density (99.8). The difference in scattering between these two extreme cases, larger than one order of magnitude, is consistent with the effect of voids as the major source of scattering. Furthermore, the slope of each curve provides information about relative pore sizes. Thus, specimen # B36 shows a larger maximum pore size compared to other samples, with pore number density somewhat less than # B33-34, while both have nearly the same measured density of 99.3%.

Despite some uncertainty in the measured densities there is a strong evidence of a systematic variation of density with extrusion temperature. The pore size in all samples, calculated from the Guinier slope, ranges from 300A to 800A and the relatively low scattering intensity indicates correspondingly low void densities. A simple calculation of void density on the basis of the given weight density yields a number of about 10^{13} voids/cm³, assuming an average void size of 500A. This number may be converted to a surface density distribution appropriate for observation by SEM or similar techniques. For the material of density 99.8%, the calculated void spacing corresponding to the above number density will be about 0.5 μ m (5000A). Attempts to observe these voids by scanning electron microscopy proved difficult because of interference from surface irregularities in the specimen.

Transmission electron microscopy was performed for direct observation of voids. This procedure is not without problems since the voids which are exposed to the surface are enlarged during the electrothinning processes and contribute to an error in the size distribution analysis. However, the interior voids remain unaffected and can provide a good estimate of number density and size.

Figures 2 and 3 demonstrate the use of two TEM methods used in the observation of voids for sample B28. In Fig. 2, the specimen is set at $S=0$ (exact Bragg condition), where S is the deviation for Bragg angle. Interference fringes from variation of sample thickness are observed. Here, the intensity contrast from voids changes alternately from white to black to white. The method is thus suitable for observation of small voids. In this micrograph voids in a range of sizes varying between 100 and 400 A along with a very large hole (3000A) are visible. In Fig. 3 a multibeam condition with $S \neq 0$, larger voids (approximately 700A) are visible. In order to minimize the adverse effects of electrothinning, a procedure consisting of electropolishing followed by ion-milling (a minimum of 1h to remove first few hundred anstrom layer from the surface) has been developed.



Figure 2 - TEM micrograph showing the interference thickness fringes and change of contrast for voids in stainless steel specimen # B28 processed at 800°C.

Figure 3 - Electron Micrographs of Voids in Powder Compacted Stainless Steel (Fe-21Cr-6Ni-9Mn-0.02C-0.25N), Processed at 800°C.



Three samples of hydropressed Ti-6Al-4V were supplied by Gould Corp. Titanium alloy powder was consolidated in autoclave at a temperature of 1275°C and at pressures of 60, 80, and 100 ksi, respectively. The powder compacted samples and a standard Ti-6Al-4V were ground to a thickness of approx. 3.3 mm, then polished on No. 400 and No. 600 Emery paper. As in the preceeding case, the sample-to-detector distance of 16 m was better suited due to the absence of significant data at larger scattering angles. Figure 4 shows SANS profiles of the three specimens.

An analysis of pore sizes gives a range of values for pore size ranging from 300A at one extreme to 1150, 1020 and 880A at the other extreme corresponding to 60, 80, and 100 ksi, processing pressures, respectively. It may be seen that at higher scattering angles the intensity associated with the 80 and 100 ksi specimens is higher than the corresponding intensity for the 60 ksi specimen. However, at very small angles the intensity from the 60 ksi sample exceeds those from the other two. This behavior indicates a refinement of pores with increasing pressure, and is consistent with the effect of compaction pressure on pore size. Transmission electron micrographs of two samples in Fig. 5 show typical pore sizes observed.

Results of this investigation clearly shows that intensity profiles of long wavelength neutrons scattered from powder compacts containing very small volume fractions of residual voids can be effectively analyzed to yield quantitative information on void size and distributions. Furthermore, the method demonstrates the potential for non-destructive evaluation of defects in rapidly solidified powder consolidates.

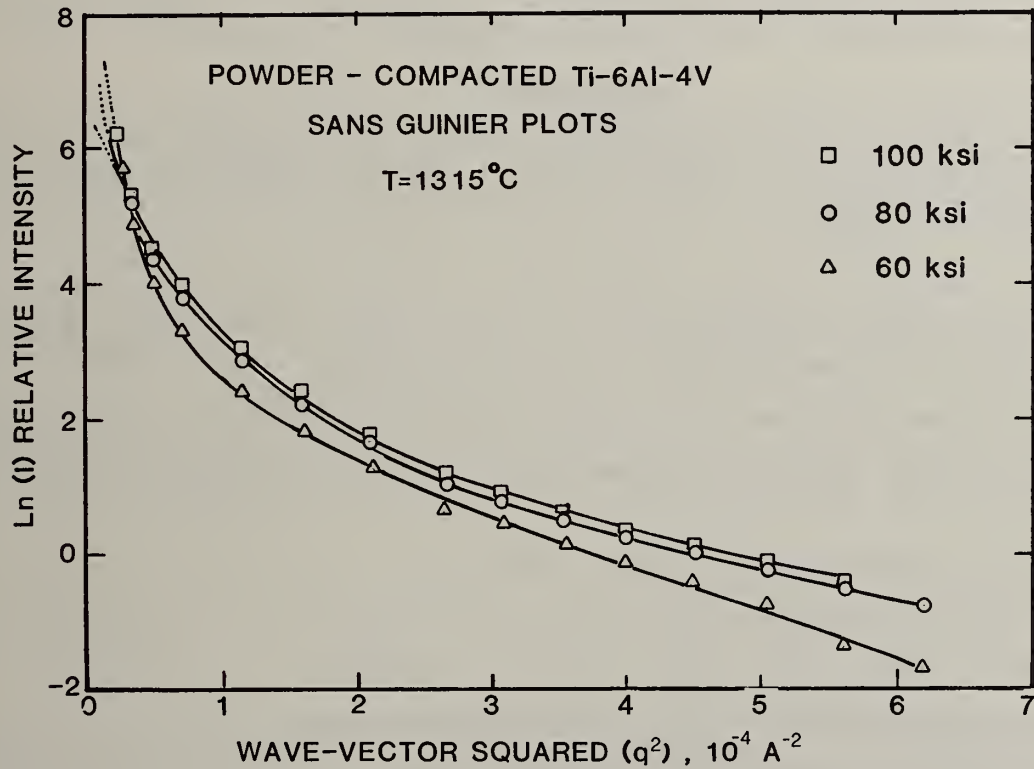


Figure 4 - Guinier plot from SANS profiles of HIPed Ti-6Al-4V alloys prepared at 60, 80, and 100 ksi.

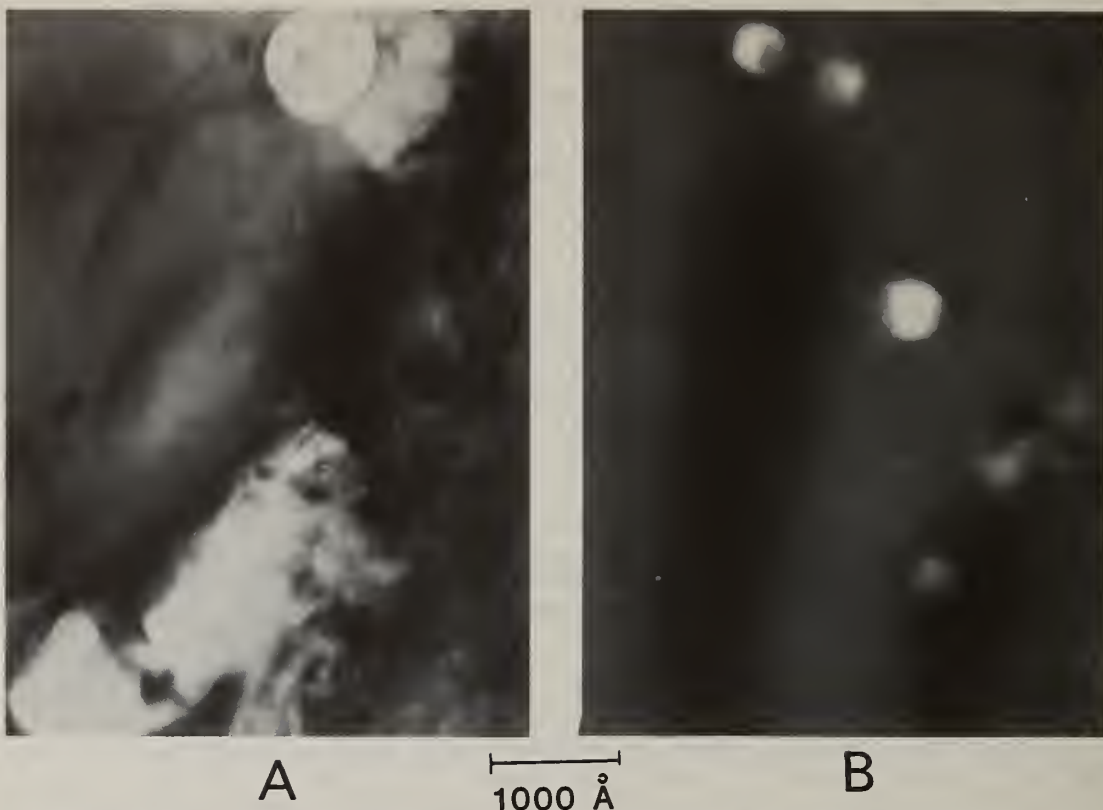


Figure 5 - Electron micrographs of voids in Ti-6Al-4V, Compacted at 2400°C (A) 60 ksi, (B) 80 ksi.

Acknowledgments

This work was funded in part by the Office of Naval Research and has been performed in cooperation with the National Science Foundation (Oak Ridge National Laboratory SANS Facility). The authors would like to thank Drs. J. E. Sumgeresky and R. Stoltz of Sandia Corporation, and Dr. M. Dustur of Imperial Clevite Corporation for supplying the alloy samples and Dr. C. S. Pande for the electron microscopic measurements.

References

1. M. Fatemi and B. B. Rath, "Non-Destructive Evaluation of Defects in Structural Materials Using Long-Wavelength Neutrons," NRL Memorandum Report No. 4226, May 1980.
2. M. Fatemi, C. S. Pande, M. A. Imam, and B. B. Rath, AIME Fall 1981 Meeting, Louisville, Ky.
3. M. Fatemi and B. B. Rath, "Non-Destructive Evaluation of Defects in Structural Materials," Report to Office of Naval Research, September 20, 1980.
4. G. C. Vonk, J. Appl. Cryst., 9, 433 (1976).
5. H. A. Mook, J. Appl. Phys., 45, 43 (1974).
6. O. Glatter, J. Appl. Cryst., 13, 7 (1980).
7. I. S. Fedorova and P. W. Schmidt, J. Appl. Cryst., 11, 405 (1978).
8. A. Guinier and G. Fournet, Small-Angle Scattering of X-Rays, J. Wiley and Sons, NY (1955).
9. D. Eylon, R. E. Omlor, R. J. Bacon and F. H. Froes, Powder Metallurgy of Titanium Alloys, Ed. F. H. Froes and J. E. Smugeresky, The Met. Soc. of AIME, Warrendale, Pa., 71, (1980).
10. H. H. Hausner, Jr. of the Japanese Soc. of Powder Met. 7 (1960).
11. M. Roth, J. Appl. Cryst., 10, 172 (1977).

RAPID SOLIDIFICATION - PAST PROMISES AND CURRENT REALITY

A. M. Adair,* L. A. Jacobson,** E. C. van Reuth,** and J. Dickson***

*AFWAL Materials Laboratory, Wright-Patterson AFB OH

**Defense Advanced Research Projects Agency (DARPA), Arlington VA

***Systems Planning Corporation, Arlington VA

ABSTRACT

A number of ongoing efforts are being conducted to develop higher performance structural alloys by means of rapid solidification processing. In almost every program, some difficulties have been encountered, and additional work has been necessary to address the fundamentals of the specific areas in which problems were not anticipated. The historical background of rapid solidification is briefly reviewed. The undertaking of development efforts to define the exploitation route for applications requiring improved materials performance is given. These efforts are described next, with emphasis on those factors which differ from our original high expectations. Recent studies which have addressed both the general aspects of current techniques for achieving and consolidating rapidly solidified materials, and the specific factors which will bear on the future application of such materials to high performance defense systems are summarized. Finally, some suggestions for future rapid solidification efforts are made. These are based on lessons learned from experience and should accelerate the application of rapidly solidified structural alloys.

Introduction

There can be little doubt that we are on the threshold of a new era in metallurgy and more broadly, in materials science, brought about by the application of Rapid Solidification Technology (RST) to the production of new and improved materials. As the introductory paper for a session concerned with applications of materials made by RST, we will treat somewhat selectively the past work that has brought us to this threshold, and outline some of the expected future advances that will come from application of RST. Concerning our choice of title for this paper, it is our feeling that over the past several years, there has been a commendable spirit of enthusiasm growing for the potential benefits of RST. Also, there has been a body of experience accumulating from efforts to apply RST to the task of developing useful new materials. We have been keenly aware of the many difficulties that have been encountered in these latter efforts, and these difficulties are what has prompted us to select our title for this review. The implication is, of course, that our current experience is not fully bearing out the past promises of RST. We do not intend to convey a pessimistic note; rather, we hope to stimulate objective examination of this new technology, and a clearer perspective as to the advantages it offers.

We will limit our discussion to those areas in which RST has been applied to structural materials. There is, of course, an additional large body of information concerning the successful production of amorphous alloys by RST. The application of such materials in a variety of useful devices also depends on the unusual physical properties of the material which play a crucial role in the achievement of significant performance improvements.

It is in the structural alloys arena that RST must face head-on the challenges posed by competitive conventional processing methods, new alloys not dependent on RST, and alternative materials such as composites that cover a wide range of temperature capability. This is a very competitive arena, one in which there is now a very keen interest in those mechanical properties which fall in the "second tier." First tier properties are those which have the most direct bearing on the performance of a component--strength, stiffness, and density. Second tier properties are those which influence the useful lifetime of the component--fatigue with its crack initiation and crack growth components, corrosion and the effects of corrosive environments on crack growth, creep and stress rupture, thermal fatigue, oxidation and hot corrosion. Somewhat further in the background, but increasing in importance, is the area of fabricability and inspectability of structural components. In the efforts to apply RST materials, we must consider how they can best be made into useful shapes and how they may differ in their ability to be inspected, based on demanding requirements to guarantee that they

are free from defects that could lead to the development of critical flaws in service.

An appropriate conclusion to this introductory section is a discussion of cost. RST involves additional costs compared to conventional structural materials processing, and we must be aware constantly of the necessity to justify these higher costs in realistic terms which balance them against achievable benefits. A recent study by Kearns has clearly put materials cost considerations into perspective [1]. When a materials choice must be made, it will invariably be the lowest cost material which will accomplish the needed performance. On the other hand, it is very difficult to resolve cost-benefit trades in a generalized context. It is almost impossible to compute the system life cycle costs saved by incorporating a higher cost, but more durable material. Judging from recent decisions in the Department of Defense, it appears that the initial acquisition cost of a system is of greater concern than the future costs of maintenance, inspection and repair. These latter costs do not clearly show up in the materials selection decision process. We expect this to be more important in the future, but we also must recognize that in the advocacy of new RST materials, we must recognize that RST is a higher cost option to conventionally processed materials. This higher cost will often have to be justified on bases over which the materials developer has little control. We suggest that this is a current reality against which the past promises of Rapid Solidification Technology need to be evaluated. Fortunately, we are faced with many moving targets of opportunity, and so we proceed with an examination of RST promises as related to some present materials challenges.

Historical Background of RST

The historical development of RST can be viewed from two perspectives--the processes by which rapid quenching from the melt (as the general field has been known until recently) can be achieved, and the application of such processes to produce useful new alloys. Examining the specific processes, one finds that in 1871 a patent was issued to E. M. Lang for a method of casting solder wire on the periphery of a rotating drum [2]. After a rather long passage of time, the next major development was a chill mold technique described by Falkenhagen and Hofmann in 1952 [3]. One year later, R. B. Pond, Sr. was awarded a patent on the melt spin method for making metallic filaments [4]. It is of interest to note that in 1958, Soviet investigators published work on the piston/anvil technique and the structure of alloys produced by this rapid solidification method [5].

In 1960, Duwez et. al. published a description of yet another rapid quenching method involving a gun or shock tube as the means of projecting molten alloy against various substrates [6]. This work is generally cited as having first recognized that unusual new solids could be achieved through rapid solidification. Duwez reported that complete (metastable) extension of solid solubility in Ag-Cu alloys could be achieved. This alloy system was examined by other investigators who were concerned with new techniques for achieving rapid quenching from the melt. A few of the more significant are: Mutsuzaki et. al. in 1963, electrical discharge machining [7]; Moss et. al. in 1964, plasma jet spraying [8]; and Pond and Maddin in 1969, rapid solidification melt spinning [9]. Aluminum alloys were the objects of investigations concerning self-substrate quenching using either an electron beam (Hiller, 1968) [10] or a laser (Jones, 1969) [11].

Amorphous metallic alloys were first reported by Duwez et. al. in 1960 [12], and research on these materials continued to increase, culminating with the recognition given to Duwez in his selection to present the American Society for Metals Campbell Memorial Lecture in 1967 [13]. The early 1970's were marked by a number of significant process and composition patents issued to investigators working at the Allied Corporation and at the Battelle Memorial Institute. In 1972, Jones and Suryanarayana published an annotated bibliography of rapid solidification work that covered the period 1958-1972 and included a total of over 400 references, many of which were from work done at universities [14].

A key link between RST and the established field of powder metallurgy was made in the mid 1970's by Cox et. al. who combined centrifugal atomization with forced convection cooling (inert gas quenching), and achieved rapid solidification rates for powders of nickel, aluminum, and iron base alloys [15]. Other powder process developments occurred subsequent to this time period, among them ultrasonic gas atomization as reported by Grant et. al. [16]. A wide variety of processes for making alloy powders are now being explored as part of the effort to advance rapid solidification technology. Of particular importance are the nickel base alloys for which increased homogeneity has demonstrable benefits (especially oxidation resistance) and aluminum alloys with high iron content and either molybdenum or cerium additions which retain higher temperature strength properties and cannot be processed by conventional ingot methods.

It has been suggested that the close ties that are developing between powder metallurgy and RST tend to detract from the stature of the latter as a separate field of endeavor. For structural alloys, however, apart from the capability of rapid solidification powder making methods, it is clear that other advancements in powder metallurgy (such as isothermal forging and hot isostatic pressing) provide the most acceptable routes to the fabrication of useful structural shapes. Thus, the many

powder consolidation methods which have been developed constitute an important part of the historical background. Without this background, much of the rapid progress in RST could not have been achieved. In fact, many would agree that the production of F100 turbine engine components from IN 100 powder beginning in 1972 was the first significant application of RST.

The promise of RST is founded on a sound basis of process techniques and exploratory applications to a wide variety of alloy systems. You have heard, and you will hear in this conference, many examples of how the promise of RST is being realized. We turn now to a few points that bear on current realities which we expect will stimulate discussion, thought, and further experimental efforts to build on the momentum already established.

Current Reality

We intend in this section to place emphasis on several lessons learned, drawing from recent experience gained on both completed efforts, and programs that have yet to be completed.

Aluminum Alloys

While there has been keen interest for some time on major programs sponsored by the DoD, there is as yet no volume application of RST aluminum alloys. Most of the effort has been on the high strength alloys of the Al-Zn-Mg compositions, and they are now undergoing a round-robin evaluation by industry. The concerns are that their overall property improvements are not sufficient to justify the additional cost, and, for specific applications, that improved fatigue crack growth resistance is needed. If these alloys are processed under properly controlled conditions, they offer a narrower variation in properties, improved fatigue strength, and improved stress corrosion resistance. We should emphasize that the final product quality is equally dependent on the initial powder quality, its careful handling, method of consolidation, and various subsequent processing steps.

Application of RST to chemical compositions which are normally used in ingot metallurgy can even have a negative effect. Most high strength aluminum alloys are used in a partially recrystallized condition, i.e., a wrought-elongated grain structure. However, rapid solidification can result in a fine dispersion of constituents that inhibit recrystallization [17]. The net result of deformation processing plus heat treatment on RST products can then result in a fully recrystallized product.

We may learn that high modulus, low density alloys based on lithium additions, processed initially by RST, can also be processable by ingot methods, depending on lithium content. Work in progress should provide the answer, as properties of materials made by each method will be compared. The high transition element content alloys for either higher modulus or higher temperature requirements will probably require all-inert processing or novel low temperature consolidation techniques, or both. Much of the benefit of RST processing has been lost due to the need for high temperature outgassing treatments that invariably result in coarsening of the strengthening particles. High temperature consolidation methods can lead to the same result. It is not yet clear whether particle surface oxide can be tolerated, given the current emphasis on both strength and toughness. Recent evidence presented by Hildeman et. al. [18] suggests that variation in oxide content which is due primarily to particulate (powder) morphology affects the alloy behavior in slow bend toughness testing; the lower oxide content giving clear indications of improved toughness. Further, they report that even for spherical products having the lowest total oxide content which were compacted by controlled vacuum hot pressing, subsequent hot deformation in excess of a 60% reduction in height would probably be required to achieve optimized mechanical properties.

Nickel Base Alloys

Production of IN 100 turbine engine components continues using a combination of extrusion and isothermal forging by a patented process. Consolidation of powder to near net shaped components by hot isostatic pressing (HIP) has been used to produce turbine engine disks for production and experimental studies; however, the use of components after HIP without any hot deformation operations ("AS HIP") has been brought into disfavor for reasons having most to do with the undesirable consequences of contamination. Most of the activity on disk alloys has been to improve the overall process or improve existing alloy compositions rather than investigate a broad range of possible approaches to utilize the advantages of RST. Such a program is planned in the near future. HIP consolidation of melt-spun ribbon has been attempted, but results indicate that more effort would be needed to achieve uniform winding, and consequent uniform consolidation shrinkage.

Improved oxidation resistant alloy compositions intended for use in turbine airfoils have required that elements such as chromium and tantalum be added (which originally had not been expected

to be needed). However, the amounts added are much lower than current casting alloy compositions, and the alloys still do not contain cobalt. Turbine airfoils produced from wafer blocks that were directionally recrystallized to elongated grain structures (similar to directionally solidified cast airfoils) had to be abandoned due to unacceptable transverse properties. While some of the compositions made by RST have also been successfully cast as single crystal test bars, the best compositions, containing small amounts of hafnium and yttrium, are not amenable to current practice for casting single crystal airfoils having complex geometry cores for cooling air distribution.

Rapid solidification plasma deposition of nickel base alloys is an emerging process, but it is too soon to give a fair assessment of its potential. Major programs on this technology are currently underway.

Iron Base Alloys

While we in the DoD may tend to be concerned with the "more exciting" alloy systems, the ferrous alloys may well be the "sleeper" in this technology. One of the first successful commercial applications of RST technology was the PM tool steels produced by Crucible. They demonstrated several years ago that the more uniform chemistry and the more evenly distributed, smaller carbide size led to more efficient cutting and longer tool life. Crucible combined this product with hot isostatic pressing to produce a variety of tool shapes. With current efforts underway to decrease machining costs by various approaches, the demand for such improved tooling materials is expected to increase significantly.

Bearing materials have always been a "very interesting" product, at times almost in an atmosphere of intrigue; due no doubt to the efficiency of the failure process associated with large bearings. AISI 52100 and M50 steels have long been industry standards; anything new never could find anyone wanting to change or willing to re-evaluate the relative cost. Most bearing problem areas center around corrosion and rolling contact fatigue failures, undoubtedly affected by the presence of corrosion product. Inherent fracture toughness is also a concern for modern turbine engine bearings. RST bearing steel compositions [19] have been produced and evaluated, whose properties suggest that attitudes may very well change, especially as the new turbine engine designs contain higher rotor speeds and fewer stages. Highly corrosion resistant bearing steel compositions have been produced which have equivalent rolling contact fatigue resistance to today's M50 steel; other compositions have shown very significant increases in rolling contact fatigue resistance. There is little doubt that these materials will be very much in demand in the future. Applications are also expected to be made where high levels of wear resistance is required, such as cam surfaces in diesel engines. As we try to get increased durability for all products we manufacture, specialty applications for these uniquely microstructured steels will evolve.

By no means should we neglect moderate to high strength steels that are quenched and tempered to achieve their properties. It has been shown that the impurity elements present in relatively low levels in cast and wrought steels take on new roles in RST produced alloys [20]. Their distribution is very uniform, they are finely divided, and they effectively prevent grain growth of the austenite phase during heating. This characteristic opens up a much larger processing and heat treatment window and offers an opportunity for more favorable combinations of strength and toughness in these steels.

Iron-aluminum alloys are not new, but achieving grain size control to effect useful room temperature ductility is new and has been a consistent result of RST technology. These materials have excellent oxidation resistance over a wide temperature range [20], their density is significantly lower than nickel base alloys, and their opportunities for the application of thermomechanical processing are many. Burner cans in turbine engines and several static structures are already under consideration for early implementation. These products must compete with the high chromium containing stainless steels and the "leaner" composition superalloys, both nickel and cobalt base.

Future Projections

An important suggestion was made at a recent Government-Industry workshop on RST. One participant expressed concern that the preponderance of Government sponsored RST efforts were addressing the application of these new materials in some of the most structurally critical components. He suggested that application efforts might proceed more smoothly if some less demanding components were selected for initial demonstration. We admit that this suggestion is eminently sensible, but is not very likely to have much effect, given the circumstances in which new RST structural alloys must compete with other materials for limited development and demonstration resources. This competitive situation is unlikely to significantly change in the future, so the efforts to achieve the highest possible payoff in performance will continue to emphasize the use of RST materials for the most challenging

components. The generation of a knowledge base for RST materials based on first-hand experience will consequently be delayed.

A more basic factor which continues to cloud the RST picture for the future is the lack of information on the unequivocal effects of higher solidification rates on the properties of consolidated shapes representative of a particular application made from a single alloy composition. Until controlled studies are performed, in which solidification rate is the single variable, other factors being held as constant as possible, we will not have a clear perspective on the real benefits of rapid solidification. For example, the recently completed work by Hildeman et. al. [18] used the same aluminum alloy compositions, and when cooling rate was varied among splat, gas atomization, and centrifugal atomization, the morphology changes associated with these processes had a greater effect than differences in cooling rate.

Another fundamental problem has to do with the effects of different powder production and handling environments on the properties of consolidated RST alloys. We expect that different alloy systems will differ in their sensitivity to environmental inertness, and might also anticipate that different alloys within a given system would also respond differently. Controlled studies are also needed to elucidate the effects of different environments on mechanical properties, especially second tier. These last two points serve to remind us that our efforts to date have been concerned with determining sufficient conditions for achieving benefits through RST, but we have not really sought out the necessary conditions. If the necessary conditions turn out to involve lower solidification rates or less stringent requirements for inert atmospheres, strict adherence to a set of sufficient conditions may impede RST materials application potential.

A final point bearing on RST structural applications is our perception of the need for more understanding of the influence of various consolidation processes on the properties of the RST material. In addition to the more well established methods of consolidation such as HIP, hot pressing and hot extrusion, other methods such as plasma spray or melt-spray deposition, dynamic compaction and ultrasonic compaction should receive greater emphasis. Work is already underway on a number of these consolidation techniques, but results are not sufficient to predict the possible advantages or disadvantages of each. Again, it can be expected that different RST alloys will respond differently to the various compaction methods.

Conclusions

Perhaps the most important lesson learned to date that applies to the field of Rapid Solidification Technology for structural alloys is that an atmosphere of optimistic over-advocacy should be carefully avoided. The principles that have guided the development of current widely used high performance structural materials are still valid ones, even for RST. However, RST processing has distinctive capabilities that have tempted us to place it outside the mainstream of past alloy developments. True, RST does offer unique new possibilities for control of alloy microstructures, but the question remains: Given this new control, what sort of microstructures should we try to produce? We do not yet seem to be capable of establishing alloy microstructure goals for the simultaneous optimization of both strength and toughness, based on clearly demonstrated fundamental principles. Perhaps the next steps needed are the devising of programs and the conducting of critical experiments, using RST materials, to shed some light on the critical microstructural parameters affecting mechanical properties of interest, both singly and in combination.

In the context of recent lessons learned, which have combined to add an air of caution to some of our enthusiasm, what can we now predict for the future of RST? It is useful to remind ourselves that actual directions which some lines of inquiry take do not always follow those that are predicted for them at their early stages. In his 1967 Campbell Memorial Lecture, Professor Duwez made the following remarks in his conclusion: "As Professor Gilman told you (in his lecture given the previous year) . . . alloy monocrystals are a reality and may be the next generation of turbine blades in jet engines. I would not dare to predict such a spectacular future for alloys quenched from the liquid state, and I am sure they will never be used in jet engines." [13]

Ten years after that prediction, a braze alloy made by rapid quenching from the melt in ribbon form had clearly shown superiority over its powder counterpart. This alloy is now used to join jet engine components. And fourteen years later, the potential of rapidly quenched nickel base alloys for turbine blades was firmly established through engine testing of two blades fabricated from Ni-Al-Mo-W alloy powder (RSR 185). Variations of this alloy are now showing the clear benefits that rapid quenching from the melt can give to high temperature strength and oxidation resistance, improvements that are due to the high degree of chemical homogeneity that results from rapid solidification.

So one past prediction has not, in fact, been borne out by later experience. There are also examples for which the actual experience has exceeded expectations. Despite our high expectations

for structural alloy performance improvements, we know that the higher cost of RST will have to be offset by some other form of economic benefit, and we suggest that the best context in which to make such cost/benefit determinations is the specific use environment. The nickel base alloy disks are the only structural alloy RST applications for which the benefits have been balanced against costs. We must have other examples of actual experience to build a broad-base economic acceptance of RST applications. Competition from other quarters will also cause the perspective and expected benefits to change.

References

- [1] Kearns, T., Private Communication.
- [2] Lang, E. M., "Machines for Casting Solder Wire," U.S. Patent No. 5,862, Reissued 1874.
- [3] Falkenhagen, G. and Hofmann, W., Z. Metallkunde 43 (1952) 69.
- [4] Pond, R. B., "Metallic Filaments and Method of Making Same," U.S. Patent No. 2,825,108; 1953.
- [5] Salli, I. V., Liteinoe Proizvodstvo, 1958, No. 7, 22-25.
- [6] Duwez, P., Willens, R. H. and Klement, W., J. Appl. Phys., 31 (1960), 1136-7.
- [7] Mutsuzaki, K., Suzuki, M., and Kawai, E., J. Jap. Inst. Metals, 27 (1963) 424-7.
- [8] Moss, M., Smith, D. L., and Lefever, R. A., Appl. Phys. Letters, 5 (1964) 120-1.
- [9] Pond, R. and Maddin, R., Trans-Met. Soc. AIME, 245 (1969) 2475-6.
- [10] Hiller, W., Met. Contr. Mecan (La Metallurgie) 100, No. 1 (1968) 35-6.
- [11] Jones, H., Mater. Sci. Eng. 5 (1969) 1-18.
- [12] Klement, W., Willens, R. H., and Duwez, P., Nature 187 (1960) 869-79.
- [13] Duwez, P. Trans. Am. Soc. Metals, 60 (1967) 607-33.
- [14] Jones H. and Suryanarayana, C., J. Materials Science, 8 (1973) 705-53.
- [15] Cox, A. et. al., Reports on Contract F33615-76-C-5136.
- [16] Anand, V., Kaufman, A. J., and Grant, N. J., "Rapid Solidification of a Modified 7075 Aluminum Alloy by Ultrasonic Gas Atomization," Rapid Solidification Processing Principles and Technologies II, Edited by R. Mehrabian, B. H. Kear and M. Cohen, Claitors Publishing Division, Baton Rouge, LA (1980) 273-286.
- [17] Jacobson, L. A., Pierce, C. M., and Cook, M. M., "Microstructures of Powder and Conventionally Processed 7075 Aluminum Alloy," AFML-TR-71-240, W-PAFB, Ohio, December 1971.
- [18] Hildeman, G. J., Lege, D. J., and Vasudevan, A. K., "Fundamentals of Compaction Processes for Rapidly Quenched Prealloyed Metal Powders," AFWAL-TR-82-4156, W-PAFB, Ohio, October 1982.
- [19] Adam, C. M., Bourdeau, R. G., and Brock, J. W., "Application of Rapidly Solidified Alloys," AFWAL-TR-81-4188, W-PAFB, Ohio, February 1982.
- [20] Proceedings of Briefing/Workshop on Rapid Solidification Technology, R. Mehrabian & Organizing Committee, COMAT; National Bureau of Standards, 1-2 July 1981.

AEROSPACE STRUCTURAL APPLICATIONS OF RAPIDLY SOLIDIFIED ALUMINUM-LITHIUM ALLOYS

R. E. Lewis^{*}, I. G. Palmer^{*}, J. C. Ekvall⁺, I. F. Sakata⁺, and W. E. Quist^{**}

^{*} Lockheed Palo Alto Research Laboratory, Palo Alto, CA, 94304

⁺ Lockheed-California Company, Burbank, CA, 91520

^{**} Boeing Commercial Airplane Company, Seattle, WA, 98124

ABSTRACT

Advanced aluminum-lithium alloys are being developed to save a significant amount of weight (10 to 20 percent) in new aircraft airframe structures, by replacing the currently used 2xxx and 7xxx high strength aluminum alloys. The weight saving of aluminum-lithium alloys is directly related to their lower density, higher modulus, and high strength. Both powder metallurgy and ingot metallurgy techniques are being used in alloy development programs. Rapid solidification processing of the alloys is currently being evaluated because improved ductility and toughness may be achieved through fine grain size, freedom from massive segregated phases, and an increased amount of elements that form fine, stable dispersoids. A number of property goals established for the development of aluminum-lithium alloys is reviewed. A comparison with these goals of the best properties of alloys in current development is presented. Specific analyses of applications of aluminum-lithium alloys to different types of aircraft are made, with particular attention to the advantage of using a variety of low density alloys exhibiting different properties. Finally, a number of technical issues regarding the development and acceptance of the materials by the supplier and user communities are reviewed.

INTRODUCTION

In the development of new aerospace structures, both increased structural efficiency and reliability are goals to be achieved, and at the lowest cost. Improvements in structural efficiency are achieved by applying more accurate or effective structural designs or by using new structural materials that will reduce weight, or a combination of these. For a majority of aerospace structures, designers believe that with currently available materials, redesign alone will not result in a significant further improvement in structural efficiency. Any substantial additional gains in weight savings will have to be achieved by applying advanced materials that are lighter, stiffer, stronger, more fatigue resistant, or more damage tolerant. The successful development of such materials will benefit all aerospace applications including aircraft, missiles, and space vehicles.

Improvements in aluminum and titanium alloys as well as composite materials are all topics of high current interest in the aerospace community. Of these, improved aluminum alloys, such as aluminum-lithium, will have obvious advantages because of their comparatively low cost and easy assimilation using the extensive existing manufacturing facilities. Lithium additions to aluminum are particularly effective as lithium reduces the density and at the same time increases the stiffness of aluminum. Both property changes are important contributions to weight savings in aerospace structures, with density decrease being the most important [1]. Only one other element, beryllium, when added to aluminum has a similar effect on the properties, but it is not an attractive choice for most applications because of its high cost and toxicity.

Rapid solidification processing (RSP) of new aluminum-lithium alloys is currently being evaluated with the objective of improving ductility, toughness, and strength. These improvements may be achieved using the attributes of RSP including finer grain size and solidification structure, extended solid solubility, and suppression of coarse second phase particles.

The status of current activities in this important alloy development and processing field is reviewed briefly below, along with appropriate aluminum-lithium ingot metallurgy developments which share the same general objectives. The major emphasis of this paper, however, is to review the airframe structural designer's assessment of the potential contributions of aluminum-lithium alloys, and why there is increasing interest on the part of both prospective suppliers and users. In the final

section, a review is presented of the technical issues that are involved in the successful development and acceptance of these new materials.

PROPERTY GOALS FOR ALLOY AND PROCESS DEVELOPMENT

Current property goals of a number of aluminum-lithium alloy development programs are shown in Table 1. Included are two powder metallurgy (PM) alloy development programs being performed by Lockheed Missiles & Space Company, Inc. (LMSC) and the Boeing Commercial Airplane Company using rapidly solidified particulate, a study by Lockheed-California Company (CALAC) in which the availability of both (PM) and ingot metallurgy (IM) alloys was assumed, and IM alloy development programs being performed by Alcoa, Alcan and British Alcan Aluminium Company (formerly British Aluminium Company). In all cases the baseline alloys are those currently being used on existing aircraft, and the property goals represent for the most part improvements in density, modulus and specific strength with other properties remaining the same, so that the new alloys would be used on a direct substitution basis for existing alloys, thereby minimizing the requirement for redesign. A number of smaller alloy development programs and programs involving mechanical alloying are not included in Table 1. Details of many of these programs are given in the proceedings of the First International Aluminum-Lithium Conference [2] and will be supplemented in the upcoming Second International Aluminum-Lithium Conference [3].

The LMSC/DARPA program started in 1978. The objectives are to develop alloys meeting the property goals shown in Table 1, and to establish a metallurgical basis for manufacturing scaleup and application to new aerospace systems. Phase 1 (Alloy Development) has been completed and reported [4,5,6]. In this phase three iterations of alloys were evaluated, involving twenty-one compositional variations made from both splat and fine atomized powders. In the first iteration of alloys Al-Li-Cu and Al-Li-dispersoid alloys were examined, made from splat particulate. In the second iteration Al-Li-Cu-Mg alloys were evaluated, also made from splat particulate. In the third iteration the most promising compositions from the first and second iterations were evaluated, made from fine atomized powders.

In Phase 2 (Scaleup) of the program two Al-Li-Cu-Mg-Zr alloys were prepared in the form of both PM and IM alloys. The target compositions were Al-3Li-1.5Cu-1Mg-0.2Zr and Al-3Cu-2Li-1Mg-0.2Zr. The PM alloys were prepared by Pratt and Whitney Aircraft from chill cast remelt stock using centrifugal atomization in helium, followed by screening, degassing, canning, and extrusion. The weight of the extrusion billets was approximately 30 lb. The IM alloys were prepared by British Alcan Aluminium by direct chill (DC) casting of 140 lb billets, followed by homogenization and extrusion. Preliminary tensile properties of the alloys have been measured, and a full spectrum of engineering property data is currently being obtained. Plans for further work on this program involve the optimization of composition in the Al-Li-Cu-Mg-Zr alloy system, including in particular the evaluation of higher zirconium levels (in the range 0.5 to 2.0 wt percent) in order to utilize the potential advantages of rapid solidification more fully than were used in the Phase 2 alloys.

The Boeing/AFWAL program started in 1982. The objective is to develop a family of aluminum alloys with significantly lower density and higher specific modulus and strength than existing high strength ingot alloys. The primary thrusts of the program are goal assessment, alloy development, and application payoff studies. Phase 1 (Team Organization and Goal Assessment) has been completed and Phase 2 (Overall Alloy and Process Development) is on-going [7]. The property goals shown in Table 1 are the preliminary goals defined at the start of the program; the actual goals have not yet been published. Three different classes of alloys are being examined, representing three different production methods. Class I comprises rapidly solidified powder alloys produced by Pratt and Whitney Aircraft by centrifugal atomization in helium, Class II comprises mechanically alloyed powder alloys produced by International Nickel Co., and Class III comprises ingot alloys produced by DC casting by British Alcan Aluminium. The primary alloy systems include Al-Li-Cu-Mg-Zr and Al-Li-Zn-Mg-Cu-Zr in Class I, Al-Li-Mg and Al-Li-Cu-Mg in Class II, and Al-Li-Mg-Zr in Class III. Powder has been prepared and consolidated for alloys in Classes I and II and mechanical property and microstructural evaluation of the alloys is currently being performed.

The CALAC/NASA program was started in 1980 and completed in 1981; the final report of the program has recently been issued [8]. The study identified the weight savings and economic benefits that would result from the incorporation of advanced aluminum alloys in future commercial aircraft. In addition an estimate was made of the future demand for new PM and IM aluminum alloy products. Realistic property goals were established for advanced aluminum alloys, in coordination with ALCOA, to maximize aircraft system effectiveness. Five alloy classes were identified to meet the requirements for future airframe design, and were classified according to the major property requirements as follows: A, strength; B, strength and corrosion resistance; C, strength, stiffness and corrosion resistance; D, durability and damage tolerance; E, low density, high stiffness. Two of these alloy classes, C and E, would contain lithium. Detailed properties were defined for all five classes of alloys for sheet, plate, extrusion and forging products, and are described in the final report [8].

TABLE 1. Abbreviated Property Goals of Current Development Programs for Aluminum-Lithium Alloys

COMPANY/SPONSOR	MFG TYPE	LOW STRENGTH	MEDIUM STRENGTH	HIGH STRENGTH	DADTA
LMSC/DARPA	PM		7075-T76 +30% E/ ρ	7075-T76 +20% E/ ρ +20% σ_y/ρ	
BOEING/AFWAL *	PM	2024-T3,T4 -10% ρ	7075-T73 +30% E/ ρ	7075-T73 +20% E/ ρ +20% σ_y/ρ	
CALAC/NASA	PM, IM	2024-T3 -10% ρ +10% FA-TIGUE		7075-T76 +10-20% σ_y +8% E	
ALCOA W/BOEING *	IM	2024-T3 -10% ρ		7075-T6 -7% ρ +10% FA-TIGUE	2324-T39 -9% ρ
BACO, RAE ALCAN, RAE BRIT, AEROSPACE	IM	2024-T3 -10% ρ	2014-T6 -10% ρ	7075-T73 -10% ρ	
ALCOA/NAVIAIR	IM	2024-T3 -8% ρ		7075-T6 8% ρ	

*PRELIMINARY PROPERTY GOALS.

TABLE 2. Tensile Properties of LMSC/DARPA Phase 2 Al-Li-Cu-Mg-Zr PM Alloys

	7075-T76 BASELINE		GOAL A		GOAL B	
	ORIGINAL	REVISED	TARGET*	ACTUAL	TARGET*	ACTUAL
F_{ty} , ksi	67	70	67	82.4	76	82.2
F_{tu} , ksi	73	80	73	90.4	87	86.1
ELONG., %	10	10	10	4.1	10	6.7
ρ , lb in. ⁻³	0.101	0.101	0.091	0.090	0.095	0.093
E, 10 ⁶ psi	10.3	10.4	12.1		11.8	
E/ ρ , 10 ⁶ lbf in. lb ⁻¹	102	103	133		124	
σ_y/ρ , 10 ³ lbf in. lb ⁻¹	663	693	736	916	796	884

*TARGET PROPERTIES SHOWN WERE DEFINED AT THE START OF THE PROGRAM AND WERE BASED ON THE ORIGINAL BASELINE VALUES FOR THE 7075-T76 ALLOY.

The ALCOA IM alloy development program started in about 1981, and represents a continuation of previous in-house work and work funded by NADC. Very little information on the program has been released, apart from the three property goals shown in Table 1, which were defined in collaboration with Boeing [9]. The intention is to have alloys commercially available by 1985. Alcoa is also performing a smaller program, sponsored by NADC, with similar property goals, as shown in Table 1.

The British Alcan Aluminium (BAACo) work started in about 1978, and was a continuation of earlier work performed by Fulmer Research Institute and High Duty Alloys. BAACo has concentrated on developing the casting and processing technology to make sheet and extrusions. A DC casting technique is being used, with some modifications to improve the safety aspects. BAACo is currently casting 800 lb ingots of dimensions 20 x 7 in, and the intention is to scale up to 4000-8000 lb rolling slabs by 1985 [10]. Initial work was performed on the Al-Mg-Li system, but most of the work is now being performed on an Al-Li-Cu-Mg-Zr alloy developed by the Royal Aircraft Establishment (RAE), Farnborough, UK. The work at ALCAN International started in 1980, and the intention is to develop the casting technology to make large ingots for plate. In order to avoid the hazards associated with DC casting an alternative casting system is currently being used. ALCAN is presently casting 310 lb ingots of dimensions 5 x 12 in, and the intention is to scale up to 6000 lb ingots by 1984 ([11]. Most of the work is currently being performed on the RAE alloy. The alloy development goals shown in Table 1 for both ALCAN and BAACo were defined in collaboration with British Aerospace.

For the alloy development programs shown in Table 1 mechanical property data is only available at the present time for the LMSC/DARPA PM program and the BAACo IM program. Mechanical property data on Phase 1 of the LMSC/DARPA program have been reported [4,5,6]. Data on Phase 2 of the program consists of preliminary tensile data generated on small scale extrusions of cross-section dimensions 0.28 x 0.56 in, made at LMSC using the same fine atomized powder as for the larger Phase 2 extrusions. Data have been obtained for alloys solution heat treated at 1000°F, water quenched, stretched 2 percent and aged at 375°F to the peak aged condition. The data are shown in Table 2 where they are also compared with the program property goals A and B. Both alloys show higher yield strengths than the program goals but lower ductility. The high yield strengths are attributed partially to unrecrystallized microstructures. The effect of various underaging treatments on strength and ductility is currently being studied, in order to define aging conditions that will produce lower strength levels that are closer to the program goals, and at the same time higher tensile ductility. Mechanical property data on the BAACo program consists of tensile and other data on an alloy of the RAE composition. Recent tensile data are shown in Table 3 for sheet, plate and extrusion products, where they are compared with data for a draft specification for sheet, and target data for plate [10]. The data for the three different property goals were obtained by different aging treatments on a single alloy composition. Strength levels are equal to or greater than the target values; however, elongations are slightly lower. The sheet data are for 0.063 in thickness, the plate data are for 1.0 in thickness equivalent in degree of reduction to 3.0 in. plate, and the extrusion data are for a cross-section 2.5 x 0.625 in. All materials were solution heat treated, water quenched, stretched and artificially aged.

APPLICATION STUDIES FOR SMALL MILITARY AIRCRAFT

The aircraft selected for the weight savings analysis was the S-3A patrol aircraft. The S-3A is a subsonic, carrier-based, anti-submarine warfare aircraft that is fully operational with the U.S.

TABLE 3. Longitudinal Tensile Properties of BAACo Al-Li-Cu-Mg Alloys Prepared from DC Cast Ingots

PROPERTIES	SHEET		PLATE		EXTRUSION	
	SPECIF.	ACTUAL	TARGET	ACTUAL	TARGET	ACTUAL
2024-T3 REPLACEMENT						
F_{ty} , ksi	39.2	48.9				51.1
F_{tu} , ksi	58.7	63.7				64.5
ELONG., %	10	8				6.5
ρ , lb in ⁻³	0.091	0.091				
2014-T6 REPLACEMENT						
F_{ty} , ksi	55.1	59				64
F_{tu} , ksi	63.8	71.4				73.5
ELONG., %	6	6				5.3
ρ , lb in ⁻³	0.091	0.091				
7075-T73 REPLACEMENT						
F_{ty} , ksi	66	67.2	63.4	60.9		73.7
F_{tu} , ksi	74	77.3	70.3	69.6		82.8
ELONG., %	6	5	10	6		6
ρ , lb in ⁻³	0.091	0.091				

TABLE 4. Simplified Formulas for Weight Ratio & Margin of Safety Correction Factors

CATEGORY NO.	FAILURE MODE	WEIGHT RATIO $\frac{W_2}{W_1}$	MARGIN OF SAFETY CORRECTION FACTOR
1	TENSILE STRENGTH	$\frac{\rho_2}{\rho_1} \frac{F_{tu1}}{F_{tu2}}$	$\frac{1}{1 + M.S.}$
2	COMPRESSIVE STRENGTH	$\frac{\rho_2}{\rho_1} \frac{F_{cy1}}{F_{cy2}}$	$\frac{1}{1 + M.S.}$
3	CRIPPLING	$\frac{\rho_2}{\rho_1} \left[\frac{E_1}{E_2} \right]^{.25} \left[\frac{F_{cy1}}{F_{cy2}} \right]^{.25}$	$\left[\frac{1}{1 + M.S.} \right]^5$
4	COMPRESSION SURFACE COLUMN & CRIPPLING	$\frac{\rho_2}{\rho_1} \left[\frac{E_1}{E_2} \right]^4 \left[\frac{F_{cy1}}{F_{cy2}} \right]^{.2}$	$\frac{1}{1 + M.S.}$
5	BUCKLING COMPRESSION OR SHEAR	$\frac{\rho_2}{\rho_1} \left[\frac{E_1}{E_2} \right]^{.33}$	$\left[\frac{1}{1 + M.S.} \right]^{.33}$
6	AEROELASTIC STIFFNESS	$\frac{\rho_2}{\rho_1} \frac{E_1}{E_2}$	$\frac{1}{1 + M.S.}$
7	DURABILITY AND DAMAGE TOLERANCE ASSESSMENT CUTOFF (DAOTA)	$\frac{\rho_2}{\rho_1} \frac{F_1}{F_2}$	$\frac{1}{1 + M.S.}$
8	GENERAL INSTABILITY, COMPRESSION OR SHEAR	$\frac{\rho_2}{\rho_1} \left[\frac{E_1}{E_2} \right]^{.5}$	$\left[\frac{1}{1 + M.S.} \right]^5$
9	MINIMUM GAGE	$\frac{\rho_2}{\rho_1} \frac{t_2}{t_1}$	$\frac{1}{1 + M.S.}$

Navy aircraft carrier fleet. It was designed and manufactured by the Lockheed-California Company and all necessary weight and structural analysis data are readily available. The S-3A structure is considered to be representative of other small military aircraft such as trainers and fighters. It is also representative of a future subsonic Vertical/Short Takeoff and Landing (V/STOL) aircraft of interest to the Navy as illustrated in Fig. 1. The S-3A performance and structure have many similarities with leading versions of the subsonic V/STOL aircraft that are currently in the preliminary design stage at several aircraft companies.

Weight Evaluation Methodology. The numerical method developed by Lockheed [1,12] for accurately predicting weight savings of an aircraft structure from properties of the advanced aluminum alloys was used for this investigation. The flow chart for this structural weight evaluation is shown in Fig. 2. The structural weight of each of the components to be evaluated is distributed according to the primary failure modes that size each component. Nine failure modes are considered. Equations that relate changes in weight to the basic material properties are then used to calculate the weight savings.

The maximum potential weight savings are determined for the improved material properties assuming that the primary failure modes do not change. The relationship between the structural weight, W_2 , for the advanced material and the structural weight, W_1 , for the baseline material is obtained by substituting the appropriate material properties into the weight ratio equations of Table 4. The potential weight savings are then determined from the following equation:

$$\text{Weight savings in pct of } W_1 = 100 (1 - W_2/W_1) \quad (1)$$



Fig. 1. An artist's rendition of one version of the subsonic V/STOL airplane

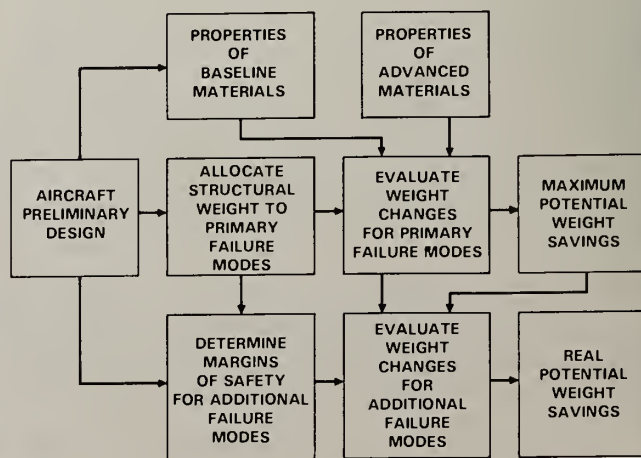


Fig. 2. Structural weight evaluation for a new material

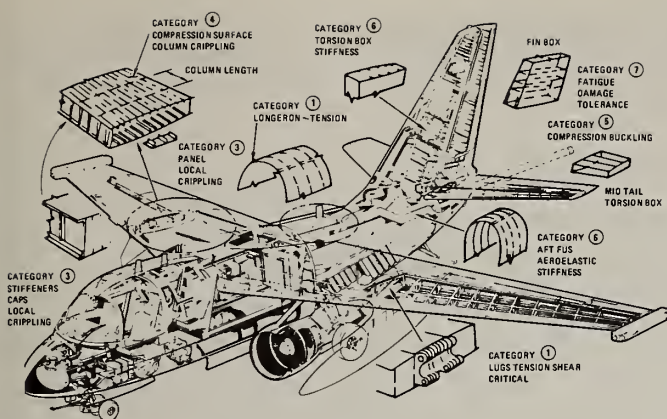


Fig. 3. Examples of critical failure modes in S-3A patrol aircraft

TABLE 5. S-3A Patrol Aircraft Weight Statement

ITEM	WEIGHT (lb)	PERCENT OF GROSS WEIGHT
STRUCTURE	13,336	27.9
(WING) *	(3,415)	(7.2)
(FUSELAGE) *	(3,388)	(7.1)
(EMPENNAGE) *	(729)	(1.5)
(CONTROL SURFACES) *	(1,393)	(2.9)
(OTHER)	(4,411)	(9.2)
PROPULSION	3,394	7.1
FIXED EQPT AND SYSTEMS	9,656	20.2
PAYLOAD, CREW, OPER. EQPT	10,420	21.8
FUEL	10,994	23.0
GROSS	47,800	

*ALUMINUM COMPONENTS CONSIDERED FOR WEIGHT SAVINGS ANALYSIS

If some primary properties are improved considerably more than others, or if some properties are improved while others remain unchanged or are degraded, other failure modes may become critical for portions of the structure. To determine the real potential weight savings, the effects of alternate failure modes must be considered. To do this, the ratio W_2/W_1 for the alternate failure mode (or modes, if more than one alternate mode is critical) is multiplied by the factor given in Table 4. The margin of safety used in these correction factors is the margin of safety of the alternate mode relative to the primary failure mode. For any given portion of structure, the lowest value of W_2/W_1 , including the effects of alternate failure modes and margins of safety, is substituted in equation (1) to obtain the real potential weight savings.

Allocation of Component Weight by Design Failure Modes. The structural arrangement and examples of the critical failure modes in the S-3A patrol aircraft are shown in Fig. 3. The weight breakdown used in the analysis is shown in Table 5. Only the primary wing, fuselage, empennage structure and the control surface structure (e.g., flap, aileron, rudder) were considered. The landing gear, nacelle and air induction system are primarily made of steel or titanium alloys. The primary and secondary structural components considered weigh 8925 lb, 67 percent of the total structure weight or 19 percent of the gross weight.

Allocation of weights of individual components into the nine design failure mode categories was made by reviewing the S-3A structural analysis reports and applying prior applicable experience. This weight breakdown is shown in Table 6. For example, thirty percent of the structure is designed by tensile strength. The primary wing structure weight consists of structure designed equally by 6 categories: (1) tensile strength, (2) crippling, (3) compression surface, (4) buckling, (5) aeroelastic stiffness and minimum gage, and (6) durability and damage tolerance. Tensile strength is dominant for the fuselage basic structure design or 55 percent of the fuselage weight.

Alternate failure modes and margins of safety for the S-3A structure were determined from stress analyses and are presented in Table 7. Note that category 7, durability and damage tolerance, is the next critical failure mode for the tensile strength critical structure.

TABLE 6. Allocation of Component Weight by Design Failure Mode for S-3A Structure

FAILURE CATEGORY	DESCRIPTION	WING (lb)	FUSELAGE (lb)	EMPENNAGE (lb)	CONTROL SURFACES (lb)	TOTAL (lb)	(%)
1	TENSILE STRENGTH	562	1873	75	178	2688	30.1
2	COMPRESSION STRENGTH						
3	CRIPPLING	581		247	452	1280	14.4
4	COMPRESSION SURFACE	583		138		721	8.1
5	BUCKLING	583	740	54	321	1698	19.0
6	AEROELASTIC STIFFNESS	445	184	80	275	984	11.0
7	QAOTA	527	476	60	47	1110	12.4
8	GENERAL INSTABILITY		91			91	1.0
9	MIN GAGE	134	24	75	120	353	4.0
	TOTAL	3415	3388	729	1393	8925	100

TABLE 7. Alternate Failure Modes and Margins of Safety for S-3A Structure

PRIMARY FAILURE MODE CATEGORY	ALTERNATE FAILURE MODES			
	NEXT CRITICAL		SECOND NEXT CRITICAL	
	CATEGORY	MS	CATEGORY	MS
1	7	0.15	6	0.30
2	NOT APPLICABLE		NOT APPLICABLE	
3	6	0.30	7	0.30
4	6	0.30	7	0.30
5	3	0.30	6	0.30
6	5	0.30	7	0.30
7	1	0.20	6	0.25
8	6	0.15	5	0.20
9	6	0.10	5	0.20

Advanced Aluminum Alloy Applications. The aforementioned weight savings evaluation methodology was used to determine the benefits from the application of advanced aluminum alloys to the baseline S-3A aircraft. The results of this analysis are shown in Fig. 4. These weight savings versus density ratio are based on the following premises.

- Baseline material properties are for 7075-T76 extrusion,
- Goal A properties are the same as baseline except for 30 percent increase in E/ρ ,
- Goal B properties are the same as baseline except for 20 percent increase in E/ρ and 20 percent increase in specific (density compensated) tensile, compression, and shear strength,
- Optimization of weight savings by combined selective use of different alloys was not attempted. However, if the alloy being evaluated resulted in a negative saving in a category, the baseline material was not replaced and the weight savings assumed zero for that category,
- The allocation of weight by design failure mode and margins of safety was in accordance with Tables 6 and 7, respectively.

The resulting weight savings for Goals A and B are presented versus density ratio. As indicated in Fig. 4, the effects of the alternate failure modes are significant for the higher density ratio materials and must be included to determine the actual weight savings.

Example Analysis of Weight Savings. An advanced aluminum-lithium alloy with an assumed material property set representing Goal B with reduced density of $\rho_2/\rho_1 = 0.94$ was selected for this analysis. Since Goal B is a 20 percent increase in E/ρ , F_{tu}/ρ , and F_{ty}/ρ ; the ratios of E_2/E_1 , F_{tu2}/F_{tu1} , and F_{cy2}/F_{cy1} are equal to $1.2 \times 0.94 = 1.128$. The values of $F_{tyDADTA}$ and t_{min} are assumed unchanged. The maximum potential weight savings for this aluminum-lithium alloy system is summarized in Table 8. The weight saving by category is shown for the S-3A structure. The use of an aluminum-lithium alloy having these assumed properties results in a calculated weight savings of 1022 lb or 11.5 percent for the S-3A aircraft. The actual weight savings and the maximum potential weight savings are equal for this example, indicating that the margins of safety are sufficiently high to preclude any influence of the next critical failure mode on weight savings.

Effect of Property Trends on Weight Savings. Since the solute content essentially fixes both the density and modulus in the candidate alloy systems, the weight savings for each alloy system can be estimated as a function of strength level. Shown in Fig. 5 is the change in modulus and weight saving plotted against density for four strength categories for Al-Li-Cu-Mg alloys and with copper content varying with lithium content, not exceeding the solid solubility limit.

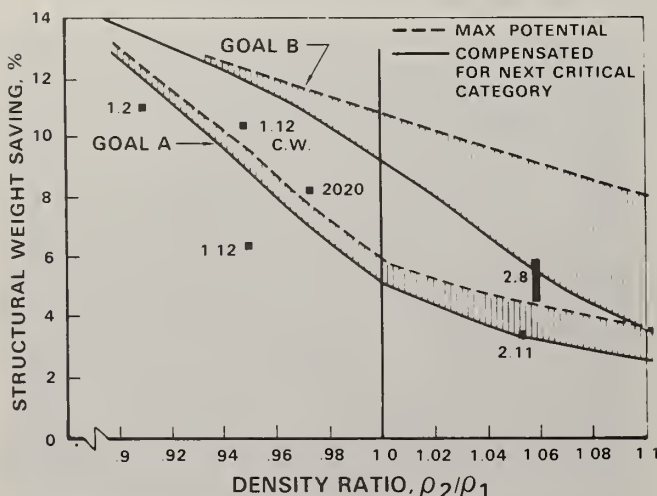


Fig. 4. Structural weight savings versus density ratio for the S-3A aircraft

TABLE 8. Weight Savings Example Analysis for S-3A Patrol Aircraft

CATEGORY	STRUCTURE WEIGHT (lb)	MAXIMUM POTENTIAL WEIGHT SAVINGS	
		(lb)	(%)
1	2688	446	16.6
2	0	0	0
3	1280	147	11.5
4	721	91	12.6
5	1698	165	9.7
6	984	163	16.6
7	1110	0	0
8	91	10	11.5
9	353	0	0
TOTAL	8925	1022*	11.5*

BASILINE ALLOY 7075-T76: F_u 75 ksi; F_y 65 ksi; E_T 10.4 Msi; ρ 101 lb/in.³
 ADVANCED Al-3Cu-2Li-1Mg-.2Zr: F_u 84 ksi; F_y 72 ksi; E_T 11.6 Msi; ρ 99 lb/in.³

*ALSO EQUALS ACTUAL WEIGHT SAVINGS

Effect of Variation of Individual Properties on Weight Savings. The effect of variation of individual property improvements on weight savings for the S-3A aircraft is illustrated in Fig. 6. Density affects the weight savings in all failure mode categories: the structural weight savings in each category is directly proportional to the density ratio. Improvements in either strength or stiffness affect structural weight by about 2.5 to 3.5 percent per 10 percent property improvement. Fig. 6 indicates that DADTA property improvements have the least impact on overall structural weight because of the small amount (10-12 percent by weight) of structure in Category 7. However, since Category 7 is often one of the next critical failure modes in Categories 1 through 6, its impact on weight savings can be considerably more significant than indicated. The results shown in Fig. 4 also indicate the importance of considering secondary failure modes on projected weight savings for new alloys.

Additional Weight Savings Due to Selective Use of Several Alloys. Maximum weight savings for aircraft structures can best be achieved by selective use of several advanced aluminum alloys. A high specific strength alloy is best for failure modes 1 and 2. A high-modulus, low-density is best for failure modes 5 and 8. A combination of strength and stiffness, both with low-density is best for failure modes 3 and 4. Finally, high DADTA properties are best for failure mode 7. A combination of advanced alloys with different improvements in specific properties would show a higher weight savings potential than the weight savings resulting from application of a single new alloy. However, the properties for new alloys should be achieved without significant reductions in the other mechanical properties or alternate failure modes with low margins of safety would become critical and limit the weight savings.

APPLICATION STUDIES FOR TRANSPORT AIRCRAFT

Several government and industry studies have recently been conducted on the use of low-density alloys in transport and other aircraft [1,4,7,8,13,14]. Each of these investigations has shown that substantial reductions in structural and total aircraft weight can be achieved through the use of low-density aluminum alloys and that aggressive alloy development on this system is appropriate. Of course, other types of large subsonic and supersonic aircraft (to Mach 2), including cargo and bomber types, can also make use of these alloys and to approximately the same degree of effectiveness as with transport aircraft. At speeds above Mach 2 aerodynamic heating becomes an increasing factor and alloys designed specifically for elevated temperatures are required.

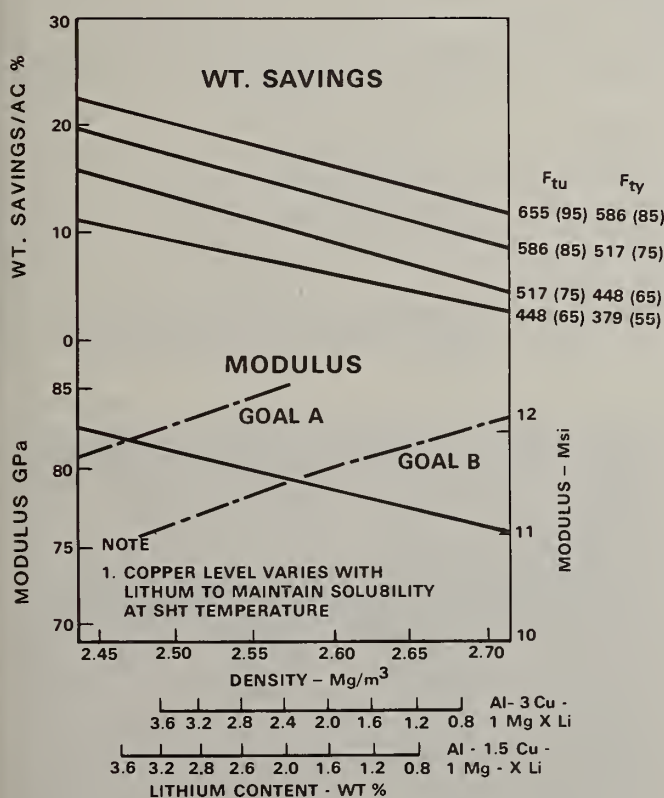


Fig. 5. Relation of density to lithium content, modulus, and S-3A aircraft weight savings for Al-XLi-YCu-IMg alloys

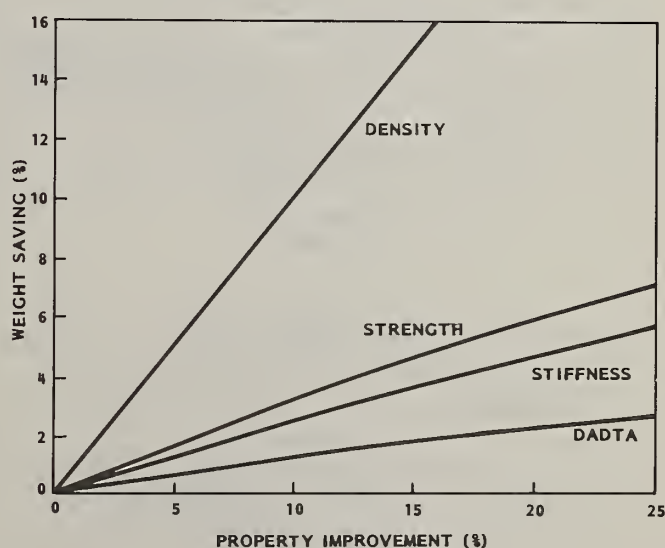


Fig. 6. Relationship of individual property improvement on S-3A aircraft weight savings

Approach. The approaches now being considered for the implementation of low-density aluminum-lithium alloys on transport aircraft are as follows:

1. Substitution of low-density aluminum alloys into current aluminum structure with little or no redesign.
2. Redesign and resizing of structure and airframes to best utilize low-density aluminum alloys. Non-aluminum components may also be incorporated into this redesign.

Both of these approaches offer certain advantages in economics, alloy design and utilization, and aircraft structural efficiency. For example, the first approach allows a more rapid introduction of new alloys into current and near production aircraft, and will yield a substantial weight saving to the user and minimize complications for the manufacturer. For alloy producers the attractive features of aluminum-lithium alloys are the immediate broad market potential and the opportunity to quickly amortize alloy development and new facility costs. The utilization method based on alloy substitution, however, does not allow optimum use of the attributes of the aluminum-lithium alloys as the new alloys must meet all of the in-place design parameters. This, in effect, dictates that density decrease is the only property that will make a substantial contribution to improved structural efficiency albeit the effect will be an important one.

The second approach can bring all the unique properties of the aluminum-lithium alloy system into play, including enhanced fatigue crack-growth-rate resistance and substantially increased modulus. With these and other alloy property attributes considered in conjunction with aircraft resizing, studies have shown that an increase of about 50% over the original weight savings may often be obtained for large transport aircraft [8]. The substitution of low-density aluminum alloys for other aircraft structural materials (principally titanium and steel) may also contribute additional weight savings but because the majority of the current transport structure is aluminum, as shown in Fig. 7, the degree of possible substitution for these materials is limited.

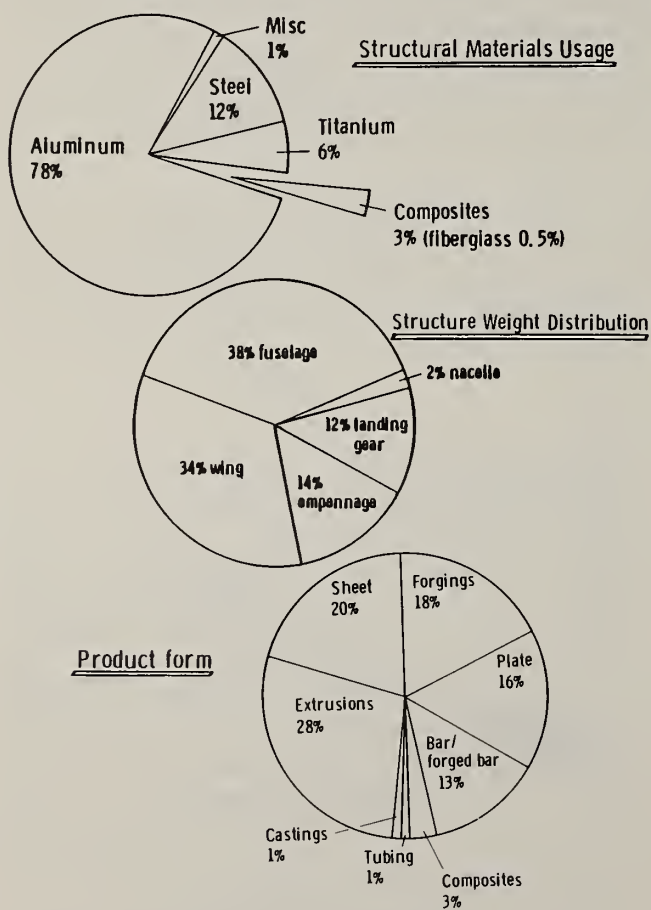


Fig. 7. Distribution and type of structural materials and forms in a typical advanced transport aircraft

TABLE 9. Airframe Applications for Aluminum-Lithium Alloys

PRODUCT FORM	TYPICAL AIRFRAME APPLICATIONS	BILLET SIZE REQUIRED (lb)
FORGING	PIN JOINTS, FITTINGS, STRUTS, FRAMES	100-1,000 SOME 5,000
EXTRUSION	STIFFENERS, SUPPORTS, RAILS	100-2,000
SHEET	FUSELAGE AND EMPENNAGE SKINS AND CONTROL SURFACES	300-2,000
PLATE	UPPER AND LOWER WING COVERS	2,000-20,000

TABLE 10. Transport Aircraft Weight Savings Studies Use of Aluminum-Lithium Alloys

BASELINE ALLOY(S)		ADVANCED Al-Li ALLOYS*		WEIGHT SAVED	
				%	lb
LOCKHEED STUDY L1011 AIRCRAFT; ELEMENTS OF WING, BODY, EMPENNAGE					
7075-T76	DENSITY	-10%		12.2	16,784
	STRENGTH	0, +20%			
	FATIGUE AND TOUGHNESS	+20%			
	MODULUS	+20%			
BOEING STUDY, 757-200 AIRCRAFT; ELEMENTS OF WING, EMPENNAGE					
2024-T3	DENSITY	-9 to -11%		10.9	1,129
7075-T6	STRENGTH	0 to + 7%			
2224-T3	FATIGUE AND TOUGHNESS	-8 to +20%			
7150-T6	MODULUS	+13 to +23%			
BOEING STUDY, 747-F AIRCRAFT; FLOOR BEAMS, SUPPORT STRUCTURE					
7075-T6	DENSITY	ALLOY 1 -10%	ALLOY 2 -10%	(1) 13.2	(1) 686
7075-T73	STRENGTH	+10%	0%	(2) 10.0	(2) 519
	FATIGUE AND TOUGHNESS	0%	0%		
	MODULUS	+10%	0%		

*PROPERTY DIFFERENCES FROM BASELINE ALLOY(S)

The major thrust of weight saving studies with rapidly solidified PM low-density alloys has been for primary structural applications, as this area offers a large and straightforward weight savings benefit. All structural subgroups as well as the entire wing, body, and empennage sections have been considered. This is possible because it is anticipated that PM aluminum-lithium alloys can be made in all common structural forms required for large transport aircraft with the possible exception of the largest plate products. These plates may require billet sizes in the 10,000 to 20,000 pound range (see Table 9). However, non-structural items or secondary structure can also provide an important increment of weight savings if constructed with low-density alloys, as a substantial increment of aircraft weight comes from small items such as clips and brackets, as well as large components such as floors, cargo handling equipment, aerodynamic smoothing surfaces, and parts of the cabin interior. Alloy development studies to date have indicated that new aluminum-lithium alloys will achieve the engineering property levels of 2024-T3, 7075-T73, and 7075-T6 with commensurate density reductions of about 10 percent.

Methodology. The methodologies used for assessing structural efficiency (weight savings) in transport aircraft obtainable with RSP or IM aluminum-lithium alloys follow procedures comparable to that described above.

Example Analyses. Three recent industry/government studies dealing with the use of aluminum-lithium alloys on transport type aircraft are the Lockheed/DARPA [13], Lockheed/NASA [8], and Boeing/AFWAL [7,14] programs. The aircraft used in these studies were the L-1011, B-737, F-27, B-747, and the B-757-200, which has received the most detailed analysis. The latter aircraft is shown in Fig. 8.

Elements of the results of three of these studies are shown in Table 10, where it will be noted that weight savings of from 10 to over 13 percent are achieved in the affected structure. This is particularly noteworthy because of the diversity of baseline alloys, and the projected properties for the aluminum-lithium alloys between the various studies. The validity of these weight saving estimates are further substantiated by the Lockheed/NASA study [8] and the most recent findings of the Boeing/AFWAL study [7]. It should be emphasized that these calculations are primarily based on simple alloy substitution and relatively small changes in design (i.e., airplane dimensions were not changed).

Structural weight savings of 10 to 13 percent have a major effect in payload and/or range improvements. For example, improvements calculated for the L-1011 aircraft are 21.3 percent (or 17,040 lbs.) in payload and 23.7 percent in range [13] (see Table 11). These impressive improvements appear to be indicative of what could be expected for other transports and/or similar aircraft, and thus underline the attractiveness of replacing currently used aluminum alloys with aluminum-lithium alloys as they become available.

If a total aircraft redesign can be considered such as downsizing of the aircraft dimensions, additional structural weight can be saved than when direct substitution only is utilized. This is because as the basic structure is made lighter, the landing gear, engines, fuel tanks, and so on, can also be made both smaller and significantly lighter. One of the iterative weight saving programs described in the literature is Lockheed's ASSET program [8,13] which projects for aluminum-lithium alloy applications an additional 1.9 to 5.3 percent reduction in total structural weight by downsizing various transport aircraft (see Table 12). For transport aircraft of the 100-passenger size and larger, total structural weight reductions are about 15 percent. For the L-1011 aircraft, a 15.9 percent re-

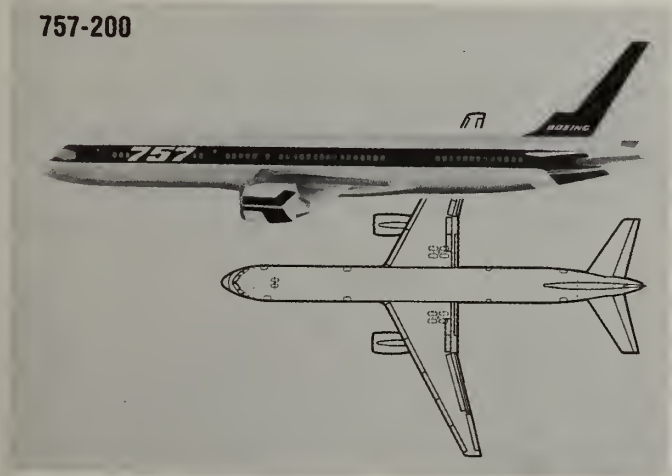


Fig. 8. The Boeing 757-200 Transport Aircraft

TABLE 11. The Effect of Aluminum-Lithium Alloys on the Payload or Range of an L-1011 Transport

PAYLOAD			RANGE		
BASELINE (lb)	CHANGE CAUSED BY APPLICATION OF AL-LI ALLOYS		BASELINE (nmi)	CHANGE CAUSED BY APPLICATION OF AL-LI ALLOYS	
	(%)	(lb)		(%)	(nmi)
80,000	+21.3	97,040	3,000	+23.7	3,711

• BASELINE ALLOY: 7075-T76

• AL-LI ALLOYS: CHANGE FROM BASELINE

	(1)	(2)	(3)	(4)
STRENGTH	+20	SAME	SAME	SAME
FATIGUE/ FRACTURE	SAME	+20	SAME	SAME
MODULUS	SAME	SAME	+20	SAME
DENSITY	-10	-10	-10	-10

TABLE 12. The Effect of Advanced Aluminum-Lithium Alloys on the Weight, Cost, and Performance of Transport Aircraft

AIRCRAFT	REDUCTION IN STRUCTURAL WEIGHT		REDUCTIONS IN FUEL AND COSTS RESULTING FROM RESIZING AIRCRAFT				REF.
	NO RESIZING (%)	WITH RESIZING (%)	PRODUCTION COSTS \$M (%)	FUEL (%)	DIRECT OPERA. COSTS (%)	TOTAL OPERA. COSTS \$M (%)	
L-1011*	-10.2	-16.1	—	-6.7%	—	—	13
L-1011*	-10.6	-15.9	-1.70 (-2.5%)	-8.4%	-5.9%	-1.68 (-3.94%)	8
B-737	-9.8	-14.6	-0.27 (-2.1%)	-5.5%	-3.7%	-0.24 (-2.17%)	8
F-27	-7.8	-9.6	-0.10 (-1.6%)	-2.6%	-1.9%	-0.05 (-0.91%)	8

*DIFFERENT BASELINE AND ADVANCED ALLOYS WERE CONSIDERED IN THESE STUDIES.

TABLE 13. Air Vehicle Structure Components Where Weight is Affected by DADTA Properties

DAOTA PROPERTY	COMMERCIAL PASSENGER AIRCRAFT	HIGH PERFORMANCE MILITARY AIRCRAFT
FATIGUE	ALL HIGHLY TENSION LOADED STRUCTURE	ALL HIGHLY TENSION LOADED STRUCTURE
PLANE STRESS FRACTURE TOUGHNESS, K_{IC}	FUSELAGE AND WING LOWER SURFACE SKINS	DOES NOT GENERALLY IMPACT WEIGHT
PLANE STRAIN FRACTURE TOUGHNESS, K_{Ic}	MOST SUBSTRUCTURE ELEMENTS NEED MINIMUM K_{Ic} PROPERTIES	MUST MEET MINIMUM K_{Ic} REQUIREMENTS IN HIGHLY TENSION LOADED STRUCTURE
CRACK GROWTH, da/dN	SKIN MATERIAL AND SOME MAJOR SUBSTRUCTURE ELEMENTS	MOST AREAS WITH MEDIUM TO HIGH TENSION LOADINGS
CORROSION, STRESS CORROSION	NEW ALUMINUM ALLOYS AND PROTECTIVE SYSTEMS GENERALLY ADEQUATE	

duction in structural weight translates into a 5.9 percent lower direct-operating cost, a 2.5 percent lower production cost, and a 4 percent lower total operating cost [8]. For the B-737 aircraft, a 14.6 percent lower structural weight translates into a 3.7 percent lower direct operating cost, a 2.1 percent lower production cost, and a 2.2 percent lower total operating cost [8].

CONSIDERATIONS FOR DURABILITY AND DAMAGE TOLERANCE ASSESSMENT (DADTA)

Evaluation of durability (fatigue) and damage tolerance characteristics of a structure requires materials property data on fatigue, fatigue crack growth, fracture toughness, and subcritical crack growth in the applicable corrosive environments. Various types of test data are required to properly evaluate these properties. The test types required include constant-amplitude fatigue, spectrum fatigue, fatigue crack growth, fracture toughness (K_{IC} and K_{Ic}), and stress corrosion cracking (K_{ISCC}). The properties obtained from these tests are required to properly evaluate potential weight savings for aircraft structural applications.

Some of the aircraft structural components sized by the DADTA properties of materials are given in Table 13. The areas of the structure where the tensile stresses are high for the normal operating service loads are particularly affected by the DADTA material properties. Based on these data, the ultimate design allowable tension stresses are reduced as required to provide adequate fatigue life and damage tolerance capability. The structural areas generally affected include wing lower surfaces and the fuselage shell structure. Since the maximum allowable stresses in these skin structures are limited, the allowable stresses in substructure elements attached to these skins are also limited even though they may not be DADTA critical. Therefore, a considerable portion of the structural weight can be affected by the DADTA material properties.

For lower wing surfaces of passenger aircraft, the plane stress (K_{IC}) fracture toughness and crack growth properties have the largest effect on the damage tolerance characteristics of the structure. The critical damage size (crack length) is of the order of the wing stiffener spacing or larger and the stiffeners are intended to provide some crack arrest capability. For high performance fighter type aircraft the critical crack sizes in the wing surfaces are smaller and flight safety is provided by inspections at intervals based on the crack growth properties of the material. Fatigue is also important for both types of aircraft: long service life requirements for passenger aircraft and severe high amplitude fatigue loadings for high performance (fighter) aircraft.

For the fuselage shell structure of passenger aircraft, the fatigue, plane stress (K_{IC}) fracture toughness, and crack growth properties all affect the durability and damage tolerance characteristics of the structure. The critical crack sizes in the skin are of the order of 20 to 40 inches. Fail safe design is provided by the frames, stringers, and in some cases reinforcements attached to the skin. The limitations in stress are based on both the fatigue and residual strength requirements. Fuselage structure for high performance military aircraft are sized to meet crack growth and fatigue requirements. Therefore, the plane stress fracture toughness properties generally do not have a weight impact in the fuselage structure of high performance military aircraft.

Protection from corrosion must be provided for aluminum alloys on aircraft structure. The corrosion protection systems in current use include anodizing or cladding of the basic material. These systems, including the use of sealants and paints, have generally provided adequate corrosion protection for most areas of the airframe structure of aircraft in current use. Cladding and anodizing, however, have a detrimental effect on the fatigue properties of the aerospace aluminum alloys which must be accounted for in establishing the allowable stresses for fatigue. The effect of corrosion

protection systems on the fatigue properties of the new advanced aluminum alloys will require careful evaluation.

TECHNICAL ISSUES RELATED TO SUCCESSFUL ALLOY DEVELOPMENT AND APPLICATION

There are a number of technical factors or issues which are related to successful development and application of the aluminum-lithium alloys. Some of these issues are peculiar to either the RSP powder metallurgy or ingot metallurgy products; many of the issues pertain to both products. It is hoped that the discussion which follows will increase awareness of the factors affecting eventual utilization and thereby contribute to the orderly, efficient establishment of this important new family of aluminum alloys.

Durability and Damage Tolerance Assessment. The durability and damage tolerance assessment of new aluminum-lithium alloys requires that fatigue, fatigue crack growth, fracture toughness, and other related properties be established. Some results have recently been reported for the 2020 aluminum alloy developed over 25 years ago by Alcoa [15]. The lithium content of this alloy is low, only 1.1 weight percent, well below the 2 to 3 weight percent in the most promising new alloys. By mid-1983, some fracture and fatigue data for the new alloys will be published by various aerospace contractors to AFWAL, DARPA and NASC.

In addition to the DADTA related data, verification of the applicability of conventional fatigue and fracture mechanics methodology will be required. This will include accuracy of predicting actual crack growth rates in structural elements from laboratory test data of the new alloys. The effects of variables such as load ratio, overloads, and chemical environment on fatigue crack growth behavior will also need to be assessed. Inspection techniques used for detecting initial crack sizes in airframe components will need to be demonstrated for the new alloys, particularly the PM alloys because of their fine grain size. Crack arrest characteristics of sheet need to be demonstrated, including the effectiveness of stringers, straps, and the frames used to support the fuselage skin. The behavior of mechanically fastened joints typically used in airframe construction will need to be evaluated. Finally, the suitability of current corrosion protection systems including paints, coatings, and surface conversion layers for the new aluminum-lithium alloys will need to be assessed.

Availability of RSP Facilities. Atomization of aluminum-lithium alloys to produce fine powder will require inert gas protection. These facilities are at present quite limited in both capacity and availability [16] and undoubtedly new capital facilities will have to be developed to support the potentially large demand. New production facilities for melting and casting will also be required. Ingot melting of aluminum-lithium alloys requires special protection of the liquid metal to avoid excessive hydrogen pickup and also special care in the casting procedure to avoid explosions due to liquid metal/water reactions.

Control of Particulate Quality. Some of the facilities used to date in the development of fine atomized aluminum-lithium powders are used for a variety of other metal alloy systems. Consequently, in some cases foreign particles 30 to 50 μm or larger in size have been found in each batch of aluminum-lithium powders. Nickel-base contamination particles in the aluminum alloy powder lot, for example, promote the formation of a brittle intermetallic shell of nickel aluminides around the particle. This feature can then act as a local defect in the final consolidated product and lower the ductility [4]. Other particulate quality factors of concern include large variations in the oxide film thickness (100 to over 1000 \AA in the splat particulate) [4,5], large variations in fineness of solidification structure (particularly in splat) [4,6], and hydrogen contamination from water vapor in the inert shielding or atomizing gas and possibly from other sources.

Consolidation of Large Powder Metallurgy Billets. Although the requirement is not unique to PM aluminum-lithium alloys, some of the component parts in aircraft airframes will need large billets for mill processing. For most extrusions, forgings, and sheet, billets weighing less than 1000 lb will satisfy a large part of the requirements. Plates for upper and lower wing covers in transport and bomber aircraft, however, will require rolling slabs weighing up to 20,000 lb. It is unlikely that powder metallurgy aluminum billets of that maximum size will be made in the foreseeable future, at least without an enormous investment.

Cost. The cost of both PM and IM aluminum-lithium alloys is an important issue. The raw material cost of an aluminum alloy containing 3 weight percent lithium is twice that of the alloy without lithium. This is due to the high current cost of lithium--\$30-\$60 per pound depending on purity level. Alcoa is hopeful that the IM aluminum-lithium alloys they are now developing will not cost more than 3 times the commercial aerospace aluminum alloys [17]. Note that Alcoa sold the 2020 aluminum-lithium alloy in plate form about 25 years ago for \$2.00 to \$2.50 per lb, at which time 7075 alloy plate sold for about \$.75 per lb [17]. The PM aluminum-lithium alloys will likely cost somewhat more than the IM aluminum-lithium alloys because of the powder metallurgy processing.

Another perspective of cost is that of the user. In general, airplane manufacturers value a pound of weight saved in an airframe at \$200 to \$600. As described in previous sections, 9 lb of aluminum-lithium alloy would typically be required to replace 10 lb of current aerospace aluminum alloy in the airframe in order to save 1 lb of weight. At the above value of a pound saved the substitution would be valued at least \$200 and possibly up to \$600. Thus, the substitution of the new aluminum-lithium alloys would be cost effective if they cost \$11 to \$33 per pound, assuming a buy-to-fly ratio of 2. The above costs must be appropriately factored to account for the user's particular efficiency of material utilization (for example, specific "buy-to-fly ratios").

A third perspective of cost is the investment capital required for the producers to develop large scale facilities and the associated production technology. One major aluminum producer has estimated the usage of aerospace grade aluminum alloys between the years 1990 and 2000 at 350-500 million lb per year [17]. Of this amount perhaps half will be alloys already in current production; the other half perhaps new materials such as PM aluminum high strength and high temperature alloys, aluminum-lithium alloys, and some materials replacing aluminum such as composites. This company suggests that the successful development of aluminum-lithium alloys which are cost effective may be expected to result in the use of between 30 and 100 million lb per year [17]. This anticipated usage is sufficient to stimulate significant private sector investment by prospective producers.

Ingot Versus Powder. Since both ingot metallurgy and RSP powder metallurgy approaches can be used to develop new aluminum-lithium alloys, some comments regarding known and prospective advantages and disadvantages of each are appropriate. Two of the IM product advantages expected in this case are lower cost and larger billet size, within some upper lithium content. Advantages of the RSP PM product include a higher lithium content potential. For example, one complex aluminum-lithium alloy designed to exhibit a yield strength of at least 65 ksi tended to crack extensively when DC cast in 8 inch dia. billet size if the lithium content was in excess of 2.7-2.8 wt percent. Such limitation in lithium content due to cracking does not apply to the PM process. Another advantage of the PM process is that higher levels of transition elements can be added for special reasons, whereas in the IM alloys, the same elements must be restricted to low levels to avoid formation of coarse, embrittling intermetallics. Such advantage for the RSP approach makes it feasible to use the technique to develop a low density, high temperature aluminum alloy by combining the attributes of lithium addition for decreased density and selective transition element addition for increased modulus and to form thermally stable dispersoids.

Ingot metallurgy disadvantages may include increased composition heterogeneity, coarser grain size and coarser solidification structure. These may in turn affect the consistency and reliability of the mechanical properties.

In addition to the higher cost of the RSP powder metallurgy product, current suppliers of aluminum-lithium powder are generally not historic producers of aluminum mill products and thus are less familiar with the requirements of producing and distributing aluminum aerospace quality material. Finally, another disadvantage is the increased effort required to establish and maintain consolidation and processing procedures to achieve consistent and reliable interparticle bonding and disruption of the preexisting oxide films covering the surface of every particle.

Obtaining Designer Confidence. The aerospace structural designer's confidence will be gained only after the following steps are accomplished.

- Verify all the property goals,
- Establish the consistency of the product and associated properties,
- Establish scaleup in product size to meet application requirements,
- Verify performance in prototype flight hardware,
- Establish supply base and acceptable cost.

These accomplishments will require close coordination between suppliers, users, and sponsors. Major additional investments will be required, particularly to establish the production base and to verify prototype hardware performance.

CONCLUSIONS

1. The application of aluminum-lithium alloys to aircraft airframe structures will result in significant (10 to 20 percent) weight savings. These weight savings are primarily due to the decreased density of the alloys.
2. Both RSP powder metallurgy and ingot metallurgy aluminum-lithium alloys have identifiable contributions, with each process having distinct advantages and disadvantages.
3. A significant interest in aluminum-lithium alloys has been established by both major users and suppliers. This is based on the promising cost effectiveness of the alloys as the result of weight savings, and the significant future market for the alloys.
4. A major effort including significant additional investment is still required to gain the aerospace structural designer's acceptance of the new aluminum-lithium alloys.

ACKNOWLEDGMENT

The authors thank Drs. T. M. F. Ronald, AFWAL/MLLS, WPAFB, OH, L. A. Jacobson and E. C. van Reuth, Materials Science Division, DARPA, Arlington, VA, for their encouragement and support for an important part of the work on which this paper is based: AFWAL Contracts F33615-78-C-5203 (DARPA Order 3417) and F33615-81-C-5053.

REFERENCES

- [1] J. C. Ekvall, J. E. Rhodes and G. G. Wald, "Methodology for Evaluating Weight Savings from Basic Material Properties," Design of Fatigue and Fracture Resistant Structures, ASTM Special Tech. Publ. 761, 1982, pp 328-341.
- [2] Aluminum-Lithium Alloys, Proc. First International Aluminum-Lithium Conference, T. H. Sanders, Jr., and E. A. Starke, Jr., eds., AIME, Warrendale, PA, 1981.
- [3] Second International Aluminum-Lithium Conference, T. H. Sanders, Jr., E. A. Starke, Jr., and R. Schmidt, organizers. Scheduled for April 12-14, 1983, Monterey, CA.
- [4] R. E. Lewis, I. G. Palmer, D. D. Crooks, H. G. Paris, F. R. Billman, L. Otto, E. A. Starke, Jr., T. H. Sanders, Jr., A. Gysler, R. Crooks, E. E. Underwood, F. S. Lin, G. Wald, E. Himmel, E. Rhodes and R. Simenz, "Development of Advanced Aluminum Alloys from Rapidly Solidified Powders for Aerospace Structural Application," Interim Technical Report for Period September 1978 - March 1981, Technical Report No. AFML-TR-81-XX, March 1981, AFWAL Contract F33615-78-C-5203, DARPA Order 3417, to be issued.
- [5] I. G. Palmer, R. E. Lewis, and D. D. Crooks, "The Design and Mechanical Properties of Rapidly Solidified Al-Li-X Alloys," Aluminum-Lithium Alloys, T. H. Sanders, Jr. and E. A. Starke, Jr., eds., AIME, Warrendale, PA, 1981, pp 241-262.
- [6] I. G. Palmer, R. E. Lewis and D. D. Crooks, "Development of Al-Li-X Alloys Using Rapidly Solidified Powders," Proc. 1982 AIME Conf. on Aluminum Powder Metallurgy, Dallas, Texas, Feb. 1982, AIME, Warrendale, PA, 1983.
- [7] G. H. Narayanan, W. E. Quist, B. L. Wilson and A. L. Wingert, "Low Density Aluminum Alloy Development," Interim Technical Report for Period 4 Jan. 1982 to 1 July 1982, AFWAL Contract No. F33615-81-C-5053, Aug. 1982.
- [8] I. F. Sakata, "Systems Study of Transport Aircraft Incorporating Advanced Aluminum Alloys - Final Report," NASA CR-165820, NASA Contract NAS1-16434, Jan. 1982.
- [9] W. C. Pohlmann, Private Communication, Sept. 1982.
- [10] C. Baker, Private Communication, Dec. 1982.
- [11] R. Jordan, Private Communication, Oct. 1982.
- [12] R. E. Lewis, et al, "Development of Advanced Aluminum Alloys from Rapidly Solidified Powders for Aerospace Structural Applications." Lockheed Palo Alto Research Laboratory Interim Technical Report for period March 1980 to December 1980, Air Force Contract F33615-78-C-5203, DARPA Order 3417, March 1980.

- [13] R. E. Lewis, D. Webster, I. G. Palmer, "A Feasibility Study for Development of Structural Aluminum Alloys from Rapidly Solidified Powders for Aerospace Structural Applications," Lockheed Palo Alto Research Laboratory, Interim Technical Report for Period June 1977-May 1978; Air Force Number AFML-TR-78-102, DARPA Order No. 3417, July 1978.
- [14] Boeing Document D6-49955-1, "Low Density Aluminum Alloy Development," Boeing Military Airplane Company, Page 4-21, May 1981.
- [15] R. C. Malcolm, A. K. Vasudevan, R. J. Bucci, P. E. Bretz, "Evaluation of the Engineering Properties of a Commercially Produced Aluminum Alloy 2020-T651 Plate," Alcoa Report for Amendment to NASC Contract N00019-79-C-0258, Dec. 18, 1981.
- [16] National Materials Advisory Board Committee on Rapid Solidification Processing, "Rapid Solidification Processing: Status and Facilities," Report NMAB-401, National Academy of Sciences, Nov. 1982.
- [17] E. Spuhler, Private Communication, Nov. 1982.

APPLICATIONS OF RAPIDLY SOLIDIFIED ALUMINUM ALLOYS AT ELEVATED TEMPERATURES

C. M. Adam*, J. W. Simon and S. Langenbeck[†]

Pratt & Whitney Aircraft/Government Products Division
West Palm Beach, Florida

[†]Lockheed California Company, Sunnyvale, California

ABSTRACT

During the past five years rapid solidification technology has been successfully applied to a number of novel aluminum alloys. By using conventional powder metallurgy techniques these alloys have been fabricated into components which appear able to compete on a specific strength basis with Ti-6Al-4V components at temperatures up to 450°F (500K). In this paper payoff studies for both airframe and gas turbine engine applications are identified and discussed.

INTRODUCTION

The use of the PWA/GPD rapid solidification technology to produce new aluminum engineering alloys has been recently reviewed in three detailed publications (References 1-3). These alloys rely on a relatively thermally stable 300-800 Å dispersion of metastable intermetallic compounds of the modified Al₃Fe type which are produced by a series of thermomechanical processing steps during consolidation of rapidly solidified aluminum alloy powder of appropriate composition. As a result of the relatively slow thermal diffusivity of the major alloying elements in the new alloys of Al-8Fe-2Mo and Al-8Fe-4Ce compositions these alloys have an extended operating temperature range beyond conventional aluminum alloys containing copper, for example alloy 2219.

It is appropriate therefore to consider whether such alloys will be viable competition on a comparative (specific) strength basis for titanium alloys, and what payoff in weight savings might result from use of the properties of these new alloys in airframe and engine applications. Early studies on gas turbine engine components in the fan and low temperature compressor, and on airframe components, indicated weight-saving payoffs ranging from 5 to 25% for the properties generated during 1980 and 1981. A second iteration of these payoff studies during 1982 (Reference 4) has identified property goals which should lead to greater weight savings if optimal strength and toughness levels can be met. In the following sections of this paper it will be clear that significantly greater market volume opportunities for rapidly solidified aluminum alloys lie in Mach 3+ airframe applications than in gas turbine engine applications, however the impact on the delicate performance/weight/cost balance for future military gas turbine engines may be such to allow superior advanced engine designs which are not feasible with conventional titanium alloys.

GAS TURBINE ENGINE APPLICATION STUDIES

Modern gas turbine engines have a complicated variety of component temperature/stress regimes. Extensive metallurgical research and development over the last three decades, coupled with increasingly sophisticated design techniques, has improved the performance of military engines from a three-to-one thrust-to-weight ratio to eight to one (figure 1). In seeking further improvement in these thrust-to-weight ratios, designers have sought to reduce engine weight with no concomitant loss of thrust. This can be achieved by development of lighter alloys with higher temperature capabilities. For rotating components, specific strength and specific stiffness are both important materials properties. Specific strength determines the maximum rotational speed for which rotating hardware can be designed; specific stiffness determines the vibrational frequency response of a rotating component, and the high-cycle fatigue damage that will be accumulated by aeroelastically induced vibration of that component. Static structures are invariably limited by Euler compressive buckling stresses which are a function of the

*Now with Allied Corporation, Corporate Technology, Morristown, NJ.

elastic modulus of the alloy selected. Development of higher specific strength and specific stiffness aluminum alloys will therefore allow engine designers to reduce engine weight in those gas-turbine areas where aluminum alloys have traditionally been used. Table 1 outlines such applications by major engine manufacturers.

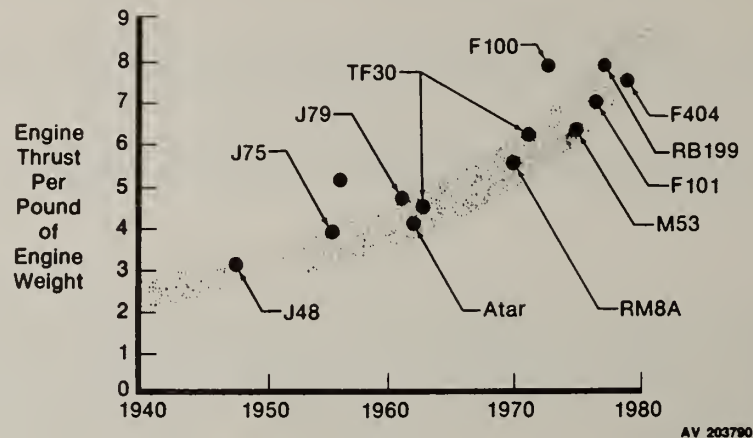


Figure 1. Military Engine Performance from 1940 to 1980

Engine induced temperature effects in nacelle and structural airframe components could be alleviated by development of higher temperature capability, and higher specific strength alloys. In general terms, several hundred pounds of aluminum alloys will be used in future advanced transport engines, and therefore up to one thousand pounds of engine related weight could conceivably be affected by alloys developed during programs related to elevated temperature strength aluminum alloys.

TABLE 1. Current Use of Aluminum Alloys in Medium-Performance Gas-Turbine Engines

Engine	Aircraft	Current Aluminum Alloy Application
PWA JT8D-15	Boeing 727-200	Second-stage fan vane, outer fan duct, third-stage compressor
PWA JT8D-209	MCD DC-9	Compressor entry guide vane, fan case, fan duct, second- and third-stage compressor vanes
PWA JT9D-7A/7F	Boeing 747	Aft fan case
PWA JT9D-59A/70A	MCD DC-10	Aft fan case
PW 2037-136	Boeing 757-200	First-stage fan vane
GE CFM-56	Boeing KC-135	First-stage fan vane, fan case
GE CFM-50	MCD DC-10; A300	First-stage fan vane, fan inlet case
GE F101-X	-	First-stage fan vane
R-R RB-211	Boeing 747; A300	First-, second-, third-, and fourth-stage intermediate compressor vanes, intermediate case

The replacement of aluminum alloys by titanium in the early 1960's resulted from higher temperature environments encountered in high-performance gas-turbine engines for military applications and from lack of strong aluminum alloys for use in the temperature range of 250 to 650°F, which were competitive with titanium alloys (References 2 and 3) on a strength-to-weight ratio basis. Figure 2 shows an engine cross section intended for development from 1985 to 1990 which was used as a baseline application engine for this payoff study. This engine is one of a generic series of demonstrator

engines, designated JT69 by Pratt & Whitney Aircraft, and has provided a series of design/analytical studies with a full engine test demonstration scheduled for late 1984. A fundamental difference between the early 1960's JT3D engine and the JT69 engine is in the thrust produced; early JT3D engines produced 19,000 lb static thrust with an engine weight of 4300 lb, while engines incorporating the advanced JT69 technology should produce some 28,000 lb thrust from an engine weight of less than 3000 lb. These performance differences arise from a substantial reduction in the number of engine parts, which combined with more efficient materials and computer-optimized design, yield thrust-to-weight ratios exceeding ten. A subsidiary benefit of lighter and less mechanically complicated engines comes from decreased manufacturing costs; current buy/fly ratios of six to ten are common for most engine components. Critical and strategic element considerations frequently increase the costs of engine alloys to prohibitive levels, and it is anticipated that a significant payoff will accrue from lower material costs and fabrication costs if advanced aluminum alloys produced by rapid solidification are utilized, rather than currently available titanium alloys.

Development of advanced powder metallurgy aluminum alloys with increased specific stiffness for the applications outlined above will require specific alloy properties substantially better than 2219 properties up to 350°F, in order to be competitive with alternate structural titanium alloys. Advanced aluminum alloys will find applications in gas turbine engines and Mach 3 airframes if they are structurally competitive with titanium on a specific strength basis at temperatures up to 650°F. In the following sections of this payoff analysis both static and rotating engine components will be examined as well as airframe applications for a super-cruiser version of a Mach 3 + airframe to determine weight-savings from application of elevated temperature aluminum alloys.

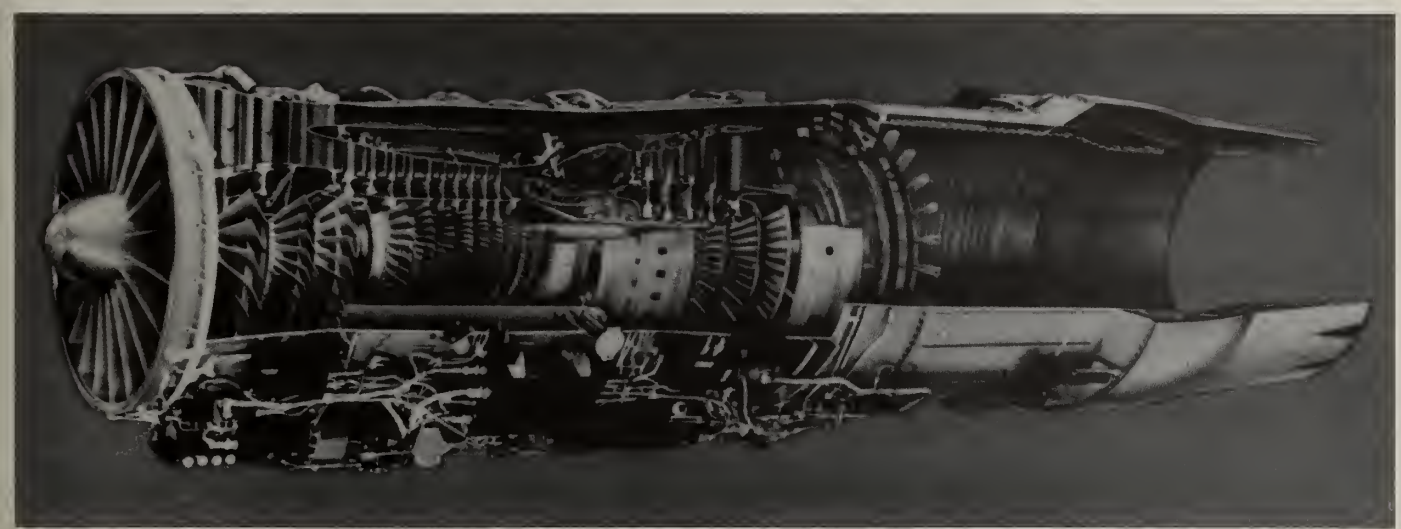


Figure 2. Gas Turbine Engine Cross-Section for Applications Study

In subsonic engines potential applications for aluminum alloys are more numerous than in high performance fighter engines which operate up to Mach 2.5. The applications listed in Table 1 are those where prolonged temperatures rarely exceed 200°F in engines with modest thrust-to-weight ratios. In higher performance engines, the fan and compressor stages produce higher aerodynamic pressures, and adiabatic heating in these stages raises component temperatures to some 450°F. In military fighter engines there is a further effect of ram airspeed at high Mach numbers which results in further aerodynamic adiabatic heating of engine components by some 250°F. In general, the steady-state temperature increment per stage in the fan and compressor section is 100 to 150°F, and these steady state operating temperatures are increased for short operational cycle times by the imposed ram temperature frequency. In military transport engines, such as that envisaged for the Long Range Cruise Aircraft (LRCA), airspeed is limited to subsonic velocities and engine components experience lower temperatures. It is therefore anticipated that a Mach 2.5 engine will provide a realistic but somewhat conservative data base for investigating the applicability of elevated temperature aluminum alloys, and that such data can be readily transferred to subsonic engines studies where applicability is anticipated to be somewhat greater.

In this application study the JT69 engine is used to compare the performance of both rotating and static aluminum hardware, using typical mechanical properties of the best alloy developed under a previous Pratt & Whitney Aircraft - Air Force Wright Aeronautical Laboratories Contract F33615-76-C-5136 "Application of Rapidly Solidified Alloys." The properties of this alloy, Al-8Fe-2Mo, are listed in Table 2, and represent a starting point for further alloy development during the course of this program. These mechanical properties are relatively modest, and fall short of specific strength

equivalency with Ti-6Al-4V.

Table 2. Typical Mechanical Properties of Al-8Fe-2Mo Used for Investigating "Base-Level" Payoff for Elevated Temperature Aluminum Alloys

	75°F	300°F	450°F	650°F
Ultimate Tensile Strength	71.3 ksi	61.8 ksi	49.1 ksi	32.2 ksi
Yield Strength	68.4	50.4	41.5	29.0
Elongation, %	6.7	7	8	10
E, Msi	12.2	11.5	11.0	10.0
0.2% Creep Stress (450°F)	-	-	-	25 ksi, 100 hr
1% Creep Stress (450°F)			35 ksi, 400 hr; 30 ksi, 1000 hr	
Creep Rupture	450°F/36 ksi/1000 hr without failure - 3% strain			
Fatigue, 10 ⁷ Cycles	-	-	20 ksi	-
R = -1.0, K _t = 1				

In the following analyses of both fan and low-pressure compressor blades and vanes, a temperature limitation of 450°F has been arbitrarily imposed in determining weight savings which would result from a direct replacement of Ti-6Al-4V with Al-8Fe-2Mo. Further temperature extensions to 650°F will require substantial alloy development, some of which are currently being developed during the AFWAL program "Elevated Temperature Aluminum Alloys" by Lockheed, Pratt & Whitney and Alcoa.

Fan and Low -Pressure Compressor Blade Analysis

In the baseline engine chosen for this application study, the 2nd- and 3rd-stage fan blades fulfill some of the compression requirements of the low-pressure compressor of engines or more modest thrust-to-weight ratios. Table 3 shows the maximum blade root stresses for Ti-6Al-4V alloys at these environmental temperatures.

Table 3. The 2nd- and 3rd Stage Ti-6Al-4V Blade Temperatures and Stresses Used as Baseline Data for Calculating Aluminum Blade Alloy Weight Savings

Blade	Temperature	Maximum Radial Stress	Peak-to-Peak Vibratory Stress Capability	Life*
Second Stage	300°F	80.5 ksi	29 ksi	3500 Cycles
Third Stage	400°F	72.4 ksi	27 ksi	7000 Cycles

*Equivalent Type 1 cycles, which roughly approximates to engine start-up, a series of engine maneuvering accelerations and decelerations, and engine shutdown.

The radial stresses in Table 3 result from centrifugal loadings and are dependent on the density, ρ , of the blade alloy and the blade geometry. If the blade has mass, m , length, l , and root area A_1 , then the blade root stress at an engine speed, ω , and radius of gyration, r , is given by

$$\begin{aligned} \text{Blade radial force, } F &= m\omega^2 r && m = A_1 l \rho \\ \text{Blade radial stress, } \sigma &= \omega^2 \rho l r \\ \text{Blade specific stress, } \sigma/\rho &= \omega^2 l r \end{aligned}$$

It is important therefore to compare the specific strength properties of an aluminum candidate blade alloy with Ti-6Al-4V in defining weight savings.

Vibratory blade stresses arise from two sources, both of which are considered in Table 5. Fluctuation in gas-flow aerodynamic loadings of approximately 1 Hz frequency lead to high-cycle

fatigue damage, and are independent of the blade material of construction. These stresses arise principally from the interaction of the rotating blades and static vanes and have been shown to be up to 15 ksi in amplitude (30 ksi peak-to-peak) in F100 engine studies. In determining applicability of advanced aluminum alloys, experience should therefore require a minimum high-cycle fatigue capability of 15 ksi amplitude at the operational steady stress level. The second vibratory stresses considered in Table 3 are basically low-cycle fatigue stresses in nature arising from engine run-up and shutdown. These low-cycle fatigue stresses have a lifetime requirement between 10^3 and 10^5 cycles, and have a maximum value equal to the blade specific stress. Comparison of Ti-6Al-4V and an advanced aluminum alloy therefore requires two sets of data. The first data set consists of a modified Goodman diagram (figure 3) showing the relationship between actual high-cycle fatigue endurance (10^7 cycles) stress amplitude, and blade specific steady-stress. The second data set consists of comparative LCF values.

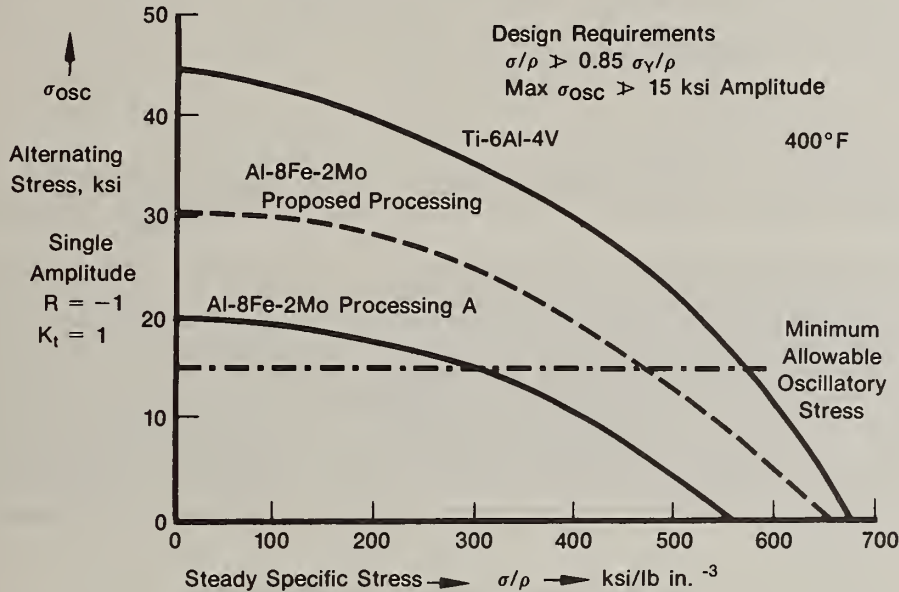


Figure 3. Modified Goodman Diagram for Ti-6Al-4V and Al-8Fe-2Mo Fan Blade Alloys

Table 4 shows calculated JT69 steady-state levels for typical engine fan blades, and comparative Al-8Fe-2Mo stresses based on the experimental fatigue data presented in Table 2. This data shows that the present alloy properties do not possess sufficient high-cycle fatigue stress capability to meet the arbitrary P&WA/GPD design stress requirement of 15 ksi single amplitude oscillatory stress at the operational steady-stress level of 47.5 ksi. Although specific steady-strength equivalency with Ti-6Al-4V at 400°F has been demonstrated (Reference 5), the required high-cycle fatigue stress amplitude endurance limit of ≈ 30 ksi has not been demonstrated and must therefore represent a desirable alloy property goal for the program. In achieving this material fatigue goal a direct substitution of Al-8Fe-2Mo for Ti-6Al-4V would be possible, leading to a hypothetical weight savings of 35%. An alternative design approach would be to adjust the steady stresses for Al-8Fe-2Mo to ≈ 32 ksi by redesigning the blade. The allowable oscillatory stress of 15 ksi would then be available, and this would result in an approximate weight saving of 7%. This hypothetical blade redesign may then result in unacceptable aerodynamic performance for this stage of the engine, and further detailed analyses of the interaction of aerodynamic losses and hypothetical weight savings would be required. The modified Goodman diagrams of figure 3 thus represent the extremes of weight saving; approximately 7% for the lower fatigue curve and approximately 35% for the upper proposed curve. It is anticipated from this analysis that fatigue curves falling between these two extremes will result in weight savings given by simple interpolation, i.e., a high-cycle fatigue endurance limit stress of 25 ksi single amplitude would lead to $\approx 20\%$ blade weight savings. The low-cycle fatigue performance of Ti-6Al-4V and Al-8Fe-2Mo should be identical when an endurance limit stress of ≈ 28 ksi single amplitude for Al-8Fe-2Mo has been achieved. At current strength levels, Al-8Fe-2Mo has approximately 75% of the specific low-cycle fatigue strength of Ti-6Al-4V, which is adequate for these blade applications.

Fan and Low-Pressure Compressor Vane Analysis

Table 5 shows a comparison of vane stress indicating that the steady aerodynamic loading on Ti-6Al-4V vanes is 39.2 ksi. To provide adequate high-cycle fatigue (10^7 cycles) vibratory capability, the existing properties of Al-8Fe-2Mo are inadequate, and the vane cross-sectional area would need to be increased 22% to reduce the steady-stresses to a value where a 15 ksi single amplitude oscillatory stress is available. As was discussed for the blade analysis, this cross section increase may incur aerodynamic penalties; however, improved processing of Al-8Fe-2Mo should produce adequate vibratory capability at increased steady stress levels. The weight savings under the Table 5 stress conditions

Table 4. Comparison of Ti-6Al-4V and Al-8Fe-2Mo Fan Blade Stresses at 400°F for 2nd- and 3rd-Stage JT69 Demonstrator Engine Blades

<u>Critical Parameter</u>	<u>Ti-6Al-4V</u>	<u>1st Generation Alloy</u>	<u>2nd Generation Alloy</u>
Centrifugal loading	72.4 ksi	47.5 ksi	47.5 ksi
Steady Stress	94% yield stress	114% yield stress*	95% yield stress
Vibratory capability 10 ⁷ cycles	14 ksi amplitude	6 ksi amplitude	15 ksi amplitude
Airfoil dimensions	A ₁ 1	A ₁ 1	A ₁ 1
Weight savings	-	7%	35%

*Yield stress is unacceptable for current blade geometry. By redesigning the blade and lowering the steady stress to 32 ksi, a 7% weight saving is hypothetically possible.

vary from 24 to 35% with intermediate weight savings possible at intermediate modified Goodman diagram stress levels. A further design consideration for vanes involves calculation of the vane deflection during aerodynamic transient pressure fluctuations of twice the steady-state aerodynamic pressure. Such surge deflections, δ , are given by Wl^3/KEI where Wl^3 is the vane loading, K is a dimensionless parameter depending on the method of vane support, E is the alloy elastic modulus, and I is the moment of inertia. For the two alloys under comparison, Al-8Fe-2Mo and Ti-6Al-4V, the respective elastic moduli are 11.5 and 15 X 10⁶ psi, respectively, at 400°F, and equivalent deflections would therefore require an increase in the Al-8Fe-2Mo vane thickness of approximately 9.3%. A set of alloy development goals for vanes thus requires two improvements: viz an increase in elastic modulus to provide enhanced surge deflection capability, and an increased high-cycle fatigue endurance limit to provide adequate fatigue strength.

Table 5. Comparison of Ti-6Al-4V and Al-8Fe-2Mo Vane Stresses at 400°F for 2nd- and 3rd-Stage JT69 Demonstrator Engine Vanes

<u>Critical Parameter</u>	<u>Ti-6Al-4V</u>	<u>1st Generation Alloy</u>	<u>2nd Generation Alloy</u>
Air loading, steady stress	39.2 ksi	39.2 ksi	39.2 ksi
Vibratory capability single amplitude	27 ksi	12 ksi*	23 ksi
Airfoil dimensions, txb	nominal, tb	1.22 tb	nominal, tb
Weight reduction	nominal	24%	35%
Equivalent surge deflection	nominal	10% increase in t/b	nominal
Weight reduction for equivalent surge deflection	nominal	25%	35%

*Direct material substitution will not allow 15 ksi single amplitude HCF vibratory capability. To increase this capability the steady stress has to be reduced to 32 ksi, requiring a 22% increase in vane cross-sectional area.

The foregoing analyses show that specific strength equivalency with Ti-6Al-4V is an important requirement for achieving direct replacement by advanced aluminum alloys. These analyses show that a high-cycle fatigue single amplitude endurance limit of ≈ 30 ksi (figure 3) will be required for blades, and a limit of ≈ 25 ksi will be required for vanes. Vane alloys should also have an improved elastic modulus to allow for deflection parity with Ti-6Al-4V, and an elastic modulus goal of 13 X 10⁶ psi at 400°F could be arbitrarily set for vane applications.

High strength aluminum alloys have been the primary structural materials in high performance fighter aircraft for many years. The relatively low material and fabrication costs combined with high strength-to-weight ratios have made the aluminum alloys most cost effective in airframe structural applications. However, degradation of strength and stiffness of aluminum alloys at elevated temperatures has been a major factor in limiting fighter speeds to the Mach 2 level. The leveling off of fighter maximum design speeds is shown in Figure 4 (Reference 5). The lone exception, which is not shown on the figure, is the YF-12 - which has a predominantly titanium structure.

Figure 4 also shows the temperatures due to aerodynamic heating over most of the skin surface of an aircraft designed for the noted maximum speeds. From this figure it can be seen that if aluminum alloys can be developed with improved high temperature strength and stiffness, the maximum operating speeds of fighters with aluminum alloy structures can be extended to beyond Mach 3. Such a development would be especially advantageous for application to a future long range supersonic-type fighter designed for a cruise speed in the range of Mach 2.7 to 2.8 with overspeed capability of Mach 3 plus. In addition, there appear to be other significant applications for elevated temperature high strength aluminum alloys in lower Mach Number aircraft. Such structures as engine inlet ducts, nacelles, and other engine heated components will benefit from aluminum alloys that maintain strength and stiffness at elevated temperatures.

A significant characteristic of a supersonic aircraft is that, for the major portion (75-90%) of the airframe structure, the subsonic and transonic loads are greater than the supersonic loads. Consequently, much of the structure is designed by room temperature properties. Design loads at speeds at which elevated structural temperatures become a significant factor may be 40 percent or less than the design loads at the lower temperatures. The actual reduction depends on a number of factors; including location (such as wing or fuselage), design maneuver load factor, gross weight reduction at high speed, and mission profile. Similarly the continuous load levels contributing to creep at elevated temperature are normally less than 25% of room temperature loads.

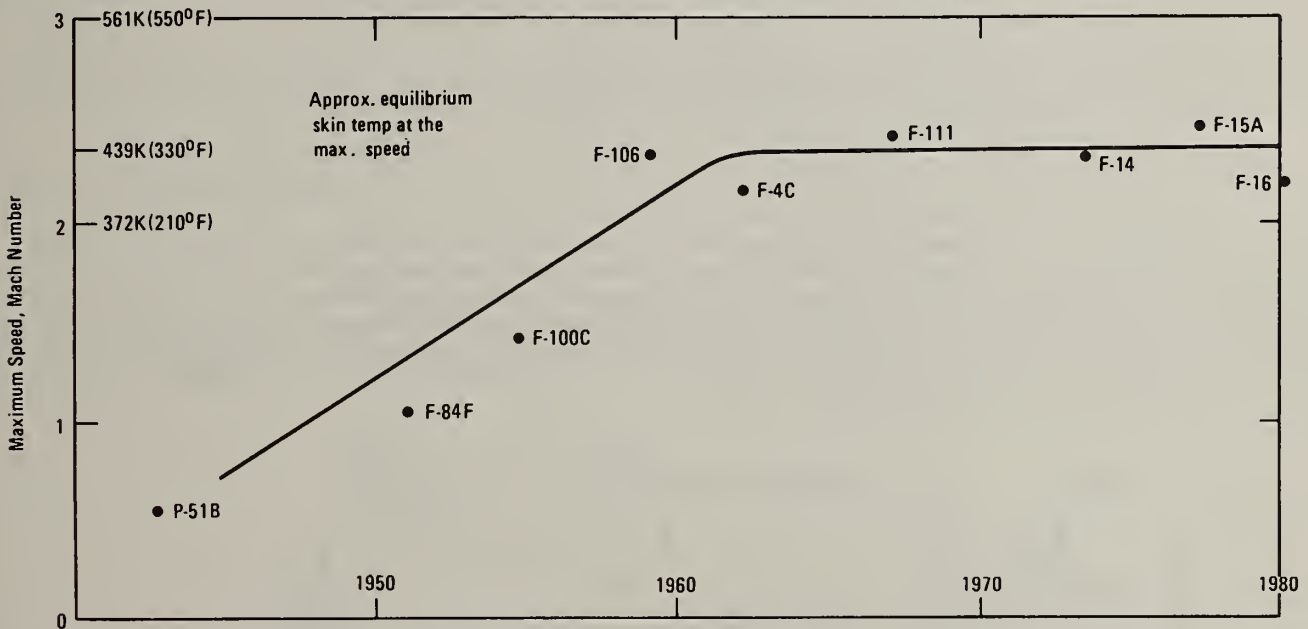


Figure 4. Fighter Maximum Design Speed Versus IOC Date

Thus, for advanced powder metallurgy (P/M) aluminum alloys to compete with titanium in airframe structures subject to elevated temperatures, the room temperature properties must be competitive on a density basis and must be unaffected by elevated temperature exposure over the life of the aircraft. In addition the alloys should possess elevated temperature properties in excess of 40% of room temperature properties and creep strength greater than 25% of room temperature strength. In contrast, parts designed by elevated temperature loads require elevated temperature properties equivalent to titanium while room temperature properties are not as critical.

Analyses have been conducted to identify the effects on structural weight of incorporating elevated temperature resistant advanced aluminum P/M alloys into the airframes of high performance fighter aircraft and selected components of military transport aircraft. In order to explore the temperature range of interest of 394 K (250°F) to 616 K (650°F) and to include a varied range of structural components, three baseline structures have been analyzed; viz. Mach 2.75-3.0 Super-

Supercruiser Airframe Weight Payoff Analysis

The Air Force has for some years been interested in the design of military aircraft with long range supersonic cruise capability. Two examples of activities in this area are: (1) the design conference titled "Technology for Supersonic Cruise Military Aircraft" held by the Air Force Flight Dynamics Laboratory in February, 1976 (Reference 7); and (2) the study program performed by Boeing for the Air Force Flight Dynamics Laboratory in 1978 (Reference 8). Industry studies were initiated recently in response to an Air Force Request for Information. As stated in the RFI the intent is "to provide interface and dialogue with industry on the projected threat, needs/deficiencies, operational concepts, and advanced technology fighter options." The information requested is intended to contribute to a basis for an advanced tactical fighter design for full scale development in 1987 with an I.O.C. of early to mid-1990's.

An important mission to be considered in this program is the strategic air defense of the USA with a mission radius of 1000, or more, nautical miles. A potential design combat profile to meet the above mission requirements has been used for the supercruiser airframe weight payoff analysis. The combat mission speed and altitude versus time diagram resulting from the mission profile consists of a cruise speed which is assumed to be Mach 2.75 with an overspeed up to Mach 3.0 for approximately 80 minutes at 60,000 feet. The design life of the aircraft under these mission profile conditions is estimated to consist of 500 flights of the basic combat mission and 4500 flights of an alternate mission. The resulting structural design skin temperature versus time spectra are shown in Figure 5.

The supercruiser configuration selected for analysis is one of a family of configurations proposed by the Boeing Company in Reference 8. It is a long range fighter with a design gross weight of 47,627 kg (105,000 lb.) and a cruise speed in the Mach 3 range. The airframe primary structural material is titanium. The wing, body and strake, and empennage structures have been investigated to determine the effect of substituting P/M aluminum alloy for the existing titanium. Allocation of weights of individual components into the design failure mode categories was made by reviewing the data in Reference 7 and applying prior applicable experience. This experience includes the design and service experience of the YF-12 and F-104, the preliminary design of a number of advanced tactical fighter type aircraft, and years of research and development of commercial supersonic cruise vehicles.

Experience with aircraft designs similar to the supercruiser fighter has shown that for the major portion of the wing, fuselage, and empennage structure the subsonic and transonic loads are greater than the supersonic loads. Consequently, most of the structure is designed by room temperature loads. Consequently, most of the structure is designed by room temperature material properties after the applicable temperature/time spectra exposure rather than the elevated temperature properties. The weight savings evaluation methodology was used to determine the weight effects of substituting P/M aluminum alloy for titanium. In actual practice, selective substitution would result in a weight saving of approximately 8%. Optimization of weight savings by combined selective use of several P/M aluminum alloys optimized for strength, stiffness, or durability and damage tolerance would increase the weight savings to an estimated 10% or 12%.

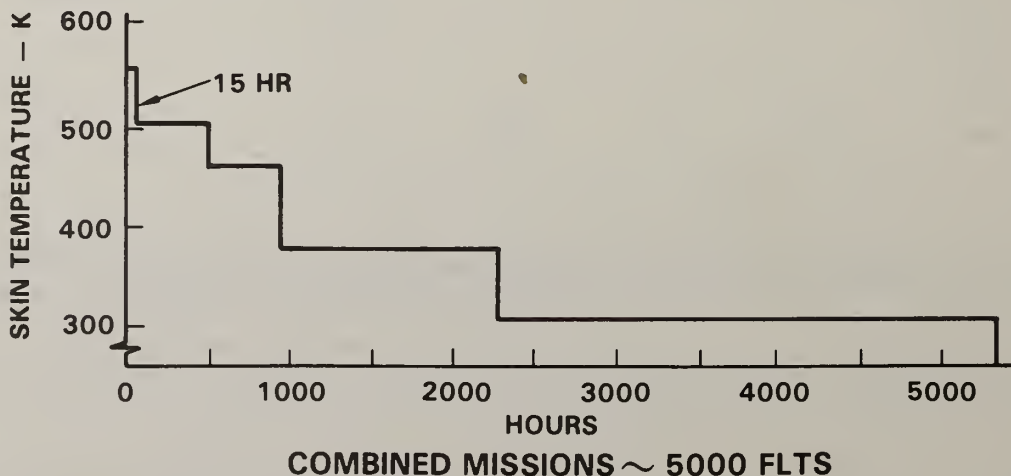


Figure 5. Supercruiser Structural Design Temperature (K) Versus Time Spectra

Advanced Tactical Fighter Aft Fuselage Structure

The Air Force Flight Dynamics Laboratory has for several years sponsored industry studies under the project "Built-Up Low-Cost Advanced Titanium Structures (BLATS)". One of these programs was a preliminary design activity conducted by Grumman Aerospace Corporation directed toward establishing advanced structural concepts for an aft fuselage of an emerging, high performance, Mach 2 class fighter airframe (Reference 9).

The conventional titanium aft fuselage developed in the BLATS program has been used as the baseline structure to evaluate the effects of using elevated temperature resistant P/M aluminum alloys in a Mach 2 plus Advanced Tactical Fighter. Temperatures of the structural elements under certain ambient temperature, speed and altitude conditions were estimated using the data of Reference 9. From these data, three temperature-time spectra have been postulated which represent the temperature-time histories in the 8000 hour life of a short to medium range advanced tactical fighter for: (1) structure with little or no engine heating; (2) structure with moderate engine heating; and (3) structure with maximum engine heating. The design speed/temperature range was assumed to be: cruise at Mach 2.2 on a standard day with overshoot to a maximum of Mach 2.5 on a hot day. The weight savings methodology previously discussed was used to determine the effects of substituting P/M aluminum alloy for titanium.

In the BLATS report (Reference 9) the structure is analyzed by assuming that critical load and temperature conditions are encountered at maximum structural temperatures. In this aft fuselage much of the structure is subjected to heat and sonic noise radiation from the engine. The engine inlet ducts are designed by air loads and elevated temperatures due to ram air. Therefore, much of the structure would be critical for maximum temperature conditions. However, the fuselage shell structure forward of the engines is likely to be critical for room temperature conditions after exposure to the higher temperatures. In this limited analysis it has not been possible to segregate the structure into the above two categories. Therefore, the structure has been evaluated for the two boundary conditions: (1) critical for operations at Mach 1.8; and (2) critical for operations at maximum temperatures.

If P/M aluminum could be selectively substituted only where it yields a weight saving, a weight saving of 13% would result. If the aluminum is substituted completely, lower net savings of 6% is shown in Table 6. In actual practice, unrestricted selected usage is not practical. A realistic, limited selective usage is estimated to result in a net weight saving of approximately 8%.

Military Transport Components

Certain structural components, currently made of titanium, stainless steel, and aluminum, are subjected to critical load-temperature design conditions in the 394 K (250°F) to 616 K (650°F) range. Several of these components, identified in Table 7 have been investigated to determine the weight impact of the use of high temperature resistant P/M aluminum alloys. Shown in this table are: the currently used materials, the structural weights; the design temperatures; and the primary structural design conditions.

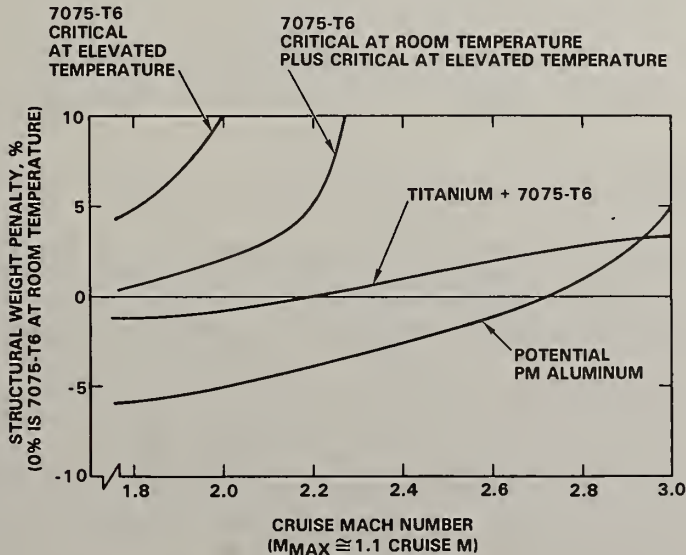


Figure 6. Estimated Potential P/M Aluminum Weight Benefits Variation With Cruise Mach Number

The results of utilizing the DARPA weight ratio equations and dominant design failure mode (or modes) have been used to determine the effect of changing the titanium structure to P/M aluminum. In the case of the C-5A Engine Nacelle, which is made of titanium and aluminum, it is estimated that half of the total weight would be converted from titanium to P/M aluminum. Weight savings of approximately one to eleven percent are possible for the remaining structures.

TABLE 6. SUMMARY OF PERCENTAGE WEIGHT SAVINGS FOR ADVANCED TACTICAL FIGHTER AFT FUSELAGE

PERCENTAGE WEIGHT SAVINGS

DEGREE OF ENGINE HEATING	CRITICAL LOAD AND TEMPERATURE CONDITIONS	UNRESTRICTED SELECTIVE USAGE	COMPLETE SUBSTITUTION
NONE	$M \leq 1.8$	12.4	5.0
	MAX. TEMP.	13.2	5.2
MODERATE	$M \leq 1.8$	13.8	7.0
	MAX. TEMP.	13.4	5.8
MAXIMUM	$M \leq 1.8$	12.8	4.5
	MAX. TEMP.	11.7	-2.0

TABLE 7. HIGH TEMPERATURE ALUMINUM APPLICATION CANDIDATES FOR MILITARY TRANSPORT AIRCRAFT

	EXISTING MATERIAL	WEIGHT KG (LB)	OPERATING TEMPERATURE K (°F)	PRIMARY DESIGN CONDITION
PYLONS - C-5A	Ti	908 (2002)	422 (300)	STIFFNESS
FWD LONGERONS/BULKHEAD	Ti/S.S.	500 (1102)	616 (650)	STIFFNESS
AFT SKINS/LONGERONS/BULKHEADS				
ENGINE NACELLE - C-5A				
DOORS	Ti/Al	381 (841)	394-644 (250-700)	AIR LOADS
FLAP SURFACES				
C-141A (T.E. ASSEMBLY)	Ti	596 (1313)	505 (450)	SONIC FATIGUE
C-130 (LOWER SURFACE)	Ti	80 (17)	422 (300)	SONIC FATIGUE

Airframe Payoff Study Conclusions

Analyses performed in this study have shown elevated temperature resistant high strength - high stiffness aluminum alloys to be viable candidates to replace titanium in aircraft structures subjected to elevated temperature environments. Weight savings in the range of 5% to 10% have consistently been calculated for a varied number of structural components ranging from the engine heated structures of subsonic transports to the entire airframe of a Mach 3 class Supercruiser/Advanced Tactical Fighter.

From these studies, combined with experience from previous studies of high performance military aircraft accumulated over the past two decades, Figure 6 has been constructed to show estimated weight versus Mach Number variations for an advanced tactical fighter airframe. Potential P/M aluminum usage is shown compared to all conventional 7075-T6 aluminum alloy and to a least weight combination of titanium and 7075-T6 aluminum. While these curves are estimates and would vary somewhat with the aircraft configuration and service life, the trends are valid. The elevated temperature resistant aluminum alloys have the potential to be the primary structural material for high performance military aircraft up to the Mach 3 cruise speed range.

In a recent publication (Reference 10) the material mixes of past and current fighter aircraft were shown with a projection to a future tactical fighter was postulated to be a Mach 2 plus supersonic cruise aircraft having an initial operating capability (IOC) between 1990 and 1995. Contrary to that prognostication, it is forecast that with the development of the P/M aluminum alloys, the material mix in the future tactical fighter will be modified. The high temperature aluminum alloys will replace much of the projected use of titanium and high strength-highstiffness aluminum alloys will reduce the use of advanced composites.

CONCLUSIONS

Application of rapid solidification technology to advanced aluminum alloys has lead to development of new alloy compositions which have significant potential weight saving payoffs for a variety of new applications.

- o For gas turbine engine vane applications weight savings of 24-35% appear feasible. Blade applications will require improved fatigue capability to achieve weight savings of 35%. Current fatigue properties will limit weight savings to approximately 7%.
- o Airframe application of elevated temperature P/M aluminum alloys will lead to weight savings of 8 to 12% depending on the degree of alloy optimization required for an aircraft of the supercruiser configuration. The advanced tactical fighter weight savings were computed to be between 6 and 13% depending on the mission profiles and alloy optimization chosen, with an expected weight saving of approximately 8%. Weight savings for various military transport components ranged from 1.2 to 10% depending on the components selected.

ACKNOWLEDGEMENTS

The initial work on elevated temperature aluminum alloys was performed under a Defense Advanced Research Projects Agency contract monitored by the Air Force Wright Aeronautical Laboratories, Contract F33615-76-C-5136, "Application of Rapidly Solidified Alloys". Subsequent work has been performed under a sub-contract from Lockheed California Company under funding from Air Force Wright Aeronautical Laboratories on contract F33615-81-C-5096, "Elevated Temperature Aluminum Alloys". The continuing encouragement and support of Dr. E. van Reuth and Dr. L. Jacobsen (DARPA), and of Mr. A. Adair and Mr. W. Griffith (AFWAL) as program monitors for these programs is gratefully acknowledged. The views and conclusions contained in this document are those of the authors and should not be interpreted as necessarily representing the official policies, either expressed or implied, of the Defense Advanced Research Projects Agency, U.S. Air Force, or the U.S. Government.

REFERENCES

1. Adam, C. M., R. G. Bourdeau and J. W. Broch, "Application of Rapidly Solidified Alloys," Final Contract Report, September 1981, Contract F33615-76-C-5136.
2. Adam, C. M., "Structure/Property Relationships and Applications of Rapidly Solidified Aluminum Alloys," Proc. 1981 Mats. Res. Soc. Symposia, North-Holland Elsevier (1982) p. 411.
3. Adam, C. M. and J. W. Simon, "Influence of Microstructure on Texture Development in an Aluminum Powder Metallurgy Alloy," A.S.M. Conference on Textures/Microstructures/Mechanical Properties, 1982, to be published.
4. Langenbeck, S., "Elevated Temperature Aluminum Alloys," Air Force Wright Aeronautical Laboratories Contract F33615-81-C-5096, Semi-Annual Technical Report, 1982.
5. Simenz, R. F., G. G. Wald, S. L. Langenbeck and E. J. Himmel, Lockheed California Company Technical Proposal, RFP F33615-80-R-5174, 23 September 1980.
6. Lewis, R. D., et al, Phase I Final Report, DARPA/AFML Contract F33615-78-C-5203, to be published.
7. Design Conference Proceedings, Technology for Supersonic Cruise Military Aircraft, Air Force Flight Dynamics Laboratory, February 17-20, 1976.
8. Hahn, Daril W., Technical Report, AFFDL-TR-78-80, Volume I, July 1978.
9. Paez, C. Technical Report, AFFDL-TR-79-3093, August 1979.
10. Hadcock, Richard N., Technical Paper, NASA Conference Publication 2162 - Part 2, Tactical Aircraft Research and Technology Conference Proceedings, October 21-23, 1980.

GAS TURBINE APPLICATIONS OF RST ALLOYS

D.B. George, R.G. Bourdeau, J.A. Miller

Pratt & Whitney Aircraft
Government Products Division
West Palm Beach, Florida 33402

ABSTRACT

Technological advances in the rapid solidification of alloys useful to the gas turbine engine show benefits related to performance, durability, and weight reduction. Implementation of this technology has been achieved successfully for superalloy turbine disks. Near-term plans for implementation have been prepared for RST high temperature aluminum alloys as a substitute for titanium and RST corrosion resistant bearings to replace conventional M50. Mid-range plans are directed toward implementation of RST superalloys for airfoils and RST intermetallics for burners and liners. The status of the RST technology is addressed in this paper and engine design benefits are described.

INTRODUCTION

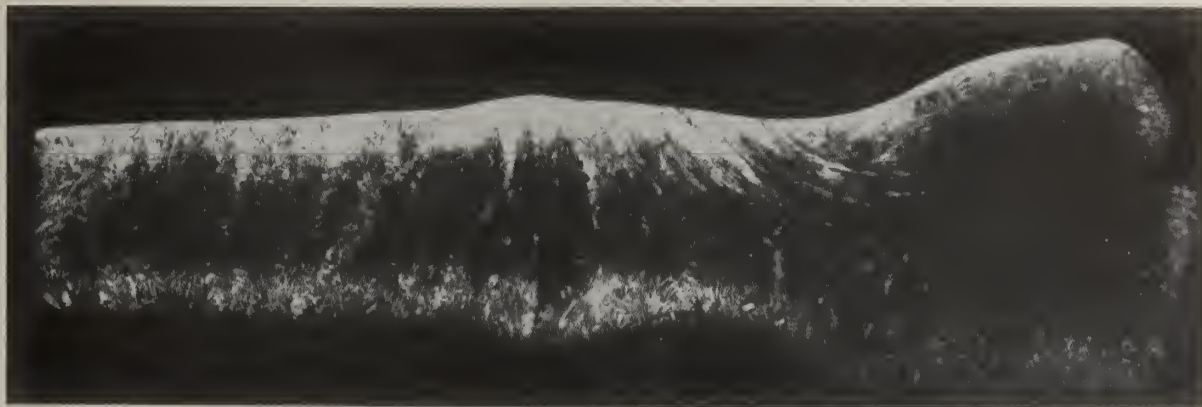
A new era of supremacy for allied tactical air forces began in the mid-1970's when the F-15 and later the F-16 entered the U.S. Air Force inventory. As of this writing, there are 727 McDonnell Douglas F-15's and 784 General Dynamics F-16's in service with free-world air forces. By the mid-1980's an estimated 925 F-15's and 1,550 F-16's will be deployed worldwide. Both of these aircraft are powered by the Pratt & Whitney Aircraft F100 engine, which featured the first production application of powder metallurgy turbine and compressor disks.

The qualitative advantage in tactical airpower provided by these and other types of aircraft in service today is not guaranteed to last indefinitely. The typical life of a high-performance fighter aircraft system is about eighteen to twenty years, so we will need a replacement for the F-15 in 1992 if we are to retain our technological lead. That may seem a long way off, but to achieve a 1992 introduction via a competitive flyoff of prototype aircraft, the program to develop the engine for the new fighter will have to start in 1983.

Improved fighter maneuverability expressed in terms of turn rate, acceleration, or rate of climb is directly related to the ratio of available engine thrust to the total aircraft weight. This ratio has nearly tripled since the 1940's as a result of the corresponding increase in the thrust-to-weight ratio of the engine itself. We believe this trend will continue due in large measure to the expanded use of powder metallurgy materials which feature higher specific strength and temperature capabilities. The revolution begun in the mid-1970's, with the introduction of powder metallurgy disks into the F100 engine, has evolved to encompass a broad spectrum of anticipated powder metallurgy applications for the next tactical engine system. Prior to discussing the potential impact of powder metallurgy on future engine systems, it is worthwhile reviewing the highly successful F100 engine experience which serves as the foundation for the further exploitation of this technology.

HISTORICAL BACKGROUND

During the early 1960's, in the development of the J58 duct-burning turbofan engine by Pratt and Whitney Aircraft, it became apparent that Waspaloy and Rene 41--the most advanced nickel-base alloys then used for forgings--did not possess the high temperature strength required for the turbine disks. A new wrought alloy, at that time known as Astroloy, did exhibit the required strength and elevated temperature operating capability. The evaluation of Astroloy forgings, however, revealed that while the desired strength potential was present, these forgings exhibited excessive scatter in mechanical properties due to gross structural segregation and lack of homogeneity as shown in Figure 1.



Bore

Rim

FIGURE 1: CROSS SECTION OF AN ASTROLOY DISK FROM 20 IN. DIA. INGOT

The segregation noted in early Astroloy forgings could be traced back to the large columnar grain structure of the ingots being produced at that time. Metallurgical evidence was compiled, showing that the segregation existing in conventional ingots was not eliminated by subsequent forging and thermal treatments.

Based on these findings, a full-scale Astroloy ingot evaluation program was initiated by Pratt and Whitney Aircraft. The results of the evaluation showed that casting parameters yielding relatively fine, equiaxed grain structure minimized macrosegregation in the ingot. Production processes were developed which produced such structures in ingots which were forged into full-scale turbine disks for the J58 engine. These disks have compiled an excellent record in the field.

Subsequent to this, in an effort to develop a stronger high temperature disk composition than Astroloy, ultrafine equiaxed grain ingots of IN100 were cast. Eight-inch diameter disks were forged from the fine-grained IN100 ingots, however, the macro- and microstructure of these disks, produced from what was considered an optimum fine-grained ingot, contained a prohibitive amount of segregation. This barrier to further development of stronger disk materials lead to consideration of a powder metallurgy approach to the production of large engine disks with a minimum of macrosegregation. The degree of macrosegregation in a small powder particle would be expected to be less by several orders of magnitude than that present in the structure of a large ingot conventionally melted and cast under optimum conditions.

A method of powder production, collection and densification was developed by Pratt and Whitney Aircraft to eliminate the problems associated with particle oxidation, scatter in properties, and lack of reproducibility which had plagued efforts up to that time to utilize powder metallurgy for superalloy parts. To avoid oxidation of individual powder particles, an "all inert" method of powder production, collection, and billet densification was developed wherein the metal powders would not be exposed to the atmosphere prior to densification (Figure 2). Astroloy, the most advanced production nickel-base superalloy disk material at that time, was selected for the investigation.

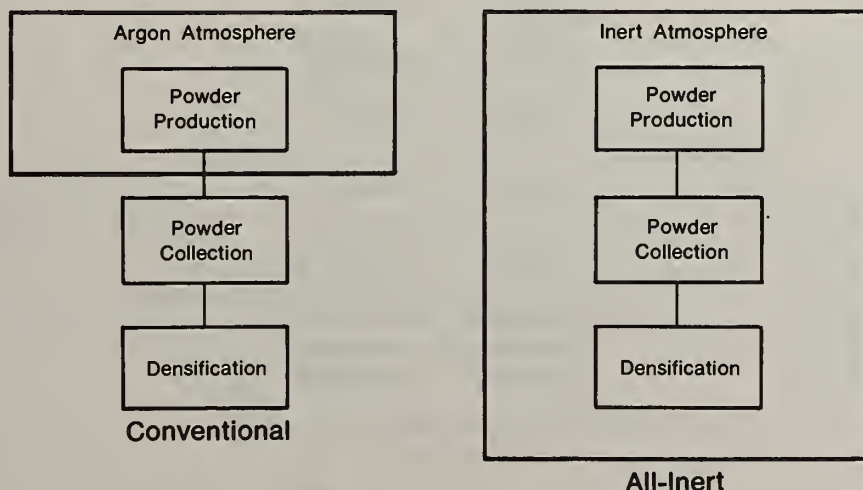


FIGURE 2: ALL-INERT POWDER METALLURGY PROCESSING PREVENTS THE FORMATION OF OXIDE FILMS ON POWDER PARTICLES

This initial program demonstrated that small Astroloy forgings (Figure 3) made by the "all inert" technique could be compacted and forged over a wide temperature range and showed uniformity of structure and mechanical properties. The macro- and microstructural segregation of the small powder disks was significantly reduced from that of even the most optimum structure seen in a disk made from a cast ingot.

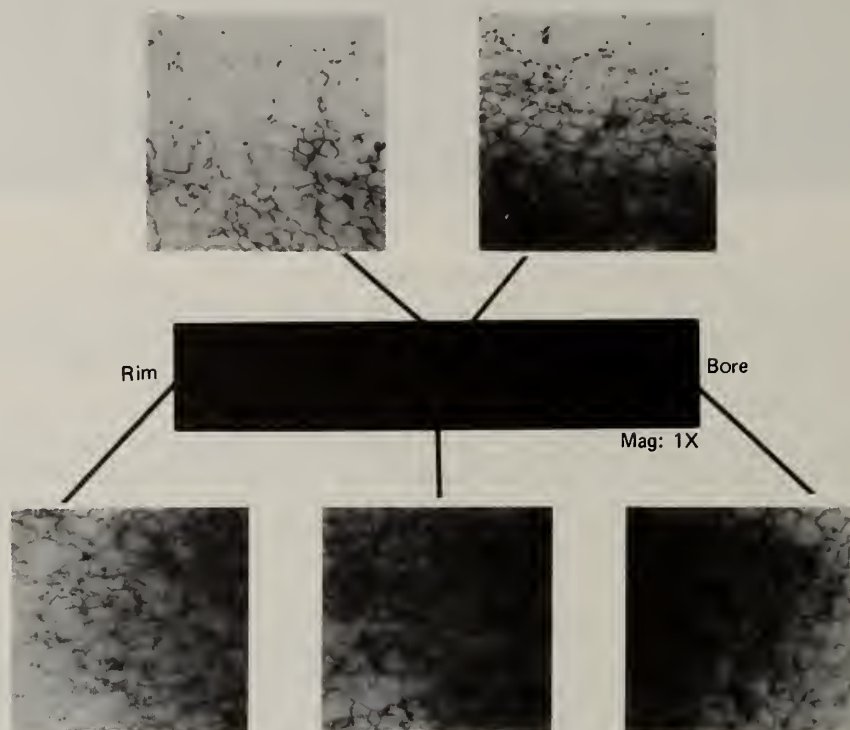
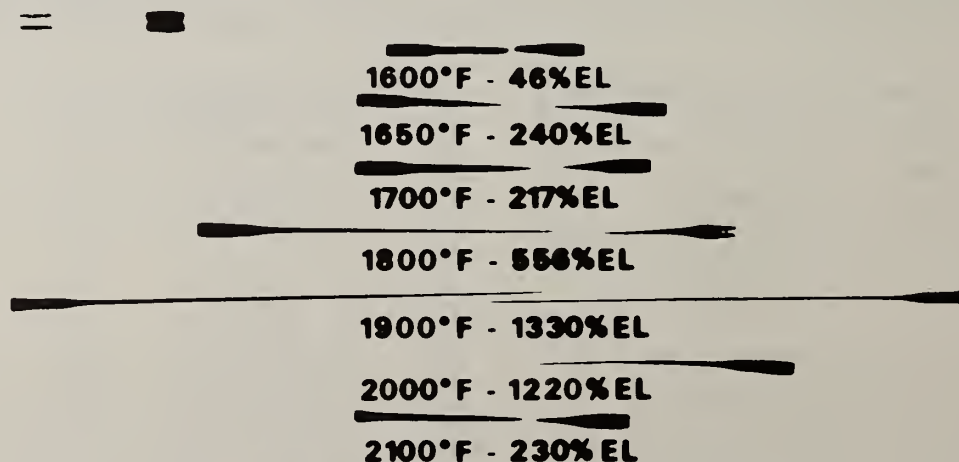


FIGURE 3: POWDER METAL PANCAKE FORGING ILLUSTRATES DRAMATIC REDUCTION IN SEGREGATION

While this Astroloy powder program was underway, it was discovered that iron, nickel, and titanium base superalloys could be made to behave superplastically. Billet and bar stock of A-286, INCO 901, Astroloy, Waspaloy, B1900, IN100, and titanium alloys 8-1-1 and 6-4 were produced by controlled processing so that they behaved in a superplastic manner over a fairly wide temperature range if the strain rates were properly controlled (Figure 4).



Note: Temperatures Shown Under Each Specimen
Are Test Temperatures

FIGURE 4: IN100 SPECIMENS AFTER STRESS RUPTURE TESTING

The next logical step was to forge these alloys isothermally in the temperature range and at the strain rate where they demonstrated superplastic behavior. It was found that billet stock previously made superplastic could be forged isothermally into complex configurations using very low unit pressures. This controlled isothermal forging practice, illustrated in Figure 5, which utilizes the superplastic behavior of the alloy being forged was given the name GATORIZING[®] by Pratt and Whitney Aircraft and is covered by U.S. Patent 3,519,503.

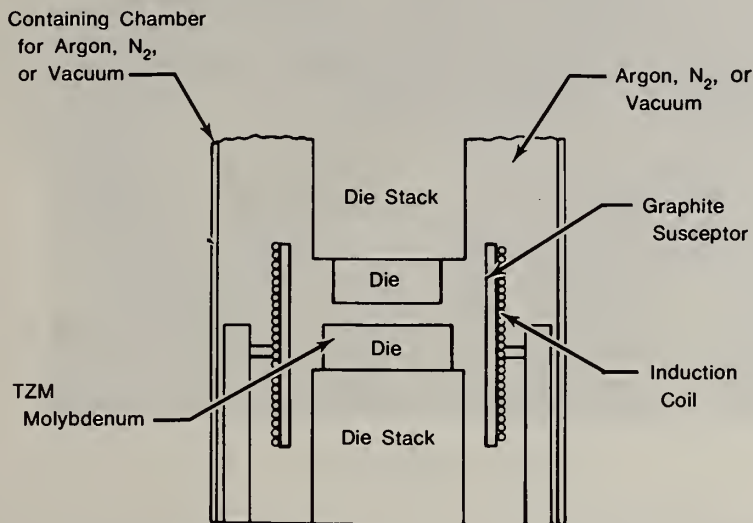
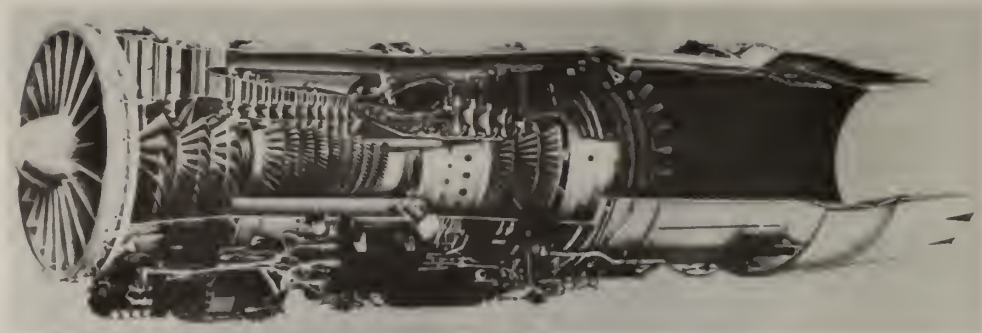


FIGURE 5: GATORIZING[®] FORGING SCHEMATIC

F100 ENGINE POWDER METALLURGY EXPERIENCE

The first application of powder metallurgy to production parts was for the high thrust-to-weight ratio F100 engine. In the early stages of the development of this engine, the materials selection was predicated on achieving the highest strength-to-weight ratio that it was possible to obtain. For the latter stage compressor disks and turbine disks, we were in need of a stronger alloy than Astroloy, then the most advanced alloy operating in a production jet engine. IN100, a nickel base superalloy developed for cast turbine blades, had the best strength-to-weight ratio at operating temperatures of available alloys. However, this highly segregation prone alloy was unusable for large engine disk forgings using conventional state-of-the-art melting and forging practices. By utilizing the "all inert" powder metallurgy concept developed in conjunction with the GATORIZING forging process, we were able to produce compressor and turbine disks and spacers from the IN100 alloy for the F100 engine with an unprecedented level and uniformity of mechanical properties. Figure 6 is a cutaway of the F100 engine with a listing of the nine IN100 parts produced by the GATORIZING process.

The first F100 engine disk from IN100 powder billet, forged by the GATORIZING process, was produced in April 1970. Since that time, 3,029 production F100 engines have been delivered to allied Air Forces worldwide each containing the nine powder metallurgy components illustrated in Figure 6 for a total of 27,261 production components. The F-15/F-16 fleet had accumulated a total of 1,385,000 engine flight hours as of November 1982, which equates to 12,465,000 hours of flight experience with powder metallurgy components. To date, there has only been one incident where a material processing related disk failure was suspected. The cause of the incident could not be established despite an extensive investigation. To say the least, the operational experience with F100 powder metallurgy components to date has been phenomenal; particularly when one remembers that this is the first production application of powder technology in a gas turbine engine. Based on the excellent experience with powder metallurgy components in the F100 engine, the stage is set to further exploit this technology in the next generation fighter engine, the development of which begins next year.



9th-Stage Compressor Disk	1st-Stage Turbine Disk
11th-Stage Compressor Disk	2nd-Stage Turbine Disk
13th-Stage Compressor Disk	3rd-Stage Turbine Disk
13th-Stage Compressor Cone Seal	4th-Stage Turbine Disk
	2nd-Stage Turbine Spacer

FIGURE 6: F100 ENGINE USED GATORIZED[®] IN100 COMPONENTS PRODUCED FROM IN100 POWDER METALLURGY BILLET

ADVANCED RST ALLOYS

Having made the revolutionary technology step from ingot to all inert powder in the F100 engine, Pratt and Whitney Aircraft with government support has embarked on a Rapid Solidification Rate (RSR) technology program aimed at further capitalizing on the potential of powder metallurgy alloys. As illustrated in Figure 7, the development of RSR alloys represents an extension of the increased cooling rate technology revolution which began with the now state-of-the-art processing of all inert powder.

A device for producing rapidly solidified alloy powders was constructed by Pratt & Whitney Aircraft which uses forced convective cooling of molten particles accelerated from a central source into a high conductivity gas quench medium. The rig is shown in Figure 8. An alloy charge is melted in the crucible at the top of the rig. The liquid metal is poured into a transfer system, which in turn supplies a continuous flow of molten metal to a disk atomizer spinning at approximately 24,000 rpm. The metal is centrifuged into particles ranging from 10 to 100 microns and is subsequently solidified by an array of helium gas-quenching jets.

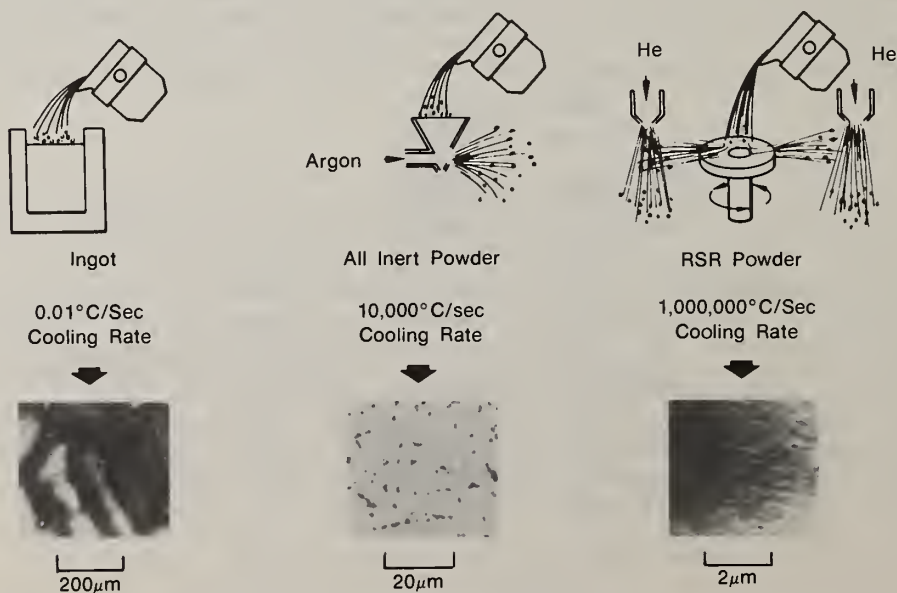


FIGURE 7: RSR POWDER PROCESSING EVOLVED FROM ALL-INERT POWDER EXPERIENCE

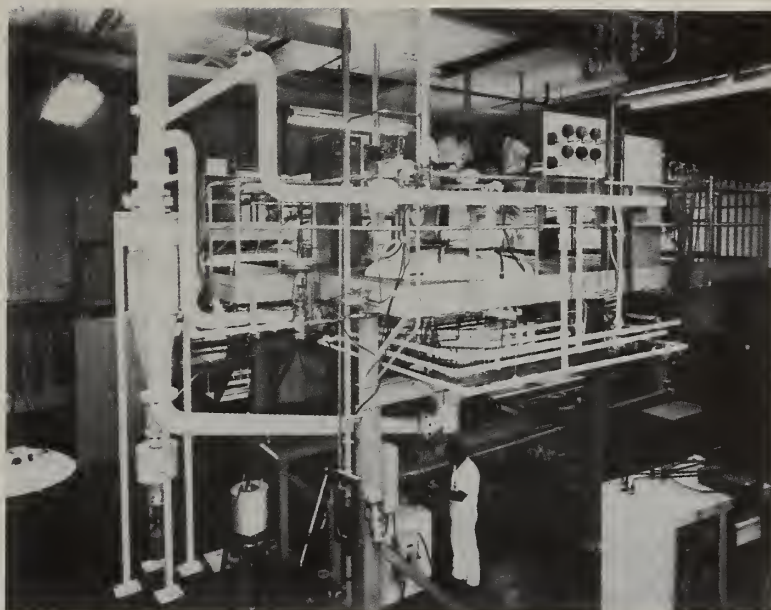


FIGURE 8: RSR POWDER PRODUCTION FACILITY

Several hundred experimental aluminum, iron, and nickel base powder metal alloy compositions have been atomized and evaluated to date under the sponsorship of the Defense Advanced Research Projects Agency (DARPA), the Air Force Materials Laboratory (AFML), the Naval Research Laboratory (NRL), the Office of Naval Research (ONR), and the Naval Air Systems Command (NAVAIR). In addition to further advances in compressor and turbine disk material capabilities, potential powder metal applications in the next generation fighter engine include lightweight aluminum fan stators, corrosion resistant bearings, oxidation resistant/lightweight burner liners, and improved durability turbine airfoils. A brief description of the alloys being pursued for these applications and the associated benefits is described in what follows.

Advanced Turbine Disks Materials

An interdivisional alloy development program has been underway at Pratt and Whitney Aircraft for several years aimed at further refining the IN100 disk material chemistry. Figure 9 illustrates one dramatic improvement which was achieved in crack growth rate reduction through the use of revised processing. Studies are proceeding to select the best combination of properties to satisfy the requirements of a wide variety of future engine disk requirements, including several derivatives of the F100 engine and the 5000 SHP Modern Technology Development Engines (MTDE) for the Army and Navy.

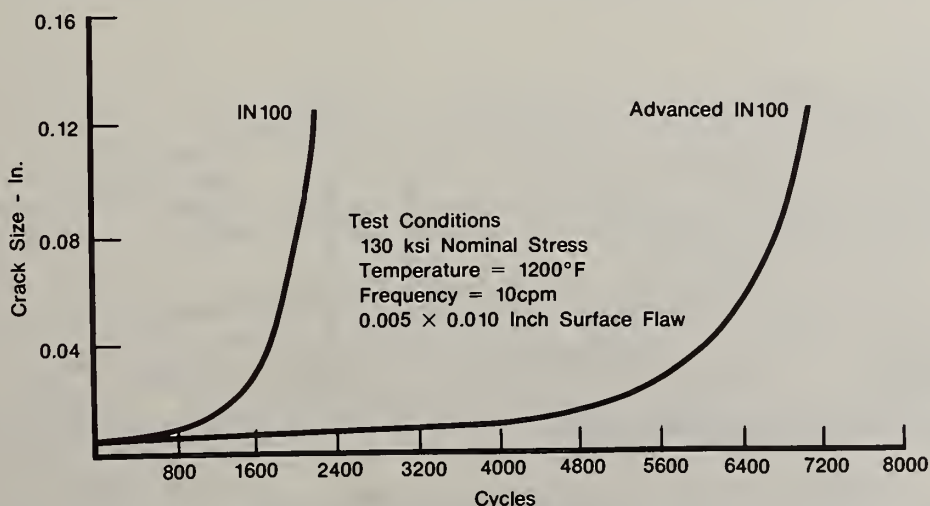


FIGURE 9: CRACK GROWTH RATE CHARACTERISTICS OF AN ADVANCED VARIANT OF IN100 (PWA 1074)

In addition to improved versions of IN100, a new chemistry disk material is being developed in support of the next generation fighter engine program to achieve the properties illustrated in Figure 10. As shown, a +50°F creep rupture capability in conjunction with a 10% improvement in tensile properties, and a crack growth rate reduction are desired. The final selection of the chemistry of this new alloy will be made in 1984.

The improved turbine disk material will permit an increase in the rotational speed of the high compressor rotor enabling elimination of one compressor stage. Alternatively, use of this material could result in extension of the disk inspection interval and/or reduced weight with an attendant reduction in operational and support costs.

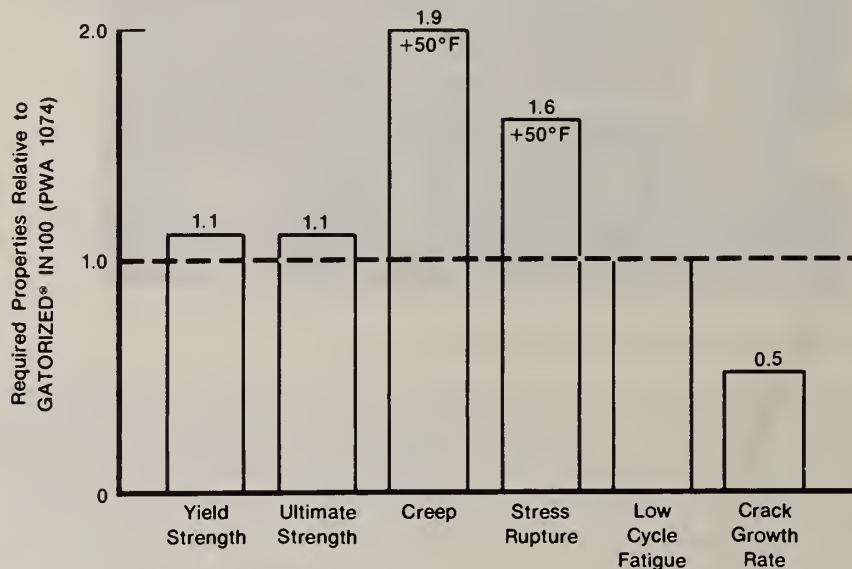


FIGURE 10: RELATIVE PROPERTY GOALS FOR NEW TURBINE DISK ALLOY

RSR Aluminum Compressor Airfoils

The development of a new high temperature aluminum alloy (Al-8Fe-2Mo) with useful strength capabilities in the 500°F range is proceeding based on the application of rapid solidification rate powder metallurgy technology. As illustrated in Figure 11, RSR aluminum alloys have been produced which provide on the order of a 150°F improvement in alloy capability relative to conventional aluminum alloys such as AA2219. Ultimately, it is believed the useful temperature range could be extended to the 650°F regime. In view of the improved temperature capability of Al-8Fe-2Mo (developed under

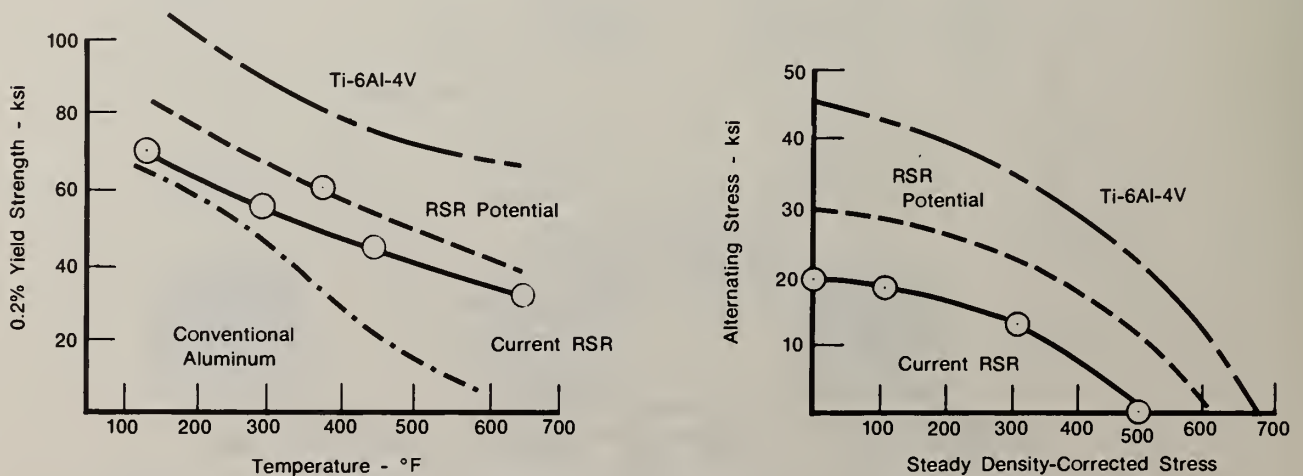


FIGURE 11: COMPARISON OF RAPID-SOLIDIFICATION-RATE ALUMINUM TO CONVENTIONAL TITANIUM AND ALUMINUM ALLOYS

AFML contract F33615-79-C-5136), the potential exists to replace heavier and more costly titanium components with aluminum in the first two fan stages.

The density of this new aluminum alloy is on the order of .104 lbs./in.³ whereas the density of Ti-6Al-4V is .160 lbs./in.³. Analyses using the strength properties achieved to date indicate a potential of up to a 20% weight savings for vane applications. During 1982, a set of 2nd stage fan stator vanes will be fabricated from the current RSR aluminum alloy for an F100 derivative engine test. If the goal alternating stress capability of Figure 11 is realized, applications to compressor blades are also envisioned with an attendant weight reduction for the supporting disk.

Corrosion Resistant Bearings

Recent Air Force Aero Propulsion Laboratory testing, (F33615-76-C-5136) of a series of RSR processed bearing alloys have demonstrated the potential of significantly improving the rolling contact fatigue (RCF) and corrosion lives of M50-like bearing steels. As illustrated in Figure 12, the alloy designated RSR 561 displayed a five-fold improvement in the B-10 rolling contact fatigue life relative to the baseline VIM-VAR M50 material. Also noteworthy is an RSR alloy which displayed a modest 20% improvement in rolling contact fatigue but which contains 19% chromium (versus 4% in M50). Due to its high chromium content, the RSR alloy should be substantially more corrosion resistant than M50, prompting the inclusion of an RSR alloy in the government-sponsored Improved Corrosion Resistant Turbine Engine Bearing Program (F33615-81-C-2023). In addition to being pursued under that program, the trial fabrication of prototype RSR bearings will also be undertaken in cooperation with the Fafnir Bearing Company.

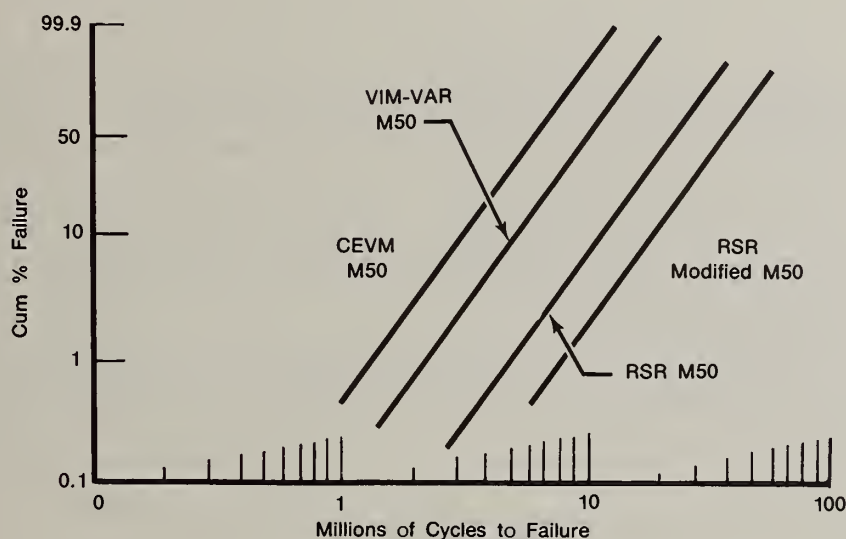


FIGURE 12. ROLLING CONTACT FATIGUE DATA FOR BEARING ALLOYS

Iron-Aluminum Alloys

Iron-aluminum alloys have been recognized for a long time as having desirable properties for high temperature applications. They have excellent oxidation and sulfidation resistance, significantly lower density than nickel or cobalt alloys (.22-.24 lbs./in.³ as opposed to .28-.33 lbs./in.³), and they contain no strategic elements. Until recently, however, iron aluminum alloys containing a sufficient amount of aluminum for good high temperature oxidation resistance were too brittle for engineering applications and their strength, especially at elevated temperature, was mediocre.

Recently, it has been shown that rapid solidification and thermomechanical processing can produce fine dispersions of titanium diboride in Fe-Al alloys. The dispersions greatly improve both the strength, ductility, and temperature capability of the iron-aluminum alloys. While the data are limited, it is believed that the dispersion strengthened iron-aluminum alloys can be developed into two classes of alloys; one class has the oxidation resistance (Figure 13) and high temperature creep strength required for use at 1800°F to 2000°F while the other class has a lower density with somewhat reduced temperature capabilities.

The lower density alloy is viewed as a candidate to replace Inconel 718 in the compressor. The high temperature oxidation resistant material will be considered for application from the combustor rearward.

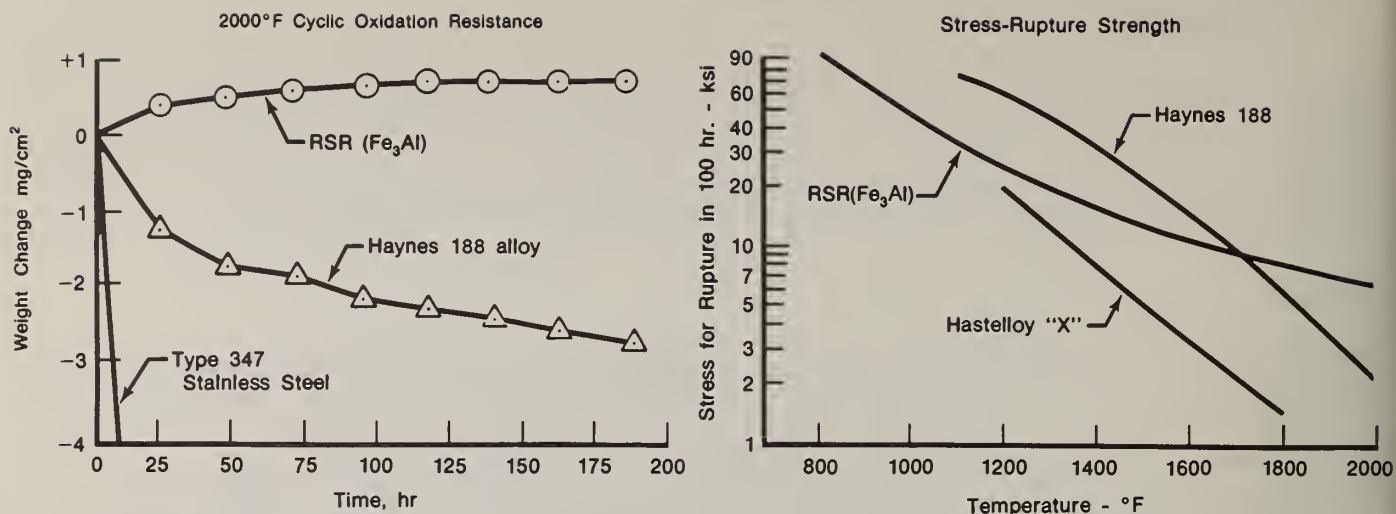


FIGURE 13. PROPERTIES OF IRON-ALUMINUM RELATIVE TO TRADITIONAL BURNER ALLOYS

Turbine Airfoil Materials

Currently both RSR vane and blade alloys are being developed under sponsorship of the Defense Advanced Research Projects Agency (DARPA) and the Air Force Materials Laboratory (AFML). The RSR vane alloy features a significant improvement in oxidation resistance (Figure 14) and a +65°F increase in incipient melting point relative to the advanced single crystal alloy PWA 1480 which has been employed in recent versions of the JT9D commercial engine and the F100 derivative engine family. The RSR blade alloy will have a +65°F advantage in creep rupture (Figure 15) and provides a significant improvement in oxidation resistance relative to PWA 1480. Both RSR processed alloys are currently undergoing detailed material property characterization scheduled for completion by the end of this year. Prototype vane and blade airfoils are scheduled to be fabricated next year for an advanced engine durability test commencing in early 1984.

The advanced RSR turbine airfoil alloys will provide cost of ownership benefits through either improved airfoil life (reduced maintenance cost) or a reduced cooling air requirement (improved SFC).

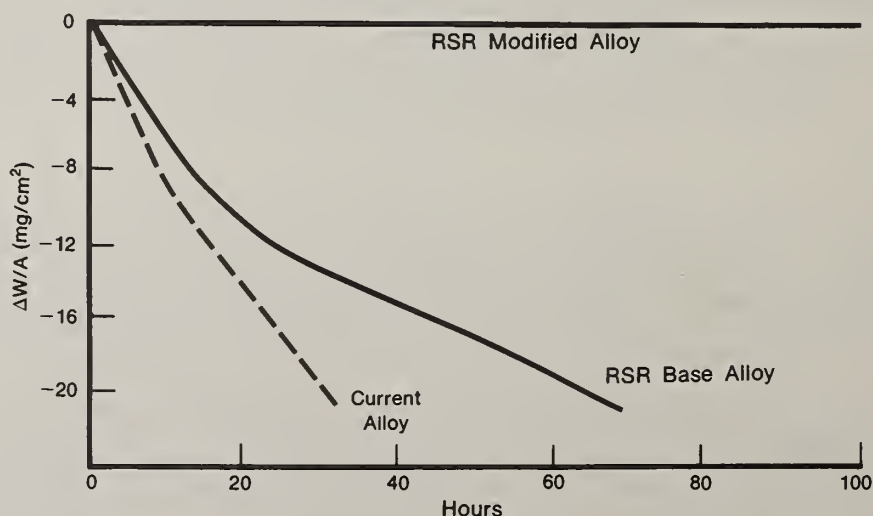


FIGURE 14. 2100°F CYCLIC OXIDATION RESISTANCE OF RSR SUPERALLOYS

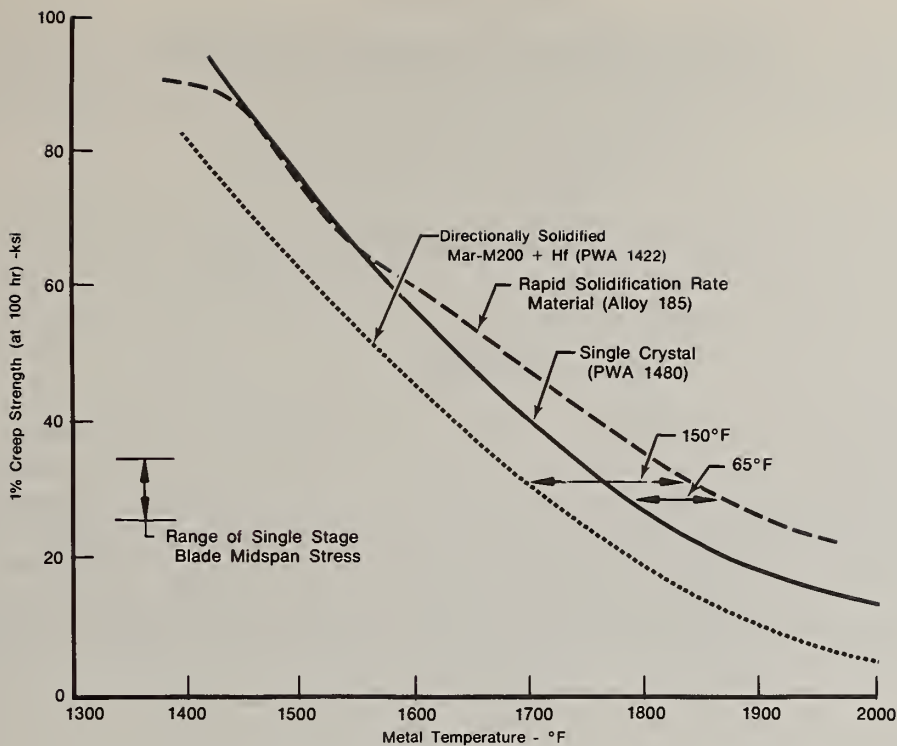


FIGURE 15. CREEP RUPTURE STRENGTH COMPARISON OF ADVANCED TURBINE BLADE MATERIALS

SUMMARY

The successful implementation of powder metallurgy disks into the production F100 engine and the excellent operational experience of those critical components has set the stage for the incorporation of a wide range of powder metal systems via rapid solidification processing into the next generation fighter engine. The timely development of advanced aluminum, iron, and nickel base powder metal superalloys under DARPA/AFML/NRL/ONR/NAVAIR sponsorship will enable the next generation fighter engine to provide a 20% improvement in engine thrust-to-weight ratio over the current F100 engine. A performance improvement of that magnitude will ensure continuance of the era of tactical fighter aircraft superiority which began with the introduction of the F100 powered F-15 aircraft.

ACKNOWLEDGEMENTS

The materials developments described herein are being supported by the Defense Advanced Research Projects Agency (under ARPA Order 3152), the Air Force Materials Laboratory (AFML), the Naval Research Laboratory (NRL), the Office of Naval Research (ONR), and the Naval Air Systems Command (NAVAIR).

The views and conclusions contained in this document are those of the authors and should not be interpreted as necessarily representing the official policies, either expressed or implied, of the Defense Advanced Research Projects Agency, U.S. Air Force, U.S. Navy or the U.S. Government.

REFERENCES

1. R.L. Athey and J.B. Moore, "Development of IN100 Powder Metallurgy Disks for Advanced Jet Engine Application," Powder Metallurgy, Syracuse University Press, 1972.
2. R.L. Athey and J.B. Moore, "Progress Report on the GATORIZING[®] Forging Process," SAE Paper 751047 presented at the National Aerospace and Manufacturing Meeting, Culver City, Los Angeles, November 17-20, 1975.
3. F.W. McAbee, Jr., "Turbine Technologies of Tomorrow," Air Force Magazine, January 1982.

AIRCRAFT ENGINE GAS TURBINE COMPONENT FABRICATION CONCEPTS USING RSPD

A.M. Johnson, J.S. Kelm, R.W. Smashey
D.V. Rigney & T.G. Wakeman

General Electric Co., Evendale, OH. 45215

ABSTRACT

The Rapid Solidification Plasma Deposition (RSPD) process offers unique opportunities for the fabrication of structural components. Injection of powder into a high velocity, low pressure plasma jet with subsequent melting and deposition of the powder onto a removable mandrel results in fine grained, homogeneous deposits. Structures of varying complexity can be made to near net shape from an extremely wide range of material compositions. Construction materials can be tailored for specific service environments within a component. Fabrication concepts using RSPD as a flexible manufacturing process for advanced aircraft gas turbine engine components are discussed as well as some of the expected benefits to be derived. Material and design aspects of RSPD are considered.

INTRODUCTION

The demands of advanced aircraft gas turbine engine operating requirements for increased performance with minimal influence on component costs present a major challenge to design, materials and manufacturing engineers. Conventional casting, forging and powder metallurgy (PM) processes have been under development for many years, and further gains in capability in these areas are difficult to obtain. Furthermore, final part costs have continued to increase at a steady rate due to accelerating material and labor costs.

Rapid Solidification (RS) technology offers improvements in alloy design and material homogeneity. A wide range of RS processes are currently under investigation throughout the world with many promising results. In most cases, rapidly solidified material is initially produced, followed by consolidation and metal working steps to reach a desired configuration from which a part is machined. Frequently, the most challenging aspect of making actual parts from rapidly solidified material is the careful handling and consolidation processing required.

The Rapid Solidification Plasma Deposition (RSPD) process under development by the General Electric Company provides the capability for flexible manufacturing of simple or complex shapes wherein the solidification and consolidation steps are combined. The essence of this technology derives from a coupling of a high energy plasma gun operated in a low pressure chamber to deposit powder material of a desired composition onto a substrate. As-deposited densities are sufficiently high that post-deposition heat treatments are normally adequate to achieve full density. Near net shapes may be formed by proper selection of mandrel configurations and deposition process control. Structures having a wide range of geometric configurations, including multiple alloy compositions within a single part, are made possible by this technique.

The development of RSPD for the fabrication of advanced aircraft gas turbine engine components is actively being pursued. The primary focus of the current effort is to provide a basic understanding of the process to establish a firm technology base for subsequent implementation. This paper addresses the key material, component design and fabrication considerations for RSPD technology.

The extremely high temperatures generated in plasma arcs have been used for a variety of purposes including: a) purification of high melting temperature materials, b) spherodization of refractory particles, c) high energy/high temperature testing, and d) deposition of specialized materials to provide unique characteristics.

Gianinni⁽¹⁾, described the atmospheric plasma jet and projected material development applications. By the early 1960's, primitive plasma generators manufactured in the United States were used to apply coatings for repair of used or mis-machined components⁽²⁾. At the same time, tungsten rocket nozzles were plasma formed. Mash and Brown⁽³⁾ describe improvements in bonding and strength of stainless steels, aluminum and other alloys in inert environments. Densities of the deposits were substantially improved from the usual range of 75-85% to as high as 92% due to minimal oxidation of the sprayed powder. Further treatment, by vacuum sintering or hot isostatic pressing (HIP), has served to increase densities of some deposits to near theoretical⁽⁴⁾.

In conventional plasma processing, the environment is maintained at atmospheric pressure. In experiments performed by Muehlberger⁽⁵⁾, 80 KW plasma jets produced at ambient pressures of ~0.1 atmosphere (76 torr) indicated a jet velocity of Mach 3, whereas previous 80 KW atmospheric plasma jet velocities seemed limited to Mach 2. More importantly, Muehlberger demonstrated the capability to produce deposits nearing 100% density with relative ease, whereas Okada and Moruo⁽⁶⁾, using inert gas shielding, reported 98-99% cast alloy density only under carefully controlled conditions. Rairden et al.⁽⁷⁾, conducted an evaluation of low pressure plasma deposition for use as a method to deposit reactive MCrAlY coating alloys at the Muehlberger facility. The deposits were near full density with little if any deposit contamination. The low pressure inert environment was acceptable for preheating components to sufficient temperature to allow deposition of MCrAlY coatings onto large industrial gas turbine blades. In 1977, simple plasma deposits of the superalloys IN738 and Rene' 80 were made⁽⁸⁾. These initial plasma deposits, after heat treatment, showed significant improvements for RSPD IN738 over conventionally cast IN738 strength and ductility at low temperature (<1200°F) as well as improved thermal fatigue resistance of RSPD Rene' 80 over cast Rene' 80.

Plasma-forming has also been used for specialty constructions, in which the base material is sprayed at atmospheric pressure onto a mandrel material to match the desired internal configuration of the component. After spraying, the mandrel material is removed by machining, leaching, or mechanical separation. The deposits are then typically finished to final dimensions. Since the plasma process relies on the deposition of molten or semi-molten material, conformation to the shape of the mandrel can be excellent. As such, the thermal spray process has been profitably used to construct dies and cast forms for specialty items such as precision plastic furniture components, decorations, and shoe soles, each of which require dimensional stability and faithful reproduction of the surface⁽⁹⁾.

PROCESSING FOR STRUCTURAL SHAPES

A typical low pressure plasma arc chamber used for RSPD processing is shown in Figure 1. The overall system includes a plasma generating gun, devices to manipulate the gun and target substrate, pumps, filters, power supplies, powder feeding equipment, plasma forming and powder carrier gas equipment, and controls to regulate the process and manipulations.

Figure 2 is a schematic of the plasma gun showing an internal injection port for the powder. External feeding of powder is a feature of other gun designs. They are generally capable of continuous operation in the 50 - 80 KW range, with short excursions to 120 KW. The position of the plasma torch is computer controlled in four axis: pitch, yaw, horizontal and vertical movement. The target mandrel can be moved laterally along the horizontal axis and rotated. Such a manipulation system is shown schematically in Figure 3.

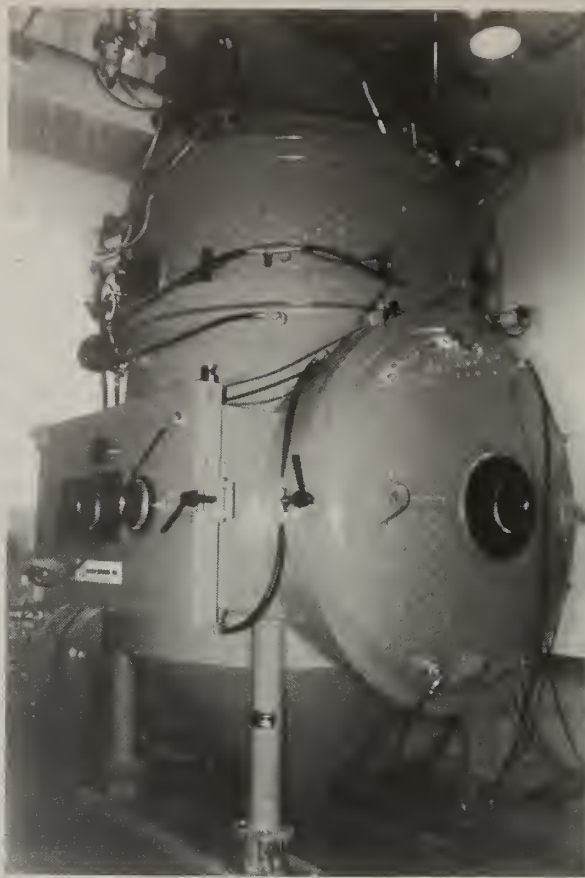


Figure 1 RSPD Development Chamber

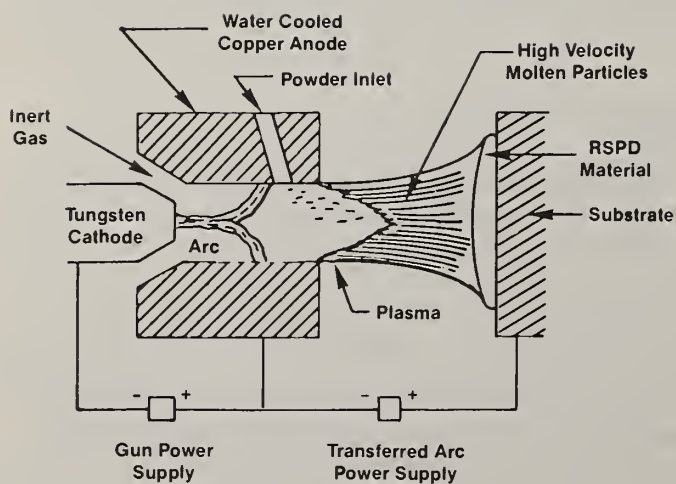


Figure 2 Schematic of a Plasma Spray System. For Reversed Transferred Arc Cleaning, the Polarity of the Transferred Arc Power Supply is Reversed

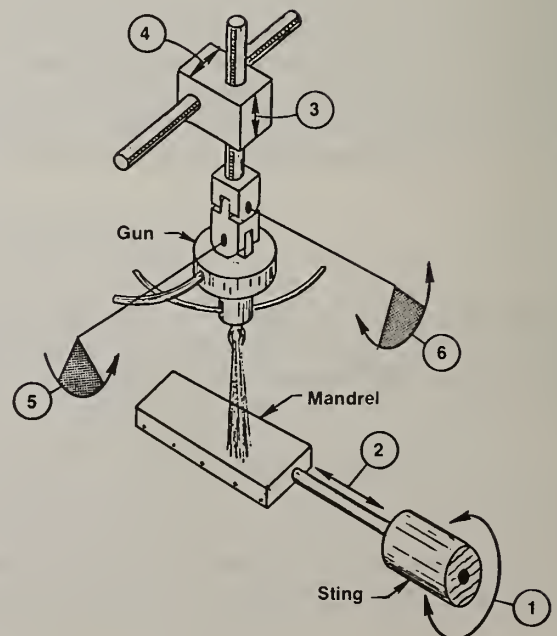


Figure 3 Schematic of Six Axis Plasma Gun and Mandrel Manipulation System

The plasma gun uses modified gas mass flow controllers to regulate the primary and secondary plasma-forming gases. Positive transferred arc, which is used to provide supplemental heating to the mandrel or component mounted on the horizontal axis, can be computer sequenced in time and position with the target mandrel. Similarly, the powder feed, vacuum pump and valve systems are also computer controlled. Thus, once a specific process program is written, an automatic sequence can be initiated for a) plasma arc initiation, b) reverse transferred arc (RTA) cleaning of the mandrel surface, c) positive transferred arc and/or plasma torch impingement preheating of the mandrel, d) spraying and e) shut-down. Pressure within the chamber is automatically maintained, and the temperature of the substrate is monitored using an optical pyrometer or contact thermocouple. Process data are acquisitioned and stored using a data-logger connected to the computer terminal.

The fabrication of RSPD structural components involves several major steps: 1) design and construction of mandrels, 2) selection of powder size and composition, 3) deposition processing and 4) post-deposition processing.

The mandrel is an important part of the RSPD process. In production modelling, the cost of mandrel fabrication and removal has a significant influence on the economic feasibility of the process. Therefore, a mandrel system must either be very simple and inexpensive so that it can be sacrificed after deposition, or durable enough to withstand many deposition cycles. The successful application of either method appears to be dependent largely on the size of the component being constructed. For example, disposable mandrels may be more suited for small components, whereas more complex reusable tooling may be required for larger components.

Near net shape deposition requires close dimensional control of both the mandrel substrate and the deposit. Conventional ambient pressure plasma forming uses mandrels which are not heated, or which are heated to a maximum of only a few hundred degrees Fahrenheit. The deposit thickness is generally much less than 0.060 inches - and the densities of the deposits are usually less than 90% of theoretical. The RSPD process, on the other hand, requires that mandrels be heated to $\sim 1600^{\circ}\text{F}$ to avoid spalling of the deposit as a result of accumulation of residual tensile cooling stresses and to facilitate adequate bonds. Delivery of powder to the plasma torch in a uniform, predictable manner requires handling methods which keep the powder free-flowing and uncontaminated with extraneous materials. Further contamination of the powder during deposition is avoided by control of interstitial impurities in plasma forming gases and the chamber environment. Typically, the superalloy powders obtained commercially in the size range of present use ($<37\text{ }\mu\text{m}$) are available with total interstitial (O_2 , N_2) contamination levels of $\sim 250\text{ ppm}$. In a properly operating system, superalloys are deposited with no increase in contamination level. Large quantities ($>10\%$) of very fine, ($<10\text{ }\mu\text{m}$) diameter powder have been found to impair the smooth delivery of powder to the plasma generator, and tend to evaporate in the plasma plume⁽¹⁰⁾.

When the molten particles impact on the substrate they "splat", forming a lenticular deposit $1\text{-}3\text{ }\mu\text{m}$ thick, and up to $100\text{ }\mu\text{m}$ in diameter. These splats are rapidly solidified at rates estimated to be $\sim 10^7\text{ }^{\circ}\text{F/sec}$, forming a chemically homogeneous and fine grained ($0.2\text{-}0.5\text{ }\mu\text{m}$) structure. The as-deposited microstructure is dependent on a large number of process variables, such as traverse rate, gun power, powder introduction method and position, chamber pressure, plasma torch orientation to the workpiece, etc. The effects of some of the variables on RSPD microstructures are discussed by Smith et al⁽¹⁰⁾ and Jackson et al⁽¹¹⁾.

After deposition, removal or separation of the deposit from the mandrel is required. Mandrels made from materials such as copper or low alloy steel can be dissolved in acid. Machining or other metal removal techniques can also be used. Since the as-deposited RSPD structures are relatively brittle, a heat treatment is given to ductilize the deposits and to reduce porosity. RSPD deposits made with substantial relative movement of the gun and substrate are generally over 98% of cast or wrought densities.

After heat treatments of $2150\text{-}2300^{\circ}\text{F}$, deposit densities generally increase to $>99\%$ of theoretical. Grain size of γ 'strengthened superalloys increases to $\sim 10\text{-}30\text{ }\mu\text{m}$. Solution strengthened alloys, such as Hastelloy X, show much larger grain growth after heat treatment to $\sim 75\text{-}300\text{ }\mu\text{m}$.

The RSPD process offers unique opportunities to be considered in the design of gas turbine components. These opportunities include increased flexibility of material utilization, near net shape capability, and graded multi-material configurations. The design, material and fabrication aspects of two widely differing gas turbine engine components are described below. Special consideration for RSPD processing and the potential benefits obtainable relative to conventional procedures are discussed.

Airfoil cooling inserts have traditionally been made from sheet metal. Due to the necessity to conform to rigid dimensional requirements, sheet metal inserts are difficult and expensive to fabricate. Advanced design blade inserts with complex shapes have dimensional requirements that are typically ± 0.002 inch and have the additional complexity of requiring variable, localized wall thickness control. To make such designs from fabricated sheet metal requires extensive machining. To reduce this machining cost, explosive forming of numerically controlled (NC) taper ground tubing has been attempted. Early in the refinement of this approach it became apparent that the amount of plastic deformation which is required to produce an insert configuration would produce a high percentage of localized tubing failures.

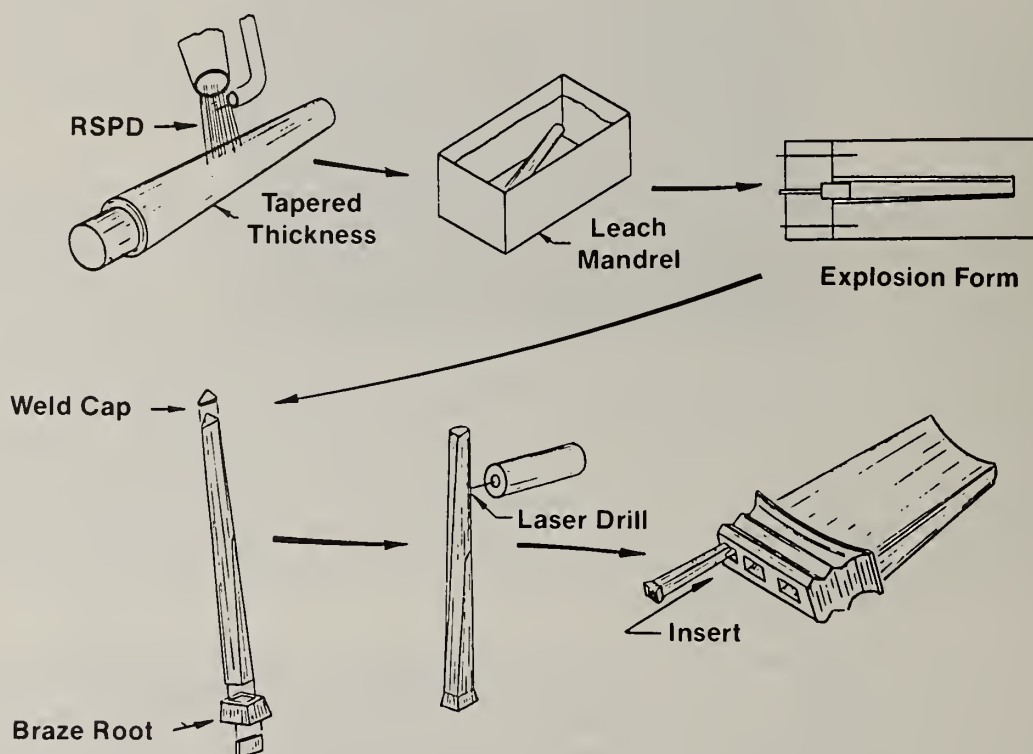


Figure 4 RSPD Blade Cooling Insert Fabrication Sequence

Tubing losses during explosive forming have been significantly reduced through the use of ultrafine grain size RSPD Waspalloy. The RSPD Waspalloy has demonstrated the capability to accommodate more high speed deformation without failure than its coarser grain, wrought counterpart. Since localized wall thickness can be controlled during the RSPD fabrication process, the expensive NC grinding operation used to produce tapers in wrought tubing was eliminated. The process used to make inserts using RSPD is schematically illustrated in Figure 4. In this process, a controlled thickness of Waspalloy was deposited onto a pre-tapered soft iron mandrel. Deposit wall thickness control was accomplished by varying the rotation speed of the mandrel and the translation speed of the plasma gun, thereby producing a barber pole type spray path about the mandrel. Fully heat-treated RSPD Waspalloy tubing used to make the inserts had an oxygen content of about 260 ppm and was between 98 to 100% dense after sintering. Typical grain size before explosive forming was about $12 \mu\text{m}$. Utilization of the RSPD Waspalloy tubing reduced manufacturing losses during explosive forming from over 75% for the wrought material to less than 5%.

A finished RSPD Waspalloy insert and a typical cross section showing the fine grained structure after all processing steps are shown in Figure 5. Finishing included the attachment of a welded tip cap and a brazed-on foot assembly. After the brazing operation, holes were lazer drilled through the leading edge and two sides of the insert.

The tensile strength of RSPD Waspalloy was determined to be about equivalent to that of forged material as shown in Figure 6. In stress rupture, the RSPD Waspalloy was about two Larson-Miller parameters weaker than forged Waspalloy. This is typical of fine grain material and is considered satisfactory for this insert application. In tensile ductility the RSPD Waspalloy behaved much like forged material to about 1000°F. Above 1000°F, the fine-grained RSPD material began to show evidence of reduced ductility, reaching a minimum at about 1600°F. Above 1600°F the tensile ductility increased. This behavior is also typical of cast superalloys exposed to elevated temperature and is believed to be caused by the presence of oxygen in grain boundaries.⁽⁸⁾ Component bench testing of the finished RSPD blade inserts showed them to be acceptable for actual engine testing which is planned for 1983.

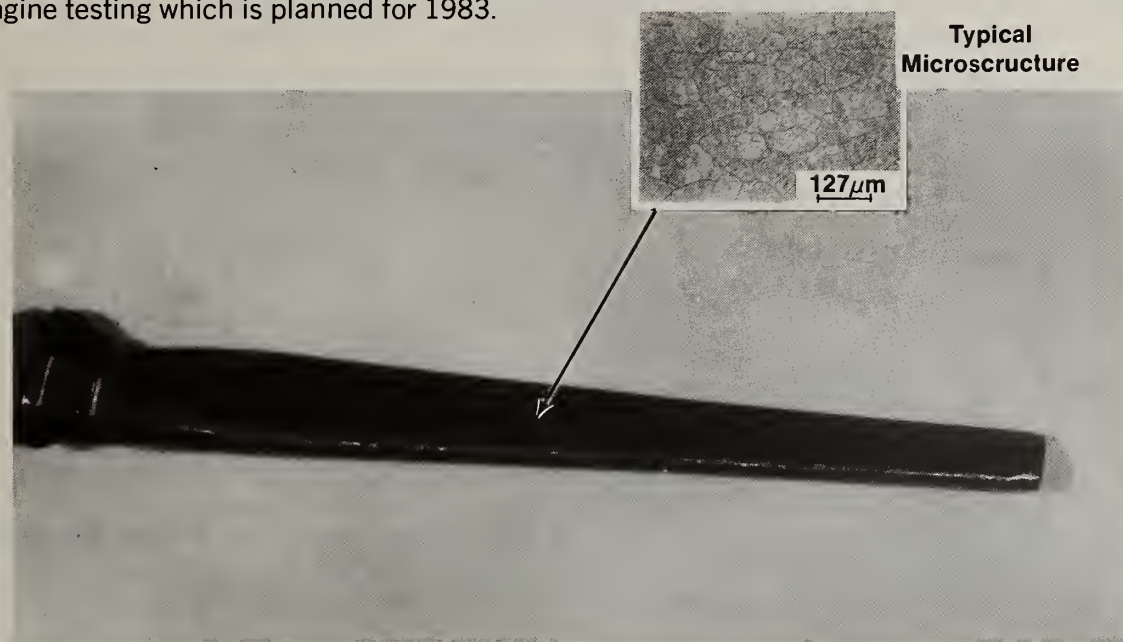


Figure 5 Finished RSPD Blade Cooling Insert

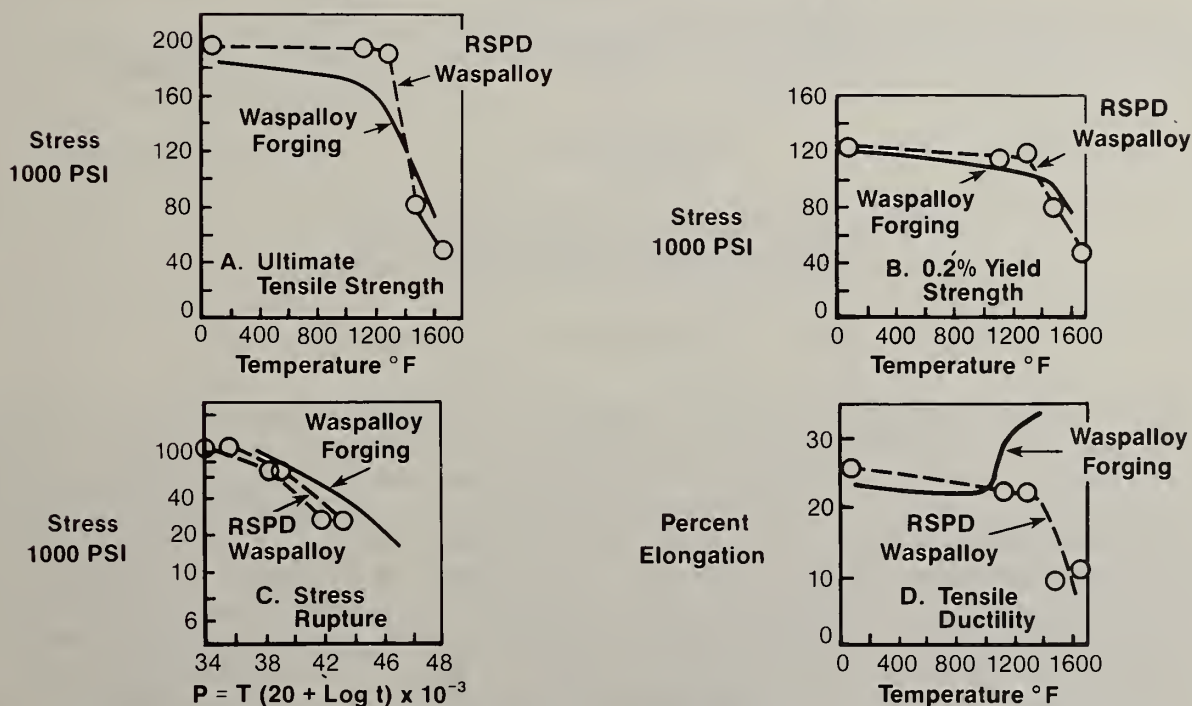


Figure 6 Comparison of RSPD Waspalloy and Forged Waspalloy Mechanical Properties

The design flexibility afforded by the RSPD process can be illustrated by considering a gas turbine combustor liner. A typical annular combustor is shown in Figure 7. At the upstream end, it consists of a dome through which fuel is introduced and a portion of the airflow passes. The downstream combustion region is contained within an annulus formed by an inner and outer combustor liner. The liners must be designed utilizing a limited amount of cooling flow for protection against the hot gases. The cooling flow is introduced through cooling rings spaced along the liner shell. Large axial thermal gradients between the hot liner shell and cooling ring are generated by the geometry and boundary conditions as illustrated in Figure 7C. Thermal gradients also exist circumferentially and are generally harmonic in nature, being a function of the number of fuel injection points in the dome. Thus, combustor liner life is limited by cracking due to hoop stress induced by axial thermal gradients and a combination of cracking, distortion, and oxidation due to circumferential thermal gradients (hot streaks).

Combustor liner materials have generally been limited to those readily available in sheet or forged form, such as Hastelloy X and HS188. The RSPD process permits designs utilizing graded, multi-material configurations. Opportunities are available to combine materials of differing strength, modulus, and thermal coefficient of expansion in unique fashions to address design requirements. For example, the designer may consider different coefficient of expansion materials in thermal gradient fields to reduce thermal stresses and thereby increase life. An example of this concept would be to fabricate the hot liner panel from Hastelloy X, while the cooling ring would be fabricated from A286 which has a higher coefficient of thermal expansion and greater low temperature (<1200°F) strength.

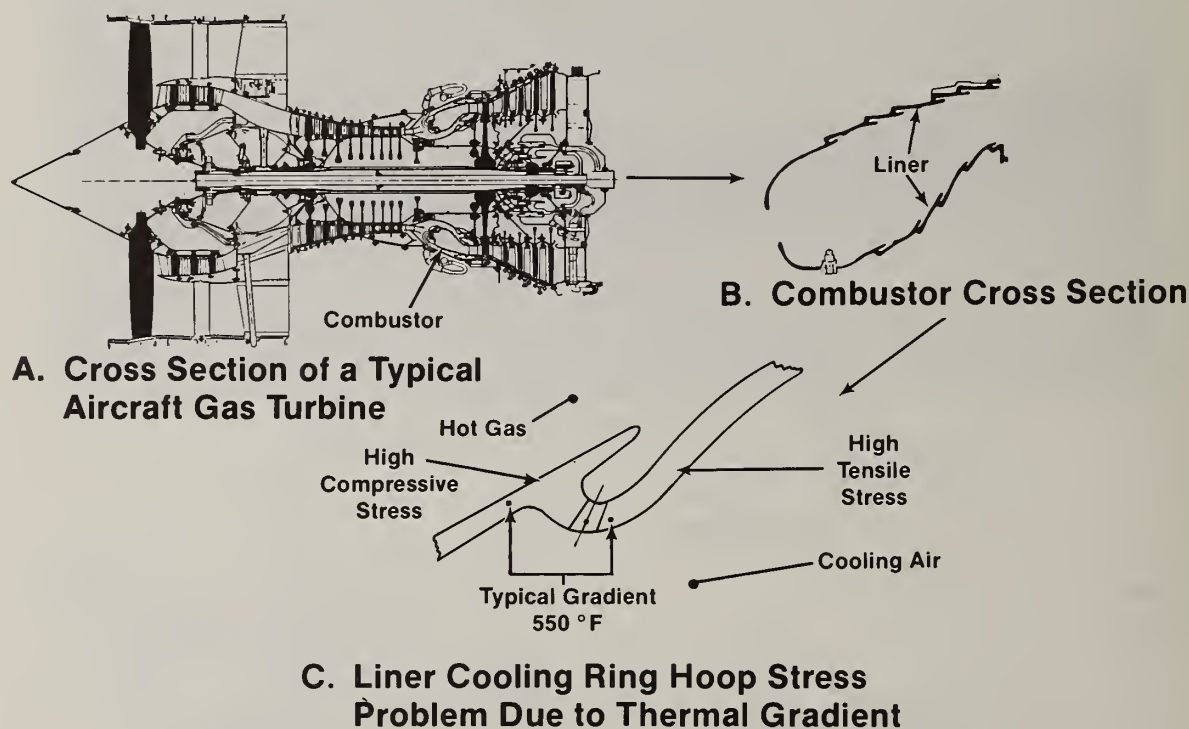


Figure 7 Combustor Liner Cooling Ring

Two concepts for manufacturing a bi-metal combustor liner by the RSPD process are shown in Figure 8. Method A is applicable to multiple material configurations, such as the Hastelloy X and A286 combination noted above. Hastelloy X sheet would be formed on a reusable mandrel and subsequently sprayed locally with a circumferential ring of A286. These local regions would then be machined to produce the cooling ring configurations. This concept is limited to materials available in sheet form. Method B illustrates a concept applicable to both multiple material and single material configurations. A reusable mandrel tool would be lined by a thin, low carbon steel sheet. The material(s) would then be sprayed to a near net shape contour. The thin low carbon steel sheet would permit removal of the sprayed liner from the reusable mandrel and could be subsequently leached or machined away. The liner form would then be final machined. Both manufacturing concepts appear viable and have been projected to be cost competitive in production with liners machined from forgings.

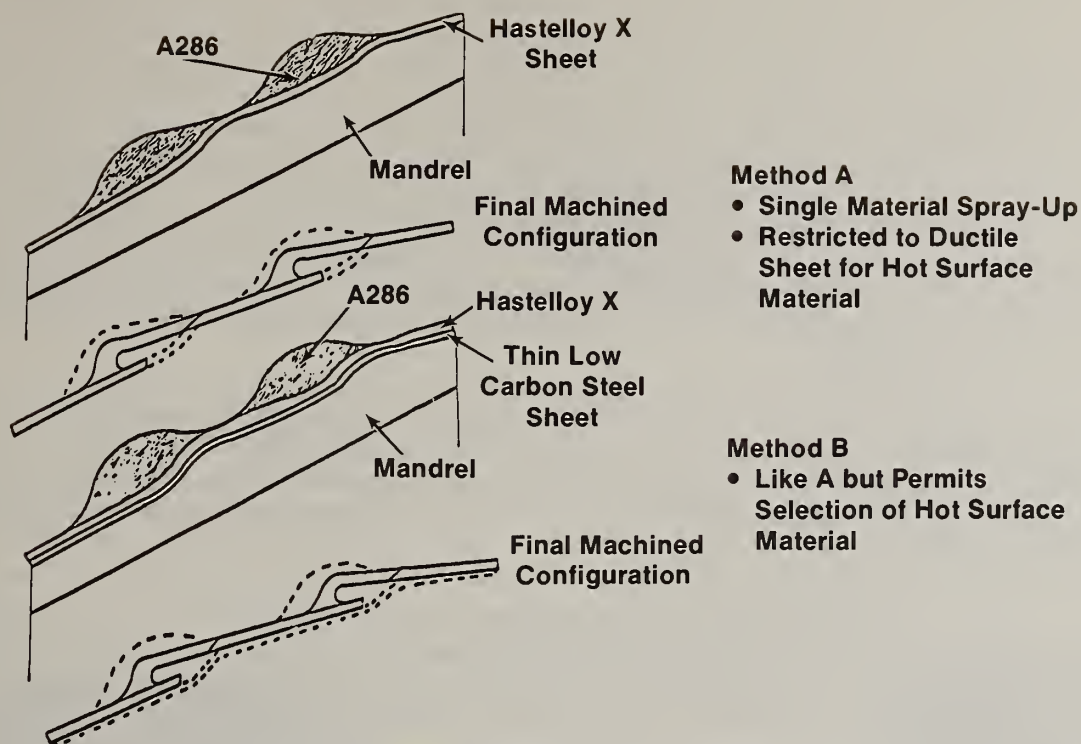


Figure 8 RSPD Combustor Manufacturing Methods

The same basic concept could be used for the fabrication of monolithic combustor liners by RSPD utilizing high temperature, high strength materials. Many high temperature superalloys were developed for turbine blade or vane applications and are available in cast form only. They are unsuitable for many structural and flow path configurations requiring thin cross-sections because of casting process limitations. The RSPD process permits fabrication of components with thin cross-sections from high strength superalloys. Benefits can be obtained from the use of available alloys, such as Rene'80, and from alloys specially formulated to take further advantage of the rapid solidification rates inherent in RSPD.

The relative tensile and stress rupture strengths of wrought Hastelloy X and RSPD Rene'80 are shown in Figure 9. Of particular interest is the excellent resistance to thermal fatigue demonstrated by high strength RSPD deposits reported elsewhere^(8, 11)

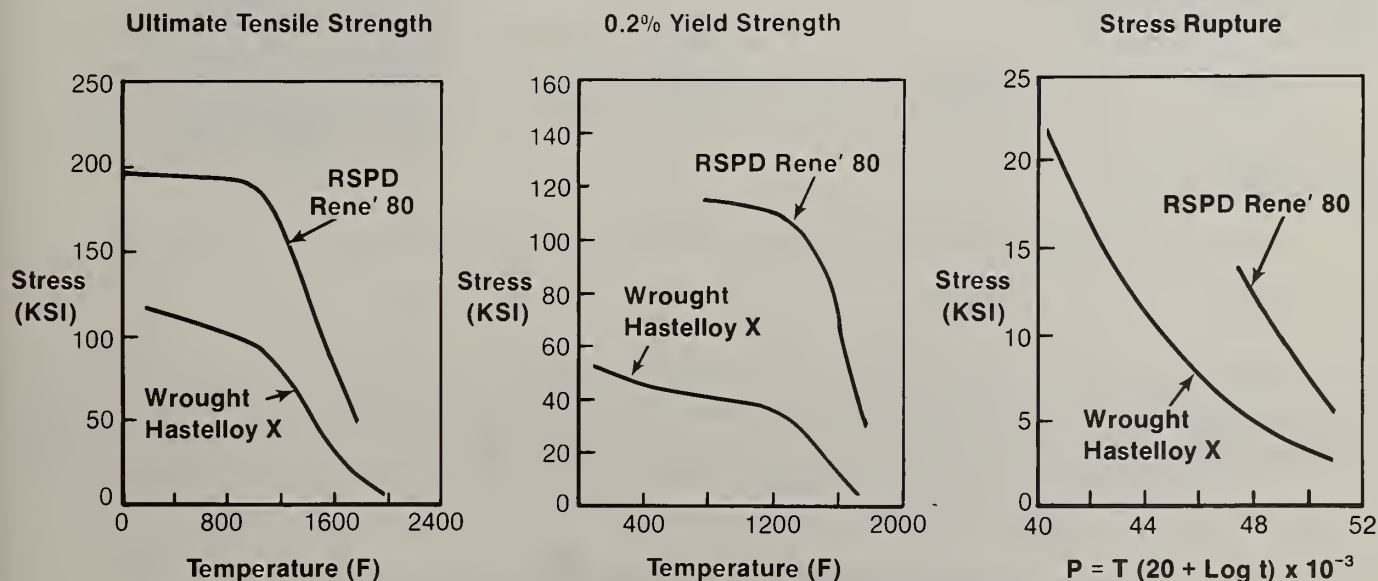


Figure 9 Comparison of RSPD Rene'80 and Wrought Hastelloy x Mechanical Properties

RSPD combustor liners offer benefits in terms of increased life and higher operating temperatures. The increases in life of either a graded material Hastelloy X/A286 (bi-metallic), monolithic MAR M509, or Rene'80 liner relative to a conventional Hastelloy X liner are shown in Figure 10. For this analysis, a relatively severe circumferential hot streak gradient and conventional material properties were assumed. If the circumferential gradient was eliminated, the life improvement obtained from the bi-metallic design could be approximately 2.5X that shown because the bi-metallic configuration significantly reduces the hoop stress resulting from axial temperature gradients. Thus, tailoring the material properties to the design problem can be a powerful design tool. Direct material substitutions such as RSPD MAR M509 or Rene'80 also indicate significant liner life improvements over wrought Hastelloy X. These improvements can result in significant savings over the life of the engine. In engine applications where Hastelloy X combustors are not life limited, improved material substitutions could permit an increase in allowable liner temperature for constant life, as illustrated in Figure 11. This translates directly into reductions in specific fuel consumption and increases in available power for the gas turbine.

In order to simulate the fabrication and thermal testing of an RSPD combustor configuration, a series of four rings about ten inches in diameter and three inches long were fabricated from Hastelloy X, Rene'80, MAR M509, and a bi-metal system, Hastelloy X/A-286. The metal rings were sprayed as cylinders on a steel ring mandrel mounted on a wheel. The sequence of manufacture is summarized in Figure 12 and the deposition results are given in Table 1.

Detailed measurements were made of the mandrels before and after deposition of the high strength alloys. These measurements indicated that, while the rings did not lose their concentricity during deposition, the inside diameter changed as a result of solidification and cooling stresses imposed by the deposits. The maximum dimensional change was about 0.1 inch reduction in diameter.

After spraying, the mandrels were dissolved using nitric acid and the deposits were heat treated at 2280°F for four hours. The Rene'80 ring was given the normal aging treatment (16 hrs. @ 1550°F), and then machined to final cross section shape. All the rings were single-point turned using a carbide bit. The machining characteristics of the Hastelloy X and the A286 were nearly indistinguishable and were similar to their wrought counterparts. The MAR M509 and the Rene'80 pieces, while requiring more energy, machined like wrought IN 718 alloy.

During the course of machining the bi-metal Hastelloy X-A286 ring, the A286 layer was inadvertently removed. This necessitated a respray to replace the A286 deposit. The Hastelloy X ring was machined to a new outside diameter configuration and A286 was deposited in a local area on the remachined ring corresponding to the position of the A286 section in the final part. This resprayed ring had less distortion as a result of deposition of the A286 than was experienced with the prior rings. The final machined cross section in Figure 12D shows the location of the Hastelloy X and A286 deposits in the simulated combustor ring.

<u>Mandrel</u>	<u>Material Deposited</u>	<u>Weight Gain lbs.</u>	<u>Efficiency (%)</u>	<u>Deposit Thickness (Inch)</u>
Steel	Rene'80	5.6	43	0.26
Steel	MAR R509	6.8	45	0.30
Steel	Hastelloy X	8.8	49	0.35
Steel	Hast X/A286	16.4	48	0.72*
Machined RSPD Hast X	A286	5.5	73	0.53

*(~0.36 mils Hast X + ~.36 mils A286)

Table 1 Results of RSPD Simulated Combustor Ring Spray Runs

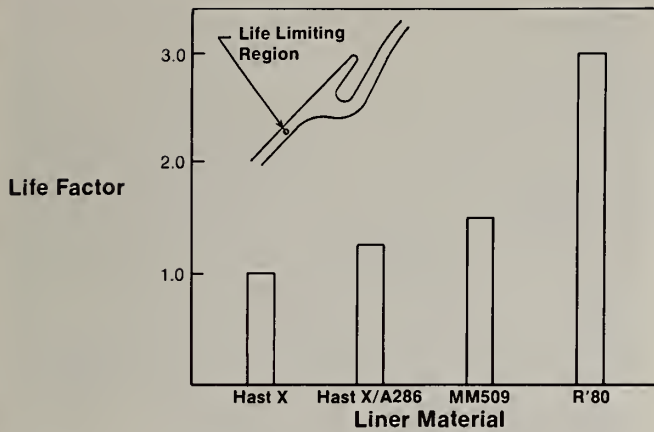


Figure 10 Relative Combustor Liner Life Comparison of Wrought Hast X to Hast X/A286, MM509, and Rene'80 Assuming a Circumferential Hot Streak

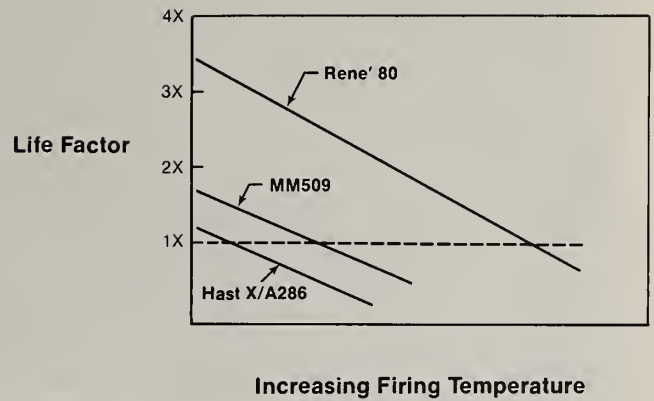


Figure 11 Increasing Allowable Firing Temperature by Substitution of Hastelloy X/A286, MM509 or Rene'80 for Hastelloy X in Combustor Liner

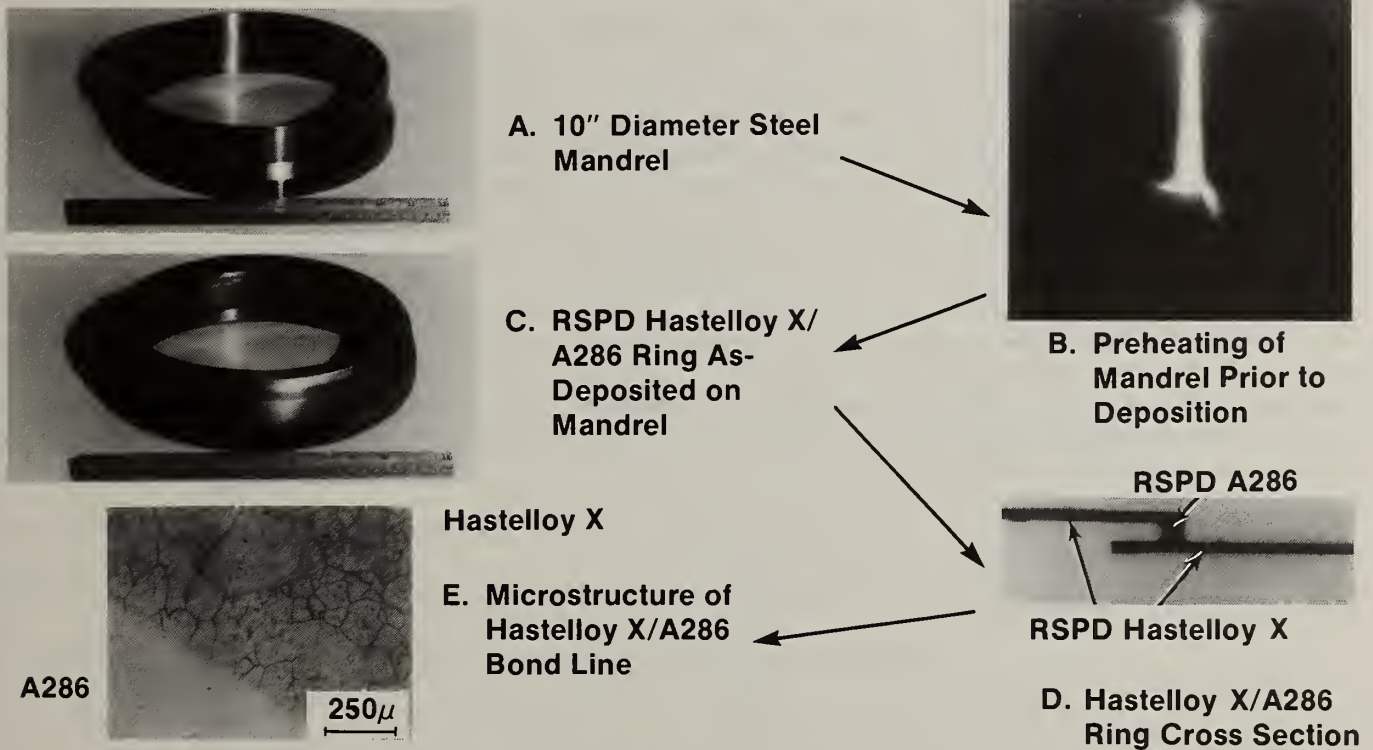
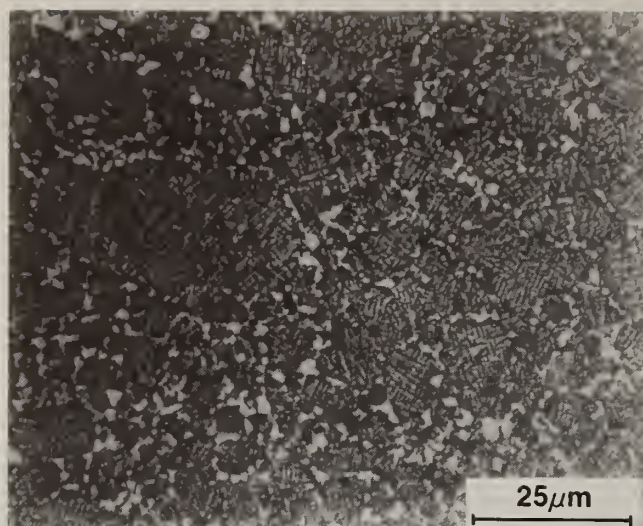
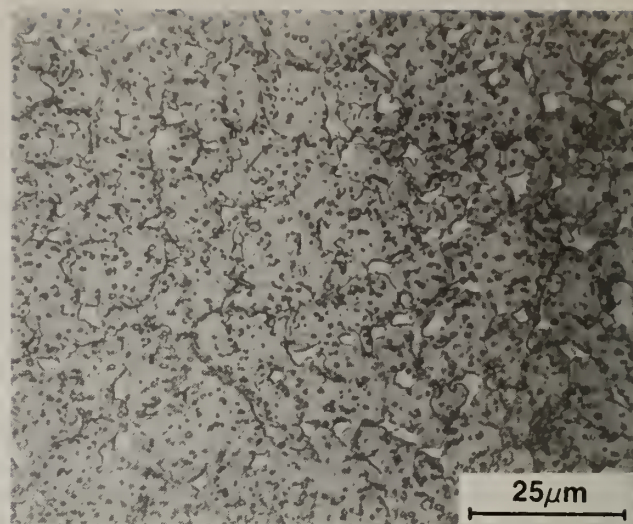


Figure 12 Fabrication of Bimetal Simulated Combustor Liner Cooling Ring by RSPD

The microstructures of the fully processed Rene'80 and MAR M509 deposits are shown in Figure 13, and the densities are given in Table 2. In all cases, the resultant deposit densities were near theoretical after heat treatment. Modest (1.0-1.5%) losses in chromium as a result of evaporation during spraying tend to increase the apparent density by 0.1 - 0.2%. The accuracy of the density measurement is about $\pm 0.2\%$.



A. RSPD Rene' 80



B. RSPD Mar M509

Figure 13 Micro Structure of RSPD Rene'80

To explore RSPD processing for modestly sized structures, a simulated combustor inner liner was fabricated from Hastelloy X. The overall dimensions of the completed ring were 7.5 inches inside diameter at the large end, 6.0 inches at the small end, and 4.2 inches in length. Normally, the ring is machined from a forging preform and is subsequently welded to the combustor dome at one end and to a flanged section at the other. A mandrel conforming to the inside contour of the liner was machined from low alloy steel and welded to a shaft. The cleaned mandrel was mounted in the low-pressure plasma system and preheated to approximately 1800°F using transferred arc. Reverse transferred arc cleaning was used to enhance bonding of the Hastelloy X to the substrate. The mandrel was sprayed with Hastelloy X and allowed to cool, then the surface was machined to form the core of the structure. Close-fitting low alloy steel bands were located at the cooling ring nuggets and a second layer of Hastelloy X was applied to the ring. After the second deposition, the part was machined to expose the steel bands and the inner and outer mandrels were leached out using nitric acid. The liner was then given a 2 hour 2150°F vacuum heat treatment, at which time one of the panel overhangs separated. Metallographic sections indicated that the separation resulted from porosity generated by low angle deposition at the bond during the second spray-on cycle. An overall view of the combustor ring is shown in Figure 14.

Deposit Material	Deposit Density g/cm ³	After Heat Treatment % of Conventional Alloy
Rene'80	8.15	99.8
MAR M509	8.80	99.3
Hastelloy X	8.25	100.4
Hastelloy X with A286 Nugget	8.21	99.9

Table 2 RSPD Simulated Combustor Rings - Heat Treated Densities

This paper has provided an overview of RSPD including a brief description of the process, some of the factors to be considered in design and fabrication, and examples of aircraft gas turbine engine components which could benefit from this approach. Work is continuing on RSPD plasma gun, process and materials development. Further advances in understanding in these areas will firmly establish the base technology required for component applications. The coupling of innovative design and manufacturing approaches utilizing the unique features of RSPD are expected to significantly impact the gas turbine engines of the 1980's and 1990's⁽¹²⁾.



Figure 14 Small RSPD Hastelloy X Combustor Liner

SUMMARY

Recent progress in the development of RSPD technology has demonstrated the feasibility of this process for the fabrication of aircraft gas turbine components. Small, thin wall parts have been made which exhibit attractive features such as improved formability and interior surface finish. Larger rings of difficult to process superalloys and combinations of material have been direct sprayed to near net shape. This flexible manufacturing process is emerging as a generic fabrication approach to be compared with casting, forging and conventional PM consolidation. The General Electric Company is pursuing this rapid solidification technology for potential application to a wide range of engine components.

ACKNOWLEDGEMENTS

Portions of this work were conducted as part of AFWAL Contract F33615-81-C-5156, U.S. Air Force Systems Command Materials Laboratory, under the direction of Dr. H.L. Gegel, and sponsored by the Defense Advanced Research Projects Agency. At DARPA the cognizant officer was Lt. Col. L.A. Jacobson. The authors appreciate the contributions of many other GE employees, particularly R.A. Amato, M.R. Jackson, L. Lievestro and J.R. Rairden.

REFERENCES

1. Gianinni, G., The Plasma Jet, Sci. Amer., August 1957.
2. The Plasma Spray Handbook, Metco Inc., Westbury, N.Y., 1963.
3. Mash, D.R. and Brown, I. MacP., Materials Engineering Quarterly, P. 18, February 1964.
4. Bittence, J.C., P. 108, Machine Design, April 1973.
5. Muehlberger, E., Proceedings 7th International Thermal Spray Conference, London, P. 245, 1973.
6. Okada, M. and Maruo, H., British Welding Journal 15 8, P., 321, 1968.
7. Rairden, J.R. and Jackson, M.R., Private Communication.
8. Jackson, M.R., Rairden, J.R., Smith, J.S., Smith, R.W., "Production Of Metallurgical Structures By Rapid Solidification Plasma Deposition", Jrnl. Of Metals, P. 23, November 1981.
9. Draskiewicz, T., Proceedings 9th International Thermal Spraying Conference, P. 244, 1981.
10. Smith, R.W., Rigney, D.V., Smith, J.S., and Rairden, J.R., "Plasma Deposition Effects On Structures and Properties of RSPD Alloys", this conference proceedings.
11. Jackson, M.R., Smashey, R.W., and Peterson, L.G., "The Mechanical Behavior of RSPD Materials", this conference proceedings.
12. Sprague, R.A., "Material and Process Impact On Aircraft Engine Designs of the 1990's", ASME Publication 82-GT-278, P. 7-8.

RECENT APPLICATIONS OF ULTRA RAPID SOLIDIFICATION
TECHNOLOGY (URST) MICROCRYSTALLINE AND AMORPHOUS POWDER MATERIALS

Julian H. Kushnick and Dulari L. Sawhney

Allied Corporation, P. O. Box 1021R, Morristown, New Jersey 07960

ABSTRACT

Amorphous Ni-Mo-B based alloy powder materials are presently being manufactured by Ultra Rapid Solidification Technology (URST*) Cast/Quenched at $\sim 10^6$ °C/sec. for a wide variety of commercial applications. Some of these powders are consolidated by hot isostatic pressing into microcrystalline solid blanks for previously described copper alloy extrusion dies, cutting tools, and aluminum die casting molds. These applications will be briefly updated. Newer applications are focused on the use of amorphous powder materials in metal-bonded abrasive wheels, corrosion and wear resistant hardfacing and as an alloy with tungsten for consolidation into experimental high specific gravity kinetic energy armor penetrators. In each instance, the amorphous characteristics of the URST powders improve performance.

Amorphous consolidation of METGLAS** alloy magnetic powders and ribbon is being developed because of the magnetic core properties obtained at high packing factors. Most recently, ultra rapid solidification is being investigated for the manufacture of aluminum microcrystalline alloys suitable for consolidation to high specific strength aircraft components. High temperature resistant alloy additives have been incorporated in these systems to improve the structure produced after the necessary thermal consolidation processing.

INTRODUCTION

As many of you are aware, Allied Corporation has been a world leader in Rapid Solidification Technology for more than 12 years. We have researched, developed, and commercialized unique Metglas amorphous metal alloy products including low loss transformer core materials, magnetic shielding and ductile brazing foils for gas turbine fabrication. All of these Metglas amorphous products are made by the rapid solidification of molten metal alloys (Figure 1) into ductile ribbons or filaments at cooling rates $\geq 1,000,000$ °C. Quenched at these rates, these special molten metal alloys do not tend to segregate or crystallize and remain amorphous---a frozen liquid or solid glass.

Technology to produce vast quantities of these amorphous materials has been developed with the assistance of the Electric Power Research Institute (EPRI) of Palo Alto, Ca. An Allied Corporation/EPRI pilot plant has been constructed which can manufacture Metglas transformer core materials (2 in., 4 in. or 7 in. wide ribbon) at rates of 3,000 ft./minute for hours while continuously winding the product. These Metglas core materials have been supplied to major transformer companies who are developing technology for the cost effective production of low core loss utility distribution and power transformers². Continuous casting technology for the manufacture of URST materials is perhaps best exemplified by the facility recently put on line at Metglas Products, Allied Technologies Company, in Parsippany, New Jersey. In this facility (Fig. 2) raw materials are melted in an induction melting furnace, the molten metal is transferred to an accumulator/feeder from which it is control fed through a casting head that is capable of depositing a 4 inch wide stream of molten metal in contact with a rotating mold. The molten stream is solidified within a millisecond to a ribbon approximately 0.0015 in. thick. The dimensions of the ribbon produced are monitored and adjusted by a computerized feedback system. There is a thread-up and winding machine to continuously wind the product at the end of the production machine. This system is designed to manufacture up to 25,000 tons/year of Metglas alloy amorphous transformer core materials³.

*Trademark of Allied Corporation

**Registered Trademark of Allied Corp.

FIGURE 1

THE RAW MATERIALS

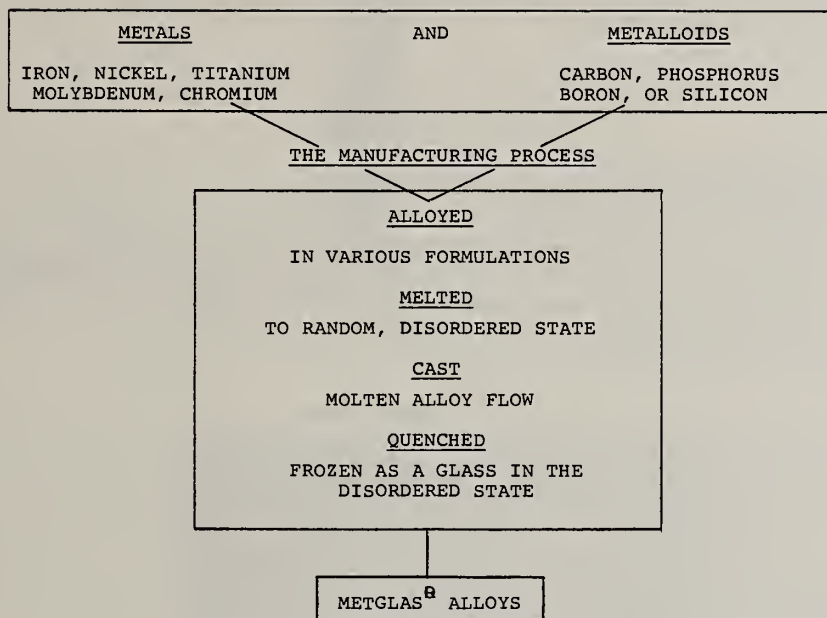
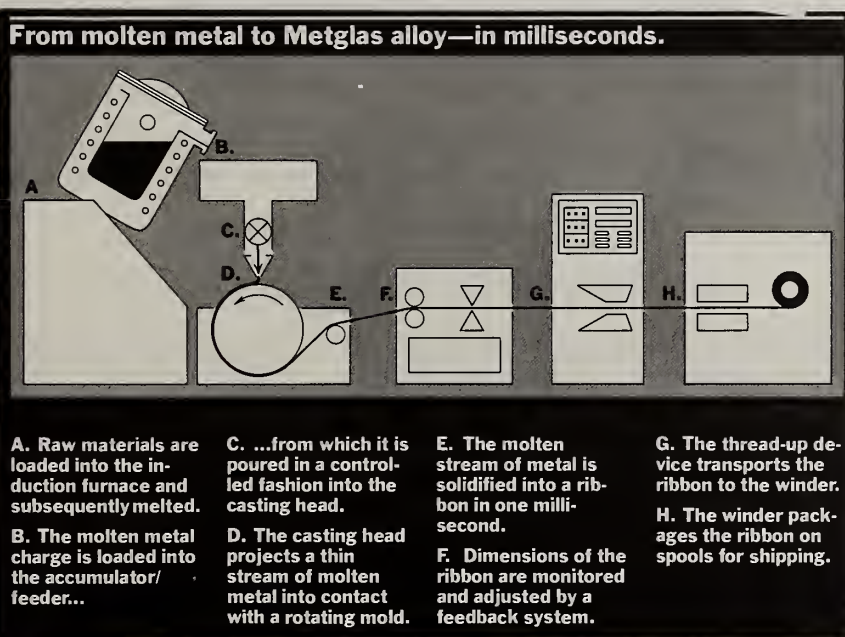


FIG. 2



The Consolidated Metal Products (CMP) group has adapted this versatile Metglas technology for a different application---powder metallurgy via ultra rapid solidification technology. We have developed low cost production technology to pulverize the URST materials so that we can market them as amorphous powders (Fig. 3)⁴ or consolidate them into new and useful bulk forms and shapes. URST powders are unique because each particle has identical composition and is amorphous. In the powder products of most so called rapid solidification processes (i.e. gas or centrifugal atomization) small particles are sometimes amorphous, medium size microcrystalline and large particles are usually segregated and dendritic. Each URST particle is homogeneous regardless of size. The CMP powders and subsequent consolidated products are marketed under the DEVITRIUM trademark⁵.

COPPER EXTRUSION DIES

In a typical bulk shape application, URST powder produced of a Ni-Fe-Mo-B alloy (DEVITRIUM*** alloy 7025) is consolidated by hot isostatic pressing (HIPping) at 1100°C and 12,500 psi pressure into microcrystalline solid bar for copper alloy extrusion dies⁶. During the HIP cycle, the powder is transformed from the amorphous to the microcrystalline state. Submicron-sized boride particles form at the grain triple points⁷ (as illustrated by the schematic of grain structure (Fig. 4). Conventional, slower cooled alloys of similar composition would consolidate as crystals of varying large grain sizes surrounded by a eutectic boride network, making the material too brittle for most engineering uses.

Devitrium alloy 7025 extrusion dies (Fig. 5) are used in the primary reduction of hot (850°C) billets of copper and brass alloys to redraw rod and shapes. The principle advantage of these dies versus dies of steel or high cobalt alloys has been their long service life (up to 300 pushes have been reported by a major copper producer) and the good surface finish of the extrudate. This reduces grinding and finishing costs prior to subsequent redraw operations. Dies of DEVITRIUM alloy 7025 have been supplied to more than six extrusion firms and are utilized when long run campaigns of extruded product are required. Unfortunately, because of the present recession this industry has not had too many opportunities to use their DEVITRIUM alloy 7025 dies in recent times.

CUTTING TOOLS

Another application that has been previously reported is cutting tools⁸. DEVITRIUM Alloy 3065, a microcrystalline Ni-Mo-B composition in its consolidated form (Figure 6) is being evaluated for the production of premium wear and chip resistant cutting tools and inserts. Cutting performance is retained at high rates of speed (up to 500 surface feet per minute) with tool life in many applications equivalent to uncoated tungsten carbide materials.

DEVITRIUM Alloy 3065 end mills produced by three major tool companies are scheduled for extensive trials with aluminum and titanium. Hobbs have been fabricated with DEVITRIUM cutting surfaces for high speed gear production.

INSERT FOR ALUMINUM DIE CASTING MOLDS

Die casting molds for Aluminum are usually machined of alloy H-13, a standard high performance steel that has generally good heat resistance. The life of an H-13 mold in a critical gate area where the hot die casting alloy enters the mold is approximately 75,000-125,000 cycles or "shots". Die casting molds typically fail by erosion and thermal fatigue. Cyclic thermal stresses cause heat checking cracks and fissures to occur in the mold surface. The checking cracks gradually worsen until they prevent good release of the molded part and cause intricate areas of the mold to break. Consolidated DEVITRIUM Alloy 7025 (Figure 6) inserts used in die casting molds have demonstrated service lives of over 250,000 shots and are still in production⁹. The improved resistance to thermal fatigue or heat checking of Consolidated DEVITRIUM Alloy 7025 is attributed to the following:

1. Consolidated DEVITRIUM Alloy 7025 is structurally homogeneous and isotropic. The microcrystals are not organized into large crystalline matrices with anisotropic characteristics that can lead to varying stresses. With uniform distribution of thermal stresses, cracks are less likely to occur during thermal expansion of the insert surface.

***Trademark of Allied Corporation

FIG. 3

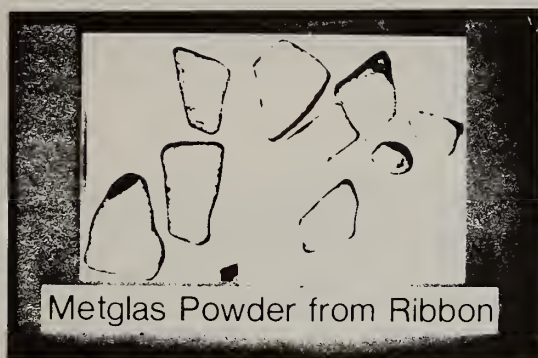


FIG. 4

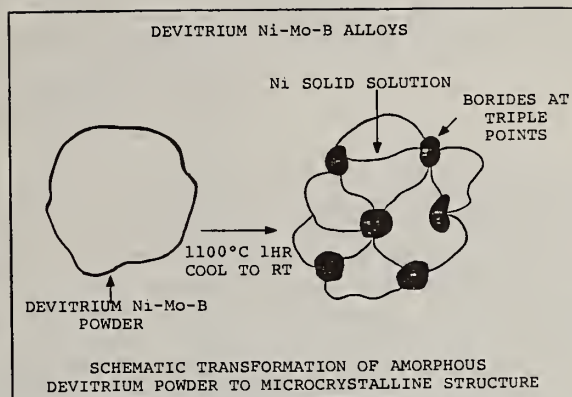


FIG. 5



FIGURE 6

Mechanical Properties of Consolidated DEVITRIUM™ ALLOYS

	<u>DVTM Alloy 7025</u>	<u>DVTM Alloy 3065</u>
	$\text{Ni}_{53}\text{Mo}_{36}\text{Fe}_9\text{B}_2$	$\text{Ni}_{54}\text{Mo}_{44}\text{B}_2$
DENSITY (G/CM ³)	9.06	9.33
HARDNESS (HRC)	47-50	60-62
TENSILE STRENGTH (KSI)	220-220	
(0.2%) YIELD STRENGTH (KSI)	175-185	
ELONGATION (%)	2-5	1%
IMPACT STRENGTH (FT-LBS.) (UNNOTCHED CHARPY)	40-50	2-5

2. DEVITRIUM Alloy 7025 as a consolidated material is a tough, elastic, high strength composition that is less likely to be torn apart by the thermal strains encountered. These properties are maintained at elevated temperatures.

3. The thermal strain in the mold material during the die casting operation is a product of the temperature difference between the bulk of the mold substrate and its surface and the coefficient of thermal expansion. The thermal expansion of DEVITRIUM Alloy 7025 is approximately 1/3 lower than that of H-13 steel. This minimizes the cyclic strain and fatigue.

METAL-BONDED ABRASIVE WHEELS

DEVITRIUM Alloy 3065 and 7025 are entering use as metal binders for diamond and other abrasive materials in oil well and mine drilling bits, masonry saws, grinding wheels, etc. Alloy 3065 and 7025 powders are amorphous and contain no crystalline structure. This is readily accomplished by ultra rapid solidification technology. Typically the DEVITRIUM powders are mixed with the abrasive material, (i.e. diamonds or silicon carbide), and are then hot pressed in graphite molds. Consolidation at 950°C and 5,000 or 7,500 psi results in about 97% of theoretical density. This temperature is maintained for relatively short periods of time to avoid degradation of the industrial diamonds contained in the matrix. During the hot pressing operation the internal structure of these powders changes from amorphous to microcrystalline at temperatures about 550°C.

Atomic movement and rearrangement occurs during the crystallization phase. There is reason to speculate that this atomic movement may generate clean surfaces and enhance the adhesion to the abrasive powder mixture. During the hot press consolidation there is rapid press ram movement as the amorphous materials consolidate and become higher density microcrystalline structures. The finished pressed matrix product is hard and wear resistant with substantial retention of hardness at elevated temperatures. This helps to increase the cutting action of the products. The pressed matrix microcrystalline materials have a substantially higher softening temperature than the original amorphous alloys. This increases the feed rates and temperatures at which the grinding tool matrix can be utilized.

An offshoot of the metal binder application has been the use of DEVITRIUM Alloys 7025 and 3065 as readily prepared hot pressed molds for the fabrication of other abrasive matrix materials. Hot pressed consolidated DEVITRIUM molds do not wear rapidly and provide a high yield of pressed parts. The finish of the pressed parts is significantly better than that obtained from graphite and other conventional die materials, probably because of the resistance of DEVITRIUM Alloys to wear and galling.

CORROSION RESISTANT PLASMA SPRAY HARDFACING

Amorphous DEVITRIUM Alloys have been developed for a wide range of corrosion resistant arc plasma hardface coatings. These coatings can be applied by a wide range of plasma spray equipment (Fig. 7) to achieve uniformly dense, well adhered amorphous coatings of unusual hardness. The data (Fig. 8) shows that the corrosion, wear resistance and nongalling characteristics of DEVITRIUM coatings are good. Ball and Cup forming tests and other bending tests indicate that the ductility of the amorphous deposited DEVITRIUM Alloy 7025 plasma coating is substantially better than that of crystalline analog materials of Ni-Mo-B alloy systems. The DEVITRIUM coatings do not tend to crack or flake from the substrate when they are deformed.

Amorphous DEVITRIUM hardfacing powders have also been used in plasma transferred arc (PTA) applied coatings and have demonstrated excellent wear resistance. Good coatings without cracks are routinely achieved. Several extruder screws and large gate valves PTA coated with DEVITRIUM Alloy 7025 are undergoing performance trials. The nongalling characteristics of the DEVITRIUM Alloys is of particular interest in the gate valve application.

KINETIC ENERGY ARMOR PENETRATORS

A program for the development of high density kinetic energy armor penetrator materials is underway with tungsten-nickel-iron-boron alloys and ultra rapid solidification technology. CMP has produced URST (Figure 9) materials containing tungsten in the range of 40-65 weight percent. Alloys containing 40 weight percent of tungsten have been cast completely amorphous. This demonstrates the beneficial effect of URST in extending the solid solubility limits by

FIGURE 7

DEVITRIUM™ Alloy 7025 Plasma Spray Powder Coating

Thickness	5-30 mils
Density % of Theoretical	98%
Microhardness VHN ₁₀₀	990
Bond Strength	12,000 psi
Percent Amorphous	80%

Substraight: Mild steel, grit blasted, degreased
 Plasma Spray Gun: Baystate PG 100; Metco 3M,
 7M; Plasmadyne SG 100
 Powder Size: Minus 80 mesh.

FIGURE 8

WEAR AND CORROSION RESISTANCE OF ARC PLASMA SPRAY COATINGS

Coating Alloys Nominal Comp. W%	Corrosion Rate of Arc Plasma Sprayed Coatings @50°C -mils/yr.- <u>1%HCl 10%H₂SO₄</u>		Selfmated Galling Threshold Stress 10 ³ PSI	Abrasive Wear Vol. Loss ASTM G-65 (sand/rubber wheel) mm ³	Abrasive Wear ASTM D2714-68 (Falex/block & ring) Vol. Loss of Sample mm ³ (Block)
DVIM 7025 Ni ₅₃ Mo ₃₆ Fe ₉ B ₂	13		20	7-10	0.05
DVIM 3065 Ni ₅₄ Mo ₄₄ B ₂	4	20	10-30	9-10	0.045
DVIM 7060 Ni ₅₄ Mo ₃₆ Cr ₈ B ₂	6	8		7	
Stellite 6B* Co ₆₁ Cr ₂₈ W ₄ C _{1.1}			50-60	9	0.03
Metco 501+ Ni ₆₁ Mo ₃₀ Cr ₁₂ Si _{2.75} B _{2.5} C _{.75}				8	0.08
Triballoy T-700* Ni ₆₁ Mo ₃₂ Cr ₁₆ Si _{3.4} Co-Fe<3.0;C<.08			50-60	9	
Hastelloy C* Ni ₆₁ Cr ₁₇ Mo ₁₇ Fe ₆ W ₅		8			

* T. M. of Cabot Corp.

+ T. M. of METCO, INC.

FIGURE 9

MECHANICAL PROPERTIES OF CONSOLIDATED URST TUNGSTEN ALLOYS

	40 Wt. % <u>Tungsten</u>	65 Wt. % <u>Tungsten</u>
DENSITY (G/CM ³)	10.75	13.1
HARDNESS (HRC)	35	40
TENSILE STRENGTH (KSI)	136	162
(0.2%) YIELD STRENGTH (KSI)	105	142
(0.2%) YIELD STRENGTH (KSI) (IN COMPRESSION)	97.5	150
TRANSVERSE RUPTURE STRENGTH (KSI)	285.5	310
IMPACT STRENGTH (FT-LBS.) (UNNOTCHED CHARPY)	25	10

OPTICAL MICROSTRUCTURE OF CONSOLIDATED URST TUNGSTEN ALLOYS



40% W



65% W

—|—|
20 μ M

comparison with the equilibrium solid solubility of ~ 27 weight percent of tungsten in nickel. Ultra rapid solidification of alloys with 65 weight percent tungsten produced a composite material, comprised of a uniform dispersion of fine tungsten particles (5-7 micron) in an essentially amorphous matrix.

Isothermal and isochronal studies of the as cast tungsten alloys, reveal that thermal treatment precipitates extremely fine tungsten particles in the supersaturated Ni-Fe-W solid solution matrix. The characteristic feature of both the alloys (i.e. with 40 percent tungsten and 65 percent tungsten) is a very stable microstructure. No substantial grain growth is observed even with long time exposure at temperatures as high as 1200°C. Figure 9 illustrates the pertinent microstructural features of URST tungsten alloys and their physical properties. In addition to the fine and thermally stable microstructure, URST prevents the formation of any brittle intermetallic phases, normally associated with either Ni-W or Fe-W binary systems. Alloys with densities of 11-13.5 has been produced via our process. Work to produce yet higher densities is in progress.

METGLAS MAGNETIC CORE MATERIALS

Amorphous consolidation of METGLAS magnetic powders is being developed so as to preserve the unique magnetic properties of the parent Metglas materials in bulk shapes. Amorphous toroidal cores have been consolidated from various Metglas magnetic materials at bulk densities ranging from 85% to 95% of theoretical. These cores have been annealed to provide potential magnetic core materials for such applications as regulator cores in switch-mode power supplies and stators for small high speed actuator motors.

Technology is also being developed to consolidate layers of thin METGLAS magnetic core ribbon into thick strip bars while retaining the Metglas amorphous structure. METGLAS alloy POWERCORE* strip bars with good magnetic properties would facilitate the construction of large transformers and motors. Power transformers typically contain from 12,000 to 300,000 lbs. of magnetic core material. Fabrication of stacked cores of the size required to provide that much magnetic flux path sometimes involves stacking the core steel as high as 6 to 8 feet. This would be very difficult with Metglas ribbon approximately 0.0015 in. thick. CMP has experimentally produced POWERCORE strip bars 0.070 in. thick with packing factors as high as 95% that could be used to fabricate large cores. We are presently developing process technology to produce POWERCORE strip in large quantities with consistent quality.

ALUMINUM MICROCRYSTALLINE ALLOYS

Within the past several years ultra rapid solidification technology has been used for the manufacture of aluminum based microcrystalline alloys cast at exceptionally high quench rates, sometimes in the order of 10^8 °C per second. The principle advantage of these high quench/casting rates is that the crystalline structure is so fine that it cannot be discerned by ordinary light microscopic techniques, (generally regarded as type A structure).⁹ The exceptional homogeneity of these microcrystalline materials is retained (with some size growth) through consolidation processes (typically by vacuum hot pressing and extrusion) into high specific strength and/or high temperature resistant fabricated aircraft components. As an integral part of these programs alloy additives are incorporated into these aluminum systems to improve their structure and prevent the formation of precipitate particle free zones during the thermal processing for consolidation and extrusion.

High specific strength alloys have been developed with greater quantities of low density alloy elements incorporated than are presently feasible with ingot metallurgy. These alloy systems can provide a cumulative weight savings of approximately 10-15% in major aircraft components. In a similar manner, high temperature resistant alloys have been developed that have maintained high use strength and exceptionally fine microcrystalline structure after prolonged thermal exposure at temperatures in excess of 450°C. These alloys could also result in significant weight savings in aircraft fabrication by reduction of Aluminum part size or displacement steel components.

We believe it feasible to manufacture ultra rapid solidification microcrystalline

*Trademark of Allied Corp.

aluminum alloys of both the high specific strength and high temperature resistant systems through integrated production casting systems similar to those capable of going from alloy raw materials to powder in line described earlier.

SUMMARY

Allied Corporation has developed a proprietary ultra rapid solidification technology process to manufacture:

1. Materials that are uniform and homogeneous in alloy composition and physical structure---amorphous or microcrystalline as required.
2. The process can be operated at cast/quench rates of 10^6 to 10^8 °C/second.
3. The URST process combined with pulverization technology provides us with high yields of products in terms of alloy composition desired powder and particle size.
4. The process is inherently rapid and low in cost to operate.
5. The process is scalable and consistent as has been demonstrated by production of our METGLAS amorphous metal alloys.

REFERENCES

- [1] S. Fass and J. Dickson, in "A Breakthrough in Powder Metallurgy at Allied Chemical Corporation", Workshop on Critical Materials, U. S. Dept. of Commerce, NBS, Gaithersburg, Md., Feb., 1981.
- [2] "Amorphous Metals: Cutting Losses in the Core" EPRI Journal, Vol 7, No. 1, Jan/Feb, 1982.
- [3] "What if?" Allied Corp., Metglas Products, Bulletin SM, Jan, 1982.
- [4] U. S. Patent 4,353,737 Method of Making Metallic Glass Powder From Glassy Alloy.
- [5] "Consolidated Metal Products - Introducing a Breakthrough in Powder Metallurgy" - Allied Corp., Nov., 1980.
- [6] "New Kind of Alloy Tested in Dies, Cutting Tools" American Metal Market/Metal Working News, May 18, 1980.
- [7] U. S. Patent 4,290,808; Metallic Glass Powders From Glassy Alloys.
- [8] "New P/M Material Extends Die Casting Die Life" Precision Metal, Vol. 40, No. 3, March, 1982.
- [9] H. Jones, Materials Science & Eng., Vol. 5, 1969, p. 91.

SHOCK COMPACTION OF FERROUS ALLOY POWDERS

T. J. Ahrens, Dan Koska, P. Kasiraj and T. Vreeland Jr.

California Institute of Technology
Pasadena, CA 91125

A. W. Hare

Northwest Technical Industries, Inc.
Sequim, WA 98382

F. D. Lemkey and E. R. Thompson

United Technologies Research Center
East Hartford, CT 06108

ABSTRACT

Experiments on the shock compaction of ferrous alloy powders have been performed using a 20 mm propellant gun system and explosive charge techniques. Spherical AISI 9310 powders were produced by various rapid solidification rate processes including inert gas, soluble gas, and centrifugal atomization. The powders were inspected microstructurally in TEM and by X-ray diffraction and found to be remarkably similar.

Propellant gun, dynamic compaction of 40% initial porosity, 100 μ m diameter powdered 9310 alloy produced consolidated specimens with ultimate tensile strengths of 0.7 to 1.3 GPa. Impact with stainless steel projectiles launched at speeds from 1 to 1.6 km/sec caused initial shock pressures in the compacted powders of 7 to 16 GPa and final shock pressures of from 19 to 34 GPa. Recovered samples demonstrated diamond pyramid hardnesses of 370 to 581 kg/mm² over this pressure range. Metallographic observations showed that the powder particles in a 2 mm thick specimen are deformed by ~50 to 200% along the direction of shock compression. Individual grains displayed evidence of inhomogeneous thermal deposition. Thermodynamic analyses indicated that for an initial distension of 1.7 for iron, a portion of the sample will have been melted upon shock recovery from direct shocks of from 7 to 16 GPa.

Flake powders from Markomet (Fe-1.35C-4.25Cr-4.5Mo-4.0V-5.75W-0.65B) and spherical 9310 steel powders were explosively compacted within the same evacuated thin wall cylindrical container. Although complete consolidation was not achieved using an ammonium nitrate and fuel oil charge ($\rho = 0.443$ gm/cm³), improved densification was achieved starting with flake rather than spherical powder geometry.

Introduction

In order to preserve the nonequilibrium nature of rapidly solidified powders and avoid extensive interactions between powder mixtures, increasing attention is being directed to the examination of shock consolidation techniques to form bulk structures. Exploratory shock compression and recovery studies [1-6] have demonstrated irreversible compaction for shock waves propagating through porous materials with amplitudes in the range of 10-20 GPa and durations of 0.1-1 sec (i.e. energy densities of ~10-100 KJ/cm³). Microscopic examination of the irreversibly compacted, initially fine-grained samples demonstrate that the irreversible work input to the porous material is nonuniformly deposited. What appears to be happening is that shock induced heating takes place along particle surfaces

presumably via strong surface frictional and deformational processes. After the shock has passed and the material is released to zero pressure, the thin molten surface layer is rapidly quenched via conduction from within the particle interiors. Depending on the width of the melted zone, cooling rates from 10^5 - 10^{10} K/sec are inferred for melt layer thicknesses of 100 to $0.2\mu\text{m}$ in metals [7]. In this way, the nonequilibrium nature of the rapidly solidified powders may be preserved.

The overall objective of this study is to exploit rapid solidification processing (RSP) technology for the purpose of fabricating an advanced helicopter gear with improved high temperature ($\sim 600^\circ\text{F}$) capability. It is believed that RSP technology applied to this situation offers the best prospects for success for two main reasons. First, rapid solidification of powders is a proven method for obtaining ultra-refined microstructures, with reduced microsegregation and extensive supersaturation of compound-forming elements. This is a prerequisite for achieving high strength without impairing fatigue and fracture toughness properties. Second, dynamic compaction is the only method currently available, albeit incompletely developed, for making fully consolidated parts from powder without incurring unacceptable coarsening of the microstructures and chemical reactions between prealloyed powders of substantially different compositions.

Experimental Program

The dynamic compaction program is divided into two areas, (1) propellant gun and (2) explosive charge techniques. Initial results on the former have been encouraging and will be published later this year [8,9]. The ferrous alloy powders compacted in this program were produced by various rapid solidification techniques. Spherical AISI 9310 (Fe-0.10C-0.65Mn-0.25Si-1.39Cr-0.13Mo-3.2Ni) powders were atomized by inert gas, soluble gas, and centrifugal processes. The powders were inspected microstructurally by TEM and X-ray diffraction and found to be remarkably similar. All size distributions contained the assumed high temperature δ -Fe phase as the major constituent, with minor amounts of f.c.c. γ -Fe and carbide. The cubic lattice parameters for the delta and gamma phases were calculated as 2.86_4 and 3.58_1\AA respectively. Actual freezing rates of NiAl-Cr eutectic powders produced by the same RSP techniques were used to calibrate liquid/solid interface velocities as is discussed elsewhere in these proceedings [10]. These experiments showed the expected dependence of α -Cr interrod spacing on powder size, Table I, indicating that coupled eutectic growth occurs to $\sim 700\text{ mm sec}^{-1}$. The average freezing velocities of argon atomized powder was observed to be equivalent to centrifugally atomized powder for equal particle size. Flake powder supplied by Marko Materials of MarkometTM 3.11 (Fe-1.35C-4.25Cr-4.5Mo-4.0V-5.75W-0.65B) was prepared from melt spun ribbon which was subsequently ball milled to form discrete flake particles.

Table I. Cr Diam. (\AA) Measurements, λ , and v Calculations, from RSP NiAl-Cr Eutectic Powders

Powder source	70-300 μm	44-70 μm	37-44 μm	<37 μm
RSR He atomized	$d = 263\text{-}1052\text{ \AA}$ range $d = 631\text{ \AA}$ $\lambda = 991\text{ \AA}$ $v \sim 0.9\text{ mm sec}^{-1}$	$d = 263\text{-}789$ $d = 526$ $\lambda = 825$ $v \sim 1.2$	$d = 105\text{-}631$ $d = 421$ $\lambda = 660$ $v \sim 1.9$	$d = 105\text{-}421$ $d = 263$ $\lambda = 412$ $v \sim 4.8$
HMI Soluble gas atomized	789-1474 $d = 947$ $\lambda = 1486$ $v \sim 0.4$	421-789 $d = 684$ $\lambda = 1074$ $v \sim 0.9$	421-789 $d = 526$ $\lambda = 826$ $v \sim 1.2$	105-263 $d = 368$ $\lambda = 577$ $v \sim 2.7$
AMDRY Argon atomized	492-1312 $d = 820$ $\lambda = 1287$ $v \sim 0.5$	263-630 $d = 526$ $\lambda = 825$ $v \sim 1.2$	420-789 $d = 420$ $\lambda = 660$ $v \sim 1.9$	<105-421 $d = 263$ $\lambda = 412$ $v \sim 4.8$

— Avg. values

A Caltech 20 mm propellant gun was used to impact a 2.5 to 5 mm thick stainless steel projectile at speeds of 0.96 to 1.8 Km/sec to compact AISI 9310 steel powder. All specimens were initially pressed to a distention of 1.7 or a volume some 1.7 times that of its crystal volume. Measured densities of the compacted samples were in the range of $7.84 \pm 0.15 \text{ Mg/m}^3$ which is close to the theoretical value of 7.86 Mg/m^3 . The transmission electron microstructure of a completely compacted specimen after ion milling is shown in Fig. 1. Dark field (g=110) transmission microscopy indicated approximately tenfold delta iron grain size reduction to $\sim 1/2 \mu\text{m}$.

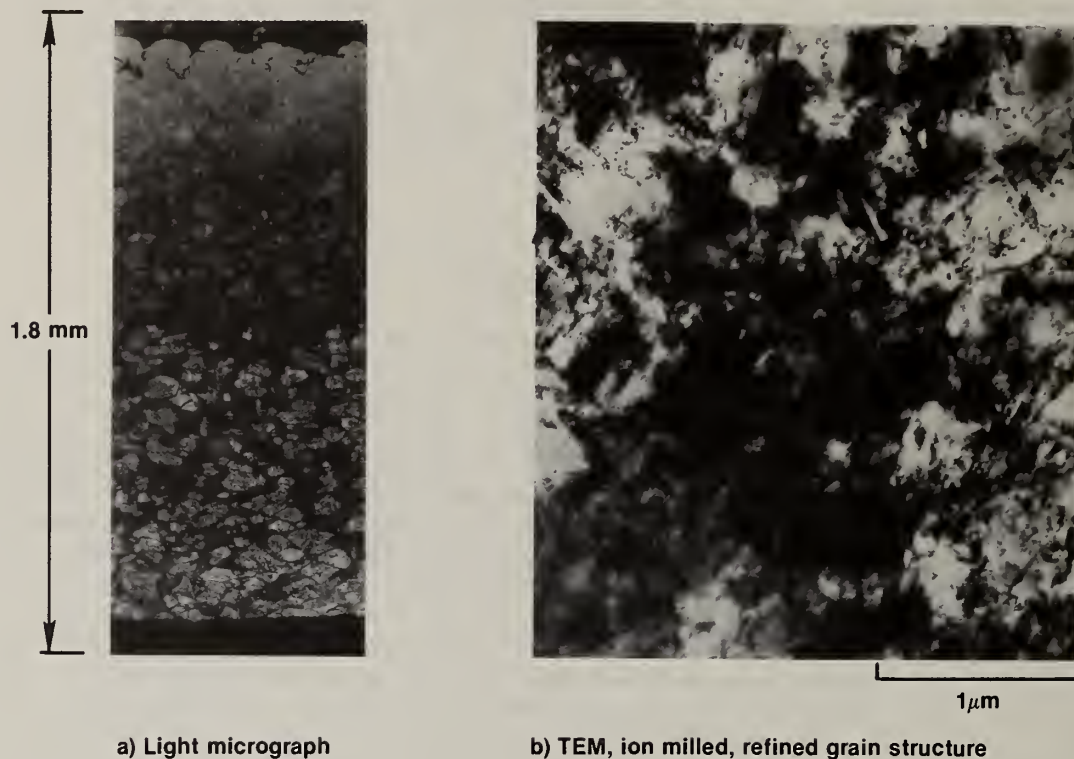


Figure 1. AISI 9310 (-200, +325 mesh) powder shocked to initial and final shock pressures of 18 and 37 GPa

Some seven tensile test specimens, cut from recovered pellets oriented parallel to the shock front were pulled to fracture. The ultimate tensile strength (Fig. 2) was observed to increase from 0.8-1.3 GPa (120-190 ksi) as the projectile velocity increased from 1 to 1.6 Km/s (initial shock pressure increased from 7 to 16 GPa). Vicker's diamond pyramid hardness (DPH) tests (Fig. 3) demonstrated a hardness increase from 370 ± 57 to 557 ± 17 at final shock pressures of 20-24 GPa. The ultimate tensile strength and DPH of dynamically compacted specimens compared favorably to conventionally quenched and tempered AISI 9310, i.e. 1.05 GPa and 300-400 DPH respectively.

To estimate the maximum mass fraction of powdered alloy which could be melted at their surfaces, it was assumed that the interiors of the powder particles become heated only as much as if they were grains in the interior of the solid alloy. This assumes no work is expended in deforming the solid particle. The excess thermal energy is assigned to the heat of fusion and the thermal content of the melt. If L is the mass fraction of the melted film it is given by:

$$L = (E_T - E'_T) / (C_p \Delta T_m + H_m - E'_T)$$

where E_T and E'_T are the thermal energy deposited in porous and nonporous powders shocked to the same high pressure respectively. Here ΔT_m is the temperature difference between the melting point, and room temperature, C_p is the specific heat, and H_m is the heat of fusion.

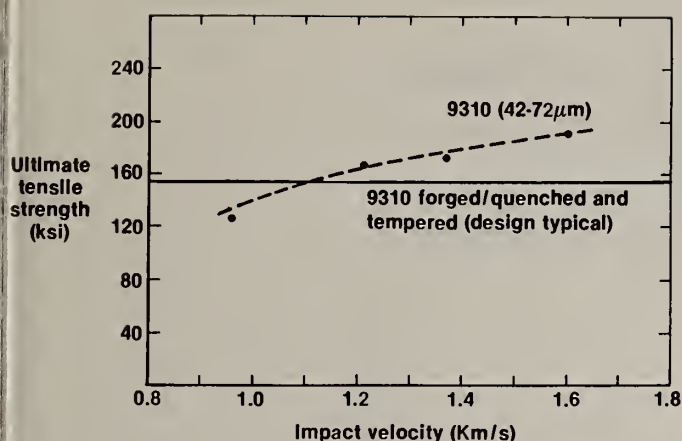


Figure 2. Ultimate tensile strength versus impact velocity

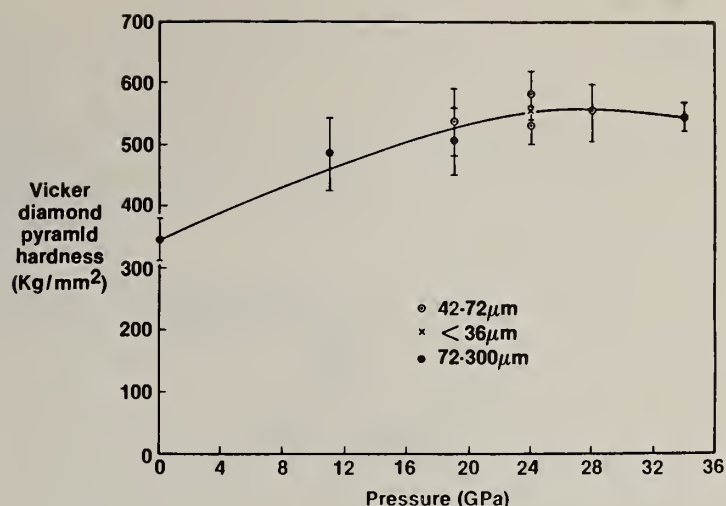


Figure 3. Diamond pyramid hardness versus final shock pressure

Using the values of 1511 K for the difference in the melting point of iron and room temperature, 0.45 MJ/g K for C_p , and 247 MJ/Mg for H_m , the post-shock temperatures and the amount of melt for iron for various initial distentions have been calculated (Fig. 4). By way of reference the present experiments were all conducted under shock pressures of from 7 to 16 GPa for initial shock propagation into the sample of distention, $m = 1.7$. Hence the maximum percentage of melt is expected to vary from 32 to 70% which is overestimated for the present experiment.

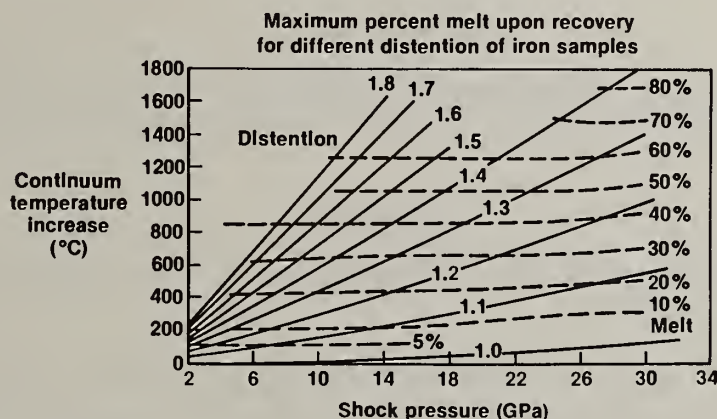


Figure 4. Continuum shock temperature increase versus initial shock pressure

It appears that in addition to the generation of a thin film of molten material at particle boundaries by the shock, in order to obtain welding of particles coated with molten material it needs to be held together under pressure for a sufficient time that the excess heat from the localized melting can be transported by Fourier conduction to within the cooler interiors of the solid particles.

Explosive Charge Compaction

Experiments to explosive compact rapidly solidified powders have been carried out using a cylindrical arrangement shown in Fig. 5. An objective was to determine the design of an assembly which yields the desired pressure-time history to achieve full densification of the powders. Initial results have not achieved full density using ammonium nitrate plus fuel oil explosives. The successful explosive consolidation of 9310 powders involves a number of alloy as well as explosive parameters

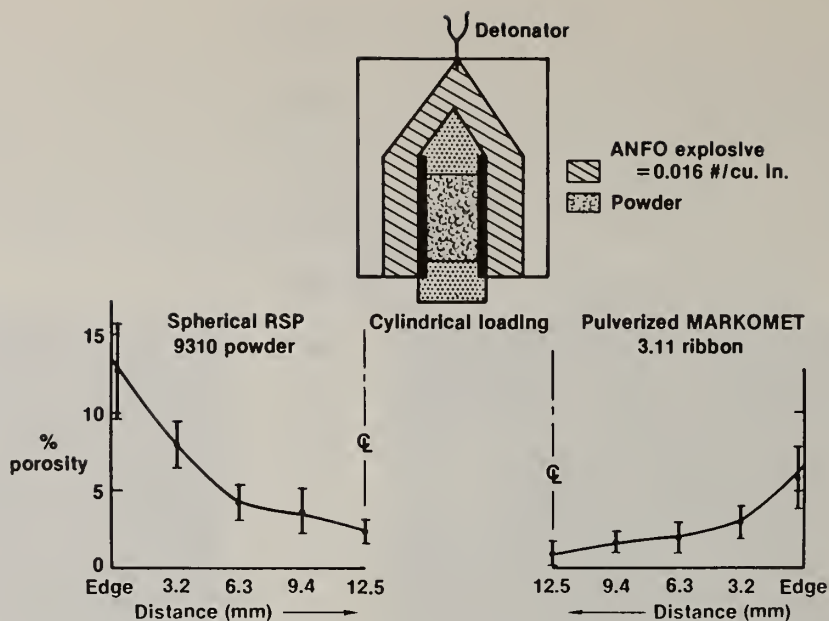


Figure 5. Explosive compaction of spherical 9310 and flake Markomet 3.11

which have just begun to be examined. For example flake Markomet 3.11 and spherical 9310 steel powders were compacted within the same evacuated thin wall cylindrical container. Although complete consolidation was not achieved, as noted in Fig. 5, improved densification was achieved starting with flake rather than spherical geometry.

Acknowledgements

This work was performed for the Department of Defense under contract DAAG46-82-C-0042 under the auspices of the Army Materials and Mechanics Research Center, Dr. Saul Isserow, technical monitor.

References

- [1] D. Raybould, 'Proceedings of the 15th International Machine Tool Design and Research Conference', Macmillan Press, London (1975).
- [2] D. Raybould, D. G. Morris and G. A. Cooper, *J. Mat. Sci.*, **14**, 2523-26 (1979).
- [3] D. Raybould, Chapter 51 in "Shock Waves and High Strain Rate Phenomena in Metals", edited by M. Meyers and L. Murr, Plenum Press (1981).
- [4] C. Cline, J. Mahler, M. Finger, W. Kuhl and R. Hooper in "Rapid Solidification Processing", edited by R. Mehrabian, B. Kear, and M. Cohen, Claitor's Press (1977).
- [5] C. Cline and R. Hooper, *Scripta Met.*, **11**, 1137 (1977).
- [6] S. W. Kieffer, 'From Regolith to Rock by Shock', *The Moon*, **13**, 301-320 (1975).
- [7] D. G. Morris, in "Proc. 2nd Int. Conf. on Rapid Solidification Processing; Principles and Technologies", edited by R. Mehrabian, B. Kear and M. Cohen, Claitor's Press (1980).
- [8] P. Kasiraj, T. Vreeland, Jr., R. B. Schwarz and T. J. Ahrens, 'Mechanical Properties of Rapidly Solidified Iron Based Powders Compacted by Shock Waves', to be presented at APS Meeting, March 1983.

- [9] R. B. Schwarz, P. Kasiraj, T. Vreeland, Jr. and T. J. Ahrens, 'Shock Wave Velocity and Temperature Measurements During Consolidation of Rapidly Solidified Iron-Based Powders', to be presented at the APS Meeting, March 1983.
- [10] W. J. Boettinger et al., 'Rapid Solidification Processing', edited by R. Mehrabian et al., 1983.
- [11] D. Raybould, J. Powder Metallurgy and Powder Technology, 16, 9-19, 1980.

ULTRASONIC GAS ATOMIZED POWDERS OF MAGNETIC ALLOYS

R. C. O'Handley, P. Domalavage, B. W. Corb, Y. Hara, and N. J. Grant

Department of Materials Science and Engineering,
MIT, Cambridge, MA 02139.

ABSTRACT

Glassy and microcrystalline powders of FeNiBSi and CoNbB alloys have been fabricated by atomization with ultrasonic He gas jets. Differential and cumulative weight distributions vs. mean particle diameter (by sieve analysis) for the $\text{Fe}_{65}\text{Ni}_{10}\text{B}_{15}\text{Si}_{10}$ alloy show the particles below $63\text{ }\mu\text{m}$ to be fully amorphous (as judged by $\text{Mo K}\alpha$ X-ray diffraction). X-ray diffraction analysis shows the crystalline particulate fraction of the FeNiBSi alloy to be composed of α -Fe-like and Fe_2B -like phases. Thermomagnetization curves indicate the additional presence of an Fe_3B -like phase. The same three phases occur - in different ratios (less α phase) - upon crystallizing the fine particulates which were glassy as atomized.

Introduction

Several reports of powder fabrication in alloy systems with favorable glass-forming tendency have appeared in the recent literature (see Table I) [1]. Miller and Murphy have gas-atomized amorphous CuZr and FeBSi alloys [2] and Yamaguchi and Narita [3] have atomized an FeBSi alloy, in both cases into the path of a water jet (effectively steam quenching). A high voltage, electrohydrodynamic (EHD) technique [4], and a spark erosion technique employing an organic medium [5,6], both making extremely fine powders, have also been reported in the literature. The EHD technique has been used to fabricate powders of several glass-forming alloys with the result that amorphous structures appeared for diameters less than $0.1\text{ }\mu\text{m}$. Spark eroded amorphous $\text{Fe}_{75}\text{B}_{10}\text{Si}_{15}$ powders were produced up to $30\text{ }\mu\text{m}$ in diameter. Patterson et al have used the Pratt and Whitney RSR technique to atomize FeBSi and NiBSi alloys. Their powders were amorphous up to approximately $15\text{ }\mu\text{m}$ [7]. Nanao has employed sub-sonic, dry gas atomization using approximately 200 psi tank pressure of Ar to produce powders of FeBSi which were amorphous below $25\text{ }\mu\text{m}$ [8]. We have recently demonstrated the suitability for glass formation of the ultrasonic gas atomization (USGA) technique [9] by the production of glassy CuZr powders up to $63\text{ }\mu\text{m}$ in diameter [10]. We report here the extension of this technique to magnetic alloys with favorable glass-forming tendency.

The ultrasonic gas atomization was effected by delivering the melt stream to an array of ultrasonically pulsed (100 kHz), high-speed (mach 2 or greater) jets of dry He gas released at a gauge pressure of approximately 1200 psi. The powder was collected at a pressure slightly above one atmosphere in a steel vessel fitted with a cyclone collector. The technique is described in more detail in Ref. [9] where it is applied to aluminum alloys.

Results

Structural Characterization.

The powder yield showed a unimodal size distribution (Fig. 1) similar to our CuZr atomization run [10] as well as to numerous microcrystalline copper and aluminum alloy runs done with this apparatus [11]. The differential weight distribution (by sieve analysis) peaks near $70\text{ }\mu\text{m}$ in the present case, higher than the peak of the distribution in our CuZr run which was at $44\text{ }\mu\text{m}$. This difference may be due to the differences in density and viscosity between the two alloy melts as well as to differences in pour speed and gas pressure at the USGA die during atomization.

$\text{Mo K}\alpha$ X-ray diffraction analysis of the sieved powders (Fig. 2) showed the particles to be fully amorphous below a diameter $d = 63\text{ }\mu\text{m}$, just as in the case of our CuZr run [10]. Above $d = 125\text{ }\mu\text{m}$ no broad diffraction peak could be discerned but only sharp crystalline peaks indicating a predominantly α -Fe structure with some Fe_2B peaks present. A quantitative analysis of the intensities suggests a 70/30 weight ratio for α to Fe_2B -like phases. In the intermediate size range the X-ray pattern is mixed. Crystallization of the originally amorphous powder fraction $d < 44\text{ }\mu\text{m}$ gave a diffraction pattern revealing a greater fraction of Fe_2B phase than exists in the

Table I

Powder fabrication in readily-glass-forming systems. Glass Cutoff refers to the particle diameter below which predominantly glassy phase was observed.

ALLOY	TECHNIQUE	T _m (°C)	GLASS CUTOFF	REF.
Cu ₆ Zr ₄	subsonic, gas/water	890	40 μm	[2]
Fe _{81.5} B _{14.5} Si ₄	subsonic, gas/water	1160	10 μm	[2]
Fe ₇₄ B ₁₁ Si ₁₅	subsonic, gas/water	1120	15-20 μm	[3]
FeSiB	EHD (<10 ⁻⁵ Torr)		0.1 μm	[4]
FeNiPB	EHD (<10 ⁻⁵ Torr)		0.1 μm	[4]
Fe ₇₅ B ₁₀ Si ₁₅	spark erosion	1130	30 μm	[5]
Fe ₇₅ B ₁₀ Si ₁₅	spark erosion	1130	>20μm	[6]
Fe ₇₉ B ₁₆ Si ₅	RSR	1150	<5-10 μm	[7]
Ni ₇₅ B ₁₇ Si ₈	RSR	1100	15μm (a)	[7]
Fe ₇₅ B ₁₀ Si ₁₅	subsonic, Argon	1130	25 μm	[8]
Cu ₆ Zr ₄	USGA, helium	890	63μm (b)	[10]
Fe ₆₅ Ni ₁₀ B ₁₅ Si ₁₀	USGA, helium	1150	63 μm (c)	present
CoNbB	USGA, helium	1250		present

(a) For Argon, 50 wt% of product is finer than 50μm whereas for He, 50 wt% of product is finer than 100μm. However, at a given d, He gives greater amorphous fraction than argon.

(b) Distribution peaks near 44 μm.

(c) Distribution peaks near 70 μm.

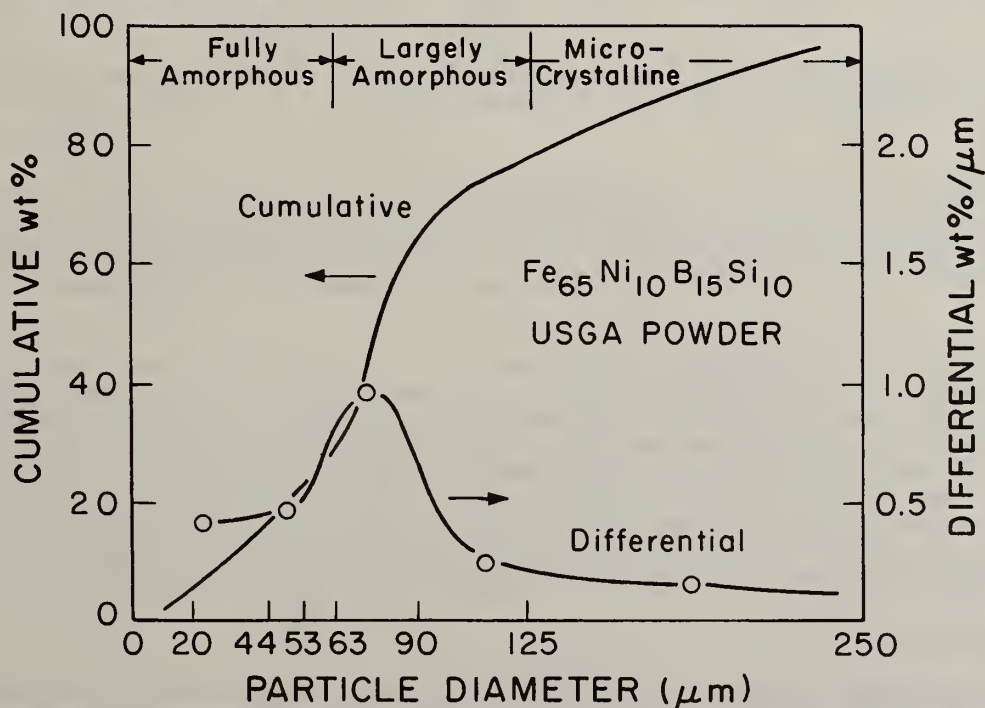


Fig. 1. Cumulative and differential particle size distributions by weight determined by sieve analysis.

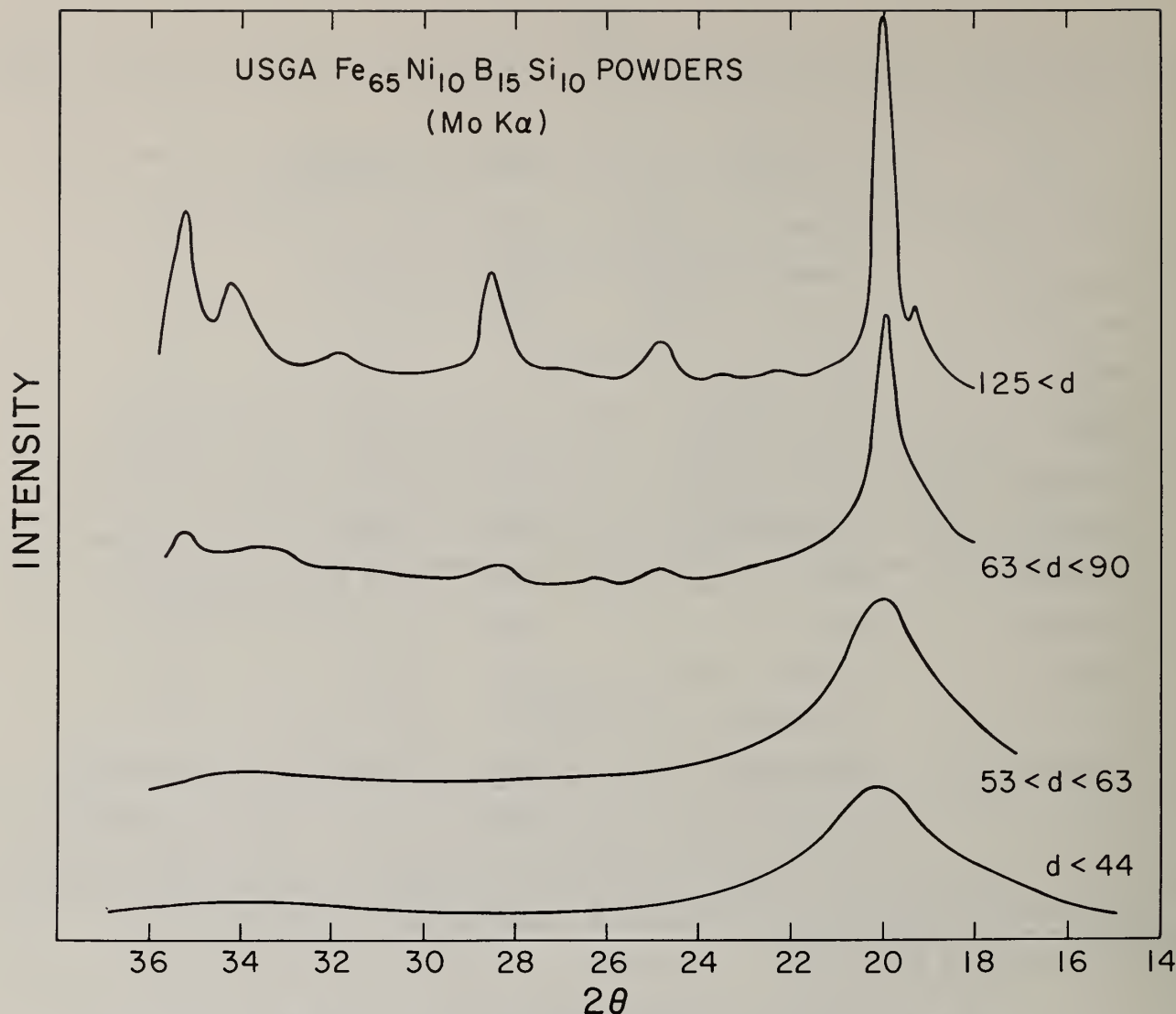


Fig. 2. X-ray diffractometer scans for four powder fractions. Crystalline peaks for $d > 125 \mu\text{m}$ index to reflections for $\alpha\text{-Fe}$ and tetragonal Fe_2B .

crystalline-as-atomized fraction. Quantitative analysis here sets the α to Fe_2B -like weight ratio at 40/60. This difference is brought out in Fig. 3 where the major $\alpha\text{-Fe}$ and Fe_2B peaks are identified. The several unidentified peaks of low intensity in the crystallized $d < 44 \mu\text{m}$ sample do not match those of either orthorhombic or tetragonal Fe_3B which are often stabilized by impurities [12].

Scanning electron micrographs (Fig. 4) of particulates show approximately spherical particles. Some of the larger particles are lightly decorated with satellites, but to a lesser extent than was the case with the CuZr powders [10] which were atomized in an earlier model apparatus. Scanning electron micrographs of subsonic atomized powders [2,7,8] show no satellites, probably because of the lower level of turbulence in that process. While our particulates greater than $125 \mu\text{m}$ in diameter show clear signs of crystallinity on their surface, some surface segregation is evident even in the size fraction less than $44 \mu\text{m}$. Electron microprobe analysis showed no compositional differences between the different size fractions (chemical analysis is being done) and marginal differences between the regions of different contrast on the surface of the crystalline particulates.

Magnetic Characteristics.

Fig. 5 shows the magnetization at 6 kOe as a function of temperature for three size fractions $d < 44 \mu\text{m}$, $53 < d < 63 \mu\text{m}$, and $d > 125 \mu\text{m}$. The two smaller size fractions, predominantly amorphous as atomized, show identical magnetization curves. The finer fraction was heated above crystallization and, upon cooling, revealed a two-magnetic phase behavior.

The magnetic data can be used to supplement the X-ray phase information given above. Turning first to the $d > 125 \mu\text{m}$ sample, glassy as atomized, we assume all of its phases to be of approximately the same composition as the parent alloy because of the rapid solidification rate. Both of the phase types identified by X-ray analysis have high Curie temperatures ($T_C(\alpha\text{-Fe}) = 1044 \text{ K}$ and $T_C(\text{Fe}_2\text{B}) = 1010 \text{ K}$) which should be moderately suppressed with small Ni or Si substitutions ($T_C(\alpha\text{-Fe}_{87}\text{Ni}_{13}) \approx 970 \text{ K}$ and $T_C((\text{Fe}_{87}\text{Ni}_{13})_2(\text{BSi})) \approx 920 \text{ K}$). Thus, the high-Curie-temperature phase is probably $\alpha\text{-FeNi(B,Si)}$ plus $(\text{FeNi})_2(\text{BSi})$ and the low-Curie-temperature phase, not seen in the X-ray diffraction pattern, remains to be identified. Its Curie temperature (750 K), while below that of Fe_3B ($T_C = 810 \text{ K}$) is reasonable for that of $(\text{Fe}_{87}\text{Ni}_{13})_3(\text{BSi})$ which can be estimated to be in the range of 730 K. Consideration of the magnetization of these phases (using the 70/30 ratio for the two high temperature phases determined by X-ray intensity analysis) suggests a 2/1 volume ratio of high temperature phases to low temperature Fe_3B -like phase. See Table II.

Table II

Relative fraction of various phases present in two powder samples. Because the densities of the iron borides are close to that of $\alpha\text{-Fe}$, the difference between volume and weight fractions is less than the uncertainty in the assigned fractions.

Sample	α	Fe_2B	Fe_3B
Crystalline, $d > 125 \mu\text{m}$	0.47	0.20	0.33
Crystallized, $d < 44 \mu\text{m}$	0.22	0.33	0.45

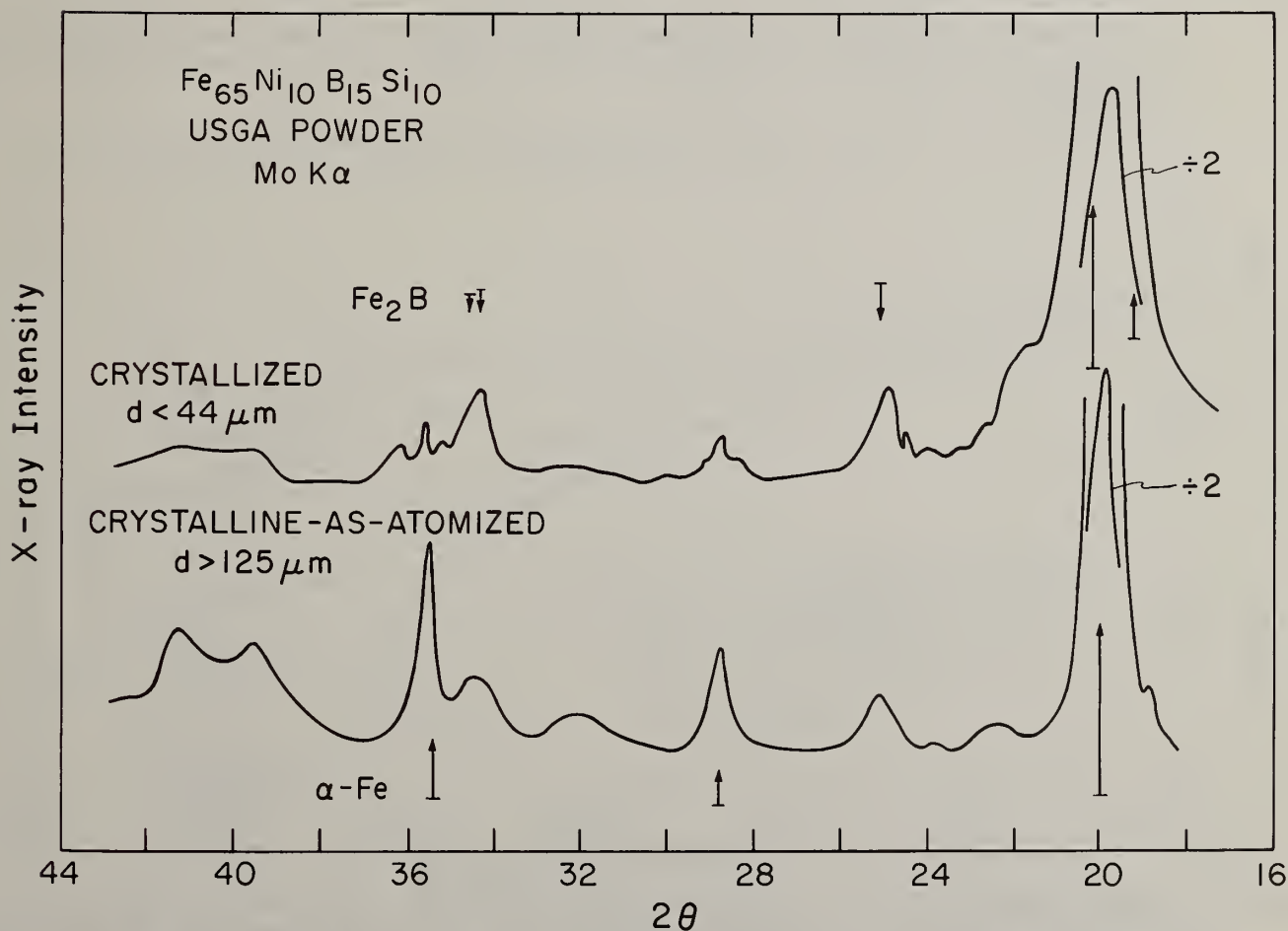
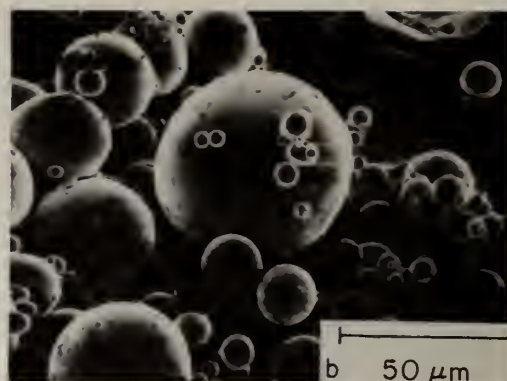
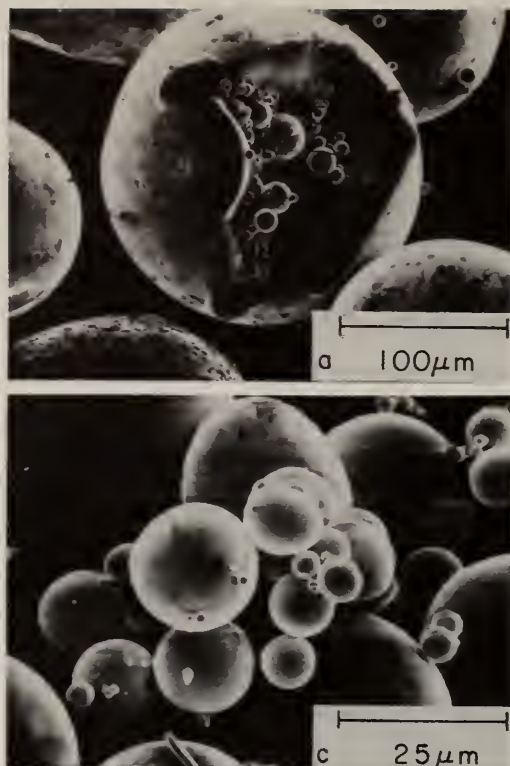


Fig. 3. Comparison of X-ray diffraction patterns for crystallized-after-atomization $d < 44 \mu\text{m}$ fraction and crystalline-as-atomized $d > 125 \mu\text{m}$ fraction. The major peaks are identified as $\alpha\text{-Fe}$ -like and Fe_2B -like phases. The lengths of the arrows indicate expected relative intensities.



- a) $d > 125 \mu\text{m}$
- b) $53 < d < 63 \mu\text{m}$
- c) $d < 44 \mu\text{m}$

Fig. 4. Scanning electron micrographs (10 kV) of FeNiBSi powders. The particle shown for the $d > 125 \mu\text{m}$ sample is not typical (it is the only one seen in thousands scanned) but is an example of an interesting but undesirable feature which can be found in some larger particulates.

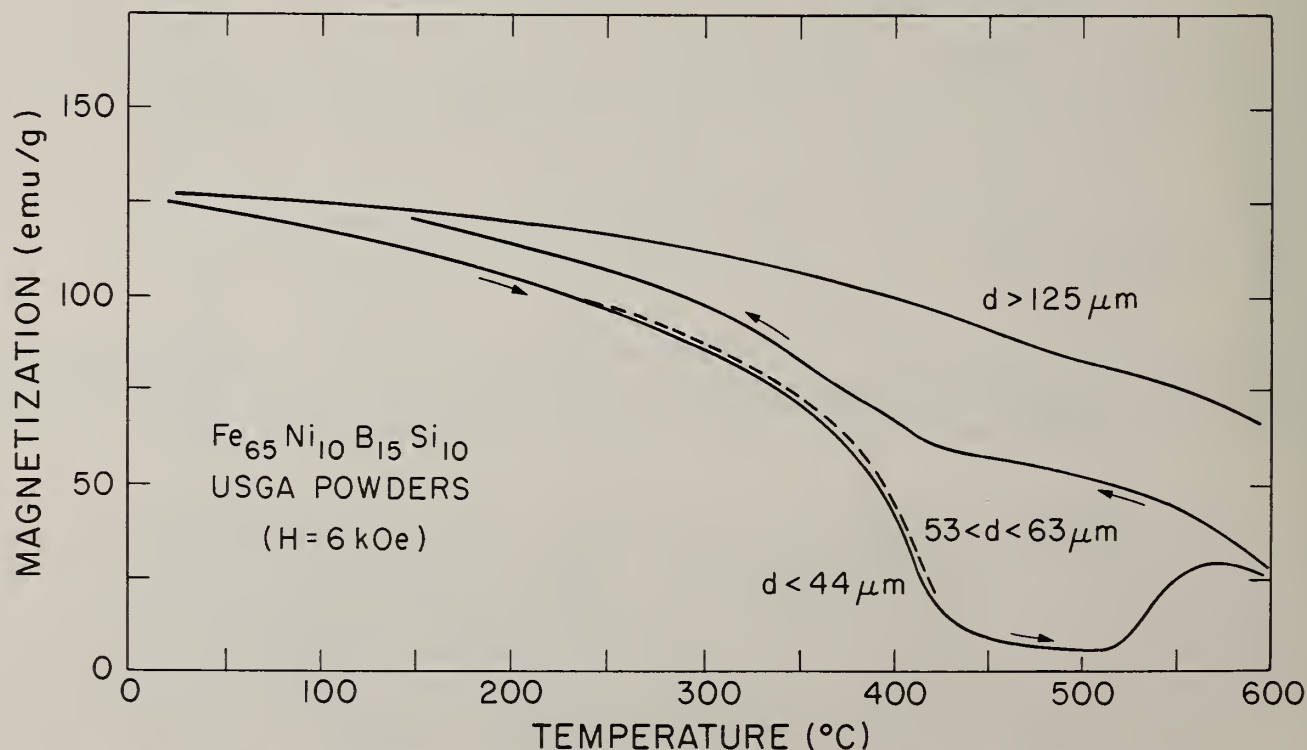


Fig. 5. Specific magnetization as a function of temperature at an applied field of 6 kOe. For $d < 44 \mu\text{m}$ (solid curve) data is shown for heating the glassy state through crystallization and cooling in the crystallized state. The behavior of the $53 < d < 63 \mu\text{m}$ glassy fraction (dashed line) is essentially identical to that of the $d < 44 \mu\text{m}$ sample. The crystalline-as-atomized fraction $d > 125 \mu\text{m}$ (solid line) shows a high Curie temperature due to the dominance of α -FeNi (probably with appreciable boron in solution).

Similar analysis for the crystallized $d < 44 \mu\text{m}$ sample (using the 40/60 weight ratio for α to Fe_2B -like phases determined by X-ray intensity analysis) points to an approximately 55/45 volume ratio of high temperature to low temperature phases. We can only speculate why the inferred Fe_3B -like phase would not appear in X-ray diffraction: it may exist in finely dispersed, microcrystallite form.

Magnetization-field loops on the packed powders revealed only minor differences between the amorphous and crystalline samples. Figure 6 shows an M-H loop for the $d < 44 \mu\text{m}$ fraction corrected for demagnetization of the contiguous spheroidal particles. Results derived from these loops for all samples are listed in Table III. The coercivities of the compacted glassy powders are three orders of magnitude greater than those of glassy ribbons of comparable compositions. Magnetic anisotropies of the different samples were estimated from the area above the magnetization curve. Although the anisotropies are two orders of magnitude greater than values obtained in the same way from amorphous ribbons [13], their principal value is as a comparison between the various size fractions. The comparison shows that in the compacted powder form the properties appear to be dominated by surface effects that mask the intrinsic magnetic softness of the amorphous magnetic state and blur the differences between the crystalline and amorphous samples.

Table III

Magnetic characteristics of compacted powder samples from three size fractions. Specific saturation magnetization σ was determined by extrapolation to infinite applied field. Values in parentheses are for crystallized particulates.

Size fraction	σ (emu/gm)	$4\pi M_s$ (kG) ^(a)	Coercivity (Oe)	Anisotropy (10^5erg/cm^3)
$d > 125 \mu\text{m}$	141	13.3	70	1.35
$53 < d < 63 \mu\text{m}$	132	12.4	45 (45)	1.4 (1.65)
$d < 44 \mu\text{m}$	135	12.7	50 (85)	1.29 (1.92)

(a) A mass density of 7.5 g/cm^3 was assumed for the alloy.

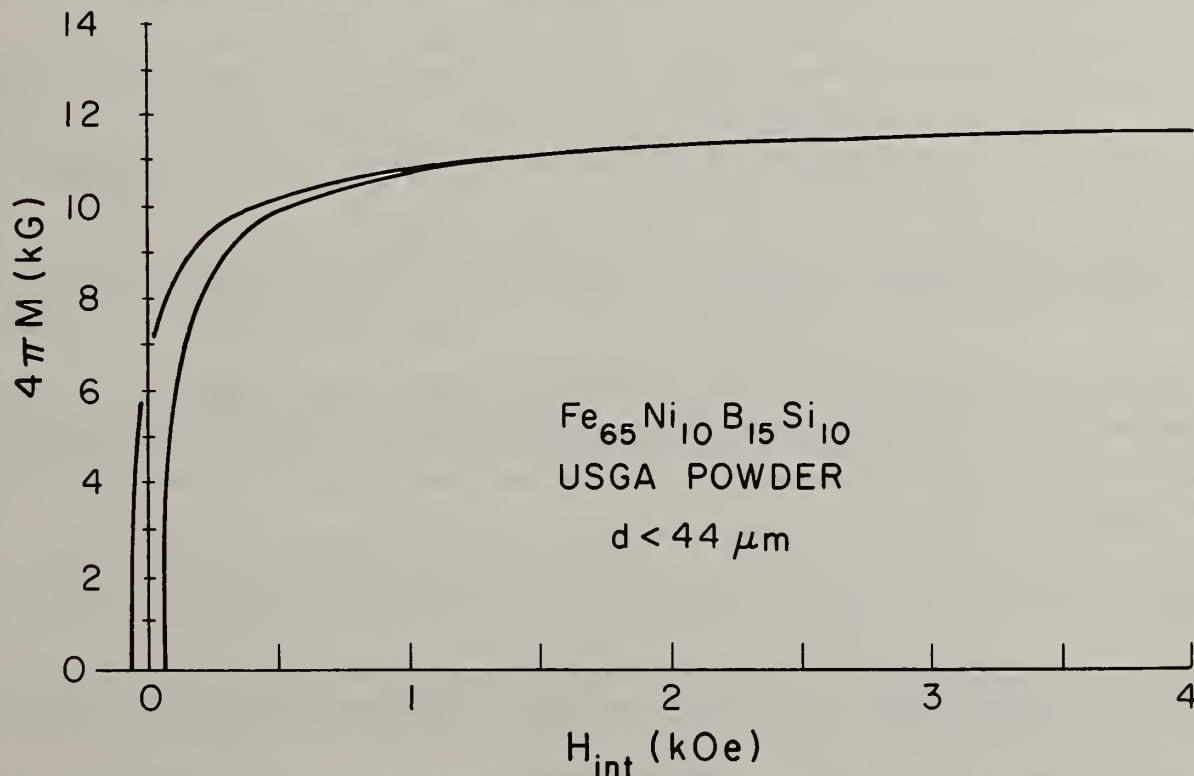


Fig. 6. Magnetization vs. applied field for compacted particulates of $d < 44 \mu\text{m}$ fraction. The correction for the demagnetization of the contiguous spheres is illustrated as is the method for estimating the magnetic anisotropy. Differences among the various samples are listed in Table III.

Discussion

Implications of magnetic measurements

The composition $\text{Fe}_{65}\text{Ni}_{10}\text{B}_{25}$ is hypereutectic according to the ternary FeNiB diagram [14]. The mode of crystallization of our alloy with $\text{B}_{15}\text{Si}_{10}$ into $\alpha\text{-FeNi}(\text{B},\text{Si}) + (\text{FeNi})_2(\text{BSi})$ with finely dispersed Fe_3B -like microcrystals possibly also present, suggests eutectic crystallization in the hypereutectic region [15]. The difference between the crystalline-as-atomized powders ($d > 125 \mu\text{m}$) and the crystallized-after-atomization powders ($d < 44 \mu\text{m}$) lies not in the phases nucleated, but in the times available for growth of existing nuclei. The crystalline-as-atomized sample shows a smaller ratio of iron boride phases to α phase than does the sample crystallized after atomization. Crystallization after atomization at a heating rate of a few degrees per minute allows more time for diffusion of the metalloids from the α phase to form more of the iron boride phases than exists in the $d > 125 \mu\text{m}$ fraction.

The increased concentration of Fe_nB ($n = 2, 3$) phases in the crystallized $d < 44 \mu\text{m}$ sample probably contributes to its greater magnetic hardness relative to the $d > 125 \mu\text{m}$ sample which contains more α phase. It is known that $\alpha\text{-Fe}$ crystallites do not have as deleterious an effect upon magnetic softness as do the lower symmetry phases Fe_3B and Fe_2B [16].

Comparison of atomization techniques

Convective undercooling ΔT_p of a droplet, per unit time Δt , can be expressed [17,18]:

$$\Delta T_p / \Delta t = 6h(T - T_0) / (d\rho C_p) \quad (1)$$

where h is the heat transfer coefficient, T_0 is the temperature of the cooling medium, d is the droplet diameter, ρ is its mass density and C_p is its specific heat as it cools. The heat transfer coefficient has been observed to vary roughly linearly with the droplet velocity [18] and can be approximated empirically as [17,18]:

$$h = 0.6k_o^{2/3}(v\rho/d)^{1/2}C_o^{1/3}(1/\eta_o)^{1/6} \quad (2)$$

where k_o , ρ_o , C_o , and η_o are respectively the thermal conductivity, mass density, specific heat and viscosity of the cooling medium and v is the relative velocity of the droplet in the medium. The factors have been arranged in order of their importance.

The difference between our USGA results (1200 psi) and those of Nanao (200 psi) (see Table I) points to the importance of droplet velocity and atomization gas in determining heat transfer and amorphous alloy formation as indicated by Eqs. (1) and (2). Clearly the greater pressure used in USGA leads to greater average relative droplet/gas velocity. The heat transfer of He relative to argon is affected by the eightfold greater thermal conductivity of He, the tenfold greater specific heat of He and the tenfold greater mass density of Ar. Based on relation (2) these differences lead to a heat transfer for He approximately 2.7 times that of argon.

Patterson found Ar gave a finer particulate distribution than He even though He gave a greater yield of amorphous material at a given droplet diameter [7]. This more efficient atomization by argon relative to helium can be understood in terms of the greater density of the argon relative to helium.

Spark erosion and the EHD process seem well suited to the production of super-fine distributions but appear to have no advantage over gas atomization techniques, especially USGA with He, in terms of heat transfer and glass forming capability. However, some of the finer particulates produced in spark erosion are believed to be quenched from the vapor state and thus experience enhanced quench rates [6].

Other differences in the upper limit to amorphous particulates (Glass Cutoff in Table I) can be understood in terms of ease of glass formation as gauged roughly by differences in alloy melting temperatures.

It is interesting to note that our cutoff diameter for glassy atomized powders is greater than the critical thickness above which ribbons of any FeBSi alloys can no longer be made glassy by melt spinning: $d_{\text{crit}} < 42 \mu\text{m}$ [19].

Acknowledgement

We are pleased to acknowledge the support of this research by the U. S. Army Research Office under contract No. DAAG-29-80-0088. Helpful discussion with C. Ashdown and E. Ting are appreciated.

References

- [1] H. H. Liebermann and J. L. Walter in Rapidly Solidified Amorphous and Crystalline Alloys, op. cit. p. 111.
- [2] S.A. Miller and R.J. Murphy, Scripta Met. 13, 673 (1979) and in Rapid Solidification Processing: Principles and Technologies II (RSP II), ed. R. Mehrabian, B. Kear and M. Cohen (Claitor's Pub. Div., Baton Rouge, LA, 1980), p. 385.
- [3] T. Yamaguchi and K. Narita, Appl. Phys. Lett. 33, 468 (1978).
- [4] J. Perel, J.F. Mahoney, P. Duwez, and B.E. Kalansher in RSP II op. cit. p. 287, J. Perel, J. F. Mahoney, S. Taylor, Z. Shanfield, and C. Levy in Rapidly Solidified Amorphous and Crystalline Alloys, Ed. B. H. Kear, B. C. Giessen, and M. Cohen, (North Holland, New York, 1982) p. 131. also p. 258 in RSP I.
- [5] T. Yamaguchi and K. Narita, IEEE Trans. MAG-13, 1621 (1977).
- [6] A. Berkowitz and J.L. Walter in RSP II op.cit. p. 294 and Mat. Sc. and Eng. 55, 275 (1982). Further results are described by A. Berkowitz, J.L. Walter and K.F. Wall, Phys. Rev. Lett. 46, 1484, 1981.
- [7] R. J. Patterson II, D. L. Ledwith and J. C. Dwyer, in Processing of Metal and Ceramic Powders, ed. K. W. Lay and R. M. German (The Metallurgical Society, Warrendale, PA, 1982) in press.
- [8] Prof. S. Nanao, Univ. of Tokyo, unpublished work.
- [9] V. Anand, A.J. Kaufman and N.J. Grant in RSP II, op. cit., p. 273.
- [10] P. Domalavage, C. Ashdown, R. C. O'Handley and N. J. Grant, J. Mat. Sc. and Eng. 57, 143 (1982).
- [11] P. Domalavage and N.J. Grant, internal report, and N. J. Grant in Advances in Powder Technology, (ASM, 1982) in press.
- [12] R. Hasegawa, R. C. O'Handley and L. I. Mendelsohn in AIP Conf. Proc. 34, (AIP, New York, 1976) p. 298.
- [13] R. C. O'Handley, AIP Conf. Proc. 29, (AIP, New York, 1976) p. 206.
- [14] H. H. Stadelmaier and C. B. Pollack, Z. Metall. 60, 960 (1969).
- [15] U. Herold and U. Koster, in Rapidly Quenched Metals III, ed. B. Cantor (The Metals Society, London, 1978) p. 281 and R. Hasegawa and R. Ray, J. Appl. Phys. 49, 4174 (1978).
- [16] A. Datta, N. J. DeCristofaro and L. A. Davis, in Rapidly Quenched Metals IV, ed. T. Masumoto and K. Suzuki (Japan Inst. of Metals, Sendai, 1982) p. 1007.
- [17] R. Mehrabian, in Rapid Solidification Processing: Principles and Technologies I (RSP I), ed. R. Mehrabian, B. Kear and M. Cohen (Claitor's Pub. Div., Baton Rouge, LA, 1978), p. 9. R. J. Patterson, in Rapidly Solidified Amorphous and Crystalline Alloys, op. cit. p. 123.
- [18] N. J. Grant, in RSP I, op. cit. p. 230.
- [19] F. E. Luborsky, H. A. Davies, H. H. Liebermann, and J. Reeve, J. Appl. Phys., Nov. 1982.

PRODUCTION APPLICATIONS OF RAPIDLY SOLIDIFIED TOOL STEELS,
SUPERALLOYS, TITANIUM ALLOYS, AND CORROSION-RESISTANT ALLOYS

J. H. Moll

Crucible Research Center
Pittsburgh, Pa. 15230

F. J. Rizzo

Crucible Compaction Metals Operation
Oakdale, Pa. 15071

ABSTRACT

While extensive work on rapidly solidified materials is being conducted in the laboratory, a number of these materials are now in production or have near-term production status. These materials include tool steels, superalloys, titanium alloys and corrosion-resistant alloys. Rapid solidification of tool steels has resulted in refined microstructures, improved performance, and advanced alloy development. Several tool steels have been developed which can be made only by rapid solidification techniques. Superalloy and titanium alloy products made from rapidly solidified powders are currently in production or near production for a number of aerospace applications. The materials offer improved quality, property capabilities and uniformity. Rapid solidification is now being evaluated for corrosion-resistant alloys. Some unique physical metallurgy aspects and applications for these materials have been established.

Introduction

In the past 20 years, processes have been developed to utilize rapid solidification technology (RST) to produce upgraded or entirely new high performance alloys. The principal advantages of these processes are (1) the ability to improve property uniformity and alloy development flexibility due to the elimination of macrosegregation, and (2) the ability to make near-net shapes which results in reduced input material and less machining to produce a finished part. To avoid segregation, solidification rates faster than those used in conventional ingot cooling are required. Fast cooling rates (10^3 to 10^6 C/sec) are attainable by making small particles with a large surface area to volume ratio. This criterion is met with powder particles ranging in size from several hundred microns to less than 37 microns. Spherical powders of this type are currently in production and are being used to produce shapes ranging from bars to complex near-net shape parts using hot-isostatic-pressing. The following are some typical production applications of rapidly solidified tool steels, titanium alloys, superalloys and corrosion-resistant materials.

RST Tool Steels

The Crucible Particle Metallurgy (CPM) process for high speed tool steels has been commercially applied since 1970. The process enables production of superior quality grades of conventional high speed steels and also lends itself to the production of new higher alloyed grades which are not practical with conventional steel making. These new grades provide unique combinations of higher red hardness, wear resistance and toughness and are proving cost effective in many commercial applications. The process involves gas atomization of prealloyed induction melted molten metal. The resulting powder is dried, screened, and loaded into steel containers which are subsequently evacuated and sealed. The powder is consolidated by hot-isostatic-pressing (HIP). The resulting compact, weighing up to 2000 lb, can be rolled or forged on conventional mill equipment or used in the as-HIP condition after the can is stripped off.

One of the most detrimental characteristics of conventionally produced high alloy tool steels is their tendency to form carbide segregation in slowly cooled ingots. Rapidly solidified powder, on the other hand, insures a very fine uniform distribution of carbide. Figure 1 compares the microstructural

appearance of conventional T15 steel with CPM T15 steel. Virtually all the carbides in the CPM product are less than 3 microns in size. In the conventional product, more than half of the carbides are larger than 6 microns and sizes up to 34 microns have been observed. The uniform distribution of fine carbides in CPM steels results in superior grindability in the hardened condition (Figure 2) without sacrifice in tool wear. For example, in form turning screw machine parts from Armco iron, CPM T15 had a tool life of 180 minutes compared to 80, 50 and 30 minutes for titanium carbide, tungsten carbide, and conventional T15, respectively. In a punching operation on T430, CPM T15 outperformed D2. Tool life (pieces/grind) for D2 was 70,000; tool life for CPM T15 was 500,000.

Rapidly solidified powder also opens development for new tool materials. A cold work steel recently developed is CPM 10V which contains 2.4% C and 10% V. The alloy could not be practically produced by conventional ingot technology. The alloy gives an unusual combination of wear resistance (Figure 3) and toughness (Figure 4). CPM 10V is outperforming conventional tool materials in such applications as cores used in molding ceramics, dies for cold compaction of steel powder, dies for cold drawing M1 high speed steel, flattening dies used in the production of drills, and punches for slots in iron oxide coated tags.

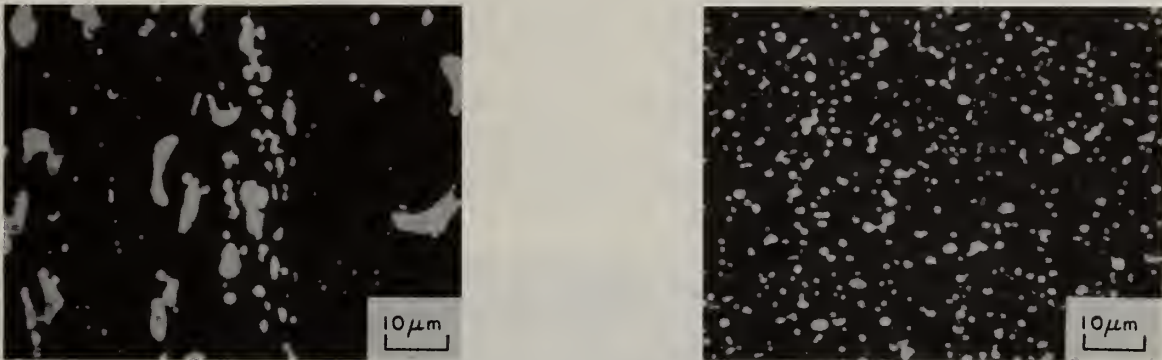


Figure 1. Comparison of Carbide Structure of Conventional T15 (left) and CPM T15 (right).

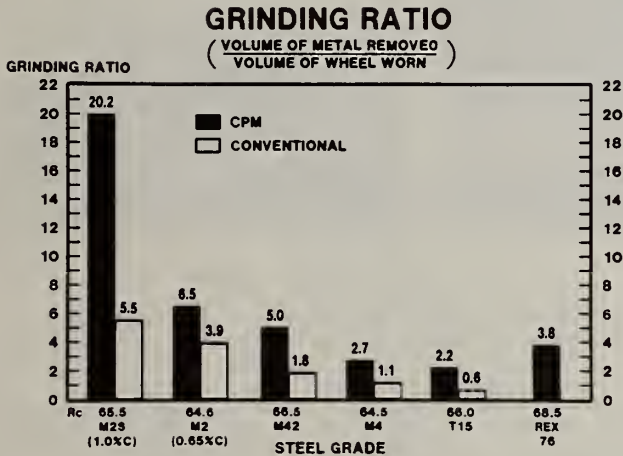


Figure 2. Comparison of Grindability of Conventional Tool Steels with CPM Tool Steels.

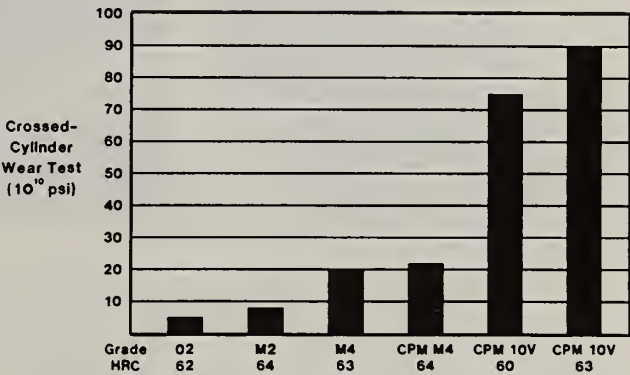
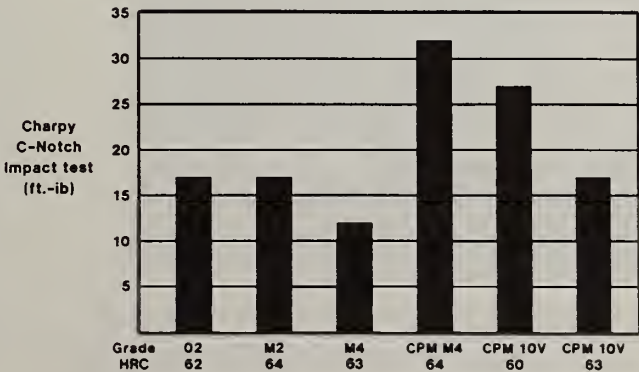


Figure 3. Wear Properties of Conventional Tool Steels and CPM Tool Steels.

Figure 4. Comparison of Toughness of Conventional Tool Steels and CPM Tool Steels.



Titanium alloys are used in the aerospace industry where high strength-to-weight ratios at moderate temperatures are required. This involves both airframe and engine applications. Conventional forgings offer attractive properties but high buy-to-fly ratios result in high cost. Casting technology has been developed to produce near-net shapes but properties of castings are often inadequate. A process, utilizing rapidly solidified powder, has been developed and is now in pilot production for producing fully dense near-net shaped parts with properties equivalent to forgings. The P/M process involves the use of a ceramic mold made by the lost wax process, powder made by PREP (Plasma Rotating Electrode Process), and hot-isostatic-pressing.

Figure 5a shows an engine compressor rotor made by using the ceramic mold process and Ti-6Al-4V powder. Using conventional processing, the part is machined from a pancake forging which weighs 30 lbs. The as-HIP near-net shape weighs only 6.2 lbs. The process is also capable of making large complex airframe parts such as the arrestor hook support fitting shown in Figure 5b. Normally made from a forging weighing 175 lbs, this as-HIP part weighed only 60 lbs. In some instances, parts made by the ceramic mold process need not be machined on all surfaces. For the fuselage braces shown in Figure 5c, only the top and bottom surfaces will be machined. The webs will require only light chemical milling to remove a thin alpha case before installation into an aircraft.

The combination of rapidly solidified powder and hot-isostatic-pressing results in an isotropic microstructure and property capability (Table I). With the advent of clean titanium alloy powder, the fatigue properties of P/M titanium have improved markedly in recent years. Figure 6 compares the fatigue properties of P/M Ti-6Al-4V with conventionally produced material. The outstanding capability of current P/M material is evident.



Figure 5. Hardware Produced Using Titanium Alloy Powder and Crucible's Ceramic Mold Process. (a) Compressor Rotor, (b) Arrestor Hook Support Fitting, and (c) Fuselage Braces.

Table I

RT Tensile and Toughness Properties
of HIP Ti-6Al-4V (Ref. 1)^a

Test Orientation	YS (ksi)	TS (ksi)	El (%)	RA (%)	K_{Ic}^b (ksi $\sqrt{\text{in}}$)
LT	132	139	13	38	73
TL	130	138	12	35	74
ST	132	139	12	36	72
AMS Spec. 4928H	120	130	10	15	-

^a1300°F/8 hr Vacuum Anneal.

^bPredicted from precracked Charpy tests.

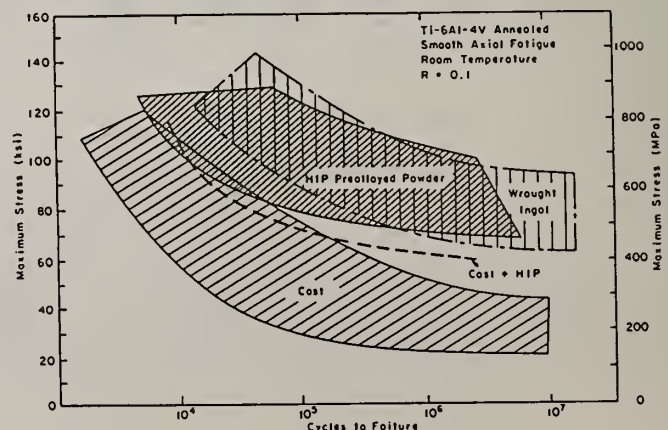


Figure 6. Room Temperature Fatigue Properties of Ti-6Al-4V (Ref. 2, 3, and 4).

Rapid solidified powder has been successfully utilized over the past five years in the production of as-HIP superalloy turbine engine hardware. A prime example of the application of powder to as-HIP superalloys is the General Electric T700 engine which powers the Army Blackhawk helicopter. Six critical rotating turbine components per engine have been produced from as-HIP Rene 95 since the onset of its production.

Rapid solidification technology has addressed the problems of critical material shortages by using less input weight. There has been a 40-lb weight savings of purchased hardware per engine over conventionally produced components. Other advantages are: (1) Shorter lead time since many processing steps are eliminated, (2) no need for heating and forging steps that could introduce detrimental conditions, (3) less finish machining because of the reduced input weight, (4) improved machinability because of greater product uniformity, and (5) lower testing costs because of mechanical property reproducibility; no parts have been rejected for failure to meet mechanical property requirements and testing has proceeded from a 1 in 25 cut-up plan to a 1 in 100 cut-up plan.

Rapidly solidified material is produced at Crucible using the inert gas atomizer depicted in the schematic in Figure 7. This material is then processed and qualified by a series of characterization tests. Once it is found acceptable, it is loaded into stamped shaped metal containers. Figure 8 shows a cut-away of the T700 disk container which was designed to use the minimum amount of input material. After the loading process, the container is outgassed and hot-isostatically-pressed to 100 percent density. This is followed by heat treatment, non-destructive testing and rough machining. A sampling of parts is cut-up for mechanical property evaluation and quality assurance. Figure 9 shows a picture of an as-HIP disk, a rough machined disk and the finish machined components made for the T700 engine.

Over 6000 parts have been produced using this technology and over 800 engines have been delivered to the field for service. There are over 200,000 operating hours accumulated on as-HIP Rene 95 parts. This engine experience is ongoing proof that rapidly solidified powder has been and will be beneficial to superalloys. Probably the most important aspect of this application of the technology is that it has resulted in a \$3000 per engine savings to the ultimate customer.

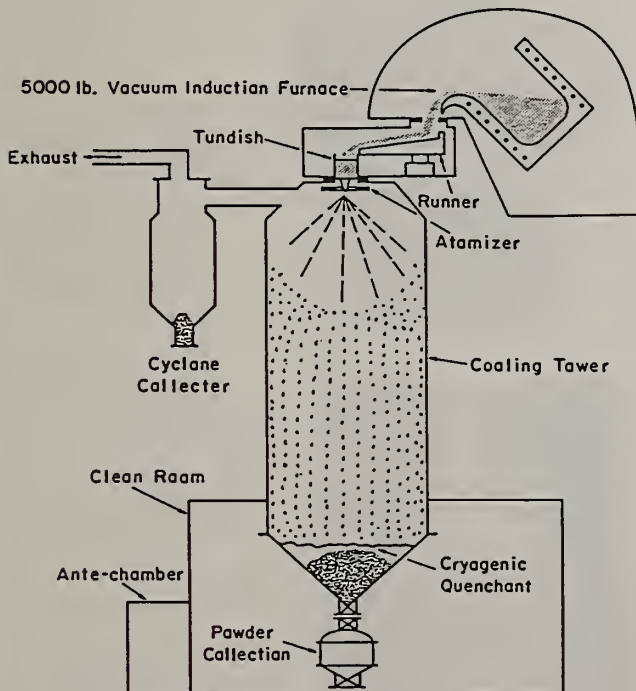


Figure 7. Schematic of Crucible's Production Inert Gas Atomizer.

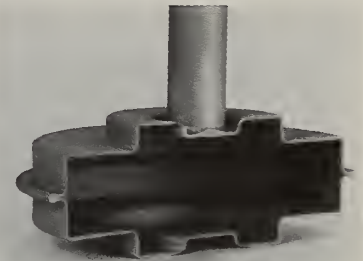
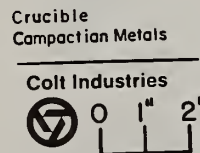


Figure 8. Sectioned Powder Container for a T700 Turbine Disk Sonic Shape.



Figure 9. P/M Rene 95 Turbine Disks. (Top left-as-HIP shape, Top right-machined sonic shape, Bottom left-final machined 1st stage disk, Bottom right-final machined 2nd stage disk.)

Powder is being considered for corrosion-resistant alloy applications. With increased exploration in sour oil and gas wells, the need for corrosion-resistant materials for use as tubing, connectors and valving has increased. The alloy steels commonly used by the oil industry do not hold up in these highly corrosive environments. Conventional production of high alloy tubing stock is expensive and time consuming. Since most sour wells are 15,000 feet and deeper, this makes obtaining the product from these wells a very costly proposition. There is currently no wellhead equipment made from corrosion-resistant alloys. So, in addition to the cost problem, there is still a materials problem.

To address the sour well materials problem, rapid solidification technology is being applied using two approaches: (1) solid tubing and near-net shape wellhead equipment, and (2) clad tubing and clad wellhead equipment. The advantages to the solid approach are tied to material usage. The application of powder for solid tubing results in higher yields from starting material than conventional processes. For wellhead equipment, powder allows the manufacturing of near-net shape parts which have never been attempted by conventional forging processes. A photograph of solid alloy C-276 tubing made by the powder process is shown in Figure 10. A solid alloy 625 valve body made using rapidly solidified powder and the Crucible ceramic mold shape process is pictured in Figure 11.

The clad approach offers the same advantage as the solid plus the economic advantage accompanying the use of less high alloy corrosion material to do the job. Processing with the clad approach may be more costly, but it offers a base material of alloy steel with a high experience level with a coating of corrosion-resistant material on surfaces which contact the hostile environment. Figure 12 shows a picture of an alloy steel valve body clad on the inside with alloy 625 powder. Clad tubing is also a feasible product using powder. Figure 13 shows a cross-section of alloy 625 clad on the outside of a lower alloy material using hot-isostatic-pressing.

Without the use of powder, it would be virtually impossible to clad a shape such as a valve body. In addition, because corrosion-resistant alloys generally develop their strength through cold work (such as in solid tubing), even forging of a valve body would not be effective in producing a component with minimum specified mechanical property levels. RST produced solid and clad valve bodies achieve property levels consistent with those specified for valve bodies made of alloy steel. Some mechanical property levels possible with rapidly solidified materials are shown in Table II.

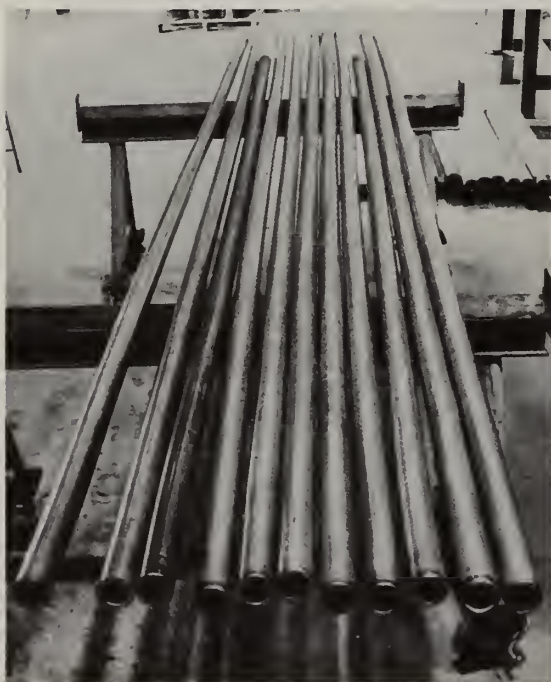


Figure 10. Alloy C-276 Tubing Produced from Hot-Isostatically-Pressed Powder.



Figure 11.
Alloy 625 Valve
Made from Hot-Isostatically-Pressed Powder
(Top-as-HIP Part, Bottom-Machined Part).

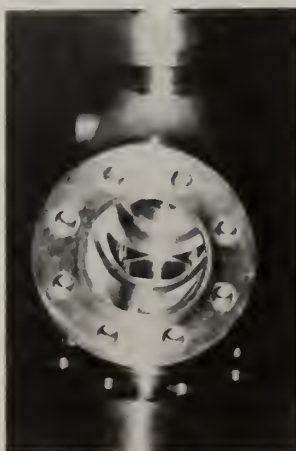




Figure 12. Alloy Steel Valve Body Clad on the Inside with Alloy 625 Powder using Hot-Isostatic-Pressing.



Figure 13. Cross-Section of Alloy 625 Powder Clad on the Outside of a Lower Alloy Material using Hot-Isostatic-Pressing.

Table II

Mechanical Properties of RST
Corrosion-Resistant Alloys

	<u>Requirement</u>		
	API Type 2	API Type 3	Typical RST Alloy 625
<u>Wellhead Equipment</u>			
TS (ksi)	90	100	144
YS (ksi)	60	75	83
El (%)	18	17	38
RA (%)	35	35	38
Hardness (R _C)	35 Max	35 Max	22
<u>Tubing</u>	<u>Requirement</u>		Typical RST Alloy C-276
TS (ksi)	-		172
YS (ksi)	150-170		161
El (%)	-		24
RA (%)	-		69
Hardness (R _C)	-		36

References

- (1) V. C. Petersen and V. K. Chandhok, "Manufacturing Process for the Hot-Isostatic-Pressing of Large Titanium PM Shapes," 1st Interim Report, Contract F33615-77-C-5005, June 1979.
- (2) F. H. Froes et al, "Developments in Titanium Powder Metallurgy," Journal of Metals, Vol. 32, February 1980.
- (3) F. H. Froes et al, "Fatigue Properties of Hot-Isostatically-Pressed Ti-6Al-4V Powders," Proceedings of 1982 National Powder Metallurgy Conference, Montreal, Canada, May 1982.
- (4) F. C. Teifke et al, "Effect of Processing on Fatigue Life of Ti-6Al-4V Castings," Advanced Processing Methods, Proceedings of 1981 TMS-AIME Fall Meeting, Louisville, Ky., 1981.

"The material contained in this paper is intended for general information only and should not be used in relation to any specific application without independent study and determination of its applicability and suitability for the intended application. Anyone making use of this material or relying thereon assumes all risk and liability arising therefrom."

COMMERCIAL RAPID SOLIDIFICATION (CRS) PROCESSING FOR ADVANCED TURBINE DISK APPLICATIONS

R. Beck, Teledyne CAE

Toledo, Ohio 43612

W. Kent, Universal Cyclops

Bridgeville, Pennsylvania 15017

C. S. Kortovich, TRW Inc.

Cleveland, Ohio 44117

ABSTRACT

Rapid solidification rate powder metallurgy processing was applied to the development of enhanced superalloys for jet engine turbine disk applications. Argon atomization employing commercially available facilities was used to produce the rapidly solidified powders. Consolidation involved the preparation of forging billets by the CAP (Consolidation at Atmospheric Pressure) process which were then isothermally forged and heat treated to develop the desired microstructure and mechanical properties in candidate alloy compositions.

The series of superalloy compositions was processed into CRS powder and was consolidated by CAP and isothermal forging techniques. The alloys included AF-115, IIB-11E, 312Hf, AF2-1DA-2, AF2-1DA-5, AF2-1DA-6, Rene' 95 and IIB-7. The CAP material exhibited excellent forgeability in channel die tooling which reduced the cylindrical shaped billets to rectangles featuring a reduction in thickness of approximately 50%. Subsequent to forging, heat treatments were developed to produce an ASTM 5-6 grain size. Mechanical property evaluations including elevated temperature tensile, stress rupture and low cycle fatigue tests were conducted on these materials. The results of these evaluations will be presented. This work was performed under Contract F33657-80-C-0124.

Introduction

Ultra-pure prealloyed superalloy powders solidified at very high rates of cooling have exhibited a strong potential to limit the alloy segregation in cast/wrought alloys to a microscopic scale. Elimination of this segregation has resulted in a stronger material exhibiting a more uniform range of mechanical properties. In order to more fully evaluate this class of materials for advanced turbine disk applications, a materials properties screening study was conducted on powder alloys produced by the commercial rapid solidification (CRS) process. The scope of this effort included the evaluation of CRS powder consolidated at atmospheric pressure (CAP), followed by isothermal forging, to provide base material for screening mechanical property tests. The program mechanical property goals included a 170 ksi 0.2% offset yield strength at 1100°F, 100 hour rupture lives at 1100°F/170 ksi and 1220°F/140 ksi, and 2400 cycles low cycle fatigue life when tested at 1100°F, with a strain range of 0.64% and a strain ratio of 1 and were selected to meet Teledyne CAE requirements for their advanced turbine disk designs.

Experimental Procedures

The nominal chemistries of the alloys chosen for evaluation are listed in Table 1.

Table 1

Nominal Chemistry (Weight Percent) of CRS Alloys⁽¹⁾

Alloy	C	Cr	W	Mo	Co	Al	Ti	Cb	B	Ta	Zr	Hf	V
AF2-1DA-2	.04	12.0	6.0	2.75	10.0	4.6	2.8	-	.015	1.5	.10	-	-
AF2-1DA-5	.04	12.0	6.0	2.75	9.0	4.6	2.8	-	.015	2.2	.10	-	-
AF2-1DA-6	.04	12.0	6.0	2.75	10.0	4.6	2.8	-	.015	1.5	.10	-	-
IIB-11E	.06	8.5	7.1	1.90	9.0	4.5	0.7	-	.013	6.4	.04	0.7	0.5
XN-312-Hf	.08	11.5	3.0	3.30	20.0	2.9	4.2	2.0	.020	2.0	.05	1.3	-
AF-115	.15	10.7	5.9	2.80	15.0	3.8	3.9	1.7	.020	-	.10	2.0	-
IIB-7	.13	9.0	7.5	2.00	9.0	3.5	.8	-	.020	10.0	.10	1.0	0.5
Rene' 95	.06	13.0	3.5	3.50	13.0	3.5	2.5	3.5	.10	-	.05	-	-

(1) Balance Nickel

The first three are modifications of AF2-1DA, a disk alloy developed by Universal Cyclops under Air Force sponsorship. The remaining alloys chosen for study were existing alloys currently in advanced development stages. The IIB-11E alloy was developed by Universal Cyclops under NASA sponsorship, the XN-312-Hf was developed by Climax-Molybdenum and the Rene' 95 and AF-115 were developed by General Electric under Air Force sponsorship.

All of the powder metal stock was produced by Universal Cyclops from high purity vacuum induction melts. The alloys were argon gas atomized using the CRS process. This process was developed to yield a greater percentage of fine powder particles. The atomized powder was screened to a -150 mesh size and blended for uniform distribution. Sieve analyses indicated generally greater than 50% of particles finer than -325 mesh (approximately 40 microns).

Powder consolidation was accomplished at Universal Cyclops using the CAP process. This is a high temperature sintering operation which is conducted on powders sealed under vacuum in glass containers. The powders are specially treated prior to encapsulation to enhance their sinterability. The powders were consolidated into 4 inch long, 1 inch diameter cylinders for subsequent isothermal forging trials.

Isothermal forging was accomplished by TRW in a channel die tooling arrangement which forged the initial cylindrical CAP preforms into rectangles exhibiting approximately 50% reduction in thickness in relation to the diameter of the CAP preforms. The dies were made from Mo-TZM and forging was conducted in a single blow under a protective argon atmosphere at temperatures ranging from 2000-2200°F.

Mechanical property testing was conducted by TRW and Teledyne CAE and consisted of 1100°F tensile tests, stress rupture tests conducted at a number of conditions and 1100°F low cycle fatigue tests.

Results and Discussion

Metallographic analysis of the CRS powders indicated that they were generally spherical in shape, with associated satellite particles and were found to be free of foreign material contamination. An example of typical CRS gas atomized powder as observed by SEM is shown in Figure 1a. The powders were characterized by dendritic and microcrystalline types of structures, with the smaller powder particles (100 microns or smaller) generally exhibiting a finer dendritic structure or a microcrystalline structure.

CAP consolidation resulted in structures exhibiting approximately 2% residual porosity. An example of a typical as-CAP structure is shown in Figure 1b. The grain sizes of the CAP materials varied somewhat, depending upon the temperature required for consolidation. The grain sizes ranged from ASTM 4-8.

The isothermal forging results over the temperature range 2000-2200°F indicated that all of the alloys exhibited excellent forgeability. Complete densification of the CAP preforms was accomplished with no forge cracking. Differences were observed, however, in terms of resultant grain size as well as time required to accomplish the forging. In general, forging at 2200°F resulted in a large (greater than ASTM 2) grain size in the material. This type of grain size would be expected to exhibit poor strength properties at 1100°F. Forging at the lower temperatures resulted in either no recrystallization or a partially recrystallized structure. This situation offered the opportunity to manipulate the structure through subsequent heat treatment operations. In terms of forging time, deformation was accomplished within 5-10 minutes at 2200°F, often taking approximately one hour at 2000°F. Long deformation times would result in poor production rates during actual parts manufacture. Because of the resultant structures and relatively short deformation times, 2100°F was selected

as the forging temperature for the production of specimens for mechanical property testing. An example of the typical as-forged structure for material forged at 2100°F is shown in Figure 1c. In order to develop optimum mechanical properties in the 1100-1220°F temperature range, solution heat treatments were selected which resulted in grain sizes in the range ASTM 5-7. A typical heat treated structure is shown in Figure 1d.

Mechanical property screening tests were conducted on forged material to characterize the effects of the various heat treatments on tensile, stress rupture and low cycle fatigue properties. Analysis of the tensile data indicated that only the AF2-1DA-2 and IIB-iiE alloys did not meet the yield strength goal of 170 ksi at 1100°F. In terms of reduction of area only the 312 Hf alloy exhibited values (3-4%) below 12%. The stress rupture results indicated that all of the alloys screened in this program exhibited good stress rupture life characteristics in the intermediate temperature range. A Larson Miller summary plot of the stress rupture data shown in Figure 2a indicates that all of the materials tested met or exceeded the Teledyne CAE design goals. The low cycle fatigue results were equally promising. The results for alloys IIB-7, AF2-1DA-6 and AF-115 are shown in the plot of Figure 2b compared to the program goal. These three alloys exhibited the highest 1100°F yield strength values. As shown in Figure 2b, the data indicated that AF2-1DA-6 and AF-1115 have very similar fatigue life characteristics. The heat treatments for both of these alloys included the following:

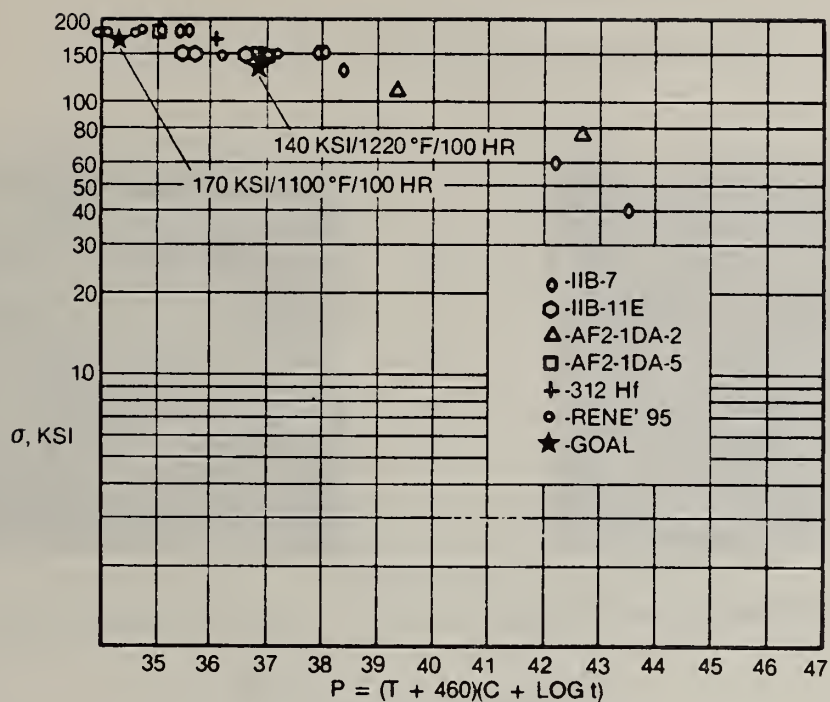
AF2-1DA-6	AF-115
2100°F/2 Hours Salt Quench to 1100°F 1400°F/16 Hours Air Cool	2100°F/2 Hours Rapid Air Cool 1400°F/6 Hours Air Cool

These heat treatments were selected to maintain a fine recrystallized (ASTM 5-7) grain size that was considered desirable for optimum tensile properties. A fine gamma-prime matrix and grain boundary precipitate was also developed throughout the microstructure.

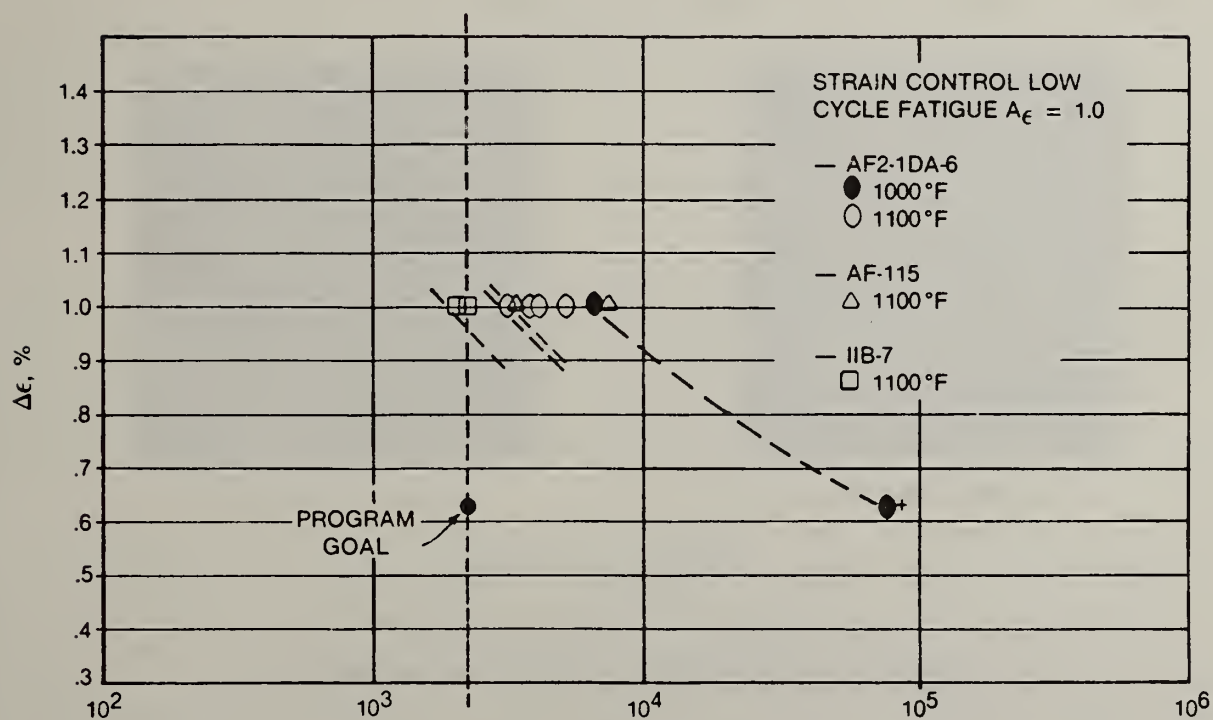
Conclusions

As a result of the material property screening conducted as part of this effort the following conclusions are offered:

1. Processed by the CAP/isothermal forge method, both CRS AF2-1DA-6 and AF-115 will meet the Teledyne CAE design requirements for advanced turbine disks.
2. The CAP/isothermal forging process is effective and has the potential to reduce powder metal forging processing costs from current industry levels.
3. In the alloys screened, a 50% reduction in preform thickness at 2100°F was adequate to eliminate powder porosity and develop the desired mechanical properties.
4. The solution heat treatments applied to these alloys exhibit sufficient flexibility to produce grain sizes that will optimize mechanical properties in the intermediate temperature range.

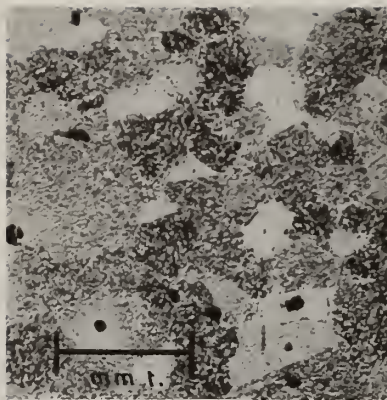


(a) Stress rupture results

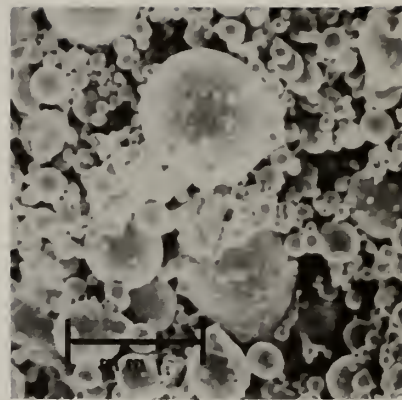


(b) Low cycle fatigue results

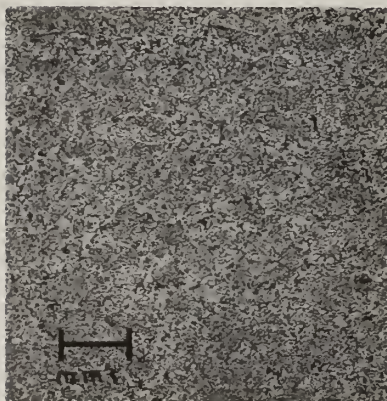
Figure 2. Summary of stress rupture and low cycle fatigue results of CAP/Isothermal forged CRS alloys.



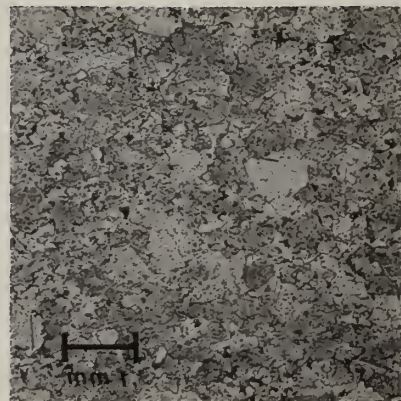
(a) As-atomized powder, 200X



(b) As-CAP powder, 200X



(c) As-forged at 2100°F, 100X



(d) Heat treated, 100X

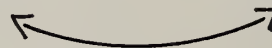


Figure 1. Photomicrographs of CRS P/M alloy AF2-1DA-6.

PANEL/WORKSHOP ON
CRITICAL QUESTIONS IN RAPID SOLIDIFICATION PROCESSING

Three overall topics were discussed in this session as follows:

1. Roadblocks to RSP, organized by M. Cohen and J. Moore

Reporters: M. Greenfield and J. Manning

2. Alternatives to RSP, organized by J. Williams and R. Sprague

Reporters: A. Adair and L. Jacobson

3. New Horizons for RSP, organized by B. Kear and L. Davis

Reporters: D. Polk and B. Rath

Various speakers were selected to address specific questions under each topic and to stimulate discussions on questions having broad implications for the field of rapid solidification. A summary of the short presentations and the resulting discussion is presented here. In the interest of completeness, conciseness, and uniformity of style, the Reporters have taken the liberty occasionally to rephrase statements made by the speakers and discussers.

TOPIC 1. Roadblocks to Rapid Solidification Processing

A. Availability of RSP Materials for R&D - T. Tietz

Results gathered during a recent NMAB study on the availability of rapidly solidified material for research and development purposes were summarized. This NMAB report will soon be available for distribution as NMAB-411. The study was undertaken to determine the current status of organizations supplying RSP materials and what problems might exist. Thus, a survey of existing facilities for production and consolidation of RS particulate is included in the report. In addition, a survey was made of R&D organizations to determine (1) past use and projected requirements for RSP materials, (2) problem areas experienced in obtaining RS particulate and/or consolidation services and (3) sources able and willing to supply RS particulate and/or consolidation services to others.

Problem areas reported by researchers included (1) most facilities produce 100-200 lb powder lots with very few facilities being available for producing small lots or custom orders for other organizations, (2) excessive delay times in obtaining test materials, (3) contamination during processing both from refractory furnace components and from cross contamination, (4) inability to obtain specific alloy compositions, (5) lack of compositional control, (6) lack of process control, (7) cost of particulate, (8) cost of consolidation, (9) difficulty or inability in obtaining larger lots of RS material (50 to 200 lb) and (10) inability to locate suitable consolidation facilities. Atomization processes appear well-developed and sufficient, although melt facilities and melting practices often are sources of problems.

With respect to the roadblock provided by an inadequate supply of rapidly solidified material, interest and approval was expressed by workshop participants in the creation of new rapid solidification facilities at the National Bureau of Standards as a source of small lots for cooperative research activities. Large commercial firms with RSP facilities are likely to see little economic benefit in supplying rapidly solidified material to other investigators. However, there is some industrial capacity for production of RSP materials by small companies. Provision of samples to universities by industrial concerns might be expected if patent and licensing questions could be clarified. Some university sources of rapidly solidified material are available, for example, melt spun alloys, but that facility provides only ribbon and not powder.

In further discussion of the production of RSP steel products, control of composition, particularly carbon and nitrogen, was emphasized as a significant problem. Since powder processing can influence the composition, redesign of starting compositions may be necessary in some instances. It was emphasized that considerable time is required to develop systems to go from powder to high quality consolidated products. Cleanliness during the powder production and consolidation stages continues to be very important.

B. Problems in Consolidation of RSP Particulates - M. DeCrescente

The current methods for the consolidation of RSP particulate were reviewed. The alternatives available to today's metal processor provide the opportunity to select a consolidation process tailored to individual need. There are still some problems preventing wide spread application, however. Concern for contamination during compaction is an issue. The increased awareness of its detrimental effect has not only spurred research toward solutions in that area, but has also created some hesitancy among current and potential users of this technology. Similar comments can be made in the areas of toxicity and safety.

In most cases, existing consolidation equipment and technology appear suitable for RSP powder having a refined microstructure. In fact, some property improvement is evident at even slightly higher, more effective pressing temperatures. Further, some of the as HIP property combinations appear unique enough to warrant greater study; post process heat treatment may not be necessary. The situation for melt spun product is currently not as positive. Additional work will be needed to efficiently process ribbon into final billet or component shape. There does not appear to be a great deal of activity addressing this problem.

Dynamic compaction, a novel low heat input technique, offers promise. In this area, questions concerning size limitations and frictional heating effects must be addressed before wide scale usage is realized.

Other techniques such as containerless processing and fluid die hot pressing are characteristic of the innovation which exists today in industry. Overall, the future is expected to bring low cost, high volume production processes yielding a superior product.

C. Surface Treatments Involving Rapid Solidification - S. Copley

Four main uses of directed energy beam (laser or electron beam) systems were described: (1) melting to produce modified surface microstructures after rapid resolidification, (2) alloying by adding solute elements in the surface melted layer, (3) cladding and (4) dispersing foreign particles in the melted layer, such as hard particles to provide improved wear resistance. Overlapping trails can be used to produce complete surface coverage. When combined with material deposition, these surface melting and resolidification processes also can produce bulk material.

To date, surface melting techniques have been demonstrated to produce microstructure refinement and modified epitaxy. Undercooling in the melt before resolidification can allow extended solubility and the production of amorphous phases in the resulting surface layer. Alloying techniques have been demonstrated to produce homogeneous alloyed layers when there is sufficient convection occurring. The feasibility of cladding and dispersion techniques have been demonstrated.

Roadblocks to further application of these surface treatment techniques include:

- (1) Residual strains that can affect the stability and integrity of the modified layer, as by causing surface cracking.
- (2) Surface relief can be produced such that an originally smooth surface loses its smoothness.
- (3) Methods for synthesis of materials need to be improved and the range of alloy systems that can be treated by the various methods still need to be defined.
- (4) Fundamental understanding of the surface processing needs to be improved, including establishment of kinetic theories, development of metastable phase diagrams and control of convection effects.
- (5) Surface absorption processes need to be understood and controlled.

D. Impediments to the Application of RSP Materials - T. Kearns

This topic began with an overview of current factors which can limit rapid implementation of RSP technology and hence decrease the opportunity for early benefit to industry. Impediments exist in all four areas of the general cycle toward advanced material utilization. Roadblocks exist in new alloy and process development, material characterization, scale up and production, and system application. The problems facing RSP, however, are not particularly unique.

University involvement is generally limited to suitable thesis topics and suffers from small new equipment budgets. Industry on the other hand is almost entirely driven by perceived economic benefit and can not justify long term basic research. The government, through its in-house

laboratories and contract programs, does offer some relief to this problem, but unfortunately must spread its limited resources and manpower among many potential advanced technologies.

One promising solution is the current increased interaction between the industrial and university community to develop the needed technologies. Although problems can exist with proprietary rights and the freedom to publish, solutions can be achieved to the benefit of all.

There has been progress in the past few years in increased availability of advanced RSP material. However, having materials to test and initially characterize is only a first step. Increased utilization of a new material requires an expensive engineering data base. In order to generate one efficiently, user needs and wants (dreams) must be made clear. This is not a simple task when a new technology may offer radically new opportunities. Innovative concepts must be developed in a parallel effort.

Scale up and production are always a major industrial risk. What is the best production process? Today, there are a number of highly touted alternatives which make a decision on large capital equipment expenditures extremely complex, not to mention the current economic state of the industry. Will there be a lasting demand? Or will a new technology (like carbon-carbon composites and fiber reinforced superalloys for high temperature gas turbine applications) supplant RSP? Certainly a heady question.

Final material application, whatever the material, rests with the designer. Industrial confidence in RSP advantages will not be achieved overnight. Generally ten to fifteen years are required to advance a technology from initial feasibility to having components in production. Opportunities for earlier implementation sometimes can occur, however, but only as a "fix" for poor initial design.

In summary, there is some successful production and application of RSP alloys in place today. Furthermore, new experimental alloys certainly appear tantalizing. What is required is more alloy development, greater awareness of the potential advantages of RSP, increased designer demand and industrial commitment. The recognition of RSP as a major government thrust area is certainly beneficial to the eventual application of this new technology.

TOPIC 2. Alternatives to Rapid Solidification Processing

A. Single Crystal Turbine Blades - C. Kortovich

Similarities between current cast single crystal turbine blades and candidate RSP blade alloys were discussed. For the cast single crystal blades (SC), compositional variations across dendrites are minimized due to the absence of grain boundary strengthening elements. However, there is more segregation in SC blades than is observed in RSP alloys; also, there are some low angle boundaries present in the SC blades. Some of the inhomogeneities found in SC blades may be beneficial to fatigue behavior in service.

The experimental RSP blade alloys with directional grain structures having high modulus orientations are superior in stress rupture to cast directionally solidified blades (DS) and cast SC blades having the <100> orientation. Based on equiaxed cast blades, and testing in stress rupture at 1800°F and 30 KSI stress level, the temperature capability increases as follows: DS + 30°F; SC + 40°F, RSP + 110°F. An appropriate reminder was made regarding the experimental status of today's RSP blade alloys (concerns of cost, inspectability, reproducibility, etc.); the same was true for cast SC blades ten years ago and they are now an established production item.

Additional competition for RSP alloy blades comes from oxide dispersion strengthened alloys, directionally solidified eutectic alloys, and from fiber reinforced superalloys.

B. Advanced Composites - C. Blankenship

Organic matrix composites (OMC) are a very strong competitor for RSP aluminum alloys. The most significant disadvantage of OMC is a low strain capability prior to fracture. Today's OMC have a strain limit of 0.004; a capability of 0.008 to 0.01 is needed. By comparing 1980 aircraft construction (about 78% aluminum, 3% OMC) with two different scenarios for the 1990's, one (which offers about a 30 percent weight reduction using OMC) has about equal use of OMC and aluminum (40% of each, with about 10% titanium), the other is more optimistic and favors OMC at 60% with aluminum and titanium at about 20% each.

Both OMC and RSP Aluminum suffer from lack of innovation in manufacturing components. For OMC, we need to use methods of carrying loads around corners, and stop using methods we use to build "metal" airplanes. For RSP Aluminum, we need to have new concepts for higher structural efficiency,

such as the superplastic forming-diffusion bonding methods available for titanium alloy construction.

Regarding automation in manufacturing, rapid progress is being made on OMC; they could easily surpass the efficiency of manufacturing using RSP Aluminum and eventually be cheaper! Thus, the pressure is on for new fabrication concepts and automated manufacturing practices for RSP Aluminum to be competitive with OMC. While organic matrix composites are a real challenge to RSP Aluminum, the jury is still out.

The major concerns for aircraft structures intended for long term service are environmental effects and structural integrity. Current experience for OMC is quite satisfactory, however, newer matrix resins are probably suspect. The clear message is that OMC components are flying and are becoming accepted.

Joining technology state-of-the-art is not equal to fabrication technology for both OMC and RSP Aluminum. Laminated metal structures would offer some structural advantages; however, the data base that would allow designer acceptance does not exist for these bonded structures.

A metal matrix composite (MMC) of short, discontinuous fibers in an aluminum matrix probably would be a competitor for OMC and RSP Aluminum. Some MMC are currently using short fiber silicon carbide in an RSP Aluminum alloy matrix.

C. Magnetic Materials - L. Johnson

Amorphous magnetic materials (AMM) for use in power distribution transformers have considerably lower core losses than anything else available today. The material in these transformers represents about 35 percent of the cost; there is a potential replacement cost for transformers in the 20 to 30 billion dollar range. The likelihood of this replacement taking place depends on both performance and cost. While the performance of the AMM is quite superior, improvements have been made in the grain oriented steels, so the performance of the competition is also improving. The cost outlook depends on whether you are "buying or selling."

The industry is very conservative; they have been making transformers the same way for 80 years. Twenty units of the 20 KVA power level have been made from AMM, at least three of them have been in service on investor owned utility poles for over one year, and they are performing very well. The historical trend is for the cost of AMM to be coming down, and they are expected to impact the market when their cost decreases to a level three times that for M4 steel; the lower the cost the larger the impact. The beginning of the earliest market penetration is expected to be 1985.

The economics for using AMM in smaller transformers, motors, etc. is not favorable. Transformers in the 25 to 50 KVA range are considered "small" and they are the market target. Motors have been built and their performance demonstrated, however, the 30 cents/lb material cost for the conventional material and the simple stamping process for laminated sheet production make it very difficult for the AMM to compete.

The cost of manufacturing transformers using AMM is estimated to be higher than for today's practice. Some investment in capital equipment will probably be required, but the future manufacturing cost is not considered a significant problem. The current down turn in housing construction and general business level makes it difficult to justify capital expenditures at this time.

D. The VADER Process - W. Boesch

The VADER process is a "ceramic-free" melting process with a current capacity of 150 lb ingots (billets) formed in a static casting mode. The process is also capable of a dynamic casting mode where the mold is slowly withdrawn giving a constant height of fall for molten droplets. The mold can also be rotated to form hollows. The process is now a fully programmable melt process using servos and a microprocessor. A 20 lb/min melt rate is in use; this is considerably higher than for other vacuum arc remelting processes (VAR).

Since no water cooled crucible is used, the VADER process requires only about 40% of the energy used for normal VAR processes. Up to 7 inch diameter ingots of IN 100 alloy have been directly ultrasonically inspected. The ingot microstructure is equiaxed and fine grained, typically ASTM 3. There is a very low residual stress present, the ingots are free from macrosegregation, the ingots are isotropic, and they have shown significantly improved hot workability. There are some ingot surface quality problems where it comes into contact with the mold. Ingots of several different alloys have been produced so far, including steels, nickel-base alloys, and aluminum alloys.

The maximum size ingot produced so far by the VADER process is 10 inches in diameter. While the process is "ceramic-less," care will be needed to minimize ceramic content in the electrodes that

are melted, since ceramic inclusions in the electrodes are likely to fall into the ingot.

The VADER process billets can be hot die forged without difficulty. Ingot sections have also been forged in a single blow from a height of 2 inches to 1/8 inch with no cracking. The same melting action, i.e., the formation of droplets and build-up of the cast ingot is available in electroslog remelting (ESR) also.

TOPIC 3. New Horizons for Rapid Solidification Processing

A. Surface Melting

1. What steps can be taken to keep residual stresses under control in surface melting treatments? - R. Schaefer

Both concerns and suggested solutions to the residual stress issue prevalent in surface melted structures were discussed. Surface melting frequently results in substrate warping, plastic deformation, hot tearing and crack initiation in the substrate. The nature of these problems have been demonstrated in 2024 aluminum alloys using an electron beam for surface melting. The extent of the problem is strongly dependent on alloy selection, substrate temperature, details of beam manipulation such as oscillations rastering patterns, and melt-zone shape. For example, it was shown that lowering the traverse rate of the electron beam or oscillating the beam during melting reduced crack density and size. Overlapped melt passes also helped in minimizing crack densities. The importance of shifting the thermal stress to the free surface by control of processing variables was also identified during the discussion.

2. Can we develop an integrated surface treatment processing method for shaped parts?-P. Strutt

The methodology was presented for the rapid processing of materials using a computer controlled electron beam system. The system incorporates features such as computer control, real-time inspection using sensors such as video, infra-red and x-ray detectors. This procedure has been used or can be used for rapid solidification, surface alloying, rapid heat treatment and joining of novel structures. For example, this procedure has been used for 52150 bearing steels to produce an ultra refined grain and martensitic microstructure in less than 0.1 sec, which would take more than an hour using bulk processing methods. The integrated materials processing allows controls over the nature and scale of solidification structure, size and distribution of high temperature carbide phases, scale of martensitic structures and degree of tempering.

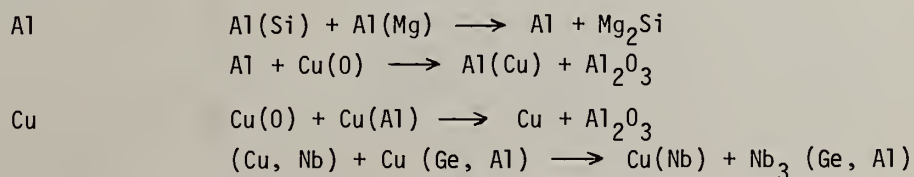
B. Melt Spinning

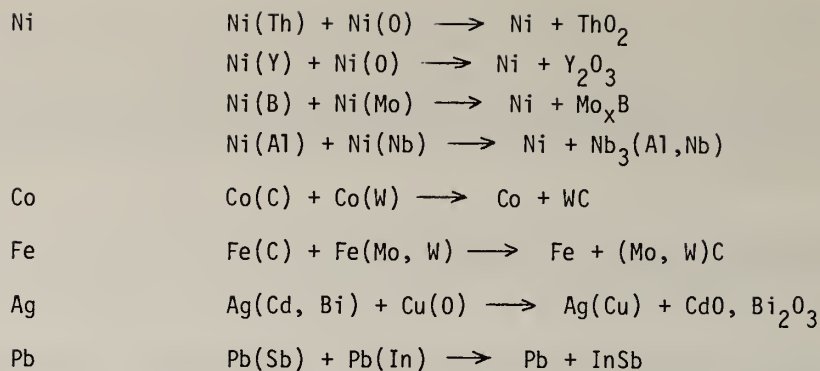
1. Can we devise methods of strip casting in the 0.005 inches to 0.050 inches thickness range? - R. Maringer

Strip casting methods have extreme flexibility and provide a number of innovative ways of fabricating structures. With proper selection of nozzle geometry, and the distance separating the molten stream outlet and the rotating wheel, it is quite possible to build up microcrystalline strips and subsequently hot roll them for full densification if necessary. It may also be possible to directly cast multilayered structures by this method.

2. What are the opportunities for materials synthesis by rapid melt mixing/quenching techniques? - B. Giessen

An approach was presented for fabricating microdispersions of high melting particles in lower melting matrices by mixing melts in suitable proportions. The microalloying approach permits rapid mixing of reaction components as solutes in the molten matrix followed by quenching. To obtain an end product of finely dispersed compound, such as AB in a matrix of C, the method proposes the mixing of two liquids, one consisting of C + A and other C + B such that both are complete solutions. Rapid quenching of the mixture of these two liquids will produce a fine dispersion of AB in a matrix of C. Examples of the liquid pairs and the reaction products in Al, Cu, Ni, Co, Fe, Ag and Pb - base alloys are:





These fabricated products may be used as dispersion strengthened alloys for elevated temperature application (Al-, Cu-, Ni-base alloy systems), wear resistant alloys for tool bits (borides, carbides, etc.), corrosion resistant alloys (Cu-Ni base alloys), electric contact materials (Ag-base alloys), superconductors [Cu + Nb₃ (Ge, Al) systems], magnetic alloys, bearing materials (Cu-Sn and Zn-base alloys) and metal-ceramic composites.

Some concerns expressed for these concepts were (a) need for complete mixing, (b) thickness of melt spun ribbons, (c) different melt temperature requirement for each molten alloy, (d) need to maintain proper ratio of mixture of liquids, and (e) existence of other methods for specific systems for which it may be simpler and easier to control the process parameters.

C. Powder Metallurgy

1. What techniques are available, and what might be tried for consolidation of metastable powders? - H. Fraser

New consolidation methods are needed in order to preserve the refined microstructure of rapidly solidified particulate. These methods should limit thermal excursions while providing a good metallurgical bond between particles. Consolidation methods such as dynamic powder compaction to include shock consolidation and vibratory compaction, and incremental consolidation such as layer glazing, in-situ consolidation of splats or osprey, VADER, and plasma spraying should be considered. Some of these processes are not without problems. These compacts have remanent voids and high dislocation densities which have to be considered in defining the fabrication parameters.

Most of the discussion on this subject dealt with process variables such as the effect of vacuum level on powder compaction, and the usefulness of an electron beam to identify the quality of the compacted product. The direct rolling of powder compacts to consolidated forms was presented as a new commercial method. Sheets and plates of 7091 aluminum alloy and titanium alloys have been fabricated directly from RSP powders.

2. Can we develop processes for optimization of undercooling before nucleation? - M. Flemings

In reference to J. Perepezko's prior oral presentation, it was suggested that RSP methods can be developed to enhance undercooling. Processes such as emulsification in molten salts or glasses can be commercially developed to improve undercooling. Undercooling up to 500°C has been achieved by such processes. Molten metals can be injected either into colder liquids or processes developed in a manner similar to electroslog remelting. Electroslog remelting has the advantage of protecting the melt from environmental contamination.

Selection of proper fluids are important for this process. Water atomization, although used extensively for stainless steel powder fabrication, is not satisfactory because of steam which acts as a barrier to rapid cooling.

- Abbaschian, G. J., 129
 Adair, A. M., 609
 Adam, C. M., 70, 629
 Adler, R. P. I., 448
 Ahrens, T. J., 672
 Aigeltinger, E. H., 186
 Amato, R. A., 547
 Anderson, I. E., 178
 Anderson, R. E., 488
 Andrus, J. S., 590
 Apelian, D., 105
 Ast, D. G., 384
 Ayers, J. D., 360
 Aziz, M. J., 113

 Bass, M., 303
 Beck, D., 303
 Beck, R., 692
 Beckerman, L. P., 579
 Biancaniello, F. S., 390, 476
 Billman, F. R., 532
 Blankenship, C., 699
 Boesch, W. J., 259, 700
 Boettinger, W. J., 45, 390, 476
 Bourdeau, R. G., 640
 Broderick, T. F., 585
 Brosius, K. S., 229

 Cavin, O. B., 264
 Chang, K. M., 337
 Chang, W. H., 500
 Chatterjee, D. K., 240
 Cheeks, T. L., 118
 Chin, H. A., 488, 590
 Clauer, A. H., 291
 Clough, R. B., 403
 Cohen, M., 1, 124, 171
 Cook, M. M., 597
 Cooper, K. P., 90
 Copley, S. M., 303, 698
 Corb, B. W., 678
 Coriell, S. R., 45
 Cote, P.J., 429

 Dabkowski, F., 435
 Das, S. K., 559
 Davis, L. A., 559
 DeCrescente, M., 698
 Dickson, J., 609
 Dimiduk, D. M., 186, 276
 Domalavage, P., 678
 Domingue, J. A., 259
 Doraivelu, S. M., 519

 Ehlers, S. K., 240
 Eiselstein, L. E., 246
 Ekvall, J. C., 615

 Fatemi, M., 603
 Flemings, M. C., 28, 702
 Fraser, H. L., 56, 702
 Froes, F. H., 585

 Gegel, H. L., 519
 George, D. B., 640

 Giamei, A. F., 186
 Giessen, B. C., 435, 439, 701
 Glasgow, T. K., 377
 Glicksman, M. E., 83, 118
 Gourdin, W. H., 565
 Grant, N. J., 209, 215, 678
 Green, H. M., 500
 Griffith, W. M., 597
 Gunasekera, J. S., 519

 Hahn, S., 443
 Hall, E. L., 118, 337, 377
 Hara, Y., 678
 Hare, A. W., 672
 Hildeman, G. J., 532
 Hirth, J. P., 135
 Horowitz, E., 416
 Horton, J. A., 264
 Hsu, S. C., 448
 Huang, S. C., 337, 377
 Hughes, J. R., 365
 Hughes, S. E., 488, 590

 Isserow, S., 323

 Jackson, A. G., 585
 Jackson, M. R., 118, 198, 270, 547
 Jacobson, L. A., 609
 Johnson, A. M., 650
 Johnson, L., 700

 Kang, S., 209
 Kapoor, D., 559
 Kasiraj, P., 672
 Kattamis, T. Z., 476
 Kear, B. H., 483
 Kearns, T., 698
 Kelly, T. F., 124
 Kelm, J. S., 650
 Kent, W., 692
 Khan, A. S., 348
 Kim, Y.-W., 597
 Kissinger, R. D., 259, 510
 Koch, C. C., 264
 Koczak, M. J., 223
 Kortovich, C. S., 692, 699
 Koska, D., 672
 Kuli, J. C., Jr., 532
 Kumar, S., 223
 Kurup, M., 312
 Kushnick, J. H., 662

 Langenbeck, S., 629
 Larson, J. L., 590
 Lawley, A., 223, 229
 LeBeau, S. E., 90
 Lederich, R. J., 281
 Lemkey, F. D., 672
 Levi, C., 458
 Lewis, B. G., 483
 Lewis, R. E., 615
 Liebermann, H. H., 365
 Lipsitt, H. A., 234, 240
 Liu, C. T., 264
 Lu, Y. Z., 286

Mahoney, J. F., 458
 Malas, J. C., 519
 Maringer, R., 701
 Martin, P. L., 252
 Masumura, R. A., 178
 Matson, L. E., 519
 Maxwell, R. E., 365
 McDevitt, D. D., 129
 Mehrabian, R., 1, 96, 397, 403, 416
 Meier, G. H., 348
 Meisel, L. V., 429
 Mendiratta, M. G., 240
 Meschter, P. J., 281
 Miller, J. A., 640
 Miracle, D. B., 234
 Mohan, S., 229
 Moll, J. H., 686
 Morgan, J. T., 519
 Moteff, J., 585

O'Handley, R. C., 678
 Olson, G. B., 171
 O'Neal, J. E., 281, 452, 579

Paik, J. S., 28
 Paliwal, M., 105
 Palmer, I. G., 615
 Panchanathan, V., 323, 443
 Pande, C. S., 360
 Patterson, R. J., II, 70
 Peng, T. C., 452, 579
 Perel, J., 458
 Perepezko, J. H., 28, 90
 Peterson, L. G., 198
 Peteves, S. D., 129
 Petit, J. I., 532
 Pettit, F. S., 348
 Pickens, J. R., 150

Quinn, D. M., 429
 Quist, W. E., 615

Rairden, J. R., 468
 Rath, B. B., 178, 603
 Ray, R., 323
 Rice, S. L., 483
 Richmond, J. J., 90
 Ridder, S. D., 96
 Rigney, D. V., 468, 650
 Ritter, A. M., 270
 Rizzo, F. J., 686
 Rosen, M., 397, 416
 Rowe, R. G., 365
 Ruano, O. A., 246

Sakata, I. F., 615
 Sastri, S., 443
 Sastry, S. M. L., 452, 579
 Sawhney, D. L., 662
 Scarbrough, J. O., 264
 Schaefer, R. J., 390, 397, 701
 Sekerka, R. F., 45
 Shanfield, Z., 458
 Shechtman, D., 96, 397, 476
 Sherby, O. D., 246

Shiohara, Y., 28
 Siemers, P. A., 547
 Simon, J. W., 629
 Smashey, R. W., 198, 650
 Smith, C. H., 215
 Smith, J. J., 397
 Smith, J. S., 468
 Smith, R. W., 105, 468
 Smugeresky, J. E., 565, 572
 Sprague, R. A., 500
 Starke, E. A., Jr., 150
 Strutt, P. R., 312, 464, 483, 701

Taquir, A., 312
 Taylor, S., 458
 Thompson, E. R., 672
 Tien, J. K., 259, 510
 Tietz, T., 697
 Tucker, T. R., 291
 Tuli, M., 464

Vander Sande, J. B., 56, 124
 van Reuth, E. C., 609
 VanStone, R. H., 365
 Vold, C. L., 178
 Voorhees, P. W., 83
 Vreeland, T., Jr., 672

Wadley, H. N. G., 403, 416
 Wadsworth, J., 246
 Wakeman, T. G., 650
 Walker, J. A., 532
 Wang, J. R. Y., 559
 Wayne, S. F., 483
 Whang, S. H., 286, 435, 439
 Williams, K. A., 234
 Williams, J. C., 135, 252
 Woodyatt, L. R., 229

Yurek, G. J., 171, 424

Zielinski, P. G., 384

